frontiers | Research Topics

Recent advances in synthetic organic chemistry at the biomedical interface: honoring Professor Iwao Ojima on the occasion of his 80th birthday

Edited by
Greta Varchi, Guigen Li, Thierry Brigaud and Naohiko Yoshikai

Published in
Frontiers in Chemistry



FRONTIERS EBOOK COPYRIGHT STATEMENT

The copyright in the text of individual articles in this ebook is the property of their respective authors or their respective institutions or funders. The copyright in graphics and images within each article may be subject to copyright of other parties. In both cases this is subject to a license granted to Frontiers.

The compilation of articles constituting this ebook is the property of Frontiers.

Each article within this ebook, and the ebook itself, are published under the most recent version of the Creative Commons CC-BY licence. The version current at the date of publication of this ebook is CC-BY 4.0. If the CC-BY licence is updated, the licence granted by Frontiers is automatically updated to the new version.

When exercising any right under the CC-BY licence, Frontiers must be attributed as the original publisher of the article or ebook, as applicable.

Authors have the responsibility of ensuring that any graphics or other materials which are the property of others may be included in the CC-BY licence, but this should be checked before relying on the CC-BY licence to reproduce those materials. Any copyright notices relating to those materials must be complied with.

Copyright and source acknowledgement notices may not be removed and must be displayed in any copy, derivative work or partial copy which includes the elements in question.

All copyright, and all rights therein, are protected by national and international copyright laws. The above represents a summary only. For further information please read Frontiers' Conditions for Website Use and Copyright Statement, and the applicable CC-BY licence.

ISSN 1664-8714
ISBN 978-2-8325-7083-8
DOI 10.3389/978-2-8325-7083-8

Generative AI statement
Any alternative text (Alt text) provided alongside figures in the articles in this ebook has been generated by Frontiers with the support of artificial intelligence and reasonable efforts have been made to ensure accuracy, including review by the authors wherever possible. If you identify any issues, please contact us.

About Frontiers

Frontiers is more than just an open access publisher of scholarly articles: it is a pioneering approach to the world of academia, radically improving the way scholarly research is managed. The grand vision of Frontiers is a world where all people have an equal opportunity to seek, share and generate knowledge. Frontiers provides immediate and permanent online open access to all its publications, but this alone is not enough to realize our grand goals.

Frontiers journal series

The Frontiers journal series is a multi-tier and interdisciplinary set of open-access, online journals, promising a paradigm shift from the current review, selection and dissemination processes in academic publishing. All Frontiers journals are driven by researchers for researchers; therefore, they constitute a service to the scholarly community. At the same time, the *Frontiers journal series* operates on a revolutionary invention, the tiered publishing system, initially addressing specific communities of scholars, and gradually climbing up to broader public understanding, thus serving the interests of the lay society, too.

Dedication to quality

Each Frontiers article is a landmark of the highest quality, thanks to genuinely collaborative interactions between authors and review editors, who include some of the world's best academicians. Research must be certified by peers before entering a stream of knowledge that may eventually reach the public - and shape society; therefore, Frontiers only applies the most rigorous and unbiased reviews. Frontiers revolutionizes research publishing by freely delivering the most outstanding research, evaluated with no bias from both the academic and social point of view. By applying the most advanced information technologies, Frontiers is catapulting scholarly publishing into a new generation.

What are Frontiers Research Topics?

Frontiers Research Topics are very popular trademarks of the *Frontiers journals series*: they are collections of at least ten articles, all centered on a particular subject. With their unique mix of varied contributions from Original Research to Review Articles, Frontiers Research Topics unify the most influential researchers, the latest key findings and historical advances in a hot research area.

Find out more on how to host your own Frontiers Research Topic or contribute to one as an author by contacting the Frontiers editorial office: frontiersin.org/about/contact

Recent advances in synthetic organic chemistry at the biomedical interface: honoring Professor Iwao Ojima on the occasion of his 80th birthday

Topic editors

Greta Varchi — Consiglio Nazionale delle Ricerche (Bologna), Italy
Guigen Li — Texas Tech University, United States
Thierry Brigaud — CY Cergy Paris Université, France
Naohiko Yoshikai — Tohoku University, Japan

Citation

Varchi, G., Li, G., Brigaud, T., Yoshikai, N., eds. (2025). *Recent advances in synthetic organic chemistry at the biomedical interface: honoring Professor Iwao Ojima on the occasion of his 80th birthday*. Lausanne: Frontiers Media SA.
doi: 10.3389/978-2-8325-7083-8

Greta Varchi was previously the co-founder of Theramol Srls and Kerline Srl. All other Topic Editors declare no competing interests with regards to the Research Topic subject.

Table of contents

06 Editorial: Recent advances in synthetic organic chemistry at the biomedical interface: honoring Professor Iwao Ojima on the occasion of his 80th birthday
Thierry Brigaud and Greta Varchi

09 Design and synthesis of phenylthiophosphoryl dichloride derivatives and evaluation of their antitumour and anti-inflammatory activities
Chunyun Xu, Na Yang, Haichun Yu and Xiaojing Wang

22 Discovery of triazole derivatives for biofilm disruption, anti-inflammation and metal ion chelation
Shuang Hong, Hongzhi Lu, Dawei Tian, Yue Chang, Qi Lu and Feng Gao

34 Design, synthesis, *in silico* studies and antiproliferative evaluation of some novel hybrids of pyrimidine-morpholine
Elaheh Ataollahi, Leila Emami, Al-Anood Mohammad Al-Dies, Fateme Zare, Alireza Poustforoosh, Mina Emami, Fateme Saadat, Fateme Motamen, Zahra Rezaei and Soghra Khabnadideh

51 Recent achievements in synthesis of anthracene scaffolds catalyzed transition metals
Fadhil Faez Sead, Vicky Jain, R. Roopashree, Aditya Kashyap, Suman Saini, Girish Chandra Sharma, Pushpa Negi Bhakuni, Mosstafa Kazemi and Ramin Javahershenas

77 Synthesis, bioactivity, and molecular docking studies: novel arylpiperazine derivatives as potential new-resistant AR antagonists
Hua Jiang, Haowei Chen, Ya Wang, Huaxin Xu and Hong Chen

89 Application of Hosomi-Sakurai allylation reaction in total synthesis of biologically active natural products
Justice Akwensi, Robert T. Kumah, Dorcas Osei-Safo and Richard K. Amewu

119 Discovery of a novel 4-pyridyl SLC-0111 analog targeting tumor-associated carbonic anhydrase isoform IX through tail-based design approach with potent anticancer activity
Hamada Hashem, Shadwa Abdelfattah, Hesham M. Hassan, Ahmed Al-Emam, Mohammed Alqarni, Ghallab Alotaibi, Ibrahim Taha Radwan, Kirandeep Kaur, Devendra Pratap Rao, Stefan Bräse and Abdullah Alkhammash

137 Antioxidant activity and selective cytotoxicity in HCT-116 and WI-38 cell lines of LC-MS/MS profiled extract from *Capparis spinosa L*
Amjad Ibrahim Oraibi, Ashour H. Dawood, Ghada Trabelsi, Ousman B. Mahamat, Leila Chekir-Ghedira and Soumaya Kilani-Jaziri

152 Modification of biopharmaceutical parameters of flavonoids: a review
Amir Taldaev, Artem A. Svotin, Semyon I. Obukhov, Roman P. Terekhov and Irina A. Selivanova

168 Design, synthesis, and biological investigation of new thiazole-based derivatives as multi-targeted inhibitors endowed with antiproliferative, antioxidant, and antibacterial properties
Hesham A. M. Gomaa, Asmaa M. Atta, Mohamed E. Shaker, Sami I. Alzarea, Tariq G. Alsahli, Eid Alatwi, Arafa Musa, Fatma A. M. Mohamed, Hayat Ali Alzahrani, Aliaa M. Mohassab, Alshaimaa Abdelmoez, Stefan Bräse and Bahaa G. M. Youssif

183 Synthesis and characterization of thymol-derived phenoxy acetamide derivatives using DFT, molecular docking, and parasitological investigations
Ahmed R. Rabee, Saied M. Soliman, Hamida Abdel-Hamid, Esraa A. Moneer, Sara H. Akl, Yahya H. Shahin, Aliaa A. Masoud, Doaa Ahmad Ghareeb, Mariusz Jaremko, Abdul-Hamid Emwas, Mazen Sherif and Mohamed Hagar

198 Neuraminidase as a novel therapeutic management strategy for Alzheimer's disease: evidenced through molecular docking, molecular dynamic simulation and gene expression analysis
Sami I. Alzarea, Omar Awad Alsaidan, Hassan H. Alhassan, Abdulaziz Ibrahim Alzarea, Tariq G. Alsahli, Metab Alharbi, Muhammad Afzal and Mohammad Jaffar Sadiq Mantargi

217 A novel thiazole-sulfonamide hybrid molecule as a promising dual tubulin/carbonic anhydrase IX inhibitor with anticancer activity
Hussam Elddin Nabeih Khasawneh, Elryah I. Ali, Ranya Mohammed Elmagzoub, Raed Fanoukh Aboqader Al-Aouadi, Wesam Taher Almagharbeh, Ghallab Alotaibi, Stefan Bräse and Abdullah Alkhammash

238 Phomaderide, a unique (6/5/4/5/6) spiro-cyclic dimer from the desert plant endophytic fungus *Phoma betae* A. B. Frank (Didymellaceae)
Hao-Di Sun, Yan-Duo Wang, Hui-Qi Fang, Jian Yang, Yu-Tong Hua, Gang Ding and Lan-Ping Guo

247 Magnetic nanocatalyst for microwave-assisted synthesis of Benzo[4,5]imidazo[1,2-*a*]pyrimidines via A3 coupling
Yuqiang Pan

265 Evaluation of newly synthesized schiff base Pd(II) complexes for prostate cancer treatment through *in vitro* cytotoxicity and molecular mechanistic studies
Damnjan Pantic, Nikola Mirkovic, Tatjana Vulovic, Danijela Jovanovic, Stefan Jakovljevic, Petar Canovic, Milan Zaric, Radica Zivkovic Zaric, Marina Kostic, Jovana Dragojevic, Vera Divac, Ziko Milanovic, Kristina Milisavljevic, Marina Mitrovic and Ivanka Zelen

288 Computational advances in the design and discovery of artemis inhibitors for radiosensitization in cancer therapy
Maryam Bashir, Usman Abdullah, Sadia Nazir, Farhan Siddique and Nasir Jalal

314 Design, synthesis, and biological assessment of a novel series of coumarin-tethered thiazole derivatives as potential antibacterial agents
Manal S. Ebaid, Hanaa Farag, Mohamed Abdelraof, Abdulrahman M. Saleh, Mohamed G. Thabit, Jarosław Dziadek, Ahmed A. Youssef and Ahmed Sabt

331 Design, synthesis, antiproliferative assessments, and computational studies of new quinolin-2(1*H*)-ones as dual EGFR/HER-2 inhibitors
Lamya H. Al-Wahaibi, Hesham A. Abou-Zied, Martin Nieger, Stefan Bräse, Bahaa G. M. Youssif and Hendawy Tawfik

354 A streamlined synthetic approach to the truncated linear trisaccharide fragment of QS-21
Jhe-Sian Lin, Zheng-Hao Tzeng, Jasper S. Dumalaog and Shang-Cheng Hung

frontiers | Frontiers in Chemistry

TYPE Editorial
PUBLISHED 16 October 2025
DOI 10.3389/fchem.2025.1721249

Check for updates

OPEN ACCESS

EDITED BY
Steve Suib,
University of Connecticut, United States

*CORRESPONDENCE
Greta Varchi,
greta.varchi@cnr.it

RECEIVED 09 October 2025
ACCEPTED 10 October 2025
PUBLISHED 16 October 2025

CITATION
Brigaud T and Varchi G (2025) Editorial: Recent advances in synthetic organic chemistry at the biomedical interface: honoring Professor Iwao Ojima on the occasion of his 80th birthday. *Front. Chem.* 13:1721249.
doi: 10.3389/fchem.2025.1721249

COPYRIGHT
© 2025 Brigaud and Varchi. This is an open-access article distributed under the terms of the Creative Commons Attribution License (CC BY). The use, distribution or reproduction in other forums is permitted, provided the original author(s) and the copyright owner(s) are credited and that the original publication in this journal is cited, in accordance with accepted academic practice. No use, distribution or reproduction is permitted which does not comply with these terms.

Editorial: Recent advances in synthetic organic chemistry at the biomedical interface: honoring Professor Iwao Ojima on the occasion of his 80th birthday

Thierry Brigaud[1,2] and Greta Varchi[3]*

[1]CY Cergy Paris Université, Centre National de la Recherche Scientifique (CNRS), BioCIS UMR 8076, Cergy-Pontoise, France, [2]Université Paris-Saclay, Centre National de la Recherche Scientifique (CNRS), BioCIS UMR 8076, Orsay, France, [3]Institute for the Organic Synthesis and Photoreactivity, Italian National Research Council, Bologna, Italy

KEYWORDS

catalysis, green chemistry, anticancer drugs, antibacterial molecules, natural products, computational chemistry

Editorial on the Research Topic
Recent advances in synthetic organic chemistry at the biomedical interface: honoring Professor Iwao Ojima on the occasion of his 80th birthday

This Research Topic brings together 20 contributions at the chemistry–biology–medicine interface honoring Professor Iwao Ojima's lifelong impact across organometallic catalysis, asymmetric synthesis, medicinal and natural products chemistry. The collection showcases how contemporary synthetic design, green chemistry, computation, and biology co-evolve to deliver selective probes, leads, and materials under milder and more sustainable conditions, while clarifying mechanisms relevant to cancer, infection, neurodegeneration, and immunology. In what follows, we outline the Topic's aims and contextualize the published articles in thematic frames, emphasizing convergences, and conclude with prospects that naturally flow from the body of work presented here.

A prominent trend across the Topic is the integration of greener synthesis with process intensification. For example, Pan and coworkers report a $NiFe_2O_4$@MCM-41@IL/Pt nanocatalyst that promotes A^3 couplings to benzo [4,5]imidazo [1,2-a]pyrimidines under microwave irradiation in water. The system allows for simple magnetic separation and efficient reuse of the catalyst. This approach exemplifies how sustainability and reaction acceleration can work hand in hand to deliver pharmaceutically relevant heterocycles with reduced environmental impact (Pan et al.).

Methodological perspective also matters. A review on transition-metal strategies for the synthesis of anthracene scaffolds highlights how Pd/Ni cross-couplings, C–H activation, and ligands selection have expanded access to functional materials and therapeutic motifs, with a clear shift toward greener protocols (Sead et al.). In parallel, the Hosomi–Sakurai allylation's enduring utility in total synthesis is recast through modern variants that deliver high yields, stereocontrol, and broad electrophile scope under mild conditions (Akwensi

et al.). These elements underscore a recurring theme in the Research Topic: revisiting classic reactivity through contemporary catalysts and conditions is one of our fastest paths to better selectivity, lower waste, and more complex architectures.

Oncology runs like a spine through the Topic with height related contributions and showcases rational polypharmacology. Ether-type arylpiperazines were tailored into potent androgen receptor (AR) antagonists with SAR insights on cycloalkyl and ortho-methyl substitutions, supported by docking in the AR ligand-binding pocket (Jiang et al.). Hypoxia biology is addressed from two angles: a tail-engineered 4-pyridyl analogue of SLC-0111 selectively inhibits CA IX, induces G0/G1 arrest and apoptosis, and shows drug-like ADMET profile (Hashem et al.); a thiazole–chalcone/sulfonamide hybrid integrates tubulin inhibition with CA IX blockade, triggering intrinsic apoptosis with favorable selectivity (Khasawneh et al.). A Schiff-base Pd(II) complex outperforms cisplatin against DU-145 and PC-3 prostate cancer cell lines while being safer on fibroblasts, with docking suggesting dual engagement of the AR and apoptotic regulators (Pantic et al.). A quinolin-2(1H)-one series supplies dual EGFR/HER-2 inhibitors; lead 5a exceeds erlotinib, with kinase assays, apoptosis markers, and long-timescale MD supporting its mechanism of action (Al-Wahaibi et al., 2025). These results collectively argue that multi-target strategies, when anchored in mechanism, can counter redundancy and resistance without compromising selectivity. A novel series of thiazole-based derivatives was synthesized and tested for antiproliferative activity as dual EGFR/VEGFR-2 inhibitors. These compounds also presented antioxidant and antibacterial activities (Gomaa et al.). Phenylthiophosphoryl dichloride derivatives have been designed and evaluated for their antitumour and anti-inflammatory activities. The study included the evaluations of the H_2S releasing capability of these compounds (Xu et al.). Novel pyrimidine-morpholine hybrids were designed and synthesized based on molecular hybridization approach. It was demonstrated that all derivatives had cytotoxic potential with IC_{50} in range of 5.12–117.04 μM. The biological activity of the compounds was confirmed by docking studies (Ataollahi et al.).

Anti-infectives and antipathogen approaches in the Research Topic emphasize antibiofilm action and complementary mechanisms. Efficiently built triazolyl heterocycles culminate in E10, which combines bactericidal activity with membrane disruption, strong antibiofilm performance, and notable anti-inflammatory effects. The same scaffold displays heavy-metal chelation capability, pointing to environmental remediation benefits and a resistance-resilient mode of action (Hong et al.). A second antibacterial approach introduces coumarin-tethered thiazoles that selectively hit problematic species and DNA gyrase, disrupt biofilms with low resistance risk, and show stable binding in docking and molecular dynamic studies (Ebaid et al.). In parasitology, thymol-anchored phenoxy-acetamides reduce oocyst burden *in vivo* and show encouraging ADME profile and docking to CpCDPK1, making 7 b a promising lead for further development (Rabee et al.).

Natural products inspired chemistry continue to expand our scaffold repertoire. From the desert endophyte *Phoma betae* comes phomaderide, a bis-spiro dimer with a rare 6/5/4/5/6 topology formed by stereoselective [2 + 2] photocycloaddition; its modest cytotoxicity and pronounced architectural novelty together make a strong case for analogue design and biosynthetic exploration. Building blocks–based molecular networking (BBMN) approach results as a modern path to targeted isolation from complex mixtures (Sun et al.). The Research Topic also probes phytochemical space functionally: LC-MS/MS-profiled *Capparis spinosa* extracts map specific phenolics to robust antioxidant performance and selective cytotoxicity in HCT-116 colon cancer cell line, and the authors show why orthogonal assays are essential to interpret antioxidant and anticancer potential rigorously (Oraibi et al.).

Computational approaches are not ancillary, representing a central theme of the Topic Research Topic, and a key tool for molecular design, prioritization of candidates, and mechanistic elucidation. Radiosensitization via Artemis inhibition is advanced through a pipeline that integrates cellular readouts, docking, ADMET, DFT, and 100-ns MD/MM-GBSA; compound 42 emerges with stable trajectories and favorable free energy, a template for converging *in silico* and *in vitro* evidence before medicinal chemistry expansion (Bashir et al.). In neurodegeneration, a repurposing-led analysis positions human neuraminidase as a tractable target for oseltamivir; docking, 50-ns MD, and enrichment of synaptic and kinase-related genes support the hypothesis while appropriately calling for experimental validation (Alzarea et al.). Across medicinal chemistry approaches elsewhere in the Topic, docking, MD, and DFT support SAR and target selectivity, evidence that computational layers are part of the prospective design loop rather than *post hoc* rationalization.

Translational determinants other than potency are also foregrounded as central considerations. A systematic review on flavonoids consolidates fragmented knowledge into comparative guidance: inclusion complexes and nanostructures boost AUC by ~4.2× and ~3.7× on average, while nanostructures and micelles can increase Cmax about 5.4×; the authors also highlight heterogeneity in solubility assays and urge standardization, a message that extends far beyond flavonoids (Taldaev et al.). In vaccine science, a streamlined route to the truncated linear trisaccharide of QS-21 removes a notorious synthetic bottleneck and opens the door to homogeneous adjuvant variants and clean SAR around a clinically important saponin (Lin et al.). Together with the green catalysis case studies above, these contributions remind us that exposure, supply, and manufacturability are decisive for translation.

Taken together, the 20 contributions span design-first medicinal chemistry, enabling synthesis, green catalysis, natural-product discovery, and computation-driven mechanism. They speak to a community increasingly comfortable blending reactivity innovation with systems-level biological thinking, all while embracing sustainability and scalability. As host editors, we are grateful to the authors and reviewers for assembling a Research Topic that both celebrates Professor Ojima's legacy and points decisively toward the future. The next steps are clear: integrate data-driven design even earlier; hard-wire greener, recyclable workflows into standard practice; pursue multi-target and multi-modal strategies where biology demands it; and keep mining biodiversity and classical reactivity alike for scaffolds that medicine has not yet explored.

Author contributions

TB: Writing – review and editing, Writing – original draft. GV: Writing – original draft, Writing – review and editing.

Funding

The author(s) declare that no financial support was received for the research and/or publication of this article.

Conflict of interest

The authors declare that the research was conducted in the absence of any commercial or financial relationships that could be construed as a potential conflict of interest.

The author(s) declared that they were an editorial board member of Frontiers, at the time of submission. This had no impact on the peer review process and the final decision.

Generative AI statement

The author(s) declare that no Generative AI was used in the creation of this manuscript.

Any alternative text (alt text) provided alongside figures in this article has been generated by Frontiers with the support of artificial intelligence and reasonable efforts have been made to ensure accuracy, including review by the authors wherever possible. If you identify any issues, please contact us.

Publisher's note

All claims expressed in this article are solely those of the authors and do not necessarily represent those of their affiliated organizations, or those of the publisher, the editors and the reviewers. Any product that may be evaluated in this article, or claim that may be made by its manufacturer, is not guaranteed or endorsed by the publisher.

frontiers | Frontiers in Chemistry

TYPE Original Research
PUBLISHED 21 January 2025
DOI 10.3389/fchem.2024.1529211

Check for updates

OPEN ACCESS

EDITED BY
Greta Varchi,
Consiglio Nazionale delle Ricerche (Bologna), Italy

REVIEWED BY
Pawan Dhote,
University of North Carolina at Chapel Hill, United States
Anis Ur Rahman,
Texas Tech University, United States

*CORRESPONDENCE
Chunyun Xu,
chunyunxu01@163.com

RECEIVED 16 November 2024
ACCEPTED 24 December 2024
PUBLISHED 21 January 2025

CITATION
Xu C, Yang N, Yu H and Wang X (2025) Design and synthesis of phenylthiophosphoryl dichloride derivatives and evaluation of their antitumour and anti-inflammatory activities. *Front. Chem.* 12:1529211. doi: 10.3389/fchem.2024.1529211

COPYRIGHT
© 2025 Xu, Yang, Yu and Wang. This is an open-access article distributed under the terms of the Creative Commons Attribution License (CC BY). The use, distribution or reproduction in other forums is permitted, provided the original author(s) and the copyright owner(s) are credited and that the original publication in this journal is cited, in accordance with accepted academic practice. No use, distribution or reproduction is permitted which does not comply with these terms.

Design and synthesis of phenylthiophosphoryl dichloride derivatives and evaluation of their antitumour and anti-inflammatory activities

Chunyun Xu*, Na Yang, Haichun Yu and Xiaojing Wang

Department of Dermatology, Maternity and Child Health Hospital of Qinhuangdao, Qinhuangdao, China

Tumours and inflammation are serious risks to human health and are importantly regulated by the gas signalling molecule hydrogen sulphide. In this work, we report the rational design and synthesis of H_2S donor molecules based on phenylthiophosphoryl dichloride nuclei and assess their efficacy against tumours and inflammation. We predicted its potential anticancer targets based on network pharmacology and then verified the inhibitory effect of the active compound **S11** on the pathway PI3K/AKT by enzyme inhibition and molecular docking assay. In addition, compound S11 exhibited a potent anti-inflammatory effect on macrophages, effectively reducing the levels of inflammatory mediators TNF-α, IL-10 and HO-1. Compound **S11** can be used as a new chemical entity for the discovery of new anti-cancer drugs or anti-inflammatory drugs.

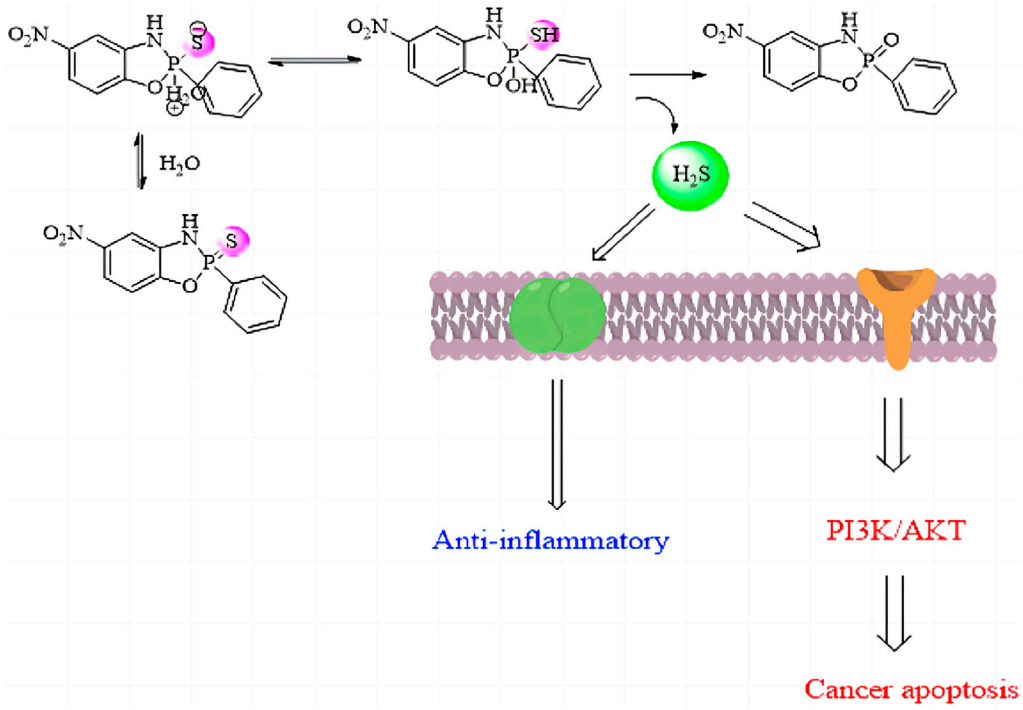
KEYWORDS

hydrogen sulfide, network pharmacology, anti-tumor, anti-inflammatory, phenylthiophosphoryl dichloride

1 Introduction

Hydrogen sulfide (H_2S) is recognized as one of the three major gas signal transmitters along with nitric oxide (NO) and carbon monoxide (CO). In the past decade, H_2S has been shown to have various biological activities, including positive regulatory effects in antioxidant mechanisms, promotion of angiogenesis, anti-inflammatory responses, and ion channel modulation (Hao et al., 2021; Li et al., 2021; Dilek et al., 2020). Furthermore, the cardioprotective effect of H_2S is associated with the inhibition of myocardial cell apoptosis following myocardial injury. The antioxidant effect of H_2S is also reflected in preserving mitochondrial function by inhibiting mitochondrial respiration (Sanchez-Aranguren et al., 2020). Moreover, H_2S plays a significant role in the hypertension (Goor et al., 2020), atherosclerosis (Munteanu, 2023), myocardial injury (Kolluru et al., 2023) and cancer apoptosis (Gao et al., 2024) as illustrated in Figure 1.

Cancer can proliferate indefinitely by maintaining reproductive signalling or overexpressing growth factors to regenerate itself. It may also be initiated by aberrant activation of downstream signalling pathways, particularly the phosphatidylinositol 3-kinase (PI3K)/mammalian target of rapamycin (mTOR) pathway, or by aberrant inactivation of suppressor genes (Siegel et al., 2018; Moses et al., 2018). The critical role of the PI3K/AKT/mTOR (PAM) pathway in cell survival, proliferation, growth, and apoptosis influences make it a promising drug target in the war against cancer (Sanchez



GRAPHICAL ABSTRACT

et al., 2019; Khan et al., 2019). Because H_2S gas is an important gas signalling transmitter, we can design a series of H_2S donors that can target and kill cancer cells by modulating the PI3K/AKT/mTOR pathway. Traditional drug discovery models can only verify the relationship between compounds and targets through a single experiment. In contrast, network pharmacology provides a "compound-protein/gene-disease" network approach, which operates on the principle of "network target, multi-component therapy" (Zhang et al., 2019). This makes it possible to analyse how small molecule drugs modulate disease at high throughput. Cyberpharmacology maps multi-drug ecological networks onto human and animal disease gene networks, providing a basis for identifying key disease-related drug targets (Nogales et al., 2022). In this study, a protein-protein interaction (PPI) network of compounds **S11** associated with cancer was constructed using publicly available databases. Subsequently, potential targets of **S11** for cancer treatment were identified. These targets were then analysed by Gene Ontology (GO) and Kyoto Encyclopedia of Genes and Genomes (KEGG) enrichment. Finally, it was validated using molecular docking methods with enzyme inhibition experiments. Similarly there is interest in the use of H_2S donors for the treatment of inflammatory diseases. Therefore, it is of great interest to know as much as possible about H_2S donors in vitro inflammatory systems. The anti-inflammatory effects of this series of hydrogen sulphide donors on macrophages *in vitro* were further tested in this context.

In a word, developing more effective organic H_2S donors is of great significance for cancer and treating inflammation. This article designs a series of novel H_2S donor molecules based on a sulfur-phosphorus core and the anti-tumor and anti-inflammatory mechanism is preliminarily explored, laying the foundation for the future design of H_2S donor-based anti-inflammatory and anticancer drugs.

2 Results and discussion

2.1 Chemical synthesis

The main donor **S1** of H_2S was efficiently and concisely synthesized using benzene as the starting material. Compound **S2**-**S16** were synthesized by reacting dichlorophenylthiophosphoryl with different amino alcohols, diols, or diamines in the presence of triethylamine (Scheme 1). In the ^{1}H NMR spectra of compounds **S1**-**S16**, the chemical shifts of hydrogen atoms in benzene ring appeared in the range of 8.88–7.28 ppm. For most compounds, the signals of protons on OCH_2 appeared in the range of 3.40–4.49 ppm. For compounds containing NH group, the chemical shifts of hydrogen in NH are in the range of 3.05–3.54 ppm. Our NMR data for compounds **S2**-**S4** in this paper are consistent with the NMR data reported in Zhang's article (Zhang et al., 2019).

2.2 H_2S release ability of the compound and its influencing factors

The H_2S-release capability of the donors was measured using the methylene blue (MB^+) method (Sun et al., 2022). This method is based on the reaction of zinc acetate with H_2S to form zinc sulfide, which then reacts with *N, N*-dimethyl-1,4-phenylenediamine sulfate to generate methylene blue in the presence of ferric ions under acid medium condition. The H_2S is quantified by measuring the

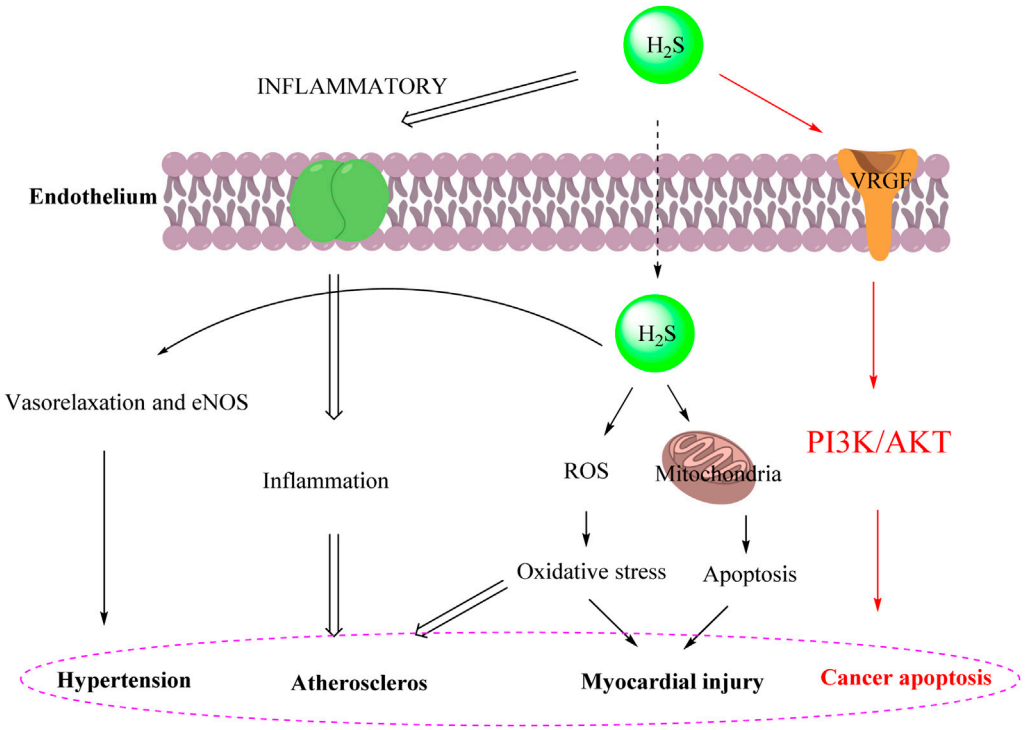


FIGURE 1
Schematic diagram of H_2S partial immunomodulatory mechanism.

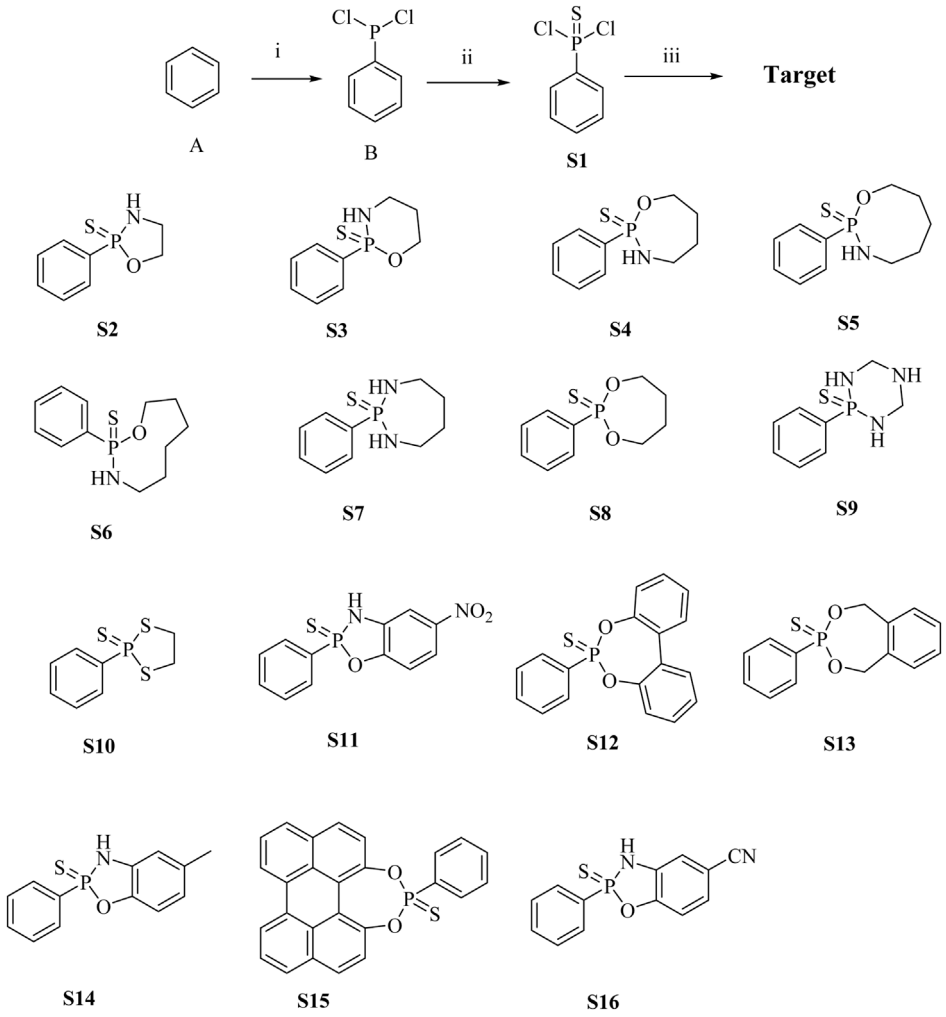
absorbance of the solution at 670 nm. Recently, literature has reported that TECP (a water-soluble phosphine reducing agent) or cysteine can promote the release of H_2S. Therefore, in the presence of TECP or cysteine, the MB^+ water titration method was used to evaluate the H_2S release ability (Nelmi et al., 2013; Hasegawa and Viles, 2014). The level of pH varies in various tissues and organs of the body; for example, the pH of the small intestine is about 8.0, whereas the pH of gastric juice is about 1.8. Therefore, we tested the release of H_2S under different temperature and pH conditions. The results, as shown in Figure 2 and Supplementary Figure 1, showed that all compounds released H_2S at room temperature. The release of H_2S increased when the temperature was 37°C, indicating that temperature affects the amount of gas released. Different pH values have relatively little effect on such H_2S donors. The release amount of compound **S11** is the highest, indicating that the size of the cyclic structure and functional groups such as esters and amides have little effect on the release of H_2S. However, the addition of a benzene ring can increase its release amount, which may be due to the electron transfer of the benzene ring increasing the release amount of H_2S. The mechanism of H_2S release was proposed, as shown in Figure 3.

2.3 The toxicity of the compounds

Compounds **S1** - **S16** were assessed for toxicities against LO2 cell lines (normal liver cell) and HepG2 cell lines (liver tumor cell) using MTT assay. Stock solutions of the tested compounds in DMSO (8,000 mM) were prepared freshly immediately prior to testing. Initially, cells were seeded in a 96-well plate at approximately 10^5 cells/well and allowed to adhere overnight. Cell survival relative to control was assessed after 24 h (Sanchez et al., 2019). The results are shown in Table 1. In summary, the toxicities of the series compounds are low to both normal cells LO2, WI38 and tumor cells HepG2, indicating that these compounds do not cause severe harm to the liver severely in the range of tested dose.

2.4 The antitumor activity of the compounds

The anti-proliferative activity of H_2S on tumor cells has been proven (Zhao et al., 2010; Faris et al., 2023; Liu et al., 2023). This experiment demonstrated that the P = S functional group is an effective functional group for releasing H_2S and has good anti-tumour activity. The results, as shown in Table 2 and Figure 2, showed that **S11** had high H_2S release and good antiproliferative activity against MCF7. Based on the highest release of H_2S with lower toxicity, we chose compound **S11** for subsequent studies. We found that the amount of hydrogen sulfide released was positively correlated with the anticancer activity, and the highest amount of hydrogen sulfide was released from **S11**, **S14** and **S16**, which showed the best activity against MCF7 cells. The activity of aminophenol derivatives was superior to that of 2,2′-dihydroxybiphenyl derivatives. The coupling of aminophenol derivatives to **S1** with electron-withdrawing groups contributed to the activity, and nitro was preferred to cyano to methyl.



Scheme 1
Synthesis of H_2S donor **S1 - S16**. Conditions and reagents: (i) $AlCl_3$, PCl_3, yield 78%; (ii) S, Benzene, yield 45%; (iii) Triethylamine, different amino alcohols, diols or diamines, yield 30%–45%.

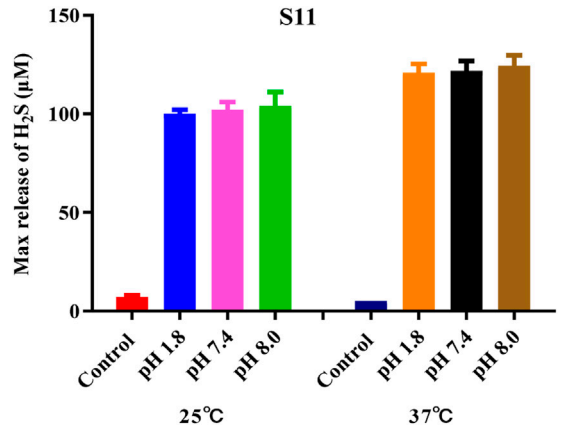


FIGURE 2
Amount of H_2S released by compound **S11**. Each bar represents the mean ± SD (standard deviation) of three independent experiments.

2.5 Assessment of anti-tumour mechanisms

2.5.1 Venn diagram construction and core PPI network screening

The Venn diagram in Figure 4A visualizes the overlap of **S11** with tumour targets, revealing 26 common genes. It is suggested that **S11** may regulate tumour cell death by interacting with these targets. We then constructed 2 networks using STRING for **S11** (Figure 4B) and an intersecting network of **S11** with cancer target (Figure 4C). Circles in Figure 4C indicate targets of drug-disease interactions; larger circles indicate more significant interactions between targets, suggesting that their respective functions are more important. Combined with Figure 4C, AKT is an important potential target for our analysed.

2.5.2 GO and KEGG pathway enrichment analysis

The results of GO (BP, CC, MF) indicated that the top 10 targets are primarily membrane-associated and involved in lipid

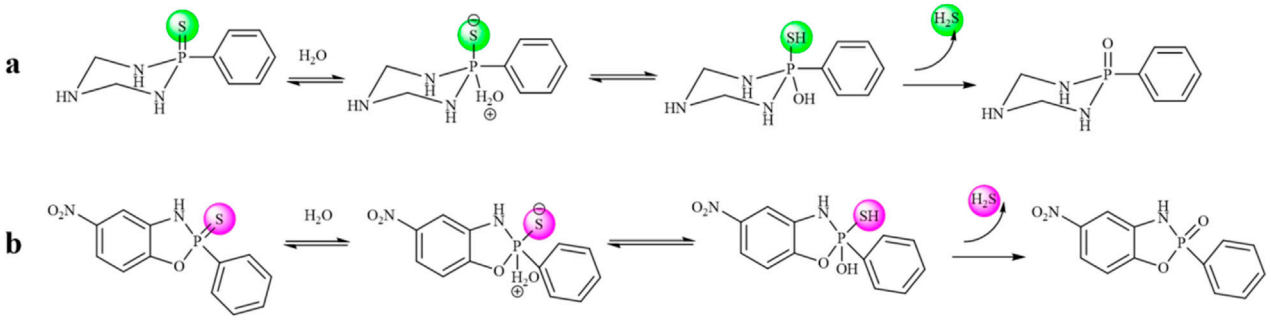


FIGURE 3
(A) Mechanism of compound **S2**-**S10** releasing H_2S. **(B)** Mechanism of compound **S11**-**S16** releasing H_2S.

TABLE 1 IC_{50} (μM) values of all the compounds.

Compound	HepG2[a,b]	LO2[a,b]	WI38[a,b]
S1	>400	>200	>200
S2	>400	>200	>200
S3	>400	>200	>200
S4	>400	>200	>200
S5	>400	>200	>200
S6	>400	>200	>200
S7	>400	>200	>200
S8	>400	>200	>200
S9	>400	>200	>200
S10	>400	>200	>200
S11	>400	>200	>200
S12	>400	>200	>200
S13	>400	>200	>200
S14	>400	>200	>200
S15	>400	>200	>200
S16	>400	>200	>200
5-FU	105	170	202

[a]Each experiment was repeated three times.
[b]*IC50* is the minimum concentration of a drug that is toxic to 50% of the cells.

TABLE 2 IC_{50} (μM) values of all compounds against cell proliferation.

Compound	HeLa[a,b]	A549[a,b]	MCF-7[a,b]
S1	726 ± 12.3	673 ± 22.4	230 ± 9.5
S2	736 ± 22.1	650 ± 32.5	455 ± 3.2
S3	826 ± 17.1	700 ± 32.3	470 ± 4.1
S4	836 ± 19.7	720 ± 22.4	472 ± 3.3
S5	622 ± 20.6	680 ± 20.5	468 ± 3.4
S6	645 ± 15.5	710 ± 22.6	471 ± 5.4
S7	655 ± 15.3	730 ± 32.3	473 ± 4.2
S8	730 ± 20.5	803 ± 20.8	480 ± 3.8
S9	730 ± 20.7	590 ± 27.1	459 ± 3.7
S10	603 ± 20.8	557 ± 18.5	455 ± 2.4
S11	260 ± 7.6	294 ± 16.6	23 ± 3.2
S12	703 ± 17.7	640 ± 15.5	164 ± 4.1
S13	633 ± 18.3	500 ± 18.2	460 ± 3.5
S14	530 ± 11.3	220 ± 20.1	31 ± 2.5
S15	733 ± 28.2	520 ± 22.7	266 ± 3.5
S16	520 ± 20.3	280 ± 28.3	28 ± 2.7
5-FU	120 ± 4.1	104 ± 5.2	136 ± 5.4

[a]Each experiment was repeated three times.
[b]*IC50* is the minimum concentration of a drug that is toxic to 50% of the cells.

metabolism and biosynthesis processes (Figure 5A). KEGG enrichment bubble diagrams analysis identified two significant pathways relevant to **S11**'s therapeutic action, notably the PI3K-AKT signaling pathway and MAPK signaling pathway related to tumor disease (Figure 5B). These analyses underscore the important role of **S11** in the treatment of tumor disease.

2.5.3 Molecular docking

For this binding site (7F7W), both GlideScore and Model scores have a significant positive correlation with biological activity. This binding site has good tuberculosis with **S11** and can form hydrogen bonding interactions (Figure 6). And the twist angle of **S11** has changed, which may be caused by newly formed hydrophobic interactions and van der Waals forces between **S11** and the ligand (Khan et al., 2022; Hu et al., 2022; Zhu et al., 2021). This indicates that our compound **S11** may induce cell apoptosis by interacting with this protein, thereby inhibiting the PI3K/AKT signaling pathway mechanism.

2.5.4 Evaluation of anti-tumour targets

PI3K pathway aberrations are the most common in cancer and one of the most widely studied pathways in cancer therapy. To date, more than 30 PI3K inhibitors have entered clinical trials for various

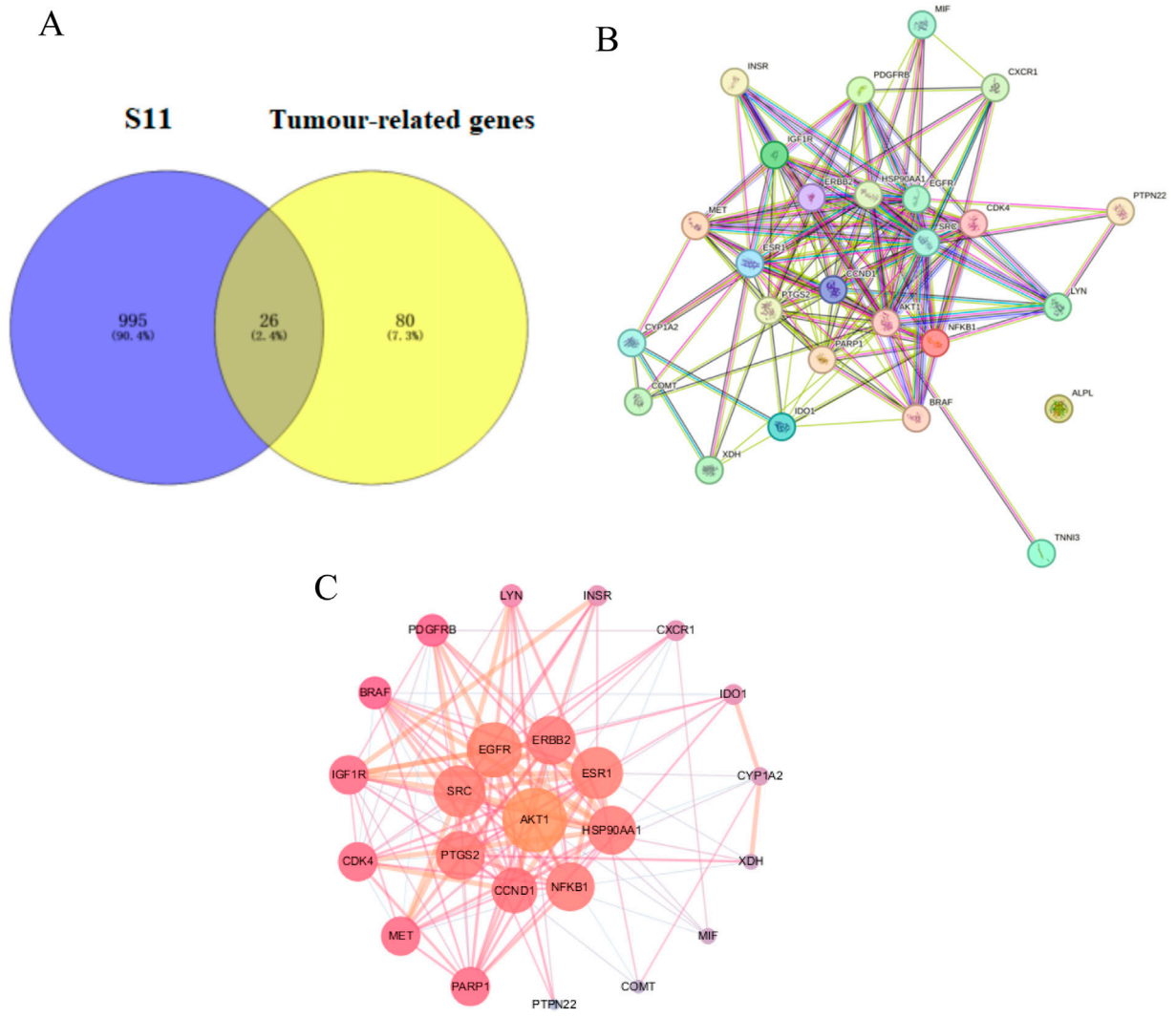


FIGURE 4
(A) Venn diagram reveals the relationship between **S11** and Tumour-related genes. **(B)** Construction of a PPI network of the interactive PPI network of **S11** and tumour targets by the STRING database. **(C)** The interactive PPI network of **S11** and tumour targets by Cytoscape software.

cancer types, and aberrant activation of PI3K and its downstream effectors, including Akt and mTOR, has been associated with a variety of cancers. AKT is a central node of the PI3K/AKT/mTOR signalling pathway, which is involved in the regulation of cell proliferation, differentiation and apoptosis and promotes tumourigenesis and metastasis, AKT is over-activated in more than 50% of tumours, including breast, lung, head and neck, endometrial, prostate and colorectal cancers (Hart et al., 2011). In conjunction with our previously predicted anticancer targets and potential mechanistic pathways, in order to further validate the antitumour mechanism of **S11**, we used a PI3K/AKT enzyme inhibition assay. The results, as shown in Table 3, showed that compound **S11** had a better inhibitory effect on PI3Kα, PI3Kβ, PI3Kγ, and AKT using PI-103 as a control, validating our predicted mechanistic pathway. We tentatively suggest that **S11** induces tumour cell death by regulating the PI3K/AKT/mTOR signalling pathway, which in turn induces tumour cell death.

2.6 The anti-inflammatory activity of the compounds

2.6.1 Effect of compounds on cell activity

To obtain more accurate anti-inflammatory results and minimize the impact of cell death caused by the test compounds on the outcomes, we first evaluated the effects of the compounds on RAW264.7 macrophage viability. The cells were divided into two groups: one treated with 1 mg/mL LPS and the other untreated. Macrophages were exposed to compounds at concentrations of 10, 50, and 100 μM for 24 h, followed by cell viability measurement using the CCK-8 assay (Huang et al., 2022; Flannigan and Wallace, 2015; Citi et al., 2020; Gemici and Wallace, 2015). The results showed that compound **S11** had low toxicity to macrophages and had no significant effect on cell growth in the absence of LPS (Figure 7). In the presence of LPS stimulation, a slight reduction of 11% cell activity was observed.

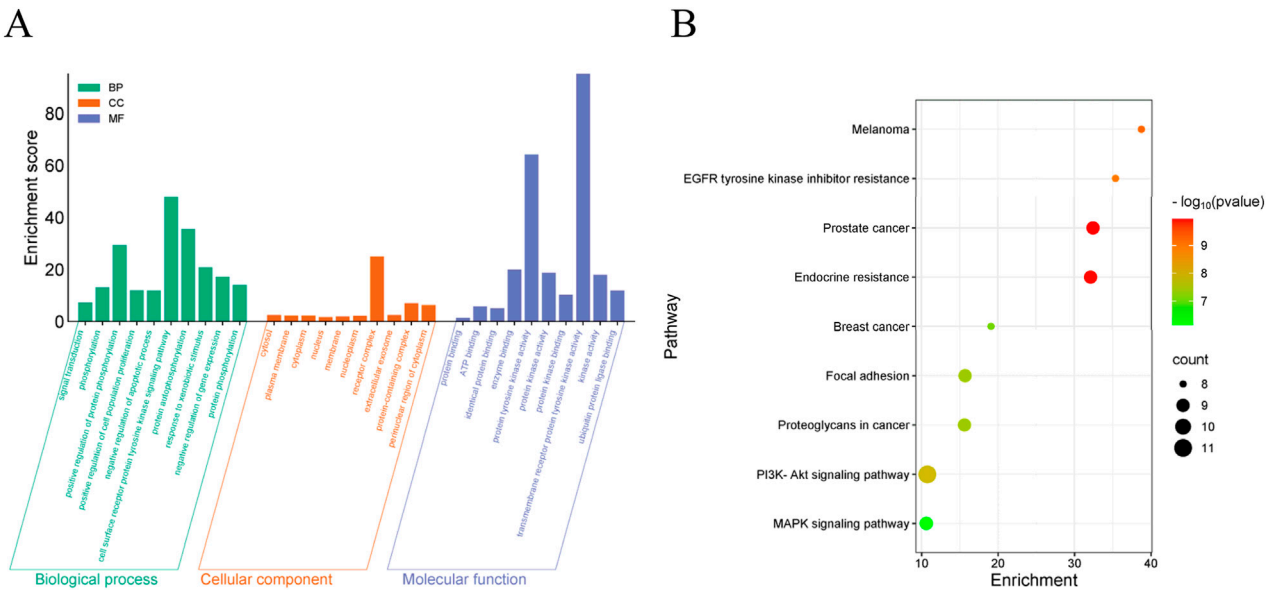


FIGURE 5
GO analysis and KEGG enrichment analysis of candidate target genes **(A)** Visualized enrichment bubble plots of biological processes (BP), cell components (CC) molecular function (MF). **(B)** Visualized enrichment bubble plots of Kyoto Encyclopedia of Genes and Genomes (KEGG). The term "RichFactor" refers to the proportion of differentially expressed transcripts found in a specific Gene Ontology (GO) entry compared to the total number of transcripts within that GO entry among all annotated transcripts. A higher RichFactor indicates a higher level of enrichment. The points on the graph are colored differently to indicate distinct P values, and the size of the points represents the number of target genes within the pathway.

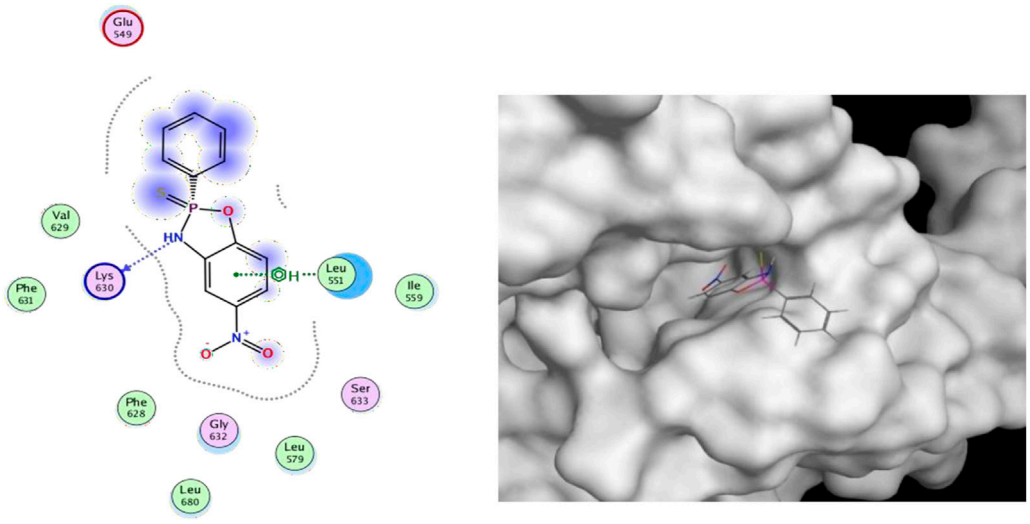


FIGURE 6
(Left) 2D ligands interaction diagram of the most active compounds (**S11**) with surrounding residues of the most probable binding site (Right) 3D diagram of compound **S11** binding to this site.

2.6.2 Impact of the compounds on nitrite production induced by LPS

Nitric oxide (NO) affects inflammation signaling pathways, regulating the intensity and timing of inflammatory responses, making it a crucial regulatory molecule in inflammation. LPS induces the production of nitric oxide (NO) by activating a series of signal transduction pathways. Upon NF-κB activation, transcription of the iNOS gene is promoted, leading to the synthesis of inducible nitric oxide synthase (iNOS). iNOS is an enzyme that produces large amounts of NO, activated under inflammatory conditions to release substantial nitric oxide (Kumar, 2023). *In vivo*, NO is easily oxidized by superoxide ions to generate nitrites. Studies have shown that H_2S not only acts to scavenge peroxides but also undergoes chemical reactions with NO,

TABLE 3 The inhibitory activity of synthesised compounds on PI3K isoforms.

Compound	PI3Kα%inhibition at 10 μM	PI3Kβ% inhibition at 10 μM	PI3Kγ% inhibition at 10 μM	AKT% inhibition at 10 μM
S11	67	75	45	61
PI-103	100	5	12	100

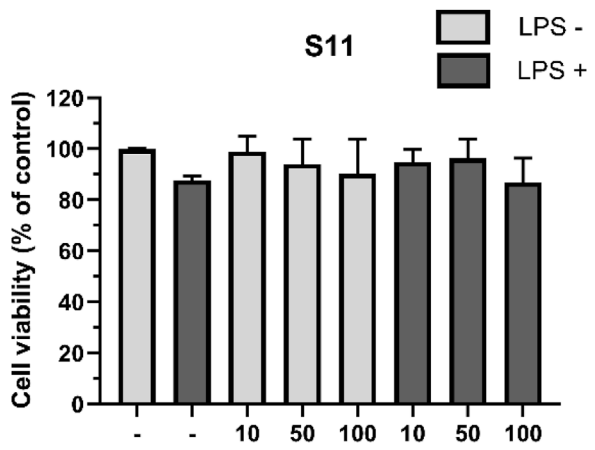


FIGURE 7
The effect of compounds on RAW264.7 cell viability. Mouse RAW264.7 macrophage cells were treated with compound **S11** at concentrations of 10, 50, and 100 μM for 24 h in the presence or absence of 1 μg/L LPS. Each bar represents the average standard deviation of three independent experiments.

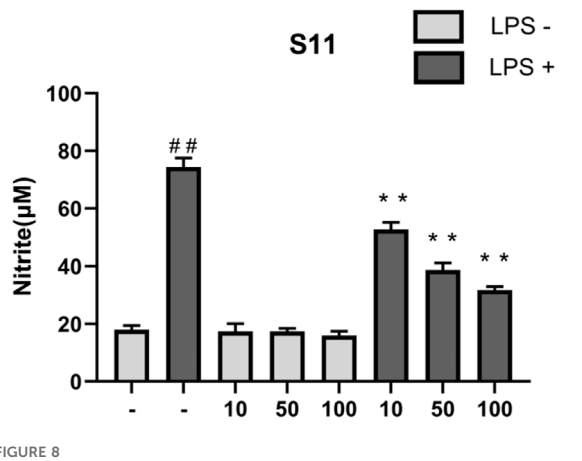


FIGURE 8
The effect of compounds on nitrite levels in RAW 264.7 cells. Mouse RAW264.7 macrophage cells were treated with compound **S11** at concentrations of 10, 50, and 100 μM for 24 h in the presence or absence of 1 μg/mL LPS. Each bar represents the mean ± SD of three independent experiments. $^{\#}p < 0.05$, $^{\#\#}p < 0.01$ vs untreated cells; $^{*}p < 0.05$, $^{**}p < 0.01$, vs LPS treated cells.

forming novel nitrosylthiol compounds. We assess the anti-inflammatory activity of compounds by measuring nitrite production (Somensi et al., 2019).

Results indicate (Figure 8) that under conditions of 1 mg/mL LPS, compound **S11** can reduce nitrite levels and showing significant inhibition of iNOS. **S11** show clear dose-dependency. At 100 μM, compound **S11** inhibits nitrite production by approximately 75%. Considering the H_2S release results, the high level of H_2S release in **S11** compounds may be the reason for their significant anti-inflammatory activity.

2.6.3 Effect of the compounds on LPS-mediated TNF-α and IL-10

Anti-inflammatory drugs typically exert their effects by inhibiting the NF-κB signaling pathway. Upon NF-κB activation, not only does it promote the transcription of the iNOS gene, but it also increases the expression of various inflammation-related genes such as TNF-α, IL-1β, etc. (Hou et al., 2006). Among these, TNF-α is a key pro-inflammatory cytokine in inflammation responses (You et al., 2022). It can activate immune cells, enhance inflammation signal transduction, and trigger inflammatory reactions, including leukocyte migration and cytokine release. Studies have shown that H_2S can significantly reduce the number of neutrophils induced by LPS in the liver and lungs, and decrease TNF-α levels (Chiba et al., 2007; Pan et al., 2023; Huang et al., 2022).

Therefore, we assessed the anti-inflammatory ability of compounds by measuring their effect on TNF-α levels in RAW264.7 cells induced by LPS. Results showed (Figure 9A) that compared to the control group, **S11** inhibited TNF-α expression (Figure 8). Compound **S11** decreased TNF-α induction levels by 80%. H_2S also promotes an increase in plasma IL-10 levels, thereby inhibiting inflammatory mediators. Comparatively (Figure 9B), compound **S11** exhibited the highest induction level of IL-10, being three times that of the control group.

2.6.4 Effect of the compounds on LPS-mediated HO-1

HO-1 is an important antioxidant enzyme involved in regulating intracellular redox balance. It reduces the generation of oxygen free radicals by degrading products such as carbon monoxide (CO) and biliverdin derived from heme, helping to inhibit oxidative stress and cell damage, and reducing the severity of inflammatory responses. Therefore, the expression level of HO-1 reflects the cell's anti-inflammatory ability to some extent (Shen et al., 2022; Hou et al., 2021; Lee et al., 2022). Nrf2 is a major regulator of the antioxidant defense system *in vivo*, and is involved in signal transduction related to various intracellular defense mechanisms. HO-1 is a target protein downstream of Nrf2, and HO-1 and its products play beneficial roles in modulating inflammatory responses. It has been shown that active compounds can attenuate lipopolysaccharide-induced cellular inflammatory responses by increasing the amount of HO-1 and thereby activating the Nrf2/HO-1 pathway (Lee et al., 2022; Ali et al., 2018). In this experiment, compound **S11** was used to treat RAW264.7 cells, and the

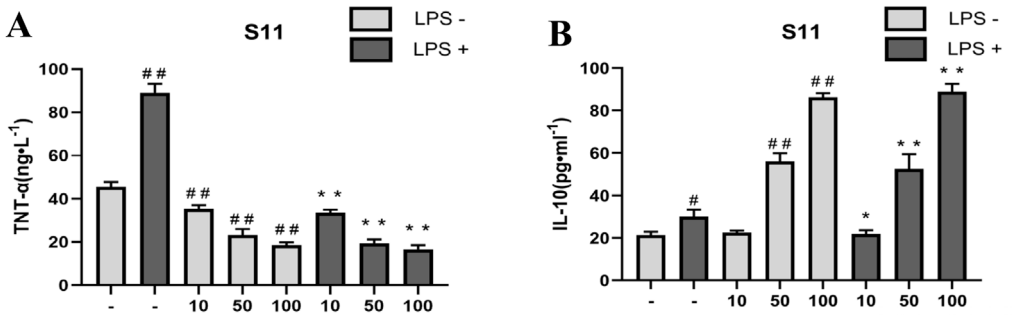


FIGURE 9
(A) The effect of compounds on TNT-α levels in RAW 264.7 cells. **(B)** The effect of compound on IL-10 level in RAW264.7 cells. Mouse RAW264.7 macrophage cells were treated with compound **S11** at concentrations of 10, 50, and 100 μM for 24 h in the presence or absence of 1 μg/mL LPS. Each bar represents the mean ± SD of three independent experiments. $^{\#}p < 0.05$, $^{\#\#}p < 0.01$ vs untreated cells; *p < 0.05, **p < 0.01, vs LPS treated cells.

expression levels of HO-1 were measured. The results showed that compound **S11** promoted HO-1 expression to approximately twice the level of the control group (Figure 10).

3 Conclusion

This experiment aimed to investigate the multifaceted effects of H_2S in anti-cancer, anti-inflammatory, and other aspects. To develop superior H_2S donor drugs, we designed a series of H_2S donor compounds based on thiol-phosphorus core and evaluated these compounds extensively. Specifically, evaluations included assessing the H_2S releasing capability of the compounds, their toxicity and activity impact on cells, anti-tumour and anti-inflammatory effects. Through these assessments, we aimed to identify H_2S donor drugs with excellent anti-tumour and anti-inflammatory activities, providing valuable references and guidance for drug development in related fields.

This experiment found that all compounds could release H_2S, with compound **S11** showing the most significant effect, possibly due to its benzene ring content. After treating LO2, HepG2, and WI38 cell lines with the compound **S1**-**S13** showed low cytotoxicity. Compound **S11** exhibited promising results in anticancer and anti-inflammatory assays. We performed target screening prediction by network pharmacology and validated it by molecular docking and enzyme inhibition assays, and found that compound **S11** may cause cancer cell death by inhibiting the PI3K/AKT pathway. *In vitro*, **S11** was found to have a better anti-inflammatory effect by the assay of some series of anti-inflammatory active factors TNF-α, IL-10 and HO-1.

4 Experimental section

All the key intermediates and final products were identified with ^{1}H NMR and ^{13}C NMR, recorded in a Bruker Avance 400 (^{1}H at 400 MHz, ^{13}C at 101 MHz), and chemical shifts were reported in parts per million using the residual solvent peaks as internal standards ($CDCl_3$ = 7.26 ppm for ^{1}H NMR and 77.16 ppm for ^{13}C NMR).

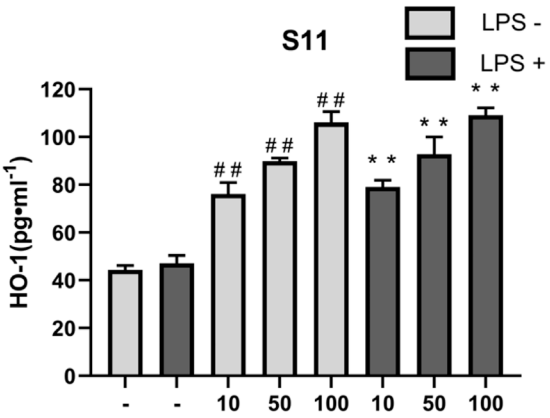


FIGURE 10
The effect of compounds on HO-1 levels in RAW 264.7 cells. Mouse RAW264.7 macrophage cells were treated with compound **S11** at concentrations of 10, 50, and 100 μM for 24 h in the presence or absence of 1 μg mL-1 LPS. Each bar represents the mean ± SD of three independent experiments. $^{\#}p < 0.05$, $^{\#\#}p < 0.01$ vs untreated cells; *p < 0.05, **p < 0.01, vs LPS treated cells.

4.1 Chemically synthetical experiments

4.1.1 Synthesis of compound dichloro (phenyl) phosphane **(B)**

We added 0.1 mmol of benzene, 0.3 mmol of phosphorus trichloride and 0.14 mmol of aluminium chloride to the reaction flask and refluxed with stirring for 5 h. Then add 0.13 mol of phosphorus trichloride and 45 mL of petroleum ether and stir the mixture at reflux for 30 min. After cooling to room temperature, filter the mixture under reduced pressure, distill the filtrate with petroleum ether at atmospheric pressure, and distill under reduced pressure. Collect fractions from 99°C–101°C with a yield of 78%. ^{1}H NMR (400 MHz, Chloroform-d) δ 7.94 (t, J = 8.6 Hz, 2H), 7.60–7.50 (m, 3H). ^{13}C NMR (101 MHz, Chloroform-d) δ 140.46 (d, J = 52.2 Hz), 132.79, 130.17 (d, J = 31.3 Hz), 129.00 (d, J = 7.9 Hz). ^{31}P NMR (162 MHz, Chloroform-d) 169.55. TOF-MS, m/z [M + H+], calcd. for $C_6H_6Cl_2P^+$, 178.9506, found: 178.9531.

4.1.2 Synthesis of compound phenylphosphonothioic dichloride **(S1)**

Slowly add the settled sulfur powder in batches to the previous product (**B**), control the vulcanization process temperature to 30°C, most of the sulfur powder disappears, and the reaction solution becomes viscous. Then, raise the temperature to 80°C and stir for 1 h. Atmospheric and vacuum distillation removes unreacted phosphorus trichloride and benzene. Collect the 90°C–91°C fraction, which is the product phenyl thiophosphine dichloride. Yield 48%. 1H NMR (400 MHz, Chloroform-d) δ 8.13 (dd, *J* = 18.6, 7.9 Hz, 2H), 7.63 (dt, *J* = 6.0, 3.0 Hz, 1H), 7.60–7.50 (m, 2H). ^{13}C NMR (101 MHz, $CDCl_3$) δ 138.07 (d, *J* = 118.2 Hz), 133.81 (d, *J* = 4.0 Hz), 129.99 (d, *J* = 15.2 Hz), 128.70 (d, *J* = 18.2 Hz). ^{31}P NMR (162 MHz, Chloroform-d) 169.56. TOF-MS, m/z [M + H+], calcd. for $C_6H_6Cl_2SP^+$, 210.9227, found: 210.9237.

4.1.3 Synthesis of compound 2-phenyl-1,3,2-oxazaphospholidine 2-sulfide **(S2)**

Di-aminoethanol (2 mmol) and triethylamine (1 mL) were dissolved in dichloromethane. Phenylphosphine dichloride (2 mmol) was added slowly in an ice bath. The reaction is then carried out at room temperature for 8 h. The precipitate was filtered and the solution was collected and concentrated. The crude product was purified by column chromatography (PE/EA = 4:1) to give a white solid. Yield 43%. Separation and purification methods can also be found in the literature (zhang et al., 2019). ^{1}H NMR (400 MHz, Chloroform-d) δ 8.00–7.75 (m, 2H), 7.54–7.29 (m, 3H), 4.53–4.40 (m, 1H), 4.38–4.23 (m, 1H), 3.80–3.60 (m, 1H), 3.54–3.34 (m, 1H), 3.16–2.99 (m, 1H). ^{13}C NMR (101 MHz, Chloroform-d) δ 135.80 (d, *J* = 135.0 Hz), 132.14 (d, *J* = 3.2 Hz), 130.89 (d, *J* = 12.3 Hz), 128.42 (d, *J* = 14.8 Hz), 68.35, 43.97.^{31}P NMR (162 MHz, DMSO) 169.50. TOF-MS, m/z [M + H$^+$], calcd. for $C_8H_{11}NOPS^+$, 199.0221, found: 200.0247.

4.1.4 Synthesis of compound 2-phenyl-1,3,2-oxazaphosphinane 2-sulfide **(S3)**

The method is the same as **S2**. Yield 47%. 1H NMR (400 MHz, Chloroform-d) δ 7.87 (ddd, *J* = 21.8, 13.8, 8.0 Hz, 2H), 7.48 (dt, *J* = 7.4, 4.8 Hz, 3H), 4.45 (td, *J* = 16.2, 7.1 Hz, 1H), 4.18–3.97 (m, 1H), 3.52–3.06 (m, 3H), 2.06 (ddt, *J* = 20.1, 10.1, 5.0 Hz, 1H), 1.62 (d, *J* = 14.3 Hz, 1H). ^{13}C NMR (101 MHz, Chloroform-d) δ 133.67 (d, *J* = 133.7 Hz), 131.90 (d, *J* = 3.2 Hz), 130.77 (d, *J* = 11.3 Hz), 128.96 (d, *J* = 14.1 Hz), 67.84, 41.33, 26.70. ^{31}P NMR (162 MHz, DMSO) 169.51. TOF-MS, m/z [M + H$^+$], calcd. for $C_9H_{13}NOPS^+$, 213.0377, found: 214.0355.

4.1.5 Synthesis of compound 2-phenyl-1,3,2-oxazaphosphepane 2-sulfide **(S4)**

The method is the same as **S2**. Yield 50%. ^{1}H NMR (400 MHz, Chloroform-d) δ 7.87 (dd, *J* = 13.8, 7.2 Hz, 2H), 7.56–7.34 (m, 3H), 4.68–4.45 (m, 1H), 4.17 (dd, *J* = 22.9, 12.0 Hz, 1H), 3.45 (s, 1H), 3.09 (dd, *J* = 30.1, 14.8 Hz, 1H), 2.74 (d, *J* = 13.9 Hz, 1H), 1.97–1.67 (m, 3H), 1.63–1.45 (m, 1H). ^{13}C NMR (101 MHz, Chloroform-d) δ 135.13 (d, *J* = 148.6 Hz), 131.41 (d, *J* = 3.2 Hz), 130.32 (d, *J* = 11.0 Hz), 128.37 (d, *J* = 14.5 Hz), 64.95, 42.65, 31.69, 29.70. ^{31}P NMR (162 MHz, DMSO) 169.50. TOF-MS, m/z [M + H$^+$], calcd. for $C_{10}H_{15}NOPS^+$, 228.0534, found: 228.0599.

4.1.6 Synthesis of compound 2-phenyl-1,3,2-oxazaphosphocane 2-sulfide **(S5)**

The method is the same as **S2**. Yield 50%. ^{1}H NMR (400 MHz, Chloroform-d) δ 7.75 (dd, *J* = 13.1, 8.2 Hz, 2H), 7.38–7.28 (m, 3H), 4.56 (qd, *J* = 9.7, 5.9 Hz, 1H), 4.07–3.85 (m, 1H), 3.49 (s, 1H), 3.02–2.84 (m, 1H), 2.78–2.62 (m, 1H), 1.98–1.82 (m, 1H), 1.73–1.33 (m, 5H). ^{13}C NMR (101 MHz, Chloroform-d) δ 134.89 (d, *J* = 149.3 Hz), 130.81 (d, *J* = 3.1 Hz), 129.87 (d, *J* = 11.0 Hz), 127.93 (d, *J* = 14.5 Hz), 65.57, 53.39, 41.80, 29.57, 28.52, 23.62. ^{31}P NMR (162 MHz, DMSO) 169.50. TOF-MS, m/z [M + H$^+$], calcd. For $C_{11}H_{17}NOPS^+$, 242.0690, found: 242.0677.

4.1.7 Synthesis of compound 2-phenyl-1,3,2-oxazaphosphonane 2-sulfide **(S6)**

The method is the same as **S2**. Yield 50%. ^{1}H NMR (400 MHz, Chloroform-d) δ 7.82 (dd, *J* = 13.7, 8.0 Hz, 2H), 7.52–7.35 (m, 3H), 4.87–4.71 (m, 1H), 4.06–3.89 (m, 1H), 3.27 (s, 1H), 2.97 (t, *J* = 15.1 Hz, 1H), 2.84 (s, 1H), 1.86 (d, *J* = 14.8 Hz, 1H), 1.77–1.61 (m, 2H), 1.59–1.31 (m, 5H). ^{13}C NMR (101 MHz, Chloroform-d) δ 134.51 (d, *J* = 149.7 Hz), 131.32 (d, *J* = 3.1 Hz), 130.66 (d, *J* = 10.8 Hz), 128.43 (d, *J* = 14.4 Hz), 62.82, 40.51, 28.53, 27.52, 20.60, 20.04.^{31}P NMR (162 MHz, DMSO) 169.51. TOF-MS, m/z [M + H$^+$], calcd. for $C_{12}H_{19}NOPS^+$, 256.0847, found: 256.0866.

4.1.8 Synthesis of compound 2-phenyl-1,3,2-diazaphosphepane 2-sulfide **(S7)**

The method is the same as **S2**. Yield 50%. ^{1}H NMR (400 MHz, Chloroform-d) δ 7.91 (dd, *J* = 13.6, 7.1 Hz, 2H), 7.47–7.31 (m, 3H), 3.34–3.11 (m, 2H), 3.09–2.84 (m, 4H), 1.73–1.52 (m, 4H). ^{13}C NMR (101 MHz, Chloroform-d) δ 136.39 (d, *J* = 126.8 Hz), 131.29 (d, *J* = 3.0 Hz), 130.32 (d, *J* = 11.0 Hz), 128.28 (d, *J* = 13.6 Hz), 41.56, 41.53, 31.72. ^{31}P NMR (162 MHz, DMSO) 169.51. TOF-MS, m/z [M + H$^+$], calcd. for $C_{10}H_{16}N_2PS^+$, 227.0694, found: 227.0780.

4.1.9 Synthesis of compound 2-phenyl-1,3,2-dioxaphosphepane 2-sulfide **(S8)**

The method is the same as **S2**. Yield 50%. ^{1}H NMR (400 MHz, Chloroform-d) δ 7.79 (dd, *J* = 13.5, 7.6 Hz, 2H), 7.46–7.29 (m, 3H), 4.24 (dd, *J* = 23.8, 5.8 Hz, 2H), 3.95 (td, *J* = 11.7, 5.9 Hz, 2H), 1.96–1.68 (m, 4H). ^{13}C NMR (101 MHz, Chloroform-d) δ 132.34 (d, *J* = 149.7 Hz), 131.82 (d, *J* = 3.1 Hz), 130.10 (d, *J* = 11.3 Hz), 128.06 (d, *J* = 14.8 Hz), 67.07, 28.96. ^{31}P NMR (162 MHz, DMSO) 169.51. TOF-MS, m/z [M + H$^+$], calcd. for $C_{10}H_{14}O_2PS^+$, 229.0374, found: 229.0398.

4.1.10 Synthesis of compound 2-phenyl-1,3,5,2-triazaphosphinane 2-sulfide **(S9)**

The method is the same as **S2**. Yield 50%. 1H NMR (400 MHz, Chloroform-d) δ 7.90–7.65 (m, 2H), 7.42–7.27 (m, 3H), 3.50–2.69 (m, 7H). ^{13}C NMR (101 MHz, Chloroform-d) δ 135.83 (d, *J* = 134.33 Hz), 132.78 (d, *J* = 13.1 Hz), 130.81 (d, *J* = 11.1 Hz), 128.11 (d, *J* = 14.1 Hz), 48.17, 42.12, 38.80. ^{31}P NMR (162 MHz, DMSO) 169.51. TOF-MS, m/z [M + H$^+$], calcd. for $C_8H_{13}N_3PS^+$, 214.0490, found: 214.0532.

4.1.11 Synthesis of compound 2-phenyl-1,3,2-dithiaphospholane 2-sulfide (S10)

The method is the same as **S2**. Yield 50%. ^{1}H NMR (400 MHz, Chloroform-d) δ 8.12 (dd, *J* = 16.9, 7.4 Hz, 2H), 7.54–7.46 (m, 3H),

3.89–3.75 (m, 2H), 3.75–3.58 (m, 2H). ^{13}C NMR (101 MHz, Chloroform-d) δ 137.18 (d, *J* = 83.5 Hz), 132.28 (d, *J* = 3.5 Hz), 131.34 (d, *J* = 12.8 Hz), 128.52 (d, *J* = 14.6 Hz), 43.00. ^{31}P NMR (162 MHz, DMSO) 169.51. TOF-MS, m/z [M + H$^+$], calcd. For $C_8H_{10}PS^+$, 232.9604, found: 232.9677.

4.1.12 Synthesis of compound 5-nitro-2-phenyl-3H-benzo [*d*][1,3,2] oxazaphosphole 2-sulfide **(S11)**

The method is the same as **S2**. Yield 50%. ^{1}H NMR (400 MHz, DMSO) δ 8.28–8.16 (m, 1H), 7.89 (d, *J* = 7.1 Hz, 2H), 7.82–7.73 (m, 1H), 7.72–7.61 (m, 1H), 6.85 (d, *J* = 9.7 Hz, 1H), 6.69 (s, 3H). ^{13}C NMR (101 MHz, DMSO-d6) δ 147.72, 134.81, 134.35 (d, *J* = 7.7 Hz), 134.11 (d, *J* = 3.1 Hz), 131.66 (d, *J* = 12.9 Hz), 131.28, 129.80, 128.99 (d, *J* = 15.6 Hz), 123.13, 117.16 (d, *J* = 4.0 Hz), 113.98. ^{31}P NMR (162 MHz, DMSO) 169.51. TOF-MS, m/z [M + H$^+$], calcd. For $C_{12}H_{10}N_2O_3PS^+$, 293.0150, found: 293.0148.

4.1.13 Synthesis of compound 6-phenyldibenzo [*d, f*][1,3,2] dioxaphosphepine 6-sulfide **(S12)**

The method is the same as **S2**. Yield 50%. ^{1}H NMR (400 MHz, Chloroform-d) δ 7.87 (dd, *J* = 14.3, 7.6 Hz, 2H), 7.59–7.47 (m, 3H), 7.42–7.24 (m, 6H), 7.10–7.01 (m, 2H). ^{13}C NMR (101 MHz, Chloroform-d) δ 148.01 (d, *J* = 11.7 Hz), 133.05 (d, *J* = 3.1 Hz), 131.33 (d, *J* = 11.5 Hz), 129.70 (d, *J* = 35.0 Hz), 129.04 (d, *J* = 1.8 Hz), 128.04 (d, *J* = 15.0 Hz), 126.27 (d, *J* = 1.8 Hz), 121.98 (d, *J* = 3.7 Hz). ^{31}P NMR (162 MHz, DMSO) 169.50. TOF-MS, m/z [M + H$^+$], calcd. For $C_{18}H_{13}PS^+$, 325.0374, found: 325.0332.

4.1.14 Synthesis of compound 3-phenyl-1,5-dihydrobenzo [e] [1,3,2] dioxaphosphepine 3-sulfide **(S13)**

The method is the same as **S2**. Yield 50%. ^{1}H NMR (400 MHz, Chloroform-d) δ 8.04–7.86 (m, 2H), 7.55 (t, *J* = 7.3 Hz, 1H), 7.50–7.41 (m, 2H), 7.40–7.37 (m, 4H), 6.00 (t, *J* = 13.1 Hz, 2H), 4.94–4.80 (m, 2H). ^{13}C NMR (101 MHz, Chloroform-d) δ 136.68, 133.02 (d, *J* = 3.1 Hz), 131.35 (d, *J* = 11.8 Hz), 129.19 (d, *J* = 53.5 Hz), 128.45 (d, *J* = 15.3 Hz). 67.47. ^{31}P NMR (162 MHz, DMSO) 169.51. TOF-MS, m/z [M + H$^+$], calcd. for $C_{14}H_{14}O_2PS^+$, 277.0374, found: 277.0331.

4.1.15 Synthesis of compound 5-methyl-2-phenyl-3H benzo [*d*][1,3,2] oxazaphosphole 2-sulfide **(S14)**

The method is the same as **S2**. Yield 30%. ^{1}H NMR (400 MHz, Chloroform-d) δ 7.82 (dd, *J* = 14.7, 7.8 Hz, 2H), 7.51–7.44 (m, 1H), 7.42–7.34 (m, 2H), 6.66 (s, 2H), 6.46 (d, *J* = 7.9 Hz, 1H), 5.82 (d, *J* = 10.2 Hz, 1H), 2.17 (s, 3H). ^{13}C NMR (101 MHz, Chloroform-d) δ 146.24 (d, *J* = 7.4 Hz), 134.05–133.51 (m), 132.15 (d, *J* = 3.2 Hz), 130.93 (d, *J* = 11.4 Hz), 128.71 (d, *J* = 14.8 Hz), 124.83, 121.53, 120.20 (d, J = 2.9 Hz), 116.40, 20.89. ^{31}P NMR (162 MHz, DMSO) 169.52. TOF-MS, m/z [M + H$^+$], calcd. for $C_{13}H_{13}NOPS^+$, 262.0455, found: 262.0459.

4.1.16 Synthesis of 2-phenylperyleno [1,12-def] [1,3,2] dioxaphosphepine 2-sulfide **(S15)**

The method is the same as **S2**. Yield 37%. ^{1}H NMR (400 MHz, Chloroform-d) δ 8.09 (d, *J* = 8.8 Hz, 1H), 8.00 (d, *J* = 8.2 Hz, 1H), 7.92 (d, *J* = 8.1 Hz, 1H), 7.73 (ddd, *J* = 35.3, 19.9, 8.8 Hz, 3H), 7.59–7.46 (m, 4H), 7.42–7.29 (m, 4H), 6.91 (d, *J* = 8.8 Hz, 1H). ^{13}C NMR (101 MHz, Chloroform-d) δ 151.05–144.86 (m), 133.39 (d, *J* = 3.1 Hz), 132.77 (d, *J* = 1.8 Hz), 132.19 (d, *J* = 1.5 Hz), 132.01 (d, *J* = 11.6 Hz), 131.73 (d, *J* = 1.3 Hz), 130.83 (dd, *J* = 42.0, 1.4 Hz), 128.51 (dd, *J* = 31.7, 14.0 Hz), 127.32 (d, *J* = 23.3 Hz), 126.76 (d, *J* = 6.5 Hz), 125.86, 122.13 (d, *J* = 2.4 Hz), 121.21 (d, *J* = 2.8 Hz). ^{31}P NMR (162 MHz, DMSO) 169.52. TOF-MS, m/z [M + H$^+$], calcd. for $C_{26}H_{16}O_2PS^+$, 423.0680, found: 423.0688.

4.1.17 Synthesis of compound 2-phenyl-3H-benzo [*d*][1,3,2] oxazaphosphole-5-carbonitrile 2-sulfide **(S16)**

The method is the same as **S2**. Yield 48%. ^{1}H NMR (400 MHz, Chloroform-d) δ 7.83 (dd, *J* = 14.7, 7.8 Hz, 2H), 7.51–7.45 (m, 1H), 7.44–7.35 (m, 2H), 6.80 (dd, *J* = 8.3, 5.6 Hz, 3H), 6.65 (t, *J* = 7.3 Hz, 1H). ^{13}C NMR (101 MHz, Chloroform-d) δ 145.65 (d, *J* = 7.8 Hz), 133.85, 132.18 (d, *J* = 3.2 Hz), 130.88 (d, *J* = 11.5 Hz), 128.76 (d, *J* = 14.8 Hz), 127.91 (d, *J* = 3.1 Hz), 123.23, 121.14, 119.40 (d, *J* = 3.2 Hz), 115.58. ^{31}P NMR (162 MHz, DMSO) 169.50. TOF-MS, m/z [M + H$^+$], calcd. for $C_{26}H_{16}O_2PS^+$, 423.0680, found: 423.0688.

4.2 Cell culture

RAW264.7 cells Cultivated in this laboratory, were cultured in Dulbecco's Modified Eagle's Medium (DMEM) (Gibco) supplemented with 10% v/v heat inactivated fetal bovine serum (FBS) (Gibco), l-glutamine (4 mM), sodium pyruvate (1 mM), HEPES buffer (20 mM) (Hyclone), penicillin (100 U/mL) and streptomycin (100 μg/mL). Cells were seeded in non-tissue culture treated Petri dishes (Biomedia) and maintained at 37°C in a 5% CO_2 humidified environment (Sanchez et al., 2019).

4.3 H_2S measurement

The H_2S-release capability of the donors was measured using the methylene blue (MB+) method. See Supplementary Material for more details (Sun et al., 2022; Hasegawa and Viles, 2014).

4.4 Venny map construction and core PPI network screening

We obtained SMILES of the active compound **S11** from PubChem database, and then obtained **S11** related information from TCSMP database, predicted and obtained related targets through PharmMapper database. Meanwhile, relevant targets were retrieved from Gene Cards database. Then five more databases were collected for cancer disease targets GenesCards database, CTD database, DisGeNET database, TTD database, OMIM database. Venn diagrams of **S11** *versus* cancer targets were obtained and visualised using the online tool Venny 2.0 (https://bioinfogp.cnb.csic.es/tools/venny/index.html). Subsequently, the identified cross-targets were uploaded to the STRING (https://cn.string-dbOrg/) database, which predicts protein interactions. The free nodes were hidden to obtain the PPI network of **S11** with cancer. This part of the data was

further analysed using Cytoscape 3.7.1 software (Zhang et al., 2019; Nogales et al., 2022).

4.5 GO and KEGG pathway enrichment analysis

To elucidate the biological significance of the gene list, we used Database Annotation, Visualisation and Integrated Discovery (DAVID), including GO and KEGG pathway enrichment analysis. We entered the cross-targets of **S11** and cancer in the PPI network into DAVID, specifying the species as "*Bos taurus*". We then performed functional analyses of graphene oxide, including biological processes (BP), cellular components (CC) and molecular functions (MF), as well as KEGG pathway enrichment analyses of the core targets, and concluded that a p-value of <0.05 was statistically significant. Finally, the OmicShare platform (https://www.omicshare.com/) was used to process the data (Zhang et al., 2019; Nogales et al., 2022).

4.6 Cell viability

The CCK-8 assay is a commonly used method for assessing cell viability, based on cellular metabolic activity. See Supplementary Material for more details (Huang et al., 2022; Flannigan and Wallace, 2015; Citi et al., 2020; Gemici and Wallace, 2015).

4.7 Nitrite level detection

The Griess assay is used to measure nitrite levels in biological samples, both *in vivo* and *in vitro*. See Supplementary Material for more details (Kumar, 2023).

4.8 Detection of cytokine levels

In this experiment, the levels of TNF-α, IL-10, and HO-1 cell factors were assessed using the ELISA method (Shen et al., 2022; Hou et al., 2021; Lee et al., 2022). See Supplementary Material for more details.

4.9 *In vitro* PI3K and ATK enzyme inhibitory assay

Enzyme activity assays were performed according to the reagent kit and references, and detailed procedures are in the Supplementary Material (Huang et al., 2022).

4.10 Docking and collecting data

Selection of previously described 7F7W targets for molecular docking with **S11**. See Supplementary Material for more details (Khan et al., 2022; Hu et al., 2022; Zhu et al., 2021).

4.11 Statistical analysis

The above experimental data are the mean ± SD of at least three independent experiments. SPSS 22.0 software was used to process the data, and one-way analysis of variance (ANOVA) was used to measure statistical differences between the two groups.

Data availability statement

The datasets presented in this study can be found in online repositories. The names of the repository/repositories and accession number(s) can be found in the article/Supplementary Material.

Author contributions

CX: Conceptualization, Data curation, Writing–original draft, Writing–review and editing. NY: Supervision, Validation, Visualization, Writing–original draft. HY: Methodology, Project administration, Resources, Supervision, Validation, Writing–original draft. XW: Data curation, Writing–original draft.

Funding

The author(s) declare that no financial support was received for the research, authorship, and/or publication of this article.

Conflict of interest

The authors declare that the research was conducted in the absence of any commercial or financial relationships that could be construed as a potential conflict of interest.

Generative AI statement

The authors declare that no Generative AI was used in the creation of this manuscript.

Publisher's note

All claims expressed in this article are solely those of the authors and do not necessarily represent those of their affiliated organizations, or those of the publisher, the editors and the reviewers. Any product that may be evaluated in this article, or claim that may be made by its manufacturer, is not guaranteed or endorsed by the publisher.

Supplementary material

The Supplementary Material for this article can be found online at: https://www.frontiersin.org/articles/10.3389/fchem.2024.1529211/full#supplementary-material

References

Ali, T., Kim, T., Rehman, S. U., Khan, M. S., Amin, F. U., Khan, M., et al. (2018). Natural dietary supplementation of anthocyanins via PI3K/Akt/Nrf2/HO-1 pathways mitigate oxidative stress, neurodegeneration, and memory impairment in a mouse model of alzheimer's disease. *Mol. Neurobiol.* 55 (7), 6076–6093. doi:10.1007/s12035-017-0798-6

Chiba, N., Masuda, A., Yoshikai, Y., and Matsuguchi, T. (2007). Ceramide inhibits LPS-induced production of IL-5, IL-10, and IL-13 from mast cells. *J. Cell Physiol.* 213 (1), 126–136. doi:10.1002/jcp.21101

Citi, V., Martelli, A., Brancaleone, V., Brogi, S., Gojon, G., Montanaro, R., et al. (2020). Anti-inflammatory and antiviral roles of hydrogen sulfide: rationale for considering H_2S donors in COVID-19 therapy. *Br. J. Pharmacol.* 177 (21), 4931–4941. doi:10.1111/bph.15230

Dilek, N., Papapetropoulos, A., Toliver-Kinsky, T., and Szabo, C. (2020). Hydrogen sulfide: an endogenous regulator of the immune system. *Pharm. Res.* 161 (12), 105119–105132. doi:10.1016/j.phrs.2020.105119

Faris, P., Negri, S., Faris, D., Scolari, F., Montagna, D., and Moccia, F. (2023). Hydrogen sulfide (H_2S): as a potent modulator and therapeutic prodrug in cancer. *Curr. Med. Chem.* 30 (40), 4506–4532. doi:10.2174/0929867330666230126100638

Flannigan, K. L., and Wallace, J. L. (2015). Hydrogen sulfide-based anti-inflammatory and chemopreventive therapies: an experimental approach. *Curr. Pharm. Des.* 21 (21), 3012–3022. doi:10.2174/1381612821666150514105413

Gao, W., Liu, Y. F., Zhang, Y. X., Wang, Y., Jin, Y. Q., Yuan, H., et al. (2024). The potential role of hydrogen sulfide in cancer cell apoptosis. *Cell Death Discov.* 10 (1), 114–119. doi:10.1038/s41420-024-01868-w

Gemici, B., and Wallace, J. L. (2015). Anti-inflammatory and cytoprotective properties of hydrogen sulfide. *Meth. Enzymol.* 555 (8), 169–193. doi:10.1016/bs.mie.2014.11.034

Goor, H., Born, J. C., Hillebrands, J. L., and Joles, J. A. (2020). Hydrogen sulfide in hypertension. *Curr. Opin. Nephrol. Hypertens.* 25 (2), 107–113. doi:10.1097/MNH.0000000000000206

Hao, Y., Wang, H., Fang, L., Bian, J., Gao, Y., and Li, C. (2021). H_2S donor and bone metabolism. *Front. Pharm.* 12 (22), 661601–661625. doi:10.3389/fphar.2021.661601

Hart, S., Goh, K. C., Novotny-Diermayr, V., Tan, Y. C., Madan, B., Amalini, C., et al. (2011). Pacritinib (SB1518), a JAK2/FLT3 inhibitor for the treatment of acute myeloid leukemia. *Blood Cancer J.* 1 (11), e44–e408. doi:10.1038/bcj.2011.43

Hasegawa, U., and Vlies, A. J. (2014). Design and synthesis of polymeric hydrogen sulfide donors. *Bio. Chem.* 25 (7), 1290–1300. doi:10.1021/bc500150s

Hou, L., Zhang, J., Liu, Y., Fang, H., Liao, L., Wang, Z., et al. (2021). MitoQ alleviates LPS-mediated acute lung injury through regulating Nrf2/Drp1 pathway. *Free. Radic. Biol. Med.* 165 (31), 219–228. doi:10.1016/j.freeradbiomed.2021.01.045

Hou, R. C., Chen, Y. S., Chen, C. H., Chen, Y. H., and Jeng, K. C. (2006). Protective effect of 1,2,4-benzenetriol on LPS-induced NO production by BV2 microglial cells. *J. Biomed. Sci.* 13 (1), 89–99. doi:10.1007/s11373-005-9039-5

Hu, M., Yang, T., Yang, L., Niu, L., Zhu, J., Zhao, A., et al. (2022). Preclinical studies of Flonoltinib Maleate, a novel JAK2/FLT3 inhibitor, in treatment of JAK2V617F-induced myeloproliferative neoplasms. *Blood. Cancer* 12 (3), 37–45. doi:10.1038/s41408-022-00628-2

Huang, J., Chen, L., Wu, J., Ai, D., Zhang, J. Q., Chen, T. G., et al. (2022). Targeting the PI3K/AKT/mTOR signaling pathway in the treatment of human diseases: current status, trends, and solutions. *J. Med. Chem.* 65 (24), 16033–16061. doi:10.1021/acs.jmedchem.2c01070

Huang, W. R., Tu, J. X., Qiao, A. Q., and Chen, L. J. (2022). GW842166X alleviates osteoarthritis by repressing LPS-mediated chondrocyte catabolism in mice. *Curr. Med. Sci.* 42 (5), 1046–1054. doi:10.1007/s11596-022-2627-z

Khan, M. A., Jain, V. K., Rizwanullah, M., Ahmad, J., and Jain, K. (2019). PI3K/AKT/mTOR pathway inhibitors in triple-negative breast cancer: a review on drug discovery and future challenges. *Drug. Discov. Today* 24 (11), 2181–2191. doi:10.1016/j.drudis.2019.09.001

Khan, N. H., Wang, D., Wang, W., Shahid, M., Khattak, S., Ngowi, E. E., et al. (2022). Pharmacological inhibition of endogenous hydrogen sulfide attenuates breast cancer progression. *Molecules* 27 (13), 4049–49. doi:10.3390/molecules27134049

Kolluru, G. K., Shackelford, R. E., Shen, X., Dominic, P., and Kevil, C. G. (2023). Sulfide regulation of cardiovascular function in health and disease. *Nat. Rev. Cardiol.* 20 (2), 109–125. doi:10.1038/s41569-022-00741-6

Kumar, M. (2023). Hydrogen sulfide: from a toxic gas to a potential therapy for COVID-19 and inflammatory disorders. *Nitric Oxide* 140 (1), 8–15. doi:10.1016/j.niox.2023.08.002

Lee, M. H., Kang, C. H., Tae, L. K., Hyun, C. Y., Lee, S., and Kim, G. Y. (2022). Acertannin attenuates LPS-induced inflammation by interrupting the binding of LPS to the TLR4/MD2 complex and activating Nrf2-mediated HO-1 activation. *Int. Immunopharmacol.* 113 (PtA), 109–124. doi:10.1016/j.intimp.2022.109344

Li, Y., Chandra, T. P., Song, X., Nie, L., Liu, M., Yi, J., et al. (2021). H_2S improves doxorubicin-induced myocardial fibrosis by inhibiting oxidative stress and apoptosis via Keap1-Nrf2. *Techno Health Care* 29 (1), 195–209. doi:10.3233/THC-218020

Liu, J., Tian, R., Sun, C., Guo, Y., Dong, L., Li, Y., et al. (2023). Microbial metabolites are involved in tumorigenesis and development by regulating immune responses. *Front. Immunol.* 19 (14), 1290414–1291134. doi:10.3389/fimmu.2023.1290414

Moses, C., Garcia, B., Harvey, A. R., and Blancafort, P. (2018). Hallmarks of cancer: the CRISPR generation. *Eur. J. Cancer.* 93 (12), 10–18. doi:10.1016/j.ejca.2018.01.002

Munteanu, C. (2023). Hydrogen sulfide and oxygen homeostasis in atherosclerosis: a systematic review from molecular biology to therapeutic perspectives. *Int. J. Mol. Sci.* 24 (9), 8376–8382. doi:10.3390/ijms24098376

Nelmi, O., Devarie-Baez, P. E. B., Bo, P., and Yu, Z. (2013). Chung-min, park. Light-induced hydrogen sulfide release from "caged" gem-dithiols. *Acs. Chem. Biol.* 15 (11), 2786–2789. doi:10.1021/ol401118k

Nogales, C., Mamdouh, Z. M., List, M., Kiel, C., Casas, A. I., and Schmidt, H. H. (2022). Network pharmacology: curing causal mechanisms instead of treating symptoms. *Trends. Pharmacol. Sci.* 43 (2), 136–150. doi:10.1016/j.tips.2021.11.004

Pan, T., Xiao, Q., Fan, H. J., Xu, L., Qin, S. C., Yang, L. X., et al. (2023). Wuzi Yanzong Pill relieves MPTP-induced motor dysfunction and neuron loss by inhibiting NLRP3 inflammasome-mediated neuroinflammation. *Metab. Brain. Dis.* 38 (7), 2211–2222. doi:10.1007/s11011-023-01266-8

Sanchez, V. E., Nichols, C., Kim, H. N., Gang, E. J., and Kim, Y. M. (2019). Targeting PI3K signaling in acute lymphoblastic leukemia. *Int. J. Mol. Sci.* 20 (2), 412–418. doi:10.3390/ijms20020412

Sanchez-Aranguren, L. C., Ahmad, S., Dias, I. H. K., Alzahrani, F. A., Rezai, H., Wang, K., et al. (2020). Bioenergetic effects of hydrogen sulfide suppress soluble Flt-1 and soluble endoglin in cystathionine gamma-lyase compromised endothelial cells. *Sci. Rep.* 10 (1), 15810–15847. doi:10.1038/s41598-020-72371-2

Shen, J., Ma, X., He, Y., Wang, Y., Zhong, T., and Zhang, Y. (2022). Anti-inflammatory and anti-oxidant properties of Melianodiol on DSS-induced ulcerative colitis in mice. *PeerJ* 25 (2), 142099–e15109. doi:10.7717/peerj.14209

Siegel, R. L., Miller, K. D., and Jemal, A. (2018). Cancer statistics, 2018. *Cancer. J. Clin.* 68 (1), 7–30. doi:10.3322/caac.21442

Somensi, N., Rabelo, T. K., Guimarães, A. G., Quintans-Junior, L. J., Moreira, J. C. F., Gelain, D. P., et al. (2019). Carvacrol suppresses LPS-induced pro-inflammatory activation in RAW 264.7 macrophages through ERK1/2 and NF-kB pathway. *Int. Immunopharmacol.* 75 (23), 105743–106143. doi:10.1016/j.intimp.2019.105743

Sun, Y., Tang, X., Zhang, K., Liu, K., Li, Z., and Zhao, L. (2022). Hydrogen sulfide detection and zebrafish imaging by a designed sensitive and selective fluorescent probe based on resorufin. *Spectrochim. Acta. Part. A.* 264 (5), 120265–120340. doi:10.1016/j.saa.2021.120265

You, Z., Yang, Z., Cao, S., Deng, S., and Chen, Y. (2022). The novel KLF4/BIG1 regulates LPS-mediated neuro-inflammation and migration in BV2 cells via PI3K/Akt/NF-kB signaling pathway. *Neuroscience* 488 (15), 102–111. doi:10.1016/j.neuroscience.2022.01.014

Zhang, J., Zhang, Q., Wang, Y., Li, J., Bai, Z., Zhao, Q., et al. (2019). Toxicity, bioactivity, release of H2S *in vivo* and pharmaco-kinetics of H2S-donors with thiophosphamide structure. *Eur. J. Med. Chem.* 15 (176), 456–475. doi:10.1016/j.ejmech.2019.05.017

Zhang, R. X., Zhu, H., Bai, K., and Ning, K. (2019). Network pharmacology databases for traditional Chinese medicine: review and assessment. *Front. Pharmacol.* 10 (8), 123–128. doi:10.3389/fphar.2019.00123

Zhao, Y., Wang, H., and Xian, M. (2010). Cysteine-activated hydrogen sulfide (H_2S) donors. *J. Am. Chem. Soc.* 133 (1), 15–17. doi:10.1021/ja1085723

Zhu, J., Yang, T., Tang, M., Yang, Z., Pei, H., Ye, H., et al. (2021). Studies on the anti-psoriasis effects and its mechanism of a dual JAK2/FLT3 inhibitor flonoltinib maleate. *Biom. Pharma.* 137 (13), 111373–112173. doi:10.1016/j.biopha.2021.111373

frontiers | Frontiers in Chemistry

TYPE Original Research
PUBLISHED 26 February 2025
DOI 10.3389/fchem.2025.1545259

Check for updates

OPEN ACCESS

EDITED BY
Stefania Villa,
University of Milan, Italy

REVIEWED BY
Francesca Quartieri,
Nerviano Medical Sciences, Italy
Željko Jaćimović,
University of Montenegro, Montenegro

*CORRESPONDENCE
Hongzhi Lu,
luhongzhi17@126.com

RECEIVED 14 December 2024
ACCEPTED 05 February 2025
PUBLISHED 26 February 2025

CITATION
Hong S, Lu H, Tian D, Chang Y, Lu Q and Gao F (2025) Discovery of triazole derivatives for biofilm disruption, anti-inflammation and metal ion chelation.
Front. Chem. 13:1545259.
doi: 10.3389/fchem.2025.1545259

COPYRIGHT
© 2025 Hong, Lu, Tian, Chang, Lu and Gao. This is an open-access article distributed under the terms of the Creative Commons Attribution License (CC BY). The use, distribution or reproduction in other forums is permitted, provided the original author(s) and the copyright owner(s) are credited and that the original publication in this journal is cited, in accordance with accepted academic practice. No use, distribution or reproduction is permitted which does not comply with these terms.

Discovery of triazole derivatives for biofilm disruption, anti-inflammation and metal ion chelation

Shuang Hong, Hongzhi Lu*, Dawei Tian, Yue Chang, Qi Lu and Feng Gao

Department of Pediatrics, Maternity and Child Health Hospital of Qinhuangdao, Qinhuangdao, China

In the face of bacterial hazards to human health and resistance to multiple antibiotics, there is an urgent need to develop new antibiotics to meet the challenge. In this paper, the triazolyl heterocyclic (3-amino-1,2,4-triazole, **D**) was synthesised efficiently using thiourea as starting material. Finally, the end product **E** was obtained by aldehyde-amine condensation reaction and the structures of all compounds were determined by spectral analysis. *In vitro* antimicrobial activity showed that **E10** had a MIC of 32 μg/mL against the tested *Escherichia coli* and 16 μg/mL against the tested *Staphylococcus aureus* strain. Meanwhile, **E10** has a good anti-biofilm effect. Antibacterial mechanism studies have shown that **E10** has a good membrane targeting ability, thus disrupting cell membranes, leading to leakage of intracellular proteins and DNA and accelerating bacterial death. In terms of anti-inflammation, **E10** dose-dependently inhibits the levels of inflammatory factors NO and IL-6, which deserves further exploration in the treatment of asthma. The study of metal ion removal capacity showed that the synthesised triazole derivatives have high capacity to remove heavy metals Pb^{2+}, Cd^{2+}, Ca^{2+}, Mg^{2+}, Fe^{3+},Cr^{3+} and Al^{3+} in the range of 42%–60%.

KEYWORDS

1,2,4-triazole derivatives, anti biofilm, anti inflammatory, antiasthmatic, metal ion detection

1 Introduction

The ESKAPE (*E. coli*/*Escherichia coli*, *S. aureus*/*Staphylococcus aureus*, *Klebsiella* pneumonia/*K. pneumoniae*, *Acinetobacter* Baumannii/A. baumannii, *Pseudomonas* aeroginosa/P. aeroginosa and *Enterobacter* species) pathogens pose an enormous health and economic threat to humans and the farming industry. These pathogens are resistant to drugs through a variety of mechanisms, rendering them invulnerable to human intervention (Ma et al., 2020; Jadimurthy et al., 2022; Patil et al., 2021). It has even been reported that bioepidermal infections account for about 2/3 of these infections (Wang et al., 2022). The emergence of multidrug-resistant (MDR), extensively drug-resistant (XDR) and pan-drug-resistant (PDR) bacteria triggered by conventional antibiotics has exacerbated the problem, and therefore there is an urgent need to develop new therapeutic approaches for the treatment of bacterial drug resistance and biofilm infections (Mulani et al., 2019; Rakesh et al., 2018).

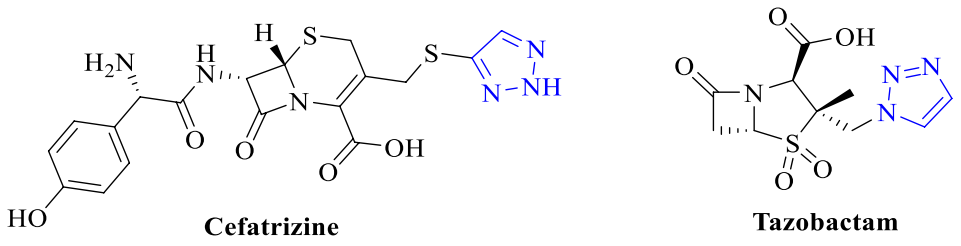


FIGURE 1
Chemical structure of triazole moiety in antibacterial.

Triazoles are common pharmacophores in many drugs and have important advantages in overcoming drug resistance, reducing toxicity and improving pharmacokinetics due to their unique molecular structure and mechanism of action (Zafar et al., 2021). Triazole derivatives have various pharmacological properties such as anti-tuberculosis (Zhang et al., 2017), anti-fungal (Dheer et al., 2017), and antibacterial (Fan et al., 2018). Triazoles can also act as stable linkage units, mimicking the electronic properties of amide bonds, carboxylic acids, etc., to link different pharmacophores (Li and Zhang, 2022). Schiff bases are an important class of organic compounds because they readily form stable complexes with most transition metals and play an important role in the development of coordination chemistry (Dalia et al., 2018). This complex has become a new type of antibacterial drug due to its better antibacterial activity and reduction of antibiotic resistance (Teran et al., 2019). Therefore, the combination of triazoles with Schiff bases is a sensible strategy in order to develop new effective drug candidates against bacterial threats (Matin et al., 2022). Therefore, the compounds designed in this paper are the couplings of triazole and Schiff bases to study their antimicrobial and anti-biofilm capabilities. As shown in Figure 1, several antimicrobial derivatives containing triazole structures have been used in clinical applications for the treatment of infections caused by a wide range of microorganisms.

Water quality is vital to human survival, as water is an essential element for life (Scorza et al., 2024). However, a major reason for the serious water pollution nowadays is the excessive heavy metal ions (Botle et al., 2023). Therefore, how to purify heavy metal ions in water is a difficult problem we face, and Schiff bases tend to have better metal chelating properties. More studies have reported that the antibacterial activity of Schiff base may be related to its complexing metals (Manhas et al., 2021). Schiff bases can chelate ions essential for microbial development or interact with DNA to cause irreversible damage to pathogens (Arag´on-Muriel et al., 2021). For these reasons, the ability of synthetic triazole derivatives coupled with Schiff bases to remove heavy metal ions from water was measured in this paper. We also know that infections are often accompanied by inflammation when they occur, and we also tested the anti-inflammatory effects of compounds.

In summary, in this paper, 3-amino-1,2,4-triazole (**D**) was synthesised using thiourea as a starting material, and finally the antimicrobial agent **E**, a coupling of triazoles and Schiff bases, was obtained by aldehyde-amine condensation reaction. The synthesised triazole derivatives have high removal rate of heavy metal ions and good antibacterial and anti-biofilm effect.

2 Results and discussion

2.1 Chemical synthesis

We used thiourea as a starting material in a three-step reaction to obtain the intermediate triazole derivative 3-amino-1,2,4-triazole (**D**) (Manning et al., 2002; Stojković et al., 2023). The reaction yields of the first three steps were above 85%, and finally the end product **E**, a coupling of triazoles and Schiff bases, was obtained by aldehyde-amine condensation reaction, and the synthetic route is showed in Scheme 1. All products were characterised by NMR and mass spectra.

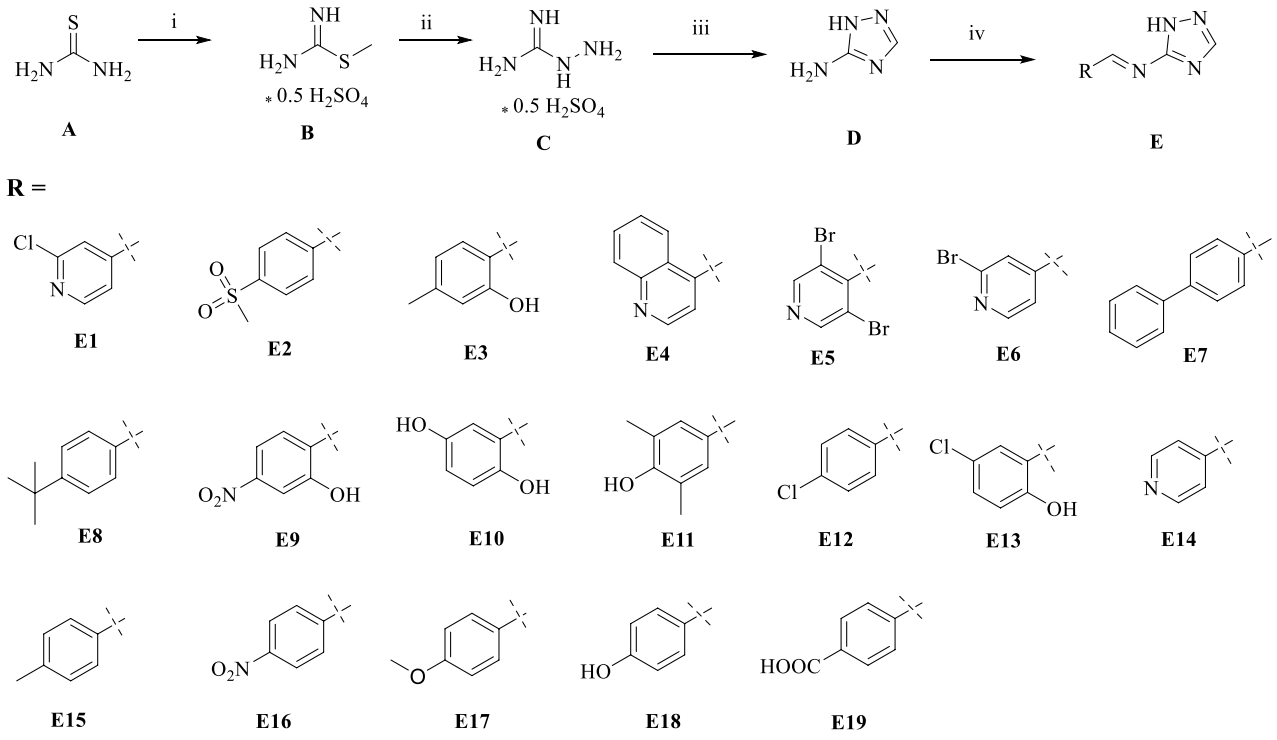
2.2 The antibacterial activity of the compounds

2.2.1 Determination of minimum inhibitory concentration

Some triazole derivatives have been reported to have good *in vitro* antibacterial activity (Tian et al., 2023). In this experiment, the *in vitro* inhibitory activity (MIC) of the Gram-positive bacteria *S. aureus* ATCC 29213, *S. aureus* ATCC 43300, *S. aureus* ATCC 33731, *S. aureus* MRSA2 and the Gram-negative bacteria *E. coli* ATCC 25922, *E. coli* DE 17 were determined using the micro broth dilution method. The antimicrobial results of the compounds are shown in Table 1. Among the tested compounds, **E10** showed good inhibitory activity against *E. coli* at a concentration of 32 μg/mL. In addition, compound **E10** showed inhibitory activity against all *S. aureus* strains at a concentration of 64 μg/mL. We found that the addition of hydroxyl group to the ligand benzaldehyde increased the antimicrobial activity by analysing the structure-activity relationship between compounds **E3**, **E9**, **E10** and **E13**.

2.2.2 Time-killing curve determinations

In order to evaluate the bactericidal ability of **E10** against *S. aureus* ATCC 29213 and *E. coli* ATCC 25922, we determined the time-kill curves of the compounds by counting the bacterial colonies at different time points using DMSO as a negative control. The results are shown in Figure 2, and the growth of *S. aureus* ATCC



SCHEME 1
Synthesis of triazole derivatives. Conditions and reagents: (i) Methanol and CH_3I, reflux, 12h, yield 93%; (ii) Ethanol, NH_2NH_2, reflux, yield 88%; (iii) Ethanol, HCOOH, reflux, yield 85%; (iV) Ethanol, different aldehyde groups, reflux, yield 50%–91%.

29213 and *E. coli* ATCC 25922 can be completely inhibited at 4-fold MIC.

2.2.3 Drug resistance study

The results of the resistance study showed that E10 had a low frequency of spontaneous resistance to *E. coli* ATCC 25922, *S. aureus* ATCC 29213 and MRSA2. As shown in Figure 3, *E. coli* ATCC 25922, *S. aureus* ATCC 29213, and MRSA2 did not increase their MIC values more than 8-fold after 28 generations. These results indicate that E10 can effectively kill bacteria and avoid the development of drug resistance.

2.3 The toxicity of the compounds

2.3.1 Hemolysis assay

To ensure the safety of our compounds, we first performed a haemolysis test on all compounds. We used 1% Triton X-100 as a positive control and sterile PBS as a negative control compounds in 4% rabbit erythrocytes after incubation at 37°C for 24 h. The results for **E10** are shown in Figure 4. Test compound **E10** at concentrations of 2–256 μg/mL showed no haemolytic properties. This indicates that **E10** does not cause haemolysis of rabbit erythrocytes even at its antibacterial concentration.

2.3.2 Cell cytotoxicity assay

We then evaluated the cytotoxicity of the active compound **E10** against the African green monkey kidney cell line (VERO cells) using the CCK8 assay (Huang et al., 2022). As shown in Figure 5, the maximum inhibitory concentration of **E10** tolerated on VERO cells was 128 μg/mL, indicating that **E10** was not cytotoxic to VERO cells at concentrations up to 64 μg/mL.

2.4 Inhibitory effects towards *S. Aureus* biofilm formation

More than 80% of chronic bacterial infections in humans are associated with biofilms, which are surface-associated bacterial communities encased in a secreted exopolysaccharide matrix that resists to environmental and chemical damage (Vishwakarma et al., 2021). Biofilm formation increases bacterial resistance to conventional antibiotic treatments and host immune responses by nearly 1,000-fold (Yang et al., 2024). Failure of antibiotics to eliminate biofilms leads to persistent chronic infections and may promote the development of antibiotic-resistant strains of bacteria. Therefore, there is an urgent need to develop drugs that are effective in preventing biofilm formation and eradicating formed biofilms.

Therefore, we investigated whether compound **E10** inhibits biofilm formation in *S. aureus* ATCC 29213. Biofilms were quantified using the crystal violet method and the inhibition of *S. aureus* ATCC 29213 biofilm by compound **E10** at concentrations ranging from 2–256 μg/mL is shown in Figure 6A. **Black** is the group without biofilm formation and **Contol** is the group that formed biofilm without drug. Compound **E10** showed significant biofilm inhibitory activity against *S. aureus* ATCC 29213 with 63.0% inhibition of biofilm at 32 μg/mL.

TABLE 1 Minimum inhibitory concentration (MIC)[a] [μg/mL] of triazole derivatives on reference bacterial strains.

Compounds	*E. coli* ATCC 25922	*E. coli* DE17>	*S. aureus* ATCC 29213	*S. aureus* ATCC 43300	*S. aureus* ATCC 33731	*S. aureus* MRSA2
Vancomycin[b]	—	—	1	2	2	2
Enrofloxacin[c]	0.0625	0.0625	—	—	—	—
E1	>256	>256	128	128	128	>256
E2	>256	>256	128	128	128	>256
E3	64	128	64	64	64	64
E4	128	128	64	64	64	64
E5	128	128	64	64	64	64
E6	128	128	64	64	128	128
E7	>256	>256	128	128	128	128
E8	>256	>256	128	128	128	128
E9	>256	>256	32	32	32	32
E10	32	32	16	16	16	16
E11	>256	>256	256	>256	>256	>256
E12	>256	>256	256	>256	>256	>256
E13	64	64	64	64	64	64
E14	>256	>256	256	256	256	>256
E15	>256	>256	256	256	256	>256
E16	64	128	64	64	64	64
E17	>256	>256	>256	>256	>256	>256
E18	>256	>256	256	>256	256	>256
E19	>256	>256	256	>256	256	>256

[a]The minimum inhibitory concentration (MIC) is the lowest concentration that completely inhibits microbial growth after 16–24 h. Each experiment was repeated three times.
[b]Vancomycin is a clinical drug against Gram-positive bacterial.
[c]Enrofloxacin is a broad-spectrum quinolone-based antibiotic.

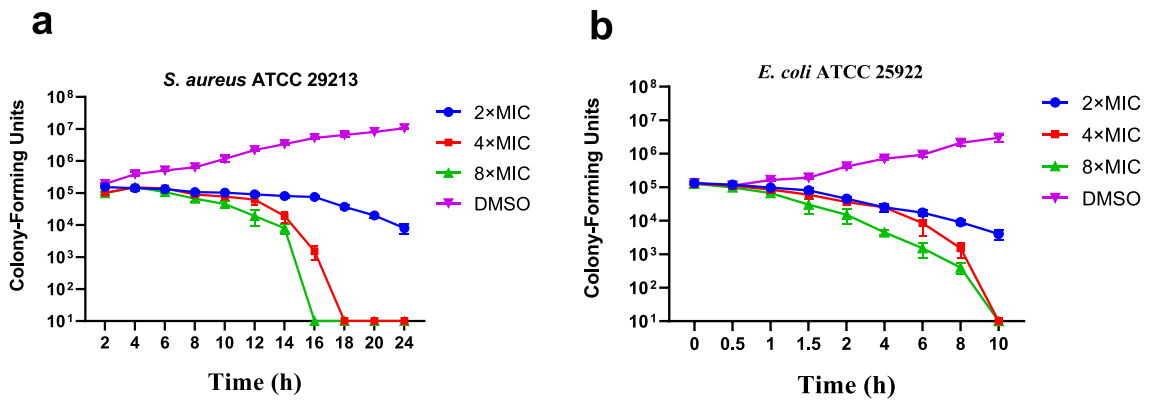


FIGURE 2
Time-kill kinetics of **E10** against **(A)** *Staphylococcus aureus* ATCC 29213 and **(B)** *Escherichia coli* ATCC 25922. Data are presented as means ± SEM (Standard Error of Mean) from three independent experiments.

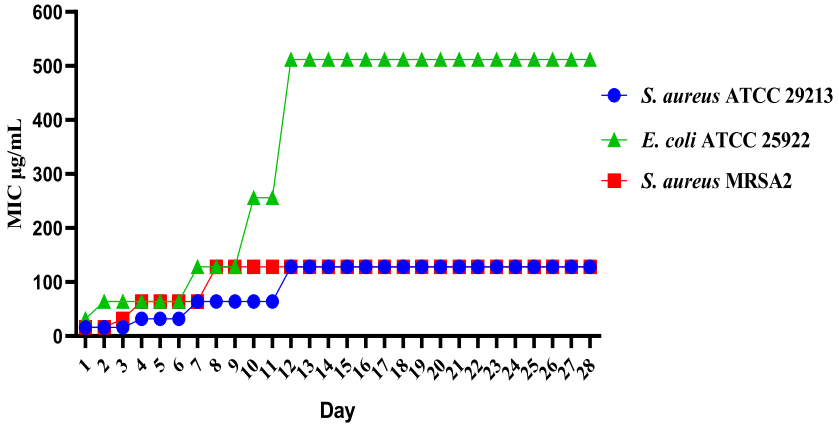


FIGURE 3
Resistance development of **E10**. Data are presented as means ± SEM from three independent experiments.

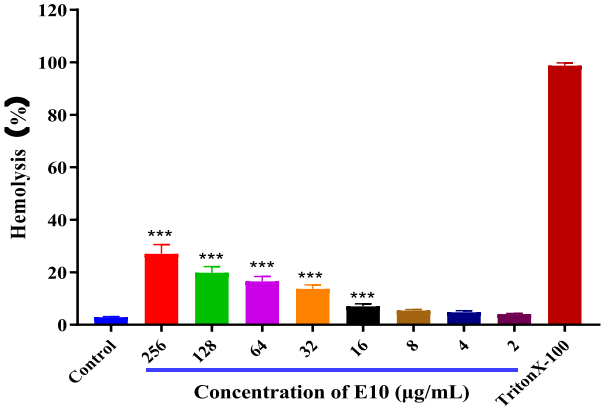


FIGURE 4
Percentage of hemolysis of rabbit blood cells at various **E10** concentrations. Difference is considered significant at *p < 0.05, **p < 0.01, ***p < 0.001. Data are presented as means ± SEM from three independent experiments.

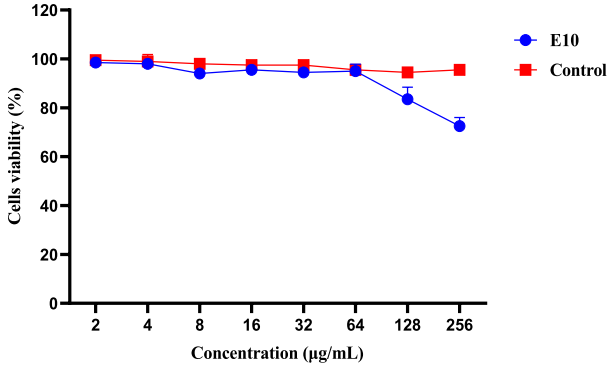


FIGURE 5
Cytotoxicity of compound **E10** against Vero cells after 24 h. Difference is considered significant at *p < 0.05, **p < 0.01, ***p < 0.001. Data are presented as means ± SEM from three independent experiments.

We next investigated whether compound **E10** could eradicate biofilms formed by *S. aureus* ATCC 29213. **E10** showed significant biofilm eradication activity against *S. aureus* ATCC 29213 by adding **E10** treatment for 24 h after complete growth of biofilm as shown in Figure 6B. Compound **E10** showed 54.5% eradication from biofilm at a concentration of 64 μg/mL.

2.5 The anti-inflammatory activity of the compounds

Inflammation often accompanies the onset of infection, and since triazole derivatives have been reported to inhibit inflammation, we further examined the effect of compound **E10** on the levels of the inflammatory factor NO (Jiaranaikulwanitch et al., 2021). The results are shown in Figure 7, where LPS alone significantly induced NO production in RAW 264.7 cells compared to NO produced by the control, and treatment with the studied compound **E10** affected NO levels. **Model** is the inflammation forming group and **Control** is the normal without inflammation group. Compound **E10** showed significant inhibition of NO production at concentrations 16 μg/mL.

To further expand the drug application scenario, we performed other inflammatory factor assays. We know that allergic asthma is the airway disease caused by some abnormal inflammatory factors. Th2 cells play an important role in triggering and pushing airway inflammation by producing, e.g., interleukin (IL)-4, (IL)-6 and TNF-α, cytokines that exacerbate the disease with immunoglobulin E (IgE) and mucus production (Li et al., 2022). We preliminarily evaluated the cytotoxicity of **E10** using the CCK8 assay, and as shown in Figure 8A, **E10** showed no significant cytotoxic effects on BEAS-2B cells at concentrations below 30 μg/mL. Next, we investigated the anti-inflammatory effect of **E10** on IL-4/TNF-α-stimulated BEAS-2B cells. As shown in Figure 8B, **E10** inhibited the IL-4/TNF-α-induced production of the pro-inflammatory cytokine IL-6. This suggests that **E10** deserves further exploration in the treatment of asthma.

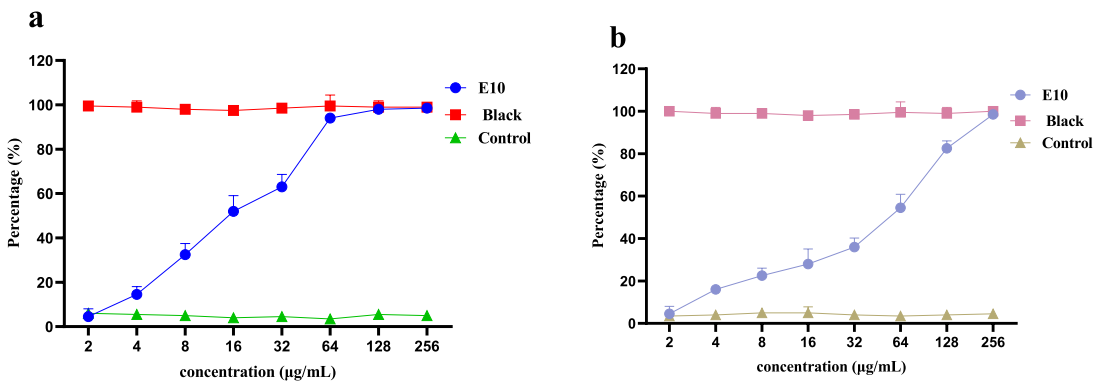


FIGURE 6
A dose-dependent response was observed in the biofilm inhibition **(A)** and eradication **(B)** activity of compound **E10** against *Staphylococcus aureus* ATCC 29213. Data are presented as means ± SEM from three independent experiments.

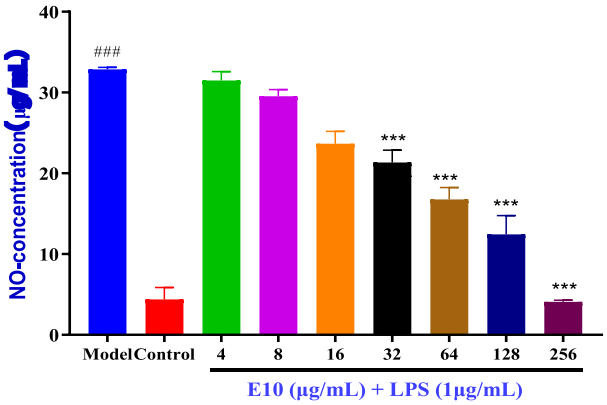


FIGURE 7
Anti-inflammatory activity of the **E10** compounds in RAW 264.7 macrophage cells was evaluated in the LPS-enhanced leukocyte migration assay. Compared with the LPS model group, *p < 0.05, **p < 0.01, ***p < 0.001; ###p < 0.001 vs. control group. Data are presented as means ± SEM from three independent experiments.

2.6 Antimicrobial mechanism investigation

2.6.1 Membrane depolarization and permeabilization assay

It has been reported that the antibacterial activity of Schiff bases is related to their hydrophobicity, which favours membrane interactions with pathogenic bacteria (Pervaiz et al., 2022). Based on the action of compound **E10** on bacterial cell membranes, it may cause changes in bacterial cell membrane depolarisation and permeability. We therefore investigated the effect of **E10** on the depolarisation and permeability of bacterial membranes using the fluorescent probes 3,3-dipropylthiodicyanoiodide (DISC35) and SYTOX Green (Yang et al., 2022; Kong et al., 2023).

After 10 min, compound **E10** was added to a solution of *S. aureus* ATCC 29213 containing the fluorescent probes DiSC35 or SYTOX Green, and the fluorescence intensity of the mixed bacterial solution continued to increase (Figures 9A, B). When the **E10** concentration was 4×MIC or 32×MIC, the fluorescence intensity of the mixed bacterial solution at 35 min was significantly increased compared to the initial fluorescence intensity, while the fluorescence intensity of the blank control without **E10** remained unchanged. This suggests that **E10** perturbs the positive and negative polarisation states of the interior and exterior of the bacterial cell membrane, thereby enhancing permeability. Similarly, the fluorescence intensity of melittin, a membrane-targeted natural antimicrobial peptide, was significantly enhanced in the positive control group. These results suggest that **E10** can affect the bacterial cell membrane, leading to bacterial death.

2.6.2 Leakage of proteins and DNA

We further determined the changes in intracellular protein and DNA concentrations after the addition of different concentrations of **E10** to *S. aureus* ATCC 29213 medium (Raman et al., 2014). Compared with the blank control group, **E10** treatment of *S. aureus* ATCC 29213 resulted in a significant and dose-dependent increase in the concentration of leaked proteins and DNA (Figures 10A, B). This suggests that **E10** can cause membrane damage in *S. aureus* ATCC 29213 cells, leading to leakage of intracellular proteins and DNA.

2.7 Screening of heavy metals and metal ion removal from aqueous solution

We previously speculated that **E10** should have good metal chelating ability to remove heavy metal ions from water, or be modified to act as a molecular probe to detect water quality. pH is a key parameter for the adsorption of heavy metals and metal ions. Since metal ions may interact with hydroxyl ions in water when the pH value is greater than 7, affecting the accuracy of our determination, the adsorption experiments in this study were carried out at a pH value of 6.0. After testing, we found that, as shown in Figure 11A, the removal amount of **E10** for divalent metal ions is 55%–60%, and the removal rate of **E10** for trivalent metal ions is 42%–45%. We infer that the removal rate of metal ions is related to the coordination form of the compound to the metal ion. One possible mechanism is shown in Figure 11B, where **E10** chelates

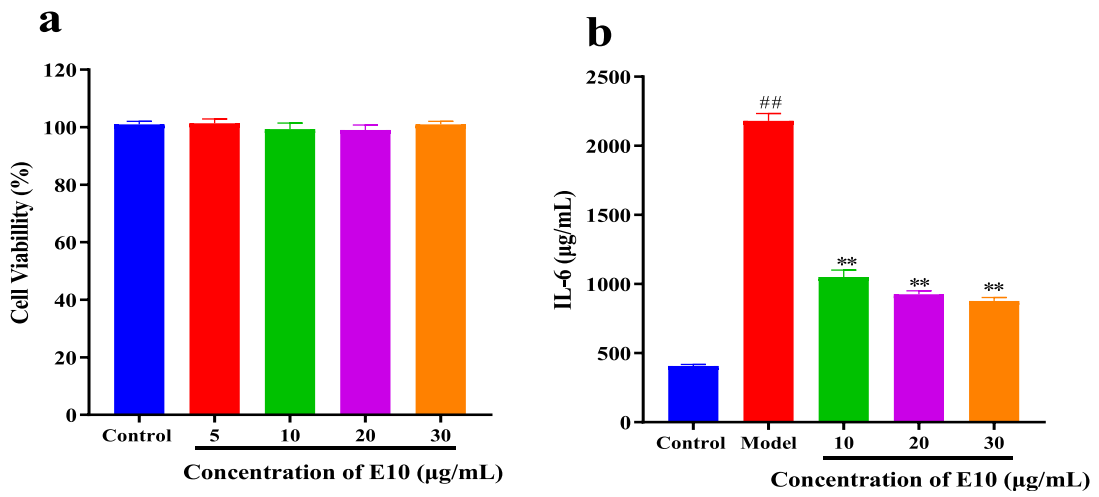


FIGURE 8
(A) Cytotoxic activity of **E10** against BEAS-2B cells. **(B)** Level of IL-6 treated with **E10** in IL-4/TNF-α-stimulated BEAS-2B cells. *p < 0.05, **p < 0.01, ***p < 0.001; ###p < 0.001 vs. control group. Data are presented as means ± SEM from three independent experiments.

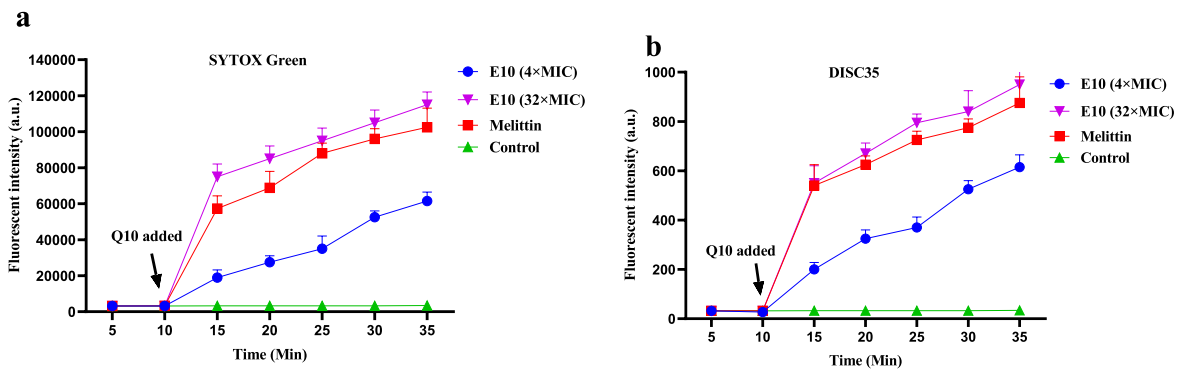


FIGURE 9
Antibacterial mechanism of **E10** against *Staphylococcus aureus* ATCC 29213. **(A)** Cytoplasmic membrane permeabilization ability of **E10** using a SYTOX Green assay. **(B)** Cytoplasmic membrane depolarization of **E10** using the DiSC35 probe. The blank control was bacteria without compound treatment, and melittin was used as a reference drug. Data are presented as means ± SEM from three independent experiments.

1:1 with divalent metal ions and 3:1 with trivalent metal ions, which also directly reduces its removal of trivalent metals.

3 Conclusion

In this paper, 3-amino-1,2,4-triazole (**D**) was synthesised using thiourea as a starting material, and finally the coupling end product **E** of triazole and Schiff base was obtained by aldolamine condensation reaction, and the structures of all the compounds were determined by spectroscopic analysis. *In vitro* antimicrobial activity showed that **E10** had a MIC of 32 μg/mL against the tested *E. coli* and 16 μg/mL against the tested *S. aureus* strains. Meanwhile, **E10** has a good anti-biofilm effect. Antibacterial mechanism studies have shown that **E10** has a good membrane targeting ability, thus disrupting cell membranes, leading to leakage of intracellular proteins and DNA and accelerating bacterial death. In terms of anti-inflammation, **E10** dose-dependently inhibits the levels of inflammatory factors NO and IL-6, which deserves further exploration in the treatment of asthma. The study of metal ion removal capacity showed that the synthesised triazole derivatives have high capacity to remove heavy metals Pb^{2+}, Cd^{2+}, Ca^{2+}, Mg^{2+}, Fe^{3+}, Cr^{3+} and Al^{3+} in the range of 42%–60%. Next step, we will use **E10** as a lead compound to further optimise its antimicrobial capacity and investigate its antimicrobial targets in depth.

4 Experimental section

4.1 Chemically synthetical experiments

4.1.1 Methyl-isothiourea (B)

We added iodomethane solution (1.7 g, 12 mmol) dropwise to an ethanol (10 mL) solution of thiourea (0.76 g, 10 mmol) at room

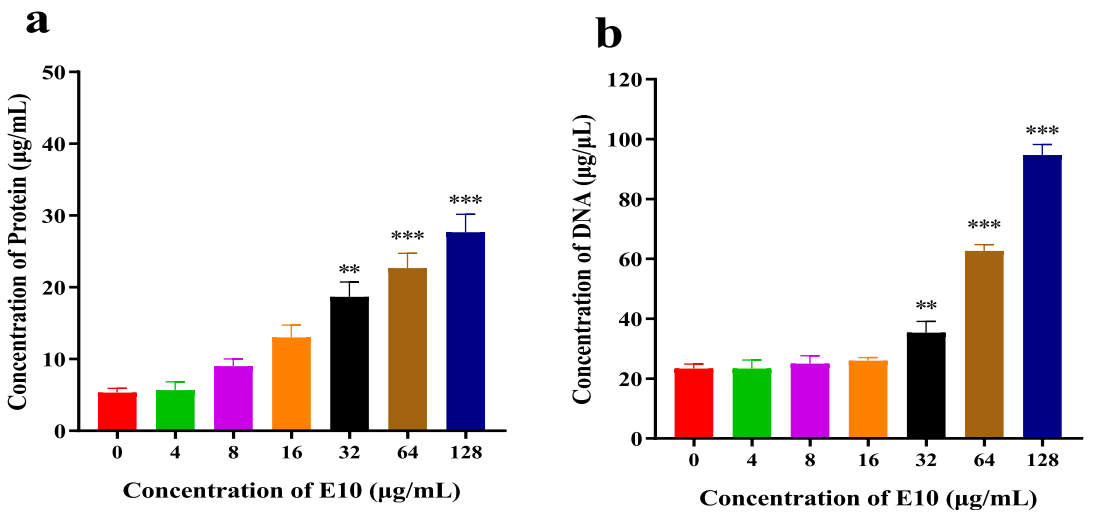


FIGURE 10
(A) DNA leakage resulting from the treatment of **E10** on *Staphylococcus aureus* ATCC 29213. **(B)** Protein leakage caused by the treatment of **E10** on *Staphylococcus aureus* ATCC 29213. *p < 0.05, **p < 0.01, ***p < 0.001. Data are presented as means ± SEM from three independent experiments.

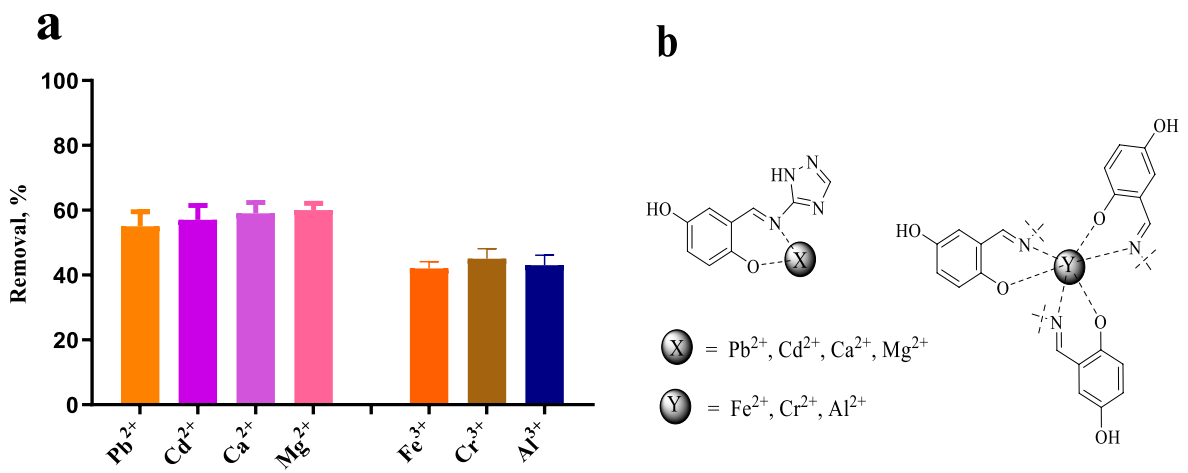


FIGURE 11
(A) Removal efficiencies of Pb^{2+}, Cd^{2+}, Ca^{2+}, Mg^{2+}, Fe^{3+}, Cr^{3+} and Al^{3+} using compound **E10**, **(B)** Possible mechanism of metal and heavy metal ion removal. Data are presented as means ± SEM from three independent experiments.

temperature. The mixture was stirred at room temperature for 12 h and the solvent was spun off at the end of the reaction. Final recrystallisation from methanol gave white solid **B** (2.2 g, yield: 93%). ^{1}H NMR (400 MHz, dmso) δ 7.76 (s, 1H), 7.21 (s, 1H), 2.69 (s, 3H). TOF-MS, m/z: [M + H^+], calcd. for $C_2H_7N_2S^+$, 91.0330, found: 91.0337.

4.1.2 Hydrazinecarboximidamide (C)

B (1 mmol) was dissolved in ethanol, appropriate amount of sodium hydroxide was added to adjust the pH to neutral and stirred for 10 min, then hydrazine hydrate (2 mmol) was added and the reaction was heated to 50°C for 6 h. The solvent was spun off, and the target product **C** (66 mg, yield: 88%) was finally recrystallised from ethanol. ^{1}H NMR (400 MHz, dmso) δ 8.82 (s, 1H), 4.67 (s, 2H). TOF-MS, m/z: [M + H^+], calcd. for $CH_7N_4^+$, 75.0670, found: 75.0675.

4.1.3 1H-1,2,4-triazol-5-amine (D)

We added sodium hydroxide 7.5 mmol, 5 mL of water to aminoguanidine **C** (7.5 mmol) and stirred the reaction for 10 min. Then formic acid (7.40 mmol) was added, and the reaction mixture was heated to 80°C to dissolve all of it, and then was dissolved at 120°C for 6 h. The reaction was stopped by the addition of ice water. After the reaction was stopped, the reaction was stopped by adding ice water and recrystallised from ethanol to give a white solid **D** (541 mg, yield: 85%) (Manning et al., 2002; Stojković et al., 2023). ^{1}H NMR (400 MHz, dmso) δ 7.43 (s, 1H), 5.75 (s, 2H). TOF-MS, m/z: [M + H^+], calcd. for $C_2H_5N_4^+$, 85.0514, found: 85.0519.

4.1.4 (E)-1-(2-chloropyridin-4-yl)-N-(1H-1,2,4-triazol-5-yl)methanimine (E1)

We dissolved the product **D** (1 mmol) in anhydrous ethanol, added aldehyde derivatives with different substituents, such as 2-chloroisonicotinaldehyde, and reacted at reflux for 8 h. After the reaction was stopped, the reaction solution was concentrated and finally the end product **E1** (104 mg, yield: 50%) was obtained by recrystallisation from ethanol. The rest of the E-series products were obtained in the same way as **E1** and will not be repeated thereafter. ^{1}H NMR (400 MHz, DMSO-d_6) δ 9.23 (s, 1H), 8.59 (s, 2H), 7.97 (d, 2H). ^{13}C NMR (100 MHz, DMSO) δ 160.16, 156.93, 148.96, 147.02, 125.31, 121.88. TOF-MS, m/z: [M + H$^+$], calcd. for $C_8H_7ClN_5^+$, 208.0390, found: 208.0395.

4.1.5 (E)-1-(4-(methylsulfonyl)phenyl)-N-(1H-1,2,4-triazol-5-yl) methanimine (E2)

Compound **E2** (205 mg, Yield: 82%). ^{1}H NMR (400 MHz, DMSO-d_6) δ 9.31 (s, 1H), 8.24 (d, J = 8.1 Hz, 2H), 8.13 (s, 1H), 8.06 (d, J = 8.1 Hz, 2H), 7.63 (s, 1H), 3.27 (s, 3H). ^{13}C NMR (101 MHz, DMSO-d6) δ 193.33, 193.12, 145.80, 139.78, 130.69, 130.22, 128.22, 128.01, 43.78. TOF-MS, m/z: [M + H$^+$], calcd. for $C_{10}H_{11}N_4O_2S^+$, 251.0602, found: 251.0609.

4.1.6 (E)-2-(((1H-1,2,4-triazol-5-yl)imino)methyl)-5-methylphenol (E3)

Compound **E3** (162 mg, Yield: 80%). ^{1}H NMR (400 MHz, DMSO-d_6) δ 9.34 (s, 1H), 8.55 (s, 1H), 7.55 (s, 1H), 7.24 (d, J = 7.9 Hz, 1H), 6.87 (d, J = 8.4 Hz, 1H), 2.25 (s, 3H). ^{13}C NMR (100 MHz, DMSO) δ 158.68, 144.74, 137.69, 132.59, 129.32, 128.54, 122.35, 117.62, 117.03, 20.37. TOF-MS, m/z: [M + H$^+$], calcd. for $C_{10}H_{11}N_4O^+$, 203.0933, found: 203.0940.

4.1.7 (E)-1-(quinolin-4-yl)-N-(1H-1,2,4-triazol-5-yl)methanimine (E4)

Compound **E4** (188 mg, Yield: 85%). ^{1}H NMR (400 MHz, DMSO-d6) δ 9.81 (s, 1H), 9.06 (d, J = 8.8 Hz, 1H), 8.63 (s, 0H), 8.11 (dd, J = 18.4, 6.3 Hz, 1H), 7.80 (dt, J = 37.7, 7.2 Hz, 1H), 4.33 (s, 1H), 3.42 (q, J = 6.9 Hz, 1H), 1.03 (td, J = 7.0, 1.1 Hz, 2H). ^{13}C NMR (101 MHz, DMSO-d_6) δ 151.14, 149.01, 144.82, 129.60, 128.58, 126.29, 125.05, 124.71, 123.80, 123.21. TOF-MS, m/z: [M + H$^+$], calcd. for $C_{12}H_{10}N_5^+$, 224.0936, found: 224.0946.

4.1.8 (E)-1-(3,5-dibromopyridin-4-yl)-N-(1H-1,2,4-triazol-5-yl)methanimine (E5)

Compound **E5** (183 mg, Yield: 55%). ^{1}H NMR (400 MHz, DMSO-d_6) δ 10.09 (s, 0H), 9.22 (s, 1H), 8.98–8.78 (m, 3H). ^{13}C NMR (100 MHz, DMSO) δ 161.07, 152.25, 151.64, 144.95, 120.95, 119.95. TOF-MS, m/z: [M + H$^+$], calcd. for $C_8H_6BrN_5^+$, 331.8969, found: 331.8975.

4.1.9 (E)-1-(2-bromopyridin-4-yl)-N-(1H-1,2,4-triazol-5-yl)methanimine (E6)

Compound **E6** (192 mg, Yield: 58%). ^{1}H NMR (400 MHz, DMSO-d6) δ 9.23 (s, 1H), 8.59 (d, J = 16.6 Hz, 2H), 8.16 (s, 1H), 7.99 (s, 1H). ^{13}C NMR (100 MHz, DMSO) δ 160.53, 159.10, 153.65, 147.52, 146.81, 132.95, 128.57, 125.34. TOF-MS, m/z: [M + H$^+$], calcd. for $C_8H_7BrN_5^+$, 251.9885, found: 251.9889.

4.1.10 (E)-1-([1,1′-biphenyl]-4-yl)-N-(1H-1,2,4-triazol-5-yl)methanimine (E7)

Compound **E7** (226 mg, Yield: 91%). ^{1}H NMR (400 MHz, DMSO-d6) δ 9.26 (d, J = 7.6 Hz, 1H), 8.53 (s, 1H), 8.08 (t, J = 8.4 Hz, 2H), 7.96–7.65 (m, 4H), 7.61–7.29 (m, 3H). ^{13}C NMR (101 MHz, DMSO) δ 166.69, 165.53, 163.18, 144.42, 143.97, 139.65, 135.05, 130.64, 130.13, 129.56, 128.65, 127.76, 127.63, 127.36. TOF-MS, m/z: [M + H$^+$], calcd. for $C_{15}H_{13}N_4^+$, 249.1140, found: 249.1146.

4.1.11 (E)-1-(4-(tert-butyl)phenyl)-N-(1H-1,2,4-triazol-5-yl)methanimine (E8)

Compound **E8** (201 mg, Yield: 88%). ^{1}H NMR (400 MHz, DMSO-d_6) δ 9.19 (s, 1H), 7.93 (d, J = 8.0 Hz, 2H), 7.57 (d, J = 8.1 Hz, 2H), 1.32 (s, 9H). ^{13}C NMR (101 MHz, DMSO-d_6) δ 164.20, 155.96, 133.16, 129.91, 129.57, 126.32, 35.34, 31.35. TOF-MS, m/z: [M + H$^+$], calcd. for $C_{13}H_{17}N_4^+$, 229.3068, found: 229.3075.

4.1.12 (E)-2-(((1H-1,2,4-triazol-5-yl)imino)methyl)-5-nitrophenol (E9)

Compound **E9** (138 mg, Yield: 62%). ^{1}H NMR (400 MHz, DMSO-d6) δ 9.49 (s, 1H), 8.76 (s, 1H), 8.23 (d, J = 12.0 Hz, 1H), 7.11 (d, J = 9.1 Hz, 1H). ^{13}C NMR (100 MHz, DMSO) δ 165.71, 162.05, 140.29, 131.07, 129.23, 126.84, 124.82, 120.25, 118.24. TOF-MS, m/z: [M + H$^+$], calcd. for $C_9H_8N_5O_3^+$, 224.0627, found: 224.0634.

4.1.13 (E)-2-(((1H-1,2,4-triazol-5-yl)imino)methyl) benzene-1,4-diol (E10)

Compound **E10** (139 mg, Yield: 68%). ^{1}H NMR (400 MHz, DMSO-d6) δ 11.63 (s, 1H), 9.32 (d, J = 20.1 Hz, 1H), 9.09 (s, 1H), 8.54 (s, 1H), 7.13 (s, 1H), 6.99–6.73 (m, 2H). ^{13}C NMR (100 MHz, DMSO) δ 164.69, 153.69, 150.31, 144.68, 124.99, 122.38, 119.75, 117.83, 116.77. TOF-MS, m/z: [M + H$^+$], calcd. for $C_9H_9N_4O_2^+$, 205.0725, found: 205.0725.

4.1.14 (E)-4-(((1H-1,2,4-triazol-5-yl)imino)methyl)-2,6-dimethylphenol (E11)

Compound **E11** (168 mg, Yield: 78%). ^{1}H NMR (400 MHz, DMSO-d6) δ 9.01 (s, 1H), 7.58 (s, 2H), 2.23 (s, 6H). ^{13}C NMR (100 MHz, DMSO) δ 158.26, 151.29, 148.40, 145.02, 130.34, 130.30, 125.15, 17.04. TOF-MS, m/z: [M + H$^+$], calcd. for $C_{11}H_{13}N_4O^+$, 217.1089, found: 217.1095.

4.1.15 (E)-1-(4-chlorophenyl)-N-(1H-1,2,4-triazol-5-yl)methanimine (E12)

Compound **E12** (165 mg, Yield: 80%). ^{1}H NMR (400 MHz, DMSO-d6) δ 9.21 (s, 1H), 8.01 (d, J = 7.9 Hz, 2H), 7.59 (d, J = 7.2 Hz, 2H). ^{13}C NMR (100 MHz, DMSO) δ 160.74, 158.57, 149.77, 136.42, 133.98, 130.60, 128.96. TOF-MS, m/z: [M + H$^+$], calcd. for $C_9H_8ClN_4^+$, 207.0617, found: 207.0625.

4.1.16 (E)-2-(((1H-1,2,4-triazol-5-yl)imino)methyl)-4-chlorophenol (E13)

Compound **E13** (138 mg, Yield: 62%). ^{1}H NMR (400 MHz, DMSO-d6) δ 10.20 (s, 0H), 9.39 (s, 1H), 7.87 (s, 1H), 7.43 (dd, J = 8.8, 2.6 Hz, 1H), 7.00 (d, J = 8.8 Hz, 1H). ^{13}C NMR (100 MHz, DMSO) δ 190.18, 163.28, 159.97, 159.31, 136.18, 127.83, 123.94, 119.99, 119.20. TOF-MS, m/z: [M + H$^+$], calcd. for $C_9H_8ClN_4O^+$, 223.0386, found: 223.0394.

4.1.17 (E)-1-(pyridin-4-yl)-N-(1H-1,2,4-triazol-5-yl)methanimine (E14)

Compound **E14** (121 mg, Yield: 70%). ^{1}H NMR (400 MHz, DMSO-d6) δ 9.24 (s, 1H), 8.87 (s, 1H), 8.76 (d, *J* = 5.3 Hz, 2H), 7.96–7.86 (m, 3H), 7.79 (d, *J* = 5.1 Hz, 1H). ^{13}C NMR (100 MHz, DMSO) δ 160.68, 158.26, 149.78, 146.71, 143.30, 124.53. TOF-MS, m/z: [M + H$^+$], calcd. for $C_8H_8N_5^+$, 174.0779, found: 174.0785.

4.1.18 (E)-1-p-tolyl-N-(1H-1,2,4-triazol-5-yl) methanimine (E15)

Compound **E15** (166 mg, Yield: 89%). ^{1}H NMR (400 MHz, DMSO-d6) δ 9.95 (s, 1H), 7.80 (d, *J* = 11.2 Hz, 2H), 7.42 (d, *J* = 10.4 Hz, 2H), 2.40 (s, 3H). ^{13}C NMR (100 MHz, DMSO) δ 160.68, 157.46, 147.23, 142.67, 130.55, 129.45, 126.36, 23.24. TOF-MS, m/z: [M + H$^+$], calcd. for $C_{10}H_{11}N_4^+$, 187.0983, found: 187.0988.

4.1.19 (E)-1-(4-nitrophenyl)-N-(1H-1,2,4-triazol-5-yl)methanimine (E16)

Compound **E16** (195 mg, Yield: 90%). ^{1}H NMR (400 MHz, DMSO-d6) δ 9.33 (s, 1H), 8.45–8.15 (m, 4H). ^{13}C NMR (100 MHz, DMSO) δ 160.53, 158.93, 149.77, 146.86, 141.38, 128.96, 124.51. TOF-MS, m/z: [M + H$^+$], calcd. for $C_9H_8N_5O_2^+$, 218.0678, found: 218.0685.

4.1.20 (E)-1-(4-methoxyphenyl)-N-(1H-1,2,4-triazol-5-yl)methanimine (E17)

Compound **E17** (141 mg, Yield: 70%). ^{1}H NMR (400 MHz, DMSO-d6) δ 9.12 (s, 1H), 8.48 (s, 1H), 7.93 (d, *J* = 7.4 Hz, 2H), 7.06 (d, *J* = 7.9 Hz, 2H), 3.82 (s, 3H). ^{13}C NMR (100 MHz, DMSO) δ 164.68, 162.92, 151.32, 144.20, 132.26, 131.35, 130.11, 114.95, 56.12. TOF-MS, m/z: [M + H$^+$], calcd. for $C_{10}H_{11}N_4O^+$, 203.0933, found: 203.0937.

4.1.21 (E)-4-(((1H-1,2,4-triazol-5-yl)imino)methyl) phenol (E18)

Compound **E18** (160 mg, Yield: 85%). ^{1}H NMR (400 MHz, DMSO-d6) δ 10.31 (s, 1H), 9.76 (s, 0H), 9.06 (s, 1H), 7.82 (d, *J* = 8.4 Hz, 2H), 6.89 (d, *J* = 8.3 Hz, 2H). ^{13}C NMR (100 MHz, DMSO) δ 163.79, 161.81, 137.04, 135.11, 132.57, 129.15, 116.31. TOF-MS, m/z: [M + H$^+$], calcd. for $C_9H_9N_4O^+$, 189.0776, found: 189.0779.

4.1.22 (E)-4-(((1H-1,2,4-triazol-5-yl)imino)methyl) benzoic acid (E19)

Compound **E19** (173 mg, Yield: 80%). ^{1}H NMR (400 MHz, DMSO-d6) δ 10.31 (s, 1H), 9.76 (s, 0H), 9.06 (s, 1H), 7.82 (d, *J* = 8.4 Hz, 2H), 6.89 (d, *J* = 8.3 Hz, 2H). ^{13}C NMR (100 MHz, DMSO) δ 170.05, 160.08, 158.65, 149.17, 141.01, 130.30, 128.74, 124.04. TOF-MS, m/z: [M + H$^+$], calcd. for $C_{10}H_9N_4O_2^+$, 217.0725, found: 217.0733.

4.2 The antibacterial activity of the compounds

4.2.1 Determination of minimum inhibitory concentration

Minimum Inhibitory Concentrations (MIC) were determined for all compounds according to Clinical and Laboratory Standards Institute (CLSI) guidelines (Mei et al., 2023). Detailed procedures can be found in the Supplementary Information.

4.2.2 Time-killing kinetics

We determined time-kill kinetics by plate colony counting. Details of the operation can be found in the previously reported literature (Song et al., 2021).

4.2.3 Drug resistance study

The drug resistance study is similar to the MIC assay, but the process needs to be repeated for 28 days, and some details can be found in the literature (Yang et al., 2024).

4.3 The toxicity of the compounds

4.3.1 Hemolysis assay

The detailed procedure for the hemolysis experiment is included in the Supplementary Information (Xu et al., 2024).

4.3.2 Cytotoxicity assay

The cytotoxicity test was conducted according to previous literature reports (Xu et al., 2024). Cell viability was assessed using the cell counting kit 8 (Beyotime, Shanghai, China) method. Cytotoxicity assay was done as described before with minor modifications. The results were calculated as follows: Cell viability (%) = (OD_{450} sample value − OD_{450} blank hole value)/(OD_{450} value of untreated control − OD_{450} blank hole value) × 100%.

4.4 Biofilm formation assay

Detailed procedures for biofilms are provided in the Supplementary Information (Etayash et al., 2021).

4.5 The anti-inflammatory activity of the compounds

LPS-stimulated RAW 264.7 cells were studied using methods reported in the literature (Jiaranaikulwanitch et al., 2021).

4.5.1 BEAS-2B Cell culture and viability. Human bronchial epithelial

Detailed procedures are provided in the Supplementary Information (Li et al., 2022).

4.5.2 Anti-inflammatory assay in BEAS-2B Cells

Detailed procedures are provided in the Supplementary Information (Li et al., 2022).

4.6 Membrane depolarization study

Detailed procedures for biofilms are provided in the Supplementary Information (Yang et al., 2024).

4.7 DNA and protein leakage

We refer to the literature for our experiments (Lu et al., 2023). Detailed procedures for biofilms are provided in the Supplementary Information.

4.8 Adsorption studies

Determination of metal ion removal was carried out with reference to previously reported methods (Xu et al., 2024; Hozien et al., 2020). We only determined a few more trivalent metal ions using the previous method. The removal percentage (Removal, %), was calculated as presented in Equation: Removal, % = $[(C_0\text{-}C_e)/C_0] \times 100$.

4.9 Statistical analysis

The above experimental data is the average ±SEM independent experiment of three data points. One-way analysis of variance was used to process the statistical differences between the two groups.

Data availability statement

The original contributions presented in the study are included in the article/Supplementary Material, further inquiries can be directed to the corresponding author.

Ethics statement

Ethical approval was not required for the studies on animals in accordance with the local legislation and institutional requirements because only commercially available established cell lines were used.

Author contributions

SH: Conceptualization, Data curation, Investigation, Methodology, Software, Supervision, Writing–original draft, Writing–review and editing. HL: Formal Analysis, Funding acquisition, Project administration, Resources, Validation, Visualization, Writing–review and editing. DT: Methodology, Supervision, Writing–review and editing. YC: Investigation, Software, Writing–review and editing. QL: Software, Supervision, Writing–review and editing. FG: Supervision, Writing–review and editing.

Funding

The author(s) declare that no financial support was received for the research, authorship, and/or publication of this article.

Conflict of interest

The authors declare that the research was conducted in the absence of any commercial or financial relationships that could be construed as a potential conflict of interest.

Generative AI statement

The author(s) declare that no Generative AI was used in the creation of this manuscript.

Publisher's note

All claims expressed in this article are solely those of the authors and do not necessarily represent those of their affiliated organizations, or those of the publisher, the editors and the reviewers. Any product that may be evaluated in this article, or claim that may be made by its manufacturer, is not guaranteed or endorsed by the publisher.

Supplementary material

The Supplementary Material for this article can be found online at: https://www.frontiersin.org/articles/10.3389/fchem.2025.1545259/full#supplementary-material

References

Arag´on-Muriel, A., Liscano, Y., Upegui, Y., Robledo, S. M., Ramírez-Apan, M. T., Morales-Morales, D., et al. (2021). *In vitro* evaluation of the potential pharmacological activity and molecular targets of new benzimidazole-based schiff base metal complexes. *Antibiotics* 10, 720–728. doi:10.3390/antibiotics10060728

Botle, A., Salgaonkar, S., Tiwari, R., Ambadekar, S., and Barabde, G. R. (2023). Brief status of contamination in surface water of rivers of India by heavy metals: a review with pollution indices and health risk assessment. *Enviro. Geochem. Hlth* 45, 2779–2801. doi:10.1007/s10653-022-01463-x

Dalia, S. A., Afsan, F., Hossain, S., Mannan, M., Haque, M., and Kudrat-E-Zahan, M. (2018). Spectral and thermal characterization of Mn(II), Ni(II) and Zn(II) complexes containing schiff base ligands towards potential biological application, *Asian J. Chem. Sci.* 4, 1–11. doi:10.9734/AJOCS/2018/42355

Dheer, D., Singh, V., and Shankar, R. (2017). Medicinal attributes of 1,2,3-triazoles: current developments. *Bioorg. Chem.* 71, 30–54. doi:10.1016/j.bioorg.2017.01.010

Etayash, H., Alford, M., Akhoundsadegh, N., Drayton, M., Straus, S. K., and Hancock, R. E. W. (2021). Multifunctional antibiotic-host defense peptide conjugate kills bacteria, eradicates biofilms, and modulates the innate immune response. *J. Med. Chem.* 25, 16854–16863. doi:10.1021/acs.jmedchem.1c01712

Fan, Y. L., Ke, X.Li. M., and Liu, M. (2018). Coumarin-triazole hybrids and their biological activities. *J. Heterocycl. Chem.* 55, 791–802. doi:10.1002/jhet.3112

Hozien, Z. A., El-Mahdy, A. F. M., Abo Markeb, A., Ali, L. S. A., and El-Sherief, H. A. H. (2020). Synthesis of Schiff and Mannich bases of news-triazole derivatives and their potential applications for removal of heavy metals from aqueous solution and as antimicrobial agents. *RSC Adv.* 10, 20184–20194. doi:10.1039/d0ra02872j

Huang, T., Jiang, H., Zhao, Y., He, J., Cheng, H., and Martyniuk, C. J. (2022). A comprehensive review of 1,2,4-triazole fungicide toxicity in zebrafish (*Danio rerio*): a mitochondrial and metabolic perspective. *Sci. Total. Environ.* 25, 151177–77. doi:10.1016/j.scitotenv.2021.151177

Jadimurthy, R., Mayegowda, S. B., Nayak, S. C., Mohan, C. D., and Rangappa, K. S. (2022). Escaping mechanisms of ESKAPE pathogens from antibiotics and their targeting by natural compounds. *Biotech. Rep.* 34, e00728–28. doi:10.1016/j.btre.2022.e00728

Jiaranaikulwanitch, J., Pandith, H., Tadtong, S., Thammarat, P., Jiranusornkul, S., Chauthong, N., et al. (2021). Novel multifunctional ascorbic triazole derivatives for amyloidogenic pathway inhibition, anti-inflammation, and neuroprotection. *Molecules* 12, 1562–1584. doi:10.3390/molecules26061562

Kong, H., Qin, S., Yan, D., Shen, B., Zhang, T., Wang, M., et al. (2023). Development of aromatic-linked diamino acid antimicrobial peptide mimics with low hemolytic toxicity and excellent activity against methicillin-resistant *Staphylococcus aureus* (MRSA). *J. Med. Chem.* 66, 7756–7771. doi:10.1021/acs.jmedchem.2c01583

Li, B., Xiao, Q., Liu, J., Mu, X., Zhang, J., Qi, Y., et al. (2022). Chemical characterization and potential mechanism of the anti-asthmatic activity of a subfraction from schisandra chinensis fruit extract. *J. Agric. Food Chem.* 70, 5015–5025. doi:10.1021/acs.jafc.2c01034

Li, J., and Zhang, J. (2022). The antibacterial activity of 1,2,3-triazole- and 1,2,4-Triazole-containingHybrids against *Staphylococcus aureus*: an updated review (2020-present). *Curr. Top. Med. Chem.* 22, 41–63. doi:10.2174/1568026621666211111160332

Lu, Y., Guan, T., Wang, S., Zhou, C., Wang, M., Wang, X., et al. (2023). Novel xanthone antibacterials: semi-synthesis, biological evaluation, and the action mechanisms. *Bioorg. Med. Chem.* 83, 117232–117248. doi:10.1016/j.bmc.2023.117232

Ma, Y. X., Wang, C. Y., Li, Y. Y., Li, J., Wan, Q., Chen, J., et al. (2020). Considerations and caveats in combating ESKAPE pathogens against nosocomial infections. *Adv. Sci.* 7, 172–182. doi:10.1002/advs.202000779

Manhas, N., Singh, P., Mocktar, C., Singh, M., and Koorbanally, N. (2021). Cytotoxicity and antibacterial evaluation of O-Alkylated/Acylated quinazolin-4-one schiff bases. *Chem. Biodivers.* 18, e2100096–e2100100. doi:10.1002/cbdv.202100096

Manning, C. O., Wadsworth, A. H., and Fellows, I. (2002). Synthesis of stable isotopically labelled versions of lamotrigine and its methylated metabolite. *J. Label. Compd. Rad.* 2002, 611–618. doi:10.1002/jlcr.590

Matin, M. M., Matin, P., Rahman, M. R., Ben Hadda, T., Almalki, F. A., Mahmud, S., et al. (2022). Triazoles and their derivatives: chemistry, synthesis, and therapeutic applications. *Front. Mol. Biosci.* 9, 864286–86. doi:10.3389/fmolb.2022.864286

Mei, R., Heng, X., Liu, X., and Chen, G. (2023). Glycopolymers for antibacterial and antiviral applications. *Molecules* 18, 985–85. doi:10.3390/molecules28030985

Mulani, M. S., Kamble, E. E., Kumkar, S. N., Tawre, M. S., and Pardesi, K. R. (2019). Emerging strategies to combat ESKAPE pathogens in the era of antimicrobial resistance: a review. *Front. Microbiol.* 10, 539–39. doi:10.3389/fmicb.2019.00539

Patil, A., Banerji, R., Kanojiya, P., Koratkar, S., and Saroj, S. (2021). Bacteriophages for ESKAPE: role in pathogenicity and measures of control. *Expert. Rev. Anti Infect. Ther.* 19, 845–865. doi:10.1080/14787210.2021.1858800

Pervaiz, M., Ahmad, I., Saeed, Z., Sagir, M., Younas, U., Tahir, M. B., et al. (2022). Amalgamation and scrutinizing of leucine derivatives schiff bases complexes as antimicrobial agent. *Comb. Chem. High. Throughput. Screen.* 25, 1167–1180. doi:10.2174/1386207325666210927092623

Rakesh, K. P., Marichannegowda, M. H., Srivastava, S., Chen, X., Long, S., Karthik, C. S., et al. (2018). Combating a master manipulator: *Staphylococcus aureus* immunomodulatory molecules as targets for combinatorial drug discovery. *Acs. Comb. Sci.* 20, 681–693. doi:10.1021/acscombsci.8b00088

Raman, N., akthivel, A., and Pravin, S. N. (2014). Exploring DNA binding and nucleolytic activity of few 4-aminoantipyrine based amino acid Schiff base complexes: a comparative approach. *Spectrochim. Acta Part A Mol. Biomol. Spectrosc.* 125, 404–413. doi:10.1016/j.saa.2014.01.108

Scorza, F. A., Chaddad, F., and Beltramim, L. (2024). Water pollution and the brain. *Clinics.* 79, 14–24. doi:10.1016/j.clinsp.2024.100424

Song, M., Liu, Y., Li, T., Liu, X., Hao, Z., Ding, S., et al. (2021). Plant natural flavonoids against multidrug resistant pathogens. *Adv. Sci.* 8, 2100749–2100760. doi:10.1002/advs.202100749

Stojković, P., Kostić, A., Lupšić, E., Jovanović, N. T., Novaković, M., Nedialkov, P., et al. (2023). Novel hybrids of sclareol and 1,2,4-triazolo[1,5-a]pyrimidine show collateral sensitivity in multidrug-resistant glioblastoma cells. *Bioorg Chem.* 138, 106605–106613. doi:10.1016/j.bioorg.2023.106605

Teran, R., Guevara, R., Mora, J., Dobronski, L., Barreiro-Costa, O., Beske, T., et al. (2019). Characterization of antimicrobial, antioxidant, and leishmanicidal activities of schiff base derivatives of 4-aminoantipyrine. *Molecules* 24, 2696–96. doi:10.3390/molecules24152696

Tian, G. M., Song, Q., Liu, Z., Guo, J., Cao, S., and Long, S. (2023). Recent advances in 1,2,3-and 1,2,4-triazole hybrids as antimicrobials and their SAR: a critical review. *Eur. J. Med. Chem.* 259, 115603–115628. doi:10.1016/j.ejmech.2023.115603

Vishwakarma, A., Dang, F., Ferrel, l A., and Barton, H. A. (2021). Peptidomimetic polyurethanes inhibit bacterial biofilm formation and disrupt surface established biofilms. *J. Am. Chem. Soc.* 16, 13–24. Epub ahead of print. doi:10.1021/jacs.1c02324

Wang, J., Jiang, Z., Wei, Y., Wang, W., Wang, F., Yang, Y., et al. (2022). Multiplexed identification of bacterial biofilm infections based on machine-learning-aided lanthanide encoding. *Acs. Nano.* 16, 3300–3310. doi:10.1021/acsnano.1c11333

Xu, C., Yang, N., Yu, H., and Wang, X. (2024). Synthesis of new triazole derivatives and their potential applications for removal of heavy metals from aqueous solution and antibacterial activities. *Front. Chem.* 23, 1473097–1473109. doi:10.3389/fchem.2024.1473097

Yang, R., Hou, E., Cheng, W., Yan, X., Zhang, T., Li, S., et al. (2022). Membrane-targeting neolignan-antimicrobial peptide mimic conjugates to combat methicillin-resistant *Staphylococcus aureus* (MRSA) infections. *J. Med. Chem.* 65, 16879–16892. doi:10.1021/acs.jmedchem.2c01674

Yang, R., Xue, Z., Li, X., Xu, T., Zhong, Y., Hu, S., et al. (2024). Novel natural ostholeinspired amphiphiles as membrane targeting antibacterials against methicillin-resistant *Staphylococcus aureus* (MRSA). *Eur. J. Med. Chem.* 5, 116449–116462. doi:10.1016/j.ejmech.2024.116449

Zafar, W., Sumrra, S. H., and Chohan, Z. H. (2021). A review: pharmacological aspects of metal based 1,2,4-triazole derived Schiff bases. *Eur. J. Med. Chem.* 12, 113602–113644. doi:10.1016/j.ejmech.2021.113602

Zhang, S., Xu, Z., Gao, C., Ren, Q. C., Chang, L., Lv, Z. S., et al. (2017). Triazole derivatives and their anti-tubercular activity. *Eur. J. Med. Chem.* 138, 501–513. doi:10.1016/j.ejmech.2017.06.051

frontiers | Frontiers in Chemistry

TYPE Original Research
PUBLISHED 28 February 2025
DOI 10.3389/fchem.2025.1537261

Check for updates

OPEN ACCESS

EDITED BY
Guigen Li,
Texas Tech University, United States

REVIEWED BY
Tao Jiang,
Ocean University of China, China
Xinwei He,
Anhui Normal University, China

*CORRESPONDENCE
Zahra Rezaei,
rezaeiza@sums.ac.ir
Soghra Khabnadideh,
khabns@sums.ac.ir

†These authors have contributed equally to this work

RECEIVED 30 November 2024
ACCEPTED 06 February 2025
PUBLISHED 28 February 2025

CITATION
Ataollahi E, Emami L, Al-Dies A-AM, Zare F, Poustforoosh A, Emami M, Saadat F, Motamen F, Rezaei Z and Khabnadideh S (2025) Design, synthesis, *in silico* studies and antiproliferative evaluation of some novel hybrids of pyrimidine-morpholine. *Front. Chem.* 13:1537261. doi: 10.3389/fchem.2025.1537261

COPYRIGHT
© 2025 Ataollahi, Emami, Al-Dies, Zare, Poustforoosh, Emami, Saadat, Motamen, Rezaei and Khabnadideh. This is an open-access article distributed under the terms of the Creative Commons Attribution License (CC BY). The use, distribution or reproduction in other forums is permitted, provided the original author(s) and the copyright owner(s) are credited and that the original publication in this journal is cited, in accordance with accepted academic practice. No use, distribution or reproduction is permitted which does not comply with these terms.

Design, synthesis, *in silico* studies and antiproliferative evaluation of some novel hybrids of pyrimidine-morpholine

Elaheh Ataollahi[1†], Leila Emami[1†], Al-Anood Mohammad Al-Dies[2], Fateme Zare[1], Alireza Poustforoosh[3], Mina Emami[1], Fateme Saadat[4], Fateme Motamen[4], Zahra Rezaei[5*] and Soghra Khabnadideh[1,5*]

[1]Pharmaceutical Sciences Research Center, Shiraz University of Medical Sciences, Shiraz, Iran, [2]Department of Chemistry, Al Qunfudah University College, UMM Al-Qura University, Mecca, Saudi Arabia, [3]Medicinal and Natural Products Chemistry Research Center, Shiraz University of Medical Sciences, Shiraz, Iran, [4]Student Research Committee, School of Pharmacy, Shiraz University of Medical Sciences, Shiraz, Iran, [5]Department of Medicinal Chemistry, Faculty of Pharmacy, Shiraz University of Medical Sciences, Shiraz, Iran

Introduction: Cancer is a complex group of diseases characterized by the uncontrolled growth and spread of abnormal cells in the body. These cells can invade nearby tissues and organs, or they may metastasize to other parts of the body through the bloodstream or lymphatic system.

Methods: In this study, eight novel pyrimidine-morpholine hybrides (**2a-2h**) were designed and synthesized based on molecular hybridization approach to identify potent cytotoxic agents. Spectroscopic methods, including infrared spectroscopy (IR), proton and carbon nuclear magnetic resonance (^{1}HNMR & ^{13}CNMR), and mass spectrometry, were employed to confirm the structures of the compounds. The cytotoxic effects of the derivatives were evaluated against cancerous cell lines, including MCF-7 and SW480, using the MTT assay.

Results and discussion: It was demonstrated that all derivatives had appropriate cytotoxic potential with IC_{50} in range of 5.12–117.04 μM. Compound **2g** was identified as the most potent compound, exhibiting IC_{50} values of 5.10 ± 2.12 μM and 19.60 ± 1.13 μM toward the SW480 and MCF-7 cell lines, respectively. Cell cycle analysis showed that **2g** could induces phase arrest in MCF-7 breast cancer cells. The apoptosis assay demonstrated the induction of apoptosis in the SW480 cell line. The biological activity of the compounds was confirmed by the docking studies. DFT analysis for compounds **2g** and **2h** was conducted at the B3LYP/6-31+G** level of theory. It was concluded that **2g** is both thermodynamically and kinetically more stable than **2h**. Moreover, the interpretation of ADME (Absorption, Distribution, Metabolism, and Excretion) indicates that these new series of compounds possess acceptable prognostic physicochemical properties. These synthesized compounds may serve as promising candidates for further investigation as anticancer agents.

KEYWORDS

pyrimidine, morpholine, synthesis, simulation, DNA, cytotoxic, cell cycle

Introduction

Cancer is a major global health issue that inflicts serious damage on human wellbeing. It is characterized by the unchecked growth of abnormal cells and ranks among the most critical health disorders globally. In fact, cancer has emerged as the second leading cause of death worldwide, with around 9.7 million fatalities reported in 2022 (Gaidai et al., 2023; Ferlay et al., 2021; Siegel et al., 2023). Despite numerous studies conducted globally on cancer treatment, achieving a complete cure remains a significant challenge. Evidence indicates that, even with an understanding of different anticancer products and the effectiveness of these medications, considerable research is yet needed to create targeted drug delivery systems and develop innovative treatments to improve diagnosis and therapy (Debela et al., 2021; Bousbaa, 2021).

The strategy of creating a hybrid compound by merging two potent biological molecules into a one has proven to be a very effective way to tackle this serious disease. This approach has garnered the attention of many medicinal chemists (Soltan et al., 2021). Motivated by the outcomes of earlier studies, researchers have recently developed and synthesized pyrimidine hybrids. These hybrids have been tested for their anticancer properties, demonstrating encouraging results against different cancer types (Sanduja et al., 2020). N_1 and N_3 are the most common positions in pyrimidine hybrids where other pharmacophores are bound either by a linkage or directly. The C_5 position, where a halogen can undergo substitution, causes cytotoxic effects (Sanduja et al., 2020; Cardona et al., 2021; Lou et al., 2021). Among the halogen substitutions, fluorine exhibited the greatest inhibitory effect (Rzepiela et al., 2020). Based on literature reports, the cytotoxic effect of 5-FU has been enhanced through the hybridization of different pharmacophores (Moreno-Quintero et al., 2022). In this regard, Figure 1 displays several uracil or 5-FU hybrids of various anticancer drugs (Sanduja et al., 2020; Huang et al., 2012; Jiang et al., 2016; Zhu et al., 2023).

Morpholine (tetrahydro-1,4-oxazine) is recognized as a valuable framework in medicinal chemistry. Due to its diverse biological activities and improved pharmacokinetic and metabolic characteristics, morpholine has emerged as one of the suitable structures being studied in structure-activity relationship (SAR) research (Lou et al., 2021; Kumari and Singh, 2020; Zhang et al., 2022). One of the key advantages of morpholine over other heterocycles with nitrogen atom, is its electrophilic ring, which results from electron-withdrawing effect of oxygen and the relatively weak basicity of nitrogen.

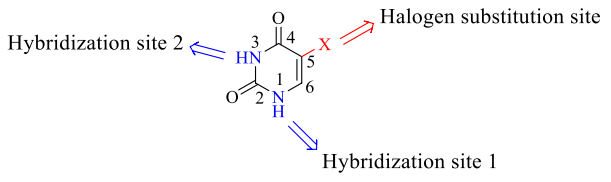


FIGURE 1
Isatin scaffold and its interaction site.

Furthermore, morpholine's capacity to create hydrogen bonds via its oxygen atom is a significant characteristic. The electron-deficient nature of its ring also enables it to engage in hydrophobic interactions (Kourounakis et al., 2020; Tzara et al., 2020). Morpholine and its related compounds have long been recognized for their various activities, such as anticancer, anti-inflammatory, antiviral, antihyperlipidemic, antioxidant, antimicrobial, antipyretic, and analgesic properties (Tzara et al., 2020; Dwivedi et al., 2022; Heiran et al., 2020; Chirra et al., 2024; SHCHERBYNA et al., 2022; Morandini et al., 2021). The antiproliferative activity of various structures containing a morpholine moiety has been extensively studied by researchers (Mao et al., 2017; Kumar et al., 2023; Killock, 2021). Some approved drugs and compounds with anticancer activity containing a morpholine moiety are listed in Figure 2.

Thymidylate synthase (TS) is a crucial enzyme involved in DNA synthesis, playing a significant role in cell survival. TS catalyzes the reductive methylation of dUMP (2′-deoxyuridine monophosphate), resulting in the production of dTMP (deoxythymidine 5′-monophosphate). dTMP undergoes subsequent phosphorylation to form dTTP (deoxythymidine triphosphate), which serves as an intermediate for DNA synthesis. TS is recognized as a target for anticancer agents that contain a pyrimidine group in their structures, used in the treatment of certain cancer cell lines (Song et al., 2021; Ferrari et al., 2018).

In this framework, we designed and synthesized various simple forms of pyrimidine-molpholine hybridizations. Fist different benzyl bromides were conjugated to the hybridization site 1. In the subsequent step to obtain the final compounds, the morpholine ring was joined to the C-6 position of the benzylated pyrimidine ring. Following confirming the structure of the synthesized compounds through spectroscopic methods, we investigated the cytotoxicity of these compounds against two cancer cell lines: MCF-7 (breast carcinoma) and SW480 (colorectal carcinoma) applying MTT assays. Cell cycle analysis and apoptosis assays were conducted to elucidate the mechanism of action. Additionally, eight molecular simulations were conducted to assess the binding energy, interactions and orientations of the compounds with the active site of thymidylate synthase (TS) as a potential therapeutic target. Furthermore, molecular dynamics simulations, density functional theory (DFT) analysis, and the drug-likeness of the compounds were investigated (Jing et al., 2024).

Experimental section

Chemistry

All chemical substances were obtained from Merck Company. The melting points of the compounds were determined using the Electrothermal 9200 device (Electrothermal, United Kingdom). The chemical structures of the compounds were analyzed using Infrared spectroscopy (VERTEX70 spectrometer), as well as ^{1}HNMR and ^{13}CNMR spectra (500 MHz, VARIAN - INOVA Bruker spectrophotometer in $CDCl_3$ as solvent).

10.3389/fchem.2025.1537261

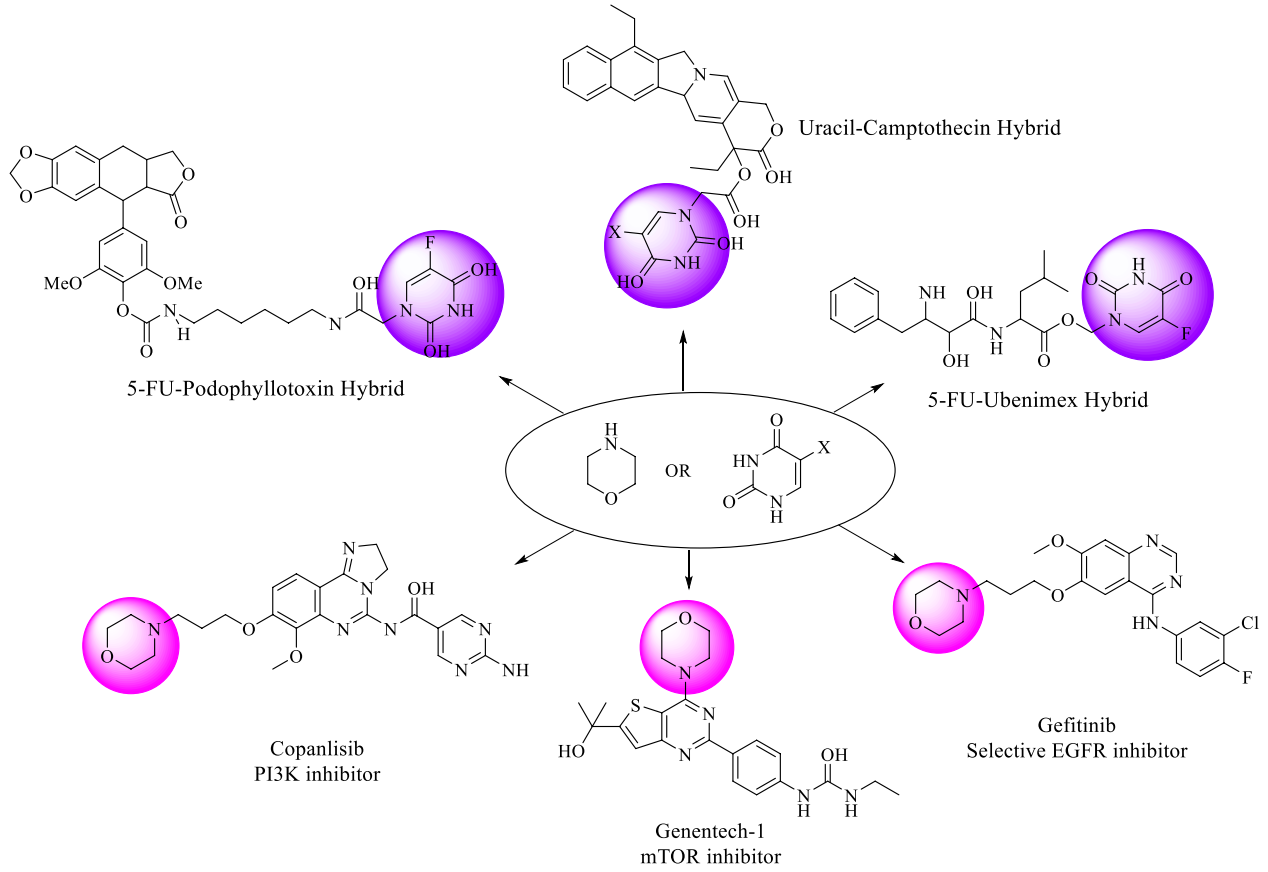


FIGURE 2
Some drugs and reported candidates with pyrimidine or morpholine scaffold exhibit diverse anticancer effects.

General procedure for the synthesis of 3-methyl-1-(substituted benzyl)-6-morpholinopyrimidine-2,4(1H,3H)-dione derivatives (**2a-2h**)

3-Methyl-6-chlorouracil (1 mmol) was combined with various benzyl bromides (1.2 mmol) (**1a-1h**) and stirred under basic conditions using diisopropylethylamine (DIPEA, 2 mmol) in tetrahydrofuran for 7 h. Upon completion of the reaction, as verified by thin-layer chromatography (TLC), the solvent was removed, yielding the intermediate without further purification (Zhu et al., 2024). Subsequently, the synthesized product from the previous step (1 mmol) was reacted with 1 mmol of morpholine in the presence of a base catalyst (potassium carbonate and triethylamine) in CH_3CN, and the mixture was refluxed for 24 h. The reaction mixture were then purified through thin layer chromatography (plates) to obtain the purified products. The chemical structures of the synthesized compound (**2a-2h**) were confirmed using ^{1}HNMR, ^{13}CNMR, and IR spectroscopy.

Spectra data

1-benzyl-3-methyl-6-morpholinopyrimidine-2,4(1H,3H)-dione (**2a**)

Yield (63%), m.p:149°C–154 °C. yellow powder. ^{1}H-NMR (500 MHz, $CDCl_3$) δ_H (ppm) = 7.33 (d, 2H, J = 8 Hz, Phenyl), 7.27-7.29 (m, 1H, Phenyl), 7.22 (d, 2H, J = 8 Hz, Phenyl), 5.38 (s, 1H, pyrimidine), 5.12 (s, 2H, CH_2), 3.75 (t, 4H, J = 4 Hz, morpholine), 3.33 (s, 3H, CH_3-pyrimidine), 2.89 (t, 4H, J = 4 Hz, morpholine). ^{13}C-NMR (125 MHz, $CDCl_3$) δ_C (ppm) = 163.28, 159.57, 152.85, 136.74, 128.81, 127.70, 126.69, 125.94, 90.18, 66.11, 51.43, 48.12, 29.70, 28.00. IR (KBr, cm^{-1}): 2923.69 (CH aromatic), 2855.02 (CH aliphatic), 1755.53–1692.52 (C=O), 1647.58 (C=N), 1605.02 (C=C), 1453.40 (C-O), 1366.66 (C-N). MS m/z (%):301.3 (57.1), 210.2 (37.5), 91.2 (100), 153.1 (36.3). Elem. Anal. Calcd. For $C_{16}H_{19}N_3O_3$ (301.35); C, 63.77; H, 6.36; N, 13.94; Found: C, 63.68; H, 6.54; N, 13.87.

1-(3-chlorobenzyl)-3-methyl-6-morpholinopyrimidine-2,4(1H,3H)-dione (**2b**)

Yield (65%), m.p:88°C–90°C. yellow powder. ^{1}H-NMR (500 MHz, $CDCl_3$) δ_H (ppm) = 7.23–7.29 (m, 3H, Phenyl), 7.10–7.12 (m, 1H, Phenyl), 5.39 (s, 1H, pyrimidine), 5.08 (s, 2H, CH_2), 3.78 (t, 4H, J = 4 Hz, morpholine), 3.32 (s, 3H, CH_3-pyrimidine), 2.89 (t, 4H, J = 4 Hz, morpholine). ^{13}C-NMR (125 MHz, $CDCl_3$) δ_C (ppm) = 163.06, 159.26, 152.75, 138.79, 134.71, 130.12, 127.98, 127.02, 124.92, 90.56, 66.09, 51.49, 47.44, 29.71, 28.02. IR (KBr) v (cm^{-1}): 2852.69 (CH aromatic), 1706.18 (C=O), 1658.40 (C=N), 1602.96 (C=C), 1441.93 (C-O), 1361.38 (C-N), 765.52 (C-Cl). MS m/z (%): 335.2 (77.0), 249.1 (3.6), 210.1 (76.18), 153.1 (82.9), 125.0 (100), 86.1 (22.3). Elem. Anal. Calcd. For

$C_{16}H_{18}ClN_3O_3$ (335.79); C, 57.23; H, 5.40; N, 12.51; Found: C, 56.97; H, 4.63; N, 12.34.

4-((3-methyl-6-morpholino-2,4-dioxo-3,4-dihydropyrimidin-1(2H)-yl)methyl)benzonitrile (**2c**)

Yield (58%), m.p:202°C–206°C. yellow powder. ^{1}H-NMR (500 MHz, $CDCl_3$) δ_H (ppm) = 7.21–7.24 (m, 2H, Phenyl), 7.02 (t, 2H, *J* = 8 Hz, Phenyl), 5.38 (s, 1H, H_5-Pyrimidine), 5.07 (s, 2H, CH_2), 3.78 (t, 4H, *J* = 4 Hz, morpholine), 3.31 (s, 3H, CH_3), 2.90 (t, 4H, *J* = 4 Hz, morpholine). ^{13}C-NMR (125 MHz, $CDCl_3$) δ_C (ppm) = 163.41, 163.13, 160.96, 159.32, 152.78, 132.48, 128.79, 115.83, 115.62, 90.36, 66.12, 51.47, 47.35, 27.97. IR (KBr, cm^{-1}): 2921.41 (CH aromatic), 2854.52 (CH aliphatic), 2227.99 (CN), 1654.52 (C=O), 1448.96 (C-O), 1364.33 (C-N). MS m/z (%): 326.2 (94.5), 240.1 (3.7), 210.1 (87.9), 153.1 (93.5), 116.1 (100), 86.1 (32.3). Elem. Anal. Calcd. For $C_{17}H_{18}N_4O_3$ (326.36); C, 62.57; H, 5.56; N, 17.17; Found: C, 62.43; H, 5.62; N, 17.32.

3-methyl-1-(4-methylbenzyl)-6-morpholinopyrimidine-2,4(1H,3H)-dione (**2d**)

Yield (53%), m.p:186°C–190°C. yellow powder. ^{1}H-NMR (500 MHz, $CDCl_3$) δ_H (ppm) = 7.10-7.14 (m, 4H, Phenyl), 5.38 (s, 1H, pyrimidine), 5.07 (s, 2H, CH_2), 3.77 (t, 4H, *J* = 4 Hz, morpholine), 3.32 (s, 3H, CH_3-pyrimidine), 2.90 (t, 4H, *J* = 4 Hz, morpholine), 2.33 (s, 3H, CH_3). ^{13}C-NMR (125 MHz, $CDCl_3$) δ_C (ppm) = 163.34, 159.61, 152.83, 137.43, 133.67, 129.46, 126.73, 90.03, 66.14, 51.42, 47.94, 30.19, 29.70, 27.98, 21.11. IR (KBr) v (cm^{-1}): 2921.80 (CH aromatic), 2853.04 (CH aliphatic), 1699.15 (C=O), 1654.08 (C=C), 1448.66 (C-O), 1380.51 (C-N). MS m/z (%): 315.1 (70.7), 210.1 (26.5), 153.1 (22.1), 105.2 (100). Elem. Anal. Calcd. For $C_{17}H_{21}N_3O_3$ (315.37); C, 64.74; H, 6.71; N, 13.32; Found: C, 64.51; H, 6.62; N, 12.97.

1-(4-fluorobenzyl)-3-methyl-6-morpholinopyrimidine-2,4(1H,3H)-dione (**2e**)

Yield (53%), m.p:172°C–175°C. yellow powder. ^{1}H-NMR (500 MHz, $CDCl_3$) δ_H (ppm) = 7.46 (d, 2H, *J* = 8 Hz, Phenyl), 7.11 (d, 2H, *J* = 8 Hz, Phenyl), 5.38 (s, 1H, H_5-Pyrimidine), 5.05 (s, 2H, CH_2), 3.76 (t, 4H, *J* = 4 Hz, morpholine), 3.31 (s, 3H, CH_3), 2.89 (t, 4H, *J* = 4 Hz, morpholine). ^{13}C-NMR (125 MHz, $CDCl_3$) δ_C (ppm) = 163.06, 159.26, 152.76, 135.75, 131.94, 128.56, 121.66, 90.38, 66.10, 51.45, 47.47, 27.99. IR (KBr, cm^{-1}): 2967.41 (CH aromatic), 2918.82–1857.15 (CH aliphatic), 1699.62 (C=O), 1654.51 (C=N), 1507.24 (C=C), 1448.68 (C-O), 1361.68 (C-N), 1160.54(C-F). MS m/z (%): 319.1 (3.5), 227.1 (100), 199.1 (88.5), 109.1 (33.6). Elem. Anal. Calcd. For $C_{16}H_{18}FN_3O_3$ (319.34); C, 60.18; H, 5.68; N, 13.16; Found: C, 60.32; H, 5.83; N, 13.37.

1-(4-bromobenzyl)-3-methyl-6-morpholinopyrimidine-2,4(1H,3H)-dione (**2f**)

Yield (78%), m.p: °C. yellow powder. ^{1}H-NMR (500 MHz, $CDCl_3$) δ_H (ppm) = 7.62 (d, 2H, *J* = 8 Hz, Phenyl), 7.33 (d, 2H, *J* = 8 Hz, Phenyl), 5.40 (s, 1H, H_5-Pyrimidine), 5.14 (s, 2H, CH_2), 3.74 (t, 4H, *J* = 4 Hz, morpholine), 3.30 (s, 3H, CH_3), 2.86 (t, 4H, *J* = 4 Hz, morpholine). ^{13}C-NMR (125 MHz, $CDCl_3$) δ_C (ppm) = 162.90, 159.04, 152.65, 142.15, 127.38, 118.40, 111.70, 90.61, 66.04, 51.45, 47.60, 28.01. IR (KBr, cm^{-1}): 3095.17 (CH aromatic), 2960.05–2852.97 (CH aliphatic), 1696.07 (C=O), 1654.36 (C=N), 1448.17 (C-O), 1358.80 (C-N), 723.91 (C-Br). MS m/z (%): 381.1 (56.0), 210.1 (70.7), 171.0 (100), 153.1 (44.8),. Elem. Anal. Calcd. For $C_{16}H_{18}BrN_3O_3$ (380.24); C, 50.54; H, 4.77; N, 11.05; Found: C, 50.37; H, 4.82; N, 11.35.

3-methyl-6-morpholino-1-(4-(trifluoromethyl) benzyl)pyrimidine-2,4(1H,3H)-dione (**2g**)

Yield (75%), m.p:144°C–150°C. white powder. ^{1}H-NMR (500 MHz, $CDCl_3$) δ_H (ppm) = 7.60 (d, 2H, *J* = 8 Hz, Phenyl), 7.34 (d, 2H, *J* = 8 Hz, Phenyl), 5.40 (s, 1H, pyrimidine), 5.16 (s, 2H, CH_2), 3.76 (t, 4H, *J* = 4 Hz, morpholine), 3.32 (s, 3H, CH_3-pyrimidine), 2.90 (t, 4H, *J* = 4 Hz, morpholine). ^{13}C-NMR (125 MHz, $CDCl_3$) δ_C (ppm) = 162.97, 159.18, 152.72, 140.79, 130.16, 129.84, 127.04, 125.79, 125.27, 122.57, 90.48, 66.07, 51.46, 47.55, 27.99. IR (KBr) v (cm^{-1}): 2981.94 (CH aromatic), 2857.32 (CH aliphatic), 1656.56 (C=O), 1452.00 (C-O), 1370.02 (C-N), 1114.99 (C-F). MS m/z (%): 369.2 (72.3), 210.1 (80.3), 153.1 (100), 159.2 (98.8). Elem. Anal. Calcd. For $C_{17}H_{18}F_3N_3O_3$ (369.34); C, 55.28; H, 4.91; N, 11.38; Found: C, 55.41; H, 5.12; N, 11.56.

3-methyl-6-morpholino-1-(4-nitrobenzyl) pyrimidine-2,4(1H,3H)-dione (**2h**)

Yield (60%), m.p:141°C–146°C. yellow powder. ^{1}H-NMR (500 MHz, $CDCl_3$) δ_H (ppm) = 8.16 (s, 2H, Phenyl), 7.61 (d, 1H, *J* = 8 Hz, Phenyl), 7.54 (t, 1H, *J* = 8 Hz, Phenyl), 5.42 (s, 1H, pyrimidine), 5.18 (s, 2H, CH_2), 3.81 (t, 4H, *J* = 4 Hz, morpholine), 3.30 (s, 3H, CH_3-pyrimidine), 2.92-2,95 (m, 4H, morpholine). ^{13}C-NMR (125 MHz, $CDCl_3$) δ_C (ppm) = 162.83, 158.92, 152.62, 148.42, 138.77, 133.28, 129.92, 122.91, 122.22, 90.95, 66.08, 51.58, 47.04, 29.69, 28.00. IR (KBr) v (cm^{-1}): 2963.56 (CH aromatic), 2854.22 (CH aliphatic), 1658.11 (C=O), 1441.38 (C-O), 1527.77 (O=N=O), 1350.38 (C-N). MS m/z (%): 346.1 (99.2), 210.1 (100), 153.1 (95.8), 136.1 (68.1). Elem. Anal. Calcd. For $C_{16}H_{18}N_4O_5$ (346.34); C, 55.49; H, 5.24; N, 16.18; Found: C, 55.37; H, 5.18; N, 16.34.

Biological evaluations

MTT assay

The MTT assay, which stands for 3-(4,5-Dimethylthiazol-yl)-2,5-Diphenyl-Tetrazolium Bromide, was employed to assess the antiproliferative effects of the synthesized derivatives (**2a-2h**) based on our established methods (Ferlay et al., 2021; Zhu et al., 2024). The cancerous cell lines MCF-7 and SW480 were sourced from the National Cell Bank of Iran (NCBI). Cancer cell lines were cultured in RPMI 1640 media supplemented with 10% fetal bovine serum (FBS) and 1% penicillin-streptomycin (Gibco, USA). Cells were harvested using a 0.5% trypsin/EDTA solution (Gibco, USA). The cells were then plated at a density of 1×10^4 cells per well in 96-well microplates (Zare et al., 2023). Treatment involved five different concentrations of the derivatives and cisplatin (ranging from 1 to 200 μM), with each concentration tested in triplicate. Three wells were left untreated to serve as negative controls. Later than 48 h, the media was replaced with 100 μL of a freshly prepared MTT mixture and incubated for 4 h at 37°C to facilitate for the formation of purple formazan crystals (Ataollahi et al., 2024). The medium was then

discarded, and 150 μL of dimethyl sulfoxide was added to dissolve the crystals, followed by a 10-minute incubation at 37°C in the dark. Absorbance was measured at 490 nm using a microplate ELISA reader. Data analysis was performed using Excel 2016 and Curve Expert 1.4, with results presented as mean ± SD for each analysis (Poustforoosh, 2025).

Apoptosis

A total of 5×10^4 SW480 cells were precultured in 24-well plates in RPMI 1640 culture medium for 16 h under standard culturing conditions. After treating cells with 2.5, 5.0, and 10.0 μM of the **2g** complex, the cells were harvested using 0.25% Trypsin, washed with PBS, and stained with propidium iodide (5 μL, 1 mg/mL), and 1U of RNase A. Cell cycle analysis was performed using flow cytometry (BD FACSCalibur Flow Cytometer, BD, USA). The DNA content was analyzed using FlowJo 10.0 software (Zhao et al., 2024a).

Cell cycle

The total number of 5×10^4 SW480 cells were precultured in 24-well plates in RPMI 1640 culture medium for 16 h under standard culturing conditions. After treating cells with 2.5, 5.0, and 10.0 μM of the **2g** complex, the cells were harvested using 0.25% Trypsin, washed with PBS, and fixed in 70% ethanol for 2 h. The cells were then centrifuged at 4,000 rpm for 2 min. In the next step, cells were permeabilized with 0.2% Triton X-100 for 15 min at 4°C. After centrifugation at 4,000 rpm for 2 min, the cells were resuspended in PBS containing propidium iodide (5 μL, 1 mg/mL) and 1U of RNase A. Cell cycle analysis was performed using flow cytometry (BD FACSCalibur Flow Cytometer, BD, USA). The DNA content was analyzed using FlowJo 10.0 software.

Computational studies

Molecular docking

The crystal structure of Thymidylate synthase (TS) was obtained from the RCSB Protein Data Bank (PDB ID: 1HVY) (Phan et al., 2001). The molecular docking process was carried out using AutoDock Vina. The compounds' structures were energy-minimized and converted to pdbqt format. For the docking analysis, a grid box measuring 40 × 40 × 40 Å and an exhaustiveness setting of 100 were applied. Discovery Studio 2016 was employed to visualize the interactions and orientations of the compounds.

MD studies

The interactions between **2g**, **2h**, and 5-FU and human thymidylate synthase (PDB ID: 1HVY) were further evaluated in a dynamic context. **2g** was the most active compound, **2h** was the compound with the lowest activity, and 5-FU was used as the positive control. Desmond by Schrödinger was used for molecular dynamics (MD) simulation. The complex system obtained from the docking analysis was utilized for the molecular dynamics simulation. The simulation was conducted within an orthorhombic box, and the solvent model used for the simulation was the Transferable Intermolecular Potential with 3 Points (TIP3P). By employing Schrödinger's system setup, the system was successfully neutralized using the precise amount of Na^+/Cl^- ions, which had a salt concentration of 0.15 M (Zhao et al., 2024a). Following the default relaxation protocol of the software, the simulation was carried out for a total of 100 nanoseconds, with the number of atoms, pressure, and temperature held constant in the NPT ensemble. Utilizing the Nose-Hoover thermostat, the temperature was precisely set to 310.15 K (37°C), and the pressure was meticulously adjusted to 1 atm through the implementation of isotropic scaling.

DFT study

Gaussian 09 was employed at the B3LYP/6-31+G** theoretical level to optimize the geometries of **2g** and **2h** without considering symmetry. DFT analyses provided calculations for total energy (Etot), enthalpy (H°), Gibbs free energy (G°), entropy (S), softness (σ), hardness (η), and electron affinity (A) at the B3LYP/6-31+G** level and a temperature of 298K.

Pharmacokinetic profiles

The physicochemical characteristics of all the synthesized compounds were assessed using the online platform http://www.swissadme.ch/, following the guidelines of Lipinski and Veber.

Results and discussion

Chemistry

Eight new pyrimidine-morpholine hybrid compounds were synthesized through a two-step process. First, various benzyl bromides (**1a-1h**) were reacted with 3-methyl-6-chlorouracil in tetrahydrofuran (THF) at 25°C to produce the benzylated pyrimidine intermediates. The ultimate derivatives (**2a-2h**) were obtained by reacting the benzylated pyrimidine with morpholine in a basic reaction system that included triethylamine and potassium carbonate, under reflux conditions for an overnight period. Figure 3 depicts the representation of the synthetic process for these compounds.

In ^{1}H-NMR spectra, the significant piece of compounds **2a-2h** are a single peak belong to the proton of pyrimidine at 5.07–5.18 ppm. Two protons of CH_2 was observed as singlet at 5.38–5.42 ppm. A key characteristic of the 13C NMR spectrum for these compounds is associated with C5 of the pyrimidine ring, which is observed in the range of 90.04–90.95 ppm.

Biological activity

MTT assay

The antiproliferative activity of eight novel pyrimidine-morpholine derivatives (**2a-2h**) were evaluated toward two human cancerous cell lines, SW480 and MCF-7. The results can be found in Figure 4 and Table 1. 5-Fluorouracil (5-FU) and Cisplatin were used as positive controls. The most potent compound was (**2g**), which demonstrated an IC_{50} value of 5.10 ± 2.12 μM, compared to 5-FU (IC_{50} = 4.90 ± 0.83 μM) and Cisplatin (IC_{50} = 16.10 ± 1.10 μM) in the SW480 cell line. Additionally, compounds **2c** and **2e** exhibited significant cytotoxic potential compared to Cisplatin. These pyrimidine-morpholine derivatives

10.3389/fchem.2025.1537261

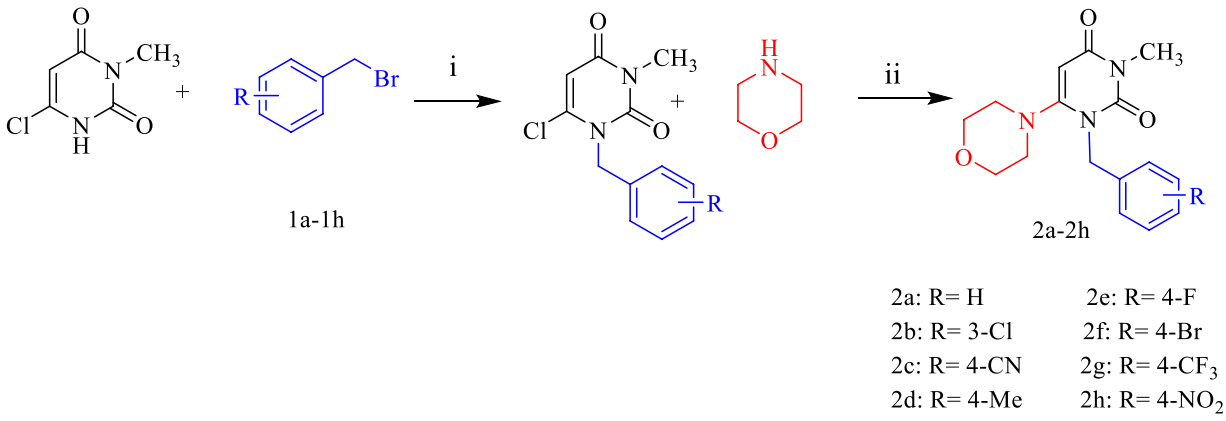


FIGURE 3
The standard reactants and condition for the synthesis of derivatives **2a-2h** are as follows: i: DIPEA in THF for 6 h at 40°C, ii: K_2CO_3/Et_3N in CH_3CN for 24 h under reflux.

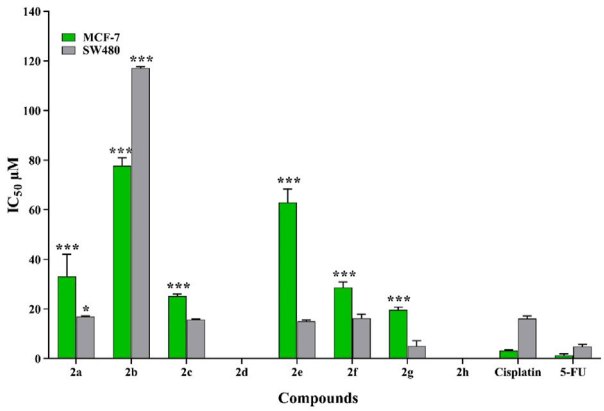
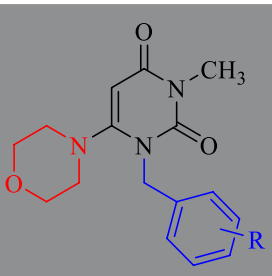


FIGURE 4
The toxic impact of the created pyrimidine-morpholine hybrids on MCF-7 and SW480 cell lines was evaluated in relation to Cisplatin and 5-FU. (*:p value <0.05, **:p value <0.01, ***:p value <0.001).

displayed higher cytotoxic activity in the SW480 cell line than in the MCF-7 cell line.

Structure-activity relationship explained that compound **2g** with CF_3 substituation (electron-withdrawing group) at *para* position of the phenyl ring showed the best cytotoxic effect. Fluorine, bromine and nitrile, as electronegative substitutions on *para* position of the phenyl ring, enhanced the toxic effect, too. The presence the eletrondonating groups in compound (**2d**) led to deteriorate the activity compared to unsubstituted derivative (**2a**). When the 4-NO_2 group was introduced on the benzyl ring, a notable decline in the activity was observed, which may be due to the large size of this functional group. The existance of eletronnegative group at *meta* position resulted in compound **2b**, cause to decrease activity. Taken togather, it was understood that the existence of electron donating substitutions at *para* position and movement the substituation from *para* to *meta* position falling down the potency and the electronnegative groups at the *para* position empowered the cytotoxic activity. These results highlight the significance of electron-withdrawing substitutions in pyrimidine-morpholine compounds for their anticancer activities. Conversely, electron-donating substitutions and substitutions with large sizes were found to decrease the activity.

TABLE 1 Antiproliferative properties of the pyrimidine-morpholine compounds (2a-2h).



Entry	R	IC_{50} ± SD (µM)	
		MCF-7	SW480
2a	H	33.15 ± 8.90	16.90 ± 0.28
2b	3-Cl	77.75 ± 3.18	117.05 ± 0.64
2c	4-CN	25.21 ± 0.85	15.72 ± 0.28
2d	4-Me	>200	>200
2e	4-F	62.90 ± 5.51	15.05 ± 0.49
2f	4-Br	28.65 ± 2.19	16.31 ± 1.56
2g	4-CF_3	19.62 ± 1.13	5.10 ± 2.12
2h	4-NO_2	>200	>200
Cisplatin	—	3.21 ± 0.27	16.10 ± 1.10
5-FU	—	1.30 ± 0.56	4.90 ± 0.83

Apoptosis

Annexin V-Propodium Iodide (PI) double staining technique was used to determine the cell death mechanism. This technique diagnosis four staining pattern: (Av^{neg}/PI^{neg}):viable:, (Av^{pos}/PI^{neg} early apoptotic, (Av^{pos}/PI^{pos}): late apoptotic and (Av^{neg}/PI^{pos}):

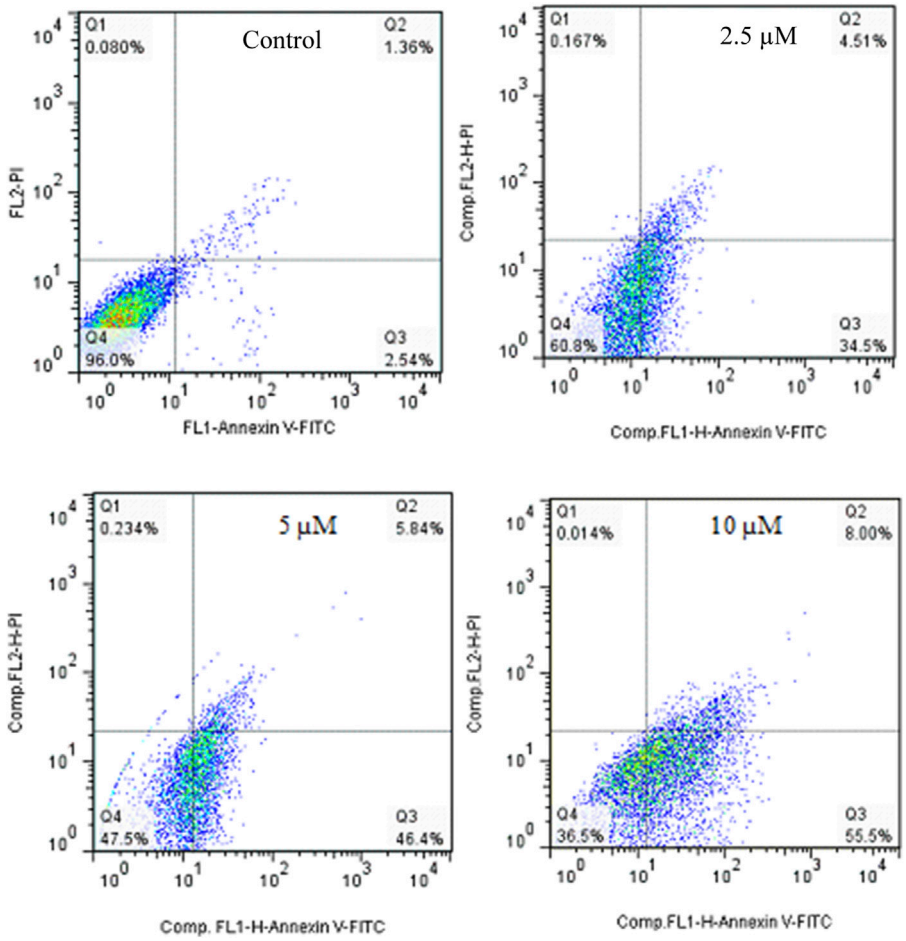


FIGURE 5
Flow cytometric studies of the apoptotic effects of 2g on the SW480 cell line after 72 h of treatment.

necrotic cells. In apoptosis stage, membrane inversion phenomena could cause that phosphatidylserine was moved to the outer membrane and so, deteted with AV-FITC staining. PI was utilized to detect both live and dead cells. The apoptotic potential of compound **2g** on SW480 cells was assessed at three different concentrations (2.5, 5, and 10 µM) following a 72-hour treatment period. The results indicated that **2g** significantly increased the percentage of Annexin V-positive cells from 3.9% to 39.1%, 52.24%, and 63.5%, demonstrating its ability to induce apoptosis in the SW480 cell line in a concentration-dependent modes (Figure 5).

The apoptosis effect of Cisplatin as positive control was performed and is shown in Figure 6. As could be seen, Cisplatin induce apoptosis and increased the percentage of Annexin V-positive cells from 3.99% to 27.35%, 42.58%, and 58.29%. taken together, **2g** could induce apoptosis in lower concetration compared to Cisplatin.

Cell cycle assessment

The cell cycle approach was employed to examine how cells are distributed among various phases (G0, G1, S, G2, M) through flow cytometry. As shown in Figure 7, SW480 cells that were treated with compound **2g** showed a rise in the population of cells in the S-phase, with percentages of 24.41%, 29.34%, and 34.38% after treatment with 2.5, 5 and 10 µM, respectively, compared to untreated cells, which had a percentage of 15.50%. These findings indicate that compound **2g** can induce an arrest in the S-phase (Table 2).

Computational studies

Molecular docking study

Molecular docking research offers a deeper insight into how molecules behave, their binding configurations, and their interactions with receptors. This leads to a more thorough analysis of the biological behavior of the compounds under study (Emami et al., 2024). All synthetic compounds were docked onto the human thymidylate synthase complexed with Raltitrexed (D16) with PDB ID: 1hvy. To determine the orientation of the synthesized compounds and the important amino acids involved in receptor binding, the interactions and positioning of the receptor's internal ligand (D16) and 5-FU were initially examined. The results are presented in Figure 8.

As observed, the compound D16 interacted through hydrogen bonding and π interactions with key residues, namely Lys 77, Phe 80,

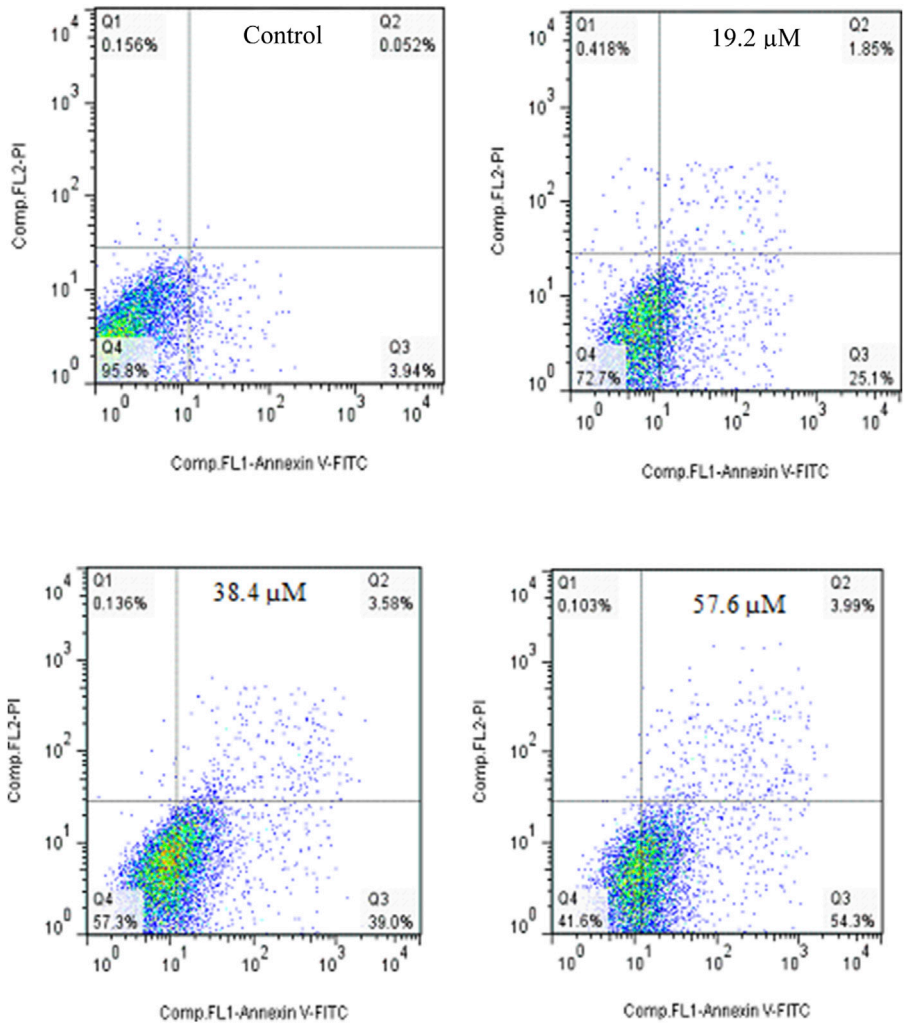


FIGURE 6
Flow cytometric studies of the apoptotic effects of Cisplatin on the SW480 cell line after 72 h of treatment.

Met 311, Gly 222, Phe 226, and Ile 108. Also, for a better interpretation of the docking results of the studied compounds, docking studies were also performed on the current anticancer drug 5-FU. That is located in the binding pocket, interacting with residues such as Ser 216, Gly 217, Gly 222, and Cys 195 through hydrophobic interactions. Additionally, it forms critical hydrogen bonds with residues Asn 226, His 196, Gln 214, and Asp 218.

The interactions and the placement of the most and least active compounds **2g** and **2h** with 1hvy are illustrated in Figure 9. Furthermore, the docking results of all compounds, including the binding energies, hydrogen bonding, and hydrophobic and π interactions, are presented in Supplementary Tables S1, S2, respectively. As expected, compound **2g** has established strong interactions with the receptor and has interacted with most of the key amino acids. The binding energy for **2g** was determined to be −8.6 kcal/mol, significantly higher than the value obtained for 5-FU (−5.2 kcal/mol). In the 2g, the morpholine ring connected to pyrimidine is situated in the binding pocket similarly to compound 5-FU. It interacts with the key amino acids His 196 and Asn 226 through hydrogen bonding. Moreover, it can be seen that most of the interactions of compound **2g** with the receptor occur in the region where the trifluorophenyl substitution is located. This substitution interacts with the amino acids Cys 195, Phe 225, Ile 108, Met 311, and Leu 213 through π interactions.

The binding energy for compound **2h** was determined to be −7.6 kcal/mol, which is the lowest value of the binding energy among all the compounds studied. Figure 9 illustrates that this compound is located in the binding pocket but establishes weak interactions with the receptor 1hvy. Important amino acids Asn 226 and His 196 are positioned around the morpholine ring connected to pyrimidine, but this motif was unable to form strong hydrogen bonds as observed in compound **2g**. Also, the nitrophenyl substitution, which likely played a crucial role in orienting this compound, did not result in the anticipated key interactions. Overall, the docking results are in good agreement with the biological findings.

MD simulation

The ligand-enzyme complex involving three compounds (2g, 2h, and 5-FU) underwent additional assessment through a 100-

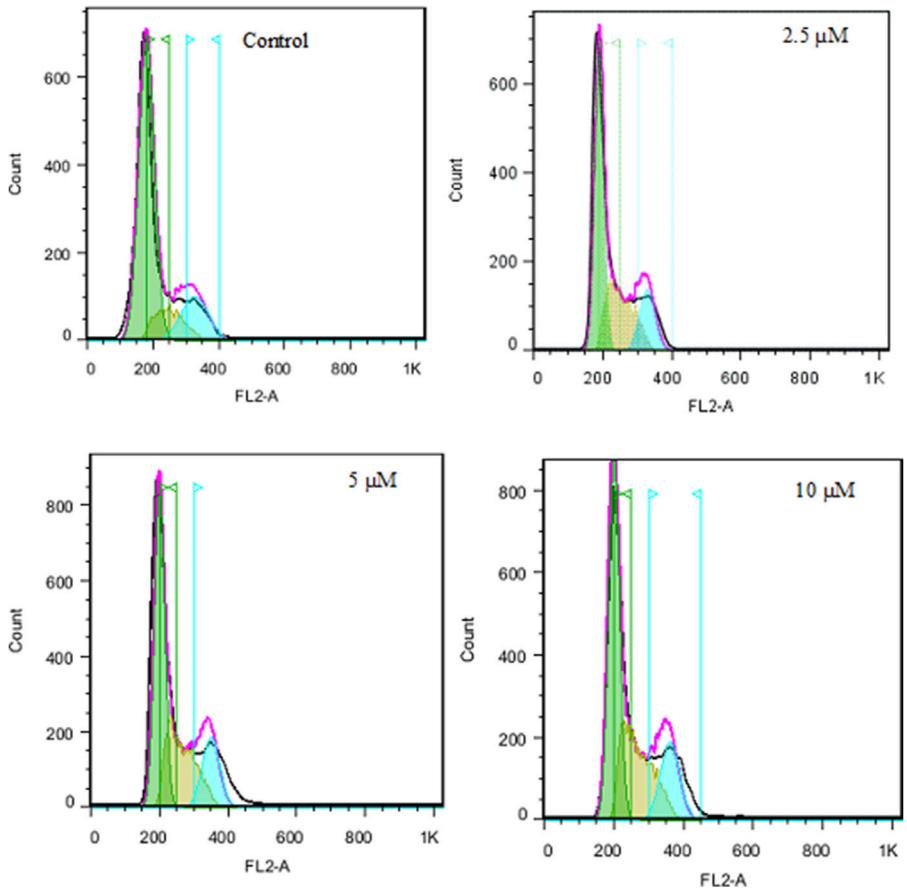


FIGURE 7
The effect of **2g** on cell cycle in SW480 cell line after 72 h treatment.

TABLE 2 The impact of 2g on the cell cycle of the SW480 cell line following a 72-hour treatment period.

Sample		SubG1/G1	S	G2/M	
1	Control	71.94	15.50	12.56	-
4	2.5 µM	58.73	24.41	16.86	Cell cycle arrest at the S phase
3	5 µM	55.08	29.34	15.58	
5	10 µM	48.88	34.38	16.74	

nanosecond MD simulation (Poustforoosh, 2024). Figure 10 displays the RMSD value for the 2g-enzyme complex during the simulation. The RMSD values show variations within a small range of 1.5–2.5 Å, suggesting that the system remained stable throughout the simulation duration.This value is almost the same for 5-fluoropyrimidine. For **2h**, similar to **2g** and 5-FU, the RMSD values fluctuate around 1.5–2 Å, but their variations are smoother compared to **2g** and 5-FU. These values indicate that simulations have reached equilibrium after some time (Kang et al., 2018; Duan et al., 2024; Gao et al., 2023).

Figure 11A shows the interactions that occurred between **2g** and the protein over a duration of 100 ns. The residues that exhibited the most significant interaction fraction are Trp109 and Asn112.Trp 109 is a crucial residue in the active site of thymidylate synthase, regulating its catalytic activity. Therefore, targeting this residue is an effective strategy for enzyme inhibition. Moreover, Tong et al. have shown that Trp109 and Asn112 are two essential residues, and targeting them can be used for enzyme inhibitors. In the case of compound **2h**, the residues exhibiting the highest interaction fraction are Ala312 and His256 (refer to Figure 11B). This observation may elucidate the diminished inhibitory activity of this compound in comparison to **2g**. The main target residues for 5-fluoropyrimidine are Glu87 and Phe225 (Figure 11C). Glu87 is also a crucial residue for targeting and enzyme inhibition.

Another important parameter that needs to be evaluated for the simulation is the percentage of secondary structure elements (SSE), which serves as an indicator of the structural compactness (Tong et al., 2022; Yin et al., 2025; Zhu et al., 2024). This parameter can be

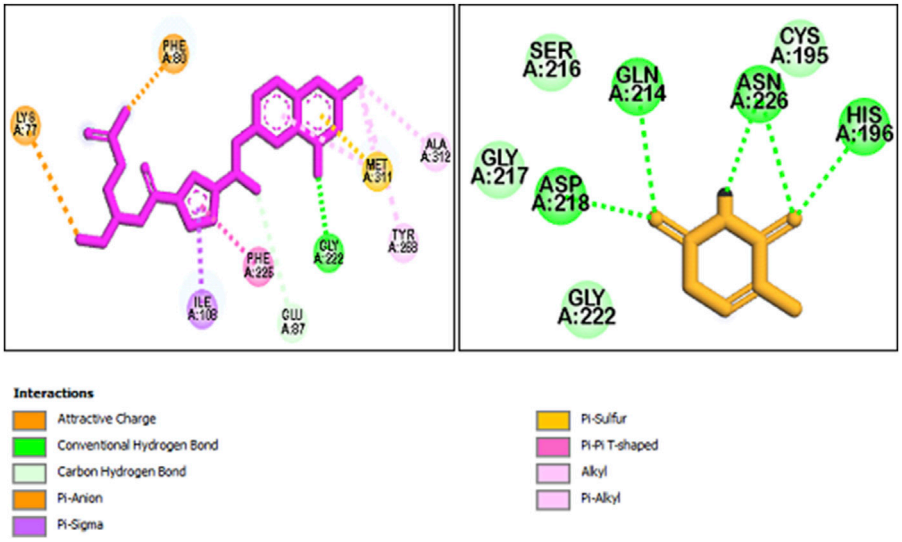


FIGURE 8
The interaction and orientation of internal ligand (D16) and 5-FU in the active site of 1hvy.

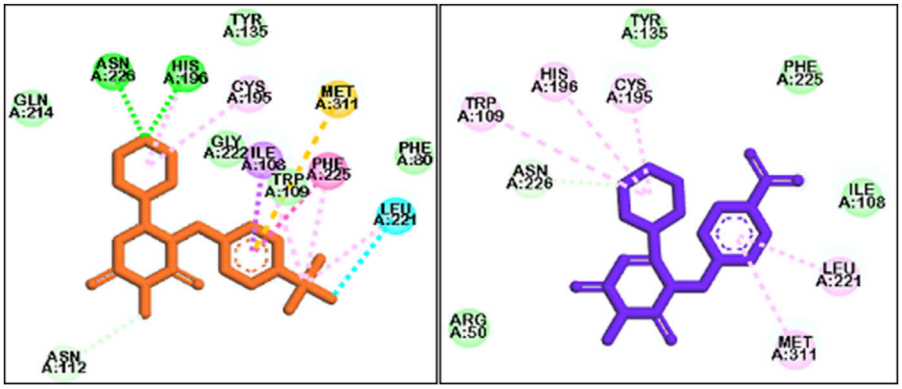


FIGURE 9
The interaction and orientation of **2g** (Red) and **2h** (Blue) in the active site of 1hvy.

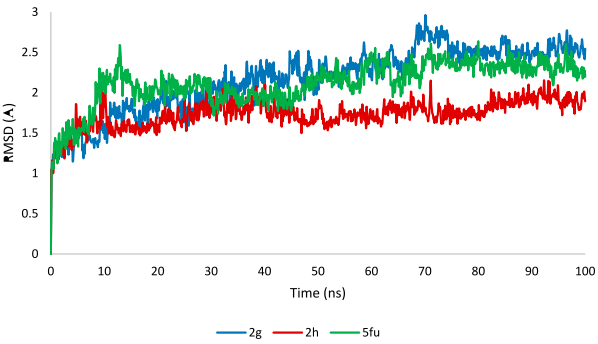


FIGURE 10
The Root Mean Square Deviation (RMSD) values of the enzyme during a 100 ns Molecular Dynamics (MD) simulation for the ligand-enzyme complexes of **2g** (blue), **2h** (red), and 5FU (green).

utilized to evaluate the stability of the protein structure throughout the simulation process (Zhang et al., 2018; Zhao et al., 2024b). The activity of the **2g** -protein complex was evaluated, and it was found to be the most active compound. The protein's alpha-helix structures, indicated by the red zone in Figure 12, and beta strands (colored in blue) exhibited minimal alterations during the simulation. As illustrated in this Figure, the proportion of SSE in the simulation is approximately 45%, a value that has remained consistent throughout the duration of the simulation. This constancy suggests a stable enzyme structure (Poustforoosh, 2025; Li et al., 2024).

DFT analysis

The HOMO and LUMO orbitals for **2g**, **2h**, and **5-FU** are depicted in Figure 13. In **2g**, HOMO is delocalized on morpholine,

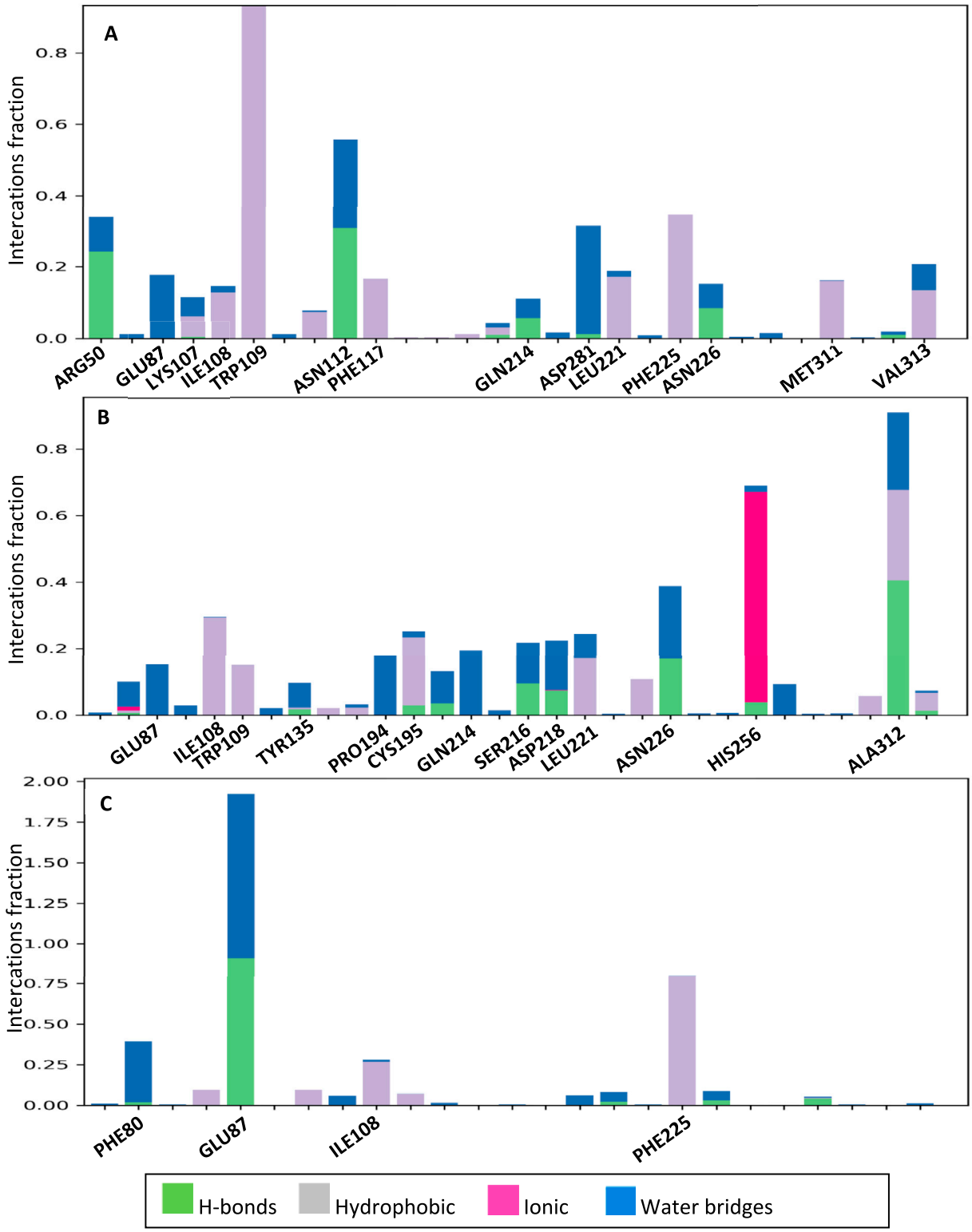


FIGURE 11
The interactions formed between the ligands and proteins during a 100 ns molecular dynamics (MD) simulation for **2g (A)**, **2h (B)**, and 5FU **(C)**.

pyrimidine, and part of triflourophenyl ring, while LUMO is delocalized over the structure of the molecule. For compound 2h, the HOMO orbital is distributed over the morpholine and pyrimidine rings, similar to compound **2g**, while the LUMO orbital is distributed over the nitrophenyl group. For 5-FU, HOMO and LUMO orbitals are delocalized throughout the molecule. The energies of HOMO, LUMO orbitals for **2g**, **2h**, and 5-FU are presented in Figure 13. Thus, the energy gap is

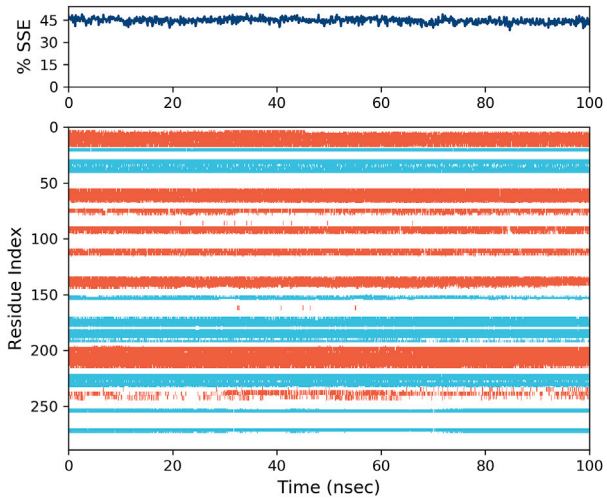


FIGURE 12
The variation in the percentage of secondary structure elements (SSE) for the protein throughout the molecular dynamics (MD) simulation is presented. The regions depicted in red correspond to alpha-helices, while those in blue indicate beta-strands.

calculated as 5.221 eV, 3.753 eV, and 5.387 eV for **2g**, **2h**, and 5-FU, respectively. The energy difference between the HOMO and the LUMO serves as an indicator of the kinetic stability and reactivity of the compounds. In this study, the energy gap order is 5-FU > **2g** > **2h**, indicating that 5-FU is more kinetically stable than **2g**, and consequently, **2g** is more stable than **2h**.

ESP plot for **2g**, **2h**, and 5-FU is indicated in Figure 14, where regions with higher electronegativity are displayed in red, and regions with lower electronegativity are displayed in blue.

Through DFT calculations, valuable insights into structural stability and reactivity can be acquired. By utilizing HOMO and LUMO energies, one can calculate parameters such as hardness (η), softness (s), and electron affinity (A). These parameters provide insights into the interplay among energy, structure, and reactivity characteristics. These parameters, along with total energy (E tot), Gibbs energy (G°), enthalpy (H°), and entropy (S), are provided in Table 3. According to the table, compound **2g** is thermodynamically more stable than **2h** and 5-FU (**2g** > **2h** > 5-FU). A hard molecule has a greater energy gap between HOMO and LUMO and is more resistant to changes in the shape of the electron cloud during chemical reactions. In contrast, a soft molecule has a lower energy gap and is more reactive. Therefore, in this study, the

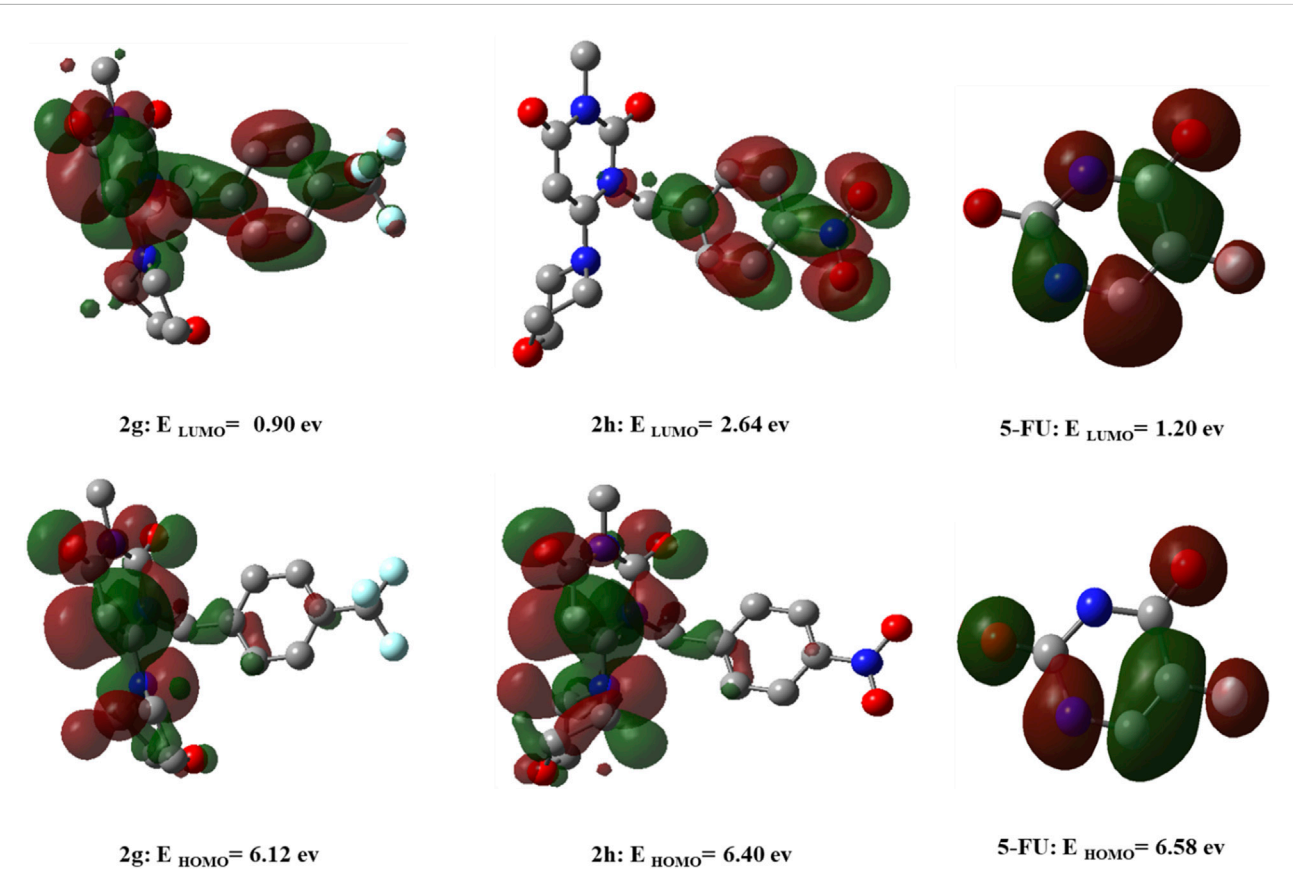


FIGURE 13
DFT calculated LUMO, HOMO, and their corresponding energy values for compounds **2g**, **2h**, and **5-FU** utilizing the B3LYP/6-31+G (d,p) computational method.

10.3389/fchem.2025.1537261

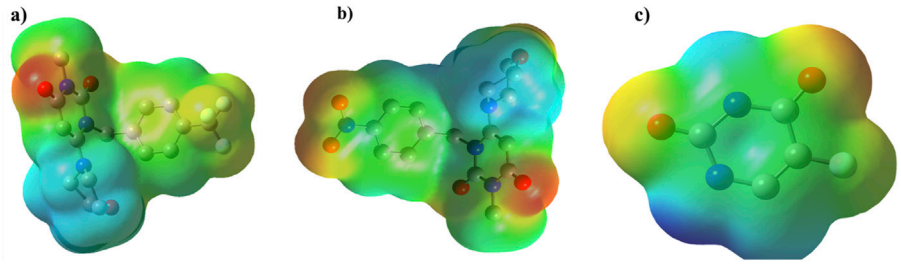


FIGURE 14
The geometry optimization and electrostatic potential (ESP) calculations for compounds **(A)** 2g, **(B)** 2h, and **(C)** 5-fluorouracil (5-FU) using the B3LYP/6-31+G (d,p) level of theory.

TABLE 3 The calculated total energy (E_{tot}), Enthalpy (H), Gibbs free energy (G), hardness (η), softness (σ, and electron affinity (A) of 2a, 2g, and 5-FU at B3LYP/6-31+G(d,p) level of theory.

Entry	E_{tot}[a]	H[a]	G[a]	S[b]	η[c]	σ[d]	A[c]
2g	−1340.379	−1340.378	−1340.456	163.680	2.61	0.38	0.899
2h	−1208.506	−1208.505	−1208.581	160.859	1.87	0.53	2.647
5-FU	−511.124	−511.123	−511.162	82.542	2.70	0.37	1.202

[a]In Hartree/particle.
[b]In cal/mol.K.
[c]In ev.
[d]In ev−1.

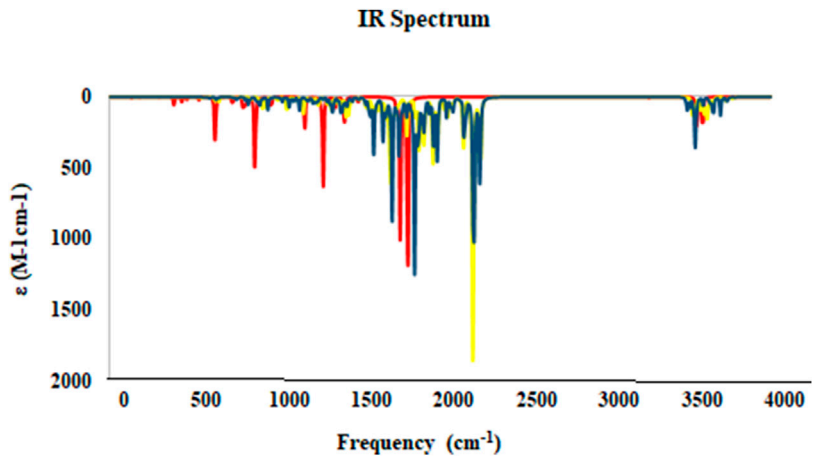


FIGURE 15
The IR Spectrum for studied compounds **2g** (blue), **2h** (yellow), and **5-FU** (red) was calculated at at B3LYP/6-31+G (d,p) level of theory.

order of hardness of compounds is as follows. 5-FU > **2g** > **2h**. Electron affinity is obtained by using the energy value of LUMO. A reduced electron affinity signifies a diminished propensity to attract electrons, which consequently enhances the likelihood of engaging in nucleophilic reactions. The findings indicate that compound **2g** exhibits a greater inclination to partake in nucleophilic reactions in comparison to the other two compounds.

The IR spectra of molecules were obtained through theoretical calculations. The frequencies were determined utilizing the B3LYP/6-311++G (d,p) theoretical framework, as illustrated in Figure 15. The assignment of bands showed C=O stretching vibrations at 1658.11 cm^{-1} (IR), 1696 cm^{-1} (DFT) for **2h**, and 1656.56 cm^{-1} (IR), 1648 cm^{-1} (DFT) for **2g**. The band of O=N=O appeared at 1527.77 cm^{-1} (IR) and 1560 cm^{-1} (DFT) for **2h** and bands of C-F appeared at 1114.99 cm^{-1} (IR) and 1088 cm^{-1} (DFT) for compound **2g**. The stretching modes of C-H aromatic, C-H aliphatic, C-O, and C-N groups have been observed to closely match the frequencies in experimental IR spectra.

TABLE 4 Physicochemical properties of the pyrimidine-morpholine derivatives (2a-2h).

Entry	MW	MLogP	HBD	HBA	n-RB	TPSA (A^2)	Lipinski Violation
2a	301.34	1.29	0	3	3	56.47	0
2b	335.79	1.80	0	3	3	56.47	0
2c	326.35	0.66	0	4	3	80.26	0
2d	315.37	1.54	0	3	3	56.47	0
2e	319.33	1.68	0	4	3	56.47	0
2f	380.24	1.92	0	3	3	56.47	0
2g	369.34	2.16	0	6	4	56.47	0
2h	346.34	0.41	0	5	4	102.29	0
Cisplatin	298.03	—	—	—	0	52.04	—
5-FU	130.08	−0.32	2	3	0	65.72	0
Rule of Lipinski	≤500	≤5	≤5	≤10	≤10	≤140	≤1

TABLE 5 In silico ADME profile of the pyrimidine-morpholin derivatives (*2a-2h*).

Entry	HIA %	Caco2 (nm/sec)	MDCK (nm/sec)	P-gp inhibition	*In vitro* skin permeability (logKp, cm h^{-1})	PPB %	BBB
2a	98.21	30.87	16.47	non	−4.06	45.18	1.10
2b	97.72	37.98	10.64	Inhibitor	−4.11	72.75	1.07
2c	98.20	20.12	16.14	Inhibitor	−4.07	52.03	0.03
2d	98.13	31.31	29.82	Inhibitor	−4.04	59.12	1.36
2e	98.20	43.56	19.71	non	−4.28	64.81	0.14
2f	97.44	43.36	0.30	Inhibitor	−4.01	74.77	0.31
2g	98.11	27.59	0.23	Inhibitor	−2.91	75.20	0.03
2h	92.45	14.03	36.06	Inhibitor	−4.01	59.60	0.02
Cisplatin	93.58	19.88	0.52	non	−4.50	73.45	0.38
5-FU	75.93	17.25	0.68	non	−5.02	8.31	0.20

Pharmacokinetic profiles

In the realm of drug design and discovery, computational methodologies are employed to forecast various properties, including molecular weight, LogP, the count of hydrogen bond acceptors, the count of hydrogen bond donors, the number of rotatable bonds, and the topological polar surface area (TPSA). This measure is implemented to avoid the design and synthesis of compounds that do not adhere to Lipinski's Rule of Five. PreADMET software and the SwissADME online server are valuable tools for predicting the pharmacokinetics and toxicity of designed compounds. These tools can assist researchers in developing drugs that are well-absorbed orally. In this study, the molecular weight of all synthesized compounds was less than 500, the number of hydrogen bond donors (HBD), hydrogen bond acceptors (HBA), and rotatable bonds (n-RB) were all less than 10, and TPSA was less than 140. All compounds meet the Lipinski Rule of Five parameters (Table 4).

Human Intestinal Absorption (HIA) refers to the process by which orally administered drugs are absorbed from the intestine. All compounds tested showed high absorption rates between 92% and 98%, indicating they are well-absorbed and can be taken up by the human intestine. To evaluate a compound's *in vitro* intestinal permeability relative to human enterocytes and to identify transporter and efflux proteins, Caco-2 cell permeability (CCP) is often used as a model. Caco-2 cells are derived from a human colon epithelial cancer line. The compounds tested demonstrated positive permeability in cell culture (CCP), indicating moderate absorption. Madin-Darby canine kidney (MDCK) cells were also used to evaluate the

TABLE 6 Toxicity prediction of the pyrimidine-morpholine derivatives (2a-2h).

Entry	Ames_test	Carcino_Mouse	HERG_Inhibition	Algae_at
2a	Mutagen	Negative	Medium-risk	0.17
2b	Mutagen	Negative	Medium-risk	0.09
2c	Mutagen	Positive	Medium-risk	0.13
2d	Mutagen	Negative	Medium-risk	0.10
2e	Mutagen	Positive	Medium-risk	0.13
2f	Mutagen	Positive	Medium-risk	0.07
2g	Mutagen	Negative	Medium-risk	0.07
2h	Mutagen	Positive	Medium-risk	0.15
Cisplatin	Non-mutagen	Negative	Medium-risk	0.19
5-FU	Mutagen	Positive	Medium-risk	0.43

human intestinal barrier and drug uptake efficiency, with all compounds showing favorable MDCK permeability values ranging from 0.23 to 36.06 nm/s. P-glycoprotein (P-gp) serves as a significant barrier to effective drug delivery by expelling toxins and foreign substances from cells. To enhance the transport of therapeutic agents, inhibiting efflux pumps is necessary. The results indicated that only compounds **2e** and **2a** were not affected by P-gp inhibition. Skin permeability (SP) is an important factor for transdermal drug delivery, as drugs must distribute through the intraepithelial lipid substance, which is the primary feature for skin absorption. All compounds showed negative skin permeability values, suggesting that transdermal administration is not required. Plasma protein binding (PPB) plays a significant role in determining the duration of a drug's presence in the body and may impact its therapeutic effectiveness. The extent of binding to plasma proteins significantly impacts a drug's pharmacodynamic and pharmacokinetic properties, with values below 90% classified as low and those at or above 90% as high. The PPB percentages for all compounds were below 90%. The capacity of therapeutic agents to penetrate the blood-brain barrier (BBB) is a critical factor in evaluating their potential side effects and toxicity. All tested compounds showed positive BBB penetration values, indicating they can cross the barrier, but their values were below 1 (CBrain/Cblood <1), suggesting they are inactive in the central nervous system (CNS) (Table 5).

Toxicity prediction is a crucial aspect of the drug discovery process, as some drug candidates may fail clinical trials due to their toxicity. The toxicity profile of the designed compounds is shown in Table 6. Mutagenicity and carcinogenicity of a compound can be predicted by the Ames test and a 2-year carcinogenicity evaluation in mice. Based on the results of the Ames test, all compounds were mutagenic. The carcinogenicity test on mice showed that compounds **2c**, **2e**, **2f**, and **2h** were carcinogenic, while the rest tested negative and were not carcinogens. The cardiac toxicity was determined using the human ether-a-go-go-related gene, HERG-inhibition assay. The blockage of the HERG leads to fatal ventricular tachyarrhythmia due to the lengthening of the QT interval. All compounds exhibited a moderate risk of HERG inhibition.

Conclusion

A novel series of morpholine-pyrimidine hybrid compounds was created as potential agents to inhibit cell growth and synthesized. The chemical structures were characterized using FT-IR, ^{1}HNMR, and ^{13}CNMR spectroscopy. The antiproliferative effects were evaluated on two human cancerous cell lines, SW480 and MCF-7. When compared to each other and to cisplatin and 5-FU as positive controls, compound 2g demonstrated the highest antiproliferative activity against the SW480 cell line, with an IC_{50} value of (IC_{50} = 5.1 ± 2.12) μM, in contrast to (IC_{50} = 16.1 ± 1.1) μM for Cisplatin and 5-FU, which had an IC_{50} of (IC50 = 4.9 ± 0.83) μM. Structure-activity relationship studies suggest that the presence of a 4-CF_3 group on the phenyl ring and an electron-withdrawing group like cyano on the benzyl part significantly enhances antiproliferative activity. The molecular docking results supported the biological activity findings. Overall, compound **2g** appears to be a propitious candidate for subsequent *in vivo* and *in vitro* anticancer research. Additionally, DFT analysis indicated that compound **2g** is more stable both thermodynamically and kinetically than compound **2h**.

Data availability statement

The original contributions presented in the study are included in the article/Supplementary Material, further inquiries can be directed to the corresponding authors.

Author contributions

EA: Supervision, Writing–review and editing. LE: Supervision, Writing–review and editing. A-AA-D: Investigation, Writing–review and editing. FZ: Investigation, Writing–review

and editing. AP: Investigation, Writing–review and editing. ME: Investigation, Writing–review and editing. FS: Investigation, Writing–original draft. FM: Investigation, Writing–original draft. ZR: Supervision, Writing–original draft. SK: Project administration, Supervision, Writing–review and editing.

Funding

The author(s) declare financial support was received for the research, authorship, and/or publication of this article. Financial assistance from the Shiraz University of Medical Sciences, grant numbers 28632 and 28633 is gratefully acknowledged.

Conflict of interest

The authors declare that the research was conducted in the absence of any commercial or financial relationships that could be construed as a potential conflict of interest.

Generative AI statement

The author(s) declare that no Generative AI was used in the creation of this manuscript.

Publisher's note

All claims expressed in this article are solely those of the authors and do not necessarily represent those of their affiliated organizations, or those of the publisher, the editors and the reviewers. Any product that may be evaluated in this article, or claim that may be made by its manufacturer, is not guaranteed or endorsed by the publisher.

Supplementary material

The Supplementary Material for this article can be found online at: https://www.frontiersin.org/articles/10.3389/fchem.2025.1537261/full#supplementary-material

References

Ataollahi, E., Behrouz, M., Mardaneh, P., Emami, M., zare, S., Zafarian, H., et al. (2024). Novel quinazolinone derivatives as anticancer agents: design, synthesis, biological evaluation and computational studies. *J. Mol. Struct.* 1295, 136622. doi:10.1016/j.molstruc.2023.136622

Bousbaa, H. (2021). Novel anticancer strategies. *Pharmaceutics* 13 (2), 275. doi:10.3390/pharmaceutics13020275

Cardona, G. W., Herrera, R. A., Castrillón, L. W., and Ramírez-Malule, H. (2021). Chemistry and anticancer activity of hybrid molecules and derivatives based on 5-fluorouracil. *Curr. Med. Chem.* 28 (27), 5551–5601. doi:10.2174/0929867328666210211164314

Chirra, N., Shanigarapu, V., Abburi, N. P., Sinegubova, E. O., Pedapati, R. K., Esaulkova, Y. L., et al. (2024). Synthesis and antiviral activity of novel imidazo [2, 1-b] thiazoles coupled with morpholine and thiomorpholines. *J. Heterocycl. Chem.* 61, 496–505. doi:10.1002/jhet.4778

Debela, D. T., Muzazu, S. G., Heraro, K. D., Ndalama, M. T., Mesele, B. W., Haile, D. C., et al. (2021). New approaches and procedures for cancer treatment: current perspectives, *SAGE Open Med.* 9, 20503121211034366.doi:10.1177/20503121211034366

Duan, J.-L., Wang, C.-C., Yuan, Y., Hui, Z., Zhang, H., Mao, N.-D., et al. (2024). Design, synthesis, and structure–activity relationship of novel pyridazinone-based PARP7/HDACs dual inhibitors for elucidating the relationship between antitumor immunity and HDACs inhibition. *J. Med. Chem.* 67 (6), 4950–4976. doi:10.1021/acs.jmedchem.4c00090

Dwivedi, A. R., Kumar, V., Prashar, V., Verma, A., Kumar, N., Parkash, J., et al. (2022). Morpholine substituted quinazoline derivatives as anticancer agents against MCF-7, A549 and SHSY-5Y cancer cell lines and mechanistic studies. *RSC Med. Chem.* 13 (5), 599–609. doi:10.1039/d2md00023g

Emami, L., Zare, F., Khabnadideh, S., Rezaei, Z., Sabahi, Z., Gheshlaghi, S. Z., et al. (2024). Synthesis, design, biological evaluation, and computational analysis of some novel uracil-azole derivatives as cytotoxic agents. *BMC Chem.* 18 (1), 3. doi:10.1186/s13065-023-01106-x

Ferlay, J., Colombet, M., Soerjomataram, I., Parkin, D. M., Piñeros, M., Znaor, A., et al. (2021). Cancer statistics for the year 2020: an overview. *Int. J. cancer* 149 (4), 778–789. doi:10.1002/ijc.33588

Ferrari, S., Severi, L., Pozzi, C., Quotadamo, A., Ponterini, G., Losi, L., et al. (2018). Human thymidylate synthase inhibitors halting ovarian cancer growth. *Vitamins Hormones* 107, 473–513. doi:10.1016/bs.vh.2017.12.002

Gaidai, O., Yan, P., and Xing, Y. (2023). Future world cancer death rate prediction. *Sci. Rep.* 13 (1), 303. doi:10.1038/s41598-023-27547-x

Gao, Y., Duan, J., Dang, X., Yuan, Y., Wang, Y., He, X., et al. (2023). Design, synthesis and biological evaluation of novel histone deacetylase (HDAC) inhibitors derived from *β* -elemene scaffold. *J. Enzyme Inhibition Med. Chem.* 38 (1), 2195991. doi:10.1080/14756366.2023.2195991

Heiran, R., Sepehri, S., Jarrahpour, A., Digiorgio, C., Douafer, H., Brunel, J. M., et al. (2020). Synthesis, docking and evaluation of *in vitro* anti-inflammatory activity of novel morpholine capped β-lactam derivatives. *Bioorg Chem.* 102, 104091. doi:10.1016/j.bioorg.2020.104091

Huang, W. T., Liu, J., Liu, J. F., Hui, L., Ding, Y. L., and Chen, S. W. (2012). Synthesis and biological evaluation of conjugates of deoxypodophyllotoxin and 5-FU as inducer of caspase-3 and -7. *Eur. J. Med. Chem.* 49, 48–54. doi:10.1016/j.ejmech.2011.12.005

Jiang, Y., Li, X., Hou, J., Huang, Y., Jia, Y., Zou, M., et al. (2016). Discovery of BC-01, a novel mutual prodrug (hybrid drug) of ubenimex and fluorouracil as anticancer agent. *Eur. J. Med. Chem.* 121, 649–657. doi:10.1016/j.ejmech.2016.05.068

Jing, R., Jiang, Z., and Tang, X. (2024). Advances in millimeter-wave treatment and its biological effects development. *Int. J. Mol. Sci.* 25 (16), 8638. doi:10.3390/ijms25168638

Kang, L., Gao, X.-H., Liu, H.-R., Men, X., Wu, H.-N., Cui, P.-W., et al. (2018). Structure–activity relationship investigation of coumarin–chalcone hybrids with diverse side-chains as acetylcholinesterase and butyrylcholinesterase inhibitors. *Mol. Divers.* 22, 893–906. doi:10.1007/s11030-018-9839-y

Killock, D. (2021). Copanlisib safe and active in combination. *Nat. Rev. Clin. Oncol.* 18 (6), 322. doi:10.1038/s41571-021-00512-1

Kourounakis, A. P., Xanthopoulos, D., and Tzara, A. (2020). Morpholine as a privileged structure: a review on the medicinal chemistry and pharmacological activity of morpholine containing bioactive molecules. *Med. Res. Rev.* 40 (2), 709–752. doi:10.1002/med.21634

Kumar, P., Mangla, B., Javed, S., Ahsan, W., Musyuni, P., Ahsan, A., et al. (2023). Gefitinib: an updated review of its role in the cancer management, its nanotechnological interventions, recent patents and clinical trials. *Recent Pat. Anti-Cancer Drug Discov.* 18 (4), 448–469. doi:10.2174/1574892818666221026164940

Kumari, A., and Singh, R. K. (2020). Morpholine as ubiquitous pharmacophore in medicinal chemistry: deep insight into the structure-activity relationship (SAR). *Bioorg Chem.* 96, 103578. doi:10.1016/j.bioorg.2020.103578

Li, S., Ling, S., Wang, D., Wang, X., Hao, F., Yin, L., et al. (2024). Modified lentiviral globin gene therapy for pediatric β0/β0 transfusion-dependent β-thalassemia: a single-center, single-arm pilot trial. *Cell Stem Cell* 31, 961–973.e8. doi:10.1016/j.stem.2024.04.021

Lou, J.-S., Zhao, L.-P., Huang, Z.-H., Chen, X.-Y., Xu, J.-T., Tai, W. C.-S., et al. (2021). Ginkgetin derived from Ginkgo biloba leaves enhances the therapeutic effect of cisplatin via ferroptosis-mediated disruption of the Nrf2/HO-1 axis in EGFR wild-type non-small-cell lung cancer. *Phytomedicine* 80, 153370. doi:10.1016/j.phymed.2020.153370

Mao, B., Gao, S., Weng, Y., Zhang, L., and Zhang, L. (2017). Design, synthesis, and biological evaluation of imidazo [1, 2-b] pyridazine derivatives as mTOR inhibitors. *Eur. J. Med. Chem.* 129, 135–150. doi:10.1016/j.ejmech.2017.02.015

Morandini, A., Leonetti, B., Riello, P., Sole, R., Gatto, V., Caligiuri, I., et al. (2021). Synthesis and antimicrobial evaluation of bis-morpholine triazine quaternary ammonium salts. *ChemMedChem* 16 (20), 3172–3176. doi:10.1002/cmdc.202100409

Moreno-Quintero, G., Castrillón-Lopez, W., Herrera-Ramirez, A., Yepes-Pérez, A. F., Quintero-Saumeth, J., and Cardona-Galeano, W. (2022). Synthesis and

chemopreventive potential of 5-fu/genistein hybrids on colorectal cancer cells. *Pharmaceuticals* 15 (10), 1299. doi:10.3390/ph15101299

Phan, J., Koli, S., Minor, W., Dunlap, R. B., Berger, S. H., and Lebioda, L. (2001). Human thymidylate synthase is in the closed conformation when complexed with dUMP and raltitrexed, an antifolate drug. *Biochemistry* 40 (7), 1897–1902. doi:10.1021/bi002413i

Poustforoosh, A. (2024). Scaffold hopping method for design and development of potential allosteric AKT inhibitors. *Mol. Biotechnol.*, 1–15. doi:10.1007/s12033-024-01307-2

Poustforoosh, A. (2025). Optimizing kinase and PARP inhibitor combinations through machine learning and *in silico* approaches for targeted brain cancer therapy. *Mol. Divers.*, 1–11. doi:10.1007/s11030-025-11114-9

Rzepiela, K., Buczek, A., Kupka, T., and Broda, M. A. (2020). Factors governing the chemical stability and NMR parameters of uracil tautomers and its 5-halogen derivatives. *Mol* 25 (17), 3931. doi:10.3390/molecules25173931

Sanduja, M., Gupta, J., and Virmani, T. (2020). Recent advancements in uracil and 5-fluorouracil hybrids as potential anticancer agents: a review. *J. Appl. Pharm. Sci.* 10 (2), 129–146. doi:10.7324/JAPS.2020.102019

Shcherbyna, R., Pruhlo, Y., Duchenko, M., Kulagĩna, M., Kudrĩa, V., and Valentyna, V. (2022). Evaluation of antioxidant activity of 1, 2, 4-triazole derivatives with morpholine moiety. *Hacettepe Univ. J. Fac. Pharm.* 42 (2), 73–82. doi:10.52794/hujpharm.1033112

Siegel, R. L., Miller, K. D., Wagle, N. S., and Jemal, A. (2023). Cancer statistics, 2023. *Ca Cancer J. Clin.* 73 (1), 17–48. doi:10.3322/caac.21763

Soltan, O. M., Shoman, M. E., Abdel-Aziz, S. A., Narumi, A., Konno, H., and Abdel-Aziz, M. (2021). Molecular hybrids: a five-year survey on structures of multiple targeted hybrids of protein kinase inhibitors for cancer therapy. *Eur. J. Med. Chem.* 225, 113768. doi:10.1016/j.ejmech.2021.113768

Song, S., Tian, B., Zhang, M., Gao, X., Jie, L., Liu, P., et al. (2021). Diagnostic and prognostic value of thymidylate synthase expression in breast cancer. *Clin. Exp. Pharmacol. Physiology* 48 (2), 279–287. doi:10.1111/1440-1681.13415

Tong, G., Peng, T., Chen, Y., Sha, L., Dai, H., Xiang, Y., et al. (2022). Effects of GLP-1 receptor agonists on biological behavior of colorectal cancer cells by regulating PI3K/AKT/mTOR signaling pathway. *Front. Pharmacol.* 13, 901559. doi:10.3389/fphar.2022.901559

Tzara, A., Xanthopoulos, D., and Kourounakis, A. P. (2020). Morpholine as a scaffold in medicinal chemistry: an update on synthetic strategies. *ChemMedChem* 15 (5), 392–403. doi:10.1002/cmdc.201900682

Yin, M., Feng, C., Yu, Z., Zhang, Y., Li, Y., Wang, X., et al. (2025). sc2GWAS: a comprehensive platform linking single cell and GWAS traits of human. *Nucleic Acids Res.* 53 (D1), D1151–D1161. doi:10.1093/nar/gkae1008

Zare, S., Emami, L., Behrouz, M., Khankahdani, R. A., Nickpour, S., Emami, M., et al. (2023). 6-Bromoquinazoline derivatives as potent anticancer agents: synthesis, cytotoxic evaluation, and computational studies. *Chem. & Biodivers.* 20 (7), e202201245. doi:10.1002/cbdv.202201245

Zhang, L., Shi, H., Tan, X., Jiang, Z., Wang, P., and Qin, J. (2022). Ten-gram-scale mechanochemical synthesis of ternary lanthanum coordination polymers for antibacterial and antitumor activities. *Front. Chem.* 10, 898324. doi:10.3389/fchem.2022.898324

Zhang, Y.-w., Zheng, X.-w., Liu, Y.-j., Fang, L., Pan, Z.-f., Bao, M.-h., et al. (2018). Effect of oridonin on cytochrome P450 expression and activities in HepaRG cell. *Pharmacology* 101 (5-6), 246–254. doi:10.1159/000486600

Zhao, C., Tang, X., Chen, X., and Jiang, Z. (2024a). Multifaceted carbonized metal–organic frameworks synergize with immune checkpoint inhibitors for precision and augmented cuproptosis cancer therapy. *ACS nano* 18 (27), 17852–17868. doi:10.1021/acsnano.4c04022

Zhao, L., Weng, Y., Zhou, X., and Wu, G. (2024b). Aminoselenation and dehydroaromatization of cyclohexanones with anilines and diselenides. *Org. Lett.* 26, 4835–4839. doi:10.1021/acs.orglett.4c01799

Zhu, J., Jiang, X., Luo, X., Zhao, R., Li, J., Cai, H., et al. (2023). Combination of chemotherapy and gaseous signaling molecular therapy: novel β-elemene nitric oxide donor derivatives against leukemia. *Drug Dev. Res.* 84 (4), 718–735. doi:10.1002/ddr.22051

Zhu, Q., Sun, J., An, C., Li, X., Xu, S., He, Y., et al. (2024). Mechanism of LncRNA Gm2044 in germ cell development. *Front. cell Dev. Biol.* 12, 1410914. doi:10.3389/fcell.2024.1410914

frontiers | Frontiers in Chemistry

TYPE Review
PUBLISHED 03 March 2025
DOI 10.3389/fchem.2025.1545252

Check for updates

OPEN ACCESS

EDITED BY
Jian-Wei Han,
East China University of Science and Technology, China

REVIEWED BY
Premkumar Gnanasekaran,
Tunghai University, Taiwan
Enol López,
University of Valladolid, Spain

*CORRESPONDENCE
Mosstafa Kazemi,
mosstafakazemi@gmail.com
Ramin Javahershenas,
jshbco@yahoo.com

RECEIVED 14 December 2024
ACCEPTED 15 January 2025
PUBLISHED 03 March 2025

CITATION
Sead FF, Jain V, Roopashree R, Kashyap A, Saini S, Chandra Sharma G, Bhakuni PN, Kazemi M and Javahershenas R (2025) Recent achievements in synthesis of anthracene scaffolds catalyzed transition metals. *Front. Chem.* 13:1545252. doi: 10.3389/fchem.2025.1545252

COPYRIGHT
© 2025 Sead, Jain, Roopashree, Kashyap, Saini, Chandra Sharma, Bhakuni, Kazemi and Javahershenas. This is an open-access article distributed under the terms of the Creative Commons Attribution License (CC BY). The use, distribution or reproduction in other forums is permitted, provided the original author(s) and the copyright owner(s) are credited and that the original publication in this journal is cited, in accordance with accepted academic practice. No use, distribution or reproduction is permitted which does not comply with these terms.

Recent achievements in synthesis of anthracene scaffolds catalyzed transition metals

Fadhil Faez Sead[1,2,3], Vicky Jain[4], R. Roopashree[5], Aditya Kashyap[6], Suman Saini[7], Girish Chandra Sharma[8], Pushpa Negi Bhakuni[9,10], Mosstafa Kazemi[11]* and Ramin Javahershenas[12]*

[1]Department of Dentistry, College of Dentistry, The Islamic University, Najaf, Iraq, [2]Department of Medical Analysis, Medical Laboratory Technique College, The Islamic University of Al Diwaniyah, Al Diwaniyah, Iraq, [3]Department of Medical Analysis, Medical Laboratory Technique College, The Islamic University of Babylon, Babylon, Iraq, [4]Marwadi University Research Center, Department of Chemistry, Faculty of Science Marwadi University, Rajkot, Gujarat, India, [5]Department of Chemistry and Biochemistry, School of Sciences, JAIN (Deemed to be University), Bangalore, Karnataka, India, [6]Centre for Research Impact and Outcome, Chitkara University Institute of Engineering and Technology, Chitkara University, Rajpura, Punjab, India, [7]Department of Chemistry, Chandigarh Engineering College, Chandigarh Group of Colleges-Jhanjeri, Punjab, India, [8]Department of Applied Sciences-Chemistry, NIMS Institute of Engineering and Technology, NIMS University Rajasthan, Jaipur, India, [9]Department of Allied Science, Graphic Era Hill University, Bhimtal, Uttarakhand, India, [10]Graphic Era Deemed to be University, Dehradun, Uttarakhand, India, [11]Young Researchers and Elite Club, Islamic Azad University, Tehran, Alborz, Iran, [12]Department of Organic Chemistry, Faculty of Chemistry Urmia University, Urmia, Iran

In the last 10 years, the synthesis of anthracene scaffolds has attracted considerable interest because of their distinctive electronic characteristics and various uses in organic electronics, photovoltaics, and therapeutics. Anthracene, a polycyclic aromatic hydrocarbon, is valued for its lightweight, stability, and electron transport capabilities, making it a key building block in advanced materials. Traditional synthesis methods often face challenges such as low selectivity and harsh conditions. However, recent advancements in transition metal-catalyzed reactions have transformed the field, offering more efficient and versatile approaches. This review examines methodologies utilizing transition metal catalysts like palladium, zinc, indium, cobalt, gold, iridium, rhodium and ruthenium, which have enabled novel synthetic pathways and selective formation of substituted anthracenes through cross-coupling reactions. The function of ligands, including phosphines and N-heterocyclic carbenes, in improving reaction efficiency and selectivity is also examined. The shift towards greener methodologies is noted, with a focus on minimizing waste and reducing toxic reagents. The shift towards greener methodologies is noted, with a focus on minimizing waste and reducing toxic reagents. Several case studies demonstrate the successful application of these techniques, highlighting the structural diversity and functional potential of anthracene derivatives in various applications.

KEYWORDS

anthracene, transition metals (Cr and Fe), synthesis, nanocatalys, catalyst

1 Introduction

The synthesis of anthracene frameworks has become a crucial field of study in organic chemistry, propelled by the compound's distinctive electronic characteristics and its wide-ranging uses in areas such as organic electronics, photovoltaics, and medicinal chemistry. Anthracene, a polycyclic aromatic hydrocarbon (PAH), features a flat structure and excellent electron mobility, positioning it as a prime candidate for the innovation of advanced materials. The growing need for effective and adaptable synthetic methods has led chemists to investigate novel ways to create anthracene derivatives, especially using transition metal catalysis. Initially isolated in the early 1800s, anthracene has attracted considerable interest because of its wide-ranging uses in different domains, such as organic electronics, photovoltaics, and medicinal chemistry (Bass et al., 2024; Aydemir et al., 2023; Shi et al., 2022; Khandaka et al., 2023; Santra et al., 2012; Zhang et al., 2014; Modi et al., 2015).

Anthracene, a tricyclic aromatic hydrocarbon consisting of three fused benzene rings, has long been a subject of fascination for chemists and materials scientists alike. Its unique electronic properties, structural rigidity, and potential for functionalization have positioned anthracene as a crucial building block in various fields, including organic electronics, photovoltaics, and medicinal chemistry. The past decade has witnessed a surge in research focused on developing efficient and versatile methods for synthesizing anthracene scaffolds, driven by the compound's diverse applications and the continuous demand for novel materials with enhanced properties (Kaewpuang et al., 2024; Modi et al., 2015; Climent et al., 2013; Climent et al., 2012).



Mosstafa Kazemi was born in Ilam, Iran. He has received MS degree in organic chemistry from Ilam University in 2013, his Ph.D. degree in organic chemistry from Ilam University in 2018. Dr. Kazemi is interested in the development of novel synthetic methods, nanocatalysts and particularly involving the application of Magnetic nanocatalysts in chemical reactions.



Ramin Javahershenas was born in Urmia, Iran, in 1971. He received his BSc in applied chemistry from Tabriz University, Tabriz, Iran in 1993, his MSc in organic chemistry from Urmia University, Urmia, Iran under the supervision of Professor Naser Ardabilchi in 1999, and his PhD in organic chemistry from Urmia University, Urmia, Iran under the supervision of Professor Jabbar Khalafy in 2017. His research interests canter around organic synthesis and include heterocyclic synthesis, asymmetric synthesis, natural products synthesis, synthetic methodology, and applications of various catalysts in multicomponent reactions.

Traditional synthetic methods for anthracene derivatives often face significant limitations, including low selectivity, harsh reaction conditions, and lengthy reaction times. These challenges have necessitated the development of more efficient strategies that can overcome these obstacles while maintaining high yields and selectivity. Recent advancements in transition metal-catalyzed reactions have revolutionized the field, providing chemists with powerful tools to construct anthracene frameworks with unprecedented efficiency and versatility.

Historically, traditional methods for synthesizing anthracene derivatives have been fraught with challenges, including low selectivity, harsh reaction conditions, and extended reaction times. These limitations have spurred the scientific community to explore more efficient and versatile synthetic strategies.

In recent years, transition metal-catalyzed reactions have revolutionized the synthesis of anthracene scaffolds, offering novel pathways that enhance both efficiency and selectivity. Traditionally, the synthesis of anthracene and its derivatives relied on classical organic reactions, such as Diels-Alder cycloadditions, Friedel-Crafts acylations, and oxidative photocyclization. While these methods have proven effective, they often suffer from limitations including low selectivity, harsh reaction conditions, and extended reaction times. Moreover, the increasing emphasis on sustainable chemistry has necessitated the development of more environmentally friendly synthetic approaches (Zhang et al., 2017; Anastas and Warner, 1998; Noyori, 2013; Anastas and Kirchhoff, 2002; Suzuki, 2011).

Transition metals, such as palladium, platinum, nickel, and copper, have been extensively utilized as catalysts in various cross-coupling reactions, including Suzuki-Miyaura, Sonogashira, and Negishi coupling. These methodologies have enabled the selective formation of substituted anthracenes, allowing for the introduction of diverse functional groups that enhance the properties of the resulting materials (Hartwig, 2008; Suzuki and Company, 2011; Jacobsen et al., 2010; Wencel-Delord et al., 2012).

The integration of these coupling strategies with other synthetic methodologies, such as cyclization and functionalization, has led to the discovery of previously inaccessible anthracene derivatives, expanding the scope of anthracene chemistry. This integration underscores the versatility of transition metal catalysis in expanding the structural diversity and functional capabilities of anthracene-based materials. The role of ligands in transition metal-catalyzed reactions cannot be overstated. Ligands play a crucial role in modulating the reactivity and selectivity of metal catalysts, influencing the overall efficiency of the synthetic process. Innovative ligand systems, including phosphines and N-heterocyclic carbenes (NHCs), have been developed to optimize catalytic performance, enabling the formation of complex anthracene structures under milder conditions. A critical aspect of these catalytic processes is the role of ligands, which are pivotal in enhancing reaction efficiency and selectivity (Hartwig, 2010; Beller and Bolm, 2004; Negishi, 2002).

Moreover, the environmental implications of these synthetic strategies cannot be overlooked. The shift towards greener methodologies that minimize waste and reduce reliance on toxic reagents is a significant trend in contemporary organic synthesis. This aligns with the broader goals of sustainable chemistry, aiming to reduce the environmental footprint of chemical processes while maintaining high efficiency and selectivity. Several case studies exemplify the successful application of transition metal catalysis in the synthesis of anthracene scaffolds. These examples not only highlight the structural diversity and functional prowess of the resulting anthracene derivatives but also demonstrate their potential in applications ranging from light-emitting diodes to

sensor technologies (Crabtree, 2009; Colacot, 2015; Johansson Seechurn et al., 2012).

In recent years, the field of anthracene synthesis has undergone a paradigm shift with the advent of transition metal-catalyzed reactions. These methodologies have opened up new avenues for constructing complex anthracene scaffolds with unprecedented efficiency and selectivity. The use of transition metals as catalysts has not only expanded the synthetic toolkit available to chemists but has also enabled the creation of previously inaccessible anthracene derivatives. The use of transition metal catalysis in organic synthesis has transformed the field, providing effective methods for creating carbon-heteroatom bonds, and carbon-carbon (Tsuji, 2005; Trost and Crawley, 2003).

In the context of anthracene synthesis, transition metals such as platinum, nickel, palladium, and copper have emerged as particularly effective catalysts. These metals enable a variety of transformations, such as cross-coupling reactions, cyclizations, and C-H activations, which are essential for building the anthracene core and adding different functionalities. In addition to enhancing synthetic efficiency, the environmental implications of these methodologies have gained increasing attention. The shift towards greener synthetic strategies that minimize waste and reduce the reliance on toxic reagents is a critical consideration in contemporary organic synthesis. Recent advancements in transition metal-catalyzed reactions have demonstrated the potential for developing sustainable methodologies that align with the principles of green chemistry, thereby addressing the environmental challenges associated with traditional synthetic approaches (Molnár, 2013; van Leeuwen, 2004).

2 Chemical structure and properties

2.1 Chemistry

Anthracene is a polycyclic aromatic hydrocarbon (PAH) made up of three interconnected benzene rings set in a linear arrangement. Anthracene has a planar structure, its chemical formula is $C_{14}H_{10}$, which allows for effective π-π stacking interactions between molecules. This planarity contributes to its electronic properties and stability. The three benzene rings are fused together, sharing two carbon atoms at each junction. This leads to a continuous conjugated system that improves its capacity to conduct electricity and absorb light. Anthracene's carbon atoms are sp^2 hybridized, creating a network of double bonds (C=C) and single bonds (C-C). The resonance structure generated by the alternating double bonds enhances the molecule's stability. Anthracene can undergo various chemical reactions, allowing for the introduction of substituents at different positions on the rings. This functionalization can modify its properties and expand its applications (Clar, 1964; Guo et al., 2018; Salam et al., 2014; Alonso et al., 2010).

The key properties of anthracene include:

- Planarity and Conjugation: The planar structure of anthracene allows for effective π-π stacking interactions, which are crucial for its performance in various applications. The extended conjugation across the three benzene rings results in a relatively low energy gap between the highest occupied molecular orbital (HOMO) and the lowest unoccupied molecular orbital (LUMO).
- Optical Properties: Anthracene shows significant absorption in the ultraviolet-visible (UV-Vis) spectrum, peaking at a wavelength of approximately 254 nm. Its high fluorescence quantum yield makes it a superb candidate for light-emitting applications.
- Thermal Stability: Anthracene is thermally stable up to approximately 300°C, which allows it to maintain its structural integrity under various processing conditions.
- Solubility: Anthracene dissolves in organic solvents like benzene, toluene, and chloroform, but its solubility in water is restricted. This property is essential for its operation in organic electronic devices.

The extended π-conjugation in anthracene leads to a relatively low energy gap between the HOMO and LUMO, facilitating efficient absorption and emission of light. This property is crucial for its applications in optoelectronic devices (Park et al., 2008).

2.2 Reactions pathways and parameters

Among the most widely employed strategies in transition metal-catalyzed anthracene synthesis are cross-coupling reactions. The Suzuki-Miyaura coupling, catalyzed primarily by palladium complexes, has proven exceptionally versatile in forming biaryl bonds, a key step in assembling the anthracene framework (Baviera and Donate, 2021; Robertson, 1930; Menendez et al., 2014).

Similarly, the Sonogashira coupling, which involves the palladium-catalyzed coupling of terminal alkynes with aryl or vinyl halides, has been instrumental in synthesizing alkynylated anthracene precursors. These intermediates can subsequently undergo cyclization to form the desired anthracene scaffolds (Oliveira et al., 2020; Zehm et al., 2008).

Another significant advancement in anthracene synthesis is the development of C-H activation methodologies. These approaches allow for the direct functionalization of C-H bonds, bypassing the need for pre-functionalized starting materials. Transition metals, particularly palladium and rhodium, have shown remarkable activity in catalyzing such transformations (Becker, 1993; Yoshizawa and Klosterman, 2014; Kastrati et al., 2023).

The success of transition metal-catalyzed reactions in anthracene synthesis is intrinsically linked to the design and selection of appropriate ligands. Ligands play a crucial role in modulating the reactivity and selectivity of the metal catalyst, often determining the outcome of the reaction. Recent years have seen significant advancements in ligand design, with a focus on developing systems that enhance catalytic performance while allowing for milder reaction conditions (Zarren et al., 2019; Floyd et al., 1976; Harvey, 2004).

Phosphine ligands have long been staples in transition metal catalysis, and their application in anthracene synthesis is no exception. The electronic and steric properties of phosphines can be finely tuned, allowing for optimization of catalyst activity and selectivity. For instance, the use of bulky, electron-rich phosphines such as SPhos and XPhos in Suzuki couplings has enabled the

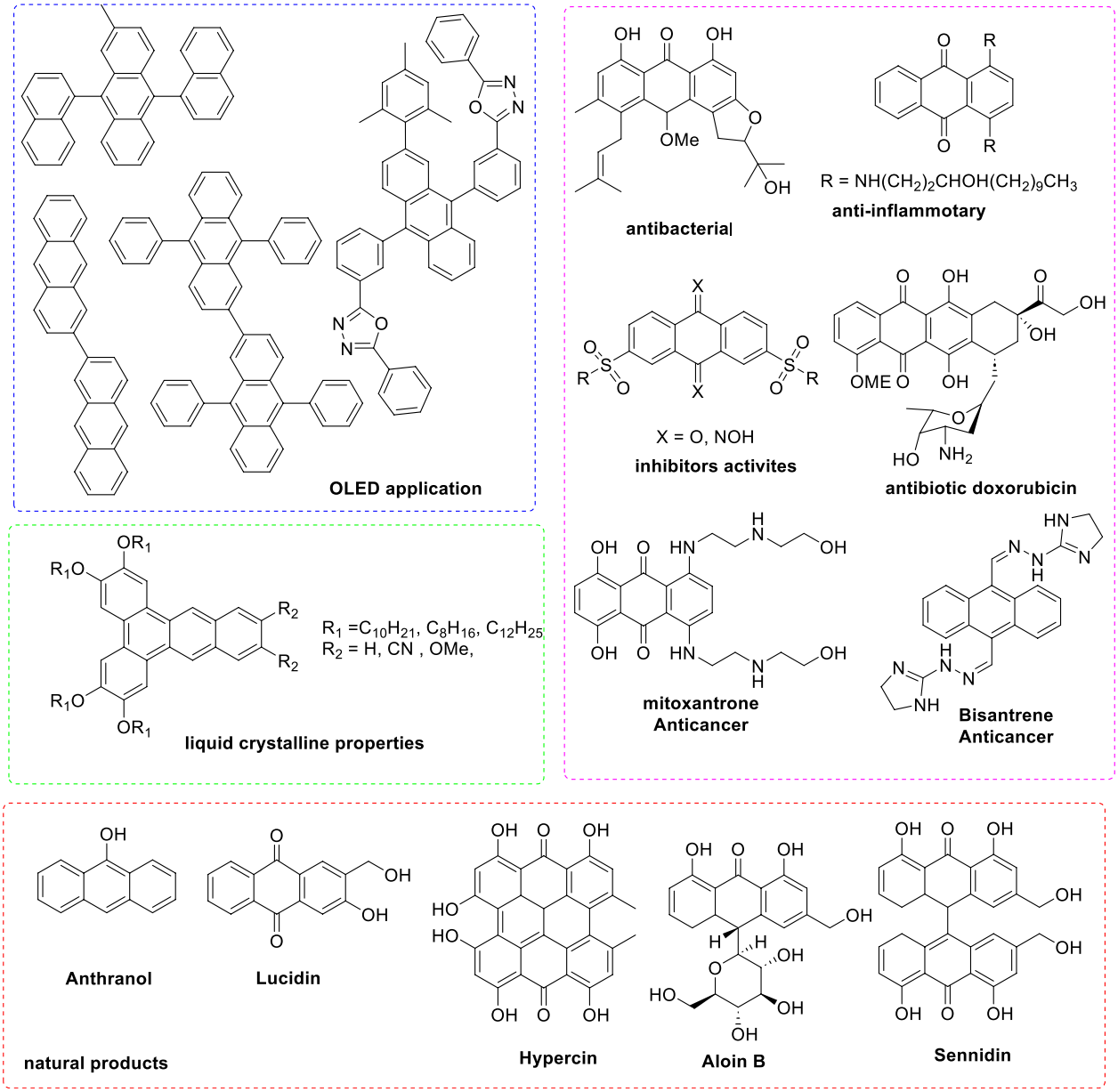


FIGURE 1
Some of anthracene derivatives.

efficient synthesis of sterically hindered anthracene derivatives (Burrell et al., 2001; Han et al., 2023).

N-Heterocyclic carbenes (NHCs) have emerged as powerful alternatives to phosphine ligands in many catalytic systems. Their strong σ-donating properties and unique steric characteristics often result in catalysts with enhanced stability and activity. In the context of anthracene synthesis, NHC-ligated palladium complexes have shown exceptional performance in challenging cross-coupling reactions (Du C.-B. et al., 2024; Fan et al., 2024).

As the field of anthracene synthesis advances, there is an increasing emphasis on developing methodologies that align with the principles of green chemistry. This shift is driven by both environmental concerns and regulatory pressures, pushing researchers to design more sustainable synthetic routes (Bass et al., 2024; Anastas and Warner, 1998; Anastas and Kirchhoff, 2002; Anastas and Kirchhoff, 2002; Zehm et al., 2008).

One approach to enhancing the sustainability of transition metal-catalyzed anthracene synthesis is the development of recyclable catalyst systems. Heterogeneous catalysts, in particular, offer the advantage of easy separation and potential reuse (Zhao et al., 2023; Khan, 2024).

The exploration of alternative reaction media, such as water or ionic liquids, represents another avenue for making anthracene synthesis more environmentally friendly. These systems can potentially reduce the use of volatile organic solvents and improve reaction efficiency (Malik and Müller, 2016; Zhu and Zhu, 2013).

2.3 Applications and future directions

The recent achievements in transition metal-catalyzed synthesis of anthracene scaffolds have not only expanded the synthetic toolkit but have also opened up new possibilities for applications. The ability to access structurally diverse and highly functionalized anthracenes has implications across various fields (Figure 1) (Wang et al., 2012; Vorona et al., 2019).

In the realm of organic electronics, anthracene derivatives synthesized through these novel methods have shown promise as materials for organic field-effect transistors (OFETs) and organic light-emitting diodes (OLEDs). The work of Wang *et al.* demonstrates how tailored anthracene scaffolds, synthesized via palladium-catalysed methods, can be utilized to create high-performance blue OLEDs (Zhang et al., 2019; Khan et al., 2023).

Anthracene's planar structure allows for effective π-π stacking interactions, which are crucial for its performance in electronic applications. The compound exhibits strong absorption in the ultraviolet-visible (UV-Vis) region, making it an excellent candidate for light-absorbing materials. Its high electron mobility and stability further enhance its utility in organic semiconductor devices. In OLEDs, anthracene derivatives are often used as emissive materials due to their ability to emit light efficiently when excited by an electric current. The incorporation of anthracene into OLEDs has led to the development of devices with improved brightness and colour purity, making them suitable for displays and lighting applications (Becker, 1993; Ihmels et al., 2000; Abou-Hatab et al., 2017).

In OFETs, anthracene serves as a semiconductor material, where its high charge carrier mobility contributes to enhanced device performance. The ability to tune the electronic properties of anthracene through chemical modifications allows for the design of materials that meet specific performance criteria, further driving advancements in organic electronics (Pozzo et al., 2001; Huang et al., 2012).

Anthracene's unique properties have led to its widespread use in various fields, including:

2.3.1 Organic electronics

In organic electronics, anthracene is valued for its high charge carrier stability and mobility. These properties make it an ideal candidate for use in (Chen et al., 2018; Van Damme and Du Prez, 2018; Fang et al., 2017):

- Organic Light-Emitting Diodes (OLEDs): Anthracene derivatives are employed as emissive materials due to their ability to emit light efficiently when excited by an electric current. The incorporation of anthracene in OLEDs enhances brightness and colour purity, making them suitable for lighting and display applications.
- Organic Field-Effect Transistors (OFETs): Anthracene serves as a semiconductor material, where its high charge carrier mobility contributes to improved device performance. The ability to chemically modify anthracene allows for the design of materials that meet specific performance criteria.

2.3.2 Photonics

Anthracene's strong absorption in the ultraviolet-visible (UV-Vis) region and its ability to emit light make it a valuable material in photonics (Kivrak et al., 2017; Zhao et al., 2017; Khazaei et al., 2015). Applications include:

- Light-Emitting Materials: Anthracene derivatives are used in the development of materials that emit light in various colours, essential for creating efficient and tuneable light sources.
- Sensors: The photophysical properties of anthracene enable its use in sensors for detecting environmental pollutants and biological molecules. The fluorescence of anthracene can be quenched or enhanced in the presence of specific analytes, allowing for sensitive detection.

The pharmaceutical industry has also benefited from these advancements. The ability to rapidly generate libraries of functionalized anthracenes has accelerated drug discovery efforts. In medicinal chemistry, anthracene and its derivatives have shown significant potential as therapeutic agents: (Brabec et al., 2011; Hurley, 2002; Ho et al., 2007; Wu et al., 2014; Okumoto et al., 2006; Ito et al., 2003; Kouam et al., 2007; Corrêa et al., 2013; Soldi et al., 2015; Lown, 1988; Venitt et al., 1998; Iyengar et al., 1997).

- Anticancer Agents: Certain anthracene derivatives have demonstrated the ability to intercalate with DNA, disrupting cellular processes and exhibiting anticancer activity. Research has focused on synthesizing novel anthracene-based compounds with enhanced efficacy against various cancer types.
- Antimicrobial and Anti-inflammatory Properties: Anthracene derivatives have also been investigated for their antimicrobial and anti-inflammatory activities. These properties make them promising candidates for developing new drugs to combat infections and inflammatory diseases.
- Drug Delivery Systems: The unique properties of anthracene allow for its incorporation into drug delivery systems, where it can enhance the solubility and bioavailability of therapeutic agents.

Anthracene's unique properties and versatility have established it as a critical compound in various scientific and industrial fields. Its role in organic electronics, photonics, and medicinal chemistry underscores its importance and potential for future innovations. Continued research and development of anthracene derivatives are expected to further expand its applications and enhance its contributions to technology and healthcare.

3 Transition metal catalysis

Over the last few decades, transition metal catalysis has transformed organic synthesis, allowing for the synthesis of new and efficient methods to build intricate molecular structures. The unique electronic properties and diverse coordination geometries of transition metals make them exceptionally versatile catalysts, capable of mediating a wide range of chemical transformations with high selectivity and efficiency. Transition metals, particularly

those in the d-block of the periodic table, possess partially filled d-orbitals that allow them to form stable complexes with organic molecules. This ability to coordinate with various ligands and substrates is fundamental to their catalytic activity. Chemists can adjust the oxidation state and coordination environment of the metal centre to fine-tune the reactivity and selectivity of these catalysts, frequently accomplishing transformations that would be difficult or unfeasible with conventional organic reagents (Heravi et al., 2021; Dandia et al., 2015; Inamdar et al., 2013; Khatun et al., 2014; Iordanidou et al., 2018; Saha et al., 2009; Hussain et al., 2017; Kumar et al., 2014).

The significance of transition metal catalysis in organic synthesis is immense. From the advancement of palladium-catalyzed cross-coupling reactions, awarded the 2010 Nobel Prize in Chemistry, to the latest progress in gold catalysis and photoredox catalysis, transition metals persist in propelling innovation in synthetic methods. As research in this field progresses, new catalysts and reactions are constantly being discovered, further expanding the boundaries of what is possible in organic synthesis. Transition metals have emerged as pivotal catalysts in organic synthesis, revolutionizing the way complex molecules are constructed. These metals, including palladium, platinum, nickel, and copper, possess unique electronic properties that enable them to facilitate a wide range of chemical transformations. Transition metals can assume different oxidation states and create stable complexes with a variety of ligands, which increases their reactivity and selectivity in catalytic reactions (Parte et al., 2024; Albaladejo et al., 2013; Sadeghzadeh, 2016; Baghbanian, 2014; Kidwai et al., 2012; Reddy and Jeong, 2016; Balwe et al., 2017; Khafaei et al., 2021; Lak et al., 2021; Sabernezhad, 2021; Du Y. et al., 2024).

The use of transition metals in catalysis offers several advantages over traditional methods. Firstly, transition metal catalysts often exhibit high activity, enabling reactions to proceed under milder conditions and with shorter reaction times. This efficiency not only reduces energy consumption but also minimizes the formation of by-products, leading to cleaner reactions. For example, palladium-catalysed cross-coupling reactions, including the Suzuki and Heck reactions, have become established techniques for creating carbon-carbon bonds in organic synthesis, enabling the swift construction of intricate molecular structures (Farokhian et al., 2021; Bakhshi et al., 2021; Amjadian et al., 2021; Kahrizi et al., 2021; Rabbani and Safdary, 2021; Sead et al., 2025; Asadi and Jalilian, 2021; Mahboub Khomami et al., 2021; Zeidali et al., 2021).

Secondly, transition metal catalysts can provide exceptional selectivity, enabling the formation of specific products in the presence of multiple functional groups. This selectivity is particularly valuable in the synthesis of pharmaceuticals and agrochemicals, where the precise control of stereochemistry and functionalization is crucial. The development of chiral transition metal catalysts has further expanded the scope of asymmetric synthesis, allowing for the production of enantiomerically pure compounds (Jalali Sarvestani and Charehjou, 2021; Saffariha et al., 2021; Hassanpour, 2021; Jalilian, 2020).

Moreover, the versatility of transition metal catalysts extends to their ability to catalyse a diverse array of reactions, including oxidation, reduction, and C–H activation. This broad applicability makes them indispensable tools in modern organic synthesis. As research continues to advance, the design and optimization of transition metal catalysts are expected to yield even more efficient and sustainable synthetic methodologies (Rasouli et al., 2020; Ali et al., 2020a; Ali et al., 2020b; Bhattacharjee et al., 2018; Noyori, 2013).

3.1 Challenges and limitations

Despite the challenges, significant progress has been made in the synthesis of anthracene scaffolds using transition metal catalysis. While transition metal catalysis has significantly advanced the field of organic synthesis, several limitations and challenges of Existing Methodologies persist (Sead, 2025; El-Remailya and Hamad, 2015; Nguyen et al., 2019; Naeimi and Didar, 2017; Bullock, 2013).

These limitations and challenges can be classified into six primary categories: (1) the development of new catalysts; (2) environmental and safety concerns; (3) reactivity and selectivity issues; (4) ligand design and optimization; (5) metal residue and purity; and (6) cost and availability.

3.2 Future directions

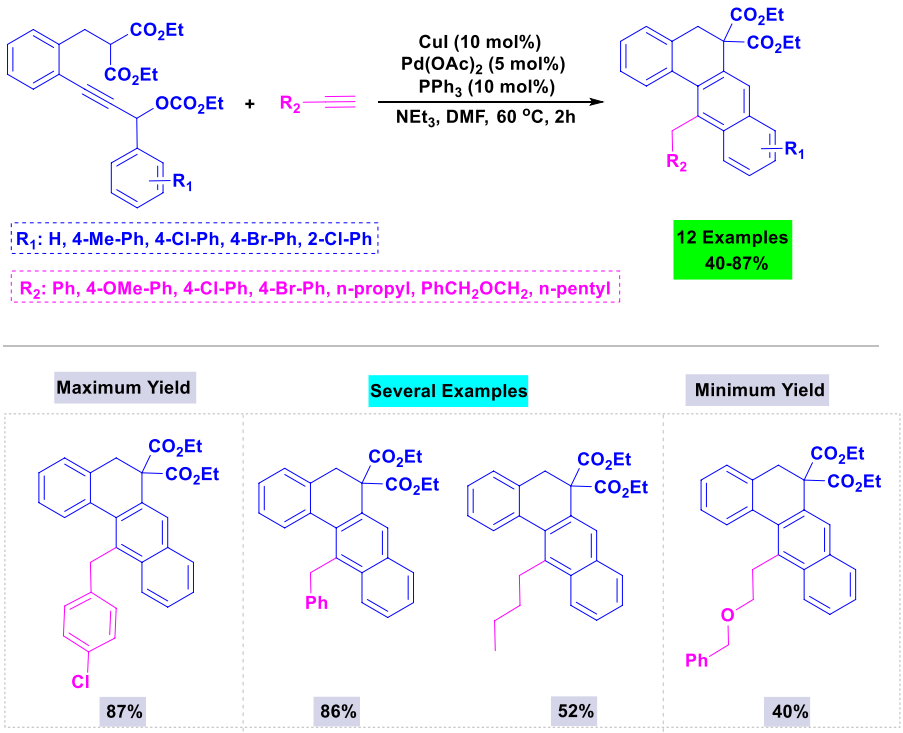
The synthesis of anthracene scaffolds catalyzed by transition metals continues to evolve, driven by the need for more efficient, selective, and sustainable methodologies. While challenges remain, recent achievements in catalyst development, C–H activation, and cross-coupling reactions have expanded the synthetic toolbox available to chemists. Future research will likely focus on further optimizing these processes, exploring new catalytic systems, and integrating emerging technologies to address the limitations of existing methodologies. Although, the use of transition metals as catalysts in organic synthesis offers numerous advantages that have transformed the landscape of chemical manufacturing. Their catalytic efficiency, selectivity, versatility, and sustainability make them indispensable tools for chemists seeking to develop innovative and efficient synthetic methodologies. As research in this field continues to advance, the discovery of new transition metal catalysts and the optimization of existing ones will undoubtedly lead to further breakthroughs in organic synthesis (Trost, 1991; Bauer and Knölker, 2015; Prier et al., 2013; Sheldon et al., 2007; Ren et al., 2009).

4 Metal catalyzed synthesis of anthracene derivatives

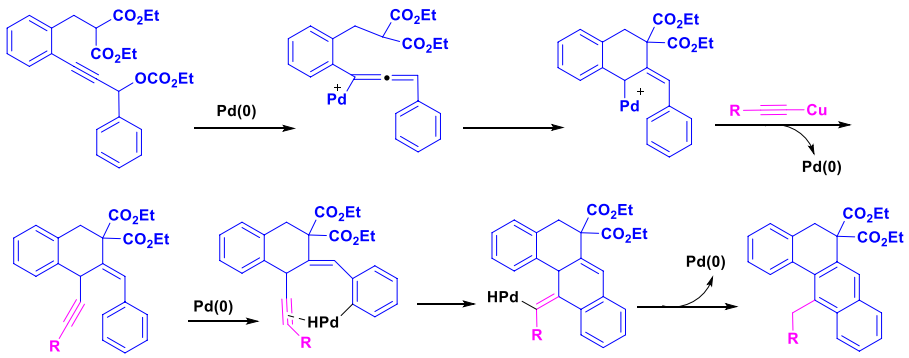
In recent times, many publications have reported in the literature for the synthesis of anthracene derivatives based on using metal complexes as the catalyst. The present review focuses on the recent developments in the metal catalyzed syntheses of anthracene scaffolds.

4.1 Palladium catalyzed synthesis of anthracenes

In 2009, Ren and colleagues reported that the combination of $Pd(OAc)_2$ and PPh_3 forms an efficient catalytic system for synthesizing tetracyclic benz [a]anthracene frameworks (Chan



SCHEME 1
Synthesis of tetracyclic benz [a] anthracenes through palladium-catalyzed tandem C-H activation/biscyclization reaction of propargylic carbonates with terminal alkynes.



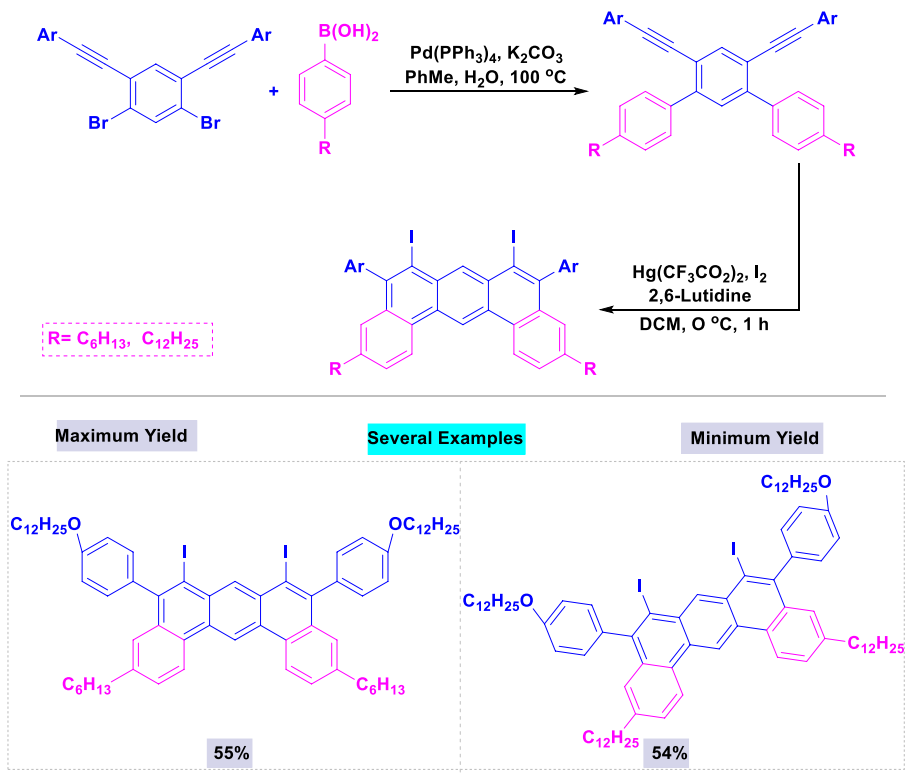
SCHEME 2
The plausible mechanism of Synthesis of tetracyclic benz [a]anthracenes through palladium-catalyzed tandem C-H activation/biscyclization reaction of propargylic carbonates with terminal alkynes.

et al., 2009). The reaction involving propargylic carbonate and phenylacetylene was carried out with various catalysts and bases in different environments; the reaction did not succeed without the palladium catalyst. Scheme 1 illustrates the details of the palladium-catalyzed tandem C-H activation/biscyclization reaction involving propargylic carbonates and terminal alkynes.

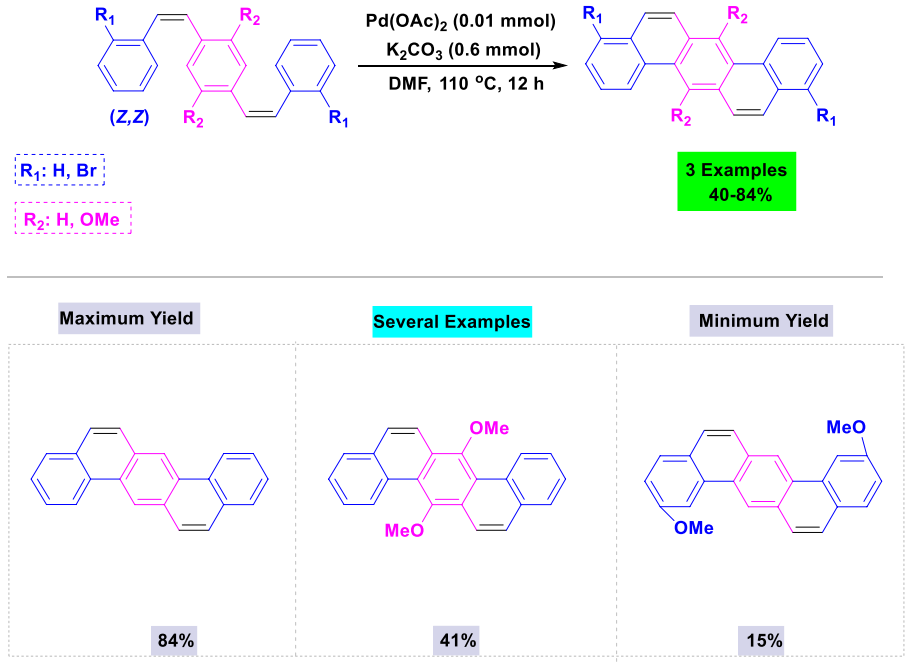
Scheme 2 depicts a palladium-catalyzed tandem C-H activation/biscyclization reaction of propargylic carbonates with terminal alkynes to synthesize tetracyclic benz[a]anthracenes. The reaction begins with the oxidative addition of a Pd(0) catalyst to a C-H bond of the propargylic carbonate. This forms a Pd(II) intermediate. The Pd(II) intermediate undergoes carbonylation, inserting a CO molecule into the Pd-C bond. The resulting acyl-Pd(II) species then undergoes migratory insertion, inserting an alkene from the terminal alkyne into the Pd-C bond. Finally, reductive elimination occurs, releasing the tetracyclic benz[a]anthracene product and regenerating the Pd (0) catalyst for the next cycle.

The use of a palladium catalyst is crucial for the C-H activation and subsequent transformations. The propargylic carbonate and terminal alkyne are the key starting materials.

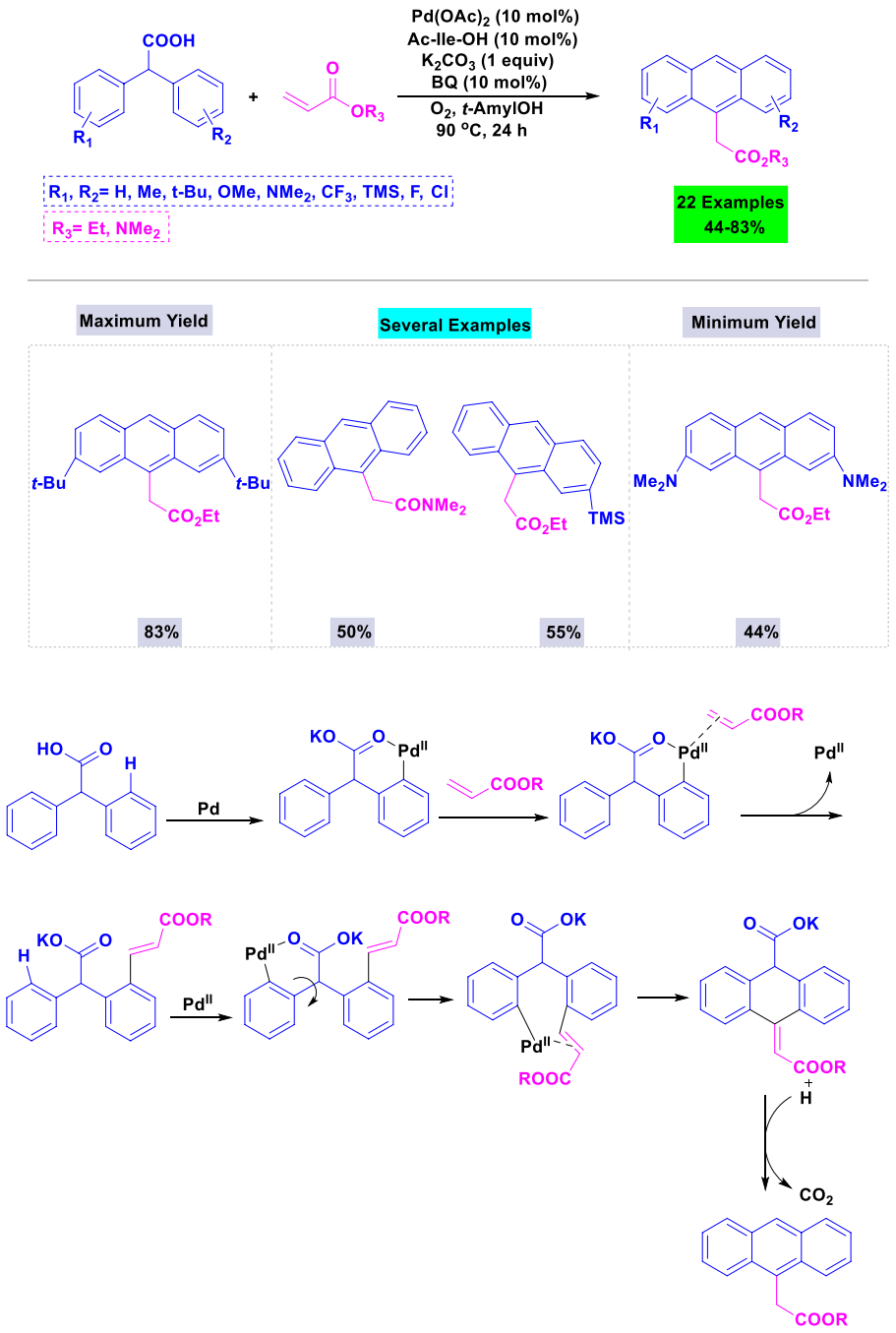
10.3389/fchem.2025.1545252



SCHEME 3
Synthesis of 6,8-diiododi-benzo [a,j]anthracenes through a multistep synthetic approach in the presence of catalytic amount of palladium.



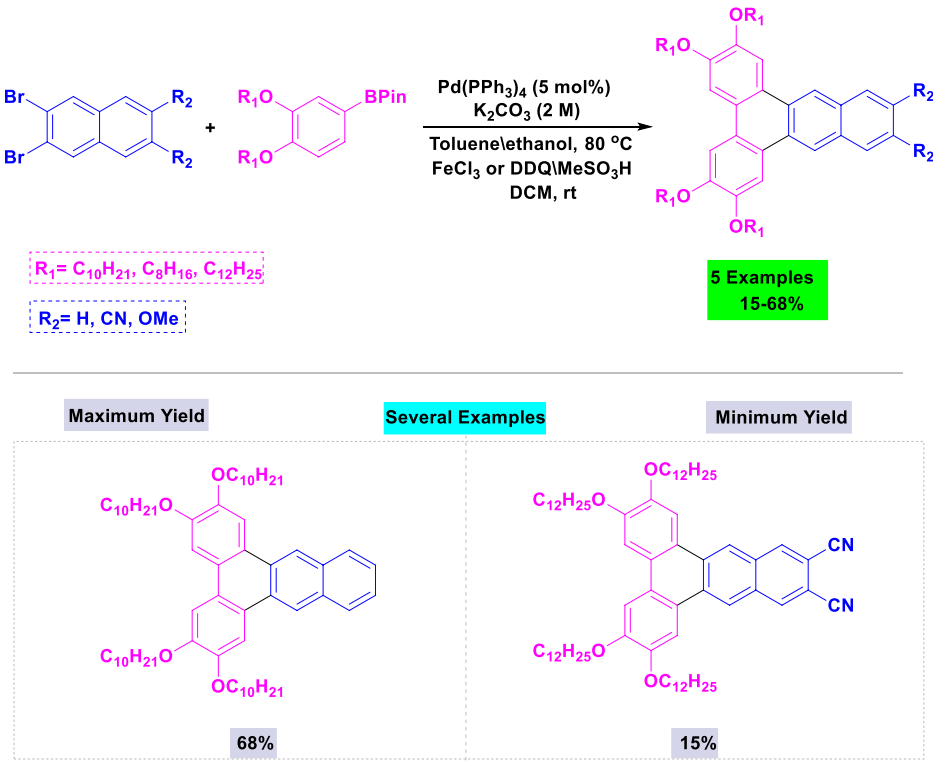
SCHEME 4
Synthesis of dibenz [*a,h*]anthracenes through Pd-catalyzed intramolecular double-cyclization of the corresponding (Z, Z)-p-styrylstilbene derivatives.



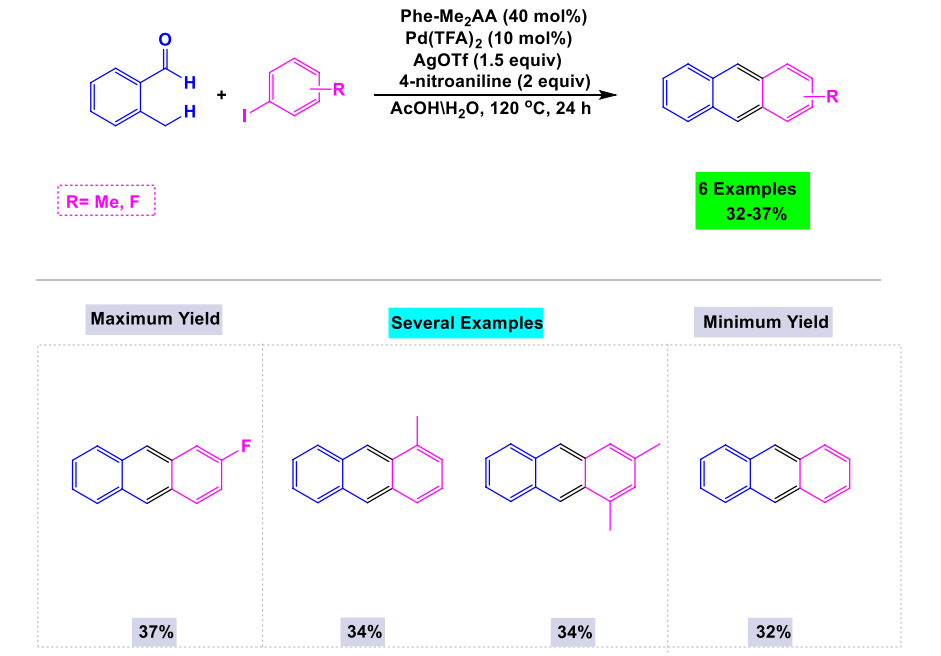
SCHEME 5
Synthesis and a plausible mechanism of synthesis of substituted anthracene derivatives through Pd(II)-catalyzed sp^3 C–H alkenylation of diphenyl carboxylic acids with acrylates.

A collection of fluorescent macrocycles constructed from 1,3-butadiyne-bridged dibenz[*a,j*]anthracene units has been synthesized with high yields via a multistep synthetic method using a catalytic amount of palladium (Umeda et al., 2012). The highest yield was observed with $Pd(PPh)_3$ in combination with potassium carbonate, among the tested palladium and bases. Scheme 3 illustrates that the corresponding 6,8-diiododi-benzo[a,j]anthracenes were synthesized with good yields through double iodonium-induced electrophilic cyclization.

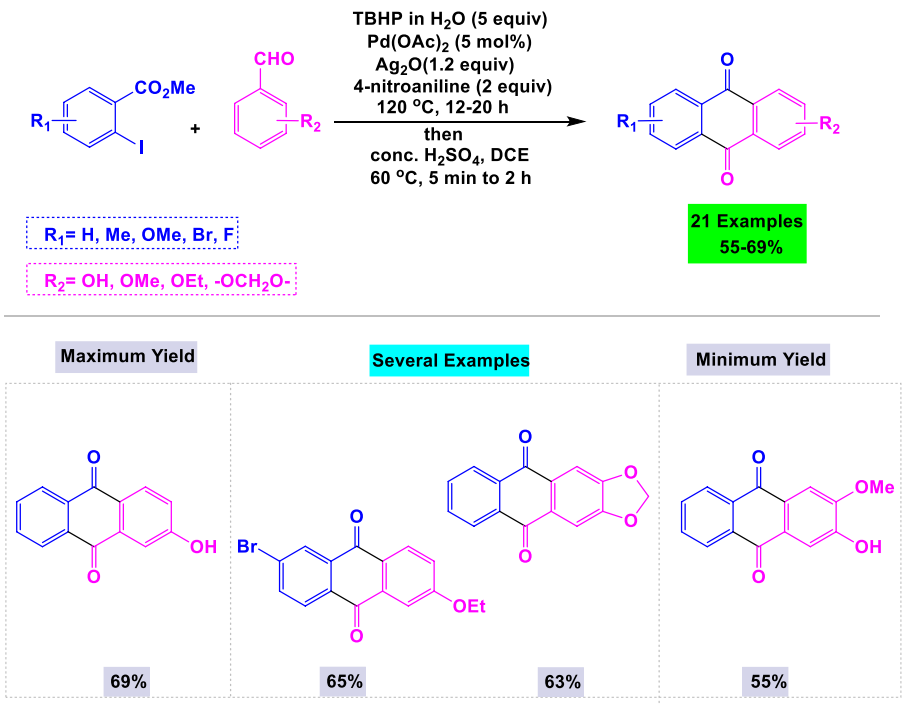
In 2012, Nishiyama and colleagues synthesized a wide variety of biologically active dibenz[a,h]anthracenes via Pd-catalyzed intramolecular double-cyclization of the respective (Z,Z)-p-styrylstilbene derivatives, which were easily prepared using the Wittig reaction (Kim et al., 2016). A variety of palladium catalysts and bases were tested in various solvents to identify the optimal conditions. The intramolecular double-cyclization of the relevant (Z,Z)-p-styrylstilbene derivatives was performed in a single



SCHEME 6
Synthesis of 2,3,5,6-tetraalkoxydi-benz [*a,c*]anthracenes through $Pd(PPh_3)_4$ catalyzed Suzuki coupling of the appropriate dibromonaphthalene and boronate ester, followed by an oxidative cyclization.



SCHEME 7
Synthesis of substituted anthracenes through Pd(I I)-Catalyzed sp^3 C-H arylation and electrophilic aromatic cyclization.



SCHEME 8
Synthesis of anthraquinones through [Pd]-catalyzed intermolecular direct acylation reaction.

pot with a catalytic quantity of $Pd(OAc)_2$ and potassium carbonate in DMF under heating conditions (Scheme 4).

In 2016, Hong and colleagues reported the synthesis of substituted anthracene derivatives via palladium(II)-catalyzed tandem transformation using carboxylic acids as traceless directing groups (Psutka et al., 2015). A variety of parameters (bases, solvents and additives) were analyzed in the template condensation of diphenyl carboxylic acid with ethyl acrylate, catalyzed by $Pd(OAc)_2$ with an amino acid-derived ligand; the highest yield was observed using potassium carbonate in t-amyl OH. Under standardized conditions, substrates featuring both electron-donating (Me-, t-Bu-, MeO-, and Me_2N-) and electron-withdrawing groups (F-, Cl-, and CF_3-) on the aryl moieties were successfully involved in these reactions, resulting in the desired anthracene products with moderate to good yields (Scheme 5).

This mechanism describes the synthesis of substituted anthracene derivatives using a palladium(II) catalyst (Scheme 5). It starts with the oxidative addition of Pd(II) to a diphenyl carboxylic acid. An acrylate then inserts into the Pd-C bond. A key step involves a C-H activation and cyclization to form the anthracene core. Finally, reductive elimination regenerates the Pd(II) catalyst and releases the substituted anthracene product, along with CO_2.

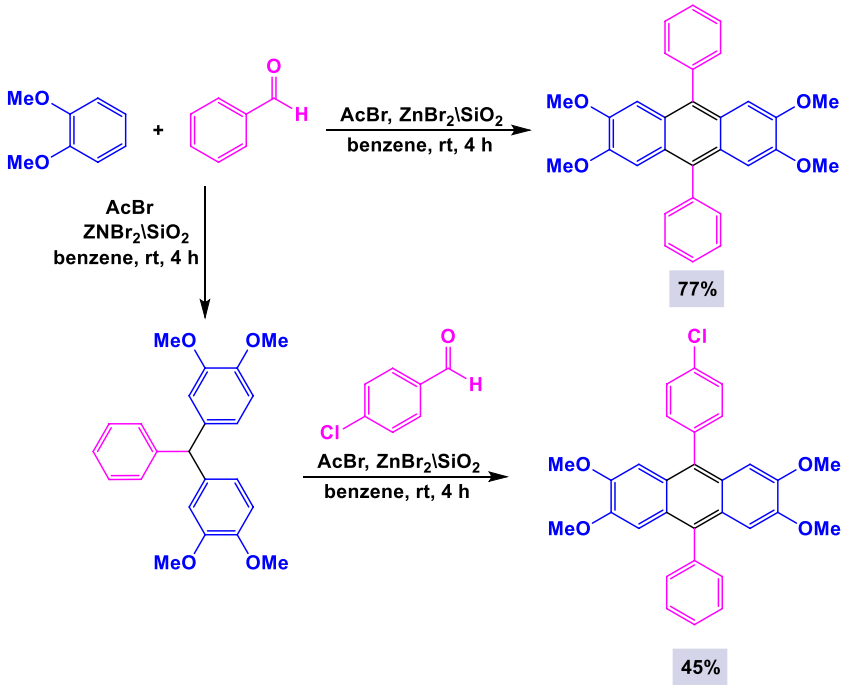
A broad range of 2,3,5,6-tetraalkoxydi-benz [a,c]anthracenes bearing substituents (H, OCH_3, or CN) in the 11- and 12-positions were successfully synthesize by Maly and coworkers with good yields through Suzuki coupling of the appropriate dibromonaphthalene and boronate ester, followed by an oxidative cyclization in the presence of palladium (Park et al., 2018). These reactions were accomplished using 5 mol% of $Pd(PPh_3)_4$ and potassium carbonate in toluene/ethanol under thermal conditions (Scheme 6).

In 2018, Park and colleagues reported that palladium catalyzes the reactions between o-tolualdehydes and aryl iodides to synthesize substituted anthracenes (Suchand and Satyanarayana, 2019). In their standardization experiments, the authors found that steric and electronic effects significantly influence the cyclization process leading to the formation of anthracenes. The details of the synthesis of substituted anthracenes from o-tolualdehydes and aryl iodides, utilizing Pd(II)-catalyzed sp^3 C-H arylation and electrophilic aromatic cyclization, are illustrated in Scheme 7.

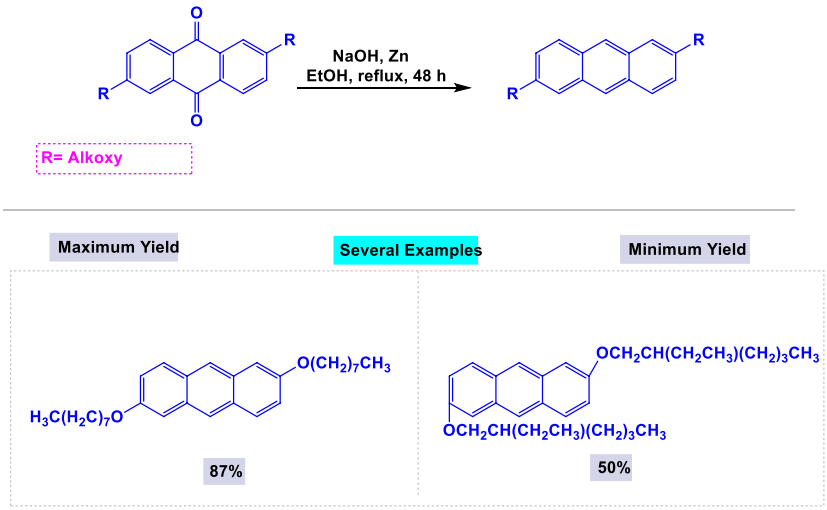
A library of biologically active anthraquinones was synthesized in good yields via a [Pd]-catalyzed intermolecular direct acylation reaction. The subsequent acylation was accomplished through intramolecular Friedel–Crafts acylation (Kodomari et al., 2008). In this methodology, Satyanarayana and Such utilized 5 mol% of $Pd(OAc)_2$ in the presence of Ag_2O/TBHP to explore the reaction scope between methyl 2-iodobenzoate and various benzaldehydes in water under reflux conditions (Scheme 8). Notably, benchtop aldehydes were employed as non-toxic acylation agents in the critical [Pd]-catalyzed acylation process.

4.2 Zinc catalyzed synthesis of anthracenes

In 2008, Kodomari and colleagues employed silica gel-supported zinc bromide as a catalyst for the synthesis of 9,10-diarylanthracene derivatives. This synthesis was accomplished through the reaction of electron-rich arenes with acetyl bromide and aldehydes under mild conditions (Bhowmik et al., 2009). The experimental studies demonstrated that the yield of diarylanthracene derivatives was influenced by the ratio of arene to aldehyde. As illustrated in



SCHEME 9
Synthesis of 9,10-diarylanthracene derivatives through $ZnBr_2/SiO_2$ catalyzed reaction of electron-rich arenes with aromatic aldehydes and acetyl bromide.

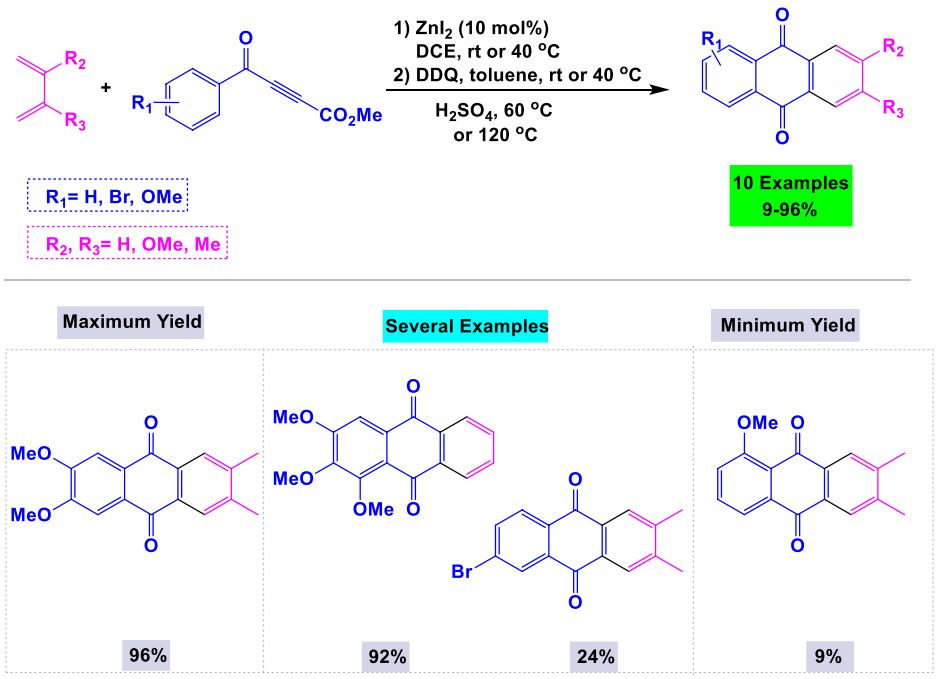


SCHEME 10
Synthesis of 9,10-diacetoxy-anthracenes through from anthraquinone and its derivatives via a single step reaction by using reductive Zn-pyridine system.

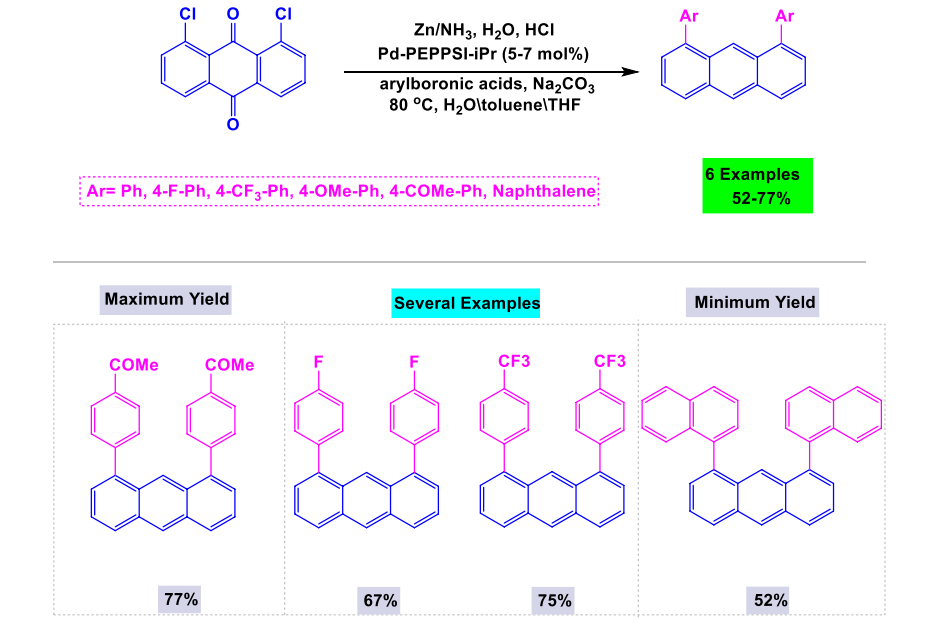
Scheme 9, the reaction of electron-rich arenes with aromatic aldehydes and acetyl bromide was catalyzed by $ZnBr_2/SiO_2$ in benzene under mild conditions, leading to favorable yields of the corresponding products.

One year later, Bhowmik and coworkers reported a facile and effective synthetic methodology for preparing 9,10-diacetoxy-anthracene derivatives from anthraquinone and its derivatives through a one-step reaction using a reductive Zn-pyridine system in ethanol under reflux conditions (Scheme 10) (Pünner et al., 2013).

Hilt and colleagues have developed an efficient synthetic route for the preparation of a wide range of symmetric and asymmetric anthraquinone derivatives, achieving good yields through zinc iodide-catalyzed Diels–Alder reactions with 1,3-dienes and



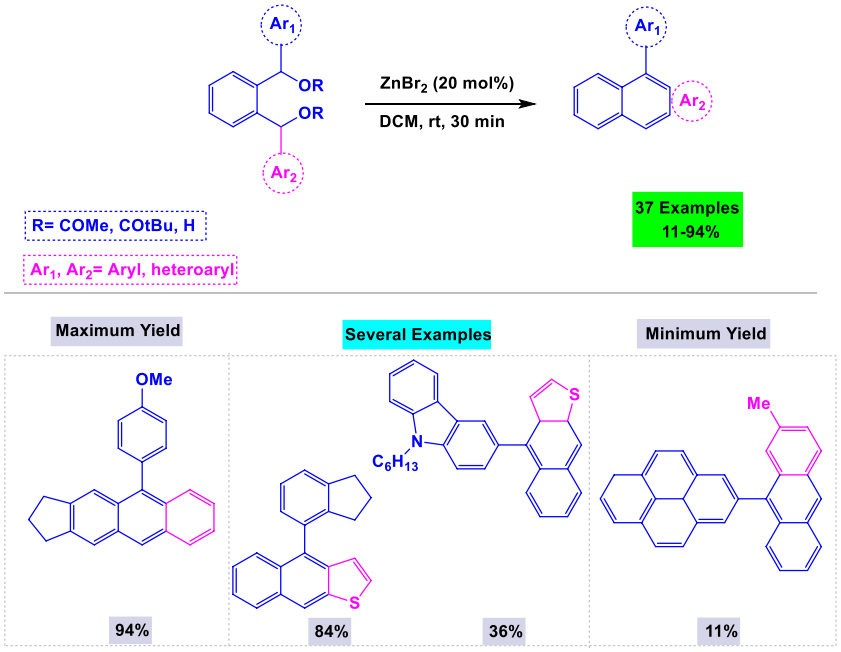
SCHEME 11
Synthesis of anthraquinone derivatives through Zinc iodide-catalyzed Diels–Alder reactions with 1,3-dienes and aroylpropiolates followed by intramolecular Friedel-Crafts cyclization.



SCHEME 12
Synthesis of 1,8 -diaryl-anthracene derivatives from anthroquinones in the presence of zinc as the catalyst.

aroylpropiolates, followed by intramolecular Friedel-Crafts cyclization (Agarwal et al., 2015). The scope and some limitations of these zinc iodide-catalyzed cyclization reactions are outlined in Scheme 11. The presence of more electron-donating alkyl or methoxy groups in the ring enhances the efficiency of the Friedel-Crafts cyclization.

In 2015, Agarwal and colleagues introduced a novel and efficient method for synthesizing biologically active 1,8-diaryl-anthracene derivatives using zinc as a catalyst (Sivasakthikumaran et al., 2015). As illustrated in Scheme 12, the method involves the reduction of 1,8-dichloroanthraquinone, followed by aryl-aryl coupling under



SCHEME 13
Synthesis of anthracenes through zinc bromide catalyzed one-pot regioselective annulation of unsymmetrical 1,2-phenylenebis (diaryl/diheteroarylmethanol).

modified Suzuki-Miyaura reaction conditions, yielding good results for 1,8-diaryl anthracene derivatives.

In a separate publication on the synthesis of anthracenes, Mohanakrishnan and colleagues introduced zinc bromide as an efficient catalyst for the one-pot regioselective annulation of unsymmetrical 1,2-phenylenebis (diaryl/diheteroarylmethanol) (Imeni et al., 2023). They investigated the influence of the catalyst and solvent to optimize the reaction conditions, ultimately determining that 20 mol% of ZnBr in dichloromethane at ambient temperature was ideal for synthesizing anthracenes (Scheme 13). This system also demonstrated high activity in the preparation of other polycyclic aromatic hydrocarbons, such as tetracenes and naphtho [b] thiophenes.

4.3 Indium catalyzed synthesis of anthracenes

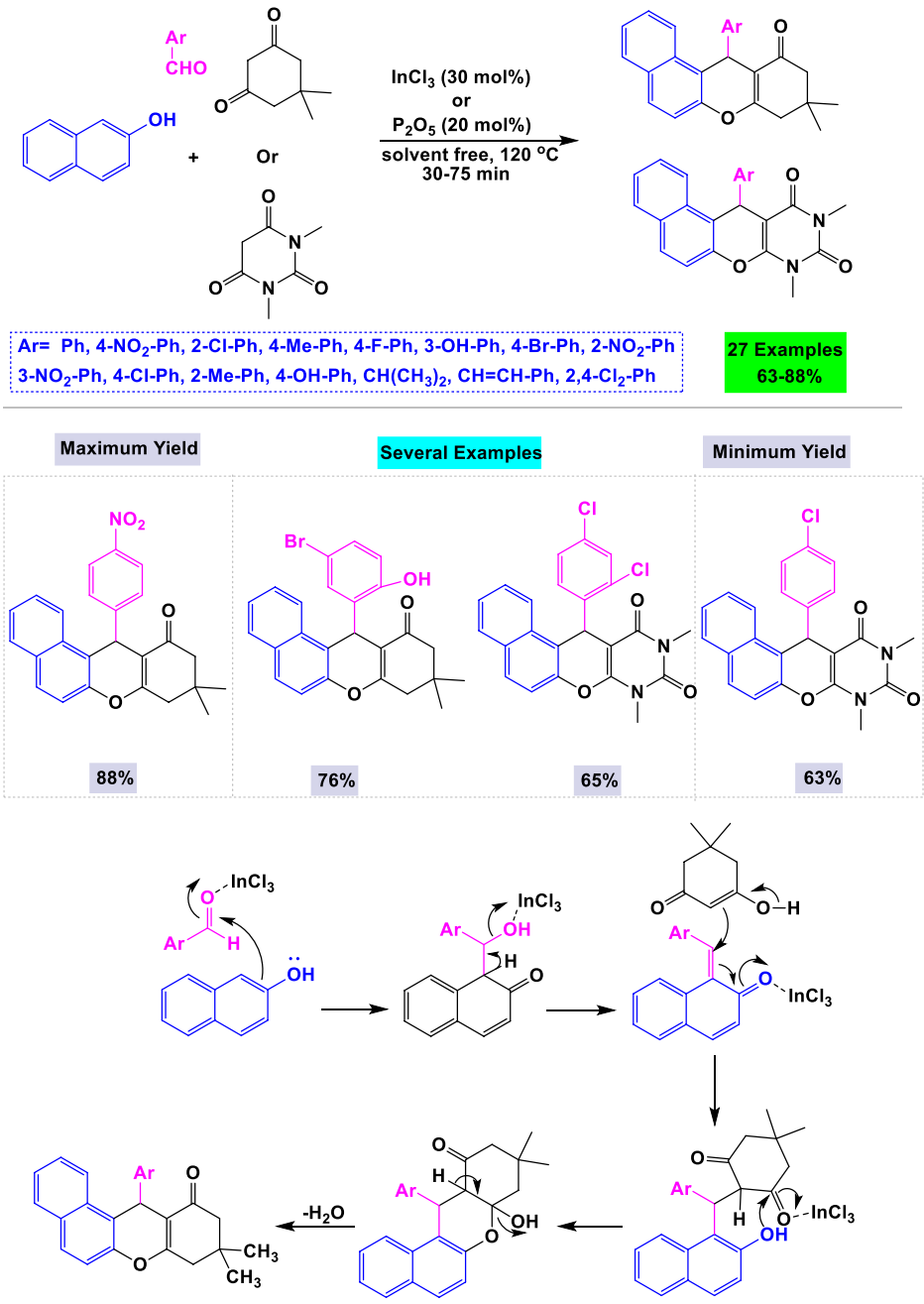
Multicomponent reactions (MCRs) are valuable tools in organic synthesis, facilitating the rapid construction of complex molecular structures from three or more reactants in a single reaction step. They are highly regarded for their efficiency, atom economy, and ability to introduce molecular diversity, rendering them essential in the development of pharmaceuticals and organic materials (Javahershenas and Nikzat, 2023; Javahershenas et al., 2024a; Javahershenas et al., 2024b; Javahershenas et al., 2024c; Nandi et al., 2009).

In 2009, Nandi and colleagues developed a general and convenient synthetic method for preparing tetrahydrobenzo[a] xanthene-11-one and diazabenzo[a]anthracene-9,11-dione derivatives. This was achieved through a one-pot three-component cyclocondensation of aldehydes, β-naphthol, and cyclic 1,3-dicarbonyl compounds, catalyzed by InCl3 under solvent-free conditions (Scheme 15). (Kuninobu et al., 2011) The advantages of this catalytic system include appropriate reaction times, higher yields, mild reaction conditions, straightforward purification, and cost-effectiveness. A mechanistic pathway for the one-pot three-component cyclocondensation involving aldehydes, β-naphthol, and cyclic 1,3-dicarbonyl compounds catalyzed by $InCl_3$ is illustrated in Scheme 14.

In 2011, Takai and colleagues developed a general and efficient synthetic methodology for the preparation of anthracene derivatives from 2-benzylic or 2-allylbenzaldehydes, utilizing a catalytic amount of In(III) or Re(I) complexes (Hueso-Falcón et al., 2014). Two key factors in optimizing the synthesis of anthracene derivatives were the concentration of the catalyst and the nature of the solvent. Details of these reactions are presented in Scheme 15. This methodology also demonstrated high efficiency in synthesizing other polycyclic aromatic hydrocarbons, including derivatives of naphthalene and naphtha [2,3-*b*]thiophene.

Estévez-Braun and colleagues reported the preparation of a library of cytotoxic dibenzo [*a,h*]anthracenes via an $InCl_3$-catalyzed one-pot three-component reaction. This reaction involved 2-hydroxy-1,4-naphthoquinone, aromatic aldehydes, and 2-naphthol as synthetic inputs, all conducted under solvent-free conditions (Scheme 16). (Javahershenas et al., 2024d) To optimize the synthesis of cytotoxic dibenzo [a,h]anthracenes, various metal catalysts and solvents were evaluated. The highest yield was achieved using 30 mol% of InCl3 without solvent under thermal conditions. A mechanistic pathway for the $InCl_3$-catalyzed one-pot three-component reaction is depicted in Scheme 16.

10.3389/fchem.2025.1545252

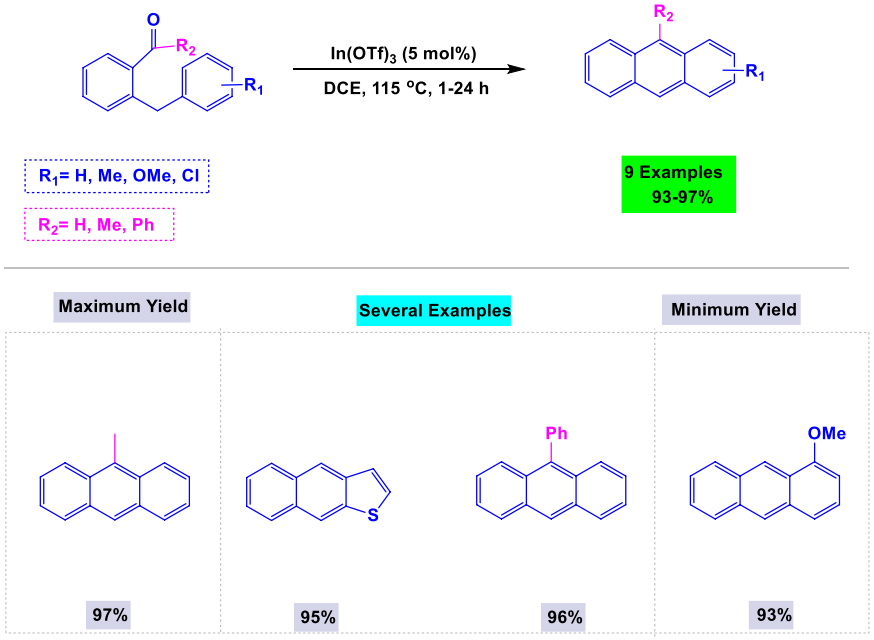


SCHEME 14
Synthesis and mechanistic rationale pathway of anthraquinone derivatives through cyclocondensation of aldehydes, *β*-naphthol and cyclic 1,3-dicarbonyl compounds catalyzed by $InCl_3$.

4.4 Cobalt catalyzed synthesis of anthracenes

Microwave-assisted synthesis is a contemporary organic technique that utilizes microwave radiation to heat reaction mixtures, resulting in significantly reduced reaction times and often enhanced product yields. This method is recognized for its efficiency, energy conservation, and capability to facilitate reactions that may be difficult to achieve under conventional thermal conditions. Zou et al. (2008) developed a general and effective microwave-assisted methodology for synthesizing substituted anthracenes and azaanthracenes in high yields through [2 + 2 + 2] cyclotrimerization reactions employing nickel and cobalt catalysts. The presence of a catalyst was essential for the synthesis of anthracene derivatives, as the template reaction was unsuccessful without nickel or cobalt. Under optimized conditions, a variety of substrates featuring functional groups such as alkyl and alkene chains, hydroxy groups, and benzene and pyridine rings were examined, resulting in the successful synthesis of the desired anthracene products in good to high yields (Scheme 17).

In a separate publication, Saino et al. (2010) reported that the combination of $CoCl_2{\cdot}6H_2O$ and Zn powder constitutes an efficient



SCHEME 15
Synthesis of anthracene derivatives from 2-benzylic- or 2-allylbenzaldehydes using a catalytic amount of In(III) or Re(I) complexes.

system for synthesizing substituted anthracenes through [2 + 2 + 2] alkyne-cyclotrimerization reactions with 2-iminomethylpyridine (dipimp) (Hoffmann et al., 2019). When the reaction was conducted using only the cobalt catalyst, the yield of the target product was unsatisfactory. As illustrated in Scheme 18, the [2 + 2 + 2] cycloaddition reaction of 1,6-diynes with 4-aryl-2-butyn-1-ols, catalyzed by the $CoCl_2{\cdot}6H_2O$/Zn reagent in the presence of dipimp, resulted in the formation of the desired substituted anthracenes with good yields. Notably, this catalytic system exhibited high activity in the synthesis of substituted pentaphenes and trinaphthylenes.

In 2019, Hoffmann and colleagues established an effective synthetic route for the preparation of 2,3- and 2,3,6,7-halogenated anthracenes through cobalt-catalyzed [2 + 2 + 2] cyclotrimerization reactions employing bis(trimethylsilyl) acetylenes (Koley et al., 2023). As depicted in Scheme 19, a crucial step involved the introduction of chlorine, bromine, or iodine substituents via halodesilylation of TMS-substituted cyclotrimerization adducts. The synthesis of 2,3- and 2,3,6,7-halogenated anthracenes achieved satisfactory yields through oxidation and aromatization processes using DDQ. Notably, this method exhibited high efficiency in producing 2,3,6,7-halogenated anthracene derivatives, which are typically difficult to obtain.

4.5 Gold catalyzed synthesis of anthracenes

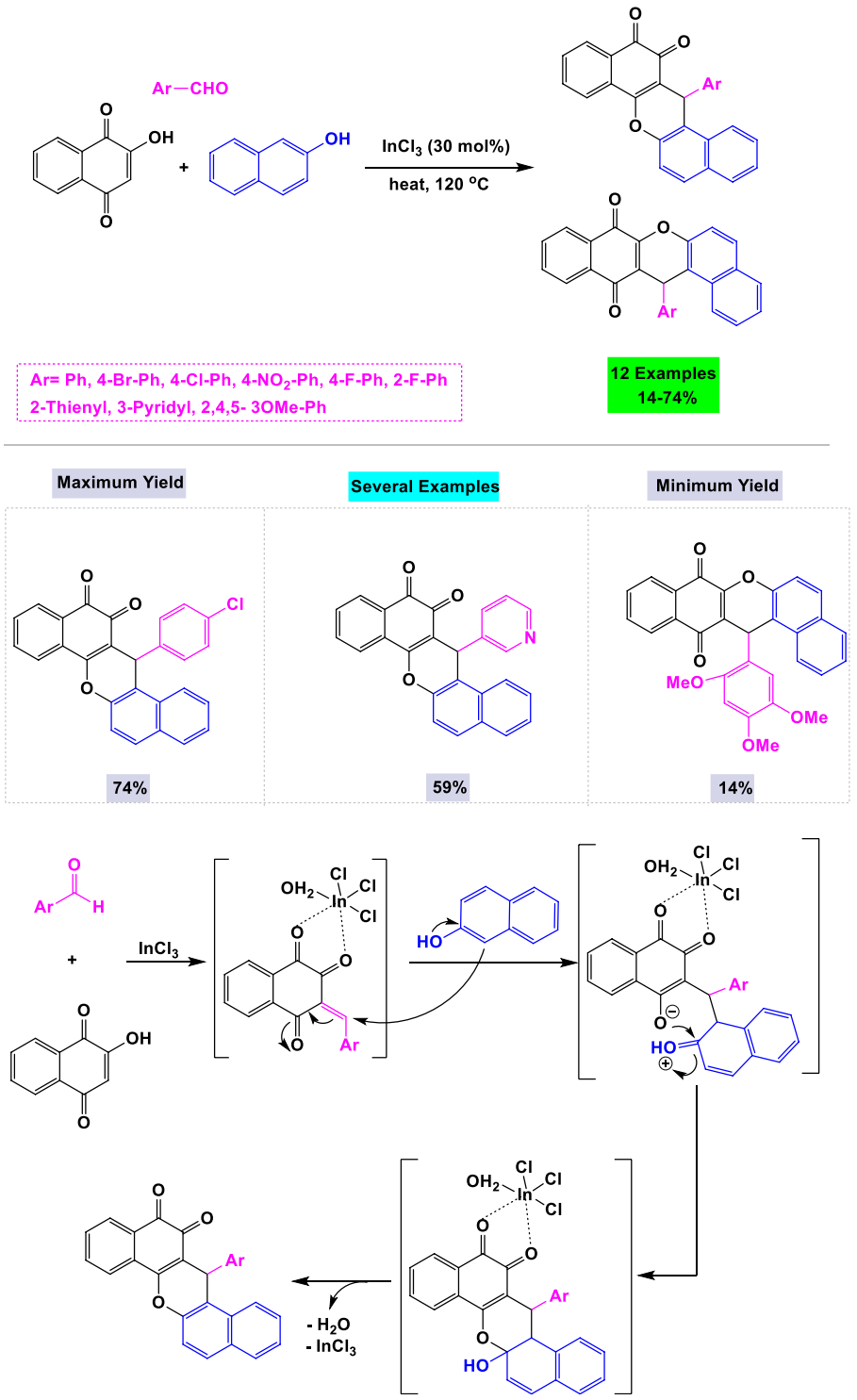
Gold-catalyzed synthesis is a specialized area of organic chemistry that utilizes gold as a catalyst to facilitate a range of chemical transformations, particularly the activation of alkynes, allenes, and alkenes (Nakae et al., 2012). This methodology is highly regarded for its capacity to promote mild and selective reactions, enabling the efficient synthesis of complex organic molecules with potential applications in drug development and materials science. In 2012, Nakae and colleagues reported the synthesis of a series of dibenzo[a, h] anthracenes through one-pot double cyclization reactions employing a catalytic amount of AuCl (Scheme 20). (Shu et al., 2013) The presence of gold catalysts was essential for these reactions, as the template double cyclization of dihaloethynylterphenyl could not be achieved in the absence of gold. These one-pot double cyclization reactions were performed using 20 mol% of AuCl in toluene at 60°C for 24 h.

Shu and colleagues have developed a novel synthetic procedure for preparing substituted anthracenes via the cyclization of o-alkynyldiarylmethanes using a catalytic amount of the gold complex ($Et_3PAuNTf_2$) (Sawano et al., 2019). They conducted template cyclization of o-alkynyldiarylmethane under various conditions to identify the optimal parameters for synthesizing substituted anthracenes. Notably, the template product was not observed in the absence of gold catalysts. Under the standardized conditions outlined in Scheme 21, functionalities such as F, Br, and Me, as well as the acid-sensitive OAc group on the aromatic ring, were all well tolerated during the cyclization process.

4.6 Iridium catalyzed synthesis of anthracene derivatives

Takeuchi and colleagues have developed a valuable synthetic method for producing biologically promising anthraquinone derivatives (Fukutani et al., 2009). This approach utilizes [Ir(cod)Cl]$_2$ (where cod is 1,5-cyclooctadiene) in combination with

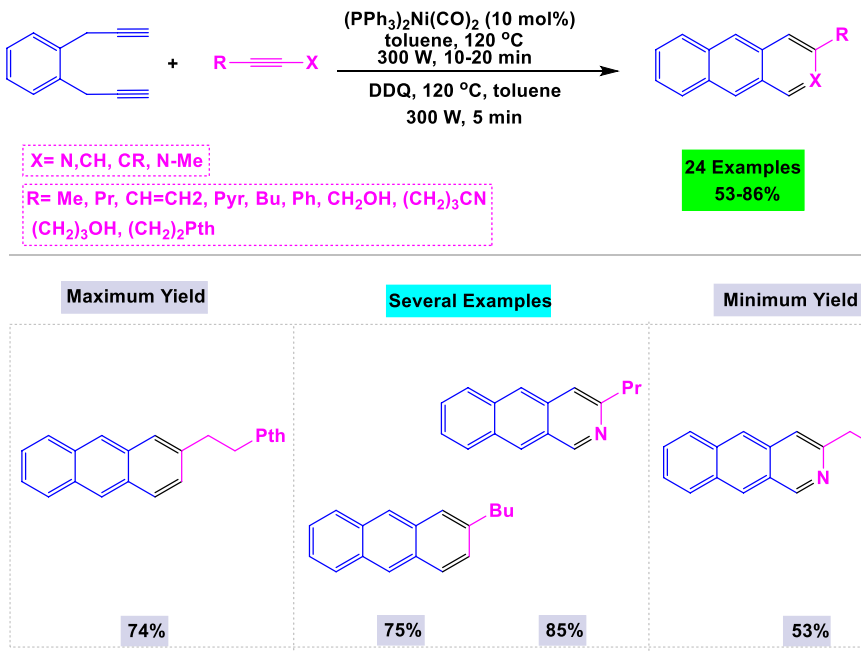
10.3389/fchem.2025.1545252



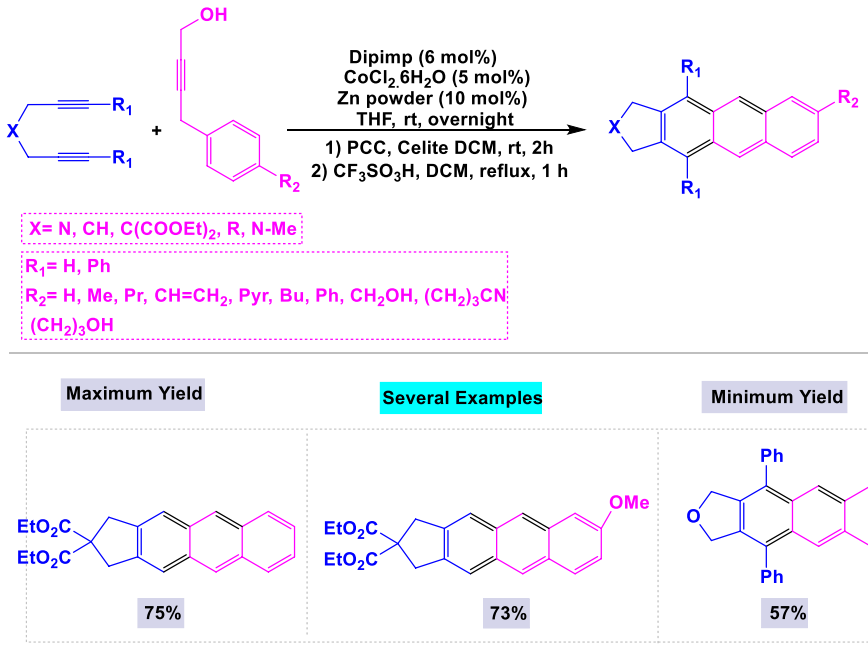
SCHEME 16
Synthesis and mechanistic rationale pathway of cytotoxic dibenzo [*a,h*]anthracenes through InCl3 catalyzed one-pot three-component reaction with 2-hydroxy-1,4-naphthoquinone, aromatic aldehydes, and 2-naphthol.

bis(diphenylphosphino)ethane (DPPE) as an effective catalytic system. The reaction of a 1,2-bis(propiolyl)benzene derivative with three equivalents of 1-hexyne was explored under various conditions, revealing that the absence of ligands resulted in a poor yield of the target product. As illustrated in Scheme 22, a range of anthraquinone derivatives can be synthesized in moderate to high yields through the $[Ir(cod)Cl]_2$/DPPE-catalyzed [2 + 2 + 2] cycloaddition of a 1,2-bis(propiolyl)benzene derivative with terminal and internal alkynes in nonpolar solvents under reflux conditions.

10.3389/fchem.2025.1545252

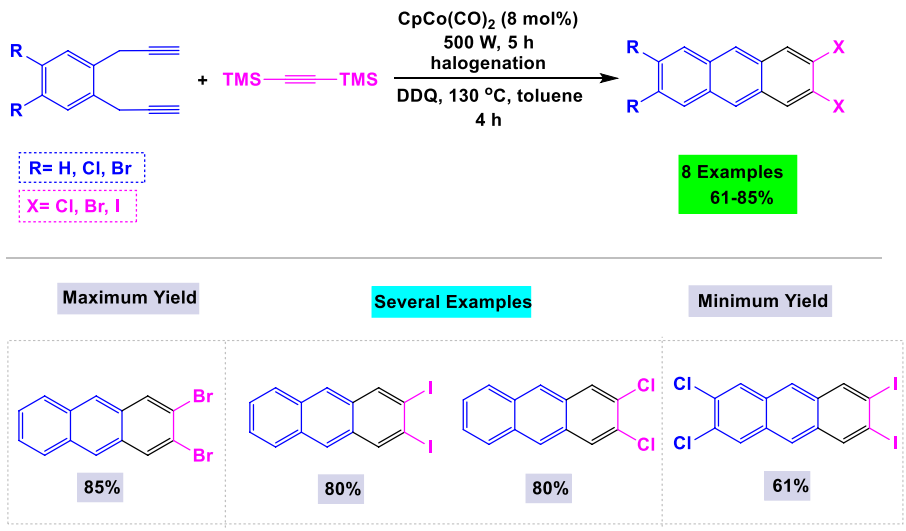


SCHEME 17
Synthesis of substituted anthracenes and azaanthracenes through Nickel/cobalt catalyzed [2 + 2 + 2] cyclotrimerization reactions.

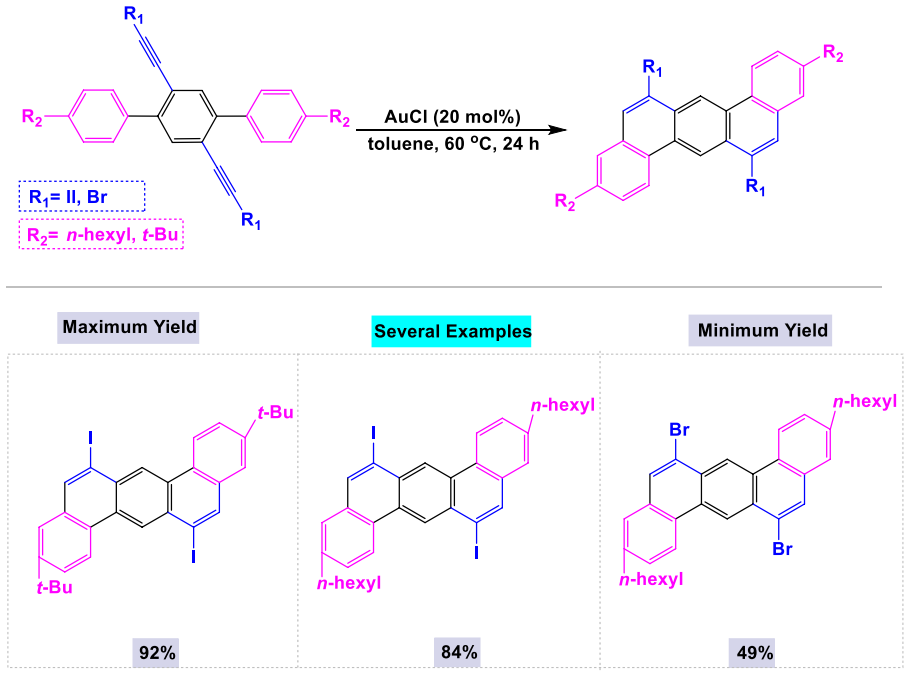


SCHEME 18
Synthesis of substituted anthracenes through $oCl_2{\cdot}6H_2O$/Zn reagent catalyzed [2 + 2 + 2] cycloaddition reaction of 1,6-diynes with 4-aryl-2-butyn-1-ols.

10.3389/fchem.2025.1545252



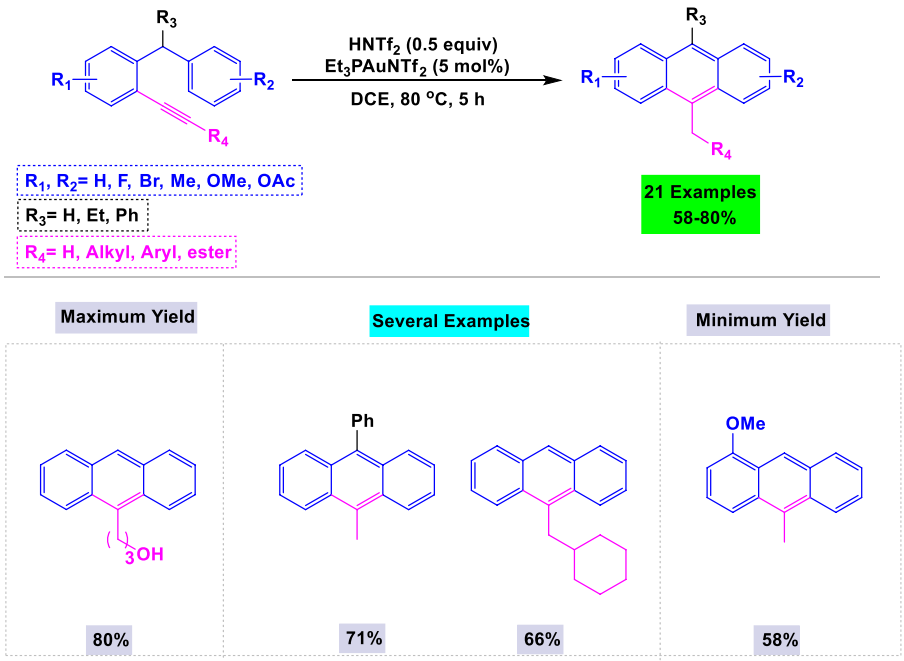
SCHEME 19
Synthesis of 2,3- and 2,3,6,7-halogenated anthracenes through cobalt-catalyzed [2 + 2 + 2] cyclotrimerization reactions with bis(trimethylsilyl) acetylenes.



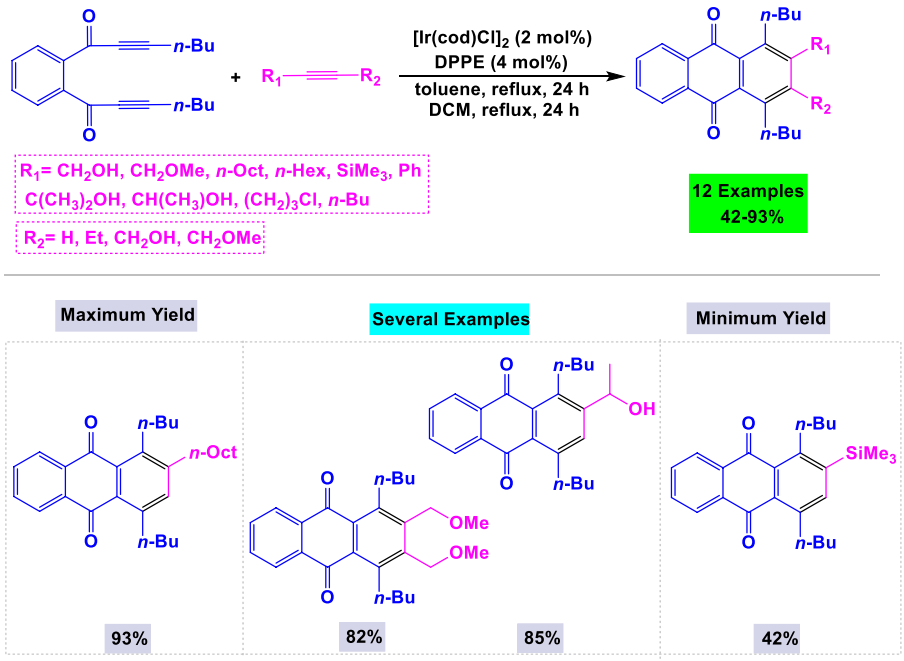
SCHEME 20
Synthesis of dibenzo [a, h]anthracenes through one-pot double cyclization reactions in the presence of catalytic amount of AuCl.

4.7 Rhodium catalyzed synthesis of anthracenes

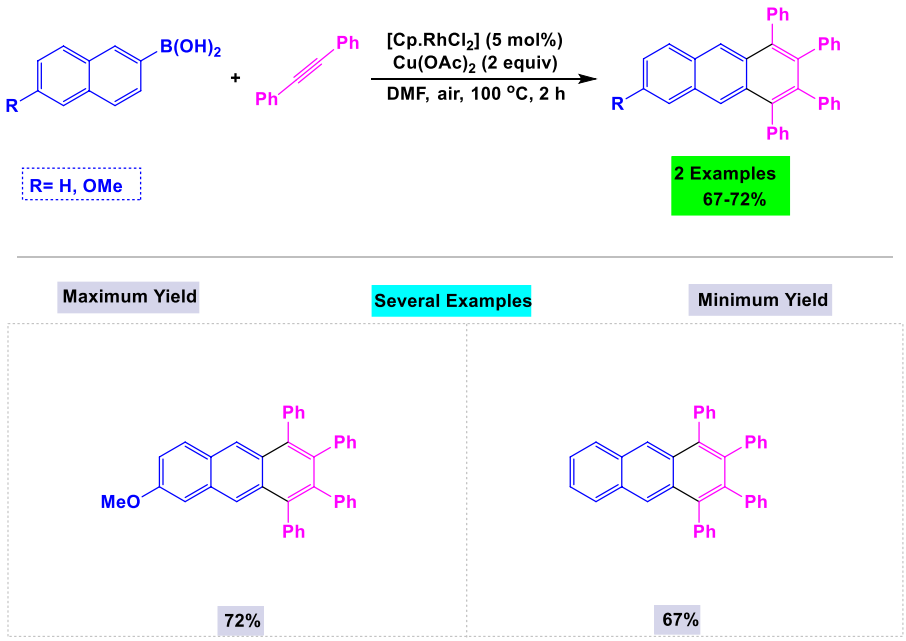
In 2009, Fukutani and his team developed a general and efficient method for synthesizing 1,2,3,4-tetrasubstituted anthracene derivatives through rhodium-catalyzed oxidative coupling reactions between aryl boronic acids and internal alkynes (Scheme 23). (Zhang et al., 2016) They investigated the effects of various catalysts and solvents to optimize the reaction conditions. This catalytic system also demonstrated high activity in the synthesis of other polysubstituted fused aromatic compounds.



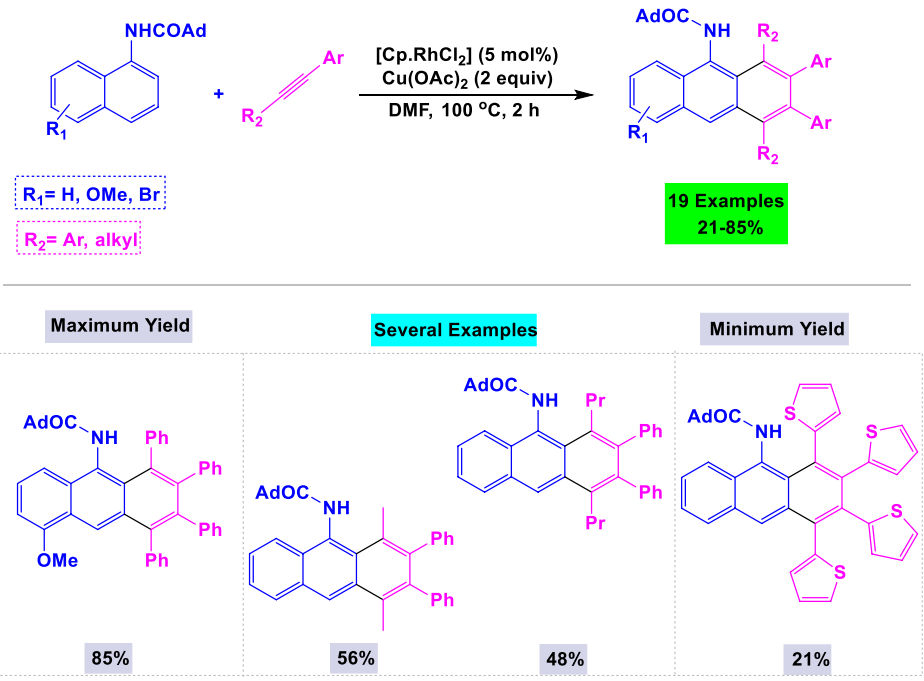
SCHEME 21
Synthesis of substituted anthracenes through gold catalyzed cyclization of o-alkynyldiarylmethanes.



SCHEME 22
Synthesis of anthraquinone derivatives through [Ir (cod)Cl]$_2$/DPPE catalyzed [2 + 2 + 2] cycloaddition of a 1,2-bis(propiolyl)benzene derivative with terminal and internal alkynes.

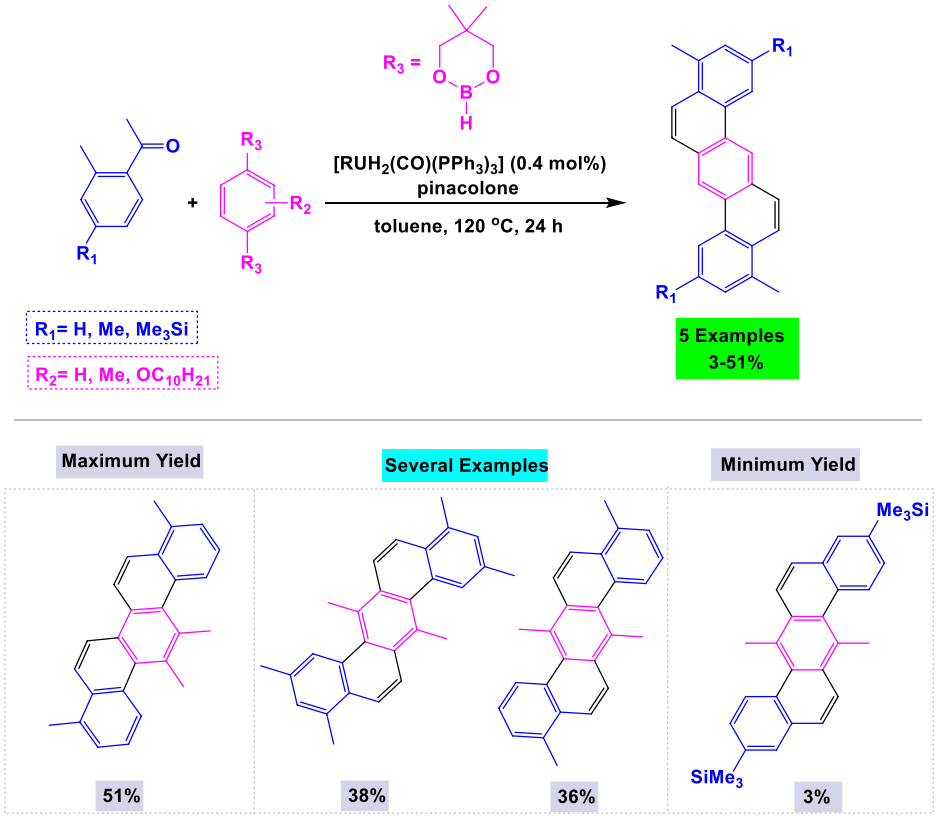


SCHEME 23
Synthesis of 1,2,3,4-tetrasubtituted anthracene derivatives through rhodium-catalyzed oxidative coupling reactions of aryl-boronic acids with internal alkynes in the presence of $Cu(OAc)_2$ as the oxidant.



SCHEME 24
Synthesis of substituted anthracenes through rhodium-catalyzed oxidative benzannulation reactions of 1-adamantoyl-1-naphthylamines with internal alkynes in the presence of $Cu(OAc)_2$ as the oxidant.

Zhang and colleagues developed an innovative and highly efficient synthetic methodology for the preparation of substituted anthracenes through rhodium-catalyzed oxidative benzannulation reactions. This process involves the reaction of 1-adamantoyl-1-naphthylamines with internal alkynes in the presence of $Cu(OAc)_2$ as the oxidant, utilizing DMF under thermal conditions (Scheme 24)



SCHEME 25
Synthesis of dibenzo [*a*,*h*] anthracenes through [$RuH_2(CO)(PPh_3)$] catalyzed one-pot regioselective C¬H arylation of aromatic ketones.

(Kitazawa et al., 2011). The reactions proceeded smoothly with alkynes containing either electron-donating or electron-withdrawing groups on the benzene ring, resulting in the formation of target anthracene products in moderate to good yields.

4.8 Ruthenium catalyzed synthesis of anthracenes

In 2011, Kitazawa and colleagues reported a one-pot, regioselective C–H arylation of aromatic ketones utilizing [$RuH_2(CO)(PPh_3)$] as the catalyst for the synthesis of dibenzo [*a*,*h*]anthracenes [159] This reaction was performed in pinacolone under reflux conditions. Additionally, they explored the effects of various substituents at specific positions on arenediboronates under standardized conditions (Scheme 25).

5 Conclusion

The synthesis of anthracene scaffolds catalyzed by transition metals has witnessed significant advancements in recent years, enhancing the efficiency, selectivity, and sustainability of these important organic compounds. Transition metal catalysis has emerged as a powerful tool for developing innovative methodologies that address challenges associated with traditional synthetic routes.

Recent achievements in this field include the implementation of C–H activation strategies, which allow for direct functionalization of anthracene derivatives, simplifying synthetic pathways and reducing the need for pre-functionalization. The evolution of cross-coupling reactions, especially using palladium and nickel catalysts, has enabled the efficient construction of complex anthracene-based structures with high yields and selectivity.

New catalytic systems, including earth-abundant metals and chiral catalysts, have further expanded the scope of anthracene synthesis, providing access to enantiomerically enriched compounds valuable in pharmaceuticals and materials science. The integration of green chemistry principles into these methodologies has led to sustainable practices, minimizing waste and environmental impact.

Looking forward, the future of anthracene scaffold synthesis appears promising, with ongoing efforts to optimize methodologies, develop novel catalysts, and explore new reaction conditions. These advancements not only enhance the utility of anthracene derivatives in various applications but also contribute to broader goals of sustainable and efficient organic synthesis. Collaboration between chemists, materials scientists, and industry will drive further innovations in this dynamic field, paving the way for new discoveries and applications of anthracene-based compounds.

Recent achievements underscore the dynamic nature of this field and its critical role in advancing modern organic synthesis. The continued exploration and optimization of these catalytic processes will pave the way for new discoveries and applications, reinforcing the importance of transition metals in synthesizing complex molecular architectures.

Author contributions

FS: Investigation, Methodology, Writing–original draft, Writing–review and editing. VJ: Investigation, Methodology, Writing–original draft, Writing–review and editing. RR: Investigation, Methodology, Writing–original draft, Writing–review and editing. AK: Investigation, Methodology, Writing–original draft, Writing–review and editing. SS: Investigation, Methodology, Writing–original draft, Writing–review and editing. GC: Investigation, Methodology, Writing–original draft, Writing–review and editing. PB: Writing–original draft, Writing–review and editing. MK: Methodology, Writing–original draft, Writing–review and editing. RJ: Project administration, Visualization, Writing–original draft, Writing–review and editing.

Funding

The author(s) declare that no financial support was received for the research, authorship, and/or publication of this article.

Conflict of interest

The authors declare that the research was conducted in the absence of any commercial or financial relationships that could be construed as a potential conflict of interest.

Generative AI statement

The author(s) declare that no Generative AI was used in the creation of this manuscript.

Publisher's note

All claims expressed in this article are solely those of the authors and do not necessarily represent those of their affiliated organizations, or those of the publisher, the editors and the reviewers. Any product that may be evaluated in this article, or claim that may be made by its manufacturer, is not guaranteed or endorsed by the publisher.

References

Abou-Hatab, S., Spata, V. A., and Matsika, S. (2017). Substituent effects on the absorption and fluorescence properties of anthracene. *J. Phys. Chem. A* 121, 1213–1222. doi:10.1021/acs.jpca.6b12031

Agarwal, N., Patil, M., and Patil, M. (2015). Synthesis of highly emissive 1,8-diaryl anthracene derivatives and fabrication of their micro/nanostructures. *RSC Adv.* 5, 98447–98455. doi:10.1039/c5ra19564k

Albaladejo, M. J., Alonso, F., and Yus, M. (2013). Synthesis of indolizines and heterocyclic chalcones catalyzed by supported copper nanoparticles. *Chem. Eur. J.* 19, 5242–5245. doi:10.1002/chem.201204305

Ali, M., Iqbal, A., and Khattak, K. K. (2020b). Pilot plant investigation on the start-up of a UASB reactor using sugar mill effluent. *Cent. Asian J. Environ. Sci. Technol. Innov.* 1, 199–205. doi:10.22034/CAJESTI.2020.04.02

Ali, M., Iqbal, A., and Waheed, A. (2020a). Co-treatment of chlorophenol and methanolic wastes. *Cent. Asian J. Environ. Sci. Technol. Innov.* 1, 277–280. doi:10.22034/CAJESTI.2020.05.04

Alonso, F., Moglie, Y., Radivoy, G., and Yus, M. (2010). Multicomponent synthesis of 1,2,3-triazoles in water catalyzed by copper nanoparticles on activated carbon. *Adv. Synth. Catal.* 352, 3208–3214. doi:10.1002/adsc.201000637

Amjadian, E., Zeinodini, A., and Doğan, H. (2021). Effect of fertilizer management systems on growth and balance of nutrients in wheat cultivation. *Cent. Asian J. Plant Sci. Innov.* 1, 56–69. doi:10.22034/CAJPSI.2021.02.01

Anastas, P. T., and Kirchhoff, M. M. (2002). Origins, current status, and future challenges of green chemistry. *Acc. Chem. Res.* 35, 686–694. doi:10.1021/ar010065m

Anastas, P. T., and Warner, J. C. (1998). *Green chemistry: theory and practice*. Oxford University Press.

Asadi, N., and Jalilian, S. (2021). Investigation of the effect of Crataegus species on diversity indices in the natural species (*Anagyris foetida L.*). *Cent. Asian J. Environ. Sci. Technol. Innov.* 2, 119–128. doi:10.22034/CAJPSI.2021.04.06

Aydemir, M., Haykir, G., Selvitopi, H., Arslan, M., Abay, B., Turksoy, F., et al. (2023). Exploring the potential of anthracene derivatives as fluorescence emitters for biomedical applications. *J. Mat. Chem. B* 11, 4287–4295. doi:10.1039/d3tb00449j

Baghbanian, S. M. (2014). Synthesis, characterization, and application of Cu_2O and NiO nanoparticles supported on natural nanozeolite clinoptilolite as a heterogeneous catalyst for the synthesis of pyrano[3,2-b]pyrans and pyrano[3,2-c]pyridones. *RSC Adv.* 4, 59397–59404. doi:10.1039/c4ra10537k

Bakhshi, B., Rostami-Ahmadvandi, H., and Fanaei, H. (2021). Camelina, an adaptable oilseed crop for the warm and dried regions of Iran. *Cent. Asian J. Plant Sci. Innov.* 1, 39–45. doi:10.22034/CAJPSI.2021.01.05

Balwe, S. G., Shinde, V. V., Rokade, A. A., Park, S. S., and Jeong, Y. T. (2017). Green synthesis and characterization of silver nanoparticles (Ag NPs) from extract of plant Radix Puerariae: an efficient and recyclable catalyst for the construction of pyrimido [1,2-b]indazole derivatives under solvent-free conditions. *Catal. Commun.* 99, 121–126. doi:10.1016/j.catcom.2017.06.006

Bass, A. D., Castellanos., D. A., Calicdan, X. A., and Cao, D. (2024). Synthesis and characterization of 1,2,3,4-naphthalene and anthracene diimides. *Beilstein J. Org. Chem.* 20, 1767–1772. doi:10.3762/bjoc.20.155

Bauer, I., and Knölker, H. J. (2015). Iron catalysis in organic synthesis. *Chem. Rev.* 115, 3170–3387. doi:10.1021/cr500425u

Baviera, G. S., and Donate, P. M. (2021). Recent advances in the syntheses of anthracene derivatives. *Beilstein J. Org. Chem.* 17, 2028–2050. doi:10.3762/bjoc.17.131

Becker, H. D. (1993). Unimolecular photochemistry of anthracenes. *Chem. Rev.* 93, 145–172. doi:10.1021/cr00017a008

Beller, M., and Bolm, C. (2004). *Transition metals for organic synthesis: building blocks and fine chemicals* (Wiley VCH).

Bhattacharjee, D., Sheet, S. K., Khatua, S., Biswas, K., Joshi, S., and Myrboh, B. (2018). A reusable magnetic nickel nanoparticle based catalyst for the aqueous synthesis of diverse heterocycles and their evaluation as potential anti-bacterial agent. *Bioorg. Med. Chem.* 26, 5018–5028. doi:10.1016/j.bmc.2018.08.033

Bhowmik, P. K., Nedeltchev, A. K., and Han, H. (2009). Synthesis, thermal, and light-emitting properties of anthracene derivatives. *Mol. Cryst. Liq. Cryst.* 501, 125–137. doi:10.1080/15421400802697707

Brabec, C. J., Heeney, M., McCulloch, I., and Nelson, J. (2011). Influence of blend microstructure on bulk heterojunction organic photovoltaic performance. *Chem. Soc. Rev.* 40, 1185–1199. doi:10.1039/c0cs00045k

Bullock, R. M. (2013). *Catalysis without precious metals*. Wiley VCH.

Burrell, A. K., Officer, D. L., Plieger, P. G., and Reid, D. C. W. (2001). Synthetic routes to multiporphyrin arrays. *Chem. Rev.* 101, 2751–2796. doi:10.1021/cr0000426

Chan, J. M. W., Tischler, J. R., Kooi, S. E., Bulović, V., and Swager, T. M. (2009). Synthesis of J-aggregating dibenz[*a*,*j*]anthracene-based macrocycles. *J. Am. Chem. Soc.* 131, 5659–5666. doi:10.1021/ja900382r

Chen, M., Yan, L., Zhao, Y., Murtaza, I., Meng, H., and Huang, W. (2018). Anthracene-based semiconductors for organic field-effect transistors. *J. Mater. Chem. C* 6, 7416–7444. doi:10.1039/c8tc01865k

Clar, E. (1964). *Polycyclic hydrocarbons*, 1. Academic Press.

Climent, M. J., Corma, A., Hernández, J. C., Hungría, A. B., Iborra, S., and Martınez-Silvestre, S. (2012). Biomass into chemicals: one-pot two- and three-step synthesis of quinoxalines from biomass-derived glycols and 1,2-dinitrobenzene derivatives using supported gold nanoparticles as catalysts. *J. Catal.* 292, 118–129. doi:10.1016/j.jcat.2012.05.002

Climent, M. J., Corma, A., Iborra, S., and Martınez-Silvestre, S. (2013). Gold catalysis opens up a new route for the synthesis of benzimidazoylquinoxaline derivatives from

biomass-derived products (glycerol). *ChemCatChem* 5, 3866–3874. doi:10.1002/cctc.201300416

Colacot, T. J. (Editors) (2015). New trends in cross-coupling: theory and applications. *The Royal Society of Chemistry*.

Corrêa, T. A., Alves, C. C. S., Castro, S. B. R., Oliveira, E. E., Franco, L. S., Ferreira, A. P., et al. (2013). Synthesis of 1,4-Anthracene-9,10-dione derivatives and their regulation of nitric oxide, IL-1β and TNF-α in activated RAW264.7 cells. *Chem. Biol. Drug Des.* 82, 463–467. doi:10.1111/cbdd.12183

Crabtree, R. H. (2009). *The organometallic chemistry of the transition metals*. John Wiley and Sons.

Dandia, A., Sharma, V., Parewa, B., Kumawat, K. S., and Sharma, A. (2015). Amidic C–N bond cleavage of isatin: chemoselective synthesis of pyrrolo[2,3,4-*kl*]acridin-1-ones using Ag NPs decorated rGO composite as an efficient and recoverable catalyst under microwave irradiation. *RSC Adv.* 5, 91888–91902. doi:10.1039/c5ra11747j

Du, C.-B., Long, Y.-J., i Han, X.-N., Han, Y., and Chen, C.-F. (2024a). Recent advances in novel chiral macrocyclic arenes. *Chem. Commun.* 60, 13492–13506. doi:10.1039/d4cc05084c

Du, Y., Mei, H., Makarem, A., Javahershenas, R., Soloshonok, V. A., and Han, J. (2024b). Copper-catalyzed multicomponent reaction of β-trifluoromethyl β-diazo esters enabling the synthesis of β-trifluoromethyl *N*,*N*-diacyl-β-amino esters. *Beilstein J. Org. Chem.* 20, 212–219. doi:10.3762/bjoc.20.21

El-Remailya, M. A. E. A. A. A., and Hamad, H. A. (2015). Synthesis and characterization of highly stable superparamagnetic CoFe2O4 nanoparticles as a catalyst for novel synthesis of thiazolo[4,5-b]quinolin-9-one derivatives in aqueous medium. *J. Mol. Catal. A Chem.* 404, 148–155. doi:10.1016/j.molcata.2015.04.023

Fan, G., Zhang, Z., Wang, G., Shao, L., Hua, B., and Huang, F. (2024). Construction of hydrocarbon belts based on macrocyclic arenes. *Chem. Sci.* 15, 10713–10723. doi:10.1039/d4sc02576h

Fang, Y., Du, X., Du, Z., Wang, H., and Cheng, X. (2017). Light- and heat-triggered polyurethane based on dihydroxyl anthracene derivatives for self-healing applications. *J. Mater. Chem. A* 5, 8010–8017. doi:10.1039/c7ta00871f

Farokhian, E., Tohidi Nejad, E., and Mohamadi Nejad, G. (2021). Studying the effect of bio-fertilizers on the yield of Sesamum indicum genotypes under drought stress. *Cent. Asian J. Plant Sci. Innov.* 1, 32–38. doi:10.22034/CAJPSI.2021.01.04

Floyd, A. J., Dyke, S. F., and Ward, S. E. (1976). The synthesis of phenanthrenes. *Chem. Rev.* 76, 509–562. doi:10.1021/cr60303a001

Fukutani, T., Hirano, K., Satoh, T., and Miura, M. (2009). Synthesis of highly substituted naphthalene and anthracene derivatives by rhodium-catalyzed oxidative coupling of arylboronic acids with alkynes. *Org. Lett.* 11, 5198–5201. doi:10.1021/ol9021172

Guo, X., Wang, L., Hu, J., and Zhang, M. (2018). CuI nanoparticle-catalyzed synthesis of tetracyclic benzo[*e*]benzo[4,5]imidazo[1,2-*c*] [1,3]thiazin-6-imine heterocycles by S_NAr-type C–S, C–N bond formation from isothiocyanatobenzenes and benzimidazoles. *RSC Adv.* 8, 22259–22267. doi:10.1039/c8ra02552e

Han, X.-N., Han, Y., and Chen, C.-F. (2023). Recent advances in the synthesis and applications of macrocyclic arenes. *Chem. Soc. Rev.* 52, 3265–3298. doi:10.1039/d3cs00002h

Hartwig, J. F. (2008). Pharma industry strategic performance: 2007–2012E. *Nat. Rev. Drug Discov.* 7, 967–977. doi:10.1038/nrd2768

Hartwig, J. F. (2010). *Organotransition metal chemistry: from bonding to catalysis*. Sausalito: University Science Books. 1160.

Harvey, R. G. (2004). Advances in the synthesis of polycyclic aromatic compounds. *Cur. Org. Chem.* 8, 303–323. doi:10.2174/1385272043485918

Hassanpour, M. (2021). Techno-economic assessment model of screening step of agricultural wastes recycling to animal feed project. *Cent. Asian J. Environ. Sci. Technol. Innov.* 2, 1–11. doi:10.22034/CAJESTI.2021.01.01

Heravi, M. R. P., Hosseinian, A., Rahmani, Z., Ebadi, A., and Vessally, E. (2021). Transition-metal-catalyzed dehydrogenative coupling of alcohols and amines: a novel and atom-economical access to amides. *J. Chin. Chem. Soc.* 68, 723–737. doi:10.1002/jccs.202000301

Ho, M.-H., Wu, Y.-S., Wen, S.-W., Chen, T.-M., and Chen, C. H. (2007). Efficient deep blue emitters for organic electroluminescent devices. *Appl. Phys. Lett.* 91, 083515. doi:10.1063/1.2773962

Hoffmann, H., Mukanov, D., Ganschow, M., Rominger, F., Freudenberg, J., and Bunz, U. H. F. (2019). 2,3-Dihalo- and 2,3,6,7-tetrahaloanthracenes by vollhardt trimerization. *J. Org. Chem.* 84, 9826–9834. doi:10.1021/acs.joc.9b01567

Huang, J., Su, J.-H., and Tian, H. (2012). The development of anthracene derivatives for organic light-emitting diodes. *J. Mater. Chem.* 22, 10977–10989. doi:10.1039/c2jm16855c

Hueso-Falcón, I., Amesty, Á., Martín, P., López-Rodríguez, M., Fernández-Pérez, L., and Estévez-Braun, A. (2014). Indium catalyzed solvent-free multicomponent synthesis of cytotoxic dibenzo[a,h]anthracenes from aldehydes, 2-hydroxy-1,4-naphthoquinone, and 2-naphthol. *Tetrahedron* 70, 8480–8487. doi:10.1016/j.tet.2014.09.076

Hurley, L. H. (2002). DNA and its associated processes as targets for cancer therapy. *Nat. Rev. Cancer* 2, 188–200. doi:10.1038/nrc749

Hussain, N., Gogoi, P., Das, M. R., Sengupta, P., Fedorov, V. E., Asanov, I. P., et al. (2017). Development of novel efficient 2D nanocomposite catalyst towards the three-component coupling reaction for the synthesis of imidazo[1,2-a]pyridines. *Appl. Catal. A* 542, 368–379. doi:10.1016/j.apcata.2017.05.033

Ihmels, H., Meiswinkel, A., and Mohrschladt, C. (2000). Novel fluorescence probes based on 2,6-Donor–Acceptor-substituted anthracene derivatives. *Org. Lett.* 2, 2865–2867. doi:10.1021/ol006291y

Imeni, S., Makarem, A., and Javahershenas, R. (2023). Recent advances in multicomponent electro-organic (electrochemical) synthesis of heterocycles. *Asian J. Org. Chem.* 12, e202300303. doi:10.1002/ajoc.202300303

Inamdar, S. M., More, V. K., and Mandal, S. K. (2013). CuO nano-particles supported on silica, a new catalyst for facile synthesis of benzimidazoles, benzothiazoles and benzoxazoles. *Tetrahedron Lett.* 54, 579–583. doi:10.1016/j.tetlet.2012.11.091

Iordanidou, T., Zarganes-Tzitzikas, C. G., Neochoritis, A., and Lykakis, I. N. (2018). Application of silver nanoparticles in the multicomponent reaction domain: a combined catalytic reduction methodology to efficiently access potential hypertension or inflammation inhibitors. *ACS Omega* 3, 16005–16013. doi:10.1021/acsomega.8b02749

Ito, K., Suzuki, T., Sakamoto, Y., Kubota, D., Inoue, Y., Sato, F., et al. (2003). Oligo(2,6-anthrylene)s: acene–oligomer approach for organic field-effect transistors. *Angew. Chem. Int. Ed.* 42, 1159–1162. doi:10.1002/anie.200390305

Iyengar, B. S., Dorr, R. T., Alberts, D. S., Solyom, A. M., Krutzsch, M., and Remers, W. A. (1997). 1,4-Disubstituted anthracene antitumor agents. *J. Med. Chem.* 40, 3734–3738. doi:10.1021/jm970308+

Jacobsen, E. N., Pfaltz, A., and Yamamoto, H. (2010). *Comprehensive asymmetric catalysis*. Springer.

Jalali Sarvestani, M., and Charehjou, P. (2021). Fullerene (C20) as a potential adsorbent and sensor for the removal and detection of picric acid contaminant: a DFT study. *Cent. Asian J. Environ. Sci. Technol. Innov.* 2, 12–19. doi:10.22034/CAJESTI.2021.01.02

Jalilian, S. (2020). Environmental risk assessment of Saman cement factory in Kermanshah in Iran by AHP and TOPSIS methods. *Cent. Asian J. Environ. Sci. Technol. Innov.* 1, 298–309. doi:10.22034/CAJESTI.2020.06.03

Javahershenas, R., Han, J., Kazemi, M., and Jervis, P. J. (2024a). Recent advances in the multicomponent synthesis of heterocycles using thiosemicarbazide. *ChemistrySelect* 9, e202401496. doi:10.1002/slct.202401496

Javahershenas, R., Han, J., Kazemi, M., and Jervis, P. J. (2024b). Recent advances in the application of 2-aminobenzothiazole to the multicomponent synthesis of heterocycles. *ChemistryOpen* 13, e202400185. doi:10.1002/open.202400185

Javahershenas, R., Makarem, A., and Klika, K. D. (2024d). Recent advances in microwave-assisted multicomponent synthesis of spiro heterocycles. *RSC Adv.* 14, 5547–5565. doi:10.1039/d4ra00056k

Javahershenas, R., and Nikzat, S. (2023). Recent advances in the multicomponent synthesis of heterocycles using tetronic acid. *RSC Adv.* 13, 16619–16629. doi:10.1039/d3ra02505e

Javahershenas, R., Soloshonok, V. A., Klika, K. D., and Jervis, P. J. (2024c). Correction: Carbon nanotubes as heterogeneous catalysts for the multicomponent reaction synthesis of heterocycles. *Carbon Lett.* doi:10.1007/s42823-024-00835-w

Johansson Seechurn, C. C., Kitching, M. O., Colacot, T. J., and Snieckus, V. (2012). Palladium-catalyzed cross-coupling: a historical contextual perspective to the 2010 Nobel prize. *Angew. Chem. Int. Ed.* 51, 5062–5085. doi:10.1002/anie.201107017

Kaewpuang, T., Hadsadee, S., Jungsuttiwong, S., Khanasa, T., and Chiang Mai, J. (2024). Anthracene and pyrene derivatives as blue fluorophores: synthesis, characterization and photophysical properties. *Scie* 51, 1–10. doi:10.12982/cmjs.2024.020

Kahrizi, S., Kahrizi, S., Rashidi, F., and Rashidi, N. (2021). Effect of 6-Benzylaminopurine on micropropagation of Nuphar lutea as an endangered species. *Cent. Asian J. Plant Sci. Innov.* 1, 70–75. doi:10.22034/CAJPSI.2021.02.02

Kastrati, A., Oswald, F., Scalabre, A., and Fromm, K. M. (2023). Photophysical properties of anthracene derivatives. *Photochem* 3, 227–273. doi:10.3390/photochem3020015

Khafaei, M., Sadeghi Hajiabadi, M., and Abdolmaleki, A. (2021). Role of 1,25-dihydroxycholecalciferol in immunological and molecular pathways involved in Multiple Sclerosis. *Cent. Asian J. Med. Pharm. Sci. Innov.* 1, 55–66. doi:10.22034/CAJMPSI/2021.02.02

Khan, J. (2024). Synthesis and applications of fluorescent chemosensors: a review. *J. Fluoresc.* 34, 2485–2494. doi:10.1007/s10895-023-03455-1

Khandaka, H., Upadhayay, Y., Soni, A., Manohardas, S., and Joshi, R. K. (2023). Facile synthesis of anthracene-based derivatives via a magnetically retrievable Fe3O4@SiO2 immobilized selenoether functionalised NHC-Pd(II) heterogenous catalyst: photophysical, electrochemical and DFT studies of novel 9,10-anthracene based derivatives. *Inorg. Chim. Acta* 565, 121840. doi:10.1016/j.ica.2023.121840

Khatun, N., Guin, S., Rout, S. K., and Patel, B. K. (2014). Divergent reactivities of o-haloanilides with CuO nanoparticles in water: a green synthesis of benzoxazoles and o-hydroxyanilides. *RSC Adv.* 4, 10770–10778. doi:10.1039/c3ra46820h

Khan, D., Xiaotao, Z., Jameel, M. H., Bin Agam, M. A., Bin Roslan, M. S., and Bajaber, M. A. (2023). Synthesis and optoelectronic properties of an anthracene derivative. *Micro and Nano Syst Lett* 11, 24. doi:10.1186/s40486-023-00187-6

Khazaei, A., Ranjbaran, A., Abbasi, F., Khazaei, M., and Moosavi-Zare, A. R. (2015). Synthesis, characterization and application of $ZnFe_2O_4$nanoparticles as a heterogeneous ditopic catalyst for the synthesis of pyrano[2,3-d] pyrimidines. *RSC Adv.* 5, 13643–13647. doi:10.1039/c4ra16664g

Kidwai, A., Jain, S., and Bhardwaj, S. (2012). Magnetic nanoparticles catalyzed synthesis of diverse N-Heterocycles. *Mol. Divers.* 16, 121–128. doi:10.1007/s11030-011-9336-z

Kim, K., Vasu, D., Im, H., and Hong, S. (2016). Palladium(II)-Catalyzed tandem synthesis of acenes using carboxylic acids as traceless directing groups. *Angew. Chem. Int. Ed.* 55, 8652–8655. doi:10.1002/anie.201603661

Kitazawa, K., Kochi, T., Nitani, M., Ie, Y., Aso, Y., and Kakiuchi, F. (2011). Convenient synthesis of dibenzo[*a*,*h*]anthracenes and picenes via C–H arylation of acetophenones with arenediboronates. *Chem. Lett.* 40, 300–302. doi:10.1246/cl.2011.300

Kivrak, A., Er, Ö. F., Kivrak, H., Topal, Y., Kuş, M., and Çamlısoy, Y. (2017). Synthesis and solar-cell applications of novel furanyl-substituted anthracene derivatives. *Opt. Mater.* 73, 206–212. doi:10.1016/j.optmat.2017.08.014

Kodomari, M., Nagamatsu, M., Akaike, M., and Aoyama, T. (2008). Convenient synthesis of triarylmethanes and 9,10-diarylanthracenes by alkylation of arenes with aromatic aldehydes using acetyl bromide and ZnBr2/SiO2. *Tetrahedron Lett.* 49, 2537–2540. doi:10.1016/j.tetlet.2008.02.117

Koley, M., Han, J., Soloshonok, V. A., Mojumder, S., Javahershenas, R., and Makarem, A. (2023). External oxidants in gold-catalyzed cross-coupling reactions. *J. Coord. Chem.* 77, 1–48. doi:10.1080/00958972.2023.2286182

Kouam, S. F., Yapna, D. B., Krohn, K., Ngadjui, B. T., Ngoupayo, J., Choudhary, M. I., et al. (2007). Antimicrobial prenylated anthracene derivatives from the leaves of *Harungana madagascariensis*. *J. Nat. Prod.* 70, 600–603. doi:10.1021/np060556l

Kumar, B., Smita, K., Cumbal, L., and Debut, A. (2014). Biogenic synthesis of iron oxide nanoparticles for 2-arylbenzimidazole fabrication. *J. Saudi Chem. Soc.* 18, 364–369. doi:10.1016/j.jscs.2014.01.003

Kuninobu, Y., Tatsuzaki, T., Matsuki, T., and Takai, K. (2011). Indium-catalyzed construction of polycyclic aromatic hydrocarbon skeletons via dehydration. *J. Org. Chem.* 76, 7005–7009. doi:10.1021/jo200861s

Lak, R., Kazemi, E., Aavani, P., Alaei, F., and Pashizeh, F. (2021). Association analysis of C677T and A1298C polymorphisms in MTHFR gene in patients with colorectal cancer susceptibility. *Cent. Asian J. Med. Pharm. Sci. Innov.* 1, 74–80. doi:10.22034/CAJMPSI.2021.02.04

Lown, J. W. (1988). *Anthracycline and anthracenedione-based anticancer agents* (Amsterdam: Elsevier).

Mahboub Khomami, A., Haddad, A., Alipoor, R., and Hojati, S. (2021). Cow manure and sawdust vermicompost effect on nutrition and growth of ornamental foliage plants. *Cent. Asian J. Environ. Sci. Technol. Innov.* 2, 68–78. doi:10.22034/CAJESTI.2021.02.03

Malik, E. M., and Müller, C. E. (2016). Anthraquinones as pharmacological tools and drugs. *Med. Res. Rev.* 36, 705–748. doi:10.1002/med.21391

Menendez, C. A., Nador, F., Radivoy, G., and Gerbino, D. C. (2014). One-step synthesis of xanthones catalyzed by a highly efficient copper-based magnetically recoverable nanocatalyst. *Org. Lett.* 16, 2846–2849. doi:10.1021/ol500964e

Modi, A., Ali, W., Mohanta, P. R., Khatun, N., and Patel, B. K. (2015). CuO nanoparticle catalyzed synthesis of 2,3-disubstituted quinazolinones via sequential *N*-arylation and oxidative C–H amidation. *ACS Sustain. Chem. Eng.* 3, 2582–2590. doi:10.1021/acssuschemeng.5b00817

Molnár, Á. (2013). Efficient, selective, and recyclable palladium catalysts in Carbon–Carbon coupling reactions. *Chem. Rev.* 111, 2251–2320. doi:10.1021/cr100355b

Naeimi, H., and Didar, A. (2017). Facile one-pot four component synthesis of pyrido [2,3-d:6,5-d′]dipyrimidines catalyzed by CuFe 2 O 4 magnetic nanoparticles in water. *J. Mol. Struct.* 1137, 626–633. doi:10.1016/j.molstruc.2017.02.044

Nakae, T., Ohnishi, R., Kitahata, Y., Soukawa, T., Sato, H., Mori, S., et al. (2012). Effective synthesis of diiodinated picene and dibenzo[a,h]anthracene by AuCl-catalyzed double cyclization. *Tetrahedron Lett.* 53, 1617–1619. doi:10.1016/j.tetlet.2012.01.071

Nandi, G. C., Samai, S., Kumar, R., and Singh, M. S. (2009). An efficient one-pot synthesis of tetrahydrobenzo[a]xanthene-11-one and diazabenzo[a]anthracene-9,11-dione derivatives under solvent free condition. *Tetrahedron* 65, 7129–7134. doi:10.1016/j.tet.2009.06.024

Negishi, E. (2002). *Handbook of organopalladium chemistry for organic synthesis*. Wiley-Interscience.

Nguyen, O. T. K., Ha, P. T., Dang, H. V., Vo, Y. H., Nguyen, T. T., Le, N. T. H., et al. (2019). Superparamagnetic nanoparticle-catalyzed coupling of 2-amino pyridines/pyrimidines with *trans*-chalcones. *RSC Adv.* 9, 5501–5511. doi:10.1039/c9ra00097f

Noyori, R. (2013). *Asymmetric catalysis in organic synthesis*. John Wiley and Sons.

Okumoto, K., Kanno, H., Hamaa, Y., Takahashi, H., and Shibata, K. (2006). Erratum: "Green fluorescent organic light-emitting device with external quantum efficiency of nearly 10%" [Appl. Phys. Lett. 89, 063504 (2006)]. *Appl. Phys. Lett.* 89, 063504. doi:10.1063/1.2359696

Oliveira, M. S., Chorociejus, G., Angeli, J. P. F., Verde, G. V., Aquino, G. L. B., Ronsein, G. E., et al. (2020). Heck reaction synthesis of anthracene and naphthalene derivatives as traps and clean chemical sources of singlet molecular oxygen in biological systems. *Photochem Photobiol. Sci.* 19, 1590–1602. doi:10.1039/d0pp00153h

Park, H., Yoo, K., Jung, B., and Kim, M. (2018). Direct synthesis of anthracenes from o-tolualdehydes and aryl iodides through Pd(II)-Catalyzed sp C H arylation and electrophilic aromatic cyclization. *Tetrahedron* 74, 2048–2055. doi:10.1016/j.tet.2018.03.006

Park, I. S., Kwon, M. S., Kim, Y., Lee, J. S., and Park, J. (2008). Heterogeneous copper catalyst for the cycloaddition of azides and alkynes without additives under ambient conditions. *Org. Lett.* 10, 497–500. doi:10.1021/ol702790w

Parte, L. G., Fernández, S., Sandonís, E., Guerra, J., and López, E. (2024). Transition-metal-catalyzed transformations for the synthesis of marine drugs. *Mar. Drugs* 22, 253. doi:10.3390/md22060253

Pozzo, J.-L., Desvergne, J.-P., Clavier, G. M., Bouas-Laurent, H., Jones, P. G., and Perlstein, J. (2001). *J. Chem. Soc. Perkin Trans.* 2, 824–826. doi:10.1039/b008084p

Prier, C. K., Rankic, D. A., and MacMillan, D. W. (2013). Visible light photoredox catalysis with transition metal complexes: applications in organic synthesis. *Chem. Rev.* 113, 5322–5363. doi:10.1021/cr300503r

Psutka, K. M., Williams, J., Paquette, J. A., Calderon, O., Bozek, K. J. A., Williams, V. E., et al. (2015). Synthesis of substituted dibenz[*a*,*c*]anthracenes and an investigation of their liquid-crystalline properties. *Eur. J. Org. Chem.* 2015, 1456–1463. doi:10.1002/ejoc.201403504

Pünner, F., Schieven, J., and Hilt, G. (2013). Synthesis of fluorenone and anthraquinone derivatives from aryl- and aroyl-substituted propiolates. *Org. Lett.* 15, 4888–4891. doi:10.1021/ol4023276

Rabbani, B., and Safdary, A. (2021). Effect of Sowing date and plant density on yield and yield components of three maize (Zea mays L.) genotypes in Takhar climatic conditions of Afghanistan. *Cent. Asian J. Plant Sci. Innov.* 1, 109–120. doi:10.22034/CAJPSI.2021.02.06

Rasouli, A., Bafkar, Z., and Chaghakaboodi, Z. (2020). Kinetic and equilibrium studies of adsorptive removal of sodium-ion onto wheat straw and rice husk wastes. *Cent. Asian J. Environ. Sci. Technol. Innov.* 1, 310–329. doi:10.22034/CAJESTI.2020.06.04

Reddy, V., and Jeong, Y. T. (2016). Copper(ii) oxide nanoparticles as a highly active and reusable heterogeneous catalyst for the construction of phenyl-1H-pyrazolo[3,4-b] pyridine derivatives under solvent-free conditions. *RSC Adv.* 6, 103838–103842. doi:10.1039/c6ra22445h

Ren, Z.-H., Guan, Z.-H., and Liang, Y.-M. (2009). Highly regioselective synthesis of benz[*a*]anthracene derivatives via a Pd-catalyzed tandem C–H activation/biscyclization reaction. *J. Org. Chem.* 74, 3145–3147. doi:10.1021/jo802712n

Robertson, J. M. (1930). Structure of naphthalene and anthracene. *Rev. Mod. Phys.* 30, 155–158. doi:10.1103/revmodphys.30.155

Sabernezhad, M. (2021). Quantitative analysis of p53 substitution mutation and breast cancer; An informative study in Iranian population. *Cent. Asian J. Med. Pharm. Sci. Innov.* 1, 8–14. doi:10.22034/CAJMPSI.2021.01.02

Sadeghzadeh, S. M. (2016). Gold (III) phosphorus complex immobilized on fibrous nano-silica as a catalyst for the cyclization of propargylic amines with CO2. *J. Mol. Catal. A Chem.* 423, 216–223. doi:10.1016/j.molcata.2016.07.001

Saffariha, M., Azarnivand, H., ZareChahouki, M., Tavili, A., NejadEbrahimi, S., and Potter, D. (2021). *Cent. Asian J. Environ. Sci. Technol. Innov.* 2, 36–44.

Saha, P., Ramana, T., Purkait, N., Ali, M. A., Paul, R., and Punniyamurthy, T. (2009). Ligand-free copper-catalyzed synthesis of substituted benzimidazoles, 2-aminobenzimidazoles, 2-aminobenzothiazoles, and benzoxazoles. *J. Org. Chem.* 74, 8719–8725. doi:10.1021/jo901813g

Saino, N., Kawaji, T., Ito, T., Matsushita, Y., and Okamoto, S. (2010). Synthesis of substituted anthracenes, pentaphenes and trinaphthylenes via alkyne-cyclotrimerization reaction. *Tetrahedron Lett.* 51, 1313–1316. doi:10.1016/j.tetlet.2009.12.130

Salam, N., Sinha, A., Roy, A. S., Mondal, P., Jana, N. R., and Islam, S. M. (2014). Synthesis of silver–graphene nanocomposite and its catalytic application for the one-pot three-component coupling reaction and one-pot synthesis of 1,4-disubstituted 1,2,3-triazoles in water. *RSC Adv.* 4, 10001–10012. doi:10.1039/c3ra47466f

Santra, S., Ranjan, P., Bera, P., Ghosh, P., and Mandal, S. K. (2012). Anchored palladium nanoparticles onto single walled carbon nanotubes: efficient recyclable catalyst for N-containing heterocycles. *RSC Adv.* 2, 7523–7533. doi:10.1039/c2ra20281f

Sawano, T., Toyoshima, Y., and Takeuchi, R. (2019). Synthesis of anthraquinones by iridium-catalyzed [2 + 2 + 2] cycloaddition of a 1,2-Bis(propiolyl)benzene derivative with alkynes. *Inorganics* 7, 138. doi:10.3390/inorganics7110138

Sead, F. F., Jain, V., Ballal, S., Singh, A., Devi, A., and Sharma, G. C. (2021). Research on transition metals for the multicomponent synthesis of benzo-fused γ-lactams. *RSC Adv.* 15, 2334–2346. doi:10.1039/D4RA08798D

Sead, F. F., Jain, V., Kumar, A., Rekha, M. M., Kundlas, M., and Gupta, S. (2025). Magnetically recoverable catalysts for efficient multicomponent synthesis of organosulfur compounds. *SC Adv.* 15, 3928–3953. doi:10.1039/d4ra08769k

Sheldon, R. A., Arends, I. W., and Hanefeld, U. (2007). *Green chemistry and catalysis*. Wiley VCH.

Shi, W., Yang, X., Li, X., Meng, L., Zhang, D., Xiao, X., et al. (2022). Syntheses of anthracene-centered large PAH diimides and conjugated polymers**. *Chem. Eur. J.* 28, e202104598. doi:10.1002/chem.202104598

Shu, C., Chen, C.-B., Chen, W.-X., and Ye, L.-W. (2013). Flexible and practical synthesis of anthracenes through gold-catalyzed cyclization of *o*-alkynyldiarylmethanes. *Org. Lett.* 15, 5542–5545. doi:10.1021/ol402713g

Sivasakthikumaran, R., Rafiq, S. M., Sankar, E., Clement, J. A., and Mohanakrishnan, A. K. (2015). Regioselective annulation of unsymmetrical 1,2-Phenylenebis(diaryl/diheteroarylmethanol): a facile synthesis of anthracene, tetracene, and naphtho[*b*]thiophene analogues. *Eur. J. Org. Chem.* 2015, 7816–7835. doi:10.1002/ejoc.201501087

Soldi, R., Horrigan, S. K., Cholody, M. W., Padia, J., Sorna, V., Bearss, J., et al. (2015). Design, synthesis, and biological evaluation of a series of anthracene-9,10-dione dioxime β-catenin pathway inhibitors. *J. Med. Chem.* 58, 5854–5862. doi:10.1021/acs.jmedchem.5b00460

Suchand, B., and Satyanarayana, G. (2019). Palladium-catalyzed direct acylation: one-pot relay synthesis of anthraquinones. *Synthesis* 51, 769–779. doi:10.1055/s-0037-1610296

Suzuki, A. (2011). Cross-coupling reactions of organoboranes: an easy way to construct C–C bonds (Nobel lecture). *Angew. Chem. Int. Ed.* 50, 6722–6737. doi:10.1002/anie.201101379

Suzuki, A., and Company, A. (2011). Palladium-catalysed hydroxylation and alkoxylation. *Chem. Soc. Rev.* 40, 4912–4921. doi:10.1039/c1cs15085e

Trost, B. M. (1991). The atom economy—a search for synthetic efficiency. *Science* 254, 1471–1477. doi:10.1126/science.1962206

Trost, B. M., and Crawley, M. L. (2003). Asymmetric Transition-Metal-Catalyzed Allylic Alkylations: Applications in Total Synthesis. *Chem. Rev.* 103, 2921–2943. doi:10.1021/cr020027w

Tsuji, J. (2005). *Transition metal reagents and catalysts: innovations in organic synthesis*. Wiley.

Umeda, R., Miyake, S., and Nishiyama, Y. (2012). Synthesis of dibenz[*a*,*h*]anthracenes by Pd-catalyzed intramolecular double-cyclization of (*Z*,*Z*)-*p*-Styrylstilbenes. *Chem. Lett.* 41, 215–217. doi:10.1246/cl.2012.215

Van Damme, J., and Du Prez, F. (2018). Anthracene-containing polymers toward high-end applications. *Prog. Polym. Sci.* 82, 92–119. doi:10.1016/j.progpolymsci.2018.02.002

van Leeuwen, P. W. (2004). *Homogeneous catalysis: understanding the art*. Springer Science and Business Media.

Venitt, S., Crofton-Sleigh, C., Agbandje, M., Jenkins, T. C., and Neidle, S. (1998). Anthracene-9,10-diones as potential anticancer Agents: bacterial mutation studies of amido-substituted derivatives reveal an unexpected lack of mutagenicity. *J. Med. Chem.* 41, 3748–3752. doi:10.1021/jm980167r

Vorona, M.Y., Yutronkie, N.J., Melville, O.A., Daszczynski, A.J., Agyei, K. T., Ovens, J.S., et al. (2019). Developing 9,10-anthracene derivatives: optical, electrochemical, thermal, and electrical characterization. *Materials (Basel)*. 12(17):2726. doi:10.3390/ma12172726

Wang, C., Dong, H., Hu, W., Liu, Y., and Zhu, D. (2012). Semiconducting π-conjugated systems in field-effect transistors: a material odyssey of organic electronics. *Chem. Rev.* 112, 2208–2267. doi:10.1021/cr100380z

Wencel-Delord, J., Nimphius, C., Wang, H., and Glorius, F. (2012). Rhodium(III) and hexabromobenzene—a catalyst system for the cross-dehydrogenative coupling of simple arenes and heterocycles with arenes bearing directing groups. *Angew. Chem. Int. Ed.* 51, 13001–13005. doi:10.1002/anie.201205734

Wu, C.-L., Chang, C.-H., Chang, Y.-T., Chen, C.-T., Chen, C.-T., and Su, C.-J. (2014). High efficiency non-dopant blue organic light-emitting diodes based on anthracene-based fluorophores with molecular design of charge transport and red-shifted emission proof. *J. Mater. Chem. C* 2, 7188–7200. doi:10.1039/c4tc00876f

Yoshizawa, M., and Klosterman, J. K. (2014). Molecular architectures of multi-anthracene assemblies. *Chem. Soc. Rev.* 43, 1885–1898. doi:10.1039/c3cs60315f

Zarren, G., Nisar, B., and Sher, F. (2019). Synthesis of anthraquinone-based electroactive polymers: a critical review. *Today Sustain.* 5, 100019. doi:10.1016/j.mtsust.2019.100019

Zehm, D., Fudickar, W., Hans, M., Schilde, U., Kelling, A., and Linker, T. (2008). 9,10-Diarylanthracenes as molecular switches: syntheses, properties, isomerisations and their reactions with singlet oxygen. *Chemistry* 14, 11429–11441. doi:10.1002/chem.200801355

Zeidali, E., MardaniKorrani, H., Alizadeh, Y., and Kamari, F. (2021). Ethnopharmacological survey of medicinal plants in semi-arid rangeland in western Iran. *Cent. Asian J. Plant Sci. Innov.* 1, 46–55. doi:10.22034/CAJPSI.2021.01.06

Zhang, W., Guo, F., Wang, F., Zhao, N., Liu, L., Li, J., et al. (2014). Synthesis of quinazoline via CuO nanoparticles catalyzed aerobic oxidative coupling of aromatic alcohols and amidines. *Org. Biomol. Chem.* 12, 5752–5756. doi:10.1039/c4ob00569d

Zhang, W., Wang, Q., Feng, X., Yang, L., Wu, Y., and Wei, X. (2017). Anthracene-based derivatives: Synthesis, photophysical properties and electrochemical properties. *Chem. Res. Chin. Univ.* 33, 603–610. doi:10.1007/s40242-017-6431-4

Zhang, X., Yu, X., Ji, D., Yamamoto, Y., Almansour, A. I., Arumugam, N., et al. (2016). Rhodium-catalyzed oxidative benzannulation of *N*-Adamantyl-1-naphthylamines with internal alkynes via dual C–H bond activation: synthesis of substituted anthracenes. *Org. Lett.* 18, 4246–4249. doi:10.1021/acs.orglett.6b01991

Zhang, Y., Ying, H., and Xu, X. (2019). Ru(II)-based antineoplastic: A "wingtip" N-heterocyclic carbene facilitates access to a new class of organometallics that are cytotoxic to common cancer cell lines. *Appl. Organomet. Chem.* 33, e4692. doi:10.1002/aoc.4692

Zhao, T., Wu, W., and Yang, C. (2023). Chiroptical regulation of macrocyclic arenes with flipping-induced inversion of planar chirality. *Chem. Commun.* 59, 11469–11483. doi:10.1039/d3cc03829g

Zhao, Y., Yan, L., Murtaza, I., Liang, X., Meng, H., and Huang, W. (2017). A thermally stable anthracene derivative for application in organic thin film transistors. *Org. Electron.* 43, 105–111. doi:10.1016/j.orgel.2017.01.005

Zhu, Y., and Zhu, W. (2013). Organic sensitizers from D–π–A to D–A–π–A: effect of the internal electron-withdrawing units on molecular absorption, energy levels and photovoltaic performances. *Chem. Soc. Rev.* 42, 2039–2058. doi:10.1039/c2cs35346f

Zou, Y., Young, D. D., Cruz-Montanez, A., and Deiters, A. (2008). Synthesis of anthracene and azaanthracene fluorophores via [2+2+2] cyclotrimerization reactions. *Org. Lett.* 10, 4661–4664. doi:10.1021/ol8019549

frontiers | Frontiers in Chemistry

TYPE Original Research
PUBLISHED 28 March 2025
DOI 10.3389/fchem.2025.1557275

Check for updates

OPEN ACCESS

EDITED BY
Greta Varchi,
Consiglio Nazionale delle Ricerche (Bologna), Italy

REVIEWED BY
Moataz Ahmed Shaldam,
Kafrelsheikh University, Egypt
Domiziana Masci,
Catholic University of the Sacred Heart, Rome, Italy

*CORRESPONDENCE
Hua Jiang,
yonghongjiang@163.com
Hong Chen,
chenwexpo@163.com

†These authors have contributed equally to this work

RECEIVED 08 January 2025
ACCEPTED 17 March 2025
PUBLISHED 28 March 2025

CITATION
Jiang H, Chen H, Wang Y, Xu H and Chen H (2025) Synthesis, bioactivity, and molecular docking studies: novel arylpiperazine derivatives as potential new-resistant AR antagonists.
Front. Chem. 13:1557275.
doi: 10.3389/fchem.2025.1557275

COPYRIGHT
© 2025 Jiang, Chen, Wang, Xu and Chen. This is an open-access article distributed under the terms of the Creative Commons Attribution License (CC BY). The use, distribution or reproduction in other forums is permitted, provided the original author(s) and the copyright owner(s) are credited and that the original publication in this journal is cited, in accordance with accepted academic practice. No use, distribution or reproduction is permitted which does not comply with these terms.

Synthesis, bioactivity, and molecular docking studies: novel arylpiperazine derivatives as potential new-resistant AR antagonists

Hua Jiang[1*†], Haowei Chen[2†], Ya Wang[2], Huaxin Xu[2] and Hong Chen[2*]

[1]Department of Urology, The Fifth Affiliated Hospital of Zunyi Medical University (Zhuhai Sixth People's Hospital), Zhuhai, China, [2]Luoyang Key Laboratory of Organic Functional Molecules, College of Food and Drug, Luoyang Normal University, Luoyang, China

The majority of patients with androgen-dependent prostate cancer (PCa) develop resistance to hormone therapy after approximately 18–24 months of androgen deprivation therapy treatment. During this process, PCa cells progressively lose their sensitivity to androgens and evolve into castration-resistant prostate cancer leading to uncontrolled tumor growth and ultimately the failure of endocrine therapy. To develop potential anti-prostate cancer agents, in this study, we identified a novel ether-type arylpiperazine derivative as a potent androgen receptor (AR) antagonist, uncovering a series of effective antiproliferative compounds. The derivatives (**7, 11, 17, 19, 20, 21, 22, 23**, and **24**) demonstrated strong cytotoxicity against cancer cells, with **17, 19, 20**, and **23** showing significant androgen receptor antagonistic activity (Inhibition% >60) and robust AR binding affinities. The structure-activity relationship (SAR) of these developed derivatives was discussed based on data. Docking study suggested that the compound **19** mainly bind to AR ligand binding pocket site through Van der Waals' force interactions. This research presents a promising lead compound for developing anticancer agents targeting prostate cancer therapy.

KEYWORDS

prostate cancer, antagonistic activity, binding affinities, docking study, AR antagonists

Highlights

- A series of arylpiperazine derivative was synthesized.
- The anti-prostate cancer activities of derivatives were investigated.
- Binding affinity and antagonistic potency of derivatives were also investigated against AR.
- Some derivatives exhibited strong activities against AR and cancer cells.
- Molecular docking and SAR of derivatives were also studied.

Introduction

According to the National Cancer Center of China's 2024 National Cancer Report, there has been an increasing trend in both the incidence and mortality rates of prostate cancer in China in

recent years, ranking sixth among the top ten malignant tumors in men (Zheng et al., 2024). The 2022 American Cancer Statistics Report estimated that prostate cancer would be the most common newly diagnosed cancer, accounting for 27%, and the second leading cause of cancer death, accounting for 11% (Siegel et al., 2022). The growth of prostate cancer cells depends on androgens, which exert their biological functions through the AR signaling pathway. Abnormal activation of the AR signaling pathway is the fundamental reason for the occurrence and development of prostate cancer (Dai et al., 2023; He et al., 2022; Jamroze et al., 2021).

Early-stage localized prostate cancer can be completely cured through surgical treatment and radiation therapy. For non-localized, inoperable prostate cancer patients, the first-line therapy is ADT (Choi et al., 2022). Endocrine therapy, while effective at controlling the progression of prostate cancer during the initial stages of treatment, leads to almost all initially hormone-sensitive tumors transforming into CRPC after 18–24 months of therapy (Vellky and Ricke, 2020). This presents significant clinical challenges, as there is currently no effective treatment regimen available for CRPC. Currently, there is no effective treatment for CRPC, although its molecular mechanisms of occurrence and development have not been fully elucidated, extensive research has found that 80% of advanced CRPC overexpress AR (Formaggio et al., 2021; Visakorpi et al., 1995), and the expression of AR in bone metastases is higher than in primary tumors (Fontana et al., 2022; Lu et al., 2020; Obinata et al., 2020). The application of next-generation ADTs (such as enzalutamide and abiraterone) can suppress the progression of CRPC by inhibiting AR in CRPC cells, and the absence of AR in CRPC cells can lead to cell death. This phenomenon indicates that the survival and growth of CRPC still depend on the AR signaling pathway, and the reactivation of AR is the fundamental cause of CRPC. Patients with CRPC constitute the main population at risk of dying from prostate cancer. Therefore, AR has become an important target for the treatment of prostate cancer. However, the development of resistance is a common issue in current endocrine therapies for prostate cancer (Schmidt et al., 2021).

Thus, finding and developing highly effective AR-targeted antagonists that combat resistance for the endocrine treatment of prostate cancer is an urgent need. Naftopidil (NAF, Figure 1), a class of arylpiperazine derivatives, selectively blocks the α1a/1d receptor subtypes, reduces the levels of dihydrotestosterone within the prostate tissue and cells, promotes apoptosis, and is currently used in the treatment of benign prostatic hyperplasia (Zhan et al., 2022). Furthermore, studies have found that NAF can effectively inhibit the proliferation of prostate cancer cells PC-3 and LNCaP, inducing apoptosis (Ishii et al., 2018; Iwamoto et al., 2017; Maesaka et al., 2021). Kinoyama et al. (2005), Kinoyama et al. (2004) reported that arylpiperazine derivatives exhibit significant AR antagonistic activity, with an IC_{50} of 0.11 μmol/L, compared to bicalutamide's IC_{50} of 50 μmol/L. They can inhibit prostate hyperplasia without affecting serum testosterone levels. In recent years, our research team has conducted extensive preliminary basic research on the anti-prostate cancer activity of arylpiperazine derivatives, discovering that some arylpiperazine derivatives show good cytotoxic activity (Chen et al., 2018a; Chen et al., 2018b; Chen et al., 2017; Chen et al., 2015; Chen et al., 2019a; Qi et al., 2022a) and exhibit better antagonistic activity and affinity for AR (Chen et al., 2019a; Chen et al., 2019b).

Although the reported arylpiperazine derivatives possess significant AR antagonistic activity, there is less research on their resistance

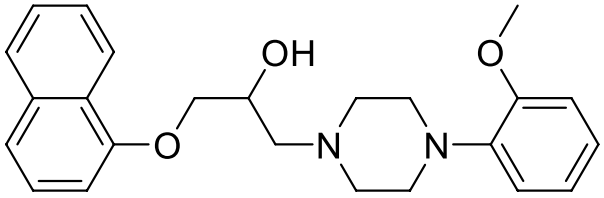


FIGURE 1
Structures of naftopidil.

evaluation and antitumor molecular mechanisms. Based on the aforementioned studies, the drug design strategy of this project is to design and synthesize a new class of arylpiperazine derivatives based on naftopidil (Scheme 1) on the foundation of previous research. The aim is to investigate their biological activity, resistance, and antitumor molecular mechanisms, thereby obtaining new drugs with stronger antagonistic activity and resistance to treat prostate cancer.

Materials and methods

General chemistry

Reagents and solvents were procured via commercial channels. Organic solvents underwent distillation before use. Melting points were determined using an uncalibrated SGW X-4 micro melting point apparatus. NMR spectra were acquired on a Bruker AVANCE-400 spectrometer in $CDCl_3$, employing TMS as an internal standard, with chemical shifts reported in δ (ppm) and coupling constants in Hertz. HRMS spectra were documented on an AB Sciex X500R QTOF mass spectrometer (Foster City, CA, United States). HPLC chromatogram was performed on UltiMate 3000 with H_2O and CH_3CN as the mobile phase. The completion of all reactions was monitored by thin-layer chromatography (TLC) performed on pre-coated silica gel 60 F_{254} TLC plates (VWR), with observations made under ultraviolet light at wavelengths of 254 and/or 365 nm (Sun et al., 2022; Sun et al., 2025).

Cell lines

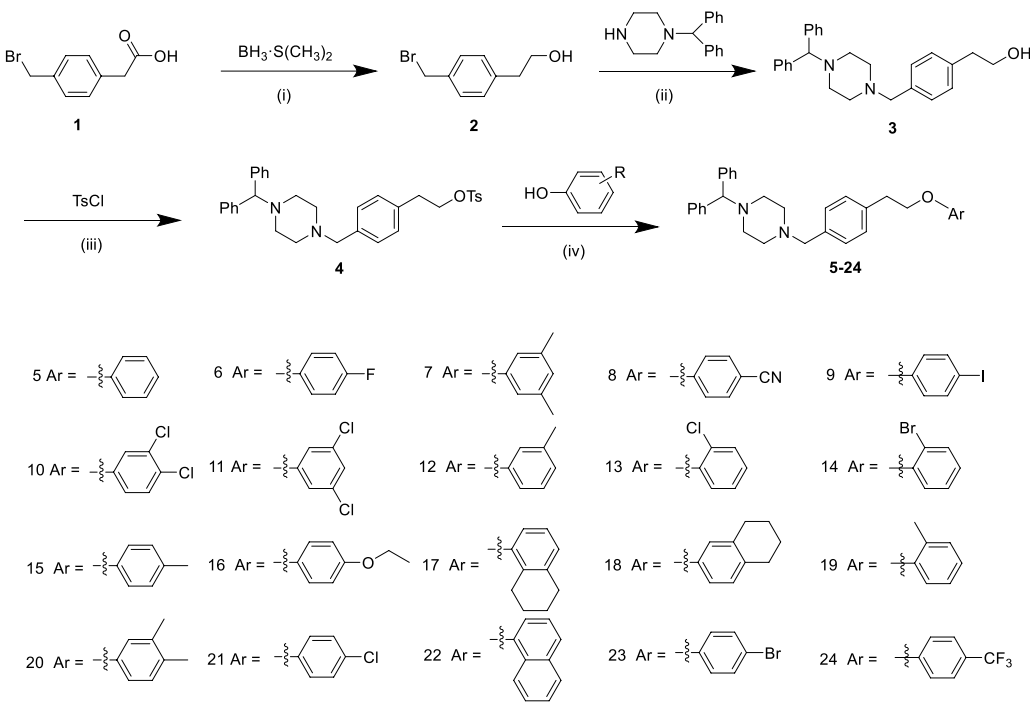
The cell lines PC-3, LNCaP, DU145 and WPMY-1 were purchased from the Cell Bank of the Chinese Academy of Sciences.

Synthesis of 2-(4-(bromomethyl)phenyl) ethanol (2)

Compound **2** was synthesized using methods reported previously in the literature (Chen et al., 2018a; Chen et al., 2014).

2-(4-((4-benzhydrylpiperazin-1-yl)methyl) phenyl)ethan-1-ol (3)

Compound **3** was synthesized using methods reported previously in the literature (Chen et al., 2018b), and sesamol was substituted with 1-(diphenylmethyl)-piperazin. White solid (ethyl



SCHEME 1
The synthesis route of derivatives **5–24**. Reagents and conditions: (i) $BH_3{\cdot}S(CH_3)_2$, THF, 0°C for 1 h, and then room temperature for 12 h; (ii) 1-(Diphenylmethyl) piperazine, K_2CO_3, CH_3CN, reflux, 12 h; (iii) TsCl, Et_3N and 4-dimethylaminopyridine, Cl_2CH_2, 0°C, 16 h; (iv) Phenol, K_2CO_3, CH_3CN, reflux, 12 h.

acetate). Yield: 70% from compound 1; M.p. 101.4°C–101.8°C; ^{1}H NMR (400 MHz, CDCl3): δ 7.38 (d, *J* = 7.4 Hz, 4H), 7.25–7.20 (m, 6H), 7.13 (t, *J* = 8.6 Hz, 4H), 4.21 (s, 1H), 3.77 (t, *J* = 6.7 Hz, 2H), 3.46 (s, 2H), 2.80 (t, *J* = 6.6 Hz, 2H), 2.45 (s, 8H). HRMS (ESI) m/z [M + H]$^+$: calcd for $C_{26}H_{31}N_2O$: 387.2431, found: 387.2448.

4-((4-benzhydrylpiperazin-1-yl)methyl) phenethyl 4-methylbenzenesulfonate (4)

Compound **4** was synthesized using methods reported previously in the literature (Chen et al., 2018b). White solid (ethyl acetate). M.p. 106.3°C–106.7°C; Yield, 87%. ^{1}H NMR (400 MHz, $CDCl_3$): *δ* 7.68 (d, *J* = 8.2 Hz, 2H), 7.39 (d, *J* = 7.4 Hz, 4H), 7.24 (t, *J* = 7.8 Hz, 6H), 7.19–7.12 (m, 4H), 7.02 (d, *J* = 7.8 Hz, 2H), 4.22 (s, 1H), 4.17 (t, *J* = 7.1 Hz, 2H), 3.48 (s, 2H), 2.90 (t, *J* = 7.1 Hz, 2H), 2.46 (s, 8H), 2.38 (s, 3H). HRMS (ESI) m/z [M + H]$^+$: calcd for $C_{33}H_{37}N_2O_3S$: 541.2519, found: 541.2601.

General procedure for the preparation of arylpiperazine derivative 5-24

Phenol (0.27 mmol, 1.5 equiv) and potassium carbonate (1.08 mmol, 6.0 equiv) were added to a solution of 4-((4-benzhydrylpiperazin-1-yl)methyl)phenethyl 4-methylbenzenesulfonate **4** (0.18 mmol, 1.0 equiv) in acetonitrile (CH_3CN, 15 mL). The reaction mixture was heated to 85°C and stirred for 12 h. Afterward, the mixture was cooled down to room temperature. The reaction mixture was then filtered, and the filtrate was concentrated under vacuum. The residue was purified by silica gel column chromatography using a petroleum ether:ethyl acetate ratio of 25:1 (v/v) to obtain the corresponding product (**5–24**).

Experimental data of 1-benzhydryl-4-(4-(2-phenoxyethyl)benzyl)piperazine (5)

White solid (ethyl acetate); M.p. 96.3°C–96.8°C; Yield, 82%. The purity = 98.5%. ^{1}H NMR (400 MHz, $CDCl_3$): *δ* 7.39 (d, *J* = 7.6 Hz, 4H), 7.27 (s, 1H), 7.25 (d, *J* = 2.3 Hz, 2H), 7.23 (d, *J* = 7.0 Hz, 5H), 7.19 (d, *J* = 8.0 Hz, 2H), 7.14 (t, *J* = 7.2 Hz, 2H), 6.92 (d, *J* = 7.3 Hz, 1H), 6.88 (d, *J* = 8.2 Hz, 2H), 4.22 (s, 1H), 4.13 (t, *J* = 7.1 Hz, 2H), 3.48 (s, 2H), 3.05 (t, *J* = 7.1 Hz, 2H), 2.46 (s, 4H), 2.40 (s, 4H). ^{13}C NMR (100 MHz, $CDCl_3$): *δ* 158.8, 142.8, 137.0, 136.2, 129.5, 128.8, 128.4, 128.0, 126.9, 120.7, 114.6, 76.2, 68.6, 62.8, 53.4, 51.9, 35.5. HRMS (ESI) m/z [M + H]$^+$: calcd for $C_{32}H_{35}N_2O$: 463.2744, found: 463.2745.

Experimental data of 1-benzhydryl-4-(4-(2-(4-fluorophenoxy)ethyl)benzyl) piperazine (6)

Light yellow solid (ethyl acetate); M.p. 90.1°C–90.4°C; Yield, 78%. The purity = 98.3%. ^{1}H NMR (400 MHz, $CDCl_3$): *δ* 7.30 (d, *J* = 7.4 Hz, 4H), 7.15 (t, *J* = 7.2 Hz, 6H), 7.10 (d, *J* = 7.7 Hz, 2H), 7.06 (t, *J* = 7.3 Hz, 2H), 6.84 (t, *J* = 8.3 Hz, 2H), 6.72–6.69 (m, 2H), 4.14 (s, 1H), 3.99 (t, *J* = 7.0 Hz, 2H), 3.41 (s, 2H), 2.94 (t, *J* = 6.9 Hz, 2H), 2.39 (s, 4H), 2.32 (s, 4H). ^{13}C NMR (100 MHz, $CDCl_3$): *δ* 158.5, 155.5 (d, *J* = 112.5 Hz), 142.8, 137.0, 136.0, 129.5, 128.8, 128.5, 128.0,

126.9, 115.8 (d, J = 22.9 Hz), 115.6 (d, J = 8.0 Hz), 76.2, 69.4, 62.7, 53.3, 51.8, 35.5. HRMS (ESI) m/z [M + H]$^+$: calcd for $C_{32}H_{34}FN_2O$: 481.2650, found: 481.2647.

Experimental data of 1-benzhydryl-4-(4-(2-(3,5-dimethylphenoxy)ethyl)benzyl) piperazine (7)

White solid (ethyl acetate); M.p. 123.2°C–123.5°C; Yield, 78%. The purity = 98%. ^{1}H NMR (400 MHz, $CDCl_3$): δ 7.39–7.37 (m, 4H), 7.21–7.18 (m, 8H), 7.12 (d, J = 7.0 Hz, 2H), 6.65–6.50 (m, 3H), 4.20 (s, 1H), 4.07 (t, J = 7.0 Hz, 2H), 3.46 (s, 2H), 3.01 (d, J = 6.6 Hz, 2H), 2.44 (s, 4H), 2.38 (s, 4H), 2.20 (s, 3H), 2.23 (s, 3H). ^{13}C NMR (100 MHz, $CDCl_3$): δ 159.0, 142.9, 139.2, 137.2, 136.2, 129.5, 128.5, 128.1, 127.0, 122.6, 122.5, 76.3, 68.6, 62.9, 53.4, 52.0, 35.7, 21.6. HRMS (ESI) m/z [M + H]$^+$: calcd for $C_{34}H_{39}N_2O$: 491.3057, found: 491.3059.

Experimental data of 4-(4-((4-benzhydrylpiperazin-1-yl)methyl) phenethoxy)benzonitrile (8)

White solid (ethyl acetate); M.p. 112.3°C–112.7°C; Yield, 51%. The purity = 98.7%. ^{1}H NMR (400 MHz, $CDCl_3$): δ 7.53 (d, J = 8.6 Hz, 2H), 7.39 (d, J = 7.4 Hz, 4H), 7.24 (t, J = 7.3 Hz, 6H), 7.19–7.13 (m, 4H),6.90 (d, J = 8.6 Hz, 2H), 4.22 (s, 1H), 4.16 (t, J = 7.0 Hz, 2H), 3.49 (s, 2H), 3.07 (t, J = 6.9 Hz, 2H), 2.46 (s, 4H), 2.40 (s, 4H). ^{13}C NMR (100 MHz, CDCl3): δ 162.1, 142.8, 136.6, 136.3, 134.0, 129.5, 128.8, 128.4, 128.0, 126.9, 119.2, 115.2, 104.0, 76.2, 69.0, 62.7, 53.4, 51.9, 35.2. HRMS (ESI) m/z [M + H]$^+$: calcd for $C_{33}H_{34}N_3O$: 488.2696, found: 488.2714.

Experimental data of 1-benzhydryl-4-(4-(2-(4-iodophenoxy)ethyl)benzyl)piperazine (9)

White solid (ethyl acetate); M.p. 113.4°C–113.9°C; Yield, 76%. The purity = 98.7%. ^{1}H NMR (400 MHz, $CDCl_3$): δ 7.51 (d, J = 8.8 Hz, 2H), 7.39 (d, J = 7.5 Hz, 4H), 7.26 (s, 1H), 7.23 (d, J = 7.0 Hz, 5H), 7.18–7.13 (m, 4H), 6.64 (d, J = 8.8 Hz, 2H), 4.22 (s, 1H), 4.08 (t, J = 7.1 Hz, 2H), 3.49 (s, 2H), 3.03 (t, J = 7.0 Hz, 2H), 2.47 (s, 4H), 2.42 (s, 4H). ^{13}C NMR (100 MHz, $CDCl_3$): δ 158.7, 142.8, 138.2, 136.7, 136.2, 129.5, 128.8, 128.4, 128.0, 126.9, 117.0, 82.7, 76.2, 68.8, 62.7, 53.3, 51.8, 35.3. HRMS (ESI) m/z [M + H]$^+$: calcd for $C_{32}H_{34}IN_2O$: 589.1710, found: 589.1740.

Experimental data of 1-benzhydryl-4-(4-(2-(3,4-dichlorophenoxy)ethyl)benzyl) piperazine (10)

Light yellow solid (ethyl acetate); M.p. 130.7°C–131.2°C; Yield, 68%. The purity = 98.8%. ^{1}H NMR (400 MHz, $CDCl_3$): δ 7.31 (d, J = 7.1 Hz, 4H), 7.19–7.13 (m, 7H), 7.09–7.04 (m, 4H), 6.86 (d, J = 2.7 Hz, 1H), 6.61 (dd, J = 8.8 Hz, J = 2.6 Hz, 1H), 4.13 (s, 1H), 3.99 (t, J = 7.0 Hz, 2H), 3.40 (s, 2H), 2.94 (t, J = 6.9 Hz, 2H), 2.37 (s, 4H), 2.31 (s, 4H). ^{13}C NMR (100 MHz, CDCl3): δ 156.8, 141.7, 135.5, 135.4, 131.8, 129.6, 128.4, 127.7, 127.4, 126.9, 125.8, 122.8, 115.3, 113.5, 75.2, 68.2, 61.7, 52.3, 50.8, 34.2. HRMS (ESI) m/z [M + H]$^+$: calcd for $C_{32}H_{33}Cl_2N_2O$: 531.1965, found: 531.1991.

Experimental data of 1-benzhydryl-4-(4-(2-(3,5-dichlorophenoxy)ethyl)benzyl) piperazine (11)

Light yellow solid (ethyl acetate); M.p. 129.5°C–130.2°C; Yield, 77%. The purity = 97.9%. ^{1}H NMR (400 MHz, $CDCl_3$): δ 7.30 (d, J = 7.5 Hz, 4H), 7.14 (d, J = 6.6 Hz, 6H), 7.08–7.04 (m, 4H), 6.83 (s, 1H), 6.67 (s, 2H), 4.14 (s, 1H), 3.99 (t, J = 6.8 Hz, 2H), 3.40 (s, 2H), 2.93 (t, J = 6.8 Hz, 2H), 2.37 (s, 4H), 2.31 (s, 4H). ^{13}C NMR (100 MHz, $CDCl_3$): δ 159.9, 142.8, 136.6, 136.3, 135.4, 129.5, 128.8, 128.4, 128.0, 126.9, 121.0, 113.7, 76.3, 69.3, 62.8, 53.4, 51.9, 35.2. HRMS (ESI) m/z [M + H]$^+$: calcd for $C_{32}H_{33}Cl_2N_2O$: 531.1965, found: 531.1985.

Experimental data of 1-benzhydryl-4-(4-(2-(m-tolyloxy)ethyl)benzyl)piperazine (12)

White solid (ethyl acetate); M.p. 125.1°C–125.6°C; Yield, 80%. The purity = 98.8%. ^{1}H NMR (500 MHz, $CDCl_3$): δ 7.45 (d, J = 7.5 Hz, 4H), 7.31 (s, 1H), 7.30 (d, J = 7.7 Hz, 5H), 7.26 (d, J = 8.0 Hz, 2H), 7.20 (dd, J = 15.0 Hz, J = 7.3 Hz, 3H), 6.79 (d, J = 7.5 Hz, 1H), 6.76–6.74 (m, 2H), 4.28 (s, 1H), 4.18 (t, J = 7.2 Hz, 2H), 3.55 (s, 2H), 3.11 (t, J = 7.1 Hz, 2H), 2.53 (s, 4H), 2.47 (s, 4H), 2.36 (s, 3H). ^{13}C NMR (125 MHz, $CDCl_3$): δ 158.9, 142.8, 139.5, 137.1, 136.1, 129.5, 129.2, 128.9, 128.5, 128.0, 126.9, 121.6, 115.5, 111.5, 76.2, 68.6, 62.7, 53.3, 51.9, 35.5, 21.6. HRMS (ESI) m/z [M + H]$^+$: calcd for $C_{33}H_{37}N_2O$: 477.2900, found: 477.2972.

Experimental data of 1-benzhydryl-4-(4-(2-(2-chlorophenoxy)ethyl)benzyl) piperazine (13)

White solid (ethyl acetate); M.p. 128.2°C–128.8°C; Yield, 74%. The purity = 98.2%. ^{1}H NMR (400 MHz, $CDCl_3$): δ 7.39 (d, J = 7.5 Hz, 4H), 7.33 (d, J = 7.3 Hz, 1H), 7.24 (t, J = 8.0 Hz, 8H), 7.15 (t, J = 6.9 Hz, 3H), 6.86 (d, J = 7.8 Hz, 2H), 4.22 (s, 1H), 4.18 (t, J = 7.0 Hz, 2H), 3.49 (s, 2H), 3.11 (t, J = 7.0 Hz, 2H), 2.46 (s, 4H), 2.39 (s, 4H). ^{13}C NMR (100 MHz, $CDCl_3$): δ 154.4, 142.8, 136.7, 136.3, 130.3, 129.4, 129.0, 128.4, 128.0, 127.6, 126.9, 123.0, 121.3, 113.4, 76.2, 69.8, 62.8, 53.3, 51.9, 35.4. HRMS (ESI) m/z [M + H]$^+$: calcd for $C_{32}H_{34}ClN_2O$: 497.2354, found: 497.2382.

Experimental data of 1-benzhydryl-4-(4-(2-(2-bromophenoxy)ethyl)benzyl) piperazine (14)

White solid (ethyl acetate); M.p. 132.1°C–132.6°C; Yield, 81%. The purity = 98.5%. ^{1}H NMR (400 MHz, $CDCl_3$): δ 7.49 (d, J = 7.7 Hz, 1H), 7.38 (d, J = 7.4 Hz, 4H), 7.22 (d, J = 9.7 Hz, 8H), 7.18–7.12 (m, 3H), 6.81–6.75 (m, 2H), 4.21 (s, 1H), 4.14 (t, J = 6.8 Hz, 2H), 3.48 (s, 2H), 3.10 (t, J = 6.8 Hz, 2H), 2.46 (s, 4H), 2.40 (s,

4H). ^{13}C NMR (100 MHz, $CDCl_3$): δ 155.3, 142.8, 136.8, 136.2, 133.4, 129.5, 129.1, 128.5, 128.4, 128.0, 126.9, 121.9, 113.2, 112.3, 76.3, 69.9, 62.8, 53.4, 51.9, 35.5. HRMS (ESI) m/z [M + H]$^+$: calcd for $C_{32}H_{34}BrN_2O$: 541.1849, found: 541.1878.

Experimental data of 1-benzhydryl-4-(4-(2-(p-tolyloxy)ethyl)benzyl)piperazine (15)

White solid (ethyl acetate); M.p. 126.4°C–126.9°C; Yield, 72%. The purity = 98.3%. ^{1}H NMR (400 MHz, $CDCl_3$): δ 7.39 (d, *J* = 7.4 Hz, 4H), 7.26–7.20 (m, 8H), 7.17 (t, *J* = 5.9 Hz, 2H), 7.05 (d, *J* = 8.3 Hz, 2H), 6.78 (d, *J* = 8.4 Hz, 2H), 4.22 (s, 1H), 4.11 (t, *J* = 7.2 Hz, 2H), 3.48 (s, 2H), 3.04 (t, *J* = 7.1 Hz, 2H), 2.46 (s, 4H), 2.40 (s, 4H), 2.26 (s, 3H). ^{13}C NMR (100 MHz, $CDCl_3$): δ 156.7, 142.8, 137.0, 136.1, 129.9, 129.4, 128.8, 128.4, 128.0, 126.9, 117.9, 114.5, 76.2, 68.8, 62.8, 53.3, 51.9, 35.5, 20.5. HRMS (ESI) m/z [M + H]$^+$: calcd for $C_{33}H_{37}N_2O$: 477.2900, found: 477.2915.

Experimental data of 1-benzhydryl-4-(4-(2-(4-ethoxyphenoxy)ethyl)benzyl) piperazine (16)

White solid (ethyl acetate); M.p. 124.7°C–125.2°C; Yield, 67%. The purity = 98%. ^{1}H NMR (400 MHz, $CDCl_3$): δ 7.39 (d, *J* = 7.4 Hz, 4H), 7.26 (s, 1H), 7.23 (d, *J* = 7.9 Hz, 5H), 7.19 (d, *J* = 8.0 Hz, 2H), 7.14 (t, *J* = 7.4 Hz, 2H), 6.80 (s, 4H), 4.22 (s, 1H), 4.08 (t, *J* = 7.0 Hz, 2H), 3.95 (q, *J* = 13.8 Hz, *J* = 6.9 Hz, 2H), 3.50 (s, 2H), 3.03 (t, *J* = 7.0 Hz, 2H), 2.47 (s, 4H), 2.40 (s, 4H), 1.37 (t, *J* = 6.9 Hz, 3H). ^{13}C NMR (100 MHz, $CDCl_3$): δ 153.2, 152.9, 142.8, 137.1, 135.9, 129.5, 128.8, 128.4, 128.0, 126.9, 115.6, 115.4, 76.2, 69.4, 64.0, 62.7, 53.3, 51.8, 35.6, 15.0. HRMS (ESI) m/z [M + H]$^+$: calcd for $C_{34}H_{39}N_2O_2$: 507.3006, found: 507.3019.

Experimental data of 1-benzhydryl-4-(4-(2-((5,6,7,8-tetrahydronaphthalen-1-yl)oxy) ethyl)benzyl)piperazine (17)

White solid (ethyl acetate); M.p. 115.8°C–116.3°C; Yield, 66%. The purity = 98.8%. ^{1}H NMR (400 MHz, $CDCl_3$): δ 7.68 (d, *J* = 8.0 Hz, 2H), 7.39 (d, *J* = 7.6 Hz, 4H), 7.27–7.22 (m, 5H), 7.17 (t, *J* = 7.6 Hz, 4H), 7.03 (d, *J* = 7.7 Hz, 2H), 4.22 (s, 1H), 4.17 (t, *J* = 7.1 Hz, 2H), 3.47 (s, 2H), 2.91 (t, *J* = 7.1 Hz, 2H), 2.45–2.40 (m, 12H), 1.42–1.28 (m, 4H). ^{13}C NMR (100 MHz, $CDCl_3$): δ 144.6, 142.8, 136.7, 134.9, 133.1, 129.8, 129.5, 128.7, 128.4, 128.0, 127.8, 126.9, 76.2, 70.6, 62.6, 53.3, 51.9, 35.0, 21.6. HRMS (ESI) m/z [M + H]$^+$: calcd for $C_{36}H_{41}N_2O$: 517.3214, found: 517.3219.

Experimental data of 1-benzhydryl-4-(4-(2-((5,6,7,8-tetrahydronaphthalen-2-yl)oxy) ethyl)benzyl)piperazine (18)

White solid (ethyl acetate); M.p. 116.0°C–116.7°C; Yield, 68%. The purity = 98.3%. ^{1}H NMR (400 MHz, $CDCl_3$): δ 7.39 (d, *J* = 7.6 Hz, 4H), 7.23 (dd, *J* = 15.2 Hz, *J* = 7.4 Hz, 8H), 7.17 (t, *J* = 6.6 Hz, 2H), 6.94 (d, *J* = 8.4 Hz, 1H), 6.64 (d, *J* = 8.4 Hz, 1H), 6.59 (s, 1H), 4.22 (s, 1H), 4.10 (t, *J* = 7.1 Hz, 2H), 3.51 (s, 2H), 3.04 (t, *J* = 7.1 Hz, 2H), 2.69 (t, *J* = 5.1 Hz, 4H), 2.49 (s, 4H), 2.43 (s, 4H), 1.75 (d, *J* = 2.6 Hz, 4H). ^{13}C NMR (100 MHz, $CDCl_3$): δ 156.6, 142.7, 138.1, 129.9, 129.5, 129.3, 128.8, 128.4, 128.0, 126.9, 114.5, 112.4, 76.2, 68.7, 62.7, 53.2, 51.7, 35.5, 28.6, 23.4, 23.2. HRMS (ESI) m/z [M + H]$^+$: calcd for $C_{36}H_{41}N_2O$: 517.3214, found: 517.3230.

Experimental data of 1-benzhydryl-4-(4-(2-(o-tolyloxy)ethyl)benzyl)piperazine (19)

White solid (ethyl acetate); M.p. 118.7°C–119.4°C; Yield, 83%. The purity = 98.9%. ^{1}H NMR (400 MHz, $CDCl_3$): δ 7.39 (d, *J* = 7.5 Hz, 4H), 7.25 (s, 2H), 7.22 (d, *J* = 7.2 Hz, 6H), 7.15 (d, *J* = 7.2 Hz, 2H), 7.10 (t, *J* = 7.6 Hz, 2H), 6.82 (t, *J* = 7.4 Hz, 1H), 6.76 (d, *J* = 8.5 Hz, 1H), 4.21 (s, 1H), 4.12 (t, *J* = 6.7 Hz, 2H), 3.50 (s, 2H), 3.06 (t, *J* = 6.7 Hz, 2H), 2.48 (s, 4H), 2.42 (s, 4H), 2.17 (s, 3H). ^{13}C NMR (100 MHz, CDCl3): δ 157.0, 142.8, 137.5, 135.8, 130.7, 129.5, 129.0, 128.5, 128.0, 127.7, 126.9, 126.7, 120.3, 110.9, 76.2, 68.7, 62.7, 53.3, 51.8, 35.7, 16.3. HRMS (ESI) m/z [M + H]$^+$: calcd for $C_{33}H_{37}N_2O$: 477.2900, found: 477.2911.

Experimental data of 1-benzhydryl-4-(4-(2-(3,4-dimethylphenoxy)ethyl)benzyl) piperazine (20)

White solid (ethyl acetate); M.p. 126.5°C–127.0°C; Yield, 81%. The purity = 98.4%. ^{1}H NMR (400 MHz, $CDCl_3$): δ 7.37 (d, *J* = 7.1 Hz, 4H), 7.24–7.19 (m, 8H), 7.14 (d, *J* = 7.2 Hz, 2H), 6.99 (d, *J* = 7.8 Hz, 1H), 6.69 (s, 1H), 6.61 (d, *J* = 6.0 Hz, 1H), 4.19 (s, 1H), 4.09 (t, *J* = 7.0 Hz, 2H), 3.52 (s, 2H), 3.02 (t, *J* = 6.9 Hz, 2H), 2.51 (s, 4H), 2.43 (s, 4H), 2.19 (s, 3H), 2.16 (s, 3H). ^{13}C NMR (100 MHz, $CDCl_3$): δ 157.0, 142.8, 137.7, 137.5, 130.4, 130.3, 129.8, 128.9, 128.7, 128.5, 128.0, 126.9, 116.3, 111.6, 76.2, 68.7, 62.6, 53.2, 51.6, 35.6, 20.0, 18.8. HRMS (ESI) m/z [M + H]$^+$: calcd for $C_{34}H_{39}N_2O$: 491.3057, found: 491.3067.

Experimental data of 1-benzhydryl-4-(4-(2-(4-chlorophenoxy)ethyl)benzyl) piperazine (21)

White solid (ethyl acetate); M.p. 129.6°C–130.1°C; Yield, 72%. The purity = 99%. ^{1}H NMR (500 MHz, $CDCl_3$): δ 7.45 (d, *J* = 7.2 Hz, 4H), 7.32 (s, 1H), 7.30 (d, *J* = 6.2 Hz, 5H), 7.26–7.24 (m, 4H), 7.21 (t, *J* = 7.4 Hz, 2H), 6.85 (d, *J* = 9.0 Hz, 2H), 4.28 (s, 1H), 4.15 (t, *J* = 7.1 Hz, 2H), 3.57 (s, 2H), 3.10 (t, *J* = 7.1 Hz, 2H), 2.54 (s, 4H), 2.47 (s, 4H). ^{13}C NMR (125 MHz, $CDCl_3$): δ 157.5, 142.8, 136.8, 136.0, 129.6, 129.3, 128.8, 128.5, 128.0, 126.9, 125.6, 115.9, 76.2, 69.0, 62.6, 53.3, 51.8, 35.4. HRMS (ESI) m/z [M + H]$^+$: calcd for $C_{32}H_{34}ClN_2O$: 497.2354, found: 497.2376.

Experimental data of 1-benzhydryl-4-(4-(2-(naphthalen-1-yloxy)ethyl)benzyl) piperazine (22)

White solid (ethyl acetate); M.p. 110.3°C–110.9°C; Yield, 75%. The purity = 98.5%. ^{1}H NMR (500 MHz, $CDCl_3$): δ 8.31 (d, *J* = 7.2 Hz, 1H),

7.83 (d, J = 7.1 Hz, 1H), 7.52–7.49 (m, 2H), 7.46 (d, J = 7.1 Hz, 5H), 7.39 (t, J = 7.8 Hz, 1H), 7.38–7.29 (m, 8H), 7.22 (t, J = 7.4 Hz, 2H), 6.84 (d, J = 7.4 Hz, 1H), 4.38 (t, J = 6.9 Hz, 2H), 4.29 (s, 1H), 3.57 (s, 2H), 3.27 (t, J = 6.9 Hz, 2H), 2.54 (s, 4H), 2.48 (s, 4H). ^{13}C NMR (125 MHz, $CDCl_3$): δ 154.6, 142.8, 137.3, 136.1, 134.5, 129.5, 128.9, 128.5, 128.0, 127.4, 126.9, 126.4, 125.9, 125.7, 125.2, 122.1, 120.3, 104.7, 76.2, 68.9, 62.7, 53.3, 51.9, 35.6. HRMS (ESI) m/z [M + H]$^+$: calcd for $C_{36}H_{37}N_2O$: 513.2900, found: 513.2927.

Experimental data of 1-benzhydryl-4-(4-(2-(4-bromophenoxy)ethyl)benzyl) piperazine (23)

White solid (ethyl acetate); M.p. 127.2°C–127.8°C; Yield, 79%. The purity = 98.6%. ^{1}H NMR (500 MHz, $CDCl_3$): δ 7.44 (d, J = 7.3 Hz, 4H), 7.38 (dd, J = 7.0 Hz, J = 2.1 Hz, 2H), 7.31 (s, 1H), 7.29 (d, J = 8.0 Hz, 5H), 7.24 (d, J = 8.1 Hz, 2H), 7.20 (t, J = 7.4 Hz, 2H), 6.80 (d, J = 9.0 Hz, 2H), 4.27 (s, 1H), 4.14 (t, J = 7.1 Hz, 2H), 3.55 (s, 2H), 3.09 (t, J = 7.1 Hz, 2H), 2.54 (s, 4H), 2.48 (s, 4H). ^{13}C NMR (125 MHz, $CDCl_3$): δ 158.0, 142.8, 136.8, 136.0, 132.3, 129.6, 128.9, 128.5, 128.0, 126.9, 116.4, 112.9, 76.2, 69.0, 62.7, 53.3, 51.8, 35.4. HRMS (ESI) m/z [M + H]$^+$: calcd for $C_{32}H_{34}BrN_2O$: 541.1849, found: 541.1884.

Experimental data of 1-benzhydryl-4-(4-(2-(4-(trifluoromethyl)phenoxy)ethyl)benzyl) piperazine (24)

White solid (ethyl acetate); M.p. 109.8°C–110.5°C; Yield, 68%. The purity = 98.7%. ^{1}H NMR (500 MHz, $CDCl_3$): δ 7.57 (d, J = 8.7 Hz, 2H), 7.46 (d, J = 7.3 Hz, 4H), 7.31 (t, J = 7.6 Hz, 6H), 7.27 (d, J = 8.0 Hz, 2H), 7.22 (t, J = 7.4 Hz, 2H), 6.98 (d, J = 8.7 Hz, 2H), 4.30 (s, 1H), 4.22 (t, J = 7.1 Hz, 2H), 3.57 (s, 2H), 3.14 (t, J = 7.1 Hz, 2H), 2.55 (s, 4H), 2.48 (s, 4H). ^{13}C NMR (125 MHz, $CDCl_3$): δ 161.3, 142.8, 136.6, 136.4, 129.6, 128.9, 128.5, 128.0, 126.9 (t, J = 4.6 Hz), 124.5 (dd, J = 539.0 Hz, J = 269.6 Hz), 122.9 (dd, J = 65.0 Hz, J = 32.5 Hz), 120.7 (d, J = 141.4 Hz), 114.5, 76.3, 68.9, 62.7, 53.4, 51.9, 35.3. HRMS (ESI) m/z [M + H]$^+$: calcd for $C_{33}H_{34}F_3N_2O$: 531.2618, found: 531.2648.

Biological evaluation

In Vitro cytotoxic assay

Cell culture

PC-3 and WPMY-1 cells were cultured in Dulbecco's modiffcation Eagle's medium (DMEM, Invitrogen, Carlsbad, CA, United States) supplemented with 10% fetal bovine serum (FBS, Hyclone, Logan, UT, United States), 100 U/mL penicillin and 0.1 mg/mL streptomycin (Invitrogen). DU145 cells were cultured in RPMI1640 media supplemented with 10% fetal bovine serum (FBS, Hyclone), 100 U/mL penicillin and 0.1 mg/mL streptomycin (Invitrogen). LNCaP cells were cultured in F12 media supplemented with 10% fetal bovine serum (FBS, Hyclone), 100 U/mL penicillin and 0.1 mg/mL streptomycin (Invitrogen). The cells were incubated at 37°C in a humidified atmosphere with 5% CO_2(Chen et al., 2025; Jiang et al., 2024).

Assessment of antitumor activity by CCK-8 assay

The proliferative capacity of cells was evaluated through the implementation of a Cell Counting Kit-8 (CCK-8) assay, supplied by Dojindo (Japan), to quantify cellular growth. Post-transfection, cells were dispensed into a 96-well microplate at a density of 3 × 10^3 cells per well and incubated for intervals of 0, 24, 48, 72, 96, and 120 h. Following this, 10 μL of the CCK-8 solution was introduced into each well and the plates were returned to the incubator for an additional 2-h period at 37°C under 5% CO_2 conditions. Absorbance readings at 450 nm were subsequently taken using an ELISA reader manufactured by Bio Tek (United States) (Chen et al., 2022; Zhou et al., 2024).

The compound concentrations were set at 30, 15, 7.5, 3.75, 1.88, and 0.94 μmol/L. The absorbance (A) was measured at 450 nm using a microplate reader. A linear regression analysis was performed plotting the logarithm of compound concentration against the inhibition rate to obtain a straight-line equation from which the half-maximal inhibitory concentration (IC_{50}) of the compound, capable of inhibiting 50% of cancer cells, was determined. All experiments were repeated three times under identical conditions, and the mean value was taken as the final result.

AR reporter gene assay

Fireffy and Renilla luciferase activities, which are indicated as RLUs, were determined using Dual-Glo luciferase assay kits (Promega) according to the manufacturer's instructions (Chen et al., 2019a; Chen et al., 2019b). RLUs were measured using a luminometer (GloMaxTM 96-Microplate Luminometer, Promega) and are reported as the mean ± SEM of three individual experiments. For agonists, fold of induction = LUinduced/RLUuninduced. For antagonists, % of control = 100 × RLU (agonist + antagonist)/RLU (agonist alone). All RLUs were normalized against ffreffy RLUs/Renilla RLUs. Data are expressed as EC_{50}/IC_{50} values in μM, and the IC_{50} of phenylephrine (μM) was calculated by plotting the data using nonlinear regression analysis in Graph-Pad Prism 5 software.

Fluorescence polarization (FP)

The fluorescence polarization technique was used to analyze the binding of **7, 11, 17, 19, 20, 21, 22, 23, 24** and enzalutamide to the AR using the PolarScreen™ AR Competitor Assay, Green (lifetechnologies, A15880) according to the manufacturer's instructions (Chen et al., 2019a; Chen et al., 2019b). Brieffy, the assay entails titration of the test compound against a preformed complex of Fluormone™AL Green and the AR-LBD (GST). The assay mixture was allowed to equilibrate at room temperature in 384-well black plates for 4 h, after which the fluorescence polarization values were measured in a SpectraMax® Paradigm® Multi-Mode Detection Platform (Molecular Devices) using an excitation wavelength of 485 nm and an emission wavelength of 535 nm. Data analysis for the ligand binding assays was performed using Prism software (GraphPad Software, Inc.).

Molecular docking simulation

Until now, three binding sites of androgen receptor have been reported, including LBP, AF2 and BF3 (Chen et al., 2019a; Chen

TABLE 1 *In vitro* cytotoxicity of compounds 5–24.

Compd.	IC_{50} (μM)[a]			
	PC-3[b]	LNCaP[b]	DU145[b]	WPMY-1[b]
5	13.08 ± 0.12	>50	>50	>50
6	34.39 ± 0.17	>50	>50	>50
7	2.95 ± 0.04	>50	24.76 ± 0.21	>50
8	12.54 ± 0.11	22.36 ± 0.20	19.83 ± 0.14	17.56 ± 0.12
9	15.23 ± 0.19	>50	>50	>50
10	17.44 ± 0.07	>50	>50	>50
11	1.59 ± 0.02	>50	17.43 ± 0.04	>50
12	>50	19.64 ± 0.23	34.43 ± 0.15	28.54 ± 0.16
13	15.35 ± 0.08	12.17 ± 0.25	21.24 ± 0.16	17.83 ± 0.17
14	19.12 ± 0.16	>50	>50	>50
15	20.49 ± 0.12	9.29 ± 0.23	13.69 ± 0.14	14.72 ± 0.14
16	13.6 ± 0.09	>50	>50	>50
17	1.89 ± 0.14	1.04 ± 0.21	7.32 ± 0.08	>50
18	5.02 ± 0.12	>50	14.36 ± 0.15	>50
19	1.23 ± 0.15	2.32 ± 0.15	0.87 ± 0.04	>50
20	1.05 ± 0.14	2.39 ± 0.13	3.89 ± 0.14	>50
21	2.83 ± 0.21	16.09 ± 0.12	13.72 ± 0.14	28.65 ± 0.13
22	10.12 ± 0.17	6.78 ± 0.14	15.76 ± 0.09	33.16 ± 0.15
23	1.78 ± 0.12	3.86 ± 0.13	1.42 ± 0.11	>50
24	3.94 ± 0.14	14.58 ± 0.18	5.76 ± 0.14	>50
Naftopidil	42.10 ± 0.79	22.36 ± 0.61	34.58 ± 0.31	>50

[a]IC_{50} refers to the half-maximal inhibitory concentration. The IC_{50} values were calculated as the mean ± standard deviation from three experimental trials.
[b]PC-3, LNCaP, and DU145 are human prostate cancer cell lines; WPMY-1, refers to human normal prostatic epithelial cells.

et al., 2019b). In order to explore the mechanism of androgen receptor antagonism by the target compound **17**, a dockingsimulation was carried out using AutoDock Vina software. The crystal structure of androgen receptor downloaded from the RCSB Protein Data Bank (http://www.rcsb.org/pdb/home/home.do) was taken as the template protein to engage in docking simulation. In prepare, the exogenous ligand was removed and the hydrogen atoms were added to the system. To ensure the reliability of docking simulation, a redock process for the exogenous ligand was performed before docking analysis. Finally, one compound target (i.e., compound **17**) with high AR antagonistic activity was docked into three potential binding sites (including LBP, AF2 and BF3) with 10 configurations.

Results and discussion

Chemistry

Scheme 1 illustrated the synthesis of arylpiperazine derivatives **5–24** *via* a four-step reaction starting from 2-(4-(bromomethyl)phenyl)acetic acid. First, 2-(4-(bromomethyl)phenyl)acetic acid one was reduced to alcohol 2 with the presence of a borane–methyl sulfide complex (2 M in tetrahydrofuran) at 0°C for 1 h and at room temperature for 12 h. After the nucleophilic substitution reaction was carried out between compound 2 and 1-(diphenylmethyl)-piperazin using CH_3CN as solvent in the presence of potassium carbonate at 85°C for 12 h gave 3 (70% yield from 1). Subsequently, compound 4 (87% yield) was obtained by reacting 3 with 4-toluene-sulfonyl chloride using CH_2Cl_2 as solvent in the presence of trimethylamine and a catalytic amount of 4-dimethylaminopyridine at 0°C for 16 h. Finally, compound 4 was treated with various phenol (1.5 equiv) in the presence of K_2CO_3 (6 eq) to obtain derivatives **5–24** in moderate yields (51%–83%). All synthesized analogs were confirmed using ^{1}H-NMR, ^{13}C-NMR, and HRMS.

Cytotoxic activity and AR antagonist activity

The cytotoxic activity of derivatives **5–24** against three human prostate cancer cell lines (PC-3, LNCaP, and DU145) and one type of human normal prostate epithelial cells was evaluated using the CCK-8 method. The results are shown in Table 1.

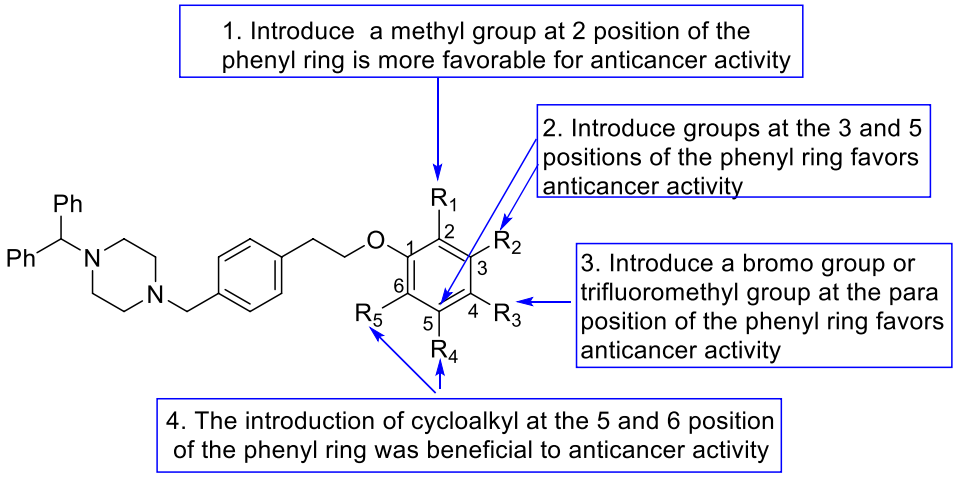


FIGURE 2
The SAR summary of the derivatives **5**–**24**.

In this study, the cytotoxic activity of ether arylpiperazine derivatives ranging from **5** to **24** was assessed against 4 cell lines: PC-3, LNCaP, DU145 (all human prostate cancer cell lines), and WPMY-1 (human normal prostatic epithelial cells) using the CCK-8 assay. The outcomes are summarized in Table 1. The data presented in the table reveal that several of these compounds exhibit pronounced cytotoxic activity against the tested cancer cell lines, with some demonstrating significantly greater potency compared to naftopidil. Notably: Compounds **7, 11, 17, 19, 20, 21, 23**, and **24** exhibit exceptionally potent activity against PC-3 cells, characterized by IC_{50} values below 5 μM. For LNCaP cells, compounds **17, 19, 20**, and **23** show particularly strong activity with IC_{50} values less than 5 μM. Compounds **19, 20, 23** and **24** also demonstrate pronounced cytotoxicity against DU145 cells. Moreover, the majority of compounds exhibited low cytotoxic character toward normal human prostate epithelial cells (WPMY-1).

The SAR investigation was mainly focused on the variation of the substitute's type on the phenyl group as a required group for antitumor activity. (1) For instance, compared to phenylpiperazine compound **5**, compounds **7** (IC_{50} = 2.95 μM) and **11** (IC_{50} = 1.59 μM), which introduce two symmetrical groups onto the phenyl ring, exhibit potent cytotoxic activity against PC-3 cells. In contrast, compound **12** (IC_{50} > 50 μM), featuring a methyl group as an electron-donating substituent in the meta position of the phenyl ring, displays significantly weaker cytotoxic activity against PC-3 than **5**. Additionally, compound **24** (IC_{50} = 5.76 μM), with a trifluoromethyl group as a strong electron-withdrawing substituent on the phenyl ring, exhibits strong cytotoxic activity against DU145 cells. These activity results indicate that variations in substituents on the phenyl ring do have a certain impact on cytotoxic activity. (2) A comparison between compounds **10** and **11** reveals that compound **11** (IC_{50} = 1.59 μM) demonstrates exceptionally strong activity against PC-3 cells, while compound **10** exhibits weaker cytotoxic activity against PC-3. These activity results suggest that the introduction of symmetrical, weakly electron-withdrawing substituents at the 3 and 5 positions of the phenyl ring favors anticancer activity. (3) When comparing compound **19** with compounds **13** and **14**, compound **19** (IC_{50} = 0.87 μM) exhibits more pronounced cytotoxic activity against DU145 cells. The results indicate that the introduction of electron-donating groups in the ortho position of the phenyl ring is more favorable for anticancer activity than the introduction of electron-withdrawing groups. (4) A comparison between compounds **12, 15**, and **19** reveals that compound **19** (IC_{50} > 50 μM) exhibits weak activity against human normal prostatic epithelial cells. These activity results suggest that when introducing a methyl group at different positions on the phenyl ring, the ortho position favors anticancer activity more than other positions. (5) Comparing compound **7** with compound **12**, compound **7** (IC_{50} = 2.95 μM) demonstrates more pronounced cytotoxic activity against PC-3 cells. These activity results indicate that the simultaneous introduction of methyl groups at the three and five positions of the phenyl ring favors anticancer activity more than the introduction of a methyl group only at the three position. (6) When comparing compounds 6, 8, 9, 15 and 21, compounds 23 and 24 exhibits more versatile and superior cytotoxic activity. These activity results suggest that the introduction of a bromo group or a trifluoromethyl group at the para position of the phenyl ring favors anticancer activity. (7) A comparison between compounds 17 and 18, compound 17 (IC50 = 1.89 μM, 1.04 μM, 7.32 μM) demonstrates better activity against the tested cell lines than compound 18 (IC50 = 5.02 μM, >50 μM, 14.36 μM). The results showed that the introduction of cycloalkyl at the 5 and 6 position of the phenyl ring was beneficial to anticancer activity (Figure 2). Above results can lead to a tool which can further design arylpiperazine derivatives as AR antagonists for *in vitro* and *in vivo* studies.

To further investigate whether these derivatives possess antagonistic activity against AR, this study adopted the scientific method of luciferase assay (Qi et al., 2022a; Qi et al., 2022b) to more accurately evaluate the antagonistic effects of these derivatives on AR (Table 2). During the implementation of the AR luciferase assay experiments, we specifically added 1 nM of the AR agonist R1881 for co-treatment, and quantitatively assessed the strength of the antagonistic activity based on the degree of inhibition of luciferase expression induced by R1881. According to the data presented in Table 2, it is evident that compounds **7, 11, 21, 22**, and **24** exhibit relatively weak antagonistic effects on AR. However, notably, compounds **17, 19, 20**, and **23** demonstrate significant antagonistic efficacy, with inhibition rates exceeding 55%. It is worth

TABLE 2 AR antagonist activity of compounds.

Compound	AR antagonistic activity% (10 μM)[a]
7	50.1 ± 1.1
11	51.2 ± 1.3
17	70.3 ± 0.8
19	71.5 ± 0.5
20	65.7 ± 1.4
21	49.4 ± 0.8
22	40.3 ± 1.2
23	62.2 ± 1.5
24	47.3 ± 0.6
R1881	N.E[b]
Naftopidil	52.2 ± 0.3
Enzalutamide	84.7 ± 1.4

[a]Inhibition rate was shown as a ratio to the R1881 control.
[b]N.E, no antagonistic effect.

TABLE 3 The binding affinity of compounds to mutant AR.

Compound	IC_{50}/μm[a]
7	2.15 ± 0.13
11	2.01 ± 0.15
17	1.14 ± 0.12
19	1.01 ± 0.03
20	1.66 ± 0.12
21	2.74 ± 0.16
22	3.02 ± 0.24
23	1.72 ± 0.12
24	2.87 ± 0.22
Naftopidil	2.13 ± 0.07
Enzalutamide	2.56 ± 0.27

[a]The data represent the mean of at least three independent determinations.

TABLE 4 The binding affinities (kcal/mol) of compound 19 in three binding sites of AR.

Binding site	Compound 19	Naftopidil
LBP (PDB ID: 2OZ7)	−11.01	−7.29
AF2 (PDB ID: 2YHD)	−4.86	−6.87
BF3 (PDB ID: 2YLO)	−6.86	−8.1

noting that these results do not entirely align with previous tests on anti-proliferative activity against cancer cells. These findings suggest that the skillful introduction of certain small molecular groups on the piperazine ring may significantly enhance their antagonistic activity against AR. The conclusions drawn from this study undoubtedly provide us with a powerful tool, which will aid us in delving deeper into the interaction mechanisms between piperazine derivatives and AR, thus laying a more solid theoretical foundation for future drug development.

Recent studies have shown that, in addition to the AR signaling pathway, estrogen receptors (ER) also play an important role in the pathogenesis of PCa(Belluti et al., 2023; Souza et al., 2023). Research by Sarswat et al. (Sarswat et al., 2011) discovered that arylpiperazines, in addition to inhibiting the transmission of AR signals, can also promote the expression of ER-β in prostate cancer cells. ER-β may function as a protective receptor, exerting inhibitory effects on the development and malignant progression of PCa(Chaurasiya et al., 2020; Lombardi et al., 2020). By acting on prostate cancer cells through these two signaling pathways simultaneously, arylpiperazines inhibit their proliferation.

Binding affinity assay of compounds 7, 11, 17, 19, 20, 21, 22, 23 and 24

To delve into the specific binding characteristics of these analogs that exhibit significant inhibitory activity against the AR, we conducted detailed binding affinity studies using fluorescence polarization (FP) technology (Chen et al., 2023; He et al., 2021; Xue et al., 2023). The experimental design was based on the competitive binding mechanism between fluorescent tracers and non-fluorescent antagonists, aiming to assess the interaction strength between a series of compounds numbered **7, 11, 17, 19, 20, 21, 22, 23** and **24** with AR (Table 3). Through this method, we were able to precisely measure the binding efficiency of each compound at different concentrations and summarize the results in Table 3. The study revealed that all tested analogs demonstrated strong binding affinity to AR, with IC_{50} values below 4 μmol (μM), indicating high binding affinity. Particularly noteworthy, compounds **17** and **19** exhibited outstanding binding performance, with IC_{50} values of 1.14 μM and 1.01 μM, respectively, surpassing not only other test samples but also the clinically used standard drug enzalutamide (IC_{50} = 2.56 μM). This suggests that these two compounds may serve as more effective candidates for AR antagonists.

Further analysis revealed a clear trend among the tested arylpiperazine derivatives: a direct correlation between the binding affinity of compounds to AR and their antagonistic activity. For instance, the tightly bound compounds **17** and **19** were also the most effective antagonists, achieving maximum inhibition rates of 70.3% and 71.5%, respectively. Additionally, while not as prominent as the former two, compounds **20** and **23** also exhibited strong antagonistic effects, with inhibition rates of 65.7% and 62.2%, respectively. These observations support the hypothesis that enhanced binding affinity may be a key factor in improving AR antagonistic activity. Based on these findings, it can be inferred that certain ether-substituted arylpiperazine derivatives, due to their excellent binding ability and antagonistic efficacy, hold potential for development as novel AR antagonists, especially in the field of prostate cancer treatment. Considering the exceptional characteristics displayed by compound **19**, we have decided to focus on it for the next phase of research to explore its specific binding sites with AR and potential mechanisms of action. This will contribute to understanding how these compounds effectively block

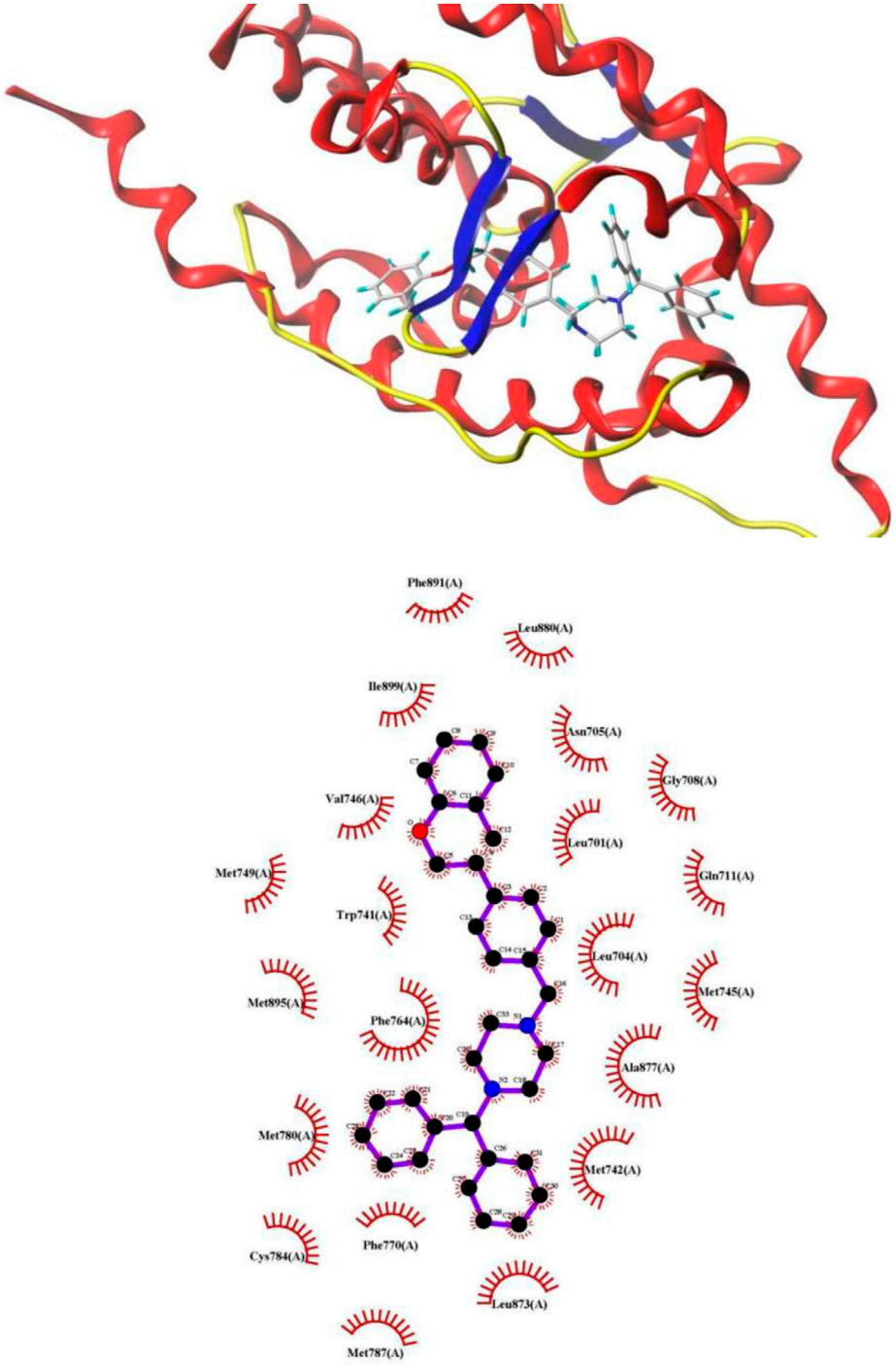


FIGURE 3
The view of compound **19**-AR interaction plots.

the AR signaling pathway, providing new strategies and methods for the treatment of prostate cancer.

Docking study

To decipher the binding mode of these compounds, as well as to explore the detailed information about their major binding interactions with AR (Zhang et al., 2014) docking simulation is performed. The optimal antagonist, compound **19** was taken as the template molecule in this process, and three binding sites of AR, including ligand binding pocket (LBP), activation function-2 (AF2) and binding function 3 (BF3) (Axerio-Cilies et al., 2011; Lack et al., 2011), were all used to explore the binding affinities of this compound. The lowest docked energy values were summarized in Table 3.

As shown in Table 4, LBP binding site had the highest binding force of −11.01 kcal/mol, which indicated that AR LBP was the major binding site for compound **19**. To better discover these binding interactions, the binding mode of compound **19** with AR was analyzed, and the detailed information was displayed in Figure 3. As shown in Figure 3, compound **19** could fit into the AR LBP site by the formation of Van der Waals' force with 14 amino acid residues, such as Val 746, Trp 741 and Phe 764, and so on. These results showed that the compound **19** mainly bind to AR LBP site through the interaction of Van der Waals' force.

Conclusion

In conclusion, this study reported the synthesis and biological evaluation of a series of novel arylpiperazine derivatives against three human prostate cancer cells and human prostate epithelial cells and AR, respectively. The results showed that the derivatives **7, 11, 17, 19, 20, 21, 22, 23** and **24** displayed strong cytotoxic activities against the tested cancer cells, and derivatives **17, 19, 20**, and **23** exhibited relatively strong antagonistic potency against AR (Inhibition % >60) and exhibited potent AR binding affinities. Structure-activity relationship (SAR) studies indicated that the introduction of cycloalkyl groups at the m,p-position on the phenyl ring and a methyl group at the o-position on the phenyl ring favored enhanced activity. Docking study suggested that the compounds **19** mainly bind to AR ligand binding pocket (LBP) site through the interaction of Van der Waals' force. These piperazine derivatives may guide the structural modification of novel anti-prostate cancer drugs.

Data availability statement

The datasets presented in this study can be found in online repositories. The names of the repository/repositories and accession number(s) can be found in the article/Supplementary Material.

Ethics statement

Ethical approval was not required for the studies on humans in accordance with the local legislation and institutional requirements because only commercially available established cell lines were used. Ethical approval was not required for the studies on animals in accordance with the local legislation and institutional requirements because only commercially available established cell lines were used.

Author contributions

HJ: Writing–original draft, Conceptualization, Funding acquisition, Formal Analysis. HaC: Conceptualization, Writing–original draft, Methodology, Software. YW: Writing–original draft, Validation. HX: Investigation, Writing–original draft. HoC: Investigation, Conceptualization, Data curation, Funding acquisition, Writing–review and editing.

Funding

The author(s) declare that financial support was received for the research and/or publication of this article. This research was funded by the Natural Science Foundation of Science and Technology Projects of Guizhou Province (Grant no. Qian Ke He Foundation-ZK [2022] General 633), the Scientific and Technological Support Project of Guizhou Province (Grant no. Qian Ke He Zhi Cheng [2023] Yi Ban 262), 2022 Guangdong Basic, Applied Basic Research Fund and Enterprises Joint Fund of Public Health and Medicine Area (Grant No. 2022A1515220218) and the Henan Province Science and Technology Attack Plan Foundation (242102231047).

Conflict of interest

The authors declare that the research was conducted in the absence of any commercial or financial relationships that could be construed as a potential conflict of interest.

The author(s) declared that they were an editorial board member of Frontiers, at the time of submission. This had no impact on the peer review process and the final decision

Generative AI statement

The author(s) declare that no Generative AI was used in the creation of this manuscript.

Publisher's note

All claims expressed in this article are solely those of the authors and do not necessarily represent those of their affiliated organizations, or those of the publisher, the editors and the reviewers. Any product that may be evaluated in this article, or claim that may be made by its manufacturer, is not guaranteed or endorsed by the publisher.

Supplementary material

The Supplementary Material for this article can be found online at: https://www.frontiersin.org/articles/10.3389/fchem.2025.1557275/full#supplementary-material

References

Axerio-Cilies, P., Lack, N. A., Nayana, M. R., Chan, K. H., Yeung, A., Leblanc, E., et al. (2011). Inhibitors of androgen receptor activation function-2 (AF2) site identified through virtual screening. *J. Med. Chem.* 54 (18), 6197–6205. doi:10.1021/jm200532b

Belluti, S., Imbriano, C., and Casarini, L. (2023). Nuclear estrogen receptors in prostate cancer: from genes to function. *Cancers (Basel)* 15 (18), 4653. doi:10.3390/cancers15184653

Chaurasiya, S., Widmann, S., Botero, C., Lin, C. Y., Gustafsson, J., and Strom, A. M. (2020). Estrogen receptor β exerts tumor suppressive effects in prostate cancer through repression of androgen receptor activity. *PLoS One* 15 (5), e0226057. doi:10.1371/journal.pone.0226057

Chen, H., Guan, X., Liu, Q., Yang, L., Guo, J., Gao, F., et al. (2022). Co-Assembled Nanocarriers of *de novo* Thiol-Activated hydrogen sulfide Donors with an RGDFF Pentapeptide for targeted therapy of non-small-cell Lung cancer. *ACS Appl. Mater Interfaces* 14 (48), 53475–53490. doi:10.1021/acsami.2c14570

Chen, H., Guo, S., Liu, Y., Jiang, H., Liao, Y.-X., Shen, J., et al. (2023). A stable NIR fluorescent probe for imaging lipid droplets in triple-negative breast cancer. *Sens. Actuat B-Chem* 398 (1), 134740. doi:10.1016/j.snb.2023.134740

Chen, H., Liang, X., Sun, T., Qiao, X., Zhan, Z., Li, Z., et al. (2018). Synthesis and biological evaluation of estrone 3-O-ether derivatives containing the piperazine moiety. *Steroids* 134, 101–109. doi:10.1016/j.steroids.2018.02.002

Chen, H., Liang, X., Xu, F., Xu, B., He, X., Huang, B., et al. (2014). Synthesis and cytotoxic activity evaluation of novel arylpiperazine derivatives on human prostate cancer cell lines. *Molecules* 19 (8), 12048–12064. doi:10.3390/molecules190812048

Chen, H., Wang, C. L., Sun, T., Zhou, Z., Niu, J. X., Tian, X. M., et al. (2018). Synthesis, biological evaluation and SAR of naftopidil-based arylpiperazine derivatives. *Bioorg Med. Chem. Lett.* 28 (9), 1534–1539. doi:10.1016/j.bmcl.2018.03.070

Chen, H., Xu, B. B., Sun, T., Zhou, Z., Ya, H. Y., and Yuan, M. (2017). Synthesis and antitumor activity of novel arylpiperazine derivatives containing the Saccharin moiety. *Molecules* 22 (11), 1857. doi:10.3390/molecules22111857

Chen, H., Xu, F., Liang, X., Xu, B. B., Yang, Z. L., He, X. L., et al. (2015). Design, synthesis and biological evaluation of novel arylpiperazine derivatives on human prostate cancer cell lines. *Bioorg Med. Chem. Lett.* 25 (2), 285–287. doi:10.1016/j.bmcl.2014.11.049

Chen, H., Yu, Y. Z., Tian, X. M., Wang, C. L., Qian, Y. N., Deng, Z. A., et al. (2019). Synthesis and biological evaluation of arylpiperazine derivatives as potential anti-prostate cancer agents. *Bioorg Med. Chem.* 27 (1), 133–143. doi:10.1016/j.bmc.2018.11.029

Chen, H., Zhang, J., Hu, P., Qian, Y., Li, J., and Shen, J. (2019). Synthesis, biological evaluation and molecular docking of 4-Amino-2H-benzo[h]chromen-2-one (ABO) analogs containing the piperazine moiety. *Bioorg Med. Chem.* 27 (20), 115081. doi:10.1016/j.bmc.2019.115081

Chen, J., Wang, C., Huang, X., Wan, R., Zhu, Z., Sun, G., et al. (2025). Quantum dots-Engineered Flexible Hydrogel as Plant-Wearable sensor for on-site Profiling Dynamic Pesticide Degradation. *Adv. Funct. Mater*, 2423643. doi:10.1002/adfm.202423643

Choi, E., Buie, J., Camacho, J., Sharma, P., and de Riese, W. T. W. (2022). Evolution of androgen deprivation therapy (ADT) and its new Emerging Modalities in prostate cancer: an Update for Practicing Urologists, Clinicians and Medical Providers. *Res. Rep. Urol.* 14, 87–108. doi:10.2147/rru.s303215

Dai, C., Dehm, S. M., and Sharifi, N. (2023). Targeting the androgen signaling Axis in prostate cancer. *J. Clin. Oncol.* 41 (26), 4267–4278. doi:10.1200/jco.23.00433

Fontana, F., Anselmi, M., and Limonta, P. (2022). Molecular mechanisms and genetic alterations in prostate cancer: from diagnosis to targeted therapy. *Cancer Lett.* 534, 215619. doi:10.1016/j.canlet.2022.215619

Formaggio, N., Rubin, M. A., and Theurillat, J. P. (2021). Loss and revival of androgen receptor signaling in advanced prostate cancer. *Oncogene* 40 (7), 1205–1216. doi:10.1038/s41388-020-01598-0

He, X., Ding, F., Sun, X., Zheng, Y., Xu, W., Ye, L., et al. (2021). Renovated multifunctional colorimetric/fluorometric sensor for simultaneous detection, imaging of pH variance and antimicrobial therapies. *Sens. Actuat B-Chem* 332, 129496. doi:10.1016/j.snb.2021.129496

He, Y., Xu, W., Xiao, Y. T., Huang, H., Gu, D., and Ren, S. (2022). Targeting signaling pathways in prostate cancer: mechanisms and clinical trials. *Signal Transduct. Target Ther.* 7 (1), 198. doi:10.1038/s41392-022-01042-7

Ishii, K., Matsuoka, I., Kajiwara, S., Sasaki, T., Miki, M., Kato, M., et al. (2018). Additive naftopidil treatment synergizes docetaxel-induced apoptosis in human prostate cancer cells. *J. Cancer Res. Clin. Oncol.* 144 (1), 89–98. doi:10.1007/s00432-017-2536-x

Iwamoto, Y., Ishii, K., Kanda, H., Kato, M., Miki, M., Kajiwara, S., et al. (2017). Combination treatment with naftopidil increases the efficacy of radiotherapy in PC-3 human prostate cancer cells. *J. Cancer Res. Clin. Oncol.* 143 (6), 933–939. doi:10.1007/s00432-017-2367-9

Jamroze, A., Chatta, G., and Tang, D. G. (2021). Androgen receptor (AR) heterogeneity in prostate cancer and therapy resistance. *Cancer Lett.* 518, 1–9. doi:10.1016/j.canlet.2021.06.006

Jiang, H., Zhang, H., and Jiang, S. (2024). CircDUSP22 Attenuates the Ferroptosis of prostate cancer cells via miR-18a-5p/SLC7A11/GPX4 signaling. *Comb. Chem. High. Throughput Screen* 27. doi:10.2174/0113862073324077240624094140

Kinoyama, I., Taniguchi, N., Kawaminami, E., Nozawa, E., Koutoku, H., Furutani, T., et al. (2005). N-Arylpiperazine-1-carboxamide derivatives: a novel series of orally active nonsteroidal androgen receptor antagonists. *Chem. Pharm. Bull. (Tokyo)* 53 (4), 402–409. doi:10.1248/cpb.53.402

Kinoyama, I., Taniguchi, N., Yoden, T., Koutoku, H., Furutani, T., Kudoh, M., et al. (2004). Synthesis and pharmacological evaluation of novel arylpiperazine derivatives as nonsteroidal androgen receptor antagonists. *Chem. Pharm. Bull. (Tokyo)* 52 (11), 1330–1333. doi:10.1248/cpb.52.1330

Lack, N. A., Axerio-Cilies, P., Tavassoli, P., Han, F. Q., Chan, K. H., Feau, C., et al. (2011). Targeting the binding function 3 (BF3) site of the human androgen receptor through virtual screening. *J. Med. Chem.* 54 (24), 8563–8573. doi:10.1021/jm201098n

Lombardi, A. P. G., Vicente, C. M., and Porto, C. S. (2020). Estrogen receptors promote Migration, Invasion and Colony formation of the androgen-independent prostate cancer cells PC-3 through β-Catenin pathway. *Front. Endocrinol. (Lausanne)* 11, 184. doi:10.3389/fendo.2020.00184

Lu, C., Brown, L. C., Antonarakis, E. S., Armstrong, A. J., and Luo, J. (2020). Androgen receptor variant-driven prostate cancer II: advances in laboratory investigations. *Prostate Cancer Prostatic Dis.* 23 (3), 381–397. doi:10.1038/s41391-020-0217-3

Maesaka, F., Tanaka, N., Nakai, Y., Asakawa, I., Tomizawa, M., Owari, T., et al. (2021). Comparison of disease-specific quality of life in prostate cancer patients treated with low-dose-rate brachytherapy: a randomized controlled trial of silodosin versus naftopidil. *Int. J. Urol.* 28 (11), 1171–1176. doi:10.1111/iju.14667

Obinata, D., Lawrence, M. G., Takayama, K., Choo, N., Risbridger, G. P., Takahashi, S., et al. (2020). Recent Discoveries in the androgen receptor pathway in castration-resistant prostate cancer. *Front. Oncol.* 10, 581515. doi:10.3389/fonc.2020.581515

Qi, Y., Chen, H., Chen, S., Shen, J., and Li, J. (2022). Synthesis, bioactivity, and molecular docking of novel arylpiperazine derivatives as potential AR antagonists. *Front. Chem.* 10, 947065. doi:10.3389/fchem.2022.947065

Qi, Y., Xue, B., Chen, S., Wang, W., Zhou, H., and Chen, H. (2022). Synthesis, biological evaluation, and molecular docking of novel hydroxyzine derivatives as potential AR antagonists. *Front. Chem.* 10, 1053675. doi:10.3389/fchem.2022.1053675

Sarswat, A., Kumar, R., Kumar, L., Lal, N., Sharma, S., Prabhakar, Y. S., et al. (2011). Arylpiperazines for management of benign prostatic hyperplasia: design, synthesis, quantitative structure-activity relationships, and pharmacokinetic studies. *J. Med. Chem.* 54 (1), 302–311. doi:10.1021/jm101163m

Schmidt, K. T., Huitema, A. D. R., Chau, C. H., and Figg, W. D. (2021). Resistance to second-generation androgen receptor antagonists in prostate cancer. *Nat. Rev. Urol.* 18 (4), 209–226. doi:10.1038/s41585-021-00438-4

Siegel, R. L., Miller, K. D., Fuchs, H. E., and Jemal, A. (2022). Cancer statistics, 2022. *CA Cancer J. Clin.* 72 (1), 7–33. doi:10.3322/caac.21708

Souza, D. S., Macheroni, C., Vicente, C. M., Cavalheiro, R. P., Campo, V. L., and Porto, C. S. (2023). Estrogen receptors regulate galectin-3 in androgen-independent DU-145 prostate cancer cells. *Oncol. Rep.* 49 (5), 93. doi:10.3892/or.2023.8530

Sun, T., Chen, R., Huang, Q., Ba, M., Cai, Z., Hu, S., et al. (2022). Chromatographic Separation of Aromatic amine Isomers: a solved issue by a new Amphiphilic pillar[6]arene stationary phase. *ACS Appl. Mater Interfaces* 14 (50), 56132–56142. doi:10.1021/acsami.2c17889

Sun, T., Zhang, Y., Liu, H., Xu, X., Cai, Z., Hu, S., et al. (2025). Separation performances of extended pillar[6]arenes, a new stationary phase for gas chromatography. *Talanta* 283, 127098. doi:10.1016/j.talanta.2024.127098

Vellky, J. E., and Ricke, W. A. (2020). Development and prevalence of castration-resistant prostate cancer subtypes. *Neoplasia* 22 (11), 566–575. doi:10.1016/j.neo.2020.09.002

Visakorpi, T., Hyytinen, E., Koivisto, P., Tanner, M., Keinänen, R., Palmberg, C., et al. (1995). *In vivo* amplification of the androgen receptor gene and progression of human prostate cancer. *Nat. Genet.* 9 (4), 401–406. doi:10.1038/ng0495-401

Xue, B., Hou, A., Du, Y., Qi, Y., Jiang, H., Zhou, H., et al. (2023). AIE donor-dependent photosensitizer for enhance photodynamic antibacterial interface. *Surf. Interfaces* 39, 102996. doi:10.1016/j.surfin.2023.102996

Zhan, H., Zhang, S., Li, L., Chen, Z., Cai, Y., Huang, J., et al. (2022). Naftopidil enantiomers suppress androgen accumulation and induce cell apoptosis via the UDP-glucuronosyltransferase 2B15 in benign prostate hyperplasia. *J. Steroid Biochem. Mol. Biol.* 221, 106117. doi:10.1016/j.jsbmb.2022.106117

Zhang, J., Li, Y., Chen, X., Pan, Y., Zhang, S., and Wang, Y. (2014). Systems pharmacology dissection of multi-scale mechanisms of action for herbal medicines in stroke treatment and prevention. *PLoS One* 9 (8), e102506. doi:10.1371/journal.pone.0102506

Zheng, R. S., Chen, R., Han, B. F., Wang, S. M., Li, L., Sun, K. X., et al. (2024). Cancer incidence and mortality in China, 2022. *Zhonghua Zhong Liu Za Zhi* 46 (3), 47–53. doi:10.1016/j.jncc.2024.01.006

Zhou, J.-W., Li, P.-L., Ji, P., Yin, K.-Y., Tan, X.-J., Chen, H., et al. (2024). Carbon quantum dots derived from resveratrol enhances anti-virulence activity against *Pseudomonas aeruginosa*. *Surf. Interfaces* 44 (1), 103662. doi:10.1016/j.surfin.2023.103662

frontiers | Frontiers in Chemistry

TYPE Review
PUBLISHED 28 March 2025
DOI 10.3389/fchem.2025.1527387

Check for updates

OPEN ACCESS

EDITED BY
Jian-Wei Han,
East China University of Science and Technology, China

REVIEWED BY
Lucia Chiummiento,
University of Basilicata, Italy
N. Vijaya Ganesh,
LGC Standards, United States

*CORRESPONDENCE
Richard K. Amewu,
ramewu@ug.edu.gh
Dorcas Osei-Safo,
dosei-safo@ug.edu.gh

RECEIVED 13 November 2024
ACCEPTED 28 February 2025
PUBLISHED 28 March 2025

CITATION
Akwensi J, Kumah RT, Osei-Safo D and Amewu RK (2025) Application of Hosomi-Sakurai allylation reaction in total synthesis of biologically active natural products.
Front. Chem. 13:1527387.
doi: 10.3389/fchem.2025.1527387

COPYRIGHT
© 2025 Akwensi, Kumah, Osei-Safo and Amewu. This is an open-access article distributed under the terms of the Creative Commons Attribution License (CC BY). The use, distribution or reproduction in other forums is permitted, provided the original author(s) and the copyright owner(s) are credited and that the original publication in this journal is cited, in accordance with accepted academic practice. No use, distribution or reproduction is permitted which does not comply with these terms.

Application of Hosomi-Sakurai allylation reaction in total synthesis of biologically active natural products

Justice Akwensi[1], Robert T. Kumah[2], Dorcas Osei-Safo[1]* and Richard K. Amewu[1]*

[1]Department of Chemistry, School of Physical and Mathematical Sciences, College of Basic and Applied Sciences, University of Ghana, Legon, Ghana, [2]Department of Chemical and Petrochemical Engineering, School of Petroleum Studies, University of Mines and Technology, Tarkwa, Ghana

The Hosomi–Sakurai allylation reaction has been widely applied in the total synthesis of biologically active natural products, especially in synthesising complex polycyclic compounds containing multi-stereogenic centres since its discovery in 1976. The Hosomi-Sakurai allylation is the allylation of ketones and aldehyde with nucleophilic allylsilanes catalyzed with Lewis acid mainly used to extend the C-C bond in a molecule and also create a new site for manipulation due to the facile transformation of the *pi* (π) bond at the end of its chain. This review highlights only portions of natural product synthetic works that feature the Hosomi-Sakurai allylation reaction or its modification as a key transformation in the synthetic route.

KEYWORDS

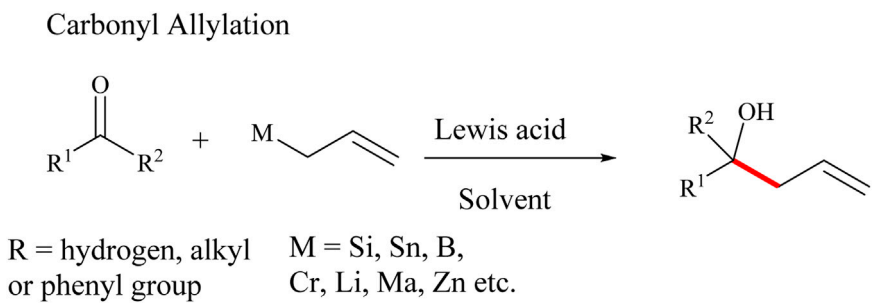
Hosomi-Sakurai allylation, carbonylation, total synthesis, stereoselectivity, natural products, lewis acid-promotors

1 Introduction

1.1 Catalytic allylation reactions

Homoallylic alcohols are a significant class of compounds with extensive applications in the synthesis of biologically active substances. Their unique structural properties make them valuable in various chemical processes, contributing to advancements in medicinal chemistry (Farina et al., 2006; Li et al., 2021; Pellissier, 2016; Shen et al., 2013). Homoallylic alcohols are products of catalytic allylation reactions that employ the use of allylic reagents under mild reaction conditions. Allylation reactions are particularly advantageous due to their use of cost-effective, nontoxic, and stable nucleophiles such as allyltrialkylsilanes, allyltrialkoxysilanes among others. Although significant advancements have been made in allylation reactions, only a limited number of catalytic asymmetric allylation reactions have been reported. This is particularly interesting due to the importance of chiral tertiary homoallylic alcohols in organic synthesis. (Fleming et al., 1989; 1997; Langkopf and Schinzer, 1995; Lee, 2020).

Allylation of carbonyl compounds is one of the most used methods of forming C-C bonds in the most versatile manner (Lee, 2020). In 1964, Mikhailov and co-workers reported the first reaction between an allyl-metal and a carbonyl catalysed by triallylborane (Stepanyan et al., 2001). A number of allyl-(semi)-metals such as Si, Mn, Sn, Sb, Mg, Bi, Al, B, Cr, Li, Zn, Ti, Zr and In have been applied in carbonyl allylation in the total synthesis of



SCHEME 1
A typical example of an HSR (allylation of carbonyl compounds) reaction catalyzed by Lewis acid to give the corresponding alcohols.

simple and complex compounds (Bols and Skrydstrup, 1995; Denmark and Fu, 2003; Dilman and Ioffe, 2003; Fleming et al., 1989; 1997; Langkopf and Schinzer, 1995; Lee, 2020; Masse and Panek, 1995; Stankevich and Cook, 2023; Yamamoto and Asao, 1993). Allylation of carbonyl compounds to produce corresponding alcohols and enols is a well-established synthetic method that employs allylic reagents in the presence of Lewis acids catalysts to form C-C bonds and alcohol derivatives in high-yields (Yamamoto and Asao, 1993). Several other allylation reactions including the Tsuji-Trost allylic reaction, Keck radical allylation, Hosomi-Sakurai allylation reactions among others have been reported in the past 2 decades. For example, the Tsuji-Trost allylic reaction is a versatile and high-yielding reaction in this category. The reaction involves the use of Pd (0) to catalyze the allylation of several nucleophilic species, including methylenes, enolates, amines, and phenols (Li, 1999; Song et al., 2007). These nucleophiles are combined with allylic compounds, such as allyl acetates and allyl bromides, (Supplementary Scheme S1a) (Hegedus et al., 1978; Keck and Yates, 1982; Trost and Van Vranken, 1996; Tsuji, 1969). Tsuji-Trost allylic reaction is applicable in the total synthesis of indole alkaloids such as Desethylibogamine, Isoquinuclidine and (±)-Catharanthine (Trost, 2015; Trost et al., 1978; Tsuji, 1986a; 1986b; Tsuji and Takahashi, 1965). Keck radical allylation is also frequently used in C-C bond formation (Supplementary Scheme S1b) (Aiqin et al., 2011; Keck and Yates, 1982). Keck radical allylation proceeds through the generation of radicals from alkyl bromides, chlorides, phenyl-selenides, and thioacylimidazoles in the presence of a radical initiator such as azobisisobutyronitrile (AIBN) and benzoyl peroxide (BPO) (Sumino et al., 2018). The application of Keck allylation is limited by the challenges associated with the purification of the corresponding products and the inherent toxic nature of organotin reagents used in the reaction (Supplementary Scheme S1b) (Fent, 1996).

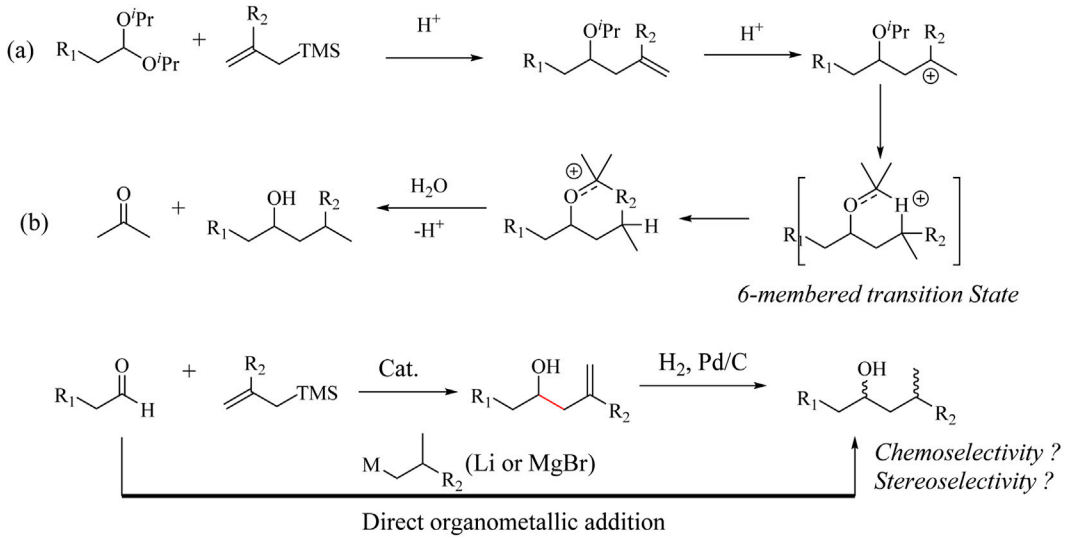
The Hosomi-Sakurai allylation reaction (HSR) is the type of allylation reaction that efficiently creates C-C bonds in the total synthesis of optically active natural products (Scheme 1) (Majetich et al., 1990). HSR involves the allylation of carbonyl compounds using allylic reagents in the presence of Lewis acid catalysts to give the corresponding alcohols in good yields. The HSR usually gives quantitative yields and hence produces fewer by-products. The substituents of the allylsilane are useful in controlling the stereochemistry of the products although the reaction is not centered on the silicon atom in most cases except for chiral allysilanes which usually yield the chiral product (Chan and Wang, 1992; Kira et al., 1990).

HSR is also applicable in the synthesis of polymers by repetitively allylating dialdehydes with bisallylsilanes to give a hydroxyl and olefinic polymer with repeating units (Supplementary Scheme S4) (Itsuno, 2005). A typical example is the preparation of Si-phenyl linkage polymers using HSR in the presence of TBAF/THF overnight (Supplementary Scheme S4). However, low molecular weight monomer units of homoallylic alcohols with high enantiomeric purity were reported (Kumagai and Itsuno, 2000).

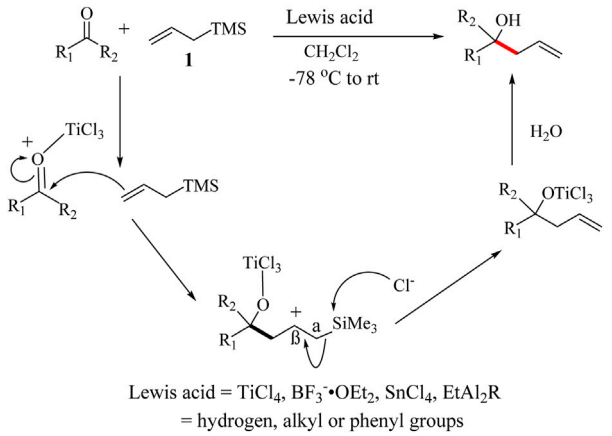
Bauer and co-workers discovered a reductive HSR of acetals (Bauer and Maulide, 2018) through the 1,5-hydride transfer transformations (Scheme 2a). The reaction exploits *in situ* generation of homoallylic ether after the HSR with the acetal substrate. Subsequent protonation to generate a carbocation at the γ-position to the ether group leads to an intramolecular 1,5-hydride transfer rearrangement to form an oxocarbenium ion. The addition of water leads to the formation of the corresponding alcohol product. The reaction mechanism yields a similar product to a direct Grignard/Alkyl-Li reagent addition to an aldehyde (Scheme 2b). Air- and water-sensitive Grignard reagents bearing functional groups such as α,β-unsaturated esters, and alkyl bromides are tolerated under these reaction conditions (Bauer and Maulide, 2018). However, the reaction is not applicable when carbonyl substrates bearing aromatic groups, unprotected alcohols, and thioethers are used, as illustrated in Supplementary Scheme S2. In addition, the homo-ether intermediate formed in the HSR could subsequently yield the desired homoallylic products with phenyl-allylsilane if the amount of catalyst was reduced to 2.7 mol%, (dr = 4.5:1) (Bauer and Maulide, 2018). It is interesting to note that this reaction was not only chemoselective but also stereoselective when pro-chiral carbonyl substrates were used (Scheme 2).

1.2 History of Hosomi-Sakurai allylation reactions

The HSR, commonly referred to as the Sakurai allylation or Sakurai reaction, was discovered in the 1970s as an alternative to the classical allylation method of C-C bond formation and has been extensively studied over the years (Bauer and Maulide, 2018). The HSR of carbonyl compounds and their derivatives with the allyl trialkylsilane as the



SCHEME 2
Reductive Hosomi-Sakurai allylation reaction **(a)** Intramolecular 1,5-hydride transfer rearrangement and **(b)** direct Grignard reaction.



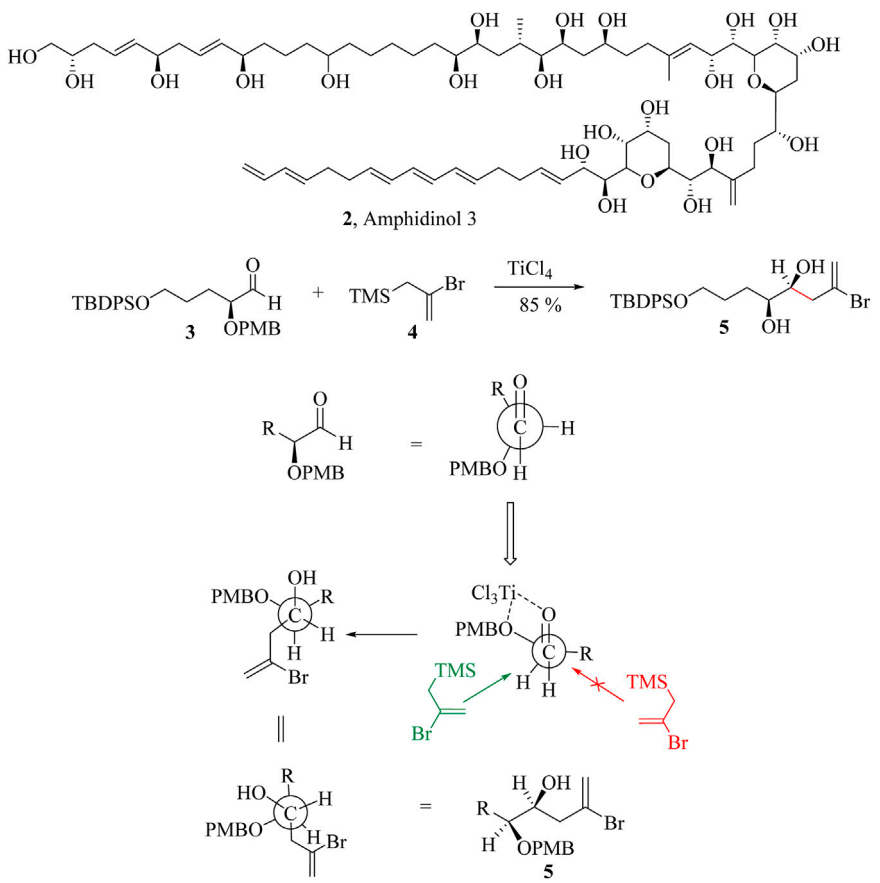
SCHEME 3
General reaction and mechanism of the HSR (Kira et al., 1990).

allylating agent in the presence of a Lewis acid as a catalyst, proceeds rapidly even at an extremely low temperature of −78°C (Hosomi and Sakurai, 1976). The H-SR is applicable in the allylation of aliphatic, alicyclic, and aromatic carbonyl compounds using allylmethylsilane and $TiCl_4$ as a catalyst. Allylsilanes are reported to be weakly nucleophilic hence the Lewis acid catalyst is used to activate and increase the reactivity of the carbon electrophile in the solution. This results in a C-C bond formation that occurs only at the γ-position to the silicon moiety (Yamamoto and Sasaki, 1989).

Allylsilanes are very useful in organic synthesis because they are easy to handle, can be used at room temperatures, and do not require special storage conditions. Their reactions are usually smooth (homogeneous) with different electrophiles under Lewis acid conditions. On the contrary, other allylating agents such as allyl-magnesium halides, -Li, -Cu, and -Ti compounds require specific temperatures and moisture-free working atmosphere and reaction conditions (Yamamoto and Sasaki, 1989). The major advantage of the HSR is that allylsilanes are readily available inexpensive starting materials. They are stable, have low toxicity, compatible with multiple functional groups, and chemically inert to atmospheric conditions (Fleming, 1991; Hosomi, 1988; Yamamoto and Asao, 1993). However, the reaction depends on the presence of Lewis acids such as $TiCl_4$, $BF_3{\cdot}OEt_2$, $SnCl_4$, and $EtAlCl_2$ as activators because allylsilanes do not readily react with non-activated electrophiles (Lade et al., 2017).

1.3 Mechanism, scope and features

A typical reaction pathway of the HSR is illustrated in Scheme 3. An oxocarbenium ion is first generated from the reaction of the carbonyl compound with the Lewis acid which makes the carbonyl carbon more electrophilic. It begins with a nucleophilic attack of the γ-carbon of the allylsilane, **1** on the carbonyl to generate a carbocation which is stabilized by the silyl group (Schweig et al., 1974). The α-Si-C bond at this stage is weak and can be easily cleaved to neutralize the carbocation, hence forming the alkene. Halide from the catalyst facilitates the facile cleavage to form the corresponding intermediate (Ponomarenko & Mironov, 1954). The reaction is usually completed by the addition of H_2O to give the desired allyl-alcohol products (Scheme 3). The propylene unit created through a reaction between an aldehyde and allylic reagents is very useful in the synthesis of optically active molecules. One of the key features of silyl groups is the ability to stabilize charges on their immediate. Specifically, this includes stabilizing geminal anions (α-effect) and vicinal cations (β-effect). The α-effect is often observed through the metalation of silanes in the α-position using strong bases (Britten et al., 2021). However, the stabilizing influence of the silyl group is significantly more pronounced



SCHEME 4
An illustration of the stereospecificity of HSR.

for the β-silicon effect compared to the α-effect (Roberts and McLaughlin, 2022).

Under Lewis acid conditions, it was observed that the reaction proceeds through a less open cyclic transition state, and more asymmetric products could be achieved (Kira et al., 1990). The HSR is regioselective due to the formation of a stable silylcarbocation intermediate (Hosomi et al., 1978a). In 1978, tetra-*n*-butylammonium fluoride (TBAF) was introduced as an alternative catalyst to Lewis acids. TBAF reacts with allylsilanes to give a stable Si-F intermediate which attacks carbonyl leading to the formation of silyl ethers (Hosomi et al., 1978b). TBAF is also effective in catalysing allylation of synthetic intermediates such as acetals, aldimines/imines/iminium ions (Shingo et al., 2002), aldehydes, acids chlorides (Yadav et al., 2003), epoxides (Yamasaki et al., 2002), ketals, keto-imines, ketones, oxocarbenium ions (Hosomi et al., 1978a) and α,β-unsaturated carbonyls (Lade et al., 2017; Roberts and McLaughlin, 2022). Allylation of α,β-unsaturated carbonyl compounds, however, generates the ketone-enol tautomers instead of the alcohol which continues the allylation cycle as illustrated in Supplementary Scheme S2 (Fürstner and Voigtländer, 2000). A number of Lewis acids have been reported as pre-catalysts in HSR in the past 3–5 decades. Lewis acid reagents such as $SnCl_4$, $AlCl_3$, $BF_3.OEt_2$, Me_3SiOTf, Me_3SiI, and $Me_3O^+BF_4^-$ or their combinations have also been used (Birch et al., 1981; Colvin, 1978; Hosomi et al., 1984; Nishiyama et al., 1982; Noyori et al., 1981; Yotsu-Yamashita et al., 1995).

Despite the numerous applications, the use of Lewis acid catalysts in HSR is limited by the inability to recover and reuse them in the subsequent reaction cycles (Supplementary Scheme S3). In addition, Lewis acids are susceptible to degenerate to allylic metal oxides and are therefore added in stoichiometric amounts to ensure the completion of the reaction (Mahlau and List, 2013). The HSR typically yields *syn*-addition products, making it highly diastereoselective in the allylation of carbonyl compounds. The Newman projection (Scheme 4) of the allylation of aldehyde **3** with (2-bromoallyl) trimethylsilane **4** to form **5**, a key intermediate in the synthesis of amphidinol 3, (**2**) demonstrates the diastereospecificity of the HSR. In the Newman projection, the intermediate coordinated to the titanium tetrachloride with the two oxygen atoms tethered together, fixing the conformation of the substrate. This is known as the Cram chelation control mechanism (Cram and Elhafez, 1952; Stanton et al., 2010). The (2-bromoallyl) trimethylsilane nucleophile then approaches along the Bürgi-Dunitz angle, but only one side of the approach is possible as the other is hindered by the R groups. This ensures the formation of only one diastereomer in high yields. Amphidinol 3 (**2**) is a potent antifungal compound produced by the dinoflagellate Amphidinium klebsii (Grisin and Evans, 2015; Huckins et al., 2007; Oishi, 2024; Wakamiya et al., 2020).

1.4 Drawbacks of the HSR

The HSR typically proceeds through an open-chain transition state mechanism, which inherently limits the scope of the method. Since carbonyl compounds are not highly reactive, there is a need to increase their reactivity by using strong Lewis acids as catalysts or by activating the allylsilane, especially those with electron-withdrawing groups (Mahlau and List, 2013). However, this approach is not favourable for late-stage functionalization, as it can be intolerant of functional groups and lead to loss of regioselectivity in some cases, resulting in low yields (Chemler and Roush, 2000). Efforts to increase the electrophilicity of carbonyl compounds often lead to a loss of regioselectivity when the allylsilane is activated by a fluoride source (Denmark and Fu, 2003). While the open anti-periplanar transition state leads to the formation of the *syn*-product in most cases, it also impedes the enantioselectivity of the mechanism (Denmark and Almstead, 1994).

1.5 Modifications to the HSR

Attempts to address the challenges of HSR have led to the discovery and use of a chiral base catalyst (**S44**), transition metal fluoride (**S45**), chiral Lewis acids (**S47**) Supplementary Figure S1, and tartrate-modified allylsilanes to improve the selectivity and versatility of the HSR (Denmark and Fu, 2001; Gauthier and Carreira, 1996; Ishihara et al., 1993; Malkov et al., 2002; 2008; Schäfers et al., 2022; Zhang et al., 1997). Due to the inherent challenges associated with the HSR, Schäfers et al. developed a dual catalytic system that uses less basic allyl chromium instead of allylsilanes (Schäfers et al., 2022). This reaction proceeds through a ring-closed Zimmerman–Traxler transition state, initiated using the sterically hindered acridinium photocatalyst and blue light-emitting diode (LED) irradiation (Supplementary Scheme S13). These reaction conditions often yield undesirable homoallylic products with different chemo- and diastereoselectivity. Mechanistic analysis showed that the reaction proceeds through a cyclic mechanism, leading to the formation of the *anti*-product.

This alternative approach using allyl chromium and photocatalytic activation represents a valuable strategy to overcome the inherent limitations of the HSR, providing access to complementary stereochemical outcomes (Schäfers et al., 2022). The HSR has seen numerous modifications to its reaction conditions since its discovery. For example, new chiral catalysts were introduced with allyltrialkylsilanes, allyltrialkoxysilanes, or allyl trichlorosilane to attain enantiomerically pure allylated products (Kaib et al., 2016; Kampen et al., 2008; Lee, 2020; Sai and Yamamoto, 2015; Schreyer et al., 2019).

The allylation of ketones to generate homoallylic alcohols through the HSR has been a challenge and has proven unsuccessful over the years. Despite these challenges, several asymmetric allylations of ketone have been reported (Niwa et al., 2019; Pellissier, 2006; Tietze et al., 1995; 2004; Wadamoto et al., 2003). The most efficient one is the use of fluoroallylsilane derivatives and Pd-based catalysts instead of the usual Lewis acids (Hayashi et al., 2010). Bismuth bromide has also been reported as a useful catalyst in the allylation of carbonyls by Komatsu and co-workers. Allylation with bismuth bromide is compatible with trimethylsilyl, trifluoromethane sulfonate (TMSOTf) (Noyori et al., 1981), and trimethylsilyl iodide (TMSI) (Komatsu et al., 1997).

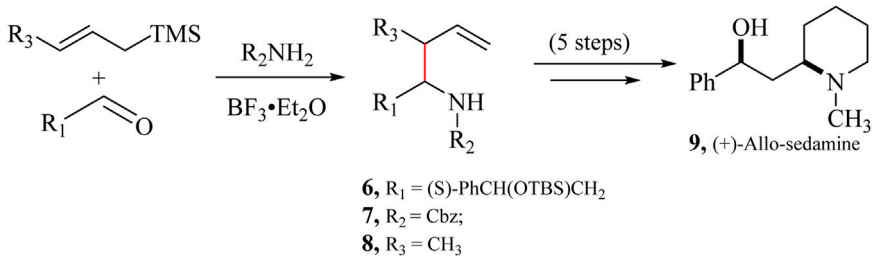
Alternatively, Sakurai-Hosomi-Yamamoto allylation has been an effective approach for the stereoselective synthesis of a number of chiral homoallylic alcohols in high yields by employing Chiral (*R*)- and (*S*)-BINAP.AgF catalysts (Supplementary Scheme S8) (Makita et al., 2003; Mirabdolbaghi and Dudding, 2012). Although the reaction mechanism for the asymmetric (*R*)- or (*S*)-BINAP.AgF Sakurai-Hosomi-Yamamoto allylation reaction remains unknown, Mirabdolbaghi et al., proposed a transition state (TS1) that rationalized the enantioselectivity of the mechanism as shown in Supplementary Scheme S8 (Mirabdolbaghi and Dudding, 2012).

Yamamoto and his coworkers further disclosed the synthesis of the γ- and *anti*-products upon using AgF and a chiral bisphosphine catalyst such as (*R*)-DIFLUOROPHOS (Nokami et al., 2003; Wadamoto et al., 2003). This reaction is also assumed to progress through the cyclic transition state that is generated *in situ* from the transmetalation of allylsilanes to AgF (Supplementary Scheme S5). This modified Ag-catalyzed asymmetric allylation reaction is amenable to ketone as well as aldehydes (Komiyama et al., 2017; Wadamoto et al., 2003).

The aza-Hosomi-Sakurai (aHS) reaction, developed by Veenstra and Schmid (1997), is an additional variation of the HSR. This method allows for the one-step synthesis of homoallylamines which involves reacting an allylsilane with an aldehyde, a carbamate, or a sulfonamide, in the presence of a Lewis acid catalyst (Scheme 5). This reaction mechanism permits the synthesis of *N*-protected homoallylamines, which can be utilised to make *N*-heteroatomic rings in a few steps (Ella-Menye et al., 2005) leading to the synthesis of pyrrolidine and piperidine rings and eventually (+)-Allosedamine (**9**) (Girard, 2015).

Onishi et al. (2002), developed a highly effective Lewis acid by combining $InCl_3$ with Me_3SiCl. The hybrid catalytic system is effective for HSR and Friedel-Crafts allylation and hydrosilylation reactions. Hexafluoroisopropanol (HFIP) has also proven to be an efficient source of a hydrogen bond donor and as a catalyst in the form HFIP–DCM (4:1 (v/v)) solution (Motiwala et al., 2022). To form the desired targeted allylated aldehyde and acetal products product, HFIP (2–5 eq.) was required (Supplementary Scheme S6) (Berkessel et al., 2006; Motiwala et al., 2022). HSR of hydroxy-aldehydes with allytrifluorosilanes was discovered to be stereospecific in the presence of triethylamine and chiral Lewis acid catalysts (Kira et al., 1990). Asymmetric Hosomi-Sakurai reactions (AHSR) could be effectively achieved with *ee* up to 92% using chiral Lewis (Denmark et al., 1994; Iseki et al., 1999; Wang et al., 1999).

Furthermore, a new trityl tetrakis (pentafluophenyl) borate $[(Ph_3C)[BPh(^F)_4]$ has been discovered as a catalyst to mediate HSR of β,γ-unsaturated α-ketoesters to yield γ,γ-disubstituted α-ketoesters in excellent yields using allylsilane reagent (Chien et al., 1991; Hollis and Bosnich, 1995; Kosugi et al., 1985; Mukaiyama et al., 1984). HSR of crotyl geminal bis(silane) with aldehydes (Supplementary Scheme S7) for instance can be carried out more efficiently by using the $(Ph_3C)[BPh(^F)_4]$ catalyst (Chu et al., 2017; Santos and Silva, 2018).



SCHEME 5
Modified Aza-Hosomi-Sakurai (aHS) allylation reaction for synthesizing (+)-Allo-sedamine (**9**) (Girard, 2015).

2 Applications of HSR in total synthesis of biologically active natural products

A plethora of synthetic methods have been studied and advanced in the synthesis of complex compounds including natural products over the past decades. Among them is HSR of carbonyl intermediates which provides a straightforward and versatile method for preparing these compounds. The HSR is characterised by the formation of a new carbon-carbon bond with high functional group compatibility. The stereoselectivity of the reaction is largely regulated by substituents on substrates under mild reaction conditions. The use of allylsilanes makes this allylation a useful tool for synthesizing complex natural products. Recently, Lee (2020) reported the application of Hosomi-Sakurai in the total synthesis of a number of natural products. In this review, we will focus only on selected examples of total synthesis of biologically active natural products that have utilized HSR as a key transformation method in the past 2 decades and were not included in Lee work.

2.1 Total synthesis of aburatubolactam A

Aburatubolactam A (**10**) is a natural product isolated from the culture broth of marine mollusc bacterium *Streptomyces* sp., SCRC-A20 in Japan (Bai et al., 2016; Henderson et al., 2008). Uemura and co-workers determined the complete structure and absolute stereochemistry of the natural product using X-ray crystallographic analysis (Bae et al., 1996). Biological screening of Aburatubolactam A (**10**) exhibited cytotoxicity properties against human cancer cells by inhibiting cell proliferation, anti-microbial activity, and the inhibition of superoxide generation (Israr et al., 2024). Aburatubolactam A (**10**) has been observed to be an inhibitor of protein kinase C in both rat brain tissue samples and rat liver cell membrane preparations (Israr et al., 2024). Additionally, Aburatubolactam A (**10**) has been found to suppress the growth of *Mycobacterium tuberculosis* bacteria by disrupting the synthesis of DNA, RNA, and proteins within the bacterial cells (Henderson et al., 2008).

A total of 23 steps were required to synthesise Aburatubolactam A (**10**) starting from commercially available ketone **11**, followed by five steps to form bicyclo [3.3.0] octene **12** with a 90% yield (Scheme 6) (Henderson et al., 2008). The fluoride-mediated Sakurai allylation using TBAF in a solvent mixture of dimethylformamide and *N,N′*-Dimethylpropyleneurea (DMF-DMPU) resulted in the formation of intermediate **13** (Majetich et al., 1986). This intermediate was obtained as a 4:1 mixture of inseparable diastereomers, achieving a yield of 78%. This ratio was then improved in favour of the desired isomer to 2:1 by the protonation of the silylketene acetyl derived from **13**. The resulting product was taken through 11 other sequential steps to achieve Aburatubolactam A (**14**) in 46% total yield (Bai et al., 2016; Henderson et al., 2008) (Scheme 6).

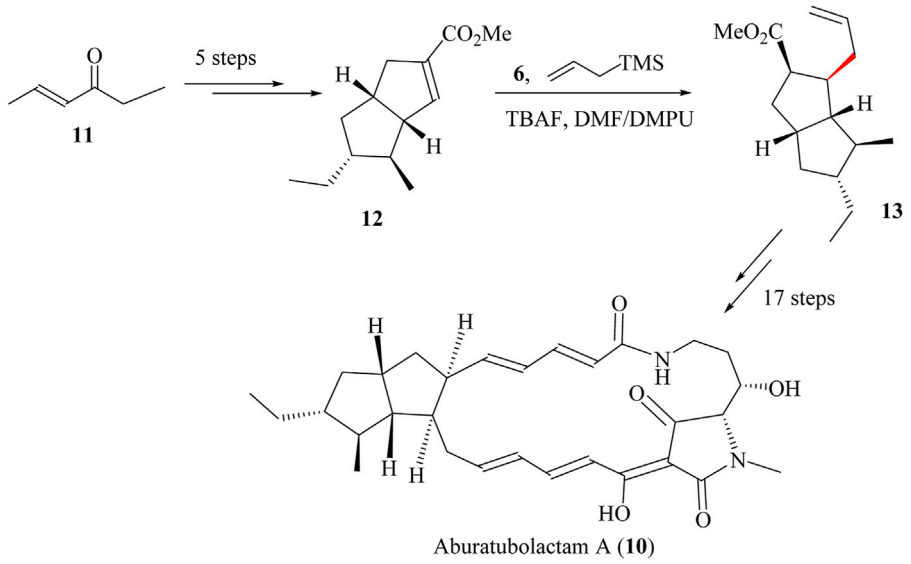
2.2 Total syntheses of (–)-acutumine

(–)-Acutumine **14**, is an alkaloid isolated first from the roots of *Sinomenium acutum* in 1929 by Goto and co-workers (Li et al., 2009). It has also been discovered in *Hypserpa nitida* and *Apis cerana*. The family of (–)-Acutumine has structural similarities to the Hasubanan family of alkaloids such as (–)-Dechloroatunine (**15**), and (–)-Hasubanonine (**16**). (–)-Acutumine (**14**) inhibits the proliferation of human T-cells and memory-enhancing properties in the Wistar rat model (Yu et al., 2002). The structure complexity with embedded chirality in the spirocyclopentenone rings 1 and 2 of (–)-Acutumines poses difficulty in its total synthesis (King et al., 2013).

In 2009, Castle and co-workers reported the total synthesis of (–)-Acutumine (**14**) (Li et al., 2009). In the build-up to the synthesis of (–)-Acutumine spirocyclopentenone ring derived from acetonide **17** was prepared in 5 steps from the starting D-ribose, **18** (Scheme 7) (Kim et al., 2020; Smith et al., 2005). Palladium was employed to catalyze the converting of 1,4-disilylation, (Ogoshi et al., 2002), and cleavage of the enoxysilane generated the *β*-dimethylsilyl ketone **19** as a single diastereomer which was taken through seven linear steps to obtain intermediate **20**. HSR was then carried out on **20** using tetrabutylammonium fluoride (TBAF) to induce an intramolecular cyclisation to obtain the key tetracycle **21** as a single diastereomer in 37% yield. The tetracycle **21** was taken through eight other linear steps to yield (–)-Acutumine, **14** (King et al., 2013).

2.3 Total synthesis of alotaketals and phorbaketals

Alotaketals and Phorbaketals are sesterterpenoid natural products that have been discovered in extracts of marine sponge species (Hubert et al., 2015; Joung et al., 2017; Shirley et al., 2018;



SCHEME 6
Total synthesis of Aburatubolactam A (**10**) (Bai et al., 2016).

Yao et al., 2020). Alotaketal A (**22**) (Scheme 8) was first isolated from a marine sponge *Hamigera sp* in Milne Bay, Papua New Guinea by Kieffer and Andersen in 2009 (Forestieri et al., 2009). To date, five Alotaketals (**A- E**) have been isolated from different other species. Alotaketals share the same tricyclic spiroketal backbone with Phorbaketals (**A- N**) which have had fourteen members isolated and structurally characterised using NMR spectroscopic techniques. Despite their structural similarity, they have different biological activity profiles. Alotaketal A (**22**) was found to increase protein kinase activity and also activate the cyclic adenosine monophosphate (cAMP) cell (*cAMP* is a derivative of adenosine triphosphate, i.e., ATP) signalling pathway in human embryonic kidney cells (HEK293T) (Beavo and Brunton, 2002; Forestieri et al., 2009). Phorbaketal (**23**) on the other hand is cytotoxic against human colorectal, hepatoma, and lung cancer cell lines (Daoust et al., 2013; Lee et al., 2014; Wang et al., 2016; Yao et al., 2020).

Yao et al., used TMSOTf as Lewis acid in catalysing the reaction between moiety **24** and **25** through an HSR to prepare a single diastereomer **26** in 75% yield (Scheme 8) (Yao et al., 2020). Yang completed the synthesis of (−)-Alotaketal A (**22**) in 30 steps with an overall yield of 2.6%. Alotaketals and Phorbaketal, i.e., Spiroketals of this nature have been very challenging to synthesise (Yao et al., 2020). Lee et al., accomplished the synthesis of (−)-Phorbaketal A (**23**) in 10 steps with a yield of 1.04% being the shortest linear sequence steps (Lee et al., 2014).

2.4 Synthesis of (+)-Amphidinolide P

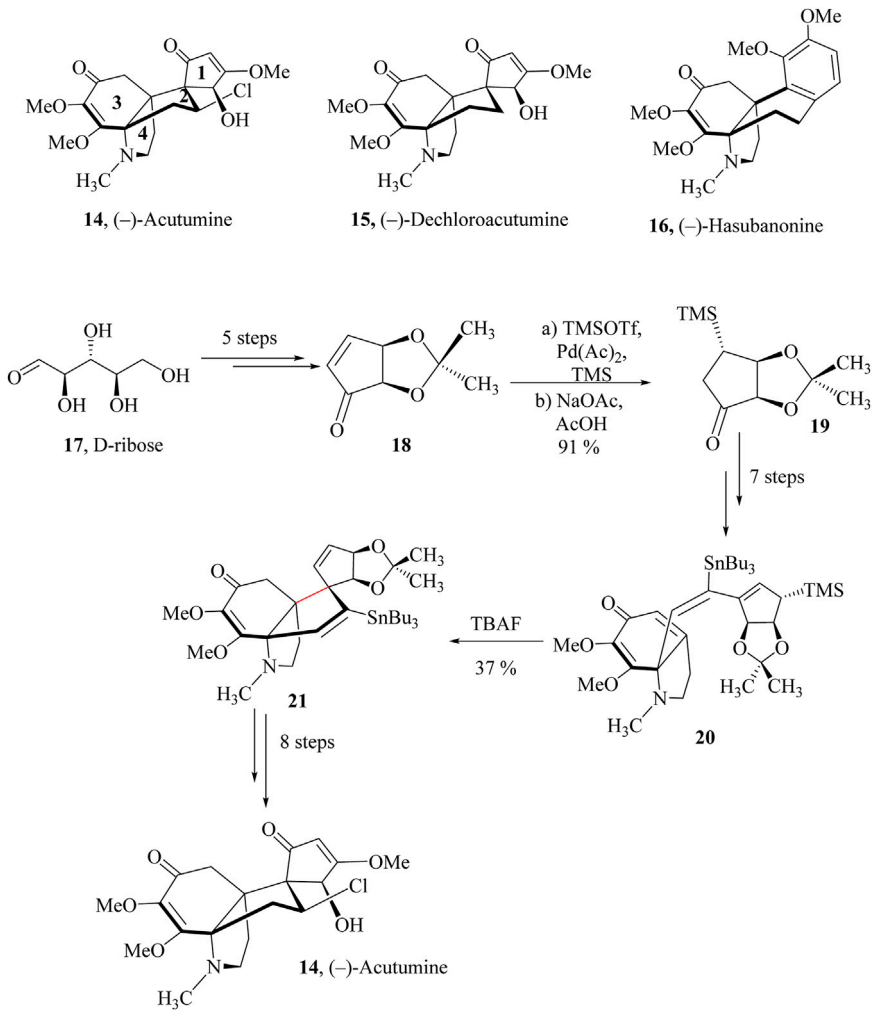
Amphidinolides are bioactive natural products isolated from marine dinoflagellates. Kobayashi and co-workers isolated the first amphidinolide A in 1986 (Ishibashi and Kobayashi, 1997; Kobayashi et al., 1986) and other amphidinolides including amphidinolides P **27** from a cultured diniflagellate *Amphidinium sp*. Amphidinolides are characterized by their unique 26-membered macrolide structure have shown antineoplastic activity against cancer cell lines and possess IC_{50} values in the low micromolar range (Heravi and Mohammadkhani, 2018).

Total synthesis of (−)-amphidinolide P, **27** was reported for the first time in 2000 by Williams and co-workers (Williams and Meyer, 2001). (+)-Amphidinolide P **27** was also prepared from a mixture of chiral precursors **29** and **30** starting from commercially available **28** (Williams et al., 2013). Aldehyde allylation with allylsilane **31** to achieve key intermediate **32** was achieved by adopting the HSR using boron trifluoride etherate as a catalyst Scheme 9 (Carreira and Joliton, 2015; Williams et al., 2013; Williams and Meyer, 2001). Traeatment of intermediate 62 through 7 steps reactions resulted in the formation of the Amphidinolides P (**27**).

2.5 Total synthesis of (±)-Aspidospermidine

(±)-Aspidospermidine (**32**) belongs to the Aspidosperma family of alkaloids (Du et al., 2017) which are made up of a pentacyclic ring system and five chiral centres. Members of this family of alkaloids possess antibiotic, anticancer, antimalarial and anti-inflammatory activities. However, the structural complexity of this class of compounds presents a challenge to successful asymmetric synthesis (Du et al., 2017; Ramirez and Garcia-Rubio, 2005).

The key intermediate in the synthetic route of (−)-Aspidospermidine **32** was first prepared by Stork and Dolfini (Stork and Dolfini, 1963). Sabot and co-workers used an alternative approach known as the "aromatic ring umpolung" which starts with polysubstituted phenol **33** which was converted to dienone **34** through HSR using allyltrimethylsilane and trifluoroethanol (TFE) or Hexafluoroisopropanol (HFIP) in the presence of $PhI(OAc)_2$ (Scheme 10). The entire total synthesis was completed in 10 steps starting from phenol **33** to give the overall yield of 5.4% (Sabot et al., 2009).



SCHEME 7
Total synthesis of (–)-Acutumine, **45** (King et al., 2013).

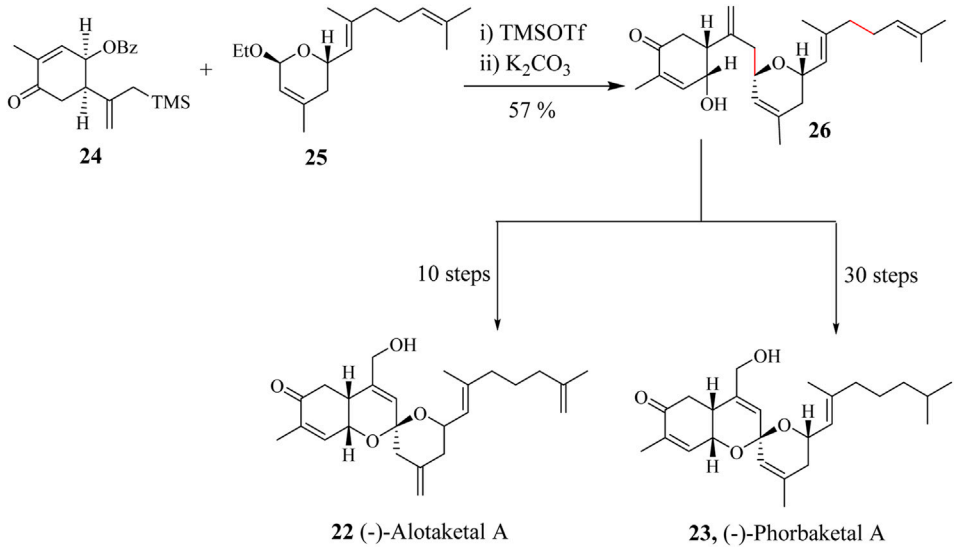
2.6 Total synthesis of Cephalotaxus diterpenoids: Cephinoid P, Cephafortoid A, 14-epi-Cephafortoid A and Fortalpinoids M-N, P

Cephalotaxus diterpenoids are structurally diverse diterpenoids. In 2016, Yue and co-workers isolated this family of compounds from *Cephalotaxus* species (Fan et al., 2017; Shao et al., 2024). This family of natural products showed potential anticancer properties. The intriguing and challenging structure of these compounds was established using X-ray crystallography techniques. Gao and coworkers have recently reported the first asymmetric total synthesis of these natural products and subgroups such as Cephinoid P (**36**), Cephafortoid A (**37**), 14-*Epi*-cephafortoid A (**38**) and Fortalpinoids M (**39**), N (**40**) and P (**41**) from the precursor (S)-trimethyl (4-methyl-2-methylenehex-5-yn-1-yl) silane (Wang et al., 2023).

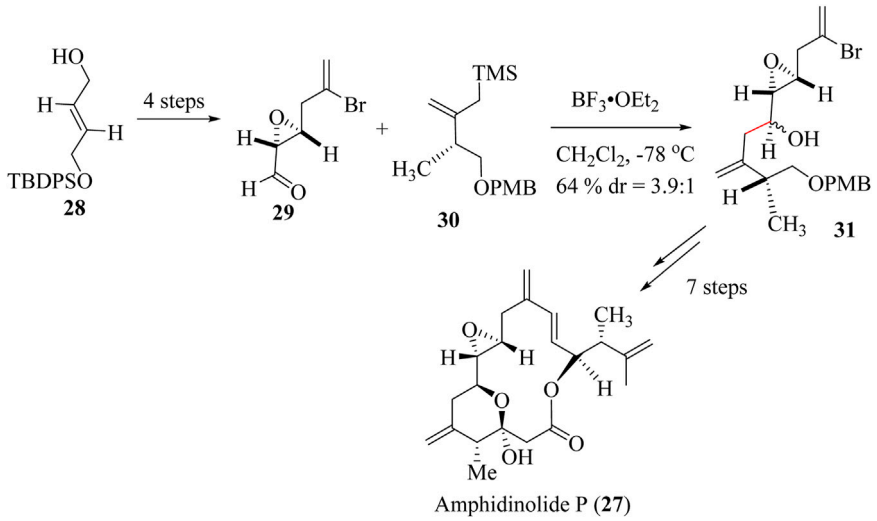
A universal strategy for the total synthesis of Cephalotaxus diterpenoids bearing unique cycloheptene A rings with chiral methyl groups was adopted. The 7-5-6 tricycle rings of the Cephalotaxus diterpenoids were obtained from the dicobalt hexacarbonyl-propargylic alcohol complex (Scheme 20). An intramolecular Nicholas/Hosomi-Sakurai cascade reaction was developed to form the cycloheptene A-ring bearing a chiral methyl group (Scheme 11). The Pauson-Khand reaction was then used to complete the skeleton of the target molecules. The asymmetric total syntheses of Cephinoid P (**36**), Cephafortoid A (**37**), 14-*Epi*-cephafortoid A (**38**) and Fortalpinoids M (**39**), N (**40**) and P (**41**) were successfully achieved over 15–18 steps from compound **42**. The proposed strategy presents a novel approach for the total synthesis of Cephalotaxus diterpenoids and structurally related akin polycyclic natural products (Wang et al., 2023).

2.7 Total Synthesis of Dehaloperophoramidine and (+)-Perophoramidine

Naturally occurring (+)-Perophoramidine **44** was isolated from marine ascidian *Perophora namei* by Ireland and co-workers in the Philippine ascidian organism, *P. namei* (Verbitski et al., 2002). Dehalogenated product Dehaloperophoramidine **44** was obtained



SCHEME 8
Total synthesis of (–)-Alotaketal A (**22**) and (–)-Phorbaketal A (**23**) involving HSR protocol (Yao et al., 2020).



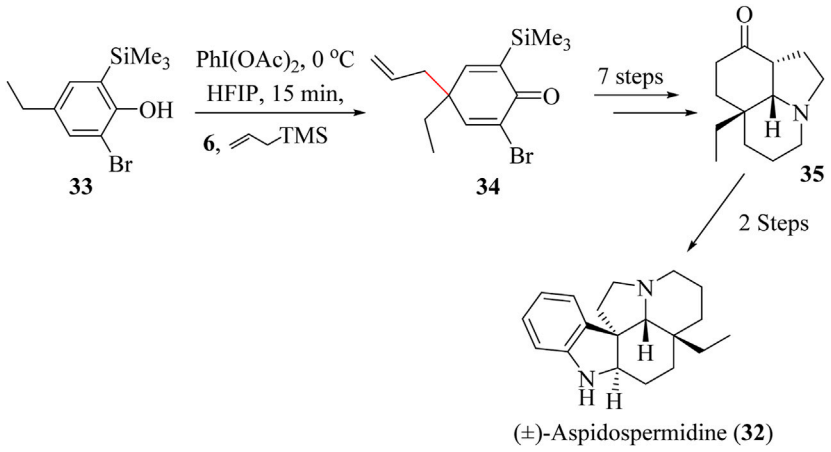
SCHEME 9
Total synthesis of Amphidinolides P (**27**) (Carreira and Joliton, 2015).

from the hydrogenation of (+)-Perophoramidine **45**. The two compounds, **44** and **45** bear a structural resemblance to a complex family of natural products called communesin alkaloids (Communesin F, **46**) (Trost and Osipov, 2015; Wilkie et al., 2016; Zuo and Ma, 2011). They both possess complex chemistry of quaternary chiral centres that makes them synthetically challenging. (+)-Perophoramidine **45** has been reported to possess anticancer activity and this has drawn the synthetic chemist's attention to them.

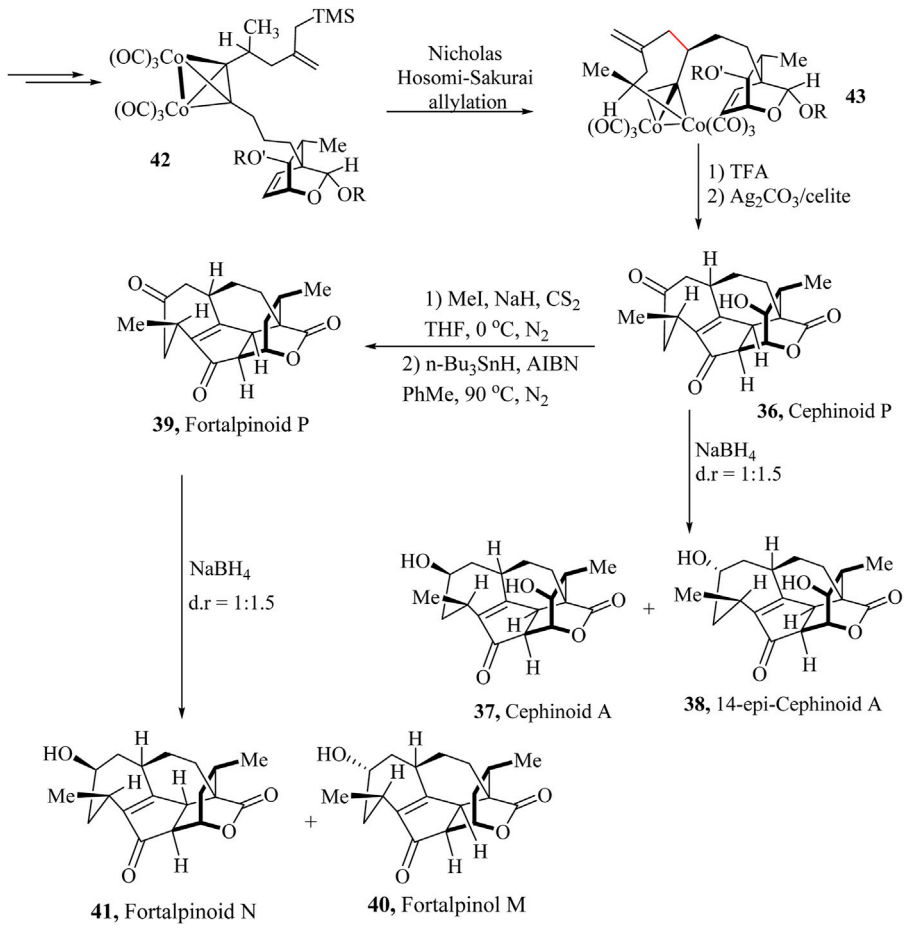
Synthesis of Dehaloperophoramidine **44** started with the reaction of commercially available **47** and **48** to make intermediate **49**, which was taken through seven steps to yield **50**. Key intermediate **51** was treated with allyltrimethylsilane in the presence of $TiCl_4$ to give **52** which was taken through 12 extra steps to achieve Dehaloperophoramidine **44** (Scheme 12) (Wilkie et al., 2016).

2.8 Total synthesis of deoxopinguisone

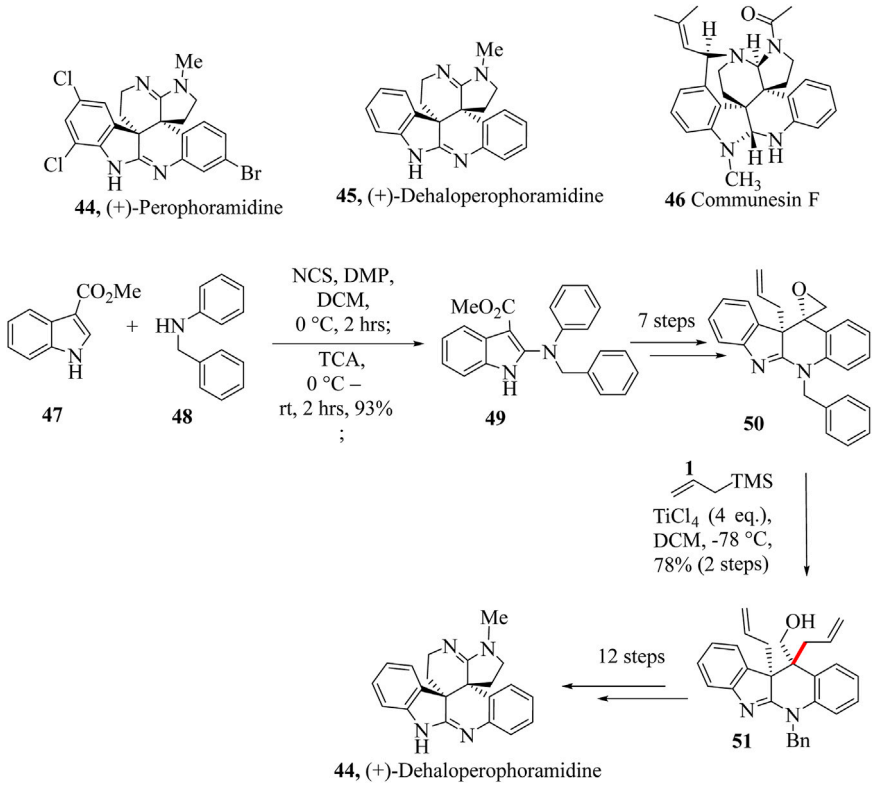
Deoxopinguisone (**52**) is a type of Pinguisanes (sesquiterpenes) that occurs naturally in liverworts (Asakawa et al., 2013). Pinguisanes was first isolated and characterised successfully using spectroscopic techniques by Krutov and co-workers in 1972 (Krutov et al., 1973; Uyehara et al., 1985). The distinctive feature of this compound is its spatial configuration of the four methyl group



SCHEME 10
Total synthesis of (±)-Aspidospermidine (**32**) (Stork and Dolfini, 1963).



SCHEME 11
Total asymmetric total synthesis of Cephalotaxus diterpenoids: Cephinoid P, Cephafortoid A, 14-*epi*-cephafortoid A and Fortalpinoids M, N, (Wang et al., 2023).



SCHEME 12
Total synthesis of (+)-Dehaloperophoramidine **51** (Wilkie et al., 2016).

substituents. These methyl groups are specifically oriented in a *β*-configuration in the molecular framework.

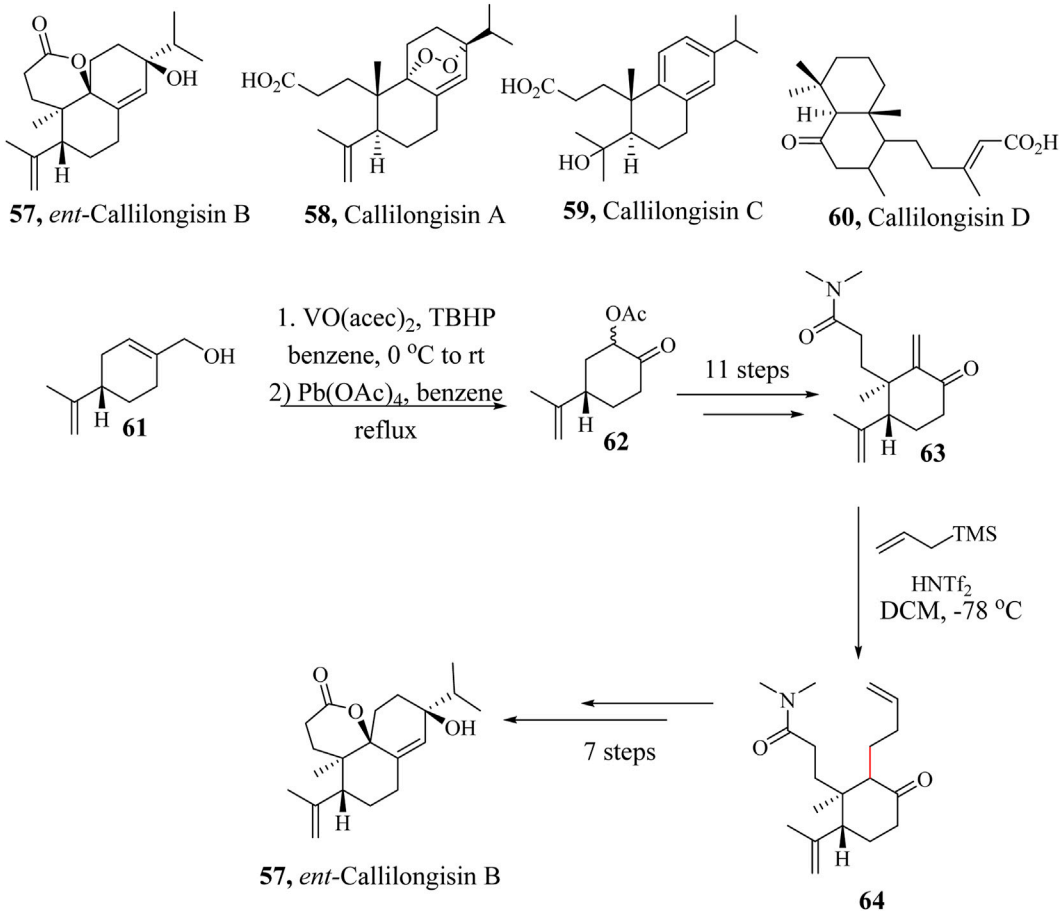
Formation of the C4–C9 bond was facilitated by the HSR to give a *cis* stereochemistry between C8 and C9 since the *cis* hindrance system is more stable in solution compared to the *trans*-derivative. The synthesis started with commercially available ketone **53** which was taken through seven sequential steps to obtain intermediate **54** (Supplementary Scheme S9). This intermediate **54** was oxidized with pyridinium dichromate and tert-butylhydroperoxide to obtain the enone intermediate **55** which was subjected to Hosomi-Sakurai cyclisation (HSC) in dry TBAF that led to the concomitant cleavage of the C-Si bond to form intermediate **55**. The HSC of **55** favoured only the formation of the desired *cis* isomer **56** as shown in Supplementary Scheme S9 below (Tori et al., 2001).

From Supplementary Scheme S10, Dthe conformation of the *cis*-isomer shows that the *β*-position from the enone is near the allylic proton that is in the *γ*-position from the TMS group. Also, *cis* -isomer of cyclohexanone is favoured due to steric hindrance (Supplementary Scheme S10) (Tori et al., 2001). The intramolecular cyclisation was accomplished by the HSR in dry TBAF as a catalyst in THF as a solvent to yield 99% compound **56**, but **56** was not formed through the *trans* conformation due to steric hindrance as shown (Supplementary Scheme S10) in the intermediate (Tori et al., 2001). Conversion of intermediate **55** to the final product Deoxopinguisone, **52** was accomplished by Uyehara and coworkers (Uyehara et al., 1985; 1986).

2.9 Total synthesis of Ent-Callilongisin B

Ent-Callilogisin B (**57**) was isolated from the leaves of *Callicarpa longissima*, along with related compounds, Callilongisin A (**58**), C (**59**), and D (60). *Ent*-Callilongisin B (**59**) is an analogue of 3,4-seco-abietane-type diterpenoid whose structure was established using NMR spectroscopic techniques (Liu et al., 2012). The natural product **57** demonstrated cytotoxic activities against a human prostate cancer cell line. An anti-inflammatory activity of **57** was also observed when tested for superoxide anion production from human neutrophil cells (Kamiya et al., 2021).

In 2021, the first asymmetric total synthesis of tricyclic diterpenoid *Ent*-callilongisin B (**57**) was reported by Kamiya et al. (2021). The synthesis started with the Sharpless oxidation of enantiomerically pure (*S*)-perillyl alcohol **61**, to form acetoxy ketone **62** (Indictor and Brill, 1965; Sharpless and Michaelson, 1973; Tanaka et al., 1974). The synthesis was accomplished following stereo-controlled Michael 1,4-addition and Hosomi–Sakurai allylation of enone **63**, followed by Wacker oxidation, and intramolecular aldol reaction of diketone to construct the six-membered ring and oxidative dearomatisation of phenol intermediate accompanied by diastereoselective δ-lactonisation (Scheme 13). The same research group is also developing enantioselective synthetic methods for other Callilongisin analogues A (**58**), C (**59**) and D (**60**) (Kamiya et al., 2022).



SCHEME 13
Total synthesis of *Ent*-callilongisin B (**57**) (Kamiya et al., 2021).

2.10 Total synthesis of eribulin mesylate

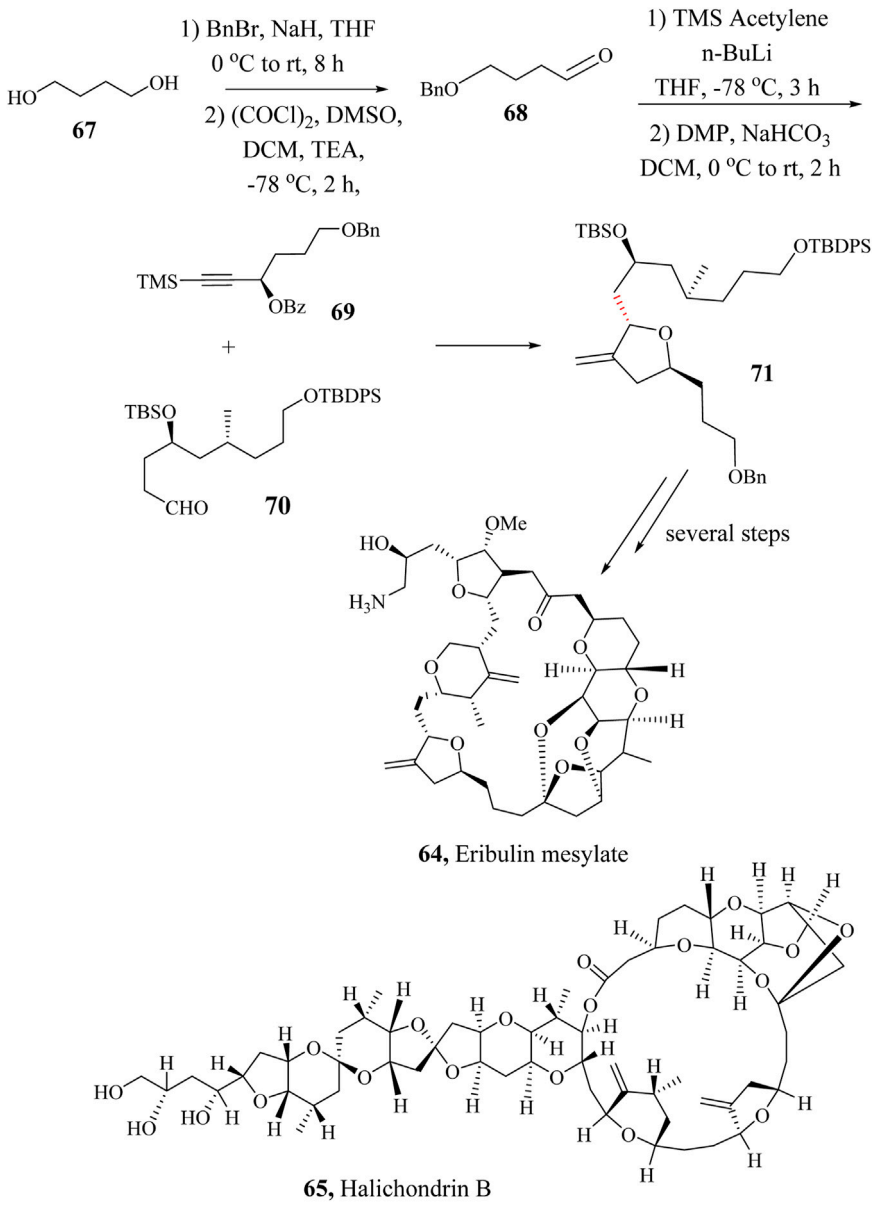
Eribulin mesylate (**65**) is an anticancer drug made from halichondrin B (**66**), a natural marine polyether macrolide product (Ortega and Cortés, 2012; Paterson et al., 2011). In 1986, halichondrin B was first isolated from the marine sponge *Halichondrin okadai* by Uemura and co-workers (Kulkarni et al., 2016). Further studies on the structure of halichondrin B led to the discovery of the analogue known as Eribulin mesylate (**65**) with improved anticancer activity against metastatic cancer cell lines. In 1997, Eisai Pharmaceutical Company in collaboration with Kishi et al., reported the total synthesis of the drug in an industrial viable way (Fang et al., 1992; Lee et al., 2016; Li et al., 2018; Stamos et al., 1997).

Currently, Pabbaraja et al., reported a more economical, and industrially scalable, approach toward the easy production of the drug (Nasam and Pabbaraja, 2024). The modified stereoselective synthetic approach to the preparation of Eribulin mesylate (**65**) involved the use of commercially available 1,4-butanediol (**67**) to generate key intermediate **68** which was coupled with intermediate **69** in HSR to achieve the key intermediate **70**. The total synthesis of Eribulin mesylate was accomplished by taking the intermediate **70** through several steps (Scheme 14) (Nasam and Pabbaraja, 2024).

2.11 Total synthesis of (–)-Galiellalactone

(–)-Galiellalactone **72**, (Scheme 15), a fungal metabolite was originally isolated from ascomycete *Galiella rufa* in 1990 (Johansson and Sterner, 2001; Kim et al., 2015). It has been found to possess inhibitory properties against STAT3 (signal transducer and activator of transcription 3) that block the DNA binding of phosphorylated STAT3 without inhibiting phosphorylation and dimerization (Don-Doncow et al., 2014). (–)-Galiellalactone also induces the apoptosis and growth inhibition of human prostate cancer cells. Sterner and co-workers were the first to report the synthesis of the (–)-Galiellalactone and confirmed its stereochemistry unambiguously (Johansson and Sterner, 2001).

Kim et al also used a modified Hosomi–Sakurai crotylation method (Hosomi and Sakurai, 1977; Shing and Li, 1997) to diastereoselectively introduce the C9 side chain with the required terminal alkene for ring closure metathesis. The intermediate **73** was reacted with (*E*)-crotyltrimethylsilane and $BF_3{\cdot}Et_2O$ as the promoter to yield compounds **74** and **75** in 88% yield in favour of the undesired **75**. However, when the catalyst was changed to $TiCl_4$, the yields dropped to 78% but favoured compound **74** to give a dr of 5:1 (Scheme 15). Further, intermolecular cyclisation of the **75** resulted in the formation of the product with the exact configuration (Kim et al., 2015).

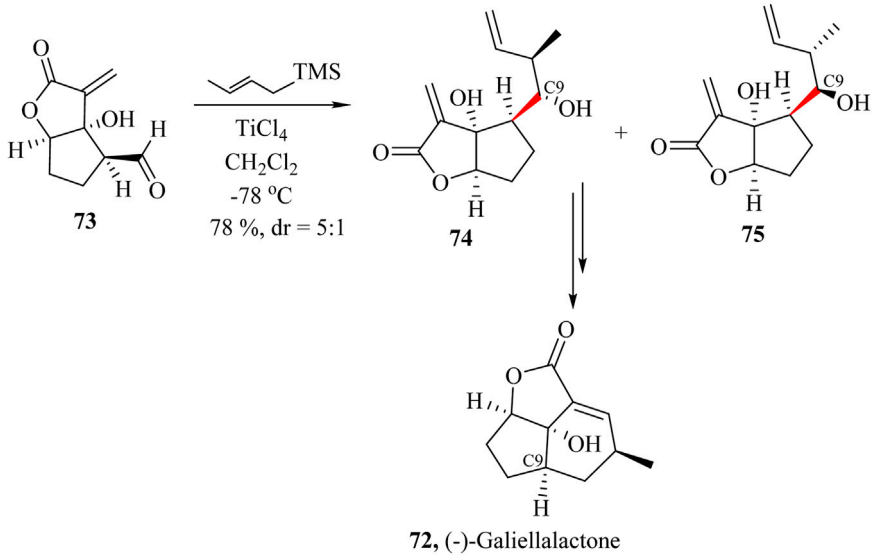


SCHEME 14
Total synthesis of Eribulin mesylate, **64** (Nasam and Pabbaraja, 2024).

2.12 Total syntheses of grayanane diterpenoids: (–)-grayanotoxin III, (+)-Principinol E, and (–)-Rhodomollein XX

Grayanane diterpenoids are naturally occurring secondary metabolites exclusively found in flowering plants of the Ericaceae family (Li et al., 2019) with over 4,000 species (Liu et al., 2024). In addition to grayanane diterpenoids (Cai et al., 2018; Ho and Lin, 1995; Lv et al., 2017; Zhou et al., 2012), Ericaceae plants contain other types of terpenoids, including triterpenoids (Teng et al., 2018; Zhang et al., 2018; Zhao et al., 2018) and meroterpenoids (Huang et al., 2018; Liao et al., 2015; Liao et al., 2017). These compounds feature a distinctive tetracyclic backbone system with an intricate 5/7/6/5 configuration, contributing to their complexity and diversity (Huang et al., 2005; Wang et al., 1998). This family of compounds exhibits various properties, including analgesic, antinociceptive, anticancer, antiviral, antifeedant, insecticidal effects, as well as toxicity and inhibition of protein tyrosine phosphatase 1B (PTP1B) (Li et al., 2019; Liu et al., 2024).

Grayanotoxins were isolated from the leaves of *Leucothoe grayana*, a poisonous shrub native to Japan, between 1930 and 1960 (Kakisawa et al., 1961; Kong et al., 2023) but the stereochemistry at the ring junction was only ambiguously determined in 1970 using X-ray crystallography by Narayanan and coworkers (Narayanan et al., 1970). Grayanotoxins are known to be toxic to both humans and animals, acting by modulating voltage-gated sodium channels. This mechanism accounts for their poisoning effects as well as their analgesic properties. Grayanotoxin III, **76** is the alkaline hydrolysed derivative of Grayanotoxin I, which naturally occurs in *L. grayana* (Kakisawa et al., 1961). Principinol E, **77** was isolated from the aerial parts of *Rhododendron principis* and exhibited significant *in vitro* inhibitory



SCHEME 15
Total synthesis of (−)-Galiellalactone (**72**) (Kim et al., 2015).

activity against PTP1B with an IC_{50} value of 3.14 ± 0.12 μM (Liu et al., 2014; Z. R; Zhang et al., 2012). Rhodomollein XX, **78** was isolated from fruits of *Rhododendron mole* (Li et al., 2000; Zhou et al., 2014) and exhibited moderate antinociceptive activity (Li et al., 2019).

The total synthesis of **76**, **77**, and **78** began with the synthesis of the key intermediate **80** from **79**. The intermediate **81** was prepared by the asymmetric 1,4-conjugated addition developed by May and co-workers (May et al., 2011) and was treated with TMSOTf in the presence of **83** to foster an intramolecular Mukaiyama aldol reaction followed by the addition of $EtAlCl_2$ which mediated the HSR to produce **82** in 62% yield (1.7:1 dr) in a one-pot. A total of 18, 19 or 20 and 18 synthetic steps were followed to obtain (−)-Grayanotoxin III, **76**, (+)-Principinol E, **77** and (−)-Rhodomollein XX, **78** (Scheme 16) (Kong et al., 2022; 2023).

2.13 Total synthesis of Heliespirone A and C

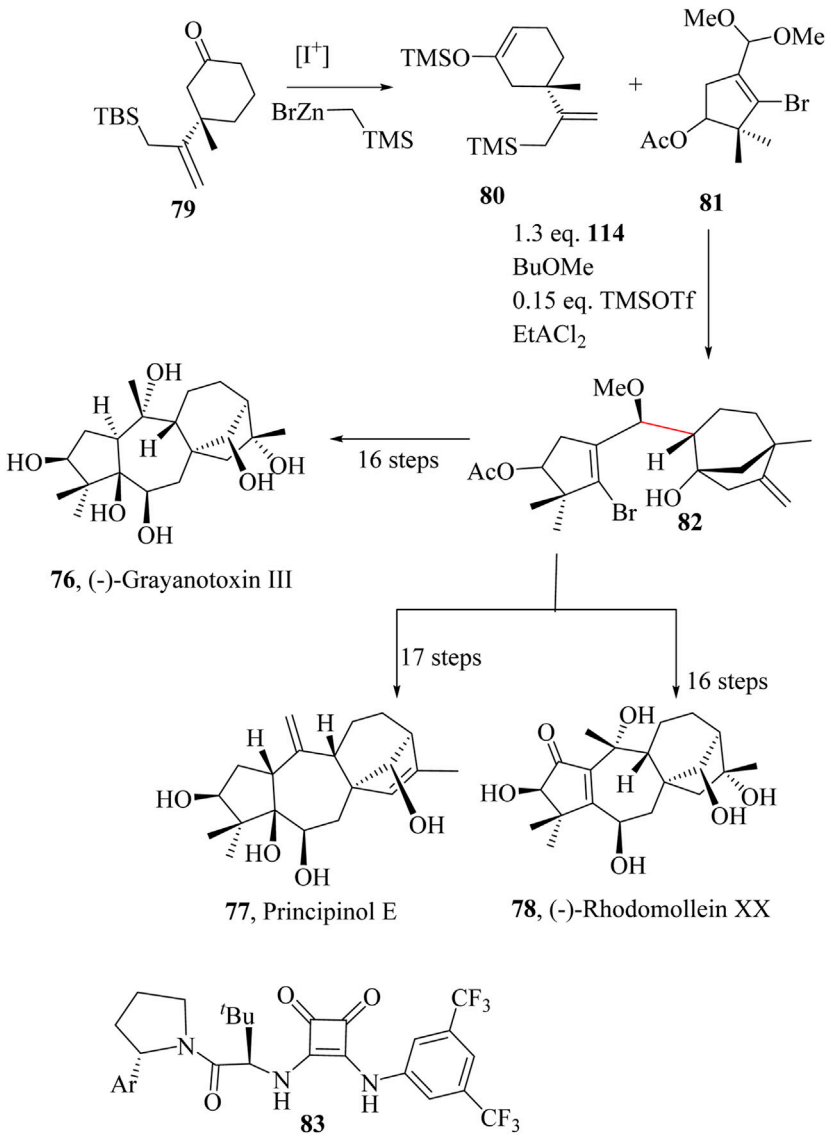
Heliespirone A (**84**) is a member of a sesquiterpene group of alkaloids that was isolated from cultivar sunflowers, i.e., *Helianthus annuus L.* by Huang et al. (2011). Heliespirone C (**85**) was isolated in the later part of 2006 and reported with six- and five-membered oxaspirocyclic skeletons, respectively (Huang and Liu, 2010). Heliespirone A (**84**) is anticipated to have a significant impact on the allelopathic action of cultivar sunflowers. Heliespirone C (**85**) demonstrated an inhibitory activity in coleoptile bioassay. Due to their intriguing structural features, biological profiles, and limited availability, these natural products present appealing targets for total synthesis (Huang and Liu, 2010).

Miyawaki et al., in 2012 reported the total synthesis of (−)-Heliespirone A (**84**) and (+)-Heliespirone C (**85**) (Miyawaki et al., 2012). A combination of several synthetic approaches including the HSR was carried out to introduce two stereogenic centers at C-8 and C-10 (Scheme 17). Intramolecular allylation of substrate **86** which had an allylsilane and *p*-benzoquinone substituents was accomplished using *tert*-butyldimethylsilyl trifluoromethanesulfonate (TBSOTf) as a catalyst in isobutyronitrile (Me_2CHCN) to give a mixture of **87** and **88** in 68% with 8:1 dr. The excellent stereoselectivity in this transformation could be attributed to the preference for transition state **T1** over **T2**. This is due to the stereoelectronically favourable antiperiplanar conformation of **T1**, as well as the steric repulsion between the allylsilane and the benzoquinone groups in **T2** as shown in Scheme 17. Intermediate **88** was taken through 4 linear steps to achieve the two diastereoisomers (±)-Heliespirones A, **84** and C, **85** (Miyawaki et al., 2012).

2.14 Total synthesis of Herboxidiene/GEX1A

Herboxidiene *GEX1A* (**89**) a potent phytotoxic polyketide was isolated from *Streptomyces chromofuscus* A7847 by Isaac and co-workers in 1992 (Isaac et al., 1992; Thirupathi and Mohapatra, 2016). Yoshida *et al.* also isolated six polyketide analogues [series (GEX1)] from *Streptomyces sp*, in 2002 (Miyawaki et al., 2012; Sakai et al., 2002; Yun and Panek, 2007). The compound exhibited selective phytotoxicity against a range of broadleaf annual weeds but harmless to wheat (Blakemore, 2002; Sakai et al., 2002). Herboxidiene/*GEX1A* (**89**) is also able to induce GAP1 and GAP2/mitosis (G1 and G2/M) cell cycle arrest in human tumour cell line WI-38 (Ghosh and Li, 2011). It also binds to SAP155, the protein responsible for the pre-mRNA splicing thereby acting as a novel slicing inhibitor (Thirupathi and Mohapatra, 2016).

The first total synthesis attempts of herboxidiene/*GEX1A*, **89** was in 1999 by Kocienski and co-workers using direct aldol reaction, Ireland-Claisen rearrangement, and hydroxy-directed epoxidation. The structural complexity of herboxidiene/*GEX1A* (**89**) comprising the presence of nine chiral centres, trisubstituted tetrahydropyran core, and conjugated diene side chain has made its synthesis particularly challenging (Smith et al., 1996). Mohapatra and

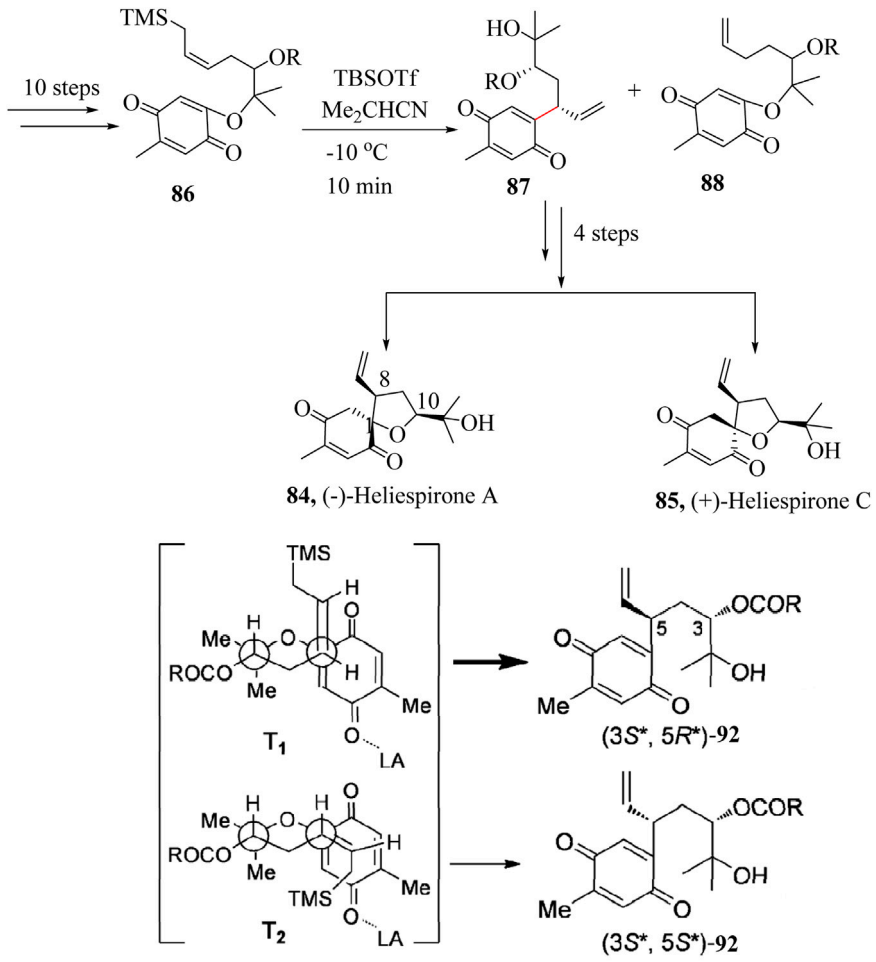


SCHEME 16
Total syntheses of Grayanane Diterpenoids: (–)-Grayanotoxin III (**76**), (+)-Principinol E (**77**), and (–)-Rhodomollein (**78**) (Kong et al., 2022; 2023).

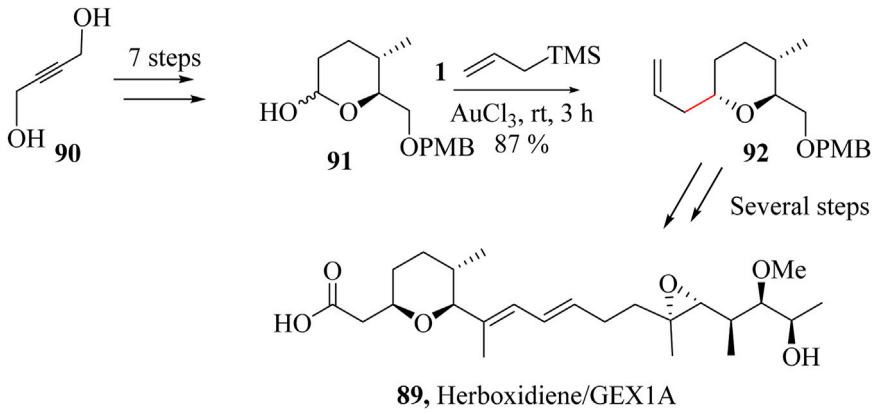
Thirupathi reported a 22 linear sequence steps toward the synthesis of herboxidiene/*GEX1A* (**89**) (Thirupathi and Mohapatra, 2016). HSR was used to couple lactol **90** which was achieved in 7 steps from 2-butyne-1,4-diol (**91**), with allyltrimethylsilane and $AuCl_3$ as a diastereoselective allylation catalyst previously developed for cyclic hemiacetals as shown in Scheme 18. Compound **92** was the key intermediate needed to synthesize Herboxidiene **89** (Thirupathi and Mohapatra, 2016).

2.15 Total synthesis of Huperserratines A and B

Lycopodium alkaloids are a large group of natural products with unique heterocyclic frameworks found in the Lycopodiaceae family. Following the isolation of lycopodine by Bödeker (1881), Harrison et al. (1961), Wada et al. (2019), more than 300 *Lycopodium* alkaloids have been isolated, and their structures established using various spectroscopic techniques including X-ray crystallography (Ma and Gang, 2004; Siengalewicz et al., 2013). These compounds exhibit distinguishable polyfused-bridged structures and demonstrate remarkable biological activities. For instance, Huperzine A, a lycodine-type lycopodium alkaloid isolated from *Huperzia serrata*, is a highly specific and potent inhibitor of AChE (Xing et al., 2014). It is also found to be effective in the treatment of Alzheimer's disease (AD) in China, and used as a dietary supplement in the United States (Liu et al., 1986; Xu et al., 1999). In 2020, ZhaO and co-workers isolated two *Lycopodium* alkaloids Huperserratines A (**93**) and B (**94**), from *H. serrata* (Wu et al., 2020). The absolute configurations of these compounds were determined using single-crystal X-ray diffraction. The compounds were the first reported macrocyclic lycopodium alkaloids with a 5-azabicyclo [10.4.0]hexadecane structure. They were also the second and third examples of



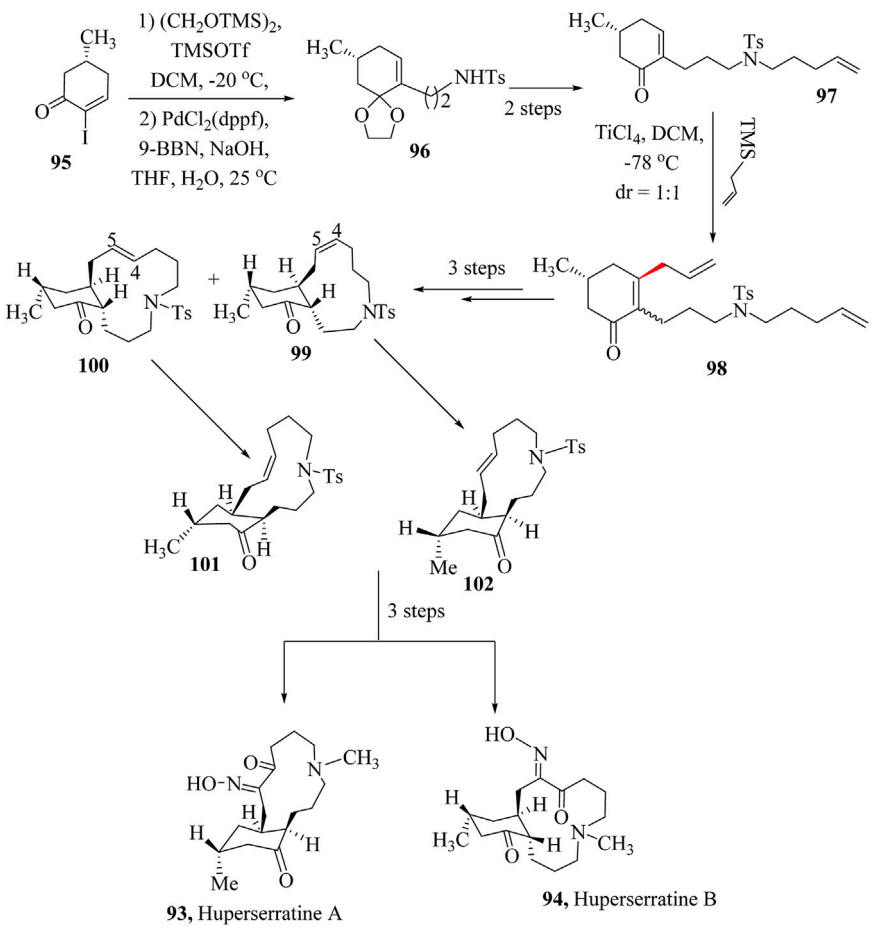
SCHEME 17
Total synthesis of (–)-Heliespirone A and C (Miyawaki et al., 2012).



SCHEME 18
Total synthesis of Herboxidiene *GEX1A*, **89** (Thirupathi and Mohapatra, 2016).

lycopodium alkaloids containing an oxime group in the molecule. In addition, Huperserratine A (**93**) showed moderate anti-HIV-1 activity with an EC_{50} value of 52.91 μg mL^{-1} (Deng et al., 2022).

ZhaO and co-workers reported the first total synthesis of Huperserratines A (**93**) and B (**94**) through a 12-step sequence including Suzuki-Miyaura coupling, the HSR, the ring-closing



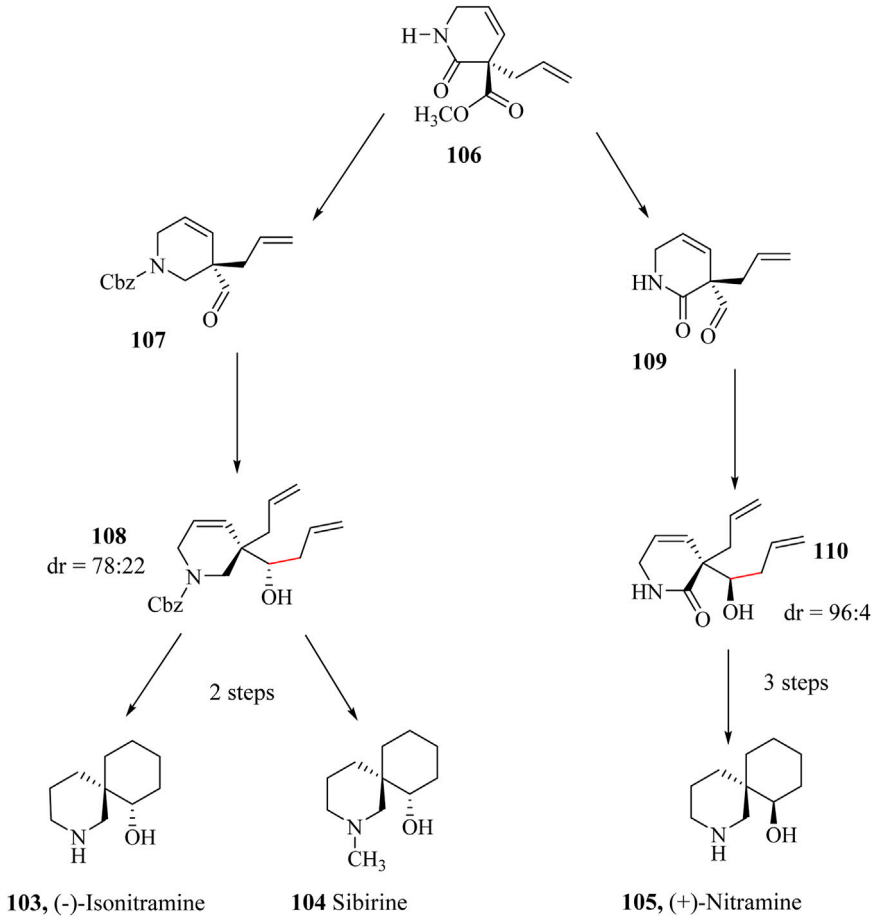
SCHEME 19
Total synthesis of Huperserratine A (**93**) and B (**94**) (Deng et al., 2022).

metathesis, the dihydroxylation, and Swern oxidation (Scheme 19) (Zhao et al., 2021). The synthesis of Huperserratines A (**93**) and B (**94**) started with (*5R*)-2-iodo-5-methyl-2-cyclohexen-1-one (**95**), which was transformed into the intermediate, **96** by a Pd-catalysed Suzuki–Miyaura reaction followed by modification through *N*-alkylation to obtain compound **97**. The 1,4-addition was completed using a $TiCl_4$-catalyzed HSR of enone **98** with allyltrimethylsilane, yielding 3,5-*trans*-cyclohexanone **99**. Epimerization at the α-position of the ketone occurred under these conditions, resulting in a 1:1 mixture of diastereomers. After three steps, diastereomers **101** and **102** were produced, respectively. After the preparation of the oxime followed by deprotection to give Huperserratines A (**93**) and B (**94**) (Deng et al., 2022; Wu et al., 2020).

2.16 Total syntheses of (±)-Isonitramine, (–)-Sibirine, and (+)-Nitramine

(±)-Isonitramine (**103**), (–)-Sibirine (**104**), and (+)-Nitramine (**105**), are spiropiperidine class of alkaloids possessing chiral quaternary carbon centres on their 2-azaspiro [5,5]undecane-7-ol core and were all isolated from *Nitraria sibrica* and *N. Schoberi* (Manske, 1960; Pandey et al., 2011). The three compounds demonstrated good biological activities against the proliferation of cancer cell lines (Boubaker et al., 2011).

The total synthesis of these alkaloids has been reported although targeted products are obtained as racemic mixtures (Westermann et al., 1993). These molecules appear simple but are challenging to synthesise due to their contiguous chiral centres. The total synthesis of (–)-Isonitramine (**103**) and (–)-Sibirine (**104**) started with the pure enantiomer **106** (Scheme 20). The ester group on **107** was reduced to an alcohol using $LiAlH_4$ followed by protection of the amine group using benzyl chloroformate in dioxane/water and subsequent oxidation to yield intermediate **108**. An allylation of intermediate **108** with allyltrimethylsilane in the presence of $BF_3{\cdot}Et_2O$ was accomplished via the HSR to give the key intermediate **109** in 92% with 78:22 diastereoselectivity. Synthesis of (+)-Nitramine (**105**) started with the conversion of the ester group of enantiopure **106** to aldehyde **109** which was treated with allyltrimethylsilane in the presence of $SnCl_4$ to yield intermediate **110** in 87% with diastereoselectivity of 96:4. The intermediates **108** and **110** were each taken through 2 and 3 steps independently to yield 42%, 38%, and 25% for (–)-Isonitramine (**103**), (–)-Sibirine (**104**), and (+)-Nitramine (**105**), respectively (Pandey et al., 2011; Yang et al., 2021).



SCHEME 20
Application of HSR total synthesis of (–)-Isonitramine (**103**), (–)-Sibirine (**104**), and (+)-Nitramine (**105**) (Pandey et al., 2011).

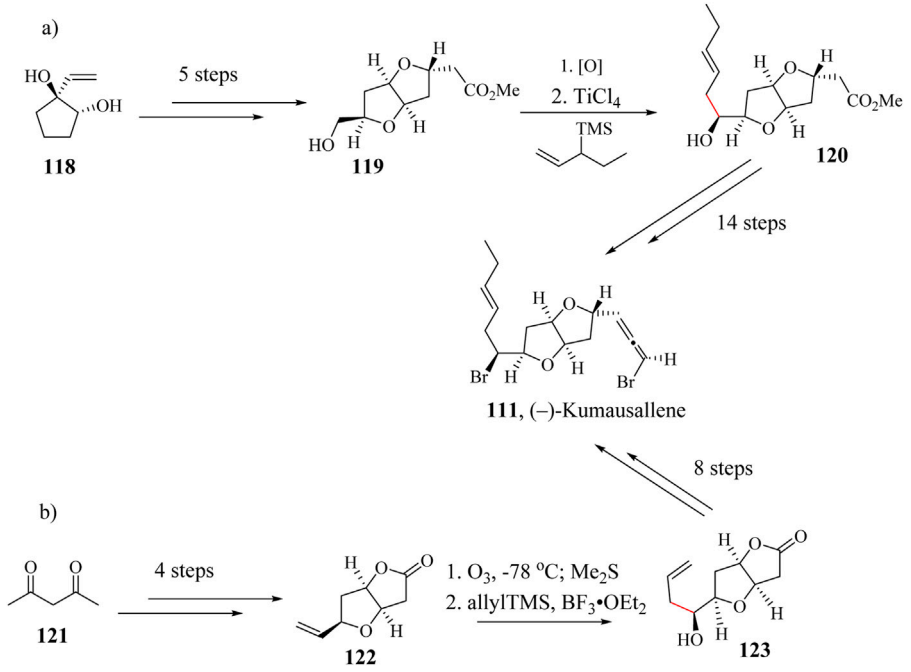
2.17 Total synthesis of (–)-Kumausallene

(–)-Kumausallene, **111** is sesquiterpene secondary metabolite belonging to a family of non-isoprenoids with a unique bromoallene or enyne moiety and also containing a dioxa-bicyclo [3.3.0] octane core (Das and Ramana, 2015; Hoffmann-Röder and Krause, 2004). Kurosawa *et* al first reported the isolation of (–)-Kumausallene, **111** from red algae *Laurencia Nipponica* Yamada collected at Kumausu, near Otaru, Hokkaido, Japan (Evans et al., 1999; Suzuki et al., 1983). Other members of the enyne containing compounds with dioxa-bicyclo [3.3.0] octane core shown in Supplementary Figure S2 include (+)-Panacene, **112** (Boukouvalas et al., 2006; Feldman, 1982; Feldman et al., 1982) and (–)-Aplysiallene, **113** (Wang and Pagenkopf, 2007); the eight- and nine-membered cyclic ethers (+)-Laurallene, **114** (Crimmins et al., 2010; Saitoh et al., 2003), (+)-Isolaurallene, **115** (Crimmins et al., 2002; Crimmins and Emmitte, 2001) (+)-Itomanallene A, **116** (Jeong et al., 2010) and (+)-Microcladallene B, **117** (Park et al., 2007).

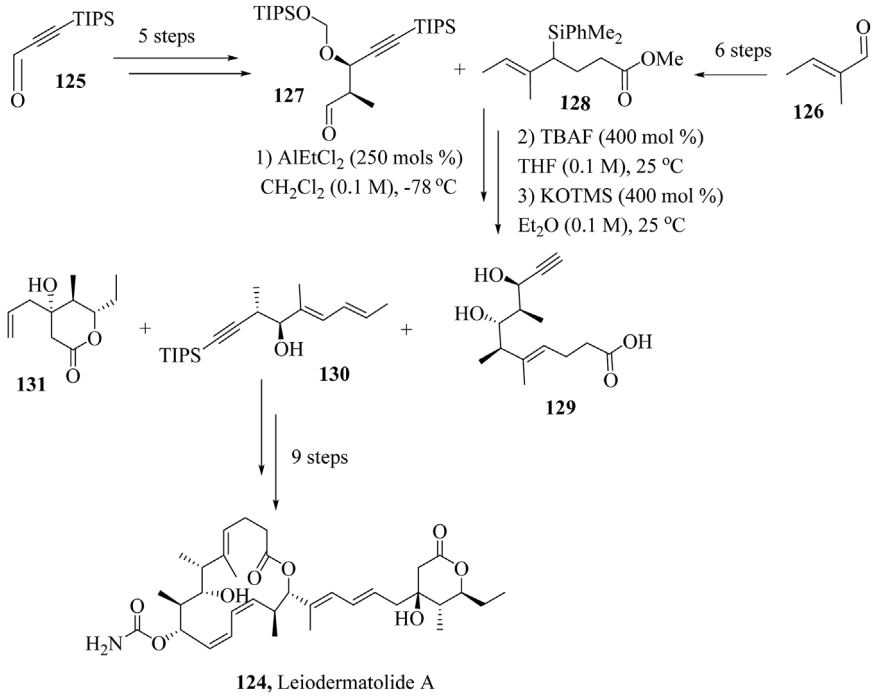
The first total synthesis of (±)-Kumausallene (**111**) was reported by Overman and his group using a ring annulation strategy (Brown et al., 1991; Grese et al., 1993). It has also been enantioselectively synthesized by Evans et al., using an acyl radical cyclization to construct the tetrahydrofuran ring followed by an efficient biomimetic strategy (Evans et al., 1999). Several other successful syntheses of (±)-Kumausallene (**111**) has been reported in literature (Grese et al., 1993; Werness and Tang, 2011). In their 20 steps synthetic attempt, Werness et al oxidized hydroxyl ester intermediate **119** which was synthesized through 5 steps starting from compound **118** to the corresponding aldehyde and subsequently installed the pentenyl side chain through (Werness et al., 2013; Werness and Tang, 2011). The final product (–)-Kumausallene was achieved after 14 sequential steps as shown in Scheme 21a. Tang *et al.*, used $BF_3{\cdot}OEt_2$ as a Lewis acid in a HSR after the ozonolysis of compound **122** which was synthesized in four steps from acetylacetone **151** to generate pentene linker with the right stereochemistry (Scheme 21b). The HSR proceeded with a diastereoselectivity of a 4:1 ratio favoring the desired stereoisomer. Compound **123** was taken through 8 extra steps to give the title compound in 5.4% yield (Werness and Tang, 2011).

2.18 Total synthesis of Leiodermatolide A

Leiodermatolide A, **124** is a 16-membered polyketide macrolide skeleton, featuring an unsaturated side chain terminating in a δ-lactone. It was isolated in 2008 from marine invertebrate sponge lithistid *Leiodermatium Sp.* in Florida (Paterson et al., 2011). It



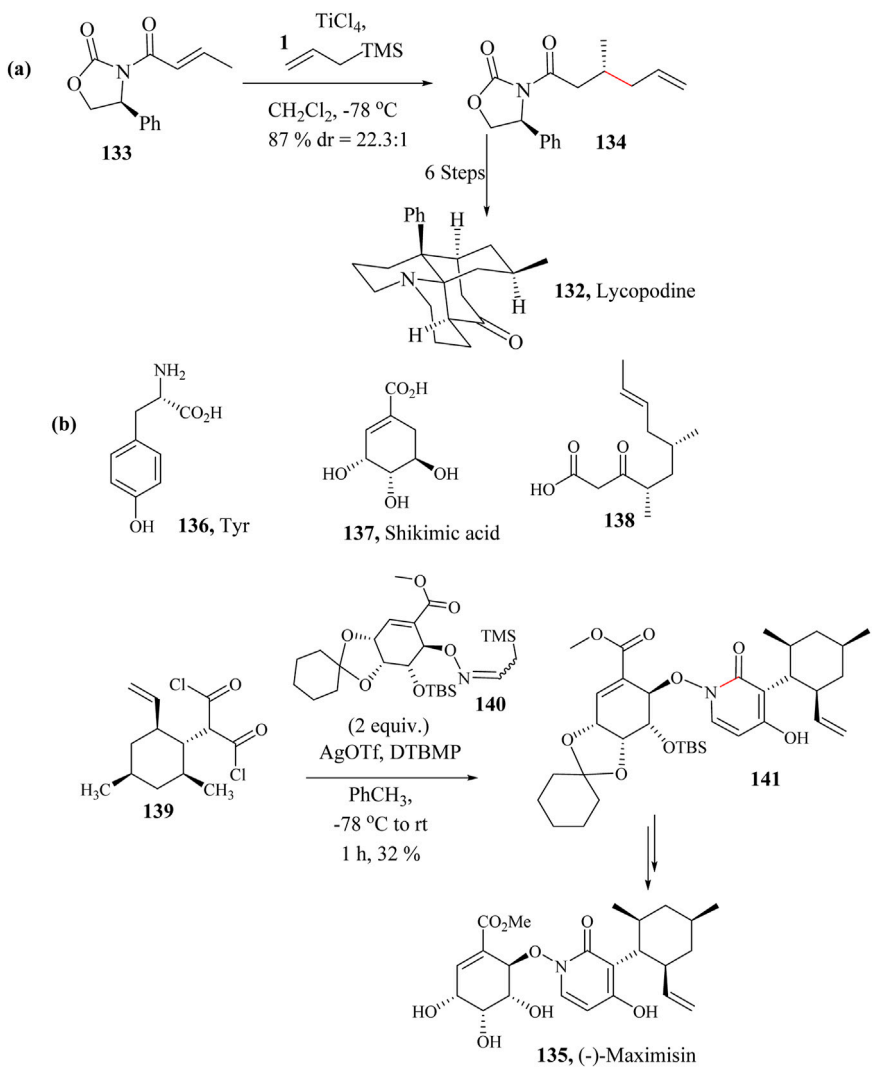
SCHEME 21
Total synthesis of Kumausallene reported by **(a)** Werness et al. (2013) and **(b)** Werness and Tang (2011).



SCHEME 22
Total synthesis of Leiodermatolide A, **124** (Siu et al., 2021).

possessed antimitotic selective cytotoxicity towards the pancreatic cancer cell lines AsPC-1, PANC-1, BxPC-3, and MIA PaCa-2, and potent cytotoxicity against skin, breast and colon cancer cell lines (Guzmán et al., 2016; Siu et al., 2021).

Krische and coworkers reported a 13-step total synthesis of leiodermatolide A, by reacting together fragments **124**, **125** and **126** synthesised independently from commercially available starting materials (Scheme 22). Intermediates **127** and **128** were synthesized



SCHEME 23
Total syntheses of **(a)** Lycopodine (**132**) and **(b)** (–)-Maximiscin (**135**) involving HSR step (Mcclymont et al., 2020; Wada et al., 2019).

from starting materials **125** and **126** independently in 5 and 6 steps respectively. Aldehyde **127** and allyl silane **158** were reacted in a chelation-controlled procedure using $AlEtCl_2$ followed by TBAF mediated HSR and exhaustive deprotection of the product to yield fragment **129**. Fragments **129, 130** and **131** were then combined sequentially to yield Leiodermatolide A, **124** (Siu et al., 2021).

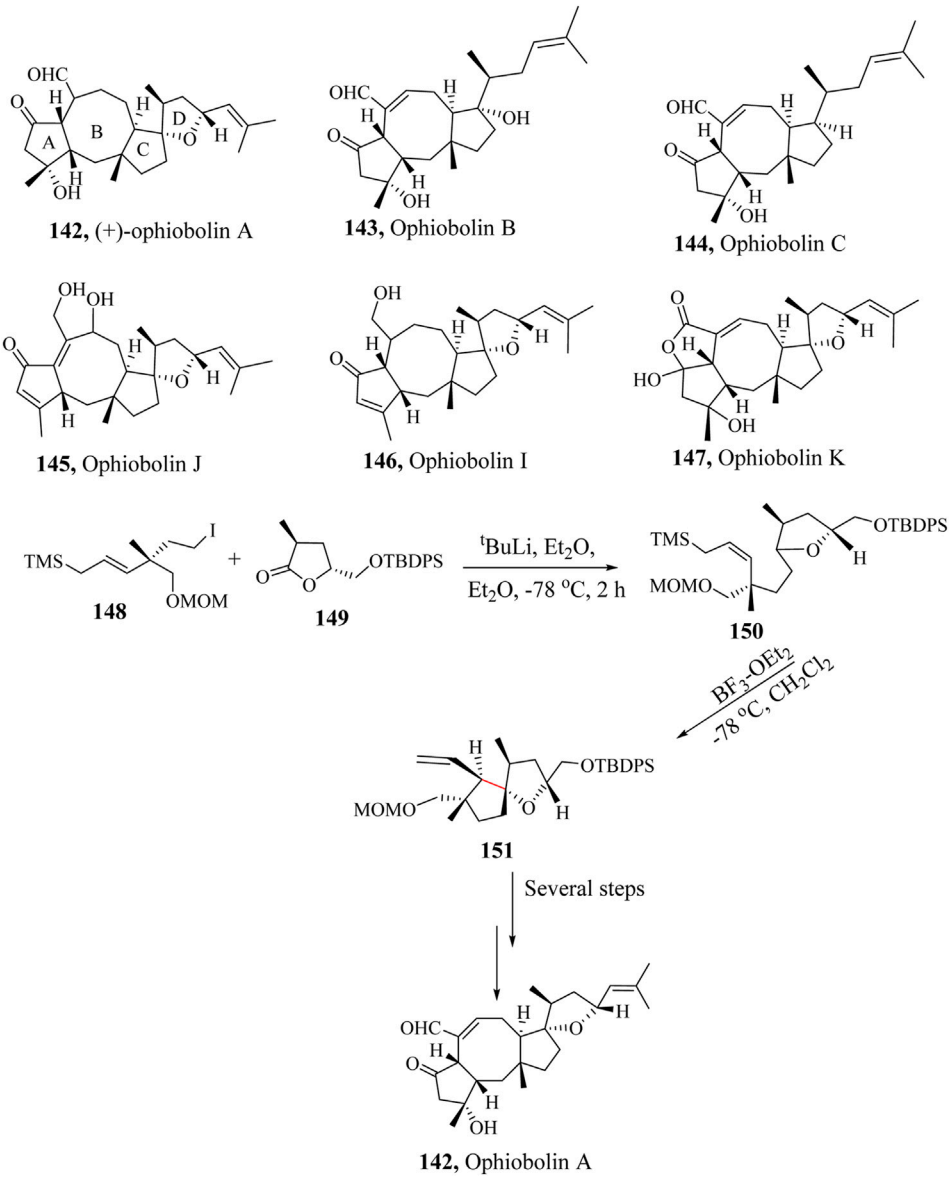
2.19 Total synthesis of Lycopodine

Lycopodine, **132** belongs to a family of over 300 naturally occurring *Lycopodium* alkaloids with a diverse structural backbone (Harrison et al., 1961). It was first isolated in 1881 by Ayer *et al* (Harrison et al., 1961; Yang and Carter, 2010) but its structure was not elucidated until 1960 by Harrison and coworkers (Ayer and Cruz, 1993). Some of the members of this family of compounds possess medicinal properties that can reversibly inhibit acetylcholinesterase and increase learning and memory efficiency (Liu et al., 1986). Lycopodine is made up of four haxacyclic rings fused with five asymmetric centres like lycodine (Liu et al., 1986).

Several total synthetic techniques have been reported for the preparation of natural **132**. Asymmetric synthesis was first reported by Yang and Carter (2010), Ma et al. (2016). Wada and co-workers also reported a concise asymmetric total synthesis of **162** by applying the HSR in the first step (Scheme 23a). Seven synthetic pathways were followed in the total synthesis of Lycopodine which started with the conversion of the commercially available crotonamide **133** to diastereoselectively make **134** (22.3: 1 dr) as shown in Scheme 23a (Wada et al., 2019).

2.20 Total synthesis of (–)-Maximiscin

(–)-Maximiscin **135** is an alkaloid made from three different metabolic pathways that incorporates a central 1,4-dihydroxy-2-pyridone derived from tyrosine 137 (Scheme 23b), attached to the ester of shikimic acid **137** and cyclohexyl of a polyketide **141** (Schmidt



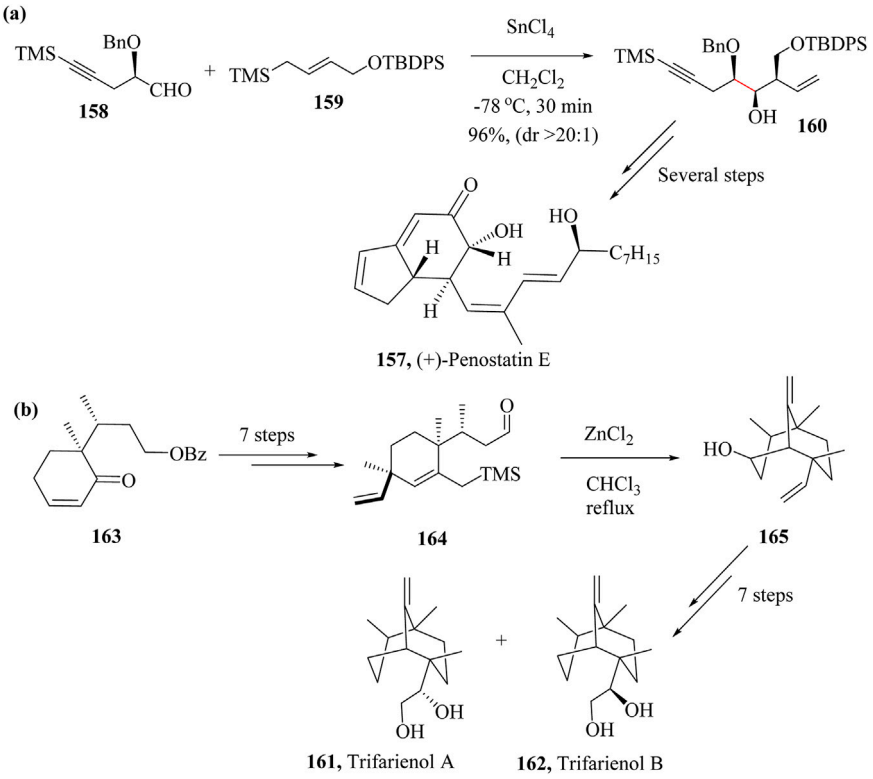
SCHEME 24
Application of HSR in total synthesis of Ophiobolin A, (**142**) (Tsuna et al., 2013).

et al., 2003). 4-Hydroxy-2-pyridone family of alkaloids (Du et al., 2014) to which (−)-Maximiscin belongs are known to be unstable and usually fragment in isolation but possess interesting biological activities (Schmidt et al., 2003). (−)-Maximiscin **135** is a fungal metabolite isolated from the fungus *Tolypocladium* which demonstrated tumor suppression activity in animal models (Du et al., 2013; Du, et al., 2014).

The total synthesis of (−)-Maximiscin **135** faced challenges due to the instability of its structure. Specifically, shikimate and pyridone residues tend to fragment when synthesised. Mcclymont and co-workers completed the total synthesis of Maximiscin **135** by following a modified enantioselective HSR using AgOTf as a promoter to activate the diacid chloride **139** as an electrophile in the presence of **140** and use the β-silicon effect of the Si–C to enhance the nucleophilicity of the nitrogen (Déléris et al., 1980; Mcclymont et al., 2020) (Scheme 23b).

2.21 Total synthesis of (+)-Ophiobolin A

Ophiobolins A-K (**142–147**) are terpenoids with 5,8,5-membered carbocyclic ring systems (Scheme 24). The complexity of the structure and intriguing biological activities of Ophiobolins A-K have attracted the attention of the organic synthetic community. (+)-Ophiobolin A, **142** has a unique 5,8,5,5 tetracyclic ring system and eight chiral centres isolated from *Ophiobolus miyabeanus* in 1958 by Ishibashi and co-workers. Its structure was fully established in 1965 by Nozoe et al. (1965), Rowley et al. (1989). Biological screening of **172** has revealed that it induces apoptotic cell death in the L1210 cell-lines, (Fujiwara et al., 2000), inhibits calmodulin-activated cyclic nucleotide phosphodiesterase, and also shows cytotoxicity to cancer cell lines A-549, Mel-20, and P-335 (IC_{50} values that range from 62.5 to 125 μM) (Li et al., 2013).



SCHEME 25
Total syntheses of **(a)** (+)-Penostatin E, **(157)** and **(b)** Trifarienols A **(161)** and B **(162)** showing applications of HSR step (Fujioka et al., 2014; Takahashi et al., 2009).

A number of synthetic attempts have been made toward the total synthesis of Ophiobolin by Kishi and co-workers (Li et al., 2013). Tsuna et al., reported the first total synthesis of (+)-ophiobolin A (**142**) in 2013. A protected *tert*-butyldiphenylsilyl (TBDPS) intermediate **148** was reacted with the methoxymethyl (MOM) intermediate **149** to generate the complex intermediate **150** which was taken through an intramolecular HSR to form the key intermediate spirocyclic compound **151** in 45% yield using $BF_3{\cdot}OEt_2$ catalytic system. Further transformation of the key intermediate result in the production of the targeted product **152** as illustrated in Scheme 24 (Tsuna et al., 2013).

2.22 Total synthesis of (+)-Paniculatine

(+)-Paniculatine **152** belongs to the Lycopodium family of alkaloids and was first isolated by Castillo and his group in 1975 (Castillo et al., 1975; 2011). Other members of the Lycopodium family such as (−)-Magellanine **153** (Loyola et al., 1979) and (+)-Magellaninone **154** (Maclean, 1985) were also isolated from *Lycopodium paniculatum* by Casillo and co-workers. (+)-Paniculatine **152** has a complicated 6-5-5-6-fused tetracyclic diquinane core structure made up of seven chiral centres woven in a tetracyclic framework (Ma and Gang, 2004). *Lycopodium* family possesses anti-inflammatory activity and acetylcholinesterase inhibitory properties and are being studied as potential drugs for the treatment of Alzheimer's and other neurodegenerative diseases (Ma and Gang, 2004; Saito et al., 2023).

The first total synthesis of (+)-Paniculatine (**152**) was reported by Sha and co-workers in 1999 using tandem cyclisation reactions that involve HSR (Sha et al., 1999). Mukai and co-workers, stereospecifically synthesized (+)-Paniculatine **152**, (−)-Magellanine **153**, (+)-Magellaninone **154** (Supplementary Scheme S12) in 43–45 unprecedented synthetic steps in 2007 (Kozaka et al., 2007). Yan et al. proposed a concise palladium-catalyzed reaction in 2014, leading to the synthesis of (+)-Paniculatine, (−)-Magellanine, and (+)-Magellaninone in 12 steps (Chen et al., 2018; Liu et al., 2019). Liu et al., developed a more concise synthetic route for the synthesis of (+)-Paniculatine, achieving the synthesis in 10 steps. This involved the HSR of compound **155** to yield the desired intermediate **156** with a high diastereoselective ratio (dr > 20:1) at −78°C using $TiCl_4$ as depicted in Supplementary Scheme S12. The overall yeild was 12%. The authors proposed that the same reaction protocol could be used to synthesise (−)-Magellanine **155** and (+)-Magellaninone **154** as well (Liu et al., 2019).

2.23 Total synthesis of (+)-Penostatin E

Penostatin E **157** was isolated from a marine-based alga *Enteromorpha intestinalis*, a strain of *Penicillium sp.* (Jansma and Hoye, 2012). The biological activity of this compound attracts much interest from the organic synthetic community. When screened against cancer cell lines (P388 leukaemia cell lines), an ED_{50} value of 0.9 μg/mL was obtained, making it a potential anticancer agent.

Fujioka et al reported the first successful synthesis of (+)-Penostatin E, **157** following the HSR method to prepare enyne **150** from aldehyde **158** and allysilane **159** which were both synthesized from (*R*)-glycidyl

isobutyrate and (*E*)-4-(trimethylsilyl)but-2-en-1-ol, respectively (Scheme 25a). Enyne **160** was diastereoselectively obtained in 96% yield after reacting **158** and **159** in the presence of $SnCl_4$ without loss of enantiopurity. The synthetic pathway was simple and could be employed in the synthesis of other Penostatin derivatives. From compound **160** to the title compound **157** took several steps (Fujioka et al., 2014; Jansma and Hoye, 2012).

2.24 Total synthesis of Trifarienols A and B

Trifarienols A (**161**), and B (**162**) are sesquiterpenes that were isolated from *Cheilolejeunea trifaria,* a liverwort of Malaysian origin with a trifarane carbon backbone (Hashimoto et al., 1994; Huang and Forsyth, 1995). These compounds **161** and **162** are structurally complicated biologically active sesquiterpenes that exhibit anticancer, antifungal, and insect antifeedant properties. The complexity of this class of compounds is hidden in the highly substituted bicyclo [3.3.1] nonane moiety and the *exo*-methylene group. The bicyclo [3.3.1] nonane backbone of Trifarienols A (**161**) and B (**162**) is also found in some naturally occurring compounds such as hyperforin, aristophenones, guttiferones, garsubellin A, papuaforin A, and upial.

The first successful Trifarienols A (**161**) and B (**162**) synthesis was by Huang and co-workers (Huang and Forsyth, 1995) in 16 steps with an overall enantiomeric yield of 3%. Tori and co-workers attempted enantioselective synthesis of Trifarienols A (**161**) and B (**162**) in 1999 where they used (2*RS*,3*R*)-2,3-dimethylcyclohexanone as starting material and had an overall yield of 1.8% and 1.4% respectively (Tori et al., 1999). In 2009, Takahashi et al., synthesised Trifarienols A (161) and B (162) from compound **165** (Scheme 25b) which was previously prepared by the group and attempted construction of the bicyclo [3.3.1] nonane ring system. HSR was employed to achieve product **165** as the sole product in 93% yield by treating intermediate **164** with $ZnCl_2$ in chloroform. The entire synthetic process took 15 steps to accomplish 2% and 9% yields of Trifarienols A (**161**) and B (**162**), respectively (Scheme 25b) (Takahashi et al., 2009).

3 Conclusion

In summary, the HSR and its applications in the total synthesis of complex and contiguous bioactive organic molecules from natural sources, have been reviewed. The HSR is applied in the formation of C-C bonds and complex transformations via activated Lewis acid-promoted allylation of various electrophiles. HSR is a facile reaction that has enabled organic chemists to undertake key transformations for the formation of complex carbocyclic compounds. Examples of such transformation include hetero-Diels–Alder (HDA), allylation of aldehydes and ketones, allylation of cyclic oxonium cation, β,γ-unsaturated α-ketoesters, carbocyclization, allylation of imines, epoxide opening/allylsilylation, cyanation of carbonyls amongst others.

The versatility of the HSR has been enhanced following the various modifications to the original method to broaden the scope of its application and molecular transformations of both intermolecularly and intramolecularly. Modifications such as the use of homoallylic allowed the preparation of a wide range of compounds including acetals, aldimines, aldehydes, carboxylic acid chlorides, epoxides, ketals, ketoimines, ketones, and α,β-unsaturated carbonyl compounds. Furthermore, HSRs occur under mild conditions and have low turnover time, are typically high yielding as well as are diastereoselective, stereoselective and installing multiple stereogenic centres concurrently.

In this review, we describe the applications of HSR in the synthesis of key intermediates and final products from several natural and synthetic products.

Author contributions

JA: Writing – original draft, Writing – review and editing. RK: Conceptualization, Writing – original draft, Writing – review and editing. DO-S: Conceptualization, Supervision, Writing – original draft, Writing – review and editing. RA: Conceptualization, Resources, Supervision, Writing – original draft, Writing – review and editing.

Funding

The author(s) declare that no financial support was received for the research, authorship, and/or publication of this article.

Conflict of interest

The authors declare that the research was conducted in the absence of any commercial or financial relationships that could be construed as a potential conflict of interest.

Generative AI statement

The author(s) declare that no Gen AI was used in the creation of this manuscript.

Publisher's note

All claims expressed in this article are solely those of the authors and do not necessarily represent those of their affiliated organizations, or those of the publisher, the editors and the reviewers. Any product that may be evaluated in this article, or claim that may be made by its manufacturer, is not guaranteed or endorsed by the publisher.

Supplementary material

The Supplementary Material for this article can be found online at: https://www.frontiersin.org/articles/10.3389/fchem.2025.1527387/full#supplementary-material

References

Aiqin, W., Jingpei, X., Wenyan, W., and Jiwen, L. (2011). Microstructural morphology and formation mechanism of rapidly solidified Al-21Si multi-alloys. *Adv. Mater. Res.* 146–147, 1597–1600. doi:10.4028/www.scientific.net/AMR.146-147.1597

Asakawa, Y., Ludwiczuk, A., and Nagashima, F. (2013). Chemical diversity of bryophytes. *Prog. Chem. Org. Nat. Prod.*, 95, pp. 21–24. doi:10.1007/978-3-7091-1084-3_3

Ayer, W. A., and Cruz, E. R. (1993). The tremulanes, a new group of sesquiterpenes from the aspen rotting fungus phellinus tremulae. *J. Org. Chem.* 58 (26), 7529–7534. doi:10.1021/jo00078a035

Bae, M. A., Yamada, K., Ijuin, Y., Tsuji, T., Yazawa, K., Tomono, Y., et al. (1996). Aburatubolactam A, a novel inhibitor of superoxide anion generation from a marine microorganism. *Heterocycl. Commun.* 2 (4), 315–318. doi:10.1515/HC.1996.2.4.315

Bai, W. J., Lu, C., and Wang, X. (2016). Recent advances in the total synthesis of tetramic acid-containing natural products. *J. Chem.* 2016 (1), 1–13. doi:10.1155/2016/8510278

Bauer, A., and Maulide, N. (2018). A stereoselective reductive hosomi-sakurai reaction. *Org. Lett.* 20 (5), 1461–1464. doi:10.1021/acs.orglett.8b00276

Beavo, J. A., and Brunton, L. L. (2002). Cyclic nucleotide research — still expanding after half a century. *Nat. Rev. Mol. Cell Biol.* 3 (9), 710–717. doi:10.1038/nrm911

Berkessel, A., Adrio, J. A., Hüttenhain, D., and Neudörfl, J. M. (2006). Unveiling the "booster effect" of fluorinated alcohol solvents: aggregation-induced conformational changes and cooperatively enhanced H-bonding. *J. Am. Chem. Soc.* 128 (26), 8421–8426. doi:10.1021/ja0545463

Birch, A. J., Kelly, L. F., and Thompson, D. J. (1981). Organometallic compounds in organic synthesis. Part 10. Preparations and some reactions of tricarbonyl-1,3- and -1,4-dimethoxycyclohexa-1,3-dieneiron and related compounds: the preparation of the tricarbonyl-3- methoxycyclohexadienyliumiron cation. *J. Chem. Soc. Perkin Trans.* 1, 1006–1012. doi:10.1039/P19810001006

Blakemore, P. R. (2002). The modified Julia olefination: alkene synthesis via the condensation of metallated heteroarylalkylsulfones with carbonyl compounds. *J. Chem. Soc. Perkin Trans.* 1, 2563–2585. doi:10.1039/b208078h

Bödeker, K. (1881). Lycopodin, das erste Alkaloïd der Gefässkryptogamen. *Justus Liebigs Ann. Der Chem.* 208 (1), 363–367. doi:10.1002/jlac.18812080308

Bols, M., and Skrydstrup, T. (1995). Silicon-tethered reactions. *Chem. Rev.* 95 (5), 1253–1277. doi:10.1021/cr00037a006

Boubaker, J., Bhouri, W., Sghaier, M. B., Bouhlel, I., Skandrani, I., Ghedira, K., et al. (2011). Leaf extracts from Nitraria retusa promote cell population growth of human cancer cells by inducing apoptosis. *Cancer Cell Int.* 11 (37), 37–2468. doi:10.1186/1475-2867-11-37

Boukouvalas, J., Pouliot, M., Robichaud, J., MacNeil, S., and Snieckus, V. (2006). Asymmetric total synthesis of (-)-panacene and correction of its relative configuration. *Org. Lett.* 8 (16), 3597–3599. doi:10.1021/ol061385e

Britten, T. K., Basson, A. J., Roberts, D. D., and McLaughlin, M. G. (2021). Aza-peterson olefinations: rapid synthesis of (E)-Alkenes. *Synthesis* 53 (19), 3535–3544. doi:10.1016/j.tet.2018.06.015

Brown, M. J., Harrison, T., and Overman, L. E. (1991). General approach to halogenated tetrahydrofuran natural products from red algae of the genus Laurencia. Total synthesis of (.+-.)-trans-kumausyne and demonstration of an asymmetric synthesis strategy. *J. Am. Chem. Soc.* 113 (14), 5378–5384. doi:10.1021/ja00014a032

Cai, Y. Q., Hu, J. H., Qin, J., Sun, T., and Li, X. L. (2018). Rhododendron Molle (Ericaceae): phytochemistry, pharmacology, and toxicology. *Chin. J. Nat. Med.* 16 (6), 401–410. doi:10.1016/S1875-5364(18)30073-6

Carreira, E. M., and Joliton, A. (2015). Total synthesis of (–)-Amphidinolide P. *Synfacts* 11 (09), 0903. doi:10.1055/s-0034-1378759

Castillo, M., Morales, G., Loyola', L. A., Calvo, C., Holland, H. L., Maclean, D. B., et al. (2011). The alkaloids of L. paniculatum and the structure of paniculatine. *Can. J. Chem.* 54 (18), 2900–2908. doi:10.1139/v76-410

Castillo, M., Morales, G., Loyola, L. A., Singh, I., Calvo, C., Holland, H. L., et al. (1975). Paniculatine. A new alkaloid from L. paniculatum desvaux. *Can. J. Chem.* 53 (16), 2513–2514. doi:10.1139/v75-357

Chan, T. H., and Wang, D. (1992). Chiral organosilicon compounds in asymmetric synthesis. *Chem. Rev.* 92 (5), 995–1006. doi:10.1021/cr00013a012

Chemler, S. R., and Roush, W. R. (2000). *Recent applications of the allylation reaction to the synthesis of natural products* 1, pp. 403–490. John Wiley and Sons, Ltd. doi:10.1002/9783527613267.ch11

Chen, S., Wang, J., and Qiu, F. G. (2018). A divergent and concise total synthesis of (-)-lycoposerramine R and (+)-lycopladine A. *Chem. Commun.* 54 (29), 3598–3600. doi:10.1039/c8cc01626g

Chien, J. C. W., Tsai, W. M., Rausch, M. D., and Rausch, M. D. (1991). Isospecific polymerization of propylene catalyzed by rac-Ethylenebis(indenyl)methylzirconium "cation.". *J. Am. Chem. Soc.* 113 (22), 8570–8571. doi:10.1021/ja00022a081

Chu, Z., Wang, K., Gao, L., and Song, Z. (2017). Chiral crotyl geminal bis(silane): a useful reagent for asymmetric Sakurai allylation by selective desilylation-enabled chirality transfer. *Chem. Commun.* 53 (21), 3078–3081. doi:10.1039/C7CC00632B

Colvin, E. W. (1978). Silicon in organic synthesis. *Chem. Soc. Rev.* 7 (1), 15–64. doi:10.1039/cs9780700015

Cram, D. J., and Elhafez, F. A. A. (1952). Studies in stereochemistry. X. The rule of "steric control of asymmetric induction" in the syntheses of acyclic systems. *J. Am. Chem. Soc.* 74 (23), 5828–5835. doi:10.1021/ja01143a007

Crimmins, M. T., and Emmitte, K. A. (2001). Asymmetric total synthesis of (−)-Isolaurallene. *J. Am. Chem. Soc.* 123 (7), 1533–1534. doi:10.1021/ja005892h

Crimmins, M. T., Emmitte, K. A., and Choy, A. L. (2002). Ring closing metathesis for the formation of medium ring ethers: the total synthesis of (-)-isolaurallene. *Tetrahedron* 58 (10), 1817–1834. doi:10.1016/S0040-4020(02)00040-6

Crimmins, M. T., Mans, M. C., and Rodríguez, A. D. (2010). Total synthesis of the proposed structure of briarellin J. *Org. Lett.* 12 (21), 5028–5031. doi:10.1021/ol102169w

Daoust, J., Chen, M., Wang, M., Williams, D. E., Chavez, M. A. G., Wang, Y. A., et al. (2013). Sesterterpenoids isolated from a northeastern pacific phorbas sp. *J. Org. Chem.* 78 (17), 8267–8273. doi:10.1021/jo4014589

Das, S., and Ramana, C. V. (2015). A formal total synthesis of (−)-kumausallene. *Tetrahedron* 71 (45), 8577–8584. doi:10.1016/j.tet.2015.09.027

Déléris, G., Pillot, J. P., and Rayez, J. C. (1980). Influence of a silyl group on an allylic position. A theoretical approach. *Tetrahedron* 36 (15), 2215–2218. doi:10.1016/0040-4020(80)80114-1

Deng, Z. T., Wu, X.De, Yuan, Z. F., Yu, N. R., Ou, Y. F., and Zhao, Q. S. (2022). Total synthesis of huperserratines A and B. *Org. Chem. Front.* 9 (14), 3664–3668. doi:10.1039/D2QO00608A

Denmark, S. E., and Almstead, N. G. (1994). Stereochemical studies on the addition of allylsilanes to aldehydes. The SE′ component. *J. Org. Chem.* 59 (18), 5130–5132. doi:10.1021/jo00097a008

Denmark, S. E., Coe, D. M., Pratt, N. E., and Griedel, B. D. (1994). Asymmetric allylation of aldehydes with chiral lewis bases. *J. Org. Chem.* 59 (21), 6161–6163. doi:10.1021/jo00100a013

Denmark, S. E., and Fu, J. (2001). Catalytic, enantioselective addition of substituted allylic trichlorosilanes using a rationally-designed 2,2'-bispyrrolidine-based bisphosphoramide. *J. Am. Chem. Soc.* 123 (38), 9488–9489. doi:10.1021/ja016552e

Denmark, S. E., and Fu, J. (2003). Catalytic enantioselective addition of allylic organometallic reagents to aldehydes and ketones. *Chem. Rev.* 103 (8), 2763–2794. doi:10.1021/cr020050h

Dilman, A. D., and Ioffe, S. L. (2003). Carbon-carbon bond forming reactions mediated by Silicon Lewis acids. *Chem. Rev.* 103 (3), 733–772. doi:10.1021/cr020003p

Don-Doncow, N., Escobar, Z., Johansson, M., Kjellström, S., Garcia, V., Munoz, E., et al. (2014). Galiellalactone is a direct inhibitor of the transcription factor STAT3 in prostate cancer cells. *J. Biol. Chem.* 289 (23), 15969–15978. doi:10.1074/jbc.M114.564252

Du, K., Yang, H., Guo, P., Feng, L., Xu, G., Zhou, Q., et al. (2017). Efficient syntheses of (−)-crinine and (−)-aspidospermidine, and the formal synthesis of (−)-minfiensine by enantioselective intramolecular dearomative cyclization. *Chem. Sci.* 8 (9), 6247–6256. doi:10.1039/C7SC01859B

Du, L., Robles, A., King, J., Powell, D., Miller, A., Mooberry, S., et al. (2013). Maximiscin, a novel shikimate-polyketide-NRPS hybrid metabolite obtained from Tolypocladium sp. with potent antitumor activities. *Planta Medica* 79 (10), CL3. doi:10.1055/s-0033-1348528

Du, L., Robles, A. J., King, J. B., Powell, D. R., Miller, A. N., Mooberry, S. L., et al. (2014). Crowdsourcing natural products discovery to access uncharted dimensions of fungal metabolite diversity. *Angew. Chem.* 126 (3), 823–828. doi:10.1002/ange.201306549

Ella-Menye, J. R., Dobbs, W., Billet, M., Klotz, P., and Mann, A. (2005). Unexpected 1,2 syn diastereoselectivity in the three-component "aza Sakurai-Hosomi" reaction. *Tetrahedron Lett.* 46 (11), 1897–1900. doi:10.1016/j.tetlet.2005.01.077

Evans, P., Murthy, V., Roseman, J., and Rheingold, A. L. (1999). Enantioselective total synthesis of the nonisoprenoid sesquiterpene (−)-Kumausallene. *Angew. Chem. Int. Ed.* 38 (21), 3175–3177. doi:10.1002/(SICI)1521-3773(19991102)38:21<3175::AID-ANIE3175>3.0.CO;2-M

Fan, Y. Y., Xu, J. B., Liu, H. C., Gan, L. S., Ding, J., and Yue, J. M. (2017). Cephanolides A-J, cephalotane-type diterpenoids from Cephalotaxus sinensis. *J. Nat. Prod.* 80 (12), 3159–3166. doi:10.1021/acs.jnatprod.7b00412

Fang, F. G., Kishi, Y., Matclich, M. C., and Scola, P. M. (1992). Synthetic studies towards halichondrins synthesis of the left halves of norhalichondrins and

homohalichondrins. *Tetrahedron Lett.* 33 (12), 1557–1560. doi:10.1016/S0040-4039(00)91673-3

Farina, V., Reeves, J. T., Senanayake, C. H., and Song, J. J. (2006). Asymmetric synthesis of active pharmaceutical ingredients. *Chem. Rev.* 106 (7), 2734–2793. doi:10.1021/cr040700c

Feldman, K. S. (1982). Biomimetic synthesis of (±) panacene. *Tetrahedron Lett.* 23 (30), 3031–3034. doi:10.1016/s0040-4039(00)87525-5

Feldman, K. S., Mechem, C. C., and Nader, L. (1982). Total synthesis of (±)-Panacene. *J. Am. Chem. Soc.* 104 (14), 4011–4012. doi:10.1021/cr040700c

Fent, K. (1996). *Ecotoxicology of organotin compounds. In critical reviews in toxicology*. 26, 3–117. doi:10.3109/10408449609089891

Fleming, I. (1991). "Allylsilanes, allylstannanes and related systems," in *Comprehensive organic synthesis* (Elsevier), 563–593. doi:10.1016/b978-0-08-052349-1.00041-x

Fleming, I., Barbero, A., and Walter, D. (1997). Stereochemical control in organic synthesis using silicon-containing compounds. *Chem. Rev.* 97 (6), 2063–2192. doi:10.1021/cr941074u

Fleming, I., Dunoguès, J., and Smithers, R. (1989). The electrophilic substitution of allylsilanes and vinylsilanes. *Org. React.* 37 (57), 57–575. doi:10.1002/0471264180.or037.02

Forestieri, R., Merchant, C. E., De Voogd, N. J., Matainaho, T., Kieffer, T. J., and Andersen, R. J. (2009). Alotaketals A and B, sesterterpenoids from the marine sponge hamigera species that activate the camp cell signaling pathway. *Org. Lett.* 11 (22), 5166–5169. doi:10.1021/ol902066e

Fujioka, K., Yokoe, H., Inoue, A., Soga, K., Tsubuki, M., and Shishido, K. (2014). Enantioselective synthesis of (+)-Penostatin E. *J. Org. Chem.* 79 (16), 7512–7519. doi:10.1021/jo501225y

Fujiwara, H., Matsunaga, K., Kumagai, H., Ishizuka, M., and Ohizumi, Y. (2000). Ophiobolin A, a novel apoptosis-inducing agent from fungus strain f-7438. *Pharm. Pharmacol. Commun.* 6 (9), 427–431. doi:10.1211/146080800128736312

Fürstner, A., and Voigtländer, D. (2000). "Halophilic activation" of chlorosilanes: allylation of aldehydes catalyzed by platinum dichloride or silver triflate. *Synthesis* 12 (7), 959–969. doi:10.1055/s-2000-6290

Gauthier, D. R., and Carreira, E. M. (1996). Catalytic, enantioselective addition of allylsilanes to aldehydes: generation of a novel, reactive TiIV complex from TiF4. *Angewandte Chemie Int. Ed. Engl.* 35 (20), 2363–2365. doi:10.1002/anie.199623631

Ghosh, A. K., and Li, J. (2011). A stereoselective synthesis of (+)-herboxidiene/GEX1A. *Org. Lett.* 13 (1), 66–69. doi:10.1021/ol102549a

Girard, N. (2015). "Synthesis of alkaloids containing a quinolizidine core by means of strategies based on a hydroformylation reaction," in *Strategies and tactics in organic synthesis*. 1st ed., Vol. 11 (Elsevier Ltd). doi:10.1016/B978-0-08-100023-6.00008-7

Grese, T. A., Hutchinson, K. D., and Overman, L. E. (1993). General approach to halogenated tetrahydrofuran natural products from red algae of the genus Laurencia. Total synthesis of (.+-.)-kumausallene and (.+-.)-1-epi-kumausallene. *J. Org. Chem.* 58 (9), 2468–2477. doi:10.1021/jo00061a021

Grisin, A., and Evans, P. A. (2015). A highly convergent synthesis of the C1–C31 polyol domain of amphidinol 3 featuring a TST-RCM reaction: confirmation of the revised relative stereochemistry. *Chem. Sci.* 6 (11), 6407–6412. doi:10.1039/C5SC00814J

Guzmán, E. A., Xu, Q., Pitts, T. P., Mitsuhashi, K. O., Baker, C., Linley, P. A., et al. (2016). Leiodermatolide, a novel marine natural product, has potent cytotoxic and antimitotic activity against cancer cells, appears to affect microtubule dynamics, and exhibits antitumor activity. *Int. J. Cancer* 139 (9), 2116–2126. doi:10.1002/IJC.30253

Harrison, W. A., Curcumelli-Rodostamo, M., Carson, D. F., Barclay, I. R. C., and MacLean, D. B. (1961). Lycopodium alkaloids x. The structure of Lycopodine. *Can. J. Chem.*, 39(1), 2086–2099. doi:10.1139/v61-277

Hashimoto, T., Koyama, H., Takaoka, S., Tori, M., and Asakawa, Y. (1994). Trifarienols A and B, Isolated from the liverwort Cheilolejeunea trifaria. Sesquiterpenes having a new carbon skeleton, trifarane. *Tetrahedron Lett.* 35 (27), 4787–4788. doi:10.1016/S0040-4039(00)76968-1

Hayashi, T., Usuki, Y., and Iio, H. (2010). 2-Fluoro-3-phenyl-allyltrimethylsilane: a new fluorinated reagent for Hosomi-Sakurai reaction. *J. Fluor. Chem.* 131 (6), 709–713. doi:10.1016/j.jfluchem.2010.03.005

Hegedus, L. S., Allen, G. F., Bozell, J. J., and Waterman, E. L. (1978). Palladium-Assisted intramolecular amination of olefins. Synthesis of nitrogen heterocycles. *J. Am. Chem. Soc.* 100 (18), 5800–5807. doi:10.1021/ja00486a035

Henderson, J. A., Phillips, A. J., Henderson, J. A., and Phillips, A. J. (2008). Total synthesis of Aburatubolactam A. *Angew. Chem. Int. Ed.* 47 (44), 8499–8501. doi:10.1002/anie.200803593

Heravi, M. M., and Mohammadkhani, L. (2018). Recent applications of Stille reaction in total synthesis of natural products: an update. *J. Organomet. Chem.* 869 (15), 106–200. doi:10.1016/j.jorganchem.2018.05.018

Ho, L.-K., and Lin, W.-N. (1995). Quercetin 5,4′-dimethyl ether from Rhododendron ellipticum. *Phytochemistry* 39 (2), 463–464. doi:10.1016/0031-9422(94)00905-9

Hoffmann-Röder, A., and Krause, N. (2004). Synthesis and properties of allenic natural products and pharmaceuticals. *Angew. Chem. - Int. Ed.* 43 (10), 1196–1216. doi:10.1002/ANIE.200300628

Hollis, T. K., and Bosnich, B. (1995). Homogeneous catalysis. Mechanisms of the catalytic Mukaiyama aldol and Sakurai allylation reactions. *J. Am. Chem. Soc.* 117 (16), 4570–4581. doi:10.1021/ja00121a015

Hosomi, A. (1988). Characteristics in the reactions of allylsilanes and their applications to versatile synthetic equivalents. *Accounts Chem. Res.* 21 (5), 200–206. doi:10.1021/ar00149a004

Hosomi, A., Endo, M., and Sakurai, H. (1978a). Selective allylations of α,β-unsaturated acetals with allylsilanes in the presence of lewis acid. *Chem. Lett.* 7 (5), 499–502. doi:10.1246/cl.1978.499

Hosomi, A., Sakata, Y., and Sakurai, H. (1984). N-(trimethylsilylmethyl)aminomethyl ethers as azomethine ylide synthons. A new and convenient access to pyrrolidine derivatives. *Chem. Lett.* 13 (7), 1117–1120. doi:10.1246/cl.1984.1117

Hosomi, A., and Sakurai, H. (1976). Syntheses of γ,δ-unsaturated alcohols from allylsilanes and carbonyl compounds in the presence of titanium tetrachloride. *Tetrahedron Lett.* 17 (16), 1295–1298. doi:10.1016/S0040-4039(00)78044-0

Hosomi, A., and Sakurai, H. (1977). Chemistry of organosilicon compounds. 99. Conjugate addition of allylsilanes to.alpha., beta.-enones. A New method of stereoselective introduction of the angular allyl group in fused cyclic.alpha., beta.-enones. *J. Am. Chem. Soc.* 99 (5), 1673–1675. doi:10.1021/ja00447a080

Hosomi, A., Shirahata, A., and Sakurai, H. (1978b). Chemistry of organosilicon compounds 113 chemoselective allylation of carbonyl compounds with allylsilanes promoted by tetra-butylammonium fluoride. A new synthesis of homoallyl alcohols. *Tetrahedron Lett.* 19 (33), 3043–3046. doi:10.1016/S0040-4039(01)94934-2

Huang, C., and Liu, B. (2010). Asymmetric total synthesis of ent-heliespirones A and C. *Chem. Commun.* 46 (29), 5280–5282. doi:10.1039/C0CC00481B

Huang, C., Zhang, W., and Liu, B. (2011). Racemic and enantioselective total synthesis of heliespirones A and C. *Sci. China Chem.* 54 (1), 43–55. doi:10.1007/s11426-010-4173-y

Huang, G. H., Hu, Z., Lei, C., Wang, P. P., Yang, J., Li, J. Y., et al. (2018). Enantiomeric pairs of meroterpenoids with diverse heterocyclic systems from Rhododendron nyingchiense. *J. Nat. Prod.* 81 (8), 1810–1818. doi:10.1021/acs.jnatprod.8b00273

Huang, H., and Forsyth, C. J. (1995). Anti selective spirocarbomercuration: synthesis and stereochemistry of the spirobicyclic sesquiterpenes spirojatamol and erythrodiene. *J. Org. Chem.* 60 (9), 2773–2779. doi:10.1021/jo00114a027

Huang, X. Z., Wang, Y. H., Yu, S. S., Fu, G. M., Hu, Y. C., Liu, Y., et al. (2005). Iridoid glycosides and grayanane diterpenoids from the roots of Craibiodendron henryi. *J. Nat. Prod.* 68 (11), 1646–1650. doi:10.1021/np050261s

Hubert, J. G., Furkert, D. P., and Brimble, M. A. (2015). Synthesis of the spirocyclic framework of sesterterpenoid natural products. *J. Org. Chem.* 80 (5), 2715–2723. doi:10.1021/jo502897u

Huckins, J. R., De Vicente, J., and Rychnovsky, S. D. (2007). Synthesis of the C1-C52 fragment of amphidinol 3, featuring a β-alkoxy alkyllithium addition reaction. *Org. Lett.* 9 (23), 4757–4760. doi:10.1021/ol7020934

Indictor, N., and Brill, W. F. (1965). Metal acetylacetonate catalyzed epoxidation of olefins with t-butyl hydroperoxide. *J. Org. Chem.* 30 (6), 2074–2075. doi:10.1021/jo01017a520

Isaac, B. G., Ayer, S. W., Elliott, R. C., and Stonard, R. J. (1992). Herboxidiene: a potent phytotoxic polyketide from Streptomyces sp. A7847. *J. Org. Chem.* 57 (26), 7220–7226. doi:10.1021/jo00052a042

Iseki, K., Mizuno, S., Kuroki, Y., and Kobayashi, Y. (1999). Asymmetric allylation with chiral formamide catalysts. *Tetrahedron* 55 (4), 977–988. doi:10.1016/S0040-4020(98)01097-7

Ishibashi, M., and Kobayashi, J. (1997). Amphidinolides: unique macrolides from marine dinoflagellates. *Heterocycles* 44 (1), 543–572. doi:10.3987/rev-96-sr1

Ishihara, K., Mouri, M., Gao, Q., Maruyama, T., Furuta, K., and Yamamoto, H. (1993). Catalytic asymmetric allylation using a chiral (Acyloxy)borane complex as a versatile lewis acid catalyst. *J. Am. Chem. Soc.* 115 (24), 11490–11495. doi:10.1021/ja00077a054

Israr, M., Kim, W. H., Kim, D. H., and Bae, H. Y. (2024). Trityl tetrakis(pentafluorophenyl) borate: a sustainable precursor for multifunctional silylium Lewis acid organocatalysis. *Chem. Catal.* 4 (4). doi:10.1016/J.CHECAT.2023.100866/ASSET/C6DF1B90-8A65-4DB5-ABA8-FFE0B53E3589/MAIN.ASSETS/SC12.SML

Itsuno, S. (2005). Chiral polymer synthesis by means of repeated asymmetric reaction. *Prog. Polym. Sci. Oxf.* 30 (5), 540–558. doi:10.1016/j.progpolymsci.2005.01.008

Jansma, M. J., and Hoye, T. R. (2012). Oxyanionic sigmatropic rearrangements relevant to cyclooctadienone formation in penostatins I and F. *Org. Lett.* 14 (18), 4738–4741. doi:10.1021/ol3019488

Jeong, W., Kim, M. J., Kim, H., Kim, S., Kim, D., and Shin, K. J. (2010). Substrate-controlled asymmetric total synthesis and structure revision of (+)-itomanallene a. *Angew. Chem. - Int. Ed.* 49 (4), 752–756. doi:10.1002/anie.200905826

Johansson, M., and Sterner, O. (2001). Synthesis of (+)-Galiellalactone. Absolute configuration of galiellalactone. *Org. Lett.* 3 (18), 2843–2845. doi:10.1021/ol016286+

Joung, S., Kim, R., and Lee, H. Y. (2017). Total synthesis of (−)-Phorbaketal A. *Org. Lett.* 19 (14), 3903–3906. doi:10.1021/ACS.ORGLETT.7B01797

Kaib, P. S. J., Schreyer, L., Lee, S., Properzi, R., and List, B. (2016). Extremely active organocatalysts enable a highly enantioselective addition of allyltrimethylsilane to aldehydes. *Angew. Chem. Int. Ed.* 55 (42), 13200–13203. doi:10.1002/anie.201607828

Kakisawa, H., Kurono, M., Takahashi, S., and Hirata, Y. (1961). Structure of grayanotoxin-I and -III. *Tetrahedron Lett.* 2 (2), 59–67. doi:10.1016/S0040-4039(01)99208-1

Kamiya, A., Kawamoto, Y., Kobayashi, T., and Ito, H. (2021). Total synthesis of ent-callilongisin B. *Org. Lett.* 23 (17), 6916–6918. doi:10.1021/acs.orglett.1c02473

Kamiya, A., Kawamoto, Y., Kobayashi, T., and Ito, H. (2022). Asymmetric syntheses of ent-callilongisins B and C. *Tetrahedron* 111 (12), 132712–141337. doi:10.1016/j.tet.2022.132712

Kampen, D., Ladépêche, A., Claßen, G., and Lista, B. (2008). Brønsted acid-catalyzed three-component hosomi–sakurai reactions. *Adv. Synthesis and Catal.* 350 (7–8), 962–966. doi:10.1002/adsc.200800036

Keck, G. E., and Yates, J. B. (1982). Carbon-carbon bond formation via the reaction of trialkylallylstannanes with organic halides. *J. Am. Chem. Soc.* 104 (21), 5829–5831. doi:10.1021/ja00385a066

Kim, C. Y., Mitchell, A. J., Glinkerman, C. M., Li, F. S., Pluskal, T., and Weng, J. K. (2020). The chloroalkaloid (−)-acutumine is biosynthesized via a Fe(II)- and 2-oxoglutarate-dependent halogenase in Menispermaceae plants. *Nat. Commun.* 11 (1), 1867–7. doi:10.1038/s41467-020-15777-w

Kim, T., Han, Y. T., An, H., Kim, K., Lee, J., and Suh, Y. G. (2015). Diastereoselective total synthesis of (-)-Galiellalactone. *J. Org. Chem.* 80 (24), 12193–12200. doi:10.1021/acs.joc.5b02121

King, S. M., Calandra, N. A., and Herzon, S. B. (2013). Total syntheses of (−)-Acutumine and (−)-Dechloroacutumine. *Angew. Chem.* 125 (13), 3642–3645. doi:10.1002/anie.201210076

Kira, M., Sato, K., and Sakurai, H. (1990). Highly stereoselective allylation of aldehydes with pentacoordinate allylsilicates in hydroxylic media. Discrimination between linear and.alpha.-branched alkanals. *J. Am. Chem. Soc.* 112 (1), 257–260. doi:10.1021/ja00157a040

Kobayashi, J., Ishibashi, M., Nakamura, H., Ohizumi, Y., Yamasu, T., Sasaki, T., et al. (1986). Amphidinolide-A, a novel antineoplastic macrolide from the marine dinoflagellate Amphidinium sp. *Tetrahedron Lett.* 27 (47), 5755–5758. doi:10.1016/S0040-4039(00)85318-6

Komatsu, N., Uda, M., Suzuki, H., Takahashi, T., Domae, T., and Wada, M. (1997). Bismuth bromide as an efficient and versatile catalyst for the cyanation and allylation of carbonyl compounds and acetals with organosilicon reagents. *Tetrahedron Lett.* 38 (41), 7215–7218. doi:10.1016/S0040-4039(97)01719-X

Komiyama, T., Minami, Y., and Hiyama, T. (2017). Recent advances in transition-metal-catalyzed synthetic transformations of organosilicon reagents. *ACS Catalysis,*, 7 (1), 631–651. doi:10.1021/acscatal.6b02374

Kong, L., Yu, H., Deng, M., Wu, F., Chen, S. C., and Luo, T. (2023). Enantioselective total syntheses of grayanane diterpenoids and (+)-Kalmanol: evolution of the bridgehead carbocation-based cyclization and late-stage functional group manipulation strategies. *J. Org. Chem.* 88 (9), 6017–6038. doi:10.1021/acs.joc.3c00365

Kong, L., Yu, H., Deng, M., Wu, F., Jiang, Z., and Luo, T. (2022). Enantioselective total syntheses of grayanane diterpenoids: (-)-Grayanotoxin III, (+)-Principinol E, and (-)-Rhodomollein XX. *J. Am. Chem. Soc.* 144 (12), 5268–5273. doi:10.1021/jacs.2c01692

Kosugi, M., Sumiya, T., Ohhashi, K., Sano, H., and Migita, T. (1985). Novel hydroxymethylation of aryl bromides by means of organotin reagents. *Chem. Lett.* 14 (7), 997–998. doi:10.1246/cl.1985.997

Kozaka, T., Miyakoshi, N., and Mukai, C. (2007). Stereoselective total syntheses of three Lycopodium alkaloids, (-)-magellanine, (+)-magellaninone, and (+)-paniculatine, based on two Pauson-Khand reactions. *J. Org. Chem.* 72 (26), 10147–10154. doi:10.1021/jo702136b

Krutov, S. M., Samek, Z., Benešova, V., and Herout, V. (1973). Isolation and the structure of deoxopinguisone from the liverwort Ptilidium ciliare. *Phytochemistry* 12 (6), 1405–1407. doi:10.1016/0031-9422(73)80574-6

Kulkarni, Y. A., Garud, M. S., Gaud, R. S., and Gaikwad, A. B. (2016). "Recent developments in using plant-derived natural products as tubulin inhibitors for the management of cancer," in *Recent developments in using plant-derived natural products as tubulin inhibitors for the management of cancer*, 1. Academic Press, 507–524. doi:10.1016/B978-0-12-802972-5.00024-X

Kumagai, T., and Itsuno, S. (2000). Asymmetric allylation polymerization: novel polyaddition of bis(allylsilane) and dialdehyde using chiral (acyloxy)borane catalyst. *Macromolecules* 33 (14), 4995–4996. doi:10.1021/ma000502x

Lade, J. J., Pardeshi, S. D., Vadagaonkar, K. S., Murugan, K., and Chaskar, A. C. (2017). The remarkable journey of catalysts from stoichiometric to catalytic quantity for allyltrimethylsilane inspired allylation of acetals, ketals, aldehydes and ketones. *RSC Adv.* 7 (13), 8011–8033. doi:10.1039/C6RA27813B

Langkopf, E., and Schinzer, D. (1995). Uses of silicon-containing compounds in the synthesis of natural products. *Chem. Rev.* 95 (5), 1375–1408. doi:10.1021/cr00037a011

Lee, J. H. (2020). Use of the Hosomi-Sakurai allylation in natural product total synthesis. *Tetrahedron* 76 (33), 131351–131367. doi:10.1016/j.tet.2020.131351

Lee, J. H., Li, Z., Osawa, A., and Kishi, Y. (2016). Extension of Pd-mediated one-pot ketone synthesis to macrocyclization: application to a new convergent synthesis of Eribulin. *J. Am. Chem. Soc.* 138 (50), 16248–16251. doi:10.1021/jacs.6b11663

Lee, Y., Wang, W., Kim, H., Giri, A. G., Won, D. H., Hahn, D., et al. (2014). Phorbaketals L-N, cytotoxic sesterterpenoids isolated from the marine sponge of the genus Phorbas. *Bioorg. Med. Chem. Lett.* 24 (17), 4095–4098. doi:10.1016/j.bmcl.2014.07.066

Li, C. H., Zhang, J. Y., Zhang, X. Y., Li, S. H., and Gao, J. M. (2019). An overview of grayanane diterpenoids and their biological activities from the Ericaceae family in the last seven years. *Eur. J. Med. Chem.* 166, 400–416. doi:10.1016/J.EJMECH.2019.01.079

Li, C. J., Wang, L. Q., Chen, S. N., and Qin, G. W. (2000). Diterpenoids from the fruits of Rhododendron molle. *J. Nat. Prod.* 63 (9), 1214–1217. doi:10.1021/NP000009E

Li, F., Tartakoff, S. S., and Castle, S. L. (2009). Enantioselective total synthesis of (-)-acutumine. *J. Org. Chem.* 74 (23), 9082–9093. doi:10.1021/jo902006q

Li, H., Zhang, J., and She, X. (2021). The total synthesis of diquinane-containing natural products. *Chem. – A Eur. J.* 27 (15), 4839–4858. doi:10.1002/chem.202003741

Li, J. J. (1999). Applications of palladium chemistry to the total syntheses of naturally occurring indole alkaloids. *Alkaloids Chem. Biol. Perspect.* 14 (C), 437–503. doi:10.1016/S0735-8210(99)80006-5

Li, K., Wang, C., Yin, G., and Gao, S. (2013). Construction of the basic skeleton of ophiobolin A and variecolin. *Org. Biomol. Chem.* 11 (43), 7550–7558. doi:10.1039/C3OB41693C

Li, X., Zhang, W., and Gao, S. (2018). Total synthesis of complex natural products: combination of chemical synthesis and biosynthesis strategies. *Chin. J. Org. Chem.* 38 (9), 2185–2198. doi:10.6023/cjoc201806019

Liao, H. B., Huang, G. H., Yu, M. H., Lei, C., and Hou, A. J. (2017). Five pairs of meroterpenoid enantiomers from Rhododendron capitatum. *J. Org. Chem.* 82 (3), 1632–1637. doi:10.1021/ACS.JOC.6B02800

Liao, H. B., Lei, C., Gao, L. X., Li, J. Y., Li, J., and Hou, A. J. (2015). Two enantiomeric pairs of meroterpenoids from Rhododendron capitatum. *Org. Lett.* 17 (20), 5040–5043. doi:10.1021/ACS.ORGLETT.5B02515

Liu, C. C., Lei, C., Zhong, Y., Gao, L. X., Li, J. Y., Yu, M. H., et al. (2014). Novel grayanane diterpenoids from Rhododendron principis. *Tetrahedron* 70 (29), 4317–4322. doi:10.1016/J.TET.2014.05.019

Liu, J., Chen, S., Li, N., and Qiu, F. G. (2019). A concise total synthesis of (+)-Paniculatine. *Adv. Synthesis Catal.* 361 (15), 3514–3517. doi:10.1002/adsc.201900376

Liu, J. S., Zhu, Y. L., Yu, C. M., Zhou, Y. Z., Han, Y. Y., Wu, F. W., et al. (1986). The structures of huperzine A and B,' two new alkaloids exhibiting marked anticholinesterase activity. *Can. J. Chem.* 64 (4), 837–839. doi:10.1139/v86-137@cjc-csc.issue01

Liu, S., Sun, L., Zhang, P., and Niu, C. (2024). Recent advances in grayanane diterpenes: isolation, structural diversity, and bioactivities from Ericaceae family (2018–2024). *Molecules* 29 (7), 1649. doi:10.3390/molecules29071649

Liu, Y. W., Cheng, Y. B., Liaw, C. C., Chen, C. H., Guh, J. H., Hwang, T. L., et al. (2012). Bioactive diterpenes from Callicarpa longissima. *J. Nat. Prod.* 75 (4), 689–693. doi:10.1021/NP200932K

Loyola, L. A., Morales, G., and Castillo, M. (1979). Alkaloids of lycopodium magellanicum. *Phytochemistry* 18 (10), 1721–1723. doi:10.1016/0031-9422(79)80193-4

Lv, X. J., Li, Y., Ma, S. G., Qu, J., Liu, Y. B., Li, L., et al. (2017). Isopimarane and nor-diterpene glucosides from the twigs and leaves of Lyonia ovalifolia. *Tetrahedron* 73 (6), 776–784. doi:10.1016/J.TET.2016.12.060

Ma, D., Zhong, Z., Liu, Z., Zhang, M., Xu, S., Xu, D., et al. (2016). Protecting-group-free total synthesis of (-)-Lycopodine via phosphoric acid promoted alkyne aza-prins cyclization. *Org. Lett.* 18 (17), 4328–4331. doi:10.1021/acs.orglett.6b02072

Ma, X., and Gang, D. R. (2004). The Lycopodium alkaloids. *Nat. Product. Rep.* 21 (6), 752–772. doi:10.1039/B409720N

Maclean, D. B. (1985). Chapter 5 lycopodium alkaloids. *Alkaloids Chem. Pharmacol.* 26 (C), 241–298. doi:10.1016/S0099-9598(08)60196-0

Mahlau, M., and List, B. (2013). Asymmetric counteranion-directed catalysis: concept, definition, and applications. *Angew. Chem. Int. Ed.* 52 (2), 518–533. doi:10.1002/anie.201205343

Majetich, G., Casares, A., Chapman, D., and Behnke, M. (1986). A general allylation procedure using trimethylallylsilane and fluoride catalysis. *J. Org. Chem.* 51 (10), 1745–1753. doi:10.1021/jo00360a021

Majetich, G., Lowery, D., and Khetani, V. (1990). A direct synthesis of (±)-neolemnanyl acetates. *Tetrahedron Lett.* 31 (1), 51–54. doi:10.1016/S0040-4039(00)94331-4

Makita, N., Hoshino, Y., and Yamamoto, H. (2003). Asymmetric epoxidation of homoallylic alcohols and application in a concise total synthesis of (-)-α-bisabolol and (-)-8-epi-α-bisabolol. *Angew. Chem. - Int. Ed.* 42 (8), 941–943. doi:10.1002/anie.200390250

Malkov, A. V., Orsini, M., Pernazza, D., Muir, K. W., Langer, V., Meghani, P., et al. (2002). Chiral 2,2′-bipyridine-type N-monoxides as organocatalysts in the enantioselective allylation of aldehydes with allyltrichlorosilane. *Org. Lett.* 4 (6), 1047–1049. doi:10.1021/ol025654m

Malkov, A. V., Ramírez-López, P., Biedermannová, L., Rulíšek, L., Dufková, L., Kotora, M., et al. (2008). On the mechanism of asymmetric allylation of aldehydes with allyltrichlorosilanes catalyzed by QUINOX, a chiral isoquinoline N-oxide. *J. Am. Chem. Soc.* 130 (15), 5341–5348. doi:10.1021/ja711338q

Manske, R. H. F. (1960). *The alkaloids. Chemistry and physiology.* Academic Press. doi:10.1016/S1876-0813(08)60018-4

Masse, C. E., and Panek, J. S. (1995). Diastereoselective reactions of chiral allyl and allenyl silanes with activated C:X.pi.-Bonds. *Chem. Rev.* 95 (5), 1293–1316. doi:10.1021/cr00037a008

May, T. L., Dabrowski, J. A., and Hoveyda, A. H. (2011). Formation of vinyl-vinylhalide-or acyl-substituted quaternary carbon stereogenic centers through NHC-Cu-catalyzed enantioselective conjugate additions of Si-containing vinylaluminums to β-substituted cyclic enones. *J. Am. Chem. Soc.* 133 (4), 736–739. doi:10.1021/ja110054q

Mcclymont, K. S., Wang, F., Minakar, A., and Baran, P. S. (2020). Total synthesis of (−)-Maximiscin. *J. Am. Chem. Soc.* 142 (19), 8608–8613. doi:10.1021/jacs.0c03202

Mirabdolbaghi, R., and Dudding, T. (2012). A catalytic asymmetric approach to C 1-chiral 3-methylene-indan-1-ols. *Tetrahedron* 68 (7), 1988–1991. doi:10.1016/j.tet.2011.12.040

Miyawaki, A., Kikuchi, D., Niki, M., Manabe, Y., Kanematsu, M., Yokoe, H., et al. (2012). Total synthesis of natural enantiomers of heliespirones A and C via the diastereoselective intramolecular Hosomi-Sakurai reaction. *J. Org. Chem.* 77 (18), 8231–8243. doi:10.1021/jo3016055

Motiwala, H. F., Armaly, A. M., Cacioppo, J. G., Coombs, T. C., Koehn, K. R. K., Norwood, V. M., et al. (2022). HFIP in organic synthesis. *Chem. Rev.* 122 (15), 12544–12747. doi:10.1021/acs.chemrev.1c00749

Mukaiyama, T., Kobayashi, S., and Murakami, M. (1984). Trityl perchlorate as an efficient catalyst in the aldol-type reaction. *Chem. Lett.* 13 (10), 1759–1762. doi:10.1246/cl.1984.1759

Narayanan, P., Röhrl, M., Zechmeister, K., and Hoppe, W. (1970). Crystal and molecular structure of grayanotoxin - I, C22H36O7. *Tetrahedron Lett.* 11 (45), 3943–3944. doi:10.1016/S0040-4039(01)98631-9

Nasam, R., and Pabbaraja, S. (2024). A convergent approach for the synthesis of C14–C26 fragment of anticancer drug Eribulin mesylate. *Synthesis* 56 (03), 462–468. doi:10.1055/a-2202-5597

Nishiyama, H., Narimatsu, S., Sakuta, K., and Itoh, K. (1982). Reaction of allylsilanes and monothioacetals in the presence of Lewis acids: regioselectivity in the cleavage of the acetals. *J. Chem. Soc. Chem. Commun.* 2 (8), 459–460. doi:10.1039/C9CC01159E

Niwa, Y., Miyake, M., Hayakawa, I., and Sakakura, A. (2019). Catalytic enantioselective Hosomi-Sakurai reaction of α-ketoesters promoted by chiral copper(ii) complexes. *Chem. Commun.* 55 (27), 3923–3926. doi:10.1039/C9CC01159E

Nokami, J., Nomiyama, K., Matsuda, S., Imai, N., and Kataoka, K. (2003). Highly enantioselective alk-2-enylation of aldehydes through an allyl-transfer reaction. *Angew. Chem. Int. Ed.* 42 (11), 1273–1276. doi:10.1002/anie.200390327

Noyori, R., Murata, S., and Suzuki, M. (1981). Trimethysilyl triflate in organic synthesis11Part 11 of this series. Part 10: S. Murata and R. Noyori, Tetrahedron Letters 2107 (1981). *Tetrahedron* 37 (23), 3899–3910. doi:10.1016/S0040-4020(01)93263-6

Nozoe, S., Morisaki, M., Tsuda, K., Iitaka, Y., Takahashi, N., Tamura, S., et al. (1965). The structure of ophiobolin, a C25 terpenoid having a novel skeleton. *J. Am. Chem. Soc.* 87 (21), 4968–4970. doi:10.1021/ja00949a061

Ogoshi, S., Tomiyasu, S., Morita, M., and Kurosawa, H. (2002). Palladium/Me3SiOTf-catalyzed bis-silylation of α,β-unsaturated carbonyl compounds without involving oxidative addition of disilane. *J. Am. Chem. Soc.* 124 (39), 11598–11599. doi:10.1021/ja0272944

Oishi, T. (2024). A long journey toward structure revision and total synthesis of amphidinol 3. *Mod. Nat. Product. Synth.* 23 (11), 55–81. doi:10.1007/978-981-97-1619-7_3

Onishi, Y., Ito, T., Yasuda, M., and Baba, A. (2002). Remarkable enhancement of Lewis acidity of chlorosilane by the combined use of indium(III) chloride. *Tetrahedron* 58 (41), 8227–8235. doi:10.1016/S0040-4020(02)00972-9

Ortega, V., and Cortés, J. (2012). Potential clinical applications of halichondrins in breast cancer and other neoplasms. *Breast Cancer Targets Ther.* 4 (2), 9–19. doi:10.2147/BCTT.S12423

Pandey, G., Prasanna Kumara, C., Kumar Burugu, S., and Puranik, V. G. (2011). Enantioselective total syntheses of (-)-Isonitramine, (-)-Sibirine, and (+)-Nitramine by ring-closing metathesis. *Eur. J. Org. Chem.* 2011 (36), 7372–7377. doi:10.1002/ejoc.201101256

Park, J., Kim, B., Kim, H., Kim, S., and Kim, D. (2007). Substrate-controlled asymmetric total synthesis of (+)-microcladallene B with a bromination strategy based on a nucleophile-assisting leaving group. *Angew. Chem. - Int. Ed.* 46 (25), 4726–4728. doi:10.1002/anie.200700854

Paterson, I., Dalby, S. M., Roberts, J. C., Naylor, G. J., Guzmán, E. A., Isbrucker, R., et al. (2011). Leiodermatolide, a potent antimitotic macrolide from the marine sponge Leiodermatium sp. *Angewandte Chemie Int. Ed. Engl.* 50 (14), 3219–3223. doi:10.1002/ANIE.201007719

Pellissier, H. (2006). Asymmetric domino reactions. Part A: reactions based on the use of chiral auxiliaries. *Tetrahedron* 62 (8), 1619–1665. doi:10.1016/j.tet.2016.04.053

Pellissier, H. (2016). Recent developments in organocatalytic dynamic kinetic resolution. *Tetrahedron* 72 (23), 3133–3150. doi:10.1016/j.tet.2016.04.053

Ponomarenko, V. A., and Mironov, V. F. (1954). Synthesis of some alkenyl- and alkylsilanes and their derivatives. *Bull. Acad. Sci. USSR Div. Chem. Sci.* 3 (3), 423–427. doi:10.1007/BF01167820

Ramirez, A., and Garcia-Rubio, S. (2005). Current progress in the chemistry and pharmacology of akuammiline alkaloids. *Curr. Med. Chem.* 10 (18), 1891–1915. doi:10.2174/0929867033457016

Roberts, D. D., and McLaughlin, M. G. (2022). Strategic applications of the β-silicon effect. *Adv. Synthesis and Catal.* 364 (14), 2307–2332. doi:10.1002/adsc.202200237

Rowley, M., Tsukamoto, M., and Kishi, Y. (1989). Total synthesis of (+)-Ophiobolin C. *J. Am. Chem. Soc.* 111 (7), 2735–2737. doi:10.1021/ja00189a069

Sabot, C., Guérard, K. C., and Canesi, S. (2009). Concise total synthesis of (±)-aspidospermidine via an oxidative Hosomi-Sakurai process. *Chem. Commun.* 20, 2941–2943. doi:10.1039/B903530C

Sai, M., and Yamamoto, H. (2015). Chiral brønsted acid as a true catalyst: asymmetric Mukaiyama aldol and hosomi–sakurai allylation reactions. *J. Am. Chem. Soc.* 137 (22), 7091–7094. doi:10.1021/jacs.5b04168

Saito, T., Awad, J. M., and Zhang, W. (2023). Synthetic studies on tetracyclic diquinane lycopodium alkaloids magellanine, magellaninone and paniculatine. *Molecules* 28 (3), 1501–1357. doi:10.3390/molecules28031501

Saitoh, T., Suzuki, T., Sugimoto, M., Hagiwara, H., and Hoshi, T. (2003). Total synthesis of (+)-laurallene. *Tetrahedron Lett.* 44 (15), 3175–3178. doi:10.1016/S0040-4039(03)00432-5

Sakai, Y., Tsujita, T., Akiyama, T., Yoshida, T., Mizukami, T., Akinaga, S., et al. (2002). GEX1 compounds, novel antitumor antibiotics related to herboxidiene, produced by Streptomyces sp. II. The effects on cell cycle progression and gene expression. *J. Antibiotics* 55 (10), 863–872. doi:10.7164/antibiotics.55.863

Santos, C. M. M., and Silva, A. M. S. (2018). Six-membered ring systems: with O and/or S atoms. *Prog. Heterocycl. Chem.* 30 (22), 473–532. doi:10.1016/B978-0-323-98410-2.00015-1

Schäfers, F., Dutta, S., Kleinmans, R., Mück-Lichtenfeld, C., and Glorius, F. (2022). Asymmetric addition of allylsilanes to aldehydes: a Cr/photoredox dual catalytic approach complementing the hosomi-sakurai reaction. *ACS Catal.* 12 (19), 12281–12290. doi:10.1021/acscatal.2c03960

Schmidt, K., Riese, U., Li, Z., and Hamburger, M. (2003). Novel tetramic acids and pyridone alkaloids, militarinones B, C, and D, from the insect pathogenic fungus Paecilomyces militaris. *J. Nat. Prod.* 66 (3), 378–383. doi:10.1021/np020430y

Schreyer, L., Properzi, R., and List, B. (2019). IDPi catalysis. *Angew. Chem. Int. Ed.* 58 (37), 12761–12777. doi:10.1002/anie.201900932

Schweig, A., Weidner, U., and Manuel, G. (1974). Theory and application of photoelectron spectroscopy. *J. Organomet. Chem.* 67 (1), C4–C6. doi:10.1016/S0022-328X(00)93659-3

Sha, C. K., Lee, F. K., and Chang, C. J. (1999). Tandem radical cyclizations initiated with α-carbonyl Radicals: first total synthesis of (+)-Paniculatine. *J. Am. Chem. Soc.* 121 (42), 9875–9876. doi:10.1021/ja992315o

Shao, H., Ma, Z. H., Cheng, Y. Y., Guo, X. F., Sun, Y. K., Liu, W. J., et al. (2024). Bioinspired total synthesis of Cephalotaxus diterpenoids and their structural analogues. *Angew. Chem. Int. Ed.* 63 (22), 2931–2948. doi:10.1002/ange.202402931

Sharpless, K. B., and Michaelson, R. C. (1973). High stereo- and regioselectivities in the transition metal catalyzed epoxidations of olefinic alcohols by tert-butyl hydroperoxide. *J. Am. Chem. Soc.* 95 (18), 6136–6137. doi:10.1021/ja00799a061

Shen, Q., Wang, L., Zhou, H., Jiang, H. D., Yu, L. S., and Zeng, S. (2013). Stereoselective binding of chiral drugs to plasma proteins. *Acta Pharmacol. Sin.* 34 (8), 998–1006. doi:10.1038/aps.2013.78

Shing, T. K. M., and Li, L. H. (1997). Asymmetric Hosomi - Sakurai reaction of allylsilanes containing arabinose-derived alcohols as chiral auxiliaries. *J. Org. Chem.* 62 (5), 1230–1233. doi:10.1021/jo962240w

Shingo, Y., Kunihiko, F., Reiko, W., Motomu, K., and Masakatsu, S. (2002). A general catalytic allylation using allyltrimethoxysilane. *J. Am. Chem. Soc.* 124 (23), 6536–6537. doi:10.1021/ja0262582

Shirley, H. J., Jamieson, M. L., Brimble, M. A., and Bray, C. D. (2018). A new family of sesterterpenoids isolated around the Pacific Rim. *Nat. Product. Rep.* 35 (3), 210–219. doi:10.1039/C7NP00049A

Siengalewicz, P., Mulzer, J., and Rinner, U. (2013). Lycopodium alkaloids – synthetic highlights and recent developments. *Alkaloids Chem. Biol.* 72 (22), 1–151. doi:10.1016/B978-0-12-407774-4.00001-7

Siu, Y. M., Roane, J., and Krische, M. J. (2021). Total synthesis of leiodermatolide A via transfer hydrogenative allylation, crotylation, and propargylation: polyketide construction beyond discrete allyl- or allenylmetal reagents. *J. Am. Chem. Soc.* 143 (28), 10590–10595. doi:10.1021/JACS.1C06062

Smith, A. B., Han, Q., Breslin, P. A. S., and Beauchamp, G. K. (2005). Synthesis and assignment of absolute configuration of (-)-oleocanthal: a potent, naturally occurring non-steroidal anti-inflammatory and anti-oxidant agent derived from extra virgin olive oils. *Org. Lett.* 7 (22), 5075–5078. doi:10.1021/ol052106a

Smith, N. D., Kocienski, P. J., and Street, S. D. A. (1996). A synthesis of (+)-Herboxidiene A. *Synthesis* 5, 652–666. doi:10.1055/s-1996-4254

Song, F., Garner, A. L., and Koide, K. (2007). A highly sensitive fluorescent sensor for palladium based on the allylic oxidative insertion mechanism. *J. Am. Chem. Soc.* 129 (41), 12354–12355. doi:10.1021/ja073910q

Stamos, D. P., Chen, S. S., and Kishi, Y. (1997). New synthetic route to the C.14-C.38 segment of halichondrins. *J. Org. Chem.* 62 (22), 7552–7553. doi:10.1021/jo971713b

Stankevich, K. S., and Cook, M. J. (2023). The Hosomi-Sakurai allylation in carbocyclization reactions. *Tetrahedron Lett.* 121 (2), 154415–154422. doi:10.1016/j.tetlet.2023.154415

Stanton, G. R., Johnson, C. N., and Walsh, P. J. (2010). Overriding felkin control: a general method for highly diastereoselective chelation-controlled additions to α-silyloxy aldehydes. *J. Am. Chem. Soc.* 132 (12), 4399–4408. doi:10.1021/ja910717p

Stepanyan, S., Burkert, V. D., Elouadrhiri, L., Adams, G. S., Anciant, E., Anghinolfi, M., et al. (2001). Observation of exclusive deeply virtual compton scattering in polarized electron beam asymmetry measurements. *APS* 87 (18), 182002. doi:10.1103/PhysRevLett.87.182002

Stork, G., and Dolfini, J. E. (1963). The Total Synthesis of *dl*-Aspidospermine and of dl-Quebrachamine. *J. Am. Chem. Soc.* 85 (18), 2872–2873. doi:10.1021/ja00901a061

Sumino, S., Uno, M., Huang, H. J., Wu, Y. K., and Ryu, I. (2018). Palladium/Light induced radical alkenylation and allylation of alkyl iodides using alkenyl and allylic sulfones. *Org. Lett.* 20 (4), 1078–1081. doi:10.1021/acs.orglett.7b04050

Suzuki, T., Koizumi, K., Suzuki, M., and Kurosawa, E. (1983). Kumausallene, A new bromoallene from the marine red alga *Laurencia Nipponica Yamada*. *Chem. Lett.* 12 (10), 1639–1642. doi:10.1246/CL.1983.1639

Takahashi, K., Akao, R., and Honda, T. (2009). Efficient diastereoselective synthesis of trifarane-type sesquiterpenes, trifarienols A and B. *J. Org. Chem.* 74 (9), 3424–3429. doi:10.1021/jo900369t

Tanaka, S., Yamamoto, H., Nozaki, H., Sharpless, K. B., Michaelson, R. C., and Cutting, J. D. (1974). Stereoselective epoxidations of acyclic allylic alcohols by transition metal-hydroperoxide reagents. Synthesis of *dl*-C18 cecropia juvenile hormone from farnesol. *J. Am. Chem. Soc.* 96 (16), 5254–5255. doi:10.1021/ja00823a042

Teng, Y., Zhang, H., Zhou, J., Zhan, G., and Yao, G. (2018). Hebecarposides A-K, antiproliferative lanostane-type triterpene glycosides from the leaves of Lyonia ovalifolia var. hebecarpa. *Phytochemistry* 151, 32–41. doi:10.1016/J.PHYTOCHEM.2018.03.012

Thirupathi, B., and Mohapatra, D. K. (2016). Gold-catalyzed Hosomi-Sakurai type reaction for the total synthesis of herboxidiene. *Org. Biomol. Chem.* 14 (26), 6212–6224. doi:10.1039/C6OB00321D

Tietze, L. F., Hölsken, S., Adrio, J., Kinzel, T., and Wegner, C. (2004). Facial-selective allylation of methyl ketones for the asymmetric synthesis of tertiary homoallylic ethers. *Synthesis*, 23, 2236–2239. doi:10.1002/1521-3765(20010316)7:63.0

Tietze, L. F., Schiemann, K., and Wegner, C. (1995). Enantioselective synthesis of tertiary homoallylic alcohols via diastereoselective addition of allylsilanes to ketones. *J. Am. Chem. Soc.* 117 (21), 5851–5852. doi:10.1021/ja00126a025

Tori, M., Hisazumi, K., Wada, T., Sono, M., and Nakashima, K. (1999). Total synthesis of optically active liverwort sesquiterpenes, trifarienols a and B, using phenylethylamine as a chiral auxiliary. *Tetrahedron Asymmetry* 10 (5), 961–971. doi:10.1016/S0957-4166(99)00067-1

Tori, M., Makino, C., Hisazumi, K., Sono, M., and Nakashima, K. (2001). Synthesis of a homochiral ketone having a pinguisane skeleton using phenylethylamine as a chiral auxiliary: a formal total synthesis of deoxopinguisone. *Tetrahedron Asymmetry* 12 (2), 301–307. doi:10.1016/S0957-4166(01)00041-6

Trost, B. M. (2015). Metal catalyzed allylic alkylation: its development in the Trost laboratories. *Tetrahedron* 71 (35), 5708–5733. doi:10.1016/j.tet.2015.06.044

Trost, B. M., Godleski, S. A., and Genet, J. P. (1978). A total synthesis of racemic and optically active ibogamine. Utilization and mechanism of a new silver ion assisted palladium catalyzed cyclization. *Chem. Inf.* 9 (38), 3930–3931. doi:10.1021/ja00480a047

Trost, B. M., and Osipov, M. (2015). Recent advances on the total syntheses of communesin alkaloids and perophoramidine. *Chem. - A Eur. J.* 21 (46), 16318–16343. doi:10.1002/chem.201501735

Trost, B. M., and Van Vranken, D. L. (1996). Asymmetric transition metal-catalyzed allylic alkylations. *Chem. Rev.* 96 (1), 395–422. doi:10.1021/cr9409804

Tsuji, J. (1969). Carbon—carbon bond formation via palladium complexes. *Accounts Chem. Res.* 2 (5), 144–152. doi:10.1021/ar50017a003

Tsuji, J. (1986a). 25 Years in the organic chemistry of palladium. *J. Organomet. Chem.* 300 (1–2), 281–305. doi:10.1016/0022-328X(86)84066-9

Tsuji, J. (1986b). New general synthetic methods involving π-allylpalladium complexes as intermediates and neutral reaction conditions. *Tetrahedron* 42 (16), 4361–4401. doi:10.1016/S0040-4020(01)87277-X

Tsuji, J., and Takahashi, H. (1965). Organic syntheses by means of noble metal compounds. XII.1 reaction of the cyclooctadiene-palladium chloride complex with ethyl malonate. *J. Am. Chem. Soc.* 87 (14), 3275–3276. doi:10.1021/ja01092a067

Tsuna, K., Noguchi, N., and Nakada, M. (2013). Enantioselective total synthesis of (+)-ophiobolin A. *Chem. - A Eur. J.* 19 (17), 5476–5486. doi:10.1002/chem.201204119

Uyehara, T., Kabasawa, Y., and Kato, T. (1986). Rearrangement approaches to cyclic skeletons. IV. The total synthesis of (±)-Pinguisone and (±)-Deoxopinguisone based on photochemical [1,3] acyl migration of a bicyclo[3.2.2]non-6-en-2-one. *Bull. Chem. Soc. Jpn.* 59 (8), 2521–2528. doi:10.1246/bcsj.59.2521

Uyehara, T., Kabasawa, Y., Kato, T., and Furuta, T. (1985). Photochemical rearrangement approach to the total synthesis of (±)-pinguisone and (±)-deoxopinguisone. *Tetrahedron Lett.* 26 (19), 2343–2346. doi:10.1016/S0040-4039(00)95094-9

Veenstra, S. J., and Schmid, P. (1997). One-pot synthesis of protected homoallyl amines. *Tetrahedron Lett.* 38 (6), 997–1000. doi:10.1016/S0040-4039(96)02458-6

Verbitski, S. M., Mayne, C. L., Davis, R. A., Concepcion, G. P., and Ireland, C. M. (2002). Isolation, structure determination, and biological activity of a novel alkaloid, perophoramidine, from the Philippine ascidian Perophora namei. *J. Org. Chem.* 67 (20), 7124–7126. doi:10.1021/jo026012f

Wada, K., Kogure, N., Kitajima, M., and Takayama, H. (2019). Concise asymmetric total synthesis of lycopodine and flabelliformine via cascade cyclization reaction. *Tetrahedron Lett.* 60 (2), 187–190. doi:10.1016/j.tetlet.2018.12.007

Wadamoto, M., Ozasa, N., Yanagisawa, A., and Yamamoto, H. (2003). BINAP/AgOTf/KF/18-crown-6 as new bifunctional catalysts for asymmetric Sakurai-Hosomi allylation and Mukaiyama aldol reaction. *J. Org. Chem.* 68 (14), 5593–5601. doi:10.1021/jo020691c

Wakamiya, Y., Ebine, M., Matsumori, N., and Oishi, T. (2020). Total synthesis of amphidinol 3: a general strategy for synthesizing amphidinol analogues and structure-activity relationship study. *J. Am. Chem. Soc.* 142 (7), 3472–3478. doi:10.1021/jacs.9b11789

Wang, D., Wang, Z. G., Wang, M. W., Chen, Y. J., Liu, L., and Zhu, Y. (1999). Asymmetric allylation of aldehydes and glyoxylates through `C-centered' chiral pentacoordinate allylsilicates or promoted by Lewis acid. *Tetrahedron Asymmetry* 10 (2), 327–338. doi:10.1016/S0957-4166(99)00004-X

Wang, H., Liu, Y., Zhang, H., Yang, B., He, H., and Gao, S. (2023). Asymmetric total synthesis of Cephalotaxus diterpenoids: cephinoid P, cephafortoid A, 14-epi-Cephafortoid A and Fortalpinoids M-N, P. *J. Am. Chem. Soc.* 145 (31), 16988–16994. doi:10.1021/jacs.3c05455

Wang, J., and Pagenkopf, B. L. (2007). First total synthesis and structural reassignment of (-)-aplysiallene. *Org. Lett.* 9 (18), 3703–3706. doi:10.1021/ol701797e

Wang, L. Q., Ding, B. Y., Qin, G. W., Lin, G., and Cheng, K. F. (1998). Grayanoids from pieris formosa1Part 2 in the series: "chemical studies on Ericaceae Plants".1. *Phytochemistry* 49 (7), 2045–2048. doi:10.1016/S0031-9422(98)00410-5

Wang, M., Tietjen, I., Chen, M., Williams, D. E., Daoust, J., Brockman, M. A., et al. (2016). Sesterterpenoids isolated from the sponge phorbas sp. activate latent HIV-1 provirus expression. *J. Org. Chem.* 81 (22), 11324–11334. doi:10.1021/acs.joc.6b02312

Werness, J. B., and Tang, W. (2011). Stereoselective total synthesis of (-)-kumausallene. *Org. Lett.* 13 (14), 3664–3666. doi:10.1021/ol201477u

Werness, J. B., Zhang, W., and Tang, W. (2013). Stereoselective addition of halogen to conjugated enynes and its application in the total synthesis of (−)-Kumausallene. *Strategies Tactics Org. Synthesis* 9 (6), 275–291. doi:10.1016/B978-0-08-099362-1.00010-2

Westermann, B., Scharmann, H. G., and Kortmann, I. (1993). Ple-catalyzed resolution of α-substituted β-ketoesters application to the synthesis of (+)-nitraniine and (-)-Isonitramine. *Tetrahedron Asymmetry* 4 (10), 2119–2122. doi:10.1016/S0957-4166(00)80054-3

Wilkie, R. P., Neal, A. R., Johnston, C. A., Voute, N., Lancefield, C. S., Stell, M. D., et al. (2016). Total synthesis of dehaloperophoramidine using a highly diastereoselective Hosomi-Sakurai reaction. *Chem. Commun.* 52 (71), 10747–10750. doi:10.1039/C6CC05747K

Williams, D. R., and Meyer, K. G. (2001). Total synthesis of (+)-Amphidinolide K. *J. Am. Chem. Soc.* 123 (4), 765–766. doi:10.1021/ja005644l

Williams, D. R., Myers, B. J., Mi, L., and Binder, R. J. (2013). Studies for the total synthesis of amphidinolide P. *J. Org. Chem.* 78 (10), 4762–4778. doi:10.1021/jo4002382

Wu, X.De, Li, X. N., Peng, L. Y., and Zhao, Q. S. (2020). Huperserratines A and B, two macrocyclic lycopodium alkaloids with an unusual skeleton from Huperzia serrata. *J. Org. Chem.* 85 (10), 6803–6807. doi:10.1021/acs.joc.0c00623

Xing, S. H., Zhu, C. X., Zhang, R., and An, L. (2014). Huperzine A in the treatment of Alzheimer's disease and vascular dementia: a meta-analysis. *Evid. Based Complement. Altern. Med.* 2014 (2), 363985–363997. doi:10.1155/2014/363985

Xu, S. S., Cai, Z. Y., Qu, Z. W., Yang, R. M., Cai, Y. L., Wang, G. Q., et al. (1999). Huperzine-A in capsules and tablets for treating patients with Alzheimer disease. *Clin. Trial* 20 (6), 486–490.

Yadav, J. S., Reddy, B. V. S., Reddy, M. S., and Parimala, G. (2003). InBr3-Catalyzed alkynylation and allylation of acid chlorides: a facile synthesis of alkynyl and allyl ketones. *Synthesis* 23 (15), 2390–2394. doi:10.1055/s-2003-42438

Yamamoto, Y., and Asao, N. (1993). Selective reactions using allylic metals. *Chem. Rev.* 93 (6), 2207–2293. doi:10.1021/cr00022a010

Yamamoto, Y., and Sasaki, N. (1989). "The stereochemistry of the Sakurai reaction," in *Chemical bonds–better ways to make them and break them* (Elsevier Science Publishers B.V), 363–441.

Yamasaki, S., Fujii, K., Wada, R., Kanai, M., and Shibasaki, M. (2002). A general catalytic allylation using allyltrimethoxysilane. *J. Am. Chem. Soc.* 124 (23), 6536–6537. doi:10.1021/ja0262582

Yang, H., and Carter, R. G. (2010). Development of an enantioselective route toward the lycopodium alkaloids: total synthesis of lycopodine. *J. Org. Chem.* 75 (15), 4929–4938. doi:10.1021/jo100916x

Yang, J., Park, Y., Yang, S., Lee, G., Ha, M. W., Kim, M. H., et al. (2021). Enantioselective total synthesis of Nitraria alkaloids: (+)-Nitramine, (+)-Isonitramine, (-)-Isonitramine, and (-)-Sibirine via asymmetric phase-transfer catalytic α-allylations of α-carboxylactams. *J. Org. Chem.* 86 (6), 4375–4390. doi:10.1021/acs.joc.0c02573

Yao, H., Zhou, N., Zhang, Z., Guan, W., Wang, H., and Cheng, H. (2020). Recent developments in syntheses of alotaketals and phorbaketals. *Tetrahedron Lett.* 61 (8), 151480–151510. doi:10.1016/j.tetlet.2019.151480

Yotsu-Yamashita, M., Yamagishi, Y., and Yasumoto, T. (1995). 5,6,11-trideoxytetrodotoxin from the puffer fish, fugu poecilonotus. *Tetrahedron Lett.* 36 (51), 9329–9332. doi:10.1016/0040-4039(95)02020-P

Yu, B. W., Chen, J. Y., Wang, Y. P., Cheng, K. F., Li, X. Y., and Qin, G. W. (2002). Alkaloids from menispermum dauricum. *Phytochemistry* 61 (4), 439–442. doi:10.1016/S0031-9422(02)00162-0

Yun, Z., and Panek, J. S. (2007). Total synthesis of herboxidiene/GEX 1A. *Org. Lett.* 9 (16), 3141–3143. doi:10.1021/ol701427k

Zhang, L. C., Sakurai, H., and Kira, M. (1997). Enantioselective allylation of aldehydes using tartrate ester modified allylsilanes. *Chem. Lett.* 26 (2), 129–130. doi:10.1246/cl.1997.129

Zhang, R., Tang, C., Li, Y., Ke, C. Q., Lin, G., Xie, H., et al. (2018). The first phytochemical investigation of Rhododendron websterianum: triterpenoids and their cytotoxic activity. *Phytochem. Lett.* 25, 43–46. doi:10.1016/J.PHYTOL.2018.03.015

Zhang, Z. R., Zhong, J. D., Li, H. M., Li, H. Z., Li, R. T., and Deng, X. L. (2012). Two new grayanane diterpenoids from the flowers of Rhododendron molle. *J. Asian Nat. Prod. Res.* 14 (8), 764–768. doi:10.1080/10286020.2012.691095

Zhao, D. R., Su, L. H., Li, R. T., Chen, X. Q., and Li, H. M. (2018). Chemical constituents from the twigs and leaves of Lyonia ovalifolia. *Biochem. Syst. Ecol.* 78, 1–4. doi:10.1016/J.BSE.2018.02.006

Zhao, S., Sirasani, G., and Andrade, R. B. (2021). Aspidosperma and strychnos alkaloids: chemistry and biology. *Alkaloids Chem. Biol.* 86 (12), 1–143. doi:10.1016/bs.alkal.2021.05.001

Zhou, C., Li, X., Li, H., and Li, R. (2012). Chemical constituents from the leaves of Craibiodendron yunnanense. *Biochem. Syst. Ecol.* 45, 179–182. doi:10.1016/J.BSE.2012.07.004

Zhou, S. Z., Yao, S., Tang, C., Ke, C., Li, L., Lin, G., et al. (2014). Diterpenoids from the flowers of Rhododendron molle. *J. Nat. Prod.* 77 (5), 1185–1192. doi:10.1021/NP500074Q

Zuo, Z., and Ma, D. (2011). Enantioselective total syntheses of communesins A and B. *Angew. Chem. - Int. Ed.* 50 (50), 12008–12011. doi:10.1002/anie.201106205

Glossary

AHSR	Asymmetric Hosomi-Sakurai reaction
AIBN	Azobisisobutyronitrile
AD	Alzheimer's disease
aSH	aza-Hosomi-Sakurai
ATP	adenosine triphosphate
BINAP	2,2′-bis(diphenylphosphino)-1,1′-binaphthyl
BPO	Benzoyl peroxide
CAB	Chiral (acyloxy)borane
cAMP	cyclic adenosine monophosphate
DCM	Dichloromethane
DIFLUOROPHOS	(2,2,2′,2′-Tetrafluoro-4,4′-bi-1,3-benzodioxole-5,5′-diyl) bis(diphenylphosphine)
DMF	Dimethylformamide
DMPU	N,N′-Dimethylpropyleneurea
DNA	Deoxyribonucleic Acid
EC_{50}	half maximal effective concentration
ED_{50}	median effective dose
GAP	GTPase-accelerating proteins
GETFund	Ghana Education Trust Fund
GNPC	Ghana National Petroleum Corporation
HDA	Hetero-Diels–Alder
HEK	human embryonic kidney cells
HFIP	Hexafluoroisopropanol
HIV	Human immunodeficiency virus
HSC	Hosomi-Sakurai cyclisation
HSR	Hosomi-Sakurai reaction
IC_{50}	Half-maximal inhibitory concentration
LED	light-emitting diode
MOM	Methoxymethyl ether
NMR	Nuclear Magnetic Resonance spectroscopy
NOE	Nuclear Overhauser effect
RNA	Ribonucleic acid
STAT3	signal transducer and activator of transcription 3
TBAF	tetrabutylammonium fluoride
TBDPS	tert-butyldiphenylsilyl
TFE	trifluoroethanol
THF	tetrahydrofuran
TMS	trimethylsilyl
TMSI	trimethylsilyl iodide
TMSO	Trimethylsulfoxonium
TMSOT	Trimethylsilyl trifluoromethanesulfonate

frontiers | Frontiers in Chemistry

TYPE Original Research
PUBLISHED 04 April 2025
DOI 10.3389/fchem.2025.1571646

Check for updates

OPEN ACCESS

EDITED BY
Naohiko Yoshikai,
Tohoku University, Japan

REVIEWED BY
Cüneyt Türkeş,
Erzincan Binali Yıldırım University, Türkiye
Sakkarapalayam Mahalingam,
Purdue University, United States

*CORRESPONDENCE
Devendra Pratap Rao,
devendrapratapprao@yahoo.com
Stefan Bräse,
stefan.braese@kit.edu

RECEIVED 05 February 2025
ACCEPTED 11 March 2025
PUBLISHED 04 April 2025

CITATION
Hashem H, Abdelfattah S, Hassan HM, Al-Emam A, Alqarni M, Alotaibi G, Radwan IT, Kaur K, Rao DP, Bräse S and Alkhammash A (2025) Discovery of a novel 4-pyridyl SLC-0111 analog targeting tumor-associated carbonic anhydrase isoform IX through tail-based design approach with potent anticancer activity. *Front. Chem.* 13:1571646. doi: 10.3389/fchem.2025.1571646

COPYRIGHT
© 2025 Hashem, Abdelfattah, Hassan, Al-Emam, Alqarni, Alotaibi, Radwan, Kaur, Rao, Bräse and Alkhammash. This is an open-access article distributed under the terms of the Creative Commons Attribution License (CC BY). The use, distribution or reproduction in other forums is permitted, provided the original author(s) and the copyright owner(s) are credited and that the original publication in this journal is cited, in accordance with accepted academic practice. No use, distribution or reproduction is permitted which does not comply with these terms.

Discovery of a novel 4-pyridyl SLC-0111 analog targeting tumor-associated carbonic anhydrase isoform IX through tail-based design approach with potent anticancer activity

Hamada Hashem[1], Shadwa Abdelfattah[2], Hesham M. Hassan[3], Ahmed Al-Emam[3], Mohammed Alqarni[4], Ghallab Alotaibi[5], Ibrahim Taha Radwan[6], Kirandeep Kaur[7], Devendra Pratap Rao[8]*, Stefan Bräse[9]* and Abdullah Alkhammash[5]

[1]Pharmaceutical Chemistry Department, Faculty of Pharmacy, Sohag University, Sohag, Egypt, [2]Department of Pharmaceutics and Industrial Pharmacy, Faculty of Pharmacy, Merit University (MUE), Sohag, Egypt, [3]Department of Pathology, College of Medicine, King Khalid University, Asir, Saudi Arabia, [4]Department of Pharmaceutical chemistry, College of Pharmacy, Taif University, Taif, Saudi Arabia, [5]Department of Pharmacology, College of Pharmacy, Shaqra University, Shaqra, Saudi Arabia, [6]Supplementary General Sciences Department, Faculty of Oral and Dental Medicine, Future University in Egypt, Cairo, Egypt, [7]Department of Chemistry, Maharaja Ranjit Singh Punjab Technical University, Bathinda, Punjab, India, [8]Coordination Chemistry Laboratory, Department of Chemistry, Dayanand Anglo-Vedic (PG) College, Kanpur, Uttar Pradesh, India, [9]Institute of Biological and Chemical Systems, Functional Molecular Systems (IBCS-FMS), Karlsruhe Institute of Technology (KIT), Karlsruhe, Germany

Introduction: Carbonic anhydrase IX (CA IX) is a tumor-associated enzyme involved in cancer progression and survival. Targeting CA IX with selective inhibitors like SLC-0111 has shown therapeutic potential. This study aimed to develop a novel 4-pyridyl analog (**Pyr**) of SLC-0111 with enhanced anticancer activity.

Methods: **Pyr** was synthesized using a tail-based design and characterized by NMR. Its cytotoxicity was tested against cancer and normal cell lines. CA inhibition, cell cycle effects, apoptosis induction, and protein expression changes were evaluated. Molecular docking and ADMET predictions assessed binding and drug-like properties.

Results and Discussion: **Pyr** showed selective cytotoxicity toward cancer cells and potent CA IX inhibition. It induced G0/G1 arrest, apoptosis, and modulated p53, Bax, and Bcl-2 levels. Docking confirmed strong CA IX binding, and ADMET analysis indicated good oral bioavailability. These results support **Pyr** as a promising anticancer candidate.

KEYWORDS

sulphonamide, SLC-0111, carbonic anhydrase, cytotoxicity, apoptosis

1 Introduction

Cancer remains one of the most challenging health conditions worldwide, characterized by uncontrolled cell growth, invasion into surrounding tissues, and potential metastasis to distant organs (Wikipedia, 2024). It affects millions of lives annually, highlighting the urgent need for effective therapeutic strategies (WHO, 2024). Advances in cancer biology have paved the way for developing anticancer agents targeting various cellular and molecular mechanisms involved in tumor initiation, progression, and metastasis (Doostmohammadi et al., 2024). Current treatments, including chemotherapy, targeted therapy, and immunotherapy, often aim to disrupt specific pathways critical to cancer survival and growth (Yang et al., 2024; P. Inc, 2024; Tilsed et al., 2022). Despite significant progress, the emergence of drug resistance and adverse side effects highlight the need for novel therapeutic targets and agents with improved efficacy and safety profiles (Targeted Cancer Therapy, 2024; Tian et al., 2024).

Among the emerging molecular targets in cancer therapy, carbonic anhydrases (CAs) have gained attention due to their critical role in maintaining the pH balance within tumor cells and their microenvironment (Pastorekova and Gillies, 2019). Carbonic anhydrases are zinc metalloenzymes with 15 known isoforms in humans, of which CA IX and CA XII are overexpressed in hypoxic tumor cells (Baranauskienė et al., 2019). These isoforms play a pivotal role in regulating intracellular and extracellular pH by catalyzing the reversible hydration of carbon dioxide to bicarbonate and protons, enabling cancer cells to thrive in acidic and hypoxic conditions (Sedlakova et al., 2014). By supporting an acidic extracellular environment, CA IX and CA XII facilitate tumor progression, invasion, and immune evasion. Consequently, carbonic anhydrase inhibitors (CAIs) have emerged as promising anticancer agents, selectively targeting tumor-associated isoforms to disrupt these critical processes (Merkx et al., 2021). Recent studies have demonstrated the potential of CAI to inhibit tumor growth, enhance the effectiveness of conventional chemotherapeutics, and overcome resistance mechanisms (Kalinin et al., 2021).

SLC-0111, a ureido-substituted benzenesulfonamide, is a potent inhibitor of CA IX, disrupting pH regulation in tumor cells and impairing their survival and invasiveness (MedChemExpress, 2024). Preclinical studies have demonstrated that SLC-0111 enhances the efficacy of chemotherapeutic agents such as cisplatin in head and neck squamous carcinoma models, leading to reduced tumor growth and invasion (Sarnella et al., 2022). Additionally, SLC-0111 has progressed to Phase I clinical trials, where it was evaluated for safety and tolerability in patients with advanced solid tumors (McDonald et al., 2020).

Building upon the success of SLC-0111, researchers have developed various analogs to enhance selectivity and potency against tumor-associated carbonic anhydrase (CA) isoforms (Angeli et al., 2023). For instance, benzofuran-based derivatives have been synthesized, exhibiting selective inhibition of CA IX and CA XII (Figure 1) and demonstrating promising anticancer activity, with compound **1** displaying significant inhibitory activity against CA IX with a Ki value of 7.1 nM (Shaldam et al., 2021). Similarly, thiazole and thiadiazole-based analogs have shown substantial inhibitory activity against tumor-associated CA isoforms with thiadiazole analog 2 exhibited remarkable Ki values of 7.9 and 9.9 nM for CA IX and CA XII inhibition, respectively (Abo-Ashour et al., 2019). These derivatives have effectively suppressed tumor cell proliferation and migration, underscoring their promise as therapeutic agents in cancer treatment by targeting carbonic anhydrases.

In parallel with the development of small molecule inhibitors targeting CA IX, immunotherapeutic strategies have also emerged as promising approaches for the treatment of CA IX-expressing tumors. Notably, bi-specific adapter molecules capable of engaging universal chimeric antigen receptor T (CAR-T) cells have been designed to facilitate the selective targeting of CA IX-positive tumor cells (Low et al., 2024). These adapters act as molecular bridges that redirect CAR-T cells to tumor sites while providing an additional layer of control, potentially reducing off-tumor toxicity and enhancing safety profiles. By enabling the specific recognition and elimination of hypoxic, CA IX-expressing tumor cells, these bi-specific adapters offer a novel immunotherapeutic avenue that could complement the effects of CA IX inhibitors and broaden the therapeutic landscape for solid tumors characterized by hypoxia and acidosis.

Inspired by these findings on SLC-0111 and its related analogs, we employed a tail approach to design and synthesize a new analog of SLC-0111, incorporating a 4-pyridyl moiety linked with sulfanilamide as the zinc-binding group. This analog was evaluated for its anticancer properties and inhibitory activity against four CA isoforms: CA I, II, IX, and XII. The design retained the zinc-binding sulfonamide motif and urea linker from SLC-0111 while introducing a 4-pyridyl moiety as a tail to enhance interactions with the hydrophobic region of the CA active site (Figure 2).

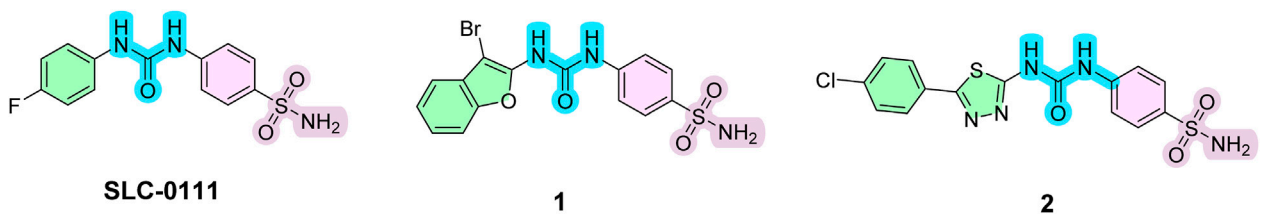


FIGURE 1
Examples of important inhibitors of tumor-associated carbonic anhydrase isoforms.

10.3389/fchem.2025.1571646

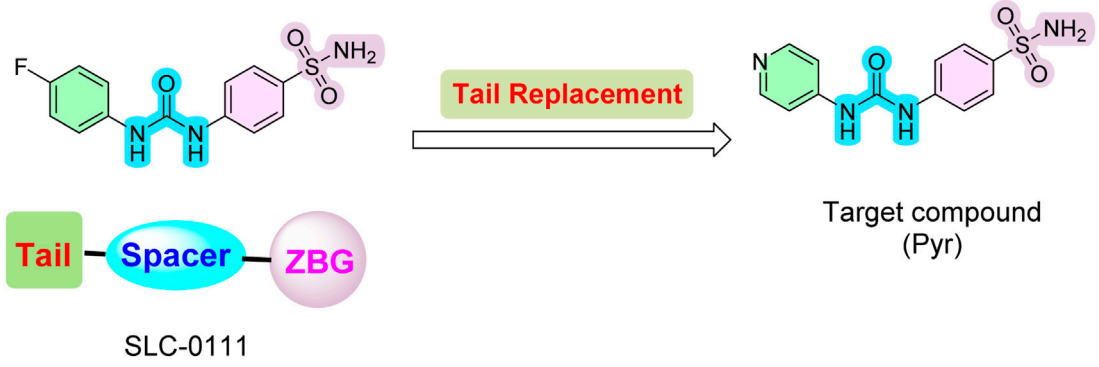
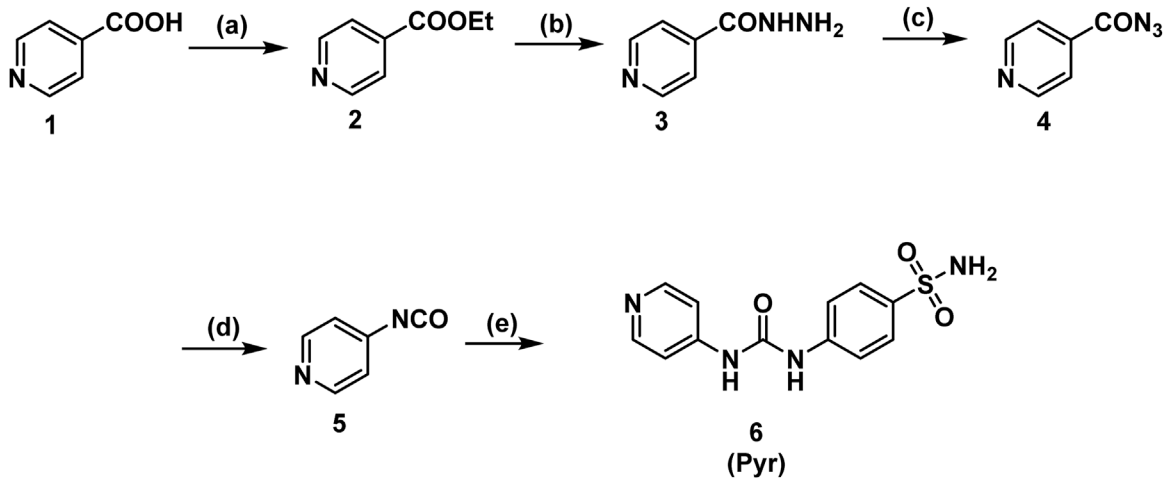


FIGURE 2
Design of novel SLC-0111 analog (**Pyr**).



SCHEME 1
Synthesis of the target compound (**Pyr**). Reagents and Conditions: (a) EtOH, H_2SO_4, reflux, 8 h; (b) hydrazine hydrate, EtOH, reflux, 18 h; (c) $NaNO_2$, HCl, 0°C, 1 h; (d) toluene, reflux, 1 h; (e) sulfanilamide, toluene, reflux, 2h.

2 Results and discussion

2.1 Chemistry

Scheme 1 illustrates the stepwise synthesis of a sulfonamide-based urea derivative starting from pyridine-4-carboxylic acid (isonicotinic acid). The synthesis begins with the Fischer esterification of isonicotinic acid, converting its carboxylic acid group into an ethyl ester using absolute ethanol in the presence of concentrated sulfuric acid as a catalyst. In the second step, the ethyl ester reacts with hydrazine hydrate, replacing the ethoxy group with a hydrazino group to form the corresponding hydrazide (Isoniazid). The hydrazide is then subjected to diazotization using sodium nitrite in the presence of hydrochloric acid, leading to the formation of the acyl azide intermediate. This reactive intermediate is key to the next transformation, the Curtius rearrangement, which is induced by heating the acyl azide in toluene. During this rearrangement, the azide undergoes nitrogen gas evolution (N_2) and acyl migration, forming an isocyanate

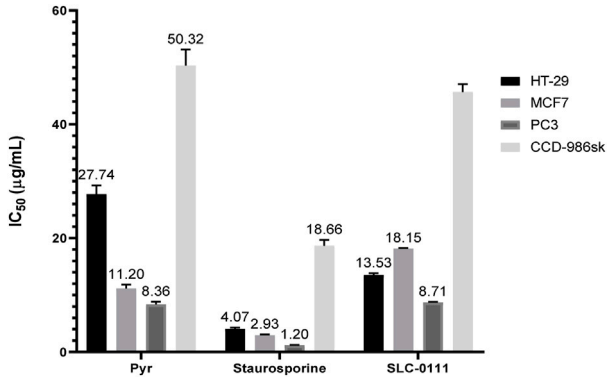


FIGURE 3
IC_{50} values (µg/mL) for **Pyr** and Staurosporine against HT-29, MCF7, PC3 cancer cells, and CCD-986sk normal cells. **Pyr** exhibited moderate cytotoxicity with better selectivity for cancer cells, while Staurosporine showed higher potency but less selectivity. Data are mean ± SEM.

TABLE 1 IC_{50} values (μg/mL) of Pyr and acetazolamide (AAZ) against CA isoforms I, II, IX, and XII. Data are expressed as mean ± SEM.

Compound	CA inhibition IC_{50} (μg/mL) ±SEM							
	CA I	R^2	CA II	R^2	CA IX	R^2	CA XII	R^2
Pyr	20.29 ± 0.92	0.9406	0.569 ± 0.03	0.9697	0.399 ± 0.02	0.9816	2.97 ± 0.17	0.9645
AAZ	0.367 ± 0.02	0.9782	0.153 ± 0.01	0.9615	0.105 ± 0.01	0.972	0.029 ± 0.001	0.9315
SLC-0111	1.36 ± 0.07	0.9935	0.498 ± 0.04	0.9767	0.048 ± 0.006	0.9642	0.096 ± 0.008	0.9873

TABLE 2 Effect of Pyr derivative on PC3 cell cycle distribution compared to DMSO-treated cells.

Compound	DNA content		
	% G0-G1	% S	% G2/M
Pyr/PC3	76.59	16.23	7.18
DMSO/PC3	53.84	28.66	17.50

intermediate. The highly reactive isocyanate is then reacted with sulfanilamide under heating in toluene to yield the final sulfonamide-based urea derivative **Pyr**. This step involves a nucleophilic attack by the amine group of sulfanilamide on the electrophilic carbon of the isocyanate group, forming the desired product.

The final compound, **Pyr**, was characterized using ^{1}H-NMR, ^{13}C-NMR, and elemental analysis. The ^{1}H-NMR spectrum confirms the structure of the compound with distinct peaks corresponding to its key protons. The urea moiety is represented by two singlets at 8.97 ppm and 9.10 ppm, confirming the presence of the urea hydrogens. The protons of the pyridine ring appear as two doublets at 8.34 ppm and 7.44 ppm, consistent with the expected splitting for this system. Similarly, the protons of the para-substituted benzene ring are represented by two doublets at 7.62 ppm and 7.73 ppm. The NH_2 group of the sulfonamide appears as a singlet at 7.24 ppm. In the ^{13}C-NMR spectrum, eight peaks are observed, consistent with the distinct carbon atoms in the molecule. Four peaks are assigned to the benzene ring carbons, while three peaks correspond to the pyridine ring carbons. The carbonyl carbon of the urea group is confirmed by a characteristic peak at 150.40 ppm, supporting the successful formation of the urea moiety. These findings from the NMR data align well with the proposed structure of the target compound.

2.2 Biological evaluation

2.2.1 Cell viability assay

Many sulfonamide-based compounds have shown promising cytotoxic activities (Güleç et al., 2024a; Güleç et al., 2024b) against various cancer cell lines. Accordingly, the cytotoxic activity of **Pyr** was evaluated against HT-29, MCF7, and PC3 cancer cell lines, as well as the normal CCD-986sk cell line. Based on the cell viability assay results shown in Figure 3, **Pyr** exhibited moderate cytotoxicity against the tested cancer cell lines (HT-29, MCF7, and PC3) with IC_{50} values of 27.74, 11.20, and 8.36 μg/mL, respectively, while showing significantly lower toxicity toward the normal cell line CCD-986sk (IC_{50} = 50.32 μg/mL), indicating good selectivity. Compared to the reference SLC-0111, Pyr demonstrated superior cytotoxicity against the MCF7 cell line (IC_{50} = 11.20 μg/mL vs. 18.15 μg/mL for SLC-0111) and comparable activity against the PC3 cell line (IC_{50} = 8.36 μg/mL vs. 8.71 μg/mL), whereas SLC-0111 exhibited better potency against the HT-29 cell line (IC_{50} = 13.53 μg/mL vs. 27.74 μg/mL for Pyr). Regarding safety, Pyr also showed slightly lower toxicity toward normal CCD-986sk cells (IC_{50} = 50.32 μg/mL) compared to SLC-0111 (IC_{50} = 45.70 μg/mL), highlighting its favorable selectivity profile. In contrast, the reference drug Staurosporine is significantly more potent across all cell lines, with much lower IC_{50} values for HT-29 (4.07 μg/mL), MCF7 (2.93 μg/mL), and PC3 (1.20 μg/mL). Still, it also exhibits considerable toxicity to normal cells (IC_{50} = 18.66 μg/mL), reflecting poor selectivity. These findings suggest that while Staurosporine is highly effective, its lack of selectivity limits its therapeutic potential. By contrast, with its selective cytotoxicity, superior or comparable efficacy to SLC-0111 in certain cancer cell lines, and reduced toxicity to normal cells, Pyr presents a more favorable profile for further development as an anti-cancer agent.

2.2.2 Evaluation of carbonic anhydrase I, II, IX, and XII inhibition

Sulfonamides are well-known inhibitors of carbonic anhydrase (CA) enzymes (Buza et al., 2024; Buza et al., 2023; Kakakhan et al., 2023) and have been widely studied for their potential therapeutic applications, particularly in cancer and other diseases. Given their significance as CA inhibitors, we evaluated **Pyr**'s inhibitory activity against various human carbonic anhydrase isoforms, specifically CA I, CA II, CA IX, and CA XII. The results in Table 1 present the IC_{50} values (μg/mL) of **Pyr** and the reference drugs acetazolamide (AAZ) and SLC-0111 against carbonic anhydrase (CA) isoforms I, II, IX, and XII. **Pyr** showed moderate inhibition of CA I (20.29 ± 0.92 μg/mL), CA II (0.569 ± 0.03 μg/mL) and CA XII (2.97 ± 0.17 μg/mL) with higher potency against the cancer-related isoform CA IX (0.399 ± 0.02 μg/mL). In comparison, AAZ, a standard carbonic anhydrase inhibitor, exhibited significantly lower IC_{50} values across all isoforms, with exceptional potency against CA II (0.153 ± 0.01 μg/mL), CA IX (0.105 ± 0.01 μg/mL), and CA XII (0.029 ± 0.001 μg/mL). Similarly, SLC-0111, a selective inhibitor of tumor-associated carbonic anhydrases, showed strong inhibition of CA IX (0.048 ± 0.006 μg/mL) and CA XII (0.096 ± 0.008 μg/mL). These results suggest that while **Pyr** is less potent than AAZ and SLC-0111 overall, it demonstrated selective inhibition of CA IX, a tumor-

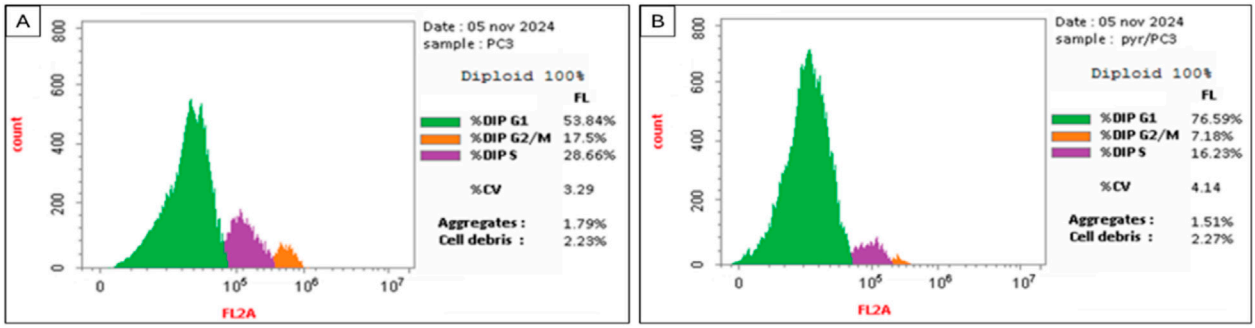


FIGURE 4
Effect of DMSO (Control, **(A)**) and **Pyr** (IC_{50}, 8.63 μg/mL, **(B)**) on cell accumulation across various phases of the cell cycle of prostate PC3 cancer cells.

TABLE 3 Effect of Pyr derivative on apoptosis and necrosis in PC3 cells compared to DMSO-treated cells.

Compound	Apoptosis			Necrosis
	Total	Early	Late	
Pyr/PC3	29.46	9.33	15.74	4.39
DMSO/PC3	2.39	0.42	0.15	1.82

associated isoform, indicating its potential as a targeted inhibitor for cancer-related applications.

2.2.3 Cell cycle analysis

The data in Table 2 and Figure 4 illustrate the impact of **Pyr** on the cell cycle distribution of PC3 cells compared to untreated cells (treated with DMSO as a control). Treatment of PC3 cells with **Pyr** significantly increased the percentage of cells in the G0-G1 phase (76.59%) compared to the control (53.84%), indicating a G0-G1 phase arrest. Correspondingly, the percentage of cells in the S phase decreased notably in **Pyr**-treated cells (16.23%) compared to the control (28.66%), suggesting inhibition of DNA synthesis and progression to the S phase. Furthermore, the percentage of cells in the G2/M phase was reduced in **Pyr**-treated cells (7.18%) compared to the control (17.50%), indicating impaired transition to mitosis. These results suggest that **Pyr** effectively induces cell cycle arrest at the G0-G1 phase in PC3 cells, thereby inhibiting cell proliferation.

2.2.4 Apoptosis assay

The data in Table 3 and Figure 5 highlight the effect of **Pyr** on apoptosis and necrosis in PC3 cells compared to untreated cells (DMSO-treated cells). Treatment of PC3 cells significantly increased total apoptosis to 29.46% compared to 2.39% in the untreated cells. This increase is driven by both early apoptosis (9.33%) and late apoptosis (15.74%), indicating that **Pyr** effectively triggers the apoptotic pathway in PC3 cells. Necrosis levels were also slightly elevated in **Pyr**-treated cells (4.39%) compared to the control (1.82%), though apoptosis remains the predominant mode of cell death. These findings suggest that **Pyr** induces substantial apoptotic cell death in PC3 cells, with minimal necrotic activity, highlighting its potential as an anti-cancer agent targeting apoptosis.

2.2.5 Effects of Pyr on p53, Bax and Bcl-2 protein expression levels

The effect of **Pyr** on the expression of pro-apoptotic (p53, Bax) and anti-apoptotic (Bcl-2) proteins in PC3 cells compared to untreated cells was studied. As shown in Table 4, **Pyr** treatment markedly increased the expression levels of p53 and Bax, while simultaneously reducing Bcl-2 levels when compared to the DMSO-treated control group. Specifically, **Pyr** treatment elevated p53 protein concentration to 1461.33 ± 10.00 pg/mL, corresponding to a 9.66-fold increase relative to control cells (151.33 ± 3.33 pg/mL). This substantial upregulation of p53 suggests the activation of a p53-dependent apoptotic pathway, which is known to play a critical role in tumor suppression through cell cycle arrest and apoptosis induction. Concurrently, Bax, a key pro-apoptotic member of the Bcl-2 family, was significantly increased to 477.27 ± 18.54 pg/mL (5.85-fold), supporting the pro-apoptotic effect of **Pyr** by promoting mitochondrial outer membrane permeabilization and the subsequent release of apoptogenic factors. In contrast, Bcl-2, an anti-apoptotic protein that antagonizes Bax and preserves mitochondrial integrity, was notably decreased following **Pyr** treatment, reaching 8.88 ± 0.30 pg/mL, which represents a 0.409-fold reduction compared to control (21.68 ± 0.70 pg/mL). This decline in Bcl-2 expression further emphasizes the potential of **Pyr** to disrupt cellular survival pathways, favoring apoptosis over proliferation in PC3 cells.

2.2.6 Effects of Pyr on caspase-3 and caspase-9 activities

To further explore the apoptotic mechanism induced by the synthesized compound **Pyr**, the activities of caspase-3 and caspase-9—two critical executioners of the intrinsic apoptosis pathway—were assessed in PC3 cells. As presented in Table 5, **Pyr** treatment led to a significant increase in the activities of both caspase-3 and caspase-9 when compared to the DMSO-treated control. The concentration of caspase-3 in Pyr-treated cells reached 573.19 ± 22.27 pg/mL, reflecting an 8.55-fold elevation relative to the control (67.02 ± 2.60 pg/mL). This notable increase underscores the activation of downstream apoptotic processes, as caspase-3 is a key effector protease responsible for the cleavage of vital cellular substrates during apoptosis. Similarly, the concentration of caspase-9, an essential

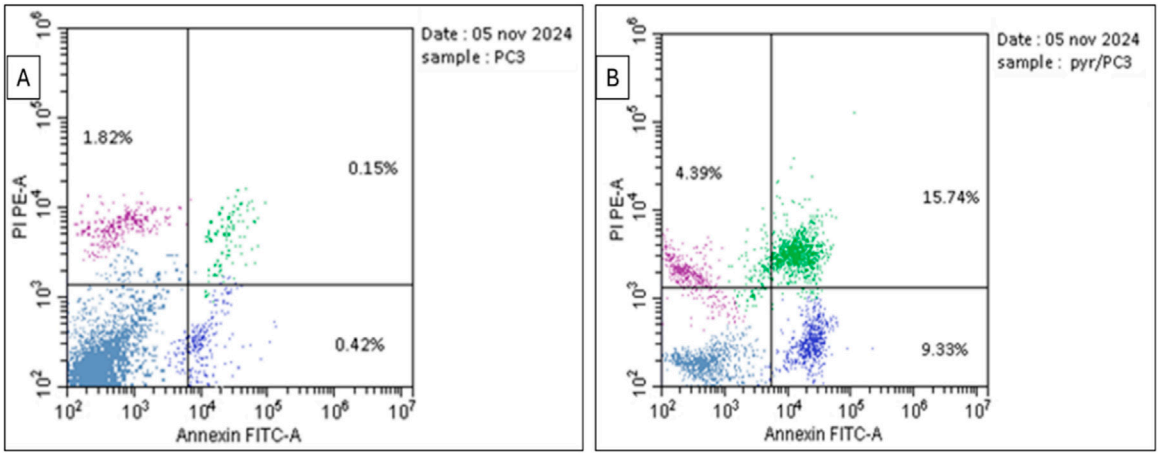


FIGURE 5
Flow cytometric dot plot for prostate PC3 cancer cells treated with **Pyr** and untreated cells following Annexin V-FITC/PI staining. **(A)** shows untreated cells, while **(B)** shows PC3 cells treated with **Pyr** at IC_{50} (8.63 µg/mL). The four quadrants are labeled as follows: Lower Left (LL) for viable cells, Lower Right (LR) for early apoptotic cells, Upper Left (UL) for necrotic cells, and Upper Right (UR) for late apoptotic cells.

TABLE 4 Effects of Pyr on p53, Bax, and Bcl-2 protein expression levels in PC3 cells.

Compound	P53		Bax		Bcl-2	
	Conc (pg/mL)	Fold change	Conc (pg/mL)	Fold change	Conc (pg/mL)	Fold change
Pyr/PC3	1461.33 ± 10.00	9.66	477.27 ± 18.54	5.85	8.88 ± 0.3	0.409
DMSO/PC3	151.33 ± 3.33	1	81.49 ± 3.16	1	21.68 ± 0.7	1

TABLE 5 Effects of Pyr on caspase-3 and caspase-9 activities in PC3 cells.

Compound	Caspase 3		Caspase-9	
	Conc (pg/mL)	Fold change	Conc (ng/mL)	Fold change
Pyr/PC3	573.19 ± 22.27	8.55	41.82 ± 0.95	8.97
DMSO/PC3	67.02 ± 2.6	1	4.66 ± 0.41	1

initiator of the mitochondrial apoptosis pathway, was significantly enhanced following **Pyr** treatment, rising to 41.82 ± 0.95 ng/mL, which corresponds to an 8.97-fold increase compared to control cells (4.66 ± 0.41 ng/mL). The activation of caspase-9 indicates the involvement of the intrinsic (mitochondrial) pathway, consistent with the observed modulation of upstream regulators, including p53, Bax, and Bcl-2.

2.3 Molecular modeling studies

2.3.1 DFT calculations

2.3.1.1 Geometrical structure and frontier molecular orbitals (FMOs)

Figure 6 illustrates the studied geometrical structural convergence of **Pyr** in the ground state using the same theoretical level. To better understand the conformational behavior of the structure under consideration, it is feasible to talk about two essential structural properties: bond lengths and bond angles. The compound's difference in planarity is explained by the face direction of the two aromatic rings, directing the sulphonyl amino group (SO_2NH_2) away from the plane of the molecule. Furthermore, an important hint to the bent structure found during optimization is provided by the CO group that considered the center of molecule bending and forms two H-bonds with the N1H5 and N2H6 with estimated bond distances of 2.367 Å and 2.370 Å, respectively. This feature may contribute to the structural stability of **Pyr**. Given that the covalent link between N and H is 1.012 Å longer than the usual bond length (Sayed and Abdelrehim, 2022), the observed N5-H and N6-H bond length validates the strength of the H-bond formation. The optimized structure's bond angle values allow for elaborating the atoms' planarity behavior. Bond angle values evaluated the similarity in the environment surrounding the molecule, as in the case of C5-N1-C7 and C7-N2-C8 with 130.77°.

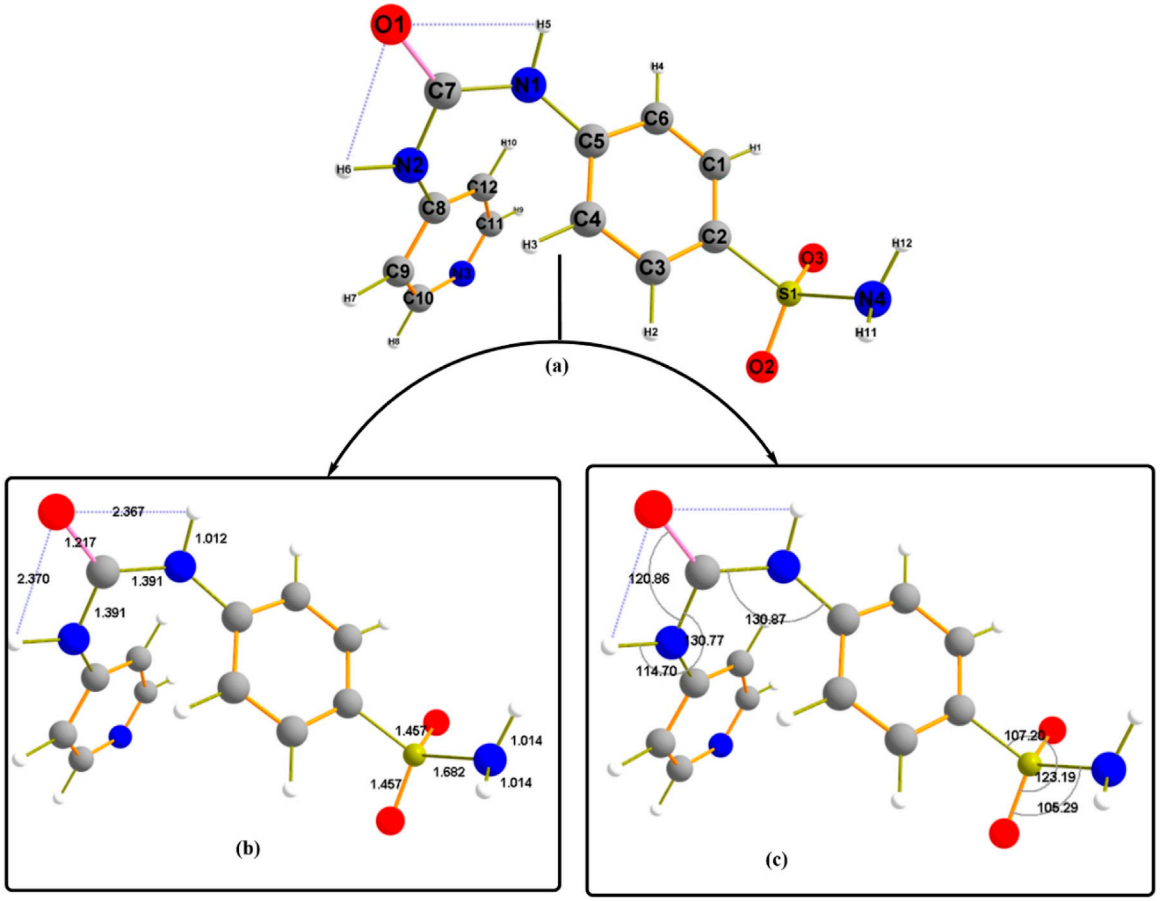


FIGURE 6
The geometrical structure of the designed compound **Pyr (a)** labeled with **(b)** bond lengths, **(c)** bond angles.

To predict the stability and reactivity of different molecules, it is essential to study the features of compounds' frontier molecular orbitals (FMOs) (Abdelrehim and El-Sayed, 2020). Figure 7 displays the energy distribution of the most significant molecular orbitals for the gaseous optimized structures (HOMO-2, HOMO-1, HOMO, LUMO, LUMO+1, and LUMO+2). The stability of the current heterocyclic complex can be predicted using the amplitude of the energy gap (ΔE = 2,558 eV) between HOMO and LUMO levels, a crucial parameter in the study of stability and reactivity (Chen et al., 2021). The orbital contribution at all examined levels was mostly observed throughout the proposed molecule, providing additional evidence for the stability of both ground and excited states. The orbital contribution in the FMOs mostly occurs around SO_2 and CONH groups, leading to the concept of successive donor-acceptor interactions in the excited states.

2.3.1.2 UV–Vis electronic spectra by TD-DFT method

The TDDFT and CPCM solvation model was used to characterize the electrical behavior of **Pyr**. The default Gaussian 09 parameters were used for the TD-DFT calculations. The software settings were adjusted for Nstate = 6 to study six states. In Figure 8, three transition bands are shown as lines. The LOG file of the Gaussian calculation shows a singlet strong absorption band for the first transition, which is the n-π* transition. With a 64.3% transition contribution, an excitation energy of 4.505 eV, and a maximum wavelength (λ_{max}) of 275 nm, the orbital contribution comprises HOMO→LUMO excitation with n-π type of electronic transition. The oscillator strength (F) revealed the strong ability of electronic achievement to LUMO excited state, where its value is higher in the first transition (0.347). Table 6 shows that while the other transitions were anticipated from HOMO→LUMO+1and from HOMO-1→LUMO with comparable contribution %, their F values differ based on the ability of electron transition from one level to another.

2.3.1.3 Electron localization function (ELF)

The electron localization function (ELF) explores the empirical concepts of electron localization, especially the localization of electron pairs, in the spirit of Lewis structures. An Electron Localization Function (ELF) in atomic space designates a point where electron confinement and bond type are known (Emara et al., 2023). One of the most important two-dimensional planes offers details on the type of bond in three distinct planes: H11-N4-H12, N1-C7-N2, N1-C7-O1, and O2-S1-O3. All the atoms of interest are exhibited at the same plane, as shown in Figure 9. The selected planes estimate a localized electronic area (red color scale) between C7 and N atoms (both N1 and N2) and the same environment (appear in the same plane). At the same time, the plane of the amino group exhibits unusual behavior as no additional atoms are observed

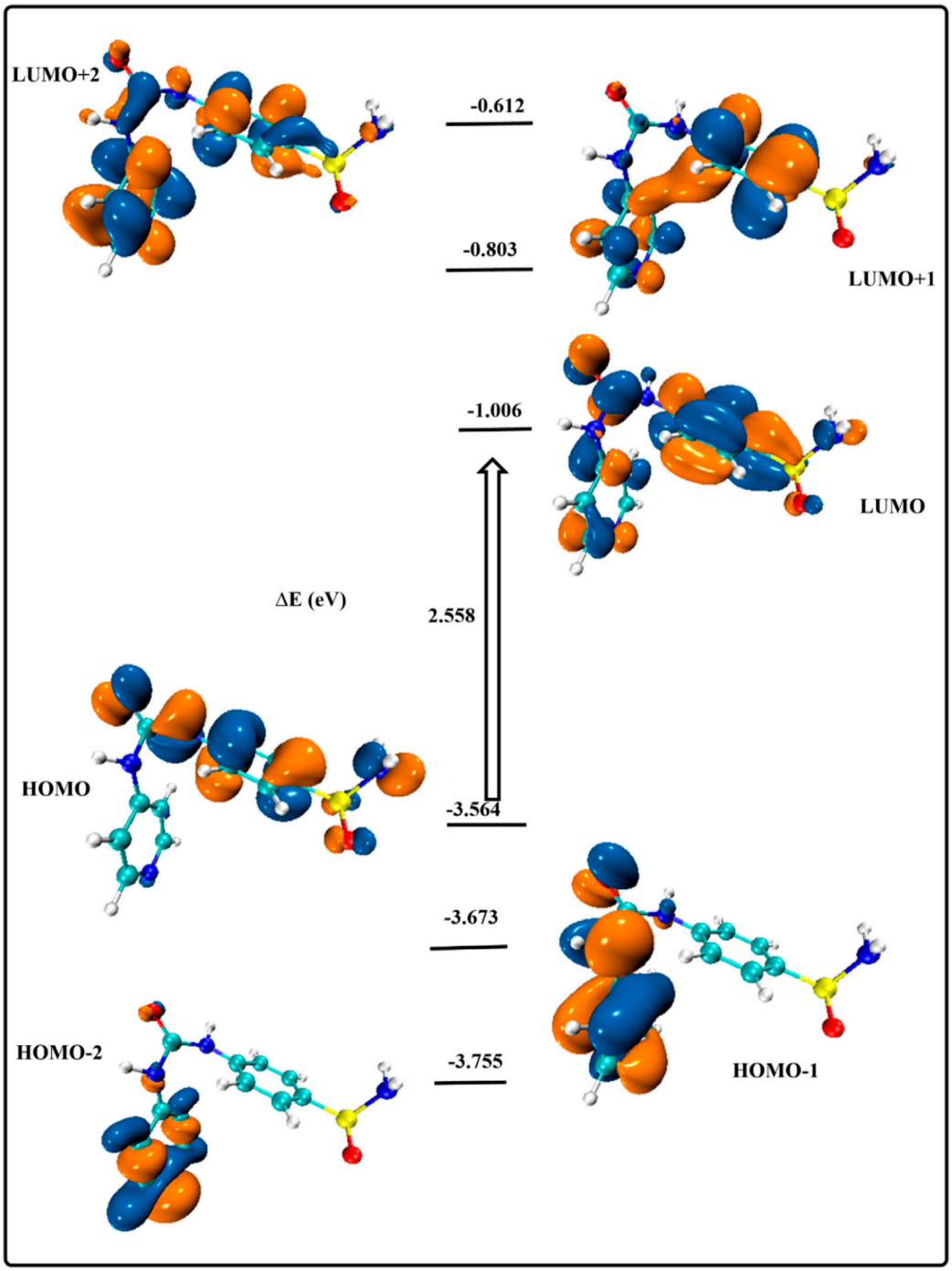


FIGURE 7
Energy excitation levels with energy values (eV).

in this plane with slightly localized electronic density in the bond of interaction between N4 and S1 (not of the same plane). So, the electron localization between N and the second coordinated atom located in the other plane is predicted by this finding, completing the geometrical structure with the optimum conditions. The map of electronic deformation around O1 decreases the electronic localization between it and C7, as displayed in Figure 9c. Another reason for this deformation is a prediction of H-bond formation between O and the other surrounded H atoms. The bond nature between S and O atoms in the O2-S1-O3 is exhibited to be less strong due to the delocalization of electrons around the two O atoms.

2.3.1.4 Molecular electrostatic potential (MEP)

The molecular electrostatic potential (MEP) 3D map is used to analyze the electronegativities of atomic locations on molecules. This topological index helps explain molecular contacts and recognition processes since long-range interactions are mostly

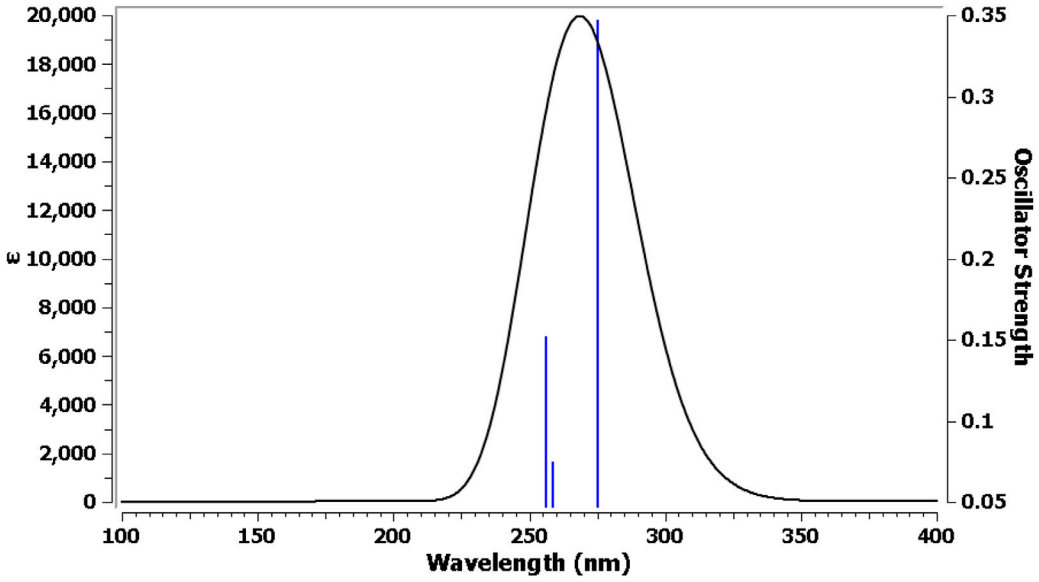


FIGURE 8
UV–Vis electronic absorption spectra for **Pyr**.

TABLE 6 Excitation energies, maximum wavelengths, oscillator strengths, and % orbital contribution for Pyr.

Spectral line number	Excitation energy (eV)	λ_{max} (nm)	F	Type of transition	% orbital contribution
1	4.505	275	0.347	HOMO→LUMO	64.3
2	4.793	259	0.074	HOMO→LUMO+1	54
3	4.839	256	0.151	HOMO-1→LUMO	64.8

caused by electrostatic forces (Issa et al., 2024). The structures of the studied compounds were visually evaluated using colors such as red, orange, yellow, green, and blue to identify potential sites of electrophilic or nucleophilic assaults (Figure 10). The following order of colors represents the decreasing potential for each atomic site: orange, red, green, yellow, and blue. As a result, a red zone indicates an electron-rich site and a blue zone indicates an electron-deficient site. More precisely, it was predicted that all oxygen atom sites in **Pyr** would have the maximum electronic richness, with the remaining portion of the molecule striving to reach a neutral state and only having a small density of π-electrons of the phenyl ring (yellow color scale). This discrepancy is believed to direct a significant electron donation from the nucleophilic O site to the electron acceptor of electrophilic sites, mainly including amino group hydrogen atoms (primary and secondary groups).

2.3.1.5 Reduced density gradient/non-covalent-interactions (RDG/NCI)

Utilizing reduced density gradient (RDG) research, noncovalent bond interactions (NCIs) between several molecular sites were identified. Different color codes were used to illustrate noncovalent interactions (El-Sayed et al., 2023). As illustrated in Figure 11, the interactions readily discernible on the surface of each molecule are vdW interactions with a green color scale and repulsion (steric) interactions with a red color scale. The sign $(\lambda_2)\rho$, obtained by multiplying the electron density by the sign of the second Hessian eigenvalue, indicates the strength of the HB interaction in compounds. In this study, vdW is visible in the cage of C1-C2-S1 and C3-C2-S1. Other electrostatic interactions appear between the two phenyl rings. In this map, H-bond spikes do not appear in the chart; the high distance between H atoms and O atoms (around 2.4 Å) may lead to less sensitivity to be estimated with reduced density parameters. The unfavorable repulsion forces in the molecule were attributed to the steric effect of phenyl rings that export closed 6-atomic system constrain behavior. This type of steric interaction can be vanished by favorable electrostatic interactions.

2.3.2 Molecular docking analysis

Molecular docking is a computational method used to predict the preferred orientation of a small molecule when bound to a receptor, such as a protein, and to evaluate the strength and stability of the interaction (Chang et al., 2023). For this study, the synthesized compound **Pyr** was docked into the active site of the carbonic anhydrase IX using PDB entry 5FL4, which contains the structure of CAIX bound to its cocrystallized ligand **9FK**. Autodock Vina, a widely used docking program, was employed to perform the docking simulations, and the results were visualized using Discovery Studio Visualizer, a tool that allows for detailed analysis of molecular interactions.

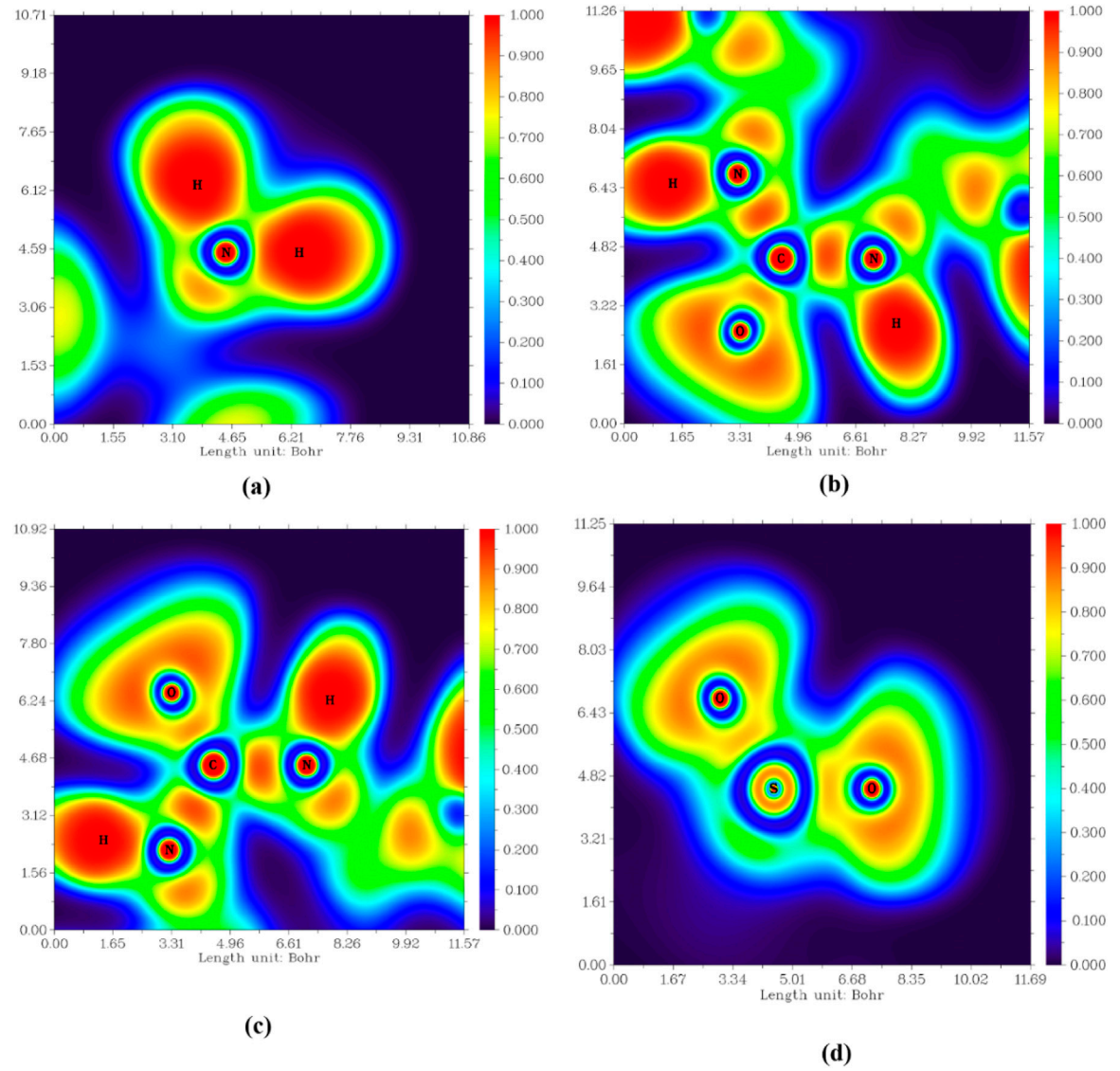


FIGURE 9
Electron localization function (ELF) colored map of **Pyr** **(a)** H11-N4-H12, **(b)** N1-C7-N2, **(c)** N1-C7-O1, and **(d)** O2-S1-O3.

To ensure the accuracy of the docking procedure, the cocrystallized ligand **9FK** was redocked into the CAIX structure. The root-mean-square deviation (RMSD) between the original and redocked ligand poses was calculated to validate the results. An RMSD of 0.9458 Å, which is well below the typical threshold of 2 Å for reliable docking, indicated that the docking procedure and the employed parameters were accurate and capable of reproducing the experimental binding mode of the ligand. The binding affinity of the redocked ligand was found to be −8.6 kcal/mol, demonstrating a stable interaction with the CAIX enzyme. The superimposition of the redocked ligand with its original conformation is shown in Figure 12.

Following the validation of the docking protocol, **Pyr** was docked into the CAIX active site, and a comparative analysis was performed with acetazolamide, the reference compound used in the *in-vitro* CA inhibition assay. The binding affinity of **Pyr** was calculated to be −7.4 kcal/mol, indicating a moderately stable interaction with the CAIX enzyme, while acetazolamide showed a binding affinity of −7.7 kcal/mol, slightly higher than **Pyr**, which suggests a similar but slightly stronger binding interaction.

Pyr exhibited several key interactions that were similar to those of acetazolamide. Specifically, the NH2 group of **Pyr**'s sulfonamide interacted with the zinc ion in the active site, mirroring the interaction of acetazolamide, where the sulfonamide group serves as the zinc-binding moiety. Additionally, both the oxygen and NH2 groups of **Pyr**'s sulfonamide formed classical hydrogen bonds with THR200, as seen with acetazolamide. The sulfur atom of **Pyr**'s sulfonamide also engaged in Pi-sulfur interactions with Trp210 and His94, akin to acetazolamide's interactions. The 2D and 3D interactions of **Pyr** are shown in Figure 13, illustrating these interactions in detail.

However, **Pyr** exhibited some unique interactions not observed with acetazolamide. The oxygen of **Pyr**'s sulfonamide formed a classical hydrogen bond with His119, a distinct interaction that was

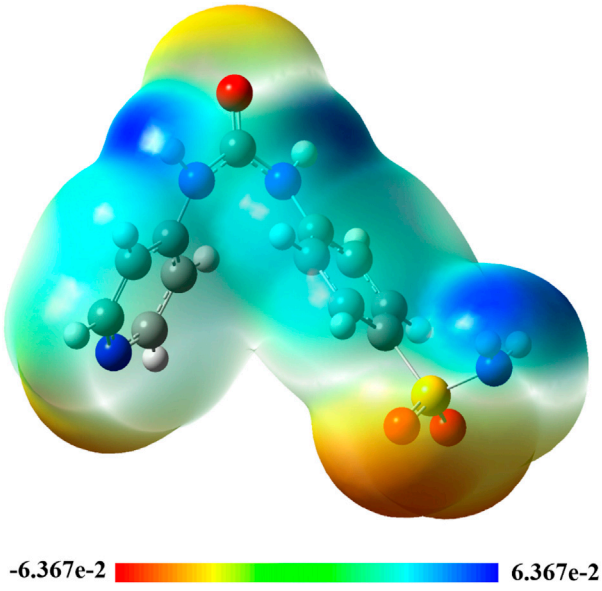


FIGURE 10
3D-colored map of the molecular electrostatic potential of **Pyr**.

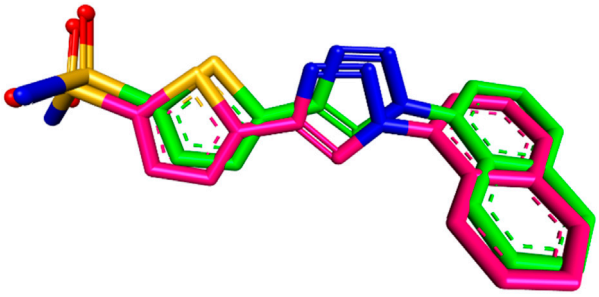


FIGURE 12
Superimposition of the redocked (green) and co-crystallized (magenta) poses of **9FK** inside the CAIX active site (RMSD = 0.9458 Å).

absent in acetazolamide. Moreover, **Pyr** formed non-classical hydrogen bonds with both Leu199 and His94, which were not seen in the acetazolamide docking. **Pyr**'s benzene ring demonstrated hydrophobic interactions with Leu199, a feature similar to the thiadiazole group of acetazolamide, but also formed additional hydrophobic interactions with both Val121 and His94, which were not present in acetazolamide.

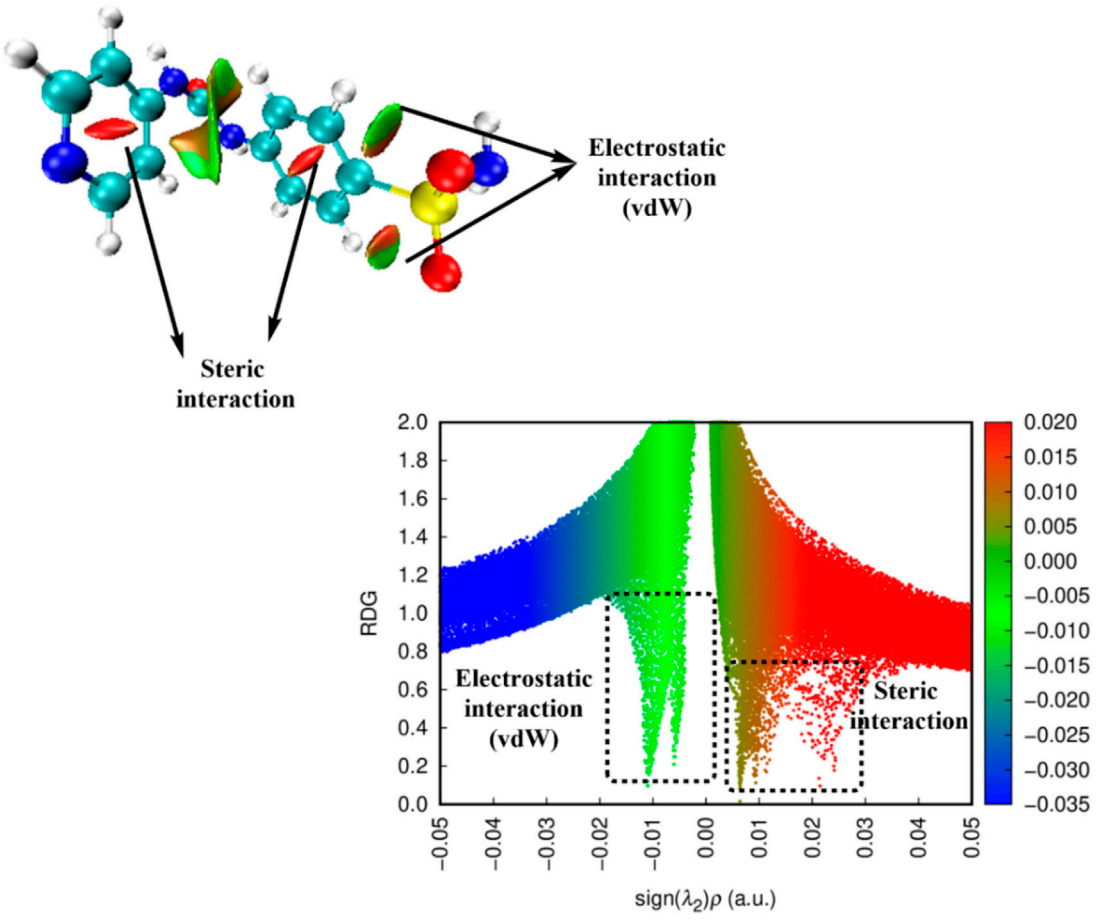
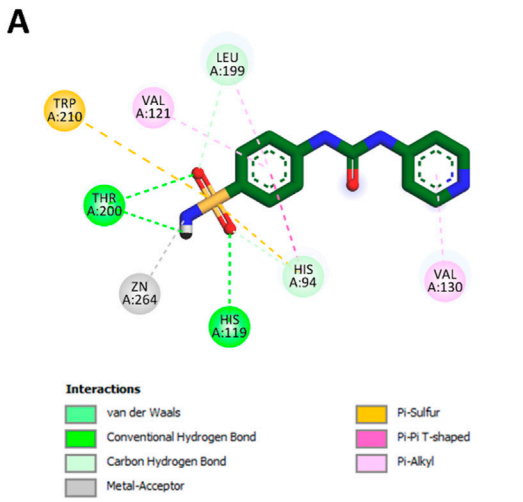


FIGURE 11
3D-NCI map and RDG plot of **Pyr**.



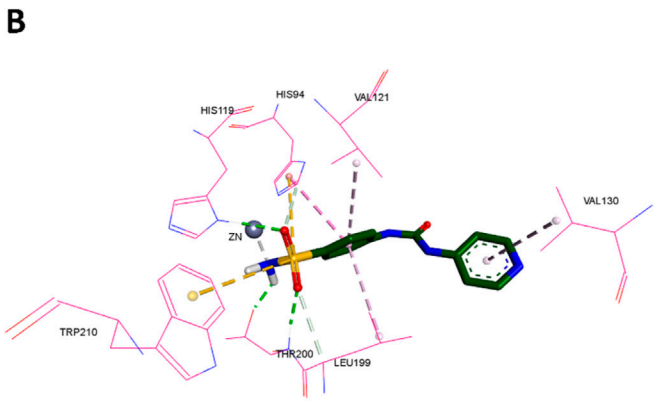
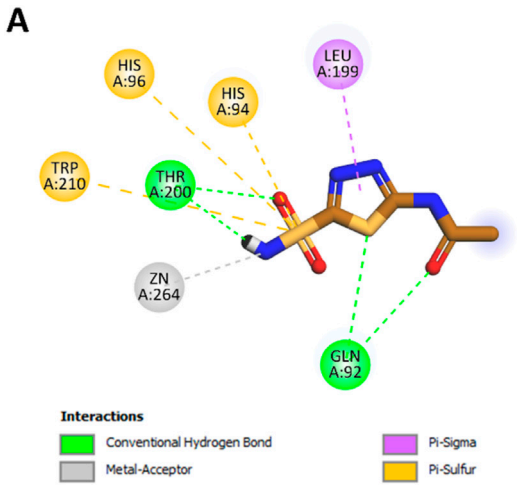


FIGURE 13
(A) 2D interaction diagram and **(B)** 3D binding mode of **Pyr** within the CAIX active site.



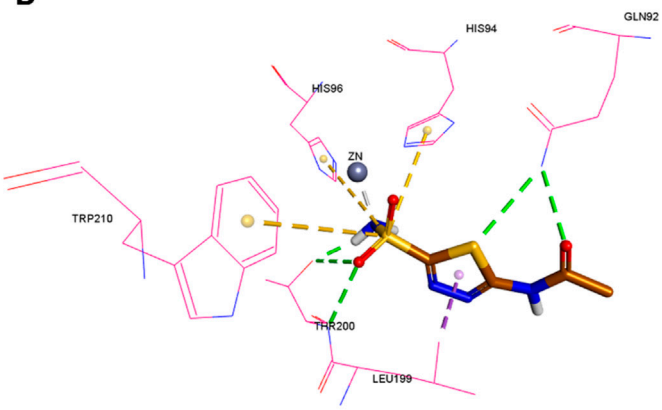


FIGURE 14
(A) 2D interaction diagram and **(B)** 3D binding mode of **Pyr** within the CAIX active site.

Finally, the pyridine ring (tail region) of **Pyr** exhibited Pi-alkyl (hydrophobic) interactions with Val130, a unique feature not observed in acetazolamide. The 2D and 3D interactions of acetazolamide are shown in Figure 14 for comparison.

2.3.3 Drug likeness and ADMET predictions

The Lipinski rule can assess the validity of the therapeutic properties in the compounds under investigation based on five determinants: molecular weight <500 Da, strong lipophilic qualities, such as LogP value <5, H-bond donors <5, H-bond acceptors <10 (Baell et al., 2013). The ligand under investigation may show signs of a drug when it meets more than two of these requirements. The drug-likeness features of PYR are shown in Table 7. It was calculated that the molecular weight of the ligand is 292.31 g/mol. It has five hydrogen bond acceptors and three hydrogen bond donors, where the investigated ligand meets these specifications. Excellent permeability across the cell membrane is indicated by the iLog P value of the molecule, which is determined to be within the range of less than 5, as predicted theoretically. It was found that the title ligand's computed TPSA value was less than 140 $Å^2$, which indicates good intestinal absorption values. Based on Lipinski's rule, these findings support the hypothesis that PYR will absorb well. Significant bioavailability is predicted based on the TPSA and number of rotatable bond values. The primary focus of medical chemistry's drug design, discovery, and contemporary drug development methods is on tiny molecules that resemble drugs and have high biological activity while being lowly harmful (Rautio et al., 2018). In silico prediction techniques, which enhance activity and toxicity study time and resource efficiency, can be used to identify (ADMET) traits (Ferreira and Andricopulo, 2019). The lipophilicity and pharmacokinetic parameters (ADMET features) are shown in Table 8. Drawing from the identified result, it can be shown that PYR exhibited a penetration capability that manifests as BBB permeant and GI absorption, indicating

TABLE 7 Drug-likeness descriptors of the studied ligand Pyr.

Hydrogen bond acceptor (HBA)	5
Hydrogen bond donor (HBD)	3
Molecular Weight (MW)	292.31 g/mol
Topological polar surface area (TPSA)	122.56 Å^2
No. of heavy atoms	20
No. of rotatable bonds	5
Partition coefficient, (ilog P)	0.73
Lipinski rule violations	yes
Bioavailability score	0.55

TABLE 8 Lipophilicity and pharmacokinetic parameters for Pyr.

XLOGP3	0.28
WLOGP	2.07
MLOGP	−0.09
Silicos-IT LogP	−0.62
Consensus LogP	0.47
CYP1A2 inhibitor	No
CYP 2C19 inhibitor	No
CYP 2C9 inhibitor	No
CYP 2D6 inhibitor	No
CYP 3A4 inhibitor	No
Skin permeability (logKp, cm/s)	−7.88
The blood-brain barrier (BBB+)	No
Human intestinal absorption (GI)	High

a reduced ability to cross the BBB and enter the central nervous system (Mani et al., 2023). The permeability value is −7.88 cm/s in human skin, showing that they cannot be absorbed within human skin. The propensity of a substance to inhibit five isoenzymes related to cytochrome P450, a major drug-metabolizing enzymes (CYP1A2, CYP2C19, CYP2C9, CYP2D6, and CYP3A4) can be evaluated using metabolic factors. CPY is utilized to develop medicinal effects and inhibit their capability. This trait is important for toxicity and other unfavorable medication interactions (Zhao et al., 2021). The predicted drug-potent ligand cannot affect these types of drug-metabolizing enzymes. **Pyr** exported a potential physicochemical characteristic that qualifies it for oral bioavailability. A suitable way to visualize this behavior is with the bioavailability radar, as shown in Figure 15. The pink zone in the bioavailability radar plot shows the optimal range for each of the six physicochemical parameters—size, solubility, lipophilicity, polarity, saturation, and flexibility. These characteristics are thought to be ideal for reaching the best oral bioavailability. A dependable model that accurately forecasts drug candidates' absorption in the gastrointestinal system and their accessibility via the blood-brain barrier is the BOILED Egg method. **Pyr** was in a white zone, suggesting a high gastrointestinal absorption, as shown in Figure 16.

3 Experimental

3.1 Chemistry

All reactions were monitored using thin-layer chromatography (TLC) on Merck (Boston, MA, United States) 9385 pre-coated aluminum silica gel plates (Kieselgel 60) measuring 5 cm × 20 cm with a 0.2 mm layer thickness. Spots were visualized under UV light at a wavelength of 254 nm. Melting points were determined using Stuart's electrothermal melting point apparatus and were uncorrected. Nuclear magnetic resonance (NMR) spectra for protons (1H, 400 MHz) were recorded in DMSO-d6 on a Bruker AM400 spectrometer, with tetramethylsilane (TMS) as the internal standard. Chemical shift values are reported in parts per million (ppm), using DMSO-d6 as the solvent, and coupling constants (J) are expressed in hertz (Hz). Signal splitting patterns are described as follows: s (singlet), d (doublet), dd (doublet of doublets), t (triplet), q (quartet), m (multiplet), and brs (broad singlet). Intermediates **1-5** were synthesized according to the reported procedures in the literature (Maconi et al., 2002).

3.1.1 Synthesis of 4-(3-(pyridin-4-yl)ureido) benzenesulfonamide (Pyr)

Freshly prepared azide derivative (**4**) (1.5 mmol, 0.178) was suspended in 10 mL of toluene, and the mixture was heated under reflux for 1 h until the evolution of N_2 gas stopped. Then sulfanilamide (1 mmol, 0.172 g) was added portionwise to the solution, and the reaction mixture was heated under reflux for 2 h. The formed fluffy precipitate was filtered off and washed extensively with boiling toluene to remove unreacted isocyanate. The crude urea product was recrystallized from absolute ethanol.

White powder; 0.216 g, 74% yield; mp: 232°C–234°C; ^{1}H NMR (400 MHz, DMSO-*d6*) δ = 9.10 (1H, s, urea-NH), 8.97 (1H, s, urea-NH), 8.34 (2H, d, pyridyl-2CH), 7.73 (2H, d, phenyl-2CH), 7.62 (2H, d, phenyl-2CH), 7.44 (2H, d, pyridyl-2CH), 7.24 (2H, s, pyridyl-NH_2); ^{13}C NMR (100 MHz, DMSO-*d6*) δ = 152.90, 150.40, 146.76, 143.78, 137.16, 126.92, 117.84, 112.15. Anal. Calcd for $C_{12}H_{12}N_4O_3S$ (292.31): C, 49.31; H, 4.14; N, 19.17. Found: C, 49.43; H, 3.99; N, 19.40.

3.2 Biological evaluation

3.2.1 Cell viability assay

The cell viability of colon HT29, breast MCF7, and prostate PC3 cancer cells, along with CCD-986sk normal cells, was evaluated for Pyr using MTT assay protocols as described in the literature (Ali et al., 2024). All cell lines were obtained from the Vacsera Cell Culture Library, Tissue Culture Unit, Cairo, Egypt, with ATCC certification. For further details, See Supplementary Appendix A in the supplementary data.

3.2.2 Evaluation of carbonic anhydrase I, II, IV, and VII inhibition

According to the assay protocol, **Pyr** was incubated at room temperature for 10 min and analyzed in triplicate. Absorbance

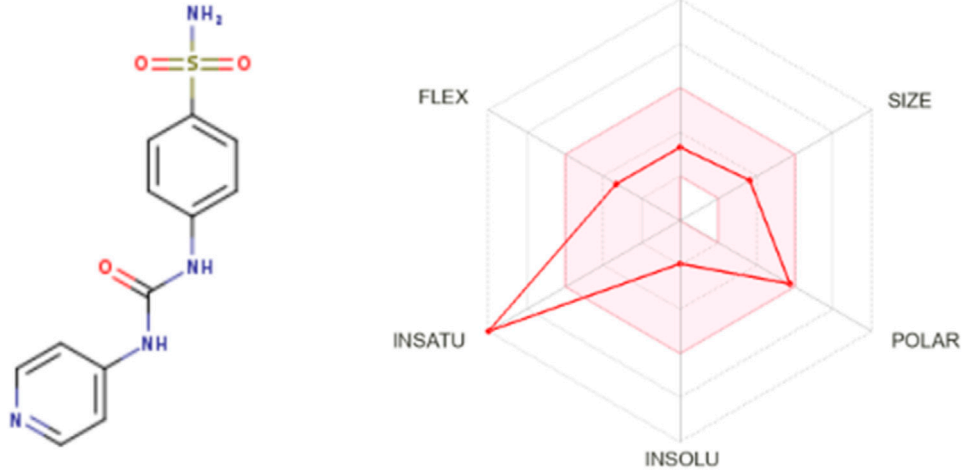


FIGURE 15
Bioavailability Radar model for **Pyr**.

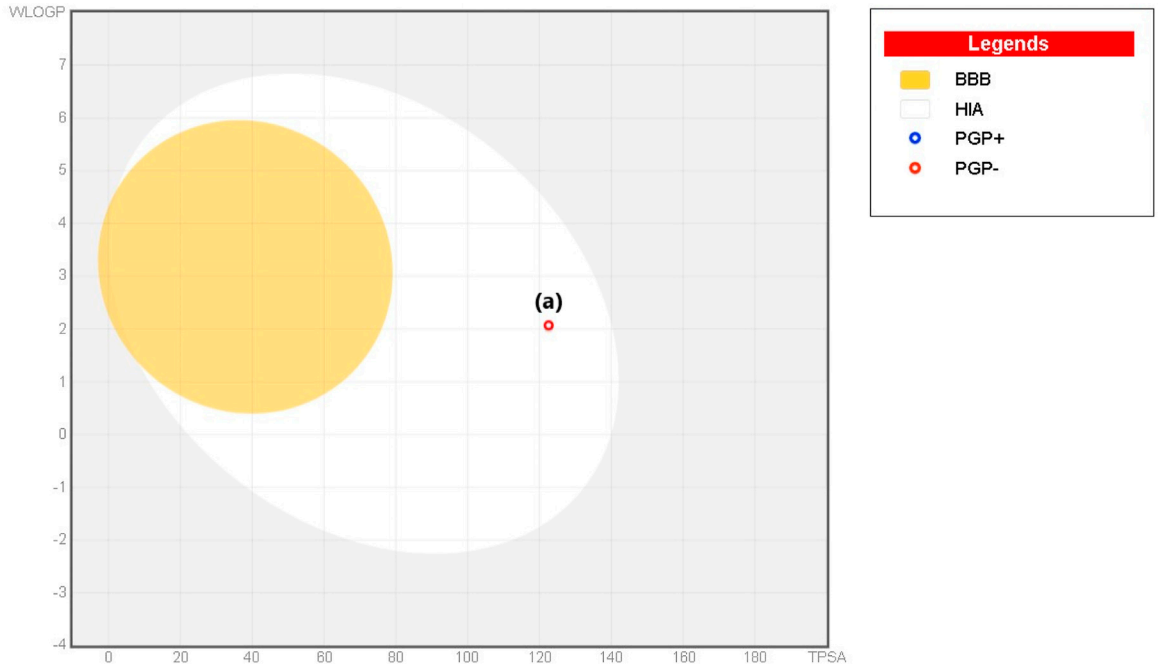


FIGURE 16
BOILED Egg plot of **Pyr**.

measurements were recorded at 405 nm in kinetic mode for 1 h at room temperature. The resulting data were plotted linearly to derive absorbance values, from which the IC_{50} value was determined using the slope of the plot (Abdelhakeem et al., 2024).

3.2.3 Cell cycle analysis

The impact of Pyr on the cell cycle progression of PC3 cells was examined by analyzing DNA content with a flow cytometer, following the procedure outlined in the literature (Ali et al., 2024). For further details, See Supplementary Appendix A in the supplementary data.

3.2.4 Determination of apoptosis

To detect apoptosis in PC3 cancer cells, the Annexin V FITC assay protocol was employed as described in the literature (Ali et al., 2024). For further details, See Supplementary Appendix A in the supplementary data.

3.2.5 Effect of Pyr on caspase-3 activity and Bax and Bcl-2 protein expression levels

The impact of Pyr on caspase-3 protein levels, Bax, and Bcl-2 was evaluated following the protocols provided in the manufacturer's kit instructions.

3.2.6 Statistical analysis

Computerized Prism 5 program was used to statistically analyzed data using one-way ANOVA test followed by Tukey's as post ANOVA for multiple comparison at $P \leq 0.05$. Data were presented as mean ± SEM.

3.3 Molecular modeling studies

3.3.1 DFT calculations

The target compound **Pyr** was subjected to a computational analysis using density functional theory (DFT) in order to provide fully optimized geometrical and electronic calculations using the hybrid B3LYP technique (Parr et al., 1980; Fayed et al., 2020). For further details, See Supplementary Appendix A in the supplementary data.

3.3.2 Molecular docking

The docking procedure essentially follows a crucial path for extremely successful results. Consequently, the docking of the investigated complexes with control comparison was simulated using the AutoDock 4.2 program (Morris et al., 2009). Additionally, Discovery Studio was used to analyze and visualize docking data. For further details, See Supplementary Appendix A in the supplementary data.

3.3.3 ADMET predictions

The ADMET parameters were calculated and *in silico* tests of the drug-like properties of **Pyr** were carried out using the open-source SwissADME server (Daina et al., 2017).

4 Conclusion

In conclusion, this study highlights the potential of a novel 4-pyridyl analog of SLC-0111 (Pyr) as a promising candidate for cancer therapy. **Pyr** exhibited selective cytotoxicity against various cancer cell lines (HT-29, MCF7, PC3) with reduced toxicity toward normal cells, demonstrating a favorable therapeutic index. Moreover, Pyr demonstrated potent and selective inhibition of tumor-associated carbonic anhydrase IX (CA IX) with an IC_{50} of 0.399 μg/mL with moderate inhibition of other CA isoforms I, II and XII. Further mechanistic investigations revealed its ability to induce G0/G1 phase cell cycle arrest and promote apoptosis in PC3 cells, supported by increased caspase-3 and caspase-9 activities and modulation of Bax/Bcl-2 and p53 protein levels. Molecular docking studies further validated Pyr's strong binding affinity and selective inhibition of tumor-associated carbonic anhydrase IX. Additionally, ADMET predictions confirmed its drug-like properties and oral bioavailability. These findings establish **Pyr** as a viable candidate for further development in anticancer drug discovery and targeted therapy applications.

Data availability statement

The original contributions presented in the study are included in the article/Supplementary Material, further inquiries can be directed to the corresponding authors.

Ethics statement

Ethical approval was not required for the studies on humans in accordance with the local legislation and institutional requirements because only commercially available established cell lines were used.

Author contributions

HH: Methodology, Writing – original draft. SA: Resources, Writing – original draft. HMH: Software, Visualization, Writing – review and editing. AA-E: Software, Visualization, Writing – review and editing. MA: Data curation, Formal Analysis, Writing – review and editing. GA: Investigation, Methodology, Writing – review and editing. IR: Conceptualization, Data curation, Writing – original draft. KK: Formal Analysis, Writing – review and editing. DR: Writing – original draft. SB: Conceptualization, Project administration, Writing – original draft. AA: Investigation, Methodology, Writing – review and editing.

Funding

The author(s) declare that financial support was received for the research and/or publication of this article. This study was funded by Deanship of Research and Graduate Studies at King Khalid University through a Large Research Project under grant number RGP2/417/45.

Acknowledgments

The authors extend their appreciation to the Deanship of Research and Graduate Studies at King Khalid University for funding this work through a Large Research Project under grant number RGP2/417/45.

Conflict of interest

The authors declare that the research was conducted in the absence of any commercial or financial relationships that could be construed as a potential conflict of interest.

Generative AI statement

The author(s) declare that no Generative AI was used in the creation of this manuscript.

Publisher's note

All claims expressed in this article are solely those of the authors and do not necessarily represent those of their affiliated organizations, or those of the publisher, the editors and the reviewers. Any product that may be evaluated in this article, or claim that may be made by its manufacturer, is not guaranteed or endorsed by the publisher.

Supplementary material

The Supplementary Material for this article can be found online at: https://www.frontiersin.org/articles/10.3389/fchem.2025.1571646/full#supplementary-material

References

Abdelhakeem, M. M., Morcoss, M. M., Hanna, D. A., and Lamie, P. F. (2024). Design, synthesis and *in silico* insights of novel 1,2,3-triazole benzenesulfonamide derivatives as potential carbonic anhydrase IX and XII inhibitors with promising anticancer activity. *Bioorg. Chem.* 144, 107154. doi:10.1016/j.bioorg.2024.107154

Abdelrehim, E.-S. M., and El-Sayed, D. S. (2020). A new synthesis of poly heterocyclic compounds containing [1,2,4]triazolo and [1,2,3,4]tetrazolo moieties and their DFT study as expected anti-cancer reagents. *Curr. Org. Synth.* 17, 211–223. doi:10.2174/1570179417666200226092516

Abo-Ashour, M. F., Eldehna, W. M., Nocentini, A., Ibrahim, H. S., Bua, S., Abdel-Aziz, H. A., et al. (2019). Novel synthesized SLC-0111 thiazole and thiadiazole analogues: determination of their carbonic anhydrase inhibitory activity and molecular modeling studies. *Bioorg Chem.* 87, 794–802. doi:10.1016/j.bioorg.2019.04.002

Ali, D. M. E., Aziz, H. A., Bräse, S., Al Bahir, A., Alkhammash, A., Abuo-Rahma, G.E.-D. A., et al. (2024). Unveiling the anticancer potential of a new ciprofloxacin-chalcone hybrid as an inhibitor of topoisomerases I and II and apoptotic inducer. *Molecules* 29, 5382. doi:10.3390/molecules29225382

Angeli, A., Paoletti, N., and Supuran, C. T. (2023). Five-membered heterocyclic sulfonamides as carbonic anhydrase inhibitors. *Molecules* 28, 3220. doi:10.3390/molecules28073220

Baell, J., Congreve, M., Leeson, P., and Abad-Zapatero, C. (2013). Ask the experts: past, present and future of the rule of five. *Future Med. Chem.* 5, 745–752. doi:10.4155/fmc.13.61

Baranauskienė, L., and Matulis, D. (2019). "Overview of human carbonic anhydrases," in *Carbonic anhydrase as drug target: thermodynamics and structure of inhibitor binding*. Editor D. Matulis (Cham: Springer International Publishing), 3–14.

Buza, A., Türkeş, C., Arslan, M., Demir, Y., Dincer, B., Nixha, A. R., et al. (2023). Discovery of novel benzenesulfonamides incorporating 1,2,3-triazole scaffold as carbonic anhydrase I, II, IX, and XII inhibitors. *Int. J. Biol. Macromol.* 239, 124232. doi:10.1016/j.ijbiomac.2023.124232

Buza, A., Türkeş, C., Arslan, M., Demir, Y., Dincer, B., Nixha, A. R., et al. (2024). Novel benzenesulfonamides containing a dual triazole moiety with selective carbonic anhydrase inhibition and anticancer activity. *RSC Med. Chem.* 16, 324–345. doi:10.1039/d4md00617h

Chang, Y., Hawkins, B. A., Du, J. J., Groundwater, P. W., Hibbs, D. E., and Lai, F. (2023). A guide to *in silico* drug design. *Pharmaceutics* 15, 49. doi:10.3390/pharmaceutics15010049

Chen, S., An, R., Li, Y., Zhu, Y., Zhu, X., Liu, R., et al. (2021). Strategy of regulating the electrophilic/nucleophilic ability by ionic ratio in poly(ionic liquid)s to control the coupling reaction of epoxide. *Catal. Sci. Technol.* 11, 6498–6506. doi:10.1039/D1CY01024G

Daina, A., Michielin, O., and Zoete, V. (2017). SwissADME: a free web tool to evaluate pharmacokinetics, drug-likeness and medicinal chemistry friendliness of small molecules. *Sci. Rep.* 7, 42717. doi:10.1038/srep42717

Doostmohammadi, A., Jooya, H., Ghorbanian, K., Gohari, S., and Dadashpour, M. (2024). Potentials and future perspectives of multi-target drugs in cancer treatment: the next generation anti-cancer agents. *Cell Commun. Signal.* 22, 228. doi:10.1186/s12964-024-01607-9

El-Sayed, D. S., Tawfik, E. M., Elhusseiny, A. F., and El-Dissouky, A. (2023). A perception into binary and ternary copper (II) complexes: synthesis, characterization, DFT modeling, antimicrobial activity, protein binding screen, and amino acid interaction. *BMC Chem.* 17, 55. doi:10.1186/s13065-023-00962-x

Emara, M. M., Hafez, S. T., Khalil, T. E., Kashyout, A.E.-H. B., El-Dissouky, A., and El-Sayed, D. S. (2023). Electronic and structural perturbations of microporous ZIF-67 nanoparticles and Cr(VI) molecule during adsorptive water decontamination unveiled by experimental and quantum computational investigations. *J. Mol. Liq.* 390, 123042. doi:10.1016/j.molliq.2023.123042

Fayed, T. A., Gaber, M., Abu El-Reash, G. M., and El-Gamil, M. M. (2020). Structural, DFT/B3LYP and molecular docking studies of binuclear thiosemicarbazide Copper (II) complexes and their biological investigations. *Appl. Organomet. Chem.* 34, e5800. doi:10.1002/aoc.5800

Ferreira, L. L. G., and Andricopulo, A. D. (2019). ADMET modeling approaches in drug discovery. *Drug Discov. Today* 24, 1157–1165. doi:10.1016/j.drudis.2019.03.015

Güleç, Ö., Türkeş, C., Arslan, M., Demir, Y., Dincer, B., Ece, A., et al. (2024a). Novel beta-lactam substituted benzenesulfonamides: *in vitro* enzyme inhibition, cytotoxic activity and *in silico* interactions. *J. Biomol. Struct. Dyn.* 42, 6359–6377. doi:10.1080/07391102.2023.2240889

Güleç, Ö., Türkeş, C., Arslan, M., Demir, Y., Dincer, B., Ece, A., et al. (2024b). Bioactivity, cytotoxicity, and molecular modeling studies of novel sulfonamides as dual inhibitors of carbonic anhydrases and acetylcholinesterase. *J. Mol. Liq.* 410, 125558. doi:10.1016/j.molliq.2024.125558

Issa, A. A., Kamel, M. D., and El-Sayed, D. S. (2024). Depicted simulation model for removal of second-generation antipsychotic drugs adsorbed on Zn-MOF: adsorption locator assessment. *J. Mol. Model* 30, 106. doi:10.1007/s00894-024-05896-2

Kakakhan, C., Türkeş, C., Güleç, Ö., Demir, Y., Arslan, M., Özkemahlı, G., et al. (2023). Exploration of 1,2,3-triazole linked benzenesulfonamide derivatives as isoform selective inhibitors of human carbonic anhydrase. *Bioorg Med. Chem.* 77, 117111. doi:10.1016/j.bmc.2022.117111

Kalinin, S., Malkova, A., Sharonova, T., Sharoyko, V., Bunev, A., Supuran, C. T., et al. (2021). Carbonic anhydrase IX inhibitors as candidates for combination therapy of solid tumors. *Int. J. Mol. Sci.* 22, 13405. doi:10.3390/ijms222413405

Low, P., Chu, H. A., Huang, B., Kasireddy, S., Singh, Y., Zheng, S., et al. (2024). Bi-specific adapters and their use with universal car-t cells in the treatment of caix-expressing tumors. Available online at: https://patents.google.com/patent/WO2024191887A2/en?oq=WO2024191887A2 (Accessed March 3, 2025).

Maconi, A., Pastorin, G., Da Ros, T., Spalluto, G., Gao, Z., Jacobson, K. A., et al. (2002). Synthesis, biological properties, and molecular modeling investigation of the first potent, selective, and water-soluble human A3 adenosine receptor antagonist. *J. Med. Chem.* 45, 3579–3582. doi:10.1021/jm020974x

Mani, N., Nicksonsebastin, D., and Prasath, M. (2023). Quantum computational, spectroscopic, ADMET, molecular docking and dynamics simulation revealing the inhibition of psoralidin against anti-tuberculosis. *Chem. Phys. Impact* 7, 100292. doi:10.1016/j.chphi.2023.100292

McDonald, P. C., Chia, S., Bedard, P. L., Chu, Q., Lyle, M., Tang, L., et al. (2020). A phase 1 study of SLC-0111, a novel inhibitor of carbonic anhydrase IX, in patients with advanced solid tumors. *Am. J. Clin. Oncol.* 43, 484–490. doi:10.1097/coc.0000000000000691

MedChemExpress (2024). MedchemExpress.Com, CA IX/XII inhibitor. U-104 (SLC-0111). Available online at: https://www.medchemexpress.com/U-104.html (Accessed November 24, 2024).

Merkx, R. I. J., Mulders, P. F. A., and Oosterwijk, E. (2021). "Carbonic anhydrase IX: current and emerging therapies," in *The carbonic anhydrases: current and emerging therapeutic targets*. Editors W. R. Chegwidden and N. D. Carter (Cham: Springer International Publishing), 205–219.

Morris, G. M., Huey, R., Lindstrom, W., Sanner, M. F., Belew, R. K., Goodsell, D. S., et al. (2009). AutoDock4 and AutoDockTools4: automated docking with selective receptor flexibility. *J. Comput. Chem.* 30, 2785–2791. doi:10.1002/jcc.21256

Parr, R. G. (1980). "Density functional theory of atoms and molecules," in *Horizons of quantum chemistry*. Editors K. Fukui and B. Pullman (Dordrecht: Springer Netherlands), 5–15.

Pastorekova, S., and Gillies, R. J. (2019). The role of carbonic anhydrase IX in cancer development: links to hypoxia, acidosis, and beyond. *Cancer Metastasis Rev.* 38, 65–77. doi:10.1007/s10555-019-09799-0

P. Inc (2024). Targeted therapy vs immunotherapy: which is Right for you, key differences and similarities - OncoDaily. Available online at: https://oncodaily.com/oncolibrary/immune-oncology/targeted-therapy-vs-immunotherapy (Accessed November 24, 2024).

Rautio, J., Meanwell, N. A., Di, L., and Hageman, M. J. (2018). The expanding role of prodrugs in contemporary drug design and development. *Nat. Rev. Drug Discov.* 17, 559–587. doi:10.1038/nrd.2018.46

Sarnella, A., Ferrara, Y., Auletta, L., Albanese, S., Cerchia, L., Alterio, V., et al. (2022). Inhibition of carbonic anhydrases IX/XII by SLC-0111 boosts cisplatin effects in hampering head and neck squamous carcinoma cell growth and invasion. *J. Exp. and Clin. Cancer Res.* 41, 122. doi:10.1186/s13046-022-02345-x

Sayed, D. S. E., and Abdelrehim, E.-S. M. (2022). Spectroscopic details on the molecular structure of pyrimidine-2-thiones heterocyclic compounds: computational and antiviral activity against the main protease enzyme of SARS-CoV-2. *BMC Chem.* 16, 82. doi:10.1186/s13065-022-00881-3

Sedlakova, O., Svastova, E., Takacova, M., Kopacek, J., Pastorek, J., and Pastorekova, S. (2014). Carbonic anhydrase IX, a hypoxia-induced catalytic component of the pH regulating machinery in tumors. *Front. Physiol.* 4, 400. doi:10.3389/fphys.2013.00400

Shaldam, M., Eldehna, W. M., Nocentini, A., Elsayed, Z. M., Ibrahim, T. M., Salem, R., et al. (2021). Development of novel benzofuran-based SLC-0111 analogs as selective cancer-associated carbonic anhydrase isoform IX inhibitors. *Eur. J. Med. Chem.* 216, 113283. doi:10.1016/j.ejmech.2021.113283

Targeted Cancer Therapy (2024). Targeted drug therapy for cancer. Available online at: https://www.cancer.org/cancer/managing-cancer/treatment-types/targeted-therapy/what-is.html (accessed November 24, 2024).

Tian, Y., Wang, X., Wu, C., Qiao, J., Jin, H., and Li, H. (2024). A protracted war against cancer drug resistance. *Cancer Cell Int.* 24, 326. doi:10.1186/s12935-024-03510-2

Tilsed, C. M., Fisher, S. A., Nowak, A. K., Lake, R. A., and Lesterhuis, W. J. (2022). Cancer chemotherapy: insights into cellular and tumor microenvironmental mechanisms of action. *Front. Oncol.* 12, 960317. doi:10.3389/fonc.2022.960317

WHO (2024). Cancer. Available online at: https://www.who.int/news-room/fact-sheets/detail/cancer (Accessed November 24, 2024).

Wikipedia (2024). The hallmarks of cancer. Wikipedia. Available online at: https://en.wikipedia.org/w/index.php?title=The_Hallmarks_of_Cancer&oldid=1259244236 (Accessed November 24, 2024).

Yang, M., Cui, M., Sun, Y., Liu, S., and Jiang, W. (2024). Mechanisms, combination therapy, and biomarkers in cancer immunotherapy resistance. *Cell Commun. Signal.* 22, 338. doi:10.1186/s12964-024-01711-w

Zhao, M., Ma, J., Li, M., Zhang, Y., Jiang, B., Zhao, X., et al. (2021). Cytochrome P450 enzymes and drug metabolism in humans. *Int. J. Mol. Sci.* 22, 12808. doi:10.3390/ijms222312808

Glossary

ADMET	Absorption, Distribution, Metabolism, Excretion, and Toxicity
AAZ	Acetazolamide
BBB	Blood-Brain Barrier
Bcl-2	B-cell lymphoma 2
CA	Carbonic Anhydrase
CA I	Carbonic Anhydrase Isoform I
CA II	Carbonic Anhydrase Isoform II
CA IX	Carbonic Anhydrase Isoform IX
CA XII	Carbonic Anhydrase Isoform XII
CAR-T	Chimeric antigen receptor T
CAIs	Carbonic Anhydrase Inhibitors
CCD-986sk	Human normal fibroblast cell line
DFT	Density Functional Theory
DMSO	Dimethyl Sulfoxide
ELF	Electron Localization Function
FMOs	Frontier Molecular Orbitals
GI	Gastrointestinal
HOMO	Highest Occupied Molecular Orbital
IC_{50}	Half-maximal Inhibitory Concentration
Ki	Inhibition Constant
LUMO	Lowest Unoccupied Molecular Orbital
MCF7	Human breast cancer cell line
MEP	Molecular Electrostatic Potential
MTT	3-(4,5-dimethylthiazol-2-yl)-2,5-diphenyltetrazolium bromide
NCI	Non-Covalent Interaction
NMR	Nuclear Magnetic Resonance
PC3	Human prostate cancer cell line
RMSD	Root-Mean-Square Deviation
TD-DFT	Time-Dependent Density Functional Theory
TLC	Thin-Layer Chromatography
TPSA	Topological Polar Surface Area
UV–Vis	Ultraviolet–Visible Spectroscopy
vdW	van der Waals

frontiers | Frontiers in Chemistry

TYPE Original Research
PUBLISHED 10 April 2025
DOI 10.3389/fchem.2025.1540174

Check for updates

OPEN ACCESS

EDITED BY
Cüneyt Türkeş,
Erzincan Binali Yıldırım University, Türkiye

REVIEWED BY
Kasireddy Sudarshan,
Purdue University, United States
Oliver Dean John,
Universiti Malaysia Sabah, Malaysia

*CORRESPONDENCE
Amjad Ibrahim Oraibi,
amjadibrahim@uomanara.edu.iq

RECEIVED 05 December 2024
ACCEPTED 12 February 2025
PUBLISHED 10 April 2025

CITATION
Oraibi AI, Dawood AH, Trabelsi G, Mahamat OB, Chekir-Ghedira L and Kilani-Jaziri S (2025) Antioxidant activity and selective cytotoxicity in HCT-116 and WI-38 cell lines of LC-MS/MS profiled extract from *Capparis spinosa L*. *Front. Chem.* 13:1540174.
doi: 10.3389/fchem.2025.1540174

COPYRIGHT
© 2025 Oraibi, Dawood, Trabelsi, Mahamat, Chekir-Ghedira and Kilani-Jaziri. This is an open-access article distributed under the terms of the Creative Commons Attribution License (CC BY). The use, distribution or reproduction in other forums is permitted, provided the original author(s) and the copyright owner(s) are credited and that the original publication in this journal is cited, in accordance with accepted academic practice. No use, distribution or reproduction is permitted which does not comply with these terms.

Antioxidant activity and selective cytotoxicity in HCT-116 and WI-38 cell lines of LC-MS/MS profiled extract from *Capparis spinosa L*

Amjad Ibrahim Oraibi[1,2,3]*, Ashour H. Dawood[4], Ghada Trabelsi[3], Ousman B. Mahamat[5], Leila Chekir-Ghedira[3] and Soumaya Kilani-Jaziri[2,3]

[1]Department of Pharmacy, Al-Manara College for Medical Sciences, Maysan, Iraq, [2]Department of Pharmaceutical Sciences A, Faculty of Pharmacy of Monastir, University of Monastir, Monastir, Tunisia, [3]Research Laboratory for Bioactive Natural Products and Biotechnology LR24ES14, Faculty of Dental Medicine of Monastir, University of Monastir, Monastir, Tunisia, [4]Department of Pharmaceutical Sciences, Al-Esraa University, Baghdad, Iraq, [5]National Federation Associations of Healers and Practitioners of Medicine, the Ministry of Public Health of Chad, N'Djamena, Chad

Introduction: *Capparis spinosa* L. is significant among the family Capparidaceae for its survival and tolerance to dry environments. In this study, we evaluate the antioxidant and anticancer activities of extracts of roots and aerial parts of *Capparis spinosa* L.

Methods: Bioactive compounds, including phenolic acids and flavonoids, in various ethyl acetate fractions from the extracted roots and aerial parts, were identified using LC-MS/MS. Principal leaf constituents characterized included Rutin, Resveratrol, Astragalin, and others. The Rutin, Resveratrol, Astragalin, (of ethyl acetate fraction), leaves, and roots were screened for antioxidant activity using DPPH, FRAP, ABTS, and CUPRAC activity assays, as well as for cytotoxicity with the MTT assay.

Result: The antioxidant and anticancer activities of the samples were evaluated using DPPH, ABTS, FRAP, CUPRAC assays, and the MTT assay. Roots and Rutin consistently exhibited the strongest antioxidant activity across all assays, with Roots (IC_{50} = 0.06–0.36 mg/mL) excelling in FRAP and CUPRAC, and Rutin (IC_{50} = 0.013 mg/mL) showing the highest DPPH activity. In contrast, Astragalin displayed the weakest antioxidant potential. For anticancer activity, the MTT assay revealed that Leaves (IC_{50} = 23.26 µg/mL) and Roots (IC_{50} = 34.65 µg/mL) were the most potent against HCT-116 cells, outperforming Nutlin (IC_{50} = 62.72 µg/mL), with minimal toxicity to normal WI-38 cells. These results highlight the therapeutic potential of Roots and Rutin as strong antioxidant and anticancer agents.

Conclusion: The results provide useful information concerning the medicinal potentials of *Capparis spinosa* L., particularly about HCT-116 and WI-38 cell line selectivity, and its relevance in the synthesis of natural antioxidants.

KEYWORDS

***Capparis spinosa* L., antioxidant activity, rutin, resveratrol, MTT assay**

1 Introduction

The *Capparis spinosa* L. is significant among the family Capparidaceae for its survival and tolerance to dry environments. Although not intensively cultivated, *C. spinosa* is grown in many places worldwide including the Mediterranean basin (Levizou et al., 2004; Sun et al., 2023). Furthermore, *C. spinosa* not only contributes to the Mediterranean diet but has also been used to treat various ailments in the traditional herbal medicine practice because of its tonic, diuretic, and antihypertensive actions (Sun et al., 2023). Different forms of *C. spinosa* are said to be beneficial when used to mitigate the challenges faced by mankind like hypolipidaemic and anti-diabetic effects (Mollica et al., 2017; Shahrajabian et al., 2021). Studies on the methanol extracts of *C. spinosa* herb had antioxidant properties and free radical scavenging properties *in vitro* which would be beneficial in conditions related to oxidative stress (Bacchetti et al., 2022; Grimalt et al., 2022). Earlier works have focused on the beneficial components of *C. spinosa* such as vitamins, flavonoids, and polyphenols which dispense antioxidant properties to the products (Mollica et al., 2017; Shahrajabian et al., 2021; Annaz et al., 2022).

Usually, both leaves and flower buds are high in Flavonoids and Phenolic substances that are the most potential antioxidants (Grimalt et al., 2022). Besides the antioxidant effect, *C. spinosa* has been reported in abundance in traditional medicine for antispasmodic, analgesic, diuretic, and expectorant properties. It has also been used for treating many conditions like curing inflammation and gastrointestinal disorders, treating anemia and liver diseases, and relieving rheumatic pain (Gull et al., 2015; Rahimi et al., 2020; Sun et al., 2023). Even within a particular region, different plant parts, such as the young shoots and other plant samples, have been incorporated into traditional medicine practices. In Greece, infusion of the young shoots was taken for relief in rheumatism, and in Libya, they focused on the tumor-curing properties of these young shoots (Rivera et al., 2003). In Syria, vinegar preparation of dried leaves was used to apply on head scabs and ulcers (Elachouri et al., 2024). The apical flower buds were utilized for respiratory problems, kidney stones, and gastrointestinal problems (Abdulridha and Saliem, 2023; Yang et al., 2023). Several researchers in different countries have studied the sections of *C. spinosa* for their antioxidant activity (Allaith, 2016). These activities are normally attributed to the high amounts of flavonoids and phenolic acids present in this plant (Alqahtani et al., 2023). These metabolites are important in understanding the medicinal aspects of the plant as well as the bioactive compounds that are responsible for the therapeutic activities. The screening employed many qualitative tests to screen for flavonoids, alkaloids, coumarins, terpenes, phenolic compounds, saponins, tannins, and cardiac glycosides. Such secondary metabolites are important they could possess valuable antioxidant, anti-inflammation, and antibacterial activities (Nazer et al., 2021).

The objective of this article is to investigate some bioactive compounds obtained from *Capparis Spinosa* L. (root and leaves), rutin, resveratrol, and astragalin for Free radical scavenging properties and anticancer effect.

2 Material and method

2.1 Plant material

The plant parts of Capparis Spinosa L. were collected from the Maysan region in southern Iraq, where it naturally grows. All plant parts were thoroughly washed and kept for drying in the shade for 3 weeks. Once dried, the plant material was ground into a fine powder using an electric grinder.

2.2 Experimental work

The experimental procedures were divided into the following steps.

2.2.1 Extraction and fractionation of leaves and stem (Soxhlet extraction)

For the extraction process, 400 g of the powdered plant material (leaves and stem) were soaked in 1,500 mL of petroleum ether (boiling point 30°C–60°C) to remove non-polar materials. The mixture was shaken frequently over 3 days. After filtering, the petroleum ether extract was set aside for further analysis, and the remaining plant material was spread on paper to evaporate any remaining solvent. The dried plant powder was then subjected to Soxhlet extraction using 80% hydroethanolic Solvent (a solution prepared with 80% ethanol and 20% water) for 12 h. The resulting extract was filtered, and the filtrates were combined. The solvent was removed under vacuum using a rotary evaporator, yielding a dark greenish residue. This residue was suspended in 500 mL of water and successively partitioned with chloroform, ethyl acetate, and n-butanol (3 × 500 mL for each fraction) using a separating funnel. The chloroform and ethyl acetate fractions were dried over anhydrous sodium sulfate, filtered, and evaporated to dryness using a rotary evaporator. The scheme of extraction is shown in Supplementary Figure S1.

2.2.2 Extraction and fractionation of roots (Soxhlet extraction)

In order to extract the roots, 150 g of powdered Capparis spinosa root were soaked in 500 mL of petroleum ether for 3 days to remove non-polar compounds. During this process, the mixture was shaken at intervals. After 3 days, the petroleum ether was separated by filtration, and the filtrate was removed from the filter paper and taken away for some hours to allow evaporation. After the hydroethanolic extract was concentrated, the solid plant residue was further liquidated by 80% ethanol for 12 h in a soxhlet thimble. The hydroethanolic extract was filtered, and the solvent was evaporated under vacuum using a rotary evaporator. This residue was dissolved in water 250 mL and further separated into several portions using chloroform, ethyl acetate, and n-butyl alcohol fractions as in the previous work for leaves and stem fractions. The fractions of petroleum ether, chloroform, ethyl acetate, and n-butanol were collected and preserved for further evaluation. Schematic diagram for fractionation of roots of *Caparis spinosa* crude extracts is shown in Supplementary Figure S2.

Step	Time (min)	A (%) (Methanol)	B (%) (0.05% TFA)
0	0	40	60
1	5	70	30
2	15	90	10
3	20	90	10
4	25	40	60
5	30	40	60

2.3 Preliminary phytochemical screening of aerial parts and roots

Phytochemical Investigation focused mostly on the presence and/or absence of various secondary metabolites in the aerial parts and the roots of *Capparis spinosa* L. and has used quite several tests. These tests aimed to slope out selected materials, particularly plant flavonoids, phenolic acids, plant alkaloids, and other plant materials.

2.4 LC-MS/MS analysis of ethyl acetate fractions

Advanced liquid chromatography-mass spectrometry (LC-MS) techniques were employed to identify and confirm the presence of flavonoids and phenolic acids within the ethyl acetate fractions derived from the aerial parts and roots. This method was employed to isolate and characterize the polar compounds from the ethyl acetate fractions and also improved the understanding of the chemical composition of these extracts.

2.5 Chromatographic analysis LC-MS/MS and GC-MS

2.5.1 LC-MS/MS analysis

2.5.1.1 Instrumentation

The analysis was performed using a liquid chromatography system (ATLAS_QTOF_ICX_V0 O4, Germany) with an Integrated ExionLC 3.61 pump system (ACCBM5671761) and a Valve model 1.0.0.0 (AB SCIEX 1). A C18–ODS column (250 mm × 4.6 mm i.d., 5 μm particle size) was used for separation.

2.5.1.2 Conditions

Ionization Mode: Negative ion mode.

Mass Range: Full scan spectra (m/z 50–900) with MS/MS fragmentation on selected ions.

Nebulization & Drying: High-purity nitrogen at optimized temperatures and flow rates.

Detector: UV at 280 nm.

2.5.1.3 Mobile phase

The mobile phase was composed of:

Solution A: Methanol.

Solution B: 0.05% Trifluoroacetic acid (TFA) in water.

2.5.1.4 Gradient elution

The separation was carried out using a gradient elution at a constant flow rate of 1.0 mL/min, as follows:

2.5.1.5 Data analysis

The acquired LC-MS/MS data were processed using Analyst 1.6.3 software (Germany-Darmstadt) for compound identification and structural elucidation (El-Elimat et al., 2024).

2.5.2 GC-MS analysis of chloroform and petroleum ether extracts

The GC-MS analysis of petroleum ether and chloroform fractions from both the aerial parts and roots of Capparis spinosa was conducted using an Agilent GC-MS system, equipped with an Agilent 190915-433UI HP-5ms Ultra Inert column.

Instrument Setup and Operating Conditions:

Column: Agilent 190915-433UI (HP-5ms Ultra Inert).

Injection Mode: Front Split/Splitless (SSZ).

Carrier Gas: High-purity helium (99.995%).

Flow Rate: 0.9 mL/min.

Carrier Gas Pressure: 7.037 psi.

Average Linear Velocity: 34,772 cm/s.

Hold-Up Time: 1.4379 min.

Temperature Program:

Initial Oven Temperature: 60°C.

Temperature Ramp 1: Increase from 60°C to 150°C at 3°C/min, hold for 10 min.

Temperature Ramp 2: Increase from 150°C to 300°C at 10°C/min.

Detection and Data Analysis:

Detector: Mass Selective Detector (MSD).

Ionization Mode: Electron Ionization (EI) at 70 eV.

Sample Injection: 1 μL of 1% extract solution (diluted in respective solvents) was injected in splitless mode.

Compound Identification: Based on mass spectral fragmentation patterns using NIST and Wiley spectral libraries.

Quantification: Relative abundance of detected compounds was expressed as a percentage based on peak area in the chromatogram (Seetharaman et al., 2025).

2.6 Antioxidant and free radical scavenging activity

2.6.1 1, 1-diphenyl-2-picrylhydrazyl radical antioxidant study

Antioxidant properties of the aerial parts, roots, resveratrol, astragalin, and rutin fractions were assessed using the DPPH radical scavenging assay. DPPH assay was performed using the following procedure (Brand-Williams et al., 1995; Baliyan et al., 2022): An amount of 0.5 mg DPPH was dissolved in 10 mL of ethanol to give a 1 mg/mL DPPH stock concentration. This solution was stored in a dark glass bottle to avoid proper temperature conditions and/or sunlight to keep it stable throughout the experiment. Four sample solutions were prepared with the following concentrations: 1 mg/mL, 0.1 mg/mL, 0.01 mg/mL, and 0.001 mg/mL in ethanol. These concentrations of the samples made it possible to use the scavenging

activity of each of the samples over a range of dilutions. The DPPH assay was performed in a 96-well microplate, which included the addition of 200 µL of DPPH solution in each well as a source of free radicals. Later, 100 µL of different sample solutions at different concentrations was added in the respective wells after the DPPH solution was added. As a control, 100 µL of ethanol was placed instead of the sample in separate wells to assess the DPPH absorbance without the addition of any antioxidant. Further blanks were carried out using 200 µL of ethanol instead of DPPH solution along with 100 µL of each of the samples, to take care of the probable absorbance of the samples themselves ethanol. Mixtures were then incubated in the dark at room temperature for 30 min to allow the reaction of the DPPH radicals with possible antioxidants in the samples in solution. Following this period, the absorbance of each of the mixtures was measured at 517 nm using a UV-Vis microplate reader. The percentage of DPPH radical scavenging activity was calculated using the following formula:

$$\text{DPPH Scavenging Activity } (\%) = \left(A \text{ control} - A \text{ sample} / A \text{ control}\right) \times 100$$

In this formula, A control refers to the absorbance of DPPH solution with ethanol whereas A sample refers to the absorbance of DPPH solution absorbed in the sample. In this manner, a calculation of the percentage of DPPH radical scavenging activity for each sample was done along with IC_{50}. The lower the IC_{50} value of the samples, the greater the antioxidant activity since it conveyed that less of the sample was needed to reduce the DPPH radicals by 50%. The DPPH scavenging effects of the aerial part, roots extract, resveratrol, astragalin, and rutin were analyzed based on their IC_{50} or extent of activity at different concentrations. They were also compared to assess their DPPH free radical scavenging ability in depth and anti-oxidative capacity as well (Moukette et al., 2015).

2.6.2 ABTS assay

The antioxidant activities of the aerial part of the plant, root, resveratrol, astragalin, and rutin were evaluated using the ABTS radical cation ($ABTS^{\cdot+}$) assay. The $ABTS^{\cdot+}$ solution preparation method was done according to (Ilyasov et al., 2020) which includes:39.2 mg ABTS dissolved in distilled water and subsequently completed with a 6.7 mM potassium persulfate solution in equal volume (We Prepared a 6.7 mM potassium persulfate solution by dissolving 17.6 mg of potassium persulfate in 5 mL of distilled water.). The solution was allowed to stand in the darkroom at a temperature for 12–16 h to form the ABTS radical cation. This resulting solution was then further diluted with ethanol to measure the maximum probable absorbance density of about 0.70 (±0.02) at 734 nm. Trolox standards were prepared in ethanol from 0.01 to 0.1 mM and sample solutions were prepared in ethanol at required concentrations. In the assay, 200 µL sample solution was taken in each cuvette, and 2 mL $ABTS^{\cdot+}$ solution was added to each tube or cuvette for mixing. Controls were prepared by mixing 2 mL of $ABTS^{\cdot+}$ solution with 200 µL of ethanol, while blanks were prepared by mixing 2 mL of ethanol with 200 µL of each sample solution (without $ABTS^{\cdot+}$). The mixtures were incubated in the dark at room temperature for 30 min before the absorbance was measured at 734 nm using a UV-Vis spectrophotometer. The percentage of ABTS radical scavenging activity was calculated using the following formula:

$$\text{ABTS Scavenging Activity } (\%) = \left(A \text{ control} - A \text{ sample } A \text{ control}\right) \times 100$$

Where A control is the absorbance of the $ABTS^{\cdot+}$ solution with ethanol, and A sample is the absorbance of the $ABTS^{\cdot+}$ solution with the sample. IC_{50} was determined by plotting the percentage of scavenging activity against the concentrations of the samples; IC_{50} is the concentration at which it shows 50% scavenging of the ABTS radicals. Based on IC_{50} values, and for some samples at definite concentrations, the antioxidant activities of the five tested samples were compared (Rumpf et al., 2023).

2.6.3 Ferric reducing antioxidant power assay

The ferric reducing antioxidant power (FRAP) assay was selected to evaluate the antioxidant activity of the aerial part, root, and fractions of resveratrol, astragalin, and rutin. For this assay, the reagents were prepared according to Skroza et al. (2015) with some modifications: The acetate buffer was prepared by adding approximately 16 mL of glacial acetic acid to 3.1 g of sodium acetate trihydrate and volumetrically making up to 1 L with distilled water. A TPTZ solution was prepared by dissolving 0.031 g in 10 mL of 40 mM HCl and a ferric chloride solution was prepared by dissolving 0.054 g of $FeCl_3{\cdot}6H_2O$ in 10 mL of distilled water. The FRAP working solution was made up immediately before use by mixing acetate buffer, TPTZ solution, and ferric chloride solution in a ratio of 10:1:1. Sample solutions from root extract, leaf extract, resveratrol, astragalin, and rutin were prepared in ethanol at a concentration of choice. The assay was carried out by first dispensing 180 µL of the FRAP working solution into each well of a 96-well microplate before adding 20 µL of each sample solution or trolox standard to the wells. The plate was then incubated for half an hour at 37°C before the absorbance reading was undertaken at 593 nm using a microplate reader. This absorbance was employed to estimate the reducing power of samples according to their capability to convert Fe^{3+} to Fe^{2+} in the presence of TPTZ (Benzie and Devaki, 2018).

2.6.4 Cupric reducing antioxidant capacity assay

Cupric reducing antioxidant capacity (CUPRAC) assay was utilized for screening additional radical scavenging activity of the aerial part, root, resveratrol, astragalin, and rutin. To perform the CUPRAC assay the following reagents were prepared according to Apak et al. (2010) 0.4262 g of copper (II) chloride dihydrate ($CuCl_2{\cdot}2H_2O$) was dissolved in 200 mL of distilled water to make a 0.01 M copper (II) chloride solution. For preparing 1 M ammonium acetate buffer (pH 7.0), 7.708 g of ammonium acetate was dissolved in 100 mL of distilled water, and about 60 mL of this buffer was supplemented with 0.0075 M neocuproine solution prepared by dissolving 0.039 g of neocuproine in 20 mL of ethanol. Trolox standard solutions were prepared in ethanol with concentrations ranging from 0.01 to 0.1 mM. Sample solutions from root extract, leaf extract, resveratrol, astragalin, and rutin were also prepared in ethanol at desired concentrations. For the assay, 150 µL of the pre-mixed reagent solution [copper (II) chloride, ammonium acetate, and neocuproine] was pipetted into each well of a 96-well microplate,

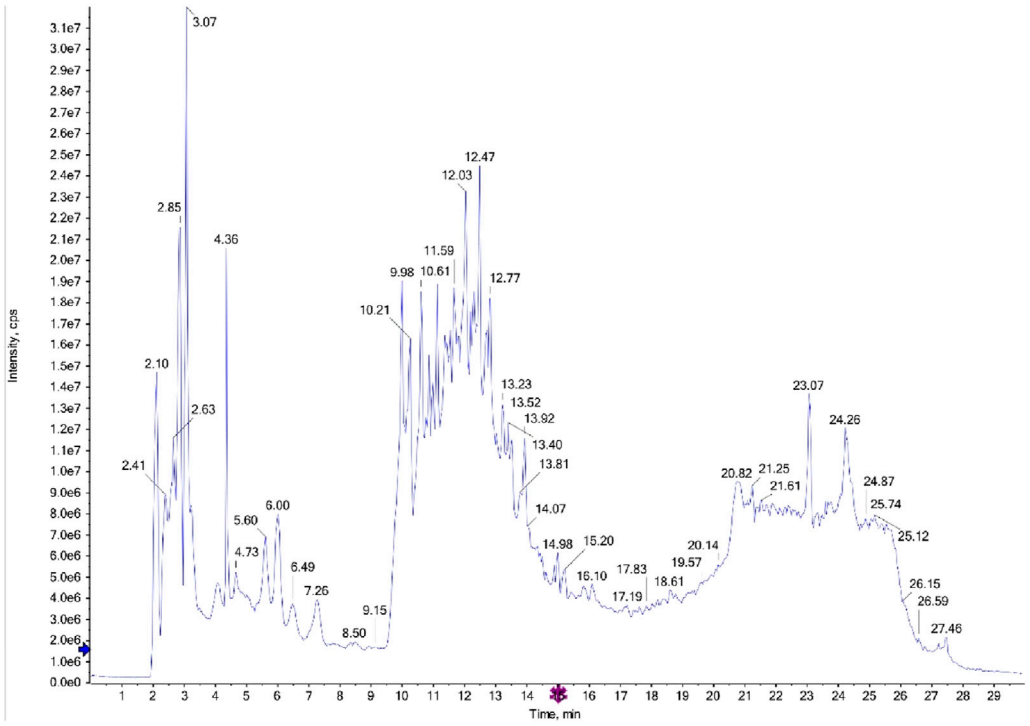


FIGURE 1
LC-MS/MS diagram of ethyl acetate fraction of the aerial parts.

followed by the addition of 50 µL of each sample solution or standard Trolox solution. The microplate was incubated at room temperature for 30 min in the dark to allow the reaction to occur. The absorbance was measured at 450 nm using a UV-Vis microplate reader. The antioxidant activity was calculated using the formula:

$$\text{CUPRAC Activity (\%)} = \left(A\,\text{sample} - A\,\text{blank} \,/\, A\,\text{control} \right) \times 100$$

Where A sample is the absorbance of the sample solution, A blank is the absorbance of the blank (without CUPRAC), and A control is the absorbance of the Trolox standard. The IC_{50} value was determined by plotting the CUPRAC activity percentage against the sample concentrations where this value represents the concentration necessary to achieve 50% of the maximum CUPRAC activity observed from the standard. The antioxidant activities of the five samples were also compared based on IC_{50} values or CUPRAC activities at a given concentration (Suktham et al., 2019).

2.7 *In vitro* MTT (3-[4, 5-dimethylthiazol-2-yl]-2, 5) diphenyl tetrazolium bromide) cell proliferation assay

2.7.1 Cell culture and media

Cell lines were purchased from the Holding Company for Biological Products and Vaccines (VACSERA, Giza, Egypt). HCT-116 and WI-38 cells were cultured in RPMI-1640 medium. Enhanced with 10% fetal bovine serum (FBS) and 1% penicillin-streptomycin mixture (100 IU/mL penicillin and 0.1 mg/mL streptomycin) (Calmeiro et al., 2021).

2.7.2 Procedure

MTT (3-(4,5-dimethylthiazol-2-yl)-2,5-diphenyl tetrazolium bromide; Sigma) was dissolved in PBS at a concentration of 5 mg/mL and filtered to sterilize and remove a small amount of insoluble residue present in some batches of MTT. At the times indicated below, the original MTT solution (10/~1 per 100/~1 medium) was added to all test wells and the plates were incubated at 37°C for 4 h. Isopropanol acid (100/~1 of 0.04 N HCI in isopropanol) was added to all wells and mixed well to dissolve the dark blue crystals. After a few minutes at room temperature to ensure all crystals were dissolved, the plates were read on a Dynatech MR580 Microelisa Reader, using a test wavelength of 570 nm, a reference wavelength of 630 nm, and a calibration setting of 1.99 (or 1.00 if the samples were strongly colored). Plates were typically read within 1 h of adding isopropanol.

2.7.3 *In vitro* MTT cell proliferation assay

The MTT assay was used to evaluate the proliferation of control and treated cells according to Ghasemi et al. (2023). 2.6~3 × 10^4 cells were added to each well of a 96-well tissue culture plate containing the appropriate media and grown for 24 h. Drug stock solutions were prepared in DMSO. Eight concentrations (300, 100, 30, 10, 3, 1, 0.3, and 0.1 µg/mL) were prepared for each compound in the growth media. The Nutlin was used as a reference compound. Cells were then treated for 72 h. Freshly prepared MTT salt (3-(4,5-dimethylthiazol-2yl)-2,5- diphenyltetrazolium bromide) (5 mg/mL; Sigma) was then added to each well to give a final concentration of 0.5 µg/µL. The plates were incubated for 4 h and the formation of formazan crystals was checked using an inverted microscope. An Equal volume of 1:1 (200 µL) DMSO and isopropanol mixture was added to each well and incubated

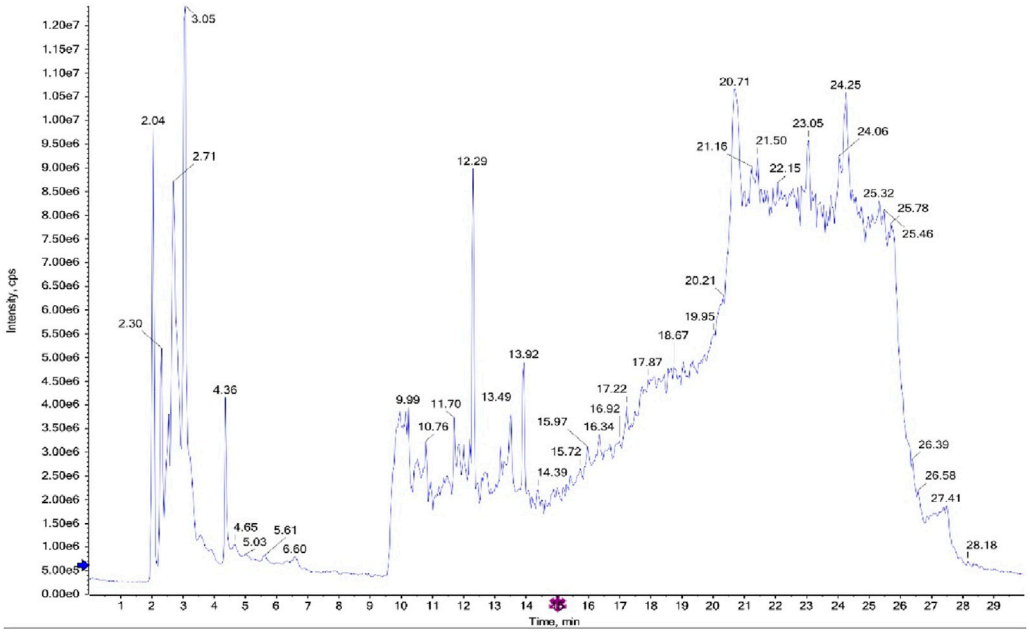


FIGURE 2
LC-MS/MS diagram of ethyl acetate fraction of the roots.

for 30–45 min. Cell proliferation was detected by measuring the absorbance of each well at 590 nm using Multiskan® EX (Thermo Scientific, United States) Microplate Reader. The Experiment was performed three times in triplicates (Ghasemi et al., 2023).

2.8 Statistical study

All methods were conducted in triplicate, and results are expressed as the mean ± standard deviation (SD). Statistical analyses, including one-way ANOVA and multiple group comparisons, were performed using GraphPad Prism version 10.4.1. Statistical significance was set at $p < 0.05$.

One-way ANOVA analysis of cytotoxic effects on HCT-116 and WI-38 cells

To assess the statistical significance of the cytotoxic effects of the tested compounds on HCT-116 (colon cancer) and WI-38 (normal) cell lines, a one-way analysis of variance (ANOVA) was performed. The ANOVA test was applied to determine whether there were statistically significant differences in cell viability among the different tested samples. Post-hoc analysis using Tukey's test was conducted when significant differences were found to identify specific group variations.

3 Result

3.1 Phytochemical screening of crude extracts

The phytochemical analysis of the crude extracts from the aerial parts and roots of *Capparis spinosa* L. was done to establish its major classes of secondary metabolites.

3.2 LC-MS/MS and GC-MS analysis: phytochemical investigation of ethyl acetate fractions from aerial parts and roots

The LC-MS/MS analysis of the ethyl acetate fractions from the aerial parts and roots revealed the presence of several bioactive compounds, with notable differences between the two fractions. The detailed results, including compound structures and their respective LC-MS/MS spectra, are provided in the Figures 1, 2; Supplementary Tables S1, S2.

A preliminary phytochemical screening of the tested fractions was conducted using GC-MS to identify various bioactive compounds, including flavonoids, phenols, alkaloids, coumarins, cardiac glycosides, and terpenoids. The table and graph are shown in the Supplementary Figures S3–S6; Supplementary Tables S3–S6.

3.3 Antioxidant and free radical scavenging activity

The IC_{50} values for the five tested samples Leaves, Roots, Rutin, Astragalin, and Resveratrol, expressed in mg/mL, provide a quantitative measure of the antioxidant capacity of each sample. These results highlight the relative potency of the tested compounds in neutralizing free radicals, with lower IC_{50} values indicating higher antioxidant activity. The data are summarized in Table 1.

3.3.1 DPPH antioxidant results for aerial part, root, rutin, astragalin, and resveratrol

The DPPH method, an established approach for evaluating the free radical scavenging activity, was carried out on the samples in different concentrations (1.0 mg/mL, 0.1 mg/mL, 0.01 mg/mL, and

TABLE 1 This table includes an antioxidant assay of DPPH, FRAP, Cuprac, and ABTS for 5 samples.

Test	Leaves	Roots	Rutin	Astragalin	Resveratrol
DPPH	0.12	0.017	0.013	1.2	0.032
ABTS	0.12	0.11	0.125	1.1	0.1
FRAP	1.4	0.36	1.06	4.08	0.7
CUPRAC	0.7	0.06	0.09	0.126	0.12

Note: The IC_{50} values were determined based on the median response from three independent experiments, with each experiment performed in triplicate to ensure accuracy and reproducibility

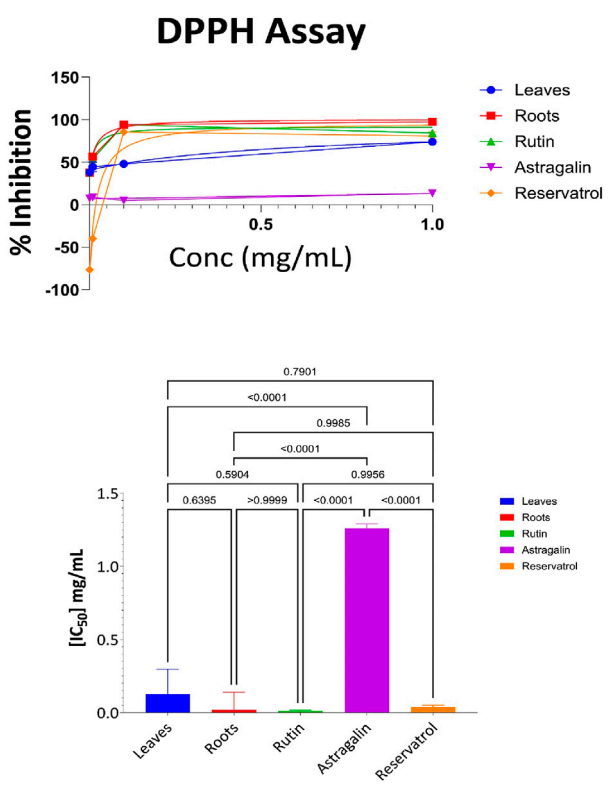


FIGURE 3
DPPH antioxidant activity: percent inhibition and IC_{50} with statistical comparisons (One-way ANOVA and Tukey's test) data are expressed as mean +- SD and n = 3.

0.001 mg/mL) in the present study. Supplementary Table S7 also shows the percent inhibition at these concentrations for each of the samples representing all the likely ranges of their antioxidant potentials.

As shown in Supplementary Table S7, the root extract exhibited the highest level of antioxidant activity at the highest concentration (97% inhibition at 1 mg/mL). Rutin also showed strong antioxidant activity, achieving 93% inhibition at 0.1 mg/mL and 84% at 1 mg/mL. Resveratrol followed closely, with 77% inhibition at 1 mg/mL and 84% at 0.1 mg/mL. The aerial parts demonstrated moderate activity, with 75% inhibition at the highest concentration. Astragalin, however, showed the weakest activity, with only 11% inhibition at 1 mg/mL and progressively lower values at lower concentrations. The IC_{50} value represents the concentration required to inhibit 50% of the DPPH radicals. Lower IC_{50} values indicate higher antioxidant potency, as less compound is required to achieve significant inhibition (Djeghim et al., 2024). The IC_{50} values for each sample were determined from the data and are depicted in Figure 3. The DPPH radical scavenging assay was conducted to evaluate the antioxidant activity of the tested samples. The IC_{50} values indicate the concentration required to scavenge 50% of DPPH radicals, with lower values representing higher antioxidant potential. Among the tested compounds, Rutin (IC_{50} = 0.013 mg/mL) and Roots (IC_{50} = 0.017 mg/mL) exhibited the strongest antioxidant activity, followed by Resveratrol (IC_{50} = 0.032 mg/mL) and Leaves (IC_{50} = 0.12 mg/mL), while Astragalin displayed the weakest activity (IC_{50} = 1.2 mg/mL). Statistical analysis using one-way ANOVA and Tukey's multiple comparison tests confirmed that the differences in antioxidant potential were statistically significant ($p < 0.0001$) between Astragalin and all other compounds, indicating its significantly lower free radical scavenging capacity. However, no significant differences were observed between Roots and Rutin ($p > 0.9999$), Leaves and Roots ($p = 0.639$), or Leaves and Resveratrol ($p = 0.791$), suggesting comparable antioxidant activity among these compounds. These results highlight the strong radical scavenging properties of Rutin and Roots, while Astragalin exhibited significantly lower antioxidant potential compared to the other samples.

3.3.2 ABTS antioxidant results for aerial part, root, resveratrol, astragalin, and rutin

The further evaluation of the antioxidant properties of the aerial parts, roots, and Resveratrol, Astragalin, and Rutin fractions was carried out using the ABTS radical cation method, which is often used in the estimation of the free radical scavenging potential of the plant. Supplementary Table S8 depicts the percentage of ABTS radicals that were effectively inhibited by the four different concentrations of the samples (1.0 mg/mL, 0.1 mg/mL, 0.01 mg/mL, and 0.001 mg/mL). According to the data in Supplementary Table S8, Resveratrol exhibited the highest antioxidant activity across all concentrations, particularly at 1 mg/mL, where it achieved 92% inhibition of ABTS radicals. The root extract followed closely, demonstrating 88% inhibition at the same concentration. Rutin also displayed strong antioxidant potential, with 78% inhibition at 1 mg/mL. However, its activity diminished more rapidly at lower concentrations compared to resveratrol and roots. In comparison, the extracts obtained from the aerial parts were only moderately active, achieving 37% inhibition at 1 mg/mL concentration and this activity decreased at lower concentrations. Astragalin demonstrated the weakest antioxidant activity, achieving only 25% inhibition at 1 mg/mL, and showing minimal effectiveness at lower concentrations.

The results from the ABTS assay, as visualized in Figure 4, provide further insights into the antioxidant capacity of the samples.

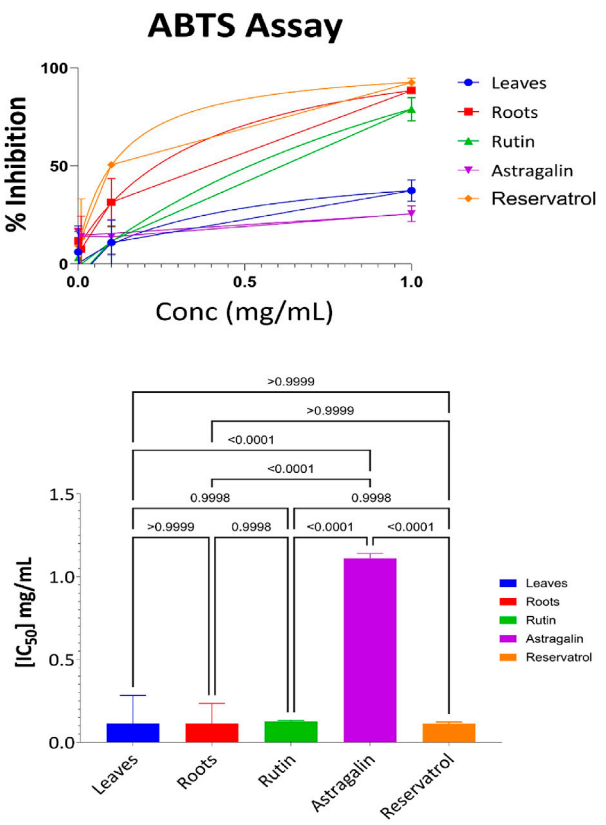


FIGURE 4
ABTS antioxidant activity: percent inhibition and IC_{50} with statistical comparisons (One-way ANOVA and Tukey's test) data are expressed as mean +- SD and n = 3.

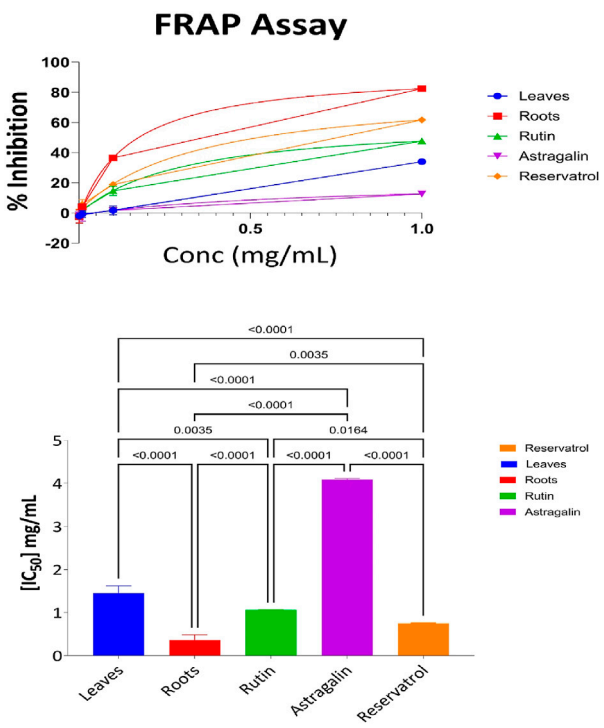


FIGURE 5
FRAP antioxidant activity: percent inhibition and IC_{50} with statistical comparisons (One-Way ANOVA and Tukey's test) data are expressed as mean +- SD and n = 3.

The ABTS radical scavenging assay was performed to evaluate the antioxidant potential of the tested samples. The IC_{50} values revealed that Resveratrol (IC_{50} = 0.1 mg/mL) exhibited the highest antioxidant activity, followed closely by Roots (IC_{50} = 0.11 mg/mL), Leaves (IC_{50} = 0.12 mg/mL), and Rutin (IC_{50} = 0.125 mg/mL), where Astragalin displayed the weakest antioxidant activity (IC_{50} = 1.1 mg/mL). Statistical analysis using one-way ANOVA and Tukey's multiple comparison test showed no significant differences between Leaves, Roots, Rutin, and Resveratrol ($p > 0.9999$), indicating similar antioxidant potential among these samples. However, Astragalin exhibited significantly lower antioxidant activity compared to all other tested compounds ($p < 0.0001$), confirming its weaker radical scavenging capacity. These findings reinforce the strong antioxidant potential of Leaves, Roots, Rutin, and Resveratrol, with Astragalin demonstrating a markedly lower ability to neutralize ABTS radicals.

3.3.3 FRAP result of the following fraction aerial part, root, resveratrol, astragalin, and rutin

The Ferric Reducing Antioxidant Power (FRAP) assay quantified the antioxidant potential of the aerial parts, roots, resveratrol, astragalin, and rutin. This assay evaluates the activity of samples in the reduction of ferric ions (Fe^{3+}) to ferrous ions (Fe^{2+}) as a defined measure of antioxidant activity. Supplementary Table S9 shows the percentage of ferric ion reduction at various concentrations for each of the samples. At the highest concentration of 1 mg/mL, the root extract was found to have the highest level of antioxidant activity with 82% ferric ion reduction. This was followed by resveratrol at 61% and Rutin at 47% respectively. The aerial parts exhibited moderate antioxidant activity with 34% ferric ion reduction, while Astragalin had the least activity reducing 12% of the ferric ions. At lower concentrations such as (0.01 mg/mL and 0.001 mg/mL), the samples in general showed a significant reduction in antioxidant activities, with some being negative values, showing a lack of or very little activity. This highlights the importance of concentration in the investigation of antioxidant screening by FRAP where high amounts of the materials are essential to produce enhanced antioxidant activities. The results presented in Figure 5 show IC_{50} of aerial parts, roots, Resveratrol, Astragalin, and Rutin as a free radical scavenging effect. The Ferric Reducing Antioxidant Power (FRAP) assay was performed to assess the reducing capacity of the tested samples. The IC_{50} values indicated that Roots (IC_{50} = 0.36 mg/mL) exhibited the highest reducing power, followed by Resveratrol (IC_{50} = 0.7 mg/mL), Rutin (IC_{50} = 1.06 mg/mL), and Leaves (IC_{50} = 1.4 mg/mL), Astragalin showed the weakest reducing capacity (IC_{50} = 4.08 mg/mL). Statistical analysis using one-way ANOVA and Tukey's multiple comparison tests confirmed significant differences ($p < 0.0001$) between Leaves and Roots, as well as between Astragalin and all other tested samples, indicating substantial variations in antioxidant potential. Additionally, significant differences were observed between Rutin and Resveratrol ($p = 0.0164$) and between Roots and Resveratrol ($p = 0.0035$), highlighting their distinct reducing capacities. These results suggest that Roots possess the strongest

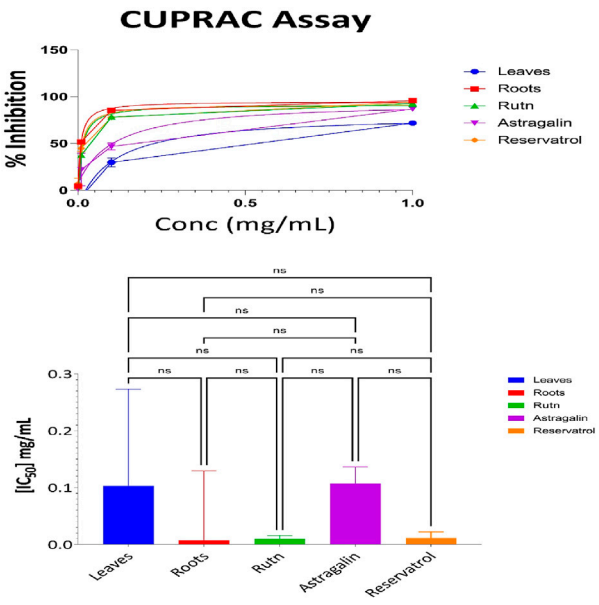


FIGURE 6
CUPRAC antioxidant activity: percent inhibition and IC_{50} with statistical comparisons (One-way ANOVA and Tukey's Test) data are expressed as mean +- SD and n = 3.

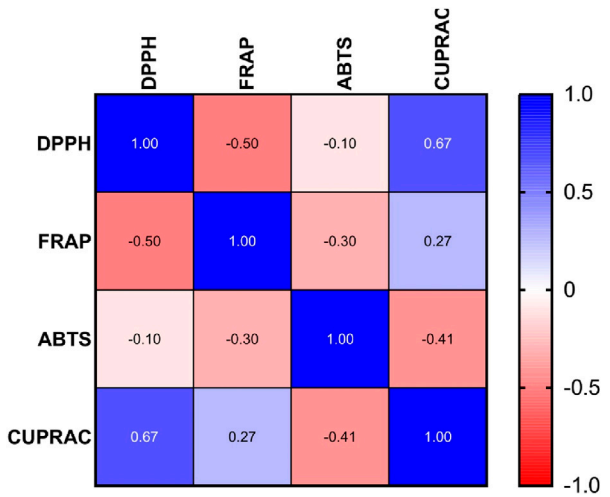


FIGURE 7
Pearson correlation coefficient analysis of IC_{50} values in DPPH, FRAP, ABTS, and CUPRAC antioxidant assays.

ferric reducing power, followed by Resveratrol, while Astragalin exhibited significantly lower antioxidant activity compared to all other samples.

3.3.4 CUPRAC antioxidant results for aerial part, root, resveratrol, astragalin, and rutin

The evaluation of the antioxidant activities of different fractions of the aerial part, root, resveratrol, astragalin, and rutin was carried out using the Cupric Reducing Antioxidant Capacity (CUPRAC) assay. This assay evaluates the ability of antioxidant compounds to reduce the cupric ions (Cu^{2+}) to the cuprous ions (Cu^{+}) which gives a good measure of its antioxidant activities. Supplementary Table S10 presents the percentage of reduction at various concentrations for each sample. At the maximum concentration (1 mg/mL), the antioxidant activity was the most substantial as 95% of the root extract was reduced with the decreasing order of activity following 94% of rutin and 93% of resveratrol. Astragalin could also display potent antioxidant effects with only an 85% reduction, whereas the aerial parts exhibited moderate activity with a 68% reduction. Decreased values of antioxidant activities were observed in samples at lower concentrations with the negative reduction values occurring at 0.01 mg/mL, and 0.001 mg/mL suggesting no activity or negligible at those concentrations.

The IC_{50} values, which represent the concentration required to achieve 50% inhibition, provide a more detailed comparison of the antioxidant efficacy of the samples. Figure 6 illustrates the IC_{50} values for the aerial parts, roots, resveratrol, astragalin, and rutin. The CUPRAC assay results indicate the antioxidant capacities of Leaves, Roots, Ruth, Astragalin, and Resveratrol, evaluated through % inhibition at concentrations of 0.001, 0.01, 0.01 and 1.0 mg/mL. All samples showed no statistically significant differences (marked as "ns") in % inhibition across the tested concentrations, suggesting comparable short-range antioxidant effects at these specific doses. The CUPRAC assay was conducted to evaluate the antioxidant capacity of the tested samples. The IC_{50} values revealed that Roots (IC_{50} = 0.06 mg/mL) exhibited the strongest antioxidant activity, followed by Rutin (IC_{50} = 0.09 mg/mL) and Resveratrol (IC_{50} = 0.12 mg/mL). Astragalin (IC_{50} = 0.126 mg/mL) demonstrated slightly weaker activity, while Leaves (IC_{50} = 0.7 mg/mL) showed the lowest antioxidant potential among the tested samples. These findings highlight the superior antioxidant activity of Roots, likely due to the presence of highly effective reducing agents, as measured by the CUPRAC method.

Statistical analysis using one-way ANOVA revealed no significant differences in antioxidant activity between Roots, Rutin, Resveratrol, and Astragalin ($p > 0.05$).

3.3.5 Statistical analysis and correlation between antioxidant activity measuring methods

Interpretation of Pearson Correlation Coefficients in the Context of Antioxidant Assays, A comparative analysis of the antioxidant potential among the samples is illustrated in Figure 7.

The Pearson correlation matrix in the provided figure represents the relationships between four used antioxidant assays DPPH, FRAP, ABTS and CUPRAC.

Each of these assays measures antioxidant potential but through different mechanisms. Correlations among them indicate similarities or differences in how antioxidants behave in different experimental conditions.

Correlations among them indicate similarities or differences in how antioxidants behave in different experimental conditions.

1. Strong Positive Correlation: DPPH vs. CUPRAC (r = 0.67)

The IC50 value for DPPH and CUPRAC shows strong linear correlation, suggesting that samples have high activity in DPPH also will have high activity in CUPRAC.

TABLE 2 Antiproliferative activity of compounds on HCT-116 and WI-38 cell lines.

Comp	Sample	*In vitro* cytotoxicity [IC_{50}, μg/mL ± SD][a]	
		HCT-116	WI-38
1	leave	23.26 ± 2.30	150.60 ± 2.90
2	Roots	34.65 ± 2.17	149.90 ± 4.75
3	Rutin	64.09 ± 2.06	205.60 ± 2.53
4	Astragalin	40.96 ± 2.23	126.70 ± 2.87
5	Resveratrol	34.03 ± 2.45	85.87 ± 2.74
Nutlin		62.72 ± 3.15	124.90 ± 3.06

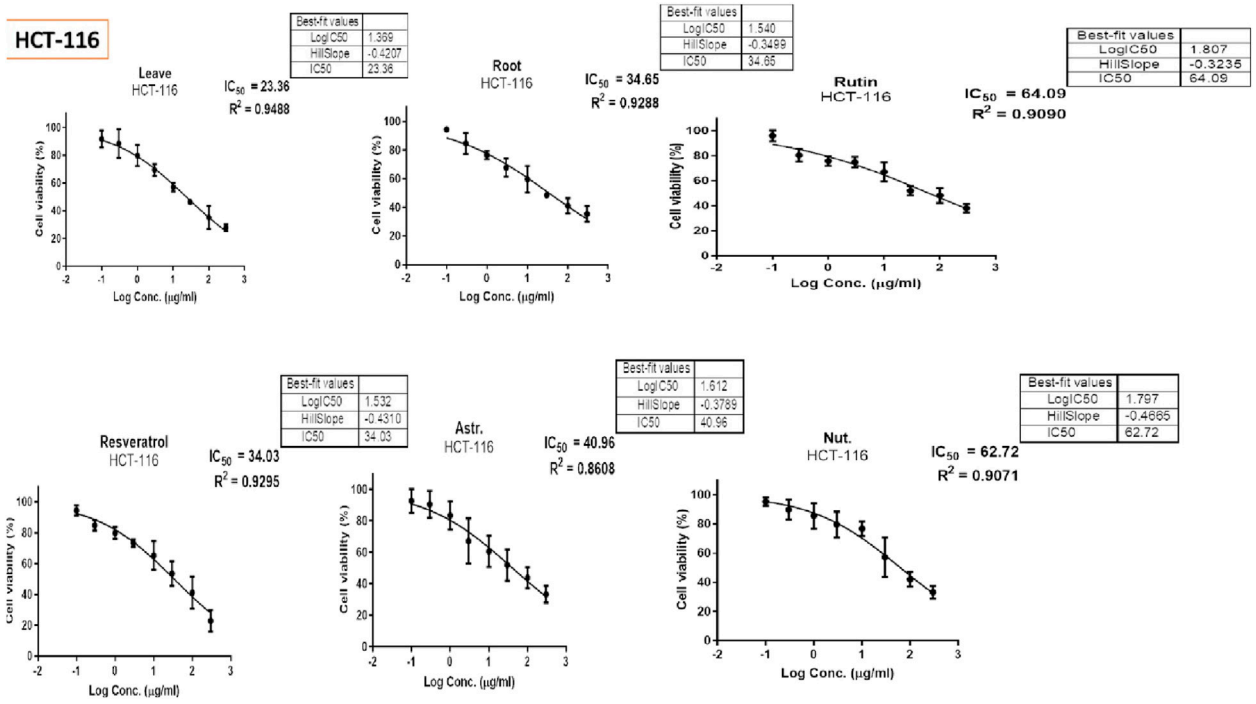


FIGURE 8
Antiproliferative activity of various extracts and compounds against HCT-116 cells.

2. Moderate Negative Correlation: DPPH vs. FRAP (r = −0.50)

A moderate inverse relationship indicates that samples with lower IC_{50} values in DPPH (higher antioxidant activity) tend to have higher IC_{50} values in FRAP meaning lower antioxidant activity 3. Weak Negative Correlation: DPPH vs ABTS (r = −0.10)

The weak negative correlation suggests minimal relationship between these assays in terms of IC_{50} values.

4. Weak Positive Correlation: FRAP vs CUPRAC (r = 0.27)

A weak but positive association exists between these two assays, indicating that some trends in antioxidant activity are shared.

5. Moderate Negative Correlation: ABTS vs. CUPRAC (r = −0.41)

A moderate inverse correlation implies that high antioxidant activity in ABTS (low IC_{50}) is moderately associated with lower antioxidant activity in CUPRAC.

6. Weak Negative Correlation: FRAP vs. ABTS (r = −0.30)

A weak inverse correlation suggests that there is little overlap in the antioxidant mechanisms measured by FRAP and ABTS.

3.4 MTT assay results and statistical analysis

The MTT assay was accomplished to assess the cell's viability in response to treatments with different extracts and compounds and the result is explained in Table 2, which shows the percent of

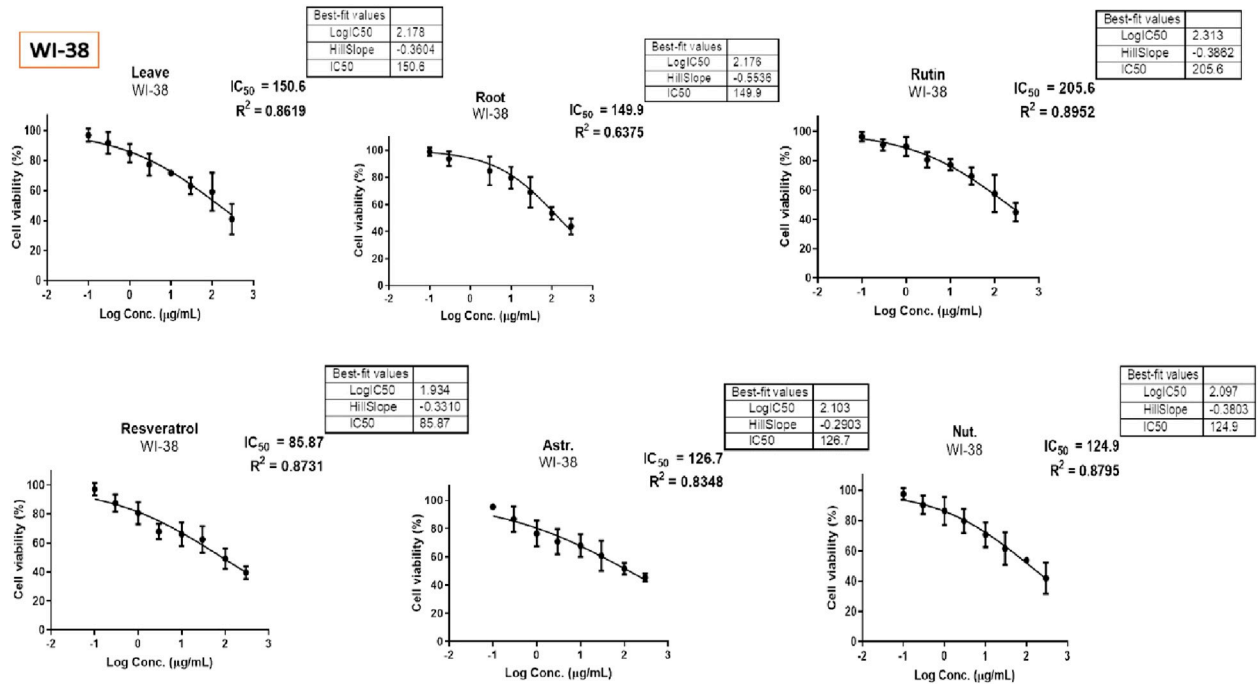


FIGURE 9
Antiproliferative activity of various extracts and compounds against WI-38 normal cells.

antiproliferation activity against the cancer cell human colon (HCT-116) (Figure 8 and effect against the normal lung fibroblast (WI-38) (Figure 9) cells to show the safety of those extracts and compounds, all cells treated for 72 h.

The cytotoxic effects of the tested compounds on HCT-116 and WI-38 cells were statistically analyzed. Significant differences among the tested samples were determined, and *post hoc* comparisons were conducted to identify group variations as shown in Figure 10 which shows the result on HCT-116 and Figure 11 explains the statistical result on the WI-38 cell line.

The MTT assay results, analyzed using one-way ANOVA and Tukey's multiple comparison tests, provide insights into the cytotoxic effects and selectivity of the tested compounds on HCT-116 colorectal cancer cells and WI-38 normal cells (Khayat et al., 2022). The analysis compared the cytotoxic activity of five natural compounds (Leaves, Roots, Rutin, Astragalin, and Resveratrol) with Nutlin, a well-established MDM2 inhibitor used as a reference compound (Basha and Mohan, 2024). In HCT-116 cells, Nutlin exhibited an IC_{50} of 62.72 ± 3.15 µg/mL, serving as the benchmark for cytotoxicity. Among the tested compounds, Leaves demonstrated the highest cytotoxicity (IC_{50} = 23.26 ± 2.30 µg/mL, $p < 0.0001$ vs. Nutlin), followed by Roots (IC_{50} = 34.65 ± 2.17 µg/mL, $p < 0.0001$ vs. Nutlin), Resveratrol (IC_{50} = 34.03 ± 2.45 µg/mL, $p < 0.0001$ vs. Nutlin), and Astragalin (IC_{50} = 40.96 ± 2.23 µg/mL, $p < 0.0001$ vs. Nutlin), whereas Rutin (IC_{50} = 64.09 ± 2.06 µg/mL, $p = 0.979$ vs. Nutlin) exhibited comparable cytotoxicity to the reference compound. These findings suggest that Leaves, Roots, Resveratrol, and Astragalin possess stronger anticancer activity than Nutlin, indicating the potential anticancer activity for those extracts and compounds.

In contrast, cytotoxicity evaluation in WI-38 normal cells revealed significantly different trends, emphasizing compound selectivity and potential therapeutic windows. Leaves and Roots exhibited high IC_{50} values (less toxicity) in WI-38 cells compared to HCT-116, indicating selective cytotoxicity toward cancer cells. Tukey's multiple comparison tests showed no significant difference between Leaves and Roots in normal cells ($p = 0.9998$), suggesting a similar safety profile. However, all other comparisons (Leaves vs. Rutin, Astragalin, Resveratrol, and Nutlin; $p < 0.0001$) indicated significant differences, highlighting the lower toxicity of Leaves and Roots in normal cells. Moreover, Rutin and Resveratrol exhibited significantly higher toxicity in WI-38 cells than in Leaves and Roots ($p < 0.0001$), suggesting a potential risk of non-selective cytotoxicity. Astragalin, while cytotoxic in cancer cells, showed a non-significant difference compared to Nutlin in normal cells ($p = 0.9796$), indicating a safety profile similar to the reference drug. Overall, these findings suggest that Leaves and Roots exhibit the best selectivity between cancer and normal cells, making them promising candidates for further anticancer investigations.

4 Discussion

The results from the phytochemical screening of the aerial part extracts indicated that there exist several classes of important metabolites such as; flavonoids and coumarins,

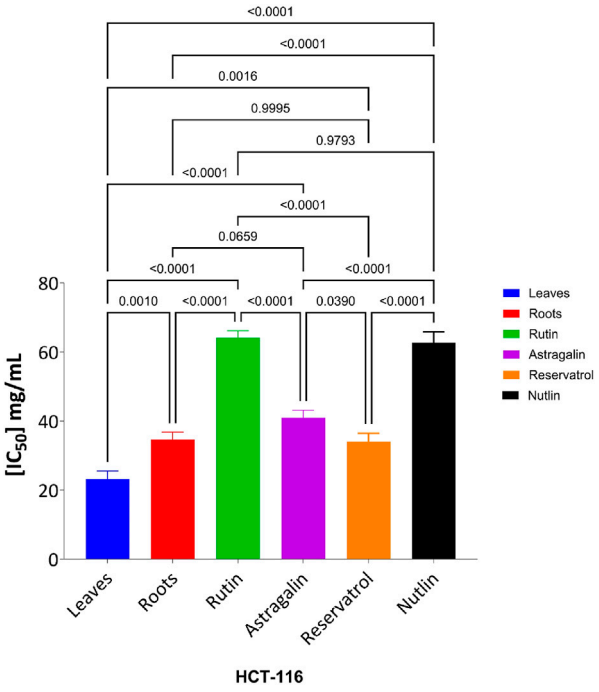


FIGURE 10
Effect of tested compounds on HCT-116 cell viability: one-way ANOVA and Tukey's post-hoc analysis.

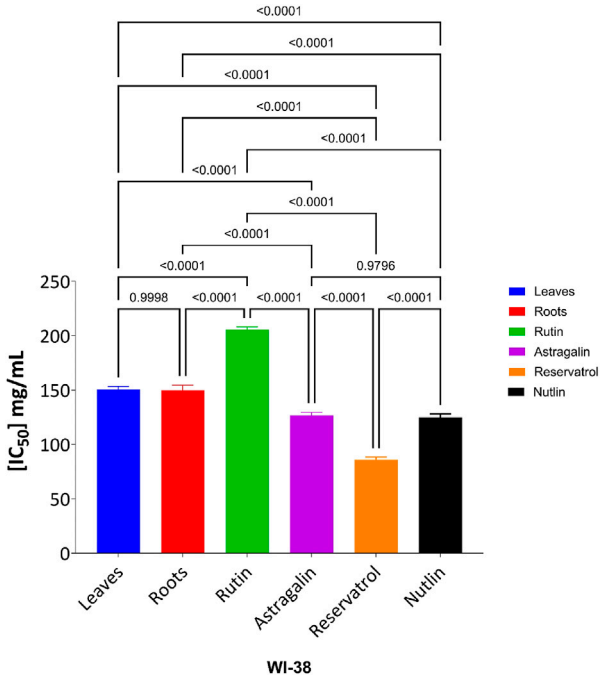


FIGURE 11
Effect of tested compounds on WI-38 cell viability: one-way ANOVA and Tukey's post-hoc analysis.

phenol derivatives, terpenes, and cardiac glycosides as shown by previous studies (Annaz et al., 2022). Similar findings have been reported in previous studies, where Capparis spinosa was recognized for its rich flavonoid and polyphenolic content, contributing to its therapeutic properties (Castillo et al., 2024).

4.1 Antioxidant activity

The five samples that were subjected to four standard antioxidant assays indicated Rutin, Roots, Resveratrol, Leaves, and Astragalin were also measured for their IC_{50} values and antioxidant potential in these assays-DPPH, FRAP, ABTS, and CUPRAC. From these tests, all the samples were assessed for their scavenging activities and reductive capabilities, and differences were observed in the Levels of Antioxidant activity in different methods used.

The DPPH method is an established approach for evaluating the free radical scavenging activity (Gulcin and Alwasel, 2023). In this assay, Rutin emerged as the potent antioxidant with the least IC_{50} having values of 0.013 mg/mL. This shows that the compound can scavenge free radicals at remarkably low concentrations; our results align with these findings (Brighente et al., 2007; Wang et al., 2021; Zhou et al., 2023). The root extract followed closely with the IC_{50} concentrations of 0.017 mg/mL, which shows that this also has a good free radical scavenging ability. Resveratrol on the other hand, although the IC_{50} value is just a bit more than for Rutin, showing 0.032 mg/mL, exhibited high efficiency in this assay as shown by other study (Yang et al., 2008). Leaves and Astragalin had much higher IC_{50} values thus implying a lower capacity to exert antioxidant effects. A particularly high IC_{50} value of astragalin which was 1.2 mg/mL; it is the least effective against DPPH radicals.

In the ABTS assay Resveratrol exhibited the highest activity with an IC_{50} value of 0.1 mg/mL that making him a potent free radical scavenging compound as approved by a previous study (Rosiak et al., 2022). This was closely followed by the Roots (0.11 mg/mL) and Leaves (0.121 mg/mL) suggesting that these samples are reasonably efficient in scavenging ABTS radicals as shown by other studies (Annaz et al., 2022). Though Astragalin did not possess ABTS scavenging activity and had a slightly higher IC_{50} value of 1.1 mg/mL confirming its consistently lower antioxidant capacity across different assays as also approved by other studies (Li et al., 2017). Rutin on the other hand also has an IC50 value close to that of roots 0.125 suggesting its high activity in ABTS assay as demonstrated by this study (Devkota et al., 2023).

In the FRAP assay which assays the ability of the samples to convert Fe3+ to Fe2+ (Mishra et al., 2022), it was observed that the roots extract had the greatest activity with an IC_{50} value of 0.36 mg/mL (Rajhi et al., 2021). This implies that there exist compounds present in the roots that enhance the effectiveness of this reduction most, rendering it the strongest in terms of ferrous reducing capacity. On the other hand, leaf extracts, with an IC_{50} of 1.4 mg/mL, showed low reducing capacity, while Rutin in the FRAP assay showed low activity with an IC50 value of 1.06 mg/mL. Resveratrol demonstrates high activity just a second after the

roots extract with IC50 0.7 mg/lm aligns with another study showing also a high activity for it in FRAP assay (Rajhi et al., 2021). The high IC_{50} value of 4.0 mg/mL for Astragalin was indicative of low antioxidant activity, which was due to a lower ability to engage in redox reactions relative to the other samples (Li et al., 2017). In CUPRAC activity test The most active out of all the tested samples turned out to be Root extract with the IC_{50} of 0.06 mg/mL as approved by Zamani et al. (2023), Followed by Rutin with IC_{50} of 0.09 mg/mL rendering them the second potent one in CUPRAC assay. This result brings out Roots cupric-reducing activity at the maximum level (Zamani et al., 2023). Resveratrol on the other hand showed also high antioxidant activities IC_{50} values of 0.012 mg/m (Zamani et al., 2023)L. In this case, the value of IC_{50} for the Leaves is higher at 0.7 mg/mL, which suggests the presence of lesser antioxidant activity despite the majority of studies showing high activity for *Capparis spinosa* leaves extract (Beldi et al., 2022). These observations reinforce the necessity of additional statistical measurements to characterize and compare any antioxidant action.

The cytotoxicity study of the two extracts (leaves and roots) of *C. spinosa* along with the three natural compounds rutin, astragalin and resveratrol were analyzed using one-way ANOVA and Tukey's multiple comparison test to provide insight into the anticancer activity and selectivity of the tested compounds (Potočnjak et al., 2022). The result revealed that the leaves and root extracts showed highest toxicity against the HCT-116 cancer cells and the lower against normal cells WI-38 normal cells. The selectivity is crucial, as an ideal therapeutic agent should effectively target cancer cells while sparing normal cells (Garg et al., 2024).

In this study, Nutlin was used as a reference compound and showed IC_{50} of 62.72 ± 3.15 μg/mL in HCT-116 cells, consistent with its role in a previous study in activity and restoring the P53 role as an anticancer agent (Kumari et al., 2022). However several of the compounds included in this study particularly the leaves and roots exhibited significantly higher activity with Leaves (IC_{50} = 23.26 ± 2.30 μg/mL) and Roots (IC_{50} = 34.65 ± 2.17 μg/mL), demonstrated significantly higher cytotoxicity than Nutlin ($p < 0.0001$) suggesting their potential activity as anticancer agent this results along with previous similar study like activity of leaves on HCT-116 (Abdul Samad, 2024; El-Berawey, 2024). The significant cytotoxicity of Resveratrol (IC_{50} = 34.03 ± 2.45 μg/mL, $p < 0.0001$ vs. Nutlin) aligns with prior findings on its ability to induce apoptosis, inhibit proliferation, and enhance oxidative stress in colorectal cancer cells (Gündoğdu and Özyurt, 2023). The differential cytotoxicity observed between HCT-116 and WI-38 cells is a crucial finding, as Leaves and Roots extracts displayed significantly higher IC_{50} values in WI-38 cells, indicating lower toxicity in normal cells. This selectivity suggests a potential therapeutic advantage, as compounds with a high cancer-to-normal cell cytotoxicity ratio are preferred in drug development to minimize systemic toxicity (Ramos et al., 2021). Additionally, Rutin (Ur Rahman and Panichayupakaranant, 2025) and Resveratrol (El Omari et al., 2021) exhibited relatively little higher toxicity in WI-38 cells but still kept their safety profile against normal cells and selectivity against HCT-116. Astragalin, which showed strong cytotoxicity against cancer cells (Chen et al., 2017), exhibited a non-significant difference compared to Nutlin in normal cells ($p = 0.9796$), suggesting a comparable safety profile to the reference MDM2 inhibitor.

The observed cytotoxic effects can be attributed to multiple mechanisms, including MDM2 inhibition, apoptosis induction, and oxidative stress modulation, which are well-documented anticancer pathways (Khan et al., 2020; Jazvinšćak Jembrek et al., 2021; Yarmohammadi et al., 2021). Our study provides a strong foundation for the further development of selective anticancer agents. Future investigations should focus on detailed mechanistic studies, including apoptosis assays, cell cycle analysis, and gene expression profiling of MDM2 and related pathways to fully elucidate the potential of these compounds.

5 Conclusion

The current study highlights the importance of performing multiple assays to assess antioxidant capacity, given the variability observed across different tests, such as DPPH, FRAP, ABTS, and CUPRAC. Among the tested samples, certain compounds, particularly Rutin, displayed strong antioxidant potential, suggesting its role in radical scavenging and reducing power. The root extract also demonstrated notable antioxidant activity. While Resveratrol and the aerial parts showed moderate activity, Astragalin exhibited minimal antioxidant capability across assays. Rutin and root extracts appear promising for further exploration as natural antioxidants, while Resveratrol may also hold potential. Additionally, the MTT assay results revealed that certain samples exhibit varying degrees of cytotoxicity against HCT-116 cancer cells, with leaf extracts showing potent and selective anticancer activity. The root extract and Resveratrol also demonstrated moderate cytotoxicity, although with slightly less selectivity. These findings suggest that the cytotoxic potential, coupled with selectivity, is crucial in identifying viable anticancer agents. Further research is necessary to elucidate the mechanisms underlying these activities and to optimize their therapeutic potential, aiming to balance efficacy with minimal toxicity to normal cells.

Data availability statement

The raw data supporting the conclusions of this article will be made available by the authors, without undue reservation.

Ethics statement

Ethical approval was not required for the studies on humans in accordance with the local legislation and institutional requirements because only commercially available established cell lines were used.

Author contributions

AO: Conceptualization, Validation, Writing–original draft. AD: Supervision, Validation, Writing–review and editing. GT: Project administration, Writing–review and editing. OM: Conceptualization, Writing–original draft. LC-G: Data curation, Funding acquisition, Resources, Writing–original draft. SK-J: Investigation, Writing–original draft.

Funding

The author(s) declare that no financial support was received for the research and/or publication of this article.

Conflict of interest

The authors declare that the research was conducted in the absence of any commercial or financial relationships that could be construed as a potential conflict of interest.

Generative AI statement

The author(s) declare that no Generative AI was used in the creation of this manuscript.

Publisher's note

All claims expressed in this article are solely those of the authors and do not necessarily represent those of their affiliated organizations, or those of the publisher, the editors and the reviewers. Any product that may be evaluated in this article, or claim that may be made by its manufacturer, is not guaranteed or endorsed by the publisher.

Supplementary material

The Supplementary Material for this article can be found online at: https://www.frontiersin.org/articles/10.3389/fchem.2025.1540174/full#supplementary-material

References

Abdulridha, R. N., and Saliem, A. H. (2023). Antidiarrheal effect of Capparis spinosa fruits extract. *Egypt. J. Hosp. Med.* 91, 3862–3869. doi:10.21608/ejhm.2023.293470

Abdul Samad, S. (2024). Anticancer activity of capparis spinosa extract against colorectal cancer.

Allaith, A. a.A. (2016). Assessment of the antioxidant properties of the caper fruit (Capparis spinosa L.) from Bahrain. *J. Assoc. Arab Univ. Basic Appl. Sci.* 19, 1–7. doi:10.1016/j.jaubas.2014.07.001

Alqahtani, A. S., Nasr, F. A., Ahmed, M. Z., Bin Mansour, M. Y., Biksmawi, A. A., Noman, O. M., et al. (2023). *In vitro* protective and anti-inflammatory effects of Capparis spinosa and its flavonoids profile. *Open Chem.* 21, 20230186. doi:10.1515/chem-2023-0186

Annaz, H., Sane, Y., Bitchagno, G. T. M., Ben Bakrim, W., Drissi, B., Mahdi, I., et al. (2022). Caper (Capparis spinosa L.): an updated review on its phytochemistry, nutritional value, traditional uses, and therapeutic potential. *Front. Pharmacol.* 13, 878749. doi:10.3389/fphar.2022.878749

Apak, R., Güçlü, K., Özyürek, M., Bektaşoğlu, B., and Bener, M. (2010). "Cupric ion reducing antioxidant capacity assay for antioxidants in human serum and for hydroxyl radical scavengers," *Advanced Protocols in Oxidative Stress II. Methods in Molecular Biology*. Editor D. Armstrong (Totowa, NJ: Humana Press) 594. doi:10.1007/978-1-60761-411-1_15

Bacchetti, T., Campagna, R., Sartini, D., Cecati, M., Morresi, C., Bellachioma, L., et al. (2022). C. spinosa L. subsp. rupestris phytochemical profile and effect on oxidative stress in normal and cancer cells. *Molecules* 27, 6488. doi:10.3390/molecules27196488

Baliyan, S., Mukherjee, R., Priyadarshini, A., Vibhuti, A., Gupta, A., Pandey, R. P., et al. (2022). Determination of antioxidants by DPPH radical scavenging activity and quantitative phytochemical analysis of Ficus religiosa. *Molecules* 27, 1326. doi:10.3390/molecules27041326

Basha, N. J., and Mohan, R. (2024). Insight on heterocycles as p53-MDM2 protein-protein interaction inhibitors: molecular mechanism for p53 activation. *ChemistrySelect* 9, e202304525. doi:10.1002/slct.202304525

Beldi, H., Gali, L., Benbott, A., Boudechicha, A., Bensouici, C., Yahia, A., et al. (2022). Variation of phenolic content and bioactivity between the different organs of the Algerian Capparis spinosa L.

Benzie, I. F., and Devaki, M. (2018). The ferric reducing/antioxidant power (FRAP) assay for non-enzymatic antioxidant capacity: concepts, procedures, limitations and applications. *Meas. Antioxid. activity and capacity Recent trends Appl.*, 77–106. doi:10.1002/9781119135388.ch5

Brand-Williams, W., Cuvelier, M.-E., and Berset, C. (1995). Use of a free radical method to evaluate antioxidant activity. *LWT-Food Sci. Technol.* 28, 25–30. doi:10.1016/s0023-6438(95)80008-5

Brighente, I., Dias, M., Verdi, L., and Pizzolatti, M. (2007). Antioxidant activity and total phenolic content of some Brazilian species. *Pharm. Biol.* 45, 156–161. doi:10.1080/13880200601113131

Calmeiro, J., Mendes, L., Duarte, I. F., Leitão, C., Tavares, A. R., Ferreira, D. A., et al. (2021). In-depth analysis of the impact of different serum-free media on the production of clinical grade dendritic cells for cancer immunotherapy. *Front. Immunol.* 11, 593363. doi:10.3389/fimmu.2020.593363

Castillo, A. B., El-Azhary, M., Sorino, C., and Levay, L. (2024). Potential ecological risk assessment of microplastics in coastal sediments: their metal accumulation and interaction with sedimentary metal concentration. *Sci. Total Environ.* 906, 167473. doi:10.1016/j.scitotenv.2023.167473

Chen, M., Cai, F., Zha, D., Wang, X., Zhang, W., He, Y., et al. (2017). Astragalin-induced cell death is caspase-dependent and enhances the susceptibility of lung cancer cells to tumor necrosis factor by inhibiting the NF-κB pathway. *Oncotarget* 8, 26941–26958. doi:10.18632/oncotarget.15264

Devkota, H. P., Belwal, T., and Bhatt, I. D. (2023). Nutraceuticals from Himalayan fruits and berries: opportunities and challenges. *Himal. Fruits Berries*, 497–505. doi:10.1016/b978-0-323-85591-4.00046-5

Djeghim, H., Benouchenne, D., Mokrani, E. H., Alsaeedi, H., Cornu, D., Bechelany, M., et al. (2024). Antioxidant, Anti-Alzheimer's, anticancer, and cytotoxic properties of peanut oil: *in vitro*, *in silico*, and GC-MS analysis. *Front. Chem.* 12, 1487084. doi:10.3389/fchem.2024.1487084

Elachouri, M., Idrissi, A., Chaachouay, N., Zidane, L., and Bussmann, R. W. (2024). "Capparis spinosa L. Capparaceae," in *Ethnobotany of northern africa and levant* (Springer), 609–623.

El-Berawey, D. Y. (2024). Phytochemical and phylogenetic perspective of medicinal plants used for cancer treatment in Egypt. *Nat. Prod. Res.*, 1–19. doi:10.1080/14786419.2024.2405012

El-Elimat, T., Olimat, S. M., Ali Agha, A. S. A., Aburjai, A., and Aburjai, T. (2024). LC-MS analysis of secondary metabolites of Asphodelus aestivus Brot. (Asphodelaceae) grown wild in Jordan. *Jordan J. Pharm. Sci.* 17, 333–343. doi:10.35516/jjps.v17i2.1850

El Omari, N., Bakrim, S., Bakha, M., Lorenzo, J. M., Rebezov, M., Shariati, M. A., et al. (2021). Natural bioactive compounds targeting epigenetic pathways in cancer: a review on alkaloids, terpenoids, quinones, and isothiocyanates. *Nutrients* 13, 3714. doi:10.3390/nu13113714

Garg, P., Malhotra, J., Kulkarni, P., Horne, D., Salgia, R., and Singhal, S. S. (2024). Emerging therapeutic strategies to overcome drug resistance in cancer cells. *Cancers* 16, 2478. doi:10.3390/cancers16132478

Ghasemi, M., Liang, S., Luu, Q. M., and Kempson, I. (2023). "The MTT assay: a method for error minimization and interpretation in measuring cytotoxicity and estimating cell viability," in *Cell viability assays: methods and protocols* (Springer), 15–33.

Grimalt, M., García-Martínez, S., Carbonell, P., Hernández, F., Legua, P., Almansa, M. S., et al. (2022). Relationships between chemical composition, antioxidant activity and genetic analysis with ISSR markers in flower buds of caper plants (Capparis spinosa L.)

of two subspecies spinosa and rupestris of Spanish cultivars. *Genet. Resour. Crop Evol.* 69, 1451–1469. doi:10.1007/s10722-021-01312-3

Gulcin, İ., and Alwasel, S. H. (2023). DPPH radical scavenging assay. *Processes* 11, 2248. doi:10.3390/pr11082248

Gull, T., Anwar, F., Sultana, B., Alcayde, M. a.C., and Nouman, W. (2015). Capparis species: a potential source of bioactives and high-value components: a review. *Industrial crops Prod.* 67, 81–96. doi:10.1016/j.indcrop.2014.12.059

Gündoğdu, A. Ç., and Özyurt, R. (2023). Resveratrol downregulates ENaCs through the activation of AMPK in human colon cancer cells. *Tissue Cell* 82, 102071. doi:10.1016/j.tice.2023.102071

Ilyasov, I. R., Beloborodov, V. L., Selivanova, I. A., and Terekhov, R. P. (2020). ABTS/PP decolorization assay of antioxidant capacity reaction pathways. *Int. J. Mol. Sci.* 21, 1131. doi:10.3390/ijms21031131

Jazvinšćak Jembrek, M., Oršolić, N., Mandić, L., Sadžak, A., and Šegota, S. (2021). Anti-oxidative, anti-inflammatory and anti-apoptotic effects of flavonols: targeting Nrf2, NF-κB and p53 pathways in neurodegeneration. *Antioxidants* 10, 1628. doi:10.3390/antiox10101628

Khan, H., Reale, M., Ullah, H., Sureda, A., Tejada, S., Wang, Y., et al. (2020). Anti-cancer effects of polyphenols via targeting p53 signaling pathway: updates and future directions. *Biotechnol. Adv.* 38, 107385. doi:10.1016/j.biotechadv.2019.04.007

Khayat, M. T., Zarka, M. A., El-Telbany, D. F. A., El-Halawany, A. M., Kutbi, H. I., Elkhatib, W. F., et al. (2022). Intensification of resveratrol cytotoxicity, pro-apoptosis, oxidant potentials in human colorectal carcinoma HCT-116 cells using zein nanoparticles. *Sci. Rep.* 12, 15235. doi:10.1038/s41598-022-18557-2

Kumari, S., Sharma, V., Tiwari, R., Maurya, J. P., Subudhi, B. B., and Senapati, D. (2022). Therapeutic potential of p53 reactivation in prostate cancer: strategies and opportunities. *Eur. J. Pharmacol.* 919, 174807. doi:10.1016/j.ejphar.2022.174807

Levizou, E., Drilias, P., and Kyparissis, A. (2004). Exceptional photosynthetic performance of Capparis spinosa L. under adverse conditions of Mediterranean summer. *Photosynthetica* 42, 229–235. doi:10.1023/b:phot.0000040594.85407.f4

Li, X., Tian, Y., Wang, T., Lin, Q., Feng, X., Jiang, Q., et al. (2017). Role of the p-coumaroyl moiety in the antioxidant and cytoprotective effects of flavonoid glycosides: comparison of astragalin and tiliroside. *Molecules* 22, 1165. doi:10.3390/molecules22071165

Mishra, Y., Amin, H. I. M., Mishra, V., Vyas, M., Prabhakar, P. K., Gupta, M., et al. (2022). Application of nanotechnology to herbal antioxidants as improved phytomedicine: an expanding horizon. *Biomed. and Pharmacother.* 153, 113413. doi:10.1016/j.biopha.2022.113413

Mollica, A., Zengin, G., Locatelli, M., Stefanucci, A., Mocan, A., Macedonio, G., et al. (2017). Anti-diabetic and anti-hyperlipidemic properties of Capparis spinosa L.: *in vivo* and *in vitro* evaluation of its nutraceutical potential. *J. Funct. foods* 35, 32–42. doi:10.1016/j.jff.2017.05.001

Moukette, B. M., Pieme, C. A., Njimou, J. R., Biapa, C. P. N., Marco, B., and Ngogang, J. Y. (2015). *In vitro* antioxidant properties, free radicals scavenging activities of extracts and polyphenol composition of a non-timber forest product used as spice: monodora myristica. *Biol. Res.* 48, 15–17. doi:10.1186/s40659-015-0003-1

Nazer, M. R., Jahanbakhsh, S., Ebrahimi, K., Niazi, M., Sepahvand, M., Khatami, M., et al. (2021). Cytotoxic and antileishmanial effects of various extracts of Capparis spinosa L. *Turkish J. Pharm. Sci.* 18, 146–150. doi:10.4274/tjps.galenos.2020.87259

Potočnjak, I., Šimić, L., Vukelić, I., Batičić, L., and Domitrović, R. (2022). Oleanolic acid induces HCT116 colon cancer cell death through the p38/FOXO3a/Sirt6 pathway. *Chemico-biological Interact.* 363, 110010. doi:10.1016/j.cbi.2022.110010

Rahimi, V. B., Rajabian, A., Rajabi, H., Vosough, E. M., Mirkarimi, H. R., Hasanpour, M., et al. (2020). The effects of hydro-ethanolic extract of Capparis spinosa (C. spinosa) on lipopolysaccharide (LPS)-induced inflammation and cognitive impairment: evidence from *in vivo* and *in vitro* studies. *J. Ethnopharmacol.* 256, 112706. doi:10.1016/j.jep.2020.112706

Rajhi, I., Hernandez-Ramos, F., Abderrabba, M., Ben Dhia, M., Ayadi, S., and Labidi, J. (2021). Antioxidant, antifungal and phytochemical investigations of Capparis spinosa L. *Agriculture* 11, 1025. doi:10.3390/agriculture11101025

Ramos, H., Soares, M. I., Silva, J., Raimundo, L., Calheiros, J., Gomes, C., et al. (2021). A selective p53 activator and anticancer agent to improve colorectal cancer therapy. *Cell Rep.* 35, 108982. doi:10.1016/j.celrep.2021.108982

Rivera, D., Inocencio, C., Obón, C., and Alcaraz, F. (2003). Review of food and medicinal uses ofCapparis L. SubgenusCapparis (capparidaceae). *Econ. Bot.* 57, 515–534. doi:10.1663/0013-0001(2003)057[0515:rofamu]2.0.co;2

Rosiak, N., Cielecka-Piontek, J., Skibiński, R., Lewandowska, K., Bednarski, W., and Zalewski, P. (2022). Antioxidant potential of resveratrol as the result of radiation exposition. *Antioxidants* 11, 2097. doi:10.3390/antiox11112097

Rumpf, J., Burger, R., and Schulze, M. (2023). Statistical evaluation of DPPH, ABTS, FRAP, and Folin-Ciocalteu assays to assess the antioxidant capacity of lignins. *Int. J. Biol. Macromol.* 233, 123470. doi:10.1016/j.ijbiomac.2023.123470

Seetharaman, J., Priya, R. A., Philip, R. R., Muthuraj, M., and Sankari, D. (2025). Evaluation of tridax procumbens secondary metabolites anti-tuberculosis activity by *in vitro* and *in silico* methods. *Curr. Microbiol.* 82, 50. doi:10.1007/s00284-024-04033-9

Shahrajabian, M. H., Sun, W., and Cheng, Q. (2021). Plant of the Millennium, Caper (Capparis spinosa L.), chemical composition and medicinal uses. *Bull. Natl. Res. Centre* 45, 131–139. doi:10.1186/s42269-021-00592-0

Skroza, D., Generalić Mekinić, I., Svilović, S., Šimat, V., and Katalinić, V. (2015). Investigation of the potential synergistic effect of resveratrol with other phenolic compounds: a case of binary phenolic mixtures. *J. Food Compos. Analysis* 38, 13–18. doi:10.1016/j.jfca.2014.06.013

Suktham, T., Jones, A., Soliven, A., Dennis, G. R., and Shalliker, R. A. (2019). A comparison of the performance of the cupric reducing antioxidant potential assay and the ferric reducing antioxidant power assay for the analysis of antioxidants using reaction flow chromatography. *Microchem. J.* 149, 104046. doi:10.1016/j.microc.2019.104046

Sun, Y., Yang, T., and Wang, C. (2023). Capparis spinosa L. as a potential source of nutrition and its health benefits in foods: a comprehensive review of its phytochemistry, bioactivities, safety, and application. *Food Chem.* 409, 135258. doi:10.1016/j.foodchem.2022.135258

Ur Rahman, A., and Panichayupakaranant, P. (2025). Antioxidants in cancer prevention. Antioxidants. *Nature's Def. Against Dis.*, 21–81. doi:10.1002/9781394270576.ch2

Wang, Z., Ding, Z., Li, Z., Ding, Y., Jiang, F., and Liu, J. (2021). Antioxidant and antibacterial study of 10 flavonoids revealed rutin as a potential antibiofilm agent in Klebsiella pneumoniae strains isolated from hospitalized patients. *Microb. Pathog.* 159, 105121. doi:10.1016/j.micpath.2021.105121

Yang, J., Guo, J., and Yuan, J. (2008). *In vitro* antioxidant properties of rutin. *LWT-Food Sci. Technol.* 41, 1060–1066. doi:10.1016/j.lwt.2007.06.010

Yang, S.-H., Tao, G., Yang, L., Wu, X., Liu, J.-W., Dagher, F., et al. (2023). Dietary phytochemical and metabolic disease prevention: focus on plant proteins. *Front. Nutr.* 10, 1089487. doi:10.3389/fnut.2023.1089487

Yarmohammadi, F., Hayes, A. W., and Karimi, G. (2021). Natural compounds against cytotoxic drug-induced cardiotoxicity: a review on the involvement of PI3K/Akt signaling pathway. *J. Biochem. Mol. Toxicol.* 35, e22683. doi:10.1002/jbt.22683

Zamani, E., Kamali Aliabad, K., Kalantar, S. M., Sodaeizadeh, H., Haghiralsadat, B. F., and Capanoglu, E. (2023). Investigating the effect of the habitat and type of extracted organ on the phytochemical compounds of caper (Capparis spinosa L.) as A medicinal and pasture plant. *Desert Manag.* 11, 57–72.

Zhou, Y., Duan, H., Chen, J., Ma, S., Wang, M., and Zhou, X. (2023). The mechanism of *in vitro* non-enzymatic glycosylation inhibition by Tartary buckwheat's rutin and quercetin. *Food Chem.* 406, 134956. doi:10.1016/j.foodchem.2022.134956

frontiers | Frontiers in Chemistry

TYPE Review
PUBLISHED 29 April 2025
DOI 10.3389/fchem.2025.1602967

Check for updates

OPEN ACCESS

EDITED BY
Ahmed A. Al-Karmalawy,
University of Mashreq, Iraq

REVIEWED BY
Kasireddy Sudarshan,
Purdue University, United States
Aya Alabdali,
UCSI University, Malaysia

*CORRESPONDENCE
Artem A. Svotin,
svotin_a_a@staff.sechenov.ru

RECEIVED 30 March 2025
ACCEPTED 21 April 2025
PUBLISHED 29 April 2025

CITATION
Taldaev A, Svotin AA, Obukhov SI, Terekhov RP and Selivanova IA (2025) Modification of biopharmaceutical parameters of flavonoids: a review.
Front. Chem. 13:1602967.
doi: 10.3389/fchem.2025.1602967

COPYRIGHT
© 2025 Taldaev, Svotin, Obukhov, Terekhov and Selivanova. This is an open-access article distributed under the terms of the Creative Commons Attribution License (CC BY). The use, distribution or reproduction in other forums is permitted, provided the original author(s) and the copyright owner(s) are credited and that the original publication in this journal is cited, in accordance with accepted academic practice. No use, distribution or reproduction is permitted which does not comply with these terms.

Modification of biopharmaceutical parameters of flavonoids: a review

Amir Taldaev[1,2,3], Artem A. Svotin[4]*, Semyon I. Obukhov[4], Roman P. Terekhov[4] and Irina A. Selivanova[4]

[1]Laboratory for the Study of Single Biomacromolecules, Institute of Biomedical Chemistry, Moscow, Russia, [2]Laboratory of Biomolecular NMR-Spectroscopy, Shemyakin-Ovchinnikov Institute of Bioorganic Chemistry, Moscow, Russia, [3]Research Center for Molecular Mechanisms of Aging and Age-Related Diseases, Moscow Institute of Physics and Technology, Dolgoprudny, Russia, [4]Nelyubin Institute of Pharmacy, Sechenov First Moscow State Medical University, Moscow, Russia

Flavonoids are natural organic compounds that are derivatives of diphenylpropane. This group of polyphenols can be found in multiple natural sources and they exhibit a variety of biological effects. Despite the wide array of beneficial properties, the development of drugs based on these compounds is hindered by their low bioavailability. Although the substantial body of information available on strategies to enhance the solubility and bioavailability of flavonoids, this knowledge remains fragmented. Therefore, the aim of this study was to consolidate and systematize scientific data on methods for increasing the solubility and bioavailability of flavonoid compounds without changing their initial molecular structures. Throughout the investigation, it was determined that the most prevalent methods for increasing solubility and bioavailability include co-crystallization, formation of phospholipid and inclusion complexes, and the creation of nanostructures. Although there were no pronounced differences observed in enhancing solubility, the impact of these methods on pharmacokinetic parameters was established. It was found that the production of inclusion complexes and nanostructures leads to the greatest increase in the area under the pharmacokinetic curve by an average of 4.2 and 3.7 times, respectively. The least effect was noted for phytosomes, where this parameter for the modified forms exceeded the initial value by only 1.7 times. Phospholipid complexes exhibited a longer average half-elimination time than all other modifications, achieving a 2.1-fold increase. For nanostructures and micelles, a substantial increase in maximum concentration of the active substance in blood plasma was observed, reaching an average of 5.4 times for both types of modifications. During the systematization and generalization of the data, a high level of heterogeneity in solubility assessment methods across various studies was revealed, complicating comparisons of original data obtained by different researchers. The findings of this review are crucial for researchers investigating the bioavailability of flavonoid compounds and will facilitate the selection of the most effective methods based on the desired outcomes for solubility and bioavailability.

KEYWORDS

flavonoids, solubility, permeability, bioavailability, biopharmaceutical properties, modification, review

1 Introduction

Flavonoids are natural organic compounds that are derivatives of diphenylpropane. This group of polyphenols can be found in multiple natural sources, including fruits (Ellwood et al., 2019), vegetables (Ahmed and Eun, 2018), berries (Whyte et al., 2019), tea (He et al., 2021), and a large number of medicinal plants (Tungmunnithum et al., 2018; Wang et al., 2018; Roy et al., 2022). Flavonoids exhibit a variety of biological effects, including anti-hepatotoxic (Gul et al., 2022), anti-ulcer (Zhang et al., 2020), and anti-inflammatory activities (Maleki et al., 2019; Al-Khayri et al., 2022), as well as wound healing properties (Carvalho et al., 2021; Zulkefli et al., 2023; Svotin et al., 2025). Several researchers claim that the anti-inflammatory effects of certain flavonoids result from the inhibition of interleukins (IL-1β, IL-6 and IL-8) and tumor necrosis factor TNF-α (Zaragozá et al., 2020). Possible mechanisms for the wound healing activity of flavonoids include their involvement in the regulation of the MAPKs and NF-kB signaling pathways (Lu et al., 2021; Ding et al., 2023). Flavonoid-related compounds, specifically isocoumarins, have been shown to exhibit anti-inflammatory activity by inhibiting enzymes involved in the leukotriene and prostaglandin pathways (Ramanan et al., 2016). Additionally, they may modulate neuronal functions through interaction with the neurotrophin receptor TrkB (Sudarshan et al., 2019). Furthermore, these compounds are potent antioxidants, capable of trapping free radicals (Masuoka et al., 2012; Tumilaar et al., 2024).

Many flavonoids are optically active compounds due to the presence of chiral carbon atoms in the benzopyranone ring. However, most researchers do not adequately address the issue of the stereochemistry of these substances. Nevertheless, this factor can lead to variations in the physicochemical, pharmacokinetic, pharmacodynamic, and pharmacological properties of various active pharmaceutical ingredients (APIs). Some scientists suggest that the lack of data regarding the stereochemistry of flavonoids may contribute to incomplete information about their safety and efficacy (Terekhov et al., 2024).

Despite the wide array of beneficial properties exhibited by flavonoids, the development of drugs based on these compounds is hindered by their low bioavailability. According to biopharmaceutical classification system (Charalabidis et al., 2019), bioavailability is influenced by the solubility of the compound in water and its permeability through the cell membrane. Most flavonoids demonstrate poor solubility in water at room temperature, which limits their bioavailability. In light of their pronounced biological effects, this limitation raises the important issue of how to enhance the solubility of this group of compounds.

An extensive search for methods to enhance the solubility and bioavailability of flavonoids is essential. Currently, variations in solubility in both polar and non-polar solvents are reported, depending on the specific structure of the flavonoid. The presence of a double bond in the ring C (Figures 1A, B), influences solubility, which is further affected by the number of hydroxyl groups in ring B. Additionally, the position of ring B within the benzopyranone structure plays a critical role. When methoxy groups are present in ring B, a decrease in flavonoid solubility is observed, regardless of the solvent used. Conversely, the existence of a single bond between the C2 and C3 atoms in ring C contributes to increased overall solubility, while the introduction of an OH group at C3 reduces solubility in water (Zhang H. et al., 2017). It is important to note that modifications in the chemical structure of these compounds may correlate with changes in biological activity. Consequently, there has been a growing interest among researchers in exploring strategies to enhance solubility without changing the original structure of flavonoids.

In addition to the physico-chemical properties of flavonoids, their bioavailability is also influenced by various other factors, including the dosage form of the drug (Stielow et al., 2023), physiological conditions (Dima et al., 2024), intestinal enzymes (Dima et al., 2020) and microflora (Kan et al., 2022). Moreover, low concentrations of flavonoids in blood plasma and their affinity for albumin hinder absorption (Naeem et al., 2022).

Despite the substantial body of information available on strategies to enhance the solubility and bioavailability of flavonoids, this knowledge remains fragmented. Therefore, it is crucial to systematize scientific information in this domain to identify new avenues for future pharmaceutical development.

The aim of this study was to consolidate and systematize scientific data on methods for increasing the solubility and bioavailability of flavonoid compounds without changing their

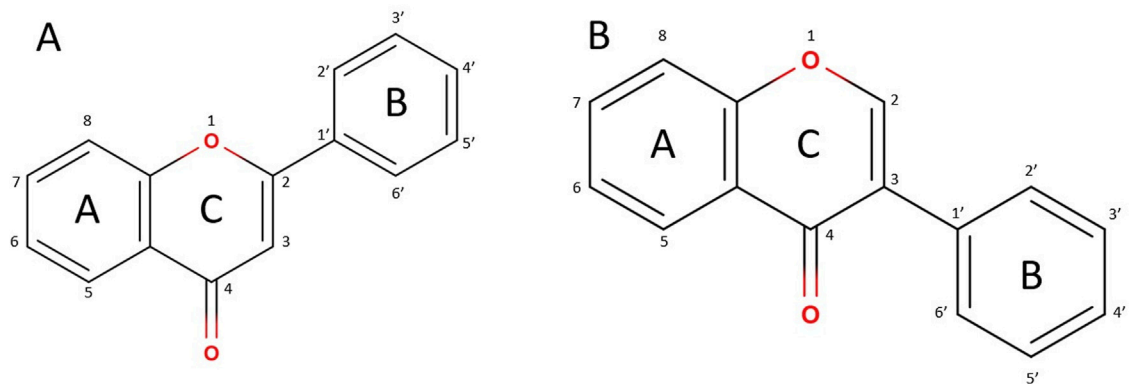


FIGURE 1
General structure: **(A)** flavonoids; **(B)** isoflavonoids.

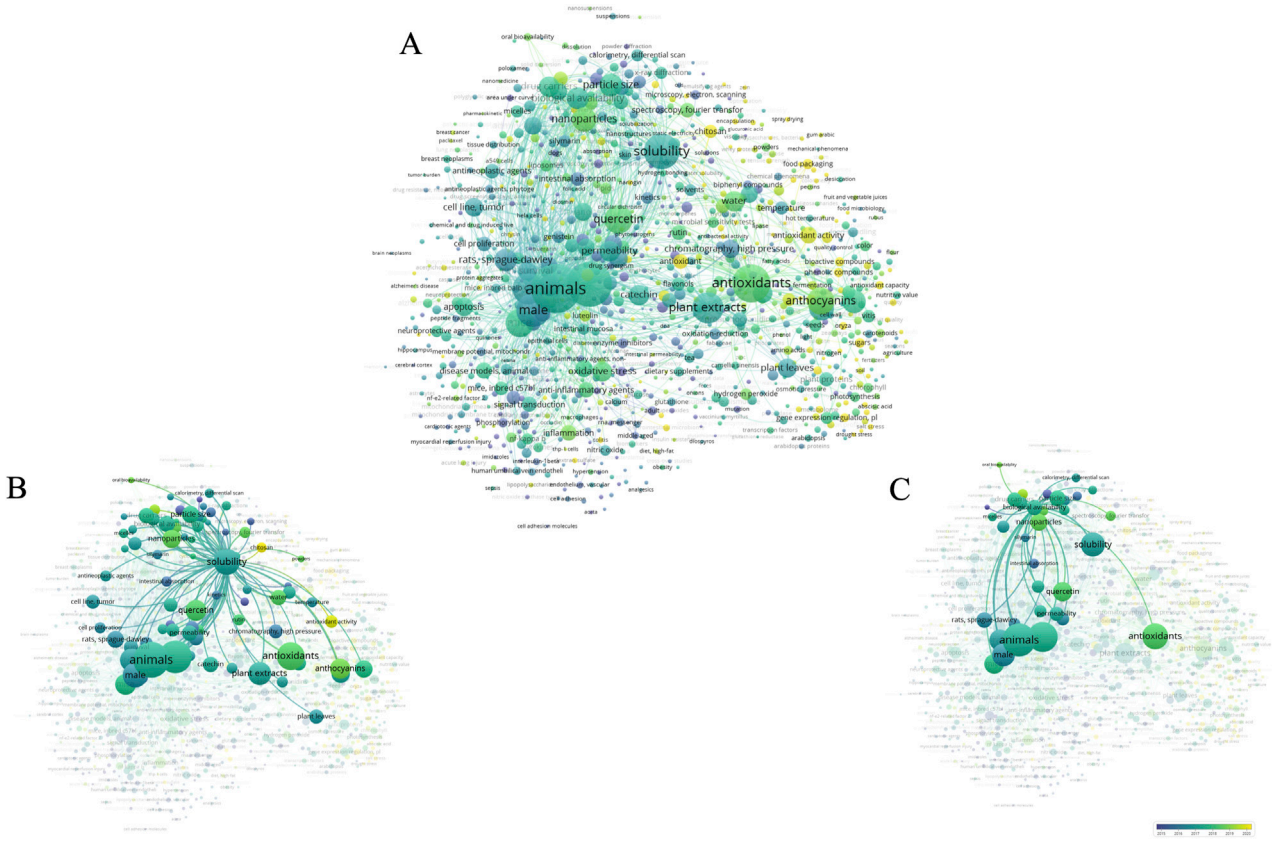


FIGURE 2
Bibliometric network on request "flavonoid AND (solubility or permeability) NOT review" in PubMed: **(A)** general view of network; **(B)** co-occurrence terms for "solubility"; **(C)** co-occurrence terms for "biological availability". Created by VOSviewer (Van Eck and Waltman, 2010; Van Eck and Waltman, 2011; Waltman and Van Eck, 2013).

initial molecular structures. Throughout this work, the main research question is to identify the most commonly encountered methods and evaluate their effectiveness in enhancing bioavailability by improving the solubility and permeability of the original flavonoids.

2 Methods

2.1 Search strategy

The following review was performed in accordance with the Preferred Reporting Items for Systematic Reviews and Meta-Analyses (PRISMA) guidelines (Page et al., 2021). To perform the literature search, the Google Scholar database was used. The following terms were applied: "flavonoid AND (solubility OR permeability) AND -review". The search was conducted on publications published no earlier than 2010.

2.2 Data processing

Two reviewers (AS and SO) independently and simultaneously performed an initial search and screening of articles by reading their tittles and abstracts to form the reference list. In case of disagreements, they were resolved by another author (RT).

Then, two authors (AS and SO) performed the data extraction of main texts, tables, figures, and Supplementary Material from the selected articles. The following data were in focus of the reviewers: method which used to increase bioavailability, initial and resulting solubility in water, multiplicity of solubility increase, initial and resulting apparent permeability, multiplicity of permeability increase, and main pharmacokinetic parameters. The sum of extracted outcomes was placed in Google Sheets. A complete consensus in the accumulated data was reached without further disagreements.

The result of the systematic analysis is presented as narrative synthesis.

3 Results

3.1 General outlook on scientific landscape

The literature indexed in MEDLINE was utilized to construct a bibliometric network based on query "flavonoid AND (solubility OR permeability) AND (NOT review)" in PubMed (Figure 2A). The term "flavonoid" was excluded from the network.

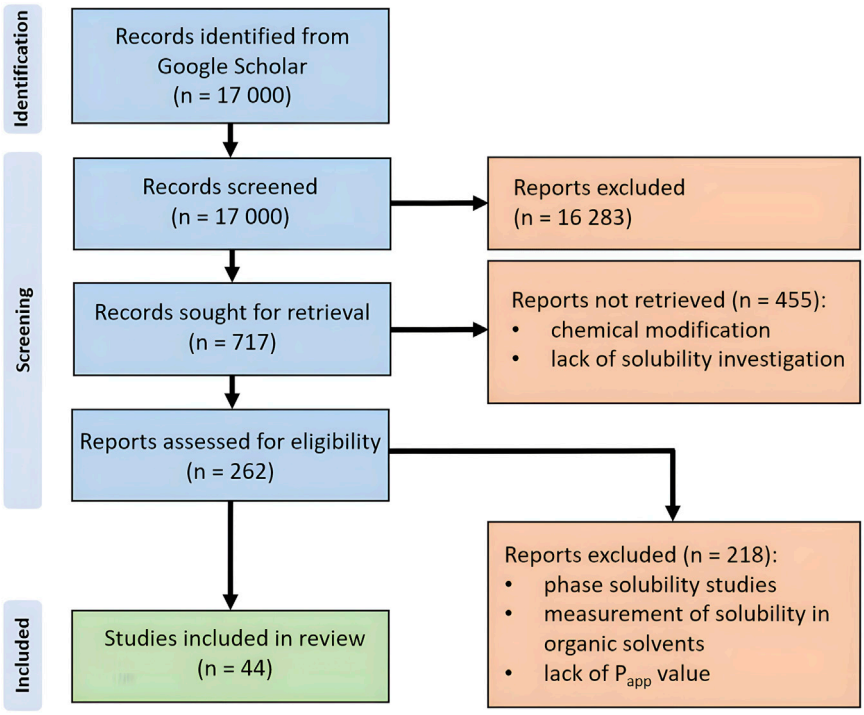


FIGURE 3
PRISMA flowchart of the search and selection process of the articles.

The size of the bubbles corresponds to the frequency of term mentions. The pseudocolor scale, ranging from blue to yellow reflects the novelty of articles from 2010 to 2024. It is evident that the primary connection to flavonoids is with the terms "animals" and "solubility". Recently, research in this area has increasingly focused on the study of antioxidant properties (Yang et al., 2024), regulation of gene expression (Bai et al., 2024; Parafati et al., 2024), and chitosan (Liu et al., 2025).

Figure 2B illustrates the interest in flavonoid solubility and related terms. It is apparent that scientists have recently shown a growing interest in the possibility of obtaining nanoparticles derived from flavonoids. Concurrently, considerable attention is given to plant extracts and quercetin as an individual component. Moreover, studies are being conducted on the antioxidant activity associated with solubility.

Figure 2C depicts the relationship between bioavailability and related terms. Over the past 6 years, connections have been observed between bioavailability and nanoparticles (Wahnou et al., 2024), indicating a strong interest among researchers in developing similar structures based on flavonoids. An important aspect is the study of oral bioavailability of flavonoids.

3.2 Process of collection and selection of the studies

The initial results of the search identified 17,000 articles in Google Scholar. After the first screening, 16,283 articles were excluded because they did not meet the inclusion criteria based on their titles and abstracts. In the subsequent review, 455 articles were eliminated for the following reasons: chemical modifications of flavonoids that resulted in the formation of new covalent bonds and the absence of solubility investigations. After reviewing the full texts, an additional 218 articles were excluded for the following reasons: reliance on phase solubility studies, measurement of solubility in organic solvents, and a lack of apparent permeability (P_{app}) values when the study was associated with permeability evaluation. Consequently, the review included 44 articles that passed through all stages of selection. The collection and selection process is illustrated in the PRISMA flow diagram (Figure 3).

3.3 General overview of the included articles

Since 2010, there has been a steady increase in the number of publications on this topic, rising from 3 in the period of 2010–2012 to 13 in both 2019–2021 and 2022–2024 (Figure 4). During the 2010–2012 timeframe, the primary focus was on the synthesis of various nanostructures; however, by 2022–2024, their representation within the total number of publications has considerable decreased. Additionally, there has been a notable rise in publications on the synthesis of cocrystals, increasing from 10.00% in 2016–2018 to 30.75% in 2022–2024. Inclusion complexes have garnered substantial attention from researchers since the period of 2013–2015. Over the past 6 years, there has been a decline in the proportion of phospholipid complexes among the methods aimed at enhancing the bioavailability of flavonoids. Recently, an increase in the diversity of modification techniques has been observed.

Among the primary groups of flavonoids, isoflavones have attracted considerable attention year after year, comprising 38.40% of all modified

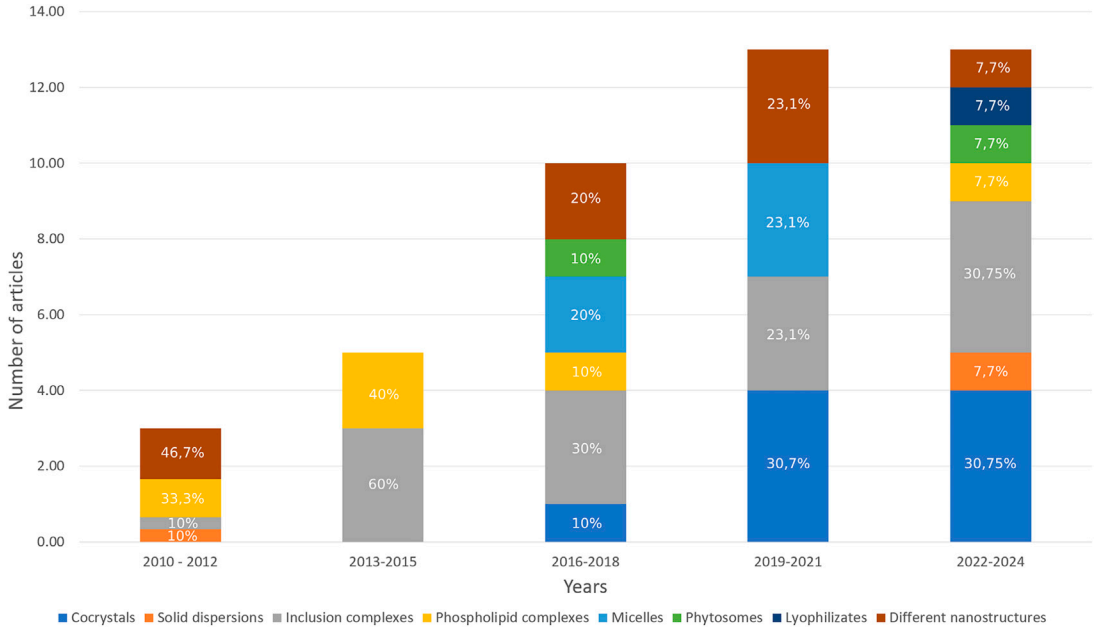


FIGURE 4
Methods used to increase the bioavailability of flavonoids included in this systematic review (% shows the proportion of the total in a given column).

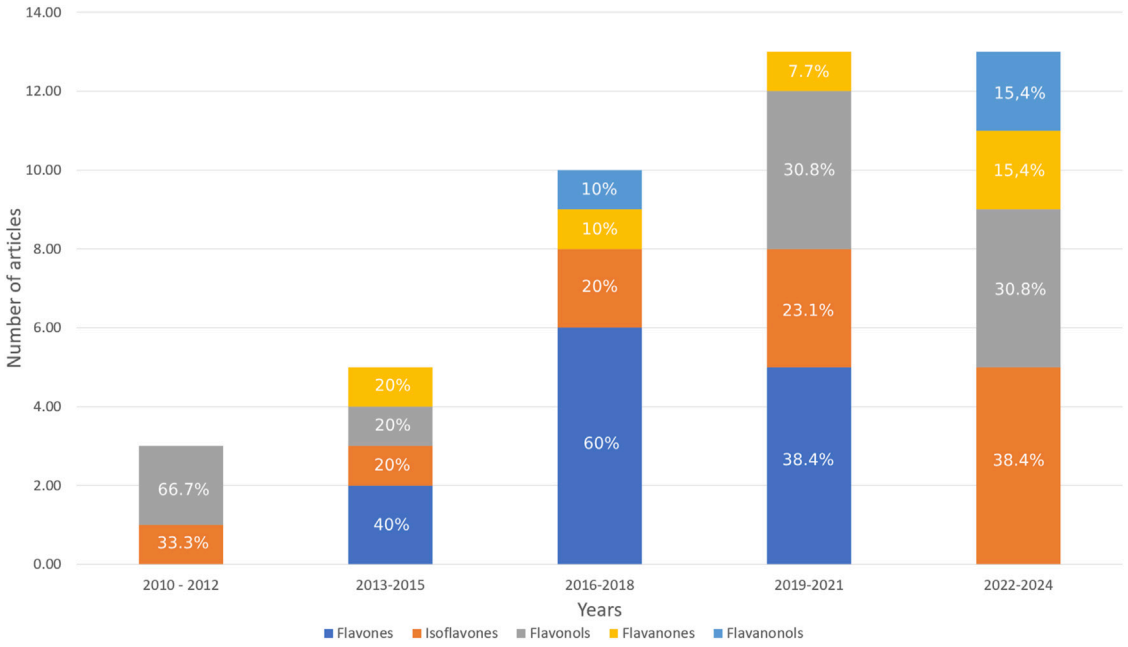


FIGURE 5
Flavonoids groups included in this review (% shows the proportion of the total in a given column).

structures in 2022–2024 (Figure 5). Although there was a surge of interest in flavones during 2013–2021, no information regarding their modification was identified for the period of 2022–2024. Over the last decade, a greater diversity of flavonoid groups has emerged compared to previous years. Moreover, 15 different flavonoids were identified in the selected articles (Figure 6).

3.4 Qualitative synthesis

The solubility of the modified objects received attention in 39 articles. Seventy-five distinct modifications were described. For the convenience of graphically representing this data, $\log_{10}$ of the multiplicative increase in the solubility of the obtained objects was

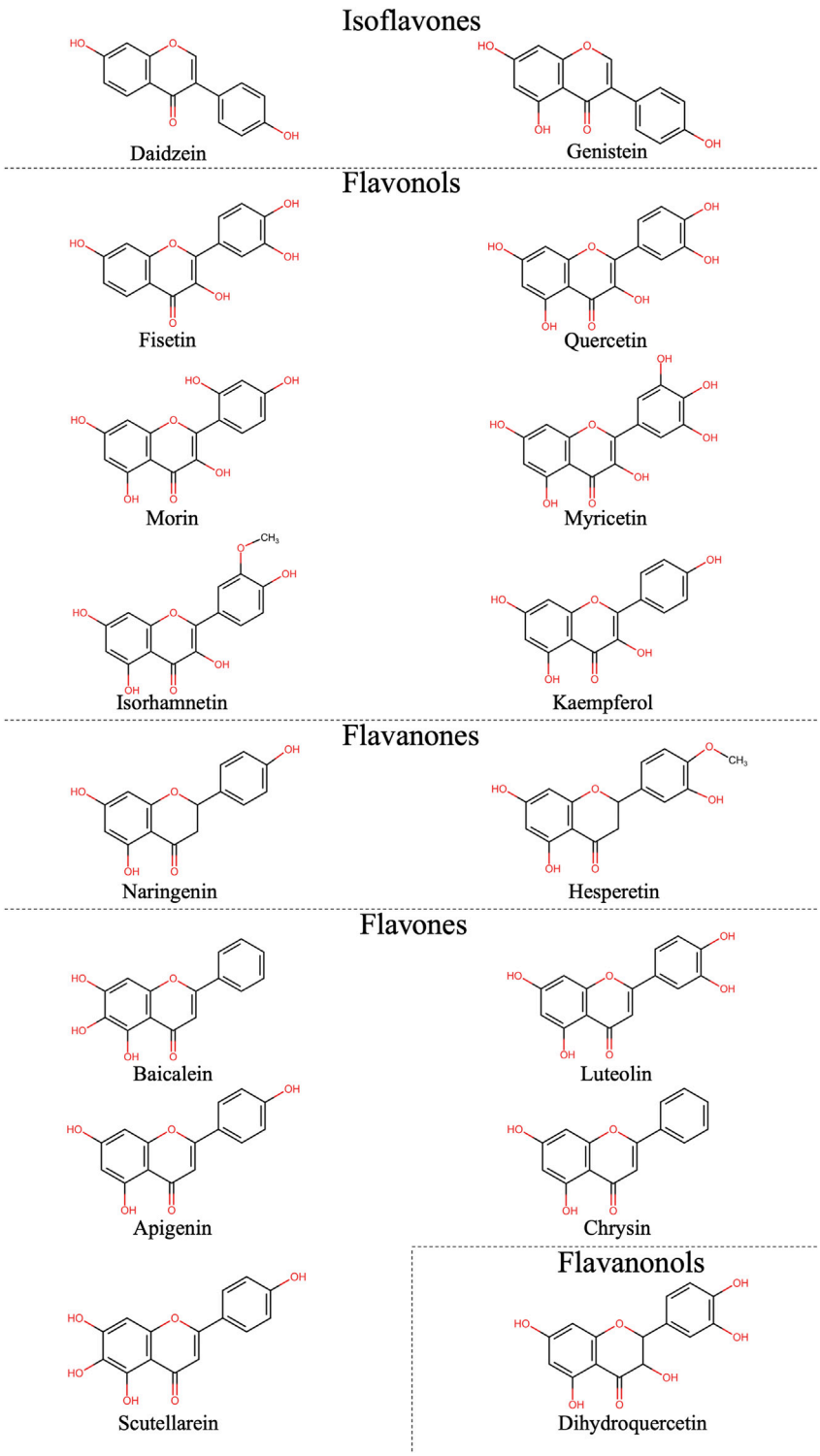


FIGURE 6
Structures of flavonoids from included articles.

used (Figure 7). All original solubility data are presented in the Supplementary Table S1.

Nine articles described and characterized 18 new flavonoid cocrystals with improved water solubility. The primary co-formers were nitrogen-containing heterocyclic compounds, including piperazine (Wang et al., 2023; Wang et al., 2024 Z.), nicotinamide (Cui et al., 2019; Ren et al., 2019), isonicotinamide (Bhalla et al., 2019; Ren et al., 2019), theobromine (Bhalla et al., 2019), cytosine (Chadha et al., 2017; Bhalla et al., 2019), caffeine (Cui et al., 2019; Luo et al., 2019; Ren et al., 2019), piperine (Liu et al.,

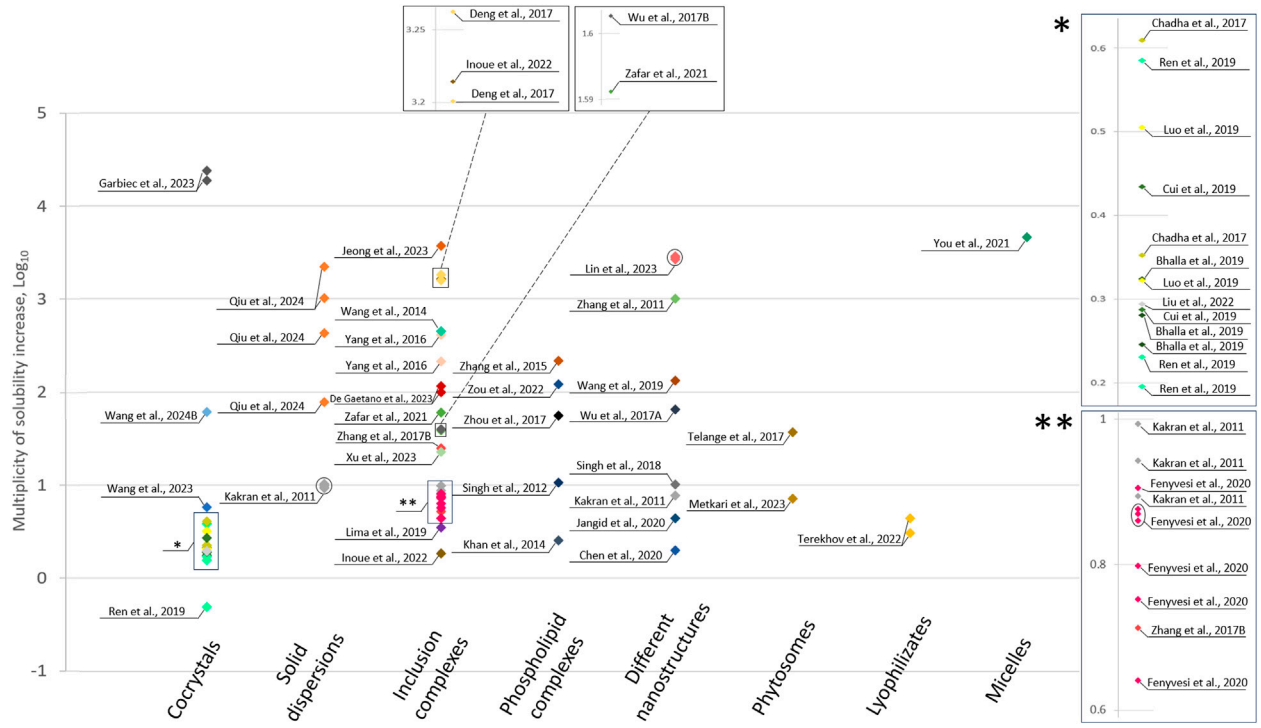


FIGURE 7
Multiplicity of solubility increase (each color shows a separate publication).

2022), isoniazid (Luo et al., 2019), and thiamine (Chadha et al., 2017). Some cocrystals were formed by combining flavonoids with amino acids such as lysine (Garbiec et al., 2023), arginine (Garbiec et al., 2023), and proline (Ren et al., 2019). The greatest increase in solubility was observed for cocrystals of genistein with proteinogenic amino acids lysine and arginine (Garbiec et al., 2023). In contrast, myricetin cocrystals with caffeine exhibited a 2-fold decrease of solubility in pure water (Ren et al., 2019).

Two articles described solid dispersions based on the flavonoids genistein (Qiu et al., 2024) and quercetin (Kakran et al., 2011) with the addition of polyvinylpyrrolidone or pluronic® F127. Qiu et al. (2024) achieved a solubility increase of over 2000 times for a 1:9 (w/w) dispersion.

The greatest number of solubility modifications (27) was represented by inclusion complexes, as detailed in 13 articles. These modifications primary involved various cyclodextrins and their derivatives, including (2-hydroxypropyl)-β-cyclodextrin (Wang et al., 2014; Yang et al., 2016; Wu et al., 2017b; Lima et al., 2019; Fenyvesi et al., 2020; Zafar et al., 2021; De Gaetano et al., 2023), γ-cyclodextrin (Inoue et al., 2022), amino-modified β-cyclodextrin (Deng et al., 2017), β-cyclodextrin (Kakran et al., 2011; Yang et al., 2016; Zhang Y. et al., 2017; Fenyvesi et al., 2020; Xu et al., 2023), sulfobutylether-β-cyclodextrin (Fenyvesi et al., 2020; De Gaetano et al., 2023), and random methyl-β-cyclodextrin (Fenyvesi et al., 2020). Additionally, some modifications were achieving using cycloamylose (Jeong et al., 2023) and lecithin (Zhang Y. et al., 2017).

Five articles reported the preparation of new flavonoid-phospholipid complexes with improved water solubility. The most notable increase was observed with kaempferol, which achieved a remarkable solubility enhancement of 216.70-fold (Zhang et al., 2015). A slightly lower increase was observed for isorhamnetin (Zou et al., 2022) and baicalein (Zhou et al., 2017), with enhancements of 122-fold and 55.45-fold, respectively. Additionally, a substantial increase (10.70 times) was noted for the phospholipid complex of quercetin (Singh et al., 2012). The smallest increase (2.54 fold) was demonstrated by the modification of luteolin (Khan et al., 2014).

Nanostructures were presented by 10 modifications in eight articles. The following objects were obtained: daidzein–phospholipid complex loaded into lipid nanocarriers (Zhang et al., 2011); nanoparticles with fisetin (Chen et al., 2020), quercetin (Kakran et al., 2011), luteolin (Wang et al., 2019), and apigenin (Wu et al., 2017a); nanosuspension with morin (Jangid et al., 2020) and naringenin (Singh et al., 2018); nanofibers of myricetin (Lin et al., 2023). The greatest increase in water solubility (more than 2600-fold) was exhibited by myricetin nanofibers produced with the addition of (2-hydroxypropyl)-β-cyclodextrin and polyvinylpyrrolidone in various ratios (Lin et al., 2023).

The enhancement of solubility through the formation of phytosomes were addressed in 2 publications. The authors (Metkari et al., 2023) successfully increased the solubility of naringenin by 7.16 times using a fraction of non-GMO soybean lecithin enriched with phosphatidylcholine (LS-75). Additionally, phytosomes containing apigenin (Telange et al., 2017) were created, demonstrating a 36.77-fold increase in solubility.

TABLE 1 Permeability of modified and native forms of flavonoids.

Group of flavonoids	Compound	Method of increasing permeability	Permeability model	Initial apparent permeability, $\times10^{-6}$ cm/s	Resulting apparent permeability, $\times10^{-6}$ cm/s	Multiplicity of permeability increase	References
Isoflavones	Genistein (GEN)	Micelle formation	Caco-2	6.33 ± 0.49 (AP-BL)	7.82 ± 0.38	1.24[a]	Shen et al. (2018)
				8.65 ± 0.51 (BL-AP)	8.29 ± 0.44	0.96[a]	
		Micelle formation (GEN-F – 1.2 mg/mL; GEN-L – 1.6 mg/mL)	Caco-2	5.28 ± 0.49 (AP-BL)	8.23 ± 0.35 (GEN-L)	1.56	Ding et al. (2019)
				7.97 ± 0.36 (BL-AP)	8.46 ± 0.43 (GEN-F)	1.06	
					7.59 ± 0.56 (GEN-L)	0.95	
		Cocrystallization with lysine (LYS) and arginine (ARG)	Cell-free permeation model	4.28 ± 0.95	0.90 ± 0.02 (GEN – LYS)	0.21[a]	Garbiec et al. (2023)
					1.13 ± 0.03 (GEN – ARG)	0.26[a]	
		Inclusion Complex with RAMEB, HP-β-CD, β-CD, and γ-CD	Caco-2	1.70 ± 0.10	17.10 ± 3.70 (GEN – β-CD)	10.00[a]	Daruházi et al. (2013)
					17.10 ± 3.50 (GEN – HP-β-CD)	10.00[a]	
					6.50 ± 1.70 (GEN – RAMEB)	3.82[a]	
					28.50 ± 1.70 (GEN – γ-CD)	16.76[a]	
	Daidzein (DDZ)	Inclusion Complex with RAMEB, HP-β-CD, β-CD, and γ-CD	Caco-2	11.90 ± 1.90	31.40 ± 4.10 (DDZ – β-CD)	2.64[a]	Daruházi et al. (2013)
					21.70 ± 9.10 (DDZ – HP-β-CD)	1.82[a]	
					24.30 ± 7.30 (DDZ – RAMEB)	2.04[a]	
					16.20 ± 1.30 (DDZ – γ-CD)	1.36[a]	
Flavones	Baicalein	Micelle formation	Caco-2	1.05 ± 0.08 (AP-BL)	1.93 ± 0.19	1.84[a]	Shen et al. (2019)
				0.97 ± 0.10 (BL-AP)	1.85 ± 0.13	1.91[a]	
		Phospholipid complex (BaPC), matrix dispersion based on phospholipid complex (BaPC-MD)	Caco-2	10.1	11.60 (BaPC)	1.15[a]	Zhou et al. (2017)
					15.30 (BaPC-MD)	1.51[a]	
	Apigenin	Micelle formation	Caco-2	5.32 ± 0.51	6.76 ± 0.56	1.27	Zhang et al. (2017c)
	Chrysin	Inclusion Complex RAMEB	Caco-2	2.32	4.65 (1:1 with RAMEB)	2.00[a]	Fenyvesi et al. (2020)
					11.00 (1:2 with RAMEB)	4.74[a]	

[a]values were calculated by the authors of current review; (CD, cyclodextrin; RAMEB, random methyl-β-cyclodextrin; HP-β-CD, 2-hydroxypropyl beta-cyclodextrin; AP, apical side; BL, basolateral side).

10.3389/fchem.2025.1602967

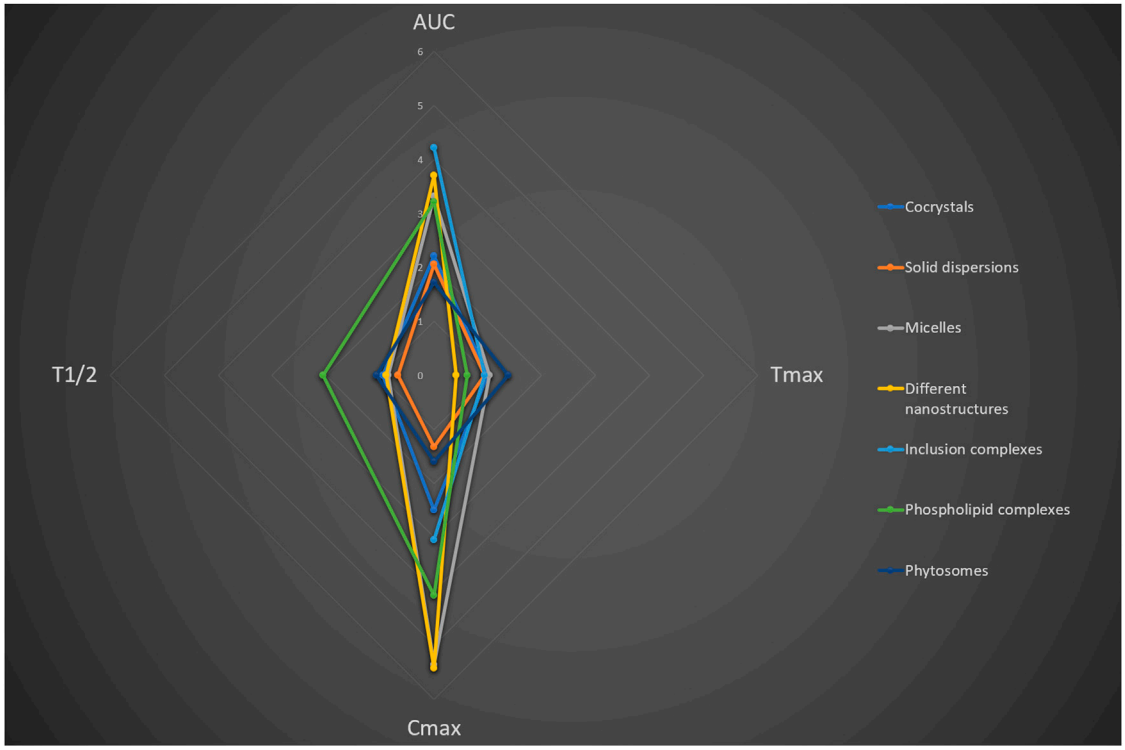


FIGURE 8
The average multiplicity of the main pharmacokinetic parameters of modified forms in comparison with native flavonoids.

The only mention regarding an enhancement in solubility involved the lyophilization of a flavonoid solution derived from organic solvents (Terekhov et al., 2022). The flavanonol dihydroquercetin exhibited water solubility increases of 4.41-fold for the aqueous ethanol and 3.06-fold for the acetonitrile lyophilizates, respectively.

A single article detailed an increase in solubility achieved by forming baicalein micelles with glycyrrhizic acid (You et al., 2021). The resulting micelles demonstrated a 4606-fold increase in solubility.

The permeability of the obtained modifications was assessed using Caco-2 cell culture in 7 articles, while 1 publication described cell-free permeation model. In 3 of these studies, the permeability assessment was conducted alongside solubility studies, while in 5 of them it was carried out separately. However, permeability studies were conducted only for two classes of flavonoids: flavones and isoflavones. Micelles (Zhang Z. et al., 2017; Shen et al., 2018; 2019; Ding et al., 2019) and inclusion complexes (Daruházi et al., 2013; Fenyvesi et al., 2020) were most frequently studied modifications in terms of permeability. The permeability of cocrystals (Garbiec et al., 2023) and phospholipid complexes (Zhou et al., 2017) was reported only once each. Most modifications increased permeability by no more than 2-folds, but the inclusion complex with daidzein (Daruházi et al., 2013) achieved 31.40-fold increase (Table 1).

Pharmacokinetic data were also extracted from articles that reported on the solubility or permeability of modifications, when available. Four primary pharmacokinetic parameters were analyzed: the area under the pharmacokinetic curve (AUC), maximum concentration of the active substance in blood plasma (C_{max}), time to reach maximum concentration (T_{max}) and half-elimination time ($T_{1/2}$). All modifications demonstrated an increased AUC (Figure 8). The greatest improvements in this parameter were observed in inclusion complexes and disassembled nanostructures, with average increases of 4.2 and 3.7 times, respectively. The least effect was noted for phytosomes, where the AUC of the modified forms exceeded the initial value by only 1.7 times. For nanostructures and micelles, a substantial increase in C_{max} of the active substance was observed, reaching an average of 5.4 times for both types of modifications. The production of solid dispersions and phytosomes exerted the least influence on this parameter, resulting in increases of 1.3 and 1.6 times, respectively. Additionally, phospholipid complexes exhibited a longer average $T_{1/2}$ than all other modifications, achieving a 2.1-fold increase. The remaining methods did not show a consistent effect on this pharmacokinetic parameter. None of the methods studied had a notable effect on T_{max}, although a slight increase was observed for phytosomes (1.4 times). A decrease in this parameter was recorded for nanostructures and phospholipid complexes, with reductions of 0.4 and 0.6 times relative to the initial time, respectively. All original pharmacokinetic data are presented in the Supplementary Table S2.

4 Discussion

A comprehensive analysis of the scientific landscape enabled the identification of several trends regarding the modification of the

biopharmaceutical properties of flavonoids in recent years. Considerable attention has been paid to their solubility, as some scientists assert that low solubility in water at room temperature constitutes one of the main obstacles to their application in pharmaceutical practice. Additionally, the objects generated through these modifications are characterized by a range of physicochemical and biological analytical methods. This allows not only for the evaluation of their structures but also for the acquisition of data regarding their bioavailability. Another important aspect is the strong connection to the term "antioxidants", because natural polyphenolic compounds are natural inhibitors of free radicals. Consequently, they may be utilized in the treatment of oxidative stress (Dhas and Mehta, 2021; Hassan et al., 2022), an area that has recently garnered considerable attention in the scientific community.

The cocrystallization method has demonstrated a considerable positive effect in enhancing the bioavailability of flavonoids. Combining ease of implementation with effectiveness in increasing water solubility, it is regarded as one of the most promising avenues for further investigation (Dutt et al., 2020). Several scientists propose that the increased solubility of these structures, compared to the initial substances, is attributable to the "spring and parachute" phenomenon (Bavishi and Borkhataria, 2016). The resulting cocrystals are supramolecular heterosynthons formed through non-covalent interactions among the components (Raheem Thayyil et al., 2020). This method is considered one of the most promising for enhancing the solubility and bioavailability of oral drugs (Emami et al., 2018; Li et al., 2021; Chhatbar et al., 2025). It is widely employed in modifying the biopharmaceutical properties of polyphenolic compounds, not only in the pharmaceutical industry (Dal Magro et al., 2021; Bu et al., 2023b; Lee et al., 2023), but also in the food industry (Chezanoglou and Goula, 2021; Dias et al., 2021; Irigoiti et al., 2021). Some studies have utilized the cocrystallization process for the subsequent joint separation of a racemic compound mixture (Zhou et al., 2021) and for enhancing the stability of moisture-sensitive drugs (Dhondale et al., 2023). Interestingly, there is a case in which this modification resulted not in an increase, but rather in a decrease in solubility (Ren et al., 2019). The authors attribute this effect to the enhanced stability of myricetin cocrystals with caffeine, resulting from the low solubility of the coformer. A similar decrease in solubility was observed for compounds of other chemical classes, such as the antifungal drug 5-fluorocytosine. (Bu et al., 2023a). In the case of using ferulic acid as a coformer, a decrease in solubility was noted due to the formation of a rigid S-shaped module, which possesses hydrophobic properties and reduced polarity. Other factors that influence the solubility of cocrystals include lattice energy and solvation free energy. For instance, in the case of the matrine modification (Wang Y. et al., 2024), it has been demonstrated that as solvation free energy increases, the solubility of cocrystals in water decreases. When assessing pharmacokinetics, it has been established that cocrystals can significantly increase the AUC and C_{max}, while having minimal impact on $T_{1/2}$ and T_{max}. This makes the obtained compounds particularly interesting when there is a need to enhance the bioavailability of a drug without affecting the rate of onset of the therapeutic effect or its elimination from the body. Compared to other methods, cocrystallization results in a relatively modest increase in solubility, typically not exceeding 10 fold. However, cocrystallization has successfully produced compounds with the most pronounced increases in solubility when compared to the original compounds, particularly in the case of genistein cocrystals with lysine. Regarding its impact on pharmacokinetic parameters, cocrystallization demonstrates a moderate effect on the enhancement of AUC and C_{max} compared to other methods.

The solid dispersion method is extensively employed in the pharmaceutical industry to improve the solubility and bioavailability of APIs (Tran et al., 2019; Gaber et al., 2022; Bajaj et al., 2023), although it has proven unpopular for flavonoids (only 2 articles). This method has found broad application in modifying the biopharmaceutical parameters of APIs (Bhujbal et al., 2021; Rusdin et al., 2024). During the development of the final product, it is possible to reduce particle size and agglomeration, enhance wettability, and alter the physical state of the substance (Janssens and Van Den Mooter, 2009). These improvements potentially lead to enhanced solubility and bioavailability. There are two primary approaches to obtaining solid dispersions: solvent evaporation-based and melting-based methods. The former includes techniques such as spray drying (Singh and Van Den Mooter, 2016; Ha et al., 2021; Weecharangsan and Lee, 2024), electrospraying (J. Hogan and Biswas, 2008), fluidized bed technology (Kwon et al., 2019), supercritical fluids (Qi et al., 2015), and spray-freeze-drying (Leuenberger, 2002). Melting-based methods comprise hot-melt extrusion (Patil et al., 2016; Gusev et al., 2022; Terenteva et al., 2024), KinetiSol® (Hughey et al., 2012), three-dimensional (3D) printing (Awad et al., 2019), and microwave heating (Hempel et al., 2020). Among these, the most well-known and widely utilized in laboratory and industrial settings are spray drying and hot-melt extrusion. Despite the substantial increase in solubility achieved through the solid dispersion method, its impact on the overall bioavailability of flavonoids was not particularly pronounced. The AUC increased on average 2-fold compared to the initial compounds. This was accompanied by a slight decrease in the $T_{1/2}$ and lack of influence on C_{max} and T_{max}. These data indicate the potential of this method in cases where it is necessary to accelerate the onset of a drug's therapeutic effect while simultaneously enhancing its bioavailability. Compared to other methods, the production of solid dispersions has a limited impact on the primary pharmacokinetic parameters, with the exception of $T_{1/2}$, which shows a reduction.

Interestingly, the method of producing inclusion complexes has gained widespread acceptance as a means to improve the solubility and bioavailability of flavonoids. These structures are formed with cyclic oligosaccharides such as cyclodextrins (CDs), cycloamylose, and its modifications (Allahyari et al., 2025). The ability of CDs to enhance solubility is attributed to their dual structure. Their internal cavity is lipophilic and capable of encapsulating molecules that are poorly soluble in polar solvents through the formation of hydrogen bonds. Meanwhile, the external surface is hydrophilic, ensuring the water solubility of the resulting complexes (Gandhi et al., 2020). Methods for obtaining such structures include co-precipitation (Hoque et al., 2022; Betlejewska-Kielak et al., 2023), kneading (Martins et al., 2020), the supercritical carbon dioxide method (Antipova et al., 2024), grinding (Hoque et al., 2022), microwave irradiation (Bin Jardan et al., 2023), and spray drying (Imam et al., 2022; Soares et al., 2023). Each method is characterized by its own

technology, advantages and disadvantages (Cid-Samamed et al., 2022; Drannikov et al., 2022). For flavonoids, this approach significantly enhanced both water solubility and permeability through cellular membranes. This led to the fact that the AUC for inclusion complexes of flavonoids increased on average by 4.2 times compared to the initial substances. This was accompanied by an increase in C_{max} by approximately 3 times. These values represent the highest enhancements among all methods considered, indicating a strong potential for modifying the biopharmaceutical properties of polyphenols. Furthermore, for the described inclusion complexes, the rate of reaching T_{max} remained virtually unchanged when compared to the initial compounds. These modifications exhibited the most pronounced improvement in solubility and bioavailability compared to all the methods studied, as indicated by the highest average AUC value across all modifications.

Another interesting set of results emerged from analyzing publications discussing various phospholipid complexes with flavonoids. There are few methods (Kuche et al., 2019) to prepare these structures for improve biopharmaceutical parameters of different APIs and plant extracts: solvent evaporation (Qiu et al., 2021; Liu et al., 2023), co-grinding (Wang et al., 2020), mechanical dispersion (Patil et al., 2024), the supercritical fluid process, co-solvent lyophilization, and anti-solvent precipitation (Saini et al., 2022). Although the increase in solubility achieved through this method was less than that attained with other approaches, its effect on pharmacokinetic parameters was quite pronounced. The average increase in AUC reached 3.2 times, falling short of the nanostructure and inclusion complex methods (3.7 and 4.2 times, respectively) while being approximately equal to that of micelles. The C_{max} increased by 3.0 times, which ranked just behind micelles and nanostructures (5.4 times, respectively). Additionally, the relative increase in $T_{1/2}$ was the largest among all the methods described for enhancing bioavailability and solubility, reaching 2.1 times. A decrease in T_{max} of nearly 2-fold was also observed. This positions this method as promising for the development of dosage forms that require prolonged release of the active substance based on flavonoids. The similar effect of phospholipid complexes enabled the development of a sustained-release formulation of dehydroandrographolide succinate for the treatment of respiratory diseases (Chen et al., 2025).

The results of the bioavailability assessment of various nanostructures showed the expected results. A significant increase in AUC and C_{max} (3.7 and 5.4 times, respectively) was observed, which is attributed to the increased surface area of the nanostructures compared to other objects. This enhancement leads to a greater completeness of absorption of the active substance and accelerates the process: T_{max} decreased by more than 2 times compared to the initial flavonoids. Thus, it can be concluded that various nanostructures may be a preferable choice for developing fast-acting drugs with high bioavailability. This was exemplified by albendazole, an antiparasitic agent, where solid lipid nanoparticles demonstrated a very rapid release of the active substance, as well as a significant increase in permeability into echinococcal cysts (Movahedi et al., 2017). The effects of increased bioavailability when obtaining nanostructured materials are also manifested at the molecular-genetic level. For instance, nanofiber frames made of polyvinyl alcohol filled with flaxseed extract exhibited a significant increase in the expression of genes that are osteogenic markers (Abdelaziz et al., 2024). This effect of nanostructures can be explained by the reduction in the size of the active substance particles during their production (Leuenberger, 2002). This reduction leads to a larger surface area and results in the aforementioned changes in solubility, bioavailability, and the biological effects of nanostructured forms. In our study, this modification method demonstrated the most pronounced increase in C_{max}, while the average AUC ranked second, following the inclusion complex. Furthermore, the major decrease in T_{max} was observed among all the methods analyzed.

Despite the fact that phytosomes are one of the types of phospholipid complexes, this review has chosen to categorize them as a separate group due to their unique characteristics, which involve covalent or hydrogen bonding between the shell and the encapsulated phytocomponent (Kuche et al., 2019; Lu et al., 2019). Because of this feature, these structures did not show a substantial increase in several pharmacokinetic parameters: AUC, C_{max}, $T_{1/2}$ (1.7, 1.6, and 1.1 times, respectively). However, these modifications showed the greatest increase in T_{max}, suggesting potential for developing dosage forms with prolonged release of the active substance. Moreover, this modification method has recently been the subject of active research for the treatment of various types of cancer (Banerjee et al., 2025; Zhao et al., 2025). Unfortunately, the number of studies investigating the use of this method for individual flavonoids has been insufficient to fully evaluate their impact on the parameters under study. A significant number of publications have focused on researching medicinal plant extracts and the production of phytosomes derived from them.

The method of lyophilization without the addition of excipients to enhance the solubility and bioavailability of flavonoids has proven to be unpopular. This method is widely used to improve the solubility and bioavailability of various APIs (Taldaev et al., 2023). One of the factors contributing to alterations in solubility and pharmacokinetic parameters is the change in the morphology of the substance and the increase in surface area during lyophilization. Moreover, this method is utilized for the production of various nanostructured materials and liposomal forms for drug delivery (Fonte et al., 2016; Franzé et al., 2018).

The method of obtaining micelles has been employed quite infrequently. However, several articles have focused not on solubility, but rather on permeability (Zhang Z. et al., 2017; Shen et al., 2019). The differing polarities within micellar structures facilitate the incorporation of poorly soluble molecules, thereby enhancing their solubilization and increasing the solubility of such compounds (Vinarov et al., 2018). It is important to note that the formation of micellar and phospholipid complexes, as well as phytosomes, are similar processes from a physical chemistry perspective. Nevertheless, we have chosen to categorize them into three distinct groups to maintain the established terminology used by the authors of the included articles.

One of the primary obstacles to systematizing information on methods for enhancing the solubility of various flavonoid modifications lies in the large differences in the methodologies employed in these analyses. Specifically, the variables such as temperature, pH value, dissolution medium, analysis duration, and methods of quantitative determination exhibited considerable

variation. Heterogeneity in the conditions and methods used for solubility analysis could led to influence the final outcome of determining the solubility of the resulting objects. This variability hindered the possibility of directly comparing results across different studies and necessitated the exclusion of publications that did not provide information on the solubility of the original compound or the solubility enhancement factor. Consequently, it seems essential to standardize the solubility determination method, for instance, utilizing high-performance liquid chromatography. Moreover, there is a paucity of research dedicated to examining the permeability of the modified flavonoids, which limits the potential for comparing the methods described in this article. The main challenge is that most studies have employed four established methods (cocrystallization, the formation of phospholipid and inclusion complexes, and the generation of nanostructures), leaving relatively little information available on other techniques.

Despite these challenges, we have compiled and summarized the literature regarding methods for enhancing the solubility and bioavailability of flavonoids, and have assessed the comparative effects of various techniques on the pharmacokinetic parameters of the resultant compounds. This information will prove valuable for scientists investigating the bioavailability of this group of natural compounds.

5 Conclusion

This review was conducted to summarize and systematize scientific data regarding the enhancement of solubility and bioavailability of flavonoids without changing their molecular structure. Throughout the investigation, it was determined that the most prevalent methods for increasing solubility and bioavailability include co-crystallization, formation of phospholipid and inclusion complexes, and the creation of nanostructures. Although there were no pronounced differences observed in enhancing solubility, the impact of these methods on pharmacokinetic parameters was established. Notably, the greatest average increase in AUC was recorded for various complexes, micelles, and nanostructures, which are the most promising for further study in the field of increasing the bioavailability of flavonoids. The most effective methods for increasing the C_{max} of the active substance in blood plasma were identified as nanostructured forms and micelles. No pronounced effect of the methods on excretion processes was established, while the rate of achieving the maximum concentration of drugs decreased for nanostructures and phospholipid complexes. During the systematization and generalization of the data, a high level of heterogeneity in solubility assessment methods across various studies was revealed, complicating comparisons of original data obtained by different researchers. Taking this into account, it would be beneficial to conduct a comparative analysis of the methods and conditions used to assess solubility in order to identify the most universal parameters for determining solubility across various flavonoids. It is also possible that similar discrepancies may be observed in the case of other groups of compounds, which necessitates further investigation. Another potential avenue for future scientific research in this field is to investigate the feasibility of integrating various methods to produce products with specific biopharmaceutical parameters. The findings of this review are crucial for researchers investigating the bioavailability of flavonoid compounds and will facilitate the selection of the most effective methods based on the desired outcomes for solubility and bioavailability.

Author contributions

AT: Funding acquisition, Resources, Writing – review and editing. AS: Data curation, Formal Analysis, Investigation, Methodology, Project administration, Software, Visualization, Writing – original draft. SO: Investigation, Software, Writing – original draft. RT: Conceptualization, Methodology, Supervision, Validation, Writing – review and editing. IS: Conceptualization, Supervision, Writing – review and editing.

Funding

The author(s) declare that financial support was received for the research and/or publication of this article. This research was funded by the Ministry of Science and Higher Education of the Russian Federation within the framework of Agreement No. 075-15-2024-643.

Conflict of interest

The authors declare that the research was conducted in the absence of any commercial or financial relationships that could be construed as a potential conflict of interest.

Generative AI statement

The author(s) declare that no Generative AI was used in the creation of this manuscript.

Publisher's note

All claims expressed in this article are solely those of the authors and do not necessarily represent those of their affiliated organizations, or those of the publisher, the editors and the reviewers. Any product that may be evaluated in this article, or claim that may be made by its manufacturer, is not guaranteed or endorsed by the publisher.

Supplementary material

The Supplementary Material for this article can be found online at: https://www.frontiersin.org/articles/10.3389/fchem.2025.1602967/full#supplementary-material

References

Abdelaziz, A. G., Nageh, H., Abdalla, M. S., Abdo, S. M., Amer, A. A., Loutfy, S. A., et al. (2024). Development of polyvinyl alcohol nanofiber scaffolds loaded with flaxseed extract for bone regeneration: phytochemicals, cell proliferation, adhesion, and osteogenic gene expression. *Front. Chem.* 12, 1417407. doi:10.3389/fchem.2024.1417407

Ahmed, M., and Eun, J.-B. (2018). Flavonoids in fruits and vegetables after thermal and nonthermal processing: a review. *Crit. Rev. Food Sci. Nutr.* 58, 3159–3188. doi:10.1080/10408398.2017.1353480

Al-Khayri, J. M., Sahana, G. R., Nagella, P., Joseph, B. V., Alessa, F. M., and Al-Mssallem, M. Q. (2022). Flavonoids as potential anti-inflammatory molecules: a review. *Molecules* 27, 2901. doi:10.3390/molecules27092901

Allahyari, R., Mahdavi, B., Rezaei-Seresht, E., and Baghayeri, M. (2025). Unlocking finasteride's potential via carboxymethyl-β-cyclodextrin inclusion complex for androgenic alopecia. *Carbohydr. Polym. Technol. Appl.* 10, 100767. doi:10.1016/j.carpta.2025.100767

Antipova, M. L., Odintsova, E. G., and Petrenko, V. E. (2024). Behavior of β-cyclodextrin/naproxen inclusion complex in supercritical carbon dioxide. Computer simulation. *J. Mol. Liq.* 407, 125234. doi:10.1016/j.molliq.2024.125234

Awad, A., Fina, F., Trenfield, S. J., Patel, P., Goyanes, A., Gaisford, S., et al. (2019). 3D printed pellets (miniprintlets): a novel, multi-drug, controlled release platform technology. *Pharmaceutics* 11, 148. doi:10.3390/pharmaceutics11040148

Bai, X., Li, L., Wu, Y., and Jie, B. (2024). Flavonoids of Euphorbia hirta inhibit inflammatory mechanisms via Nrf2 and NF-κB pathways. *Cell. biochem. Biophys.* 83, 1167–1183. doi:10.1007/s12013-024-01551-y

Bajaj, J. S., Hassanein, T. I., Pyrsopoulos, N. T., Sanyal, A. J., Rahimi, R. S., Heimanson, Z., et al. (2023). Dosing of rifaximin soluble solid dispersion tablets in adults with cirrhosis: 2 randomized, placebo-controlled trials. *Clin. Gastroenterol. Hepatol.* 21, 723–731.e9. doi:10.1016/j.cgh.2022.05.042

Banerjee, S., Mukhopadhyay, S., Das, A., Banerjee, S., Bose, S., Banerjee, S., et al. (2025). Preparation, characterisation, anticancer potential and safety evaluation of a soy lecithin phytosome delivery system loaded with constituents from *Barleria lupulina*. *J. Microencapsul.*, 1–21. doi:10.1080/02652048.2025.2467046

Bavishi, D. D., and Borkhataria, C. H. (2016). Spring and parachute: how cocrystals enhance solubility. *Prog. Cryst. Growth Charact. Mat.* 62, 1–8. doi:10.1016/j.pcrysgrow.2016.07.001

Betlejewska-Kielak, K., Bednarek, E., Budzianowski, A., Michalska, K., and Maurin, J. K. (2023). Comprehensive characterisation of the flurbiprofen/β-cyclodextrin inclusion complex using X-ray techniques and NMR spectroscopy. *J. Mol. Struct.* 1285, 135450. doi:10.1016/j.molstruc.2023.135450

Bhalla, Y., Chadha, K., Chadha, R., and Karan, M. (2019). Daidzein cocrystals: an opportunity to improve its biopharmaceutical parameters. *Heliyon* 5, e02669. doi:10.1016/j.heliyon.2019.e02669

Bhujbal, S. V., Mitra, B., Jain, U., Gong, Y., Agrawal, A., Karki, S., et al. (2021). Pharmaceutical amorphous solid dispersion: a review of manufacturing strategies. *Acta Pharm. Sin. B* 11, 2505–2536. doi:10.1016/j.apsb.2021.05.014

Bin Jardan, Y. A., Ahad, A., Raish, M., Al-Mohizea, A. M., and Al-Jenoobi, F. I. (2023). Microwave-Assisted formation of ternary inclusion complex of pterostilbene. *Pharmaceuticals* 16, 1641. doi:10.3390/ph16121641

Bu, F.-Z., Yu, Y.-M., Shen, Y.-L., Wu, Z.-Y., and Li, Y.-T. (2023a). Cocrystallization with nutrient ferulic acid towards reducing the dissolubility behaviors of antifungal drug 5-fluorocytosine: an integrated theoretical and experimental case research. *J. Mol. Struct.* 1275, 134601. doi:10.1016/j.molstruc.2022.134601

Bu, F.-Z., Yu, Y.-M., Zhang, M., Yan, C.-W., Wu, Z.-Y., and Li, Y.-T. (2023b). Directed self-assembly with gallic acid provides first phenolic acid cocrystals for the antiviral drug acyclovir toward increasing pharmaceutical features and synergy: a theoretical and experimental integration research. *Cryst. Growth Des.* 23, 5868–5882. doi:10.1021/acs.cgd.3c00489

Carvalho, M. T. B., Araújo-Filho, H. G., Barreto, A. S., Quintans-Júnior, L. J., Quintans, J. S. S., and Barreto, R. S. S. (2021). Wound healing properties of flavonoids: a systematic review highlighting the mechanisms of action. *Phytomedicine* 90, 153636. doi:10.1016/j.phymed.2021.153636

Chadha, R., Bhalla, Y., Nandan, A., Chadha, K., and Karan, M. (2017). Chrysin cocrystals: characterization and evaluation. *J. Pharm. Biomed. Anal.* 134, 361–371. doi:10.1016/j.jpba.2016.10.020

Charalabidis, A., Sfouni, M., Bergström, C., and Macheras, P. (2019). The biopharmaceutics classification system (BCS) and the biopharmaceutics drug disposition classification system (BDDCS): beyond guidelines. *Int. J. Pharm.* 566, 264–281. doi:10.1016/j.ijpharm.2019.05.041

Chen, L.-F., Xu, P.-Y., Fu, C.-P., Kankala, R. K., Chen, A.-Z., and Wang, S.-B. (2020). Fabrication of supercritical antisolvent (SAS) process-assisted fisetin-encapsulated poly (vinyl pyrrolidone) (PVP) nanocomposites for improved anticancer therapy. *Nanomaterials* 10, 322. doi:10.3390/nano10020322

Chen, W.-Y., Wei, J.-X., Yu, C.-Y., Liu, C.-Y., and Liao, Y.-H. (2025). Inhalable spray-dried porous microparticles containing dehydroandrographolide succinate phospholipid complex capable of improving and prolonging pulmonary anti-inflammatory efficacy in mice. *Drug Deliv. Transl. Res.* 15, 670–687. doi:10.1007/s13346-024-01626-6

Chezanoglou, E., and Goula, A. M. (2021). Co-crystallization in sucrose: a promising method for encapsulation of food bioactive components. *Trends Food Sci. Technol.* 114, 262–274. doi:10.1016/j.tifs.2021.05.036

Chhatbar, M., Borkhataria, C., Patel, O., Raichura, K., Pethani, T., Parmar, G., et al. (2025). Enhancing the solubility and bioavailability of itraconazole through pharmaceutical cocrystallization: a promising strategy for drug formulation. *J. Pharm. Sci.* 114, 103770. doi:10.1016/j.xphs.2025.103770

Cid-Samamed, A., Rakmai, J., Mejuto, J. C., Simal-Gandara, J., and Astray, G. (2022). Cyclodextrins inclusion complex: preparation methods, analytical techniques and food industry applications. *Food Chem.* 384, 132467. doi:10.1016/j.foodchem.2022.132467

Cui, W., He, Z., Zhang, Y., Fan, Q., and Feng, N. (2019). Naringenin cocrystals prepared by solution crystallization method for improving bioavailability and anti-hyperlipidemia effects. *AAPS PharmSciTech* 20, 115. doi:10.1208/s12249-019-1324-0

Dal Magro, C., Dos Santos, A. E., Ribas, M. M., Aguiar, G. P. S., Volfe, C. R. B., Lopes, M. L. L. C., et al. (2021). Production of curcumin-resveratrol cocrystal using cocrystallization with supercritical solvent. *J. Supercrit. Fluids* 171, 105190. doi:10.1016/j.supflu.2021.105190

Daruházi, Á. E., Kiss, T., Vecsernyés, M., Szente, L., Szőke, É., and Lemberkovics, É. (2013). Investigation of transport of genistein, daidzein and their inclusion complexes prepared with different cyclodextrins on Caco-2 cell line. *J. Pharm. Biomed. Anal.* 84, 112–116. doi:10.1016/j.jpba.2013.05.012

De Gaetano, F., Margani, F., Barbera, V., D'Angelo, V., Germanò, M. P., Pistarà, V., et al. (2023). Characterization and *in vivo* antiangiogenic activity evaluation of morin-based cyclodextrin inclusion complexes. *Pharmaceutics* 15, 2209. doi:10.3390/pharmaceutics15092209

Deng, Y.-H., Su, L.-N., Pang, Y.-H., Guo, Y.-F., Wang, F., Liao, X.-L., et al. (2017). Preparation, characterization and water solubility of inclusion complexes of daidzein with amino-modified β -cyclodextrins. *Chin. J. Anal. Chem.* 45, 648–653. doi:10.1016/S1872-2040(17)61012-0

Dhas, N., and Mehta, T. (2021). Intranasal delivery of chitosan decorated PLGA core/shell nanoparticles containing flavonoid to reduce oxidative stress in the treatment of Alzheimer's disease. *J. Drug Deliv. Sci. Technol.* 61, 102242. doi:10.1016/j.jddst.2020.102242

Dhondale, M. R., Thakor, P., Nambiar, A. G., Singh, M., Agrawal, A. K., Shastri, N. R., et al. (2023). Co-crystallization approach to enhance the stability of moisture-sensitive drugs. *Pharmaceutics* 15, 189. doi:10.3390/pharmaceutics15010189

Dias, J. L., Lanza, M., and Ferreira, S. R. S. (2021). Cocrystallization: a tool to modulate physicochemical and biological properties of food-relevant polyphenols. *Trends Food Sci. Technol.* 110, 13–27. doi:10.1016/j.tifs.2021.01.035

Dima, C., Assadpour, E., Dima, S., and Jafari, S. M. (2020). Bioavailability of nutraceuticals: role of the food matrix, processing conditions, the gastrointestinal tract, and nanodelivery systems. *Compr. Rev. Food Sci. Food Saf.* 19, 954–994. doi:10.1111/1541-4337.12547

Dima, C., Assadpour, E., Nechifor, A., Dima, S., Li, Y., and Jafari, S. M. (2024). Oral bioavailability of bioactive compounds; modulating factors, *in vitro* analysis methods, and enhancing strategies. *Crit. Rev. Food Sci. Nutr.* 64, 8501–8539. doi:10.1080/10408398.2023.2199861

Ding, C., Liu, Z., Zhao, T., Sun, S., Liu, X., Zhang, J., et al. (2023). A temperature-sensitive hydrogel loaded with taxifolin promotes skin repair by modulating MAPK-mediated autophagic pathway. *J. Mat. Sci.* 58, 14831–14845. doi:10.1007/s10853-023-08951-0

Ding, P., Chen, Y., Cao, G., Shen, H., Ju, J., and Li, W. (2019). Solutol®HS15+pluronicF127 and Solutol®HS15+pluronicL61 mixed micelle systems for oral delivery of genistein. *Drug Des. devel. Ther.* 13, 1947–1956. doi:10.2147/DDDT.S201453

Drannikov, A. A., Vatlin, I. S., Trusova, M. E., Di Martino, A., Krivoshchekov, S. V., Guriev, A. M., et al. (2022). Investigation of the influence of formulation method on technological parameters of gramicidin S and β-cyclodextrin inclusion complexes. *Drug Dev. Regist.* 11, 102–108. doi:10.33380/2305-2066-2022-11-2-102-108

Dutt, B., Choudhary, M., and Budhwar, V. (2020). Cocrystallization: an innovative route toward better medication. *J. Rep. Pharm. Sci.* 9, 256. doi:10.4103/jrptps.JRPTPS_103_19

Ellwood, L., Torun, G., Bahar, Z., and Fernandez, R. (2019). Effects of flavonoid-rich fruits on hypertension in adults: a systematic review. *JBI Database Syst. Rev. Implement. Rep.* 17, 2075–2105. doi:10.11124/JBISRIR-D-19-00050

Emami, S., Siahi-Shadbad, M., Adibkia, K., and Barzegar-Jalali, M. (2018). Recent advances in improving oral drug bioavailability by cocrystals. *BioImpacts* 8, 305–320. doi:10.15171/bi.2018.33

Fenyvesi, F., Nguyen, T. L. P., Haimhoffer, Á., Rusznyák, Á., Vasvári, G., Bácskay, I., et al. (2020). Cyclodextrin complexation improves the solubility and caco-2 permeability of chrysin. *Materials* 13, 3618. doi:10.3390/ma13163618

Fonte, P., Reis, S., and Sarmento, B. (2016). Facts and evidences on the lyophilization of polymeric nanoparticles for drug delivery. *J. Control. Release* 225, 75–86. doi:10.1016/j.jconrel.2016.01.034

Franzé, S., Selmin, F., Samaritani, E., Minghetti, P., and Cilurzo, F. (2018). Lyophilization of liposomal formulations: still necessary, still challenging. *Pharmaceutics* 10, 139. doi:10.3390/pharmaceutics10030139

Gaber, D. A., Alnwiser, M. A., Alotaibi, N. L., Almutairi, R. A., Alsaeed, S. S., Abdoun, S. A., et al. (2022). Design and optimization of ganciclovir solid dispersion for improving its bioavailability. *Drug Deliv.* 29, 1836–1847. doi:10.1080/10717544.2022.2083723

Gandhi, S. R., Quintans, J. D. S. S., Gandhi, G. R., Araújo, A. A. D. S., and Quintans Júnior, L. J. (2020). The use of cyclodextrin inclusion complexes to improve anticancer drug profiles: a systematic review. *Expert Opin. Drug Deliv.* 17, 1069–1080. doi:10.1080/17425247.2020.1776261

Garbiec, E., Rosiak, N., Zalewski, P., Tajber, L., and Cielecka-Piontek, J. (2023). Genistein Co-amorphous systems with amino acids: an investigation into enhanced solubility and biological activity. *Pharmaceutics* 15, 2653. doi:10.3390/pharmaceutics15122653

Gul, S., Maqbool, M. F., Zheng, D., Li, Y., Khan, M., and Ma, T. (2022). Alpinetin: a dietary flavonoid with diverse anticancer effects. *Appl. Biochem. Biotechnol.* 194, 4220–4243. doi:10.1007/s12010-022-03960-2

Gusev, K. A., Maimistov, D. N., Pavlovsky, V. I., Aliev, A. R., Pavlovsky, A. V., Ivanova, O. V., et al. (2022). Development of the composition and technology for production a solid dispersion system by hot melt extrusion to increase the bioavailability of the active substance. *Drug Dev. Regist.* 11, 108–115. doi:10.33380/2305-2066-2022-11-4-108-115

Ha, E.-S., Choi, D. H., Baek, I., Park, H., and Kim, M.-S. (2021). Enhanced oral bioavailability of resveratrol by using neutralized eudragit E solid dispersion prepared via spray drying. *Antioxidants* 10, 90. doi:10.3390/antiox10010090

Hassan, S. S. U., Samanta, S., Dash, R., Karpiński, T. M., Habibi, E., Sadiq, A., et al. (2022). The neuroprotective effects of fisetin, a natural flavonoid in neurodegenerative diseases: focus on the role of oxidative stress. *Front. Pharmacol.* 13, 1015835. doi:10.3389/fphar.2022.1015835

He, H.-F., Wei, K., Yin, J., and Ye, Y. (2021). Insight into tea flavonoids: composition and chemistry. *Food Rev. Int.* 37, 812–823. doi:10.1080/87559129.2020.1721530

Hempel, N.-J., Knopp, M. M., Berthelsen, R., and Löbmann, K. (2020). Convection-induced vs. Microwave radiation-induced *in situ* drug amorphization. *Molecules* 25, 1068. doi:10.3390/molecules25051068

Hogan, J., and Biswas, P. (2008). Narrow size distribution nanoparticle production by electrospray processing of ferritin. *J. Aerosol Sci.* 39, 432–440. doi:10.1016/j.jaerosci.2008.01.002

Hoque, M. J., Toda, M., and Mase, N. (2022). Comparative study of inclusion complex formation between β-cyclodextrin (host) and aromatic diamines (guests) by mixing in hot water, co-precipitation, and solid-state grinding methods. *J. Carbohydr. Chem.* 41, 249–272. doi:10.1080/07328303.2022.2068026

Hughey, J. R., Keen, J. M., Miller, D. A., Brough, C., and McGinity, J. W. (2012). Preparation and characterization of fusion processed solid dispersions containing a viscous thermally labile polymeric carrier. *Int. J. Pharm.* 438, 11–19. doi:10.1016/j.ijpharm.2012.08.032

Imam, S. S., Alshehri, S., Mahdi, W. A., Alotaibi, A. M., Alhwaifi, M. H., Hussain, A., et al. (2022). Formulation of multicomponent chrysin-hydroxy propyl β cyclodextrin-poloxamer inclusion complex using spray dry method: physicochemical characterization to cell viability assessment. *Pharmaceuticals* 15, 1525. doi:10.3390/ph15121525

Inoue, Y., Yoshida, M., Ezawa, T., Tanikawa, T., Arce, F., See, G. L., et al. (2022). Inclusion complexes of daidzein with cyclodextrin-based metal–organic framework-1 enhance its solubility and antioxidant capacity. *AAPS PharmSciTech* 23, 2. doi:10.1208/s12249-021-02151-2

Irigoiti, Y., Yamul, D. K., and Navarro, A. S. (2021). Co-crystallized sucrose with propolis extract as a food ingredient: powder characterization and antioxidant stability. *LWT* 143, 111164. doi:10.1016/j.lwt.2021.111164

Jangid, A. K., Agraval, H., Gupta, N., Jain, P., Yadav, U. C. S., Pooja, D., et al. (2020). Amorphous nano morin outperforms native molecule in anticancer activity and oral bioavailability. *Drug Dev. Ind. Pharm.* 46, 1123–1132. doi:10.1080/03639045.2020.1776318

Janssens, S., and Van Den Mooter, G. (2009). Review: physical chemistry of solid dispersions. *J. Pharm. Pharmacol.* 61, 1571–1586. doi:10.1211/jpp.61.12.0001

Jeong, H.-M., Kang, H.-N., Lee, Y.-R., Kim, E.-A., Lee, E.-H., and Shim, J.-H. (2023). Improved low water solubility of fisetin by enzymatic encapsulation reaction using cycloamylose produced by cyclodextrin glucanotransferase. *Process Biochem.* 130, 138–146. doi:10.1016/j.procbio.2023.04.005

Kakran, M., Sahoo, N. G., and Li, L. (2011). Dissolution enhancement of quercetin through nanofabrication, complexation, and solid dispersion. *Colloids Surf. B Biointerfaces* 88, 121–130. doi:10.1016/j.colsurfb.2011.06.020

Kan, J., Wu, F., Wang, F., Zheng, J., Cheng, J., Li, Y., et al. (2022). Phytonutrients: sources, bioavailability, interaction with gut microbiota, and their impacts on human health. *Front. Nutr.* 9, 960309. doi:10.3389/fnut.2022.960309

Khan, J., Alexander, A., Saraf, S., and Saraf, S. (2014). Luteolin-phospholipid complex: preparation, characterization and biological evaluation: luteolin-phospholipid complex. *J. Pharm. Pharmacol.* 66, 1451–1462. doi:10.1111/jphp.12280

Kuche, K., Bhargavi, N., Dora, C. P., and Jain, S. (2019). Drug-phospholipid complex—a go through strategy for enhanced oral bioavailability. *AAPS PharmSciTech* 20, 43. doi:10.1208/s12249-018-1252-4

Kwon, H. J., Heo, E.-J., Kim, Y.-H., Kim, S., Hwang, Y.-H., Byun, J.-M., et al. (2019). Development and evaluation of poorly water-soluble celecoxib as solid dispersions containing nonionic surfactants using fluidized-bed granulation. *Pharmaceutics* 11, 136. doi:10.3390/pharmaceutics11030136

Lee, C., Hee Lim, J., Young Cho, A., Yoon, W., Yun, H., Won Kang, J., et al. (2023). Molecular structures of flavonoid co-formers for cocrystallization with carbamazepine. *J. Ind. Eng. Chem.* 118, 309–317. doi:10.1016/j.jiec.2022.11.015

Leuenberger, H. (2002). Spray freeze-drying – the process of choice for low water soluble drugs? *J. Nanoparticle Res.* 4, 111–119. doi:10.1023/A:1020135603052

Li, J., Hao, X., Wang, C., Liu, H., Liu, L., He, X., et al. (2021). Improving the solubility, dissolution, and bioavailability of metronidazole via cocrystallization with ethyl gallate. *Pharmaceutics* 13, 546. doi:10.3390/pharmaceutics13040546

Lima, B. D. S., Campos, C. D. A., Da Silva Santos, A. C. R., Santos, V. C. N., Trindade, G. D. G. G., Shanmugam, S., et al. (2019). Development of morin/hydroxypropyl-β-cyclodextrin inclusion complex: enhancement of bioavailability, antihyperalgesic and anti-inflammatory effects. *Food Chem. Toxicol.* 126, 15–24. doi:10.1016/j.fct.2019.01.038

Lin, T.-C., Yang, C.-Y., Wu, T.-H., Tseng, C.-H., and Yen, F.-L. (2023). Myricetin nanofibers enhanced water solubility and skin penetration for increasing antioxidant and photoprotective activities. *Pharmaceutics* 15, 906. doi:10.3390/pharmaceutics15030906

Liu, L., Nie, J., and Li, L. (2023). Phospholipid complexation for bioavailability improvement of albendazole: preparation, characterization and *in vivo* evaluation. *AAPS PharmSciTech* 24, 36. doi:10.1208/s12249-022-02497-1

Liu, X., Xu, F., Yong, H., Chen, D., Tang, C., Kan, J., et al. (2025). Recent advances in chitosan-based active and intelligent packaging films incorporated with flavonoids. *Food Chem. X* 25, 102200. doi:10.1016/j.fochx.2025.102200

Liu, Y., Yang, F., Zhao, X., Wang, S., Yang, Q., and Zhang, X. (2022). Crystal structure, solubility, and pharmacokinetic study on a hesperetin cocrystal with piperine as coformer. *Pharmaceutics* 14, 94. doi:10.3390/pharmaceutics14010094

Lu, M., Qiu, Q., Luo, X., Liu, X., Sun, J., Wang, C., et al. (2019). Phyto-phospholipid complexes (phytosomes): a novel strategy to improve the bioavailability of active constituents. *Asian J. Pharm. Sci.* 14, 265–274. doi:10.1016/j.ajps.2018.05.011

Lu, S., Zhou, S., Chen, J., Zheng, J., Ren, J., Qi, P., et al. (2021). Quercetin nanoparticle ameliorates lipopolysaccharide-triggered renal inflammatory impairment by regulation of Sirt1/NF-KB pathway. *J. Biomed. Nanotechnol.* 17, 230–241. doi:10.1166/jbn.2021.3031

Luo, Y., Chen, S., Zhou, J., Chen, J., Tian, L., Gao, W., et al. (2019). Luteolin cocrystals: characterization, evaluation of solubility, oral bioavailability and theoretical calculation. *J. Drug Deliv. Sci. Technol.* 50, 248–254. doi:10.1016/j.jddst.2019.02.004

Maleki, S. J., Crespo, J. F., and Cabanillas, B. (2019). Anti-inflammatory effects of flavonoids. *Food Chem.* 299, 125124. doi:10.1016/j.foodchem.2019.125124

Martins, L. N. S. B., Venceslau, A. D. F. A., Carvalho, L. B., Jaime, C., Cardoso, M. D. G., and Pinto, L. D. M. A. (2020). Inclusion complex of Callistemon viminalis essential oil prepared by kneading. *J. Incl. Phenom. Macrocycl. Chem.* 97, 109–119. doi:10.1007/s10847-020-00989-w

Masuoka, N., Matsuda, M., and Kubo, I. (2012). Characterisation of the antioxidant activity of flavonoids. *Food Chem.* 131, 541–545. doi:10.1016/j.foodchem.2011.09.020

Metkari, V., Shah, R., Salunkhe, N., and Gurav, S. (2023). QBD approach for the design, optimization, development, and characterization of naringenin-loaded phytosomes to enhance solubility and oral bioavailability. *J. Pharm. Innov.* 18, 2083–2097. doi:10.1007/s12247-023-09775-w

Movahedi, F., Li, L., Gu, W., and Xu, Z. P. (2017). Nanoformulations of albendazole as effective anticancer and antiparasite agents. *Nanomed* 12, 2555–2574. doi:10.2217/nnm-2017-0102

Naeem, A., Ming, Y., Pengyi, H., Jie, K. Y., Yali, L., Haiyan, Z., et al. (2022). The fate of flavonoids after oral administration: a comprehensive overview of its bioavailability. *Crit. Rev. Food Sci. Nutr.* 62, 6169–6186. doi:10.1080/10408398.2021.1898333

Page, M. J., McKenzie, J. E., Bossuyt, P. M., Boutron, I., Hoffmann, T. C., Mulrow, C. D., et al. (2021). The PRISMA 2020 statement: an updated guideline for reporting systematic reviews. *BMJ* n71, n71. doi:10.1136/bmj.n71

Parafati, M., La Russa, D., Lascala, A., Crupi, F., Riillo, C., Fotschki, B., et al. (2024). Dramatic suppression of lipogenesis and No increase in beta-oxidation gene expression are among the key effects of bergamot flavonoids in fatty liver disease. *Antioxidants* 13, 766. doi:10.3390/antiox13070766

Patil, H., Tiwari, R. V., and Repka, M. A. (2016). Hot-melt extrusion: from theory to application in pharmaceutical formulation. *AAPS PharmSciTech* 17, 20–42. doi:10.1208/s12249-015-0360-7

Patil, J., Pawde, D. M., Bhattacharya, S., and Srivastava, S. (2024). Phospholipid complex formulation technology for improved drug delivery in oncological settings: a comprehensive review. *AAPS PharmSciTech* 25, 91. doi:10.1208/s12249-024-02813-x

Qi, J., Wang, B., Ding, S., Daintree, L. S., Ledger, D. M., Zhao, W., et al. (2015). Itraconazole solid dispersion prepared by a supercritical fluid technique: preparation, *in vitro* characterization, and bioavailability in beagle dogs. *Drug Des. devel. Ther.* 2801, 2801. doi:10.2147/DDDT.S81253

Qiu, C., Zhang, Y., Fan, Y., Li, S., Gao, J., He, X., et al. (2024). Solid dispersions of genistein via solvent rotary evaporation for improving solubility, bioavailability, and amelioration effect in HFD-induced obesity mice. *Pharmaceutics* 16, 306. doi:10.3390/pharmaceutics16030306

Qiu, X.-L., Fan, Z.-R., Liu, Y.-Y., Wang, D.-F., Wang, S.-X., and Li, C.-X. (2021). Preparation and evaluation of a self-nanoemulsifying drug delivery system loaded with heparin phospholipid complex. *Int. J. Mol. Sci.* 22, 4077. doi:10.3390/ijms22084077

Raheem Thayyil, A., Juturu, T., Nayak, S., and Kamath, S. (2020). Pharmaceutical Co-crystallization: regulatory aspects, design, characterization, and applications. *Adv. Pharm. Bull.* 10, 203–212. doi:10.34172/apb.2020.024

Ramanan, M., Sinha, S., Sudarshan, K., Aidhen, I. S., and Doble, M. (2016). Inhibition of the enzymes in the leukotriene and prostaglandin pathways in inflammation by 3-aryl isocoumarins. *Eur. J. Med. Chem.* 124, 428–434. doi:10.1016/j.ejmech.2016.08.066

Ren, S., Liu, M., Hong, C., Li, G., Sun, J., Wang, J., et al. (2019). The effects of pH, surfactant, ion concentration, coformer, and molecular arrangement on the solubility behavior of myricetin cocrystals. *Acta Pharm. Sin. B* 9, 59–73. doi:10.1016/j.apsb.2018.09.008

Roy, A., Khan, A., Ahmad, I., Alghamdi, S., Rajab, B. S., Babalghith, A. O., et al. (2022). Flavonoids a bioactive compound from medicinal plants and its therapeutic applications. *Biomed. Res. Int.* 2022, 5445291. doi:10.1155/2022/5445291

Rusdin, A., Mohd Gazzali, A., Ain Thomas, N., Megantara, S., Aulifa, D. L., Budiman, A., et al. (2024). Advancing drug delivery paradigms: polyvinyl pyrolidone (PVP)-Based amorphous solid dispersion for enhanced physicochemical properties and therapeutic efficacy. *Polymers* 16, 286. doi:10.3390/polym16020286

Saini, V., Bala, R., and Arora, S. (2022). Formulation and characterization of phytophospholipid complex of andrographis paniculata extract. *ECS Trans.* 107, 9119–9126. doi:10.1149/10701.9119ecst

Shen, H., He, D., Wang, S., Ding, P., Wang, J., and Ju, J. (2018). Preparation, characterization, and pharmacokinetics study of a novel genistein-loaded mixed micelles system. *Drug Dev. Ind. Pharm.* 44, 1536–1542. doi:10.1080/03639045.2018.1483384

Shen, H., Liu, Y., Zhang, H., Ding, P., Zhang, L., Zhang, L., et al. (2019). Enhancing the oral bioavailability of baicalein via Solutol® HS15 and Poloxamer 188 mixed micelles system. *J. Pharm. Pharmacol.* 71, 765–773. doi:10.1111/jphp.13058

Singh, A., and Van Den Mooter, G. (2016). Spray drying formulation of amorphous solid dispersions. *Adv. Drug Deliv. Rev.* 100, 27–50. doi:10.1016/j.addr.2015.12.010

Singh, D., Rawat, M., S. M., Semalty, A., and Semalty, M. (2012). Quercetin-phospholipid complex: an amorphous pharmaceutical system in herbal drug delivery. *Curr. Drug Discov. Technol.* 9, 17–24. doi:10.2174/157016312799304507

Singh, M. K., Pooja, D., Ravuri, H. G., Gunukula, A., Kulhari, H., and Sistla, R. (2018). Fabrication of surfactant-stabilized nanosuspension of naringenin to surpass its poor physiochemical properties and low oral bioavailability. *Phytomedicine* 40, 48–54. doi:10.1016/j.phymed.2017.12.021

Soares, R. N., Ximenes, E. C. P. D. A., Araújo, S. B., Silva, R. L. D., Souza, V. M. O. D., Coelho, L. C. B. B., et al. (2023). Evaluation of β-lapachone-methyl-β-cyclodextrin inclusion complex prepared by spray drying and its application against different developmental stages of Schistosoma mansoni in murine model. *Chem. Biol. Interact.* 373, 110374. doi:10.1016/j.cbi.2023.110374

Stielow, M., Witczyńska, A., Kubryń, N., Fijałkowski, Ł., Nowaczyk, J., and Nowaczyk, A. (2023). The bioavailability of drugs—the current state of knowledge. *Molecules* 28, 8038. doi:10.3390/molecules28248038

Sudarshan, K., Boda, A. K., Dogra, S., Bose, I., Yadav, P. N., and Aidhen, I. S. (2019). Discovery of an isocoumarin analogue that modulates neuronal functions via neurotrophin receptor TrkB. *Bioorg. Med. Chem. Lett.* 29, 585–590. doi:10.1016/j.bmcl.2018.12.057

Svotin, A. A., Taldaev, A., Nikitin, I. D., Korochkina, M. D., Terekhov, R. P., and Selivanova, I. A. (2025). Insights in wound healing properties of water-soluble composition of dihydroquercetin and L-lysine. *J. Pharm. Pharm. Sci.* 28, 13831. doi:10.3389/jpps.2025.13831

Taldaev, A., Pankov, D. I., Terekhov, R. P., Zhevlakova, A. K., and Selivanova, I. A. (2023). Modification of the physicochemical properties of active pharmaceutical ingredients via lyophilization. *Pharmaceutics* 15, 2607. doi:10.3390/pharmaceutics15112607

Telange, D. R., Patil, A. T., Pethe, A. M., Fegade, H., Anand, S., and Dave, V. S. (2017). Formulation and characterization of an apigenin-phospholipid phytosome (APLC) for improved solubility, *in vivo* bioavailability, and antioxidant potential. *Eur. J. Pharm. Sci.* 108, 36–49. doi:10.1016/j.ejps.2016.12.009

Terekhov, R. P., Ilyasov, I. R., Beloborodov, V. L., Zhevlakova, A. K., Pankov, D. I., Dzuban, A. V., et al. (2022). Solubility enhancement of dihydroquercetin via "green" phase modification. *Int. J. Mol. Sci.* 23, 15965. doi:10.3390/ijms232415965

Terekhov, R. P., Savina, A. D., Pankov, D. I., Korochkina, M. D., Taldaev, A., Yakubovich, L. M., et al. (2024). Insights into the stereoisomerism of dihydroquercetin: analytical and pharmacological aspects. *Front. Chem.* 12, 1439167. doi:10.3389/fchem.2024.1439167

Terenteva, O. A., Kotsur, Yu. M., Narkevich, I. A., and Flisyuk, E. V. (2024). Production sustained release dosage forms from deliquescent substances by solid dispersion systems. *Drug Dev. Regist.* doi:10.33380/2305-2066-2024-13-4-1951

Tran, P., Pyo, Y.-C., Kim, D.-H., Lee, S.-E., Kim, J.-K., and Park, J.-S. (2019). Overview of the manufacturing methods of solid dispersion technology for improving the solubility of poorly water-soluble drugs and application to anticancer drugs. *Pharmaceutics* 11, 132. doi:10.3390/pharmaceutics11030132

Tumilaar, S. G., Hardianto, A., Dohi, H., and Kurnia, D. (2024). A comprehensive review of free radicals, oxidative stress, and antioxidants: overview, clinical applications, global perspectives, future directions, and mechanisms of antioxidant activity of flavonoid compounds. *J. Chem.* 2024, 1–21. doi:10.1155/2024/5594386

Tungmunnithum, D., Thongboonyou, A., Pholboon, A., and Yangsabai, A. (2018). Flavonoids and other phenolic compounds from medicinal plants for pharmaceutical and medical aspects: an overview. *Medicines* 5, 93. doi:10.3390/medicines5030093

Van Eck, N. J., and Waltman, L. (2010). Software survey: VOSviewer, a computer program for bibliometric mapping. *Scientometrics* 84, 523–538. doi:10.1007/s11192-009-0146-3

Van Eck, N. J., and Waltman, L. (2011). Text mining and visualization using VOSviewer. doi:10.48550/ARXIV.1109.2058

Vinarov, Z., Katev, V., Radeva, D., Tcholakova, S., and Denkov, N. D. (2018). Micellar solubilization of poorly water-soluble drugs: effect of surfactant and solubilizate molecular structure. *Drug Dev. Ind. Pharm.* 44, 677–686. doi:10.1080/03639045.2017.1408642

Wahnou, H., Limami, Y., and Oudghiri, M. (2024). Flavonoids and flavonoid-based nanoparticles for osteoarthritis and rheumatoid arthritis management. *Biochem.* 4, 38–61. doi:10.3390/biochem4010003

Waltman, L., and Van Eck, N. J. (2013). A smart local moving algorithm for large-scale modularity-based community detection. *Eur. Phys. J. B* 86, 471. doi:10.1140/epjb/e2013-40829-0

Wang, F., Yang, B., Zhao, Y., Liao, X., Gao, C., Jiang, R., et al. (2014). Host-guest inclusion system of scutellarein with 2-hydroxypropyl-beta-cyclodextrin: preparation, characterization, and anticancer activity. *J. Biomater. Sci. Polym. Ed.* 25, 594–607. doi:10.1080/09205063.2014.884875

Wang, L., Zhong, C., Zu, Y., Zhao, X., Deng, Y., Wu, W., et al. (2019). Preparation and characterization of luteolin nanoparticles for enhance bioavailability and inhibit liver microsomal peroxidation in rats. *J. Funct. Foods* 55, 57–64. doi:10.1016/j.jff.2019.01.054

Wang, T., Li, Q., and Bi, K. (2018). Bioactive flavonoids in medicinal plants: structure, activity and biological fate. *Asian J. Pharm. Sci.* 13, 12–23. doi:10.1016/j.ajps.2017.08.004

Wang, W., Zhang, W., Jiang, Y., Wang, X., Zhang, X., Liu, H., et al. (2020). Preparation of ursolic acid–phospholipid complex by solvent-assisted grinding method to improve dissolution and oral bioavailability. *Pharm. Dev. Technol.* 25, 68–75. doi:10.1080/10837450.2019.1671864

Wang, Y., Zhang, B., Wang, W., Yuan, P., Hu, K., Zhang, L., et al. (2024a). Improvement of the thermal stability and aqueous solubility of three matrine salts assembled by the similar structure salt formers. *Pharmaceuticals* 17, 94. doi:10.3390/ph17010094

Wang, Z., Li, Q., An, Q., Gong, L., Yang, S., Zhang, B., et al. (2023). Optimized solubility and bioavailability of genistein based on cocrystal engineering. *Nat. Prod. Bioprospecting* 13, 30. doi:10.1007/s13659-023-00397-w

Wang, Z., Li, S., Li, Q., Wang, W., Liu, M., Yang, S., et al. (2024b). A novel cocrystal of daidzein with piperazine to optimize the solubility, permeability and bioavailability of daidzein. *Molecules* 29, 1710. doi:10.3390/molecules29081710

Weecharangsan, W., and Lee, R. J. (2024). Surface solid dispersion of ketoconazole on trehalose dihydrate using spray drying to achieve enhanced dissolution rate. *AAPS PharmSciTech* 25, 220. doi:10.1208/s12249-024-02941-4

Whyte, A. R., Cheng, N., Butler, L. T., Lamport, D. J., and Williams, C. M. (2019). Flavonoid-Rich mixed berries maintain and improve cognitive function over a 6 h period in young healthy adults. *Nutrients* 11, 2685. doi:10.3390/nu11112685

Wu, W., Zu, Y., Wang, L., Wang, L., Wang, H., Li, Y., et al. (2017a). Preparation, characterization and antitumor activity evaluation of apigenin nanoparticles by the liquid antisolvent precipitation technique. *Drug Deliv.* 24, 1713–1720. doi:10.1080/10717544.2017.1399302

Wu, W., Zu, Y., Zhao, X., Zhang, X., Wang, L., Li, Y., et al. (2017b). Solubility and dissolution rate improvement of the inclusion complex of apigenin with 2-hydroxypropyl-β-cyclodextrin prepared using the liquid antisolvent precipitation

and solvent removal combination methods. *Drug Dev. Ind. Pharm.* 43, 1366–1377. doi:10.1080/03639045.2017.1318900

Xu, Y., Wang, Y., Li, C., Han, T., Chen, H., Chen, W., et al. (2023). Preparation, characterization, and biological activity of the inclusion complex of dihydroquercetin and β-Cyclodextrin. *AAPS Open* 9, 16. doi:10.1186/s41120-023-00083-8

Yang, L.-J., Xia, S., Ma, S.-X., Zhou, S.-Y., Zhao, X.-Q., Wang, S.-H., et al. (2016). Host–guest system of hesperetin and β-cyclodextrin or its derivatives: preparation, characterization, inclusion mode, solubilization and stability. *Mat. Sci. Eng. C* 59, 1016–1024. doi:10.1016/j.msec.2015.10.037

Yang, T., Zhang, Z., Ning, F., Yuan, L., Yang, X., and Luo, L. (2024). New theoretical perspective for easy evaluation of the antioxidant properties of typical flavonoids. *Microchem. J.* 197, 109786. doi:10.1016/j.microc.2023.109786

You, G., Feng, T., Zhang, G., Chen, M., Liu, F., Sun, L., et al. (2021). Preparation, optimization, characterization and *in vitro* release of baicalein-solubilizing glycyrrhizic acid nano-micelles. *Int. J. Pharm.* 601, 120546. doi:10.1016/j.ijpharm.2021.120546

Zafar, A., Alruwaili, N. K., Imam, S. S., Alsaidan, O. A., Alkholifi, F. K., Alharbi, K. S., et al. (2021). Formulation of genistein-HP β cyclodextrin-poloxamer 188 ternary inclusion complex: solubility to cytotoxicity assessment. *Pharmaceutics* 13, 1997. doi:10.3390/pharmaceutics13121997

Zaragozá, C., Villaescusa, L., Monserrat, J., Zaragozá, F., and Álvarez-Mon, M. (2020). Potential therapeutic anti-inflammatory and immunomodulatory effects of dihydroflavones, flavones, and flavonols. *Molecules* 25, 1017. doi:10.3390/molecules25041017

Zhang, H., Wang, M., Chen, L., Liu, Y., Liu, H., Huo, H., et al. (2017a). Structure-solubility relationships and thermodynamic aspects of solubility of some flavonoids in the solvents modeling biological media. *J. Mol. Liq.* 225, 439–445. doi:10.1016/j.molliq.2016.11.036

Zhang, K., Gu, L., Chen, J., Zhang, Y., Jiang, Y., Zhao, L., et al. (2015). Preparation and evaluation of kaempferol–phospholipid complex for pharmacokinetics and bioavailability in SD rats. *J. Pharm. Biomed. Anal.* 114, 168–175. doi:10.1016/j.jpba.2015.05.017

Zhang, W., Lian, Y., Li, Q., Sun, L., Chen, R., Lai, X., et al. (2020). Preventative and therapeutic potential of flavonoids in peptic ulcers. *Molecules* 25, 4626. doi:10.3390/molecules25204626

Zhang, Y., Yu, J., Dong, X.-D., and Ji, H.-Y. (2017b). Research on characteristics, antioxidant and antitumor activities of dihydroquercetin and its complexes. *Molecules* 23, 20. doi:10.3390/molecules23010020

Zhang, Z., Cui, C., Wei, F., and Lv, H. (2017c). Improved solubility and oral bioavailability of apigenin via Soluplus/Pluronic F127 binary mixed micelles system. *Drug Dev. Ind. Pharm.* 43, 1276–1282. doi:10.1080/03639045.2017.1313857

Zhang, Z., Huang, Y., Gao, F., Bu, H., Gu, W., and Li, Y. (2011). Daidzein–phospholipid complex loaded lipid nanocarriers improved oral absorption: *in vitro* characteristics and *in vivo* behavior in rats. *Nanoscale* 3, 1780. doi:10.1039/c0nr00879f

Zhao, H., Bao, S., Chen, S., Yang, Q., Lou, K., Gai, Y., et al. (2025). Phytosomes loaded with mastoparan-M represent a novel strategy for breast cancer treatment. *Int. J. Nanomedicine* 20, 109–124. doi:10.2147/IJN.S481871

Zhou, F., Shemchuk, O., Charpentier, M. D., Matheys, C., Collard, L., Ter Horst, J. H., et al. (2021). Simultaneous chiral resolution of two racemic compounds by preferential cocrystallization. *Angew. Chem.* 133, 20426–20430. doi:10.1002/ange.202107804

Zhou, Y., Dong, W., Ye, J., Hao, H., Zhou, J., Wang, R., et al. (2017). A novel matrix dispersion based on phospholipid complex for improving oral bioavailability of baicalein: preparation, *in vitro* and *in vivo* evaluations. *Drug Deliv.* 24, 720–728. doi:10.1080/10717544.2017.1311968

Zou, F., Zhao, H., Ma, A., Song, D., Zhang, X., and Zhao, X. (2022). Preparation of an isorhamnetin phospholipid complex for improving solubility and anti-hyperuricemia activity. *Pharm. Dev. Technol.* 27, 842–852. doi:10.1080/10837450.2022.2123510

Zulkefli, N., Che Zahari, C. N. M., Sayuti, N. H., Kamarudin, A. A., Saad, N., Hamezah, H. S., et al. (2023). Flavonoids as potential wound-healing molecules: emphasis on pathways perspective. *Int. J. Mol. Sci.* 24, 4607. doi:10.3390/ijms24054607

frontiers | Frontiers in Chemistry

TYPE Original Research
PUBLISHED 06 May 2025
DOI 10.3389/fchem.2025.1595997

Check for updates

OPEN ACCESS

EDITED BY
Marko Jukic,
University of Maribor, Slovenia

REVIEWED BY
Mesut Işık,
Bilecik Şeyh Edebali University, Türkiye
Meryem Topal,
Gümüşhane University, Türkiye

*CORRESPONDENCE
Hesham A. M. Gomaa,
hasoliman@ju.edu.sa
Bahaa G. M. Youssif,
bgyoussif2@gmail.com
Stefan Bräse,
braese@kit.edu

RECEIVED 19 March 2025
ACCEPTED 18 April 2025
PUBLISHED 06 May 2025

CITATION
Gomaa HAM, Atta AM, Shaker ME, Alzarea SI, Alsahli TG, Alatwi E, Musa A, Mohamed FAM, Alzahrani HA, Mohassab AM, Abdelmoez A, Bräse S and Youssif BGM (2025) Design, synthesis, and biological investigation of new thiazole-based derivatives as multi-targeted inhibitors endowed with antiproliferative, antioxidant, and antibacterial properties. *Front. Chem.* 13:1595997. doi: 10.3389/fchem.2025.1595997

COPYRIGHT
© 2025 Gomaa, Atta, Shaker, Alzarea, Alsahli, Alatwi, Musa, Mohamed, Alzahrani, Mohassab, Abdelmoez, Bräse and Youssif. This is an open-access article distributed under the terms of the Creative Commons Attribution License (CC BY). The use, distribution or reproduction in other forums is permitted, provided the original author(s) and the copyright owner(s) are credited and that the original publication in this journal is cited, in accordance with accepted academic practice. No use, distribution or reproduction is permitted which does not comply with these terms.

Design, synthesis, and biological investigation of new thiazole-based derivatives as multi-targeted inhibitors endowed with antiproliferative, antioxidant, and antibacterial properties

Hesham A. M. Gomaa[1]*, Asmaa M. Atta[2], Mohamed E. Shaker[1], Sami I. Alzarea[1], Tariq G. Alsahli[1], Eid Alatwi[1], Arafa Musa[3], Fatma A. M. Mohamed[4], Hayat Ali Alzahrani[5], Aliaa M. Mohassab[6], Alshaimaa Abdelmoez[7], Stefan Bräse[8]* and Bahaa G. M. Youssif[7]*

[1]Department of Pharmacology, College of Pharmacy, Jouf University, Sakaka, Aljouf, Saudi Arabia, [2]Pharmaceutical Chemistry Department, Faculty of Pharmacy, Badr University in Cairo (BUC), Badr City, Cairo, Egypt, [3]Department of Pharmacognosy, College of Pharmacy, Jouf University, Sakaka, Aljouf, Saudi Arabia, [4]Department of Clinical Laboratory Sciences, College of Applied Medical Sciences at Al-Qurayyat, Jouf University, Al-Qurayyat, Saudi Arabia, [5]Applied Medical Science College, Medical Laboratory Technology Department, Northern Border University, Arar, Saudi Arabia, [6]Department of Medicinal Chemistry, Faculty of Pharmacy, Minia University, Minia, Egypt, [7]Department of Pharmaceutical Organic Chemistry, Faculty of Pharmacy, Assiut University, Assiut, Egypt, [8]Institute of Biological and Chemical Systems, IBCS-FMS, Karlsruhe Institute of Technology, Karlsruhe, Germany

Introduction: A novel series of thiazole-based derivatives **11a-f** and **12a-f** was developed, synthesized, and tested for antiproliferative activity as dual EGFR/VEGFR-2 inhibitors, antioxidants, and antibacterial agents.

Methods: The structures of the new compounds **11a-f** and **12a-f** were validated using NMR spectroscopy and elemental microanalysis. The antiproliferative activity of **11a-f** and **12a-f** was tested against a panel of four cancer cell lines using MTT assay.

Results and Discussion: Compounds **11d** and **11f** had the highest antiproliferative activity, with GI_{50} values of 30 and 27 nM, respectively, making them more potent than erlotinib (GI_{50} = 33 nM). Inhibitory studies for EGFR and VEGFR-2 demonstrated that compounds **11d** and **11f** were the most potent derivatives with dual inhibitory activity. Furthermore, compounds **11d** and **11f** exhibited significant antioxidant activity at 10 μM, with radical scavenging activity of 71% and 73%, respectively, compared to the reference Trolox (78%). Moreover, compounds **11a-f** and **12a-f** exhibit significant inhibitory activity against *E. coli* DNA gyrase, with compounds **11b**, **11e**, and **12b** displaying the highest inhibitory efficacy, yielding IC_{50} values of 182, 190, and 197 nM, respectively, in comparison to the reference novobiocin (IC_{50} = 170 nM). Compounds **11b** and **11e** have significant antibacterial efficacy against both Gram-positive and Gram-negative bacterial strains, as demonstrated by a twofold serial dilution experiment. They

exhibit similar efficacy against *S. aureus, E. coli*, and *P. aeruginosa*, demonstrating more potency than ciprofloxacin, however displaying reduced effectiveness against *B. subtilis* compared to ciprofloxacin.

KEYWORDS

anticancer, antioxidant, antibacterial, EGFR, VEGFR-2

1 Introduction

Nitrogen-containing heterocyclic molecules are crucial in drug development, with around 75% of FDA-approved small-molecule medicines comprising one or more nitrogen-based heterocycles (Al-Wahaibi et al., 2024a; Mohamed et al., 2024). Thiazole, also known as 1,3-thiazole, is an azole heterocyclic moiety that includes one sulfur and one nitrogen atom at positions one and 3, respectively. Their varied biological activity is evidenced by numerous clinically authorized thiazole-containing drugs exhibiting various pharmacological effects. Most of these compounds are 2,4-disubstituted thiazole derivatives, with just a limited number being 2,5-disubstituted or 2,4,5-trisubstituted thiazoles (Arshad et al., 2022; Alateeq et al., 2024; Abdelazeem et al., 2017; Abdel-Aziz et al., 2021; Abdel-Aziz et al., 2022). Several medicines having antibacterial, antiparkinsonian, antithrombotic, antifungal, antiulcer, anti-inflammatory, anticancer, antiparasitic, and antigout action contain one thiazole moiety in their structure (Figure 1) (Jadhav et al., 2021; Chugh et al., 2022).

Enzyme inhibition has recently been recognized as a vital and important target method for tumor treatment (Liu et al., 2024; Wang et al., 2021). Thiazole-based derivatives in cancer therapy have been shown to efficiently inhibit many enzymes and enzymatic pathways, including tyrosine kinase inhibitors, B-RAF enzyme inhibitors, and microtubule function suppression (Rana et al., 2023; Sharma et al., 2020). Several risk factors contribute to molecular variations or mutations in critical proteins, such as tyrosine kinases, initiating carcinogenesis. These tyrosine kinases play crucial roles in proper cell proliferation, differentiation, metabolism, migration, and cell-cycle regulation by phosphorylating tyrosine residues in proteins (Theivendren et al., 2021; Pang et al., 2022). Conversely, receptor tyrosine kinases (RTKs) are high-affinity cell surface receptors that facilitate transmembrane signalling and play a transformative role in a variety of malignancies (Batool et al., 2023; Qi et al., 2024). The FDA (Food and Drug Administration) has approved numerous medications to treat cancer caused by activated RTKs (Zhong et al., 2021; Kumar et al., 2024).

Epidermal Growth Factor Receptor (EGFR) is a type of membrane RTK that is overexpressed in many cancers. Cancer progression is intimately tied to EGFR TK signal transmission, therefore blocking receptor activation can effectively stop tumor growth (Al-Wahaibi et al., 2023a; Al-Wahaibi et al., 2024b). VEGFR-2 (Vascular Endothelial Growth Factor Receptor) is a RTK that can promote angiogenesis (Marzouk et al., 2020). VEGFR-2, a member of the VEGFR family, regulates the proliferation of blood vessels in tumors and is required to form solid tumors. Blocking VEGFR-2 has been proposed as a potential method to reduce angiogenesis (Mahmoud et al., 2023; Mahmoud et al., 2024).

EGFR and VEGFR-2 have been identified as viable therapeutic targets in cancer treatment. They are essential in signalling networks that regulate tumor cell angiogenesis, motility, differentiation, and proliferation (Al-Wahaibi et al., 2024a; Xie et al., 2018). EGFR and VEGFR-2 often share similar signalling pathways in a complicated network of interconnections. Inhibiting EGFR can diminish VEGF synthesis and obstruct angiogenesis. Simultaneously increasing VEGFR-2 expression may ultimately result in resistance to EGFR treatments. Thus, the concurrent inhibition of both EGFR and VEGFR-2 has arisen as an effective cancer therapeutic strategy, producing a synergistic impact (Liu Z.-L. et al., 2023; Liu X.-J. et al., 2023).

Bacterial infections, caused by Gram-positive or Gram-negative bacteria, are the predominant form of infections contracted in hospitals or by the general populace (Al-Wahaibi et al., 2024c; Al-Wahaibi et al., 2024d). Furthermore, bacteria have acquired resistance to almost all presently utilized antibiotics due to their prolonged, extensive, and improper application, intensifying the issue (Al-Wahaibi et al., 2024e). Each year, drug-resistant infections kill approximately 0.7 million people worldwide, a figure that might rise to 10 million by 2050 if current trends continue (Agrawal and Patel, 2024). Consequently, it is critical to speed up the development of new antibacterials that are highly efficient against both susceptible and resistant pathogens.

DNA gyrase, a topoisomerase II enzyme, modifies the topology of DNA. It has two parts, called GyrA and GyrB, that are important for separating two DNA strands and starting a process called negative supercoiling during DNA replication (Abdel-Aziz et al., 2023; Al-Wahaibi et al., 2021). Antibacterial medications that particularly target DNA gyrase work through two mechanisms: gyrase poisoning, as reported with Ciprofloxacin, and inhibiting the ATP binding site, as demonstrated in Novobiocin (Tiz et al., 2019). Because of its profound relevance, DNA gyrase has emerged as a fascinating target for developing antibacterial medications.

The prevalence of cancer-related mortality as well as new cases associated with treatment or chronic infections highlight the link between infection and cancer. Infectious agents including bacteria and viruses cause approximately 2 million new cancer cases (Seong et al., 2025; Portela et al., 2025). Individuals with persistent infections are more likely to develop cancer because their immune systems are unable to battle both the pathogen and the development of cancer cells (Woo et al., 2025). This weakness may also result from overly aggressive cancer treatments such as chemotherapy, radiotherapy, and surgical resection, which make patients susceptible to pathogenic infections. Furthermore, chronic infection causes inflammation, which contributes to the development of cancer (Zolfi et al., 2025).

Considering these precedents, this report presents an efficient synthesis of a new series of thiazole-based derivatives hybridized with coumarin or benzofuran (**11a-f** and **12a-f**, Figure 2), in line

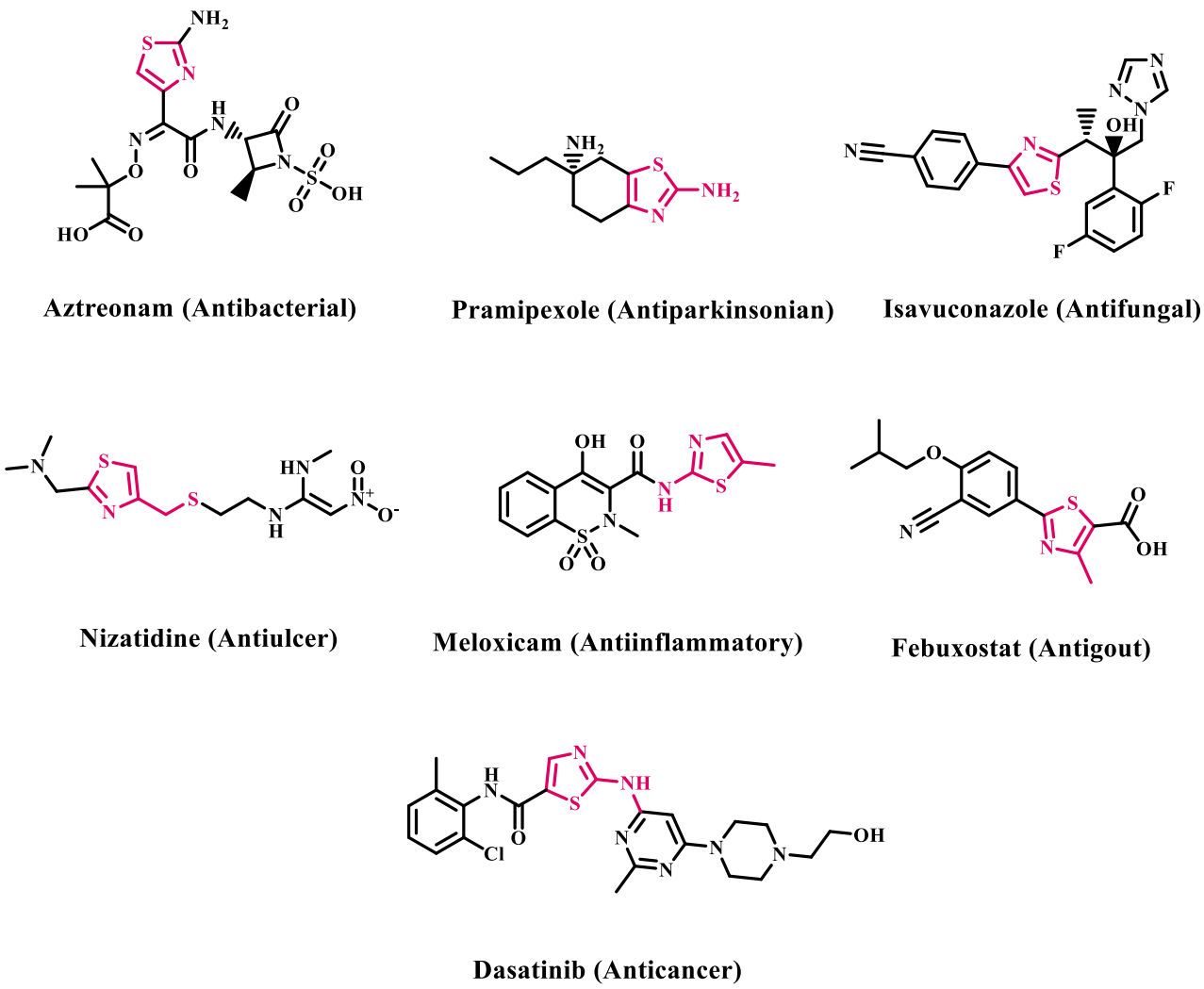


FIGURE 1
Structures of some clinically approved thiazole-based drugs.

with our research objectives of developing innovative methodologies for synthesizing heterocyclic systems with promising pharmacological properties (Al-Wahaibi et al., 2023b; Al-Wahaibi et al., 2023c; Aly et al., 2024; Aly et al., 2023; Elbastawesy et al., 2015; El-Sheref et al., 2023; Frejat F. O. A. et al., 2022). Furthermore, we investigated the biological activities of the newly synthesized compounds, which have potential anticancer, antibacterial, and antioxidant effects.

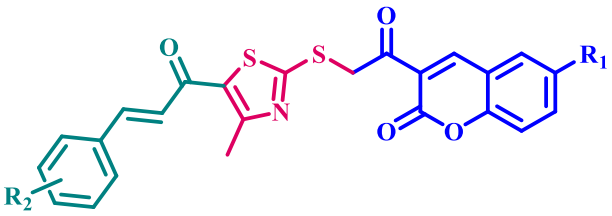
The newly synthesized compounds were examined for their impact on cell viability in a normal cell line to evaluate their safety profile. The antiproliferative efficacy of novel compounds was evaluated against a panel of four different cancer cell lines. The most effective compounds were assessed for their dual inhibition of EGFR and VEGFR-2, in addition to their antioxidant properties. All newly synthesized compounds were evaluated as DNA gyrase inhibitors, and the most effective derivatives were examined for their antibacterial activity against Gram-positive bacteria (*S. aureus* and *B. subtilis*) and Gram-negative bacteria (*E. coli* and *P. aeruginosa*).

2 Results and discussion

2.1 Chemistry

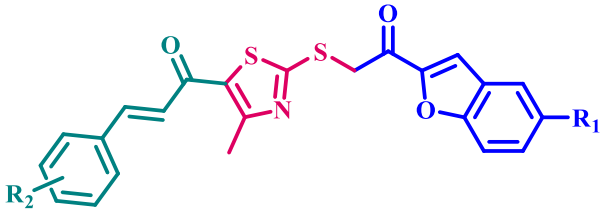
Scheme 1 highlights the schematic pathway employed for synthesizing the target compounds **11a-f** and **12a-f**. The synthesis was initiated with the condensation of 2-hydroxy benzaldehyde derivatives **2a-b** with ethyl acetoacetate in the presence of piperidine, employing ethanol as the solvent. The reaction was performed at 0°C for 24 h to yield 3-acetyl-2*H*-chromen-2-one derivatives **3a-b** (Sahu et al., 1996). Following this, the bromination of **3a-b** was conducted using *N*-bromosuccinimide (NBS) and *p*-toluene sulfonic acid (PTSA) in acetonitrile under reflux for 12 h, resulting in the formation of 3-(2-bromoacetyl)-2*H*-chromen-2-ones **4a-b** (Kakkar et al., 2018).

Similarly, compounds **7a-b** were synthesized by condensing compounds **2a-b** with bromoacetone **five** in ethanolic KOH at 0°C for 4 h to yield compounds **6a-b** (Chidan Kumar et al., 2015), which were then brominated with a mixture of NBS and



11a-f

11a: R_1= H, R_2= H
11b: R_1= Cl, R_2= H
11c: R_1= OCH_3, R_2= H
11d: R_1= H, R_2= Br
11e: R_1= Cl, R_2= Br
11f: R_1= OCH_3, R_2= Br



12a-f

12a: R_1= H, R_2= H
12b: R_1= Cl, R_2= H
12c: R_1= OCH_3, R_2= H
12d: R_1= H, R_2= Br
12e: R_1= Cl, R_2= Br
12f: R_1= OCH_3, R_2= Br

FIGURE 2
Structures of new compounds **11a-f** and **12a-f**.

PTSA to yield the benzofuran derivatives **7a-b** (Kakkar et al., 2018). The synthesis of chalcone intermediates **10a-c** is depicted in Scheme 1, commencing with the cyclization of 3-chloropentane-2,4-dione (8) into 1-(2-mercapto-4-methylthiazol-5-yl)ethan-1-one (**9**) *via* reacting with ammonia and carbon disulfide in absolute ethanol (Hashem et al., 2024). The acetyl group of the thiazole ring in **9** then participates in a Claisen-Schmidt condensation reaction with various substituted benzaldehydes in ethanol under basic conditions, yielding chalcone derivatives **10a-c** (Hashem et al., 2024). The thiazole chalcones **10a-c** are subjected to *S*-alkylation with 3-(2-bromoacetyl)-2*H*-chromen-2-ones **4a-b** or benzofuran derivatives **7a-b**, utilizing sodium carbonate and sodium iodide in acetone at room temperature for 6 h. This reaction gives the novel compounds **11a-f** and **12a-f** in substantial yields.

Reagents and conditions: (i) Piperidine, EtOH, 0°C, 24 h; (ii) NBS, PTSA.H_2O, acetonitrile, reflux, 12 h; (iii) KOH, EtOH, 0°C, 4 h; (iv) CS_2, NH_3, ethanol, 20°C, 6 h; (v) appropriate aromatic aldehyde, 60% NaOH, EtOH, 0°C, 18 h; (vi) **4a-b**/**7a-b**, Na_2CO_3, NaI, acetone, r.t., 5 h.

The structures of the target compounds **11a-f** and **12a-f** were confirmed by ^{1}H NMR, ^{13}C NMR, and elemental analysis. The ^{1}H NMR spectra exhibited characteristic peaks, including a singlet for the methylene group at δ 4.92–4.98 ppm, a singlet for the methyl protons at δ 2.55–2.61 ppm, the chalcone moiety displays distinct resonances, with the α-proton at δ 7.32–7.63 ppm and the β-proton at δ 7.48–7.77 ppm. In some cases, these signals were well-defined, whereas in others, they overlapped with aromatic protons. The aromatic protons corresponding to the coumarin, benzofuran, and benzene rings appeared in their expected region of δ 6.5–8.5 ppm, while the characteristic singlet for the C5 proton of the coumarin moiety was observed at a higher chemical shift (8.73–8.81 ppm). The ^{13}C NMR spectra further supported the structural elucidation, revealing distinctive signals for the carbonyl moiety of the chalcone moiety at δ 180–183 ppm, the methylene carbon at δ 38–39 ppm, the methyl carbon at δ 16–19 ppm, and the methoxy carbon at approximately δ 55 ppm.

As a representative example, compound **11f** exhibited well-defined NMR spectral features. In the ^{1}H NMR spectrum, the C5 proton of the coumarin core resonated as a singlet at δ 8.73 ppm, whereas the α-proton of the chalcone moiety appeared at δ 7.63 ppm and the β-proton at δ 7.72 ppm, both as doublets. The methylene (-CH_2-) group was observed as a singlet at δ 4.92 ppm, while the methoxy group exhibited a singlet at δ 3.77 ppm. The methyl group attached to the thiazole ring was also detected as a singlet at δ 2.59 ppm, aligning with its expected chemical shift. The ^{13}C NMR spectrum of **11f** further confirmed its structure, displaying a carbonyl signal for the chalcone moiety at δ 193.48 ppm and another carbonyl signal adjacent to the coumarin ring at δ 182.10 ppm. The methoxy carbon was observed at δ 55.94 ppm, the methylene carbon at δ 38.11 ppm, and the methyl carbon at δ 19.03 ppm. These chemical shifts were entirely consistent with the proposed structure, confirming the successful synthesis of **11a-f** and **12a-f**.

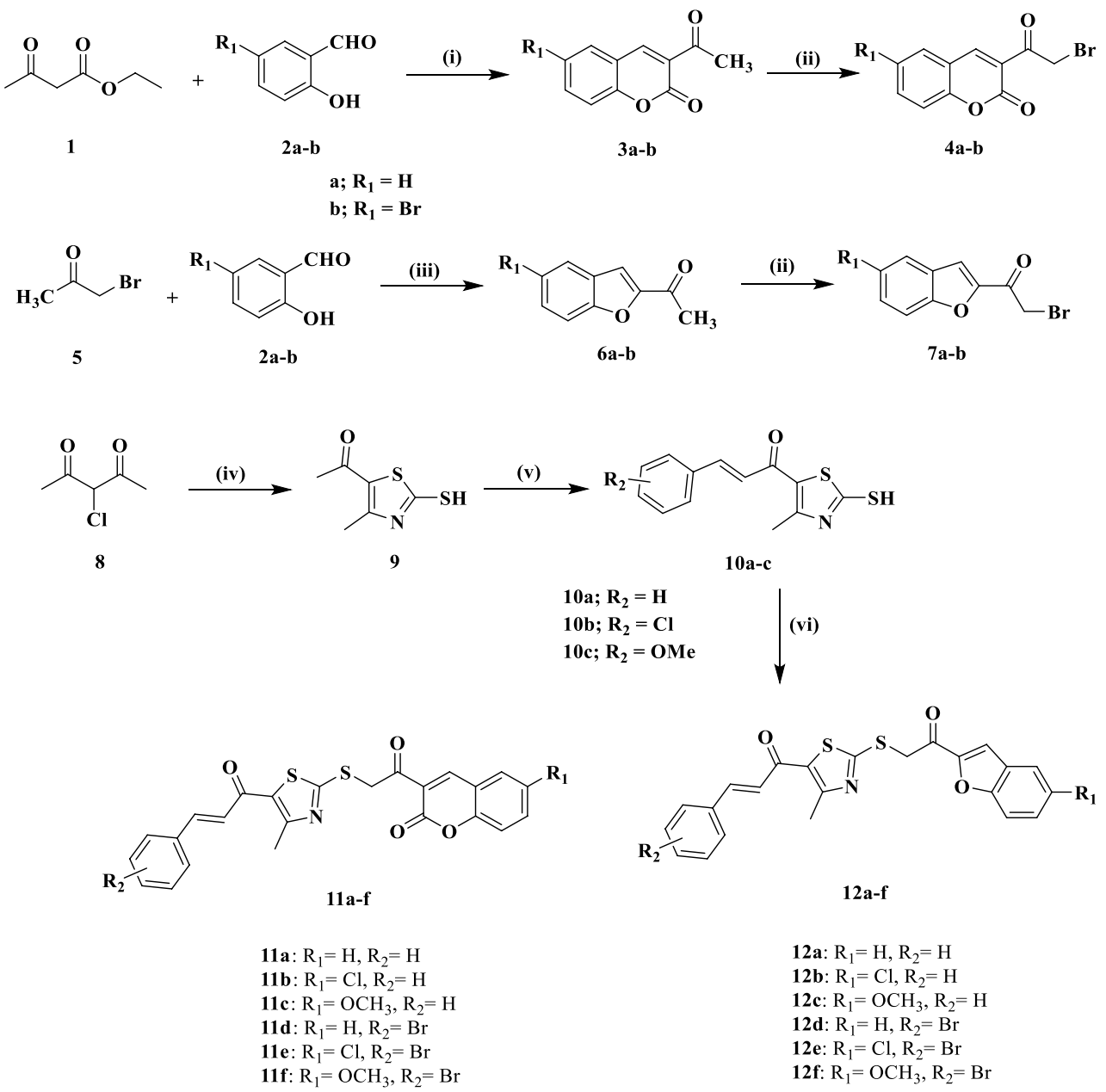
2.2 Biology

2.2.1 Evaluation of cell viability effect

To assess the viability impact of new targets **11a-f** and **12a-f**, the human mammary gland epithelial (MCF-10A) normal cell line was used. The MTT test was applied to assess the cell viability of **11a-f** and **12a-f** following 4 days of incubation with MCF-10A cells (El-Sherief et al., 2019; Ramadan et al., 2020). Table 1 indicates that none of the analyzed compounds exhibited cytotoxicity since all compounds maintained over 90% cell viability at a concentration of 50 μM.

2.2.2 Antiproliferative assay

The MTT assay was employed to assess the antiproliferative effects of targets **11a-f** and **12a-f** on four human cancer cell lines: colon cancer (HT-29), pancreatic cancer (Panc-1), lung cancer (A-549), and breast cancer (MCF-7), with erlotinib serving as a



SCHEME 1
Synthesis of new compounds **11a-f** and **12a-f**.

reference compound (Mahmoud et al., 2023; Alshammari et al., 2022). Table 1 presents each compound's median inhibitory concentration (IC_{50}) and average IC_{50} (GI_{50}) for each compound against the four cancer cell lines.

Results from Table 1 revealed that compounds **11a-f** and **12a-f** exhibited notable antiproliferative efficiency, with GI_{50} values between 27 nM and 71 nM relative to the reference Erlotinib (GI_{50} = 33 nM), and all evaluated compounds demonstrated greater sensitivity towards the lung cancer (A-549) cell line compared to the other cell lines assessed. Furthermore, coumarin-based compounds (**11a-f**) exhibit greater reactivity than benzofuran counterparts (**12a-f**). Compounds **11a**, **11d**, **11e**, **11f**, **12c**, and **12d** exhibited the most potent antiproliferative activity, with GI_{50} values of 44, 30, 41, 27, 36, and 48 nM, respectively, rendering compounds **11d** and **11f** more potent than erlotinib (GI_{50} = 33 nM).

Compound **11f** (R_1 = 4-OMe, R_2 = Br, coumarin-based) had the highest efficacy among all synthesized derivatives, demonstrating a GI_{50} value of 27 nM, which is 1.2-fold more active than erlotinib (GI_{50} = 33 nM) against the four tested cancer cell lines.

Compound **11f** exhibited more potency than erlotinib against the four evaluated cancer cell lines. It demonstrated optimal efficacy against lung cancer (A-549) and breast cancer (MCF-7) cell lines. Compound **11f** exhibited IC_{50} values of 25 nM for A-549 and 29 nM for MCF-7, demonstrating 1.2- and 1.4-fold more potency than erlotinib (IC_{50} values = 30 and 40 nM, respectively).

TABLE 1 Cell viability assay and IC_{50} values of compounds 11a-f and 12a-f against four cancer cell lines.

Comp	Cell viability %	Antiproliferative activity IC_{50} ± SEM (nM)				
		A-549	MCF-7	Panc-1	HT-29	Average (GI_{50})
11a	91	40 ± 2	48 ± 3	44 ± 3	44 ± 3	44
11b	92	69 ± 6	74 ± 6	70 ± 6	72 ± 6	71
11c	90	52 ± 4	56 ± 4	54 ± 4	57 ± 4	55
11d	95	28 ± 1	31 ± 1	30 ± 1	30 ± 1	30
11e	91	37 ± 2	43 ± 2	40 ± 2	42 ± 2	41
11f	93	25 ± 1	29 ± 1	26 ± 1	28 ± 1	27
12a	93	65 ± 5	70 ± 5	66 ± 5	66 ± 5	67
12b	90	61 ± 5	68 ± 5	64 ± 5	65 ± 5	65
12c	91	33 ± 2	39 ± 2	36 ± 2	37 ± 2	36
12d	90	45 ± 3	50 ± 3	48 ± 3	48 ± 3	48
12e	94	60 ± 5	64 ± 5	62 ± 5	62 ± 5	62
12f	92	55 ± 4	59 ± 4	56 ± 4	56 ± 4	57
Erlotinib	ND	30 ± 3	40 ± 3	30 ± 3	30 ± 3	33

The substitution pattern at the fourth position of the phenyl group in the chalcone moiety (R_1), along with the type of substitution in the phenyl groups of the coumarin or benzofuran moieties (R_2), significantly influences the antiproliferative activity of compounds **11a-f** and **12a-f**. For example, compounds **11d** (R_1 = H, R_2 = Br, coumarin-based) and **11e** (R_1 = Cl, R_2 = Br, coumarin-based), which share identical structural characteristics with compound **11f** but possess different R_1 substituents, exhibited diminished antiproliferative activity. Compounds **11d** and **11e** had GI_{50} values of 30 and 41 nM, respectively, which are 1.1- and 1.5-fold lower than compound **11f**. The data reveal that the electron-donating group (OMe) is more tolerant of activity than the electron-withdrawing group, with the order of activity (R_1) being OMe > H > Cl.

Compound **11c** (R_1 = 4-OMe, R_2 = H, coumarin-based), which features an unsubstituted coumarin ring, demonstrated a marked decrease in antiproliferative efficacy. Compound **11c** showed a GI_{50} value of 55 nM, demonstrating a twofold inferior potency to that of compound **11f**. This result demonstrates the importance of the bromine atom in the coumarin moiety for antiproliferative action. Moreover, compound **12f** (R_1 = 4-OMe, R_2 = Br, benzofuran-based), which shares the same structure as **11f** but incorporates a benzofuran moiety in place of coumarin, exhibited a significant reduction in antiproliferative efficacy. Compound **12f** exhibited a GI_{50} value of 57 nM, indicating it is 2.1-fold less effective than compound **11f**, illustrating that the coumarin moiety is superior for antiproliferative activity than the benzofuran moiety.

A similar principle can be used to compare compounds **11d** (R_1 = H, R_2 = Br, coumarin-derived) and **11e** (R_1 = Cl, R_2 = Br, coumarin-derived), both of which are coumarin derivatives, to compounds **12d** (R_1 = H, R_2 = Br, benzofuran-derived) and **12e** (R_1 = Cl, R_2 = Br, benzofuran-derived), both of which are benzofuran derivatives. Compound **12d** showed a GI_{50} value of 48 nM, which was 1.6-fold less effective than the coumarin-based derivative **11d** (GI_{50} = 30 nM), while compound **12e** demonstrated a GI_{50} value of 62 nM, which was 1.5-fold less efficient than its coumarin counterpart, derivative **11e** (GI_{50} = 41 nM).

2.2.3 Evaluation of EGFR inhibitory activity

The most effective antiproliferative compounds, **11a**, **11d**, **11e**, **11f**, and **12c**, were evaluated for their capacity to inhibit EGFR utilizing the EGFR-TK assay (Al-Wahaibi et al., 2022). The findings are presented in Table 2.

The results of this assay correspond with the antiproliferative assay findings, indicating that compounds **11d** (R_1 = H, R_2 = Br, coumarin-based) and **11f** (R_1 = OMe, R_2 = Br, coumarin-based) are the most effective derivatives of EGFR inhibitors, exhibiting IC_{50} values of 76 ± 3 and 71 ± 3 nM, respectively, surpassing the potency of the reference drug Erlotinib (IC_{50} = 80 ± 5 nM). Compounds **11d** and **11f** were the most effective derivatives exhibiting antiproliferative effects. Compounds **11e** (R_1 = Cl, R_2 = Br, coumarin-based) and **12c** (R_1 = OMe, R_2 = H, benzofuran-based) exhibited significant anti-EGFR activity, with IC_{50} values of 89 ± 3 nM and 83 ± 3 nM, respectively. In contrast compound **11a** showed the lowest potency as an EGFR inhibitor, with an IC_{50} value of 93 ± 4 nM, compared to Erlotinib (IC_{50} = 80 nM). The results indicate that compounds **11d** and **11f** have significant antiproliferative activity and may serve as EGFR inhibitors.

2.2.4 Evaluation of VEGFR-2 inhibitory action

Compounds **11a**, **11d**, **11e**, **11f**, and **12c** were evaluated for their capacity to inhibit VEGFR-2, with Sorafenib serving as the control agent (Al-Wahaibi et al., 2024a). The results are displayed as IC_{50} values in Table 2. The findings indicated that the examined compounds had moderate to good VEGFR-2 inhibitory activity, with IC_{50} values between 2.90 and 5.20 μM, compared to Sorafenib,

TABLE 2 IC_{50} values of compounds 11a, 11d, 11e, 11f, and 12c against EGFR and VEGFR-2.

Compound	EGFR inhibition $IC_{50} \pm$ SEM (nM)	VEGFR-2 inhibition $IC_{50} \pm$ SEM (μM)
11a	93.00 ± 4	5.20 ± 0.030
11d	76.00 ± 3	3.60 ± 0.020
11e	89.00 ± 4	4.90 ± 0.030
11f	71.00 ± 3	2.90 ± 0.010
12c	83.00 ± 3	4.05 ± 0.020
Erlotinib	80.00 ± 5	--
Sorafenib	--	0.17 ± 0.001

which had an IC_{50} value of 0.17 μM. In all cases, the evaluated compounds exhibit a potency 17-fold inferior to the reference Sorafenib. Compound **11f** (R_1 = OMe, R_2 = Br, coumarin-based), the most effective antiproliferative and EGFR inhibitor, also exhibited the highest potency as a VEGFR-2 inhibitor, with an IC_{50} value of 2.90 ± 0.010 μM. Based on the *in vitro* experiments, we infer that compound **11f** exhibits significant antiproliferative activity and functions as a dual inhibitor of EGFR and VEGFR-2, necessitating structural modifications to enhance its efficacy.

2.3 Evaluation of antioxidant activity

Antioxidant agents have become essential in medicine due to their extensive preventative and therapeutic usage across many diseases. Free radicals are integral to cancer, cardiovascular diseases, autoimmune illnesses, and age-related issues, prompting novel medical strategies (Goyal et al., 2025). The scavenging of stable free radicals by DPPH (2,2-diphenyl-1-picrylhydrazyl) (El-Sheref et al., 2023) was employed to assess the possible antioxidant capabilities of compounds **11d**, **11f**, and **12c**, with Trolox serving as a reference, Table 3. The assay was performed at three distinct concentrations of the examined compounds (100, 50, and 10 μM).

Compounds **11d** and **11f**, derivatives of coumarin, had substantial antioxidant activity at 10 μM, scavenging DPPH radicals by 71% and 73%, respectively, compared to Trolox (78%). Moreover, compounds **11d** and **11f** exhibited comparable radical scavenging activity to Trolox at concentrations of 100 and 50 μM, respectively (Table 3). Conversely, compound 9, a benzofuran derivative, was identified as the least active derivative regarding antioxidant activity, underscoring the significance of the coumarin moiety for such action. The results suggested that compounds **11d** and **11f** may be considered effective antiproliferative agents with antioxidant properties.

TABLE 3 Antioxidant activity of compounds 11d, 11f, and 12c.

Antioxidant (DPPH radical scavenging activity %)			
Comp	100 μM	50 μM	10 μM
11d	92	80	71
11f	94	82	73
12c	85	73	66
Trolox	95	83	78

2.4 Evaluation of antimicrobial activity

2.4.1 *E. coli* DNA gyrase inhibitory action

A supercoiling experiment was performed to assess the inhibitory efficacy of compounds **11a-f** and **12a-f** against *E. coli* DNA gyrase (Abdel-Aziz et al., 2023). Results are presented as residual activity (RA) of the enzyme at 1 μM of compounds or IC_{50} values for compounds with RA < 50% as presented in Table 4.

Compounds **11a-f** and **12a-f** show notable inhibitory activity against *E. coli* DNA gyrase, with IC_{50} values ranging from 182 to 208 nM, compared to the reference novobiocin, which has an IC_{50} value of 170 nM. The evaluated compounds exhibited lower potency in all cases than the reference novobiocin. Compounds **11b**, **11e**, and **12b** demonstrated the most significant inhibitory activity against *E. coli* DNA gyrase, with IC_{50} values of 182, 190, and 197 nM, respectively. Compound **11b** (R_1 = Cl, R_2 = H, coumarin-based) exhibited the highest efficacy as a DNA gyrase inhibitor, with an IC_{50} value of 182 nM, which is 1.1-fold less effective than the reference novobiocin, which has an IC_{50} value of 170 nM. Compound **11e** (R_1 = Cl, R_2 = Br, coumarin-based) exhibited the second highest activity as a DNA gyrase inhibitor, with an IC_{50} value of 190 nM, demonstrating equipotency with compound **11b**, so underscoring the significance of halogen atoms in the inhibitory action against DNA gyrase.

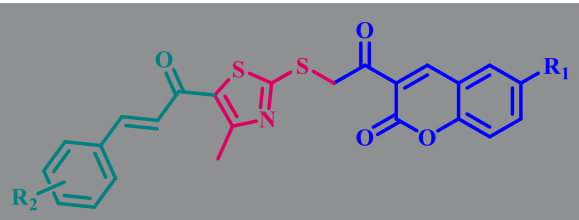
Compound **12b**, a benzofuran-based derivative (R_1 = Cl, R_2 = H), possesses identical structural characteristics to compound **11b**, but includes a benzofuran moiety instead of a coumarin moiety. It exhibits an IC_{50} value of 197 nM, indicating reduced potency compared to compound **11b** (IC_{50} = 182 nM). The data reaffirmed the significance of the coumarin moiety in the efficacy of these compounds as antiproliferative and antibacterial agents. Compounds **12e** and **12f**, both benzofuran derivatives, exhibited significant inhibitory activity against DNA gyrase, with IC_{50} values of 217 and 208 nM, respectively, approximately 1.2-fold less effective than compound **11b**.

2.4.2 Antibacterial activity

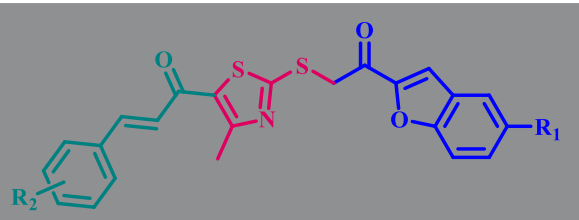
The antibacterial efficacy of compounds **11b**, **11e**, and **12b** was evaluated against Gram-positive bacteria (*S. aureus* and *B. subtilis*) and Gram-negative bacteria (*E. coli* and *P. aeruginosa*). Table 5 presents the MICs (nM) of these compounds against the evaluated bacteria, utilizing ciprofloxacin as the reference drug, determined through a twofold serial dilution approach on a 96-well microtiter plate (Frejat F. O. et al., 2022).

Compound **11b** (R_1 = Cl, R_2 = H, coumarin-based) had the highest potency among the compounds evaluated, with MIC values of 23, 42, and 45 nM against *S. aureus*, *E. coli*, and *P. aeruginosa*, respectively. It exhibited superior efficacy to ciprofloxacin against the examined species but had a MIC value of 18 nM against *B. subtilis*, which is 1.8-fold less efficient than ciprofloxacin

TABLE 4 IC_{50} values of compounds 11a-f and 12a-f against *E. Coli* DNA gyrase.



11a-f



12a-f

Compound	R_1	R_2	IC_{50} (nM) or RA (%)
			E. Coli DNA gyrase
11a	H	H	72%
11b	Cl	H	182 ± 13
11c	OMe	H	68%
11d	H	Br	54%
11e	Cl	Br	190 ± 13
11f	OMe	Br	71%
12a	H	H	61%
12b	Cl	H	197 ± 12
12c	OMe	H	59%
12d	H	Br	65%
12e	Cl	Br	217 ± 15
12f	OMe	Br	208 ± 15
Novobiocin	----	----	170 ± 11 nM

10.3389/fchem.2025.1595997

TABLE 5 MIC values of compounds 11b, 11e, and 12b against four bacterial species.

Minimum inhibitory concentration (MIC) in nM				
Compound	Bacterial species			
	(G^+)		(G^-)	
	B. subtilis	*S. aureus*	*E. coli*	*P. aeruginosa*
11b	18 ± 1	23 ± 1	42 ± 3	45 ± 3
11e	22 ± 1	27 ± 1	48 ± 3	53 ± 3
12b	29 ± 1	34 ± 2	62 ± 4	64 ± 4
Ciprofloxacin	10 ± 1	30 ± 2	60 ± 4	60 ± 4

(MIC = 10 nM). Compound **11e** (R_1 = Cl, R_2 = Br, coumarin-based) demonstrated the second highest efficacy. The MIC values were similar to those of compound **11b** against *S. aureus* and *E. coli*, as shown in Table 5. Nonetheless, it was 2.2 times less efficacious than ciprofloxacin against *B. subtilis*. Ultimately, the benzofuran-based derivative, compound **12b** (R_1 = Cl, R_2 = H), exhibited the lowest potency among the derivatives, demonstrating MIC values inferior to those of ciprofloxacin against all tested species. The observations indicate that compounds **11b** and **11e** are effective antibacterial agents with a broad spectrum of activity against Gram-positive and Gram-negative species, potentially functioning as DNA gyrase inhibitors.

2.5 Molecular docking

The molecular docking studies were conducted to rationalize the *in vitro* potency of the most active compound (**11f**) against three distinct biological targets: EGFR, VEGFR-2, and *E. coli* DNA gyrase. Docking was performed using Auto-Dock Vina (Sharma et al., 2025), and the docking poses were visualized and analyzed with Discovery Studio Visualizer (Rustagi et al., 2025). Initially, docking protocols were validated by redocking the cocrystallized ligands into the corresponding protein active sites to ensure accuracy and reliability. For EGFR, the crystal structure with PDB code 5D41 (Bhanja and Patra, 2025) was utilized. Redocking of the native ligand, EAI001, yielded a binding affinity of −9.3 kcal/mol and an RMSD of 1.1 Å, confirming the validity of the docking conditions. The superimposition between the redocked and cocrystallized ligand is depicted in Figure 3.

Subsequently, docking of compound **11f** into the allosteric site of EGFR, previously identified as the binding pocket for EAI001, demonstrated a binding affinity of −8.5 kcal/mol. Detailed interaction analysis revealed that the coumarin ring of **11f** engaged in significant hydrophobic interactions with Leu718, Leu844, and Ala743. Additionally, the thiazole moiety formed hydrophobic contacts with Ala743 and Lys745, alongside a pi-sulfur interaction with Met790 and a sulfur-X interaction with Asp855. The benzene ring of **11f** further stabilized the binding through hydrophobic interactions with Met766, Leu858, and Leu788. Notably, the methoxy group appeared to contribute to the compound's enhanced potency by participating in hydrophobic interactions with Leu747, Ile759, and Leu788, potentially improving binding affinity compared to other derivatives. A summary of these interactions is presented in Figure 4.

For VEGFR-2, docking was conducted using the crystal structure with PDB code 3U6J (Reang et al., 2023), which represents the ATP-binding site of the kinase. Validation through redocking of the cocrystallized ligand yielded a binding affinity of −7.2 kcal/mol and an RMSD of 0.512 Å, confirming the accuracy of the docking protocol. The superimposition of the redocked and cocrystallized ligand is also shown in Figure 3. Docking of compound **11f** into VEGFR-2 produced a binding affinity of −8.9 kcal/mol, with several notable interactions observed, as presented in Figure 5. The coumarin moiety of **11f** exhibited

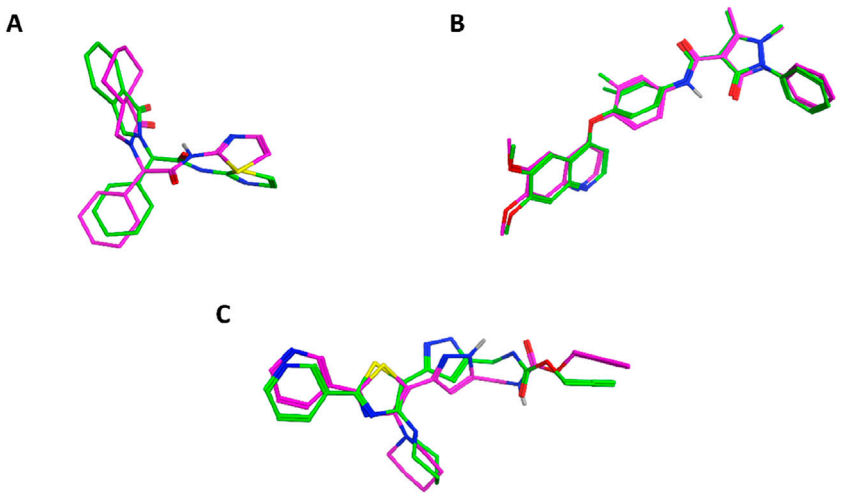


FIGURE 3
Superimposition of redocked (magenta) and cocrystallized (green) ligands in the active sites of **(A)** EGFR (5D41), **(B)** VEGFR-2 (3U6J), and **(C)** *E. coli* DNA gyrase (3G7E).

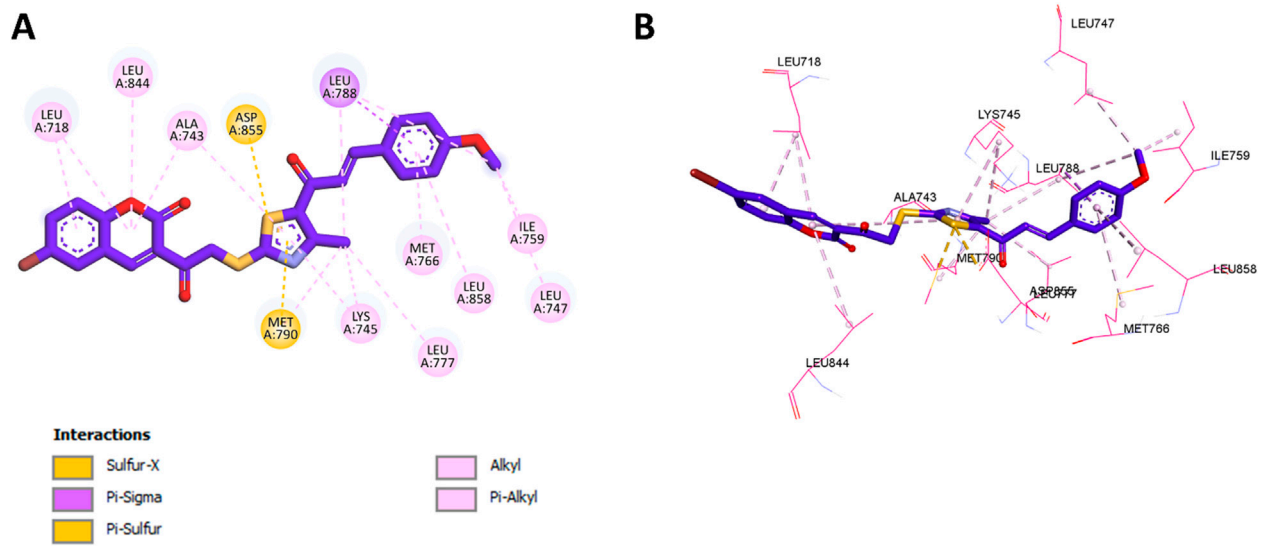


FIGURE 4
(A) 2D interaction diagram and **(B)** 3D binding mode of **11f** within the allosteric site of EGFR.

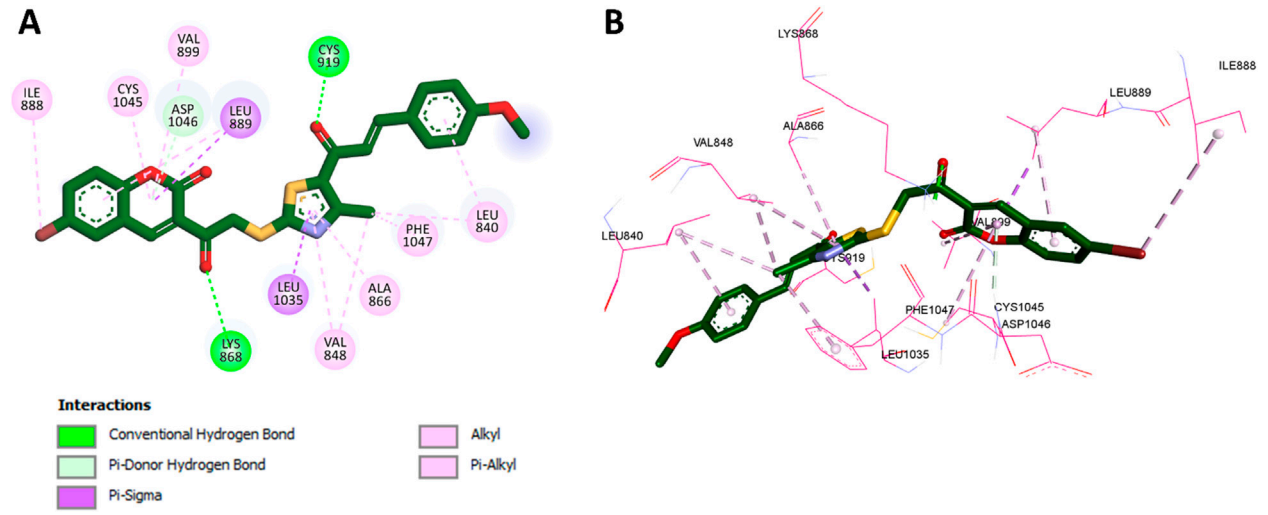


FIGURE 5
(A) 2D interaction diagram and **(B)** 3D binding mode of **11f** within the VEGFR-2 ATP-binding site.

hydrophobic interactions with Leu889, Val899, and Cys1045 and formed a pi-donor hydrogen bond with Asp1046. Additionally, the bromine substituent on the coumarin ring engaged in hydrophobic interaction with Ile888. The carbonyl groups of **11f** formed classical hydrogen bonds with key residues Cys919 and Lys868, further stabilizing the complex. Moreover, the thiazole ring contributed to the binding through hydrophobic interactions with Leu1035, Val848, Ala866, Phe1047, and Leu840.

For *E. coli* DNA gyrase, docking studies were performed using the crystal structure with PDB code 3G7E (Sofi et al., 2025), which represents the ATP-binding site of the GyrB subunit. Redocking of the native ligand resulted in a binding affinity of −6.7 kcal/mol and an RMSD of 1.126 Å, confirming the suitability of the docking settings. The superimposition of the redocked and cocrystallized ligand is included in Figure 3. Docking of compound **11b**, which exhibited the highest *in vitro* potency against DNA gyrase, resulted in a binding affinity of −9.3 kcal/mol. The coumarin moiety of **11b** was found to establish extensive hydrophobic interactions with Val120, Val43, Ile78, Val167, Leu132, and Ala47, along with a pi-sulfur interaction with Met95. The thiazole ring of **11b** further contributed hydrophobic interactions with Ile78 and Pro79. Notably, the sulfur atom adjacent to the thiazole moiety formed a classical hydrogen bond with Gly77. In addition, both the phenyl ring and the chlorine substituent in **11b** engaged in hydrophobic

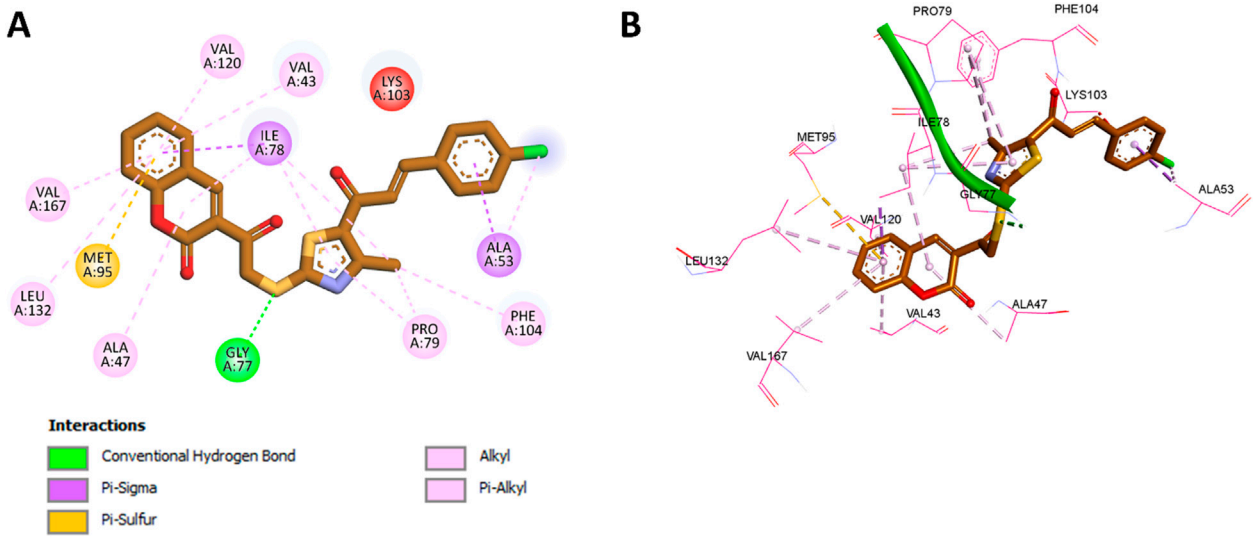


FIGURE 6
(A) 2D interaction diagram and **(B)** 3D binding mode of **11b** within the ATP-binding site of the GyrB subunit.

interactions with Ala53. A comprehensive summary of these interactions is depicted in Figure 6.

3 Conclusion

In this study, we designed, synthesized, and biologically evaluated a novel series of thiazole-based derivatives (**11a-f** and **12a-f**) as multi-targeted inhibitors with potent antiproliferative, antioxidant, and antibacterial activities. Compounds **11d** and **11f** exhibited the strongest antiproliferative effects (GI_{50} = 30 and 27 nM, respectively), surpassing Erlotinib, through dual EGFR/VEGFR-2 inhibition. Structure-activity relationship analysis highlighted the critical role of the coumarin moiety and electron-donating substituents in enhancing activity. Additionally, **11d** and **11f** demonstrated robust antioxidant potential. This dual antiproliferative and antioxidant profile is particularly valuable, as oxidative stress plays a significant role in cancer pathogenesis and progression. Furthermore, **11b**, **11e**, and **12b** exhibited potent antibacterial activity, inhibiting *E. coli* DNA gyrase and displaying broad-spectrum efficacy. The multi-target profile of these derivatives underscores their potential as versatile therapeutic agents against cancer and bacterial infections. Further studies are required to assess their *in vivo* efficacy, pharmacokinetics, and toxicity. Future research will focus on optimizing VEGFR-2 inhibition while retaining the compounds' anticancer, antioxidant, and antibacterial properties.

In summary, these thiazole-based derivatives represent a promising class of multi-targeted inhibitors with significant potential for the development of new therapeutic agents addressing both cancer and bacterial infections, two major global health challenges. The dual EGFR/VEGFR-2 inhibition mechanism, coupled with antioxidant and antibacterial properties, positions these compounds as versatile candidates for further development in medicinal chemistry and drug discovery pipelines.

4 Experimental

4.1 Chemistry

General Details: Refer to Appendix A.

4.1.1 General procedure for the synthesis of target compounds (11a-f) and (12a-f)

A mixture of thiazole chalcones **10a-c** (1 mmol) and the corresponding coumarins **4a-b** or benzofurans **7a-b** (1 mmol) in acetone containing sodium carbonate (1.5 mmol, 0.159 g) and sodium iodide (2 mmol, 0.3 g) was stirred at room temperature for 5 h. After the reaction was complete, the mixture was refrigerated overnight. The precipitate was filtered, washed with distilled water, and recrystallized using ethanol.

4.1.1.1 (*E*)-3-(2-((5-Cinnamoyl-4-methylthiazol-2-yl)thio) acetyl)-2*H*-chromen-2-one (11a)

Yellow powder; 0.312 g, 70% yield; m.p. 215°C–217°C; ^{1}H NMR (500 MHz, DMSO-d_6) δ 8.81 (s, 1H, coumarin-C_4-H), 8.02–7.98 (m, 2H, Ar-H), 7.76 (d, J = 15.3 Hz, 1H, chalcone-β C=H), 7.66–7.58 (m, 5H, Ar-H & chalcone-α C=H), 7.39–7.31 (m, 3H, Ar-H), 4.95 (s, 2H, CH_2), 2.60 (s, 3H, CH_3); ^{13}C NMR (100 MHz, DMSO-d_6) δ 190.33, 181.78, 166.60, 164.28, 159.32, 155.06, 145.08, 138.06, 137.05, 134.06, 132.07, 130.84, 130.09, 126.06, 125.11, 124.38, 122.83, 120.13, 119.32, 116.85, 38.45, 18.81. Anal. Calc. (%) for $C_{24}H_{17}NO_4S_2$: C, 64.41; H, 3.83; N, 3.13. Found: C, 64.33; H, 3.87; N, 3.17.

4.1.1.2 (*E*)-3-(2-((5-(3-(4-Chlorophenyl)acryloyl)-4-methylthiazol-2-yl)thio)acetyl)-2*H*-chromen-2-one (11b)

Yellow powder; 0.366 g, 76% yield; m.p. 222°C–223°C; ^{1}H NMR (500 MHz, DMSO-d_6) δ 8.81 (s, 1H, coumarin-C_4-H), 8.02–7.97 (m, 2H, Ar-H), 7.72 (d, J = 15.4 Hz, 1H, chalcone-β C=H), 7.66–7.59 (m, 3H, Ar-H & chalcone-α C=H), 7.54 (d, J = 8.2 Hz, 2H, Ar-H), 7.43 (d, J = 8.4 Hz, 2H, Ar-H), 4.95 (s, 2H, CH_2), 2.61 (s, 3H, CH_3); ^{13}C

NMR (100 MHz, DMSO-d_6) δ 191.02, 180.88, 166.56, 163.87, 157.18, 153.19, 147.11, 141.15, 137.16, 133.47, 131.68, 130.30, 129.04, 126.04, 125.33, 124.62, 121.89, 120.85, 119.44, 116.97, 38.68, 19.25. Anal. Calc. (%) for $C_{24}H_{16}ClNO_4S_2$: C, 59.81; H, 3.35; N, 2.91. Found: C, 59.74; H, 3.39; N, 2.84.

4.1.1.3 (*E*)-3-(2-((5-(3-(4-Methoxyphenyl)acryloyl)-4-methylthiazol-2-yl)thio) acetyl)-2*H*-chromen-2-one (11c)

Yellow powder; 0.329 g, 69% yield; m.p. 229°C–231°C; ^{1}H NMR (500 MHz, DMSO-d_6) δ 8.80 (s, 1H, coumarin-C_4-H), 8.01–7.98 (m, 2H, Ar-H), 7.72 (d, *J* = 15.3 Hz, 1H, chalcone-β C=H), 7.66–7.62 (m, 2H, Ar-H & chalcone-α C=H), 7.61–7.59 (m, 2H, Ar-H), 7.58 (s, 1H, Ar-H), 6.92 (d, *J* = 8.4 Hz, 2H, Ar-H), 4.94 (s, 2H, CH_2), 3.79 (s, 3H, OCH_3), 2.58 (s, 3H, thiazole-CH_3); ^{13}C NMR (100 MHz, DMSO-d_6) δ 192.16, 180.16, 166.18, 160.61, 156.76, 153.26, 150.68, 143.56, 138.33, 137.03, 134.17, 131.25, 130.55, 127.31, 125.69, 124.07, 123.11, 122.19, 119.22, 118.58, 55.92, 38.43, 19.02. Anal. Calc. (%) for $C_{25}H_{19}NO_5S_2$: C, 62.88; H, 4.01; N, 2.93. Found: C, 62.76; H, 4.13; N, 3.87.

4.1.1.4 (*E*)-6-Bromo-3-(2-((5-cinnamoyl-4-methylthiazol-2-yl)thio)acetyl)-2*H*-chromen-2-one (11d)

Yellow powder; 0.405 g, 77% yield; m.p. 255°C–257°C; ^{1}H NMR (500 MHz, DMSO-d_6) δ 8.73 (s, 1H, coumarin-C_4-H), 8.22 (s, 1H, Ar-H), 7.97 (d, *J* = 8.9 Hz, 1H, Ar-H), 7.77–7.74 (m, 2H, Ar-H & chalcone-βC = H), 7.63 (d, *J* = 15.4 Hz, 1H, chalcone-αC = H), 7.59 (dd, *J* = 6.9, 2.4 Hz, 2H, Ar-H), 7.39–7.31 (m, 3H, Ar-H), 4.93 (s, 2H, CH_2), 2.59 (s, 3H, CH_3); ^{13}C NMR (100 MHz, DMSO-d_6) δ 190.55, 180.84, 169.14, 164.58, 158.37, 151.95, 145.48, 144.16, 140.91, 140.33, 137.05, 134.46, 132.17, 129.87, 129.29, 128.27, 124.76, 120.54, 119.24, 116.94, 37.18, 18.73. Anal. Calc. (%) for $C_{24}H_{16}BrNO_4S_2$: C, 54.67; H, 3.06; N, 2.66. Found: C, 54.58; H, 3.15; N, 2.57.

4.1.1.5 (*E*)-6-Bromo-3-(2-((5-(3-(4-chlorophenyl)acryloyl)-4-methylthiazol-2-yl)thio)acetyl)-2*H*-chromen-2-one (11e)

Yellow powder; 0.398 g, 71% yield; m.p. 236°C–237°C; ^{1}H NMR (500 MHz, DMSO-d_6) δ 8.73 (s, 1H, coumarin-C_4-H), 8.22 (d, *J* = 2.3 Hz, 1H, Ar-H), 7.90 (dd, *J* = 8.9, 2.4 Hz, 1H, Ar-H), 7.80 (d, *J* = 8.5 Hz, 2H, Ar-H), 7.62 (d, *J* = 15.5 Hz, 1H, chalcone-β C=H), 7.47 (dd, *J* = 8.7, 2.5 Hz, 3H, Ar-H), 7.34 (d, *J* = 15.5 Hz, 1H, chalcone-α C=H), 4.93 (s, 2H, CH_2), 2.59 (s, 3H, CH_3); ^{13}C NMR (100 MHz, DMSO-d_6) δ 190.57, 181.22, 171.59, 160.41, 155.56, 148.87, 144.02, 138.80, 135.91, 134.31, 132.84, 132.10, 131.13, 130.19, 128.72, 124.24, 121.66, 118.65, 117.19, 113.43, 37.84, 18.14. Anal. Calc. (%) for $C_{24}H_{15}BrClNO_4S_2$: C, 51.40; H, 2.70; N, 2.50. Found: C, 51.28; H, 2.76; N, 2.44.

4.1.1.6 (*E*)-6-Bromo-3-(2-((5-(3-(4-methoxyphenyl) acryloyl)-4-methylthiazol-2-yl)thio)acetyl)-2*H*-chromen-2-one (11f)

Yellow powder; 0.456 g, 82% yield; m.p. 232°C–235°C; ^{1}H NMR (500 MHz, DMSO-d_6) δ 8.73 (s, 1H, coumarin-C_4-H), 8.10 (d, *J* = 2.4 Hz, 1H, Ar-H), 7.97 (d, *J* = 8.9 Hz, 1H, Ar-H), 7.75 (dd, *J* = 8.9, 2.5 Hz, 1H, Ar-H), 7.72 (d, *J* = 15.3 Hz, 1H, chalcone-β C=H), 7.63 (d, *J* = 15.4 Hz, 1H, chalcone-α C=H), 7.58 (d, *J* = 8.0 Hz, 2H, Ar-H), 6.93 (d, *J* = 8.7 Hz, 2H, Ar-H), 4.92 (s, 2H, CH_2), 3.77 (s, 3H, OCH_3), 2.59 (s, 3H, thiazole-CH_3); ^{13}C NMR (100 MHz, DMSO-d_6) δ 193.48, 182.10, 166.58, 159.74, 152.98, 144.81, 143.56, 139.65, 139.26, 136.44, 135.40, 132.16, 130.56, 129.58, 127.68, 125.70, 124.10, 122.17, 119.90, 114.66, 55.94, 38.11, 19.03. Anal. Calc. (%) for $C_{25}H_{18}BrNO_4S_2$: C, 53.96; H, 3.26; N, 2.52. Found: C, 53.84; H, 3.37; N, 2.57.

4.1.1.7 (*E*)-1-(2-((2-(Benzofuran-2-yl)-2-oxoethyl)thio)-4-methylthiazol-5-yl)-3-phenylprop-2-en-1-one (12a)

Yellow powder; 0.281 g, 67% yield; m.p. 219°C–221°C; ^{1}H NMR (500 MHz, DMSO-d_6) δ 8.12 (s, 1H, Ar-H), 7.73 (d, *J* = 15.3 Hz, 1H, chalcone-β C=H), 7.68 (d, *J* = 8.0 Hz, 1H, Ar-H), 7.62 (d, *J* = 8.4 Hz, 2H, Ar-H), 7.53 (d, *J* = 8.0 Hz, 1H, Ar-H), 7.48 (d, *J* = 15.3 Hz, 1H, chalcone-α C=H), 7.48–7.43 (m, 5H, Ar-H), 4.98 (s, 2H, CH_2), 2.55 (s, 3H, CH_3); ^{13}C NMR (100 MHz, DMSO-d_6) δ 183.56, 179.86, 167.21, 162.02, 151.27, 144.53, 142.87, 140.32, 138.59, 136.45, 135.09, 133.22, 130.88, 129.63, 127.97, 126.08, 124.40, 119.92, 118.90, 38.49, 16.74. Anal. Calc. (%) for $C_{23}H_{17}NO_3S_2$: C, 65.58; H, 4.08; N, 3.34. Found: C, 65.66; H, 4.02; N, 3.29.

4.1.1.8 (*E*)-1-(2-((2-(Benzofuran-2-yl)-2-oxoethyl)thio)-4-methylthiazol-5-yl)-3-(4-chlorophenyl)prop-2-en-1-one (12b)

Yellow powder; 0.349 g, 77% yield; m.p. 215°C–216°C; ^{1}H NMR (500 MHz, DMSO-d_6) δ 8.11 (s, 1H, Ar-H), 7.85 (d, *J* = 7.8 Hz, 1H, Ar-H), 7.78 (d, *J* = 8.6 Hz, 2H, Ar-H), 7.72 (d, *J* = 8.4 Hz, 1H, Ar-H), 7.61 (d, *J* = 15.5 Hz, 1H, chalcone-β C=H), 7.54 (t, *J* = 7.2 Hz, 1H, Ar-H), 7.46 (d, *J* = 8.5 Hz, 2H, Ar-H), 7.36 (t, *J* = 7.2 Hz, 1H, Ar-H), 7.32 (d, *J* = 15.5 Hz, 1H, chalcone-α C=H), 4.97 (s, 2H, CH_2), 2.54 (s, 3H, CH_3); ^{13}C NMR (100 MHz, DMSO-d_6) δ 183.41, 181.80, 168.48, 158.39, 156.21, 150.98, 142.51, 136.05, 133.48, 132.49, 131.18, 129.55, 127.29, 125.37, 124.75, 123.78, 117.27, 115.62, 112.76, 37.84, 18.73. Anal. Calc. (%) for $C_{23}H_{16}ClNO_3S_2$: C, 60.85; H, 3.55; N, 3.09. Found: C, 60.94; H, 3.67; N, 3.13.

4.1.1.9 (*E*)-1-(2-((2-(Benzofuran-2-yl)-2-oxoethyl)thio)-4-methylthiazol-5-yl)-3-(4-methoxyphenyl)prop-2-en-1-one (12c)

Yellow powder; 0.386 g, 86% yield; m.p. 227°C–229°C; ^{1}H NMR (500 MHz, DMSO-d_6) δ 8.11 (s, 1H, Ar-H), 7.71 (d, *J* = 9.7 Hz, 1H, Ar-H), 7.59 (d, *J* = 8.6 Hz, 2H, Ar-H), 7.52 (d, *J* = 7.8 Hz, 1H, Ar-H), 7.48 (d, *J* = 15.9 Hz, 1H, chalcone-β C=H), 7.44–7.38 (m, 2H, Ar-H & chalcone-α C=H), 7.30–7.25 (m, 1H, Ar-H), 6.93 (d, *J* = 8.7 Hz, 2H, Ar-H), 4.96 (s, 2H, CH_2), 3.76 (s, 3H, OCH_3), 2.54 (s, 3H, thiazole-CH_3); ^{13}C NMR (100 MHz, DMSO-d_6) δ 184.09, 181.77, 169.79, 165.26, 158.74, 154.58, 152.29, 151.26, 142.90, 142.21, 137.02, 130.53, 129.51, 127.97, 124.08, 123.41, 119.47, 114.68, 112.75, 55.92, 37.55, 16.45. Anal. Calc. (%) for $C_{24}H_{19}NO_4S_2$: C, 64.12; H, 4.26; N, 3.12. Found: C, 64.19; H, 4.33; N, 3.04.

4.1.1.10 (*E*)-1-(2-((2-(5-Bromobenzofuran-2-yl)-2-oxoethyl)thio)-4-methylthiazol-5-yl)-3-phenylprop-2-en-1-one (12d)

Yellow powder; 0.438 g, 88% yield; m.p. 245°C–246°C; ^{1}H NMR (500 MHz, DMSO-d_6) δ 7.94 (t, *J* = 2.0 Hz, 1H, Ar-H), 7.84 (d, *J* = 2.1 Hz, 1H, Ar-H), 7.72 (d, *J* = 15.9 Hz, 1H, chalcone-β C=H), 7.60–7.54 (m, 4H, Ar-H), 7.47 (d, *J* = 15.9 Hz, 1H, chalcone-α C=H), 7.39–7.31 (m, 3H, Ar-H), 4.97 (s, 2H, CH_2), 2.54 (s, 3H, CH_3); ^{13}C

NMR (100 MHz, DMSO-d_6) δ 183.71, 181.49, 164.94, 163.59, 159.07, 155.83, 154.22, 150.02, 141.96, 138.34, 131.86, 130.26, 128.93, 127.03, 126.06, 119.21, 117.88, 116.64, 112.34, 37.16, 16.72. Anal. Calc. (%) for $C_{23}H_{16}BrNO_3S_2$: C, 55.43; H, 3.24; N, 2.81. Found: C, 55.39; H, 3.27; N, 2.79.

4.1.1.11 (*E*)-1-(2-((2-(5-bromobenzofuran-2-yl)-2-oxoethyl)thio)-4-methylthiazol-5-yl)-3-(4-chlorophenyl) prop-2-en-1-one (12e)

Yellow powder; 0.362 g, 68% yield; m.p. 251°C–252°C; ^{1}H NMR (500 MHz, DMSO-d_6) δ 8.10 (d, J = 1.9 Hz, 1H, Ar-H), 8.05 (s, 1H, Ar-H), 7.79 (d, J = 8.5 Hz, 2H, Ar-H), 7.74 (d, J = 8.9 Hz, 1H, Ar-H), 7.69 (dd, J = 8.9, 2.0 Hz, 1H, Ar-H), 7.62 (d, J = 15.5 Hz, 1H, chalcone-β C=H), 7.47 (d, J = 8.5 Hz, 2H, Ar-H), 7.33 (d, J = 15.5 Hz, 1H, chalcone-α C=H), 4.97 (s, 2H, CH_2), 2.54 (s, 3H, CH_3); ^{13}C NMR (100 MHz, DMSO-d_6) δ 183.09, 179.21, 164.94, 157.79, 155.17, 153.90, 148.03, 143.85, 140.30, 139.32, 138.33, 133.47, 131.85, 127.02, 126.13, 124.75, 123.76, 121.50, 116.94, 37.57, 16.44. Anal. Calc. (%) for $C_{23}H_{15}BrClNO_3S_2$: C, 51.84; H, 2.84; N, 2.63. Found: C, 51.91; H, 2.89; N, 2.59.

4.1.1.12 (*E*)-1-(2-((2-(5-Bromobenzofuran-2-yl)-2-oxoethyl)thio)-4-methylthiazol-5-yl)-3-(4-methoxyphenyl)prop-2-en-1-one (12f)

Yellow powder; 0.417 g, 79% yield; m.p. 238°C–239°C; ^{1}H NMR (500 MHz, DMSO-d_6) δ 7.94 (t, J = 2.4 Hz, 1H, Ar-H), 7.84 (d, J = 2.1 Hz, 1H, Ar-H), 7.58 (d, J = 8.6 Hz, 3H, Ar-H), 7.55 (dd, J = 8.5, 2.1 Hz, 1H, Ar-H), 7.48 (d, J = 15.9 Hz, 1H, chalcone-β C=H), 7.41 (d, J = 15.9 Hz, 1H, chalcone-α C=H), 6.93 (d, J = 8.7 Hz, 2H, Ar-H), 4.96 (s, 2H, CH_2), 3.76 (s, 3H, OCH_3), 2.58 (s, 3H, thiazole-CH_3); ^{13}C NMR (100 MHz, DMSO-d_6) δ 183.71, 181.49, 165.27, 157.82, 156.21, 146.82, 138.04, 136.73, 134.13, 133.17, 130.25, 129.60, 128.26, 127.31, 123.42, 122.18, 119.89, 119.22, 117.25, 55.99, 37.84, 16.14. Anal. Calc. (%) for $C_{24}H_{18}BrNO_4S_2$: C, 54.55; H, 3.43; N, 2.65. Found: C, 54.64; H, 3.40; N, 2.67.

4.2 Biology

4.2.1 Assay for cell viability

The viability effects of **11a-f** and **12a-f** on the human mammary gland epithelial (MCF-10A) normal cell line were evaluated using the MTT test (El-Sherief et al., 2019; Ramadan et al., 2020). Refer to Appendix A for additional information.

4.2.2 Antiproliferative assay

The MTT assay was employed to assess the antiproliferative efficacy of **11a-f** and **12a-f** against four human cancer cell lines, utilizing Erlotinib as a reference control (Mahmoud et al., 2023; Alshammari et al., 2022). Dose-response assays determined the IC_{50} values for the novel compounds. We derived the reported data from a minimum of two separate experiments, each consisting of three repetitions per concentration. Appendix A provides experimental details.

4.2.3 Assay for EGFR inhibitory action

The most effective antiproliferative compounds, **11a**, **11d**, **11e**, **11f**, and **12c**, were evaluated for their capacity to inhibit EGFR utilizing the EGFR-TK assay (Al-Wahaibi et al., 2022). Refer to Appendix A for more details.

4.2.4 Assay for VEGFR-2 inhibitory action

Compounds **11a**, **11d**, **11e**, **11f**, and **12c** were assessed for their ability to inhibit VEGFR-2, using sorafenib as the control agent (Al-Wahaibi et al., 2024a). The outcomes are presented as IC_{50} values. Appendix A outlines more experimental details.

4.2.5 Antioxidant assay

The scavenging of stable free radicals by DPPH (El-Sheref et al., 2023) was employed to assess the antioxidant activities of compounds **11d**, **11f**, and **12c**, with Trolox serving as a reference. The assay was performed at three different concentrations of the examined compounds (100, 50, and 10 μM). Appendix A contains more details.

4.2.6 DNA gyrase inhibitory assay

A supercoiling experiment was performed to assess the inhibitory efficacy of compounds **11a-f** and **12a-f** against *E. coli* DNA gyrase (Abdel-Aziz et al., 2023). Results are presented as RA of the enzyme at 1 μM of compounds or IC_{50} values for compounds with RA < 50%. Refer to Appendix A for more information.

4.2.7 Antibacterial assay and MIC calculations

The antibacterial efficacy of compounds **11b**, **11e**, and **12b** was evaluated against Gram-positive bacteria (*S. aureus* and *B. subtilis*) and Gram-negative bacteria (*E. coli* and *P. aeruginosa*). The MICs (nM) of the tested compounds against the evaluated bacteria were determined through a twofold serial dilution approach on a 96-well microtiter plate (Frejat F. O. et al., 2022). See Appendix A for more details.

Data availability statement

The original contributions presented in the study are included in the article/Supplementary Material, further inquiries can be directed to the corresponding authors.

Author contributions

HG: Software, Funding acquisition, Writing – original draft, Data curation. AA: Methodology, Software, Writing – original draft. MS: Investigation, Writing – original draft, Resources. SA: Investigation, Writing – original draft, Formal Analysis, Visualization. TA: Validation, Software, Writing – original draft, Data curation. EA: Software, Data curation, Resources, Writing – review and editing. AM: Conceptualization, Writing – review and editing, Formal Analysis. FM: Formal Analysis, Visualization, Conceptualization, Methodology, Writing – review and editing. HA: Formal Analysis, Methodology, Writing – review and editing, Validation, Visualization. AM: Methodology, Validation, Investigation, Software, Writing – original draft, Formal Analysis, Writing – review and editing, Visualization. AA: Investigation, Data curation, Writing – review and editing, Validation, Visualization, Writing – original draft, Formal Analysis,

Methodology. SB: Writing – review and editing, Supervision. BY: Resources, Conceptualization, Investigation, Writing – review and editing, Data curation, Visualization, Validation, Writing – original draft, Formal Analysis, Software, Supervision, Methodology.

Funding

The author(s) declare that financial support was received for the research and/or publication of this article. This work was funded by the Deanship of Graduate Studies and Scientific Research at Jouf University under grant No. (DGSSR-2024-01-01014). The authors also acknowledge support from the KIT-Publication Fund of the Karlsruhe Institute of Technology.

Conflict of interest

The authors declare that the research was conducted in the absence of any commercial or financial relationships that could be construed as a potential conflict of interest.

Generative AI statement

The authors declare that no Generative AI was used in the creation of this manuscript.

Publisher's note

All claims expressed in this article are solely those of the authors and do not necessarily represent those of their affiliated organizations, or those of the publisher, the editors and the reviewers. Any product that may be evaluated in this article, or claim that may be made by its manufacturer, is not guaranteed or endorsed by the publisher.

Supplementary material

The Supplementary Material for this article can be found online at: https://www.frontiersin.org/articles/10.3389/fchem.2025.1595997/full#supplementary-material

References

Abdelazeem, A. H., El-Saadi, M. T., Said, E. G., Youssif, B. G., Omar, H. A., and El-Moghazy, S. M. (2017). Novel diphenylthiazole derivatives with multi-target mechanism: synthesis, docking study, anticancer and anti-inflammatory activities. *Bioorg. Chem.* 75, 127–138. doi:10.1016/j.bioorg.2017.09.009

Abdel-Aziz, S. A., Cirnski, K., Herrmann, J., Abdel-Aal, M. A., Youssif, B. G., and Salem, O. I. (2023). Novel fluoroquinolone hybrids as dual DNA gyrase and urease inhibitors with potential antibacterial activity: design, synthesis, and biological evaluation. *J. Mol. Struct.* 1271, 134049. doi:10.1016/j.molstruc.2022.134049

Abdel-Aziz, S. A., Taher, E. S., Lan, P., Asaad, G. F., Gomaa, H. A., El-Koussi, N. A., et al. (2021). Design, synthesis, and biological evaluation of new pyrimidine-5-carbonitrile derivatives bearing 1, 3-thiazole moiety as novel anti-inflammatory EGFR inhibitors with cardiac safety profile. *Bioorg. Chem.* 111, 104890. doi:10.1016/j.bioorg.2021.104890

Abdel-Aziz, S. A., Taher, E. S., Lan, P., El-Koussi, N. A., Salem, O. I., Gomaa, H. A., et al. (2022). New pyrimidine/thiazole hybrids endowed with analgesic, anti-inflammatory, and lower cardiotoxic activities: design, synthesis, and COX-2/sEH dual inhibition. *Arch. Pharm.* 355 (7), 2200024. doi:10.1002/ardp.202200024

Agrawal, A., and Patel, A. K. (2024). *Antibiotic resistance profile and detection in ESKAPE pathogens, ESKAPE pathogens: detection, mechanisms and treatment strategies*. Springer, 33–77.

Alateeq, A. M., Al-Faiyz, Y. S., McNair, O. D., Wiggins, J. S., and Sayed, A. R. (2024). Synthesis, reaction, and biological activity of thiazoles. *Curr. Org. Synth.* 22, 481–515. doi:10.2174/0115701794322192240905093650

Alshammari, M. B., Aly, A. A., Youssif, B. G., Bräse, S., Ahmad, A., Brown, A. B., et al. (2022). Design and synthesis of new thiazolidinone/uracil derivatives as antiproliferative agents targeting EGFR and/or BRAFV600E. *Front. Chem.* 10, 1076383. doi:10.3389/fchem.2022.1076383

Al-Wahaibi, L. H., Amer, A. A., Marzouk, A. A., Gomaa, H. A., Youssif, B. G., and Abdelhamid, A. A. (2021). Design, synthesis, and antibacterial screening of some novel heteroaryl-based ciprofloxacin derivatives as DNA gyrase and topoisomerase IV inhibitors. *Pharmaceuticals* 14 (5), 399. doi:10.3390/ph14050399

Al-Wahaibi, L. H., Elshamsy, A. M., Ali, T. F., Youssif, B. G., Brase, S., Abdel-Aziz, M., et al. (2024a). Design and synthesis of new dihydropyrimidine derivatives with a cytotoxic effect as dual EGFR/VEGFR-2 inhibitors. *ACS omega* 9 (32), 34358–34369. doi:10.1021/acsomega.4c01361

Al-Wahaibi, L. H., El-Sheref, E. M., Hammouda, M. M., and Youssif, B. G. (2023a). One-pot synthesis of 1-Thia-4-azaspiro [4.4/5] alkan-3-ones via schiff base: design, synthesis, and apoptotic antiproliferative properties of dual EGFR/BRAFV600E inhibitors. *Pharmaceuticals* 16 (3), 467. doi:10.3390/ph16030467

Al-Wahaibi, L. H., El-Sheref, E. M., Tawfeek, H. N., Abou-Zied, H. A., Rabea, S. M., Bräse, S., et al. (2024b). Design, synthesis, and biological evaluation of novel quinoline-based EGFR/HER-2 dual-target inhibitors as potential anti-tumor agents. *RSC Adv.* 14 (45), 32978–32991. doi:10.1039/d4ra06394e

Al-Wahaibi, L. H., Mahmoud, M. A., Alzahrani, H. A., Abou-Zied, H. A., Abdelmoez, A., Youssif, B. G., et al. (2024c). Synthesis, enzyme inhibition, and docking studies of new schiff bases of disalicylic acid methylene-based derivatives as dual-target antibacterial agents. *Front. Chem.* 12, 1493906. doi:10.3389/fchem.2024.1493906

Al-Wahaibi, L. H., Mahmoud, M. A., Alzahrani, H. A., Abou-Zied, H. A., Gomaa, H. A., Youssif, B. G., et al. (2024d). Discovery of new Schiff bases of the disalicylic acid scaffold as DNA gyrase and topoisomerase IV inhibitors endowed with antibacterial properties. *Front. Chem.* 12, 1419242. doi:10.3389/fchem.2024.1419242

Al-Wahaibi, L. H., Mahmoud, M. A., Mostafa, Y. A., Raslan, A. E., and Youssif, B. G. (2023b). Novel piperine-carboximidamide hybrids: design, synthesis, and antiproliferative activity via a multi-targeted inhibitory pathway. *J. Enzyme Inhibition Med. Chem.* 38 (1), 376–386. doi:10.1080/14756366.2022.2151593

Al-Wahaibi, L. H., Mohammed, A. F., Abdelrahman, M. H., Trembleau, L., and Youssif, B. G. (2023c). Design, synthesis, and biological evaluation of indole-2-carboxamides as potential multi-target antiproliferative agents. *Pharmaceuticals* 16 (7), 1039. doi:10.3390/ph16071039

Al-Wahaibi, L. H., Mostafa, Y. A., Abdelrahman, M. H., El-Bahrawy, A. H., Trembleau, L., and Youssif, B. G. (2022). Synthesis and biological evaluation of indole-2-carboxamides with potent apoptotic antiproliferative activity as egfr/cdk2 dual inhibitors. *Pharmaceuticals* 15 (8), 1006. doi:10.3390/ph15081006

Al-Wahaibi, L. H., Rabea, S. M., Mahmoud, M. A., Youssif, B. G., Brase, S., and Abdel-Aziz, S. A. (2024e). Synthesis and antimicrobial evaluation of new 1, 2, 4-triazolo [1, 5-a] pyrimidine-based derivatives as dual inhibitors of bacterial DNA gyrase and DHFR. *ACS omega* 9 (47), 47261–47273. doi:10.1021/acsomega.4c08365

Aly, A. A., Abdallah, E. M., Ahmed, S. A., Rabee, M. M., Fuhr, O., Ibrahim, M. A., et al. (2024). Synthesis and characterization of new palladium (II) and silver (I) thiosemicarbazone derived by acenaphthenequinone complexes and their antimicrobial activity. *Polyhedron* 251, 116851. doi:10.1016/j.poly.2024.116851

Aly, A. A., Alshammari, M. B., Ahmad, A., Gomaa, H. A., Youssif, B. G., Braese, S., et al. (2023). Design, synthesis, docking and mechanistic studies of new thiazolyl/thiazolidinylpyrimidine-2, 4-dione antiproliferative agents. *Arabian J. Chem.* 16 (4), 104612. doi:10.1016/j.arabjc.2023.104612

Arshad, M. F., Alam, A., Alshammari, A. A., Alhazza, M. B., Alzimam, I. M., Alam, M. A., et al. (2022). Thiazole: a versatile standalone moiety contributing to the development of various drugs and biologically active agents. *Molecules* 27 (13), 3994. doi:10.3390/molecules27133994

Batool, Z., Azfal, A., Liaquat, L., Sadir, S., Nisar, R., Inamullah, A., et al. (2023). *Receptor tyrosine kinases (RTKs): from biology to pathophysiology, receptor tyrosine kinases in neurodegenerative and psychiatric disorders*. Elsevier, 117–185.

Bhanja, K. K., and Patra, N. (2025). Identification of novel fourth-generation allosteric inhibitors targeting inactive state of EGFR T790M/L858R/C797S and T790M/L858R mutations: a combined machine learning and molecular dynamics approach. *J. Phys. Chem. B* 129, 3610–3629. doi:10.1021/acs.jpcb.4c07651

Chidan Kumar, C., Then, L. Y., Chia, T. S., Chandraju, S., Win, Y.-F., Sulaiman, S. F., et al. (2015). Benzofuranyl esters: synthesis, crystal structure determination, antimicrobial and antioxidant activities. *Molecules* 20 (9), 16566–16581. doi:10.3390/molecules200916566

Chugh, V., Pandey, G., Rautela, R., and Mohan, C. (2022). Heterocyclic compounds containing thiazole ring as important material in medicinal chemistry. *Mater. Today Proc.* 69, 478–481. doi:10.1016/j.matpr.2022.09.150

Elbastawesy, M., Youssif, B., Abdelrahman, M. H., and Hayallah, A. M. (2015). Synthesis and biological evaluation of some new coumarin derivatives as potential antimicrobial, analgesic and anti-inflammatory agents. *Der. Pharma. Chem.* 7, 337–349.

El-Sheref, E. M., Bräse, S., Tawfeek, H. N., Alasmary, F. A., and Youssif, B. G. (2023). Synthesis, antioxidant and antiproliferative actions of 4-(1, 2, 3-Triazol-1-yl) quinolin-2 (1 H)-ones as multi-target inhibitors. *Int. J. Mol. Sci.* 24 (17), 13300. doi:10.3390/ijms241713300

El-Sherief, H. A., Youssif, B. G., Abdelazeem, A. H., Abdel-Aziz, M., and Abdel-Rahman, H. M. (2019). Design, synthesis and antiproliferative evaluation of novel 1, 2, 4-triazole/schiff base hybrids with EGFR and B-RAF inhibitory activities. *Anti-Cancer Agents Med. Chem.* 19 (5), 697–706. doi:10.2174/1871520619666181224115346

Frejat, F. O., Cao, Y., Wang, L., Zhai, H., Abdelazeem, A. H., Gomaa, H. A., et al. (2022b). New 1, 2, 4-oxadiazole/pyrrolidine hybrids as topoisomerase IV and DNA gyrase inhibitors with promising antibacterial activity. *Arch. Pharm.* 355 (7), 2100516. doi:10.1002/ardp.202100516

Frejat, F. O. A., Cao, Y., Zhai, H., Abdel-Aziz, S. A., Gomaa, H. A., Youssif, B. G., et al. (2022a). Novel 1, 2, 4-oxadiazole/pyrrolidine hybrids as DNA gyrase and topoisomerase IV inhibitors with potential antibacterial activity. *Arabian J. Chem.* 15 (1), 103538. doi:10.1016/j.arabjc.2021.103538

Goyal, S., Thirumal, D., Singh, S., Kumar, D., Singh, I., Kumar, G., et al. (2025). Basics of antioxidants and their importance, antioxidants. *Nat's Def. Against Dis.*, 1–20. doi:10.1002/9781394270576.ch1

Hashem, H., Hassan, A., Abdelmagid, W. M., Habib, A. G., Abdel-Aal, M. A., Elshamsy, A. M., et al. (2024). Synthesis of new thiazole-privileged chalcones as tubulin polymerization inhibitors with potential anticancer activities. *Pharmaceuticals* 17 (9), 1154. doi:10.3390/ph17091154

Jadhav, P. M., Kantevari, S., Tekale, A. B., Bhosale, S. V., Pawar, R. P., and Tekale, S. U. (2021). A review on biological and medicinal significance of thiazoles. *Phosphorus, Sulfur, Silicon Relat. Elem.* 196 (10), 879–895. doi:10.1080/10426507.2021.1945601

Kakkar, S., Kumar, S., Lim, S. M., Ramasamy, K., Mani, V., Shah, S. A. A., et al. (2018). Design, synthesis and biological evaluation of 3-(2-aminooxazol-5-yl)-2 H-chromen-2-one derivatives. *Chem. Central J.* 12, 130–213. doi:10.1186/s13065-018-0499-x

Kumar, R., Goel, H., Solanki, R., Rawat, L., Tabasum, S., Tanwar, P., et al. (2024). Recent developments in receptor tyrosine kinase inhibitors: a promising mainstay in targeted cancer therapy. *Med. drug Discov.* 23, 100195. doi:10.1016/j.medidd.2024.100195

Liu, B., Zhou, H., Tan, L., Siu, K. T. H., and Guan, X.-Y. (2024). Exploring treatment options in cancer: tumor treatment strategies. *Signal Transduct. Target. Ther.* 9 (1), 175. doi:10.1038/s41392-024-01856-7

Liu, X.-J., Zhao, H.-C., Hou, S.-J., Zhang, H.-J., Cheng, L., Yuan, S., et al. (2023b). Recent development of multi-target VEGFR-2 inhibitors for the cancer therapy. *Bioorg. Chem.* 133, 106425. doi:10.1016/j.bioorg.2023.106425

Liu, Z.-L., Chen, H.-H., Zheng, L.-L., Sun, L.-P., and Shi, L. (2023a). Angiogenic signaling pathways and anti-angiogenic therapy for cancer. *Signal Transduct. Target. Ther.* 8 (1), 198. doi:10.1038/s41392-023-01460-1

Mahmoud, M. A., Mohammed, A. F., Salem, O. I., Almutairi, T. M., Bräse, S., and Youssif, B. G. (2024). Design, synthesis, and apoptotic antiproliferative action of new 1, 2, 3-triazole/1, 2, 4-oxadiazole hybrids as dual EGFR/VEGFR-2 inhibitors. *J. Enzyme Inhibition Med. Chem.* 39 (1), 2305856. doi:10.1080/14756366.2024.2305856

Mahmoud, M. A., Mohammed, A. F., Salem, O. I., Rabea, S. M., and Youssif, B. G. (2023). Design, synthesis, and antiproliferative properties of new 1, 2, 3-triazole-carboximidamide derivatives as dual EGFR/VEGFR-2 inhibitors. *J. Mol. Struct.* 1282, 135165. doi:10.1016/j.molstruc.2023.135165

Marzouk, A. A., Abdel-Aziz, S. A., Abdelrahman, K. S., Wanas, A. S., Gouda, A. M., Youssif, B. G., et al. (2020). Design and synthesis of new 1, 6-dihydropyrimidin-2-thio derivatives targeting VEGFR-2: molecular docking and antiproliferative evaluation. *Bioorg. Chem.* 102, 104090. doi:10.1016/j.bioorg.2020.104090

Mohamed, A. M., Abou-Ghadir, O. M., Mostafa, Y. A., Dahlous, K. A., Bräse, S., and Youssif, B. G. (2024). Design and synthesis of new 1, 2, 4-oxadiazole/quinazoline-4-one hybrids with antiproliferative activity as multitargeted inhibitors. *Front. Chem.* 12, 1447618. doi:10.3389/fchem.2024.1447618

Pang, K., Wang, W., Qin, J. X., Shi, Z. D., Hao, L., Ma, Y. Y., et al. (2022). Role of protein phosphorylation in cell signaling, disease, and the intervention therapy. *MedComm* 3 (4), e175. doi:10.1002/mco2.175

Portela, R., Borovnik, K., Costa, C. M., Grilo, I. R., and Pereira, P. M. (2025). High-priority pathogens: where do we stand? in *Nanotherapeutics for Infectious Diseases*. Jenny Stanford Publishing New York, 93–140.

Qi, Y., Deng, S.-M., and Wang, K.-S. (2024). Receptor tyrosine kinases in breast cancer treatment: unraveling the potential. *Am. J. Cancer Res.* 14 (9), 4172–4196. doi:10.62347/kivs3169

Ramadan, M., Abd El-Aziz, M., Elshaier, Y. A., Youssif, B. G., Brown, A. B., Fathy, H. M., et al. (2020). Design and synthesis of new pyranoquinolinone heteroannulated to triazolopyrimidine of potential apoptotic antiproliferative activity. *Bioorg. Chem.* 105, 104392. doi:10.1016/j.bioorg.2020.104392

Rana, R., Kumar, N., Gulati, H. K., Sharma, A., Khanna, A., Badhwar, R., et al. (2023). A comprehensive review on thiazole based conjugates as anti-cancer agents. *J. Mol. Struct.* 1292, 136194. doi:10.1016/j.molstruc.2023.136194

Reang, J., Sharma, K., Sharma, P. C., Yadav, V., Sharma, V., and Majeed, J. (2023). Discovery of VEGFR inhibitors through virtual screening and energy assessment. *J. Biochem. Mol. Toxicol.* 37 (5), e23321. doi:10.1002/jbt.23321

Rustagi, V., Gupta, S. R., Singh, A., and Singh, I. K. (2025). Beyond trial and error: leveraging advanced software for Therapeutic discovery. *Chem. Biol. Lett.* 12 (1), 1251. doi:10.62110/sciencein.cbl.2025.v12.1251

Sahu, S. K., Mishra, A., and Behera, R. K. (1996). Synthesis of thiazole, benzothiazole, oxadiazole, thiadiazole, triazole and thiazolidinone incorporated coumarins. *Indian J. Heterocycl. Chem.*, 91–94.

Seong, H., Izutsu, R., Osaki, M., and Okada, F. (2025). Cancer prevention: past challenges and future directions. *Genes Environ.* 47 (1), 4. doi:10.1186/s41021-025-00326-y

Sharma, P. C., Bansal, K. K., Sharma, A., Sharma, D., and Deep, A. (2020). Thiazole-containing compounds as therapeutic targets for cancer therapy. *Eur. J. Med. Chem.* 188, 112016. doi:10.1016/j.ejmech.2019.112016

Sharma, V., Gupta, A., Singh, A., Tyagi, S., Panday, H., Srivastava, S., et al. (2025). Virtual perspectives of sanguinarine on cancer prevention and treatment through molecular dynamic study. *Silico Pharmacol.* 13 (1), 33. doi:10.1007/s40203-025-00315-7

Sofi, F. A., Masoodi, M. H., and Tabassum, N. (2025). Recent advancements in the development of next-generation dual-targeting antibacterial agents. *RSC Med. Chem.* doi:10.1039/D4MD00934G

Theivendren, P., Kunjiappan, S., Hegde, Y. M., Vellaichamy, S., Gopal, M., Dhramalingam, S. R., et al. (2021). *Importance of protein kinase and its inhibitor: a review, protein kinases: promising targets for anticancer drug research*. IntechOpen, 75–100.

Tiz, D. B., Skok, Ž., Durcik, M., Tomašič, T., Mašič, L. P., Ilaš, J., et al. (2019). An optimised series of substituted N-phenylpyrrolamides as DNA gyrase B inhibitors. *Eur. J. Med. Chem.* 167, 269–290. doi:10.1016/j.ejmech.2019.02.004

Wang, C., Zhang, J., Yin, J., Gan, Y., Xu, S., Gu, Y., et al. (2021). Alternative approaches to target Myc for cancer treatment. *Signal Transduct. Target. Ther.* 6 (1), 117. doi:10.1038/s41392-021-00500-y

Woo, S., Park, P.-G., An, T., Fatima, M., Moon, Y.-E., Lee, S.-Y., et al. (2025). Mini-review on the therapeutic vaccines targeting chronic infectious diseases: evaluation system of therapeutic vaccines targeting HPV and EBV-related cancers. *Hum. Vaccines Immunother.* 21 (1), 2457187. doi:10.1080/21645515.2025.2457187

Xie, C., Wan, X., Quan, H., Zheng, M., Fu, L., Li, Y., et al. (2018). Preclinical characterization of anlotinib, a highly potent and selective vascular endothelial growth factor receptor-2 inhibitor. *Cancer Sci.* 109 (4), 1207–1219. doi:10.1111/cas.13536

Zhong, L., Li, Y., Xiong, L., Wang, W., Wu, M., Yuan, T., et al. (2021). Small molecules in targeted cancer therapy: advances, challenges, and future perspectives. *Signal Transduct. Target. Ther.* 6 (1), 201–248. doi:10.1038/s41392-021-00572-w

Zolfi, E., Khaleghi Mehr, F., Emtiazi, N., and Moradi, Y. (2025). A review of the carcinogenic potential of human papillomavirus (HPV) in urological cancers. *Virology J.* 22 (1), 53. doi:10.1186/s12985-025-02682-1

frontiers | Frontiers in Chemistry

TYPE Original Research
PUBLISHED 21 May 2025
DOI 10.3389/fchem.2025.1579923

Check for updates

OPEN ACCESS

EDITED BY
Guigen Li,
Texas Tech University, United States

REVIEWED BY
Pradeep Kumar Jaiswal,
Texas A&M University, United States
Yasmine Fernine,
Sidi Mohamed Ben Abdellah University, Morocco
Chenyang Lu,
Purdue University, United States

*CORRESPONDENCE
Ahmed R. Rabee,
ahmedrabee@alexu.edu.eg,
ahmedramadanrabee@gmail.com
Mohamed Hagar,
mohamedhaggar@gmail.com

RECEIVED 19 February 2025
ACCEPTED 28 April 2025
PUBLISHED 21 May 2025

CITATION
R. Rabee A, M. Soliman S, Abdel-Hamid H, A. Moneer E, H. Akl S, H. Shahin Y, A. Masoud A, Ghareeb DA, Jaremko M, Emwas A-H, Sherif M and Hagar M (2025) Synthesis and characterization of thymol-derived phenoxy acetamide derivatives using DFT, molecular docking, and parasitological investigations. *Front. Chem.* 13:1579923. doi: 10.3389/fchem.2025.1579923

COPYRIGHT
© 2025 R. Rabee, M. Soliman, Abdel-Hamid, A. Moneer, H. Akl, H. Shahin, A. Masoud, Ghareeb, Jaremko, Emwas, Sherif and Hagar. This is an open-access article distributed under the terms of the Creative Commons Attribution License (CC BY). The use, distribution or reproduction in other forums is permitted, provided the original author(s) and the copyright owner(s) are credited and that the original publication in this journal is cited, in accordance with accepted academic practice. No use, distribution or reproduction is permitted which does not comply with these terms.

Synthesis and characterization of thymol-derived phenoxy acetamide derivatives using DFT, molecular docking, and parasitological investigations

Ahmed R. Rabee[1]*, Saied M. Soliman[1], Hamida Abdel-Hamid[1], Esraa A. Moneer[2], Sara H. Akl[2], Yahya H. Shahin[3], Aliaa A. Masoud[4], Doaa Ahmad Ghareeb[4], Mariusz Jaremko[5], Abdul-Hamid Emwas[6], Mazen Sherif[1] and Mohamed Hagar[1]*

[1]Chemistry Department, Faculty of Science, Alexandria University, Alexandria, Egypt, [2]Department of Medical Laboratory Technology, Faculty of Applied Health Sciences Technology, Pharos University in Alexandria, Alexandria, Egypt, [3]Department of Medical Laboratory Technology, Faculty of Health and Medical Techniques, Almaaqal University, Basrah, Iraq, [4]Bio-Screening and Preclinical Trial Lab, Biochemistry Department, Faculty of Science, Alexandria University, Alexandria, Egypt, [5]Biological and Environmental Sciences and Engineering Division, King Abdullah University of Science and Technology, Makkah, Saudi Arabia, [6]KAUST Core Laboratories, King Abdullah University of Science and Technology, Thuwal, Saudi Arabia

Novel phenoxy acetamide derivatives based on a thymol moiety were synthesized for target parasitological investigation. The newly synthesized compounds, **5a**, **5b**, **7a**, **7b**, and **9**, were synthesized as phenoxy acetamide derivatives containing a phthalimide or naphthalimide ring through a condensation reaction with various acid anhydrides. Their structures were confirmed based on spectral data derived through Fourier-transform infrared, proton and carbon-13 nuclear magnetic resonance, and elemental analyses. The parasitological, biochemical, and immunological activities of the compounds were measured. The screened compounds were subjected to molecular docking in the active site of CpCDPK1, in addition to analyses based on Lipinski's rule and SwissADME. The results showed that compounds **5a**, **5b**, and **7b** demonstrated promising antiparasitic activity, characterized by high gastrointestinal absorption and favorable drug-likeness profiles. Furthermore, **5a** and **7b** exhibited higher binding affinities than that of the reference drug. In practical assessments, compound **7b** exhibited the highest percentage reduction in oocyst counts (67%). Density functional theory calculations were performed to assess the thermodynamic stability, molecular geometry, frontier molecular orbital energy gaps, and molecular electrostatic potentials of compounds **5a**, **5b**, **7a**, **7b**, and **9**.

KEYWORDS

thymol, naphthalimide and phthalimide derivatives, anti-parasites, molecular docking, DFT

1 Introduction

Thymol (2-isopropyl-5-methylphenol) is a white crystalline aromatic compound with a distinct scent that is produced *via* the terpene pathway and typically found in the genera *Thymus* and *Origanum*. Its direct biosynthetical link with p-cymene has been demonstrated through the aromatization of c-terpinene in *Thymus vulgaris* L. (Poulose and Croteau, 1978)

According to the United States Food and Drug Administration (US-FDA), thymol is safe with low toxicity. (Cohen, 1984). Thymol has been known to exert therapeutic effects on humans, (Jyoti et al., 2019), with a range of biological activities, such as antibacterial, (Dong et al., 2024), antifungal, (Alves Eloy et al., 2021), antioxidant, (Sathe et al., 2019), antiprotozoal, (Clemente et al., 2021), anti-inflammatory, (Chen et al., 2020), antiviral, (Nandi and Khanna, 2022), antiparasitic, (Hikal et al., 2021; Sennouni et al., 2022), and anticancer (Lv and Chen, 2017; Chauhan et al., 2017) activities. Additionally, thymol has shown efficacy against *C. parvum (Cryptosporidium parvum)* in cell cultures. (Dominguez-Uscanga et al., 2021).

Phenoxy acetamide derivatives exhibit antioxidant activity and may protect biological systems against oxidative damage. (Al-Ostoot et al., 2021a; Arshad et al., 2022). Molecules containing acetamide linkages and their derivatives as core structures display a wide range of biological activities, (Al-Ostoot et al., 2021b), especially antitrypanosomal effects. (Capelini et al., 2021). Phthalimides, which are neutral, lipophilic compounds exhibiting antimicrobial (Akgün et al., 2012) and anti-inflammatory (Alanazi et al., 2015) properties readily penetrate biological membranes. Thus, phthalimides have been used as platforms for developing anti-*Trypanosoma cruzi* and antiplasmodial drugs. (González et al., 2014; Singh et al., 2015).

Naphthalimide derivatives have conventionally been used as fluorescent fibers and dyes. In prior decades, these derivatives were used as medicines and sensors. (Qian et al., 2010). The tricyclic planar ring structure of the naphthalimide class facilitates intercalation with DNA and disruption of biological processes. (Kamal et al., 2013). Hence, naphthalimides exhibit a range of biological attributes, such as antiviral, (Chanh et al., 1994), antioxidant, (Ghosh et al., 2015), and antimicrobial activities. (Staneva et al., 2019).

Thymol, characterized as a safe compound, (Aljohani et al., 2022), exhibits various advantages, such as abundance and low toxicity to mammalian cells. Consequently, thymol and related substances may represent promising candidates for developing novel antiparasitic therapies (Chauhan and Kang, 2014).

The zoonotic protozoan parasite *C. parvum*, which is the second-most common cause of foodborne and waterborne diarrheal illnesses globally, is a member of the phylum Apicomplexa. (Ryan et al., 2016). Its adverse effects are particularly severe for immunocompromised individuals. (Wang et al., 2018).

Considering these aspects, this study was aimed at synthesizing newly phenoxy acetamide derivatives based on a thymol moiety through condensation reactions with a series of acid anhydrides and assessing their antiparasitic effects through experimental and molecular docking studies. One of the challenges with thymol is its rapid absorption and metabolism, which can limit its effectiveness *in vivo*. The phenoxy acetamide derivatives based on thymol can potentially create prodrugs that release thymol more slowly, allowing for sustained therapeutic effects. Moreover, density functional theory (DFT) calculations were performed to explore their thermodynamic stability, molecular geometry, frontier molecular orbital (FMO) energy gaps, and molecular electrostatic potential (MEP).

2 Results and discussion

2.1 Chemistry

Phenoxy acetamide derivatives based on a thymol moiety were synthesized through condensation reactions with a series of acid anhydrides. As shown in Scheme 1, 2-(2-isopropyl-5-methylphenoxy)acetohydrazide (**3**) was reacted with different acid anhydrides, including phthalic anhydride (**4a**), 1,2,4-benzene tricarboxylic acid anhydride (**4b**), 1,8-naphthalic anhydride (**6a**), 4-amino-1,8-naphthalic anhydride (**6b**), and pyromellitic dianhydride (**8**) in dimethylformamide (DMF) and glacial acetic acid under reflux conditions for 4–6 h to afford compounds **5a**, **5b**, **7a**, **7b**, and **9**, respectively.

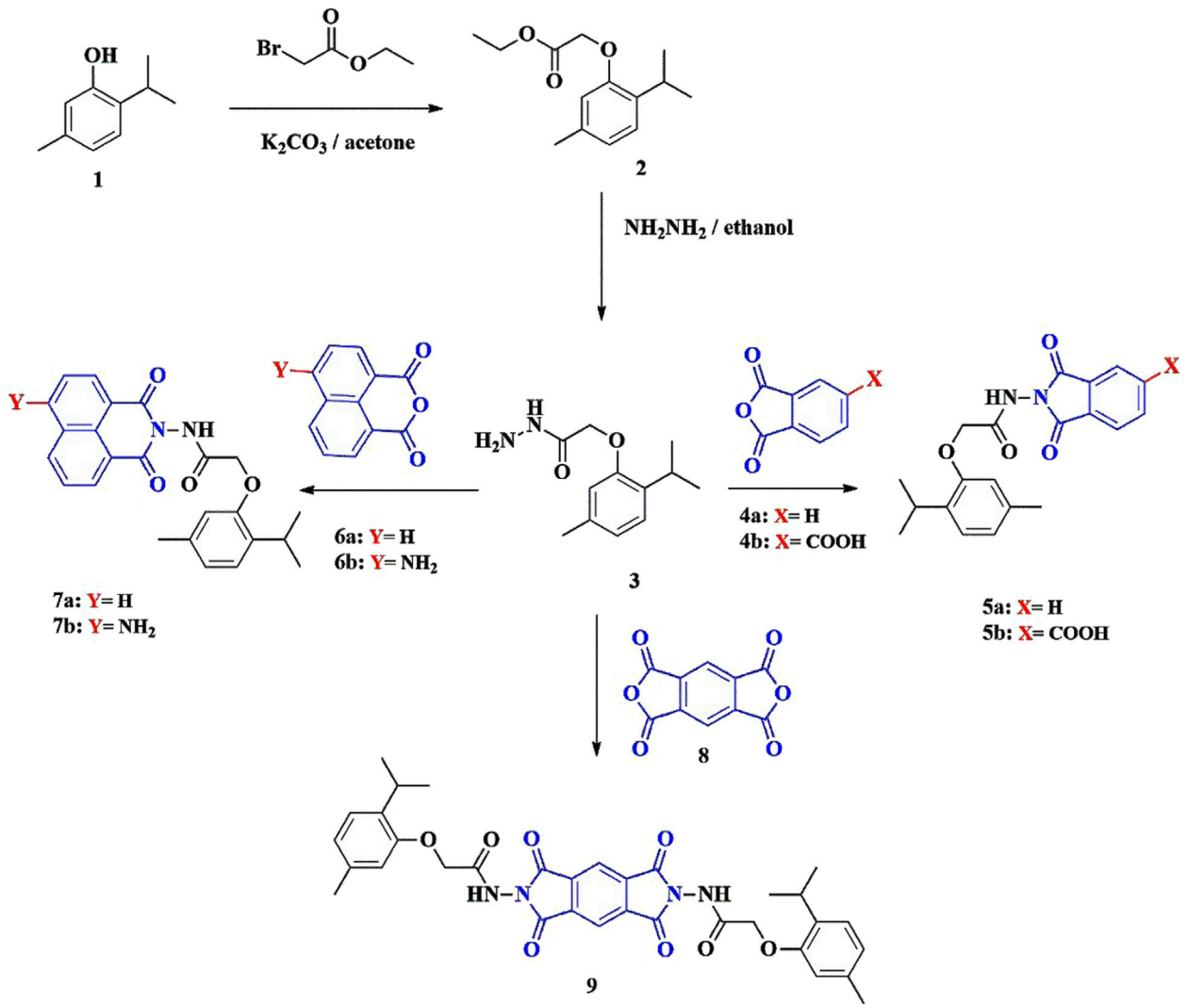
The structures of the synthesized compounds **5a**, **5b**, **7a**, **7b**, and **9** were confirmed using spectroscopic data. The proton nuclear magnetic resonance (^{1}H-NMR) spectrum showed characteristic singlet peaks for NH (10.08–10.90 ppm) and aliphatic CH_3 (1.13–2.27 ppm). The infrared (IR) spectra of all synthesized compounds showed two sharp bands of C=O (conjugated anhydride) at ν = 1,792 cm^{-1} and 1,744 cm^{-1}.

For compound **5b**, the ^{1}H-NMR spectrum showed a singlet peak of COOH at 10.13 ppm and the ^{13}C-NMR spectrum showed a peak at δ_C: 168.4 (COOH). The ^{1}H-NMR spectrum of compound **7b** showed a singlet peak of NH_2 at 7.71 ppm. For compound **9**, the ^{1}H-NMR spectrum showed two singlet peaks at 8.45 and 8.29 ppm, corresponding to pyromellitic protons.

2.2 *In silico* physicochemical and pharmacokinetic predictions

An absorption, distribution, metabolism, excretion, toxicity (ADMET) study was performed to assess the pharmacokinetic, physicochemical, and drug-likeness profiles of compounds **5a**, **5b**, **7a**, **7b**, and **9**. As indicated in Table 1, compounds **5a**, **5b**, **7a**, and **7b** demonstrated high gastrointestinal (GI) absorption, whereas compound **9** exhibited low GI absorption. Blood–brain barrier (BBB) permeability was observed only for **5a** and **7a**. None of the compounds were substrates for P-glycoprotein. Selective inhibition of cytochrome P450 enzymes was noted, with compound **5b** inhibiting CYP1A2 and compounds **5a**, **7a**, and **7b** inhibiting CYP2C19. Furthermore, all compounds inhibited CYP2C9 and compound **9** uniquely inhibited CYP3A4. Drug-likeness analysis revealed no violations of Lipinski's rule of five for **5a**, **5b**, **7a**, and **7b**, although compound **9** exhibited two violations. Bioavailability scores were consistent for **5a**, **5b**, **7a**, and **7b**, ranging from 0.55 to 0.56, whereas compound 9 had a significantly lower score (0.17). Medicinal chemistry assessments indicated that **5b** had the fewest lead-likeness violations, followed by **5a**, **7a**, and **7b**, with compound **9** exhibiting the most violations. Synthetic accessibility scores showed that **5a** was the easiest to synthesize and **9** posed the greatest challenge. Physicochemical analysis revealed that compound **9** had the highest molecular weight (626.66 g/mol) and topological polar surface area (TPSA) (154.8 $Å^2$), correlating with low membrane permeability. Compound **5a** exhibited the lowest molecular weight and TPSA, contributing to its favorable pharmacokinetic profile. Compound **9** also had the highest number of rotatable bonds, indicating greater molecular flexibility, while **5a**, **7a**, **7b** was more rigid. Lipophilicity was most pronounced in compound **9**

10.3389/fchem.2025.1579923



SCHEME 1
Synthesis of phenoxy acetamide derivatives containing a thymol unit.

(consensus log Po/w of 4.06) and **5b** exhibited the lowest value (2.54). Solubility predictions categorized **5a**, **5b**, **7a**, and **7b** as moderately soluble, while **9** was noted to be poorly soluble (ESOL log S of −6.64). Among the tested compounds, **5a, 7a, 7b** emerged as the most promising owing to their high GI absorption, moderate solubility (ESOL log S of −4.24, −5.46, −5.11), balanced lipophilicity (consensus log Po/w 2.95, 3.91, 3.39), and TPSA (75.71, 77.4, 103.42 Å^2). It selectively inhibited CYP2C19 and CYP2C9 and did not interact with CYP1A2, CYP2D6, or P-gp, resulting in enhanced therapeutic safety profile. However, compound **7b** stands out as a safer candidate due to its lack of BBB permeability, which may reduce potential central nervous system side effects.

2.3 Molecular docking studies

Molecular docking results were validated by re-docking the native ligand VGG into the CDPK1 active site, considered a key target for antiparasitic drug development owing to its essential role in the lifecycle of parasites. The analysis yielded a root mean square deviation (RMSD) of 0.52 Å and docking score of −7.27 kcal/mol, validating the proposed methodology. The binding affinity of each compound (**5a**, **5b**, **7a**, **7b**, and **9**) is outlined in Table 2. As shown in Figure 1, compound **5a** demonstrated the highest binding affinity (−7.42 kcal/mol), forming strong hydrogen bonds with critical catalytic residues Asp219, Met136 and Lys105, along with stabilizing π-alkyl and van der Waals interactions highlighting its potential as a potent inhibitor. Compound **5b** showed the second-highest binding affinity (−6.45 kcal/mol) and interacted with Asp219, Lys105, and Phe220, indicating a slightly weaker but still significant binding conformation. Compound **7b** exhibited a comparable binding affinity (−6.41 kcal/mol), with conventional hydrogen bond interactions involving Tyr155 and Asp219, suggesting a stable binding profile. In contrast, compounds **7a** and **9** displayed notably weaker binding profiles. Compound **7a** had a lower binding affinity (−5.39 kcal/mol), with limited hydrogen bond interactions involving Asp219, reflecting a less stable binding mode. Compound **9** demonstrated a highly unfavorable binding affinity (32.66 kcal/mol) owing to steric clashes and unfavorable conformations within the active

10.3389/fchem.2025.1579923

TABLE 1 ADMET study of compounds 5a, 5b, 7a, 7b, and 9.

Pharmacokinetics	5a	5b	7a	7b	9
GI absorption	High	High	High	High	Low
BBB permeability	Yes	No	Yes	No	No
P-gp substrate	No	No	No	No	No
CYP1A2 inhibitor	No	Yes	No	No	No
CYP2C19 inhibitor	Yes	No	Yes	Yes	No
CYP2C9 inhibitor	Yes	Yes	Yes	Yes	Yes
CYP2D6 inhibitor	No	No	No	No	No
CYP3A4 inhibitor	No	No	No	No	Yes
Drug Likeness	**5a**	**5b**	**7a**	**7b**	**9**
Lipinski violations	0	0	0	0	2
Bioavailability score	0.55	0.56	0.55	0.55	0.17
Medicinal Chemistry	**5a**	**5b**	**7a**	**7b**	**9**
Lead likeness violations	2	1	2	2	3
Synthetic accessibility	2.75	2.98	3.08	3.19	4.27
Physicochemical Properties	**5a**	**5b**	**7a**	**7b**	**9**
Formula	$C_{20}H_{20}N_2O_4$	$C_{21}H_{20}N_2O_6$	$C_{24}H_{22}N_2O_4$	$C_{24}H_{23}N_3O_4$	$C_{34}H_{34}N_4O_8$
MW	352.38	396.39	402.44	417.46	626.66
Num. heavy atoms	26	29	30	31	46
Num. aromatic heavy atoms	12	12	19	19	24
Fraction Csp3	0.25	0.24	0.21	0.21	0.29
Num. rotatable bonds	6	7	6	6	12
Num. H-bond acceptors	4	6	4	4	8
Num. H-bond donors	1	2	1	2	2
MR	100.09	107.05	118.78	123.18	176.11
TPSA	75.71	113.01	77.4	103.42	154.8
Lipophilicity	**5a**	**5b**	**7a**	**7b**	**9**
Consensus log $P_{o/w}$	2.95	2.54	3.91	3.39	4.06
Water Solubility	**5a**	**5b**	**7a**	**7b**	**9**
ESOL log S	−4.24	−4.11	−5.46	−5.11	−6.64
ESOL solubility (mg/mL)	$2.04E^{-02}$	$3.10E^{-02}$	$1.38E^{-03}$	$3.22E^{-03}$	$1.44E^{-04}$
ESOL solubility (mol/L)	$5.78E^{-05}$	$7.81E^{-05}$	$3.44E^{-06}$	$7.71E^{-06}$	$2.29E^{-07}$
ESOL class	Moderately soluble	Moderately soluble	Moderately soluble	Moderately soluble	Poorly soluble

site, indicating a lack of inhibitory potential. Although compound **7b** had a slightly lower binding affinity than **5a** and **5b**, it demonstrated the highest *in vivo* antiparasitic activity, attributable to its balanced ADMET profile, including high GI absorption, moderate solubility, and selective cytochrome P450 inhibition, which enhanced its bioavailability and efficacy. In our *in silico* analyses, compounds **5a, 7a,** and **7b** emerged as the most promising candidates; however, compound **7b** was particularly notable because, in addition to its favorable ADMET properties, it selectively bound to Tyr155 in the active site which is the same residue to which the co-crystallized ligand VGG binds. This selective interaction suggests that Tyr155 plays a key role in CpCDPK1 activity, and even though **7b** exhibited slightly lower binding energy, its engagement with Tyr155 likely contributes to its enhanced antiparasitic effects. Conversely, the experimental results of compounds 7a and 9, which

10.3389/fchem.2025.1579923

TABLE 2 Docking scores of compounds and types of interactions with 2WEI.

Ligand compound	Binding energy score (S) (Kcal/mol)	RMSD (RefRMSD)	Inhibition constant (Ki) (μM)	Type of binding interactions	Residues involved in the interactions
Ligand (VGG)	−7.27	0.52	4.7	Hydrogen bonds	Pyrimidine nitrogen with Tyr155, amine hydrogen with Glu153.
5a	−7.42	0.0	3.65	Hydrogen bond	Methyl hydrogen with Asp219, carbonyl oxygen with Lys105, and amide proton with Met136.
5b	−6.45	0.0	18.6	Hydrogen bond	Carbonyl oxygen with Lys105, carboxyl proton with Phe220, and carbonyl oxygen with Asp219.
7a	−5.39	0.0	111.9	Hydrogen bond	Methyl hydrogen with Asp219.
7b	−6.41	0.0	20.03	Hydrogen bond	Amine with Tyr155 and ether oxygen with Asp219
9	32.66	0.0	0.0	Unfavorable bumps	Multiple bumps

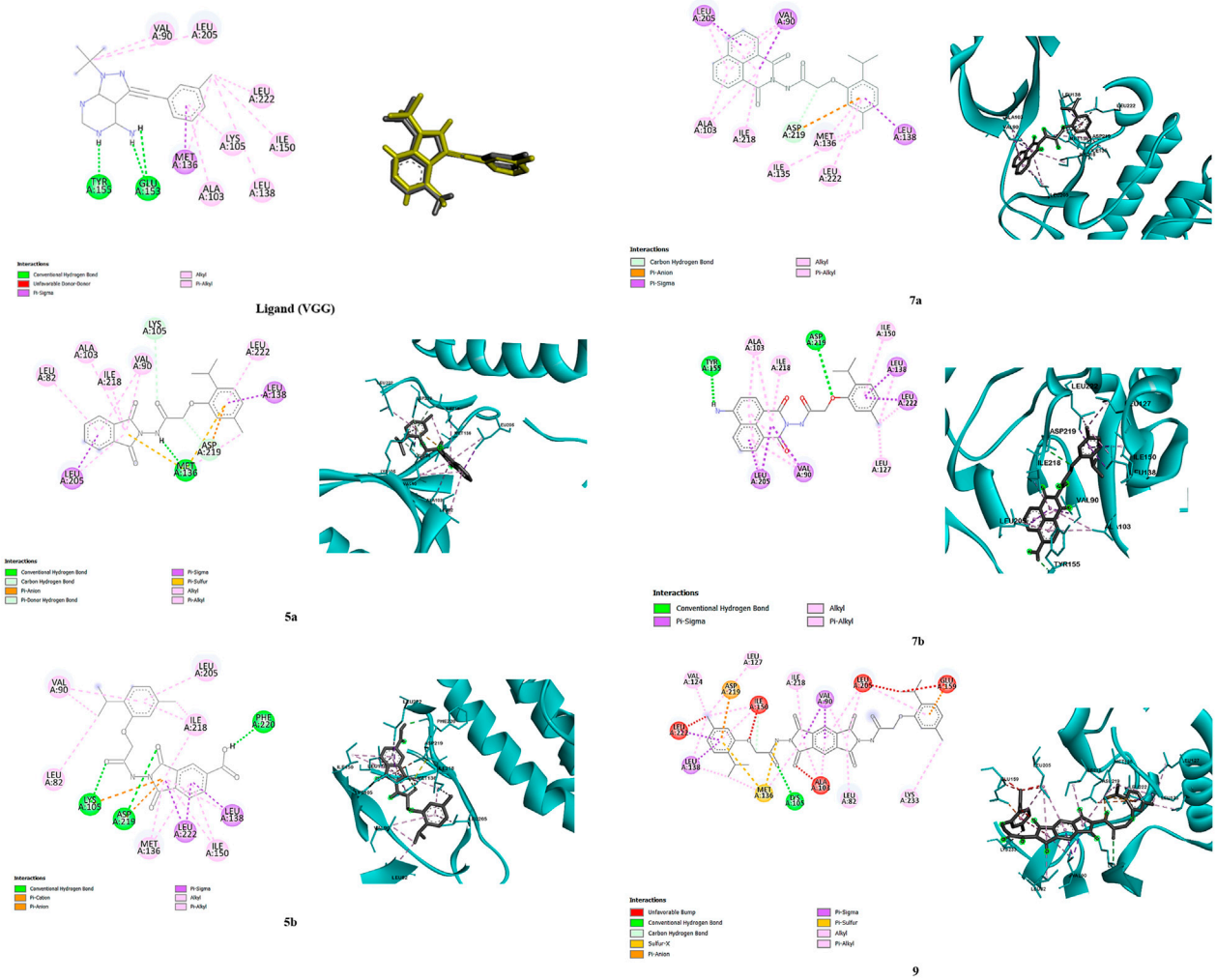


FIGURE 1
Binding poses of compounds **5a**, **5b**, **7a**, **7b**, and **9**, and ligand (VGG) in the 2WEI active site (2D and 3D representations).

showed the lowest antiparasitic activities, correlated with their poorer docking scores and weaker binding interactions within the active site. These findings underscore the critical role of stable binding interactions, particularly with key residues, and favorable pharmacokinetic profiles in achieving potent *in vivo* activity, thereby highlighting compound 7b as a promising candidate for further drug development.

10.3389/fchem.2025.1579923

TABLE 3 *In vitro* hemolytic activity and IC_{50} values (cytotoxicity on RBCs).

Concentration (µg/mL)	Hemolysis %				
	5a	7a	5b	7b	9
62.5	0	0	0	0	0
125	0	0	0	0	0
250	0	0	0	0	0
500	0	5.0167	0	0	0
1,000	0	6.1873	0	0	34.95
IC $_{50}$ (µg/mL)	ND	6754.9	ND	ND	1,556.6

IC_{50} (µg/mL): sample concentration causing 50% hemolysis of RBCs. ND, not determined.

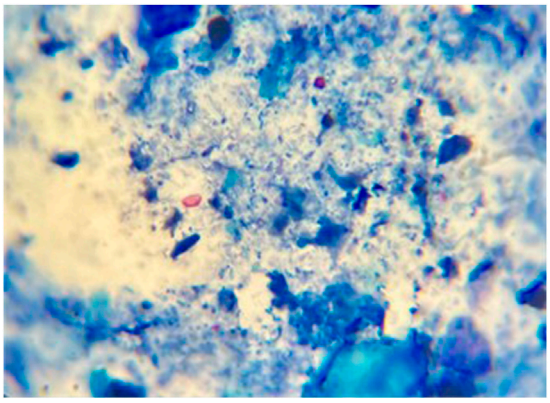


FIGURE 2
Fecal smear stained with modified Ziehl–Neelsen stain, showing *Cryptosporidium* oocysts (black arrows). Magnification: 1,000×.

2.4 Biological evaluation

2.4.1 Cytotoxic effects on red blood cells (RBCs)

The *in vitro* cytotoxic effects of the newly synthesized compounds on RBCs were assessed through hemolytic activity. The hemolysis percentages at 1,000 µg/mL were zero for **5a**, **5b**, and **7b**; 6.18% for **7a**; and 34.95% for **9** (Table 3).

2.4.2 Parasitological results

Using the modified Ziehl–Neelsen staining technique, oocysts were identified as bright-pink oval or round structures against a bluish background (Figure 2).

Table 4 indicates significant statistical differences among all groups. The mean oocyst count in the infected, non-treated group (G2) was 34.4 ± 0.69, while the corresponding value in the nitazoxanide (NTZ)-treated group was 10.4 ± 0.51, indicating the highest reduction in oocyst count. Among the tested compounds, the **7b**- and **7a**-treated groups exhibited the highest (67%) and lowest (51%) percentage reduction in the oocyst count, respectively.

2.4.2.1 Ultrastructural analysis

Scanning electron microscopy (SEM) was used to evaluate the ultrastructural morphological features of oocysts in fecal samples for each group. Oocysts from the control group exhibited a uniform spherical shape with smooth cyst surfaces. In contrast, cysts extracted from treated mice exhibited varying degrees of morphological changes (Figure 3).

2.4.2.2 Transmission electron microscopy (TEM)

TEM images (Figure 4) of ultrathin sections of small intestinal epithelial cells from the non-infected, non-treated control group revealed typical prominent microvilli, regular euchromatic nuclei, and well-developed cell junctions. In contrast, all treated groups revealed different levels of

TABLE 4 Number of *Cryptosporidium*-oocyst-shedding immunosuppressed mice in different study groups.

Shed oocysts/mg	G2	G3	G 4	G5	G6	G7	G8	F	P
Mean ± SD	34.4 ± 0.69	10.4 ± 0.51	13.2 ± 1.034	14.7 ± 0.67	16.8 ± 0.63	11.5 ± 0.85	15.4 ± 0.52	389.597	0.000
(R%)		70%	62%	57%	51%	67%	55%		
P within groups		P_1 0.000**	P_2 0.000**	P_3 0.000**	P_4 0.000**	P_5 0.000**	P_6 0.000**		
			P_7 0.004*	P_8 0.000**	P_9 0.000**	P_{10} 0.519^{ns}	P_{11} 0.000**		
				P_{12} 0.022*	P_{13} 0.000**	P_{14} 0.011*	P_{15} 0.002*		
					P_{16} 0.003*	P_{17} 0.000**	P_{18} 0.250^{ns}		
						P_{19} 0.000**	P_{20} 0.031*		
							P_{21} 0.000**		

F: One-way ANOVA, test.
P_1: G2 vs G3, P_2: G2 vs G4, P_3: G2 vs G5, P_4: G2 vs G6, P_5: G2 vs G7, P_6: G2 vs G8, P_7: G3 vs G4, P_8: G3 vs G5, P_9: G3 vs G6, P_{10}: G3 vs G7, P_{11}: G3 vs G8, P_{12}: G4 vs G5, P_{13}: G4 vs G6, P_{14}: G4 vs G7, P_{15}: G4 vs G8, P_{16}: G5 vs G6, P_{17}: G5 vs G7, P_{18}: G5 vs G8, P_{19}: G6 vs G7, P_{20}: G6 vs G8 and P_{21}: G7 vs G8.
R%: reduction percent in oocyst count.
Ns not significant, * significant at $p < 0.05$, ** significant at $p < 0.001$.

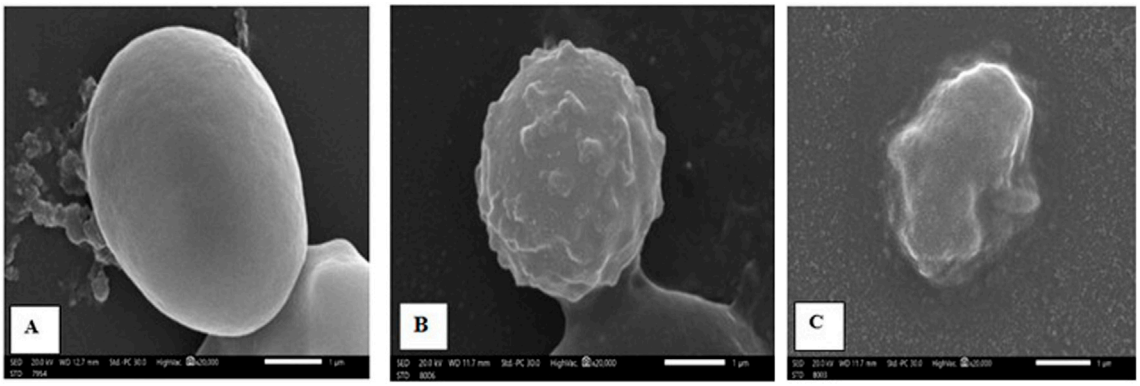


FIGURE 3
Scanning electron micrography images of *Cryptosporidium* oocysts from the **(A)** infected control group (G2), displaying a spherical shape with an extremely smooth surface; **(B)** NTZ-treated group (G3), showing rough, irregular surfaces with bleb formation; and **(C) 7b**-treated group, exhibiting complete distortion with irregular shapes and outlines.

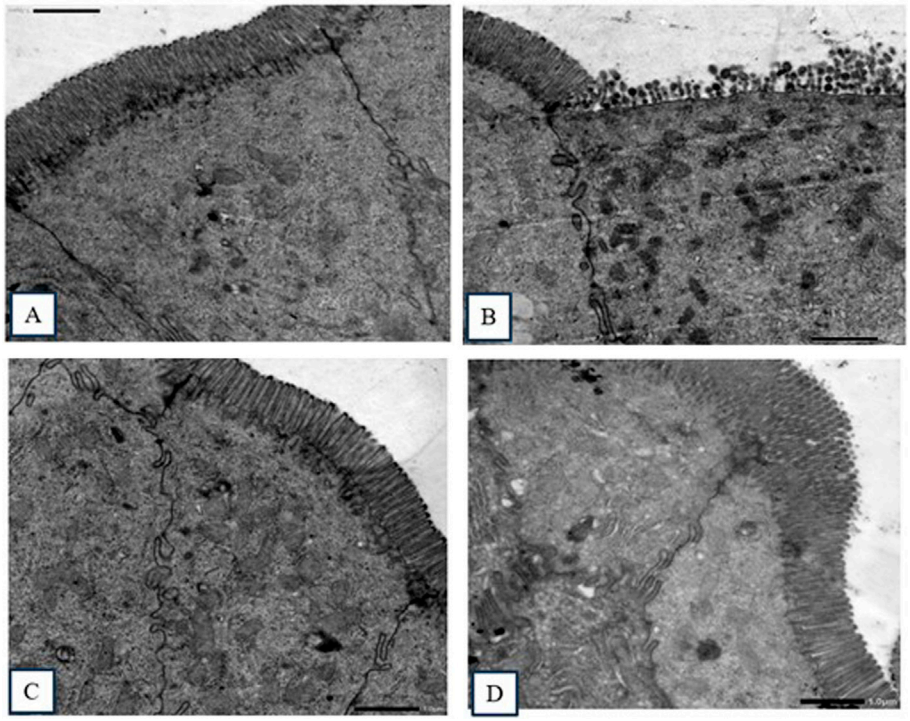


FIGURE 4
Transmission electron micrography images of sections in the small intestine. **(A)** Non-infected, non-treated group, showing intestinal columnar epithelial cells with normal prominent microvilli and well-developed cell junctions. **(B)** Infected, non-treated group, showing ileal epithelial cells with significantly damaged epithelial lining and distorted and blunted microvilli. **(C)** NTZ-treated group, showing normal ultrastructure and regularly arranged apical microvilli with oval euchromatic nuclei. **(D) 7b**-treated group, showing healthy microvilli (slightly disfigured and disarranged).

abnormalities, ranging from slight disarrangement to completely damaged atrophied microvilli.

2.4.3 Biochemical measurements

Biochemical parameter levels were significantly increased in the infected, non-treated control group compared with the negative control group. All treated groups showed significant changes in the biochemical parameter levels compared with the positive control group (Table 4).

2.4.4 Immunological measurements

In the serum cytokine analysis (Table 5), the levels of interferon-gamma (IFN-γ), tumor necrosis factor-alpha (TNF-α), interleukin-6 (IL-6), and interleukin-10 (IL-10) were significantly higher ($P < 0.001$) in the infected control group compared with the negative control group. The mean levels of IFN-γ, IL-6, and IL-10 were significantly reduced ($P < 0.001$) in the treated groups compared with the infected control group (Table 6).

TABLE 5 Cytokine levels in mice groups.

Group	TNF-α (pg/mL)	IFN-γ (pg/mL)	IL-6 (pg/mL)	IL-10 (pg/mL)
G1	9.3 ± 0.94	342.5 ± 4.16	88.1 ± 0.87	253.4 ± 1.17
G2	33.25 ± 0.79	717.4 ± 2.67	260.5 ± 0.70	397.4 ± 1.42
G3	7.8 ± 0.91	422.1 ± 3.21	111.4 ± 1.17	276.5 ± 0.97
G4	13.1 ± 0.99	477.8 ± 1.61	176.8 ± 0.91	327.6 ± 1.34
G5	13.7 ± 1.25	494.2 ± 3.15	181.7 ± 149	387.8 ± 0.78
G6	15.9 ± 0.87	608.8 ± 2.48	237.4 ± 2.23	434.2 ± 1.13
G7	11.8 ± 1.03	415.2 ± 2.57	143.1 ± 1.1	277.2 ± 1.47
G8	16.2 ± 1.03	534.2 ± 1.26	215.7 ± 1.15	416.8 ± 0.63
F	165.828*	1,232.828*	736.518*	1,224.031*
P	<0.001*	<0.001*	<0.001*	<0.001*

F, One-way ANOVA *P value < 0.05 significant.

TABLE 6 Biochemical analysis of mice groups.

Group	ALT (U/L)	AST (U/L)	Urea (mg/dL)	Creatinine (mg/dL)	Total protein (g/dL)	Albumin (g/dL)
G1	8.11 ± 0.61	25 ± 0.56	19 ± 0.89	0.15 ± 0.93	2.32 ± 1.21	4.1 ± 1.32
G2	14.35 ± 0.63	68.32 ± 0.85	41.42 ± 0.98	0.69 ± 0.39	2.62 ± 0.96	5.16 ± 1.11
G3	25.69 ± 0.92	86.36 ± 0.81	22.59 ± 0.93	1.26 ± 0.73	2.33 ± 0.68	4.56 ± 0.71
G4	24.6 ± 1.22	97.55 ± 0.55	26.45 ± 0.51	1.36 ± 0.14	2.46 ± 0.43	4.63 ± 0.93
G5	23.58 ± 0.08	94.63 ± 0.26	24.33 ± 0.38	1.52 ± 0.45	2.49 ± 1.22	4.87 ± 1.12
G6	39.68 ± 0.82	130.5 ± 0.67	45.34 ± 0.36	1.76 ± 0.36	2.4 ± 0.62	4.8 ± 0.84
G7	21.53 ± 0.31	95.63 ± 1.63	25.3 ± 0.92	0.96 ± 0.71	2.53 ± 0.64	4.74 ± 0.38
G8	30.21 ± 0.64	105.96 ± 0.81	35.85 ± 0.63	1.46 ± 0.33	2.32 ± 0.47	4.66 ± 0.41
F	122.815	667.930	597.905	136.462	321.651	14.631
P	<0.001*	<0.001*	<0.001*	<0.001*	<0.001*	<0.001*

F, One-way ANOVA, *P value < 0.05 significant.

2.5 DFT study

2.5.1 Geometrical structure

Compounds **5a**, **5b**, **7a**, **7b**, and **9** were theoretically examined using DFT calculations. Gauss View 6.016 (Dennington et al., 2016) was used to draw the molecular structures. Computations were performed in the gas phase using Gaussian 09 Revision D.01 software, (Caricato et al., 2009), adopting the DFT/B3LYP method at a 6–311 g basis set.

This method facilitated the optimization of the molecular geometry to determine the lowest energy and most stable structures, commonly referred to as convergence. In addition, a frequency process was applied to the optimized structures using the same basis sets to compute their thermodynamic parameters. The absence of imaginary frequencies confirmed the stability of the optimized compounds, and all synthesized compounds displayed non-coplanar structures. The optimized compounds are presented in Figure 5.

2.5.2 Polarizability and dipole moment

Molecular polarizability refers to the degree to which the electron cloud of a molecule can be distorted by an external charge, leading to the development of an electric dipole moment. (Katariya et al., 2024). The electronic nature and polarity of terminal substituents considerably affect the polarizability and dipole moment of the compound. (Soni et al., 2024). The calculated polarizability values for the investigated compounds are presented in Table 7.

Dipole moment calculations were conducted along the x, y, and z axes. It is observed that **5a** which contains only one phthalimide ring has a very low dipole moment. Meanwhile, **5b** and **7b**. have higher dipole moment values due to the presence of COOH and NH_2 groups.

2.5.3 MEP mapping

MEP mapping serves as a valuable tool for assessing electron density and charge distribution in a molecule, enabling the prediction of intermolecular and intramolecular interactions, as well as the extent of molecular packing and formal and partial charge of atoms. (Butera, 2024).

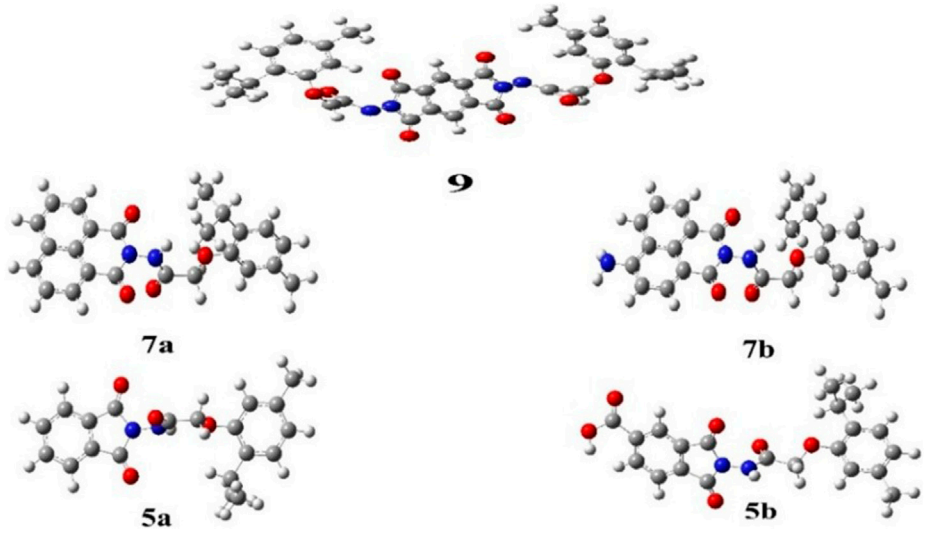


FIGURE 5
Optimized geometrical structures of synthesized phenoxy acetamide derivative compounds **5a**, **5b**, **7a**, **7b**, and **9** (gray, carbon; white, hydrogen; red, oxygen, and blue, nitrogen).

TABLE 7 Calculated polarizability (a.u.) and dipole moment (Debye) of compounds 5a, 5b, 7a, 7b, and 9.

Compound	Dipole moment				Polarizability
	X	Y	Z	Total	
5a	−0.4286	−0.7157	−1.9086	2.0830	244.40
5b	−0.6944	−6.1862	0.1809	6.2277	265.59
7a	−3.0859	1.4869	1.3867	3.6955	295.54
7b	5.5612	0.8400	−0.9210	5.6992	310.61
9	−1.9875	3.3012	1.8926	4.2930	484.64

Following the same basis set, charge distribution maps for all compounds were derived. In the maps, regions of electron density were illustrated in ascending order: red > orange > yellow > green > blue. Specifically, regions with high electronegativity appeared in red, whereas regions with the least negative charge appeared in blue. (Politzer and Murray, 2021).

All synthesized compounds (**5a**, **5b**, **7a**, **7b**, and **9**) exhibited a high negative charge in the center regions owing to the presence of acetamide and phthalimide groups, each contributing a half-negative charge on their oxygen atoms. In compound **5b**, the highest negative charge was localized on the oxygen atom of the COOH group. The MEP maps are shown in Figure 6.

2.5.4 FMO analysis

FMOs refer to the highest occupied molecular orbital (HOMO), which donates electrons, and the lowest unoccupied molecular orbital (LUMO), which accepts electrons (Figure 7). These orbitals are essential for studying the reactivity of molecules, as they can be used to predict the electron transfer and excitation processes between orbitals based on the energy gap between HOMO and LUMO. As the energy gap widens, excitation energy rises, while reactivity falls (Tanaka, 2024).

Several physical parameters can be calculated from FMOs using the same computational method and basis sets. These parameters include the energy gap [$(\Delta E) = (E_{LUMO}–E_{HOMO})$], hardness [$(\eta) = (E_{LUMO}–E_{HOMO})/2$], softness [$(S) = 1/(E_{LUMO}–E_{HOMO})$], electronegativity [$(X) = (–E_{HOMO}–E_{LUMO})/2$], electronic chemical potential [$(\mu) = –X$], and fractional number of electrons transferred [$(\Delta N) = - \mu/\eta$]. The results of FMO reactivity descriptors are summarized in Table 8.

Softness indicates the sensitivity of the π-electron cloud of a molecule to potential disruptions from chemical processes. Consequently, the electronic characteristics of terminal substituents may influence softness. (Ahmed et al., 2020). For example, compounds **5b** and **9** exhibited higher softness values owing to the presence of the COOH group in **5b** and high molecular weight of compound **9**. Moreover, the electronegativity and fractional number of electrons transferred were greater in **9** than those in the other compounds, attributable to the higher electron density in this compound.

3 Materials and methods

3.1 Materials and equipment

Details regarding the materials and equipment characterization are provided in the Supplementary Material.

3.2 General procedure for condensation

A mixture containing 2-(2-isopropyl-5-methylphenoxy) acetohydrazide (**3**) (0.01 mol) and different acid anhydrides (0.01 mol), i.e., phthalic anhydride (**4a**), 1,2,4-benzene tricarboxylic acid anhydride (**4b**), 1,8-naphthalic anhydride (**6a**), 4-amino-1,8-naphthalic anhydride (**6b**), and pyromellitic dianhydride (**8**) in 15 mL DMF and a few drops of glacial acetic acid was refluxed for 4–6 h. The excess solvent was removed under reduced pressure, and the residue was poured into cold water (200 mL). The obtained solid was filtered and crystallized from ethanol to yield compounds **5a**, **5b**, **7a**, **7b**, and **9**.

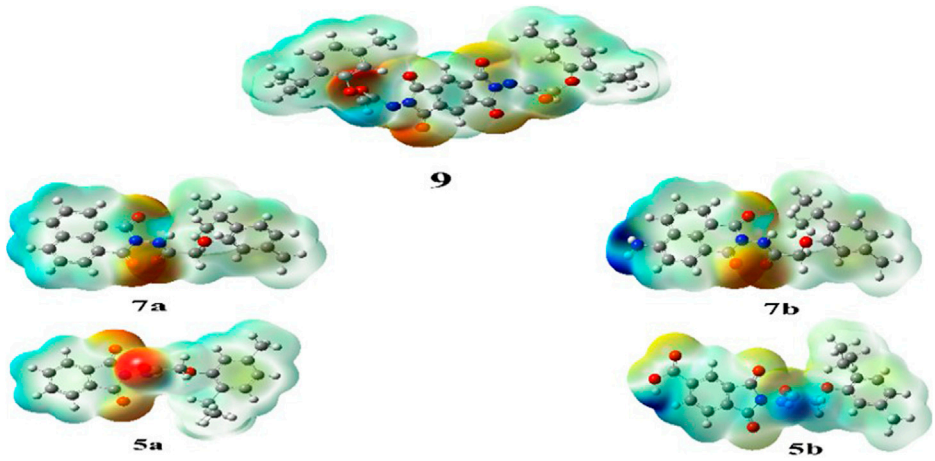


FIGURE 6
Molecular electrostatic potential (MEP) maps of synthesized compounds.

3.2.1 *N*-(1,3-dioxoisoindolin-2-yl)-2-(2-isopropyl-5-methylphenoxy)acetamide (5a)

Compound **5a** as white crystals (79% yield); R_f = 0.44 (n-hexane: ethyl acetate, 1:2, V/V); m.p = 148°C–150°C; IR(KBr) ν_{max} (cm^{-1}): 3427 (NH), 2955 (CH), 1792, 1744 (C=O, conjugated anhydride) observed as strong bands; ^{1}H-NMR (500 MHz, DMSO-d_6) δ_H: 10.86 (s, 1H, **NH**), 7.95 (d, *J* = 2.5 Hz, 2H, Ar-H), 7.91 (d, *J* = 3.0 Hz, 2H, Ar-H), 7.07 (d, *J* = 7.5 Hz, 1H, Ar-H), 6.79 (s, 1H, Ar-H), 6.75 (d, *J* = 7.0 Hz, 1H, Ar-H), 4.80 (s, 2H, **CH_2**), 3.23 (m, 1H, **CH**), 2.27 (s, 3H, **CH_3**), 1.13 (d, *J* = 6.5 Hz, 6H, **CH_3**-CH-**CH_3**); ^{13}C-NMR (125 MHz, DMSO- d_6) δ_C: 168.4, 165.5, 156.3 (C=O, amide), 136.5, 135.9, 134.1, 129.9, 126.3, 124.3, 122.6, 113.7 (Ar-**C**), 66.8 (OCH_2), 26.2, 23.3, 21.4; Anal. calculated for $C_{20}H_{20}N_2O_4$: C, 68.17; H, 5.72; N, 7.95; Found: C, 67.94; H, 5.59; N, 8.02.

3.2.2 2-(2-(2-Isopropyl-5-methylphenoxy) acetamido)-1,3-dioxoisoindoline-5-carboxylic acid (5b)

Compound **5b** as yellowish-white crystals (80% yield); R_f = 0.48 (n-hexane:ethyl acetate, 1:3, V/V); m.p = 190°C–192°C; IR(KBr) ν_{max} (cm^{-1}): 3358 (NH), 3420 cm^{-1} (OH), 1773, 1732 (C=O, conjugated anhydride) observed as strong bands; ^{1}H-NMR (500 MHz, DMSO-d_6) δ_H: 10.99 (bs, 1H, **COOH**), 10.13 (bs, 1H, **NH**), 8.41 (d, *J* = 3.0 Hz, 1H, Ar-H), 8.32 (d, *J* = 1.5 Hz, 1H, Ar-H), 8.07 (s, 1H, Ar-H), 7.42–6.91 (m, 1H, Ar-H), 6.74–6.28 (m, 2H, Ar-H), 4.80 (m, 2H, **CH_2**), 3.31 (m, 1H, **CH**), 2.23 (s, 3H, **CH_3**), 1.13 (s, 6H, **CH_3**-CH-**CH_3**); ^{13}C-NMR (125 MHz, DMSO-d_6) δ_C: 168.4 (COOH), 167.6, 164.8, 155.4 (C=O, amide), 136.5, 136.4, 134.1, 130.3, 126.2, 126.1, 124.8, 124.3, 122.6, 122.2, 113.6, 113.4 (Ar-**C**), 66.8 (OCH_2), 26.2, 23.3, 21.4; Anal. calculated for $C_{21}H_{20}N_2O_6$: C, 63.63; H, 5.09; N, 7.07; Found: C, 63.52; H, 4.97; N, 7.19.

3.2.3 *N*-(1,3-dioxo-*1H*-benzo[*de*]isoquinolin-2(*3H*)-yl)-2-(2-isopropyl-5-methylphenoxy) acetamide (7a)

Compound **7a** as off-white crystals (82% yield); R_f = 0.52 (n-hexane:ethyl acetate, 1:3, V/V); m.p = 198°C–200°C; IR(KBr) ν_{max} (cm^{-1}): 3191 (NH), 2961 (CH), 1773, 1732 (C=O, conjugated anhydride) observed as strong bands; ^{1}H-NMR (500 MHz, DMSO-d_6) δ_H: 10.89 (s, 1H, **NH**), 8.52 (d, *J* = 7.5 Hz, 2H, Ar-H), 8.48 (d, *J* = 7.5 Hz, 2H, Ar-H), 7.87 (t, *J* = 7.5 Hz, 2H, Ar-H), 7.06 (d, *J* = 7.5 Hz, 1H, Ar-H), 6.90 (s, 1H, Ar-H), 6.75 (d, *J* = 7.5 Hz, 1H, Ar-H), 4.81 (s, 2H, **CH_2**), 3.34 (m, 1H, **CH**), 2.30 (s, 3H, **CH_3**), 1.14 (d, *J* = 7.0 Hz, 6H, **CH_3**-CH-**CH_3**); ^{13}C-NMR (125 MHz, DMSO-d_6) δ_C: 167.8, 162.1, 155.4 (C=O, amide), 136.5, 135.9, 135.8, 134.1, 132.9, 132.1, 128.1, 127.9, 127.7, 126.2, 122.5, 122.1, 113.8 (Ar-**C**), 66.9 (OCH_2), 26.2, 23.3, 21.5; Anal. calculated for $C_{24}H_{22}N_2O_4$: C, 71.63; H, 5.51; N, 6.96; Found: C, 71.54; H, 5.42; N, 7.01.

3.2.4 *N*-(6-amino-1,3-dioxo-*1H*-benzo[*de*] isoquinolin-2(*3H*)-yl)-2-(2-isopropyl-5-methylphenoxy)acetamide (7b)

Compound **7b** as pale yellow crystals (84% yield); R_f = 0.54 (n-hexane:ethyl acetate, 1:3, V/V); m.p = 290°C–292°C; IR(KBr) ν_{max} (cm^{-1}): 3436, 3350 (NH_2), 3191 (NH), 1740, 1,698 (C=O, conjugated anhydride) observed as strong bands; ^{1}H-NMR (500 MHz, DMSO-d_6) δ_H: 10.09 (s, 1H, **NH**), 8.61 (d, *J* = 8.5 Hz, 1H, Ar-H), 8.35 (d, *J* = 7.0 Hz, 1H, Ar-H), 8.11 (d, *J* = 7.5 Hz, 1H, Ar-H), 7.71 (s, 2H, **NH_2**), 7.60 (t, *J* = 7.0 Hz, 1H, Ar-H), 7.01 (d, *J* = 7.0 Hz, 1H, Ar-H), 6.81 (d, *J* = 7.5 Hz, 2H, Ar-H), 6.71 (s, 1H, Ar-H), 4.54 (s, 2H, **CH_2**), 2.84 (m, 1H, **CH**), 2.19 (s, 3H, **CH_3**), 1.10 (s, 6H, **CH_3**-CH-**CH_3**); ^{13}C-NMR (125 MHz, DMSO-d_6) δ_C: 162.5, 160.8, 154.4 (C=O, amide), 136.4, 134.1, 133.5, 133.0, 131.3, 131.2, 126.1, 124.8, 122.3, 119.7, 118.7, 113.4, 109.2 (Ar-**C**), 102.6 (CNH_2), 66.8 (OCH_2), 26.1, 23.3, 21.4; Anal. calculated for $C_{24}H_{23}N_3O_4$: C, 69.05; H, 5.55; N, 10.07; Found: C, 68.85; H, 5.43; N, 10.19.

3.2.5 *N,N′*-(1,3,5,7-tetraoxopyrrolo[3,4-*f*] isoindole-2,6(*1H,3H,5H,7H*)-diyl)bis(2-(2-isopropyl-5-methylphenoxy)acetamide) (9)

Compound **9** as yellowish-white crystals (85% yield); R_f = 0.44 (n-hexane:ethyl acetate, 1:3, V/V); m.p > 300°C; IR(KBr) ν_{max} (cm^{-1}): 3358 (NH), 2962 (CH), 1744, 1715 (C=O, conjugated anhydride) observed as strong bands; ^{1}H-NMR (500 MHz, DMSO-d_6) δ_H: 11.96 (s, 1H, **NH**), 11.03 (s, 1H, **NH**), 8.45

10.3389/fchem.2025.1579923

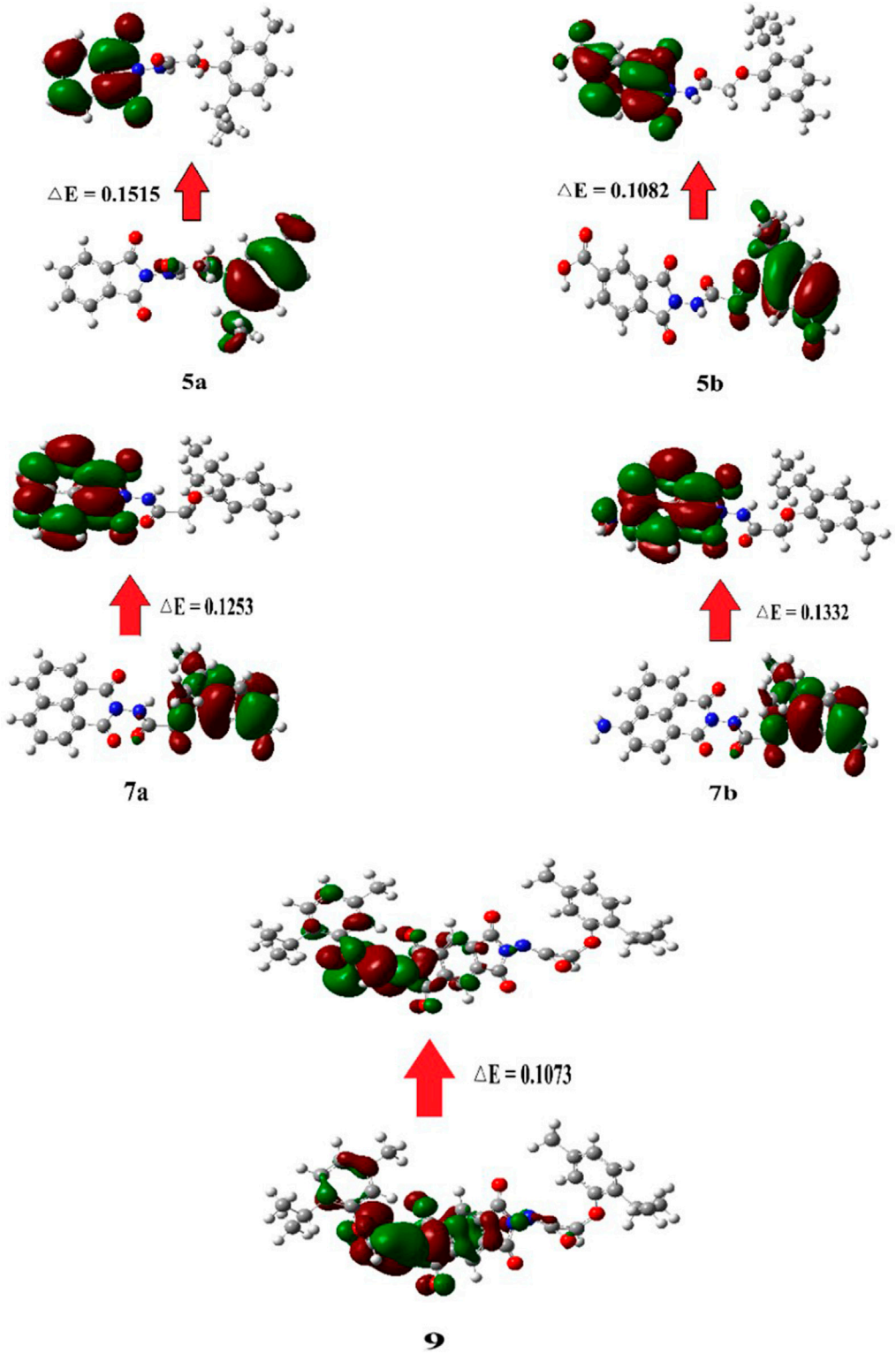


FIGURE 7
Graphical representation of the frontier molecular orbitals (FMOs) of compounds **5a**, **5b**, **7a**, **7b**, and **9**.

(s, 1H, pyromellitic-H), 8.29 (s, 1H, pyromellitic-H), 7.07–6.59 (m, 6H, Ar-H), 4.82 (s, 4H, 2**CH$_2$**), 3.07 (m, 2H, 2**CH**), 2.27 (s, 6H, 2**CH$_3$**), 1.13 (d, J = 6.5 Hz, 12H, 2**CH$_3$**-CH-**CH$_3$**); ^{13}C-NMR (125 MHz, DMSO-d_6) δ_C: 168.3, 166.8, 163.9, 163.8, 155.2 (C=O, amide), 138.4, 136.5, 135.7, 135.6, 134.9, 134.1, 126.3, 122.6, 119.7, 118.5, 118.4, 113.6, 113.5 (Ar-**C**), 66.7, 66.6 (OCH$_2$), 26.3, 24.8, 23.3, 23.2, 21.5, 21.3; Anal. calculated for $C_{34}H_{34}N_4O_8$: C, 65.17; H, 5.47; N, 8.94; Found: C, 65.02; H, 5.34; N, 9.01.

TABLE 8 FMO energies (eV), energy difference (eV), and corresponding parameters of investigated compounds.

Compound	E_{HOMO}	E_{LUMO}	ΔE	η	S = 1/η	X	μ = - X	ΔN = -μ/η
5a	−0.2423	−0.0909	0.1515	0.0757	13.2031	0.1666	−0.1666	2.1995
5b	−0.2239	−0.1157	0.1082	0.0541	18.4860	0.1698	−0.1698	3.1381
7a	−0.2260	−0.1008	0.1253	0.0626	15.9681	0.1634	−0.1634	2.6094
7b	−0.2232	−0.0900	0.1332	0.0666	15.0161	0.1566	−0.1566	2.3519
9	−0.2329	−0.1256	0.1073	0.0537	18.6393	0.1793	−0.1793	3.3418

3.3 *In silico* physicochemical and pharmacokinetic predictions

The method of ADMET study is provided in the Supplementary Material.

3.4 *In silico* molecular docking

The method of *In silico* Molecular Docking study is provided in the Supplementary Material.

3.5 Biological evaluation

3.5.1 Hemolytic activity assay

The hemolytic effect of different compounds was evaluated using an existing method. (Diaconu et al., 2020). One milliliter of rat blood was collected, added to a sterile, screw-top EDTA tube, and centrifuged at 3000 rpm for 20 min. The upper layer was decanted, and the erythrocytes were rinsed several times with 10 mL of cooled isotonic and sterile phosphate-buffered saline (PBS) with a pH of 7.4. The rinsed cells were re-suspended in 20 mL sterile, cold PBS. The compounds (serial dilutions of 62.5–1,000 μg/mL in DMSO) were added to the erythrocyte solution and incubated for 60 min at 37°C. After centrifugation at 3000 rpm for 10 min, the absorbance of hemoglobin in the supernatant at 540 nm was used to calculate the hemolysis rate. Triton X-100 (0.1% in PBS) was used as a positive control, and the vehicle (PBS/DMSO) was used as the negative control. The hemolysis percentage was calculated as follows: Hemolysis percentage = (Ab of sample − Ab of negative control)/(Ab of positive control–Ab of negative control) × 100.

3.5.2 Drugs

NTZ was orally administered as a reference drug at a dose of 250 mg/kg/d for 10 successive days, starting from the 7th day of infection. (Fahmy et al., 2021).

3.5.3 Preparation of *Cryptosporidium* oocysts

Cryptosporidium oocysts were obtained from the Parasitology Lab, Theodor Bilharz Research Institute, Giza, Egypt. Before infection, the oocysts were concentrated and counted in PBS using a hemocytometer. To maintain the organism cycle, five mice were inoculated with 3000–3500 oocysts using a tuberculin syringe in an intra-esophageal manner. (Operario et al., 2015).

3.5.4 Experimental animals

Eighty healthy laboratory-bred adult male Swiss albino mice weighing 30–40 g were purchased from the animal house of the Faculty of Pharmacy, Pharos University. The animals were allowed to acclimatize for 1 week to the environmental conditions and housed in grouped plastic cages away from direct sunlight, under appropriate sanitary conditions and controlled temperature and humidity.

3.5.5 Immunosuppression

Immune suppression was induced and maintained throughout the experiment by administering dexamethasone (Dexazone, Al Kahira Pharmaceutical and Chemical Industries) through oral-gastric gavage at a dose of 0.25 mg/g/d for 14 consecutive days prior to inoculation with *Cryptosporidium* oocysts. (Najoom et al., 2021).

3.5.6 Infection

On day 15 of dexamethasone treatment, mice in the infected groups were inoculated with 10^4 *Cryptosporidium* oocysts using oral-gastric gavage. Before infection, oocysts were concentrated and counted in PBS using a hemocytometer.

3.5.7 Study design

Mice were distributed equally into eight groups of 10 each. At the end of the experiment, all animals were anesthetized for parasitological, ultrastructural, immunological, and biochemical studies. Mice grouping details are provided in the Supplementary Material.

3.5.8 Parasitological examination

On the final day of the experiment (30 days post infection), fresh fecal pellets from the infected mice in each group were collected to count the number of oocysts. Every sample was homogenized through suspension in double-distilled H_2O. Subsequently, a fecal smear of 1 mg feces was prepared and stained using the modified Ziehl–Neelsen staining method. The stained fecal smear was examined microscopically, and the *Cryptosporidium* oocysts were counted. The number of oocysts per mg feces for each mouse was tabulated as the mean value for each group. All reported data represent the means of three independent trials.

3.5.9 Ultrastructural analysis

3.5.9.1 SEM

Fecal samples from each group were harvested in a 2.5% glutaraldehyde solution and examined using a scanning electron

microscope (Hassan et al., 2023) to detect morphological changes. An aliquot (20 μL) of dispersed flow cell biofilm sample was fixed in an equal volume of 5.0% glutaraldehyde in sterile 1× PBS. The samples were immobilized and attached to 0.01% poly-L-lysine (Sigma, USA) coated round coverslips (12 mm) and subjected to high-resolution imaging using an in-lens secondary electron detector at an accelerating voltage of 3 kV (Zeiss 55 VP field-emission SEM).

3.5.9.2 TEM

The small intestine of each mouse was removed, cut into small pieces (1 mm^3), fixed in 2% glutaraldehyde in 0.1 M phosphate buffer, postfixed in 1% osmium tetraoxide for 2 h at 4°C, dehydrated, and embedded in Epon. Semi-thin and ultrathin sections (two samples per mouse) were prepared using an ultramicrotome. The sections were stained and analyzed using a transmission electron microscope.

3.5.9.3 Biochemical measurements

Blood samples were collected from each group, transferred into tubes, and centrifuged at 3000 rpm for 5 min. The clear, non-hemolyzed supernatant serum was separated into clean tubes and stored at −20°C until use. Alanine aminotransferase (ALT) and aspartate aminotransferase (AST) levels were determined using commercially available spectrophotometric diagnostic kits (Sigma-Aldrich) according to the manufacturer instructions.

3.5.9.4 Immunological measurements

Serum concentrations of IFN-γ, TNF-α, IL-6, and IL-10 for each group were determined using an enzyme-linked immunosorbent assay reader, following the manufacturer's protocol.

3.5.9.5 Statistical analysis

The results were calculated, tabulated, and statistically analyzed using the statistical computer program SPSS version 24 (Windows 10). Data were expressed as mean ± standard deviation (SD). Differences between groups were determined using a one-way analysis of variance (ANOVA) to compare one variable across groups. The level of significance was defined as $P < 0.05$.

3.5.9.6 Ethics approval

The experiments were performed in accordance with the guidelines of the Institutional Animal Care and Use Committee (IACUC) at the Faculty of Medicine, Alexandria University (AU 04/24/12/30/3/03) as well as the Animal Research: Reporting of *In Vivo* Experiments (ARRIVE) guidelines. The mice anesthetized through intraperitoneal injections of ketamine hydrochloride (100 mg/kg) and xylazine (10 mg/kg).

5 Conclusion

This study reports the design and synthesis of novel phenoxy acetamide derivatives (**5a**, **5b**, **7a**, **7b**, and **9**) based on a thymol moiety for target parasitological treatments. All synthesized compounds demonstrated a reduction in oocyst counts, with compound **7b** exhibiting the highest percentage reduction (67%). Moreover, all treated groups showed significant changes in the biochemical parameter levels compared with the positive control group. The mean serum levels of INF-γ, IL-6, and IL-10 were significantly reduced in all treated groups compared with the infected control group. DFT calculations indicated that compounds **5a**, **5b**, and **7b** exhibited a high energy gap between FMOs and high dipole moment values, which may be strongly correlated with their bioactivity. Therefore, compounds **5a**, **5b**, and **7b** represent promising candidates for the development of efficient antiparasitic drugs.

Data availability statement

The raw data supporting the conclusions of this article will be made available by the authors, without undue reservation.

Ethics statement

The present experiment was performed in accordance with the Animal Care and Use Committee at the Faculty of Medicine (Institutional Animal Care and Use Committee (IACUC) Alexandria University (AU 04/24/12/30/3/03). The study was conducted in accordance with the local legislation and institutional requirements.

Author contributions

AR: Methodology, Writing – original draft, Writing – review and editing. SM: Supervision, Writing – review and editing, Validation. HA-H: Supervision, Writing – review and editing. EA: Investigation, Writing – review and editing. SH: Investigation, Writing – review and editing. YH: Data curation, Writing – review and editing. AA: Formal Analysis, Writing – review and editing. DG: Data curation, Writing – review and editing. MJ: Funding acquisition, Writing – review and editing. A-HE: Funding acquisition, Writing – review and editing. MS: Software, Writing – review and editing. MH: Writing – original draft.

Funding

The author(s) declare that financial support was received for the research and/or publication of this article. Open access funding provided by The Science, Technology & Innovation Funding Authority (STDF) in cooperation with The Egyptian Knowledge Bank (EKB) with (ID 46267).

Conflict of interest

The authors declare that the research was conducted in the absence of any commercial or financial relationships that could be construed as a potential conflict of interest.

Generative AI statement

The author(s) declare that no Generative AI was used in the creation of this manuscript.

Publisher's note

All claims expressed in this article are solely those of the authors and do not necessarily represent those of their affiliated organizations, or those of the publisher, the editors and the reviewers. Any product that may be evaluated in this article, or claim that may be made by its manufacturer, is not guaranteed or endorsed by the publisher.

Supplementary material

The Supplementary Material for this article can be found online at: https://www.frontiersin.org/articles/10.3389/fchem.2025.1579923/full#supplementary-material

References

Ahmed, N. H., Saad, G. R., Ahmed, H. A., and Hagar, M. (2020). New wide-stability four-ring azo/ester/Schiff base liquid crystals: synthesis, mesomorphic, photophysical, and DFT approaches. *RSC Adv.* 10, 9643–9656. doi:10.1039/c9ra10499b

Akgün, H., Karamelekoğlu, İ., Berk, B., Kurnaz, I., Sarıbıyık, G., Öktem, S., et al. (2012). Synthesis and antimycobacterial activity of some phthalimide derivatives. *Bioorg. & Med. Chem.* 20, 4149–4154. doi:10.1016/j.bmc.2012.04.060

Alanazi, A. M., El-Azab, A. S., Al-Suwaidan, I. A., ElTahir, K. E. H., Asiri, Y. A., Abdel-Aziz, N. I., et al. (2015). Structure-based design of phthalimide derivatives as potential cyclooxygenase-2 (COX-2) inhibitors: anti-inflammatory and analgesic activities. *Eur. J. Med. Chem.* 92, 115–123. doi:10.1016/j.ejmech.2014.12.039

Aljohani, F. S., Rezki, N., Aouad, M. R., Elwakil, B. H., Hagar, M., Sheta, E., et al. (2022). Synthesis, characterization and nanoformulation of novel sulfonamide-1, 2, 3-triazole molecular conjugates as potent antiparasitic agents. *Int. J. Mol. Sci.* 23, 4241. doi:10.3390/ijms23084241

Al-Ostoot, F. H., Sherapura, A., V, V., Basappa, G., Hk, V., Bt, P., et al. (2021a). Targeting HIF-1α by newly synthesized Indolephenoxyacetamide (IPA) analogs to induce anti-angiogenesis-mediated solid tumor suppression. *Pharmacol. Rep.* 73, 1328–1343. doi:10.1007/s43440-021-00266-8

Al-Ostoot, F. H., Zabiulla, M., Salah, S., and Khanum, S. A. (2021b). Recent investigations into synthesis and pharmacological activities of phenoxy acetamide and its derivatives (chalcone, indole and quinoline) as possible therapeutic candidates. *J. Iran. Chem. Soc.* 18, 1839–1875. doi:10.1007/s13738-021-02172-5

Alves Eloy, M., Ribeiro, R., Martins Meireles, L., Antonio de Sousa Cutrim, T., Santana Francisco, C., Lirian Javarini, C., et al. (2021). Thymol as an interesting building block for promising fungicides against Fusarium solani. *J. Agric. Food Chem.* 69, 6958–6967. doi:10.1021/acs.jafc.0c07439

Arshad, M. F., Alam, A., Alshammari, A. A., Alhazza, M. B., Alzimam, I. M., Alam, M. A., et al. (2022). Thiazole: a versatile standalone moiety contributing to the development of various drugs and biologically active agents. *Molecules* 27, 3994. doi:10.3390/molecules27133994

Butera, V. (2024). Density functional theory methods applied to homogeneous and heterogeneous catalysis: a short review and a practical user guide. *Phys. Chem. Chem. Phys.* 26, 7950–7970. doi:10.1039/d4cp00266k

Capelini, C., de Souza, K. R., Barbosa, J. M., Salomão, K., Sales Junior, P. A., Murta, S. M., et al. (2021). Phenoxyacetohydrazones against trypanosoma cruzi. *Med. Chem. Res.* 30, 1703–1712. doi:10.1007/s00044-021-02768-9

Caricato, M., Frisch, M. J., Hiscocks, J., and Frisch, M. J. (2009). *Gaussian 09: IOps reference*. CT, USA: Gaussian Wallingford.

Chanh, T. C., Lewis, D. E., Judy, M. M., Sogandares-Bernal, F., Michalek, G. R., Utecht, R. E., et al. (1994). Inhibition of retrovirus-induced syncytium formation by photoproducts of a brominated 1,8-naphthalimide compound. *Antivir. Res.* 25, 133–146. doi:10.1016/0166-3542(94)90102-3

Chauhan, A. K., Bahuguna, A., Paul, S., and Kang, S. C. (2017). Thymol elicits HCT-116 colorectal carcinoma cell death through induction of oxidative stress. *Anti-Cancer Agents Med. Chem. Former. Curr. Med. Chemistry-Anti-Cancer Agents* 17, 1942–1950. doi:10.2174/1871520617666170327121228

Chauhan, A. K., and Kang, S. C. (2014). Thymol disrupts the membrane integrity of Salmonella ser. typhimurium *in vitro* and recovers infected macrophages from oxidative stress in an *ex vivo* model. *Res. Microbiol.* 165, 559–565. doi:10.1016/j.resmic.2014.07.001

Chen, J., Li, D.-L., Xie, L.-N., Ma, Y.-r., Wu, P.-P., Li, C., et al. (2020). Synergistic anti-inflammatory effects of silibinin and thymol combination on LPS-induced RAW264.7 cells by inhibition of NF-κB and MAPK activation. *Phytomedicine* 78, 153309. doi:10.1016/j.phymed.2020.153309

Clemente, C. M., Ravetti, S., Allemandi, D. A., Hergert, L. Y., Pineda, T., and Robledo, S. M. (2021). Synthesis, *in vitro* antiprotozoal activity and cytotoxicity of new thymol carbonate derivatives. *ChemistrySelect* 6, 6597–6600. doi:10.1002/slct.202101461

Cohen, S. (1984). *US Environmental Protection Agency, office of pesticide programs*. Pomerantz (Environmental Prot. Agency, Off, 5–13.

Dennington, R., Keith, T. A., and Millam, J. M. (2016). *GaussView, version 6.0. 16*. Semichem Inc Shawnee Mission KS.

Diaconu, M., Pavel, L. V., Hlihor, R.-M., Rosca, M., Fertu, D. I., Lenz, M., et al. (2020). Characterization of heavy metal toxicity in some plants and microorganisms—a preliminary approach for environmental bioremediation. *New Biotechnol.* 56, 130–139. doi:10.1016/j.nbt.2020.01.003

Dominguez-Uscanga, A., Aycart, D. F., Li, K., Witola, W. H., and Laborde, J. E. A. (2021). Anti-protozoal activity of Thymol and a Thymol ester against Cryptosporidium parvum in cell culture. *Int. J. Parasitol. Drugs Drug Resist.* 15, 126–133. doi:10.1016/j.ijpddr.2021.02.003

Dong, H., You, Y., Wang, N., Wang, M., Song, T., He, Y., et al. (2024). Development of amphipathic derivatives of thymol and carvacrol as potent broad-spectrum antibacterial agents. *Eur. J. Med. Chem.* 276, 116716. doi:10.1016/j.ejmech.2024.116716

Fahmy, M.-E. A., Abdelaal, A. A., Hassan, S. I., Shalaby, M. A., Ismail, M. A. M., Khairy, R. A., et al. (2021). Antiparasitic and immunomodulating effects of nitazoxanide, ivermectin and selenium on Cryptosporidium infection in diabetic mice. *Rev. Bras. Parasitol. Veterinária* 30, e012121. doi:10.1590/s1984-29612021087

Ghosh, P., Singha Roy, S., Basu, A., Bhattacharjee, A., and Bhattacharya, S. (2015). Sensitization of cisplatin therapy by a naphthalimide based organoselenium compound through modulation of antioxidant enzymes and p53 mediated apoptosis. *Free Radic. Res.* 49, 453–471. doi:10.3109/10715762.2015.1012079

González, M. A., Clark, J., Connelly, M., and Rivas, F. (2014). Antimalarial activity of abietane ferruginol analogues possessing a phthalimide group. *Bioorg. & Med. Chem. Lett.* 24, 5234–5237. doi:10.1016/j.bmcl.2014.09.061

Hassan, E. M., Soliman, S. M., Moneer, E. A., Hagar, M., Barakat, A., Haukka, M., et al. (2023). Synthesis, X-ray structure, hirshfeld, DFT conformational, cytotoxic, and anti-toxoplasma studies of new indole-hydrazone derivatives. *Int. J. Mol. Sci.* 24, 13251. doi:10.3390/ijms241713251

Hikal, W. M., Tkachenko, K. G., Said-Al Ahl, H. A., Sany, H., Sabra, A. S., Baeshen, R. S., et al. (2021). Chemical composition and biological significance of thymol as antiparasitic. *Open J. Ecol.* 11, 240–266. doi:10.4236/oje.2021.113018

Jyoti, D. D., Singh, D., Kumar, G., Karnatak, M., Chandra, S., Prakash Verma, V., et al. (2019). Thymol chemistry: a medicinal toolbox. *Curr. Bioact. Compd.* 15, 454–474. doi:10.2174/1573407214666180503120222

Kamal, A., Bolla, N. R., Srikanth, P. S., and Srivastava, A. K. (2013). Naphthalimide derivatives with therapeutic characteristics: a patent review. *Expert Opin. Ther. Pat.* 23, 299–317. doi:10.1517/13543776.2013.746313

Katariya, K., Soni, R., Nakum, K. J., Patel, D., Nada, S., and Hagar, M. (2024). New symmetric/unsymmetrical self-assembling salicylaldimine-chalcones: synthesis, photophysical study and DFT approach. *J. Mol. Struct.* 1295, 136610. doi:10.1016/j.molstruc.2023.136610

Lv, R., and Chen, Z. (2017). Thymol inhibits cell migration and invasion by downregulating the activation of PI3K/AKT and ERK pathways in human colon cancer cells. *Trop. J. Pharm. Res.* 16, 2895–2901. doi:10.4314/tjpr.v16i12.13

Najoom, S., Fozia, F., Ahmad, I., Wahab, A., Ahmad, N., Ullah, R., et al. (2021). Effective antiplasmodial and cytotoxic activities of synthesized zinc oxide nanoparticles using Rhazya stricta leaf extract. *Evidence-Based Complementary Altern. Med.* 2021, 1–9. doi:10.1155/2021/5586740

Nandi, T., and Khanna, M. (2022). Anti-viral activity of thymol against influenza A virus. *EC Microbiol.* 18, 98–103.

Operario, D. J., Bristol, L. S., Liotta, J., Nydam, D. V., and Houpt, E. R. (2015). Correlation between diarrhea severity and oocyst count via quantitative PCR or fluorescence microscopy in experimental cryptosporidiosis in calves. *Am. J. Trop. Med. Hyg.* 92, 45–49. doi:10.4269/ajtmh.14-0488

Politzer, P., and Murray, J. S. (2021). "Molecular electrostatic potentials: significance and applications," in *Chemical reactivity in confined systems: theory, modelling and applications*, 113–134.

Poulose, A., and Croteau, R. (1978). Biosynthesis of aromatic monoterpenes: conversion of γ-terpinene to p-cymene and thymol in Thymus vulgaris L. *Archives Biochem. Biophysics* 187, 307–314. doi:10.1016/0003-9861(78)90039-5

Qian, X., Xiao, Y., Xu, Y., Guo, X., Qian, J., and Zhu, W. (2010). "Alive" dyes as fluorescent sensors: fluorophore, mechanism, receptor and images in living cells. *Chem. Commun.* 46, 6418–6436. doi:10.1039/c0cc00686f

Ryan, U., Zahedi, A., and Paparini, A. (2016). Cryptosporidium in humans and animals—a one health approach to prophylaxis. *Parasite Immunol.* 38, 535–547. doi:10.1111/pim.12350

Sathe, P. S., Rajput, J. D., Gunaga, S. S., Patel, H. M., and Bendre, R. S. (2019). Synthesis, characterization, and antioxidant activity of thymol-based paracetamol analogues. *Res. Chem. Intermed.* 45, 5487–5498. doi:10.1007/s11164-019-03914-0

Sennouni, C. I., Oukouia, M., Jabeur, I., Hamdani, H., Chami, F., and Remmal, A. (2022). *In vitro* and *in vivo* study of the antiparasitic effect of thymol on poultry drinking water. *Acta Sci. Biol. Sci.* 44, e58571. doi:10.4025/actascibiolsci.v44i1.58571

Singh, A. K., Rajendran, V., Pant, A., Ghosh, P. C., Singh, N., Latha, N., et al. (2015). Design, synthesis and biological evaluation of functionalized phthalimides: a new class of antimalarials and inhibitors of falcipain-2, a major hemoglobinase of malaria parasite. *Bioorg. & Med. Chem.* 23, 1817–1827. doi:10.1016/j.bmc.2015.02.029

Soni, R., Nakum, K. J., Katariya, K. D., Gergis, M., Hagar, M., and Sharma, V. S. (2024). Biphenyls embedded Schiff base-bis esters: self-assembling behaviour, impact of additional aromatic ring and ester linkage and their DFT investigations. *Liq. Cryst.* 51, 1215–1229. doi:10.1080/02678292.2024.2350044

Staneva, D., Vasileva-Tonkova, E., and Grabchev, I. (2019). A new bioactive complex between Zn (II) and a fluorescent symmetrical benzanthrone tripod for an antibacterial textile. *Materials* 12, 3473. doi:10.3390/ma12213473

Tanaka, K. (2024). New strategy for lowering the energy levels of one frontier molecular orbital in conjugated molecules and polymers based on Aza-substitution at the isolated HOMO or LUMO. *Polym. J.* 56, 61–70. doi:10.1038/s41428-023-00843-z

Wang, Z.-D., Liu, Q., Liu, H.-H., Li, S., Zhang, L., Zhao, Y.-K., et al. (2018). Prevalence of Cryptosporidium, microsporidia and Isospora infection in HIV-infected people: a global systematic review and meta-analysis. *Parasites & vectors* 11, 28–19. doi:10.1186/s13071-017-2558-x

frontiers | Frontiers in Chemistry

TYPE Original Research
PUBLISHED 30 May 2025
DOI 10.3389/fchem.2025.1574702

Check for updates

OPEN ACCESS

EDITED BY
Naohiko Yoshikai,
Tohoku University, Japan

REVIEWED BY
Pranab Kishor Mohapatra,
C. V. Raman Global University, India
Mamdouh F. A. Mohamed,
Sohag University, Egypt

*CORRESPONDENCE
Muhammad Afzal,
afzalgufran@gmail.com

RECEIVED 11 February 2025
ACCEPTED 01 May 2025
PUBLISHED 30 May 2025

CITATION
Alzarea SI, Alsaidan OA, Alhassan HH, Alzarea AI, Alsahli TG, Alharbi M, Afzal M and Sadiq Mantargi MJ (2025) Neuraminidase as a novel therapeutic management strategy for Alzheimer's disease: evidenced through molecular docking, molecular dynamic simulation and gene expression analysis. *Front. Chem.* 13:1574702. doi: 10.3389/fchem.2025.1574702

COPYRIGHT
© 2025 Alzarea, Alsaidan, Alhassan, Alzarea, Alsahli, Alharbi, Afzal and Sadiq Mantargi. This is an open-access article distributed under the terms of the Creative Commons Attribution License (CC BY). The use, distribution or reproduction in other forums is permitted, provided the original author(s) and the copyright owner(s) are credited and that the original publication in this journal is cited, in accordance with accepted academic practice. No use, distribution or reproduction is permitted which does not comply with these terms.

Neuraminidase as a novel therapeutic management strategy for Alzheimer's disease: evidenced through molecular docking, molecular dynamic simulation and gene expression analysis

Sami I. Alzarea[1,2], Omar Awad Alsaidan[3,2], Hassan H. Alhassan[4], Abdulaziz Ibrahim Alzarea[5], Tariq G. Alsahli[1], Metab Alharbi[6], Muhammad Afzal[7]* and Mohammad Jaffar Sadiq Mantargi[7]

[1]Department of Pharmacology, College of Pharmacy, Jouf University, Sakaka, Al-Jouf, Saudi Arabia, [2]King Salman Centre for Disability Research, Riyadh, Saudi Arabia, [3]Department of Pharmaceutics, College of Pharmacy, Jouf University, Sakaka, Al-Jouf, Saudi Arabia, [4]Department of Clinical Laboratory Sciences, College of Applied Medical Sciences, Jouf University, Sakaka, Al-Jouf, Saudi Arabia, [5]Department of Clinical Pharmacy, College of Pharmacy, Jouf University, Sakaka, Al-Jouf, Saudi Arabia, [6]Department of Pharmacology and Toxicology, College of Pharmacy, King Saud University, Riyadh, Saudi Arabia, [7]Department of Pharmaceutical Sciences, Pharmacy Program, Batterjee Medical College, Jeddah, Saudi Arabia

Introduction: Neuraminidase in humans is studied to see how well repurposed oseltamivir works for treating Alzheimer's disease (AD) using methods like molecular docking, molecular dynamic (MD) simulation, and gene expression analysis. Gene enrichment analysis was also studied to understand the behaviour of neuraminidases in humans.

Methods: Molecular docking was done using oseltamivir and the neuraminidase proteins with the *PyRx* tool, and the results were analysed using BIOVIA Discovery Studio. MD simulation (50 ns) of the oseltamivir and neuraminidase complex was performed using GROMACS tools. The gene expression analysis and gene enrichment study were done using GEO2R, which showed the results as log FC and significant values. Enricher tool-based gene enrichment analysis was done to determine the gene behaviour related to the AD.

Results: The molecular docking showed a strong connection between oseltamivir and neuraminidase (–6.5 kcal/mol), acetylcholinesterase (–7.9 kcal/mol), CDKs (–6.5 kcal/mol), and GSKs (–6.6 kcal/mol), interacting with different amino acids in the protein sequences. MD simulations showed a strong interaction between the ligand and neuraminidase, with stable measurements indicating that both the protein and ligand remained consistent in size and energy, which is better explained through the results of MM_PBSA and MM_GBSA analysis of the complex, resulting in the ΔE_vdW, ΔE_elec, ΔG_polar, ΔG_nonpolar, ΔG_gas, (ΔE_vdW + ΔEEL), ΔG_solvation: (ΔG_polar + ΔG_nonpolar) and ΔG_bind: total energies suggesting the complex stayed stable in conditions similar to those resembling natural cell. The gene expression analysis expressed

TUBB3 (formation of beta-tubulin), FABP3 (regulates alpha-synuclein uptake in dopaminergic neurons), and CALM1 (calcium signal transduction pathway) to be highly upregulated in the given conditions with kinase binding (p = 0.0006541) and protein phosphatase regulatory activity (p = 0.001357) were highly upregulated, implicating their importance in the AD.

Discussion: The study ends on a hopeful note for using oseltamivir to treat neurological diseases, but it suggests that future research should include a solid cell line study, an *in vitro* study, and a clinical study.

KEYWORDS

Alzheimer's disease, oseltamivir, neuraminidase, molecular docking, molecular dynamic simulation, gene expression analysis, gene enrichment analysis, insilico study

Introduction

Alois Alzheimer pioneered the study of memory loss. He observed the existence of amyloid plaques and an immense harm to neurons during brain examinations of his very first patient who was suffering from cognitive loss and personality change before the patient died. Alois Alzheimer defined this particular condition as a disease of the cortical neurons in the cerebrum. Emil Kraepelin named this condition of serious concern as Alzheimer's disease (AD), taken after the name of Alois Alzheimer (DeTure and Dickson, 2019; Breijyeh and Karaman, 2020). Advanced reduction in cognition can be brought about by cerebro-cortical disorder like AD (Kelley and Petersen, 2007). Other suggested causes are boozing, microorganism infections, anomaly of cardiovascular and/or pulmonary systems that can reduce oxygen supply to the brain, nutritional deficit, cyanocobalamin deficiency and cancers (Baazaoui and Iqbal, 2022; Holtzman et al., 2011; Rathod et al., 2016). Currently, about 50 million people are affected globally by AD. The numbers are expected to double every 5 years and to almost triple by 2050 (Livingston et al., 2020; Nichols et al., 2022). AD overburden the affected individuals, their families and countries' economies. In fact, the total health expenditure of AD alone as per researchers is over US$1 trillion per annum (Chen et al., 2024). Until now, AD is incurable. The existing pharmacological interventions can only manage AD's signs and symptoms (Passeri et al., 2022). Researchers classified AD as multifactorial disease; two main etiologies were hypothesised: the acetyl cholinergic and amyloid beta (Singh et al., 2024). At present, drugs which are approved to treat AD are acetylcholinesterase inhibitors and *N*-methyl d-aspartate (NMDA) antagonists (Barthold et al., 2020). Globally, researchers are trying to explore the mechanism involved behind the progressive neurodegeneration of cerebral cholinergic neurons, abnormal tau protein metabolism, beta-amyloid, inflammation and oxidative free radical damage. The aim is to develop promising pharmacological entities that can stop or modify the neurodegeneration in AD (Forsyth and Ritzline, 1998)

Oseltamivir is an antiviral, which acts by inhibiting viral neuraminidase that is required for the virus to be released from the host cells. Researchers reported that oseltamivir reduces inflammation. It is one of the mechanisms suggested in the reduction of influenza symptoms (Bird et al., 2015) and in the production of antipyretic effect (Treanor et al., 2000). Oseltamivir is primarily used for the treatment of influenza A and B infections. Oseltamivir's target viral enzyme neuraminidase cleaves the sialic acid residues present terminally on carbohydrate moieties of host cell membrane and influenza virus envelop (Treanor et al., 2000). This process breaks down the membrane barriers and causes the release of progeny viruses from the host cells. Through the same process, new virion infects other cells. The neuraminidase inhibitors bring about the static infectious condition and make available these virions to the macrophages intracellularly (McKimm-Breschkin, 2013).

Sialidases are recognised as analogues to viral neuraminidase in humans, and they have been termed as human neuraminidases (hNEU). Exploration of hNEU chemistry and pharmacology revealed to exhibit the same structure and function as that of viral neuraminidase (Magesh et al., 2009; Glanz et al., 2018; Keil et al., 2022). Four isomers of sialidase, which are now known as hNEU, have been recognised, and they hydrolyse sialosides, gangliosides and glycoproteins in humans (Seo et al., 2021). These enzymes were found to play pivotal roles in different pathological states such as diabetes, (Easwaran et al., 2023a), cancers (Reddy et al., 2015) and neurodegenerative disorders (Miyagi and Taniguchi, 2008). hNEU-1 is the most abundant isoform of enzyme among all hNEU, which is present in lysosomes and plasma membrane and is a part of membrane complex (Maurice et al., 2016). hNEU-1 cleaves sialic acid from oligosaccharides and glycoproteins, and it has no effect on gangliosides. Sialidase (hNEU-2) localises in cytosol and catalyses sialic acid from verities of glycans. Sialidase (hNEU-3) is predominantly associated with plasma membrane and it selectively causes desialylation of gangliosides. Fourth isoform of sialidase (hNEU-4) exists mainly on membranes of cell organelles and possesses broad choice of glycan selectivity (Magesh et al., 2006).

Sialidases mediate cleavage reaction of glycoproteins, oligosaccharides and gangliosides. Sialidases also release sialic acid, which has been found to be involved in verities of biological processes including cancers, diabetes, neurodegeneration, inflammation and many more (Seo et al., 2021). Sialic acid releases play homeostatic as well as pathological roles. Sialic acid's influence on neurons has been extensively studied by the researchers, and it has been found that sialidase mutations and generations of sialic acid are negatively associated with AD (Zhu et al., 2024). Sialic acid is required to activate many Siglec genes (primarily downregulated inflammation), which are required in stressful microglial environment and to protect the microglial cells (Khatua et al., 2013). However, this balance of microglial activation and inflammation disrupts in chronic cases and becomes the basis of

neurodegeneration due to inflammatory upregulation (Gao et al., 2023). Sialic acid on gangliosides interacts with Ca^{+2} and facilitates the synaptic transmission, which in excess can lead to excitoxicity (Chahinian et al., 2024). Studies with increased serum sialic acid concentration in AD exhibited sialic to mediate the amyloid β (Aβ) association with gangliosides, which in turn leads to the Aβ plaque formation (Xiao et al., 2022). Sialic acid has been found to downregulate Siglec-3 (CD33). The stimulation of Siglec-3 is very well established in microglial protection (Puigdellívol et al., 2020).

By reviewing the abovementioned literature and other related studies about the sialidase (hNEU), we came to hypothesise that hNEU can be a good target to inhibit the neurodegeneration from multiple fronts which are opened because of neuraminidase stimulation and liberation of sialic acid. Considering the fact that oseltamivir is a viral neuraminidase (vNEU) inhibitor and sialidases in humans are the structural analogues to (vNEU), we aimed to study the impact of neuraminidase inhibitor, i.e., oseltamivir against neuraminidase and different analogues of human neuraminidase including secretases, glycogen synthase kinase, cyclin dependent kinase, protein phosphatase 2A, sialyltransferase, acetylcholinesterase, interleukin-1B and tumour necrosis factor through preliminary pharmacological and toxicity profiling, molecular docking and molecular dynamic simulations. We aim to understand the role of different genes through gene expression analysis to establish the strength of interaction of oseltamivir against various enzymes mentioned and to shed light on its behaviour resembling cellular nature and its expression in the influence of different genes which are pivotal in human biology.

Methods

Preparing the protein for insilico processing

Proteins of interest, which play a significant role in the dysregulated metabolism, were identified as follows: neuraminidase (PDB ID: 2HTY), responsible for the entry of viral particles inside the healthy mammalian cells; (McAuley et al., 2019); beta secretase (PDB ID: 5YGX), responsible for the proteolytic cleavage of AD amyloid precursor; (Sambamurti et al., 2007); gamma secretase (PDB ID: 6YHF), responsible for the breakdown of the amyloid precursor protein to amyloid beta; (Carroll and Li, 2016); alpha secretase (PDB ID: 6BE6), responsible for the breakdown of amyloid precursor protein to soluble amyloid precursor protein alpha; (Corbo et al., 2011); glycogen synthase kinase – 3 beta (GSK3B) (PDB ID: 1PYX), responsible for the regulation of signalling post endocytic transport; (Partonen and Kushida, 2023); cyclin dependent kinase – 5 (CDK5) (PDB ID: 1H4L), responsible for organising the cytoskeleton and cellular growth; (Tian et al., 2022); protein phosphatase 2A (PP2A) (PDB ID: 1B3U), responsible for the cellular processes like autophagy, apoptosis, cell proliferation and DNA repair; (Dzulko et al., 2020); sialyltransferase (PDB ID: 5BO6), responsible for the hydrolysis of sialic acid; (Zhang et al., 2010); acetylcholinesterase (PDB ID: 1ACJ), responsible for the metabolism of acetylcholine at the synapse of two different neurons; (Volkow et al., 2001); interleukin 1B (PDB ID: 1IOB), responsible for the endocrine and reproductive dysfunction; (Baraskar et al., 2021); and, tumour necrosis factor (PDB ID: 1TNF), responsible for the modulation of various gene expression cellularly. (Schütze et al., 1992). The protein pdb files were downloaded from the RCSB PDB database (https://www.rcsb.org/) and (Berman et al., 2000) visualised through BIOVIA discovery studio (Baroroh et al., 2023) application, where the hetatms, water and co-crystals were removed and polar hydrogens were added to induce the charge around the protein structure to facilitate perfect interaction with the ligand in case of molecular docking and MD simulations.

Preparing oseltamivir as ligand

The structure of oseltamivir was downloaded in the .sdf format, which will be formatted as ligand of the study. Furthermore, it was downloaded from structural information rich databases like 'PubChem' directory (https://pubchem.ncbi.nlm.nih.gov/), (Kim et al., 2024) particularly oseltamivir (ethyl (3*R*,4*R*,5*S*)-4-acetamido-5-amino-3-pentan-3-yloxycyclohexene-1-carboxylate) (Green et al., 2008). The processing of the molecule for the conversion into the pdbqt was done by employing open babel tool (O'Boyle et al., 2011).

Identification of pharmacological and toxicological activity employing PASS tool

The prediction of activity spectra of substances (PASS) (https://www.way2drug.com/passonline/), an online tool, was selected to predict the possible activity of oseltamivir. The molecular SMILES formula was given as input in the interface of PASS, which predicts the possible pharmacological actions and toxicological activities. The structure-activity relationship was denoted by Pa: probability of activity and Pi: probability of inactivity. This approach provided an idea concerning the possible targets and activity for approaching through preparing the biomolecules of interest (enzymes) for further processing, employing molecular docking and MD simulation studies to develop an understanding with the evidence (Poroikov et al., 2007).

Performing the proteins - ligand molecular docking

The processed protein crystal structures were uploaded into the PyRx interface (https://pyrx.sourceforge.io/) and converted into pdbqt format as a macromolecule of the study (Dallakyan et al., 2015). The ligands.sdf file was uploaded through the 'Open Babel' and was processed into pdbqt format to make ligand molecule for molecular docking after energy minimisation. The molecular docking was performed by creating a grid dimension (Table 2), and selecting complete protein. Twenty core CPUs with effectiveness were selected, and final docked molecules were saved for further processing. BIOVIA and discovery studios were the preferred methods to analyse the results obtained after molecular docking, including the 2D structures of proteins and ligands interactions, protein-ligand interactions and pocket identification (Murugan et al., 2022; Germoush et al., 2024).

Preparing the enzyme and oseltamivir for MD simulation

Pymol interface was selected for converting the.dsv files into.pdb files. The separately imported protein and ligand files after molecular docking were joined through pymol. It was then saved in the form of pdb file for performing the MD simulation by means of GROMACS for a time period of 50 nanoseconds (ns), temperature of 300K, solvent–water, ions–sodium and chlorine, with one random seed and selected seed of seed_1234 for duality (Bytheway et al., 2008; Coutsias and Wester, 2019; Sasumana and Kaushik, 2018; Varghese et al., 2024; Yuan et al., 2017; Bekker et al., 1993).

The molecular dynamic (MD) simulation of a oseltamivir-neuraminidase complex was performed using GROMACS 2024, installed on linux (ubuntu) operating system, supported by the NIVIDIA RTX 4060 graphical processing unit and 16 GB RAM. Firstly, the topology files of the protein was generated using GROMACS compatible forcefield such as CHARMM36 and the ligand topology files were generated using Swissparam tools (Bugnon et al., 2023; Zoete et al., 2011; Yesselman et al., 2012). Secondly, the ligand-protein complex was assembled and a simulation box was defined maintaining a minimum distance of 1.0 nm from the edges. TIP3P water model was chosen to solvate the simulation box was used. Sodium and chlorine was used as counterions to neutralise the system. To reduce steric clashes, energy minimising of the system was performed employing the steepest descent algorithm, followed by two equilibration steps such as NVT and NPT for a time period of 100 ps (picoseconds) to stabilise the temperature and pressure of the system using the V-rescale and Parrinello–Rahman algorithms. The production MD simulation run was conducted for 50 ns (nanoseconds) with a time step of 2 fs under stable boundary conditions saving the results every 10 ps.

Build in GROMACS utilities were used to perform post simulation analysis. The structural stability of the complex was assessed by calculating the root mean square deviation (RMSD) of the ligand and protein over time. While flexibility was evaluated using root mean square fluctuation (RMSF) per residue and the radius of gyration was assessed to determine the compactness of the protein. Binding free energies were carried employing the gmx_MMPBSA tool, externally installed using anaconda3 packages. The MD trajectory and topology files were used for processing gmx_MMPBSA (Molecular Mechanics Generalized Born Surface Area) and gmx_MMGBSA (Molecular Mechanics Poisson–Boltzmann Surface Area) binding free energies over represented snapshots. (Miller et al., 2012). The energies included van der Waals, electrostatic, polar solvation and non-polar solvation contributions. This protocol provided insights into the stability, dynamics, and binding energetics of the ligand–protein complex.

Performing the gene expression analysis of sialyltransferase (analogue of neuraminidase)

Gene expression analysis was executed by means of GEO2R (https://www.ncbi.nlm.nih.gov/geo/geo2r/), an online tool of national centre for biotechnological information (NCBI) database (https://www.ncbi.nlm.nih.gov/) for variance expression analysis of huge datasets from gene expression omnibus (GEO). Datasets were normalised and comparisons between case and control groups were achieved. Significant genes were identified based on p-values (<0.05) and log 2-fold change thresholds for the gene analysis (Kalyan et al., 2023). The GEO series accessions involving sialyltransferase genes expression data, i.e., GSE5281 (Liang et al., 2007; Liang et al., 2008a; Readhead et al., 2018; Liang et al., 2008b), were selected for the study. The gene expression data was examined using dataset GSE5281, bearing the genes responsible for the development of AD and bearing the data of 61 control samples and 44 case samples. Differential expressional analysis was performed to recognise significant gene regulated within the groups. The study was completed using Benjamini and Hochberg method with NCBI generated data following the statistically significant level cut-off of p-values (<0.05), log 2-fold change threshold 'zero' with volcano and mean difference plot for control group vs. case group. The results are expressed in Table 4, bearing the data of twenty highly significant genes associated with the development or that played a crucial role in the pathway related to AD.

Gene enriching analysis

To identify the biological impact of twenty significant genes derived out of GEO analysis associated with AD, the gene enrichment analysis was performed employing the enrichr tool. The significant gene codes were given as input into the enrichr interface, (Kuleshov et al., 2016; Chen et al., 2013), which integrates the data from various databases. The analysis involves selecting relevant categories like gene ontology (GO), (Ashburner et al., 2000), terms for cellular components, molecular functions and biological processes. Furthermore, disease specific annotations were explored employing Jensen diseases and Jensen tissue databases to understand the link of the genes with the AD pathology. Adjusted p-values (Padj) were used to ensure statistical significance. Combined scores, which integrate p-values and z-scores, were used to rank the enriched outcomes so that the results provide insights into the role of synaptic function, protein phosphorylation, lipid metabolism and neuroinflammation, which are critical in understanding the pathology of AD (Xie et al., 2021). The findings were visualised using volcano plots to understand and recognise key pathways and phenotypes for further investigation.

Results

The PASS prediction analysis points out several important pharmacological activities with high probable activities (Pa) and low possibility of inactivity (Pi), which suggests the oseltamivir is highly active against the targets like Neuraminidase inhibitor (Pa = 0.931) and Alpha-N-acetylglucosaminidase inhibitor (Pa = 0.455). The aforementioned targets could be of prime interest as the enzyme may be involved in the transferase reaction and may result in the production of abnormal proteins. Three different variants were identified based on the mutated gene expression, which could result in the development of neuronal disorders (Alroy et al.,

TABLE 1 The activity prediction of oseltamivir.

Pharmacological activity prediction		
Pa	Pi	Predicted activity
0.931	0.000	Neuraminidase (Influenza B) inhibitor
0.932	0.001	Antiviral (Influenza)
0.920	0.001	Antiviral (Influenza A)
0.685	0.000	Neuraminidase (influenza) inhibitor
0.652	0.005	Macrophage stimulant
0.455	0.013	Alpha-N-acetylglucosaminidase inhibitor
0.473	0.048	Muramoyltetrapeptide carboxypeptidase inhibitor
0.461	0.042	Antiviral (Rhinovirus)
0.447	0.034	Peptide-N4-(N-acetyl-beta-glucosaminyl) asparagine amidase inhibitor
0.434	0.034	Antimyopathies
Toxicity Prediction		
Pa	Pi	Predicted activity
0.511	0.063	Acidosis, metabolic
0.463	0.082	Sneezing
0.517	0.190	Twitching
0.417	0.110	Weight loss
0.359	0.065	Hypocalcaemic
0.375	0.097	Dyspnea
0.333	0.127	Gastrointestinal disturbance
0.326	0.129	Ototoxicity
0.259	0.084	Sensitization
0.363	0.195	Thrombophlebitis

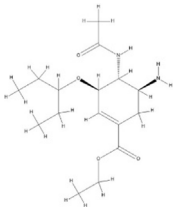
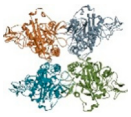
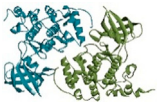
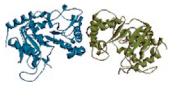
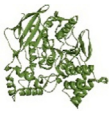
Pa: probably activity, Pi: possibly inactivity, data derived through an online tool, i.e., PASS program (http://www.way2drug.com/PASSOnline/).

2014). Inhibition of enzymes, highlighting its role in neuronal protection, misrepresentation or misexpression of the gene related to this enzyme, may result in neurological disorders, which is the point of interest of the current study Deficiency of the said enzyme may result in various other neurological disorders (Zhao and Neufeld, 2000). Additionally, it may result in toxicities like metabolic acidosis (0.511), sneezing, twitching, weight loss, hypocalcemia, dyspnea, gastrointestinal disturbance, ototoxicity, sensitization and thrombophlebitis with lower intensity, which are needed to be taken care of during the evaluation of the study. These activities express oseltamivir's resourcefulness and therapeutic potential in diverse biological contexts related to Alzheimer's disease (Table 1). (Annexure 1).

Molecular docking

The oseltamivir interacted with neuraminidase at a hydrogen bond length of 2.06Å with GLU C:174, expressing the lowest binding score of −6.5 kcal/mol at given grid values mentioned in Table 2. Further, the interaction between protein and ligand was formed even through Vander wall's interaction with ARG C:172 along with six other amino acids. The oseltamivir also interacted with beta secretase at a hydrogen bond length of 1.86Å with TYR A:71, expressing the lowest binding score of −6.2 kcal/mol. Further, the interaction between protein and ligand was formed even through Vander wall's interaction with ILE 118 along with nine other amino acids. The oseltamivir interacted with gamma secretase as well at a hydrogen bond length of 3.02Å with ALA 42, expressing the lowest binding score of −3.5 kcal/mol, a bit weaker interaction in comparison with other proteins. Further, the interaction between protein and ligand was formed even through Vander wall's interaction with ILE 45 along with three other amino acids. Similarly, the oseltamivir interacted with alpha secretase at a hydrogen bond length of 2.14Å with ARG A:239, expressing the lowest binding score of - 6.4 kcal/mol. Further, the interaction between protein and ligand was formed even through Vander wall's interaction with THR A:238 along with eight other amino acids. The oseltamivir interacted with glycogen synthase kinase 3 beta (GSK-3B) too at a hydrogen bond length of 2.05Å with GLY B:202, expressing the lowest binding score of - 6.6 kcal/mol. Further, the interaction between protein and ligand was formed even

TABLE 2 Protein (Neuraminidase) -Ligand (Oseltamivir) Docking Results of '*PyRx Python Prescription 0.8*' Analysed Through '*BIOVIA-Discovery Studios Visualiser v.21.1.0.20298*'.

Name of ligand (Oseltamivir)	Name of protein	Various receptor enzymes associated with Alzheimer's as target proteins and oseltamivir as ligands						
		Highest affinity score Kcal/mol	*RMSD*	*Ionic or wander wall's interactions (Å units)*	*Hydrogen bond interactions (Å units)*	*Amino acids*	*Grid dimensions Centre Dimensions*	
Oseltamivir 	Neuraminidase (PDB ID: 2HTY) 	−6.5	0	ARG C:172, LEU A:127, SER A:101, ASN C:208, GLU C:209, GLU A:128, THR C:191	2.30 2.06 2.47 2.82	PHE C: 173, GLU C:174, LYS C:206, TYR A:100	x = 1.5994 y = 50.1814 z = 100.559	x = 103.0816 y = 102.4211 z = 53.8510
	Beta secretase (PDB ID: 5YGX) 	−6.2	0	ILE 118, ARG 128, SER36, GLY 34, TYR 198, ILE 226, ASP 228, VAL 332, ASP 32, THR 231	1.86 2.15	TYR A:71 GLY A:230	x = 14.3015 y = 41.0494 z = 0.1888	x = 56.1419 y = 64.6465 z = 45.9909
	Gamma secretase (PDB ID: 6YHF) 	−3.5	0	ILE 45, GLY 38, LEU 34, MET 35	3.02	ALA 42	x = - 2.2973 y = −3.2008 z = 11.7049	x = 26.2145 y = 48.5674 z = 13.6442
	Alpha secretase (PDB ID: 6BE6) 	−6.4	0	THR A:238, LYS A:518, GLU A:240, ILE A:243, SER A:506, SER A:504, CYS A:473, ASP A:481, LYS A:480	2.14	ARG A:239	x = 31.7668 y = 33.1965 z = 18.0663	x = 94.5299 y = 109.4674 z = 123.8035
	GSK-3B (PDB ID: 1PYX) 	−6.6	0	LYS A:292, ASN B:95, GLN B:89, VAL B:87, LYS B:85, SER B:203, PHE B:67	2.51 2.57 2.05	ARG B:96 GLU B:97 GLY B:202	x = 24.2110 y = −0.3042 z = 21.4266	x = 72.9735 y = 80.3676 z = 103.6807
	CDK-5 (PDB ID: 1H4L) 	−6.3	0	GLU A:81, ALA A:143, ASP A:84, GLN A:85, ILE A:10, GLN A:130, ASN A:131, ASP A:144, LYS A:33, VAL A:18	2.87	ASP A:86	x = 35.4578 y = −32.768 z = 26.1504	x = 77.4488 y = 60.5521 z = 49.0611
	PP2A (PDB ID: 1B3U) 	−5.5	0	THR A:141, ALA A:183, SER A:186, LYS A:187, GLY A:148, CYS A:143, VAL A:108, SER A:145, THR A:101, ARG A:182, MET A:179, PHE A:140	2.54 2.37 1.94	ASP A:105 THR A: 144 ARG A:104	x = 34.6630 y = 46.7673 z = 23.0447	x = 97.3458 y = 107.1759 z = 122.2308
	Sialyltransferase (PDB ID: 5BO6) 	−6.4	0	ALA B:192, LEU B:238, GLU B:195, SER B:234, ASN B; 230, PRO B:190	2.12	THR B:194	x = −3.5210 y = 9.8904 z = −11.0690	x = 61.7766 y = 59.4714 z = 102.3049
	Acetylcholine-esterase (PDB ID: 1ACJ) 	−7.9	0	GLU A: 199, GLY A:441, TYR A:130, HIS A:440, GLY A:117, TYR A:442, LEU A:127, SER A:124, GLY A:118, GLY A:123, SER A:122, ASN A:85, GLN A:69, TYR A:121,	2.55	TRP A:84	x = 4.7576 y = 65.5208 z = 56.8290	x = 64.6127 y = 61.3047 z = 56.9408

(Continued on following page)

TABLE 2 (*Continued*) Protein (Neuraminidase) -Ligand (Oseltamivir) Docking Results of '*PyRx Python Prescription 0.8*' Analysed Through '*BIOVIA-Discovery Studios Visualiser v.21.1.0.20298*'.

Name of ligand (Oseltamivir)	Name of protein	Various receptor enzymes associated with Alzheimer's as target proteins and oseltamivir as ligands						
		Highest affinity score Kcal/mol	*RMSD*	*Ionic or wander wall's interactions (Å units)*	*Hydrogen bond interactions (Å units)*	*Amino acids*	*Grid dimensions Centre Dimensions*	
				ASP A:72, GLY A:80, TRP A:432, SER A:81, TYR A:334				
	Interleukin 1B (PDB ID: 1IOB) 	−5.3	0	VAL A:85, ASN A:66, TYR A:90, ASN A:7, SER A:5, SER A:43, GLY A:61, GLU A:64, LYS A:65	2.02 2.39	LEU A:62 LYS A:63	x = 15.9224 y = 13.5665 z = 1.1895	x = 44.2915 y = 37.7782 z = 44.89.24
	TNF alpha (PDB ID: 1TNF) 	−7.4	0	LYS C:98, PRO B:110, LYS A:98, GLU C:116, GLU B:116, SER B:99, GLU A:116, PRO A:100, TYR A:115, TRP A:114, CYS A:110, PRO C:100, GLN C:102, GLU C:104	2.37 3.02	SER C:99 GLN B:102	x = 19.9745 y = 49.6645 z = 39.9343	x = 62.7877 y = 63.9782 z = 61.4350

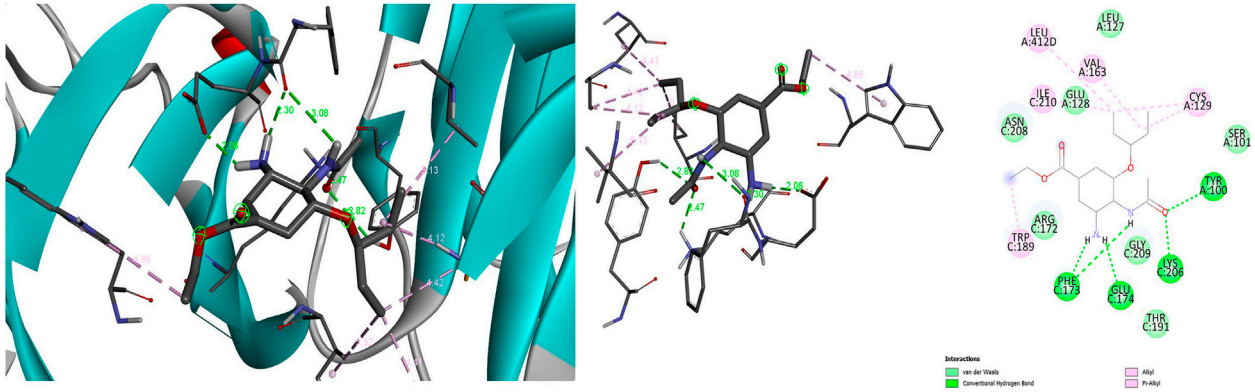


FIGURE 1
shows the interaction between the ligand (oseltamivir) and the enzyme protein (neuraminidase); first from left shows the receptor interaction with ligand, middle image shows the protein interactive pocket atoms with ligand and the third image shows the 2D illustration of amino acids interacting with ligand through hydrogen, Vander Waal's, among other interactions.

through Vander wall's interaction with LYS A:292 along with six other amino acids. Additionally, the oseltamivir interacted with cyclin dependant kinase 5 (CDK-5) at a hydrogen bond length of 2.87Å with ASP A:86, expressing the lowest binding score of - 6.3 kcal/mol. Further, the interaction between protein and ligand was formed even through Vander wall's interaction with 10 other amino acids. There was also an interaction of oseltamivir with protein phosphatase 2A (PP2A) at a hydrogen bond length of 1.94Å with ARG A:104, expressing the lowest binding score of - 5.5 kcal/mol. Further, the interaction between protein and ligand was formed even through Vander wall's interaction with 12 other amino acids. Correspondingly, the oseltamivir interacted with sialyltransferase at a hydrogen bond length of 2.12Å with THR B:194, expressing the lowest binding score of - 6.4 kcal/mol. Further, the interaction between protein and ligand was formed even through Vander wall's interaction with six other amino acids. In the same manner, the oseltamivir interacted with acetylcholinesterase at a hydrogen bond length of 2.55Å with TRP A:84, expressing the lowest binding score of - 7.9 kcal/mol, which is the highest binding affinity of the current study. Further, the interaction between protein and ligand was formed even through Vander wall's interaction with 19 other amino acids. Adding to the list, the oseltamivir interacted also with interleukin 1B at a hydrogen bond length of 2.02Å with LEU A:62, expressing the lowest binding score of - 5.3 kcal/mol. Further, the interaction between protein and ligand was formed even through Vander wall's interaction with nine other amino acids.

TABLE 3 Molecular dynamic (MD) simulation of oseltamivir and neuraminidase.

Seed	Protein	Ligand	Root mean square deviation (RMSD) nm	Root mean square fluctuations (RMSF) nm	Radius of gyration (Rg) nm
Random seed	Neuraminidase	Oseltamivir	P: 0.128424–0.493372 L: 0.122013–0.838708	P: 0.0451–0.2189 L: 0.0153–0.1925	P: 3.391135–3.518412 L: 0.354091–0.37452
Seed_1234	Neuraminidase	Oseltamivir	P: 0.161276–2.858013 L: 0.208401–3.217241	P: 1.2986–2.2136 L: 0.0160–0.2210	P: 3.390434–4.271447 L: 0.341893–0.371202

nm = Nanometres, P = protein, L = ligand.

Lastly, the oseltamivir interacted with tumour necrosis factor - alpha at a hydrogen bond length of 2.37Å with SER C:99, expressing the lowest binding score of - 7.4 kcal/mol, which is also one of the best results of the current study. Further, the interaction between protein and ligand was formed even through Vander wall's interaction with 14 other amino acids. (Table 2) (Figure 1).

The summary of the dual MD simulation (random simulation and seed_1234) of the oseltamivir-neuraminidase complex is explained in Table 4, which consist a of binding free energies components as integral part of MM-PBSA analysis. Significant high magnitude of van der Waals interactions (ΔE_vdW) changed form the negligible phase in pre-dynamic MM-PBSA (−0.00 ± 1.26 for random and 0.00 ± 0.40 for seed_1234) to a considerable negative value post-simulation (−20.22 ± 0.73 and −19.05 ± 0.50), which indicates high binding confirmation and attractive ness between the ligand and protein. Similar observations were noticed for electrostatic interactions (ΔE_elec), the energy quotient shifts from negligible to highly promising post-dynamic i.e., −284.37 ± 0.95 for random and −255.35 ± 1.46 for seed_1234, these results confirm the strong bonding between the ligand and protein. However, in case of polar solvation energy (ΔG_polar) the post simulation results of random seed was increased and seed_1234 was decreased, showing a system determined correction was pointed to the seed_1234 simulation being more favourable. The total gas-phase energy (ΔG_gas), transforms in to significantly favourable value post simulation, indicating stronger intermolecular connections in the complex environment. Finally, the binding free energies (ΔG_bind) change from the positive in pre-MM-PBSA value to negative in post MM-PBSA value exhibits improved binding characteristics post molecular dynamics.

The results MM-GBSA analysis of pre and post dual MD simulation of random seed and seed_1234 for determining their binding free energies is expressed in Table 5, the van der Waals interaction energy (ΔE_vdW) demonstrated shift from undermined values in pre dynamic simulation (0.00 ± 0.00 random and −0.00 ± 0.00 seed_1234) to recognisable post dynamic simulation (−18.78 ± 0.01 for random and −19.18 ± 0.78 for seed_1234) values representing better packing between ligand and protein post simulation. Electrostatic interactions (ΔE_elec) showed similar results, shifting from insignificant range of values to desirable values (−266.20 ± 0.46 for random and −259.86 ± 1.81 for seed_1234) post simulation. Conclusively, the total binding free energies (ΔG_bind) remained constantly negative in both pre and post MM-GBSA states, suggesting the stable and promising binding between the ligand and protein.

The MM-GBSA decomposition analysis for the ligand and protein complex, pre and post MD simulations in random and fixed (seed_1234) conditions revealed that key amino acid fragments such as GLU:276 and GLU:277 developed strong interactions in pre-MD simulation analysis with values −10.36 and −11.98 kcal/mol under random conditions. A great shift in the energies of the amino acids was identified in post MD simulation, i.e., GLU:276 reaching −15.61 kcal/mol and GLU:277 displaying a positive value of 3.87 kcal/mol, highlighting important changes. Residues like ARG:224 and ARG:292 better binding energies post MD simulations and LEU:134, TRP:178, SER:179, and ILE:222 maintained constant negative energies throughout simulations.

The interaction of ligand, oseltamivir, and enzyme protein, neuraminidase, was analysed through molecular dynamic simulation employing GROMACS tool. Various crucial parameters have been identified such as RMSD, radius of gyration (Rg), Vander Waal's surface area (VSA) and the potential energy of the complex (PE). The protein RMSD ranged for Protein: P: 0.128424–0.493372 nm, ligand 0.122013–0.838708 nm under random seed simulation and under seed_1234 simulation it ranged from Protein 0.161276–2.858013 nm and Ligand 0.208401–3.217241 nm, which explains that the ligand-protein complex has undergone minimal structural disorientation and exhibited stable binding throughout the test. The radius of gyration remained constant between for protein at a range of 3.391135–3.518412 nm and for the ligand at a range of 0.354091–0.37452 nm under random simulation conditions, however, the protein and ligand showed the radius of gyration of about 3.390434–4.271447 nm and 0.341893–0.371202 nm under seed_1234 simulation conditions which explains minimal disorientation in seed_1234 simulation. The RMSF of protein and ligand under random and seed_1234 MD simulation conditions exhibited a value of P: 0.0451–0.2189 nm, L: 0.0153–0.1925 nm for random simulation and P: 1.2986–2.2136 nm and ligand L: 0.0160–0.2210 nm under seed_1234 simulation conditions exhibiting vigorous molecular interactions between the ligand and protein in a complex, which justify the results expressed in Tables 2, 3. Through this current simulation results, it is evident that the oseltamivir forms a stable and favourable bond with the enzyme protein like neuraminidase, which underscores the oseltamivir as a suitable candidate for development of pharmacophore against the enzyme protein of neuraminidase (Figure 2).

Through these results, it can be explained that targeting the neuraminidase can ensure effective modulation of pathological pathway related to AD (Du et al., 2024), as neuraminidase or similar enzymes like sialic acid modifying agents are involved in neurodegenerative pathways (Zhang et al., 2023).

The dataset validation performed through GEO employing the accession number GSE5281 and focusing on the gene expression related to the Alzheimer's disease for sialyltransferase, which is an



FIGURE 2
(Continued).

analogue of neuraminidase in humans, has shown significant differential expression results. Based on their low p-value and high log fold-change (Log FC) ranging between 6.25×10^{-10} to 3.92×10^{-8}, significant statistical evidence for changes related to gene expression was found. The log FC values of 1 shows two folds, 1.5 three folds and 2 four folds in the gene upregulation in the given dataset. The significantly expressed genes like tubulin beta 3 class III (TUBB3) and synaptosome associated protein 25 (SNAP25) are important for normal neuronal structure and function even at the synaptic level (Duly et al., 2022; Olsson et al., 2011), the processes which are dysregulated in AD. The four folds upregulation of ubiquitin C-terminal hydrolase L1 (UCHL1) and PPP2R2D, a subunit of protein phosphatase 2A, suggests altered signalling pathways and protein turnover in human brain (Bishop et al., 2016), which are associated with neurodegenerative diseases. The neurexin 3 (NRXN3) and calmodulin 1 (CALM1) are associated with synaptic connectivity, calcium signalling and disrupting, which are highly associated with AD. (Mu et al., 2024; Chin and Means, 2000) Other genes like fatty acid binding protein 3 (FABP3), (Lee et al., 2020), which represents the lipid metabolism, and somatostatin (SST) (Samson et al., 2008) have neuromodulatory function highly affecting the cognitive processes. Dysregulation of which may develop the AD. (Samson et al., 2008) Aggregation of certain protein and inflammation of developing genes such as reticulon 3 (RTN3) (Grumati et al., 2017) and C1q and tumour necrosis factor-related protein 4 (C1QTNF4) (Vester et al., 2021) can act as central to the development and prognosis of AD. Through this analysis, the network of dysregulated genes involved in synaptic function, neuroinflammation, calcium function and protein homeostasis can be explained. The significant alteration in the gene expression and homeostasis emphasises potential targets for novel therapeutic intervention in relation to AD. (Table 4) The volcano plot expresses the differential expressing gene between Alzheimer's disease samples and normal samples obtained from the dataset GSE5281 (Figure 3), which shows distinct upregulated and downregulated genes in the context of AD. In the log FC values, positive values (red) show upregulated genes while negative values (blue) show downregulated genes. The y-axis (p-value) shows the significance of the study samples, where the non-significant genes are shown in grey colour. These genes may be involved in inflammation, synaptic dysfunction, amyloid metabolism or impaired neuroprotection. These findings provide potential biomarkers for the development of novel therapeutic agents. (Annexure II).

The enricher-based analysis of 20 highly significant genes has revealed an enriching analysis of genes implicated in Alzheimer's disease, highlighting significant association among the cellular components, molecular function, mammalian phenotypes, tissues and related diseases. Within the cellular components, vesicles (adjusted p-value = 0.04964, combined score = 115.27) and glutamatergic synapses (adjusted p-value = 0.04964, combined score = 200.25) emerged as critical, emphasising the known roles of synaptic dysfunction in AD. In molecular function, kinase binding (adjusted p-value = 0.03205, combined score = 89.70) and protein phosphatase regulator activity (adjusted p-value = 0.03324, combined score = 278.70) highlighted the disruption in

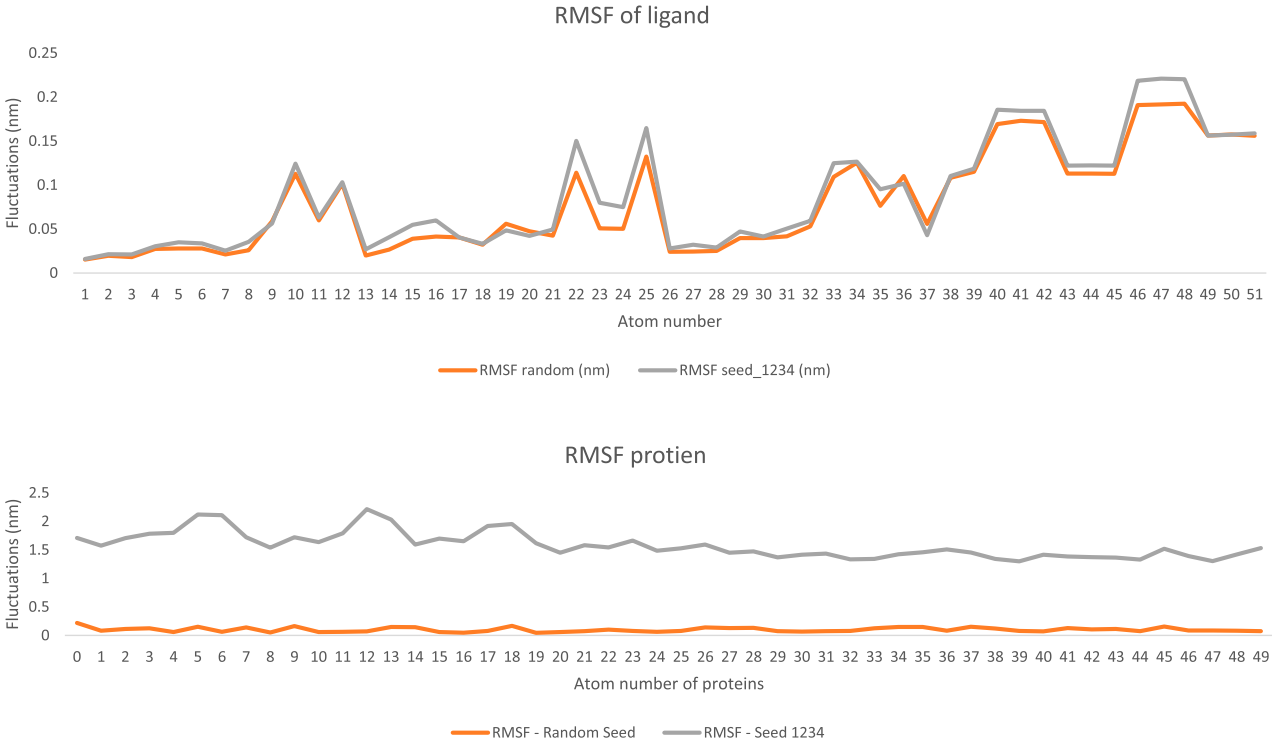


FIGURE 2
(Continued).

protein phosphorylation as a tau-related AD precursor (Iqbal et al., 2010). Long chain fatty acid binding and phosphoserine residue binding showed strong results (adjusted p-value = 0.04964 for both, combined scores = 828.65), suggesting metabolic and post-translational monitoring dysregulation. In the case of mammalian phenotype level, the abnormal peripheral nervous system synaptic transmission with values (adjusted p-value = 0.008775, combined score = 3208.63) and abnormal endplate potential with values (adjusted p-value = 0.01166, combined score = 1658.66) were significant, which is consistent with the impact of AD on the synaptic transmission. Decreased paired-pulse facilitation with values (adjusted p-value = 0.01781, combined score = 961.11) proves impaired synaptic plasticity, further assisting neurodegeneration. From the tissue specific analysis, the cortex of the brain (adjusted p-value = 0.0001872, combined score = 511.81) and the ganglia with values (adjusted p-value = 0.0007525, combined score = 280.10) showed significant involvement, which are shown to be critically affected in AD. Within the disease association, strong links were noticed related to brain disease, pineoblastoma, dumping syndrome and dysembryoplastic neuroepithelial tumour, hinting at overlapping pathways of neurodegeneration. The analysis has given a hint related to the metabolic causes of the development of AD, where neuraminidase analogues like sialyltransferase plays a crucial role in disrupting the metabolism of various proteins and lipids. Hence, the enricher-based analysis of highly significant genes has revealed various potential targets for the novel development of therapeutic agents (Table 5).

Discussion

Oseltamivir, which inhibits neuraminidase and facilitates the viral entry into the cells, disarranges sialic acid from the glycoproteins. The sialic acid is also produced by the action of various human enzymes, such as secretases, glycogen synthesis kinases, cycling dependent kinases, protein phosphatase 2A, sialyltransferase, acetylcholinesterase, interleukin 1B and tumour necrosis factor, which plays a vital role either in the formation of insoluble sialic acid or in the production of neurodegeneration through inflammation. Hence, the current study was taken up to analyse the inhibitory potential of oseltamivir against all of the enzymes or cytokines related to Alzheimer's disorders.

The PASS online tool was used to predict the pharmacological activity of a compound. It was predicted that oseltamivir functions as neuraminidase inhibitor and that it was a preferred antiviral agent against influenza A and B viruses. The 'Pa' values exceeding 0.9 were well-aligned with documented role of oseltamivir. A study published by Patricia et al. highlighted the antiviral activity of oseltamivir against influenza (Schirmer and Holodniy, 2009). The findings of this study confirmed the mechanism of action, which helped us in choosing the required topic.

However, the secondary activities such as macrophages stimulation (Hama, 2016) and alpha-N-acetylglucosaminidase inhibition had to settle with lower Pa values, which could be considered as the off-target effects and related to oseltamivir. The secondary activities are not yet well-developed or published, which opens up a potential change of studying the molecular-related

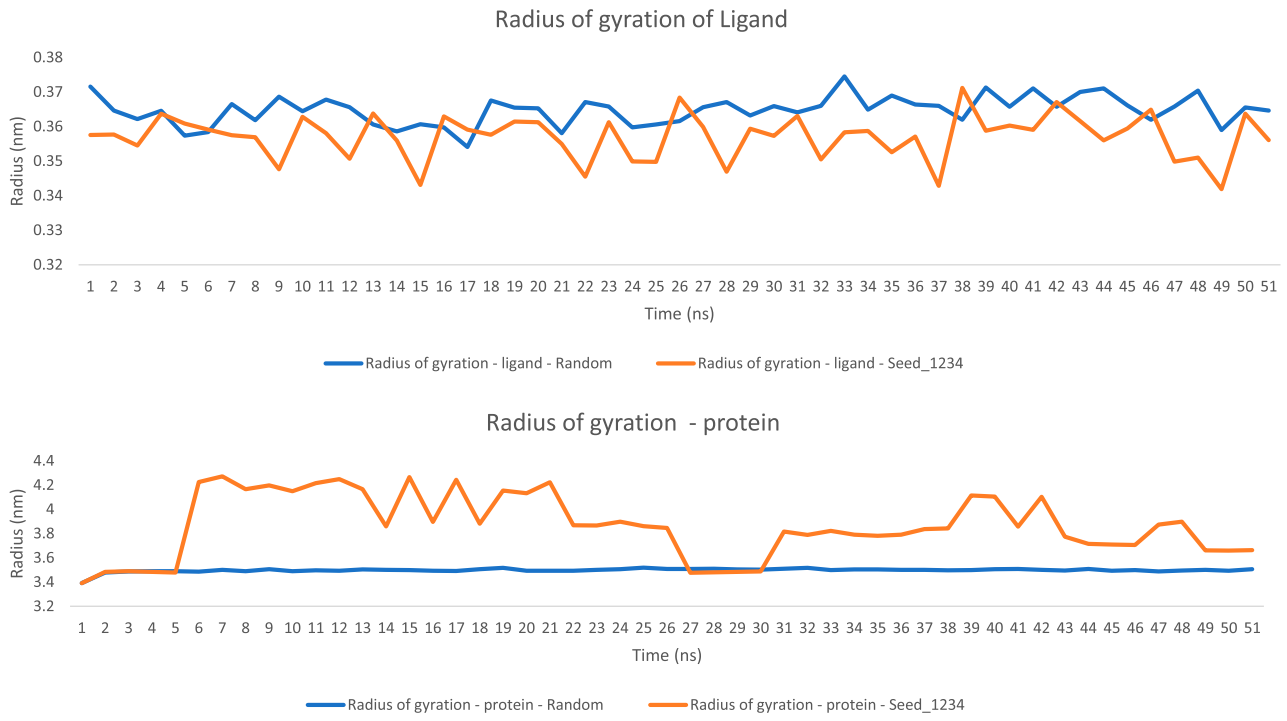


FIGURE 2
(Continued). Represents the molecular dynamic simulation interactions of the ligand and protein complex as RMSD of protein and ligand, RMSF of protein and ligand, radius of gyration.

TABLE 4 Results of pre and post MM-PBSA binding free energy components in kcal/mol of the MD simulated molecular complex of Oseltamivir and Neuraminidase.

Energy components	Pre MM-PBSA (Mean ± SD); random seed	Post MM-PBSA (Mean ± SD); random seed	Pre MM-PBSA (Mean ± SD); Seed_1234	Post MM-PBSA (Mean ± SD); Seed_1234
ΔE_vdW (van der Waals)	−0.00 ± 1.26	−20.22 ± 0.73	0.00 ± 0.40	−19.05 ± 0.50
ΔE_elec (Electrostatic)	−0.00 ± 2.22	−284.37 ± 0.95	0.00 ± 3.20	−255.35 ± 1.46
ΔG_polar (Polar solvation)	246.03 ± 17.02	289.19 ± 1.33	267.15 ± 11.36	263.47 ± 0.31
ΔG_nonpolar (Non-polar solvation)	−3.56 ± 0.03	−3.25 ± 0.04	−3.57 ± 0.03	−3.31 ± 0.05
ΔG_gas (Energy in vacuum)	−229.62 ± 20.44	−304.59 ± 1.20	−269.62 ± 6.13	−274.40 ± 1.56
ΔG_solvation (Total solvation energy)	242.47 ± 17.02	285.95 ± 1.33	263.58 ± 11.36	260.16 ± 0.31
ΔG_bind (Total Binding Free Energy)	12.84 ± 26.60	−18.65 ± 1.79	−6.04 ± 12.91	−14.24 ± 1.59

ΔE_vdW: van der Waals interaction energy between the ligand and the protein.
ΔE_elec: electrostatic interaction energy.
ΔG_polar: solvation free energy due to polar interactions, calculated using the Poisson–Boltzmann (PB) or Generalized Born (GB) models.
ΔG_nonpolar: non-polar solvation free energy, often estimated from the solvent-accessible surface area (SASA).
ΔG_gas: Total energy in vacuum (ΔE_vdW + ΔEEL).
ΔG_solvation: Total solvation energy (ΔG_polar + ΔG_nonpolar).
ΔG_bind: total binding free energy, sum of the above components.

activities concerning other diseases for the patient's safety (Easwaran et al., 2023b).

The toxicity prediction has expressed that the oseltamivir may develop metabolic acidosis (Pa = 0.511), twitching (Pa = 0.517) and dyspnoea (Pa = 0.375). These effects were also noted in the clinical setting with higher doses or with prolonged use of oseltamivir. A published meta-analysis highlights gastrointestinal disturbances and no neuropsychiatric effects of oseltamivir in patients. Such studies confirm the application of oseltamivir with proper dose management (Malosh et al., 2017). Certain predicted toxicities,

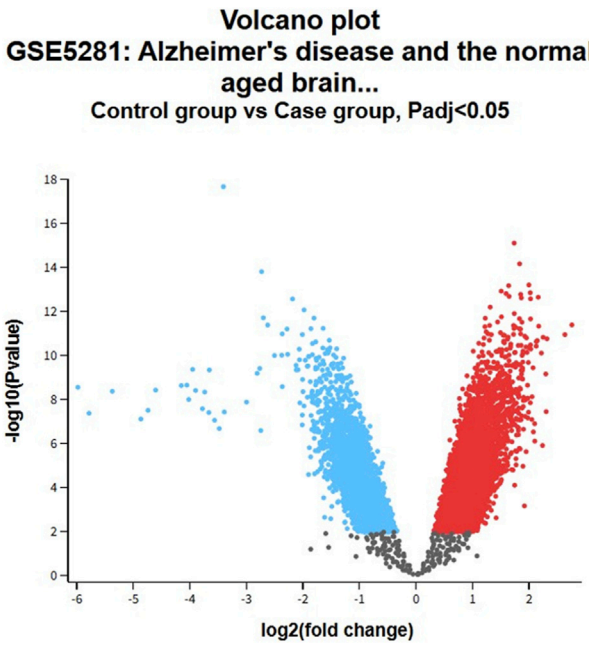


FIGURE 3
Volcano plot of gene expression related to sialyltransferase; red colour shows the upregulation of genes and the blue colour shows the downregulation of genes.

like thrombophlebitis and ototoxicity, lack substantial clinical evidences. To overcome these limitations of the insilico studies, a necessary clinical validation is recommended. Further, a published study explains that the adverse events related to oseltamivir are milder in intensity, which can be managed clinically (Smith et al., 2011). Nevertheless, the concerns raised by the predictive models as a part of insilico studies cannot be counted less. Hence, a thorough discussion and drug repurposing must be considered (Jhee et al., 2008). In order to avoid the adverse drug reactions or drug interactions of the oseltamivir with those that are milder in action, the drug can be formulated into a lipid or polymer-based carriers as targeted drug. Delivery system implicates its action directly in the targets like neuraminidase analogues or acetylcholinesterase (Farid and Jaffar, 2019; Farid and Jaffar, 2020; Fouad et al., 2017; Jaffar and Farid, 2019) for the application of novel molecules clinically in order to improve the quality of life of those with neurological disorders (Srujana et al., 2017).

The molecular docking studies that employed the PyRx revealed a wide range of binding affinities of oseltamivir to various proteins, included those which are of importance in Alzheimer's disease. One such target of oseltamivir was acetylcholinesterase (−7.9 kcal/mol), followed by TNF-alpha (−7.4 kcal/mol), GSK-3B (−6.6 kcal/mol) and neuraminidase (−6.5 kcal/mol). These findings suggest the potential off-target interactions of oseltamivir outside its main mechanism of action and antiviral target (Walczak-Nowicka and Herbet, 2021).

Binding affinity to acetylcholinesterase and neuraminidase is particularly important as it highlights the possible role of oseltamivir in controlling cholinergic pathway and neurodegeneration, which explains the involvement of acetylcholinesterase in the development of Alzheimer's disease (Walczak-Nowicka and Herbet, 2021). The observations of the current study provide high binding affinity of the oseltamivir with acetylcholinesterase; the said action can be validated through the pre-clinical or clinical investigations. Furthermore, the binding affinity of oseltamivir with neuraminidase of −6.5 kcal/mol was consistent with the role of oseltamivir as neuraminidase inhibitor. The observed amino acid interaction with ARG C:172 and GLU A: 128 confirms stable ligand

TABLE 5 Results of pre and post MM-GBSA binding free energy components in kcal/mol of the MD simulated molecular complex of Oseltamivir and Neuraminidase.

Energy components	Pre MM-GBSA (Mean ± SD); random seed	Post MM-GBSA (Mean ± SD); random seed	Pre MM-GBSA (Mean ± SD); Seed_1234	Post MM-GBSA (Mean ± SD); Seed_1234
ΔE_vdW (van der Waals)	0.00 ± 0.00	−18.78 ± 0.01	−0.00 ± 0.00	−19.18 ± 0.78
ΔE_elec (Electrostatic)	0.00 ± 0.00	−266.20 ± 0.46	−0.00 ± 0.00	−259.86 ± 1.81
ΔG_polar (Polar solvation, EGB)	242.01 ± 5.04	252.84 ± 0.07	249.12 ± 6.73	250.85 ± 0.52
ΔG_nonpolar (Non-polar solvation, ESURF)	−4.21 ± 0.51	−3.94 ± 0.04	−4.67 ± 0.12	−4.51 ± 0.08
ΔG_gas (Gas-phase energy)	−270.30 ± 3.88	−284.98 ± 0.48	−279.86 ± 3.25	−279.04 ± 1.97
ΔG_solvation (Total solvation)	237.80 ± 5.06	248.91 ± 0.08	244.45 ± 6.73	246.34 ± 0.52
ΔG_bind (Total binding energy)	−32.50 ± 6.38	−36.07 ± 0.49	−35.41 ± 7.47	−32.70 ± 2.04

ΔE_vdW: van der Waals interaction energy between the ligand and the protein.
ΔE_elec: electrostatic interaction energy.
ΔG_polar: solvation free energy due to polar interactions, calculated using the Poisson–Boltzmann (PB) or Generalized Born (GB) models.
ΔG_nonpolar: non-polar solvation free energy, often estimated from the solvent-accessible surface area (SASA).
ΔG_gas: Total energy in vacuum (ΔE_vdW + ΔEEL).
ΔG_solvation: Total solvation energy (ΔG_polar + ΔG_nonpolar).
ΔG_bind: total binding free energy, sum of the above components.

TABLE 6 Results of pre and post MM-GBSA binding free energy components in kcal/mol of the MD simulated molecular complex of Oseltamivir and Neuraminidase.

Residue	Random seed pre-simulation results		Random seed post-simulation results		Seed_1234 pre-simulation results		Seed_1234 post-simulation results	
	Total Avg.	Total Std. Dev.	Total Avg.	Total Std. Dev.	Total Avg.	Total Std. Dev.	Total Avg.	Total Std. Dev.
ARG:118	0.160709673	20.6970533	0.073136364	10.86711143	0.4862628	12.27216531	0.160709673	20.6970533
GLU:119	0.145217055	16.97288771	0.312664145	19.51603618	0.0962056	13.84325406	0.145217055	16.97288771
LEU:134	−0.100363636	5.004673121	−0.050090909	5.228447377	−0.0945	4.94543138	−0.100363636	5.004673121
GLN:136	−0.000954545	7.763218447	0.0045	5.5218969	0.018	3.367739887	−0.000954545	7.763218447
ASP:151	0.298093891	8.950598719	0.215914473	7.73179094	1.0444396	4.99261937	0.298093891	8.950598719
ARG:152	−1.308884473	13.31951908	0.528265964	14.93811591	−1.7658424	4.183743335	−1.308884473	13.31951908
ARG:156	0.177119345	11.31163594	0.100202145	17.29397933	−0.053198	10.6508142	0.177119345	11.31163594
TRP:178	−0.781931927	6.321986742	−0.316781782	4.945035206	−0.779634	1.907511047	−0.781931927	6.321986742
SER:179	−0.177992	5.067683233	−0.252709673	7.109482835	−0.2032008	6.822918681	−0.177992	5.067683233
ALA:180	−0.126545455	3.673033655	−0.058454545	4.181619527	−0.118	5.358094251	−0.126545455	3.673033655
ILE:194	−0.217727273	5.611584371	−0.128136364	4.297757474	−0.151	4.03092049	−0.217727273	5.611584371
ILE:222	−0.806077745	4.719285829	−1.333992982	5.225018381	−0.7242256	4.429854294	−0.806077745	4.719285829
LEU:223	0.037590909	4.216363729	0.062454545	3.445386751	0.066	1.001068429	0.037590909	4.216363729
ARG:224	1.984467455	11.9544286	2.420310036	10.85285635	0.9764916	4.983251277	1.984467455	11.9544286
THR:225	−0.315034182	5.214389646	−0.096469236	5.560143728	−0.039	3.686086622	−0.315034182	5.214389646
GLU:227	−1.129660982	16.40106878	0.251115018	12.70363795	−0.6225964	5.087889271	−1.129660982	16.40106878
SER:246	0.017864982	16.35876677	0.086831455	7.270088086	0.0887052	2.333831796	0.017864982	16.35876677
ASN:247	−0.007402909	6.693001681	−0.015727273	5.982405279	0.0077264	13.05948338	−0.007402909	6.693001681
HIS:274	−0.036954545	6.725702928	−11.95182465	9.375090448	−0.0515	3.514541713	−0.036954545	6.725702928
GLU:276	−10.35734345	10.12830086	−15.6124636	13.24161797	−10.5700584	3.694668202	−10.35734345	10.12830086
GLU:277	−11.97835425	9.960964089	3.874111455	13.02749532	−11.2034756	12.73485215	−11.97835425	9.960964089
ARG:292	3.614850218	12.26243563	−0.4706028	10.75649373	2.5030608	14.28342655	3.614850218	12.26243563
ASN:294	0.026062909	8.481015303	−0.226556036	7.736542115	−1.137642	3.21043479	0.026062909	8.481015303
TYR:347	−0.617738473	6.642141102	−0.172151127	4.10205902	−0.954044	6.307583365	−0.617738473	6.642141102
GLY:348	−0.118318182	6.118548282	0.151545455	8.723824196	−0.0255	3.935544276	−0.118318182	6.118548282
ARG:371	0.162681818	11.27644502	0.265398218	17.65578963	0.6629548	5.726531147	0.162681818	11.27644502
TYR:406	−0.048908909	5.856747652	−0.424290836	6.079761746	0.2029712	5.262203844	−0.048908909	5.856747652
PRO:431	−0.0085	4.373965825	−0.014954545	4.81802992	−0.047	1.539013945	−0.0085	4.373965825
LIG:469	−12.39375356	11.25346838	0.019090909	9.532751049	−14.1827488	4.869457648	−12.39375356	11.25346838

binding aligning with structural studies of Larisa et al (Gubareva and Mohan, 2022) Comparatively, the binding energies with beta and alpha secretase suggest weaker but potentially significant interaction with amyloid precursors protein-processing enzymes. These findings align with the results provided by Kioke et al., that antiviral agents may provide neuroprotective effect through off-target interactions, i.e., sialidase (Hata et al., 2008).

The stability of neuraminidase-oseltamivir complex was confirmed by molecular dynamic simulations studies, as evident RMSD values for Protein: 0.128424–0.493372 nm, ligand 0.122013–0.838708 nm under random seed simulation and for seed_1234 simulation it ranged from Protein 0.161276–2.858013 nm and Ligand 0.208401–3.217241 nm confirming stability of the complex. The result of radius of gyration (for protein at a range of 3.391135–3.518412 nm and for the ligand at a range of 0.354091–0.37452 nm and 3.390434–4.271447 nm and 0.341893–0.371202 nm for seed_1234 simulation) further supports the structural stability of the complex. These findings

TABLE 7 Gene expression analysis of sialyltransferase gene with accession number GSE5281.

Accession number	Groups	ID	Adj. P-value	Log FC	Gene symbol	Gene title
GSE5281 Focusing on the Alzheimer's disease	Control groups: 61 samples Case group: 44 samples	213476_x_at	6.25E-10	1.999	TUBB3	Tubulin beta 3 class III
		202257_s_at	9.34E-10	2.022	CD2BP2	CD2 cytoplasmic tail binding protein 2
		230656_s_at	1.00E-09	2.163	UTP4	UTP4, small subunit processome component
		207232_s_at	1.00E-09	2.027	DZIP3	DAZ interacting zinc finger protein 3
		205738_s_at	5.07E-09	2.028	FABP3	Fatty acid binding protein 3
		213921_at	8.05E-09	2.759	SST	Somatostatin
		202785_at	8.40E-09	2.172	NDUFA7	NADH: ubiquinone oxidoreductase subunit A7
		223708_at	1.30E-08	2.636	C1QTNF4	C1q and tumour necrosis factor related protein 4
		221772_s_at	1.44E-08	1.926	PPP2R2D	Protein phosphatase 2 regulatory subunit B delta
		1568603_at	1.56E-08	2.250	CADPS	Calcium dependent secretion activator
		201387_s_at	1.63E-08	1.956	UCHL1	Ubiquitin C-terminal hydrolase L1
		202507_s_at	1.72E-08	2.319	SNAP25	Synaptosome associated protein 25
		215020_at	1.94E-08	2.147	NRXN3	Neurexin 3
		1568604_a_at	2.08E-08	2.130	CADPS	Calcium dependent secretion activator
		219549_s_at	2.58E-08	2.027	RTN3	Reticulon 3
		213710_s_at	2.84E-08	2.127	CALM1	Calmodulin 1
		200638_s_at	3.00E-08	1.948	YWHAZ	Tyrosine 3-monooxygenase/tryptophan 5-monooxygenase activation protein zeta
		219408_at	3.15E-08	1.989	PRMT7	Protein arginine methyltransferase 7
		215021_s_at	3.44E-08	2.031	NRXN3	Neurexin 3
		209953_s_at	3.92E-08	1.893	CDC37	Cell division cycle 37

can be related to the results of a research study published by Putra et al. (2018), which demonstrated similar RMSD for the neuraminidase inhibition forming protein-ligand complex. These results are similar with other earlier published computational studies, affirming strong interaction of oseltamivir with the primary target, i.e., neuraminidase. Similarly, the RMSF values P: 0.0451–0.2189 nm, L: 0.0153–0.1925 nm for random simulation and P: 1.2986–2.2136 nm and ligand L: 0.0160–0.2210 nm under seed_1234 explains extensive molecular interactions, which further validates the oseltamivir's potency as neuraminidase inhibitor (Abdullahi et al., 2023).

Moreover, with regards to the acetylcholinesterase, the binding energies (-7.9 kcal/mol) also stands as an add-on to the off-target effects of oseltamivir. Combination of inhibition of neuraminidase and acetylcholinesterase in humans may prove to be beneficial in the management of neurological disorders like Alzheimer's disease (Khunnawutmanotham et al., 2024).

Analysis of the results obtained post MD simulation MM-PBSA and MM-GBSA revealed increased binding affinities of the oseltamivir with Neuraminidase complex. Important energy components such as van der Waals (ΔE_vdW), electrostatic (ΔE_elec) interactions have shown a shift form the negligible (0 ± 0.00) to a favourable value in both productions and trajectories. Which indicates a stronger ligand-protein interactions post MD simulations. On the other hand, polar solvent energy (ΔG_polar) was identified with variable changes, and non-polar energies remains consistently constant. The total binding energies (ΔG_bind) became significantly favourable in random as well as seed_1234 simulations, which confirms improved complex stability. Decomposition level MM-GBSA analysis highlighted critical moieties like GLU:376, GLU:277 and LIG:469 with great shifts in the residual energies of ARG224 and ARG292 post MD simulations. These finding emphasize the value of MD simulations in capturing realistic energetic and structural refinements in ligand binding (Tables 5, 6).

The genes, which play a vital role in the TUBB3 (formation of beta-tubulin), FABP3 (regulates alpha-Synuclein uptake in dopaminergic neurons) and CALM1 (Calcium signal transduction pathway) in Alzheimer's disease, were upregulated. These findings align with the earlier studies published by Shu et al., which reported similar gene expression patterns in AD. The upregulation of neuronal structure and calcium signalling

TABLE 8 The results of significant gene expression from the data of 20 highly upregulated and significantly expressed genes.

Index	Name	P-value	Adjusted p-value	Odds Ratio	Combined score
Cellular components					
1	Vesicle	0.001147	0.04964	17.03	115.27
2	Glutamatergic Synapse	0.002206	0.04964	32.74	200.25
Molecular function					
1	Kinase Binding	0.0006541	0.03205	12.23	89.70
2	Protein Phosphatase Regulator Activity	0.001357	0.03324	42.21	278.70
3	Adenylate Cyclase Regulator Activity	0.004492	0.04964	293.79	1588.07
4	Long-Chain Fatty Acid Binding	0.007179	0.04964	167.86	828.65
5	Phosphoserine Residue Binding	0.007179	0.04964	167.86	828.65
6	Omega Peptidase Activity	0.008072	0.04964	146.87	707.80
Mammalian phenotype level 4					
1	Abnormal PNS Synaptic Transmission	0.00003428	0.008775	312.09	3208.63
2	Abnormal Endplate Potential	0.00009112	0.01166	178.29	1658.66
3	Decreased Paired-Pulse Facilitation	0.0002087	0.01781	113.41	961.11
Jensen tissue					
1	Brain cortex cell line	9.549e-7	0.0001872	36.92	511.81
2	Ganglion	0.000007678	0.0007525	23.78	280.10
3	Interstitial cell of Cajal	0.00002361	0.001543	29.76	317.08
4	Temporal lobe	0.0004218	0.01516	6.88	53.46
5	Parietal lobe	0.0005833	0.01516	8.14	60.61
Jensen diseases					
1	Brain disease	0.002151	0.03929	33.18	203.78
2	Pineoblastoma	0.005388	0.03929	235.02	1227.64
3	Dumping syndrome	0.007179	0.03929	167.86	828.65
4	Dysembryoplastic neuroepithelial tumour	0.007179	0.03929	167.86	828.65

pathways provides further insights into the molecular basics of AD (Wang et al., 2012). Oseltamivir's potential to modulate the gene expression, particularly in sialyltransferase-related pathways, requires further investigation (Fang et al., 2014). The current study does not directly demonstrate the ligands' impact on the genes. The observed docking ability of ligand against sialyltransferase (−6.4 kcal/mol) suggests a possible role in controlling glycosylation process related to neurodegeneration. This aligns with the study published by Jannis et al., which highlights the importance of sialylation in brain function and pathological development (Wißfeld et al., 2024) (Tables 7, 8).

Functional enrichment analysis revealed significant association with molecular function, such as kinase binding ($p = 0.0006541$) and protein phosphatase regulatory activity ($p = 0.001357$). These findings explore the role of oseltamivir in modulating signal pathways indirectly through protein interactions. Additionally, the action on the cellular components, such as vesicle and glutaminergic synapse, underlines the potential impact of oseltamivir on synaptic transmission. Furthermore, the association of oseltamivir's activity with brain cortex cell lines and disease such as dysembryoplastic neuroepithelial tumour ($p = 0.007179$) raises a point regarding the higher implications of the oseltamivir use in neurological conditions. These findings also align with the earlier published studies by Pamela et al., which reported off-target effects on the neural pathways. However, a thorough experimental validation is still required to justify these activities obtained through *in silico* studies (Ferreira et al., 2020).

Conclusion

The current study aims to explore the impact of oseltamivir as an inhibitor on neuraminidase and its analogues in humans, along with the significant genes and pathways involved in the AD. The results highlight the binding affinities of oseltamivir with neuraminidase, acetylcholinesterase and sialyltransferase, along with the importance

of synaptic functions, vesicle transport and kinase-regulating genes, suggesting their pivotal role in the progression of AD. The binding affinities, synaptic functions, vesicle transport and kinase regulating are prior expressed in various research publications linking to cognition decline and development of AD. The identified enzymes can be considered as important molecular targets for developing novel drugs to treat AD in humans. However, a small number of target proteins and insilico methods employed in the study needs to be validated experimentally. Future research anchoring on the same idea should focus on the understanding of molecular mechanisms and clinical validations to solidify the findings with the therapeutic potential of these targets in AD. The current study provides a deeper understanding of the various patterns related to AD, which could help in the future development of novel agents.

Limitations and future directions

This study provides comprehensive yet limited insights regarding oseltamivir's pharmacology and toxicology profile. The insilico predictions and docking studies require experimental validations to confirm their applicability in clinical settings. Additionally, the observed gene expression analysis and pathway association are correlative and do not establish causality.

Future studies should focus on experimental validation of the pharmacological and toxicological activities predicted related to oseltamivir, along with its off-target interaction. For oseltamivir repurposing, both *in vitro* and *in vivo* studies are required to confirm its effect on the neurological pathways and to correct the neurological diseases. Additionally, integrating multi-omics data such as proteomics and metabolomics could possibly elucidate the molecular mechanisms highlighting oseltamivir's pharmacological effects. However, through this study, the potential pharmacological, toxicological and gene regulatory activities of the oseltamivir are uncovered as neuraminidase inhibitor. Likewise, the potential secondary activities and off-target interactions are also uncovered. These findings provide a broader therapeutic applications and safety profile of oseltamivir. Moreover, experimental validation is being considered in collaboration with renowned research institutes and we hope to explore this aspect in the upcoming series works.

Data availability statement

The data can be found in the given link below: https://figshare.com/s/e2b28ab2503735cd6302.

Author contributions

SA: Conceptualization, Formal Analysis, Funding acquisition, Writing – original draft. OA: Conceptualization, Investigation, Resources, Writing – original draft. HA: Writing – review and editing. AA: Methodology, Project administration, Writing – review and editing. TA: Conceptualization, Formal Analysis, Investigation, Writing – review and editing. MeA: Writing – original draft. MuA: Methodology, Visualization, Writing – original draft, Writing – review and editing. MJ: Formal Analysis, Methodology, Software, Writing – original draft.

Funding

The author(s) declare that financial support was received for the research and/or publication of this article. The authors extend their appreciation to the King Salman center For Disability Research for funding this work through Research Group no KSRG-2024-340.

Acknowledgments

The authors extend their appreciation to the King Salman center For Disability Research for funding this work through Research Group no KSRG-2024-340.

Conflict of interest

The authors declare that the research was conducted in the absence of any commercial or financial relationships that could be construed as a potential conflict of interest.

The author(s) declared that they were an editorial board member of Frontiers, at the time of submission. This had no impact on the peer review process and the final decision.

Generative AI statement

The author(s) declare that Generative AI was used in the creation of this manuscript. During the preparation of this work the authors used SciSpace (https://typeset.io/) in order to improve the quality of english language, and to align the names of drugs with the text. After using this tool/service, the authors reviewed and edited the content as needed and takes full responsibility for the content of the publication.

Publisher's note

All claims expressed in this article are solely those of the authors and do not necessarily represent those of their affiliated organizations, or those of the publisher, the editors and the reviewers. Any product that may be evaluated in this article, or claim that may be made by its manufacturer, is not guaranteed or endorsed by the publisher.

Supplementary material

The Supplementary Material for this article can be found online at: https://www.frontiersin.org/articles/10.3389/fchem.2025.1574702/full#supplementary-material

References

Abdullahi, M., Uzairu, A., Shallangwa, G. A., Mamza, P. A., Ibrahim, M. T., Chandra, A., et al. (2023). Unveiling 1,3-thiazine derivative as a potential neuraminidase inhibitor: molecular docking, molecular dynamics, ADMET and DFT studies. *Chem. Afr.* 6 (6), 2957–2967. doi:10.1007/s42250-023-00713-4

Alroy, J., García-Moliner, M. L., and Lee, R. E. (2014). "The pathology of the skeleton in lysosomal storage diseases," in *Pathobiology of human disease*. Editors L. M. McManus and R. N. Mitchell (San Diego: Academic Press), 874–892.

Ashburner, M., Ball, C. A., Blake, J. A., Botstein, D., Butler, H., Cherry, J. M., et al. (2000). Gene Ontology: tool for the unification of biology. *Nat. Genet.* 25 (1), 25–29. doi:10.1038/75556

Baazaoui, N., and Iqbal, K. (2022). Alzheimer's disease: challenges and a therapeutic opportunity to treat it with a neurotrophic compound. *Biomolecules* 12 (10), 1409. doi:10.3390/biom12101409

Baraskar, K., Thakur, P., Shrivastava, R., and Shrivastava, V. K. (2021). Female obesity: association with endocrine disruption and reproductive dysfunction. *Obes. Med.* 28, 100375. doi:10.1016/j.obmed.2021.100375

Baroroh, S. S. M. B. U., Muscifa, Z. S., Destiarani, W., Rohmatullah, F. G., and Yusuf, M. (2023). Molecular interaction analysis and visualization of protein-ligand docking using Biovia Discovery Studio Visualizer. *Indonesian J. Comput. Biol. (IJCB)* 2 (1), 22. doi:10.24198/ijcb.v2i1.46322

Barthold, D., Joyce, G., Ferido, P., Drabo, E. F., Marcum, Z. A., Gray, S. L., et al. (2020). Pharmaceutical treatment for alzheimer's disease and related dementias: utilization and disparities. *J. Alzheimers Dis.* 76 (2), 579–589. doi:10.3233/jad-200133

Bekker, H., Berendsen, H. J. C., Dijkstra, E. J., Achterop, S., Vondrumen, R., Vanderspoel, D., et al. (1993). "Gromacs - a parallel computer for molecular-dynamics simulations," in *4th international conference on computational physics (PC 92)*. Editors R. A. DeGroot and J. Nadrchal (World Scientific Publishing: SINGAPORE), 252–256.

Berman, H. M., Westbrook, J., Feng, Z., Gilliland, G., Bhat, T. N., Weissig, H., et al. (2000). The protein data bank. *Nucleic Acids Res.* 28 (1), 235–242. doi:10.1093/nar/28.1.235

Bird, N. L., Olson, M. R., Hurt, A. C., Oshansky, C. M., Oh, D. Y., Reading, P. C., et al. (2015). Oseltamivir prophylaxis reduces inflammation and facilitates establishment of cross-strain protective T cell memory to influenza viruses. *PLOS ONE* 10 (6), e0129768. doi:10.1371/journal.pone.0129768

Bishop, P., Rocca, D., and Henley, J. M. (2016). Ubiquitin C-terminal hydrolase L1 (UCH-L1): structure, distribution and roles in brain function and dysfunction. *Biochem. J.* 473 (16), 2453–2462. doi:10.1042/bcj20160082

Breijyeh, Z., and Karaman, R. (2020). Comprehensive review on Alzheimer's disease: causes and treatment. *Molecules* 25 (24), 5789. doi:10.3390/molecules25245789

Bugnon, M., Goullieux, M., Röhrig, U. F., Perez, M. A. S., Daina, A., Michielin, O., et al. (2023). SwissParam 2023: a modern web-based tool for efficient small molecule parametrization. *J. Chem. Inf. Model.* 63 (21), 6469–6475. doi:10.1021/acs.jcim.3c01053

Bytheway, I., Darley, M. G., and Popelier, P. L. A. (2008). The calculation of polar surface area from first principles: an application of quantum chemical topology to drug design. *ChemMedChem* 3 (3), 445–453. doi:10.1002/cmdc.200700262

Carroll, C. M., and Li, Y.-M. (2016). Physiological and pathological roles of the γ-secretase complex. *Brain Res. Bull.* 126, 199–206. doi:10.1016/j.brainresbull.2016.04.019

Chahinian, H., Yahi, N., and Fantini, J. (2024). Glutamate, gangliosides, and the synapse: electrostatics at work in the brain. *Int. J. Mol. Sci.* 25 (16), 8583. doi:10.3390/ijms25168583

Chen, E. Y., Tan, C. M., Kou, Y., Duan, Q., Wang, Z., Meirelles, G. V., et al. (2013). Enrichr: interactive and collaborative HTML5 gene list enrichment analysis tool. *BMC Bioinforma.* 14 (1), 128. doi:10.1186/1471-2105-14-128

Chen, S., Cao, Z., Nandi, A., Counts, N., Jiao, L., Prettner, K., et al. (2024). The global macroeconomic burden of Alzheimer's disease and other dementias: estimates and projections for 152 countries or territories. *Lancet Glob. Health* 12 (9), e1534–e1543. doi:10.1016/s2214-109x(24)00264-x

Chin, D., and Means, A. R. (2000). Calmodulin: a prototypical calcium sensor. *Trends Cell Biol.* 10 (8), 322–328. doi:10.1016/s0962-8924(00)01800-6

Corbo, C. P., and Alonso, A. d.C. (2011). "Chapter 2 - therapeutic targets in alzheimer's disease and related tauopathies," in *Progress in molecular biology and translational science*. Editor S. Rahman (Academic Press), 47–83.

Coutsias, E. A., and Wester, M. J. (2019). RMSD and symmetry. *J. Comput. Chem.* 40 (15), 1496–1508. doi:10.1002/jcc.25802

Dallakyan, S., and Olson, A. J. (2015). "Small-molecule library screening by docking with PyRx," in *Chemical biology: methods and protocols*. Editors J. E. Hempel, C. H. Williams, and C. C. Hong (New York, NY: Springer New York), 243–250.

DeTure, M. A., and Dickson, D. W. (2019). The neuropathological diagnosis of Alzheimer's disease. *Mol. Neurodegener.* 14 (1), 32. doi:10.1186/s13024-019-0333-5

Du, J., Shui, H., Chen, R., Dong, Y., Xiao, C., Hu, Y., et al. (2024). Neuraminidase-1 (NEU1): biological roles and therapeutic relevance in human disease. *Curr. Issues Mol. Biol.* 46 (8), 8031–8052. doi:10.3390/cimb46080475

Duly, A. M. P., Kao, F. C. L., Teo, W. S., and Kavallaris, M. (2022). Biii-tubulin gene regulation in health and disease. *Front. Cell Dev. Biol.* 10, 851542. doi:10.3389/fcell.2022.851542

Dzulko, M., Pons, M., Henke, A., Schneider, G., and Krämer, O. H. (2020). The PP2A subunit PR130 is a key regulator of cell development and oncogenic transformation. *Biochimica Biophysica Acta (BBA) - Rev. Cancer* 1874 (2), 188453. doi:10.1016/j.bbcan.2020.188453

Easwaran, V., Almeleebia, T. M., Mantargi, M. J. S., Khan, N. A., Alshahrani, S. M., Orayj, K., et al. (2023b). Patient safety culture in the southern region of Saudi arabia: a survey among community pharmacies. *Healthcare* 11 (10), 1416. doi:10.3390/healthcare11101416

Easwaran, V., Khan, N. A., Iqbal, M. J., Alshahrani, S. M., Orayj, K., Almeleebia, T. M., et al. (2023a). The study of healthcare professionals' perspective towards the quality of diabetic care services in Abha. *Eur. Rev. Med. Pharmacol. Sci.* 27 (10), 4328–4336. doi:10.26355/eurrev_202305_32437

Fang, Q., Gao, Y., Chen, M.-f., Guo, X.-l., Yang, X., Yang, X., et al. (2014). Molecular epidemiology and evolution of A(H1N1)pdm09 and H3N2 virus during winter 2012–2013 in Beijing, China. *J. Mol. Epidemiol. Evol. Genet. Infect. Dis.* 26, 228–240. doi:10.1016/j.meegid.2014.05.034

Farid, M., and Jaffar, M. (2019). Creation and assessment of buccal mucoadhesive sustained release oral films. *Int. J. Pharm. Pharm. Res.* 16 (2), 30–41.

Farid, M., and Jaffar, M. (2020). Formulation and evaluation of ofloxacin loaded chitosan nanoparticles. *WORLD J. Pharm. Pharm. Sci.* 9 (10), 1–13.

Ferreira, P. C. L., De Bastiani, M. A., Bellaver, B., Povala, G., Brum, W. S., Ramos, V. G., et al. (2020). Functional enrichment analysis of differentially expressed genes leads to dysregulation in biological processes networks in Alzheimer's disease continuum. *Alzheimer's & Dementia* 16 (S2), e039506. doi:10.1002/alz.039506

Forsyth, E., and Ritzline, P. D. (1998). An overview of the etiology, diagnosis, and treatment of alzheimer disease. *Phys. Ther.* 78 (12), 1325–1331. doi:10.1093/ptj/78.12.1325

Fouad, M., Zaki, A., Shabana, S., El-Haggar, R., Haggar, M., and Jaffar, S. (2017). Evaluation of oral hypoglycemic potency of Medicago polymorpha and Zygophyllum simplex: a Drug-Drug interaction study. *Medicine* 6 (6), 648–651.

Gao, C., Jiang, J., Tan, Y., and Chen, S. (2023). Microglia in neurodegenerative diseases: mechanism and potential therapeutic targets. *Signal Transduct. Target. Ther.* 8 (1), 359. doi:10.1038/s41392-023-01588-0

Germoush, M. O., Mantargi, M. J. S., Sarhan, M., Alrashdi, B. M., Massoud, D., Alzwain, S., et al. (2024). Molecular docking of eleven snake venom peptides targeting human immunodeficiency virus capsid glycoprotein as inhibitors. *Open Veterinary J.* 14 (11), 2936–2949. doi:10.5455/ovj.2024.v14.i11.22

Glanz, V. Y., Myasoedova, V. A., Grechko, A. V., and Orekhov, A. N. (2018). Inhibition of sialidase activity as a therapeutic approach. *Drug Des. Devel Ther.* 12, 3431–3437. doi:10.2147/dddt.s176220

Green, M. D., Nettey, H., and Wirtz, R. A. (2008). Determination of oseltamivir quality by colorimetric and liquid chromatographic methods. *Emerg. Infect. Dis. J.* 14 (4), 552–556. doi:10.3201/eid1404.061199

Grumati, P., Morozzi, G., Hölper, S., Mari, M., Harwardt, M.-L. I. E., Yan, R., et al. (2017). Full length RTN3 regulates turnover of tubular endoplasmic reticulum via selective autophagy. *eLife* 6, e25555. doi:10.7554/elife.25555

Gubareva, L., and Mohan, T. (2022). Antivirals targeting the neuraminidase. *Cold Spring Harb. Perspect. Med.* 12 (1), a038455. doi:10.1101/cshperspect.a038455

Hama, R. (2016). The mechanisms of delayed onset type adverse reactions to oseltamivir. *Infect. Dis.* 48 (9), 651–660. doi:10.1080/23744235.2016.1189592

Hata, K., Koseki, K., Yamaguchi, K., Moriya, S., Suzuki, Y., Yingsakmongkon, S., et al. (2008). Limited inhibitory effects of oseltamivir and zanamivir on human sialidases. *Antimicrob. Agents Chemother.* 52 (10), 3484–3491. doi:10.1128/aac.00344-08

Holtzman, D. M., Morris, J. C., and Goate, A. M. (2011). Alzheimer's disease: the challenge of the second century. *Sci. Transl. Med.* 3 (77), 77sr1. doi:10.1126/scitranslmed.3002369

Iqbal, K., Liu F Fau - Gong, C. X., Gong Cx Fau - Grundke-Iqbal, I., and Grundke-Iqbal, I. (2010). Tau in Alzheimer disease and related tauopathies. *Curr. Alzheimer Res.* 7 (8), 656–664. doi:10.2174/156720510793611592

Jaffar, M., and Farid, M. (2019). Formulation and *in vivo* evaluation of risperidone spherical agglomerates prepared for earlier absorption of risperidone. *World J. Pharm. Res.* 8 (13), 1430–1444.

Jhee, S. S., Yen, M., Ereshefsky, L., Leibowitz, M., Schulte, M., Kaeser, B., et al. (2008). Low penetration of oseltamivir and its carboxylate into cerebrospinal fluid in healthy Japanese and caucasian volunteers. *Antimicrob. Agents Chemother.* 52 (10), 3687–3693. doi:10.1128/aac.00327-08

Kalyan, G. U., Reddy, D. P., Chandrakanth, G., Pooja, B., Anitha, V., and Vivek, D. (2023). "Gene association disease prediction by GEO2R tool," in *2023 international conference on evolutionary algorithms and soft computing techniques (EASCT)*.

Keil, J. M., Rafn, G. R., Turan, I. M., Aljohani, M. A., Sahebjam-Atabaki, R., and Sun, X.-L. (2022). Sialidase inhibitors with different mechanisms. *J. Med. Chem.* 65 (20), 13574–13593. doi:10.1021/acs.jmedchem.2c01258

Kelley, B. J., and Petersen, R. C. (2007). Alzheimer's disease and mild cognitive impairment. *Neurol. Clin.* 25 (3), 577–609. doi:10.1016/j.ncl.2007.03.008

Khatua, B., Roy, S., and Mandal, C. (2013). Sialic acids siglec interaction: a unique strategy to circumvent innate immune response by pathogens. *Indian J. Med. Res.* 138 (5), 648–662.

Khunnawutmanotham, N., Sooknual, P., Batsomboon, P., Ploypradith, P., Chimnoi, N., Patigo, A., et al. (2024). Synthesis, antiacetylcholinesterase activity, and molecular dynamics simulation of aporphine–benzylpyridinium conjugates. *ACS Med. Chem. Lett.* 15 (1), 132–142. doi:10.1021/acsmedchemlett.3c00467

Kim, S., Chen, J., Cheng, T., Gindulyte, A., He, J., He, S., et al. (2024). PubChem 2025 update. *Nucleic Acids Res.* 53, D1516–D1525. doi:10.1093/nar/gkae1059

Kuleshov, M. V., Jones, M. R., Rouillard, A. D., Fernandez, N. F., Duan, Q., Wang, Z., et al. (2016). Enrichr: a comprehensive gene set enrichment analysis web server 2016 update. *Nucleic Acids Res.* 44 (W1), W90–W97. doi:10.1093/nar/gkw377

Lee, S.-M., Lee, S. H., Jung, Y., Lee, Y., Yoon, J. H., Choi, J. Y., et al. (2020). FABP3-mediated membrane lipid saturation alters fluidity and induces ER stress in skeletal muscle with aging. *Nat. Commun.* 11 (1), 5661. doi:10.1038/s41467-020-19501-6

Liang, W. S., Dunckley, T., Beach, T. G., Grover, A., Mastroeni, D., Ramsey, K., et al. (2008b). Altered neuronal gene expression in brain regions differentially affected by Alzheimer's disease: a reference data set. *Physiol. Genomics* 33 (2), 240–256. doi:10.1152/physiolgenomics.00242.2007

Liang, W. S., Dunckley, T., Beach, T. G., Grover, A., Mastroeni, D., Walker, D. G., et al. (2007). Gene expression profiles in anatomically and functionally distinct regions of the normal aged human brain. *Physiol. Genomics* 28 (3), 311–322. doi:10.1152/physiolgenomics.00208.2006

Liang, W. S., Reiman, E. M., Valla, J., Dunckley, T., Beach, T. G., Grover, A., et al. (2008a). Alzheimer's disease is associated with reduced expression of energy metabolism genes in posterior cingulate neurons. *Proc. Natl. Acad. Sci.* 105 (11), 4441–4446. doi:10.1073/pnas.0709259105

Livingston, G., Huntley, J., Sommerlad, A., Ames, D., Ballard, C., Banerjee, S., et al. (2020). *Lancet. Lancet* 396 (10248), 413–446. doi:10.1016/s0140-6736(20)30367-6

Magesh, S., Savita, V., Moriya, S., Suzuki, T., Miyagi, T., Ishida, H., et al. (2009). Human sialidase inhibitors: design, synthesis, and biological evaluation of 4-acetamido-5-acylamido-2-fluoro benzoic acids. *Bioorg. & Med. Chem.* 17 (13), 4595–4603. doi:10.1016/j.bmc.2009.04.065

Magesh, S., Suzuki, T., Miyagi, T., Ishida, H., and Kiso, M. (2006). Homology modeling of human sialidase enzymes NEU1, NEU3 and NEU4 based on the crystal structure of NEU2: hints for the design of selective NEU3 inhibitors. *J. Mol. Graph. Model.* 25 (2), 196–207. doi:10.1016/j.jmgm.2005.12.006

Malosh, R. E., Martin, E. T., Heikkinen, T., Brooks, W. A., Whitley, R. J., and Monto, A. S. (2017). Efficacy and safety of oseltamivir in children: systematic review and individual patient data meta-analysis of randomized controlled trials. *Clin. Infect. Dis.* 66 (10), 1492–1500. doi:10.1093/cid/cix1040

Maurice, P., Baud, S., Bocharova, O. V., Bocharov, E. V., Kuznetsov, A. S., Kawecki, C., et al. (2016). New insights into molecular organization of human neuraminidase-1: transmembrane topology and dimerization ability. *Sci. Rep.* 6 (1), 38363. doi:10.1038/srep38363

McAuley, J. L., Gilbertson, B. P., Trifkovic, S., Brown, L. E., and McKimm-Breschkin, J. L. (2019). Influenza virus neuraminidase structure and functions. *Front. Microbiol.* 10, 39. doi:10.3389/fmicb.2019.00039

McKimm-Breschkin, J. L. (2013). Influenza neuraminidase inhibitors: antiviral action and mechanisms of resistance. *Influenza Other Respir. Viruses* 7 (s1), 25–36. doi:10.1111/irv.12047

Miller, B. R., III, McGee, T. D., Jr., Swails, J. M., Homeyer, N., Gohlke, H., and Roitberg, A. E. (2012). MMPBSA.py: an efficient program for end-state free energy calculations. *J. Chem. Theory Comput.* 8 (9), 3314–3321. doi:10.1021/ct300418h

Miyagi, T. (2008). "Aberrant expression of sialidase in cancer and diabetes," in *Experimental glycoscience: glycobiology*. Editor N. Taniguchi, (Tokyo: Springer Japan), 329–332.

Mu, M., Sun, H., Geng, S., Xu, T., Sun, C., Zhang, Z., et al. (2024). Neurexin-3 in the paraventricular nucleus of the hypothalamus regulates body weight and glucose homeostasis independently of food intake. *Mol. Brain* 17 (1), 49. doi:10.1186/s13041-024-01124-3

Murugan, N. A., Podobas, A., Gadioli, D., Vitali, E., Palermo, G., and Markidis, S. (2022). A review on parallel virtual screening softwares for high-performance computers. *Pharmaceuticals* 15 (1), 63. doi:10.3390/ph15010063

Nichols, E., Steinmetz, J. D., Vollset, S. E., Fukutaki, K., Chalek, J., Abd-Allah, F., et al. (2022). Estimation of the global prevalence of dementia in 2019 and forecasted prevalence in 2050: an analysis for the Global Burden of Disease Study 2019. *Lancet Public Health* 7 (2), e105–e125. doi:10.1016/s2468-2667(21)00249-8

O'Boyle, N. M., Banck, M., James, C. A., Morley, C., Vandermeersch, T., and Hutchison, G. R. (2011). Open Babel: an open chemical toolbox. *J. Cheminformatics* 3 (1), 33. doi:10.1186/1758-2946-3-33

Olsson, B., Zetterberg, H., Hampel, H., and Blennow, K. (2011). Biomarker-based dissection of neurodegenerative diseases. *Prog. Neurobiol.* 95 (4), 520–534. doi:10.1016/j.pneurobio.2011.04.006

Partonen, T. (2023). "Medication effects," in *Encyclopedia of sleep and circadian rhythms*. Editor C. A. Kushida Second Edition) (Oxford: Academic Press), 755–760.

Passeri, E., Elkhoury, K., Morsink, M., Broersen, K., Linder, M., Tamayol, A., et al. (2022). Alzheimer's disease: treatment strategies and their limitations. *Int. J. Mol. Sci.* 23 (22), 13954. doi:10.3390/ijms232213954

Poroikov, V., Filimonov, D., Lagunin, A., Gloriozova, T., and Zakharov, A. (2007). PASS: identification of probable targets and mechanisms of toxicity†. *SAR QSAR Environ. Res.* 18 (1-2), 101–110. doi:10.1080/10629360601054032

Puigdellívol, M., Allendorf, D. H., and Brown, G. C. (2020). Sialylation and galectin-3 in microglia-mediated neuroinflammation and neurodegeneration. *Front. Cell. Neurosci.* 14, 162. doi:10.3389/fncel.2020.00162

Putra, R., Imaniastuti, R., Nasution, M., Kerami, D., and Tambunan, U. (2018). "Molecular docking simulation of neuraminidase influenza A subtype H1N1 with potential inhibitor of disulfide cyclic peptide (DNY, NNY, LRL)," in *IOP conference series: materials science and engineering* (Bristol, United Kingdom: IOP Publishing).

Rathod, R., Kale, A., and Joshi, S. (2016). Novel insights into the effect of vitamin B12 and omega-3 fatty acids on brain function. *J. Biomed. Sci.* 23 (1), 17. doi:10.1186/s12929-016-0241-8

Readhead, B., Haure-Mirande, J.-V., Funk, C. C., Richards, M. A., Shannon, P., Haroutunian, V., et al. (2018). Multiscale analysis of independent Alzheimer's cohorts finds disruption of molecular, genetic, and clinical networks by human herpesvirus. *Neuron* 99 (1), 64–82.e7. doi:10.1016/j.neuron.2018.05.023

Reddy, Y. P., Chandrasekhar, K. B., and Mohammed Jaffar, S. (2015). A study of nigella sativa induced growth inhibition of MCF and HepG2 cell lines: an anti-neoplastic study along with its mechanism of action. *Pharmacogn. Res.* 7 (2), 193. doi:10.4103/0974-8490.150541

Sambamurti, K. (2007). "Beta secretase," in *xPharm: the comprehensive pharmacology reference*. Editors S. J. Enna and D. B. Bylund (New York: Elsevier), 1–8.

Samson, W. K., Zhang, J. V., Avsian-Kretchmer, O., Cui, K., Yosten, G. L. C., Klein, C., et al. (2008). Neuronostatin encoded by the somatostatin gene regulates neuronal, cardiovascular, and metabolic functions. *J. Biol. Chem.* 283 (46), 31949–31959. doi:10.1074/jbc.m804784200

Sasumana, J., and Kaushik, V. (2018). "Molecular dynamics simulation by using NAMD-VMD and gromacs," in *Journal of emerging technologies and innovative research*.

Schirmer, P., and Holodniy, M. (2009). Oseltamivir for treatment and prophylaxis of influenza infection. *Expert Opin. Drug Saf.* 8 (3), 357–371. doi:10.1517/14740330902840519

Schütze, S., Machleidt, T., and Krönke, M. (1992). Mechanisms of tumor necrosis factor action. *Semin. Oncol.* 19 (2 Suppl. 4), 16–24.

Seo, N., Lee, H., Oh, M. J., Kim, G. H., Lee, S. G., Ahn, J. K., et al. (2021). Isomer-specific monitoring of sialylated N-glycans reveals association of α2,3-linked sialic acid epitope with behcet's disease. *Front. Mol. Biosci.* 8, 778851. doi:10.3389/fmolb.2021.778851

Singh, M. K., Shin, Y., Ju, S., Han, S., Kim, S. S., and Kang, I. (2024). Comprehensive overview of Alzheimer's disease: etiological insights and degradation strategies. *Int. J. Mol. Sci.* 25 (13), 6901. doi:10.3390/ijms25136901

Smith, J. R., Rayner, C. R., Donner, B., Wollenhaupt, M., Klumpp, K., and Dutkowski, R. (2011). Oseltamivir in seasonal, pandemic, and avian influenza: a comprehensive review of 10-years clinical experience. *Adv. Ther.* 28 (11), 927–959. doi:10.1007/s12325-011-0072-7

Srujana, M. P., Vigneshwaran, E., Kumar, G. S., Jyoshna, K., and Jaffar Sadiq, M. J. (2017). Assessment of quality of life in children with epilepsy in rural settings of South India: a cross sectional study. *CHRISMED J. Health Res.* 4 (2), 110–116. doi:10.4103/2348-3334.201980

Tian, Z., Feng, B., Wang, X.-Q., and Tian, J. (2022). Focusing on cyclin-dependent kinases 5: a potential target for neurological disorders. *Front. Mol. Neurosci.* 15, 1030639. doi:10.3389/fnmol.2022.1030639

Treanor, J. J., Hayden, F. G., Vrooman, P. S., Barbarash, R., Bettis, R., Riff, D., et al. (2000). Efficacy and safety of the oral neuraminidase inhibitor oseltamivir in treating acute InfluenzaA randomized controlled trial. *JAMA* 283 (8), 1016–1024. doi:10.1001/jama.283.8.1016

Varghese, A. F., Chockalingam, M. P., Viswaksenan, S., Santhappan, J. S., Ravindran, A. L., Balac, B., et al. (2024). Experimental determination of radius of gyration of an object using compound pendulum technique. *AIP Conf. Proc.* 3059 (1), 030005. doi:10.1063/5.0193845

Vester, S. K., Beavil, R. L., Lynham, S., Beavil, A. J., Cunninghame Graham, D. S., McDonnell, J. M., et al. (2021). Nucleolin acts as the receptor for C1QTNF4 and

supports C1QTNF4-mediated innate immunity modulation. *J. Biol. Chem.* 296, 100513. doi:10.1016/j.jbc.2021.100513

Volkow, N. D., Ding, Y.-S., Fowler, J. S., and Gatley, S. J. (2001). Imaging brain cholinergic activity with positron emission tomography: its role in the evaluation of cholinergic treatments in Alzheimer's dementia. *Biol. Psychiatry* 49 (3), 211–220. doi:10.1016/s0006-3223(00)01112-4

Walczak-Nowicka, Ł. J., and Herbet, M. (2021). Acetylcholinesterase inhibitors in the treatment of neurodegenerative diseases and the role of acetylcholinesterase in their pathogenesis. *Int. J. Mol. Sci.* 22 (17), 9290. doi:10.3390/ijms22179290

Wang, S., Qaisar, U., Yin, X., and Grammas, P. (2012). Gene expression profiling in Alzheimer's disease brain microvessels. *J. Alzheimer's Dis.* 31 (1), 193–205. doi:10.3233/jad-2012-120454

Wißfeld, J., Abou Assale, T., Cuevas-Rios, G., Liao, H., and Neumann, H. (2024). Therapeutic potential to target sialylation and SIGLECs in neurodegenerative and psychiatric diseases. *Front. Neurology* 15, 1330874. doi:10.3389/fneur.2024.1330874

Xiao, M., Yao, C., Liu, F., Xiang, W., Zuo, Y., Feng, K., et al. (2022). Sialic acid ameliorates cognitive deficits by reducing amyloid deposition, nerve fiber production, and neuronal apoptosis in a mice model of Alzheimer's disease. *NeuroSci* 3 (1), 28–40. doi:10.3390/neurosci3010002

Xie, Z., Bailey, A., Kuleshov, M. V., Clarke, D. J. B., Evangelista, J. E., Jenkins, S. L., et al. (2021). Gene set knowledge discovery with enrichr. *Curr. Protoc.* 1 (3), e90. doi:10.1002/cpz1.90

Yesselman, J. D., Price, D. J., Knight, J. L., and Brooks Iii, C. L. (2012). MATCH: an atom-typing toolset for molecular mechanics force fields. *J. Comput. Chem.* 33 (2), 189–202. doi:10.1002/jcc.21963

Yuan, S., Chan, H. C. S., and Hu, Z. (2017). Using PyMOL as a platform for computational drug design. *WIREs Comput. Mol. Sci.* 7 (2), e1298. doi:10.1002/wcms.1298

Zhang, R., Yip, V. L. Y., and Withers, S. G. (2010). "8.11 - mechanisms of enzymatic glycosyl transfer," in *Comprehensive natural products II*. Editors H.-W. Liu and L. Mander (Oxford: Elsevier), 385–422.

Zhang, W., Xiao, D., Mao, Q., and Xia, H. (2023). Role of neuroinflammation in neurodegeneration development. *Signal Transduct. Target. Ther.* 8 (1), 267. doi:10.1038/s41392-023-01486-5

Zhao, K.-W., and Neufeld, E. F. (2000). Purification and characterization of recombinant human α-N-acetylglucosaminidase secreted by Chinese hamster ovary cells. *Protein Expr. Purif.* 19 (1), 202–211. doi:10.1006/prep.2000.1230

Zhu, W., Zhou, Y., Guo, L., and Feng, S. (2024). Biological function of sialic acid and sialylation in human health and disease. *Cell Death Discov.* 10 (1), 415. doi:10.1038/s41420-024-02180-3

Zoete, V., Cuendet, M. A., Grosdidier, A., and Michielin, O. (2011). SwissParam: a fast force field generation tool for small organic molecules. *J. Comput. Chem.* 32 (11), 2359–2368. doi:10.1002/jcc.21816

frontiers | Frontiers in Chemistry

TYPE Original Research
PUBLISHED 26 June 2025
DOI 10.3389/fchem.2025.1606848

Check for updates

OPEN ACCESS

EDITED BY
Guigen Li,
Texas Tech University, United States

REVIEWED BY
Deepender Kaushik,
University of Nebraska Medical Center, United States
Ata Makarem,
University of Hamburg, Germany

*CORRESPONDENCE
Ranya Mohammed Elmagzoub,
ranya.idrees@nbu.edu.sa
Stefan Bräse,
stefan.braese@kit.edu

RECEIVED 06 April 2025
ACCEPTED 09 June 2025
PUBLISHED 26 June 2025

CITATION
Khasawneh HEN, Ali EI, Elmagzoub RM, Al-Aouadi RFA, Almagharbeh WT, Alotaibi G, Bräse S and Alkhammash A (2025) A novel thiazole-sulfonamide hybrid molecule as a promising dual tubulin/carbonic anhydrase IX inhibitor with anticancer activity.
Front. Chem. 13:1606848.
doi: 10.3389/fchem.2025.1606848

COPYRIGHT
© 2025 Khasawneh, Ali, Elmagzoub, Al-Aouadi, Almagharbeh, Alotaibi, Bräse and Alkhammash. This is an open-access article distributed under the terms of the Creative Commons Attribution License (CC BY). The use, distribution or reproduction in other forums is permitted, provided the original author(s) and the copyright owner(s) are credited and that the original publication in this journal is cited, in accordance with accepted academic practice. No use, distribution or reproduction is permitted which does not comply with these terms.

A novel thiazole-sulfonamide hybrid molecule as a promising dual tubulin/carbonic anhydrase IX inhibitor with anticancer activity

Hussam Elddin Nabeih Khasawneh[1], Elryah I. Ali[2], Ranya Mohammed Elmagzoub[2]*, Raed Fanoukh Aboqader Al-Aouadi[3], Wesam Taher Almagharbeh[4], Ghallab Alotaibi[5], Stefan Bräse[6]* and Abdullah Alkhammash[5]

[1]Chemical Engineering Department, Al-Huson University College, Al-Balqa' Applied University, Al-Salt, Jordan, [2]Department of Medical Laboratory Technology, College of Applied Medical Sciences, Northern Border University, Arar, Saudi Arabia, [3]College of Medicine, Al-Ayen Iraqi University, AUIQ, An Nasiriyah, Iraq, [4]Medical and Surgical Nursing Department, Faculty of Nursing, University of Tabuk, Tabuk, Saudi Arabia, [5]Department of Pharmacology, College of Pharmacy, Al-Dawadmi Campus, Shaqra University, Shaqra, Saudi Arabia, [6]Institute of Biological and Chemical Systems, Functional Molecular Systems (IBCS-FMS), Karlsruhe Institute of Technology (KIT), Karlsruhe, Germany

Introduction: Multitargeted anticancer agents can overcome resistance by simultaneously modulating key pathways. This study reports a novel thiazole - chalcone/sulfonamide hybrid (compound 7) designed to inhibit both tubulin polymerization and carbonic anhydrase IX (CA IX).

Methods: Compound 7 was synthesized through a five-step sequence and characterized by NMR and elemental analysis. Its cytotoxicity was assessed against cancer (HT-29, A549, 786-O, MCF-7) and normal (WI-38) cell lines. Tubulin polymerization and CA isoform inhibition (I, II, IX, XII) were evaluated. Apoptosis induction was confirmed by measuring p53, Bax, Bcl-2, and caspases 3 and 9. Molecular docking, ADMET, and DFT studies supported mechanistic insights.

Results and discussion: Compound 7 showed potent activity against HT-29 cells (IC_{50} = 0.98 μM) and low toxicity toward WI-38 cells. It inhibited tubulin polymerization (IC_{50} = 2.72 μM) and selectively targeted CA IX (IC_{50} = 0.021 μM) and CA XII, while sparing CA I and II. Apoptotic effects were confirmed by increased p53 and Bax, reduced Bcl-2, and activation of caspases. Docking studies revealed key interactions within the colchicine-binding site of tubulin and CA IX's zinc-binding pocket. ADMET and DFT results supported its drug-like properties and electronic suitability. These findings suggest that compound 7 is a promising lead for dual-targeted anticancer therapy with selective cytotoxicity and mechanistic efficacy.

KEYWORDS

thiazole, chalcone, sulphonamide, tubulin, carbonic anhydrase, cytotoxicity, apoptosis

1 Introduction

Cancer is a complex and heterogeneous disease involving multiple dysregulated pathways that contribute to uncontrolled proliferation, evasion of apoptosis, angiogenesis, and metastasis (Hanahan and Weinberg, 2011; Vogelstein et al., 2013). Traditional chemotherapeutics often target a single pathway, which can be bypassed by cancer cells, leading to resistance and limited long-term efficacy. Among other advanced theranostic methods (Sgouros et al., 2020; Klika et al., 2021; Makarem et al., 2019), multitarget-directed ligands (MTDLs) have emerged as a promising strategy, offering the ability to modulate multiple cancer-related targets with a single compound (Doostmohammadi et al., 2024; Brindisi et al., 2022). This approach enhances therapeutic efficacy, reduces the likelihood of resistance, and improves treatment outcomes compared to monotherapies or combination regimens. Thus, the rational design of multitarget anticancer agents holds great potential in cancer drug discovery, enabling the simultaneous disruption of multiple tumor-promoting mechanisms and providing a comprehensive approach to address the complexity of tumor biology (Li et al., 2021; Lembo and Bottegoni, 2024).

Among the diverse molecular targets explored in recent years, carbonic anhydrase (CA), particularly the tumor-associated isoforms IX and XII, has garnered significant attention (Supuran, 2018). These membrane-bound enzymes are crucial for regulating pH homeostasis in hypoxic tumor microenvironments by the reversible hydration of carbon dioxide (Mboge et al., 2018). Overexpression of CA IX, driven by hypoxia-inducible factors, is strongly associated with tumor aggressiveness, poor prognosis, and resistance to conventional therapies, as it facilitates extracellular acidification and promotes invasion and metastasis (Chiche et al., 2008). Selective inhibition of CA IX/XII disrupts the acidic pH gradient essential for tumor survival, leading to impaired proliferation and increased sensitivity to other anticancer agents while sparing normal tissues (Neri and Supuran, 2011; Lou et al., 2011).

Sulfonamides represent the most extensively studied class of CA inhibitors (Carta et al., 2014; Khokhlov et al., 2023), with several derivatives demonstrating promising anticancer activity through selective inhibition of CA IX/XII (McDonald et al., 2022). The ureido-substituted sulfonamide SLC-0111 has advanced to Phase Ib/II clinical trials for metastatic pancreatic cancer, demonstrating the clinical viability of this approach (Kalinin et al., 2021). In recent investigations, the structural optimization of sulfonamide frameworks has led to the development of significantly improved inhibitors. Compound **I** displayed stronger inhibition than SLC-0111 against CA IX and exhibited potent antiproliferative activity against HCT-116 and MCF-7 cells (Elbadawi et al., 2021). Compound **II**, a benzofuran-based sulfonamide, exhibited exceptional CA IX selectivity with a K_i of 5.5 nM and favorable selectivity over CA II (Shaldam et al., 2021). The thiadiazole analogue **III** demonstrated a K_i of 7.9 nM against CA IX, outperforming SLC-0111 (K_i = 45 nM) (Abo-Ashour et al., 2019). Furthermore, compound **IV**, a pyrazole benzenesulfonamide, exhibited potent inhibition of CA XII with an IC_{50} of 0.101 μM and notable anticancer efficacy across several tumor cell lines (Ahmed et al., 2023). Lastly, compound **V**, a 1,2,3-triazole benzenesulfonamide, achieved a K_i of 0.03 μM for CA IX and demonstrated dual cytotoxic activity against MCF-7 and Hep-3B cells with high selectivity indices (Abdelhakeem et al., 2024). Examples of such sulfonamide-based inhibitors are illustrated in Figure 1.

In addition to targeting metabolic adaptation, disrupting mitotic progression has long been an effective strategy in cancer treatment (van Vuuren et al., 2015). Among the most validated targets in this context is tubulin, a structural protein essential for the formation of the mitotic spindle and cell division. The dynamic polymerization and depolymerization of microtubules during cell cycle progression render tubulin particularly susceptible to pharmacological intervention (Jordan and Wilson, 2004). Tubulin-binding agents, such as paclitaxel and vinblastine, have demonstrated significant clinical efficacy by inducing mitotic arrest and apoptosis in rapidly dividing cells (Dumontet and Jordan, 2010). However, limitations, including dose-limiting toxicities and the emergence of resistance mechanisms (Kavallaris, 2010)—such as changes in β-tubulin isoforms and increased drug efflux—highlight the need for novel tubulin inhibitors with improved specificity and tolerability.

In response to these challenges, various heterocyclic scaffolds have been explored for their ability to disrupt tubulin dynamics (Hawash, 2022; Elshamsy et al., 2023), with thiazole derivatives standing out as particularly promising candidates. Thiazole derivatives, a class of nitrogen- and sulfur-containing heterocycles, have emerged as valuable pharmacophores in anticancer drug discovery (Kaur and Jaitak, 2022) due to their structural rigidity, electronic properties, and ability to engage in specific interactions with biological targets. In particular, their affinity for the colchicine-binding site on tubulin has made them attractive scaffolds for designing inhibitors of tubulin polymerization (Figure 2). The disruption of microtubule dynamics by these agents leads to mitotic arrest and apoptosis in cancer cells. Several potent thiazole-based tubulin inhibitors have been reported. For instance, compound **VI**, a thiazole-naphthalene hybrid, inhibited tubulin polymerization with an IC_{50} of 3.3 μM (Wang et al., 2021). Compound **VII**, a thiazole-hydrazone-indole conjugate, showed even stronger inhibition (IC_{50} = 1.68 μM) (Wang et al., 2024), while compound **VIII**, a 2,4-disubstituted thiazole, exhibited comparable activity (IC_{50} = 2.00 μM) (El-Abd et al., 2022). These examples underscore the potential of thiazole-based molecules as effective antimitotic agents.

Chalcones have also emerged as important scaffolds in the design of multitargeted anticancer agents, particularly for disrupting microtubule dynamics. These α,β-unsaturated carbonyl compounds are well recognized for their ability to interfere with tubulin polymerization by binding to the colchicine site (Liu et al., 2022; Al-Wahaibi et al., 2025), thereby inducing mitotic arrest and apoptosis. Several chalcone-based compounds have demonstrated potent tubulin inhibitory activity (Figure 2). For instance, compound **IX**, a 2′,5′-dimethoxychalcone, has been shown to interfere with tubulin polymerization and induce cell cycle arrest in cancer cells (Lin et al., 2011). In another study, compound **X**, a benzofuran-chalcone hybrid, demonstrated tubulin-binding potential, as supported by molecular docking analyses (Mphahlele et al., 2018). Another notable example is compound **XI**, a benzo[d]imidazo (Vogelstein et al., 2013) thiazole-chalcone conjugate, which effectively inhibits tubulin assembly and induces

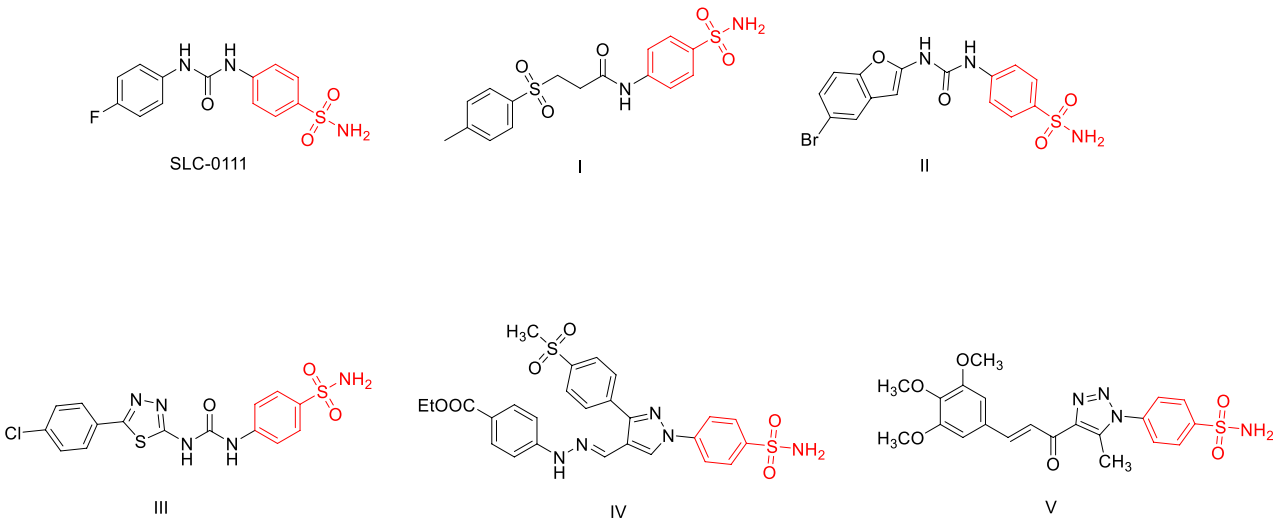


FIGURE 1
Examples of reported sulphonamides as carbonic anhydrase inhibitors.

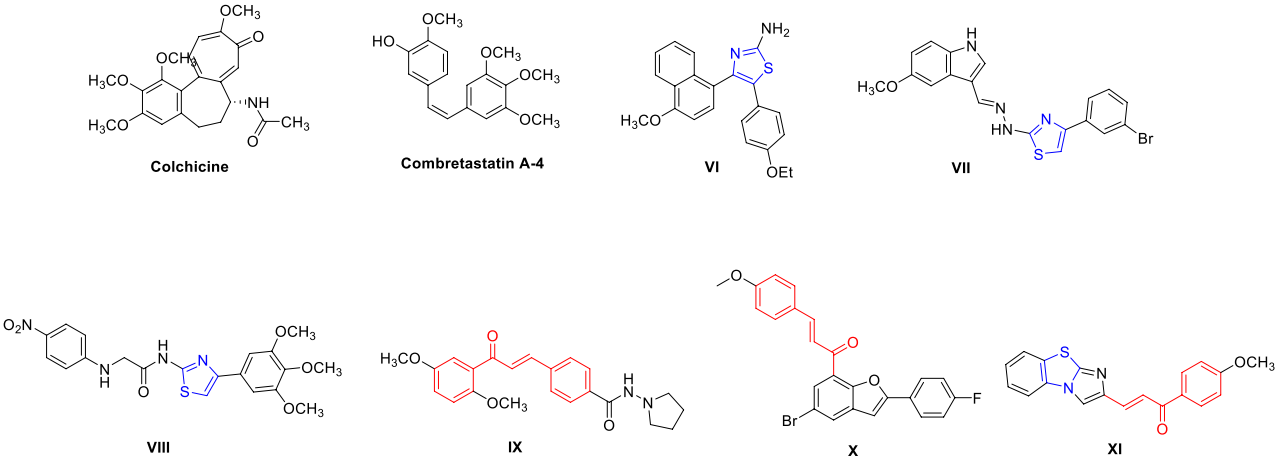


FIGURE 2
Examples of reported thiazoles and chalcones as inhibitors of tubulin polymerization.

apoptosis (Sultana et al., 2018). Collectively, these findings highlight the structural and functional relevance of both thiazoles and chalcones as foundational scaffolds for the development of novel tubulin-targeting anticancer agents.

In our earlier investigation aimed at discovering novel antitubulin agents, we identified the lead compound **2e**—hereafter referred to as **Tz**—as a promising thiazole–chalcone derivative with potent inhibitory activity against tubulin polymerization (Hashem et al., 2024). **Tz** demonstrated significant inhibition of tubulin polymerization (IC_{50} = 7.78 μM), although it was slightly less potent than the reference compound Combretastatin A-4. Motivated by the goal of developing a multitargeted anticancer agent, we aimed to enhance the activity of **Tz** by introducing a para-substituted sulfonamide group in place of the original 3-chlorophenyl moiety. This design strategy was inspired by the structural features of the known CA IX inhibitor SLC-0111, where the sulfonamide group coordinates with the active-site zinc ion and engages in hydrogen bonding with polar residues. Recent studies have shown that dual inhibition of tubulin and CA IX/XII within a single molecular framework can produce enhanced anticancer effects through complementary mechanisms (Elkotamy et al., 2025), further supporting our rationale. In our design, the resulting hybrid—compound **7**—retained the thiazole–chalcone pharmacophore essential for inhibiting tubulin polymerization while mimicking both the para-sulfonamide and urea carbonyl groups of SLC-0111 (Figure 3). This structural convergence was intended to allow dual interaction within the colchicine-binding site of tubulin and the active site of CA IX, with the sulfonamide potentially enhancing tubulin binding through additional polar contacts.

To evaluate its biological potential, compound **7** was synthesized and subjected to a comprehensive panel of biological assays,

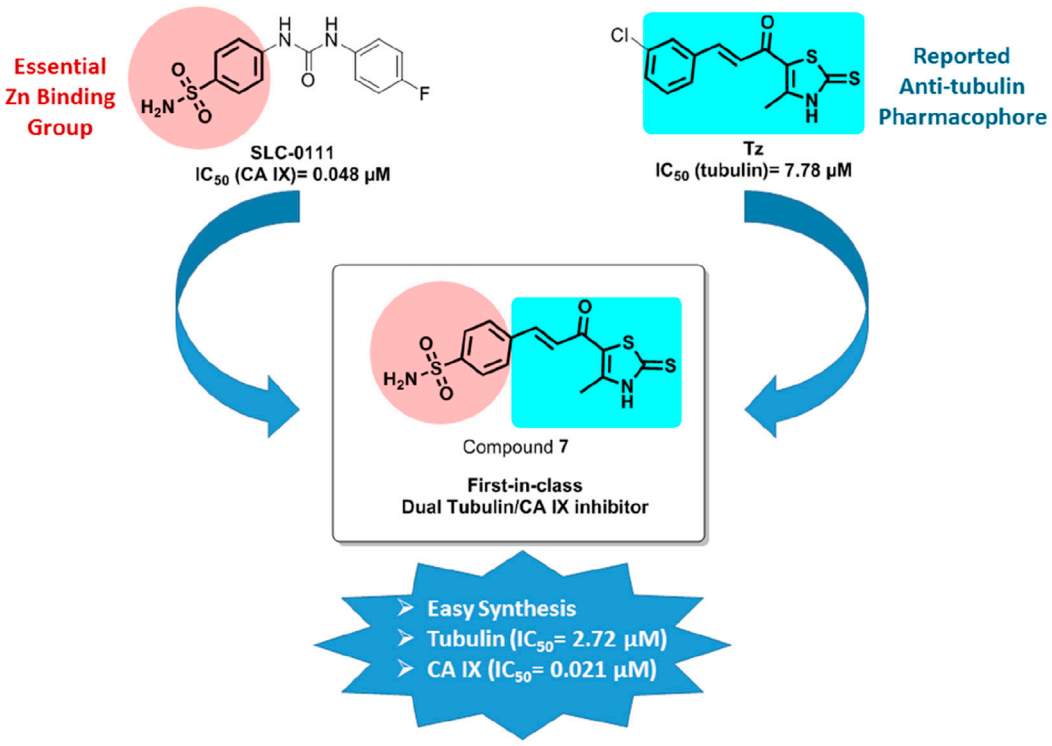


FIGURE 3
Design of the target compound (compound **7**).

including cytotoxicity screening, tubulin polymerization inhibition, and inhibition of CA isoforms. Additionally, mechanistic studies were carried out to assess its potential to induce apoptosis, followed by a detailed set of molecular modeling studies, including molecular docking to investigate binding interactions, ADMET analysis to predict pharmacokinetic behavior, and DFT calculations to examine its electronic properties.

2 Results and discussion

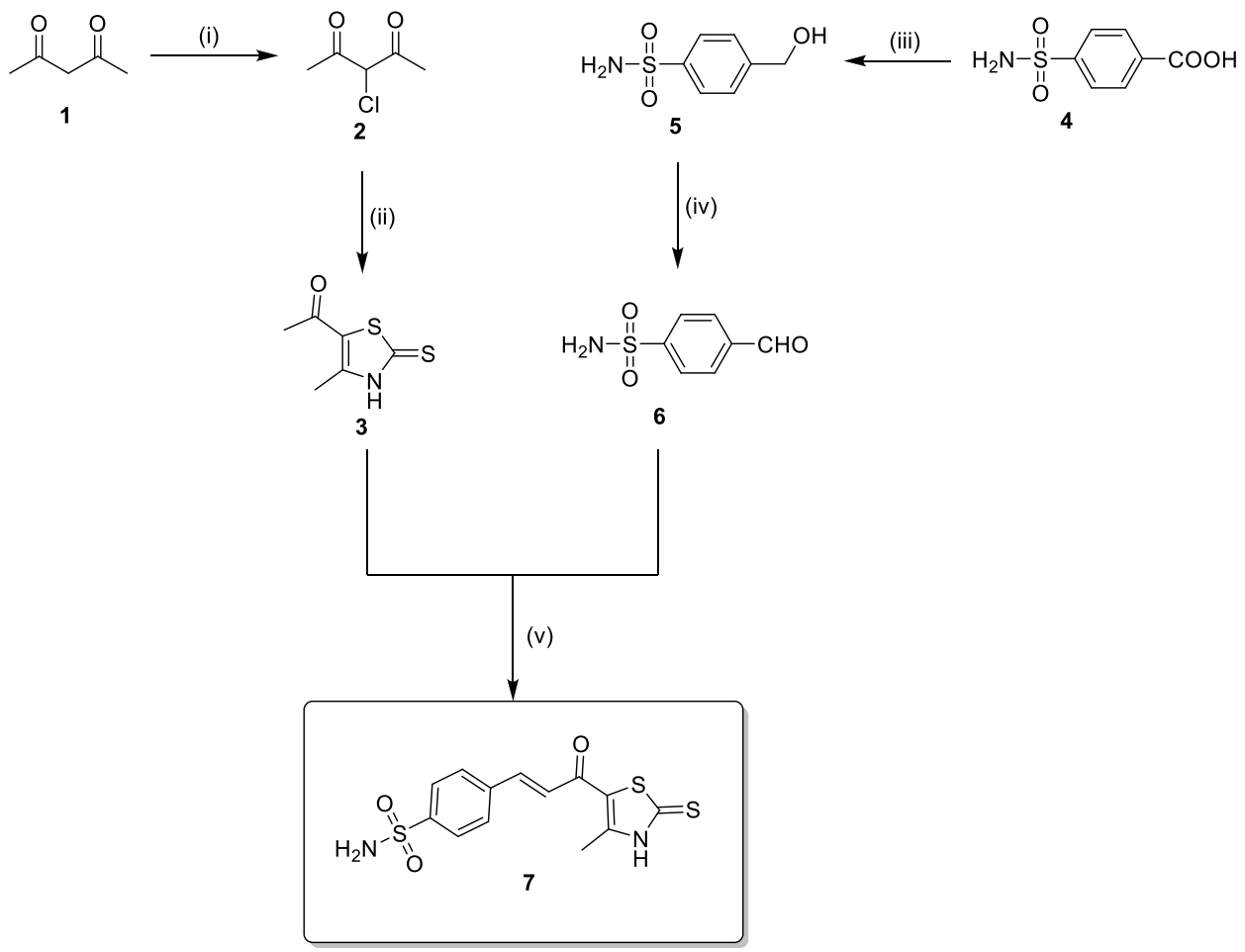
2.1 Chemistry

The synthetic pathway for the chalcone derivative (**7**) is illustrated in Scheme 1 and proceeds through a multi-step sequence starting from commercially available acetylacetone. Initially, acetylacetone (**1**) was subjected to chlorination using sulfuryl chloride in toluene at room temperature for 16 h, affording 3-chloroacetylacetone (**2**) as the key electrophilic intermediate. This chlorinated derivative subsequently underwent cyclization with ammonium hydroxide and carbon disulfide in ethanol under reflux conditions, leading to the formation of the thiazole intermediate (**3**) with a moderate yield of 69%.

Parallel to this, 4-sulfamoylbenzoic acid (**4**) was reduced using borane in tetrahydrofuran at 0°C for 19 h to afford the corresponding benzyl alcohol (**5**) in excellent yield (93%). Subsequent oxidation of this alcohol with pyridinium chlorochromate in dichloromethane under reflux for 6 h afforded the aldehyde intermediate (**6**) in 76% yield, serving as a key precursor for the final condensation step. The final chalcone derivative (**7**) was synthesized through a base-catalyzed Claisen–Schmidt condensation between the thiazole intermediate (**3**) and the aldehyde (**6**). The reaction was conducted in ethanol with 60% sodium hydroxide at 0°C for 12 h, facilitating the formation of the α,β-unsaturated carbonyl system characteristic of chalcone scaffolds. The final compound was isolated in good yield (73%), demonstrating the efficiency of the overall synthetic route.

Reagents and Conditions: (i) SO_2Cl_2, toluene, RT, 16 h; (ii) NH_3, CS_2, EtOH, reflux, 6 h; (iii) BH_3, THF, 0°C, 19 h; (iv) PCC, DCM, reflux, 6 h; (v) 60% NaOH, ethanol, 0°C, 12 h.

The structure of the final compound was characterized by ^{1}H NMR, ^{13}C NMR, and elemental analysis. The ^{1}H NMR spectrum, recorded in DMSO-d_6, displayed distinct signals consistent with the proposed structure. A downfield singlet appeared at δ 13.64 ppm, corresponding to the thiazole N-H proton, confirming the formation of the thiazole ring. Aromatic protons from the sulfonamide phenyl ring appeared as two doublets at δ 7.93 and δ 7.83 ppm. The olefinic protons of the α,β-unsaturated carbonyl system were observed as two trans-coupled doublets at δ 7.51 and δ 7.41 ppm, indicating the *E*-configuration of the double bond. A singlet at δ 7.23 ppm corresponded to the sulfonamide protons, while the methyl group resonated as a singlet at δ 2.59 ppm. The ^{13}C NMR spectrum further supported the structure of compound 7, displaying key carbon resonances in DMSO-d_6. A characteristic signal appeared at δ 189.50 ppm, corresponding to the thiocarbonyl carbon of the thiazole ring, while the carbonyl carbon of the chalcone moiety resonated at δ 180.17 ppm. Additionally, the



SCHEME 1
Synthesis of the target compound (**7**).

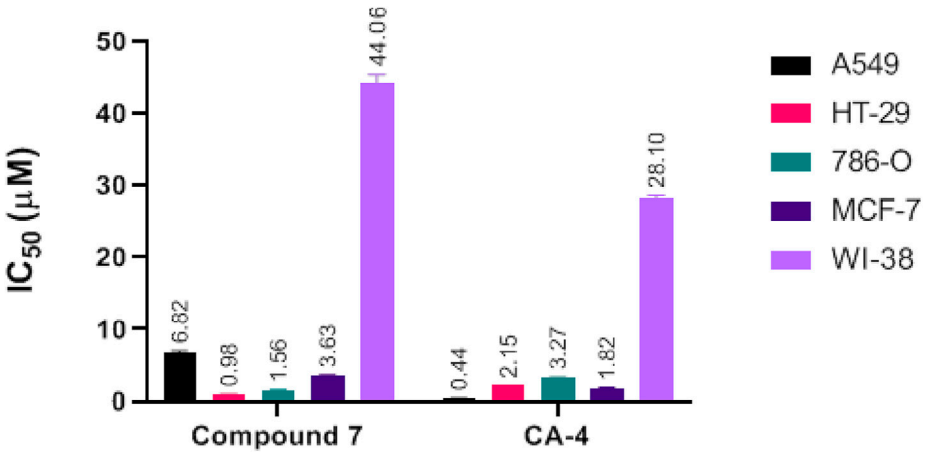


FIGURE 4
Comparative IC_{50} values of compound **7** and combretastatin A-4 (CA-4) against A549 (lung), HT-29 (colorectal), 786-O (renal), and MCF-7 (breast) cancer cell lines, as well as the WI-38 normal fibroblast cell line, determined by MTT assay. Data are mean ± SEM.

TABLE 1 Tubulin polymerization inhibition (IC_{50}, μM) of compound 7 and combretastatin A-4, as determined by an *in vitro* assay. Data are presented as mean ± SEM.

Compound	Tubulin polymerization inhibition IC_{50} ± SEM (μM)
7	2.72 ± 0.16
CA-4	2.97 ± 0.09

methyl group carbon was observed at δ 15.57 ppm, consistent with the presence of the methyl-substituted thiazole.

2.2 Biological evaluation

2.2.1 Antiproliferative assay

The antiproliferative activity of Compound **7** was evaluated against A549, HT-29, 786-O, and MCF-7 cancer cell lines, as well as the normal WI-38 fibroblast cell line, using the MTT assay and compared with combretastatin A-4 (CA-4) as a reference compound (Huo et al., 2021). As shown in Figure 4, compound **7** exhibited considerable cytotoxic activity across the tested cancer cell lines, with the most pronounced effect observed against the HT-29 colorectal cancer cells, where it achieved an IC_{50} value of 0.98 μM. Notably, this potency surpassed that of CA-4 against the same cell line (IC_{50} = 2.15 μM), indicating a preferential effect of compound **7** toward colorectal carcinoma.

Compound **7** also displayed good activity against 786-O renal cancer cells (IC_{50} = 1.56 μM) and moderate inhibition of A549 lung (IC_{50} = 6.82 μM) and MCF-7 breast cancer cells (IC_{50} = 3.63 μM). In contrast, CA-4 exhibited higher potency against A549 (IC_{50} = 0.44 μM) and MCF-7 cells (IC_{50} = 1.82 μM), confirming its well-known broad cytotoxic profile. However, selectivity analysis revealed that compound **7** had a more favorable therapeutic index. When tested against WI-38 normal fibroblasts, compound **7** showed an IC_{50} of 44.06 μM, resulting in a remarkably high selectivity index (SI) of 44.96 for HT-29 and 28.25 for 786-O cells. These values were significantly higher than those calculated for CA-4, which showed an SI of 13.06 for HT-29 and 8.59 for 786-O.

2.2.2 Effect of compound 7 on tubulin polymerization

To investigate the potential mechanism underlying its antiproliferative activity, compound **7** was evaluated for its ability to inhibit tubulin polymerization (Huo et al., 2021). As presented in Table 1, the compound exhibited notable tubulin polymerization inhibition with an IC_{50} value of 2.72 μM, which is comparable to that of CA-4 (IC_{50} = 2.97 μM). This result suggests that compound **7** may exert its antiproliferative effects, at least in part, through interference with microtubule dynamics, similar to CA-4. It is noteworthy that compound 7 was developed through the structural optimization of our previously reported thiazole–chalcone derivative, Tz, which showed moderate tubulin polymerization inhibition (IC_{50} = 7.78 μM). Compared to **Tz**, compound **7** incorporates a para-substituted sulfonamide group designed to enhance polar interactions within the colchicine-binding site. This modification appears to have significantly improved its tubulin inhibitory potency. The introduction of the electron-withdrawing sulfonamide moiety likely enhances binding affinity by establishing additional hydrogen bonds and reinforcing anchorage within the active site, resulting in a lower IC_{50} value.

TABLE 2 IC_{50} values (μM) of compound 7, acetazolamide (AAZ), and SLC-0111 against CA isoforms I, II, IX, and XII. Data are expressed as mean ± SEM.

Compound	CA inhibition IC_{50} (μM) ±SEM			
	CA I	CA II	CA IX	CA XII
7	1.90 ± 0.25	0.381 ± 0.045	0.021 ± 0.004	0.114 ± 0.012
AAZ	0.367 ± 0.02	0.153 ± 0.01	0.105 ± 0.01	0.029 ± 0.001
SLC-0111	1.36 ± 0.07	0.498 ± 0.04	0.048 ± 0.006	0.096 ± 0.008

2.2.3 Evaluation of carbonic anhydrase I, II, IX, and XII inhibition

To further investigate the biological profile of compound **7**, its inhibitory activity against a panel of human carbonic anhydrase (CA) isoforms was evaluated, including the physiologically relevant isoforms CA I and CA II, as well as the tumor-associated isoforms CA IX and CA XII (Albelwi et al., 2024). As summarized in Table 2, compound **7** exhibited selective and potent inhibition toward the tumor-associated CA IX isoform with an IC_{50} value of 0.021 ± 0.004 μM, outperforming the reference inhibitors acetazolamide (AAZ) and SLC-0111, which showed IC_{50} values of 0.105 ± 0.01 μM and 0.048 ± 0.006 μM, respectively. This remarkable potency against CA IX suggests that compound **7** may effectively target the hypoxic microenvironment of solid tumors, where CA IX is overexpressed and contributes to tumor progression, invasion, and metastasis.

Additionally, compound **7** showed potent inhibition of CA XII (IC_{50} = 0.114 ± 0.012 μM), another tumor-associated isoform, indicating a potential dual inhibitory effect that could enhance anticancer efficacy. In contrast, its activity against the ubiquitous and off-target isoforms CA I and CA II was significantly lower, with IC_{50} values of 1.90 ± 0.25 μM and 0.381 ± 0.045 μM, respectively. This selectivity profile is favorable compared to AAZ, which displayed strong inhibition of CA I (IC_{50} = 0.367 ± 0.02 μM) and CA II (IC_{50} = 0.153 ± 0.01 μM), raising concerns about potential off-target effects and toxicity.

To better illustrate this selectivity, selectivity indices (SI) were calculated as the ratio of IC_{50} values for the off-target isoforms to those for the tumor-associated isoforms, as presented in Table 3. Compound **7** demonstrated outstanding selectivity toward CA IX, with SI values of CA I/CA IX = 90.5 and CA II/CA IX = 18.1. These values markedly exceeded those of AAZ (CA I/CA IX = 3.5, CA II/CA IX = 1.5) and SLC-0111 (CA I/CA IX = 28.3, CA II/CA IX = 10.4), confirming the superior tumor-targeting potential of compound **7**. Moreover, the CA I/CA XII selectivity ratio of compound **7** reached 16.7, surpassing AAZ (12.7) and closely aligning with SLC-0111 (14.2), further supporting its preferential targeting of tumor-associated isoforms.

Interestingly, this strong and selective inhibition of CA IX correlates well with the MTT assay results, where compound **7**

TABLE 3 Selectivity indices (SI) of compound 7, acetazolamide (AAZ), and SLC-0111 for tumor-associated CA IX and CA XII over off-target isoforms CA I and CA II.

Compound	Selectivity index (SI)			
	CA I/CA IX	CA II/CA IX	CA I/CA XII	CA II/CA XII
7	90.5	18.1	16.7	3.3
AAZ	3.5	1.5	12.7	5.3
SLC-0111	28.3	10.4	14.2	5.2

TABLE 4 Effects of Compound 7 on p53, Bax, and Bcl-2 protein expression levels in HT-29 cells.

Compound	P53		Bax		Bcl-2	
	Conc (pg/mL)	Fold change	Conc (pg/mL)	Fold change	Conc (pg/mL)	Fold change
7/HT-29	1,224.00 ± 6.67	8.12	392.25 ± 14.58	5.73	6.212 ± 0.093	0.323
DMSO/HT-29	150.66 ± 3.33	1	68.50 ± 1.67	1	19.25 ± 0.43	1

demonstrated its most potent antiproliferative activity against HT-29 (IC_{50} = 0.98 μM) and 786-O (IC_{50} = 1.56 μM) cancer cell lines. Both of these tumor types are known to constitutively express high levels of CA IX, suggesting that the remarkable cytotoxicity of Compound 7 toward these cells may be partially attributed to its potent inhibition of CA IX. This mechanistic link further supports the potential of Compound 7 to act selectively against CA IX-expressing tumors, offering a targeted approach to anticancer therapy.

2.2.4 Effects of compound **7** on p53, Bax and Bcl-2 protein expression levels

To further explore the potential apoptotic mechanism underlying the antiproliferative effects of compound **7**, its impact on key apoptosis-related proteins—p53, Bax, and Bcl-2—was investigated in HT-29 cells (Ahmed et al., 2024). As shown in Table 4, treatment with compound **7** resulted in a substantial upregulation of the tumor suppressor protein p53, increasing its concentration from 150.66 ± 3.33 pg/mL in the DMSO-treated control to 1,224.00 ± 6.67 pg/mL, representing an 8.12-fold elevation. This significant induction of p53 suggests activation of a p53-mediated apoptotic pathway, which is known to play a critical role in controlling cell cycle arrest and promoting apoptosis in response to cellular stress and DNA damage. Similarly, compound **7** significantly increased the expression of the pro-apoptotic protein Bax, resulting in a 5.73-fold increase in its level compared to the control. Bax concentration reached 392.25 ± 14.58 pg/mL, up from 68.50 ± 1.67 pg/mL in DMSO-treated cells. The elevation of Bax further supports the pro-apoptotic effect of compound **7**, as Bax promotes mitochondrial outer membrane permeabilization, leading to the release of cytochrome c and caspase activation. Conversely, the anti-apoptotic protein Bcl-2 was significantly downregulated following treatment with compound 7. Bcl-2 concentration decreased from 19.25 ± 0.43 pg/mL in control cells to 6.212 ± 0.093 pg/mL, reflecting a 0.323-fold change. This notable reduction in Bcl-2 levels favors the apoptotic process by diminishing its protective effect against mitochondrial-mediated apoptosis.

Collectively, these findings demonstrate that compound **7** effectively shifts the Bax/Bcl-2 ratio in favor of apoptosis and activates p53-mediated pathways in HT-29 cells. The combined upregulation of p53 and Bax, along with the suppression of Bcl-2, provides strong evidence that compound **7** induces apoptosis as a major mechanism contributing to its potent antiproliferative activity against colorectal cancer cells.

2.2.5 Effects of compound 7 on caspase-3 and caspase-9 activities

To further confirm the apoptotic pathway induced by compound **7** in HT-29 cells, the activation of caspase-3 and caspase-9—key executioner and initiator caspases, respectively—was evaluated (Abdel-Motaal et al., 2024). As detailed in Table 5, treatment with compound **7** resulted in a significant increase in caspase-3 levels, reaching 511.27 ± 13.18 pg/mL, compared to 57.64 ± 1.36 pg/mL in DMSO-treated control cells. This represents an 8.87-fold increase, indicating robust activation of the downstream effector caspase, which is essential for the execution phase of apoptosis. In parallel, caspase-9, a central mediator of the intrinsic mitochondrial apoptotic pathway, was significantly activated following treatment with compound 7. The caspase-9 level increased from 5.09 ± 0.26 ng/mL in control cells to 49.39 ± 1.13 ng/mL, corresponding to a 9.70-fold elevation. This pronounced increase strongly suggests that compound **7** triggers the intrinsic apoptotic pathway, likely *via* mitochondrial damage and cytochrome c release, leading to caspase-9 activation and subsequent caspase-3 cleavage.

Together, the significant activation of both caspase-9 and caspase-3 provides compelling evidence that compound **7** induces apoptosis in HT-29 cells through the intrinsic mitochondrial pathway. These findings are consistent with the observed upregulation of p53 and Bax and the downregulation of Bcl-2, reinforcing the role of mitochondrial-mediated apoptosis as a key mechanism underlying the potent anticancer activity of compound **7**.

TABLE 5 Effects of Compound 7 on caspase-3 and caspase-9 activities in HT-29 cells.

Compound	Caspase 3		Caspase-9	
	Conc (pg/mL)	Fold change	Conc (ng/mL)	Fold change
7/HT-29	511.27 ± 13.18	8.87	49.39 ± 1.13	9.70
DMSO/HT-29	57.64 ± 1.36	1	5.09 ± 0.26	1

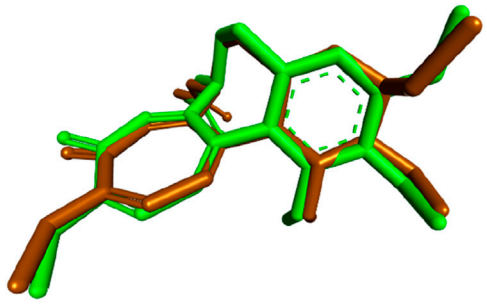


FIGURE 5
Superimposition of the redocked (brown) and cocrystallized (green) poses of colchicine within the binding site of tubulin.

2.3 Molecular modeling studies

2.3.1 Molecular docking studies

2.3.1.1 Docking of compound **7** into the colchicine binding site of tubulin

To gain further insights into the molecular basis of the tubulin polymerization inhibition observed for compound 7, molecular docking studies were conducted targeting the colchicine-binding site of tubulin. The crystal structure of the tubulin–colchicine complex (PDB ID: 4O2B) was utilized for this purpose (Boichuk et al., 2021). Docking was performed using AutoDock Vina (Trott and Olson, 2010), and the resulting ligand–protein interactions were visualized using Discovery Studio Visualizer. Before docking the test compound, the docking protocol was validated by redocking the co-crystallized ligand colchicine into its native binding site. The redocked pose showed a binding affinity of −8.5 kcal/mol and a root-mean-square deviation (RMSD) of 0.7173 Å compared to the crystallographic orientation, confirming the reliability of the docking approach. The superimposition of the docked and experimental poses is illustrated in Figure 5.

Compound 7 was subsequently docked into the colchicine-binding site and yielded a binding affinity of −9.8 kcal/mol, which is slightly more favorable than that of the reference compound combretastatin A-4 (CA-4, −9.6 kcal/mol), suggesting a strong interaction with the target site. As depicted in Figure 6, compound 7 exhibited several critical interactions that underlie its high binding affinity. Notably, the thiocarbonyl group formed a classical hydrogen bond with Cys241, an interaction previously highlighted as essential for the tight binding of tubulin inhibitors such as colchicine and CA-4. In addition, compound 7 retained several important hydrophobic interactions observed in both CA-4 and **Tz**, including contacts with Leu255, Leu248, Ala180, and Val181 (Figures 7, 8).

Beyond these conserved interactions, compound 7 introduced additional hydrogen bonding contacts not seen in CA-4 or **Tz**. Specifically, the thiocarbonyl group formed hydrogen bonds with Val238, while the sulfonamide group at the para position of the phenyl ring formed new hydrogen bonds with Ser178, Asn101, and Lys254. These unique interactions not only enhance the binding affinity but also serve to anchor compound 7 more securely within the colchicine-binding pocket, thereby stabilizing the ligand–protein complex. The presence of the sulfonamide moiety, in particular, appears to reinforce molecular recognition and may contribute to the slightly superior tubulin inhibition profile of compound 7 compared to both CA-4 and the previously reported **Tz**.

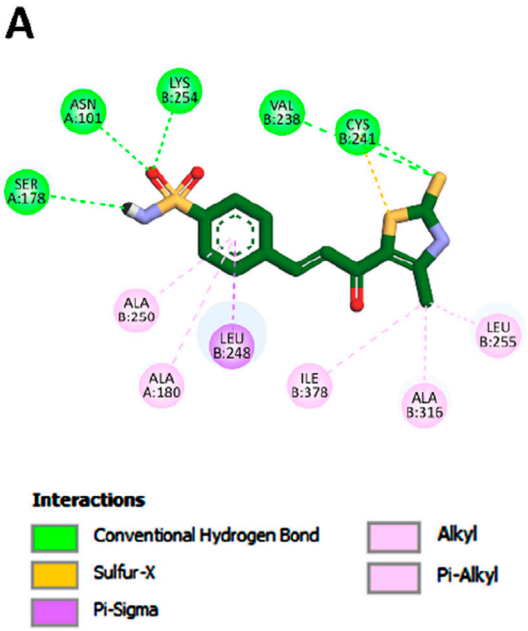
2.3.1.2 Docking of compound **7** into the carbonic anhydrase IX active site

To complement the experimental findings on the potent and selective inhibition of CA IX by compound 7, molecular docking was performed to explore its binding interactions within the active site of CA IX (PDB ID: 5FL4). The docking protocol was first validated by redocking the co-crystallized ligand into the CA IX crystal structure, resulting in a binding affinity of −6.8 kcal/mol and an RMSD of 0.8532 Å relative to the crystallographic pose, as illustrated in Figure 9. This result confirmed the accuracy of the docking methodology.

Upon docking, compound 7 exhibited a binding affinity of −8.1 kcal/mol, consistent with its experimentally observed submicromolar inhibition of CA IX. The sulfonamide moiety of compound 7 played a central role in anchoring the molecule within the active site. Its amino group directly coordinated with the catalytic zinc ion and formed classical hydrogen bonds with key residues His119 and Thr200. Additionally, the sulfonyl group contributed two more hydrogen bonds with these same residues, further stabilizing the complex. The sulfur atom of the sulfonamide also participated in π–sulfur interactions with His94 and Trp210, which further contributed to the overall affinity of the ligand within the active site.

The docking pose further revealed that the phenyl ring of compound 7 contributed to hydrophobic stabilization through a π–σ interaction with Leu199 and a π–alkyl interaction with Val121. These interactions are comparable to those observed with the reference inhibitor SLC-0111, which also employs a sulfonamide pharmacophore and a hydrophobic tail (Figure 10). Additionally, the carbonyl of the chalcone linker of compound 7 formed a non-classical carbon–hydrogen bond with Pro203, mirroring an analogous interaction observed with the urea carbonyl of SLC-0111.

A notable structural divergence between the two compounds lies in the tail region: compound 7 features a thiazole ring bearing a methyl substituent, whereas SLC-0111 incorporates a fluorophenyl moiety. This thiazole ring engaged in a π–alkyl interaction with



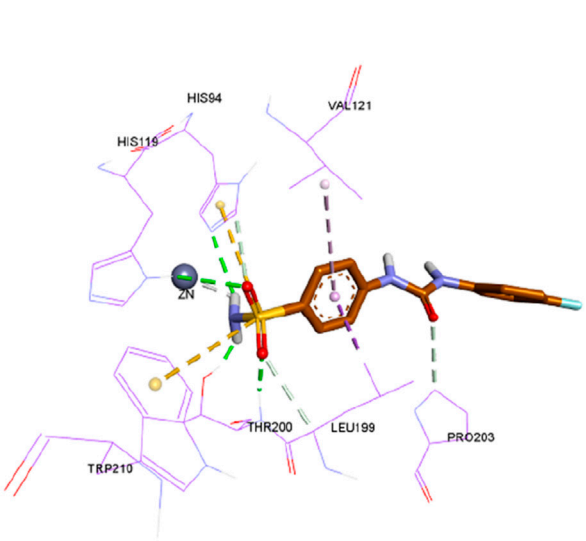
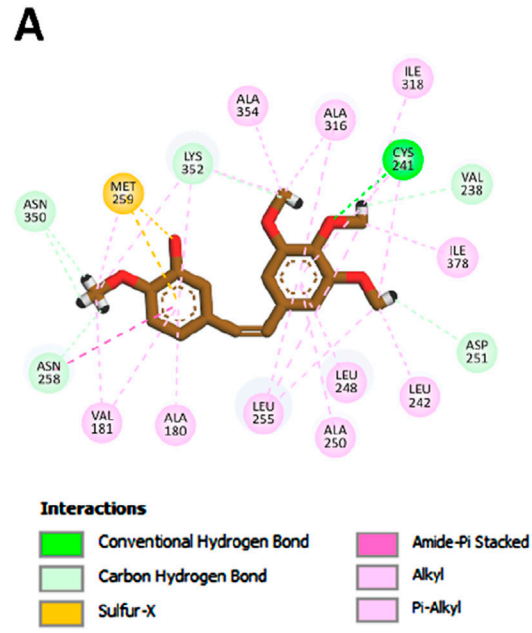


FIGURE 6
2D **(A)** and 3D **(B)** interactions of compound **7** within the colchicine binding site of tubulin.



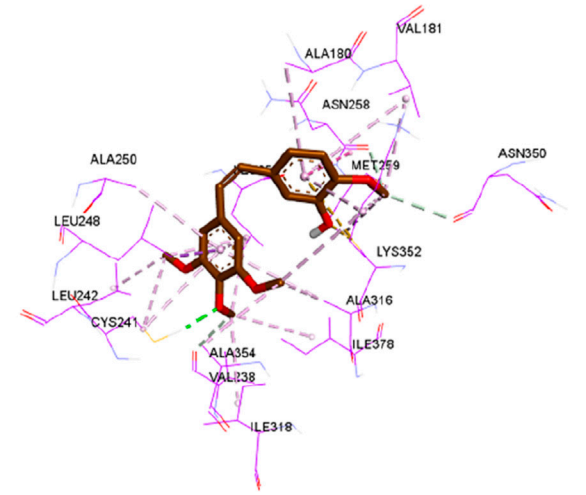


FIGURE 7
2D **(A)** and 3D **(B)** interactions of compound CA-4 within colchicine binding site of tubulin.

Val130, and its methyl group formed an additional alkyl interaction with the same residue. These unique contacts are visualized in Figure 11 and likely contribute to anchoring compound 7 more firmly within the CA IX active site, thereby enhancing its binding strength and selectivity. Overall, the docking results provide a structural rationale for the experimentally observed potency and specificity of compound 7, reinforcing its promise as a dual-targeted anticancer agent.

2.3.2 Drug likeness and ADMET predictions

The drug-likeness and ADMET profile of compound 7 were evaluated using SwissADME (Daina et al., 2017) to assess its

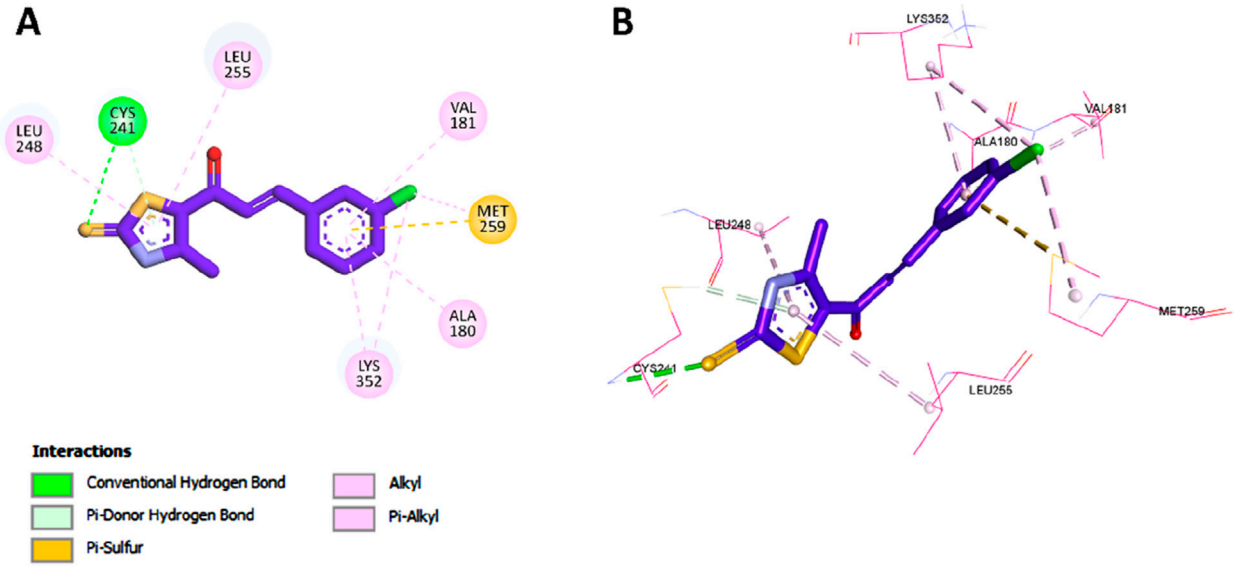


FIGURE 8
2D **(A)** and 3D **(B)** interactions of compound **Tz** within the colchicine binding site of tubulin.

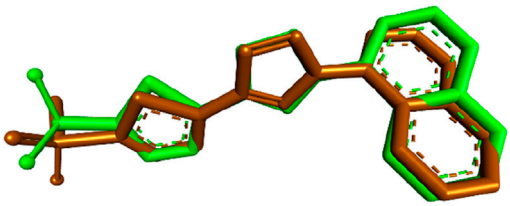


FIGURE 9
Superimposition of the redocked (brown) and cocrystallized (green) poses of the native ligand within the CAIX active site.

suitability as an orally bioavailable anticancer agent. With a molecular weight of 340.44 g/mol, four rotatable bonds, and acceptable aromatic content, compound 7 satisfies key drug-likeness criteria, including Lipinski, Ghose, and Muegge rules. Its topological polar surface area (TPSA) of 161.73 Å^2, though exceeding classical thresholds, is consistent with enzyme-targeted scaffolds, where elevated polarity enhances binding within hydrophilic active sites, such as the zinc-containing pocket of CA IX.

The compound exhibits a favorable lipophilicity profile, with a consensus Log P_ow of 2.20, indicating a well-balanced hydrophilic–lipophilic character conducive to membrane permeability and solubility. It is predicted to be soluble or moderately soluble across three models, supporting its potential for oral administration.

Although compound 7 shows low predicted gastrointestinal absorption, this may reduce systemic off-target exposure while favoring localized tumor accumulation—particularly when paired with targeted delivery platforms. The compound does not cross the blood–brain barrier and is not a P-gp substrate, limiting CNS exposure and efflux-related resistance. It is predicted to inhibit several CYP450 isoforms, a property that warrants attention during development but may be beneficial for prolonging systemic half-life under controlled regimens.

The bioavailability score (0.55) and synthetic accessibility (3.30) suggest good oral drug potential and moderate ease of synthesis. Medicinal chemistry filters report no PAINS alerts and only two Brenk flags, both associated with functional groups essential for biological activity. The bioavailability radar, as depicted in Figure 12, highlights optimal values for size, flexibility, solubility, and lipophilicity, with slight deviations in polarity and unsaturation, reflecting the structural features necessary for target engagement.

In summary, compound 7 exhibits a favorable drug-likeness and ADMET profile. Its physicochemical and pharmacokinetic attributes, combined with its dual-targeting activity, support its potential as a promising lead in anticancer drug development.

2.3.3 DFT calculations

2.3.3.1 Geometrical structure and frontier molecular orbitals (FMOs)

Figure 13 presents the investigated geometrical structural convergence of compound 7 in its ground state, utilizing the same theoretical level. To develop a deeper understanding of the conformational behavior of this structure, it is essential to examine two fundamental structural properties: bond lengths and bond angles. These parameters provide significant insights into the molecular geometry and its deviation from planarity. The compound's deviation from a completely planar structure can be attributed to the orientation of its sulfonamide group (SO_2NH_2), which is positioned in C5 of the parent part. This spatial arrangement influences the overall stability and electronic distribution within the molecule. Additionally, a CO group at the molecular core plays a pivotal role in inducing a bent geometry. This CO group not only acts as the central point of molecular bending but also forms two hydrogen bonds with the H1 atom, with estimated bond distances of 2.041 Å. The formation of these H-bonds is a

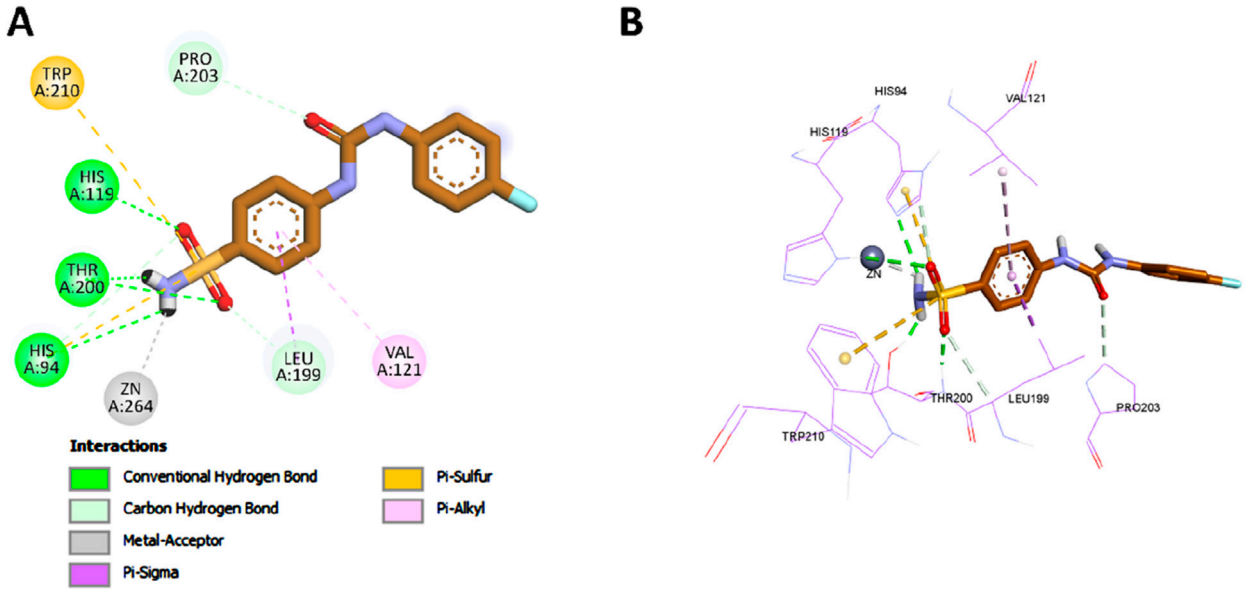


FIGURE 10
2D **(A)** and 3D **(B)** interactions of SLC-0111 within the CA IX active site.

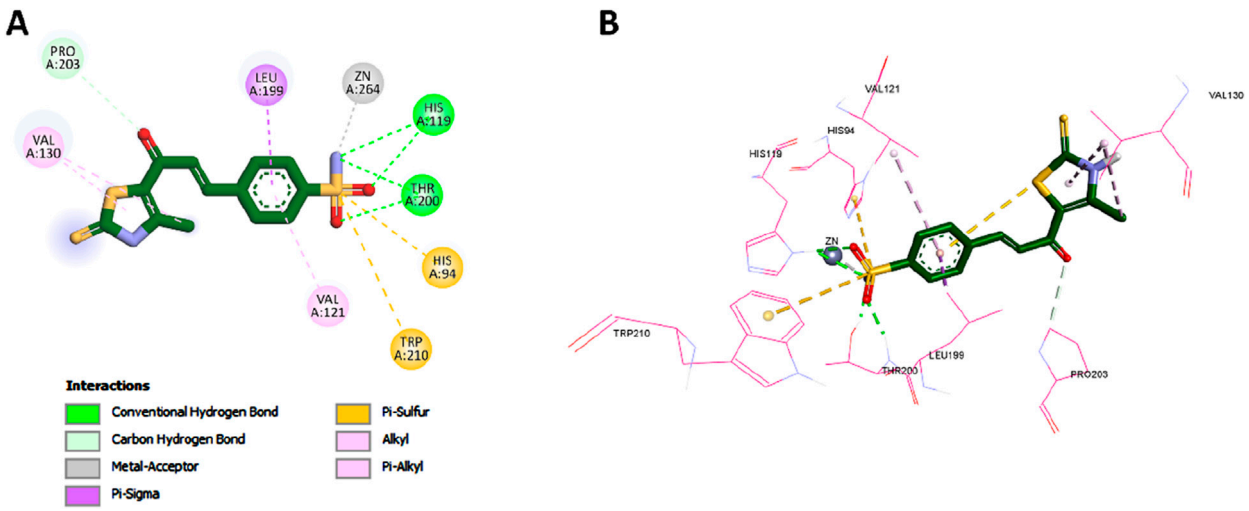


FIGURE 11
2D **(A)** and 3D **(B)** interactions of compound **7** within the CA IX active site.

critical factor in stabilizing the optimized molecular structure. An important aspect of this structural stability is the validation of the strength of hydrogen bond formation. Other bond length values were estimated for C5-S2 and C12-S3 at 1.806 Å and 1.662 Å, respectively. This difference is attributed to the bond order between atoms. A very slight difference was observed in S2-O1 and S2-O2, where the geometrical environment is similar, facilitating a symmetric electronic distribution with the NH_2 group. Furthermore, analyzing the bond angle values provides additional clarity regarding the planarity behavior of the atoms within the structure. The bond angles help assess the degree of similarity in the molecular environment surrounding specific atoms. For instance, the angles C11-C13-N1 and C9-N10-S1 measured 117.50° and 116.21°, respectively. This finding suggests a relatively consistent spatial arrangement that contributes to the overall molecular geometry. The angles around the SO2 group also export the same stability results. These findings collectively enhance our understanding of the compound's structural characteristics and contribute to predicting its stability and reactivity in various chemical contexts.

To accurately predict the stability and reactivity of various molecular systems, a comprehensive analysis of the frontier molecular orbitals (FMOs) is essential. These orbitals play a crucial role in determining the electronic properties of a

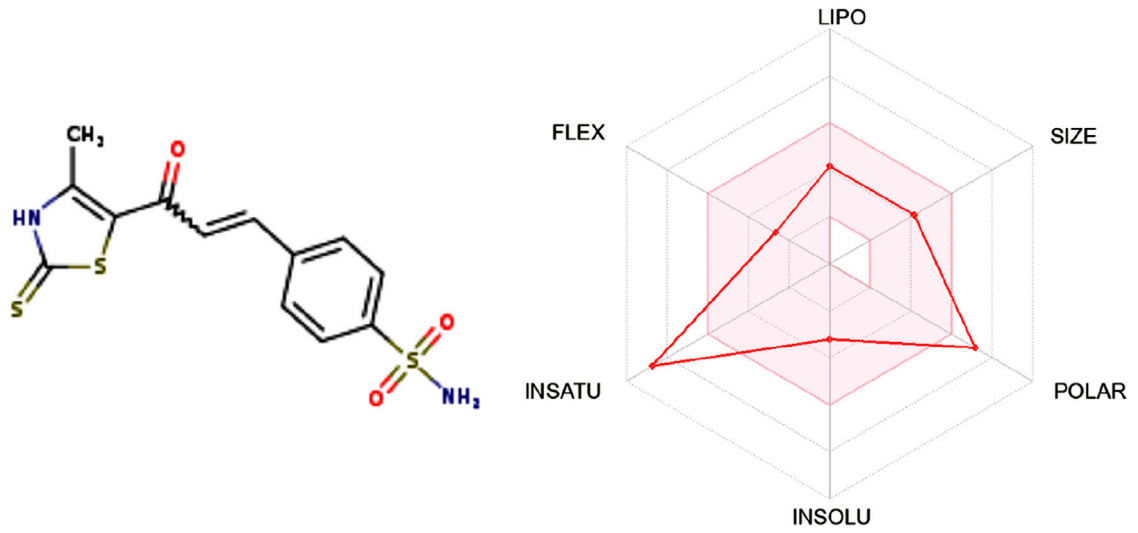


FIGURE 12
Bioavailability radar of compound **7** showing overall drug-like properties with minor deviations in polarity and saturation.

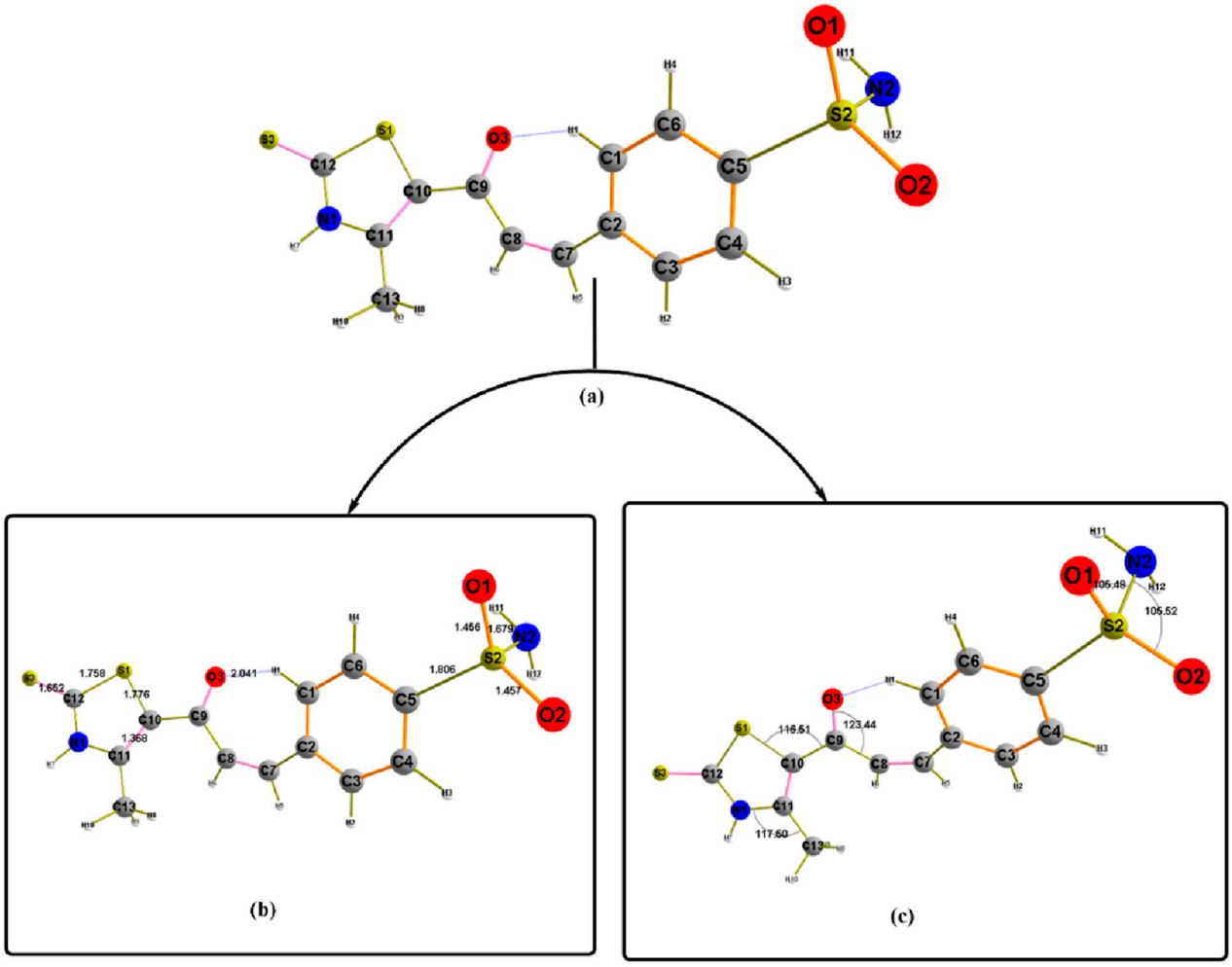


FIGURE 13
Geometrical structure of compound **7** **(a)** labeled with **(b)** bond lengths, **(c)** bond angles.

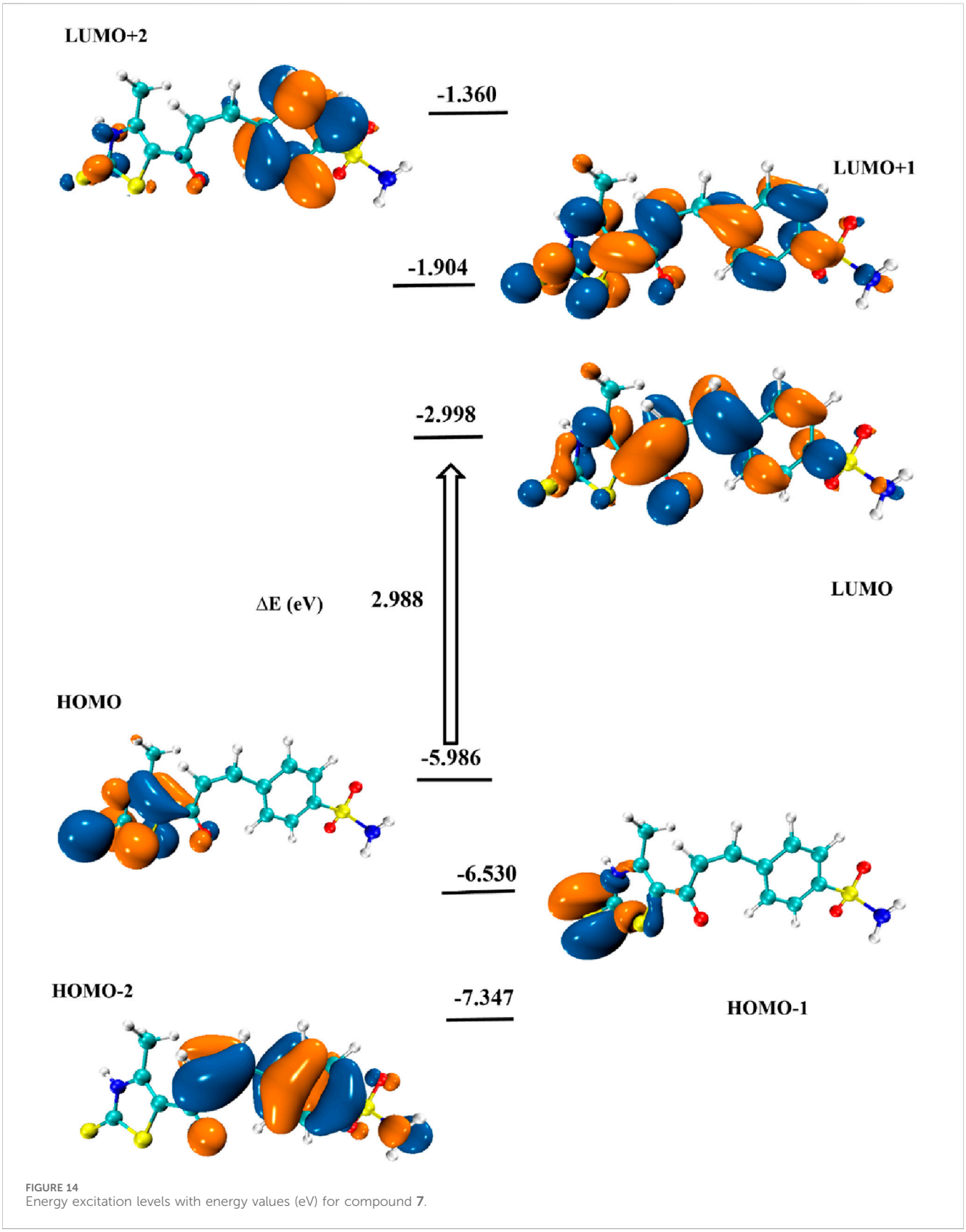


FIGURE 14
Energy excitation levels with energy values (eV) for compound **7**.

compound, influencing its chemical behavior, interaction potential, and overall stability in different environments. Figure 14 illustrates the energy distribution of the most significant molecular orbitals for the optimized gaseous-phase structure, including HOMO-2, HOMO-1, HOMO, LUMO, LUMO+1, and LUMO+2. By examining these orbitals, valuable insights can be gained into the

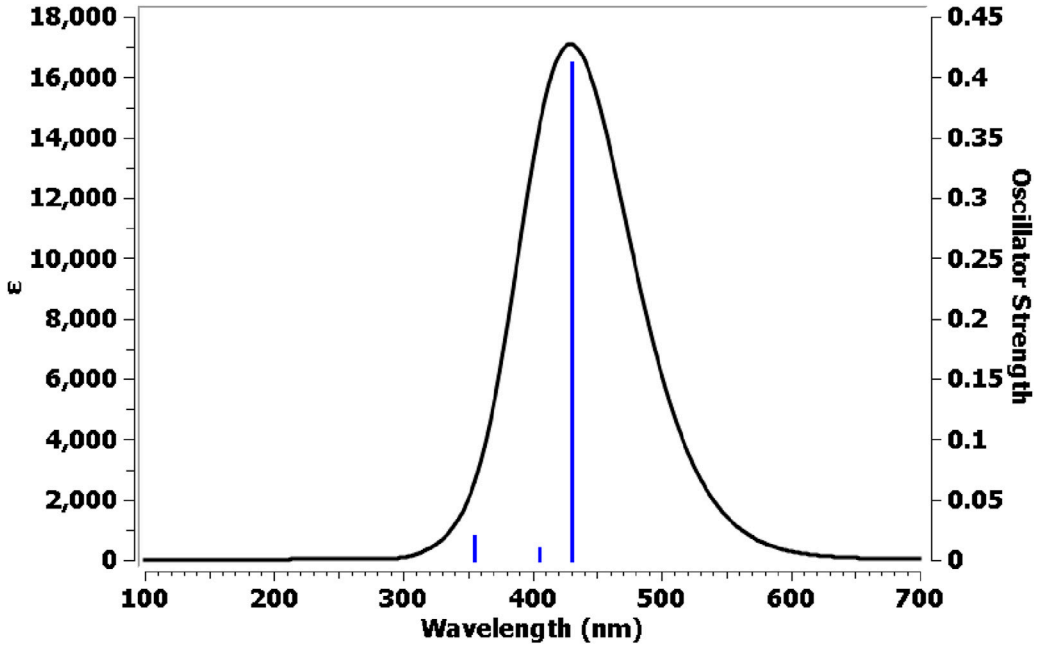


FIGURE 15
UV–Vis electronic absorption spectra for compound **7**.

electronic transitions and potential reactivity sites within the molecule. One of the key factors in assessing the molecular stability of compound **7** is the energy gap (ΔE) between the highest occupied molecular orbital (HOMO) and the lowest unoccupied molecular orbital (LUMO). In this case, the calculated energy gap of 2.988 eV serves as a strong indicator of molecular stability, as a larger gap generally correlates with lower reactivity and greater resistance to electronic excitation. Furthermore, the distribution and contribution of molecular orbitals across different regions of the molecule provide additional evidence supporting the stability of both ground and excited states. The localization of FMOs predominantly around the thiazole ring and carbonyl functional groups suggests a significant role of these moieties in the electronic transitions of the molecule. This observation aligns with the concept of successive donor-acceptor interactions occurring in the excited states, where electron density shifts between these key functional groups. Such interactions are fundamental in determining the electronic excitation pathways and potential photochemical behavior of the compound.

2.3.3.2 UV–vis electronic spectra by TD-DFT method

To comprehensively analyze the electronic properties of compound **7**, the time-dependent density functional theory (TD-DFT) method, combined with the conductor-like polarizable continuum model (CPCM), was employed to account for solvation effects. These computational approaches enable an accurate description of the molecule's electronic behavior in solution, providing valuable insights into its optical absorption characteristics. The calculations were performed using the Gaussian 09 software, maintaining the default parameter settings for TD-DFT simulations. To capture the essential electronic transitions, the number of excited states was set to Nstate = 6, ensuring a detailed evaluation of the lowest six electronic states. Figure 15 presents three distinct transition bands corresponding to the observed electronic excitations. The Gaussian calculation's LOG file confirms the presence of a strong singlet absorption band in the first electronic transition, attributed to an n-π* transition. This transition occurs with a significant contribution of 70%, an excitation energy of 2.88 eV, and a corresponding maximum absorption wavelength (λ_{max}) of 430 nm. The HOMO→LUMO excitation predominantly drives this electronic transition, highlighting the participation of non-bonding (n) orbitals in the excitation process. A critical parameter in determining the intensity and probability of electronic transitions is the oscillator strength (F), which provides insight into the transition dipole moment and the likelihood of photon absorption. For the first electronic transition, the oscillator strength is calculated as 0.411, indicating a strong electronic transition efficiency from the ground state to the excited state (LUMO). This higher F value suggests a significant electronic coupling, facilitating effective absorption in the UV-Vis spectrum. Furthermore, Table 6 outlines additional electronic transitions, particularly those involving excitations from HOMO-1 to LUMO and HOMO-2 to LUMO. These transitions exhibit comparable percentage contributions to the overall absorption spectrum, signifying their relevance in the electronic excitation process. However, their respective oscillator strength (F) values differ, reflecting variations in electron transition probabilities between different molecular orbitals. The variations in F values further emphasize the differential ability of electronic transitions based on the spatial and energetic alignment of frontier orbitals.

2.3.3.3 Electron localization function (ELF)

The Electron Localization Function (ELF) serves as a powerful analytical tool for investigating the empirical concepts of electron

TABLE 6 Excitation energies, maximum wavelengths, oscillator strengths, and % orbital contribution for compound 7.

Spectral line number	Excitation energy (eV)	λ_{max} (nm)	F	Type of transition	% Orbital contribution
1	2.88	430	0.411	HOMO→LUMO	70
2	3.06	405	0.01	HOMO-1→LUMO	66
3	3.49	355	0.019	HOMO-2→LUMO	55

localization, particularly the spatial confinement of electron pairs in molecular systems. This approach aligns closely with Lewis structures, offering a deeper understanding of chemical bonding by mapping electron density distributions. The ELF provides a quantitative measure of electron localization at specific points in atomic space, shedding light on bond characteristics and electronic interactions within the molecule. One of the most insightful ways to analyze ELF is through two-dimensional cross-sectional planes, which offer crucial details about bonding interactions across different molecular regions. In this study, the analysis focuses on four distinct planes: C1-H1-O3, C5-S2-O1, C5-S2-O2, and H11-N2-H12, as well as N1-C12-S3, each of which provides a unique perspective on electron distribution and bond strength. As illustrated in Figure 16, all atoms of interest are located within the same molecular plane, providing a coherent view of both localized and delocalized electron density. The selected ELF planes reveal a strongly localized electronic region (represented by the red color scale) between the S2, O1, and O2 atoms with some difference in the planes of C5-S2-O1 and C5-S2-O2, indicating a high degree of electron confinement in this bonding region. This suggests a stable electronic environment in which N2, located in the NH2 plane, plays a crucial role in molecular connectivity through the electronic delocalization effect. Generally, the plane involving the amino group (N4) exhibits an atypical electron localization pattern. The plane of C1-H1-O3 exhibits a significant H-bond formation between H1 and O3 that appears in the electronic deformation area around O3. The delocalization effect implies a dynamic charge distribution, leading to a more flexible electronic structure rather than a rigid, strongly localized bond.

2.3.3.4 Molecular electrostatic potential (MEP)

The Molecular Electrostatic Potential (MEP) 3D-map is a valuable computational tool used to analyze the electrostatic properties of molecules by mapping the electronegativities of atomic locations. This topological approach offers crucial insights into molecular interactions, charge distribution, and the prediction of reactive sites, thereby enhancing our understanding of molecular recognition and non-covalent interactions. Since electrostatic forces predominantly govern long-range molecular interactions, MEP plays a significant role in predicting electrophilic and nucleophilic attack sites within a given structure. To visually assess the electrostatic distribution, color-coded MEP maps were generated for compound **7**, as shown in Figure 17. These maps employ a spectrum of colors—red, orange, yellow, green, and blue—each representing different electrostatic potential values across the molecular surface. The color sequence follows the decreasing order of electrostatic potential, with orange and red indicating the most electron-rich (nucleophilic) regions. Yellow and green represent regions of moderate electronic density, typically found in neutral areas. Blue signifies electron-deficient (electrophilic) zones, which are likely to attract electron-donating species. By interpreting the MEP map, it was observed that the oxygen atoms in compound **7** exhibit the highest electron density, as highlighted by intense red zones. These regions act as strong electron-donor sites, making them highly reactive toward electrophilic attack. The remaining molecular regions, particularly the N and S atoms, exhibit a lower density of π-electrons, as represented by the yellow color scale. This suggests that these atoms are less nucleophilic compared to oxygen-rich sites. However, the area of N1 bearing H was indicated in blue, suggesting an electron donor or H-bonding formation with other molecules.

2.3.3.5 Reduced density gradient/non-covalent interactions (RDG/NCI)

The Reduced Density Gradient (RDG) method is a valuable computational tool for identifying and visualizing non-covalent interactions (NCIs) within a molecular system. These interactions play a crucial role in stabilizing molecular structures and influencing their chemical behavior. By analyzing the RDG function, it is possible to distinguish between different types of weak interactions, such as van der Waals (vdW) forces, hydrogen bonding, and steric repulsions. This method provides a detailed perspective on molecular stability and intra- and intermolecular forces, which are essential for predicting reactivity and interaction mechanisms. To effectively interpret the nature of non-covalent interactions, color-coded RDG isosurfaces were generated, as depicted in Figure 18. The different interaction types were classified based on their corresponding colors: Green regions indicate the presence of weak van der Waals (vdW) interactions, which typically contribute to molecular packing and stability. Red regions represent steric repulsions, which arise from unfavorable close contacts between atoms, often due to spatial constraints. Blue regions, if present, would indicate strong attractive interactions, such as hydrogen bonding, but were not observed in this analysis. A key parameter in this study is $\text{sign}(\lambda_2)\rho$, which is derived by multiplying the electron density (ρ) by the sign of the second Hessian eigenvalue (λ_2). This value serves as an indicator of interaction strength, particularly in identifying hydrogen bonding (HB) interactions within the system. From the RDG analysis, significant vdW interactions were observed, notably in the C1 and C9 regions, indicating the presence of weak attractive forces that contribute to molecular cohesion. Interestingly, hydrogen bond (H-bond) spikes were prominently detected in the RDG chart in the region between H1 and O3. The non-intense blue color is attributed to the relatively H-bearing C atom, which is predicted to be less positively charged. This reduces the sensitivity of these interactions when analyzed using

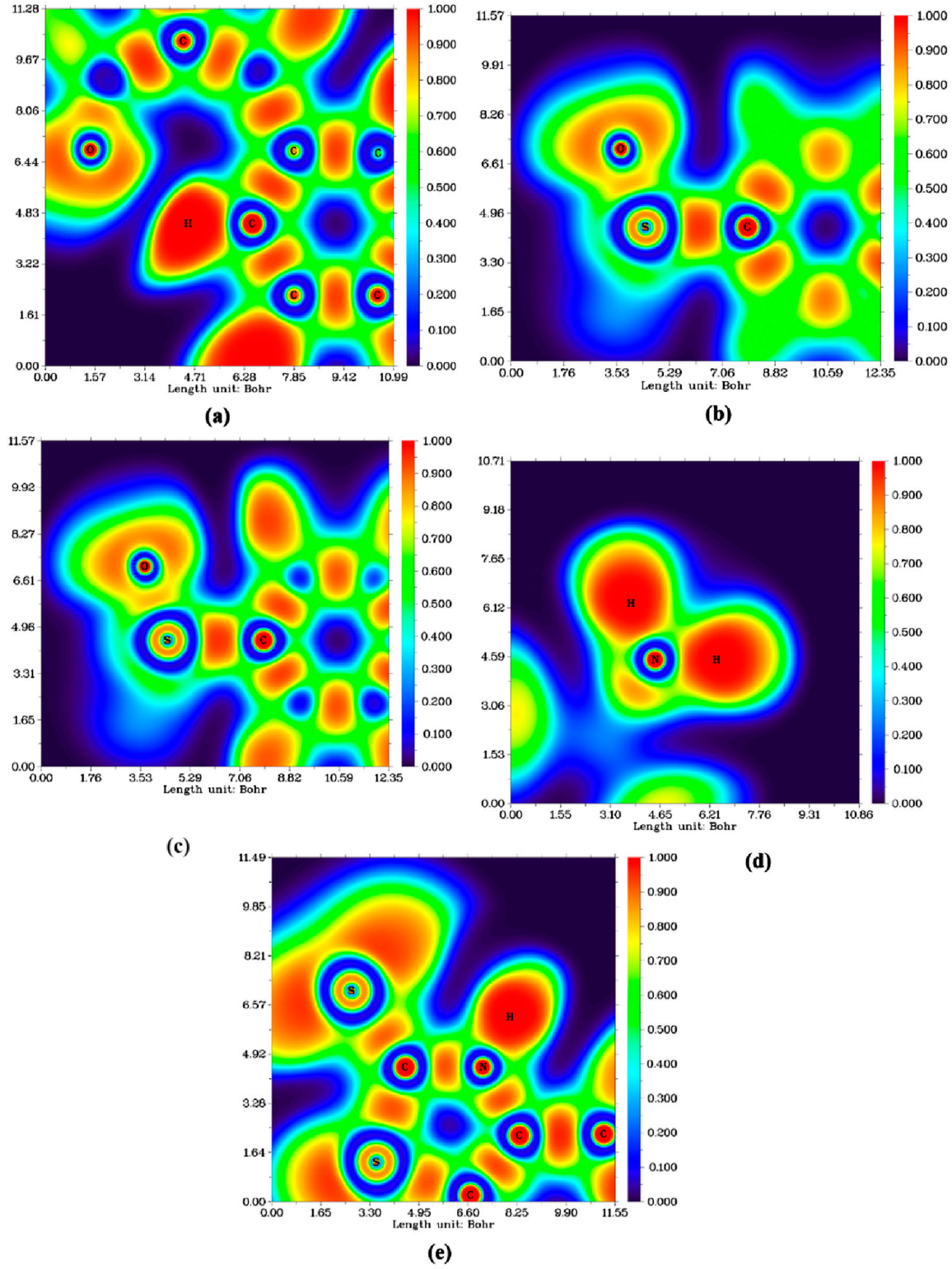


FIGURE 16
Electron localization function (ELF) colored map of compound **7** **(a)** C1-H1-O3, **(b)** C5-S2-O1, **(c)** C5-S2-O2, **(d)** H11-N2-H12, and **(e)** N1-C12-S3.

the reduced density gradient approach. Although hydrogen bonding is a well-known stabilizing factor in many systems, in this case, the distance constraints prevent its strong contribution to molecular stabilization. Furthermore, steric repulsion forces were noted in regions surrounding the phenyl rings, as indicated by red zones in the RDG analysis. These repulsive interactions stem from the rigid 6- and 5-membered rings, which impose spatial constraints on molecular flexibility. However, such unfavorable steric

10.3389/fchem.2025.1606848

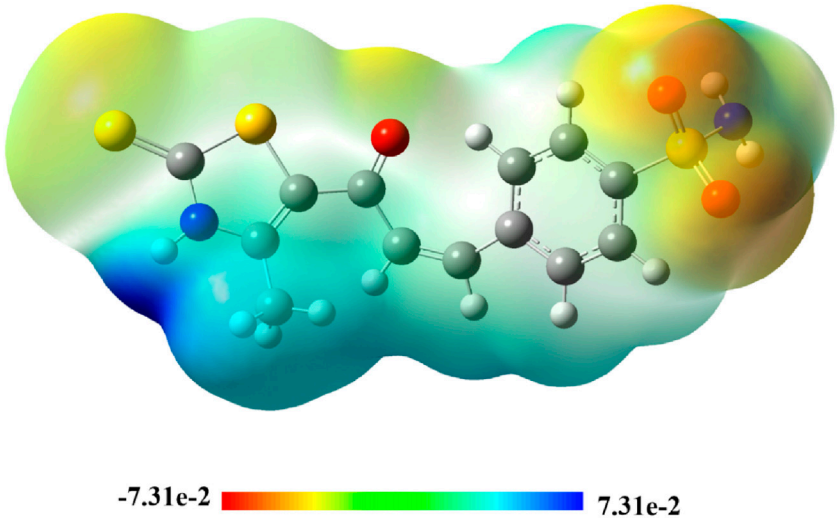


FIGURE 17
3D-colored map of the molecular electrostatic potential of compound **7**.

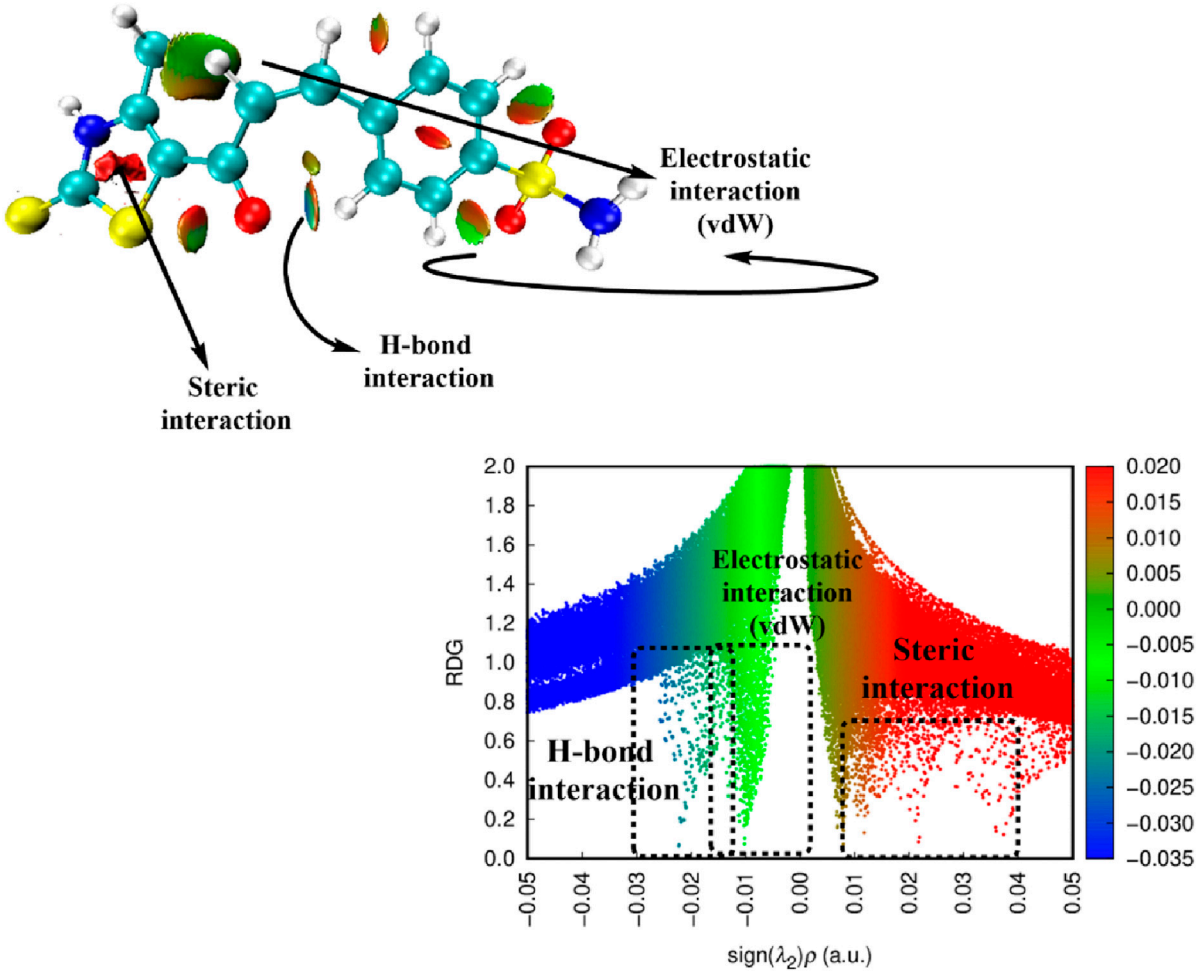


FIGURE 18
3D-NCI map and RDG plot of compound **7**.

interactions can be counterbalanced by favorable electrostatic interactions, ensuring overall molecular stability. This suggests that while steric hindrance limits certain conformational changes, the presence of stabilizing non-covalent forces, such as vdW interactions and H-bond formation, allows the structure to maintain its optimized conformation.

3 Conclusion

This study reports the design, synthesis, and biological evaluation of a novel thiazole–chalcone/sulfonamide hybrid (compound **7**) as a promising dual inhibitor of tubulin polymerization and carbonic anhydrase IX. The compound exhibited potent cytotoxicity against cancer cell lines, particularly HT-29 colorectal cells, with favorable selectivity over normal cells. Mechanistic investigations revealed activation of the intrinsic apoptotic pathway through modulation of p53, Bax, Bcl-2, and caspases. Molecular docking confirmed strong and specific interactions with both biological targets, while *in silico* ADMET and DFT analyses indicated suitable drug-like properties, stability, and electronic characteristics. Collectively, the data highlight compound **7** as a promising scaffold for further development as a dual-targeted anticancer agent with potential therapeutic relevance in tumors characterized by cytoskeletal dysregulation and CA IX overexpression.

4 Experimental

4.1 Chemistry

General Details: Refer to Appendix A (Supplementary Material).

3-Chloroacetylacetone (**2**) (Cativiela et al., 1995), 1-(2-mercapto-4-methylthiazol-5-yl)ethan-1-one (**3**) (Hashem et al., 2024), 4-(hydroxymethyl)benzenesulfonamide (**5**) (Procopiou et al., 2010) and 4-formylbenzenesulfonamide (**6**) (Zuo et al., 2022) were prepared according to reported procedures.

Synthesis of (*E*)-4-(3-(4-methyl-2-thioxo-2,3-dihydrothiazol-5-yl)-3-oxoprop-1-en-1-yl)benzenesulfonamide (7).

An aqueous NaOH solution (140 mg, 3.5 mmol 60%) was added dropwise to a solution of the thiazole intermediate **3** (173 mg, 1 mmol) and the aldehyde **6** (185 mg, 1 mmol) in absolute ethanol at 0°C. The reaction mixture was stirred in an ice bath for 12 h. The solvent was evaporated under reduced pressure, and the mixture was redissolved in distilled water and acidified by diluted acetic acid. The formed precipitate was filtered off, washed with distilled water, and recrystallized from acetonitrile.

Yellow powder; 0.248 g, 73% yield; mp 267–269°C; ^{1}H NMR (400 MHz, DMSO-d_6) δ 13.64 (s, 1H, N-*H*), 7.93 (d, *J* = 9.7 Hz, 2H, Ar-*H*), 7.83 (d, *J* = 9.2 Hz, 1H, Ar-*H*), 7.51 (d, *J* = 15.9 Hz, 1H, =C*H*), 7.41 (d, *J* = 15.9 Hz, 1H, =C*H*), 7.23 (s, 2H, SO_2NH_2), 2.59 (s, 3H, CH_3); ^{13}C NMR (100 MHz, DMSO-d_6) δ 189.50, 180.17, 147.73, 143.96, 134.14, 131.78, 130.28, 126.41, 125.16, 123.60, 15.57. ESI-MS (*m/z*): Calcd. 340.00, found 340.41 $[M]^+$. Anal. Calcd. For $C_{13}H_{12}N_2O_3S_3$: C, 45.87%; H, 3.55%; N, 8.23%. Found: C, 45.99%; H, 3.71%; N, 8.04%. HPLC analysis: 97.4%.

4.2 Biological evaluation

4.2.1 Antiproliferative assay

The cytotoxic potential of compound **7** was assessed using a propidium iodide fluorescence assay across A-549, HT-29, 786-O, MCF-7, and WI-38 cell lines. All cell lines were obtained from the Vacsera Cell Culture Library, Tissue Culture Unit, Cairo, Egypt, with ATCC certification. The assay enabled the detection of membrane-compromised cells based on the fluorescence intensity of DNA binding. Check Appendix A for additional information.

4.2.2 Tubulin polymerization assay

The effect of compound **7** on tubulin polymerization was evaluated using the Tubulin Polymerization Assay Kit (Cytoskeleton Inc., United States). Fluorescence-based measurements were used to monitor its impact on microtubule dynamics. Details are presented in Appendix A (Supplementary Material).

4.2.3 Evaluation of carbonic anhydrase I, II, IV, and VII inhibition

The inhibitory effect of compound **7** on carbonic anhydrase isoforms I, II, IX, and XII was evaluated using the Carbonic Anhydrase Inhibitor Screening Kit (Colorimetric, BioVision, Cat# K473-100), which measures enzymatic activity *via* substrate hydrolysis and measures absorbance at 405 nm. The assay was conducted under standard conditions as outlined by the manufacturer. Further methodological details can be found in Appendix A (Supplementary Material).

4.2.4 Effect on Bax expression levels

The effect of compound **7** on pro-apoptotic Bax protein expression was evaluated using the Human Bax ELISA Kit (DRG, EIA-4487), which employs a biotin-streptavidin-HRP detection system and colorimetric measurement at 450 nm. Changes in Bax levels were quantified in treated cell lysates to assess the apoptotic response. Comprehensive assay details are available in Appendix A (Supplementary Material).

4.2.5 Effect on Bcl-2 expression levels

To assess the anti-apoptotic effect of compound 7, Bcl-2 protein levels were quantified using the Zymed Bcl-2 ELISA Kit (Invitrogen, Cat. No. 99-0042), a sandwich ELISA format with streptavidin-HRP detection. Absorbance was measured at 450 nm to determine changes in Bcl-2 expression in response to treatment. A full description of the assay protocol is included in Appendix A (Supplementary Material).

4.2.6 Effect on p53 expression levels

The influence of compound **7** on p53 protein levels was investigated using the Human p53 ELISA Kit (Thermo Fisher Scientific, Cat. No. BMS256), which employs a dual-antibody sandwich format with HRP-based colorimetric detection at 450 nm. The assay enabled the sensitive quantification of p53 expression following exposure to the compound. Detailed procedures and reagent preparation can be found in Appendix A (Supplementary Material).

4.2.7 Effect of caspase-3 activity

The effect of compound **7** on apoptosis was further assessed by quantifying active caspase-3 levels using the Human Caspase-3

(Active) ELISA Kit (Invitrogen, Cat. No. KHO1091). This sandwich ELISA detects caspase-3 cleaved at Asp175/Ser176, enabling sensitive colorimetric measurement at 450 nm. Additional procedural details are provided in Appendix A (Supplementary Material).

4.2.8 Effect on caspase-9 activity

The involvement of compound 7 in apoptosis induction was further examined by quantifying caspase-9 levels using the Human Caspase 9 ELISA Kit (Thermo Fisher Scientific, Cat. No. BMS 2025). This assay employs a sandwich ELISA format, utilizing a specific capture antibody and an HRP-conjugated detection system, with absorbance measured at 450 nm. A detailed methodology is provided in Appendix A (Supplementary Material).

4.3 Molecular modeling

4.3.1 Molecular docking

Molecular docking of compound 7 was performed against tubulin (PDB ID: 4O2B) and carbonic anhydrase IX (PDB ID: 5FL4) using AutoDock Vina. Protein and ligand preparations, grid setup, and visualization were conducted using standard molecular modeling tools. Detailed procedures are described in Appendix A (Supplementary Material).

4.3.2 ADMET predictions

The pharmacokinetic properties of compound 7 were predicted using the SwissADME web tool (http://www.swissadme.ch). The SMILES notation of the compound was input into the platform to evaluate key absorption, distribution, metabolism, and excretion (ADME) parameters. These included gastrointestinal (GI) absorption, blood-brain barrier (BBB) permeability, prediction of P-glycoprotein substrate, cytochrome P450 enzyme inhibition, and physicochemical descriptors such as lipophilicity (LogP), solubility (LogS), and topological polar surface area (TPSA). Drug-likeness was also assessed based on Lipinski's rule of five and related filters.

4.3.3 DFT calculations

The structural and electronic properties of compound 7 were investigated using density functional theory (DFT) with the B3LYP/6-311++G(d,p) level of theory. Visualization and topological analyses, including MEP mapping, RDG, NCI, and ELF, were carried out using Chemcraft, VMD, and Multiwfn software. Further computational details are provided in Appendix A (Supplementary Material).

Data availability statement

The original contributions presented in the study are publicly available. This data can be found here: https://doi.org/10.6084/m9.figshare.29369423.

Ethics statement

Ethical approval was not required for the studies on humans in accordance with the local legislation and institutional requirements because only commercially available established cell lines were used.

Author contributions

HK: Conceptualization, Writing – original draft. EA: Funding acquisition, Resources, Writing – review and editing. RE: Funding acquisition, Resources, Writing – review and editing. RA-A: Investigation, Software, Writing – original draft. WA: Data curation, Formal Analysis, Validation, Writing – original draft. GA: Investigation, Software, Writing – original draft. SB: Conceptualization, Project administration, Supervision, Writing – review and editing. AA: Investigation, Software, Writing – original draft.

Funding

The author(s) declare that financial support was received for the research and/or publication of this article. This study was funded by the Deanship of Scientific Research at Northern Border University, Arar, Kingdom of Saudi Arabia, through project number NBU-FFR-2025-435-01.

Acknowledgments

The authors extend their appreciation to the Deanship of Scientific Research at Northern Border University, Arar, KSA, for funding this research work through the project number "NBU-FFR-2025-435-01."

Conflict of interest

The authors declare that the research was conducted in the absence of any commercial or financial relationships that could be construed as a potential conflict of interest.

Generative AI statement

The author(s) declare that no Generative AI was used in the creation of this manuscript.

Publisher's note

All claims expressed in this article are solely those of the authors and do not necessarily represent those of their affiliated organizations, or those of the publisher, the editors and the reviewers. Any product that may be evaluated in this article, or claim that may be made by its manufacturer, is not guaranteed or endorsed by the publisher.

Supplementary material

The Supplementary Material for this article can be found online at: https://www.frontiersin.org/articles/10.3389/fchem.2025.1606848/full#supplementary-material

References

Abdelhakeem, M. M., Morcoss, M. M., Hanna, D. A., and Lamie, P. F. (2024). Design, synthesis and *in silico* insights of novel 1,2,3-triazole benzenesulfonamide derivatives as potential carbonic anhydrase IX and XII inhibitors with promising anticancer activity. *Bioorg Chem.* 144, 107154. doi:10.1016/j.bioorg.2024.107154

Abdel-Motaal, M., Aldakhili, D. A., Abo Elmaaty, A., Sharaky, M., Mourad, M. A. E., Alzahrani, A. Y. A., et al. (2024). Design and synthesis of novel tetrabromophthalimide derivatives as potential tubulin inhibitors endowed with apoptotic induction for cancer treatment. *Drug Dev. Res.* 85, e22197. doi:10.1002/ddr.22197

Abo-Ashour, M. F., Eldehna, W. M., Nocentini, A., Ibrahim, H. S., Bua, S., Abdel-Aziz, H. A., et al. (2019). Novel synthesized SLC-0111 thiazole and thiadiazole analogues: determination of their carbonic anhydrase inhibitory activity and molecular modeling studies. *Bioorg Chem.* 87, 794–802. doi:10.1016/j.bioorg.2019.04.002

Ahmed, N. M., Mohamed, M. S., Awad, S. M., Abd El-Hameed, R. H., El-Tawab, N. A. A., Gaballah, M. S., et al. (2024). Design, synthesis, molecular modelling and biological evaluation of novel 6-amino-5-cyano-2-thiopyrimidine derivatives as potent anticancer agents against leukemia and apoptotic inducers. *J. Enzyme Inhib. Med. Chem.* 39, 2304625. doi:10.1080/14756366.2024.2304625

Ahmed, R. F., Mahmoud, W. R., Abdelgawad, N. M., Fouad, M. A., and Said, M. F. (2023). Exploring novel anticancer pyrazole benzenesulfonamides featuring tail approach strategy as carbonic anhydrase inhibitors. *Eur. J. Med. Chem.* 261, 115805. doi:10.1016/j.ejmech.2023.115805

Albelwi, F. F., Nafie, M. S., Albujuq, N. R., Hourani, W., Aljuhani, A., Darwish, K. M., et al. (2024). Design and synthesis of chromene-1,2,3-triazole benzene sulfonamide hybrids as potent carbonic anhydrase-IX inhibitors against prostate cancer. *RSC Med. Chem.* 15, 2440–2461. doi:10.1039/d4md00302k

Al-Wahaibi, L. H., Elshamsy, A. M., Ali, T. F. S., Youssif, B. G. M., Bräse, S., Abdel-Aziz, M., et al. (2025) Design, synthesis, in silico studies, and apoptotic antiproliferative activity of novel thiazole-2-acetamide derivatives as tubulin polymerization inhibitors. *Front. Chem.* 13:1565699. doi:10.3389/fchem.2025.1565699

Boichuk, S., Galembikova, A., Syuzov, K., Dunaev, P., Bikinieva, F., Aukhadieva, A., et al. (2021). The design, synthesis, and biological activities of pyrrole-based carboxamides: the novel tubulin inhibitors targeting the colchicine-binding site. *Molecules* 26, 5780. doi:10.3390/molecules26195780

Brindisi, M., Kessler, S. M., Kumar, V., and Zwergel, C. (2022). Editorial: multi-target directed ligands for the treatment of cancer. *Front. Oncol.* 12, 980141. doi:10.3389/fonc.2022.980141

Carta, F., Supuran, C. T., and Scozzafava, A. (2014). Sulfonamides and their isosters as carbonic anhydrase inhibitors. *Future Med. Chem.* 6, 1149–1165. doi:10.4155/fmc.14.68

Cativiela, C., Serrano, J. L., and Zurbano, M. M. (1995). Synthesis of 3-substituted pentane-2,4-diones: valuable intermediates for liquid crystals. *J. Org. Chem.* 60, 3074–3083. doi:10.1021/jo00115a023

Chiche, J., Ilc, K., Laferrière, J., Trottier, E., Dayan, F., Mazure, N. M., et al. (2008). Hypoxia-inducible carbonic anhydrase IX and XII promote tumor cell growth by counteracting acidosis through the regulation of the intracellular pH. *Cancer Res.* 69, 358–368. doi:10.1158/0008-5472.CAN-08-2470

Daina, A., Michielin, O., and Zoete, V. (2017). SwissADME: a free web tool to evaluate pharmacokinetics, drug-likeness and medicinal chemistry friendliness of small molecules. *Sci. Rep.* 7, 42717. doi:10.1038/srep42717

Doostmohammadi, A., Jooya, H., Ghorbanian, K., Gohari, S., and Dadashpour, M. (2024). Potentials and future perspectives of multi-target drugs in cancer treatment: the next generation anti-cancer agents. *Cell Commun. Signal.* 22, 228. doi:10.1186/s12964-024-01607-9

Dumontet, C., and Jordan, M. A. (2010). Microtubule-binding agents: a dynamic field of cancer therapeutics. *Nat. Rev. Drug Discov.* 9, 790–803. doi:10.1038/nrd3253

El-Abd, A. O., Bayomi, S. M., El-Damasy, A. K., Mansour, B., Abdel-Aziz, N. I., and El-Sherbeny, M. A. (2022). Synthesis and molecular docking study of new thiazole derivatives as potential tubulin polymerization inhibitors. *ACS Omega* 7, 33599–33613. doi:10.1021/acsomega.2c05077

Elbadawi, M. M., Eldehna, W. M., Nocentini, A., Abo-Ashour, M. F., Elkaeed, E. B., Abdelgawad, M. A., et al. (2021). Identification of *N*-phenyl-2-(phenylsulfonyl) acetamides/propanamides as new SLC-0111 analogues: synthesis and evaluation of the carbonic anhydrase inhibitory activities. *Eur. J. Med. Chem.* 218, 113360. doi:10.1016/j.ejmech.2021.113360

Elkotamy, M. S., Abdelrahman, M. A., Giovannuzzi, S., Alkabbani, M. A., Nocentini, A., Supuran, C. T., et al. (2025). Development of pyrazolo[1,5-*a*]pyrimidine-grafted coumarins as selective carbonic anhydrase inhibitors and tubulin polymerization inhibitors with potent anticancer activity. *Int. J. Biol. Macromol.* 303, 140462. doi:10.1016/j.ijbiomac.2025.140462

Elshamsy, A. M., Ali, T. F. S., Osman, M., and El-Koussi, N. A. (2023). Recent progress in biological activities of dihydropyrimidine derivatives: an updated mini-review. *J. Adv. Biomed. Pharm. Sci.* 6, 114–123. doi:10.21608/jabps.2023.198467.1183

Hanahan, D., and Weinberg, R. A. (2011). Hallmarks of cancer: the next generation. *Cell* 144, 646–674. doi:10.1016/j.cell.2011.02.013

Hashem, H., Hassan, A., Abdelmagid, W. M., Habib, A. G. K., Abdel-Aal, M. A. A., Elshamsy, A. M., et al. (2024). Synthesis of new thiazole-privileged chalcones as tubulin polymerization inhibitors with potential anticancer activities. *Pharm. (Basel)* 17, 1154. doi:10.3390/ph17091154

Hawash, M. (2022). Recent advances of tubulin inhibitors targeting the colchicine binding site for cancer therapy. *Biomolecules* 12, 1843. doi:10.3390/biom12121843

Huo, X.-S., Jian, X.-E., Ou-Yang, J., Chen, L., Yang, F., Lv, D.-X., et al. (2021). Discovery of highly potent tubulin polymerization inhibitors: design, synthesis, and structure-activity relationships of novel 2,7-diaryl-[1,2,4]triazolo[1,5-*a*]pyrimidines. *Eur. J. Med. Chem.* 220, 113449. doi:10.1016/j.ejmech.2021.113449

Jordan, M. A., and Wilson, L. (2004). Microtubules as a target for anticancer drugs. *Nat. Rev. Cancer* 4, 253–265. doi:10.1038/nrc1317

Kalinin, S., Malkova, A., Sharonova, T., Sharoyko, V., Bunev, A., Supuran, C. T., et al. (2021). Carbonic anhydrase IX inhibitors as candidates for combination therapy of solid tumors. *Int. J. Mol. Sci.* 22, 13405. doi:10.3390/ijms222413405

Kaur, K., and Jaitak, V. (2022). Thiazole and related heterocyclic systems as anticancer agents: a review on synthetic strategies, mechanisms of action and SAR studies. *Curr. Med. Chem.* 29, 4958–5009. doi:10.2174/0929867329666220318100019

Kavallaris, M. (2010). Microtubules and resistance to tubulin-binding agents. *Nat. Rev. Cancer* 10, 194–204. doi:10.1038/nrc2803

Khokhlov, A. L., Shetnev, A. A., Korsakov, M. K., Fedorov, V. N., Tyushina, A. N., Volkhin, N. N., et al. (2023). Pharmacological properties of sulfonamide derivatives, new inhibitors of carbonic anhydrase. *Bull. Exp. Biol. Med.* 175, 205–209. doi:10.1007/s10517-023-05835-w

Klika, K. D., Pieve, C. D., Kopka, K., Smith, G., and Makarem, A. (2021). Synthesis and application of a thiol-reactive HBED-type chelator for development of easy-to-produce Ga-radiopharmaceutical kits and imaging probes. *Org. Biomol. Chem.* 19, 1722–1726. doi:10.1039/D0OB02513E

Lembo, V., and Bottegoni, G. (2024). Systematic investigation of dual-target-directed ligands. *J. Med. Chem.* 67, 10374–10385. doi:10.1021/acs.jmedchem.4c00838

Li, X., Li, X., Liu, F., Li, S., and Shi, D. (2021). Rational multitargeted drug design strategy from the perspective of a medicinal chemist. *J. Med. Chem.* 64, 10581–10605. doi:10.1021/acs.jmedchem.1c00683

Lin, C.-N., Tu, H.-Y., Huang, a-M., Hoar, T.-C., Yang, S.-C., Pu, Y.-S., et al. (2011). Synthesis and biological evaluation of 2′,5′-dimethoxychalcone derivatives as microtubule-targeted anticancer agents. *US2011306775A1.*

Liu, W., He, M., Li, Y., Peng, Z., and Wang, G. (2022). A review on synthetic chalcone derivatives as tubulin polymerisation inhibitors. *J. Enzyme Inhib. Med. Chem.* 37, 9–38. doi:10.1080/14756366.2021.1976772

Lou, Y., McDonald, P. C., Oloumi, A., Chia, S., Ostlund, C., Ahmadi, A., et al. (2011). Targeting tumor hypoxia: suppression of breast tumor growth and metastasis by novel carbonic anhydrase IX inhibitors. *Cancer Res.* 71, 3364–3376. doi:10.1158/0008-5472.CAN-10-4261

Makarem, A., Sarvestani, M. K., Klika, K. D., and Kopka, K. (2019). A multifunctional HBED-type chelator with dual conjugation capabilities for radiopharmaceutical development. *Synlett* 30, 1795–1798. doi:10.1055/s-0039-1690194

Mboge, M. Y., Mahon, B. P., McKenna, R., and Frost, S. C. (2018). Carbonic anhydrases: role in pH control and cancer. *Metabolites* 8, 19. doi:10.3390/metabo8010019

McDonald, P. C., Chafe, S. C., Supuran, C. T., and Dedhar, S. (2022). Cancer therapeutic targeting of hypoxia induced carbonic anhydrase IX: from bench to bedside. *Cancers (Basel)* 14, 3297. doi:10.3390/cancers14143297

Mphahlele, M. J., Maluleka, M. M., Parbhoo, N., and Malindisa, S. T. (2018). Synthesis, evaluation for cytotoxicity and molecular docking studies of benzo[c]furan-chalcones for potential to inhibit tubulin polymerization and/or EGFR-tyrosine kinase phosphorylation. *Int. J. Mol. Sci.* 19, 2552. doi:10.3390/ijms19092552

Neri, D., and Supuran, C. T. (2011). Interfering with pH regulation in tumours as a therapeutic strategy. *Nat. Rev. Drug Discov.* 10, 767–777. doi:10.1038/nrd3554

Procopiou, P. A., Barrett, V. J., Bevan, N. J., Biggadike, K., Box, P. C., Butchers, P. R., et al. (2010). Synthesis and Structure−Activity relationships of long-acting β_2Adrenergic receptor agonists incorporating metabolic inactivation: an antedrug approach. *J. Med. Chem.* 53, 4522–4530. doi:10.1021/jm100326d

Sgouros, G., Bodei, L., McDevitt, M. R., and Nedrow, J. R. (2020). Radiopharmaceutical therapy in cancer: clinical advances and challenges. *Nat. Rev. Drug Discov.* 19, 589–608. doi:10.1038/s41573-020-0073-9

Shaldam, M., Eldehna, W. M., Nocentini, A., Elsayed, Z. M., Ibrahim, T. M., Salem, R., et al. (2021). Development of novel benzofuran-based SLC-0111 analogs as selective cancer-associated carbonic anhydrase isoform IX inhibitors. *Eur. J. Med. Chem.* 216, 113283. doi:10.1016/j.ejmech.2021.113283

Sultana, F., Reddy Bonam, S., Reddy, V. G., Nayak, V. L., Akunuri, R., Rani Routhu, S., et al. (2018). Synthesis of benzo[d]imidazo[2,1-b]thiazole-chalcone conjugates as microtubule targeting and apoptosis inducing agents. *Bioorg Chem.* 76, 1–12. doi:10.1016/j.bioorg.2017.10.019

Supuran, C. T. (2018). Carbonic anhydrase inhibitors as emerging agents for the treatment and imaging of hypoxic tumors. *Expert Opin. Investig. Drugs* 27, 963–970. doi:10.1080/13543784.2018.1548608

Trott, O., and Olson, A. J. (2010). AutoDock Vina: improving the speed and accuracy of docking with a new scoring function, efficient optimization and multithreading. *J. Comput. Chem.* 31, 455–461. doi:10.1002/jcc.21334

van Vuuren, R. J., Visagie, M. H., Theron, A. E., and Joubert, A. M. (2015). Antimitotic drugs in the treatment of cancer. *Cancer Chemother. Pharmacol.* 76, 1101–1112. doi:10.1007/s00280-015-2903-8

Vogelstein, B., Papadopoulos, N., Velculescu, V. E., Zhou, S., Diaz, L. A., and Kinzler, K. W. (2013). Cancer genome landscapes. *Science* 339, 1546–1558. doi:10.1126/science.1235122

Wang, G., Liu, W., Fan, M., He, M., Li, Y., and Peng, Z. (2021). Design, synthesis and biological evaluation of novel thiazole-naphthalene derivatives as potential anticancer agents and tubulin polymerisation inhibitors. *J. Enzyme Inhib. Med. Chem.* 36, 1693–1701. doi:10.1080/14756366.2021.1958213

Wang, Y.-T., Huang, X., Cai, X.-C., Kang, X.-X., and Zhu, H.-L. (2024). Synthesis, biological evaluation and molecular docking of thiazole hydrazone derivatives grafted with indole as novel tubulin polymerization inhibitors. *J. Mol. Struct.* 1301, 137343. doi:10.1016/j.molstruc.2023.137343

Zuo, D., Do, N., Hwang, I., Ann, J., Yu, J.-W., and Lee, J. (2022). Design and synthesis of an N-benzyl 5-4-sulfamoylbenzylidene-2-thioxothiazolidin-4-one scaffold as a novel NLRP3 inflammasome inhibitor. *Bioorg Med. Chem. Lett.* 65, 128693. doi:10.1016/j.bmcl.2022.128693

frontiers | Frontiers in Chemistry

TYPE Original Research
PUBLISHED 07 July 2025
DOI 10.3389/fchem.2025.1583666

Check for updates

OPEN ACCESS

EDITED BY
Ahmed A. Al-Karmalawy,
University of Mashreq, Iraq

REVIEWED BY
Saad Shaaban,
King Saud University, Saudi Arabia
Ghina'A. Abu Deiab,
Yarmouk University, Jordan
Aya Alabdali,
UCSI University, Malaysia

*CORRESPONDENCE
Gang Ding,
gding@implad.ac.cn
Lan-Ping Guo,
glp01@126.com

†These authors have contributed equally to this work

RECEIVED 27 February 2025
ACCEPTED 20 May 2025
PUBLISHED 07 July 2025

CITATION
Sun H-D, Wang Y-D, Fang H-Q, Yang J, Hua Y-T, Ding G and Guo L-P (2025) Phomaderide, a unique (6/5/4/5/6) spiro-cyclic dimer from the desert plant endophytic fungus *Phoma betae* A. B. Frank (Didymellaceae). *Front. Chem.* 13:1583666. doi: 10.3389/fchem.2025.1583666

COPYRIGHT
© 2025 Sun, Wang, Fang, Yang, Hua, Ding and Guo. This is an open-access article distributed under the terms of the Creative Commons Attribution License (CC BY). The use, distribution or reproduction in other forums is permitted, provided the original author(s) and the copyright owner(s) are credited and that the original publication in this journal is cited, in accordance with accepted academic practice. No use, distribution or reproduction is permitted which does not comply with these terms.

Phomaderide, a unique (6/5/4/5/6) spiro-cyclic dimer from the desert plant endophytic fungus *Phoma betae* A. B. Frank (Didymellaceae)

Hao-Di Sun[1†], Yan-Duo Wang[2†], Hui-Qi Fang[2], Jian Yang[3], Yu-Tong Hua[3], Gang Ding[2*] and Lan-Ping Guo[1*]

[1]State Key Laboratory for Quality Ensurance and Sustainable Use of Dao-di Herbs, Institute of Chinese Materia Medica China Academy of Chinese Medical Sciences, China Academy of Chinese Medical Sciences, Beijing, China, [2]State Key Laboratory of Bioactive Substance and Function of Natural Medicines, Institute of Medicinal Plant Development, Chinese Academy of Medical Sciences and Peking Union Medical College, Beijing, China, [3]State Key Laboratory for Quality Ensurance and Sustainable Use of Dao-di Herbs, National Resource Center for Chinese Materia Medica, China Academy of Chinese Medical Sciences, Beijing, China

Introduction: Endophytic fungi from desert plants are prolific producers of structurally unique stress-responsive metabolites. This study investigates the secondary metabolites of Phoma betae A. B. Frank (Didymellaceae), a desert plant endophytic fungus, aiming to discover novel bioactive compounds through advanced molecular networking strategies.

Methods: A building blocks-based molecular network (BBMN) strategy was employed to screen the fungal extract. Target compounds were isolated using silica gel and ODS column chromatography, followed by semi-preparative HPLC purification. Structural elucidation was achieved through comprehensive NMR spectroscopy, mass fragmentation pathway analysis, and electronic circular dichroism (ECD) calculations. Cytotoxicity was evaluated against HeLa and A549 cancer cell lines using CCK-8 assays.

Results: Three compounds were characterized:Phomaderide (3), a unique (6/5/4/5/6) spiro-cyclic dimer formed via stereoselective [2+2] photocycloaddition of two phaeosphaeride A (1) monomers. Its biosynthetic precursor phaeosphaeride A (1). A new hydroxylated analog, phaeosphaeride C (2). Compounds 2 and 3 exhibited moderate cytotoxicity against HeLa (IC_{50} 29.97–39.15 μM) and A549 cells (IC_{50} 30.47–58.33 μM).

Discussion: This work highlights the metabolic versatility of extremophilic fungi, demonstrating Phoma betae's capacity to generate architecturally complex molecules. Phomaderide's unprecedented spiro-cyclic dimer scaffold positions it as a promising lead for anticancer drug discovery, with structural modifications (hydroxylation and dimerization) significantly influencing bioactivity. The BBMN strategy proved effective for targeted isolation of structurally related analogs from complex extracts.

KEYWORDS

phomaderide, desert plant endophytic fungus, building block-based molecular network, cytotoxicity, structural elucidation, natural products

1 Introduction

Endophytic fungi of desert plants, under extreme environmental stress, frequently biosynthesize structurally unique stress-responsive metabolites. During the long-term evolutionary adaptation to these environments, these fungi have produced a variety of secondary metabolites that are a promising resource of biologically active natural products (Li et al., 2020; Xu et al., 2022; Tan Y. et al., 2022; Zhang et al., 2021; Tan et al., 2019; Tan X. M. et al., 2022). In our prior research, a series of undescribed diphenyl ethers were isolated from the endophytic fungus *Phoma betae* A. B. Frank (Didymellaceae) inhabiting a desert plant, and an empirical rule about the shielding effects induced by an aromatic ring in diphenyl ethers was first observed and analyzed (Tan Y. et al., 2022; Liu et al., 2023).

In a previous study, ten diphenyl ethers (DPEs) were isolated from the desert plant endophytic fungus *P. betae* A. B. Frank (Didymellaceae) (Tan Y. et al., 2022). Bioactivity evaluation revealed moderate cytotoxicity and potent antioxidant activities, highlighting their potential as antioxidant agents.

In the continued exploration of secondary metabolites with novel structures from this fungus, phaeosphaeride A (**1**) was isolated from the endophytic fungus *Phaeosphaeria avenaria*. This metabolite, with a unique ring system, exhibited strong inhibitory activity of signal transducer and activator of transcription **3** (STAT3) (Maloney et al., 2006). Its unique ring system and excellent bioactivities attracted different groups for total synthesis, which established its correct relative and absolute configurations (Chatzimpaloglou et al., 2012; Chatzimpalogou et al., 2014; Kobayashi et al., 2015). The building block-based molecular network (BBMN) method integrates molecular networking with the concept of building blocks (He et al., 2021; Zhu et al., 2023). By extracting fragments containing characteristic fragment ions or neutral losses from MS^2 spectra, this approach simplifies large amounts of raw data and generates more targeted molecular network results.

In this study, a BBMN strategy was employed to rapidly screen analogs phaeosphaeride C (**2**) and phomaderide (**3**) related to phaeosphaeride A (**1**) from the extract of *P. betae* A. B. Frank (Didymellaceae) of these compounds (Figure 1). Phomaderide (**3**) is a structurally unprecedented (6/5/4/5/6) spiro-cyclic dimer formed via a [2 + 2] photocycloaddition of two phaeosphaeride A monomers. Its complex architecture includes a cyclobutane core, multiple stereocenters, and fused heterocyclic systems, reflecting significant structural divergence. While DPEs primarily exhibited antioxidant properties, phomaderide and its precursor analog phaeosphaeride C (**2**) demonstrated moderate cytotoxicity against HeLa and A549 cells, suggesting distinct bioactive mechanisms. This comparison underscores the metabolic versatility of *P. betae* A. B. Frank. The isolation, structural elucidation, possible biogenetic pathways, and biological activities of compounds (**1**–**3**) are presented in this study.

2 Materials and methods

2.1 General experimental procedures

1D and 2D NMR data were recorded on a Bruker AVANCE III 500 MHz (Bruker, Massachusetts, America) or a Varian Inova 600 MHz spectrometer (Varian, California, America), using $CDCl_3$ or DMSO-d_6 signals as references (δ_H/δ_C 7.26/77.2, 2.50/39.5). HR-ESI-MS spectra were obtained on a UPLC-Q-TOF-MS/MS (Waters Xevo G2-s QTOF, United States). In addition, optical rotations were obtained on a 241 polarimeter (PerkinElmer, Waltham, America), and UV spectra were measured on a UV-2102 (Unico, Shanghai, China) instrument. IR spectra were recorded on an FTIR-8400S spectrophotometer (Shimadzu, Kyoto, Japan), and the J-815 spectropolarimeter (JASCO, Tokyo, Japan) was used for collecting CD spectra. For purification, semi-preparative high-performance liquid chromatography (HPLC) was performed on a SEP LC-52 instrument with an MWD UV detector (Separation (Beijing) Technology Co Ltd., Beijing, China) which was packed with an Octadecylsilyl (ODS) column (YMC-pack ODS-A, 5 μm, 250 × 10 mm, Kyoto, Japan).

2.2 Fungal material fermentation and extraction

The strain of *P. betae* A. B. Frank (Didymellaceae) was isolated from the desert plant and provided by the Chinese Academy of Agricultural Sciences.

Phoma betae A. B. Frank was cultured on PDA plates at 25°C for 7 days. Then, the cells were transformed into a sterilized solid medium containing rice (60.0 g) and distilled water (80 mL) in Fernbach flasks (500 mL) for further fermentation at 25°C for 30 days. Finally, the whole fermented material was extracted with ethyl acetate (EtOAc) three times, and the extract was concentrated under reduced pressure to yield 150 g of the crude extract.

2.3 Purification of structures

The original extract was fractionated on a silica gel column chromatograph using dichloromethane (CH_2Cl_2) ether and methanol (MeOH) (1:0–0:1, each 5.0 L) to obtain nine fractions (Fr.C1–Fr.C9). Fr.C2 (0.56 g) was separated on an ODS column chromatography with MeOH in H_2O (20:80–80:20, each 260 mL) to get seven subfractions. Fr.C2.3 (39.3 mg) was further purified by semi-preparative HPLC (58% MeOH in H_2O, v/v, 2 mL/min) to yield **1** (19.9 mg, t_R 26.1 min). Fr.C3 (2.29 g) was fractionated on an ODS column chromatograph using MeOH in H_2O elution (30:70–90:10, each 500 mL) to get eight subfractions. Fr.C3.3 (14.4 mg) was further purified by semi-preparative HPLC (60% MeOH in H_2O, v/v, 2 mL/min) to obtain **2** (2.8 mg, t_R 12.4 min). Fr.C3.6 (111.4 mg) was further separated by semi-preparative HPLC (78% MeOH in H_2O, 2 mL/min) to yield **3** (11.5 mg, t_R 28.7 min).

2.4 Preparation of (*R*)- and(*S*)-MTPA esters of compound 2

(*R*)-MTPACl (8 μL) was added to a solution of compound **2** (0.8 mg) in pyridin-d_5 (200 μL) and placed at room temperature for 24 h. The crude product was purified by HPLC (60% acetonitrile in H_2O, 2 mL/min) to afford (*S*)-MTPA ester (≈0.5 mg, t_R = 15.4 min). (*S*)-MTPACl (8 μL) was added to a solution of compound **1** (0.5 mg)

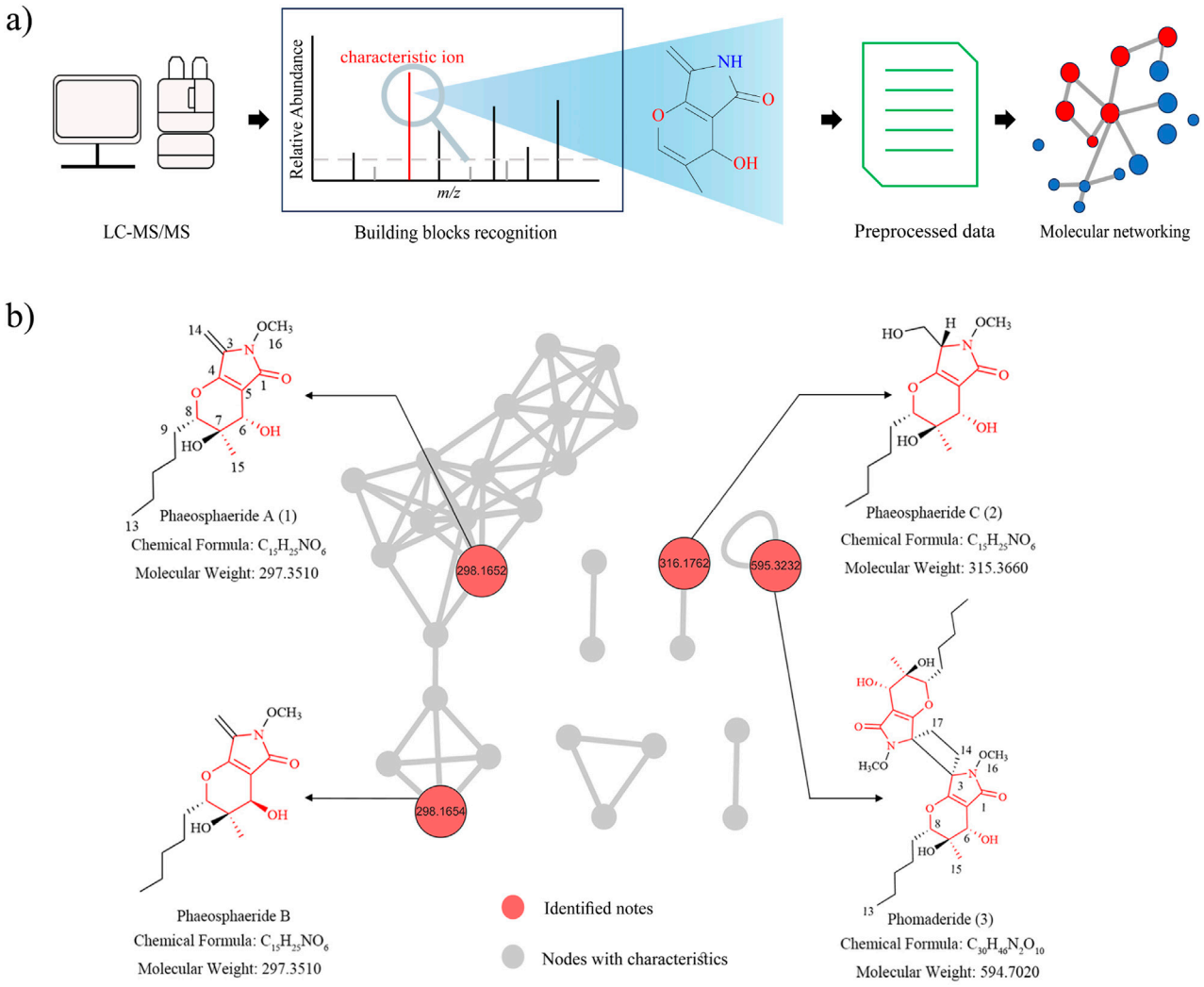


FIGURE 1
(A) Schematic workflow of the application of the building block-based molecular network (BBMN). **(B)** BBMN of the spectra with the refined features.

in pyridin-d_5 (200 μL) and placed at room temperature for 24 h. The crude product was purified by HPLC (60% acetonitrile in H_2O, 2 mL/min) to afford (*R*)-MTPA ester (≈0.4 mg, t_R = 18.51 min). ^{1}H NMR data from the (*S*)- and (*R*)-MTPA ester derivatives of phaeosphaeride C (**2**) are shown in Supplementary Figure S12.

2.5 Identification of building blocks by characteristic fragmentations filtration

The building blocks were identified by comparing the MS data of compound **1** reported in previous studies. A series of fragments with relatively high abundance and stability were observed in the mass spectrum of **1**. After deducing the fragmentation pathway of **1**, the product ions at (m/z) 180.0671 were selected to recognize the building blocks of phaeosphaeride A (**1**) from the LC-MS dataset. The script for product ion and ion intensity filtering was written in Python (version 3.10.2) and ran on Cursor. Considering the quantity limitation of subsequent isolation and structural elucidation procedures, an additional filter was used with the following settings: m/z tolerance = 0.02, minimum peak area = 1.0E4. Additionally, we designed two versions of the extraction tool, allowing users to select the appropriate tool based on the file format of the raw data (https://github.com/mujinyu233/BBMN-extract).

2.6 Biological activities of 2 and 3

A549 and HeLa cells were seeded in 96-well plates at a density of 8,000 cells per well and incubated in Dulbecco's modified Eagle medium (DMEM) for 24 h. After incubation, the cells were treated with compounds **2** and **3** for 48 h. Subsequently, the culture medium was removed, and 100 μL of CCK-8 reagent (diluted 10-fold in DMEM) was added to each well. The plates were further incubated at 37°C for 1 h. Finally, the optical density was measured at 450 nm using a microplate reader. The **2** and **3** stock solutions (100 mM) were prepared with dimethyl sulfoxide (DMSO). The indicated concentrations were prepared immediately before use.

2.7 Photo-induced synthetic reactions

A solution of phaeosphaeride A (**1**) (20 mg, 0.17 mmol) in 1,4-dioxane (1.0 mL) was irradiated with a 500-W high-pressure mercury lamp for 6 h. The solvent was evaporated under vacuum, and the residue was purified by semi-preparative HPLC (54% acetonitrile in H_2O, 2 mL/min) to yield **3** (0.3 mg, tR 26 min).

3 Results and discussion

3.1 Construction of building block-based molecular networking

UPLC-Q-TOF-MS/MS analysis was first employed to study the secondary metabolites of *P. betae* A. B. Frank (Didymellaceae). Initially, known compounds were annotated based on featured-based molecular networking, leading to the identification of phaeosphaeride A (**1**) from the fungal extract. In order to determine the characteristic fragment ions of BBMN, the protonated parent ion (*m/z* 298) of compound **1** was observed in the UPLC-Q-TOF-MS/MS spectra with a relatively low abundance. The fragmentation routes showed that the fragment ion (*m/z* 280) was produced from the protonated parent ion (*m/z* 298) through the loss of one molecule of H_2O (−18). Then, the fragment ion (*m/z* 280) undergoes successive neutral losses of a CH_2O (−30) molecule and a C_5H_{10} (−70) molecule, resulting in the formation of characteristic fragment ions (*m/z* 180) (Supplementary Figure S1) (corresponding to the pyranopyrrole unit). Hence, the diagnostic ion at (*m/z*) 180 was used to filter the MS^2 data to construct the BBMN network (Figure 1), and several nodes were selected with significant features (red nodes) for further investigation. Under the guidance of the BBMN strategy, compounds **2** and **3** were subsequently isolated following quick pinpointing. In this study, a Python-coded building blocks extraction tool was developed to filter and identify MS^2 data containing target ions and output results based on ion intensity.

3.2 Structural elucidation of the new compounds

The molecular formula of compound **2** was determined to be $C_{15}H_{25}NO_6$, indicating that there was one more hydroxyl in **2** than in compound **1**. In addition, the molecular formula of compound **3** was determined to be $C_{30}H_{46}N_2O_{10}$, which might be a dimeric phaeosphaeride. Phaeosphaeride C (**2**) and phomaderide (**3**) were then isolated from the extract.

Compound **2** was isolated as a yellow oil. Comparison of the NMR data with those of pheosphaeride A (**1**) indicated structural similarities, with key differences that included the disappearance of the exocyclic double bond signal at C-3 and the emergence of a multiplet integrating for one proton in the mid-field region (δ_H = 4.12). The ^{13}C-NMR spectrum displayed a CH signal at δ_C = 62.6, suggesting structural modification at C-3. Further analysis of heteronuclear multiple bond coherence (HMBC) correlations between H-14 (δ_H 4.04, 3.90) and C-3 (δ_C 62.6)/C-14 (δ_C 58.3), combined with heteronuclear single quantum coherence (HSQC) cross peaks ($\delta_{H\text{-}14a,b}$ = 4.04, 3.90; $\delta_{C\text{-}14}$ = 58.3), confirmed the attachment of a -CH_2-OH moiety at C-3 (Supplementary Figures S2, S3), which was supported by 2D-NMR spectral data (Supplementary Figures S5, S6). The relative configuration of **2** was the same as that of **1** based on rotating-frame nuclear Overhauser enhancement spectroscopy (ROESY) correlations (Supplementary Figure S7). Weak spatial interactions between 15-Me and 6-OH, as well as between H-8 and H-6, confirmed that **2** shares the same relative configuration as **1**. The stereochemistry of **2** was determined to be 3*R*, 6*S*, 7*R*, and 8*S* according to modified Mosher's reactions (Supplementary Figures S12, S13).

TABLE 1 ^{1}H and^{13}C NMR data (DMSO-d_6) of 3.

No.	δ_H, (*J* in Hz)	δ_C
1		170.3, C
3		70.7, C
4		167.7, C
5		103.7, C
6	3.96, d (6.0)	65.9, CH
7		70.4, C
8	4.05, m	86.0, CH
9	1.71, m	27.8, CH_2
10	1.55, m 1.39, m	26.2, CH_2
11	1.30, m	31.2, CH_2
12	1.30, m	22.0, CH_2
13	0.87, t (6.5)	13.9, CH_3
14	2.64, m 1.99, m	24.9, CH_2
15	1.08, s	18.2, CH_3
16	3.71, s	65.2, CH_3
6-OH	5.27, d (6.0)	
7-OH	4.76, d (3.5)	

[a]Recorded at 500 MHz.
[b]Recorded at 125 MHz.

Phomaderide (**3**) was isolated as a colorless oil, and its molecular formula was assigned as $C_{30}H_{46}N_2O_{10}$ through the HR-ESI-MS $[M + H]^+$ (*m/z* 595.3267, calculated 595.3231) with nine degrees of unsaturation. The ^{1}H and ^{13}C spectra of **3** (Table 1) gave only 23 protons and 15 carbons, suggesting that compound **3** might be a symmetrical dimer. The HSQC spectrum of **3** revealed the presence of a carbonyl carbon, two olefinic carbons, two quaternary carbons, two oxygenated methines, five methylenes, two methyl groups, a methoxy group, and two exchangeable protons.

The ^{1}H–^{1}H COSY correlations of **3** gave two isolated fragments corresponding to OH-CH-6 and -CH-8–CH_2-9–CH_2-10–CH_2-11–CH_2-12–CH_3-13 (Figure 2), and the remaining connectivity was established by HMBC correlations. The correlations from 15-Me and 7-OH to C-6, C-7, and C-8 supported that C-7 was an oxygenated quaternary carbon connected with C-6, C-8, C-15, and

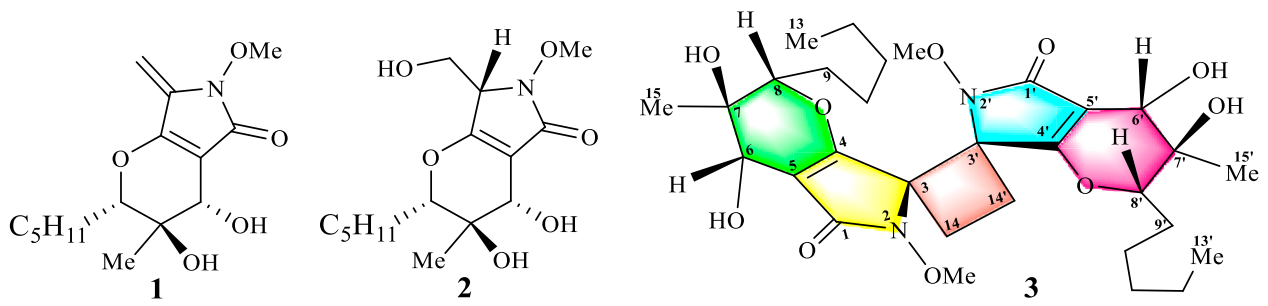


FIGURE 2
Structures of phaeosphaeride A **(1)**, phaeosphaeride C **(2)**, and phomaderide **(3)**.

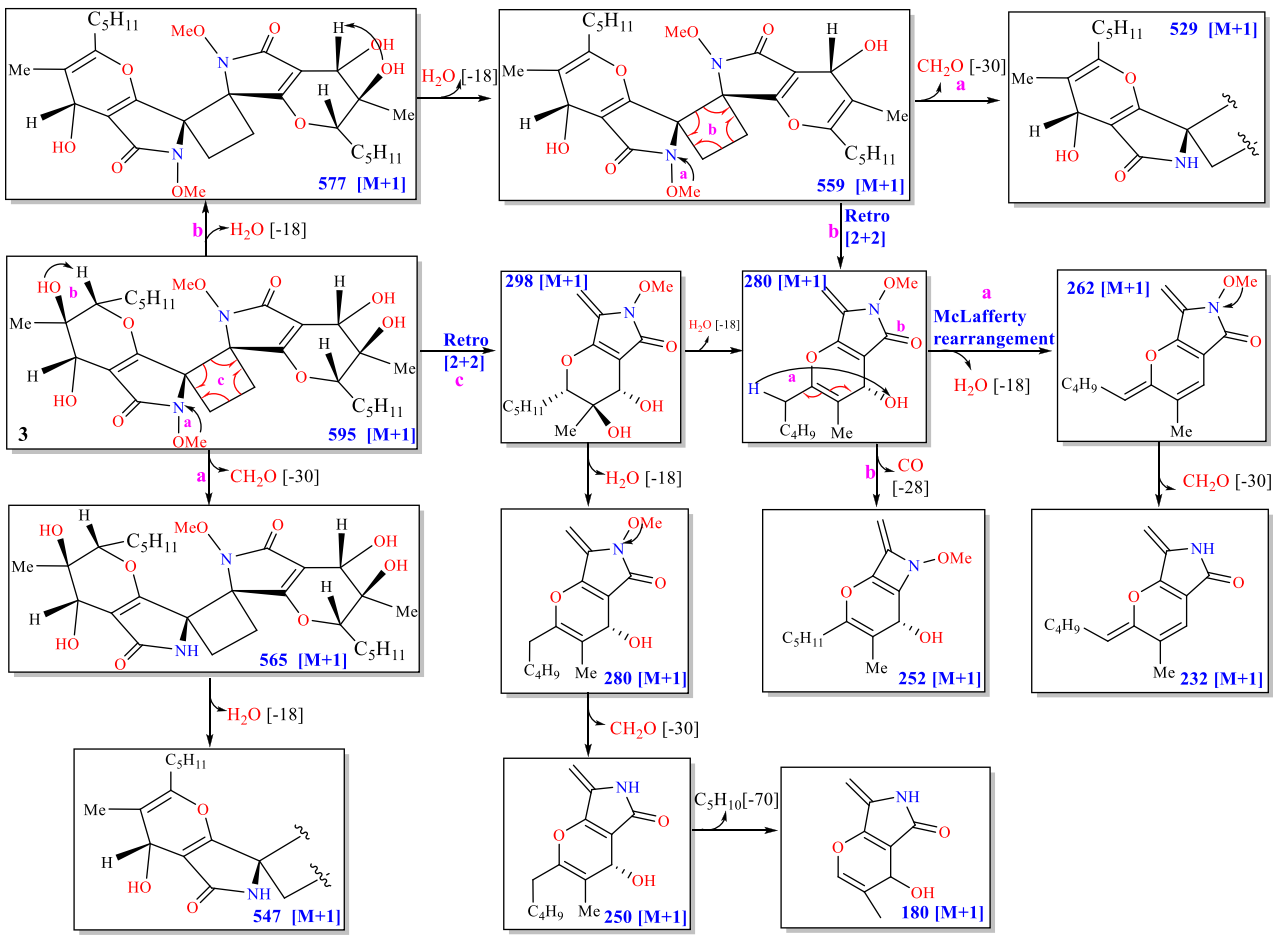


FIGURE 3
Mass fragmentation pathways of **3**.

7-OH. The HMBC correlations of 6-OH with C-5, C-6, and C-7 confirmed the connectivity of C-6 with C-5 and C-7. The cross peaks in the HMBC spectrum from H-6 to C-1, C-4, and C-5 suggested the connection of C-5 with C-1, C-4, and C-6. The correlation from H-8 to C-4 led to an ether linkage between C-4 and C-8 that constructed a 3,4-dihydro-2*H*-pyran ring. The correlations from -CH_2-14 to C-3 and C-4 determined the connectivity of C-3 with C-4 and C-14. Considering the chemical shift values of the -OMe and C-3 ($\delta_{H/C}$ = 3.71/65.2; $\delta_{C\text{-}3}$ = 70.7) and similar NMR spectra between **3** and **1**/**2**, the *N*-methoxypyrrolidin-2-one was suggested to exist in **3** the same way it did in **1** and **2**. By accounting for the multiplets (three doublets overlapped in the ^{1}H-NMR spectrum) of H-14a and H-14b, a head-to-head and tail-to-tail [2 + 2]-cycloaddition adduct of two identical monomers (**1**) was suggested to be the structure of **3** (Zhang et al., 2016; Shen et al., 1994; Yang et al., 2023). This conclusion was also supported by MS/MS experiments. The mass

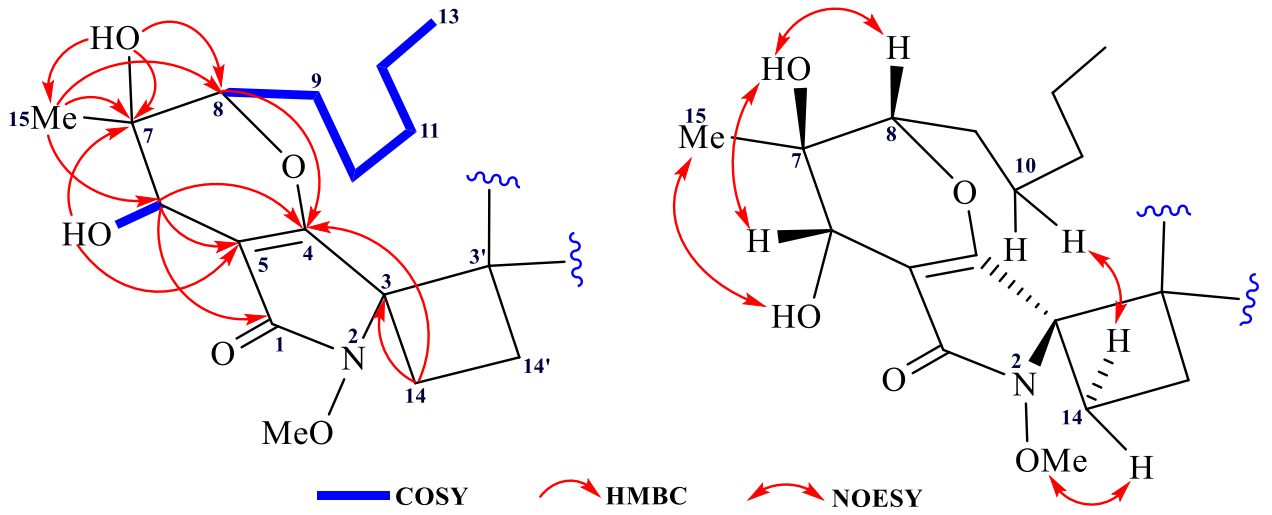
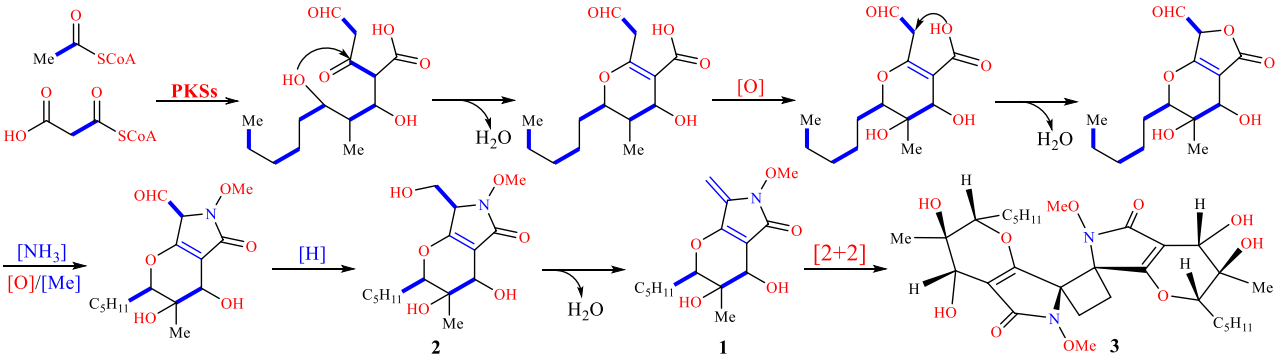


FIGURE 4
Key 2D-NMR correlations of **3**.



SCHEME 1
Plausible biosynthetic pathways of **1**–**3**.

fragmentation pathways of **3** revealed that a Retro [2 + 2] reaction, a neutral loss (H_2O, CO, and HCOH), and a McLafferty rearrangement (-H_2O) were the main cleavage patterns (Figure 3).

The relative configuration of phomaderide (**3**) was determined by the NOESY correlation (Figure 4). The correlations from 7-OH to H-6 and H-8 revealed that these groups were on the same face of the 3,4-dihydro-2*H*-pyran ring, whereas the correlations from 15-Me to 6-OH suggested that the two groups were on the other side of the pyran ring. The weak NOESY correlations from H-14a to -OMe and from H-14b to CH_2-10- indicated that these protons were close in space. Theoretically, the stereochemistry of **3** was similar to that of **1** and **2** based on their structural features and possible biosynthetic pathways. The proposed biosynthetic pathway for compounds **1**, **2,** and **3** (Scheme 1) aligns with fungal secondary metabolism logic. The N-methoxypyrrolidin-2-one core in **1** likely originates from a hybrid polyketide-amino acid pathway (Miyanaga et al., 2018), with O-methylation at C-3 mediated by enzymes (You et al., 2024). The stereoselective [2 + 2] photocycloaddition forming **3** represents a rare but mechanistically coherent step. While abiotic photodimerization is plausible (supported by photocatalytic experiments), enzymatic mediation via ROS-generating oxidases could enforce stereocontrol, as evidenced by the exclusive isolation of a single stereoisomer. The head-to-head/tail-to-tail dimerization minimizes steric clashes, preserving stereochemistry at C-6/C-8.

Despite coherence, key questions remain: the timing of O-methylation, enzymatic *versus* abiotic dimerization triggers and ecological drivers of dimer selectivity. Resolving these requires gene cluster analysis and isotopic labeling studies. Overall, the pathway exemplifies fungal innovation in merging polyketide logic with radical-mediated cycloadditions, underscoring desert endophytes as reservoirs of structurally unique metabolites shaped by environmental pressures. To further support this hypothesis, modified Mosher's reactions were tried but were not successful. Thus, the absolute configuration of **3** was determined by the comparison of the ECD spectrum recorded in MeOH and the DT-DFT-calculated spectrum of **3** at the B3LYP16-311+G (d, p) level. The calculated ECD spectrum of **3** matched with the

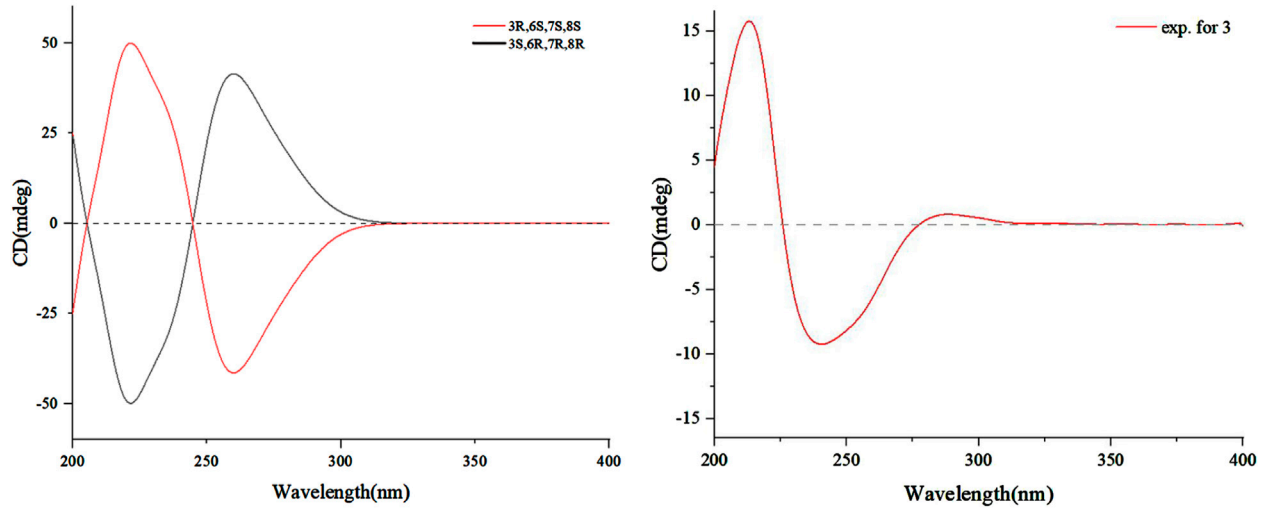


FIGURE 5
Calculated and experimental ECD spectra of **3**.

experimental ECD spectrum (Figure 5), which suggested its stereochemistry to be 3*R*, 6*S*, 7*R*, and 8*S*.

To verify whether **3** is an artificial product, a photocatalytic approach was employed to induce the [2 + 2] cycloaddition reaction of **1**. Theoretically, four stereoisomers could be formed considering two chiral carbons at C-3/C-3′. However, natural products possessing cyclobutane skeletons typically exist in only a few predominant stereoisomeric forms, which might be due to stereoselectivity influenced by steric hindrance, electronic effects, *E*/*Z* tautomerization, and ring strain of olefinic bonds (Yang et al., 2023; Sun et al., 2024; Liu and Hu, 2024). Due to the low yield of the products, only the MS analysis was investigated (Supplementary Figure S23), which suggested that biomimetic synthesis yielded a single stereoisomer through light-induced [2 + 2] cycloaddition. Furthermore, phaeosphaeride A (**1**) without dimeric structures was co-isolated in previous reports (Maloney et al., 2006), indicating that **1** could not undergo spontaneous [2 + 2] cycloaddition to shape the dimer phomaderide (**3**). More importantly, the low yield of phomaderide (**3**) in the photocatalytic synthesis implied that this dimer with a unique ring system was not an artifact.

3.3 Bioactivity assay

Compound **1** displayed strong inhibitory activity against STAT3 related to oncogeneis and also inhibited the myeloma cell growth, whereas its diastereomer phaeosphaeride B did not show activity against STAT3 (Maloney et al., 2006). Considering the structural similarity, the cytotoxic activities of compounds **2** and **3** were evaluated against several cancer cell lines. Compounds **2** and **3** exhibit moderate inhibitory activity against HeLa cells with half-maximal inhibitory concentration (IC_{50}) values ranging from 29.97 μmol/L to 39.15 μmol/L. In addition, compounds **2** and **3** exhibited weak inhibitory activity against non-small cell lung cancer cells A549, with IC_{50} values ranging from 30.47 μ mol/L to 58.33 μ mol/L (Supplementary Tables S2, S3).

4 Conclusion

In summary, guided by the BBMN strategy, a chemical investigation was performed on the plant endophytic fungus *P. betae* A. B. Frank (Didymellaceae), which led to the discovery of phomaderide (**3**) with a unique 6/5/4/5/6 pentacyclic system, featuring two spiro rings and multiple heteroatoms. Phomaderide (**3**) is formed by the linkage of two identical precursors through a double bond [2 + 2] cycloaddition, resulting in a cyclobutane structure with a symmetric structure and eight stereocenters. This complex carbon skeleton possesses ten oxygen atoms forming different functional groups, including amide, ether bonds, -OH, and -NOMe, which implies it as a potential star molecule for organic synthesis. The structural modifications of hydroxylation and dimerization exert significant impacts on biological activity. Consistent with prior analogous studies, the hydroxylation at C-14 in compound **2** may enhance hydrogen bonding capacity and lipophilicity (Liu et al., 2025; Kim et al., 2025), providing a theoretical rationale for its moderate cytotoxicity against HeLa cells (IC50 29.97 μM). Conversely, the [2 + 2] dimerization in **3** introduces a strained cyclobutane core and bis-spirocyclic fused N-methoxypyrrolidone systems, resulting in heightened molecular rigidity and polarity. These structural alterations likely compromise membrane permeability (Haruna et al., 2021), thereby accounting for the attenuated cytotoxicity (IC50 39.15 μM). These findings underscore the critical balance between hydrophilicity, molecular topology, and bioactivity in natural products. Our result further implied that fungi from unique bio-environmental fields, such as under-investigated endophytic fungi from desert plants, will be a potent new resource for novel and bioactive secondary metabolites. In future studies, establishing a framework for rational analog design with optimized pharmacokinetic profiles and fully elucidating the mechanistic implications of these structural features will be essential.

Data availability statement

The original contributions presented in the study are included in the article/Supplementary Material; further inquiries can be directed to the corresponding authors.

Ethics statement

Ethical approval was not required for the studies on humans in accordance with the local legislation and institutional requirements because only commercially available established cell lines were used. Ethical approval was not required for the studies on animals in accordance with the local legislation and institutional requirements because only commercially available established cell lines were used.

Author contributions

H-DS: writing – original draft. Y-DW: writing – review and editing. H-QF: writing – review and editing. JY: writing – review and editing. Y-TH: writing – review and editing. GD: funding acquisition, resources, and writing – review and editing. L-PG: funding acquisition and writing – review and editing.

Funding

The author(s) declare that financial support was received for the research and/or publication of this article. This work was financially supported by the National Key Research and Development Program of China (2023YFC3503801), Scientific and Technological Innovation Project of China Academy of Chinese Medical Sciences (CI2024C007YN), Innovation Team and Talents Cultivation Program of the National Administration of Traditional Chinese Medicine (ZYYCXTD-D-202005), CAMS Innovation Fund for Medical Sciences (CIFMS, 2021-I2M-1-029), China Agricultural Research System of MOF and MARA (CARS-21), and Key project at the central government level: The ability establishment of sustainable use for valuable Chinese medicine resources (2060302).

Conflict of interest

The authors declare that the research was conducted in the absence of any commercial or financial relationships that could be construed as a potential conflict of interest.

Generative AI statement

The author(s) declare that no Generative AI was used in the creation of this manuscript.

Publisher's note

All claims expressed in this article are solely those of the authors and do not necessarily represent those of their affiliated organizations, or those of the publisher, the editors and the reviewers. Any product that may be evaluated in this article, or claim that may be made by its manufacturer, is not guaranteed or endorsed by the publisher.

References

Chatzimpaloglou, A., Yavropoulou, M. P., Rooij, K. E., Biedermann, R., Mueller, U., Kaskel, S., et al. (2012). Total synthesis and biological activity of the proposed structure of phaeosphaeride A. *J. Org. Chem.* 77, 9659–9667. doi:10.1021/jo301662e

Chatzimpalogou, A., Kolosov, M., Eckols, T. K., Tweardy, D. J., and Sarli, V. (2014). Synthetic and biological studies of phaeosphaerides. *J. Org. Chem.* 79, 4043–4054. doi:10.1021/jo500545d

Haruna, K., Muthu, S., Aayisha, S., Peedikakal, A., AL-Saadi, A. A., et al. (2021). Molecular docking, spectroscopic, and quantum chemical studies on aromatic heterocycle tetrakis(4-pyridyl)cyclobutane regioisomers: potential membrane-permeable inhibitors. J. Mol. Model. *3* 94. doi:10.1007/s00894-021-04687-3

He, Q. F., Wu, Z. L., Li, L. R., Sun, W., Wang, G., Jiang, R., et al. (2021). "Discovery of neuritogenic securinega alkaloids from flueggea suffruticosa by a building blocks-based molecular network strategy,". Editor J. Angew. Chem. Int., 60, 19609–19613. doi:10.1002/anie.202103878*Angew. Chem. Int. Ed.*

Kim, K. G., Lee, K. H., Yang, E. J., Lee, G. W., Lee, T., Kim, M.J., et al. (2025). Novel enzymatic synthesis of 3-Hydroxybutyryl Naringin and its molecular identification and bioactive characterization. Food Chem. *15* 143590. doi:10.1016/j.foodchem.2025.143590

Kobayashi, K., Kobayashi, Y., Nakamura, M., Tamura, O., and Kogen, H. (2015). Establishment of relative and absolute configurations of phaeosphaeride A: total synthesis of ent-phaeosphaeride A. *J. Org. Chem.* 80, 1243–1248. doi:10.1021/jo5025046

Liu, S. Q., Li, Q. Q., Wang, Y. H., Yu, X.Y., Li, S.Y., Geng, R.Y., et al. (2020). Bioactive seco-sativene sesquiterpenoids from an artemisia desertorum endophytic fungus, cochliobolus sativus. *J. Nat. Prod.* 83, 1488–1494. doi:10.1021/acs.jnatprod.9b01148

Liu, J. W., and Hu, Y. C. (2024). Discovery and evolution of [4 + 2] cyclases. Curr opin chem biol. *81* 102504. doi:10.1016/j.cbpa.2024.102504

Liu, J. Z., Sun, H. D., Chen, L., and Ding, G. (2023). Shielding effects of aromatic (indole) ring for structural analysis. *J. N. Prod.* 86, 2238–2245. doi:10.1021/acs.jnatprod.3c00434

Liu, S. Q., Li, Q. Q., Wang, Y. H., et al. (2025). Unveiling the formation capacity and characterization of pentacyclic triterpene-structured oleogels: role of the molecular configuration and oil profile. Food Res. Int. *203* 115803. doi:10.1016/j.foodres.2025.115803

Maloney, K. N., Hao, W. S., Xu, J., Gibbons, J., Hucul, J., Roll, D., et al. (2006). Phaeosphaeride A, an inhibitor of STAT3-dependent signaling isolated from an endophytic fungus. *Org. Lett.* 8, 4067–4070. doi:10.1021/ol061556f

Miyanaga, A. M., Kudo, F. T., and Eguchi, T. S. (2018). Protein-protein interactions in polyketide synthase-nonribosomal peptide synthetase hybrid assembly lines. *Nat. Prod. Rep.* 35, 1185–1209. doi:10.1039/c8np00022k

Shen, X. Y., Isogai, A., Furihata, K., Sun, H. D., Suzuki, A., et al. (1994). Maoecrystal M: a naturally occurring symmetric *ent*-kaurane dimer from *Rabdosia eriocalyx*. PHYTOCHEMISTRY. *35* 725. doi:10.1016/S0031-9422(00)90595-8

Sun, X. W., Li, Y., Lu, M. X., Zhao, W., Ma, H. W., Yang, X. J., et al. (2024). "Quantitative Formation of octa-substituted cyclobutanes by the [2+2] photocycloaddition of stiff-stilbenes". *J. Angew. Chem. Int.* doi:10.1002/anie.202421472

Tan, X. M., Li, Q., Wang, Y. D., Wang, T., Yang, J., Sun, B., et al. (2022b). UPLC-Q-TOF-MS/MS analysis of the guaiane sesquiterpenoids oxytropiols A–J and detection of undescribed analogues from the locoweed endophytic fungus Alternaria oxytropis (Pleosporaceae). *Phytochem. Anal.* 33, 344–354. doi:10.1002/pca.3092

Tan, X. M., Zhang, X. Y., Yu, M., Yu, Y. T., Guo, Z., Gong, T., et al. (2019). Sesquiterpenoids and mycotoxin swainsonine from the locoweed endophytic fungus Alternaria oxytropis. PHYTOCHEMISTRY. *164* 154. doi:10.1016/j.phytochem.2019.05.012

Tan, Y., Wang, Y. D., Li, Q., Xing, X. K., Niu, S. B., Sun, B. D., et al. (2022a). Undescribed diphenyl ethers betaethrins A-I from a desert plant endophytic strain of the fungus Phoma betae A.B. Frank (Didymellaceae). phytochemistry. *201* 113264, 10. doi:10.1016/j.phytochem.2022.113264

Xu, L. Z., Yan, D. J., Tan, X. M., Niu, S. B., Yu, M., Sun, B. D., et al. (2022). Phaeosphspirone (1/1′), a pair of unique polyketide enantiomers with an unusual 6/5/5/6 tetracyclic ring from the desert plant endophytic fungus Phaeosphaeriaceae sp. PHYTOCHEMISTRY. *194* 112969. doi:10.1016/j.phytochem.2021.112969

Yang, P. Y., Jia, Q., Song, S. J., and Huang, X. X. (2023). [2 + 2]-Cycloaddition-derived cyclobutane natural products: structural diversity, sources, bioactivities, and biomimetic syntheses. *Nat. Prod. Rep.* 40, 1094–1129. doi:10.1039/d2np00034b

You, C., Pan, Y. J., Liu, R. X., Li, S., and Feng, Y. (2024). Structural basis for substrate flexibility of the O-methyltransferase MpaG' involved in mycophenolic acid biosynthesis. *Protein Sci.* 33, e5144. doi:10.1002/pro.5144

Zhang, H., Liu, J., Gan, L. S., Dalal, S., Cassera, M. B., and Yue, J. M. (2016). Antimalarial diterpenoid dimers of a new carbon skeleton from Aphanamixis grandifolia. *Org. Biomol. Chem.* 14, 957–962. doi:10.1039/C5OB02296G

Zhang, X. Y., Tan, X. M., Yu, M., Yang, J., Sun, B. D., Qin, J. C., et al. (2021). Bioactive metabolites from the desert plant-associated endophytic fungus Chaetomium globosum (Chaetomiaceae). PHYTOCHEMISTRY. *185* 112701. doi:10.1016/j.phytochem.2021.112701

Zhu, D. F., Yuan, J., Yue, Q. Q., Zhao, Y., Yu, S., Zhamilya, A., et al. (2023). Building block extractor: an MS/MS data mining tool for targeted discovery of natural products with specified features. *J. Anal. Chem.* 95, 10939–10946. doi:10.1021/acs.analchem.3c00744

frontiers | Frontiers in Chemistry

TYPE Original Research
PUBLISHED 14 July 2025
DOI 10.3389/fchem.2025.1631183

Check for updates

OPEN ACCESS

EDITED BY
Umamahesh Balijapalli,
Kyulux,Inc., Japan

REVIEWED BY
Sagnik Sengupta,
University of Texas Southwestern Medical Center, United States
N. Vijaya Ganesh,
LGC Standards, United States

*CORRESPONDENCE
Yuqiang Pan,
pany42976@gmail.com,
yu2028qiang@163.com

RECEIVED 19 May 2025
ACCEPTED 11 June 2025
PUBLISHED 14 July 2025

CITATION
Pan Y (2025) Magnetic nanocatalyst for microwave-assisted synthesis of Benzo[4,5]imidazo[1,2-*a*]pyrimidines via A3 coupling. *Front. Chem.* 13:1631183.
doi: 10.3389/fchem.2025.1631183

COPYRIGHT
© 2025 Pan. This is an open-access article distributed under the terms of the Creative Commons Attribution License (CC BY). The use, distribution or reproduction in other forums is permitted, provided the original author(s) and the copyright owner(s) are credited and that the original publication in this journal is cited, in accordance with accepted academic practice. No use, distribution or reproduction is permitted which does not comply with these terms.

Magnetic nanocatalyst for microwave-assisted synthesis of Benzo[4,5]imidazo[1,2-*a*] pyrimidines via A3 coupling

Yuqiang Pan*

Guangxi Guida Agricultural Technology Co., Ltd., Nanning, Guangxi, China

This manuscript introduces an innovative and environmentally benign magnetic nanocatalyst ($NiFe_2O_4$@MCM-41@IL/Pt(II)) designed to synthesize benzoimidazo [1,2-*a*]pyrimidines via a microwave-assisted, one-pot A3 coupling reaction. The methodology employs aromatic and heteroaromatic aldehydes, 2-aminobenzimidazole derivatives, and terminal alkynes in water as a green solvent, leveraging the synergistic effects of nanocatalysis and microwave irradiation. The magnetic nanocatalyst, characterized by its robust structure and high surface reactivity, facilitates rapid reaction kinetics, achieving excellent yields while significantly reducing energy consumption and reaction time compared to conventional thermal approaches. Its inherent magnetic properties enable straightforward separation and reuse across multiple cycles without appreciable loss in catalytic efficiency, aligning with sustainable chemistry principles. The protocol demonstrates broad substrate compatibility, successfully accommodating diverse aldehydes, including challenging heteroaromatic systems, to furnish a library of pharmaceutically relevant heterocycles. This broad substrate compatibility underscores the versatility of the nanocatalyst, making it a valuable tool for a wide range of chemical synthesis applications. This work highlights the transformative role of hybrid methodologies in addressing both efficiency and environmental impact in chemical synthesis.

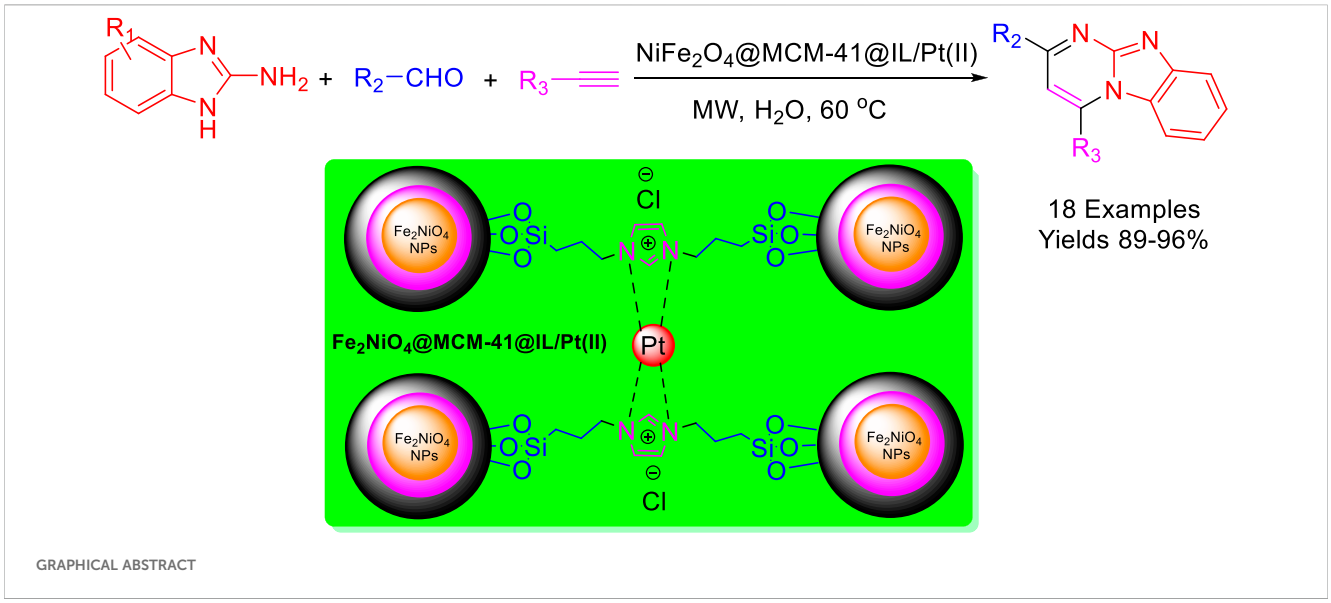
KEYWORDS

NiFe2O4@MCM-41@IL/pt, A3 coupling reactions, nanomagnetic catalyst, microwave-assisted, imidazo[1,2-a]pyrimidines

1 Introduction

The field of organic synthesis is increasingly embracing greener and more efficient methodologies, primarily driven by green chemistry principles. This shift aims to minimize hazardous substances and waste, utilize sustainable resources, and improve the efficiency of chemical reactions (Rotstein et al., 2014; Javahershenas and Nikzat, 2023; Zhu et al., 2015). Among the innovative strategies emerging, one-pot multicomponent reactions (MCRs) stand out as a powerful approach in organic synthesis, inspiring new possibilities. MCRs enable the simultaneous condensation of multiple reagents to create complex structures while reducing the formation of by-products (Georg Thieme Verlag KG, 2014; Javahershenas et al., 2024a).

Imidazo[1,2-a]pyrimidines are a notable class of heterocyclic compounds that have attracted attention for their diverse biological activities and potential applications in



GRAPHICAL ABSTRACT

medicinal chemistry and materials science (Berson et al., 2001; Harrison and Keating, 2005; Hanson et al., 2008; Monti et al., 2009; Enguehard-Gueiffier and Gueiffier, 2007; Denora et al., 2008; Trapani et al., 2005). These fused ring systems exhibit various pharmacological properties, including antibacterial (Rival et al., 1992), anticancer (Panda et al., 2022), antimicrobial (Revankar et al., 1975), and antifungal (Rival et al., 1991) activities. Traditional synthetic routes to these valuable scaffolds often involve multi-step procedures that require harsh reaction conditions and environmentally harmful reagents. Therefore, there is a pressing need for more sustainable and efficient methods to synthesize these important molecular frameworks, underscoring the significance of our work in the field (Figure 1) (Tully et al., 1991; Rupert et al., 2003; Feely et al., 1989; O'Connor et al., 2010; Linton et al., 2011).

Microwave-assisted organic synthesis (MAOS) stands out as a potent technique, accelerating chemical reactions with its unique advantages. It offers enhanced reaction rates, higher yields, and superior selectivity compared to conventional heating methods. By employing microwave irradiation, MAOS facilitates chemical reactions, resulting in increased reaction rates, reduced energy consumption, and improved yields (Gulati et al., 2021; Javahershenas et al., 2024b). The technique's ability to interact uniquely with polar reactants and solvents, promoting uniform heating and accelerating reaction kinetics, is a game-changer. The underlying mechanism of microwave-assisted synthesis involves rapid and uniform heating of reaction mixtures, which enhances molecular interactions under mild conditions. In green chemistry, microwave-assisted reactions are particularly advantageous as they reduce energy consumption and minimize reaction times, making them ideal for scalable industrial processes. The ability to perform reactions efficiently within short timeframes positions microwave-assisted synthesis as a valuable tool for producing complex organic molecules (Kappe and Dall'Acqua, 2019; Zhang and Cai, 2020; Kappe and Stadler, 2006).

The role of nanotechnologies, particularly nanocatalysis, in revolutionizing the optimization of chemical reactions cannot be overstated. Developing efficient and reusable catalysts is essential for achieving sustainable chemical processes. Nanocatalysts, such as $NiFe_2O_4$, offer distinct advantages, including high catalytic activity, stability, and ease of separation from reaction mixtures through magnetic decantation (Amrutkar et al., 2022; Kanithan et al., 2022; Chandra, 2021). This capability significantly reduces waste and enhances catalyst recovery, aligning with one of the core principles of green chemistry—minimizing waste. When combined with mesoporous materials like MCM-41, nanocatalysts can form an efficient catalyst system, enhancing reaction rates and product selectivity (Kazemi, 2020; Wang et al., 2021).

Integrating mesoporous materials, like MCM-41, with metal oxides creates a synergistic effect that enhances the dispersion and accessibility of active catalytic sites. Mesoporous materials' high surface area and favorable pore structure are essential for accommodating reactants and facilitating catalytic activity (Snoussi et al., 2018; Kefayati et al., 2016). Furthermore, when combined with ionic liquids (ILs), known for their low volatility and high thermal stability, these composites exhibit enhanced efficiency and selectivity, often surpassing traditional catalytic systems. Ionic liquids, composed of organic cations and inorganic anions, possess unique properties such as negligible vapor pressure and tunable solubility, making them versatile in catalysis and green chemistry. In heterogeneous catalysis, ILs can function as both reaction media and catalyst modifiers, boosting the stability and activity of supported metal species (Sead et al., 2025e; Zhu et al., 2010; Javahershenas et al., 2025).

By merging the magnetic properties of $NiFe_2O_4$ with the mesoporosity of MCM-41 and the solvation capabilities of ionic liquids, novel catalytic systems such as the $NiFe_2O_4$@MCM-41@IL/Pt(II) complex can be developed. This multi-faceted approach maximizes the benefits of each component, leading to a robust and versatile catalytic framework (Rogers and Seddon, 2002; Parvulescu and Hardacre, 2007; ; Saha et al., 2009; Zare et al., 2009; Hasaninejad et al., 2010).

The synthesis of fused imidazo[1,2-*a*]pyrimidines via A3 coupling reactions is a remarkable advancement in one-pot

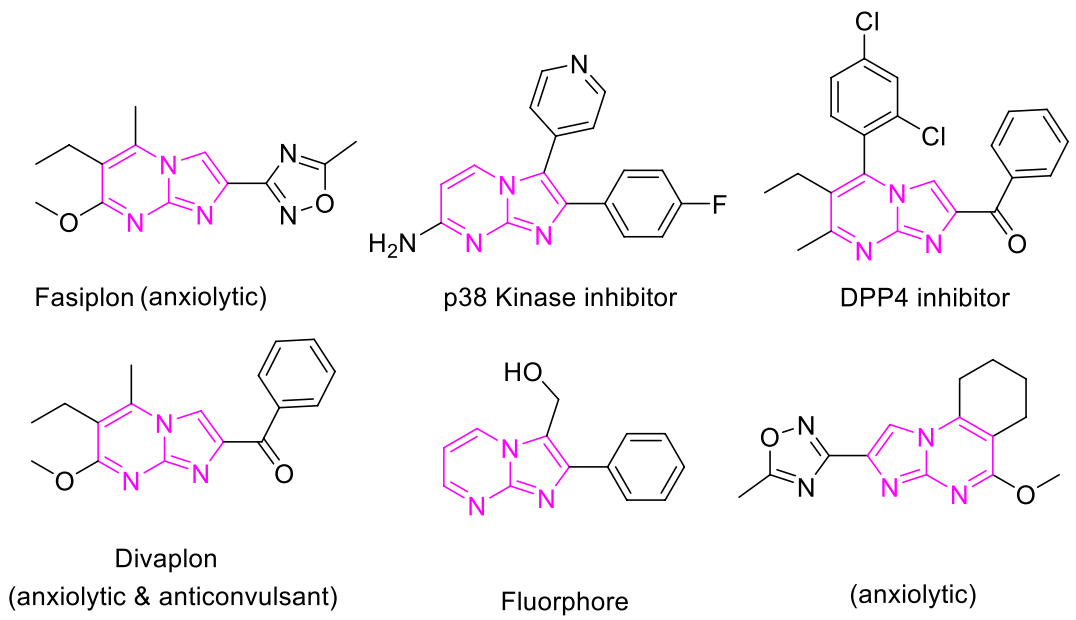


FIGURE 1
Biologically potent imidazo[1,2-*a*]pyrimidines.

multicomponent reactions (MCRs). The A3 coupling process, which integrates an aldehyde, an alkyne, and an amine, showcases the efficiency of atom-economical methodologies. These methodologies allow for the construction of complex molecular architectures in a single synthetic step, a feat that was previously challenging to achieve (Javahershenas and Mole, 2023; Khan et al., 2019; Zheng et al., 2020).

Utilizing the $NiFe_2O_4$@MCM-41@IL/Pt (II) complex as a catalyst within this MCR framework can significantly improve the reaction's efficiency and sustainability. The incorporation of platinum (Pt) further enhances the catalytic properties of this nanocomposite. Platinum is well-known for its effectiveness as a catalyst in cross-coupling reactions, including A3 coupling, where it facilitates the condensation of an aldehyde, an amine, and an alkyne to form intricately fused imidazo[1,2-*a*]pyridine frameworks. The appeal of the A3 coupling reaction lies in its operational simplicity and minimal waste production (Pourhasan-Kisomi et al., 2018; Kazemi and Ghobadi, 2017; Kazemi, 2023; Wang et al., 2021; Abedi et al., 2021; Huang et al., 2021; Sead et al., 2025a).

However, challenges such as Pt leaching and catalyst recovery have highlighted the need for robust catalytic systems that effectively address these issues. Developing a stable and recyclable catalyst is crucial for optimizing the sustainability of the A3 coupling reaction while maintaining high catalytic activity (Sead et al., 2025b; Sead et al., 2025c; Sead F. F. et al., 2025).

In this study, we introduce the synthesis and application of a promising microwave-assisted $NiFe_2O_4$@MCM-41@IL/Pt(II) complex nanomagnetic catalyst for the one-pot green synthesis of fused imidazo[1,2-a]pyrimidines through A3 coupling reactions. The hybrid catalyst, meticulously crafted by combining $NiFe_2O_4$ nanoparticles with MCM-41 and then functionalizing with ionic liquid components and platinum, demonstrates superior catalytic performance, high recyclability, and environmental compatibility. This catalyst holds great promise for advancing sustainable chemistry principles in the field of organic synthesis.

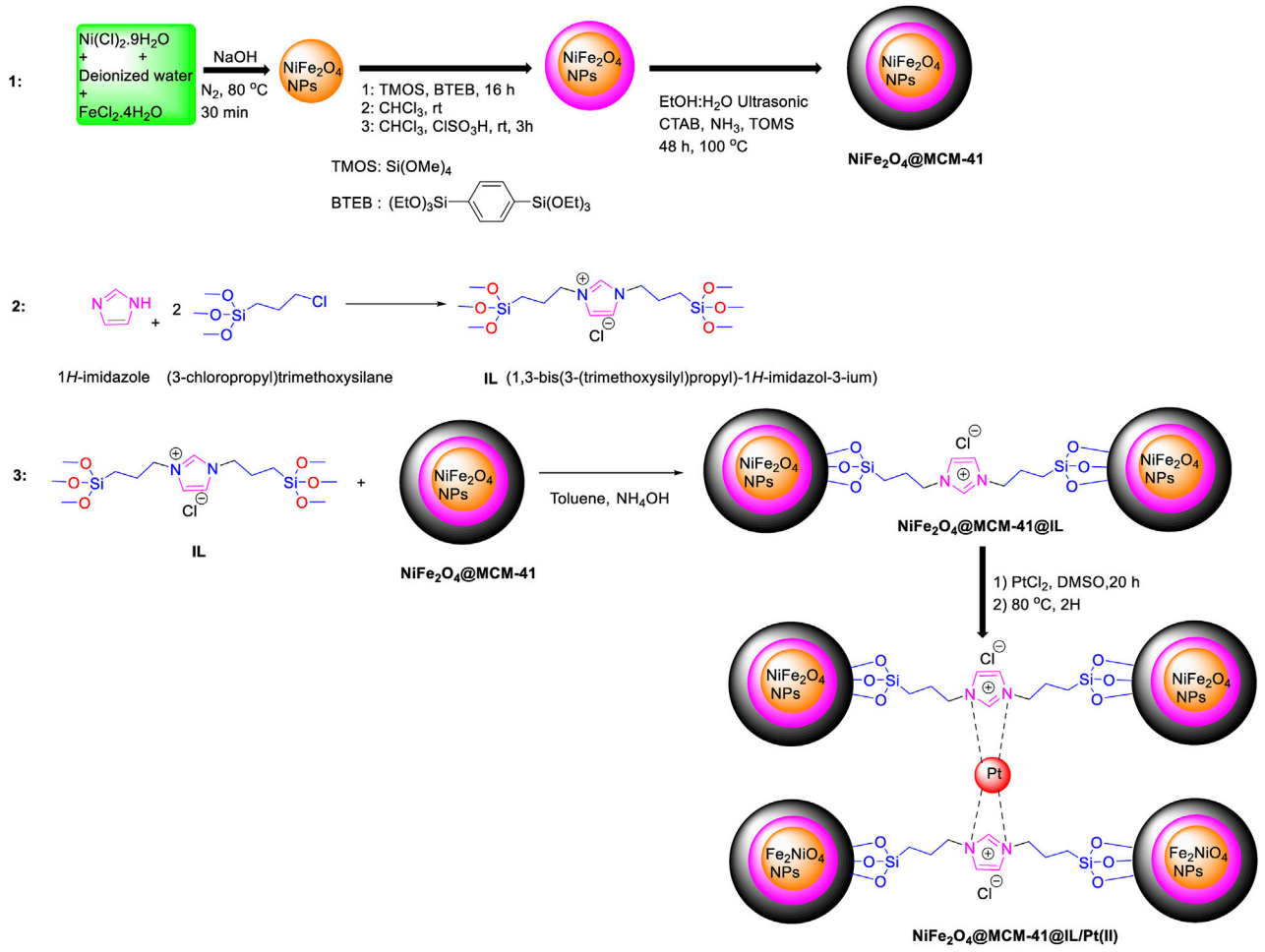
The primary objective of this research is to investigate the efficiency and reusability of the $NiFe_2O_4$@MCM-41@IL/Pt (II) catalyst in various A3 coupling reactions under microwave irradiation. The rapid reaction times and enhanced yields achieved using this system highlight the potential of microwave-assisted synthesis for the efficient construction of valuable fused imidazo[1,2-*a*]pyridine derivatives. Additionally, the catalyst's magnetic properties facilitate easy recovery from reaction mixtures, significantly simplifying the purification process and enhancing the sustainability of the overall synthetic pathway.

Understanding the A3 coupling reaction's mechanistic aspects is crucial. It provides insights into each component's contributions within the catalyst system. This understanding is key to how the synergistic interactions among $NiFe_2O_4$, MCM-41, ionic liquids, and platinum enhance catalytic performance. It will pave the way for designing even more advanced catalytic systems.

In summary, developing the $NiFe_2O_4$@MCM-41@IL/Pt (II) complex nanomagnetic catalyst significantly advances sustainable organic synthesis. By leveraging the advantages of microwave-assisted synthesis, nanocatalysis, and the unique properties of ionic liquids, this work offers a robust and efficient method for synthesizing fused imidazo[1,2-a]pyrimidines. The implications of this research extend beyond immediate synthetic applications, potentially influencing a broader range of catalytic processes and initiatives aimed at environmental sustainability in organic chemistry.

2 Result and discussion

Scheme 1 outlined the synthetic route for preparing a novel nanocatalyst, $NiFe_2O_4$@MCM-41@IL/Pt. Nickel chloride



SCHEME 1
Preparation of $NiFe_2O_4$@MCM41@IL/Pt (II) nanocatalyst.

hexahydrate ($NiCl_2{\cdot}9H_2O$) and iron chloride tetrahydrate ($FeCl_2{\cdot}4H_2O$) were dissolved in deionized water. Sodium hydroxide (NaOH) was added to the solution, and the mixture was heated at 80°C for 30 min, leading to the formation of $NiFe_2O_4$ nanoparticles.

For the functionalization of SiO_2 with organic groups, tetramethoxysilane (TMOS) and bis (triethoxysilyl) benzene (BTEB) were added to the $NiFe_2O_4$ nanoparticles. The mixture was stirred for 16 h. Subsequently, chlorosulfonic acid ($ClSO_3H$) was introduced, and the mixture was stirred in chloroform ($CHCl_3$) for 3 h.

The functionalized MCM-41 was mixed with a solution containing $NiFe_2O_4$ nanoparticle nanoparticles, cetyltrimethylammonium bromide (CTAB), ammonia (NH_3), and toluene. The mixture was sonicated for 48 h at 100°C, resulting in the attachment of $NiFe_2O_4$ nanoparticles to the MCM-41 support via the organic functional groups.

For immobilization of $NiFe_2O_4$@MCM-41 nanoparticles onto the ionic liquid (IL), (3-chloropropyl)trimethoxysilane was reacted with 1H-imidazole to produce IL (1,3-bis(3-(trimethoxysilyl)propyl)-1H-imidazol-3-ium). The mixture of $NiFe_2O_4$@MCM-41 with this IL was then added to a dispersion of toluene and NH_4OH and stirred for 24 h.

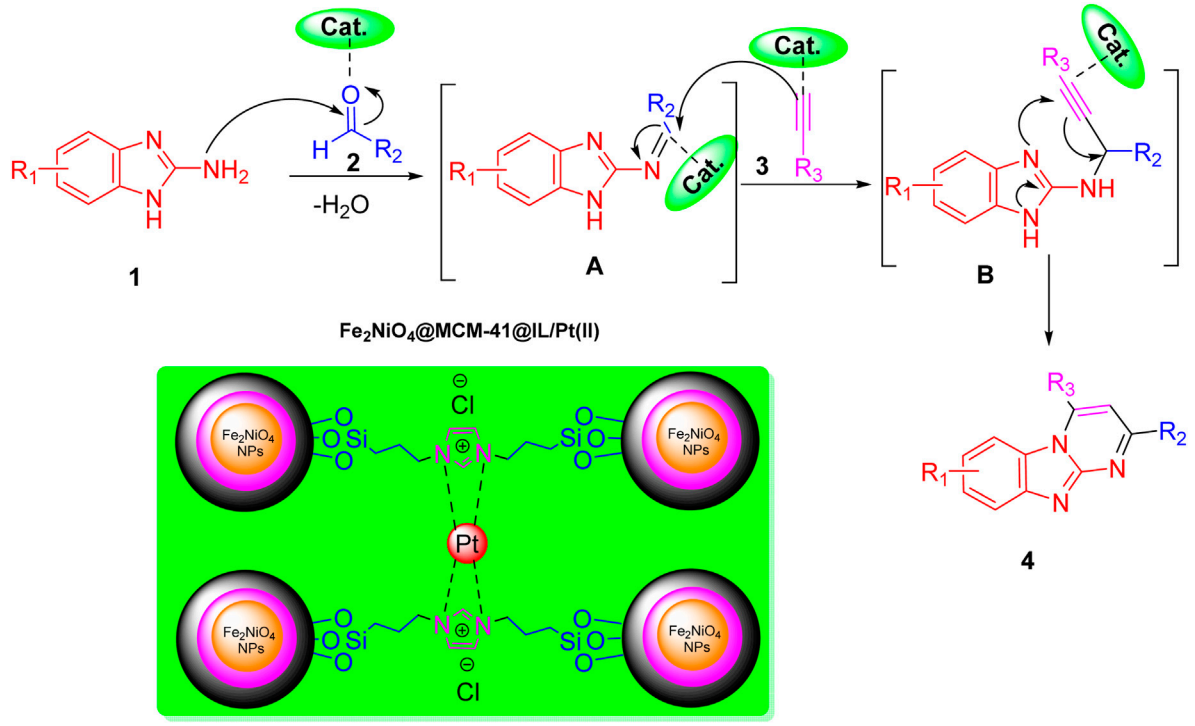
The final nanocatalyst, $NiFe_2O_4$@MCM-41@IL, was dispersed in a solution containing $PtCl_2$ and DMSO. The mixture was stirred for 20 h at room temperature, then heated at 80°C for 2 h. The product was filtered and washed with ethanol to obtain the final $NiFe_2O_4$@MCM-41@IL/Pt nanocatalyst.

This nanocatalyst was expected to exhibit unique catalytic properties owing to the synergistic effects of $NiFe_2O_4$ nanoparticles, the MCM-41 support, the ionic liquid, and platinum nanoparticles.

This study presents a comprehensive analysis of the Fourier-transform infrared (FT-IR) spectra of various nickel-iron oxide nanocomposites, as illustrated in Figure 2. The spectra encompass $NiFe_2O_4$ nanoparticles (NPs) and their functionalized derivatives, including $NiFe_2O_4$@SiO_2, $NiFe_2O_4$@MCM-41, $NiFe_2O_4$@MCM-41@IL, and $NiFe_2O_4$@MCM-41@IL/Pt(II). Each spectrum provides insights into the structural and functional characteristics of these materials.

The spectrum for pure $NiFe_2O_4$ nanoparticle NPs (curve a) displays characteristic absorption bands corresponding to the metal-oxygen vibrations typical of spinel ferrites. Notably, the peaks around 580 cm^{-1} indicate the Fe-O bonds in the octahedral sites, while those near 400 cm^{-1} correspond to the tetrahedral sites. These features confirm the successful synthesis of $NiFe_2O_4$ with its expected crystalline structure.

Additional peaks emerge that signify Si-O stretching vibrations upon functionalization with silica in curve b ($NiFe_2O_4$@SiO_2). This



SCHEME 2
A plausible mechanism for the synthesis of imidazo[1,2-a]pyrimidines derivatives catalyzed by $NiFe_2O_4$@MCM-41@IL/Pt nanocomposite.

indicates successful incorporation of silica onto the nickel iron oxide framework, enhancing its stability and inspiring potential applications in catalysis and adsorption processes.

The spectrum for $NiFe_2O_4$@MCM-41 (curve c) reveals further modifications. The presence of MCM-41, a mesoporous silica material, is evidenced by distinct absorption bands associated with silanol groups and the characteristic pore structure of MCM-41. This modification increases surface area and facilitates enhanced interaction with reactants in catalytic applications.

In curve d, representing $NiFe_2O_4$@MCM-41@IL, we observe additional peaks related to ionic liquid functionalities. Incorporating ionic liquids is significant as it can improve solubility and enhance catalytic activity by providing a unique environment for reaction processes. This modification suggests a tailored approach to optimize catalytic performance through solvent effects.

Finally, curve e illustrates the FT-IR spectrum of $NiFe_2O_4$@MCM-41@IL/Pt (II), introducing platinum species into the composite. The presence of Pt(II) is confirmed by new absorption bands that emerge in this spectrum, indicating successful loading of platinum onto the nanocomposite. This addition is crucial as platinum is known for its exceptional catalytic properties, particularly in hydrogenation reactions and fuel cells.

Comparative analysis of these spectra reveals significant insights into how each modification impacts the structural integrity and functionality of the nickel-iron oxide nanocomposites. The progressive introduction of silica, mesoporous structures, ionic liquids, and platinum enhances not only the physical properties but also expands their applicability across various fields, such as catalysis and environmental remediation.

This FT-IR analysis highlights the importance of each component within these nanocomposites and underscores how systematic modifications, a crucial part of the research process, can lead to materials with tailored properties suitable for advanced applications. Such insights contribute to ongoing research to optimize catalyst design for improved efficiency and effectiveness in chemical processes.

Examining the morphology and structure of the catalyst is a critical aspect of contemporary catalysis research. In this regard, SEM and TEM analyses were used to investigate the morphology and shape of the $NiFe_2O_4$@MCM-41@IL/Pt (II) catalyst particles in Figure 3. The SEM images reveal a porous, agglomerated structure with a rough surface. The higher magnification image (100 nm scale bar) shows a more detailed view of the individual particles, which appear spherical or slightly irregular. The TEM image provides a closer look at the nanocatalyst's morphology. It shows a well-dispersed distribution of nanoparticles, with some agglomeration visible. The particles exhibit a spherical or slightly elongated shape with a relatively uniform size distribution.

Morphology: Both techniques confirm the presence of a porous structure with agglomerated particles. The TEM image offers a more detailed insight into the individual particle morphology, revealing their spherical or slightly elongated shape.

Particle Size Distribution: The TEM image suggests the nanoparticles' relatively uniform size distribution, consistent with the SEM observations.

Dispersion: The TEM image shows a well-dispersed distribution of nanoparticles, indicating good dispersion within the support material.

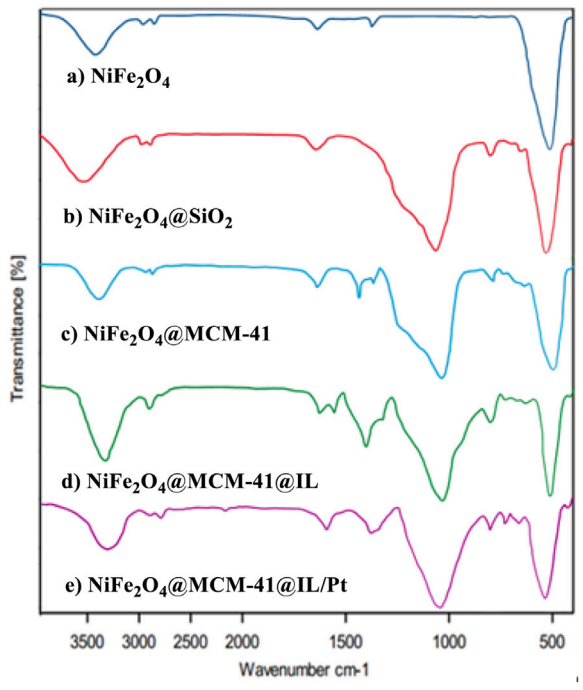


FIGURE 2
FT-IR spectrums of $NiFe_2O_4$ NPs, $NiFe_2O_4$@SiO_2, $NiFe_2O_4$@MCM-41, $NiFe_2O_4$@MCM-41@IL, and $NiFe_2O_4$@MCM-41@IL/Pt (II) nanocomposites.

The SEM and TEM images provide valuable information about the morphology and structure of the $NiFe_2O_4$@MCM-41@IL/Pt nanocatalyst. The porous structure observed in both images is likely beneficial for catalytic applications as it can provide a large surface area for reactant adsorption and product desorption. The uniform size distribution and good dispersion of the nanoparticles are also desirable features for catalytic activity.

Figure 4 presents the magnetization curves obtained from Vibrating Sample Magnetometry (VSM) measurements for Fe_3O_4 NPs and $NiFe_2O_4$@MCM-41@IL/Pt nanocatalyst. The magnetization (M) is plotted against the applied magnetic field (H) in units of emu/g and Oe, respectively.

Saturation Magnetization: The saturation magnetization (Ms) is the maximum magnetization achieved when a material is subjected to a strong magnetic field. From the curves, it is evident that the $NiFe_2O_4$@MCM-41@IL/Pt nanocatalyst exhibits a significantly higher Ms compared to Fe_3O_4 NPs. This suggests that the $NiFe_2O_4$@MCM-41@IL/Pt nanocatalyst possesses a stronger magnetic response than the Fe_3O_4 NPs.

Hysteresis Loop: The hysteresis loop is the curve traced by the magnetization as the applied magnetic field increases and then decreases. The area enclosed by the hysteresis loop represents the energy loss during a magnetization cycle. The $NiFe_2O_4$@MCM-41@IL/Pt nanocatalyst exhibits a narrower hysteresis loop than Fe_3O_4 NPs, indicating a lower energy loss during magnetization reversal. This is beneficial for applications where energy efficiency is a concern.

Coercivity (Hc) is the magnetic field required to reduce the magnetization of a material to zero after it has been saturated. The $NiFe_2O_4$@MCM-41@IL/Pt nanocatalyst shows a lower Hc than Fe_3O_4 NPs. This suggests that the $NiFe_2O_4$@MCM-41@IL/Pt nanocatalyst is more straightforward to magnetize and demagnetize, which is desirable for applications requiring rapid magnetic switching. The enhanced magnetic properties of the $NiFe_2O_4$@MCM-41@IL/Pt nanocatalyst compared to Fe_3O_4 NPs can be attributed to several factors:

$NiFe_2O_4$ nanoparticles within the MCM-41 support matrix can contribute to an increase in Ms and a decrease in Hc. $NiFe_2O_4$ is known for its high magnetic moment and low coercivity. The MCM-41 support can provide a large surface area for the deposition of $NiFe_2O_4$ nanoparticles, leading to a higher concentration of magnetic material and, consequently, a higher Ms. The IL coating on the $NiFe_2O_4$@MCM-41 nanoparticles can further enhance the magnetic properties by improving the dispersion of the nanoparticles and reducing interparticle interactions. The presence of Pt nanoparticles on the surface of the $NiFe_2O_4$@MCM-41@IL nanoparticles can also influence the magnetic properties, although the exact mechanism is not fully understood.

The VSM results demonstrate that the $NiFe_2O_4$@MCM-41@IL/Pt nanocatalyst exhibits superior magnetic properties to Fe_3O_4 NPs. These enhanced properties make the $NiFe_2O_4$@MCM-41@IL/Pt nanocatalyst a promising material for various applications, including magnetic separation, catalysis, and drug delivery.

X-ray diffraction (XRD) is a powerful technique for characterizing the crystalline structure of materials. In this study, XRD patterns were obtained for Fe_3O_4 nanoparticles (NPs) and v $NiFe_2O_4$@MCM-41@IL/Pt nanocatalyst in Figure 5. These patterns provide insights into the samples' phase purity, crystallinity, and lattice parameters.

The XRD patterns of Fe_3O_4 NPs and $NiFe_2O_4$@MCM-41@IL/Pt nanocatalyst are presented in Figure 5. The XRD pattern of Fe_3O_4 NPs exhibits a series of sharp peaks, indicating a highly crystalline nature. The positions and relative intensities of these peaks match well with the standard XRD pattern of magnetite (Fe_3O_4), confirming the phase purity of the sample. The absence of additional peaks suggests minimal impurities in the sample. The XRD pattern of $NiFe_2O_4$@MCM-41@IL/Pt nanocatalyst shows a distinct difference compared to the Fe_3O_4 NPs. The peaks are broader and less intense, suggesting a lower degree of crystallinity. This is likely due to the MCM-41 support and the incorporation of IL and Pt nanoparticles, which can disrupt the long-range order of the crystal lattice.

Fe_3O_4 NPs exhibit higher crystallinity compared to the $NiFe_2O_4$@MCM-41@IL/Pt nanocatalyst. This is evident from the sharper and more intense peaks in the Fe_3O_4 pattern. Both samples appear phase pure, as no additional peaks corresponding to impurities are observed in either pattern. The positions of the peaks in the XRD patterns can be used to calculate the lattice parameters of the samples. However, this analysis is beyond the scope of this brief description.

XRD analysis confirms the successful synthesis of Fe_3O_4 NPs and $NiFe_2O_4$@MCM-41@IL/Pt nanocatalyst. The Fe_3O_4 NPs exhibit high crystallinity and phase purity. At the same time, the $NiFe_2O_4$@MCM-41@IL/Pt nanocatalyst shows a lower degree of crystallinity due to the MCM-41 support and incorporated IL and Pt nanoparticles.

Figure 6 presents the thermogravimetric analysis (TGA) spectra of the $NiFe_2O_4$@MCM-41@IL/Pt nanocatalyst. The TGA curve

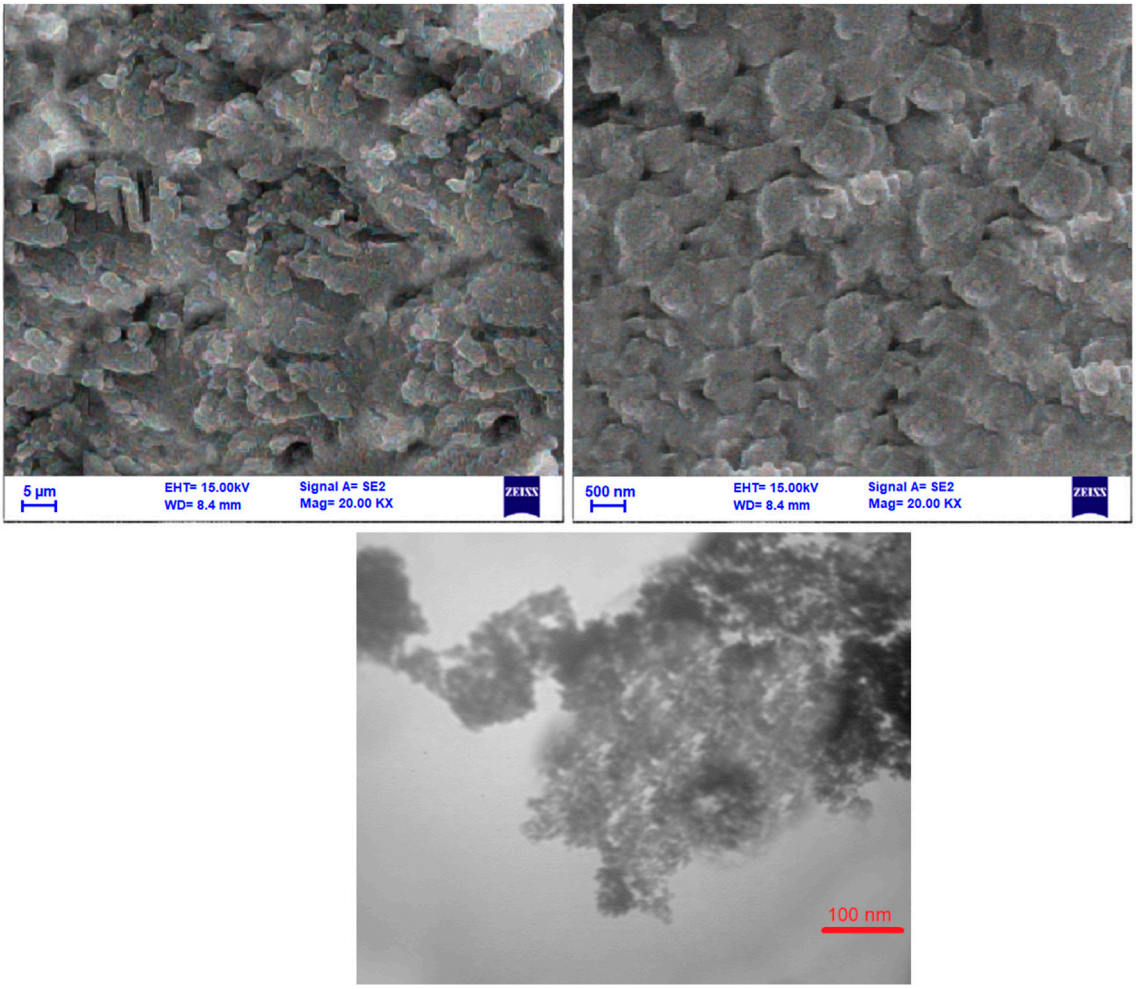


FIGURE 3
SEM and TEM images of $NiFe_2O_4$@MCM-41@IL/Pt nanocatalyst at different magnifications.

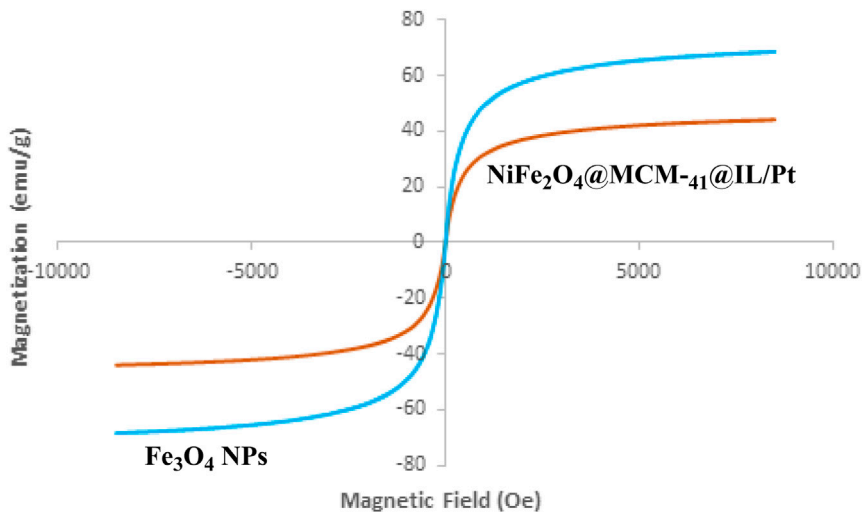


FIGURE 4
VSM analysis of Fe_3O_4 NPs and $NiFe_2O_4$@MCM-41@IL/Pt nanocatalyst.

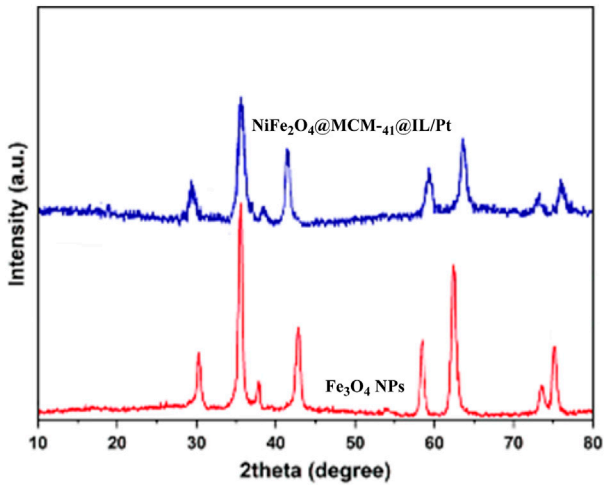


FIGURE 5
XRD patterns of Fe_3O_4 NPs and $NiFe_2O_4$@MCM-41@IL/Pt nanocatalyst.

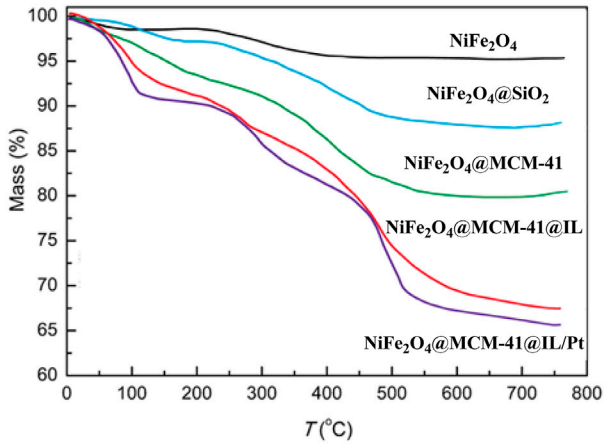


FIGURE 6
TGA spectrums of $NiFe_2O_4$@MCM-41@IL/Pt nanocatalyst.

reveals a multi-step weight loss pattern, indicating the presence of various components with different thermal stabilities.

Initial Weight Loss (Up to ~200°C): A slight weight loss is observed in the initial temperature range, likely due to removing adsorbed water and volatile organic compounds. First Major Weight Loss (200°C–500°C): A significant weight loss occurs in this temperature range, which can be attributed to the decomposition of the ionic liquid (IL) component. The IL acts as a stabilizing agent and provides a confined environment for the growth of nanoparticles, but its thermal decomposition leads to a substantial mass loss. Second Major Weight Loss (500°C–700°C): A further weight loss in this temperature range can be associated with the decomposition of the organic template (MCM-41) used to synthesize the mesoporous support. The MCM-41 structure provides a high surface area for the dispersion of active nanoparticles, but its removal at higher temperatures results in

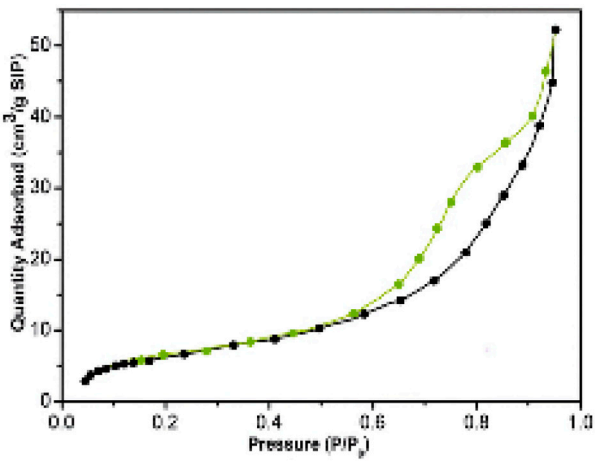


FIGURE 7
BET analysis of $NiFe_2O_4$@MCM-41@IL/Pt nanocatalyst.

additional mass loss. Final Weight Loss (Above 700°C): A minimal weight loss is observed at temperatures above 700°C, indicating the presence of a highly stable residual phase. This phase is likely composed of the $NiFe_2O_4$ nanoparticles and possibly residual Pt nanoparticles, which exhibit high thermal stability.

The TGA analysis confirms the presence of multiple components in the $NiFe_2O_4$@MCM-41@IL/Pt nanocatalyst. The multi-step weight loss pattern highlights the composite material's complex nature, with each step corresponding to the thermal decomposition of specific components.

The TGA analysis provides valuable insights into the thermal stability and composition of the $NiFe_2O_4$@MCM-41@IL/Pt nanocatalyst. The multi-step weight loss pattern confirms the presence of various components, including the IL, mesoporous support, and active nanoparticles. Understanding the catalyst's thermal behavior is crucial for optimizing its synthesis and application in various catalytic processes.

Figure 7 presents the BET analysis of the $NiFe_2O_4$@MCM-41@IL/Pt nanocatalyst. The BET (Brunauer-Emmett-Teller) analysis is a widely used technique to determine porous materials' specific surface area, pore size distribution, and pore volume. In this case, the BET analysis provides insights into the nanocatalyst's textural properties.

The adsorption isotherm in Figure 7 shows a Type IV curve, characteristic of mesoporous materials. This indicates that the nanocatalyst possesses a network of interconnected pores with a relatively uniform size distribution. The specific surface area of the nanocatalyst, as determined by the BET analysis, is expected to be high due to the presence of mesopores. A high surface area is crucial for catalytic applications, as it provides more active sites for reactant adsorption and interaction with the catalyst surface. The pore size distribution of the nanocatalyst can be estimated from the adsorption isotherm. The presence of mesopores in the nanocatalyst is beneficial for catalytic reactions, as they can facilitate the diffusion of reactants and products within the pores.

The $NiFe_2O_4$@MCM-41@IL/Pt nanocatalyst can be compared with the BET analysis of other materials, such as pristine $NiFe_2O_4$,

MCM-41, and Pt nanoparticles. This comparison can help understand the different components' impact on the nanocatalyst's textural properties. As revealed by the BET analysis, the nanocatalyst's textural properties can correlate with its catalytic performance in various reactions. A high surface area and well-developed pore structure can enhance the nanocatalytic activity and selectivity of the nanocatalyst.

In conclusion, the BET analysis provides valuable information about the textural properties of the $NiFe_2O_4$@MCM-41@IL/Pt nanocatalyst. The presence of mesopores with a high surface area is expected to contribute to this material's excellent catalytic performance.

Figure 8 presents the Energy Dispersive X-ray (EDX) spectrum obtained from the $NiFe_2O_4$@MCM-41@IL/Pt nanocatalyst, confirming the presence of the constituent elements. The spectrum displays distinct peaks corresponding to Nickel (Ni), Iron (Fe), Oxygen (O), Silicon (Si), and Platinum (Pt), which are consistent with the expected composition of the synthesized material. Notably, the presence of Pt peaks (Pt Mα, Pt Mβ, Pt Lα, and Pt Lβ) substantiates the successful incorporation of platinum onto the catalyst support. The peaks observed for Ni and Fe indicate the presence of the $NiFe_2O_4$ component, while the Si and O peaks are attributed to the MCM-41 support. Additionally, peaks corresponding to Carbon (C) and Nitrogen (N) are observed, likely originating from the ionic liquid (IL) component of the catalyst. The relative intensities of the peaks provide a semi-quantitative estimate of the elemental composition, suggesting a higher concentration of Si than the other metallic elements. This observation is consistent with the expected structure of the catalyst, where the $NiFe_2O_4$ nanoparticles are supported on the MCM-41 matrix and further functionalized with the ionic liquid and platinum.

The EDX spectrum is direct evidence for successfully synthesizing the intended composite material. The presence of peaks for all expected elements (Ni, Fe, O, Si, Pt, and likely C and N) confirms the successful incorporation of each component into the final catalyst structure.

While EDX is not ideal for precise quantification, the relative peak intensities offer insight into the relative abundance of elements. The higher intensity of Si peaks suggests that it is the most abundant element detected, which is reasonable considering that MCM-41 is the primary support material.

The clear presence of Pt peaks is crucial, as it confirms the successful loading of platinum onto the catalyst. The intensity and shape of the Pt peaks can potentially provide information about the platinum's oxidation state and distribution, although more detailed analysis might be required for a deeper understanding.

The relatively strong Si and O signals, attributed to the MCM-41 support, are expected to be more intense than the signals from the $NiFe_2O_4$ and Pt components, which are present as nanoparticles or surface modifications.

C and N peaks suggest the successful incorporation of the ionic liquid. However, it is important to note that these elements are common and could originate from adventitious carbon or other sources.

EDX is a surface-sensitive technique and may not accurately represent the bulk composition. Also, light elements like Lithium (if present in the ionic liquid) might not be detected accurately.

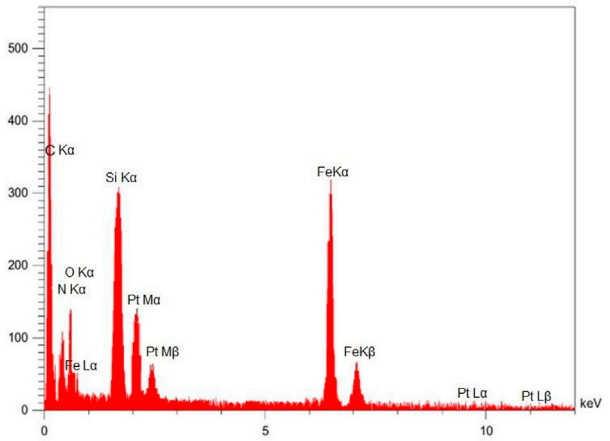


FIGURE 8
EDX analysis of $NiFe_2O_4$@MCM-41@IL/Pt nanocatalyst.

The EDX spectrum provides valuable preliminary information about the $NiFe_2O_4$@MCM-41@IL/Pt nanocatalyst composition. It confirms the presence of all expected components and offers a semi-quantitative insight into their relative abundance.

Figure 9 presents the elemental mapping analysis of the $NiFe_2O_4$@MCM-41@IL/Pt nanocatalyst. This technique allows for the visualization and spatial distribution of individual elements within the complex nanostructure, providing crucial insights into the material's composition and morphology.

The mapping reveals the presence and distribution of the following elements:

Fe (Iron): The iron distribution (red) indicates its presence primarily within the $NiFe_2O_4$ component. The relatively concentrated areas suggest the successful incorporation of iron into the spinel structure.

C (Carbon): The carbon mapping (teal) highlights the presence of the organic components, including the ionic liquid (IL) and the MCM-41 matrix. A uniform distribution suggests a homogeneous dispersion of these components within the catalyst structure.

N (Nitrogen): Nitrogen (blue) serves as an indicator for the presence of the ionic liquid (IL) component, confirming its successful incorporation into the catalyst system. The co-localization of nitrogen with carbon supports this assignment.

O (Oxygen): Oxygen (purple) is associated with the metal oxides ($NiFe_2O_4$ and potentially the silica of MCM-41). Its widespread distribution is consistent with the oxygen content in these components.

Si (Silicon): Silicon (yellow) is a distinctive marker for the MCM-41 mesoporous silica support. The distribution pattern reflects the structure of the silica matrix and confirms its successful integration into the catalyst.

Pt (Platinum): Platinum (green) mapping reveals the distribution of the platinum nanoparticles, which are a critical catalytic component. The distribution pattern suggests the dispersion of platinum throughout the catalyst structure, potentially supported on the MCM-41 or within the ionic liquid environment.

The elemental mapping provides valuable information regarding the successful synthesis of the $NiFe_2O_4$@MCM-41@IL/

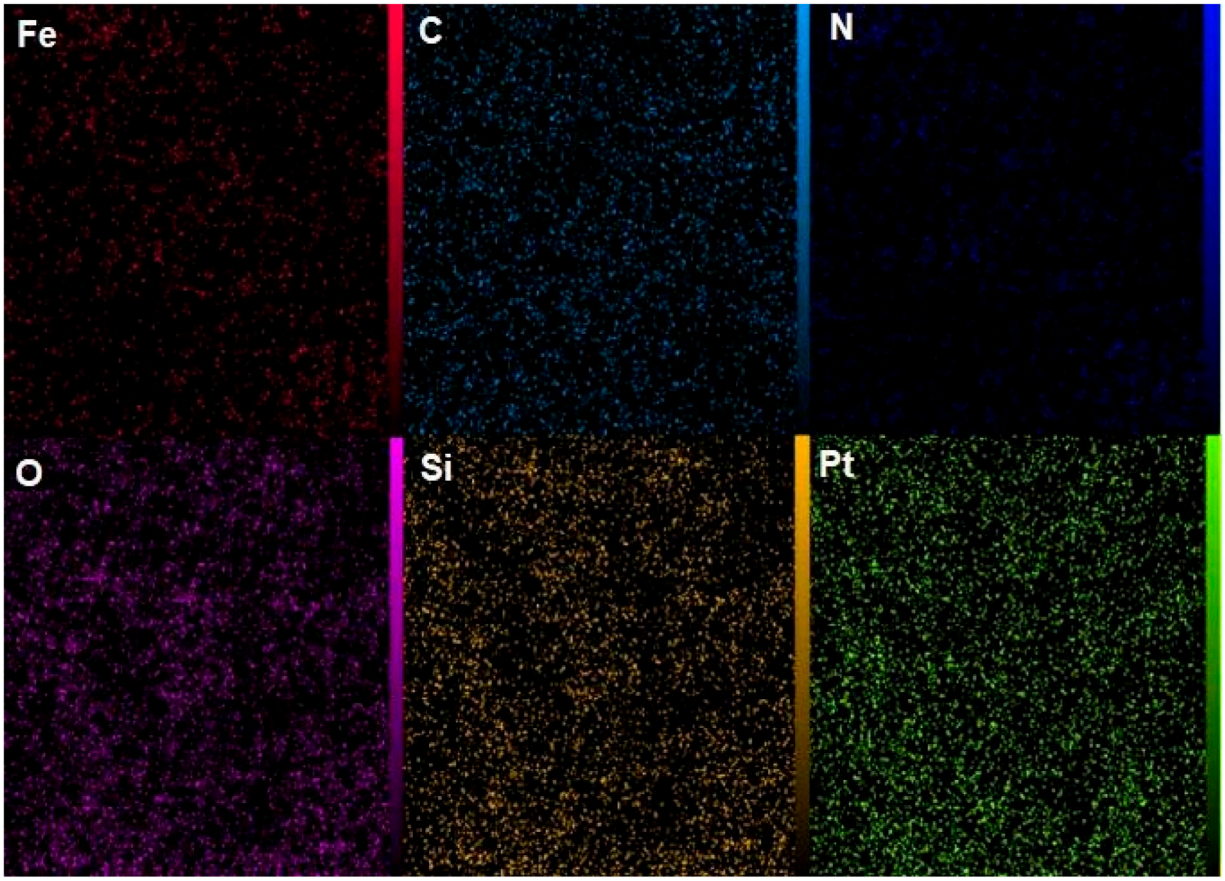


FIGURE 9
Elemental mapping analysis of $NiFe_2O_4$@MCM-41@IL/Pt nanocatalyst.

Pt nanocatalyst. The distinct signals for Fe, Si, and O confirm the presence of the $NiFe_2O_4$ and MCM-41 components. The detection of C and N and their co-localization confirm the successful incorporation of the ionic liquid. Notably, the Pt mapping demonstrates the presence and distribution of the platinum nanoparticles, which are essential for the material's catalytic activity.

The elemental mapping presented in Figure 9 provides valuable insight into the composition and structure of the $NiFe_2O_4$@MCM-41@IL/Pt nanocatalyst. The successful mapping of each constituent element confirms the composite material's successful synthesis and provides a basis for understanding its catalytic properties.

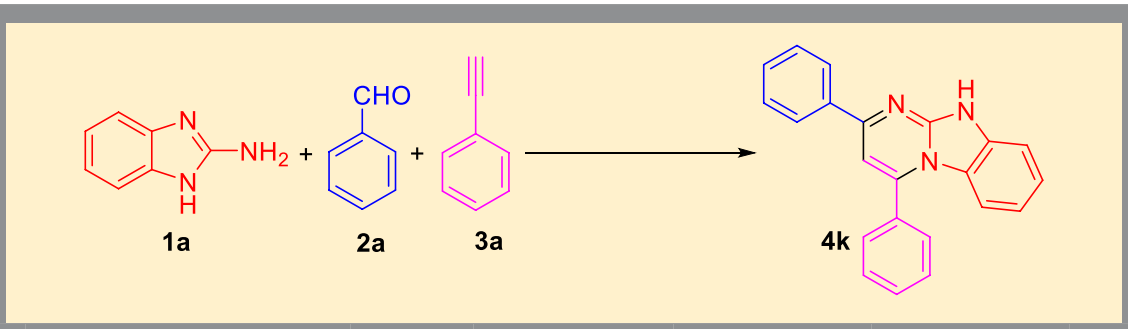
After identifying the structure of the $NiFe_2O_4$@MCM-41@IL/Pt nanocomposite, its catalytic performance in the preparation of imidazo[1,2-a]pyrimidines was evaluated. Table 1 shows a summary of the optimization conditions for the synthesis of imidazo[1,2-a]pyrimidines (product 4k). The reaction involves 2-aminobenzimidazole (1) (1 mmol), benzaldehyde (2) (1 mmol), phenylacetylene (3) (1 mmol), $NiFe_2O_4$@MCM-41@IL/Pt NPs (0–15 mg) water as a solvent (2 mL) was stirred at mentioned temperatures was evaluated under microwave irradiation. The table includes 21 entries, each detailing different catalysts, solvents, conditions (temperature and time), and yields.

A variety of organic solvents were explored, including 1,4-dioxane, methanol, ethanol, isopropanol, n-butanol, DMF, acetonitrile, chloroform, dichloromethane, DMSO, ethyl acetate, THF, and toluene. The best results were consistently obtained with water, yielding 94% product at 60°C. Without a catalyst, water proved to be an ineffective solvent for the reaction, yielding no product. However, when the $NiFe_2O_4$@MCM-41@IL/Pt catalyst was introduced, water proved a suitable solvent, with yields increasing with temperatures up to 60°C. Higher temperatures generally led to higher yields, with the optimal temperature being 60°C for most solvents. The $NiFe_2O_4$@MCM-41@IL/Pt catalyst was essential for the reaction to proceed. Without it, no product was formed. Based on the data, the following conditions are identified as the best for synthesizing compound (4k) is water in the presence of $NiFe_2O_4$@MCM-41@IL/Pt NPs (0.10 mol%) at 60°C under MW.

In a controlled and precise experiment, we investigated the production of a broad and diverse range of imidazo[1,2-*a*]pyridine derivatives. This process used a one-step, three-component reaction method that included the use of aromatic and heteroaromatic aldehydes, along with 2-aminobenzimidazole derivatives, as well as terminal alkyne. This method allowed us to more accurately follow the production process of the desired derivatives and analyze the results carefully. The data in Table 2 demonstrates the successful creation of benzimidazole products with remarkably high yields.

The electronic effects observed in the synthesis of imidazo[1,2-a] pyrimidines using the $NiFe_2O_4$@MCM-41@IL/Pt(II) catalyst are of significant importance, as they can greatly influence the reaction's reactivity and selectivity. The table presented showcases the impact

TABLE 1 Optimization condition for synthesis of imidazo[1,2-a]pyrimidines (product 4k).



Entry	Catalyst (mol%)	MW	Solvent	Temp. (°C)	Time (min)	Yield (%) [a]
1	No catalyst	-	H_2O	40°C	200	No
2	No catalyst	-	H_2O	60°C	200	No
3	No catalyst	-	H_2O	80°C	200	No
4	No catalyst	-	H_2O	100°C	200	No
5	$NiFe_2O_4$@MCM-41@IL/Pt (0.05)	100w	H_2O	40°C	20	53
6	$NiFe_2O_4$@MCM-41@IL/Pt (0.05)	100w	H_2O	60°C	20	65
7	$NiFe_2O_4$@MCM-41@IL/Pt (0.05)	100w	H_2O	80°C	20	70
8	$NiFe_2O_4$@MCM-41@IL/Pt (0.10)	100w	H_2O	40°C	20	68
9	$NiFe_2O_4$@MCM-41@IL/Pt (0.10)	100w	H_2O	60°C	20	94
10	$NiFe_2O_4$@MCM-41@IL/Pt (0.10)	100w	H_2O	80°C	20	91
11	$NiFe_2O_4$@MCM-41@IL/Pt (0.15)	100w	H_2O	40°C	20	72
12	$NiFe_2O_4$@MCM-41@IL/Pt (0.15)	100w	H_2O	60°C	20	92
13	$NiFe_2O_4$@MCM-41@IL/Pt (0.15)	100w	H_2O	80°C	20	90
14	$NiFe_2O_4$@MCM-41@IL/Pt (0.10)	80w	H_2O	60°C	20	86
15	$NiFe_2O_4$@MCM-41@IL/Pt (0.10)	120w	H_2O	60°C	20	90
16	$NiFe_2O_4$@MCM-41@IL/Pt (0.10)	150w	H_2O	60°C	20	87
17	$NiFe_2O_4$@MCM-41@IL/Pt (0.10)	100w	CH_3CN	60°C	20	64
18	$NiFe_2O_4$@MCM-41@IL/Pt (0.10)	100w	DMF	60°C	20	52
19	$NiFe_2O_4$@MCM-41@IL/Pt (0.10)	100w	CH_2Cl_2	60°C	20	57
20	$NiFe_2O_4$@MCM-41@IL/Pt (0.10)	100w	EtOH	60°C	20	90
21	$NiFe_2O_4$@MCM-41@IL/Pt (0.10)	100w	EtOH:H_2O (1:1)	60°C	20	86
22	No catalyst	100w	H_2O	60°C	20	No
23	$NiFe_2O_4$@MCM-41@IL/Pt (0.10)	-	H_2O	60°C	20	No
Reaction conditions: 2-aminobenzimidazole (1 mmol), aldehyde (1 mmol), and terminal alkyne (1 mmol)						

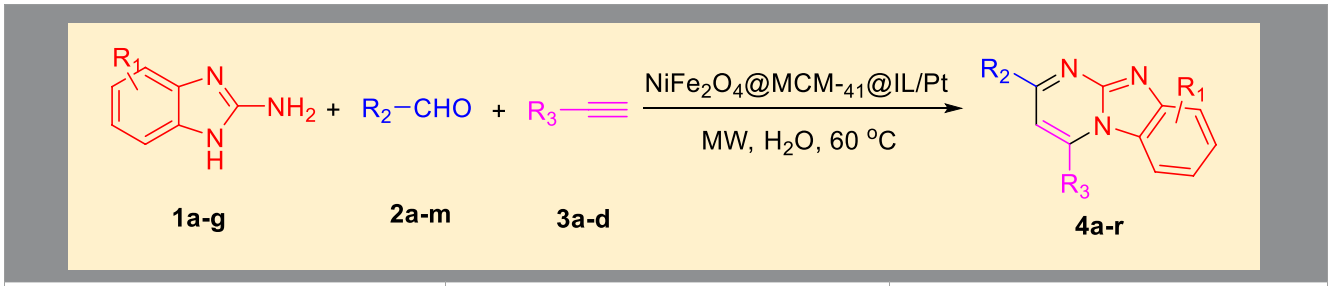
[a]Yields referred to isolated products.

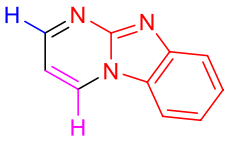
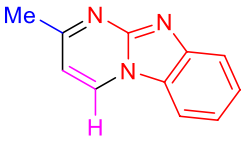
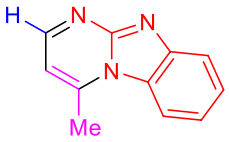
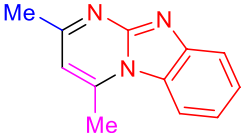
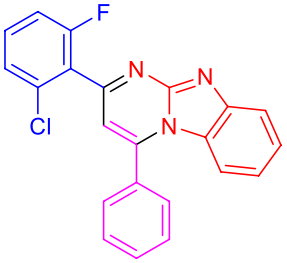
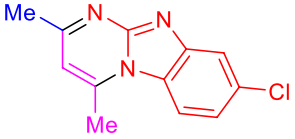
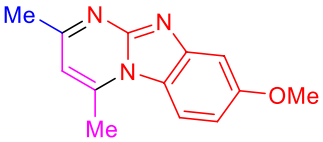
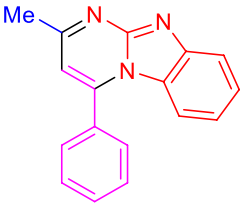
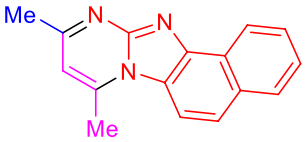
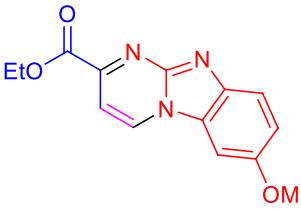
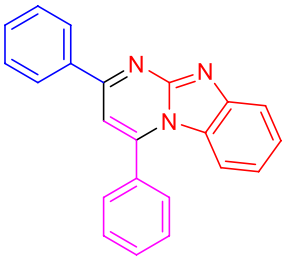
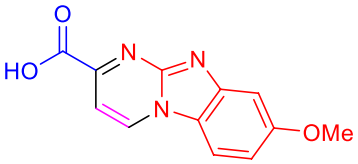
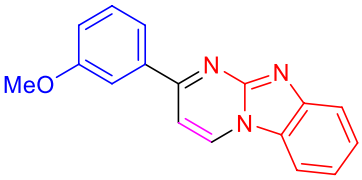
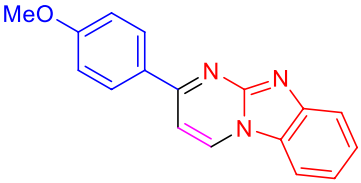
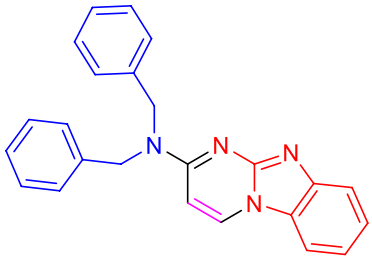
of various substituents on the aromatic rings of the reactants, providing a clear understanding of how electronic properties affect the overall yield and reaction time.

Firstly, electron-donating groups (EDGs), such as alkyl or methoxy substituents, enhance nucleophilicity in amines or electrophilicity in carbonyl compounds. This increased nucleophilicity can lead to faster reaction rates, as seen in entries where these groups are present. For instance, in a reaction involving [specific reactants], compounds with methoxy groups show shorter reaction times and higher yields than those with electron-withdrawing groups (EWGs) like [specific reactants]. EDGs stabilize positive charges that may develop during intermediate formation, facilitating smoother transitions through reactive states.

Conversely, electron-withdrawing groups like nitro or halogens can decrease nucleophilicity and increase electrophilicity. Due to their inductive effects, these groups can create a less favorable environment for nucleophilic attacks, which can result in longer reaction times and lower yields. For example, when a nitro group is

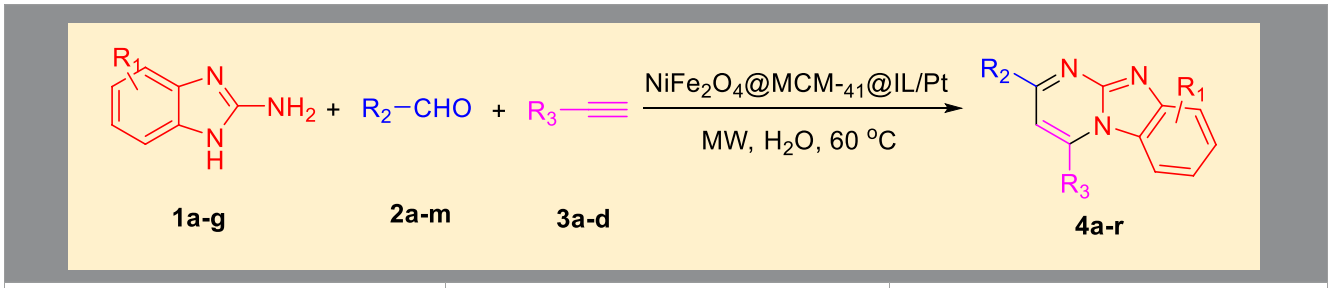
TABLE 2 Scope of synthesis of imidazo[1,2-a]pyrimidines using $NiFe_2O_4$@MCM-41@IL/Pt catalyst.

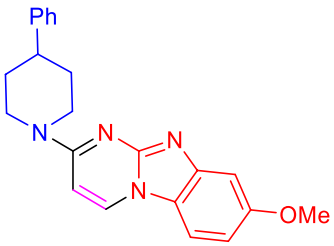
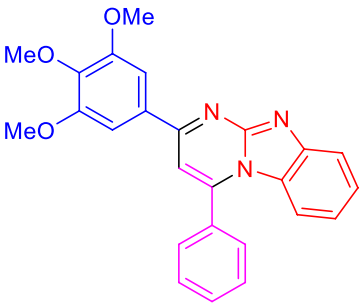
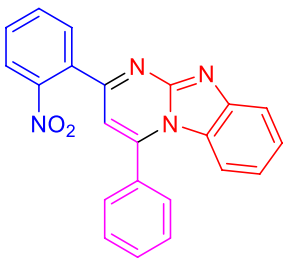


		
4a, 18 min, 95% (Shinde and Jeong, 2015)	4b, 17 min, 94%, (Kumar et al., 2014)	4c, 17 min, 92%, (Kumar et al., 2014)
		
4days, 18 min, 93% (Rawat and Rawat, 2018)	4e, 18 min, 91% (Rawat and Rawat, 2018)	4f, 16 min, 90% (Shinde and Jeong, 2015)
 4g, 15 min, 91% (Jayashree and Shivashankar, 2019)	 4h, 18 min, 90% (Jayashree and Shivashankar, 2019)	 4i, 16 min, 91% (Shinde and Jeong, 2015)
		
4j, 19 min, 90% (Rawat and Rawat, 2018)	4k, 20 min, 94% (Rawat and Rawat, 2018)	4L, 21 min, 89% (Kumar et al., 2014)
		
4m, 17 min, 94% (Kumar et al., 2014)	4n, 18 min, 96% (Shinde and Jeong, 2015)	4o, 22 min, 92% (Jayashree and Shivashankar, 2019)

(Continued on following page)

TABLE 2 (*Continued*) Scope of synthesis of imidazo[1,2-a]pyrimidines using $NiFe_2O_4$@MCM-41@IL/Pt catalyst.



		
4p, 23 min, 90% (Rawat and Rawat, 2018)	4q, 15 min, 95% (Shinde and Jeong, 2015)	4r, 22 min, 90% (Jayashree and Shivashankar, 2019)

[a]Yields referred to isolated products.

present on one of the aromatic rings, the reaction proceeds more slowly because it destabilizes intermediates by increasing electron deficiency.

Moreover, steric effects also play a role alongside electronic factors. Bulky substituents can hinder access to reactive sites on the substrate or catalyst, further influencing reaction kinetics. The combination of steric hindrance with electronic effects often dictates the overall efficiency of the synthesis.

Understanding these electronic effects is an academic exercise and a crucial step toward optimizing conditions for synthesizing imidazo[1,2-a]pyrimidines. By strategically selecting substituents based on their electronic properties, chemists can tailor reactions to achieve desired products more efficiently while maximizing yields. The table's data highlights this interplay between electronic effects and catalytic performance and provides practical insights for future research and applications.

As depicted in the provided Scheme 2, the mechanism for synthesizing imidazo[1,2-a]pyrimidine derivatives involves several critical steps. These steps are significantly facilitated by the Fe_2NiO_4@MCM-41@IL/Pt (II) nanocomposite catalyst, a pivotal element that enhances the reaction efficiency and selectivity. Understanding the role of this catalyst is crucial for a comprehensive grasp of the synthesis process.

The reaction begins with the nucleophilic attack of an amine (compound 1) on a carbonyl or imine intermediate, leading to the formation of an intermediate denoted as A. In this step, water is eliminated, and the catalyst facilitates the activation of the substrates by providing a suitable environment that lowers the activation energy required for bond formation. Platinum within the catalyst structure enhances its Lewis acidity, promoting electrophilic character in the substrate and thus facilitating this initial nucleophilic attack.

Subsequently, intermediate A undergoes further transformation, where another amine reacts with it in a subsequent step. This reaction leads to another intermediate (denoted as B), where additional water is released. The catalyst's role here is crucial; it not only accelerates the reaction but also ensures high regioselectivity toward desired products by stabilizing transition states and intermediates through coordination interactions. This reassures us of the catalyst's effectiveness in the synthesis process.

In the final stage of the mechanism, intermediate B undergoes cyclization to yield imidazo[1,2-a]pyrimidine derivatives (compound 4). This step is critical as it involves forming new bonds that define the final product's structure. The catalytic support provided by Fe_2NiO_4@MCM-41@IL/Pt(II) ensures that these reactions proceed smoothly by maintaining a favorable reactant microenvironment while facilitating effective substrate alignment. Effective substrate alignment refers to the arrangement of the reactants in a way that maximizes the chances of successful reaction, and the catalyst ensures this alignment, thereby promoting the formation of the desired product.

The role of the catalyst throughout this mechanism is paramount. It provides active sites for substrate binding and stabilizes intermediates through coordination interactions, significantly enhancing both reaction rates and yields. This underscores the catalyst's crucial contribution to the reaction, instilling confidence in its effectiveness.

This mechanism illustrates how Fe_2NiO_4@MCM-41@IL/Pt (II) serves as a facilitator of chemical transformations and as a means to improve overall process efficiency in synthesizing valuable imidazo [1,2-*a*]pyrimidine derivatives.

Simple catalyst separation and reusability are important factors in modern catalyst science. Consequently, the reusability of the v@MCM-41@IL/Pt catalyst was evaluated in the synthesis of product 4k. Following the reaction, the $NiFe_2O_4$@MCM-41@IL/Pt catalyst was recovered through magnetic decantation, washed with ethyl acetate and ethanol, dried, and reused. The results of the reusability tests reflected that the $NiFe_2O_4$@MCM-41@IL/Pt catalyst could be employed up to 6 times without substantially reducing its efficiency (Figure 10). FT-IR, VSM, and BET analyses were used to investigate the

TABLE 3 Comparison of the efficiency of this method with reported methods for the synthesis of imidazo[1,2-a]pyridine derivatives (product 4k) as the model reaction.

Entry	Catalyst	Condition	Time (min)	Yield (%)	Ref.
1	CuO NPs	Solvent-free, 100°C	60	84	56
2	CuI/Ag_2CO_3	CH_3CN, reflux	300	72	57
3	MSA	Solvent-free, 85°C	120	68	58
4	sulfated copper oxide	CH_3CN, reflux	180	85	59
5	$NiFe_2O_4$@MCM-41@IL/Pt	MW, 60°C	20	94	This Method

structure of the recovered catalyst (Figure 10). VSM analysis confirmed that the regenerated catalyst still has high magnetic properties. Also, FT-IR and BET analyses confirmed that the recovered catalyst has remarkable stability because the structure and shape of the particles in the analyses before and after recovery were almost the same.

The left SEM image provides a visual representation of the morphology and microstructure of the recovered $NiFe_2O_4$@MCM-41@IL/Pt nanocatalyst in Figure 11. The image reveals a porous and agglomerated structure with particles ranging from approximately 5–10 μm. The surface appears rough and uneven, indicating the presence of numerous pores and cavities.

The VSM (Vibrating Sample Magnetometer) curve on the right shows the magnetic hysteresis loop of the recovered catalyst. The curve exhibits a typical S-shaped behavior, characteristic of ferromagnetic materials. The following observations can be made from the VSM data:

Saturation Magnetization (Ms): The saturation magnetization value is approximately 45 emu/g. This indicates a relatively high magnetic moment of the catalyst.

Coercivity (Hc): The coercivity is around 10 Oe. This value suggests that the catalyst possesses a moderate degree of magnetic hardness.

Remanence (Mr): The remanence is approximately 20 emu/g. This value signifies residual magnetization in the catalyst even after the applied magnetic field is removed.

The VSM analysis suggests that the recovered catalyst retains its magnetic properties after six use cycles. The high saturation magnetization and moderate coercivity indicate that an external magnetic field can easily separate the catalyst from the reaction mixture. However, the presence of agglomeration in the SEM image might hinder the separation process to some extent.

Additional VSM measurements at different temperatures would be beneficial to gain a deeper understanding of the catalyst's magnetic properties. This would provide insights into the temperature dependence of the magnetic parameters and the nature of magnetic interactions within the catalyst.

The BET (Brunauer-Emmett-Teller) analysis, not shown in the image, determines the catalyst's specific surface area and pore size distribution. This information is crucial for understanding the catalyst's activity and stability.

The image indicates that the catalyst was recovered after six cycles. It would be interesting to compare the VSM and BET data of the fresh and recovered catalysts to assess the impact of multiple cycles on their properties.

The recovered $NiFe_2O_4$@MCM-41@IL/Pt nanocatalyst's SEM and VSM analysis suggest that it retains its magnetic properties after six cycles of use. However, further analysis, including BET analysis and VSM measurements at different temperatures, is required to understand the catalyst's properties and behavior fully.

The FT-IR spectrum of the recovered catalyst shows significant differences compared to the fresh catalyst. The observed differences between the fresh and recovered catalyst spectra suggest that the catalyst undergoes significant changes during the reaction process. The decrease in intensity of the O-H and C-H stretching peaks indicates a potential loss of active sites on the catalyst surface. Additionally, the broadening and reduction in intensity of the carbonyl and aromatic peaks suggest changes in the catalyst's electronic structure and surface properties.

The FT-IR spectra of the fresh and recovered catalyst (Figure 12) revealed significant differences, particularly in the regions corresponding to O-H and C-H stretching vibrations. The decrease in intensity of these peaks in the recovered catalyst suggests a potential loss of active sites due to coking and/or metal leaching. Additionally, the broadening and reduction in intensity of the carbonyl and aromatic peaks indicate changes in the catalyst's electronic structure and surface properties. Further investigations are necessary to elucidate the exact mechanisms of these changes and their impact on the catalyst's performance.

2.1 Hot filtration test (leaching)

To assess nickel leakage from the catalyst during the reaction, a leaching test was conducted using a hot filtration method for the click reaction involving 2-aminobenzimidazole (1), aldehyde (2), and terminal alkyne (3). After 10 min, the catalytically active particles were removed from the reaction mixture through hot filtration, and the filtrate was observed for any continued activity. Following the hot filtration, the reaction yield stabilized at approximately 46% and showed no further changes (Figure 13).

Table 3 compares the efficiency of different methods for synthesizing 2-(phenylthio)benzo [*d*]thiazole (product 4k). Efficiency is evaluated based on the time required for the reaction and the product yield. The table shows that the method developed in this study, using $NiFe_2O_4$@MCM-41@IL/Pt as a catalyst, is the most efficient. It requires only 3 h to complete and yields 95%. Other methods reported in the literature typically require longer reaction times and lower yields.

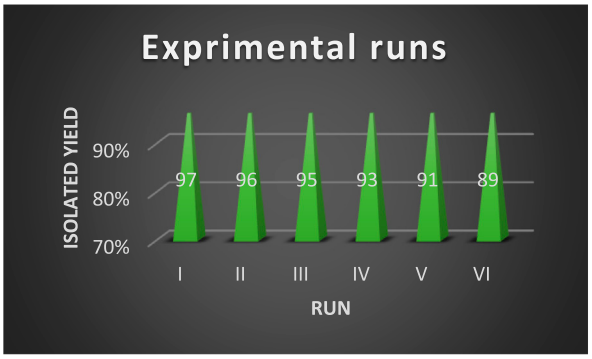


FIGURE 10
Reusability of $NiFe_2O_4$@MCM-41@IL/Pt catalyst on the model reaction (product 4k).

3 Experimental

All chemicals were purchased from Sigma and Merck. The reagents and solvents used in this work were obtained from Sigma-Aldrich, Fluka, or Merck and used without further purification. The samples' infrared spectra (IR) were recorded in KBr disks using a NICOLET impact 410 spectrometer. ^{1}HNMR and ^{13}CNMR spectra were recorded with a Bruker DRX-400 spectrometer at 400 and 100MHz, respectively.

3.1 Synthesis of nanocatalyst

3.1.1 Synthesis of $NiFe_2O_4$ nanoparticles

$NiFe_2O_4$ was fabricated via a co-precipitation chemical process. $FeCl_2{\cdot}4H_2O$ and $Ni(Cl)_2{\cdot}9H_2O$ were initially dissolved in 100 mL of water, maintained under a nitrogen atmosphere at 80°C with a molar ratio of 2:1. Following this, 10 mL of 0.2 M NaOH solution was incrementally added over 10 min to the agitated mixture, achieving a final pH of 12. After 30 min of continuous stirring, the $NiFe_2O_4$ MNPs were magnetically separated, washed multiple times with deionized water, and dried at 75°C overnight.

3.1.2 Synthesis of $NiFe_2O_4$@SiO_2

The interlayers of SiO_2 were prepared through a modified Stober method (Dai et al., 2017). In order to synthesize $NiFe_2O_4$@MCM-41, first, $NiFe_2O_4$@SiO_2 NPs were prepared according to a well-known procedure (Cui et al., 2013). Then, 0.6 g of $NiFe_2O_4$@SiO_2 nanoparticles were added to distilled water (50 mL) and EtOH (110 mL) and dispersed under ultrasonic irradiation at 30°C for 30 min. In the next step, 3 mL of aqueous ammonia solution (25%) and 1 g of cetyltrimethylammonium bromide (CTAB) were added to the resulting mixture, and it was mechanically stirred at room temperature for 10 min. Then 0.7 mL of tetraethoxysilane (TMOS) was added dropwise, and the resulting mixture was stirred for 2 h at room temperature. After that, this was statically heated at 100°C for 48 h. Finally, the resulting material was separated using an external magnet, washed with deionized water, and dried at 70°C for 10 h. The CTAB template was removed from the synthesized material by calcination at 400°C for 6 h [62].

3.1.3 Synthesis of $NiFe_2O_4$@MCM-41@IL

The $NiFe_2O_4$@MCM-41@IL nanomaterial was prepared: 1.0 g of $NiFe_2O_4$@MCM-41 nanoparticles were suspended in 50 mL of toluene and sonicated for 20 min at room temperature. Then, 0.53 mmol of 1,3-bis(3-(trimethoxysilyl)propyl)-1*H*-imidazol-3-ium chloride was added, and the mixture was refluxed under an argon atmosphere for 24 h in an oil bath. The resulting solid was separated using an external magnet, washed thoroughly with ethanol, and labeled $NiFe_2O_4$@MCM-41@IL.

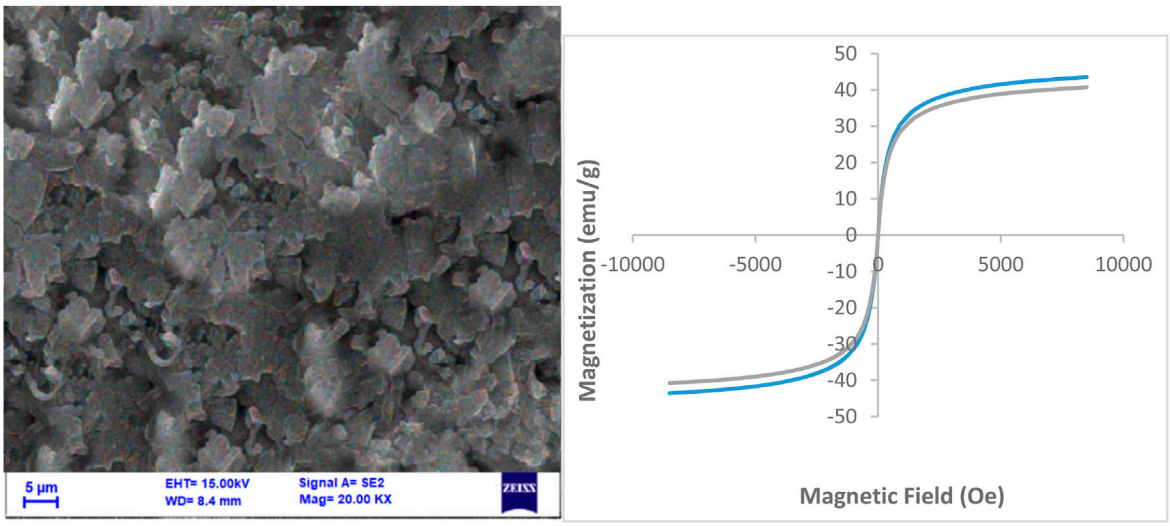


FIGURE 11
VSM and BET analysis of the recovered $NiFe_2O_4$@MCM-41@IL/Pt nanocatalyst after 6 times.

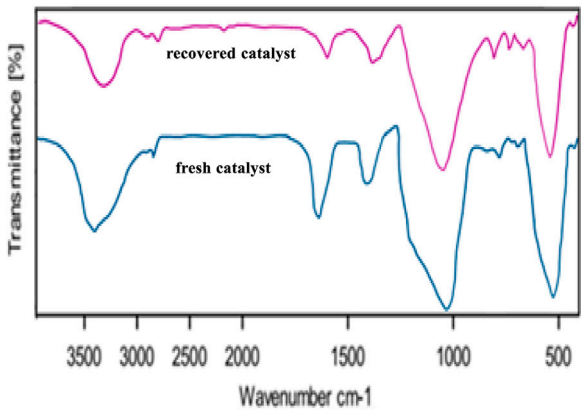


FIGURE 12
FT-IR spectrums of fresh catalyst and recovered catalyst (after 6 times).

3.1.4 Synthesis of $NiFe_2O_4$@MCM-41@IL/Pt

For the preparation of $NiFe_2O_4$@MCM-41@IL/Pt nanocatalyst, typically 1 g of $NiFe_2O_4$@MCM-41@IL was added in dimethyl sulfoxide (DMSO, 20 mL) and sonicated for 10 min at room temperature. After the complete dispersion of this material, 1.5 mmol of $Pt(Cl)_2$ salt was added into the reaction vessel and the obtained mixture was first stirred at room temperature for 24 h and then heated for 2 h at 80°C. After that, the resulting material was magnetically separated, washed thoroughly with DMSO, dried at 65°C for 10 h, and labeled as $NiFe_2O_4$@MCM-41@IL/Pt.

3.2 General procedure for the preparation of imidazo [1,2-*a*]pyridine derivatives

2-Aminobenzimidazole (1 mmol), arylaldehyde (1 mmol), and phenylacetylene (2 mmol) were combined with $NiFe_2O_4$@MCM-41@IL/Pt nanocatalyst (10 mg) and 5 mL of distilled water in a 10 mL initiator reaction vial. The vial was hermetically sealed and pressurized for 20 s before microwave irradiation at 60°C with a power output of 100 W. The vial was microwaved until thin-layer chromatography (TLC) using n-hexane–ethyl acetate (2:1) showed complete consumption of the starting substances. After cooling the reaction mixture to room temperature, the magnetic organocatalyst was separated using a magnetic field. The remaining residue was subsequently purified through recrystallization from ethanol to obtain the desired product with high yields.

4 Conclusion

This study demonstrates the successful development of a novel, eco-friendly $NiFe_2O_4$@MCM-41@IL/Pt magnetic nanocatalyst for the efficient synthesis of benzo[4,5]imidazo[1,2-a]pyrimidines via microwave-assisted A^3 coupling reactions. By integrating the magnetic properties of $NiFe_2O_4$, the high surface area of MCM-41, the stabilizing effects of ionic liquids, and the catalytic activity of platinum, this hybrid system achieves exceptional performance in water as a green solvent, energy-efficient conditions. The microwave irradiation protocol significantly accelerated reaction kinetics, enabling the formation of target heterocycles in 15–25 min with yields of 89%–96%, while the catalyst's magnetic core allowed facile recovery and reuse over five cycles without appreciable loss in activity. The methodology exhibits an impressive broad substrate compatibility, accommodating diverse aromatic and heteroaromatic aldehydes, 2-aminobenzimidazole derivatives, and terminal alkynes to generate pharmaceutically relevant scaffolds. This versatility of the catalyst instills optimism about its potential applications. This approach aligns with green chemistry principles by eliminating toxic solvents, minimizing waste, and reducing energy consumption. Mechanistic insights into the synergistic roles of the catalyst components underscore the importance of Pt-mediated alkyne activation and IL-enhanced stabilization of intermediates. This work represents a significant advancement in sustainable

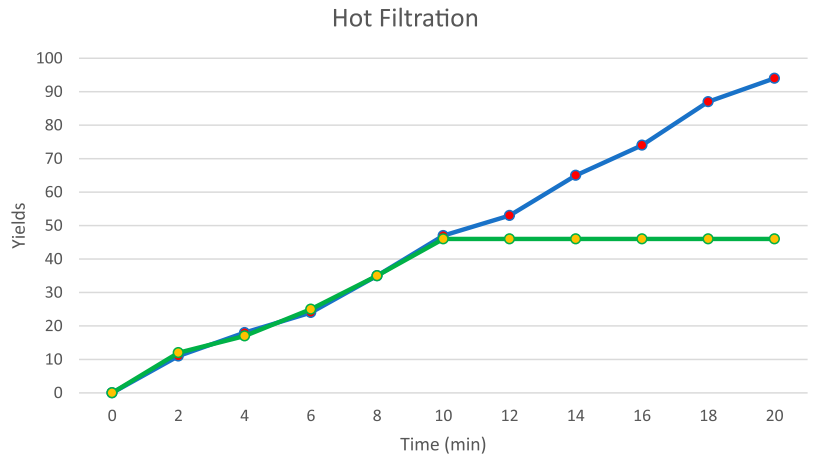


FIGURE 13
Hot filtration test (leaching) catalyst.

heterocyclic chemistry, offering a scalable, environmentally benign alternative to traditional multi-step syntheses. The developed protocol streamlines access to bioactive imidazopyridine and highlights the potential of integrating microwave technology with recyclable nanocatalysts for diverse organic transformations. Future studies will explore applications in industrial-scale synthesis and adaptations to other multicomponent reactions.

Data availability statement

The original contributions presented in the study are included in the article/Supplementary Material, further inquiries can be directed to the corresponding author.

Author contributions

YP: Formal Analysis, Investigation, Methodology, Supervision, Visualization, Writing – original draft, Writing – review and editing.

Funding

The author(s) declare that no financial support was received for the research and/or publication of this article.

Conflict of interest

Author YP was employed by Guangxi Guida Agricultural Technology Co., Ltd.

Generative AI statement

The author(s) declare that no Generative AI was used in the creation of this manuscript.

Publisher's note

All claims expressed in this article are solely those of the authors and do not necessarily represent those of their affiliated organizations, or those of the publisher, the editors and the reviewers. Any product that may be evaluated in this article, or claim that may be made by its manufacturer, is not guaranteed or endorsed by the publisher.

Supplementary material

The Supplementary Material for this article can be found online at: https://www.frontiersin.org/articles/10.3389/fchem.2025.1631183/full#supplementary-material

References

Abedi, M., Hosseini, M., Arabmarkadeh, A., and Kazemi, M. (2021). 15-Membered macrocyclic schiff-base-Pd(0) complex immobilized on Fe3O4 MNPs: an novel nanomagnetic catalyst for the one-pot three-component C–H chalcogenation of azoles by S8 and aryl iodides. *Synth. Commun.* 51, 835–855. doi:10.1080/00397911.2020.1858320

Amrutkar, R. D., Bhalerao, S. S., Bhoir, A. S., Bhusare, R. H., Bodhare, S. S., and Borse, J. N. (2022). Role of catalyst in organic synthesis. *Curr. Trends Pharm. Pharm. Chem.* 4, 115–119. doi:10.18231/j.ctppc.2022.019

Berson, A., Descatoire, V., Sutton, A., Fau, D., Maulny, B., Vadrot, N., et al. (2001). Toxicity of alpidem, a peripheral benzodiazepine receptor ligand, but not zolpidem, in rat hepatocytes: role of mitochondrial permeability transition and metabolic activation. *J. Pharmacol. Exp. Ther.* 299, 793–800. doi:10.1016/s0022-3565(24)29292-2

Chandra, P. (2021). Recent Advancement in the Copper Mediated Synthesis of Heterocyclic Amides as Important Pharmaceutical and Agrochemicals. *ChemistrySelect*, 6, 10274–10322. doi:10.1002/slct.202103035

Cui, Z.-M., Chen, Z., Cao, C.-Y., Jiang, L., and Song, W.-G. (2013). A yolk–shell structured Fe2O3@mesoporous SiO2 nanoreactor for enhanced activity as a Fenton catalyst in total oxidation of dyes. *Chem. Commun.* 49, 2332. doi:10.1039/c3cc38649j

Dai, J., Zou, H., Wang, R., Wang, Y., Shi, Z., and Qiu, S. (2017). Yolk–shell Fe_3O_4@SiO_2@PMO: amphiphilic magnetic nanocomposites as an adsorbent and a catalyst with high efficiency and recyclability. *Green Chem.* 19, 1336–1344. doi:10.1039/c6gc02926d

Denora, N., Laquintana, V., Pisu, M. G., Dore, R., Murru, L., Latrofa, A., et al. (2008). 2-Phenyl-imidazo[1,2-*a*]pyridine compounds containing hydrophilic groups as potent and selective ligands for peripheral benzodiazepine receptors: synthesis, binding affinity and electrophysiological studies. *J. Med. Chem.* 51, 6876–6888. doi:10.1021/jm8006728

Enguehard-Gueiffier, C., and Gueiffier, A. (2007). Recent progress in the pharmacology of imidazo[1,2-a]pyridines. *Mini Rev. Med. Chem.* 7, 888–899. doi:10.2174/138955707781662645

Feely, M., Boyland, P., Picardo, A., Cox, A., and Gent, J. P. (1989). Lack of anticonvulsant tolerance with RU 32698 and Ro 17-1812. *Eur. J. Pharmacol.* 164, 377–380. doi:10.1016/0014-2999(89)90482-2

Georg Thieme Verlag KG (2014). Multicomponent reactions 1: reactions involving a carbonyl compound as electrophilic component, vol 1. In *Science of synthesis: multicomponent reactions*, Georg Thieme Verlag KG, Stuttgart.

Gulati, S., John, S. E., and Shankaraiah, N. (2021). Microwave-assisted multicomponent reactions in heterocyclic chemistry and mechanistic aspects. *Beilstein J. Org. Chem.* 17, 819–865. doi:10.3762/bjoc.17.71

Hanson, S. M., Morlock, E. V., Satyshur, K. A., and Czajkowski, C. (2008). Structural requirements for eszopiclone and zolpidem binding to the γ-aminobutyric acid type-A ($GABA_A$) receptor are different. *J. Med. Chem.* 51, 7243–7252. doi:10.1021/jm800889m

Harrison, T. S., and Keating, G. M. (2005). Zolpidem: a review of its use in the management of insomnia. *CNS Drugs* 19, 65–89. doi:10.2165/00023210-200519010-00008

Hasaninejad, A., Zare, A., Shekouhy, M., and Rad, J. A. (2010). Catalyst-Free one-pot four component synthesis of polysubstituted imidazoles in neutral ionic liquid 1-Butyl-3-methylimidazolium bromide. *J. Comb. Chem.* 12, 844–849. doi:10.1021/cc100097m

Huang, W., Jiang, J., and Mandal, T. (2021). Ferrite nanoparticles: catalysis in multicomponent reactions (MCR). *Synth. Commun.* 51, 2397–2422. doi:10.1080/00397911.2021.1939883

Javahershenas, R., Han, J., Kazemi, M., and Jervis, P. J. (2024a). Recent advances in the application of 2-aminobenzothiazole to the multicomponent synthesis of heterocycles. *ChemistryOpen* 13, e202400185. doi:10.1002/open.202400185

Javahershenas, R., Makarem, A., and Klika, K. D. (2024b). Recent advances in microwave-assisted multicomponent synthesis of spiro heterocycles. *RSC Adv.* 14, 5547–5565. doi:10.1039/d4ra00056k

Javahershenas, R., and Mole, J. (2023). Recent advances in the application of deep eutectic solvents for the synthesis of Spiro heterocyclic scaffolds via multicomponent reactions. *J. Mol. Liq.* 385, 122398. doi:10.1016/j.molliq.2023.122398

Javahershenas, R., and Nikzat, S. (2023). Recent advances in the multicomponent synthesis of heterocycles using tetronic acid. *RSC Adv.* 13, 16619–16629. doi:10.1039/d3ra02505e

Javahershenas, R., Soloshonok, V. A., Klika, K. D., and Jervis, P. J. (2025). Carbon nanotubes as heterogeneous catalysts for the multicomponent reaction synthesis of heterocycles. *Carbon Lett.* 35, 385–870. doi:10.1007/s42823-024-00835-w

Jayashree, S., and Shivashankar, K. (2019). Sulfated copper oxide catalyzed one-pot synthesis of*N*-fused benzimidazolo/benzothiazolo pyrimidines. *Polycycl. Aromat. Compd.* 41, 858. doi:10.1080/10406638.2019.1625065

Kanithan, S., ArunVignesh, N., Katubi, K. M., Subudhi, P. S., Yanmaz, E., ArockiaDhanraj, J., et al. (2022). Enhanced optical, magnetic, and photocatalytic activity of Mg2+ substituted NiFe2O4 spinel nanoparticles. *J. Mol. Struct.* 1265, 133289. doi:10.1016/j.molstruc.2022.133289

Kappe, C. O., and Dall'Acqua, F. (2019). *ChemSusChem* 12, 1948–1968.

Kappe, C. O., and Stadler, A. (2006). *Microwaves in organic and medical chemistry*. Wiley-VCH.

Kazemi, M. (2020). *Synthetic communications*, 50.2114.

Kazemi, M. (2023). Copper catalysts immobilized on magnetic nanoparticles: catalysis in synthesis of tetrazoles. *Nanomater. Chem.* 1, 1–11. doi:10.22034/nc.2023.416867.1003

Kazemi, M., and Ghobadi, M. (2017). Magnetically recoverable nano-catalysts in sulfoxidation reactions. *Nanotechnol. Rev.* 6, 549–571. doi:10.1515/ntrev-2016-0113

Kefayati, H., Bazargard, S. J., Vejdansefat, P., Shariati, S., and Kohankar, A. M. (2016). Fe3O4@MCM-41-SO3H@[HMIm] [HSO4]: an effective magnetically separable nanocatalyst for the synthesis of novel spiro[benzoxanthene-indoline]diones. *Dyes Pigm.* 125, 309–315. doi:10.1016/j.dyepig.2015.10.034

Khan, A., Saeed, K., and Khan, I. (2019). Nanoparticles: properties, applications and toxicities. *Arab. J. Chem.* 12, 908–931. doi:10.1016/j.arabjc.2017.05.011

Kumar, A., Kumar, M., Maurya, S., and Khanna, R. S. (2014). Regioselective synthesis of fused imidazo[1,2-*a*]pyrimidines via intramolecular C–N bond formation/6-*endo*-*Dig*Cycloisomerization. *J. Org. Chem.* 79, 6905–6912. doi:10.1021/jo5007762

Linton, A., Kang, P., Ornelas, M., Kephart, S., Hu, Q., Pairish, M., et al. (2011). Systematic structure modifications of imidazo[1,2-*a*]pyrimidine to reduce metabolism mediated by aldehyde oxidase (AO). *J. Med. Chem.* 54, 7705–7712. doi:10.1021/jm2010942

Monti, J. M., Warren, S. D., Pandi Perumal, S. R., Langer, S. Z., and Hardeland, R. (2009). Pharmacotherapy of insomnia: focus on zolpidem extended release. *Clin. Med. Ther.* 1, 123–140. doi:10.4137/cmt.s2040

O'Connor, S. P., Wang, Y., Simpkins, L. M., Brigance, R. P., Meng, W., Wang, A., et al. (2010). Synthesis, SAR, and atropisomerism of imidazolopyrimidine DPP4 inhibitors. *Bioorg. Med. Chem. Lett.* 20, 6273–6276. doi:10.1016/j.bmcl.2010.08.090

Panda, J., Raiguru, B. P., Mishra, M., Mohapatra, S., Nayak, S., et al. (2022). Recent advances in the synthesis of imidazo[1,2-a]pyridines: a brief review. *ChemistrySelect* 7, e202103987. doi:10.1002/slct.202103987

Parvulescu, V. I., and Hardacre, C. (2007). Catalysis in ionic liquids. *Chem. Rev.* 107, 2615–2665. doi:10.1021/cr050948h

Pourhasan-Kisomi, R., Shirini, F., and Golshekan, M. (2018). Introduction of organic/inorganic Fe3O4@MCM-41@Zr-piperazine magnetite nanocatalyst for the promotion of the synthesis of tetrahydro-4H-chromene and pyrano[2,3-d]pyrimidinone derivatives. *Appl. Organomet. Chem.* 32, e4371. doi:10.1002/aoc.4371

Rawat, M., and Rawat, D. S. (2018). Copper oxide nanoparticle catalysed synthesis of imidazo[1,2-a]pyrimidine derivatives, their optical properties and selective fluorescent sensor towards zinc ion. *Tetrahedron Lett.* 59, 2341–2346. doi:10.1016/j.tetlet.2018.05.005

Revankar, G. R., Matthews, T. R., and Robins, R. K. (1975). Synthesis and antimicrobial activity of certain imidazo[1,2-a]pyrimidines. *J. Med. Chem.* 18, 1253–1255. doi:10.1021/jm00246a018

Rival, Y., Grassy, G., and Michel, G. (1992). Synthesis and antibacterial activity of some imidazo(1,2-a)pyrimidine derivatives. *Chem. Pharm. Bull.* 40, 1170–1176. doi:10.1248/cpb.40.1170

Rival, Y., Grassy, G., Taudou, A., and Ecalle, R. (1991). Antifungal activity *in vitro* of some imidazo[1,2-a]pyrimidine derivatives. *Eur. J. Med. Chem.* 26, 13–18. doi:10.1016/0223-5234(91)90208-5

Rogers, R. D., and Seddon, K. R. (2002). *Ionic liquids: industrial applications to green chemistry*. Washington, DC.Journal of the American Chemical Society.

Rotstein, B. H., Zaretsky, S., Rai, V., and Yudin, A. K. (2014). Small heterocycles in multicomponent reactions. *Chem. Rev.* 114, 8323–8359. doi:10.1021/cr400615v

Rupert, K. C., Henry, J. R., Dodd, J. H., Wadsworth, S. A., Cavender, D. E., Olini, G. C., et al. (2003). Imidazopyrimidines, potent inhibitors of p38 MAP kinase. *Bioorg. Med. Chem. Lett.* 13, 347–350. doi:10.1016/s0960-894x(02)01020-x

Saha, D., Saha, A., and Ranu, B. C. (2009). Ionic liquid-promoted dehydration of aldoximes: a convenient access to aromatic, heteroaromatic and aliphatic nitriles. *Tetrahedron Lett.* 50, 6088–6091. doi:10.1016/j.tetlet.2009.08.069

Sead, F. F., Jain, V., Ballal, S., Singh, A., Gupta, S., Sharma, G. C., et al. (2025b). ZnFe2O4-SiO2@PC-Ni nanoparticles for one-pot, solvent-free synthesis of imidazo[1,2-a]pyridines by A3 coupling reactions under ultrasound conditions. *J. Indian Chem. Soc.* 102, 101653. doi:10.1016/j.jics.2025.101653

Sead, F. F., Jain, V., Kumar, A., Ganesan, S., Shankhyan, A., Kumari, M., et al. (2025a). Green utilizing AlFeO3 nanoparticles-catalyzed for sustainable biginelli synthesis of 3, 4-dihydropyrimidin-2(1H)-thiones in glycerol. *catal. Surv. Asia*. doi:10.1007/s10563-025-09450-9

Sead, F. F., Jain, V., Kumar, A., Ganesan, S., Shankhyan, A., Sharma, G. C., et al. (2025d). One-pot, for the green preparation of benzimidazoles and 2,3-dihydroquinazolin-4(1H)-ones catalyzed by In2O3 NPs/glycerol. *J. Inorg. Organomet. Polym.* doi:10.1007/s10904-025-03604-y

Sead, F. F., Jain, V., Roopashree, R., Devi, A., Kashyap, A., Sharma, G. C., et al. (2025c). Fe3O4@SiO2-Diol/AQ-Pd(0) nanocomposite catalyzed ecofriendly synthesis of thioesters via three-component thiocarbonylation-coupling reactions. *J. Inorgmet. Chem* 1034, 123654. doi:10.1016/j.jorganchem.2025.123654

Sead, F. F., Jain, V., V, A., Devi, R. R., Kashyap, A., Sharma, G. C., Negi, B. P., et al. (2025e). Fe3O4@SiO2-Diol/AQ-Pd(0) nanocomposite catalyzed ecofriendly synthesis of thioesters via three-component thiocarbonylation-coupling reactions. *J Inorgmet. Chem.* 1034, 123654. doi:10.1016/j.jorganchem.2025.123654

Shinde, V. V., and Jeong, Y. T. (2015). Molybdate sulfuric acid (MSA): an efficient solid acid catalyst for the synthesis of diversely functionalized fused imidazo[1,2-a] pyrimidines under solvent-free conditions. *New J. Chem.* 39, 4977–4986. doi:10.1039/C5NJ00516G

Snoussi, Y., Bastide, S., Abderrabba, M., and Chehimi, M. M. (2018). Sonochemical synthesis of FeO@NH-mesoporous silica@Polypyrrole/Pd: a core/double shell nanocomposite for catalytic applications. *Ultrason. Sonochem.* 41, 551–561. doi:10.1016/j.ultsonch.2017.10.021

Trapani, G., Laquintana, V., Denora, N., Trapani, A., Lopedota, A., Latrofa, A., et al. (2005). Structure–Activity relationships and effects on neuroactive steroid synthesis in a series of 2-Phenylimidazo[1,2-*a*]pyridineacetamide peripheral benzodiazepine receptors ligands. *J. Med. Chem.* 48, 292–305. doi:10.1021/jm049610q

Tully, W. R., Gardner, C. R., Gillespie, R. J., and Westwood, R. (1991). 2-(Oxadiazolyl)- and 2-(thiazolyl)imidazo[1,2-a]pyrimidines as agonists and inverse agonists at benzodiazepine receptors. *J. Med. Chem.* 34, 2060–2067. doi:10.1021/jm00111a021

Wang, Y., Liu, X., Yu, X., and Lakshman, M. (2021). Ferrite nanocatalysts in coupling reactions. *Synth. Commun.* 51, 2106–2126. doi:10.1080/00397911.2021.1928219

Zare, A., Parhami, A., Moosavi-Zare, A. R., Hasaninejad, A., Khalafi-Nezhad, A., and Beyzavi, M. H. (2009). A catalyst-free protocol for the green and efficient condensation of indoles with aldehydes in ionic liquids. *Can. J. Chem.* 87, 416–421. doi:10.1139/v08-172

Zhang, Q., and Cai, W. (2020). *ChemCatChem* 12, 6181–6196.

Zheng, Y., Liu, Y., Guo, X., Chen, Z., Zhang, W., Wang, Y., et al. (2020). Sulfur-doped g-C3N4/rGO porous nanosheets for highly efficient photocatalytic degradation of refractory contaminants. *J. Mater. Sci. Technol.* 41, 117–126. doi:10.1016/j.jmst.2019.09.018

Zhu, J., Wang, Q., and Wang, M. X. (2015). *Multicomponent reactions in organic synthesis* (Weinheim: Wiley-VCH), 1.

Zhu, Y., Fang, Y., and Kaskel, S. (2010). Folate-conjugated Fe_3O_4@SiO_2 hollow mesoporous spheres for targeted anticancer drug delivery. *J. Phys. Chem. C* 114, 16382–16388. doi:10.1021/jp106685q

frontiers | Frontiers in Chemistry

TYPE Original Research
PUBLISHED 17 July 2025
DOI 10.3389/fchem.2025.1636477

Check for updates

OPEN ACCESS

EDITED BY
Waquar Ahsan,
Jazan University, Saudi Arabia

REVIEWED BY
Kasireddy Sudarshan,
Purdue University, United States
Ata Makarem,
University of Hamburg, Germany
Li Ma,
Xingimaging, United States

*CORRESPONDENCE
Tatjana Vulovic,
tatjana_vulovic@yahoo.com
Danijela Jovanovic,
danijeladrjovanovic@gmail.com

†These authors have contributed equally to this work and share first authorship

RECEIVED 28 May 2025
ACCEPTED 26 June 2025
PUBLISHED 17 July 2025

CITATION
Pantic D, Mirkovic N, Vulovic T, Jovanovic D, Jakovljevic S, Canovic P, Zaric M, Zaric RZ, Kostic M, Dragojevic J, Divac V, Milanovic Z, Milisavljevic K, Mitrovic M and Zelen I (2025) Evaluation of newly synthesized schiff base Pd(II) complexes for prostate cancer treatment through *in vitro* cytotoxicity and molecular mechanistic studies.
Front. Chem. 13:1636477.
doi: 10.3389/fchem.2025.1636477

COPYRIGHT
© 2025 Pantic, Mirkovic, Vulovic, Jovanovic, Jakovljevic, Canovic, Zaric, Zaric, Kostic, Dragojevic, Divac, Milanovic, Milisavljevic, Mitrovic and Zelen. This is an open-access article distributed under the terms of the Creative Commons Attribution License (CC BY). The use, distribution or reproduction in other forums is permitted, provided the original author(s) and the copyright owner(s) are credited and that the original publication in this journal is cited, in accordance with accepted academic practice. No use, distribution or reproduction is permitted which does not comply with these terms.

Evaluation of newly synthesized schiff base Pd(II) complexes for prostate cancer treatment through *in vitro* cytotoxicity and molecular mechanistic studies

Damnjan Pantic[1,2†], Nikola Mirkovic[1,3†], Tatjana Vulovic[1,4*], Danijela Jovanovic[1,4*], Stefan Jakovljevic[1,5], Petar Canovic[6], Milan Zaric[6], Radica Zivkovic Zaric[7,8], Marina Kostic[9], Jovana Dragojevic[10], Vera Divac[10], Ziko Milanovic[9], Kristina Milisavljevic[9,10], Marina Mitrovic[6] and Ivanka Zelen[6]

[1]Department of Surgery, Faculty of Medical Sciences, University of Kragujevac, Kragujevac, Serbia, [2]Department of Urology, Clinic of Urology and Nephrology, University Clinical Center Kragujevac, Kragujevac, Serbia, [3]Department of Vascular Surgery Center, University Clinical Center Kragujevac, Kragujevac, Serbia, [4]Department of Anesthesia and Resuscitation, University Clinical Center Kragujevac, Kragujevac, Serbia, [5]Department of General Surgery, University Clinical Center Kragujevac, Kragujevac, Serbia, [6]Department of Biochemistry, Faculty of Medical Sciences, University of Kragujevac, Kragujevac, Serbia, [7]Department of Pharmacology and Toxicology, Faculty of Medical Sciences, University of Kragujevac, Kragujevac, Serbia, [8]Department of Clinical Pharmacology, University Clinical Center Kragujevac, Kragujevac, Serbia, [9]Department of Science, Institute for Information Technologies, University of Kragujevac, Kragujevac, Serbia, [10]Department of Chemistry, Faculty of Sciences, University of Kragujevac, Kragujevac, Serbia

Introduction: Palladium (II) complexes are promising anticancer agents with potential advantages over platinum drugs. This study aimed to synthesize and characterize three new Pd(II) complexes (**2a–2c**) with Schiff base ligands derived from salicylic acid and amine scaffolds, and to evaluate their antitumor activity against prostate cancer cells.

Methods: The Pd(II) complexes were synthesized and structurally characterized. Cytotoxicity was tested on two human prostate cancer cell lines (PC-3, DU-145) and healthy fibroblasts (MRC-5). Apoptosis induction was assessed by flow cytometry, with a focus on Bcl-2 and caspase proteins. Molecular docking was used to examine binding to the androgen receptor (AR) and apoptotic regulators (CASP3, BCL2, BAX). DNA and human serum albumin (HSA) binding were also investigated.

Results: All complexes showed significant cytotoxicity. Notably, complex **2c** exhibited more potent cytotoxic activity than cisplatin in prostate cancer cell lines, with lower IC_{50} values after 72 h exposure in DU-145 (7.1 μM vs. 8.2 μM) and PC-3 cells (8.6 μM vs. 21.9 μM), while showing reduced toxicity in normal MRC-5 cells (42.3 μM vs. 24.4 μM). Apoptosis was confirmed as the primary cytotoxic mechanism, involving the activation of Bcl-2 and caspases. Docking studies revealed that complex **2c** had the strongest binding affinity to AR and apoptotic proteins, mediated by hydrogen bonds, π–π stacking, and hydrophobic interactions. DNA and HSA binding supported their biological relevance.

Conclusion: Complex **2c** exhibits potent anticancer activity through the induction of apoptosis and dual targeting of the AR and apoptotic pathways, making it a promising candidate for further development of anticancer drugs.

KEYWORDS

palladium, schiff bases, DNA, albumin, cytotoxicity, apoptosis, prostate cancer

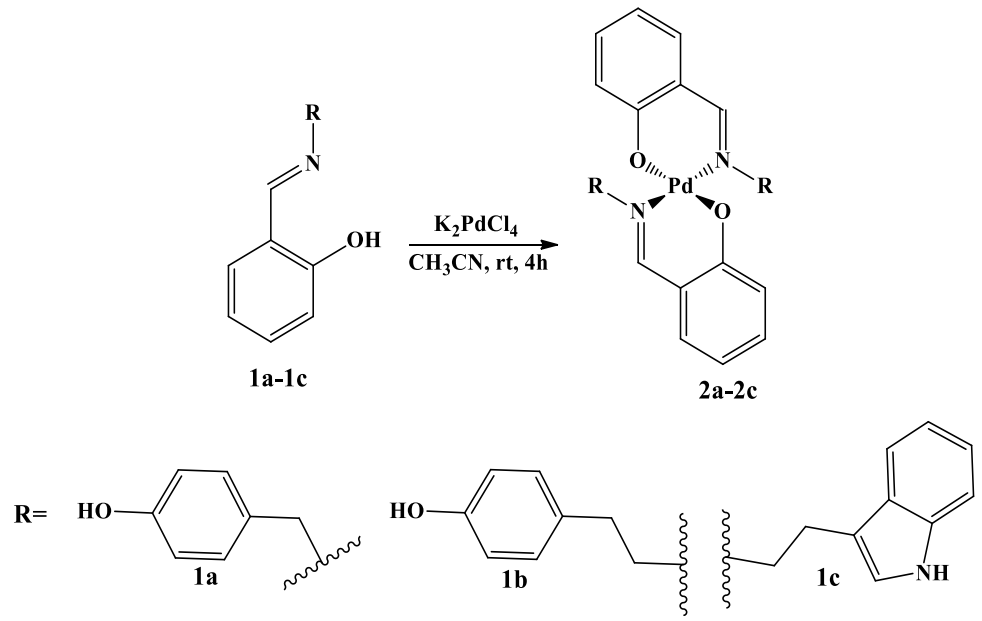
1 Introduction

The treatment of cancer is the most challenging issue of modern science, particularly due to the resistance of tumor cells to many utilized protocols and treatments, as well as due to serious side effects. Metal complexes have emerged as a suitable alternative for the treatment of different ailments due to their unique properties (Makarem et al., 2025; Klika et al., 2022). Among them, platinum-based drugs still represent the most explored options for cancer treatment, but the new studies concentrate on other metal drugs with better efficacy (Gupta et al., 2018; Cross et al., 2016; Galanski et al., 2003; Raza et al., 2021; Prathima et al., 2023). The idea behind the design of new metalotherapeutics with increased activity and lowered toxicity is based mainly on the elucidation of antitumor molecular mechanisms different from those expressed by platinum compounds (Prathima et al., 2023). The last two decades have brought increased interest in the design and synthesis of palladium complexes that could serve as alternative anticancer drugs (Lazarević et al., 2017; Vojtek et al., 2019; Carneiro et al., 2020) inspired by their coordination mode similar to that of platinum, but, according to some studies performed on rats, significantly lower toxicity (Abu-Surrah and Kettunen, 2006). As it undergoes a redox reaction, the palladium is also capable of forming reactive oxygen species (ROS). Despite the obvious similarity of these two metalotherapeutic groups, the palladium complexes are much more reactive, therefore, imposing the need for their stabilization through the utilization of specific chelating ligands. The choice of a suitable ligand is a crucial step in the development of a promising antitumor candidate, knowing that finely tuned physicochemical properties of the used ligand, its biological potential, and the strength of the ligand-metal bond directly influence the selectivity and mechanism of the antitumor activity at a molecular level.

The Schiff bases represent molecules widely utilized in many biological studies as pharmacophores capable of forming stable complexes with a variety of metals. Besides the nitrogen atom from imino groups, the molecular scaffold of Schiff bases can be easily manipulated to contain other donor atoms, such as oxygen and sulfur, and, in that way, provide the desired physicochemical or pharmaceutical properties necessary for the establishment of targeted biological activity. There are numerous reports evidencing the pharmacological potential of these compounds reflected in pronounced antitubercular, anti-inflammatory, antiviral, anticholinesterase, antibacterial, anticancer, and antioxidant activities (Aslan et al., 2020; Hosseini-Yazdi et al., 2017; Gowdhami et al., 2021; Kamel et al., 2010; Liu et al., 2019; Thiriveedhi et al., 2019; Amin et al., 2019; Lahmidi et al., 2019). When it comes to the tumor cells, Schiff bases can be selectively hydrolyzed by tumor cells or provide the release of active amines as antimetabolites (Shi et al., 2020). Other antitumor effects of Schiff bases include the cell cycle arrest by the production of free radicals and damage to proteins and nucleic acids (Panchsheela Ashok et al., 2020; Dhivya et al., 2015; Ma et al., 2012). These multiple biological actions make Schiff bases particularly attractive ligands for the design of metal complexes with enhanced therapeutic profiles. Despite the significant number of studies on Schiff base metal complexes, the exploration of palladium (II) complexes incorporating biogenic amine motifs such as tryptamine and tyramine remains limited, providing an opportunity for the development of new structures with potentially improved selectivity and reduced toxicity. Moreover, the rational inclusion of *p*-hydroxybenzylamine, structurally related to tyramine but with an additional hydroxyl group, could further modulate the physicochemical properties and biological activity of the resulting complexes.

As a consequence of above mentioned, the Schiff bases are also utilized as a ligand for the design of palladium complexes as promising candidates for photodynamic therapy (Demirbağ et al., 2024), as well as effective anticancer agents against a variety of cancer cell lines through the different molecular pathways, such as inhibition of proteasomes, enzymes, and cancer protein markers (Podolski-Renić et al., 2024). There are numerous literature examples describing the potential of Schiff base-derived palladium complexes as promising anticancer agents. For example, palladium complex derived from 2-[({2-[(2-hydroxyethyl)amino]ethyl}imino)methyl] phenol has demonstrated potent anticancer activity against several cancer cell lines, with respective IC_{50} values of 13.24 ± 1.21, 25.24 ± 0.91, 38.14 ± 1.19, and 31.21 ± 2.56 μM against HT-1080, A-549, MCF-7, and MDA-MB-231 (Khaldoune et al., 2023). The Schiff base made from (*S*)-2-amino-3-phenyl-1-propanol with 2-hydroxybenzaldehyde and 2-hydroxy-1-naphthaldehyde has been utilized for the synthesis of a palladium complex that exhibited anticancer activity against DLD-1 and MDA-MB-231 cell lines with IC_{50} values of 4.07 and 9.97 μM, respectively (Basaran et al., 2022). Also, palladium complex made from Schiff base comprising heterocyclic core in the structure was more efficient than cisplatin in killing breast cancer cells with an IC_{50} dose (31.80 ± 4.05 μM) (Al-Azzawi et al., 2025).

Among the cancers, prostate cancer is one of the leading causes of male death. The existing therapeutic strategies, such as androgen deprivation therapy, are associated with increased resistance, and new approaches in the treatment are necessary. One of the current promising ways in this domain is the development of strategies for the effective delivery of miR-34 to prostate cancer cells (Abdelaal et al., 2024). Although these attempts are very often associated with delivery vehicle-associated toxicity and non-adequate stability and cell uptake, one of the possible solutions is an approach based on small molecule ligand conjugation to miR-34 without a delivery vehicle, a way that enables high affinity and specificity for receptors (Abdelaal et al., 2024; Li et al., 2024).



SCHEME 1
Synthesis of Schiff base palladium (II) complexes **2a–2c**.

In the light of the foregoing, herein we report the synthesis, characterization, and results of *in vitro* cytotoxic assay of three new palladium (II) complexes bearing Schiff base ligands combining salicylic aldehyde and tryptamine/tyramine and *p*-OH benzylamine structural motifs. The novelty of this study lies in the strategic selection of biologically relevant amine scaffolds and the investigation of their combined effects with palladium (II) coordination on anticancer potential. While tryptamine and tyramine represent examples of biogenic amines, *p*-OH benzylamine was used due to the structural resemblance to the tyramine scaffold. The cytotoxic activity was assessed on two human prostate cancer cell lines, PC-3 and DU-145, and the results were compared with those obtained with the healthy fibroblast cell line MRC-5. It was of interest to compare the influence of the palladium metal ion coordination to the Schiff base ligand on their antitumor potential. To gain further insight into their possible mode of action, we focused on one of the key molecular targets in prostate cancer–the androgen receptor (AR). This receptor plays a central role in disease progression by regulating the transcription of genes involved in cell growth, survival, and differentiation upon binding with androgens such as testosterone and dihydrotestosterone (Chatterjee, 2003). Notably, AR signaling remains active even under androgen-deprived conditions in tumor cells, facilitating continued tumor proliferation and the emergence of therapy resistance (Li et al., 2025). Taking into consideration the strong connection between androgen-AR signaling and prostate cancers, some of the available options for treatments are based on the application of androgen deprivation therapy (ADT) or direct targeting by anti-androgens. Although these approaches result in cell cycle arrest and apoptosis induction, due to the disease progression and drug resistance, new therapeutic strategies are needed (Culig and Puhr, 2024; Fujita and Nonomura, 2019; Mehralivand et al., 2024).

Given its critical role, a molecular docking study was undertaken to evaluate the interaction of the synthesized palladium complexes with AR, aiming to elucidate their potential as modulators of androgen receptor activity and their contribution to the observed cytotoxic effects.

2 Results and discussion

2.1 Synthesis of Pd complexes 2a–2c

The targeted Pd(II) complexes **2a–2c** have been prepared in a one-pot procedure comprising the reaction between corresponding imine **1a–1c** as ligands and K_2PdCl_4 as a metal source in acetonitrile, at room temperature in a 1:1 ratio (ligand vs. metal salt), as indicated in Scheme 1. The ligands **1a–1c** were synthesized and structurally characterized in our previous studies (Babić et al., 2025; Marjanović et al., 2024). Besides the salicylic part, the ligands were composed of imine patterns–tryptamine, tyramine, and *p*-OH benzyl moiety, structurally related to the tyramine molecular scaffold. All complexes are new compounds obtained in the form of powders and fully characterized by the IR, ^{1}H NMR, ^{13}C NMR, mass spectrometry, and elemental analysis (Experimental part, Supplementary Material).

2.2 NMR studies

A detailed overview of the NMR characterization data for all synthesized compounds is provided in the Materials and Methods section, as well as in the Supplementary Material (SI), while representative examples are discussed herein to highlight key structural changes upon complexation. The representative ^{1}H NMR spectra of palladium complex **2b** were analyzed by

10.3389/fchem.2025.1636477

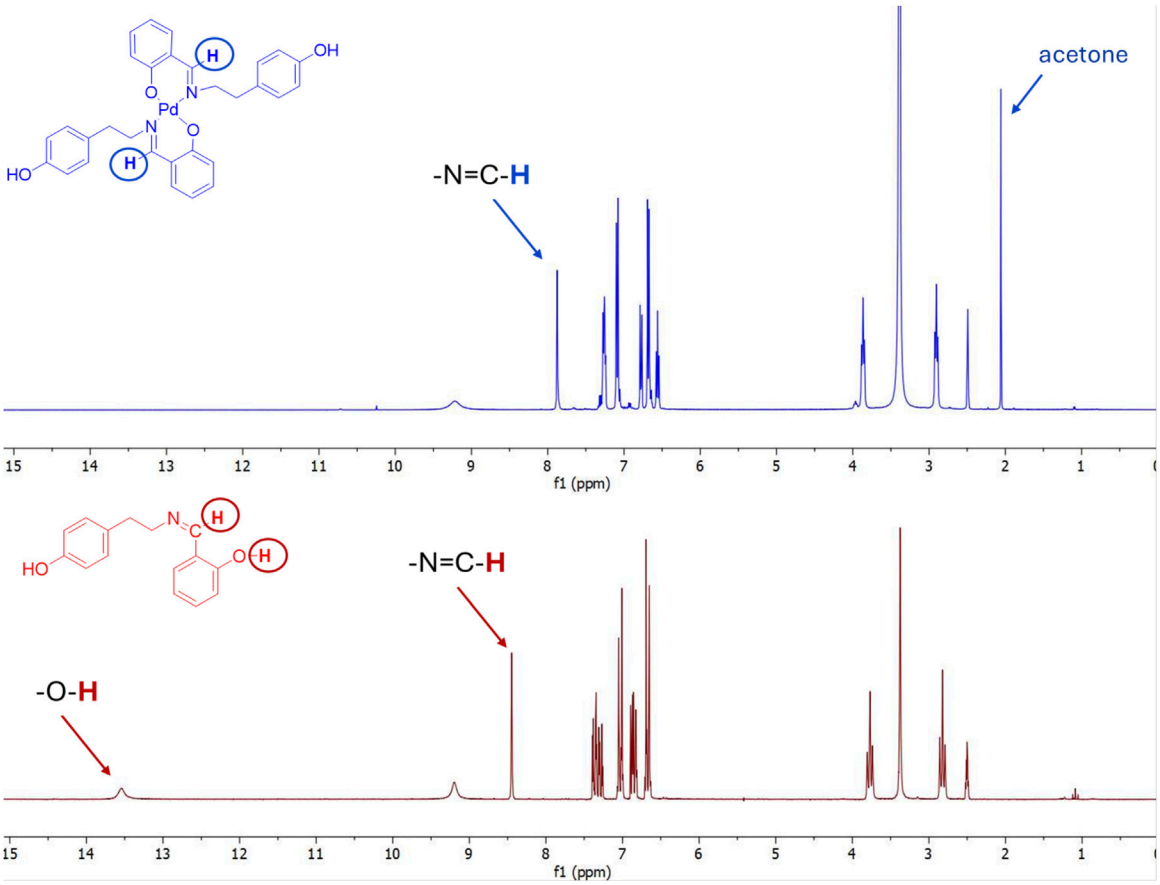


FIGURE 1
Comparison of ^{1}H NMR spectra of starting ligand **1b** and complex compound **2b**.

comparison with the spectra of ligand compound **1b**, as depicted in Figure 1. The azomethine proton–**CH = N** from the Schiff base located at 8.45 ppm is, in the case of the palladium complex, shifted to 7.88 ppm, confirming the involvement of the imino group in the coordination with the palladium metal ion. The–OH proton peaks from the salicylic moiety appearing at 13.54 ppm in the ligand spectra completely disappear in the case of palladium complex spectra, undoubtedly confirming the coordination of the palladium ion with the phenolate anion. Additionally, subtle changes in the aromatic region (6.5–8.0 ppm) further support coordination-induced electronic redistribution. The multiplet pattern of aromatic protons becomes slightly broadened and shifts marginally, which can be attributed to changes in magnetic environment and restricted rotation upon complexation. Taken together, these spectroscopic features strongly support the formation of a stable square planar Pd(II) complex, in which the ligand coordinates through both imine nitrogen and deprotonated phenolic oxygen, in agreement with the proposed structure shown in Figure 1.

In the ^{13}C NMR spectra, clear changes in the chemical shifts of characteristic carbon atoms were observed upon complexation with Pd(II), supporting the proposed coordination mode. In the free ligand 1b, the signal for the azomethine carbon (–CH = N) appears at 165.82 ppm, while the phenolic carbon bearing the–OH group (–C–OH) resonates at 155.68 ppm (Figure 2). Upon complex formation, the azomethine carbon signal shifts slightly upfield to 163.54 ppm, indicating a decrease in electron density due to the coordination of the imine nitrogen to the palladium center, which is consistent with the formation of a Pd–N bond. The phenolic carbon signal shows a negligible shift (from 155.68 ppm to 155.72 ppm), which suggests that while deprotonation of the hydroxyl group occurs, the local electronic environment of the carbon remains largely stabilized, possibly due to resonance delocalization within the chelate ring and Pd–O bond formation. Additionally, several aromatic carbon signals appear in the 120–140 ppm region, with slight shifts compared to the free ligand, reflecting electronic redistribution upon coordination. These observations provide further evidence of ligand binding and the resulting structural reorganization. Overall, the ^{13}C NMR data, in conjunction with the ^{1}H NMR results, support the successful coordination of ligand 1b to Pd(II) through the imine nitrogen and phenolate oxygen atoms in complex **2b**. The corresponding ^{1}H NMR spectral data for the CH = N and–C-OH protons, as most relevant shifts in complex structure determination for all complexes **2a–2c,** are given in Table 1.

2.3 IR analysis

The experimental IR spectra of all investigated ligands and their corresponding Pd(II) complexes are provided in the Supplementary

10.3389/fchem.2025.1636477

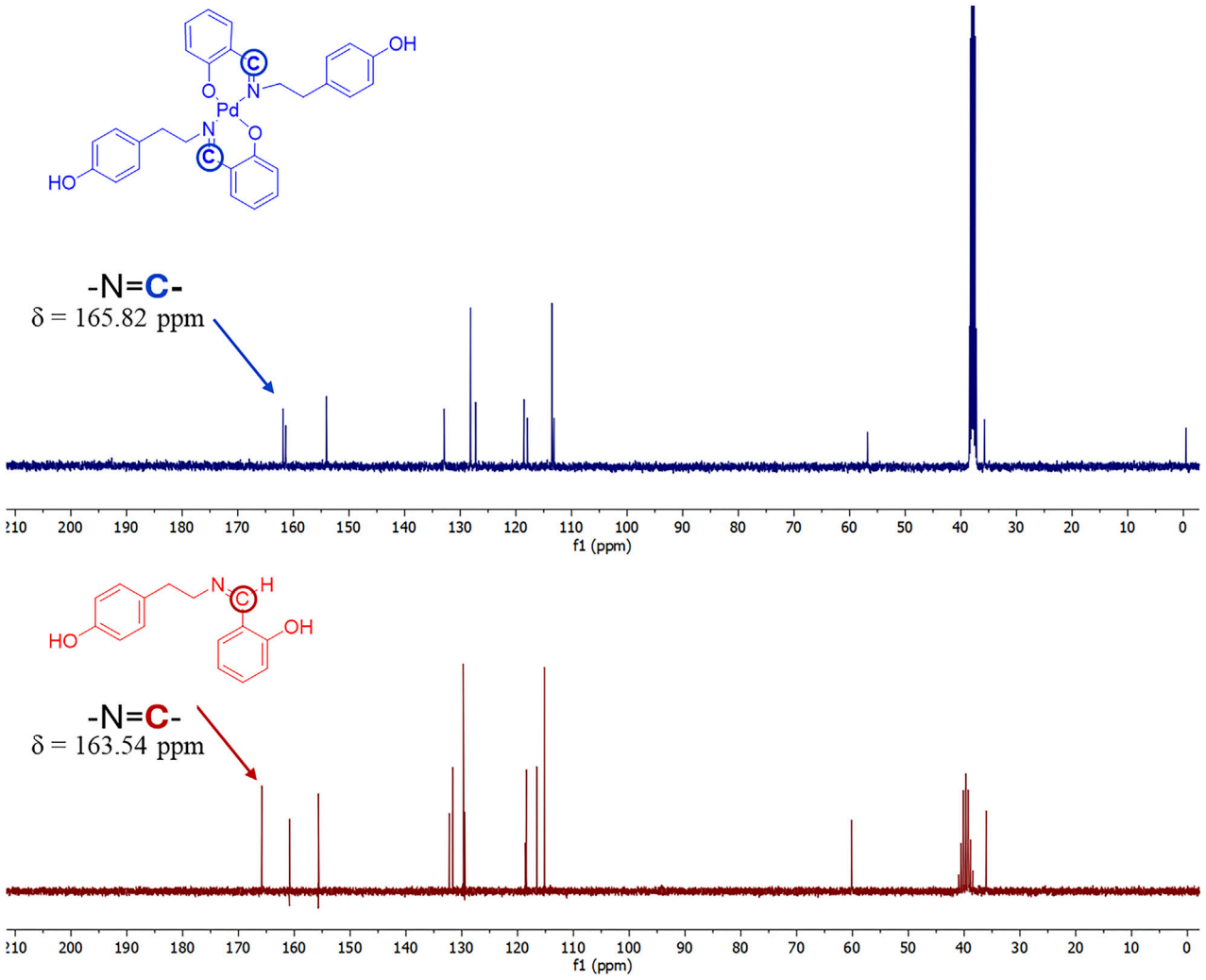


FIGURE 2
Comparison of ^{13}C NMR spectra of starting ligand **1b** and complex compound **2b**.

TABLE 1 ^{1}H NMR spectral data of ligands 1a–1c and complex compounds 2a–2c.

Compound	Imine proton-HC = N	Salicylic OH proton
1a	8.65 ppm, s	13.56 ppm, s
2a	8.20 ppm, s	missing
1b	8.45 ppm, s	13.54 ppm, s
2b	7.88 ppm, s	missing
1c	8.48 ppm, s	13.69 ppm, s
2c	7.96 ppm, s	missing

Material (SI). IR spectral analysis offers valuable insights into the coordination behavior of ligands during complex formation with Pd(II) ions. One of the most significant vibrational bands in the FTIR spectra of Schiff base ligands is the imine stretching band (νC = N), typically observed in the range of 1,610–1,650 cm^{-1}. This functional group plays a key role in metal coordination, and any shift in its position upon complexation serves as strong evidence of such interaction. The extent of the νC = N shift correlates with the strength of azomethine nitrogen coordination to the Pd(II) center, further supporting its direct involvement in complex formation. The uniform trend observed across all examined systems confirms that the ligands coordinate with the palladium ion via the imine nitrogen. The FTIR spectral data for free ligands (**1a–1c**) and Pd(II)-complexes **(2a–2c)** are given in Table 2, and these spectral features collectively confirm the bidentate coordination mode of the Schiff base ligand via the imine nitrogen and phenolic oxygen atoms to the Pd(II) center. Upon coordination of palladium via the nitrogen's imino group, the strong C=N stretching band shifts to lower wavenumbers, indicating a weakening of the bond due to donation of the nitrogen lone pair to Pd(II). Also, the appearance of two new weak bands, attributed to Pd–N stretching and Pd–O stretching vibrations, affirms the formation of complexes. These IR findings are consistent with the ^{1}H and ^{13}C NMR data previously

TABLE 2 FTIR spectral data for ligands 1a–1c and Pd(II)-complexes 2a–2c.

Compound	$\nu_{(C=N)}$/cm-1	$\nu_{(Pd-N)}$/cm-1	$\nu_{(Pd-O)}$/cm-1
1a	1,641	–	–
1b	1,631	–	–
1c	1,631	–	–
2a	1,615	513	461
2b	1,611	506	460
2c	1,618	559	453

TABLE 3 UV-visible spectral data for the Schiff base 1b and its Pd(II)-complex 2b.

Compound	Λ (nm)	Band asignment
1b	262, 282, 290	π→π* aromatic
	317	π→π* imine
	410	π→π* imine
2b	262, 282, 290	π→π* aromatic
	313	π→π* imine
	393	LMCT

discussed, providing complementary experimental evidence for the formation of bidentate N, O-chelated palladium (II) complexes.

2.4 Mass spectrometry

The electrospray ionization mass spectrometry (ESI-MS) analysis was performed to confirm the molecular composition and stoichiometry of the synthesized palladium (II) complexes. In the mass spectrum of complex **2a** (Mol.Wt 558.08), a dominant signal was observed at *m/z* = 559.0857, which corresponds to the protonated molecular ion $[M + H]^+$, confirming the formation of the proposed bis-Schiff base Pd(II) complex (ESI, Supplementary Figure SI13). Similarly, for complex **2c** (Mol.Wt 632.14), a strong peak at *m/z* = 633.1490 was detected, also corresponding to the [M + H]+species (ESI, Supplementary Figure SI22), while the spectra of compound **2b** (Mol.Wt 586.11) revealed the peak at 587.03 (ESI, Supplementary Figure SI18). The presence of these molecular ion peaks, which match the calculated molecular masses of the respective complexes, confirms the proposed coordination of two Schiff base ligands to the Pd(II) ion in a 2:1 ligand-to-metal ratio. These results provide direct evidence for the successful formation of the target Pd(II) complexes and are in full agreement with the spectroscopic data (NMR and IR), thereby supporting the proposed coordination environment illustrated in the structural models.

2.5 Molar conductivity

The molar conductivity of complexes **2a–2c** was measured in DMSO and demonstrated values ranging from 15.4 16.3–17.2 S cm2 mol^{-1}, respectively. This is in agreement with the reports where the palladium is coordinated with two ligand compounds forming complexes that are neutral in nature and that behave as nonelectrolytes in solution (Ali et al., 2013; Geary, 1971).

2.6 Absorption spectroscopy

UV-Vis spectra were recorded in DMSO as a solvent, at room temperature, and the data of the absorption wavelength maxima (λ max) are given in Table 3 and Figure 3. Both Schiff base **1b** and its Pd(II) complex **2b** exhibited strong bands corresponding to π → π* aromatic transitions. Further, two more bands are attributed to the

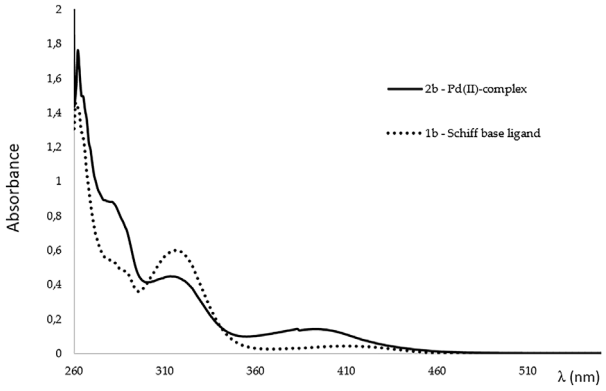


FIGURE 3
UV-Vis spectra of the Schiff base **1b** (···) and its Pd(II)-complex **2b** (–).

ligand **1b**, the medium intensity π → π* and very weak and broad n→π* transition of the imine group. Upon coordination, the π → π* band of the imine group decreases in intensity, while the new band at 393 nm, attributed to Ligand-to-Metal Charge Transfer (LMCT), appears (Felicio et al., 2001; Hussain et al., 2019). The stability of Schiff base metal complexes is a key factor influencing their performance during biological evaluations. Unstable complexes, prone to hydrolysis or degradation, may lead to reduced efficacy, altered mechanisms of action, or false-positive/negative outcomes. Palladium (II), typically adopting a square-planar geometry (Kostić et al., 2003), forms stable complexes with bidentate Schiff base ligands, but its coordination environment can be sensitive to ligand exchange. Considering that Pd(II) is a soft Lewis acid and has affinity for soft donor atoms (like sulfur) it was necessary to evaluate the stability of synthetized complexes in DMSO, as all stock solutions for biological experiments were prepared in DMSO as a solvent. Possible ligand exchange may lead to complex decomposition or formation of Pd–DMSO adducts. In order to determine the stability of selected complex **2b** in DMSO, a series of UV-Vis spectra in the range of 200–600 nm were recorded after t = 0, 24, and 48 h (Supplementary Figure SI17) (Marjanović et al., 2023). Spectroscopic data confirms the preservation of the complex's stability in DMSO, retaining its structural integrity without signs of ligand displacement or decomposition.

TABLE 4 IC_{50} values in μM for Pd(II) complexes 2a–2c and cisplatin (CP) after 24, 48, and 72 h of drug exposure. Results are presented as mean ± SD and determined from the results of MTT assay in three independent experiments.

Cell line	Time	2a	2b	2c	CP
DU-145	24 h	83.6 ± 9.2	75.9 ± 7.3	48.4 ± 5.1	22.3 ± 2.4
	48 h	17.5 ± 1.6	19.2 ± 2.1	11.0 ± 1.2	11.4 ± 1.1
	72 h	9.3 ± 0.9	8.7 ± 0.8	7.1 ± 0.8	8.2 ± 0.8
PC-3	24 h	94.1 ± 9.1	75.2 ± 7.2	38.4 ± 3.6	15.6 ± 1.4
	48 h	89.8 ± 8.8	58.6 ± 5.6	12.5 ± 1.1	29.7 ± 3.1
	72 h	79.3 ± 7.7	29.1 ± 2.8	8.6 ± 0.9	21.9 ± 2.2
MRC-5	24 h	94.3 ± 9.7	87.7 ± 8.8	80.7 ± 8.1	90.1 ± 9.2
	48 h	92.4 ± 9.1	78.5 ± 7.7	75.6 ± 7.7	41.9 ± 4.4
	72 h	83.0 ± 8.1	49.2 ± 5.1	42.3 ± 4.1	24.4 ± 0.8

2.7 Stability assay

As one of the essential features of compounds with drug-like potential is their stability in a physiological environment, the stability screening should be an integral part of the comprehensive assessment of a compound's pharmaceutical properties. For this assay, compound **2b** was selected as a representative. In Supplementary Figure SI23, time-dependent UV-Vis absorption spectra of complex **2b** are presented. Tested compounds have shown sufficient stability in solution under physiologically relevant conditions, where slight changes may be attributed to the solvent evaporation as absorbance slightly decreases over time.

2.8 Viscosity measurement

To examine the nature of the interaction of the obtained compound **2c** and deoxyribonucleic acid sodium salt from calf thymus (CT-DNA), the viscosity measurements were done. The viscosity of DNA is sensitive to length changes, and it is regarded as the least ambiguous and the most critical clue of DNA binding mode in solution (Li et al., 2010). As the intercalation strength is usually proportional to the increase in the viscosity of the DNA, from the data presented in Supplementary Figure SI24, it can be concluded that compound **2c** intercalates very weakly with the DNA strands, as the addition of increasing concentrations of **2c** to the DNA solution led to a moderate increase in viscosity. These data indicate that the interaction of complex **2c** with DNA is with a strong preference for the minor groove binding rather than intercalation, which is in accordance with the competitive fluorescence quenching studies.

2.9 *In vitro* cytotoxic study

The cytotoxicity of the three synthesized Pd(II) complexes (**2a–2c**) was assessed *in vitro* using human prostate carcinoma cells lacking prostate-specific membrane antigen (PSMA) and androgen receptor independence (DU-145), human prostate carcinoma cells (PC-3), and non-cancerous human fibroblasts (MRC-5). It is important to note that PSMA receptors are extensively used in prostate cancer research (Klika et al., 2024). The evaluation was conducted via the MTT assay following 24, 48, and 72 h of treatment. For comparative purposes, the cytotoxic profile of cisplatin was also examined. The findings unequivocally demonstrate that all Pd(II) complexes, as well as cisplatin, exhibit dose-dependent cytotoxic effects against DU-145 and PC-3 cell lines. The IC_{50} values for these Pd(II) complexes and cisplatin are summarized in Table 4, reinforcing their potential as anticancer agents (Figure 4).

All tested Pd(II) complexes, as well as cisplatin, significantly reduced the viability of DU-145 and PC-3 prostate carcinoma cell lines following 24, 48, and 72 h of treatment. Among the synthesized complexes, compound **2c** exhibited the most pronounced cytotoxic activity across all exposure durations and against both cell lines. Notably, the cytotoxic effect of complex **2c** surpassed that of cisplatin after 48 and 72 h of treatment under identical experimental conditions (Figure 4; Table 4). Furthermore, while all Pd(II) complexes demonstrated a relatively lower cytotoxic impact on non-cancerous human fibroblasts (MRC-5) compared to cisplatin, exceptions were observed for complexes **2b** and **2c** at the 24-h mark. These findings underscore the selective anticancer potential of the newly synthesized Pd(II) complexes (**2a–2c**), particularly their preferential activity against human prostate cancer cell lines. Although compounds **2b** and **2c** exhibited moderate cytotoxicity toward MRC-5 fibroblasts at 24 h, their activity against prostate cancer cell lines significantly increased at 48 h and 72 h, resulting in improved selectivity over time. For example, at 72 h, compound **2c** showed IC_{50} values of 7.1 μM (DU-145) and 8.6 μM (PC-3) compared to 42.3 μM in MRC-5, suggesting a preferential cytotoxic effect on malignant cells. In contrast, cisplatin demonstrated potent cytotoxicity across all tested cell lines, with only limited differences between cancerous and non-cancerous cells (e.g., 8.2 μM in DU-145 vs. 24.4 μM in MRC-5 at 72 h), indicating lower selectivity. These findings highlight the potential therapeutic advantage of compounds **2b** and **2c**, particularly **2c**, which combines increased anticancer activity with reduced impact on non-tumorigenic cells over extended exposure times. The subsequent phase of our investigation focused on determining the mode of cell death induced by the Pd(II) complexes in DU-145 and PC-3 prostate carcinoma cells. To achieve this, an annexin V/PI staining assay was employed. The results revealed that all tested Pd(II) complexes effectively triggered apoptosis (Figure 5). Notably, in DU-145 cells, treatment with an IC_{50} dose of complex **2c** resulted in the highest proportion of necrotic cells. Further analyses were conducted to investigate whether these Pd(II) complexes affected the intracellular levels of the anti-apoptotic protein Bcl-2 and the pro-apoptotic protein Bax. Additionally, caspase-3 activation was assessed in DU-145 cells exposed to the Pd(II) complexes. The findings demonstrated a significant reduction in Bcl-2 levels and a concomitant increase in BAX concentrations in cells treated with IC_{50} doses of the Pd(II) complexes compared to untreated controls (Figure 5). Moreover, a marked elevation in the percentage of cells exhibiting active caspase-3 was observed following treatment with the Pd(II) complexes (Figure 6). Collectively, these results indicate that the Pd(II) complexes (**2a–2c**) decreased the Bcl-2/BAX ratio, thereby

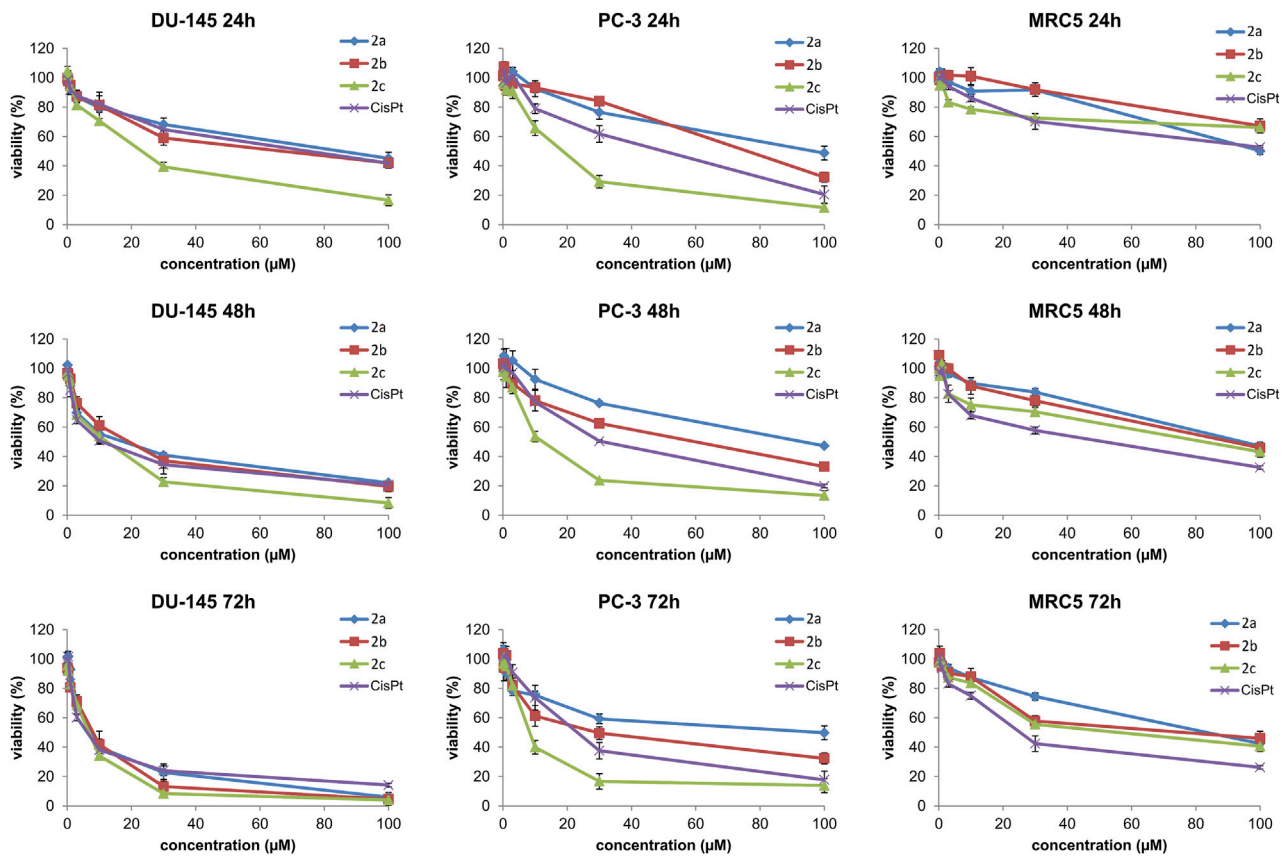


FIGURE 4
The effects of Pd(II) complexes (**2a–2c**) and cisplatin (CisPt) on the viability of human prostate carcinoma cells without prostate-specific membrane antigen (PSMA) and androgen receptor-independent (DU-145), human prostate carcinoma cells (PC-3), and human non-tumor cells (MRC-5).

promoting caspase-3 activation and inducing apoptosis via intrinsic apoptotic pathways.

The induction of apoptosis and/or cell cycle arrest is a well-established mechanism for reducing cancer cell viability (Kacar et al., 2017; Deljanin et al., 2016). Notably, cancer cells exhibit a heightened reliance on DNA damage repair mechanisms and the abrogation of the G2 checkpoint. Arrest in the G0/G1 phase typically halts cellular proliferation while allowing for the repair of damage caused by anticancer agents. In contrast, G2/M phase arrest is often associated with the initiation of apoptosis. In our study, we investigated the effects of IC_{50} concentrations of Pd(II) complexes **2a–2c** on the cell cycle of DU-145 prostate cancer cells 24 h post-treatment. Flow cytometric analysis was performed on propidium iodide (PI)-stained cells to evaluate cell cycle distribution (Figure 7). The results revealed that all Pd(II) complexes induced G0/G1 phase arrest in DU-145 cells, highlighting their ability to interfere with cell cycle progression. Furthermore, variations in the mechanisms of action among the Pd(II) complexes (**2a–2c**) were observed, underscoring their distinct biological activities.

The long-term antiproliferative effect of Pd(II) complexes was tested by using a clonogenic assay. All tested compounds showed a significant antiproliferative effect, which was dose-dependent, and the most pronounced effect was detected after treatment with complex **2c** (Figure 8).

Different palladium complexes have demonstrated the ability to induce apoptosis by activating the intrinsic mitochondrial pathway (Czarnomysy et al., 2021). Mitochondria combine death signals from both intrinsic and extrinsic apoptotic pathways. The dysregulation of mitochondrial membrane potential (ΔΨM) is crucial in the activation of mitochondrial apoptosis. We examined the capacity of palladium complexes **2a–2c** to induce mitochondrial apoptosis in DU-145 cells by assessing changes in ΔΨM using the fluorescent dye JC-10. In living cells, JC-10 mainly produces red fluorescent aggregates within the mitochondrial matrix. In contrast, in dying cells, it mainly diffuses from the mitochondria into the cytoplasm, leading to the production of a green monomeric form. Treatment with complexes **2a–2c** resulted in a significant rise in JC-10 green fluorescence and a reduction in JC-10 red fluorescence, indicating a loss of ΔΨM. Specifically, our results demonstrated that all tested compounds significantly increased the JC10 green/JC-10 red ratio by 2.1-, 2.9-, and 3.2-fold, respectively, compared to untreated cells (Figure 9). These findings suggest that the complexes **2a–2c** effectively induce apoptosis in DU-145 cells via the intrinsic mitochondrial pathway by disrupting ΔΨM.

The query outlines the synthesis and evaluation of three new Pd(II) complexes (**2a–2c**) for their cytotoxicity and mechanisms of action against human prostate carcinoma cells (DU-145 and PC-3) and non-cancerous fibroblasts (MRC-5). The findings demonstrate

10.3389/fchem.2025.1636477

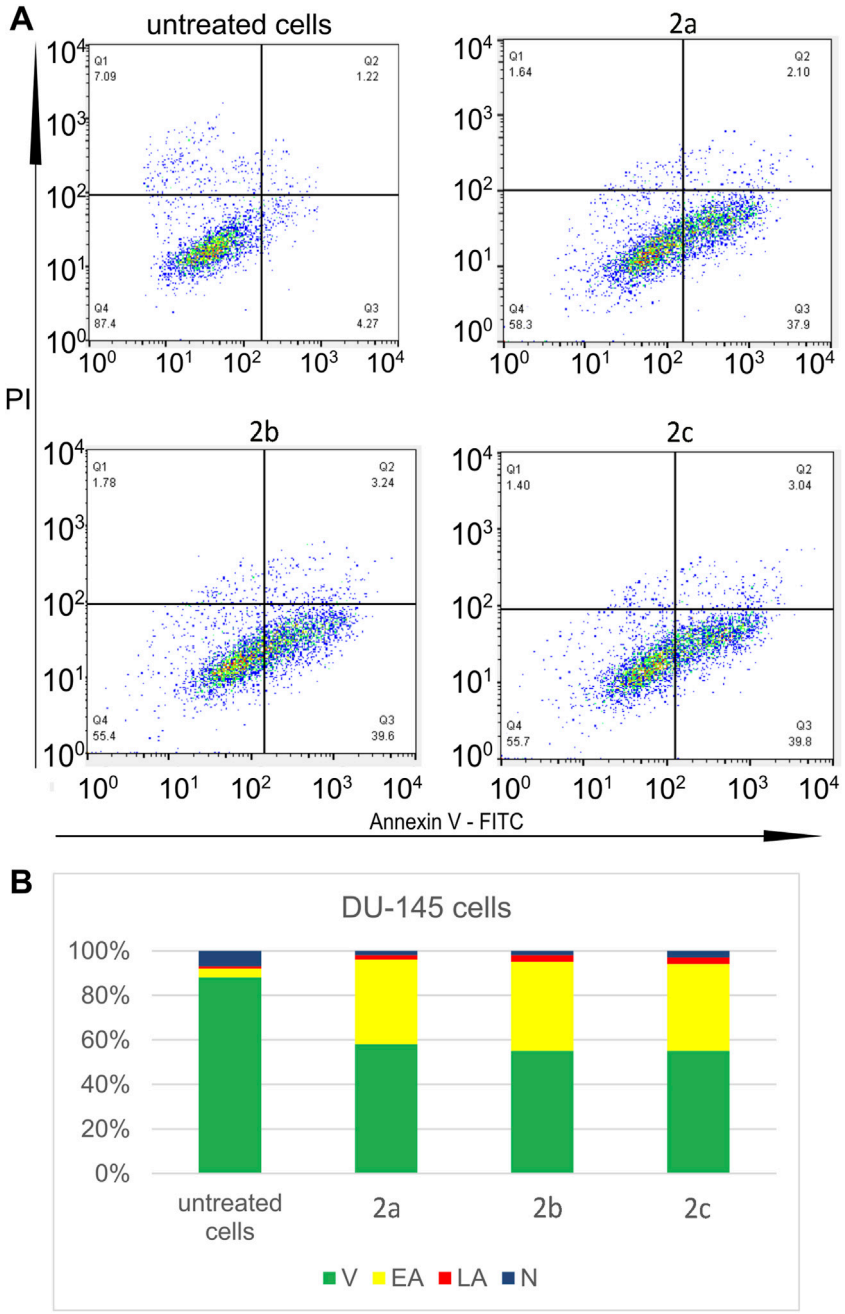
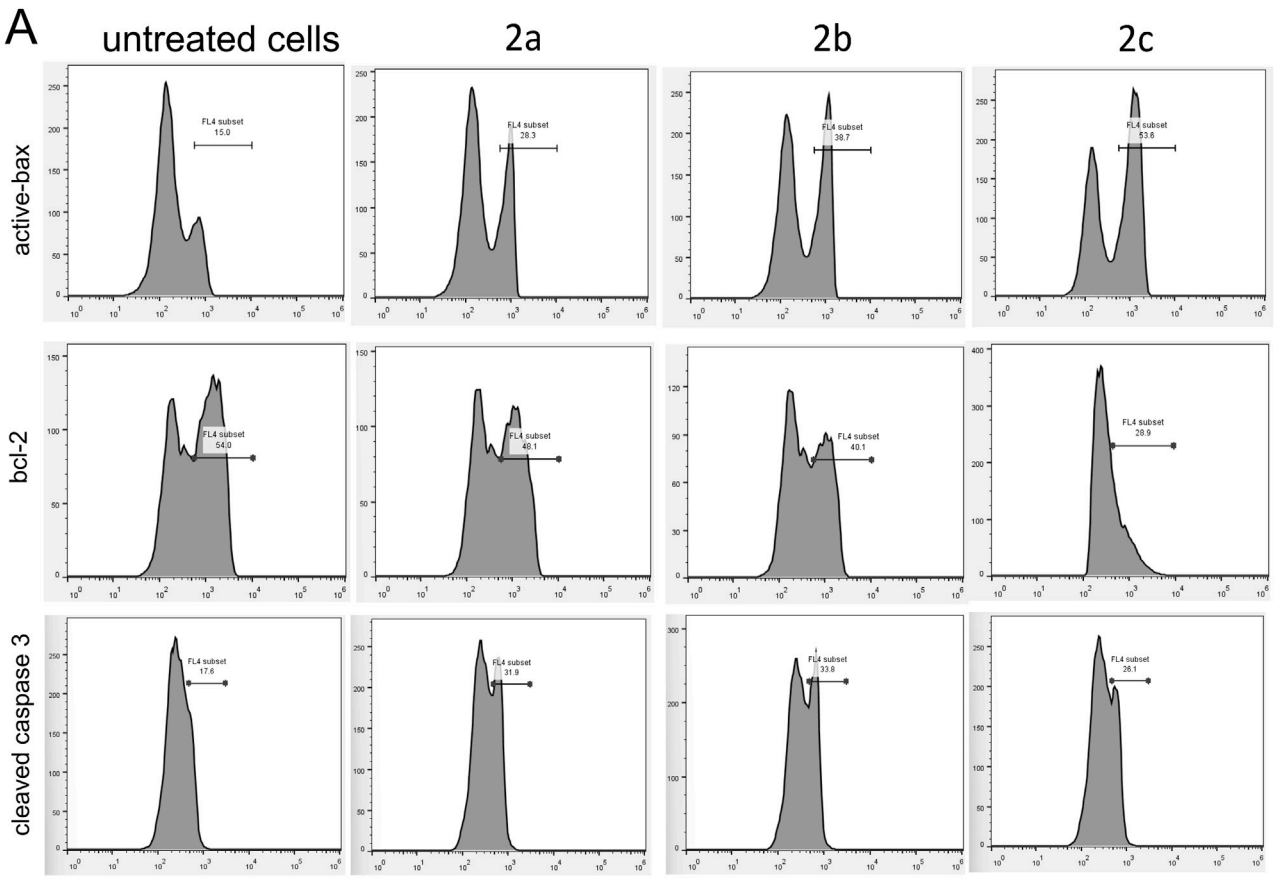


FIGURE 5
Three tested Pd(II) complexes (**2a–2c**) decrease viability of treated human prostate carcinoma cells without prostate-specific membrane antigen (PSMA) and androgen receptor-independent (DU-145); **(A)** Representative flow-cytometry plots using Annexin V-FITC/PI staining for apoptosis. **(B)** The average percentage of DU-145 viable cells (V), early apoptotic cells (EA), late apoptotic cells (LA) and necrotic cells (N) after 24 h treatment with IC_{50} of Pd(II) complexes (**2a–2c**).

that all three complexes exhibit potent and selective cytotoxic effects on prostate carcinoma cells, with complex **2c** showing superior efficacy against DU-145 cells after 72 h compared to cisplatin. The cytotoxic potency follows the order **2a** < **2b** < **2c**, potentially due to the presence of an indole ring in the ligand of complex **2c** (Kandeel et al., 2025; Kamel et al., 2019). Conversely, the selectivity increases in the reverse order (**2c** < **2b** < **2a**), with all Pd(II) complexes displaying greater selectivity than cisplatin.

The search results corroborate the potential of Pd(II) complexes as anticancer agents. For instance, studies have shown that Pd(II) complexes induce apoptosis through mechanisms such as mitochondrial membrane depolarization, Bax upregulation, and Bcl-2 downregulation in prostate cancer cells like DU-145 and PC-3 (Valentini et al., 2009; Ulukaya et al., 2013). Additionally, some Pd(II) complexes demonstrate selective cytotoxicity against cancer cells while sparing non-cancerous cells. The observed

A



B

	untreated cells	2a	2b	2c
bax MFI	15	29	39	53
bcl-2 MFI	54	48	40	29
cleaved cas-3 % of cells	18	32	34	26

FIGURE 6
Pd(II) complexes **2a–2c** induce apoptosis of human prostate carcinoma cells without prostate-specific membrane antigen (PSMA) and androgen receptor-independent (DU-145) via a caspase-dependent pathway. **(A)** MFI values (mean fluorescence intensity) for anti-apoptotic protein bcl-2, proapoptotic protein Bax and cleaved caspase 3 of DU-145 cells treated with IC_{50} of Pd(II) complexes **2a–2c**. **(B)** Overview of MFI values for pro-apoptotic protein active bax, antiapoptotic bcl-2 and active (cleaved) caspase-3 of DU-145 cells treated with IC_{50} of Pd(II) complexes **2a–2c**.

differences in efficacy and selectivity among Pd(II) complexes may be attributed to structural variations in their ligands, as highlighted in other research on similar compounds. These findings underscore the therapeutic potential of Pd(II) complexes for prostate cancer treatment.

Pd(II) complexes exhibit substantial anticancer potential against DU-145 human prostate cancer cells, primarily through the induction of apoptosis, particularly early apoptosis (Plutín et al., 2014). This mechanism was confirmed in our study, where treatment with Pd(II) complexes resulted in a significant transition of cells from viability to the early apoptotic stage. These complexes demonstrate both cytotoxic and antiproliferative properties by disrupting cellular metabolism and inducing cell death (Valentini et al., 2009). Furthermore, Pd(II) complexes exert both short-term and long-term antiproliferative effects, significantly impairing cell growth and abolishing long-term proliferation. Their action also includes inhibition of cell migration and adhesion, induction of morphological changes such as cellular shrinkage, and interaction with DNA, leading to double-stranded DNA cleavage–a key contributor to their cytotoxic effects (Laginha et al., 2023).

Studies corroborate these findings, highlighting that Pd(II) complexes induce apoptosis via mitochondrial membrane depolarization, Bax upregulation, and Bcl-2 downregulation (Carneiro et al., 2020). Additionally, their ability to disrupt DNA integrity without activating DNA repair enzymes further emphasizes their therapeutic potential (Sharma et al., 2016). These results collectively position Pd(II) complexes as promising candidates for prostate cancer treatment due to their multifaceted anticancer mechanisms.

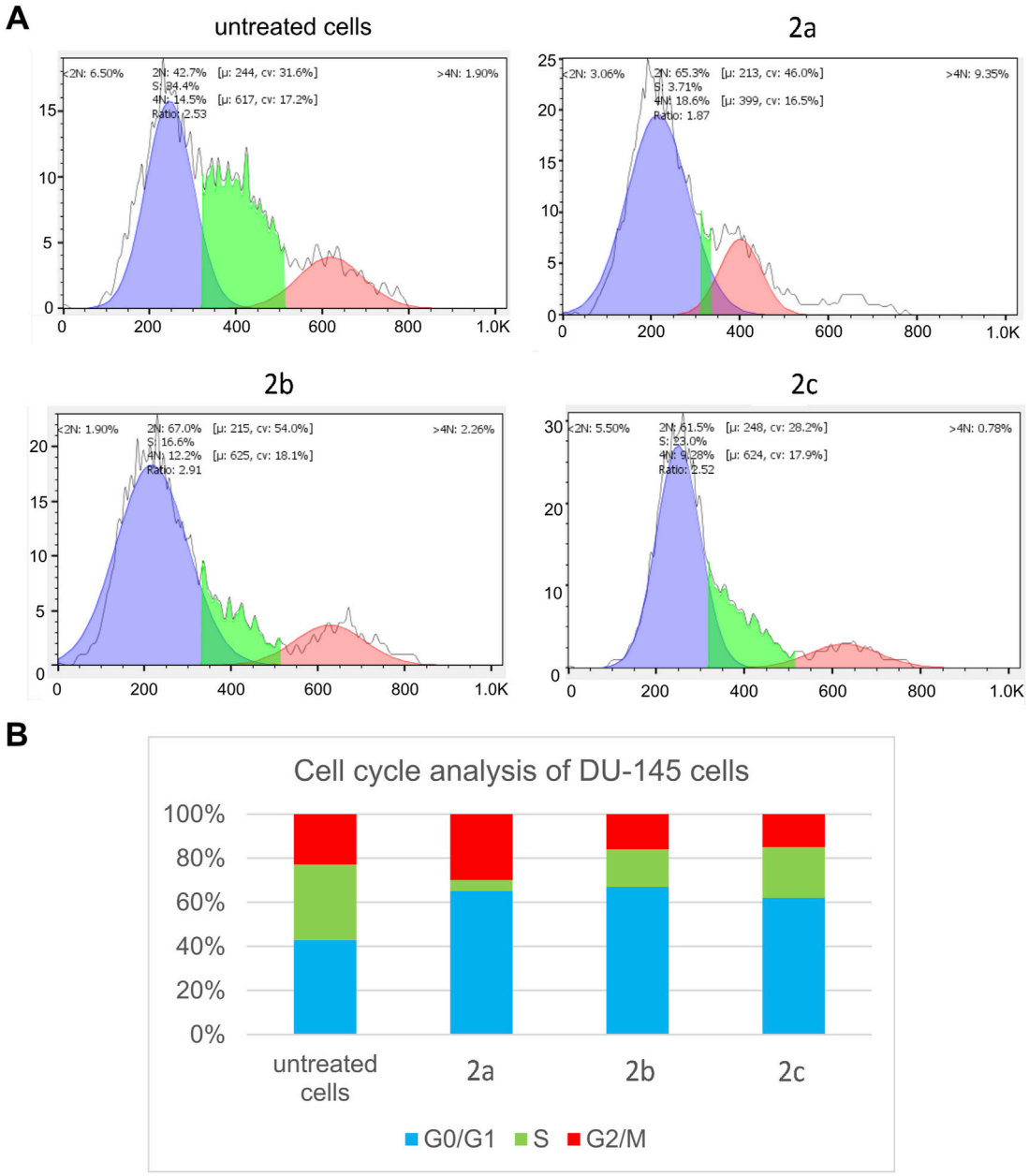


FIGURE 7
Pd(II) complexes (**2a–2c**) induce G2/M cell cycle arrest of treated tumour DU-145 cells. **(A)** Representative flow-cytometry plots using PI staining for cell cycle phase detection. **(B)** The average percentage of DU-145 cells in G0/G1 cell cycle phase (blue), S cell cycle phase (green) and G2/M cell cycle phase (red) after 24 h treatment with IC_{50} of Pd(II) complexes (**2a–2c**).

Research has demonstrated that Pd(II) complexes can induce apoptosis through multiple pathways, including the activation of cell death receptors and the generation of reactive oxygen species (ROS). These complexes have shown significant efficacy against DU-145 prostate cancer cells, highlighting their potential as anticancer agents. The metabolic effects triggered by Pd(II) complexes can be more rapid compared to those of cisplatin, which may result in faster patient recovery. This rapid metabolic response is advantageous as it could potentially reduce the duration and severity of side effects associated with chemotherapy.

Studies on various Pd(II) complexes have revealed diverse mechanisms of action, including DNA interaction, ROS-mediated mitochondrial dysfunction, and the activation of intrinsic and extrinsic apoptotic pathways (Carneiro et al., 2020; Espino et al., 2020). The ability of Pd(II) complexes to induce apoptosis without relying on DNA damage, as seen with cisplatin, suggests they may offer a distinct therapeutic approach with potentially fewer side effects (Espino et al., 2020). Additionally, the activation of cell death receptors and the induction of apoptosis through ROS production underscore the versatility of Pd(II) complexes in targeting cancer cells (Carneiro et al., 2020; Aydinlik et al., 2021).

Palladium (II) complexes have demonstrated significant cytotoxic and growth-inhibitory effects on the DU-145 human prostate adenocarcinoma cell line, primarily through mechanisms

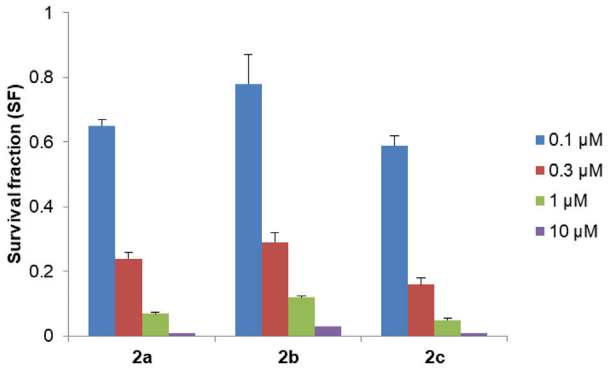


FIGURE 8
Survival fraction (SF) for Pd(II) complexes **2a–2c** tested in four different concentrations in DU-145 cells. Results are presented as mean ± standard deviation.

such as DNA interaction and apoptosis induction. These complexes induce cellular changes, including reduced cell numbers and morphological alterations, which are indicative of their cytotoxic effects. The formation of DNA adducts following the interaction of Pd(II) complexes with DNA is a key contributor to their anticancer activity. Studies highlight that complexation with thiosemicarbazone ligands enhances the antitumor potential of Pd(II) complexes, making this a promising strategy for developing new anticancer agents. For instance, Pd(II)-thiosemicarbazone complexes have shown potent cytotoxicity against DU-145 cells, with IC_{50} values significantly lower than those of cisplatin (Hernández et al., 2013). Furthermore, Pd(II) complexes have been shown to modulate protein expression in DU-145 cells, potentially influencing pathways critical to cancer progression (Kontek et al., 2011). These findings underscore the therapeutic potential of Pd(II) complexes and the need for further research to optimize their efficacy and selectivity.

2.10 DNA interaction study

Many metal-based anticancer agents have DNA as a primary potential biological target. Accordingly, it is very important to understand the binding properties of different transition metal ion complexes. Two possible binding modes of the transition metal ion complexes toward DNA are defined as covalent and non-covalent types of interactions. The covalent bindings consider the replacement of the labile ligand of the complex by a nitrogen base of DNA, and noncovalent are intercalation, electrostatic, or groove binding. The most employed method for determination of binding mode between complexes and DNA is fluorescence quenching (Recio Despaigne et al., 2014). For this investigation competitive studies with EB and Hoechst, 33,258 (Hoe) were made using fluorescence quenching experiments.

Ethidium bromide (EB) is a classical intercalator that gives significant fluorescence emission intensity when it intercalates into the base pairs of DNA. The fluorescence titration of EB-DNA with increasing amounts of **2c** is shown in Figure 10. The decrease in the emission intensity of the band at 611 nm suggests that complex **2c** can replace EB from EB-DNA and interact with DNA by the interactive mode (Tarushi et al., 2010; Tarushi et al., 2013).

The Stern-Volmer quenching constants (K_{sv}) are calculated from the slopes of the plots of I_0/I vs. (**4**) from Equation 1 (Lakowicz and Weber, 1973)

$$I_0/I = 1 + K_{sv}[Q] \quad (1)$$

and presented in Table 5. Quenching rate constants, k_q are calculated through the correlation (Klika et al., 2022), since its known that the average fluorescence lifetime of the DNA without a quencher (τ_0) is 10^{-8} s (Equation 2) (Aydinlik et al., 2021; Lakowicz et al., 1999)

$$K_{sv} = k_q \times \tau_0 \quad (2)$$

The obtained values for K_{sv} suggest that **2c** can interact with DNA molecules in interactive mode (Tarushi et al., 2013).

In order to further elucidate the binding mode of complex **2c** with CT-DNA, competitive fluorescence quenching studies were also conducted using Hoechst 33,258 (Hoe), a synthetic derivative of N-methylpiperazine known to bind specifically within the minor groove of DNA (Vojtek et al., 2019). Minor groove binding represents a non-covalent interaction typical for small-molecule drugs and bioactive compounds, often associated with sequence-selective recognition (Kandeel et al., 2025). The fluorescence titration of the pre-formed Hoe–DNA complex with increasing concentrations of complex **2c** is shown in Figure 11. A gradual decrease in fluorescence intensity suggests that complex **2c** can effectively displace Hoe from the minor groove, indicating a possible groove-binding mode of interaction with DNA.

The decrease in fluorescence intensity, as shown in Figure 11, indicates that the palladium complex **2c** is capable of displacing Hoe from the Hoe–DNA complex. The Stern–Volmer quenching constant (K_{sv}), calculated and presented in Table 5, supports this observation and further confirms the proposed interaction between complex **2c** and DNA through minor groove binding.

By comparing the K_{sv} values obtained from the EB and Hoe fluorescence quenching experiments (Table 5), it can be concluded that the complexes interact with double-stranded DNA through both binding modes–intercalation and minor groove binding. However, the higher Stern–Volmer constant observed for the Hoe displacement assay compared to the EB assay suggests that complex **2c** exhibits a stronger preference for minor groove binding over interactive interaction.

2.11 Molecular docking study

The inhibition of the AR plays a crucial role in the treatment of androgen-dependent diseases, particularly prostate cancer. Targeting AR with small molecules can modulate its activity, thereby disrupting androgen signaling pathways critical for tumor growth and progression. In this context, our molecular docking study aimed to evaluate the binding affinity of Pd-based complexes as potential AR inhibitors. As shown in Table 6, molecular docking results indicate that the **2c** complex exhibits the strongest interaction with the receptor, as evidenced by its lowest

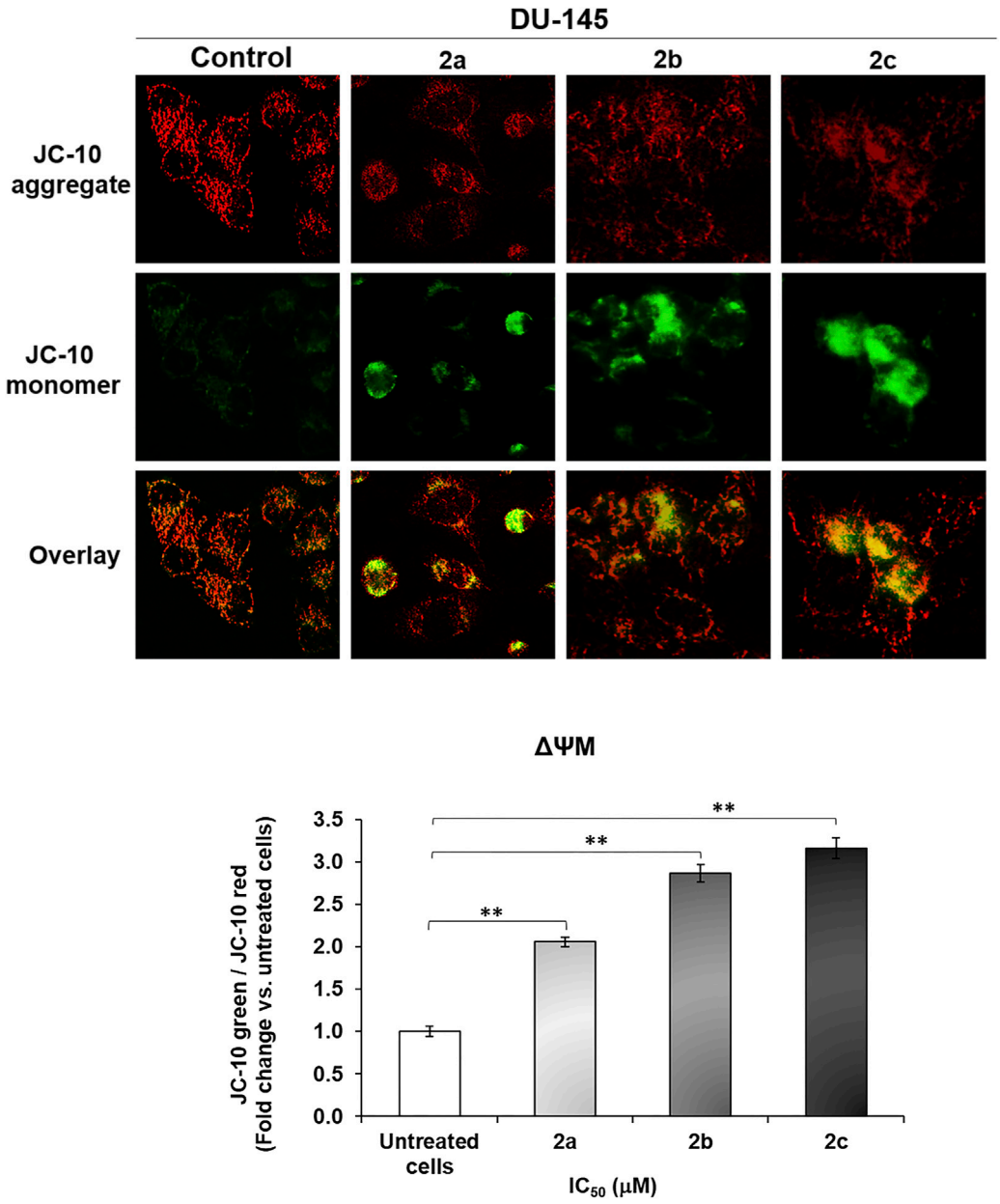


FIGURE 9
Palladium complexes **2a–2c** induce changes in mitochondrial membrane potential (ΔΨM) in DU-145 cells. DU-145 cells were treated with palladium complexes **2a–2c** (IC_{50}-μM) for 48 h and stained with the mitochondrial fluorescent probe JC-10. Pd complexes reduced the red fluorescence of the JC-10 aggregate within the mitochondria while increasing the green fluorescence of the JC-10 monomer in the cytoplasm. The MFI of the red and green forms of JC-10 was measured using ImageJ. The histogram shows the mean fold change of the MFI JC-10 green/MFI JC-10 red ratio. The bars show the mean ± SE; (N = 3). Significance levels are indicated as **p < 0.01 compared to control. Scale bar: 100 μm; magnification: ×40.

binding free energy value. Its inhibition constant, the smallest among the tested compounds, suggests a high potential for enzyme inhibition, making it the most promising candidate in this study. The **2b** complex also demonstrates significant inhibitory activity, albeit slightly weaker than **2c**, yet it still forms stable interactions with the receptor, highlighting its relevance as a potential inhibitor. In contrast, the **2a** complex shows the highest binding free energy value and the largest inhibition constant, indicating a weaker affinity for the enzyme's active site. For comparison, bicalutamide (**BIC**) was used as a reference inhibitor, and the results reveal that **2c** exhibits a stronger receptor binding affinity. These findings underscore the potential of **Pd** complexes as **AR** receptor inhibitors, with **2c** emerging as the most promising candidate for further investigation.

The molecular interactions between Pd derivatives and **AR**, illustrated in Figure 12, offer valuable insights into the potential inhibitory properties of these compounds. Non-covalent interactions contribute significantly to the stability of the ligand-protein complex by reinforcing the binding affinity within the enzyme's active site. Hydrophobic interactions predominantly

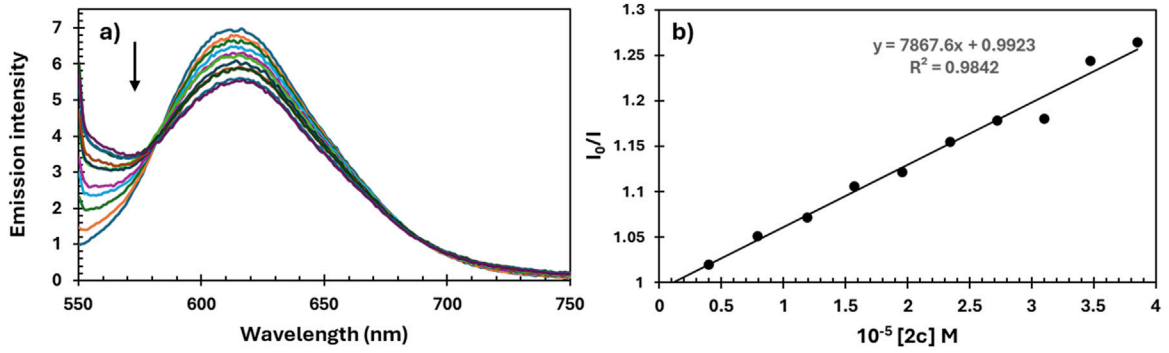


FIGURE 10
(a) Emission spectra of EB-DNA in the absence and presence of complex **2c**. pH = 7.4; λex = 550 nm; **(b)** plots of I_0/I versus concentration of quencher [**2c**].

TABLE 5 The bimolecular quenching rate constant (k_q), Stern–Volmer constant (K_{sv}), and correlation coefficient (R) for complex 2c as a quencher.

Complex	Test	$k_q[M^{-1}s^{-1}]$	$K_{sv}[M^{-1}]$	R^2
2c	EB	0.8 × 1,012	0.8 × 104	0.9842
	Hoe	3.1 × 1,012	3.1 × 104	0.9455

enhance the stability of the complex by facilitating favorable packing and minimizing solvent exposure, while conventional hydrogen bonds provide additional stabilization through directional electrostatic forces, further strengthening the ligand-enzyme interaction.

The hydrophobic segments of palladium derivatives enable interactions with various amino acids, such as A:LEU 704, A:VAL 746, and A:ILE 899, leading to the formation of alkyl/π-alkyl contacts. Additionally, other types of non-covalent interactions, including π-sigma and π-sulfur interactions, play a crucial role in ligand stabilization. π-sigma interactions arise due to the interaction between the electron cloud of aromatic rings and sigma bonds within the molecule (Ferreira de Freitas and Schapira, 2017), as observed in **2c** interacting with A:MET 742, A:VAL 746, and A:MET 895. Similarly, **2a** and **2b** also establish interactions with these amino acids, in addition to A:LEU 873. π-sulfur interactions, which involve interactions between sulfur atoms and the π-electron systems of aromatic rings (Meyer et al., 2003), are characteristic of enzymes containing methionine residues, including A:MET 742, A:MET 745, A:MET 749, A:MET 787, and A:MET 895.

Conventional hydrogen bonds are essential for maintaining the stability of ligand–enzyme complexes (Ferreira de Freitas and Schapira, 2017; Bissantz et al., 2010). These interactions arise between the hydroxyl groups of **2a** and **2b** derivatives and polar amino acid residues within the enzyme's active site, such as A:MET 742 and A:MET 787. Moreover, a distinct carbon-hydrogen bond is formed between the **2a** derivative and A:ASN 705, further stabilizing the complex and ensuring the proper alignment of the ligand within the catalytic pocket. All these interactions collectively play a crucial role in stabilizing the ligand within the enzyme complex.

The observed interactions with the androgen receptor (**AR**) suggest that **Pd** complexes can effectively modulate receptor activity. Overall, these diverse binding modes highlight the potential of palladium derivatives for therapeutic applications, particularly in targeting key regulatory proteins like **AR**. The molecular docking results indicate that all examined Pd complexes exhibit significant interactions with key regulators of apoptosis–caspase 3 (**CASP3**), Bcl-2-associated X protein (**BAX**), and the anti-apoptotic B-cell lymphoma 2 (**BCL2**) protein. The negative values of the binding free energy (ΔG_{bind}) suggest the stability of the formed complexes, while variations in the obtained parameters provide insight into the binding preferences of these compounds for pro-apoptotic (**CASP3**, **BAX**) and anti-apoptotic (**BCL2**) proteins.

Analysis of the data in Table 7 highlights **2c** as the strongest binding ligand, exhibiting the lowest ΔG_{bind} values for **CASP3** (−8.81 kcal/mol) and **BAX** (−8.44 kcal/mol). These results suggest that **Pd3** preferentially targets pro-apoptotic proteins, which may indicate its potential to induce cell death by activating apoptosis. These findings suggest that **2c** exhibits selectivity toward pro-apoptotic proteins, highlighting its potential role as a pro-apoptotic modulator in anticancer strategies. In contrast, **2a** and **2b** display a more balanced binding affinity between pro-apoptotic and anti-apoptotic proteins, which may imply a different mechanism of action.

Since **2c** exhibited the most favorable binding results, it was selected to represent the intermolecular interactions with the active sites of **CASP3**, **BCL2**, and **BAX**, as shown in Figure 13. These interactions involve a combination of hydrophobic, electrostatic, and hydrogen bonding forces. Hydrophobic interactions play a central role in driving the binding process, while electrostatic forces aid in the precise alignment of **2c** within the enzyme's active site. Additionally, hydrogen bonds further stabilize the complex, enhancing both the strength and specificity of the binding. These findings underscore the molecular factors that contribute to **2c**'s potential as an effective modulator of apoptotic pathways.

In the context of **CASP3** (Figure 13a), **2c** engages in a conventional hydrogen bond with A:ARG 207, along with carbon-hydrogen interactions involving A:SER 205 and A:ARG 207. Additionally, alkyl/π-alkyl interactions are observed with A:CYS 163, A:ARG 207, and A:TRP 214. The π-π interactions can adopt different configurations, such as edge-to-face (T-shape) or

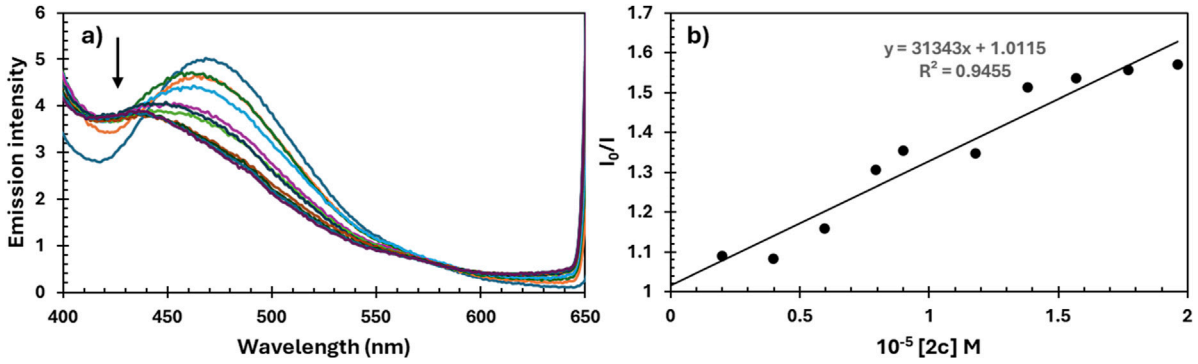


FIGURE 11
(a) Emission spectra of Hoe-DNA in the absence and presence of complex **2c**. pH = 7.4; λex = 346 nm; **(b)** plots of I_0/I versus concentration of quencher [**2c**].

TABLE 6 Thermodynamic parameters (kcal/mol) of Pd complexes at the active site of Androgen Receptor (AR) determined after molecular docking simulation.

Complex	ΔG_{bind}	K_i (μM)	ΔG_{inter}	$\Delta G_{vdw\ +\ hbond\ +\ desolv}$	ΔG_{elec}	ΔG_{total}	ΔG_{tor}	ΔG_{unb}
AR								
2a	−5.56	83.36	−7.21	−7.23	0.02	−1.29	1.65	−1.29
2b	−8.44	0.65	−10.64	−10.62	−0.02	−1.74	2.20	−1.74
2c	−10.51	0.02	−12.16	−12.21	0.05	−2.47	1.65	−2.47
BIC	−9.11	0.21	−10.76	−10.65	−0.11	−1.92	1.65	−1.92

offset stacking (shifted parallel alignment), depending on the local geometry and chemical environment of the binding site (Meyer et al., 2003; Tsuzuki et al., 2002). Notably, A:HIS 121 participates in one of these π-π interactions, adopting an edge-to-face (T-shape) configuration. **2c** also establishes a π-sulfur interaction with A:CYS 163, further stabilizing its binding. Moreover, electrostatic interactions play a critical role in ligand stabilization, particularly π-anion and π-cation interactions, which arise when the electron cloud of an aromatic ring interacts with an anion or cation (Ferreira de Freitas and Schapira, 2017; Mahadevi and Sastry, 2013). In this context, **2c** forms a π-cation interaction with A:ARG 207, underscoring the selectivity of its binding. Together, these diverse interaction types contribute to a strong binding affinity, aligning with the observed activation of caspase-3. More broadly, they are essential for the stability and specificity of protein-ligand complexes, as they enhance charge complementarity between the ligand and active-site residues, ultimately strengthening overall binding affinity.

For **BCL2** (Figure 13b), **2c** establishes a conventional hydrogen bond with A:ASN 102 and a carbon-hydrogen bond with A:ARG 105. Additionally, alkyl/π-alkyl interactions are observed with A:VAL 92, A:LEU 96, A:ARG 105, and A:ALA 108, while π-sulfur hydrophobic interactions occur with A:MET 74. Notably, characteristic π-sigma interactions are also present with A:VAL 92. The inhibition of **BCL2** disrupts mitochondrial membrane stability, triggering the release of pro-apoptotic factors such as cytochrome c, a key molecule in the initiation of apoptosis.

In the case of **BAX** (Figure 13c), **2c** establishes a carbon-hydrogen bond with A:ALA 104 and engages in T-shaped π-π interactions with A:PHE 146. Additionally, alkyl/π-alkyl interactions are observed with multiple residues, including A:PHE 97, A:VAL 126, A:LEU 130, and A:ALA 149. These stabilizing interactions enhance **BAX** activation, promoting pore formation in the mitochondrial membrane, which facilitates the release of apoptotic factors and drives the process of programmed cell death.

The molecular interactions of **Pd**-based complexes with **CASP3**, **BCL2**, and **BAX** offer valuable insights into their potential role in modulating apoptotic pathways. Through diverse binding modes–including hydrogen bonding, π-π stacking, alkyl/π-alkyl interactions, π-sulfur interactions, and electrostatic forces–these complexes contribute to the stability and specificity of protein-ligand interactions. Collectively, these findings underscore the ability of **Pd**-based complexes to regulate key apoptotic proteins, highlighting their potential as therapeutic agents for apoptosis-related diseases. The specificity and strength of their interactions with critical residues further reinforce their significance in fine-tuning apoptotic signaling pathways.

The integrated results of cytotoxicity assays, DNA interaction studies, and molecular docking analyses demonstrate that Pd(II) complex **2c** exhibits the most potent and selective anticancer activity among the tested compounds. Complex **2c** reduced the viability of DU-145 and PC-3 prostate cancer cells more effectively than cisplatin at later time points while showing lower toxicity toward

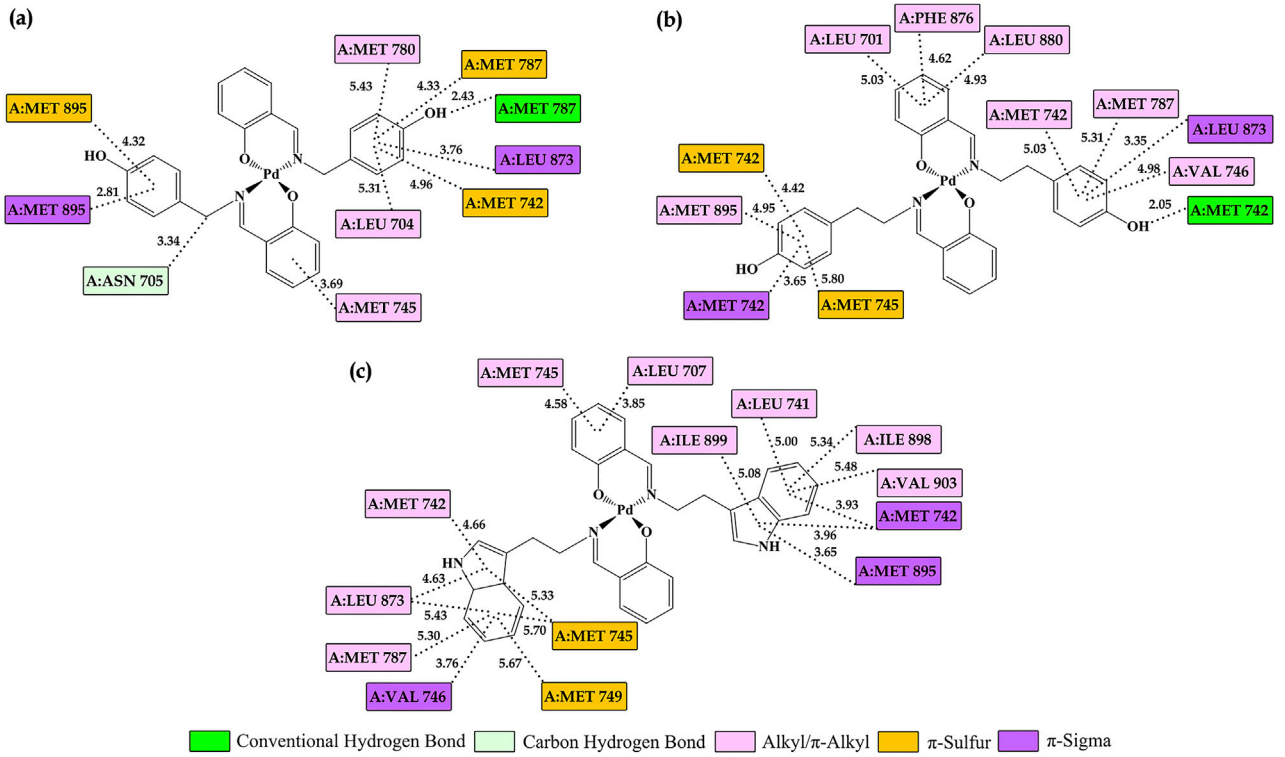


FIGURE 12
Visualization of key interactions between the Androgen Receptor **(AR)** and **(a) 2a**, **(b) 2b**, and **(c) 2c** in a 2D representation. Interatomic distances are measured in Å, with different colors indicating various interaction types, as described in the legend.

TABLE 7 Thermodynamic parameters (kcal/mol) of Pd complexes at the active sites of caspase 3 (CASP3), Bcl-2-associated X protein (BCL2), and anti-apoptotic B-cell lymphoma 2 (BAX) determined after molecular docking simulations.

Complex	ΔG_{bind}	Ki (μM)	ΔG_{inter}	$\Delta G_{vdw\ +\ hbond\ +\ desolv}$	ΔG_{elec}	ΔG_{total}	ΔG_{tor}	ΔG_{unb}
2a								
CASP3	−7.88	1.66	−9.53	−9.49	−0.04	−1.18	1.65	−1.18
BCL2	−7.92	1.56	−9.57	−9.39	−0.18	−1.39	1.65	−1.39
BAX	−7.68	2.36	−9.32	−9.27	−0.05	−1.54	1.65	−1.54
2b								
CASP3	−7.98	1.42	−10.17	−9.92	−0.25	−1.90	2.20	−1.90
BCL2	−8.08	1.20	−10.27	−10.22	−0.06	−1.87	2.20	−1.87
BAX	−6.86	9.31	−9.06	−8.98	−0.08	−2.18	2.20	−2.18
2c								
CASP3	−8.81	0.35	−10.46	−10.41	−0.05	−2.89	1.65	−2.89
BCL2	−8.26	0.88	−9.91	−9.85	−0.06	−2.91	1.65	−2.91
BAX	−8.44	0.65	−10.09	−10.11	0.02	−2.72	1.65	−2.72

non-cancerous fibroblasts, suggesting improved therapeutic selectivity. Mechanistically, **2c** triggered apoptosis via the intrinsic mitochondrial pathway, as evidenced by Bax upregulation, Bcl-2 downregulation, caspase-3 activation, mitochondrial membrane potential loss, and G0/G1 cell cycle arrest. Fluorescence displacement assays confirmed that **2c** interacts with DNA via both intercalation and minor groove binding, with a preference for the latter. Molecular docking supported these findings, revealing strong and specific binding of **2c** to pro-apoptotic proteins (caspase-3, Bax), with moderate affinity for anti-apoptotic Bcl-2. Although AR-negative cell lines were used in this study, complex **2c** also showed a high predicted binding affinity for the androgen receptor,

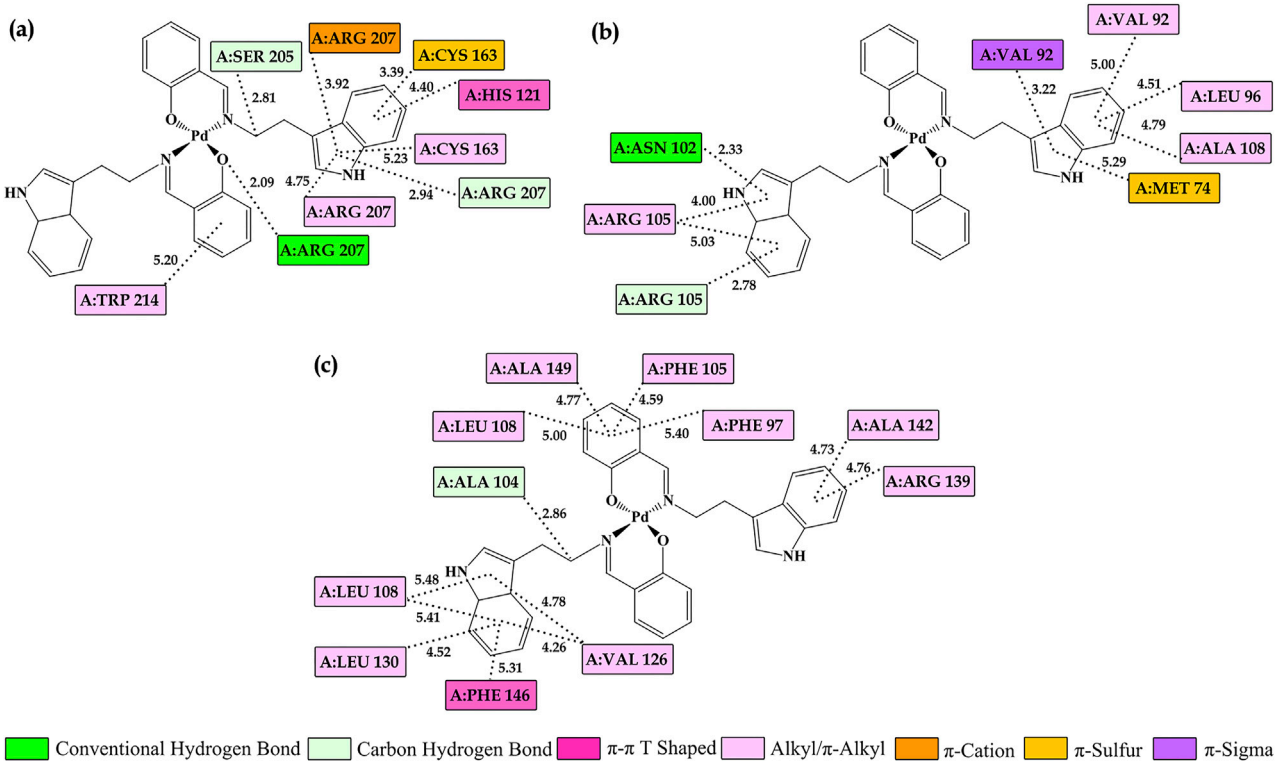


FIGURE 13
Visualization of key interactions between the **2c** and **(a)** caspase 3 **(CASP3)**, **(b)** Bcl-2-associated X protein **(BCL2)**, and **(c)** anti-apoptotic B-cell lymphoma 2 **(BAX)** in a 2D representation. Interatomic distances are measured in Å, with different colors indicating various interaction types, as described in the legend.

suggesting potential applicability in AR-positive prostate cancer models. These combined results suggest that complex **2c** exerts its cytotoxic effects through a multi-targeted mechanism involving DNA engagement, apoptosis induction, and modulation of key signaling proteins, highlighting its promise as a candidate for further development in prostate cancer therapy.

3 Materials and Methods

3.1 General procedures

3.1.1 General procedures and materials

All chemicals were used without purification, and all of them are commercially available. ^{1}H NMR and ^{13}C NMR spectra were recorded in DMSO-d_6 as a solvent with a Bruker Ascend 400 (400 MHz) spectrometer. Chemical shifts are given in parts per million (δ) down from tetramethylsilane as the internal standard. For elemental analyses (C, H, O, N) were used Elementar Vario MICRO elemental analyzer. IR spectra were obtained on Perkin Elmer FT-IR spectrometer, two equipped with a DTGS detector. Mass spectra were recorded at 6546 LC/Q-TOF (Agilent, Santa Clara, CA, SAD) equipped with Jet Stream ion source and connected with 1,290 Infinity II HPLC (Agilent, Santa Clara, CA, AD). Data were collected every second in the mass area 100–1,000 Da. Molar conductance of the Pd(II) complexes was measured on freshly prepared 10^{-3} M solutions in DMSO at room temperature using Crison EC-Meter basic 30+conductivity cell. The viscosity of the DNA solution was measured in the absence and presence of increasing amounts of **2c**. To the 0.01 mM DNA solution in PBS, a corresponding ratio of examinated compound was added at ratio [**2c**]/[DNA]: 0.1; 0.2; 0.3; 0.4; 0.5; 0.6; 0.7; 0.8; 0.9 and 1. Data are presented as a plot of (η/η0)1/3 vs. ratio of [**2c**]/[DNA], where η is the DNA viscosity in the presence of the compound, η0 is the viscosity of DNA in buffer alone.

3.1.2 General procedure for the synthesis of ligand compounds 1a–1c

15 mL of absolute ethanol and 1 mmol of the corresponding amine (*p*-OH benzyl amine for **1a**, tyramine for **1b**, and tryptamine for **1c**) were added to a 50 mL flask. After dissolving the amine, an equal amount of salicylic aldehyde was added, and the reaction mixture was stirred at room temperature overnight. The obtained solid products were filtered, washed with cold ethanol, and dried in an air atmosphere. The spectral data for the compounds were in agreement with those previously published (Babić et al., 2025; Marjanović et al., 2024). The corresponding spectra of all ligands compounds are given in Supplementary Material.

3.1.3 Experimental procedure for the synthesis of palladium complexes 2a–2c

0.0001 mol of the corresponding Schiff base ligand (**1a–1c**) was dissolved in 5 mL of acetonitrile and subsequently equivalent of K_2PdCl_4 was added in one portion. The resulted mixture was stirred

at room temperature for 4 h. The obtained solid products were filtered, washed thoroughly with ethanol and dried under air atmosphere. The obtained palladium complexes **2a–2c** were characterized by ^{1}H and ^{13}C NMR, IR, MS spectra and elemental analysis.

2a: Yellow powder. Yield 84%. ^{1}H NMR (400 MHz, DMSO-d_6) δ 9.35 (s, 2H, *p*-OH-benzylamine-O-H), 8.20 (s, 2H, -N=C-H), 7.56–7.05 (m, 4H, from salicylaldehyde-Ar-H and 4H from *p*-OH-benzylamine-Ar-H), 6.93–6.47 (m, 8H, 4H from salicylaldehyde-Ar-H and 4H from *p*-OH-benzylamine-Ar-H), 4.82 (s, 4H, -CH2-).^{13}C NMR (101 MHz, DMSO-d_6) δ 163.69, 163.26, 157.68, 156.56, 134.66, 130.47, 129.56, 129.12, 124.04, 120.30, 119.68, 115.21, 114.93, 57.41. IR (cm^{-1}): 1,615 ν(C=N), 513 ν(Pd–N), 461 ν(Pd–O).Anal. Found: C, 60.28; H, 4.41; N, 5.12. Calc. for $C_{28}H_{24}N_2O_4Pd$: C, 60.17; H, 4.33; N, 5.01.

2b: Orange powder. Yield 75%. ^{1}H NMR (400 MHz, DMSO-d_6) δ 9.21 (s, 2H, tyramine-OH), 7.88 (s, 2H, -N=C-H), 7.27 (dd, J = 7.5, 5.7 Hz, 4H from tyramine-ArH and salicilal. ArH), 7.10 (d, J = 8.4 Hz, 4H, *p*-OH-benzylamine-Ar-H), 6.82–6.52 (m, 8H, 4H, salicilal.-ArH and tyramine-Ar-H), 3.87 (t, J = 7.4 Hz, 4H -CH_2-), 2.91 (t, J = 7.5 Hz, 4H -CH_2-). ^{13}C NMR (101 MHz, DMSO-d_6) δ 163.54 (-N=C-), 163.06, 155.72, 134.55, 129.83, 128.90, 120.21, 119.59, 115.19, 114.82, 58.44, 37.42. IR (cm^{-1}): 1,611 ν(C=N), 506 ν(Pd–N), 460 ν(Pd–O). Anal. Found: C, 61.49; H, 4.74; N, 4.85. Calc. for $C_{30}H_{28}N_2O_4Pd$: C, 61.39; H, 4.81; N, 4.77.

2c: Dark red-brown powder. Yield 78%. ^{1}H NMR (400 MHz, DMSO-d_6) δ 10.96 (s, 2H, -N-H), 7.96 (s, 2H, -N=C-H), 7.6–6.90 (m, 2H, tryptamine-Ar-H; m, 6H, 4H from salicyal.-Ar-H, 2H from tryptamine Ar-H; 2H, tryptamine-Ar-H and 2H, tryptamine-Ar-H, 2H, tryptamine-Ar-H; 4H, salicylal.-Ar-H), second triplet from the CH_2 group overlapped with the H_2O peak, 3.02 (t, J = 8.0 Hz, 4H, -CH_2-). ^{13}C NMR (101 MHz, DMSO-d_6) δ 164.06 (-N=C-), 163.34, 136.76, 136.66, 129.73, 127.24, 123.83, 121.66, 118.97, 118.54, 117.70, 115.24, 112.02, 111.68, 57.85, 28.51. IR (cm^{-1}): 1,618 ν(C=N), 559 ν(Pd–N), 453 ν(Pd–O). Anal. Found: C, 64.38; H, 4.72 N 8.79. Calc. for $C_{34}H_{30}N_4O_2Pd$: C, 64.51; H, 4.78; N, 8.85.

3.2 *In vitro* cytotoxic study

3.2.1 Cell cultures

In this investigation, two experimental groups of cancer cell lines were employed: human prostate carcinoma cells lacking prostate-specific membrane antigen (PSMA) and androgen receptor independence (DU-145 and HTB-81™), alongside human prostate carcinoma cells (PC-3 and CRL-1435™). The control group comprised non-cancerous human fibroblasts (MRC-5 and CCL-171™). All cell lines utilized in this study were procured from the American Type Culture Collection (ATCC, Manassas, VA, United States). The cells were maintained in a complete medium containing high-glucose DMEM, supplemented with 10% fetal bovine serum and 200 mM L-glutamine (reagents sourced from Sigma-Aldrich, St. Louis, MO, United States). Cultivation of the cells was conducted in 25 cm^2 flasks (Thermo Fisher Scientific, Waltham, MA, United States) at 37°C under conditions of absolute humidity and a 5% CO_2 atmosphere.

3.2.2 MTT assay

The cytotoxic effects of three newly synthesized Pd(II) complexes were assessed on DU-145, PC-3, and MRC-5 cell lines using the MTT assay. For comparison, the cytotoxicity of cisplatin, a clinically established chemotherapeutic agent, was also evaluated across all cell lines. Cells were harvested during their exponential growth phase, counted, and seeded at a density of 5 × 10^3 cells per well in 96-well culture plates. Following an initial 24-h incubation at 37°C in a humidified atmosphere with 5% CO_2, the cells were treated with varying concentrations of Pd(II) complexes and cisplatin (0.3, 1, 3, 10, 30, and 100 μM), alongside a control group maintained in complete medium. The treated cells were incubated under identical conditions (37°C, 5% CO_2, absolute humidity) for durations of 24, 48, and 72 h. After incubation, the medium was removed, and an MTT solution was added to each well. The cells were then incubated for an additional 2 h to facilitate the reduction of thiazolyl blue tetrazolium bromide in the MTT solution. Subsequently, the MTT solution was carefully removed, and the resulting formazan crystals were solubilized in DMSO. The plates were shaken in the dark for 10 min before measuring the absorbance of the purple-colored solution at 595 nm using a microplate reader (Zenyth 3,100, Anthos Labtec Instruments, Salzburg, Austria). All experiments were performed in triplicate and repeated across three independent runs. Cell viability was calculated as a percentage by dividing the absorbance of treated cells (minus blank absorbance) by the average absorbance of untreated control cells (minus blank absorbance) and multiplying by 100.

$$\%\ \text{of the viable cells} = (\,(\text{absorbance of treated cell} - \text{absorbance of blank}) \,/\, (\text{absorbance of untreated cell} - \text{absorbance of blank})\,) * 100$$

The IC_{50} values, representing the concentration required to reduce cell viability by 50% relative to the control, were calculated by fitting the logarithmically transformed dose-response data obtained from the MTT assay. This analysis was performed using Microsoft Office Excel 2010, leveraging its curve-fitting capabilities to determine precise inhibitory concentrations.

3.2.3 Annexin V/7AAD assay

The mode of cell death triggered by Pd(II) complexes **2a–2c** was assessed using the Annexin V–fluorescein isothiocyanate (FITC)/propidium iodide (PI) Apoptosis Kit (BD Biosciences, Franklin Lakes, NJ, United States). DU-145 cells were exposed to the respective IC_{50} concentrations of the **2a–2c** complexes or cultured in media alone as a control for 24 h at 37°C in a humidified atmosphere with 5% CO_2. Following incubation, the cells were trypsinized, washed with phosphate-buffered saline (PBS), centrifuged, and resuspended in 100 μL of ice-cold binding buffer. Subsequently, the cells were stained with 10 μL of Annexin V-FITC and 20 μL of PI, incubated for 15 min at room temperature in the dark, and then supplemented with 400 μL of binding buffer per tube. Flow cytometric data were analyzed using a standardized gating strategy to ensure accurate identification of cell populations. Initially, cell debris and doublets were excluded based on forward and side scatter properties. Subsequent gating was performed on singlet populations to minimize aggregation artifacts. For apoptosis assessment using Annexin V-FITC and propidium iodide (PI),

compensation was applied using single-stained controls to correct for spectral overlap. Unstained and untreated control samples were used to establish baseline fluorescence and define quadrant boundaries. Cells were then categorized into four populations: viable (Annexin V−/PI−), early apoptotic (Annexin V+/PI−), late apoptotic or secondary necrotic (Annexin V+/PI+), and necrotic (Annexin V−/PI+). A minimum of 10,000 events per sample were recorded, and all gates were applied consistently. The samples were analyzed using a Cytomics FC500 flow cytometer (Beckman Coulter, Brea, CA, United States), and the data were processed with FlowJo V10 Software. The results were presented as density plots illustrating Annexin V-FITC and PI staining patterns.

3.2.4 Cell cycle

The next phase of the research involved investigating the effects of Pd(II) complexes **2a–2c** on the cell cycle progression of DU-145 cells. DU-145 cells were treated with IC_{50} concentrations of Pd(II) complexes **2a–2c** and cisplatin, or cultured in media alone as a control, for 24 h at 37°C under conditions of 5% CO_2 and absolute humidity. Following incubation, the cells were harvested, washed with phosphate-buffered saline (PBS), and fixed in 70% ethanol at +4°C. The fixed cells were aggregated and resuspended in 1 mL PBS containing RNAse A (500 μg/mL). After a 30-min incubation at 37°C, the cells were stained with 5 μL propidium iodide (PI) solution (10 mg/mL PBS). The samples were incubated for an additional 15 min in the dark and subsequently analyzed using a flow cytometer. Cell cycle distribution data were processed using FlowJo V10 Software and presented as histograms.

3.2.5 Assessment of apoptosis

Our research focused on examining the expression levels of the pro-apoptotic protein Bax, the anti-apoptotic protein Bcl-2, and the percentage of cells containing active caspase-3. DU-145 cells were incubated for 24 h with the IC_{50} concentrations of Pd(II) complexes **2a–2c** or in complete cell culture medium as a control. Following incubation, the cells were washed three times with ice-cold PBS, resuspended, fixed, and permeabilized using a Fixation and Permeabilization Kit (eBioscience, San Diego, CA, United States). For Bcl-2 staining, cells were incubated with a 1:1,000 Bcl-2 fluorescein isothiocyanate (FITC) primary antibody (mhbcl01, Life Technologies, Thermo Fisher Scientific, Waltham, MA, United States) for 15 min at room temperature. Additional staining involved incubating permeabilized DU-145 cells for 30 min with 1:1,000 primary antibodies for active Bax (N20, sc-493; Santa Cruz Biotech Inc., Dallas, TX, United States) and cleaved caspase-3 (#9661, Cell Signaling Technology, Danvers, MA, United States). Cells were then washed with PBS and incubated with a 1:2000 secondary goat anti-rabbit IgG-FITC antibody (Ab6717-1, Abcam, Cambridge Biomedical Campus, Cambridge, United Kingdom) for 30 min. Subsequently, cells were washed in PBS and analyzed by flow cytometry. Fluorescence from at least 15,000 events per sample was measured using a Cytomics FC500 flow cytometer (Beckman Coulter, Brea, CA, United States). Fluorescence intensity was standardized using isotype-matched negative control antibodies. The mean fluorescence intensities (MFIs) for Bax and Bcl-2 were calculated as the ratio of raw mean channel fluorescence to isotype control levels, respectively, and represented the expression levels of these proteins. The concentrations of cleaved caspase-3 were evaluated as the percentages of cells displaying fluorescence.

3.2.6 Clonogenic assay

In this assay (Franken et al., 2006), cells are seeded at low densities and incubated for 2 weeks to allow colony formation, with colonies defined as clusters of ≥50 cells. Treated and untreated cells are compared to assess survival fractions (SF), calculated by normalizing the plating efficiency (PE) of treated cells to that of controls. Colonies are fixed with 6% glutaraldehyde, stained with 0.5% crystal violet, and colonies were quantified using ImageJ software version 1.54 with a standardized macro. Images were first converted to 8-bit grayscale, and background noise was reduced using the "Subtract Background" function. Thresholding was applied to isolate colonies, and the "Analyze Particles" tool was used to count colonies based on defined size and circularity parameters. Only colonies with an area corresponding to ≥50 cells and a circularity range of 0.3–1.0 were included. Overlapping or merged colonies were excluded unless distinct borders were visually discernible. All image processing steps were applied consistently across samples to ensure reproducibility. Data are represented as dose-response survival curves.

Plating efficiency is calculated by the following formula:

$$PE = \frac{Number\ of\ colonies}{Number\ of\ cells\ seeded} \times 100\%$$

Survival fraction is calculated when all plating efficiencies are calculated according to the formula:

$$SF = \frac{PE_{treated}}{PE_{control}}$$

3.2.7 Assessment of mitochondrial membrane potential by JC-10 immunofluorescence staining

JC-10 gathers in the mitochondria of living cells, forming red fluorescence aggregates. On the other hand, JC-10 is also present in a monomeric cytosolic form and dyes cells green in necrotic and apoptotic cells. Mitochondrial membrane potential was assessed using the dye JC-10. DU-145 cells were seeded at a density of 2×10^4 cells per well in 24-well cell culture plates and incubated in complete DMEM medium at 37°C with 5% CO_2 for 24 h. The cells were treated with palladium complexes **2a–2c** at their IC_{50} concentrations for a duration of 48 h. The cells were treated for 20 min with 2.5 μM JC-10 dye in warm PBS. JC-10 accumulation in cells was evaluated using a Gramma Libero FLUO500T trinocular inverted fluorescence microscope. We used the 525/590 nm fluorescence emission ratio for our quantification analysis. We captured images using the 2020 S-EYE Setup Microscope camera and the S-EYE_Setup-1.6.0.11 software. The ImageJ program was used to analyse the images.

3.3 DNA interaction study

The EB/Hoe-competitive studies of complex **2c** were made using fluorescence emission spectroscopy. DNA-EB and DNA-Hoe solutions were prepared by mixing 100 μM EB/Hoe and 40 μM

CT-DNA in phosphate buffered saline buffer at pH = 7.4. The fluorescence spectra were recorded immediately after the addition of an increasing amounts of compound **2c** (0–100) into the solution of DNA-EB or DNA-Hoe to investigate the possible binding effect of tested compound. The excitation wavelength was 527 nm for EB and 346 nm for Hoe, respectively, while emission was recorded in the wavelengths ranges 550–750 nm for EB and 360–600 nm for Hoe.

3.4 Stability assay

The complex used for the testing was dissolved in the minimal amount of DMSO (dimethylsulfoxide) possible and diluted with PBS of ~10^{-5} M in concentration and less than 0.7% DMSO. UV-Vis spectra were recorded after 0, 24 and 48 h in the range 200–600 nm. Absorption spectra were recorded on UV–Vis Perkin–Elmer Lambda 35 spectrophotometer equipped with water thermostated cell.

3.5 Computational study

A computational approach was employed to assess the binding affinity and inhibitory potential of **2a–2c** complexes toward androgen receptor (AR), caspase 3 (CASP3), B-cell lymphoma 2 (BCL2), and Bcl-2-associated X protein (BAX). The molecular structures of the studied complexes were initially optimized using the *Gaussian16* software package (Frisch et al., 2019), applying the B3LYP–D3BJ functional (Zhao et al., 2006). The 6–311+G (d,p) basis set was applied for C, N, O, and H atoms, while Pd atoms were treated with the def2-TZVPD basis set (Becke and Johnson, 2005) incorporating an effective core potential. This optimization ensured accurate geometric and electronic properties, providing a solid foundation for further computational studies. The crystallographic structures of the target proteins were retrieved from the RCSB Protein Data Bank: AR (PDB code: 1Z95) (Bohl et al., 2005), CASP3 (PDB code: 3KJF) (Wang et al., 2010), BCL2 (PDB code: 2W3L) (Porter et al., 2009), and BAX (PDB code: 2YXJ) (Lee et al., 2007). The preparation of protein structures was carried out using BIOVIA Discovery Studio 4.0 (BIOVIA, 2024), where non-essential heteroatoms, co-crystallized ligands, and water molecules were removed. This step ensured unobstructed access to the active site, creating optimal conditions for docking. Molecular docking simulations were performed using AutoDock Tools 1.5.7, integrated with AutoDock 4.2.6 (Morris et al., 1998). The Lamarckian Genetic Algorithm (LGA) (Fuhrmann et al., 2010) optimized ligand conformations within a rigid protein framework. To comprehensively encompass the binding regions, docking grids were defined for each target protein: AR (69 × 69 × 69 $Å^3$, centered at 27.977 × 2.357 × 6.252 Å), CASP3 (56 × 56 × 56 $Å^3$, centered at 21.577 × −5.202 × 10.866 Å), BCL2 (66 × 66 × 66 $Å^3$, centered at 39.806 × 26.936 × −12.415 Å), and BAX (69 × 69 × 69 $Å^3$, centered at −9.874 × −14.522 × 10.799 Å), with a uniform grid spacing of 0.375 Å. During the docking process, ligand flexibility was allowed, while the protein structure remained rigid, ensuring the identification of potential binding modes accurately. The LGA parameters were set to include a population size of 150, a maximum of 2,500,000 energy evaluations over 27,000 generations, a mutation rate of 0.02, and a crossover rate of 0.8. This approach enabled a comprehensive analysis of ligand-protein interactions, providing valuable insights into the inhibitory potential of Pd-based complexes.

4 Conclusion

Three new palladium complexes **2a–2c**, derived from Schiff base ligands combing salicylic and tyramine/tryptamine or *p*-hydroxyl benzylamine scaffolds in structure, have been synthesized and characterized. The complexes displayed potent anti-proliferative activity against both human prostate cancer cell lines PC-3 and DU-145 and good selectivity between cancer and normal cells. Complex **2c,** combining salicylic and tryptamine structural motifs, has demonstrated even better activity than cisplatin for both tested cell lines, with IC_{50} values of 7.1 μM (DU-145) and 8.6 μM (PC-3). The apoptotic assay has revealed the potential of complexes for apoptosis induction through the Bcl-2 and caspase family activation pathways. Molecular docking studies revealed that complex **2c** exhibits the strongest binding affinity toward the androgen receptor (AR), surpassing the reference inhibitor bicalutamide. Additionally, **2c** showed selective interactions with pro-apoptotic proteins **CASP3** and **BAX**, involving stable non-covalent forces such as hydrophobic contacts, π-π stacking, π-sulfur, and hydrogen bonds. These interactions suggest a dual mechanism of action–AR inhibition and pro-apoptotic modulation–supporting **2c**'s potential as a multifunctional anticancer agent. Taken together, these findings highlight the therapeutic potential of palladium complex **2c** as a promising lead compound for the development of new, multitarget anticancer agents, particularly in the treatment of prostate cancer. In conclusion, the synthesized palladium complexes demonstrated promising *in vitro* anticancer activity, indicating their potential as lead compounds for further development. However, a limitation of the present study is the absence of *in vivo* data, which is essential to fully assess the therapeutic potential and safety profile of these complexes under physiological conditions. Future research should focus on evaluating the efficacy and toxicity of these compounds in appropriate *in vivo* models to support their progression toward clinical relevance.

Data availability statement

The original contributions presented in the study are included in the article/Supplementary Material, further inquiries can be directed to the corresponding authors.

Ethics statement

Ethical approval was not required for the studies on humans in accordance with the local legislation and institutional requirements because only commercially available established cell lines were used.

Author contributions

DP: Methodology, Investigation, Conceptualization, Writing – original draft, Formal Analysis, Writing – review and editing, Project administration, Funding acquisition. NM: Investigation, Writing – review and editing, Project administration, Funding acquisition, Writing – original draft, Formal Analysis, Methodology. TV: Investigation, Validation, Writing – original draft, Funding acquisition, Writing – review and editing, Resources. DJ: Validation, Investigation, Writing – review and editing, Funding acquisition, Writing – original draft, Resources. SJ: Resources, Writing – review and editing, Writing – original draft, Software. PC: Project administration, Methodology, Data curation, Formal Analysis, Supervision, Validation, Visualization, Funding acquisition, Writing – original draft, Conceptualization, Investigation, Writing – review and editing, Resources. MZ: Writing – review and editing, Writing – original draft, Visualization, Software. RZ: Formal Analysis, Writing – review and editing, Writing – original draft. MK: Writing – original draft, Visualization, Methodology, Validation, Investigation, Writing – review and editing, Resources. JD: Formal Analysis, Writing – review and editing, Writing – original draft. VD: Methodology, Writing – review and editing, Writing – original draft, Formal Analysis. ZM: Writing – review and editing, Methodology, Writing – original draft, Software, Validation. KM: Writing – original draft, Software, Formal Analysis, Writing – review and editing. MM: Writing – review and editing, Formal Analysis, Writing – original draft, Investigation, Validation. IZ: Visualization, Funding acquisition, Resources, Validation, Investigation, Writing – original draft, Writing – review and editing.

Funding

The author(s) declare that financial support was received for the research and/or publication of this article. This work was supported by the Ministry of Science, Technological Development, and Innovations of the Republic of Serbia [Agreements No. 451-03-137/2025-03/200111; 451-03-136/2025-03/200111; 451-03-136/2025-03/200378; 451-03-137/2025-03/200122 and 451-03-136/2025-03/200122].

Acknowledgments

We would like to thank Professor Darko Anđelković for the generous help in the realization and interpretation of mass analysis.

Conflict of interest

The authors declare that the research was conducted in the absence of any commercial or financial relationships that could be construed as a potential conflict of interest.

Generative AI statement

The author(s) declare that no Generative AI was used in the creation of this manuscript.

Publisher's note

All claims expressed in this article are solely those of the authors and do not necessarily represent those of their affiliated organizations, or those of the publisher, the editors and the reviewers. Any product that may be evaluated in this article, or claim that may be made by its manufacturer, is not guaranteed or endorsed by the publisher.

Supplementary material

The Supplementary Material for this article can be found online at: https://www.frontiersin.org/articles/10.3389/fchem.2025.1636477/full#supplementary-material

References

Abdelaal, A. M., Sohal, I. S., Iyer, S. G., Sudarshan, K., Orellana, E. A., Ozcan, K. E., et al. (2024). Selective targeting of chemically modified miR-34a to prostate cancer using a small molecule ligand and an endosomal escape agent. *Mol. Ther. Nucleic Acids* 35, 102193. doi:10.1016/j.omtn.2024.102193

Abu-Surrah, A., and Kettunen, M. (2006). Platinum group antitumor chemistry: design and development of new anticancer drugs complementary to cisplatin. *Curr. Med. Chem.* 13, 1337–1357. doi:10.2174/092986706776872970

Al-Azzawi, M., Yılmaz, İ., and Bostancı, H. E. (2025). Synthesis and anti-cancer properties of Pd(II) and Pt(II) coordination compounds of heterocyclic Schiff base ligands. *J. Mol. Struct.* 1337, 142199. doi:10.1016/j.molstruc.2025.142199

Ali, I., Wani, W. A., and Saleem, K. (2013). Empirical formulae to molecular structures of metal complexes by molar conductance. *Synth. React. Inorg. Met. Nano-Met Chem.* 43, 1162–1170. doi:10.1080/15533174.2012.756898

Amin, L. H. T., Shawer, T. Z., El-Naggar, A. M., and El-Sehrawi, H. M. A. (2019). Design, synthesis, anticancer evaluation and docking studies of new pyrimidine derivatives as potent thymidylate synthase inhibitors. *Bioorg Chem.* 91, 103159. doi:10.1016/j.bioorg.2019.103159

Aslan, H. G., Akkoç, S., and Kökbudak, Z. (2020). Anticancer activities of various new metal complexes prepared from a Schiff base on A549 cell line. *Inorg. Chem. Commun.* 111, 107645. doi:10.1016/j.inoche.2019.107645

Aydinlik, S., Erkisa, M., Ari, F., Celikler, S., and Ulukaya, E. (2021). Palladium(II) complex enhances ROS-dependent apoptotic effects via autophagy inhibition and disruption of multiple signaling pathways in colorectal cancer cells. *Anticancer Agents Med. Chem.* 21, 1284–1291. doi:10.2174/1871520620666200929153804

Babić, S., Marjanović, J. S., Divac, V. M., Klisurić, O. R., Milivojević, D., Bogojeski, J. V., et al. (2025). Molecular docking study and *in vitro* evaluation of apoptotic effect of biogenic-amine-based N,O-Cu(II) complexes as potent antitumor agents. *J. Coord. Chem.* 78, 1007–1026. doi:10.1080/00958972.2025.2477589

Basaran, E., Gamze Sogukomerogullari, H., Cakmak, R., Akkoc, S., Taskin-Tok, T., and Köse, A. (2022). Novel chiral Schiff base palladium(II), nickel(II), copper(II) and iron(II) complexes: synthesis, characterization, anticancer activity and molecular docking studies. *Bioorg Chem.* 129, 106176. doi:10.1016/j.bioorg.2022.106176

Becke, A. D., and Johnson, E. R. (2005). A density-functional model of the dispersion interaction. *J. Chem. Phys.* 123, 154101. doi:10.1063/1.2065267

BIOVIA (2024). *Dassault systèmes BIOVIA*.

Bissantz, C., Kuhn, B., and Stahl, M. (2010). A medicinal chemist's guide to molecular interactions. *J. Med. Chem.* 53, 5061–5084. doi:10.1021/jm100112j

Bohl, C. E., Gao, W., Miller, D. D., Bell, C. E., and Dalton, J. T. (2005). Structural basis for antagonism and resistance of bicalutamide in prostate cancer. *Proc. Natl. Acad. Sci. U. S. A.* 102, 6201–6206. doi:10.1073/pnas.0500381102

Carneiro, T. J., Martins, A. S., Marques, M. P. M., and Gil, A. M. (2020). Metabolic aspects of palladium(II) potential anti-cancer drugs. *Front. Oncol.* 10, 590970. doi:10.3389/fonc.2020.590970

Chatterjee, B. (2003). The role of the androgen receptor in the development of prostatic hyperplasia and prostate cancer. *Mol. Cell Biochem.* 253, 89–101. doi:10.1023/A:1026057402945

Cross, J. M., Blower, T. R., Gallagher, N., Gill, J. H., Rockley, K. L., and Walton, J. W. (2016). Anticancer Ru II and Rh III piano-stool complexes that are histone deacetylase inhibitors. *Chempluschem* 81, 1276–1280. doi:10.1002/cplu.201600413

Culig, Z., and Puhr, M. (2024). Androgen receptor–interacting proteins in prostate cancer development and therapy resistance. *Am. J. Pathol.* 194, 324–334. doi:10.1016/j.ajpath.2023.12.003

Czarnomysy, R., Radomska, D., Szewczyk, O. K., Roszczenko, P., and Bielawski, K. (2021). Platinum and palladium complexes as promising sources for antitumor treatments. *Int. J. Mol. Sci.* 22, 8271. doi:10.3390/ijms22158271

Deljanin, M., Nikolic, M., Baskic, D., Todorovic, D., Djurdjevic, P., Zaric, M., et al. (2016). Chelidonium majus crude extract inhibits migration and induces cell cycle arrest and apoptosis in tumor cell lines. *J. Ethnopharmacol.* 190, 362–371. doi:10.1016/j.jep.2016.06.056

Demirbağ, B., Ballı, E., Yıldırım, M., Ünver, H., Temel, G., Yılmaz, M. K., et al. (2024). Investigation of the anticancer of photodynamic therapy effects by using the novel Schiff base ligand palladium complexes on human breast cancer cell line. *Chem. Pap.* 78, 7611–7621. doi:10.1007/s11696-024-03622-z

Dhivya, R., Jaividhya, P., Riyasdeen, A., Palaniandavar, M., Mathan, G., and Akbarsha, M. A. (2015). *In vitro* antiproliferative and apoptosis-inducing properties of a mononuclear copper(II) complex with dppz ligand, in two genotypically different breast cancer cell lines. *BioMetals* 28, 929–943. doi:10.1007/s10534-015-9877-1

Espino, J., Fernández-Delgado, E., Estirado, S., de la Cruz-Martinez, F., Villa-Carballar, S., Viñuelas-Zahínos, E., et al. (2020). Synthesis and structure of a new thiazoline-based palladium(II) complex that promotes cytotoxicity and apoptosis of human promyelocytic leukemia HL-60 cells. *Sci. Rep.* 10, 16745. doi:10.1038/s41598-020-73488-0

Felicio, R., Cavalheiro, E. T., and Dockal, E. (2001). Preparation, characterization and thermogravimetric studies of [N,N′-cis-1,2-cyclohexylene bis(salicylideneaminato)] cobalt(II) and [N,N′-(±)-trans-1,2-cyclo-hexylene bis(salicylideneaminato)]cobalt(II). *Polyhedron* 20, 261–268. doi:10.1016/S0277-5387(00)00620-3

Ferreira de Freitas, R., and Schapira, M. (2017). A systematic analysis of atomic protein–ligand interactions in the PDB. *Medchemcomm* 8, 1970–1981. doi:10.1039/C7MD00381A

Franken, N. A. P., Rodermond, H. M., Stap, J., Haveman, J., and van Bree, C. (2006). Clonogenic assay of cells *in vitro*. *Nat. Protoc.* 1, 2315–2319. doi:10.1038/nprot.2006.339

Frisch, M. J., Trucks, G. W., Schlegel, H. B., Scuseria, G. E., Robb, M. A., Cheeseman, J. R., et al. (2019). *Gaussian 16, revision C.01*. Wallingford: Gaussian, Inc.

Fuhrmann, J., Rurainski, A., Lenhof, H., and Neumann, D. (2010). A new Lamarckian genetic algorithm for flexible ligand-receptor docking. *J. Comput. Chem.* 31, 1911–1918. doi:10.1002/jcc.21478

Fujita, K., and Nonomura, N. (2019). Role of androgen receptor in prostate cancer: a review. *World J. Mens. Health* 37, 288–295. doi:10.5534/wjmh.180040

Galanski, M. S., Arion, V. B., Jakupec, M. A., and Keppler, B. K. (2003). Recent developments in the field of tumor-inhibiting metal complexes. *Curr. Pharm. Des.* 9, 2078–2089. doi:10.2174/1381612033454180

Geary, W. J. (1971). The use of conductivity measurements in organic solvents for the characterisation of coordination compounds. *Coord. Chem. Rev.* 7, 81–122. doi:10.1016/S0010-8545(00)80009-0

Gowdhami, B., Ambika, S., Karthiyayini, B., Ramya, V., Kadalmani, B., Vimala, R. T. V., et al. (2021). Potential application of two cobalt (III) Schiff base complexes in cancer chemotherapy: leads from a study using breast and lung cancer cells. *Toxicol Vitro* 75, 105201. doi:10.1016/j.tiv.2021.105201

Gupta, G., Cherukommu, S., Srinivas, G., Lee, S. W., Mun, S. H., Jung, J., et al. (2018). Bodipy-based Ru(II) and Ir(III) organometallic complexes of avobenzone, a sunscreen material: potent anticancer agents. *J. Inorg. Biochem.* 189, 17–29. doi:10.1016/j.jinorgbio.2018.08.009

Hernández, W., Paz, J., Carrasco, F., Vaisberg, A., Spodine, E., Manzur, J., et al. (2013). Synthesis and characterization of new palladium(II) thiosemicarbazone complexes and their cytotoxic activity against various human tumor cell lines. *Bioinorg. Chem. Appl.* 2013, 1–12. doi:10.1155/2013/524701

Hosseini-Yazdi, S. A., Mirzaahmadi, A., Khandar, A. A., Eigner, V., Dušek, M., Lotfipour, F., et al. (2017). Synthesis, characterization and *in vitro* biological activities of new water-soluble copper(II), zinc(II), and nickel(II) complexes with sulfonato-substituted Schiff base ligand. *Inorganica Chim. Acta* 458, 171–180. doi:10.1016/j.ica.2017.01.005

Hussain, I., Ullah, A., Khan, A. U., Khan, W. U., Ullah, R., Almoqbil, A., et al. (2019). Synthesis, characterization and biological activities of hydrazone Schiff base and its novel metals complexes. *Sains Malays.* 48, 1439–1446. doi:10.17576/jsm-2019-4807-13

Kacar, O., Cevatemre, B., Hatipoglu, I., Arda, N., Ulukaya, E., Yilmaz, V. T., et al. (2017). The role of cell cycle progression for the apoptosis of cancer cells induced by palladium(II)-saccharinate complexes of terpyridine. *Bioorg Med. Chem.* 25, 1770–1777. doi:10.1016/j.bmc.2017.01.033

Kamel, M. M., Abdel-hameid, M. K., El-Nassan, H. B., and El-Khouly, E. A. (2019). Synthesis and cytotoxicity evaluation of novel indole derivatives as potential anti-cancer agents. *Med. Chem. (Los Angeles)* 15, 873–882. doi:10.2174/1573406415666190408125514

Kamel, M. M., Ali, H. I., Anwar, M. M., Mohamed, N. A., and Soliman, A. M. (2010). Synthesis, antitumor activity and molecular docking study of novel sulfonamide-Schiff's bases, thiazolidinones, benzothiazinones and their C-nucleoside derivatives. *Eur. J. Med. Chem.* 45, 572–580. doi:10.1016/j.ejmech.2009.10.044

Kandeel, M. M., AbdElhameid, M. K., Adel, M., Al-Shorbagy, M. Y., and Negmeldin, A. T. (2025). Design, synthesis, and cytotoxicity evaluation of novel indolin-2-one based molecules on hepatocellular carcinoma HepG2 cells as protein kinase inhibitors. *Molecules* 30, 1105. doi:10.3390/molecules30051105

Khaldoune, K., Hasnaoui, A., Fdil, N., Oubella, A., Lafhal, K., Oubahmane, M., et al. (2023). Exploring anticancer activity, acute toxicity, and molecular docking of synthesized Schiff bases and Schiff base-palladium complex. *Inorg. Chem. Commun.* 156, 111089. doi:10.1016/j.inoche.2023.111089

Klika, K. D., Alsalim, R., Eftekhari, M., and Makarem, A. (2022). Synthesis of a polyaminocarboxylate-based aluminum complex and its structural studies using 1H {13C}-HMBC NMR and a Karplus-type function. *Dalton Trans.* 51, 12436–12441. doi:10.1039/d2dt01702d

Klika, K. D., Han, J., Busse, M. S., Soloshonok, V. A., Javahershenas, R., Vanhaecke, F., et al. (2024). Inductively coupled plasma-mass spectrometry (ICP-MS): an emerging tool in radiopharmaceutical science. *J. Am. Chem. Soc.* 146, 30717–30727. doi:10.1021/jacs.4c12254

Kontek, R., Matławska-Wasowska, K., Kalinowska-Lis, U., Kontek, B., and Ochocki, J. (2011). Evaluation of cytotoxicity of new trans-palladium(II) complex in human cells *in vitro*. *Acta Pol. Pharm.* 68, 127–136.

Kostić, N. M., and Dutcă, L. M. (2003). "Palladium,". *Comprehensive coordination chemistry II*. Editors J. A. McCleverty and T. J. Meyer (Pergamon), 6, 555–672. doi:10.1016/B0-08-043748-6/05124-0

Laginha, R. C., Martins, C. B., Brandão, A. L. C., Marques, J., Marques, M. P. M., Batista de Carvalho, L. A. E., et al. (2023). Evaluation of the cytotoxic effect of Pd_2Spm against prostate cancer through vibrational microspectroscopies. *Int. J. Mol. Sci.* 24, 1888. doi:10.3390/ijms24031888

Lahmidi, S., Anouar, E. H., El Hafi, M., Boulhaoua, M., Ejjoummany, A., El Jemli, M., et al. (2019). Synthesis, X-ray, spectroscopic characterization, DFT and antioxidant activity of 1,2,4-triazolo[1,5-a]pyrimidine derivatives. *J. Mol. Struct.* 1177, 131–142. doi:10.1016/j.molstruc.2018.09.046

Lakowicz, J. R., Gryczynski, I., Gryczynski, Z., and Dattelbaum, J. D. (1999). Anisotropy-based sensing with reference fluorophores. *Anal. Biochem.* 267, 397–405. doi:10.1006/abio.1998.3029

Lakowicz, J. R., and Weber, G. (1973). Quenching of fluorescence by oxygen. Probe for structural fluctuations in macromolecules. *Biochemistry* 12, 4161–4170. doi:10.1021/bi00745a020

Lazarević, T., Rilak, A., and Bugarčić, Ž. D. (2017). Platinum, palladium, gold and ruthenium complexes as anticancer agents: current clinical uses, cytotoxicity studies and future perspectives. *Eur. J. Med. Chem.* 142, 8–31. doi:10.1016/j.ejmech.2017.04.007

Lee, E. F., Czabotar, P. E., Smith, B. J., Deshayes, K., Zobel, K., Colman, P. M., et al. (2007). Crystal structure of ABT-737 complexed with Bcl-XL: implications for selectivity of antagonists of the Bcl-2 family. *Cell Death Differ.* 14, 1711–1713. doi:10.1038/sj.cdd.4402178

Li, C., Cheng, D., and Li, P. (2025). Androgen receptor dynamics in prostate cancer: from disease progression to treatment resistance. *Front. Oncol.* 15, 1542811. doi:10.3389/fonc.2025.1542811

Li, D. D., Tian, J. L., Gu, W., Liu, X., and Yan, S. P. (2010). A novel 1,2,4-triazole-based copper(II) complex: synthesis, characterization, magnetic property and nuclease activity. *J. Inorg. Biochem.* 104, 171–179. doi:10.1016/j.jinorgbio.2009.10.020

Li, W., Wang, Y., Liu, X., Wu, S., Wang, M., Turowski, S. G., et al. (2024). Developing folate-conjugated miR-34a therapeutic for prostate cancer: challenges and promises. *Int. J. Mol. Sci.* 25, 2123. doi:10.3390/ijms25042123

Liu, P., Yang, Y., Tang, Y., Yang, T., Sang, Z., Liu, Z., et al. (2019). Design and synthesis of novel pyrimidine derivatives as potent antitubercular agents. *Eur. J. Med. Chem.* 163, 169–182. doi:10.1016/j.ejmech.2018.11.054

Ma, Z. Y., Qiao, X., Xie, C. Z., Shao, J., Xu, J. Y., Qiang, Z. Y., et al. (2012). Activities of a novel Schiff base copper(II) complex on growth inhibition and apoptosis induction toward MCF-7 human breast cancer cells via mitochondrial pathway. *J. Inorg. Biochem.* 117, 1–9. doi:10.1016/j.jinorgbio.2012.08.007

Mahadevi, A. S., and Sastry, G. N. (2013). Cation–π interaction: its role and relevance in chemistry, biology, and material science. *Chem. Rev.* 113, 2100–2138. doi:10.1021/cr300222d

Makarem, A., Han, J., and Klika, K. D. (2025). Byproducts in the synthesis of [68Ga] Ga-PSMA-11. *Nat. Protoc.* doi:10.1038/s41596-025-01164-6

Marjanović, J. S., Ćoćić, D., Petrović, N., Kosanić, M., Kostić, M. D., and Divac, V. M. (2023). Histamine derived Schiff bases and corresponding spinaceamines – synthesis, characterization and biological evaluation. *J. Mol. Struct.* 1290, 135926. doi:10.1016/j.molstruc.2023.135926

Marjanović, J. S., Matić, J. D., Milanović, Ž., Divac, V. M., Kosanić, M. M., Petković, M. R., et al. (2024). Molecular modeling studies, *in vitro* antioxidant and antimicrobial assay and BSA affinity of novel benzyl-amine derived scaffolds as CYP51B inhibitors. *Mol. Divers.* doi:10.1007/s11030-024-11074-6

Mehralivand, S., Thomas, C., Puhr, M., Claessens, F., van de Merbel, A. F., Dubrovska, A., et al. (2024). New advances of the androgen receptor in prostate cancer: report from the 1st International Androgen Receptor Symposium. *J. Transl. Med.* 22, 71. doi:10.1186/s12967-024-04878-5

Meyer, E. A., Castellano, R. K., and Diederich, F. (2003). Interactions with aromatic rings in chemical and biological recognition. *Angew. Chem. Int. Ed.* 42, 1210–1250. doi:10.1002/anie.200390319

Morris, G. M., Goodsell, D. S., Halliday, R. S., Huey, R., Hart, W. E., Belew, R. K., et al. (1998). Automated docking using a Lamarckian genetic algorithm and an empirical binding free energy function. *J. Comput. Chem.* 19, 1639–1662. doi:10.1002/(SICI)1096-987X(19981115)19:14<1639::AID-JCC10>3.0.CO;2-B

Panchsheela Ashok, U., Prasad Kollur, S., Prakash Arun, B., Sanjay, C., Shrikrishna Suresh, K., Anil, N., et al. (2020). *In vitro* anticancer activity of 4(3H)-quinazolinone derived Schiff base and its Cu(II), Zn(II) and Cd(II) complexes: preparation, X-ray structural, spectral characterization and theoretical investigations. *Inorganica Chim. Acta* 511, 119846. doi:10.1016/j.ica.2020.119846

Plutín, A. M., Mocelo, R., Alvarez, A., Ramos, R., Castellano, E. E., Cominetti, M. R., et al. (2014). On the cytotoxic activity of Pd(II) complexes of N,N-disubstituted-N′-acyl thioureas. *J. Inorg. Biochem.* 134, 76–82. doi:10.1016/j.jinorgbio.2014.01.022

Podolski-Renić, A., Čipak Gašparović, A., Valente, A., López, Ó., Bormio Nunes, J. H., Kowol, C. R., et al. (2024). Schiff bases and their metal complexes to target and overcome (multidrug) resistance in cancer. *Eur. J. Med. Chem.* 270, 116363. doi:10.1016/j.ejmech.2024.116363

Porter, J., Payne, A., de Candole, B., Ford, D., Hutchinson, B., Trevitt, G., et al. (2009). Tetrahydroisoquinoline amide substituted phenyl pyrazoles as selective Bcl-2 inhibitors. *Bioorg Med. Chem. Lett.* 19, 230–233. doi:10.1016/j.bmcl.2008.10.113

Prathima, T. S., Choudhury, B., Ahmad, M. G., Chanda, K., and Balamurali, M. M. (2023). Recent developments on other platinum metal complexes as target-specific anticancer therapeutics. *Coord. Chem. Rev.* 490, 215231. doi:10.1016/j.ccr.2023.215231

Raza, M. K., Noor, A., and Samantaray, P. K. (2021). Ir(III) and Ru(II) complexes in photoredox catalysis and photodynamic therapy: a new paradigm towards anticancer applications. *ChemBioChem* 22, 3270–3272. doi:10.1002/cbic.202100469

Recio Despaigne, A., Da Silva, J., Da Costa, P., Dos Santos, R., and Beraldo, H. (2014). ROS-mediated cytotoxic effect of copper(II) hydrazone complexes against human glioma cells. *Molecules* 19, 17202–17220. doi:10.3390/molecules191117202

Sharma, N. K., Ameta, R. K., and Singh, M. (2016). Biological impact of Pd(II) complexes: synthesis, spectral characterization, *in vitro* anticancer, CT-DNA binding, and antioxidant activities. *Int. J. Med. Chem.* 2016, 1–10. doi:10.1155/2016/9245619

Shi, S., Yu, S., Quan, L., Mansoor, M., Chen, Z., Hu, H., et al. (2020). Synthesis and antitumor activities of transition metal complexes of a bis-Schiff base of 2-hydroxy-1-naphthalenecarboxaldehyde. *J. Inorg. Biochem.* 210, 111173. doi:10.1016/j.jinorgbio.2020.111173

Tarushi, A., Lafazanis, K., Kljun, J., Turel, I., Pantazaki, A. A., Psomas, G., et al. (2013). First- and second-generation quinolone antibacterial drugs interacting with zinc(II): structure and biological perspectives. *J. Inorg. Biochem.* 121, 53–65. doi:10.1016/j.jinorgbio.2012.12.009

Tarushi, A., Raptopoulou, C. P., Psycharis, V., Terzis, A., Psomas, G., and Kessissoglou, D. P. (2010). Zinc(II) complexes of the second-generation quinolone antibacterial drug enrofloxacin: structure and DNA or albumin interaction. *Bioorg Med. Chem.* 18, 2678–2685. doi:10.1016/j.bmc.2010.02.021

Thiriveedhi, A., Nadh, R. V., Srinivasu, N., Bobde, Y., Ghosh, B., and Sekhar, KVGC (2019). Design, synthesis and anti-tumour activity of new pyrimidine-pyrrole appended triazoles. *Toxicol Vitro* 60, 87–96. doi:10.1016/j.tiv.2019.05.009

Tsuzuki, S., Honda, K., Uchimaru, T., Mikami, M., and Tanabe, K. (2002). Origin of attraction and directionality of the π/π interaction: model chemistry calculations of benzene dimer interaction. *J. Am. Chem. Soc.* 124, 104–112. doi:10.1021/ja0105212

Ulukaya, E., Frame, F. M., Cevatemre, B., Pellacani, D., Walker, H., Mann, V. M., et al. (2013). Differential cytotoxic activity of a novel palladium-based compound on prostate cell lines, primary prostate epithelial cells and prostate stem cells. *PLoS One* 8, e64278. doi:10.1371/journal.pone.0064278

Valentini, A., Conforti, F., Crispini, A., De Martino, A., Condello, R., Stellitano, C., et al. (2009). Synthesis, oxidant properties, and antitumoral effects of a heteroleptic palladium(II) complex of curcumin on human prostate cancer cells. *J. Med. Chem.* 52, 484–491. doi:10.1021/jm801276a

Vojtek, M., Marques, M. P. M., Ferreira, IMPLVO, Mota-Filipe, H., and Diniz, C. (2019). Anticancer activity of palladium-based complexes against triple-negative breast cancer. *Drug Discov. Today* 24, 1044–1058. doi:10.1016/j.drudis.2019.02.012

Wang, Z., Watt, W., Brooks, N. A., Harris, M. S., Urban, J., Boatman, D., et al. (2010). Kinetic and structural characterization of caspase-3 and caspase-8 inhibition by a novel class of irreversible inhibitors. *Biochim. Biophys. Acta Proteins Proteom* 1804, 1817–1831. doi:10.1016/j.bbapap.2010.05.007

Zhao, Y., Schultz, N. E., and Truhlar, D. G. (2006). Design of density functionals by combining the method of constraint satisfaction with parametrization for thermochemistry, thermochemical kinetics, and noncovalent interactions. *J. Chem. Theory Comput.* 2, 364–382. doi:10.1021/ct0502763

frontiers | Frontiers in Chemistry

TYPE Original Research
PUBLISHED 28 July 2025
DOI 10.3389/fchem.2025.1597454

Check for updates

OPEN ACCESS

EDITED BY
Massimiliano Meli,
National Research Council (CNR), Italy

REVIEWED BY
Aashish Soni,
Essen University Hospital, Germany
Samanta Makurat,
University of Gdansk, Poland

*CORRESPONDENCE
Farhan Siddique,
drfarhansiddique@bzu.edu.pk
Nasir Jalal,
nasir.jalal@alumni.colostate.edu

RECEIVED 21 March 2025
ACCEPTED 09 July 2025
PUBLISHED 28 July 2025

CITATION
Bashir M, Abdullah U, Nazir S, Siddique F and Jalal N (2025) Computational advances in the design and discovery of artemis inhibitors for radiosensitization in cancer therapy.
Front. Chem. 13:1597454.
doi: 10.3389/fchem.2025.1597454

COPYRIGHT
© 2025 Bashir, Abdullah, Nazir, Siddique and Jalal. This is an open-access article distributed under the terms of the Creative Commons Attribution License (CC BY). The use, distribution or reproduction in other forums is permitted, provided the original author(s) and the copyright owner(s) are credited and that the original publication in this journal is cited, in accordance with accepted academic practice. No use, distribution or reproduction is permitted which does not comply with these terms.

Computational advances in the design and discovery of artemis inhibitors for radiosensitization in cancer therapy

Maryam Bashir[1], Usman Abdullah[2], Sadia Nazir[3], Farhan Siddique [1]* and Nasir Jalal [4]*

[1]Department of Pharmaceutical Chemistry, Faculty of Pharmacy, Bahauddin Zakariya University, Multan, Pakistan, [2]Department of Biomedical Sciences, Pak-Austria Fachhochschule, Haripur, Pakistan, [3]Atta ur Rahman School of Applied Biosciences, National University of Sciences and Technology, Islamabad, Pakistan, [4]Baiao Kuntai Biotechnology, China-Europe Innovation Center, Hangzhou, Zhejiang, China

Introduction: Artemis is a key scaffold repair protein involved in the non-homologous end-joining (NHEJ) DNA repair pathway and is encoded by the DCLRE1C gene in humans. Its inhibition disrupts double-strand break (DSB) repair, sensitizing cancer cells to ionizing radiation (IR). However, no Artemis-targeted inhibitors are currently available for therapeutic use. This study aims to identify and characterize novel small-molecule Artemis inhibitors that act as potential radiosensitizers in cancer treatment.

Methods: Micronuclei formation was assessed in Artemis-deficient (CJ179), proficient (1BR3), and mutant (48BR) cell lines following 1 Gy IR exposure. Initial in vitro screening identified HMAD as a potential Artemis inhibitor. A focused virtual screening of 69 compounds was performed using AutoDock4 and Glide to evaluate binding affinity to Artemis. The top 16 compounds ($\Delta G < -8.0$ kcal/mol) were further analyzed. Density Functional Theory (DFT) calculations at the B3LYP/6–311+G(d,p) level were used to assess frontier molecular orbitals and reactivity. ADMET profiling was conducted to evaluate pharmacokinetic properties. Compounds 42 and 51 were subjected to 100 ns molecular dynamics (MD) simulations with MMGBSA binding free energy calculations, PCA, and FEL analysis.

Results: CJ179 cells exhibited significantly higher micronuclei post-irradiation, confirming Artemis's role in DNA repair. Among the top hits, compound 42 showed a highly stable binding profile, with a favorable MMGBSA binding energy of −36.94 kcal/mol. ADMET analysis indicated optimal drug-like properties. MD simulations revealed stable interaction trajectories, hydrogen bonding, and a narrow binding pocket. PCA and FEL analysis further supported the dynamic stability of compound 42.

Discussion: This study identifies compound 42 as a promising Artemis inhibitor with potential as a radiosensitizing agent. The integrated *in vitro* and computational findings offer a foundation for further preclinical development, contributing to more effective radiotherapy strategies in cancer treatment.

KEYWORDS

ARTEMIS, radiosensitizers, DNA repair mechanism, DFT, MM-GBSA, free energy landscape

Introduction

Radiotherapy has been established as a highly effective treatment strategy for tumors. The ionizing radiation, used for radiotherapeutic purposes, relies on generating DNA double-strand breaks (DSB) in the target cancerous tissue (van de Kamp et al., 2021) that leads to eventual cell death. Radiosensitizers are believed to increase the therapeutic ratio by inhibiting the repair protein activation of DNA-PKcs, XRCC-ligase IV, and Artemis, which are involved in the DNA repair mechanism (van de Kamp et al., 2021). Several chemical inhibitors of DNA-dependent protein kinase catalytic subunit (DNA-PKcs), specifically NU7026 and AZD7648, have been used in versatile experimental scenarios as radiosensitizers (GLORIEUX, 2020). Recently, Artemis inhibition has been reported as a therapeutic strategy for acute lymphoblastic leukemia (Watanabe et al., 2022; Liu et al., 2018; Li et al., 2014) that effectively halted the DNA repair mechanism in irradiated cells, with negligible clinical consequences on normal cells (Watanabe et al., 2022). The small interfering RNA (siRNA) mediated Artemis inhibition increases the radiosensitivity of target colorectal cell line (RKO) cells *in vitro* (Liu et al., 2018). Small organic compounds such as ampicillin, ceftriaxone, ebselen, disulfiram, and auranofin hindered Artemis functioning with modest IC_{50} values (Li et al., 2014; Yosaatmadja et al., 2021), which has caught the attention of researchers who are seeking to identify small molecules as Artemis inhibitors in the development of radiosensitizers.

As part of the DNA double-strand break repair (DSBR) cascade, Artemis is phosphorylated for repair activation at S516 and S645 in unirradiated cells. Following treatment with DSB-inducing drug bleomycin, this phosphorylation is enhanced 10-15-fold (Soubeyrand et al., 2006). In addition to being a phosphorylation target of Ataxia-Telangiectasia Mutated (ATM) and DNA-PKcs, Artemis can also be phosphorylated by the Ataxia-Telangiectasia and Rad3-Related (ATR) kinase. However, it interacts with known cell cycle checkpoint proteins and becomes a target of ATM or ATR after exposure to ionizing radiation (IR) or ultraviolet (UV) radiation, respectively (Zhang et al., 2004). DSBs are among the most lethal forms of DNA damage, and their efficient repair is essential for the survival of cancer cells. One of the primary mechanisms for repairing these DSBs in mammalian cells is the non-homologous end joining (NHEJ) pathway, which is active during the G1 phase of the cell cycle. The NHEJ pathway is largely mediated by a complex of proteins, including DNA-PK, Ku70/80, and Artemis. Artemis plays a critical role in processing DNA ends to accelerate ligation during NHEJ, making it a needed component of the DNA repair machinery. DNA PK-dependent phosphorylation of Artemis after treatment with DSB-inducing agents increased the cellular retention of Artemis, maintained its interaction with DNA at DSBs, and also activated its endonucleolytic activity (Ma et al., 2005). While NHEJ is critical for maintaining genomic stability, it also contributes to the survival of cancer cells after radiation-induced damage. As such, targeting Artemis and other components of the NHEJ pathway has emerged as a promising strategy to enhance the efficacy of radiotherapy. Inhibiting Artemis could impair DNA repair, rendering cancer cells more susceptible to the lethal effects of radiation. This concept of radiosensitization, achieved through the inhibition of DNA repair pathways, could potentially improve treatment outcomes and overcome radioresistance in tumors that are refractory to radiation.

Artemis is a small (78 kDa) protein, a member of the metallo-β-lactamase family. It has both endonuclease and intrinsic 5′-exonuclease activity, while point mutation of the putative active site residue (H115A) can markedly reduce both endo and exonuclease activities. But it can be blocked by small yet specific molecule inhibitors (Li et al., 2014). The protein plays a role in the non-homologous end-joining pathway of DNA repair through its nuclease activity, facilitating the double-strand end processing following ionizing radiation exposure (Riballo et al., 2004). However, identifying and developing specific Artemis inhibitors remains a significant challenge. Traditional drug discovery approaches are time-consuming and expensive, making it essential to utilize computational methods to accelerate the identification of potential inhibitors.

Virtual high-throughput (vHTS) (Prieto-M et al., 2019; Aziz et al., 2022a) screening represented one of the most straightforward applications in drug design (Schmidtke and Barril, 2010; Agoni et al., 2020), employing a molecular docking program to determine how an entire database of existing or virtual compounds will bind to a specific target protein (Zoete et al., 2009). The commonly used docking programs, such as DOCK (Allen et al., 2015), AutoDock (Huey et al., 2007), Glide (Friesner et al., 2004), FlexX (Cross, 2005), GOLD (Verdonk et al., 2003), Surflex-Dock, MOE-Dock, and UCSF DOCK (Pagadala et al., 2017) rely on sampling algorithms (Huang and Zou, 2010) along with scoring functions (Schulz-Gasch and Stahl, 2004) to evaluate molecular interactions. This approach accelerated the drug discovery process by narrowing down vast libraries to a manageable number of promising candidates for detailed experimental testing (Zoete et al., 2009; Anwar et al., 2021). Artificial intelligence (AI) further aids in drug screening by predicting key physicochemical properties, influencing pharmacokinetics, and receptor target specificity (Zang et al., 2017). AI web-based tools like LimTox, SwissADME, admetSAR, ADMETlab3.0, Toxtree, and pkCSM can be used to predict physicochemical properties, thereby effectively reducing costs in drug development (Yang et al., 2019). Density Functional Theory (DFT)-based computations played a pivotal role by providing insights into the electronic properties (Tandon et al., 2019; Arshad et al., 2021), which are fundamental to understanding key molecular interactions, including covalent bonding, dipole-dipole and ion-dipole interactions, hydrogen bonding, hydrophobic effects, and charge transfer mechanisms. Such detailed analysis is crucial for elucidating the interaction dynamics between drug-like molecules and their biological targets, thereby enhancing therapeutics' rational design and optimization (Reimers et al., 2003; Tuma et al., 1999; Ejaz et al., 2023). Furthermore, Molecular Dynamics (MD)-based binding free energy calculations help prioritize potential drug candidates during the hit identification phase (Li et al., 2019; Abel et al., 2017; Aziz et al., 2023). This approach provides a comprehensive understanding of atomic-level interactions and the dynamic behavior of biomolecular systems (Badar et al., 2022). The combined use of Free Energy Landscapes (FEL) and Principal Component Analysis (PCA) has proven to be a highly effective method for comprehensively exploring the conformational landscape of a protein and identifying its representative substrates.

In this study, we reported the *in silico* studies of 69 small-molecule inhibitors of Artemis, taken from a library with ZINC ID 846591, which was previously developed in the Sanford-Burnham Center for Chemical Genomics (the University of Southern California, Los Angeles, CA). The data was provided to the NIH Molecular Libraries Probe Production Network (https://www.broadinstitute.org/mlpcn/). Initially, virtual high-throughput screening (vHTS) was carried out using AutoDock and Glide docking programs, resulting in the identification of 16 hit compounds with high binding affinities. These compounds were further evaluated through *in silico* ADMET profiling using ADMETlab 3.0 (Valencia et al., 2023), followed by density functional theory (DFT) analysis. Based on favorable physicochemical properties and DFT results, compounds 42 and 51 were selected for MD simulations, FEL, and PCA analysis to assess their stability and interaction dynamics. The current study aims to find an Artemis inhibitor as a potential radiosensitizer adjuvant to cancer chemotherapy by employing the above computational techniques. According to the best of our knowledge, no experimental data have yet been defined on the role of an Artemis inhibitor as a radiosensitizer by *in vitro* or *in vivo* studies. This research can potentially lead to new therapeutic strategies targeting DNA repair mechanisms, offering new hope for patients with radioresistant cancers.

Experimental methodology

Sampling and processing of primary ductal carcinoma cells

Five Samples of invasive ductal carcinoma were collected from patients with grade 3 breast cancer after consent from the patients and surgeons from 4 hospitals in Rawalpindi/Islamabad. Samples were named as 1MOS, 3PRF, 2PRF, 1PTN, and 2PTN and collected in ice-cold Roswell Park Memorial Institute (RPMI) 1,640 (Life Technologies® Cat No: 91800-014) supplemented with 10% horse serum (HS). And were processed as per the protocol of Potdar and Chaugule (Potdar et al., 2011) however, the protocol was modified in the lab according to the requirement. Samples were washed twice with 1X PBS. Tissues of 2 mm^2 around the blood vessels were taken and fed in 10 mL RPMI+10 %HS and 1% Penicillin/Streptomycin (PenStrep) at 37°C and 5% CO_2. Tissues were checked for logarithmic growth of cells for over a week.

Primary cell culture

Four cancerous tissues obtained after surgical resection, with patients' consent (from Jinnah hospital, Islamabad) were washed with ice cold 1XPBS three times; cut in small pieces of 5 × 5 mm and incubated in 4 mL of 0.25% trypsin EDTA (Gibco by Life technologies, reference # 25200-056) for 15 min followed by addition of 1XPBS 10 mL. The tissue pieces were chopped down further and were collected along with 1XPBS in a 15 mL tube and were spun at 1,000 rpm for 5 min. The supernatant and tissue debris were discarded. The cells were collected in the form of a pellet and were suspended in cell culture complete medium (RMPI 1640 medium and supplemented with 10% Horse Serum). Cells were cultured at 37°C and 5% CO_2 in a humidified incubator in a sterile environment. After 5 days of development of primary culture, the cells were serum-starved. Serum starvation was done by changing the concentration of serum from 10% to 8% for 5 days and from 8% to 6% for the next 5 days, from 6% to 4% for the next 5 days, and then finally, 2% serum was provided. The idea behind the treatment was that the cancerous cell growth was independent of growth factor availability. Viable cells were used for culturing at each step at 1.0 x 10^5 cells/mL of complete cell culture medium.

Cell culture of artemis cell lines

The cell lines (CJ179, 1BR3, and 48BR) were obtained from Penelope Jeggo's lab at the Genome Damage and Stability Centre, University of Sussex, United Kingdom. The Artemis-defective fibroblast CJ179 primary cell line was cultured in DMEM, supplemented with 10% FBS at 37°C with 5% CO_2 (Krempler, 2004). Artemis proficient cell lines 1BR3 and 48BR were cultured by culture conditions mentioned by the United Kingdom Health Security Agency (https://www.culturecollections.org.uk/nop/product/1br3): briefly, we used DMEM + 2 mM L-glutamine +100 units/mL Penicillin, 100 µg/mL streptomycin, 0.4 µg.mL puromycin. Cells were seeded at 5 × 10,000 cells/cm^2, using 0.05% trypsin/EDTA for splitting. The Artemis mutant (ATR-proficient) fibroblasts 48BR were cultured in DMEM, supplemented with 15% FBS (Burdak-Rothkamm et al., 2008).

Micronuclei (MN) quantification

We exposed Artemis deficient (CJ179), proficient (1BR3), and mutated (48BR) cell lines to 1Gy of ionizing radiation and fixed them in methanol acetic acid (3:1 ratio), and spread them onto cold, dried glass slides. The cells were observed under ×100 magnification using oil immersion (Podrimaj-Bytyqi et al., 2018). The cells that were observed under the randomly selected field of view were analyzed for counting micronuclei.

siRNA inhibition of artemis

Inhibition of Artemis was done at the transcription level by introducing siRNA into the invasive ductal carcinoma cell lines. Lipofectamine ™ 2000(Cat No 1668-027) was purchased from Invitrogen, and siRNA with sequence 5′-UUAGGAGUCCAGGUUCAUG-3′ (Zhang, et al., 2004) was purchased in duplex from Eurofins Operon. Two days before transfection, cells were grown in DMEM complete growth medium (Biowest: Cat No S181H-100) supplemented with 10% FBS. Lipofectamine ™ 2000 (3ul) was mixed with 150 µL of DMEM (without FBS) and left at room temperature for 5 min. After 5 min, 20 µL of 20 pmol/µL siRNA stock was added to the lipofectamine solution and incubated at room temperature for 20 min. The complex of siRNA and lipofectamine was added to 1 mL of cell suspension with 60%-70% confluence and incubated for 4 h in cell culture conditions. Then warm 1.5 mL of DMEM +10% FBS was added, and cells were incubated for 48-96 h.

TABLE 1 qPCR primer sequences of p53, DNA-PKcs, and Artemis.

Serial no.	Gene	Sequence 5′→3′	Opt Tm- °C-PCR	References
1	Artemis-forward	GGACAAGGGTGGTTGGGAGTAGA	49.5	Zhang et al. (2009)
	Artemis-reverse	CCCAATTGCAGGTAAAACAGTCAAG	49.5	
2	DNA-PKcs-forward	CCGGACGGACCTACTACGACT	57.1	Yasaei and Slijepcevic (2010)
	DNA-PKcs-reverse	AGAACGACCTGGGCATCCT	57.1	
3	p53-forward	TAACAGTTCCTGCATGGGCGGC	57	Węglarz et al. (2006)
	p53-reverse	AGGACAGGCACAAACACGCACC	57	

RNA extraction and cDNA synthesis

RNA was extracted by Trizol method (Sambrook et al., 1989) and was checked on 1% agarose gel by looking for two bands of 28S and 18S. For semi-quantitative analysis of gene expression cDNA was prepared from chemicals purchased from Thermoscientific. Oligo dt (2.5 µL), 5 µL Diethylpyrocarbonate water (DEPC), and RNA (17 µL) were mixed to make 25 µL of total volume, and PCR tubes were incubated at 70°C for 10 min and then chilled on ice for 5 min. Reverse Transcriptase (RT) buffer (10 µL), dNTPs (2.5 µL), DEPC water (8.75 µL), RNase inhibitor (1.25 µL), and RT enzyme (2.5 µL) were added to tubes and PCR was run for 1 h at 42°C. Tubes were stored at −20°C.

Semi-quantitative analysis of gene expression

PCR of p53, DNA-PKcs, and Artemis Primer sequence and annealing temperatures (Table 1) was performed (Sambrook et al., 1989). These PCR products were then run on a 2% agarose gel as the product lengths were 121, 280, and 260 base pairs for p53, Artemis and DNA-PKcs, respectively. Bands were analyzed by the software ImageJ.

Artemis inhibitor

The Artemis inhibitor used for *in vitro* experiments was (2-hydroxy-5-methoxybenzaldehyde 4-anilino-6-(3,5-dimethyl-H-pyrazol--yl)-,3,5-triazin-2-ylhydrazone, referred to as HMAD and purchased from the University of California San Diego.

Chromosomal aberration assay

Chromosomal aberrations in Artemis-inhibited and exponentially growing cell lines were determined by metaphase spreads (Xiong et al., 2015). The cells were harvested by trypsinization (using 0.25% trypsin) 24 h after treatment and incubation with 1 µg of Colcemid/mL for 1 h to collect metaphase spreads for analysis. The cells were fixed after treatment with hypotonic solution (0.56% KCl) in Methanol-glacial acetic acid (3:1). Air-dried preparations were used, and slides were stained with 4′, 6-diamidino-2-phenylindole/ Vectashield antifade mixture. For chromosomal aberrations, 25 mitotic cells were analyzed for each treatment per cell line at a magnification of ×100.

Irradiation

a. Radiation of Artemis cell lines

The Artemis cell lines (CJ179, 1BR3, 48BR) were grown to 1 × 10^6 cells/mL, irradiated with a ^{137}Cs source at a dose rate of 1.0 Gy/min, brought into the lab, and then evaluated for Micronucleus (MN) formation, and performed at Colorado State University, United States.

b. Radiation of Primary cells

Each sample of primary cells was split into 13 subgroups for irradiation. The first group was the absolute, which was not given any treatment. The next 4 groups (2-5) were incubated with NU7026 for 12 h before irradiation. The next 4 groups (6-9) were treated with artemis inhibitor for 12 h before irradiation. The rest of the 4 groups (10-13) were designated as control groups. Group 2 of each sample was irradiated with a radiation dose of 0.5 Gy, Group 3 of each sample was irradiated with a radiation dose of 1 Gy, Group 4 of each sample was irradiated with a radiation dose of 2 Gy and Group 5 of each sample was irradiated with a radiation dose of 4 Gy. The rest of the parameters were kept the same. Table 2 summarizes the treatment strategy for subgroups of sample 1. The rest of the subgroups from the three samples were treated accordingly. These irradiations utilized a Cobalt source and were performed at the Nuclear Medicine, Oncology Radiotherapy Institute (NORI) Hospital, Pakistan. A^{60}Co source (Model: Theratron Phoenix) was used for irradiation of samples at the Nuclear Medicine, Oncology Radiotherapy Institute (NORI), Islamabad, Pakistan. The source diameter was 2 cm, and the source activity was 8,382 Ci.

Comet assay

Cells were incubated at standard conditions for the next 24 h after irradiation. Cells were then collected in a 15 mL tube after trypsinization. The cell suspension was then centrifuged at 1,000 rpm for 5 min to collect the cell pellet. The pellet was

TABLE 2 Inhibitor treatment strategies for primary cells coupled with irradiation dose.

Sample/Group	Radiation dose	Chemical inhibitor
Sample1/Group1	0.0 Gy	None
Sample1/Group2	0.5 Gy	DNA PK (inhibitor NU7026)
Sample1/Group3	1 Gy	DNA PK (inhibitor NU7026)
Sample1/Group4	2 Gy	DNA PK (inhibitor NU7026)
Sample1/Group5	4 Gy	DNA PK (inhibitor NU7026)
Sample1/Group6	0.5 Gy	Artemis inhibitor (HMAD)
Sample1/Group7	1 Gy	Artemis inhibitor (HMAD)
Sample1/Group8	2 Gy	Artemis inhibitor (HMAD)
Sample1/Group9	4 Gy	Artemis inhibitor (HMAD)
Sample1/Group10	0.5 Gy	None
Sample1/Group11	1 Gy	None
Sample1/Group12	2 Gy	None
Sample1/Group13	4 Gy	None

The different parameters calculated in dosimetry (Parallel Opposed Beam Pair Calculation Results) are given below in Table 3.

TABLE 3 Dosimetry calculations for irradiation of primary cells.

Parameter	[a]Calculated result	
Total dose	0.5 Gy/1Gy/2Gy/4Gy	
Fraction	0.5 Gy	
Field size (collimator opening)	Rt lateral	20 cmX28cm
	Lt lateral	20 cmX28cm
Depth of dose prescription point	Rt lateral	9 cm
	Lt lateral	9 cm
Dose fraction at Zmax	Rt lateral	0.28Gy
	Lt lateral	0.28Gy
Beam weight	50%	
Current beam output	1.848 Gy/min	

[a]Parameters related to irradiation were calculated by a professional dosimetrist.

resuspended in 200 µL of 1XPBS and mixed with 1% Low Melting Point Agarose in a 1:10 ratio. Glass Slides were coated with 1% normal melting point agarose (molten) and allowed to dry on ice. The cell suspension was added to slides in the form of six drops per slide with a space in between. Cover slips were placed on the drops to embed the cells and allow gel solidification. After 10 min, the cover slips were removed. Slides were then immersed completely in ice-cold lysis solution and placed at 4°C for 1 hour in the dark. The slides were then placed in neutralization buffer for 15 min in the dark at 4 C. Slides were then shifted into 1X TAE buffer in the horizontal electrophoresis tank. The voltage was set to 1 V/cm, and current was supplied for 25 min. Staining was performed with 80 µL 1X Ethidium Bromide staining solution prepared from 10X (20 µg/mL) stock solution. The stain was left for 5 min, and slides were then washed in ice-cold water to remove excess stain. After drying at room temperature in the dark, the slides were observed at a ×40 objective lens in the blue channel of the fluorescence microscope for comet analysis, and images were captured. ImageJ and CASP software were used to analyze the images for comet tail analysis and the percentage of DNA in the comet tail. Multiple slides were prepared for one sample in three independent experiments to ensure the reproducibility of results.

MTT assay

1.0×10^5 Cells/mL were seeded 1 day before irradiation in 10 mL of RPMI1640 medium supplemented with 10% horse serum in T-25 flask. After 12 h, cells were processed for irradiation as explained above. Followed by irradiation, 100 µL of medium from the culture flask containing cells was taken and plated in a microplate (96-well plate) for 24 h. After 24 h, 20 µL of filter-sterilized MTT (5 mg/mL in PBS) was added to the micro wells containing cells. Following 3 h of incubation with MTT, the cell culture medium was discarded and the purple formazan crystals were dissolved in sterile DMSO (50 µL) by incubating at 37°C for 10-15 min. The absorbance at 490 nm was measured with a spectrophotometric plate reader. The absorbance values were converted to %Cell survival by the following formula;

$$\%\text{Cell survival} = \frac{\text{Absorbance of sample} - \text{Absorbance of blank}}{\text{Absorbance of control} - \text{Absorbance of blank}}$$

Statistical analysis

Statistical analysis of gene expression was done on GraphPad Prism 5.04, and a tailed paired *t-test* was run between control and siRNA-transfected cells of the same sample for all three genes. For the cell viability and comet assay a two-way ANOVA was used. The

p-values were calculated, and graphs were plotted with standard error mean values at a significance level of <0.05.

Computational methodology

Tanimoto similarity

The structural similarity between the investigated 69 compounds was evaluated using the RDKit program (Kunnakkattu et al., 2023). For each compound, the Tanimoto similarity index (Ts-index) (Vogt and Bajorath, 2017) was calculated against all studied compounds, and the results were visualized using a plot generated with OriginLab 2018 (RCSB, 2025).

Molecular docking

The predictions obtained by docking simulations can provide useful information about the presence or absence of protein-ligand interactions, how these interactions are established (electrostatic, Van der Waals, hydrogen bonds, hydrophobic interactions), and which residues of the protein are involved. A representative protein X-ray crystal structure of Artemis with Uniprot ID: X6R6W9 and PDB ID: 7ABS (Yosaatmadja et al., 2021) was retrieved from the Uniprot (https://www.uniprot.org/) and RCSB Protein Data Bank (https://www.rcsb.org/), respectively. The BLAST program performed pairwise sequence alignment of these two Artemis proteins (https://blast.ncbi.nlm.nih.gov/Blast.cgi#). For molecular docking, the protein was prepared using the Protein Preparation Wizard module implemented in the Maestro (Schrödinger Release 2016-4: Maestro, Schrödinger, LLC, New York, United States) and optimized with OPLS-2005 force field. The zinc library of 69 compounds was downloaded from the ZINC database (Irwin and Shoichet, 2005) in SDF format and prepared by the LigPrep module in Maestro. The Receptor Grid Generation tool was employed to create a grid box around amino acid residues involved in interaction with the DNA. Finally, ligands were docked at the binding site with the Glide module, and G-scores and E-model scores were recorded for each ligand (Friesner et al., 2004). To perform a docking with AutoDock4, the protein and ligand structure were prepared using MGL tools and saved in. pdbqt format. The grid box was created around the key amino acid residues, and box size/dimensions were recorded to generate a grid parameter file. Finally, a docking parameter file was generated to perform docking. The results were saved as the docking log file, containing information about the binding energies for energetically favorable ten conformational poses of each ligand (Siddique et al., 2024; Farhan et al., 2024).

ADMET studies

The ADMET properties of the compound library were predicted with the online web server tool ADMETlab-3.0 (Valencia et al.; Zadorozhnii et al., 2022; Xiong et al., 2021). Employing a quantitative structure-property relationship (QSPR) model trained by a multi-task graph attention (MGA) framework (Xiong et al., 2021).

Density function theory

In the current study, all the computations were done using the Gaussian 09 W software program (Frisch et al., 2009). The molecular geometry of the investigated compounds was subjected to convergence using DFT with the B3LYP functional (Becke, 1993) and 6-311 + g (d,p) basis set (Clark et al., 1983), (Tirado-Rives and Jorgensen, 2008). The vibrational frequencies of the studied compounds were recorded at the same theoretical level to confirm the true global minima of optimized structures. To define the molecular reactivity/kinetic stability of investigated compounds, DFT was employed to calculate global and local reactivity descriptors such as frontier molecular orbital (FMO) energies, HOMO/LUMO energy gaps, and corresponding softness/hardness parameters. Furthermore, the chemical potential, electronegativity, ionization potential, and electron affinity were recorded as reactivity parameters (Bilal et al., 2022; Aziz et al., 2022b), followed by visualization of molecular electrostatic potential (MEP) maps to investigate the nucleophilic and electrophilic attack sites (Yaqoob et al., 2025).

Molecular dynamics simulation

The 3-D models of protein-ligand complexes were generated in. pdb format using Maestro. They were subjected to molecular dynamics (MD) simulation in the GROMACS 2022.2 software program (Abraham et al., 2022) to evaluate the dynamic behavior of these complexes. The topology parameters for protein were established by the pdb2gmx module, employing the CHARMM27 force field (MacKerell et al., 1998), whereas ligand topology parameters were established using the cegenFF server (https://cgenff.com/). The simulation box of cubic shape was developed, and complexes were centered here under periodic boundary conditions. The system was solvated with water molecules using the TIP3P model (Jorgensen et al., 1983), and Cl^- ions were added to neutralize the system. The 50,000 energy minimization steps were conducted using the steepest descent methodology, which is then followed by NVT/NPT equilibration steps, each for 100-ps time duration. The Leapfrog method was employed during NPT equilibration to couple protein, ligand, and other system components. The system's temperature was maintained at 300K with 1 bar pressure using Berendsen thermostat and barostat coupling constants. The PME algorithm was employed to correct truncation errors arising from the Coulomb interaction cutoffs at 1.2 nm. Finally, MD simulation was performed for a 100 ns period at isothermal/isobaric conditions, and trajectories were visualized in VMD1.9.2 (Humphrey et al., 1996). The MM-GBSA binding free energy calculations were performed using a dielectric constant of 80 for the solvent and 1 for the solute, which are standard values for implicit solvent models (Sun et al., 2014). The Xmgrace 5.1.19 (Turner, 2005) was employed for graph analysis (Lindahl et al., 2001).

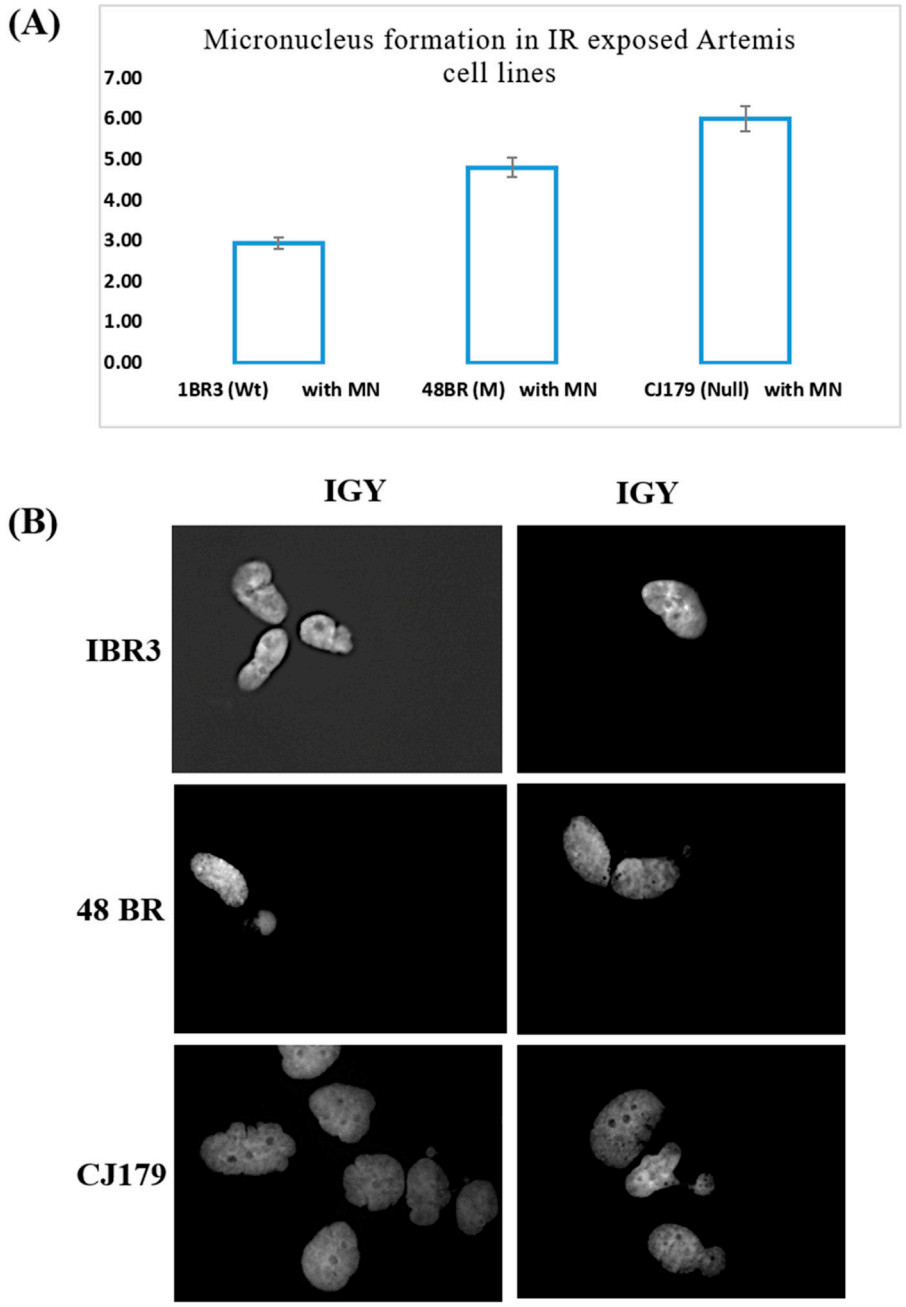


FIGURE 1
Micronucleus frequency assay: **(A)** Micronucleus formation in IR (1 Gy) exposed Artemis cell lines. The percentage frequency in each cell line was plotted. **(B)** Representative micrographs of micronucleation in Artemis cell lines following exposure to 1 Gy ionizing radiation (Mag x 400).

PCA and FEL

To conduct the PCA (Abdi and Williams, 2010), the gmx covar tool within the GROMACS suite was employed to compute the covariance matrix, which helped to assess the correlation between atomic fluctuations in the protein-ligand complex. The corresponding eigenvalues and eigenvectors were extracted via the gmx analog module, and projections on principal component (PC) coordinates were visualized for each frame. Additionally, the FEL analysis was carried out using the gmx sham module in GROMACS, allowing us to identify equilibrium and transition states that characterize protein-ligand complex stability (Papaleo et al., 2009).

Result and discussion

Micronucleus (MN) frequency assay

Our investigation showed that gamma-ray irradiated (1 Gy) Artemis-deficient cell line CJ179 had a higher number of unresolved DNA damage as measured indirectly using MN frequency assay,

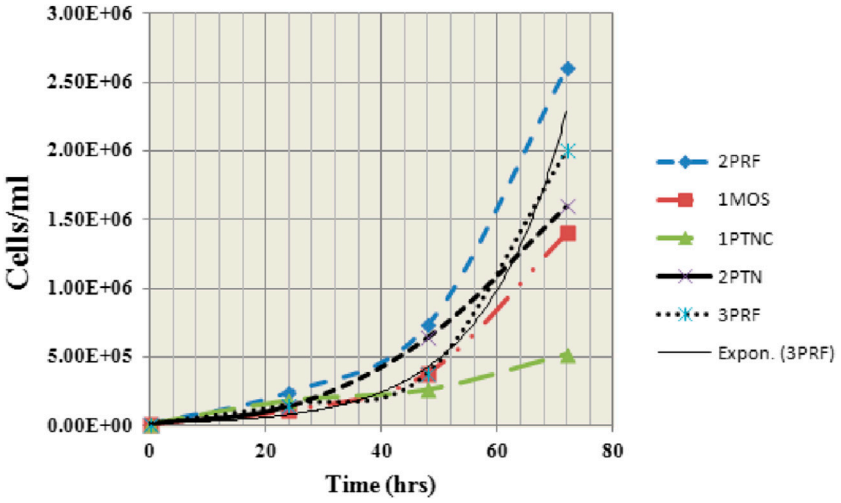


FIGURE 2
Graph showing growth curves of 5 primary cell lines (derived from invasive ductal carcinomas) at 0, 24, 48, and 72 h. Most aggressive growth is demonstrated by 1MOS and 2PRF whereas 1PTNC is shown to be the slowest in growth.

while Artemis-mutated 48BR cell line could resolve only some of the damage as compared to the Artemis wild-type cell line 1BR3 (Figure 1A), highlighting the potential of Artemis protein as a target for cancer therapy. The Figure 1B represented the micrographs of micronucleation in Artemis cell lines following exposure to 1 Gy ionizing radiation.

Primary cell culture

Samples (1MOS, 1PTNC, 2PTN, 3PRF and 2PRF) were observed for exponential growth starting from 1×10^{4} cells/mL to$1x10^{6}$ cells/mL. Each sample showed a different growth pattern (Figure 2). 2PRF and 1MOS showed the most aggressive growth, reaching 5 times of initial number (2.4×10^{6} and 1.9×10^{6} cells/mL) after 24 h and 48 h of incubation, respectively. 1PTNC and 2PTN appeared to be slow growers, with almost double the number of cells after 24 and 48 h 3PRF was doubled thrice of the initial concentration at 24 and 48 h intervals. Morphological analysis of picked colonies after growth showed similarities with their parent colonies. Small cells clumped together to form colonies. Viable cells and colonies appeared to be transparent, whereas dead cells were seen as black and suspended in the medium.

Artemis siRNA transfection of cells

Expression analysis was done for the Artemis gene by preparing the cDNA. Artemis gene expression values were divided by the Actin gene to normalize, while analysis of gene expression on ImageJ provided the results of a 40 percent decrease in Artemis gene expression level as compared to control in 1MOS and 1PTNC. In 2PTN, 30 percent whereas around 20 percent decrease in 3PRF and 2PRF samples was observed (Figures 3A,B). Statistical analysis provided significance in samples except 3PRF as compared to the control. The *p*-value of all samples except 3PRF was less than 0.05.

Gene expression analysis of DNA-PKcs

In gene expression analysis of DNA-PKcs, 1MOS and 2PRF showed an increase in DNA-PKcs gene expression by 10 and 30 percent, respectively. The increase in gene expression shown by IMOS was not significant compared to 2PRF. whereas, other 3 samples had a downregulation effect. 1PTN showed no decreasing trend as compared to 2PTN and 3PRF, which showed almost up to 15 percent and 30 percent decrease, respectively (Figures 3C,D). The *p*-value of all samples was greater than 0.05.

Gene expression analysis of TP53

Increase or decrease in the TP53 gene, which encodes p53 protein, was also checked before and after inhibition of Artemis. Interestingly, all samples of breast cancer showed a significant increase in p53 gene expression after Artemis inhibition. 2PTN was seen to have the highest increase in p53 gene expression, which was almost 46%. Almost similar trend was observed in 2PRF, whereas 1PTN and 1MOS showed a similarity in increased expression of 38%. 3PRF conferred the lowest increase in expression level of 20% as compared to the control (Figures 3E,F). The *p*–values are >0.05.

MTT assay

The percentage viability of siRNA-transfected cells was determined with an MTT assay, in which conversion of yellow tetrazolium MTT to purple formazan was quantified at dual optical densities of 490 nm and 630 nm. Control has the darkest color of purple formazan, which means that the darkest the color, the higher the optical density, because of a high number of proliferating cells. The highest decrease in percentage cell viability was observed in 1PTN and 3PRF, in which cells lost 50% viability. IMOS and 2PTN

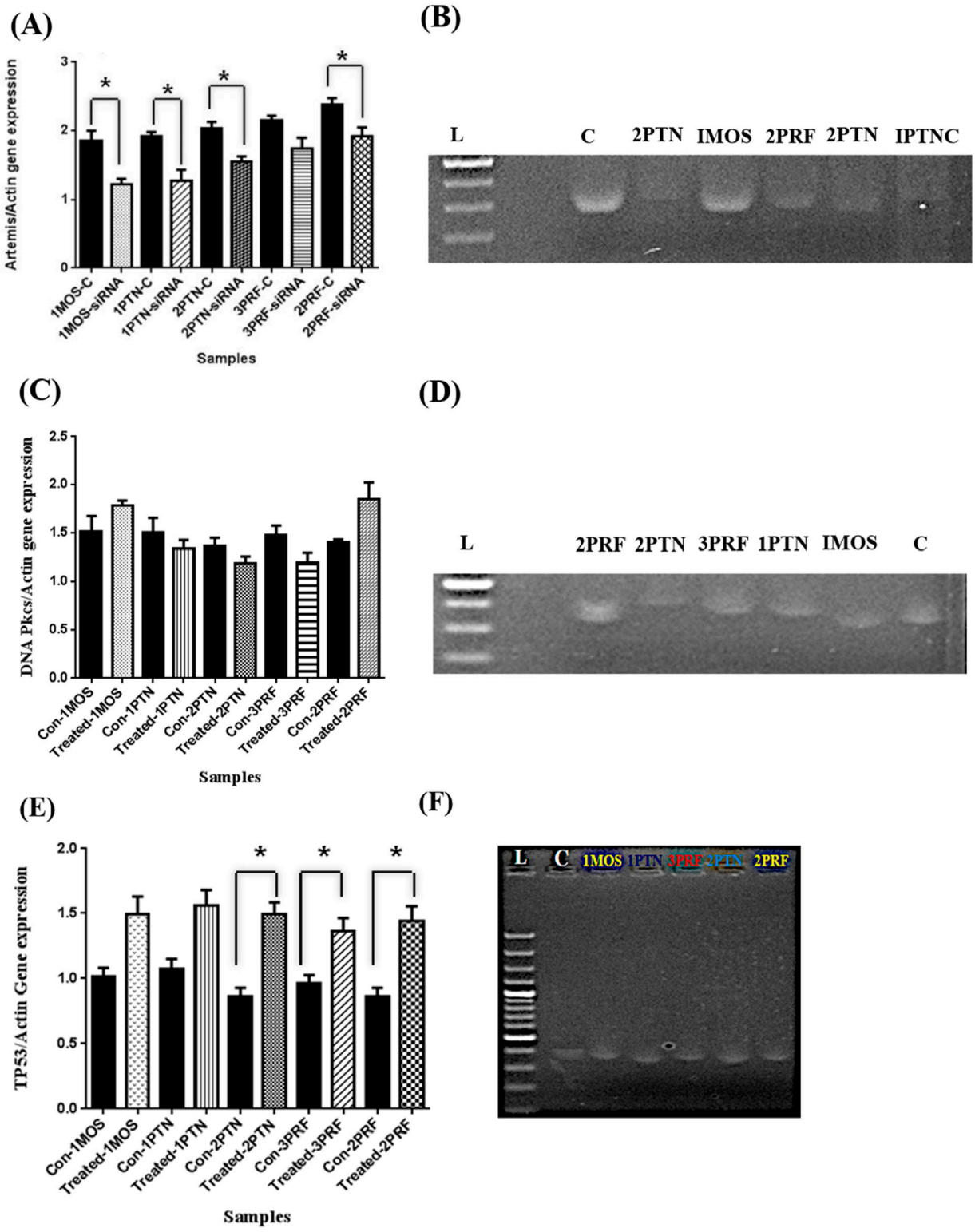


FIGURE 3
Artemis inhibition expression analysis after siRNA transfection in primary cell lines, Gene expression analysis of DNA-PKcs after inhibition of Artemis, and Gene expression analysis of TP53 after Artemis inhibition. **(A)** The graph represents the expression of the Artemis gene after siRNA transfection. Error bars are Standard Error Mean (SEM). X-axis has samples and Y-axis has Artemis/Actin gene expression values **(B)** Gel electrophoresis picture of amplified cDNA of Artemis gene and inhibition in the Breast cancer samples as compared to control, bands were analyzed by ImageJ (C = control, L = ladder 1000bps and dot in lPTN is gel doc error) **(C)** Graph shows the change in expression of DNA-PKcs with no significance. Values were calculated by dividing DNA PKcs bands measurement by Actin values and **(D)** Gel electrophoresis of DNA-PKcs amplified PCR products (C = control, L = ladder 1000bps) **(E)** Bar graph shows the expression analysis done by ImageJ and TP53 values divided by Actin band values, error bars are Standard error mean (SEM) with

(*Continued*)

FIGURE 3 (Continued)
significance (p-value <0.05) in 2PTN, 2PRF and 3PRF in paired t-test. **(F)** TP53 amplified on a 2% agarose gel, which shows an increase in gene expression. (C = control, L = Ladder 1000bps, and the dot in mid of the bands is a gel doc error).

showed 60% cell viability, which was decreased by 40%, and lastly, 2PRF showed 70% cell viability (Figure 4).

COMET assay

To confirm if Artemis inhibitor could be used a novel radiosensitizer we analyzed the DNA damage against different doses of radiation and the results indicated more DNA damage at low dosage of radiation compared to the higher doses. This consequence could be explained due to the activation of DNA repair pathways at high dose of radiation. To check this possibility we blocked NHEJ pathway by inhibiting key factor of NHEJ repair i.e., DNA PKcs; As a result, there was significant increase in accumulated damage over 24 h after high dose radiations. These results ensure that the NHEJ is the main pathway for repair of IR induced damage and that repair system activation at high dose of radiation is the reason for less DNA damage and cell killing rather than low dose of radiation. We also inhibited the NHEJ by using same strategy followed by low dose of radiation but the effect was not remarkable leading to the conclusion that at low dose DNA repair pathways are not activated. We observe that DNA PKcs inhibition impairs cells in IR induced damage repair. The effect of 10 μM concentration of DNA PKcs specific chemical inhibitor (NU7026) was analyzed for its effect on percent cell survival against different dose of radiation and it was found out that it almost decrease the cell survival by 50% at 4Gy of radiation. In the second aspect of our study, we analyzed the effect of artemis inhibition in response to IR induced DNA damage. In this approach we inhibited artemis by using 2-hydroxy-5-methoxybenzaldehyde-4-anilino-6-(3,5-dimethyl-H-pyrazol--yl)-,3,5-triazin-2-ylhydrazone chemical inhibitor.

Single Cell gel electrophoresis assay and MTT assay carried out after IR predicted that role of artemis in cell cycle arrest/apoptosis that is independent of DNA damage repair as shown in Figure 5 (Panel A and Panel B). Repair process was seen to be little defective in response to artemis inhibition as compared to control and the change was negligible. Percentage cell proliferation after IR was remarkably decreased which predicts the role of Artemis in cell cycle check points. Artemis inhibition caused almost 50% decrease in cell survival at 0.5 Gy of IR. This sensitivity does not affect the NHEJ as DNA damage was not accumulated in cells when analyzed after 24 h.

Tanimoto similarity

The Ts-index was computed for the 69 compounds, including the reference. The Figure 6 presented a heatmap that visualizes the pairwise similarity of these compounds using the Ts-index. The Ts-index, widely applied in cheminformatics, measures molecular similarity by comparing structural features. These features are typically represented as binary fingerprints, where each bit signifies the presence or absence of a particular molecular attribute.

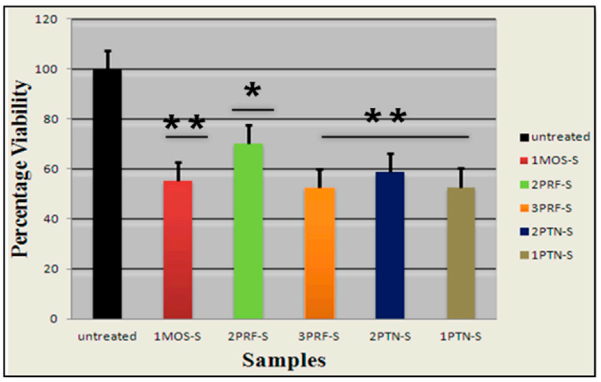


FIGURE 4
Percentage viability of the cells transfected with siRNA is plotted on the Graph. (p-value <0.05 one star significance and p-value <0.01, two star significance).

On both the x-axis and y-axis, the 69 compounds were numbered from 0 to 68, and the reference was labeled as cef. The heatmap displayed the similarity score for the compounds corresponding to the intersecting data points. The scores ranged from 0 to 1, with a score of 1 (purple highlighted) indicating identical or highly similar compounds, while a score of 0 (red highlighted) represented no similarity. The diagonal line running from the top-left to the bottom-right represents each compound's comparison with itself, resulting in a purple line with a perfect similarity score of 1. The off-diagonal line indicated the varying levels of similarity between different compounds, with colors transitioning from purple to red as the similarity decreases.

Docking studies

The Artemis protein comprised two major domains: the Metallo-β-lactamase domain (MBL) and the β-CASP domain. The Zn ion in the MBL domain served as a catalytic center for the endonuclease activity of Artemis. The motif I–motif IV (ASP17, HIS33, HIS35, ASP37, HIS38, HIS115, ASP136) and motif C (VAL341), in the MBL domain, were involved in co-ordination with Zn ion in the catalytic site. In contrast, motifs A and B (ASP165 and HIS319) stabilize the product during catalytic reactions. The zinc-finger motif in the β-CASP domain (HIS228, HIS254, CYS256, CYS272) is involved in structural changes in Artemis, constituting the non-catalytic binding site. DNA's highly negative phosphate groups coordinate with the Zn ion in the catalytic site. In addition to this, the positively charged amino acid residues, including ARG18, ARG21, LYS36, LYS40, ARG43, and LYS74 of the MBL domain and residues such as ARG 172, ASN205, LYS207, and LYS288 of β-CASP domain recognized

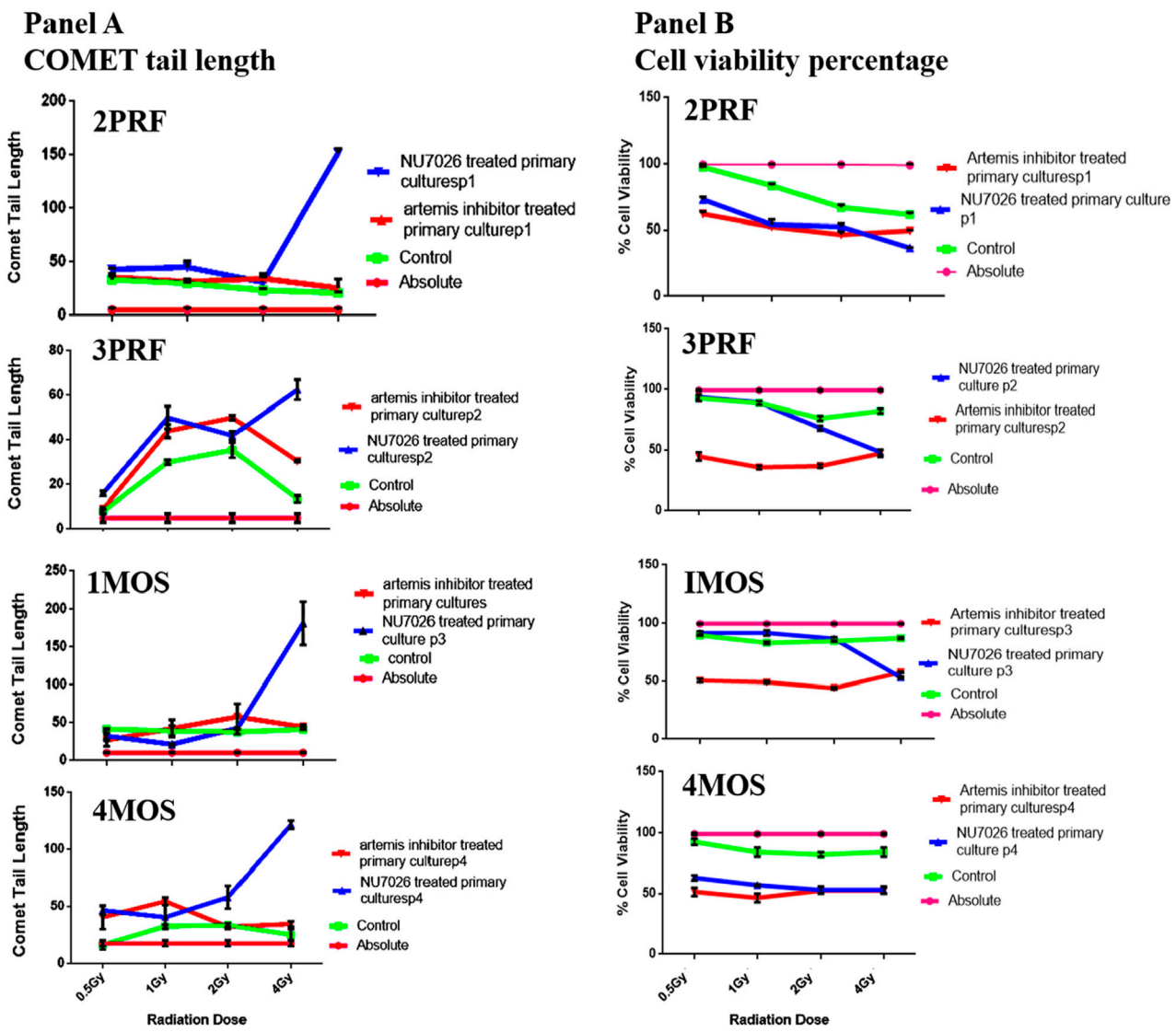


FIGURE 5
Panel **(A)** shows the graphical plots of comet tail lengths (in A.U.) for 4 primary cell lines (2PRF, 3PRF, 1MOS, and 4MOS), while panel **(B)** shows the cell viability measured with the MTT assay in these primary cell lines. These cell lines were treated with either Artemis inhibitor or DNA PK inhibitor to compare the effects of radiation exposure at 0.5, 1.0, 2.0, and 4.0 Gy.

negatively charged DNA as the substrate. This represented the extended open substrate binding pocket of Artemis located between the MBL domain and β-CASP domain (Yosaatmadja et al., 2021; Karim et al., 2020). The 7ABS incorporates Zn ion, crucial for protein activity, in its structure that is not present in X6R6W9. Furthermore, the sequence alignment analysis represented the 100% similarity of amino acid residues (120–203) of 7ABS with amino acid residues (1-84) of X6R6W9, indicating the metallo-β-lactamase domain of Artemis protein only, as shown in Figure 7. Based on the above analysis, which was 100% similar, the Artemis protein with PDB ID 7ABS was selected to understand better compound interactions with Zn ions within the binding pocket.

Molecular docking studies revealed the significant binding affinity of investigated compounds with 7ABS that displayed coordinate covalent bonds, ionic interactions with Zn ions, and H-bonding interaction with key amino acid residues. The compounds 01, 02, 04, 05, 42, 43, 44, 46, 51, and 58 were identified as top hits by the Glide module with ΔG-scores ranging from −9.1 kcal/mol to −8.0 kcal/mol. The compounds 23, 46, and 49 were selected by AutoDock4 screening with docking scores above −8.0 kcal/mol. However, compounds 28, 55, 59, and 67 demonstrated comparable binding affinities in both, Glide and Autodock4 predictions. The G-scores, Emodel scores, hydrogen bonding, hydrophobic, and ionic interactions of top hits with Artemis endonuclease are outlined in Table 4.

The ligands 01 and 02 showed H-bonding interactions with ASP136 via conserved water molecules. In contrast, the inhibitory activity of ligand 04 is attributed to the hydrogen bonding with the amino acid residue of motif B (HIS319). Supplementary Figure S1 illustrates the 2D and 3D interaction of ligands 01, 02, and 04 with the target protein. The substantial binding affinity of compound 42,

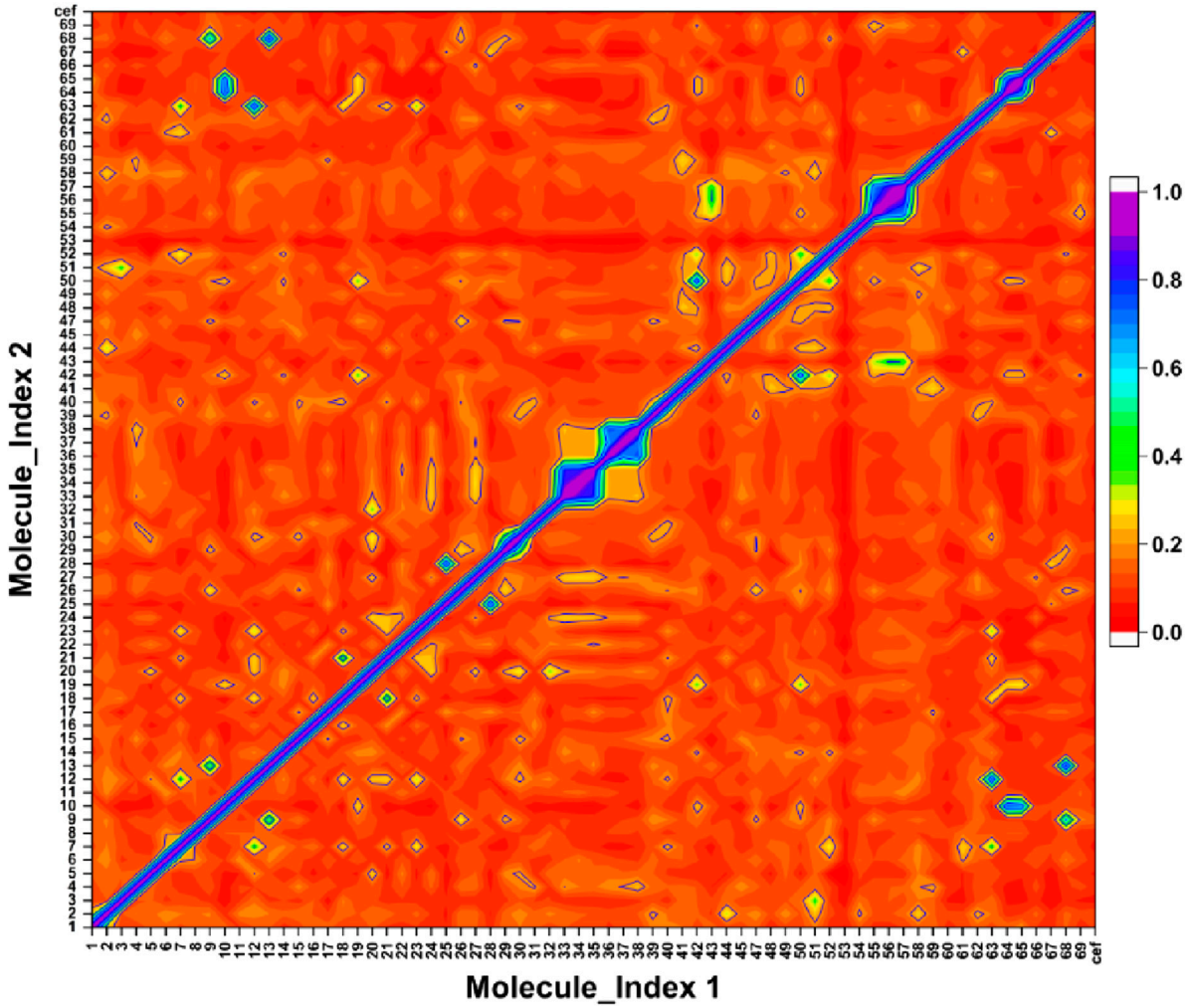


FIGURE 6
The symmetric matrix shows self-similarity values of 1.0 on the diagonal. The color scale represents pairwise similarity, with purple indicating high similarity and red indicating low similarity.

A)

Score	Expect	Method	Identities	Positives	Gaps
180 bits(457)	4e-62	Compositional matrix adjust.	84/84(100%)	84/84(100%)	0/84(0%)

```
X6R6W9  1    MFLFQGNNGTVLYTGDFRLAQGEAARMELLHSGGRVKDIQSVYLDTTFCDPRFYQIPSRE  60
             MFLFQGNNGTVLYTGDFRLAQGEAARMELLHSGGRVKDIQSVYLDTTFCDPRFYQIPSRE
7ABS    120  MFLFQGNNGTVLYTGDFRLAQGEAARMELLHSGGRVKDIQSVYLDTTFCDPRFYQIPSRE  179

X6R6W9  61   ECLSGVLELVRSWITRSPYHVVWL  84
             ECLSGVLELVRSWITRSPYHVVWL
7ABS    180  ECLSGVLELVRSWITRSPYHVVWL  203
```

B)

Score	Expect	Method	Identities	Positives	Gaps
180 bits(457)	4e-62	Compositional matrix adjust.	84/84(100%)	84/84(100%)	0/84(0%)

```
X6R6W9  1    MFLFQGNNGTVLYTGDFRLAQGEAARMELLHSGGRVKDIQSVYLDTTFCDPRFYQIPSRE  60
7ABS    120  ............................................................  179

X6R6W9  61   ECLSGVLELVRSWITRSPYHVVWL  84
7ABS    180  ........................  203
```

FIGURE 7
The sequence alignment of investigated Artemis proteins (Uniprot ID: X6R6W9 and PDB ID: 7ABS) in **(A)** pairwise and **(B)** dot representations.

TABLE 4 Molecular Glide score, Hydrogen bonding interactions (Å), hydrophobic and other interacting residues for ligands with Artemis protein (PDB ID: 7ABS).

Ligands	G-score (kcal/mol)	Emodel	Autodock4	Ionic/H.B.I residue (distance Å)	Hydrophobic and other interacting residues
01	−8.5	−81.83	−5.88	ASP136 (2.44) THR167 (1.89) Zn 101 (2.00) Zn 402 (3.89)	HIS35, ASP37, THR167, LYS207, ALA209, TYR212, PRO289, SER290, THR291, PHE318, HIS319, VAL341, PRO343, VAL344
02	−8.1	−86.60	−5.62	ASP136 (2.44) THR291 (2.74) Zn 101 (2.20) Zn 402 (3.45)	HIS35, LYS36, ASP37, HIS115, THR167, PHE168, LYS207, ALA208, THR291, SER317, PHE318, HIS319, VAL341, PRO343, VAL344
04	−8.6	−93.86	−5.89	HIS115 (3.09) HIS319 (2.38) Zn402 (2.02)	HIS35, ASP37, HIS115, ASP136, LYS207, ALA209, PHE318, HIS319
05	−8.5	−97.93	−7.20	ASP136 (2.44) PHE318 (3.17) Zn 101 (2.23) Zn 402 (3.37)	HIS35, ASP37, HIS115, PHE168, LYS207, TYR212, SER290, THR291, TRP293, PHE318, HIS319
23	−4.5	−51.63	−8.1	CYS34 (3.20) HIS35 (3.02) HIS35 (3.06) LYS36 (2.17) LYS207 (4.53) TYR212 (2.44) PHE318 (3.11)	HIS35, LYS36, LYS207, ALA209, PHE318
28	−6.8	−73.87	−7.0	LYS36 (2.64) ASP37 (1.67) ASP37 (3.81) LYS207 (2.02) LYS207 (4.63)	LYS207, ALA209, PHE318
42	−8.6	−139.47	−8.03	LYS36 (1.92) LYS36 (3.47) ASP136 (2.44) ALA208 (2.79) TYR210 (1.81) TYR210 (3.25) HIS319 (2.40) HIS319 (4.72) Zn 101 (2.04) Zn 402 (3.43)	CYS34, HIS35, ASP37, LEU68, SER72, PRO73, HIS115, THR167, LYS207, ALA208, ALA209, TYR210, PHE318
43	−8.1	−114.32	−6.26	ASP37 (2.32) ASP136 (2.44) HIS319 (4.72) Zn 101 (2.04) Zn 402 (3.43)	CYS34, HIS35, LYS36, ASP37, HIS115, THR167, LYS207, ALA208, ALA209, TYR210, PHE318, HIS319
44	−8.0	−81.99	−6.29	ASP136 (2.44) PHE318 (2.62) HIS319 (4.46) Zn101 (2.19)	HIS35, ASP37, THR167, LYS207, ALA209, TYR212, THR291, SER317, PHE318, HIS319, VAL341, PRO343
46	−9.1	−112.52	−7.00	PRO289 (2.77) HIS319 (2.10) PHE316 (2.44) Zn402 (3.91)	HIS35, LYS36, ASP37, LYS207, TYR212, PRO289, SER290, THR291, PHE316, SER317, PHE318
49	−6.2	−86.81	−8.1	HIS35 (3.24) LYS36 (2.06) ASP37 (2.13) LYS207 (4.87) ALA208 (1.92)	HIS35, LYS36, LYS207, ALA209, PHE318

(Continued on following page)

TABLE 4 (*Continued*) Molecular Glide score, Hydrogen bonding interactions (Å), hydrophobic and other interacting residues for ligands with Artemis protein (PDB ID: 7ABS).

Ligands	G-score (kcal/mol)	Emodel	Autodock4	Ionic/H.B.I residue (distance Å)	Hydrophobic and other interacting residues
51	−9.4	−133.21	−7.69	HIS319 (4.59) Zn402 (3.89)	HIS35, LYS36, ASP37, THR167, LYS207, ALA208, ALA209, VAL341, PRO343, VAL344
55	−7.6	−99.68	−7.1	ASP37 (1.89) ASP136 (1.92) THR219 (3.07) SER317 (3.79) PHE318 (1.91)	PHE168, LYS207, ALA208, ALA209, PHE318
58	−8.4	−105.72	−6.68	ASP136 (2.44) PHE316 (2.56) THR291 (1.82) HIS319 (3.07) Zn101 (2.13) Zn 402 (3.06)	HIS35, THR167, LYS207, TYR212, SER290, THR291, TRP293, PHE316, SER317, PHE318
59	−7.1	−99.68	−6.8	HIS35 (3.37) HIS35 (3.79) ASP37 (3.36) ASP37 (5.19) ASP136 (2.07) ASP136 (1.73) PHE318 (2.36) HIS319 (2.40)	LYS36, LYS207, ALA208, ALA209, TYR212, PHE318
67	−6.5	−93.25	−6.4	HIS35 (3.17) ASP37 (4.00) ALA208 (2.31)	HIS35, LYS36, ALA209, TYR210, PHE318
Ceftriaxone	−9.9	−165.02	−6.6	HIS35 (1.54) LYS36 (2.13) HIS115 (3.29) PHE318 (3.63) HIS319 (2.20) Zn402 (3.93)	CYS34, HIS35, ASP37, THR167, PHE168, LYS207, ALA208, ALA209, TYR210, TYR212, THR291

with a ΔG-score of −8.6 kcal/mol, is attributed to strong electrostatic and H-bonding interactions with LYS 36 and HIS319 in the catalytic domain. Compound 43 displayed H-bonding interactions with ASP37 and ASP136 in the MBL domain and ionic interaction with HIS319 in the catalytic binding site, as shown in Supplementary Figure S2. Compound 44 displayed π-π interaction with amino acid LYS207 of the β-CASP domain that stabilizes the substrate. It also exhibited halogen and ionic interactions with PHE318 and HIS319 with a bond distance of 2.62Å and 4.46Å, respectively. The compound 46 exhibited π-hydrogen bonding interactions with amino acid residues PRO289 and HIS 319 with distances of 2.77Å and 2.44Å, respectively. Similarly, compound 51 exhibited ionic interactions and π-π stacking with amino acid residue HIS319 (Supplementary Figure S3). The residue HIS319 of motif B interacts with ASP165 (motif-A) via H-bonding and is considered critical for Artemis's endonuclease activity. Additionally, the inhibitory activity of all top hits is attributed to the coordination with the Zn ion, which is crucial for the enzyme's catalytic activity. The high binding affinity was observed for compounds 42, 46, and 51 with ΔG-scores of −8.6 kcal/mol, −9.1 kcal/mol, and −9.4 kcal/mol, respectively. The similar binding affinities (−8.1 kcal/mol) were recorded for compounds 23 and 49 by the AutoDock4 program, showcasing H-bonding interactions with key residues such as HIS35, ASP37 (MBL domain), and LYS 207 (β-CASP domain). Compounds 28, 42, 55, 59, and 67 demonstrated significant binding affinities, recorded by both software programs (AutoDock4 and Glide), showing a docking score deviation of −0.5 kcal/mol. The ceftriaxone exhibited moderate inhibitory activity against Artemis protein with an IC_{50} value of 65 μM (Yosaatmadja et al., 2021; Melenotte et al., 2021) by *in-vivo* studies, used as a reference for result comparison. The significant binding affinity of ceftriaxone with a Glide score of −9.9 kcal/mol is attributed to its metal co-ordination as well as H-bonding interaction with conserved amino acid residues such as HIS35, HIS115, and HIS319, as illustrated in Supplementary Figure S4. The 2D and 3D interactions of compounds 42, 46, 51, and ceftriaxone with the target protein are illustrated in Figure 8. The docking scores of all compounds, recorded by AutoDock4 and the Glide program, were tabulated in Supplementary Table S2 (Supplementary Material).

ADMET analysis

The ADMET properties of top-hit compounds are presented in Table 5 and Table 6. All the top hits exhibited molecular weight of less than 500 Da except for compound 42 and the reference drug. The compounds 43 and 67 showed significant

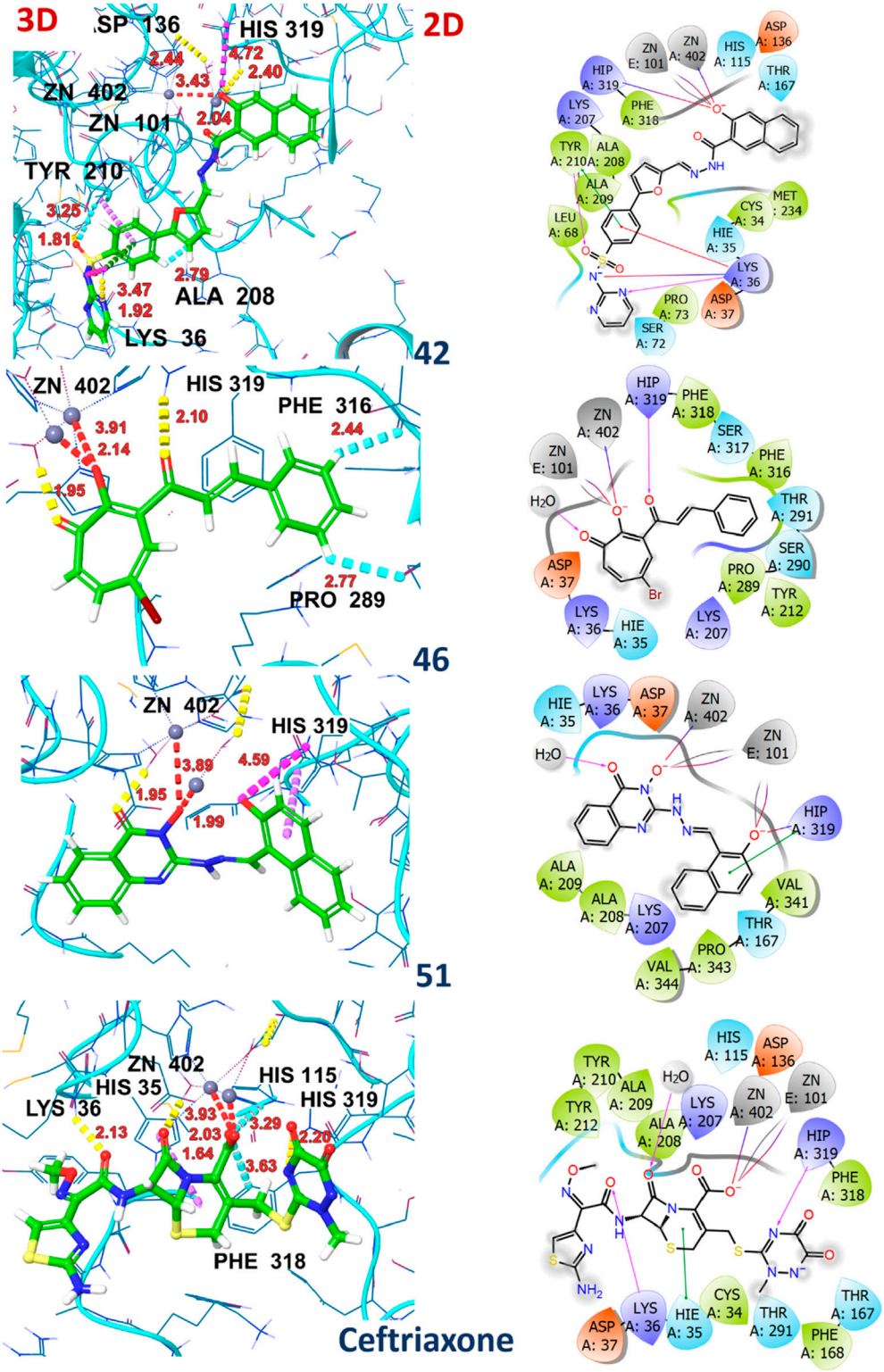


FIGURE 8
2D and 3D interactions of compounds 42, 46, 51, and ceftriaxone with 7ABS protein.

lipid solubility with high log P values of 4.84 and 4.73, respectively, representing their passive absorption from the GI tract. The TPSA value indicates the polarity of compounds and should be less than 140Å for optimal pharmacokinetic properties. The compound 59 and reference compounds are considered highly polar among the investigated compounds with TPSA values of 152.84Å and 215.69 Å. Almost all the compounds were found to be the substrate of P-glycoprotein,

TABLE 5 The ADMET properties include physicochemical parameters, absorption, distribution, and bioavailability of top-hits.

Compounds	MW	TPSA	LogP	P-gp inhibitor	P-gp substrate	HIA	F (20%)	Caco-2	PPB
1	357.17	104.45	2.27	0.39	0.00	0.02	0.11	−5.10	97.93
2	348.12	100.01	2.74	0.09	0.02	0.01	0.01	−5.16	98.10
4	179.06	69.89	0.72	0.00	0.04	0.02	0.06	−5.42	71.21
5	324.11	77.92	1.12	0.69	0.11	0.72	0.09	−4.56	87.62
23	349.13	56.49	3.41	0.61	0.00	0.00	0.02	−4.13	97.48
28	321.1	72.47	3.22	0.90	0.00	0.34	0.04	−4.97	97.59
42	513.11	146.78	3.74	0.00	0.04	0.00	0.92	−5.85	98.81
43	430.19	122.37	4.84	0.05	0.06	0.00	0.64	−5.14	98.87
44	342.1	101.16	3.60	0.03	0.00	0.00	0.03	−4.86	98.62
46	329.99	54.37	3.29	0.99	0.00	0.00	0.04	−4.89	98.88
49	355.11	96.7	3.97	0.00	0.02	0.00	0.01	−4.97	98.67
51	346.11	99.74	3.33	0.00	0.19	0.00	0.81	−4.94	98.86
55	360.13	110.39	3.07	0.05	0.00	0.00	0.04	−4.85	98.20
58	345.11	94.48	2.78	0.02	0.04	0.00	0.04	−4.99	97.95
59	462.15	152.84	2.59	0.00	0.51	0.00	0.99	−5.46	97.73
67	433.13	88.9	4.73	0.56	0.00	0.00	0.11	−5.03	98.23
Ceftriaxone	554.05	214.96	−0.60	0.01	0.00	0.99	0.97	−6.58	92.00

MW, Molecular Weight; TPSA, Topological polar surface area; P-gp, p-glycoprotein; HIA, Human intestinal absorption; F20%, Bioavailability; Caco-2, Caco-2, cell membrane permeability; PPB, plasma protein binding.

resulting in decreased bioavailability. In contrast, the inhibition of P-glycoprotein may enhance the bioavailability of compounds. However, compounds 28 and 46 were found to mimnimally inhibit P-glycoprotein among the investigated compounds, with values of 0.90 and 0.99, respectively, affecting their bioavailability. Compounds 05 and ceftriaxone demonstrated poor human intestinal absorption among the top hits. Most compounds displayed high Caco-2 membrane permeation with values > −5.0 cm/s, contributing to increased oral absorption. The investigated compounds exhibited significant plasma protein binding affinity (>90%), indicating a lower unbound fraction in plasma. However, compounds 04 and 05 showed 71.21% and 87.62% fractions bound with plasma protein, allowing a significant fraction of free drug to reach its target site.

The low probability of crossing the blood-brain barrier is observed for compounds 28, 46, and 49 and is considered not associated with CNS-related toxicities. The CYP2D6 and CYP3A4 enzymes inhibition or induction may affect drug metabolism, therapeutic effect, and related toxicities. The high enzyme inhibition probability was observed with compounds 23, 28, 43, 51, 55, and 58. In contrast, the compounds 01, 05, 23, 42, and 58 were found to be the substrate of CYP2D6 and CYP3A4 metabolizing enzyme. The top hits demonstrated short half-lives with T½values ranging from 0.69 h to 1.53 h, representing their rapid elimination. The details of ADMET properties for all compounds are outlined in Supplementary Table S2 and Supplementary Table S3 (Supplementary Material).

DFT results

Optimized geometries

The bond lengths and angles were computed at DFT/B3LYP/6-311 + g (d,p) level of theory and are considered accurate from HF calculations, attributed to the inclusion of electron correlation. The optimized geometries of top hits at their most stable conformations are illustrated in Supplementary Figure S5. The optimization energies were computed as −628.95 a. u to −2,856.39 a. u with the lowest Hartree optimization energy value of −1773.27a.u., recoded for compound 67. Most top hits displayed non-planar geometry, particularly observed with compounds 01, 05, 42, 58, 67, and ceftriaxone, likely due to steric hindrance imposed by the adjacent substituents. However, compounds 02, 04, 23, 28, 43, 44, 51, and 55 showed somewhat planar conformations. Table 7 presented the top-hit compounds' optimization energies, dipole moment, polarizability, and HOMO-LUMO gap values. The dipole moment (μ) is one of the significant electronic parameters that illustrates the uneven distribution of charges among atoms in a given compound and is often involved in intermolecular interactions such as dipole-dipole interactions. It is frequently used to study the intermolecular interactions involving the non-bonded type dipole-dipole interactions because the higher the dipole moment is, the stronger the intermolecular interactions. The compounds 01 and 02 displayed higher dipole moments of 9.33 and 10.22 debye, indicating stronger intermolecular interactions, a prerequisite for significant binding affinity with

TABLE 6 The ADMET properties include Blood-brain penetration, metabolism, and excretion regarding the half-life of top hits.

Compounds	BBB	CYP2D6 inhibitor	CYP2D6 substrate	CYP3A4-inhibitor	CYP3A4-substrate	T1/2 (hr)	Lipinski violation
1	0.00	0.00	0.00	0.00	0.99	0.69	0
2	0.66	0.00	0.00	0.00	0.72	1.10	0
4	0.00	0.00	0.00	0.00	0.26	1.53	0
5	0.10	0.00	0.96	0.51	0.01	1.20	0
23	0.81	0.06	0.99	0.98	0.37	0.69	0
28	0.00	0.99	0.00	0.95	0.00	0.52	0
42	0.00	0.00	0.00	0.00	0.99	0.63	1
43	0.00	0.00	0.02	0.99	0.01	0.54	0
44	0.00	0.00	0.24	0.00	0.00	0.71	0
46	0.83	0.01	0.01	0.00	0.00	0.98	0
49	0.78	0.00	0.00	0.02	0.06	0.86	0
51	0.00	0.01	0.01	0.89	0.01	0.78	0
55	0.00	0.10	0.00	0.98	0.00	0.90	0
58	0.09	0.99	0.98	0.99	0.01	1.25	0
59	0.00	0.00	0.00	0.01	0.00	1.08	2
67	0.00	1.00	0.74	1.00	0.09	0.73	0
Ceftriaxone	0.01	0.01	0.00	0.00	0.00	1.92	1

BBB, Blood Brain Barrier (enhanced penetration with values close to 1). T1/2: half life.

TABLE 7 Energetic parameters of top hits using DFT in the gas phase.

Compounds	Optimization energy (a.u.)	Dipole moment (debye)	Polarizability (a.u.)	HOMO (eV)	LUMO (eV)	HOMO-LUMO (ΔeV)
01	−1,203.45	9.33	250.49	−6.15	−1.42	4.74
02	−1,178.75	10.22	299.02	−5.61	−2.55	3.06
04	−628.95	4.54	125.25	−7.34	−1.97	5.37
05	−1,106.30	7.70	245.19	−6.95	−3.11	3.83
23	−1,121.46	4.17	318.89	−6.32	−2.27	4.05
28	−1,089.04	6.89	270.76	−6.48	−3.34	3.15
42	−2050.71	6.64	470.71	−5.84	−2.38	3.46
43	−1,440.46	5.73	385.81	−5.92	−1.76	4.17
44	−1,482.96	5.17	307.50	−5.67	−2.20	3.47
49	−1,194.51	6.80	295.79	−6.19	−2.20	3.99
51	−1,177.42	1.34	308.20	−5.89	−2.21	3.68
55	−1,212.92	0.32	348.05	−5.71	−2.22	3.49
58	−1,161.42	4.09	288.30	−5.81	−2.35	3.45
59	−1,598.61	2.84	376.82	−5.86	−1.82	4.03
67	−1773.27	5.34	355.51	−5.91	−1.61	4.30
Ceftriaxone	−2,856.39	3.99	375.11	−6.09	−2.32	3.78

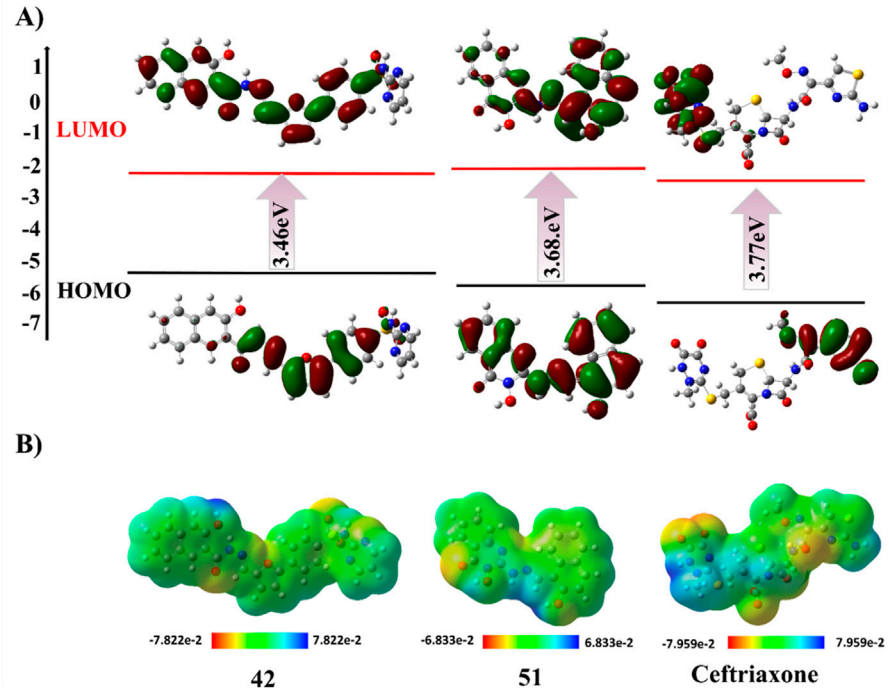


FIGURE 9
DFT studies of compounds 42, 51, and ceftriaxone. **(A)** HOMO-LUMO contour plot. **(B)** Molecular electrostatic potential map.

the target protein. However, compound 51 displayed a high binding affinity with the target protein with the lower dipole moment of 1.34 debye, representing that this parameter is not directly correlated with activity. Polarizability (α) refers to the ease with which electrons can be displaced from the compounds by an external electric field, reflecting the compound's softness and reactivity. In general, high polarizability is associated with the softer nature of the compound (Chattaraj et al., 2003). Compound 42 displayed the highest polarizability of 470.71 a. u, among the top hits, with a lower energy gap of 3.46 eV. However, significant polarizability is also perceived for compounds 43, 59, and 67, along with high HOMO energy values ranging from −5.86eV to −5.92eV. The higher HOMO energies of these compounds were accompanied by easy electron displacement, attributed to their high electron-donating capability. The compound 04 showed lower HOMO energy values of −7.34eV indicating its inferior ability to lose electrons, considered to be less reactive as evidenced by a large energy gap of 5.37 eV. The lowest energy gap of 3.15eV is computed for compound 28, attributed to significantly minimum LUMO energy values of −3.34 eV, representing its greater competency to accept electrons. The energy gap of compound 02 is calculated as 3.06 eV, which is suggested to be the soft compound with electron-donating capacity and high reactivity.

The Supplementary Figure S6 illustrates the HOMO-LUMO orbitals and their corresponding energy gap values for compounds 01, 02, 04, 05 and 23. The HOMO contour maps in compound 02 presented the electron density of electron-rich benzimidazole moiety, while LUMO contour maps were centered on the 2-oxo-quinoline moiety, highlighting its charge transfer character. Similarly, compound 23 showed a shift of electron density from electron-rich to electron-deficient regions in HOMO to LUMO contour maps. This charge transfer type is also observed with compounds 28, 42, and 43, as shown in Supplementary Figure S7. In compounds 01, 04, 44, 46, and 51, the HOMO/LUMO contour maps are located across the entire structure, attributed to extended conjugated systems in these compounds (Supplementary Figure S6; Supplementary Figure S8). Conversely, in compound 05, the HOMO and LUMO orbitals were centered on the particular moiety of the structure, indicating the reactive sites. Interestingly, the non-planar rings displayed negligible electron density with respect to the main nucleus in the chemical structures of compounds 58 and 67 (Supplementary Figure S9). The optimized geometries, HOMO-LUMO contour maps, and MEP plots of compounds 42, 51, and ceftriaxone are presented in Figure 9.

The physiochemical properties and quantum chemical descriptors for top hits are outlined in Table 8. The chemical potential (μ) represents the molecule's inclination to lose or gain electrons, whereas lower μ values signify the greater tendency to capture electrons. The compound 05 and 28 showed lower chemical potentials of −5.03 and −4.91 eV, respectively; compound 01 and reference ceftriaxone exhibited the same chemical potential of −3.78 eV, whereas compound 67 demonstrated the highest potential (μ = −3.76 eV) in comparison to other compounds. Furthermore, compounds 02 and 28 were softer, with chemical softness values of 0.33eV and 0.32 eV, respectively, reflecting their high reactivity. In contrast, the softness potential was the same for compound 05 and ceftriaxone (0.26 eV). Substantive reactivity is also observed with compounds 42 and 51, correlated with their significant binding affinities. Compound 04 was considered the least reactive, with a hardness value of 2.69eV among the top hits. The

TABLE 8 Physiochemical properties and Quantum chemical descriptors for top hits using DFT in the gas phase.

Compounds	Chemical potential (μ) (eV)	Electro-negativity (χ) (eV)	Chemical hardness (η) (eV)	Chemical softness (ζ) (eV)	Electro-philicity index (ω)	Ionization potential (I) (eV)	Electron affinity (A)
01	−3.78	3.78	2.37	0.21	3.02	6.15	1.42
02	−4.08	4.08	1.53	0.33	5.43	5.61	2.55
04	−4.66	4.66	2.69	0.19	4.04	7.34	1.97
05	−5.03	5.03	1.92	0.26	6.60	6.95	3.11
23	−4.30	4.30	2.03	0.25	4.55	6.32	2.27
28	−4.91	4.91	1.57	0.32	7.66	6.48	3.34
42	−4.11	4.11	1.73	0.29	4.89	5.84	2.38
43	−3.84	3.84	2.08	0.24	3.54	5.92	1.76
44	−3.93	3.93	1.73	0.29	4.46	5.67	2.20
46	0.00	0.00	0.00	0.00	0.00	0.00	0.00
49	−4.20	4.20	2.00	0.25	4.41	6.19	2.20
51	−4.05	4.05	1.84	0.27	4.45	5.89	2.21
55	−3.97	3.97	1.75	0.29	4.51	5.71	2.22
58	−4.08	4.08	1.73	0.29	4.82	5.81	2.35
59	−3.84	3.84	2.02	0.25	3.66	5.86	1.82
67	−3.76	3.76	2.15	0.23	3.29	5.91	1.61
Ceftriaxone	−3.78	4.20	1.89	0.26	4.68	6.09	2.32

high electronegativity for compound 05 (χ = 5.03 eV) indicates its greater electron-attracting ability, as evidenced by low LUMO energy and high electron affinity (A = 3.11eV). In contrast, compounds 01 and 67 showed low electronegativity values of 3.78eV and 3.76eV, respectively, representing their lower capacity to attract electrons. Electrophilicity (ω) quantifies the stabilization energy of a compound as it gains electrons. The results displayed high electrophilicity (ω = 7.66) for compound 28, suggested to be a good electrophile compared to other top-hit compounds. These reactivity parameters illustrated the chemical behavior of top-hit compounds and possible interaction types involved in their significant binding affinity.

The molecular electrostatic potential (MEP) surface is invaluable for understanding the allocation of electrostatic potential over the molecule's isoelectronic density surface and aids in determining the regions of the molecule that are likely to be involved in binding interactions. The MEP maps displayed the molecule's high and low electron density regions, presented by a standard color coding system. The red region indicated high electron density with a partial negative charge. In contrast, the blue region signified low electron density with a partial positive charge, turning yellow to green towards neutral regions. In the case of compounds 01, 02, 42, 43, 58, and 59, the positive blue region is centered on the hydrogen atoms bonded to phenolic oxygen, suggested to be a nucleophilic attack site with a maximum of positive electrostatic potential. However, the positive potential is localized on hydrogen atoms bonded to hydroxyl amine in compound 04 and on aromatic hydrogens of compounds 23, 28, 49, and 67, which are suggested to be susceptible to nucleophilic attack. Furthermore, compounds 51 and 55 displayed positive potential sites around the hydrazine and amino groups, respectively, indicating their significant interaction with nucleophiles. Furthermore, the MEP analysis revealed electrophilic attack sites with the most negative potential, centered on carbonyl oxygen and nitrogen atoms of diazole and azo functional groups in the chemical structure of top-hit compounds. The MEP maps of investigated compounds are illustrated in Supplementary Figure S10.

MD-simulation analysis

The MD simulation analysis of compounds 42, 51, and ceftriaxone was performed by plotting root mean square deviation (RMSD), root mean square fluctuation (RMSF), number of H-bond contacts, and % occupancy of H-bonds with key amino acid residues over 100 ns molecular dynamic simulation along with MMGBSA binding energy calculations at various trajectories.

The RMSD plots of backbone atoms of Artemis in complex with investigated compounds revealed the structural stability of protein during the entire simulation, as shown in Supplementary Figure S11. The protein structure in complex with compound 51 and ceftriaxone showed great stability, with RMSD values of about 0.2 nm. In contrast, the Artemis 42 complex showed slight variation during 32ns–55 ns of simulation, with RMSD values of about 0.25 nm.

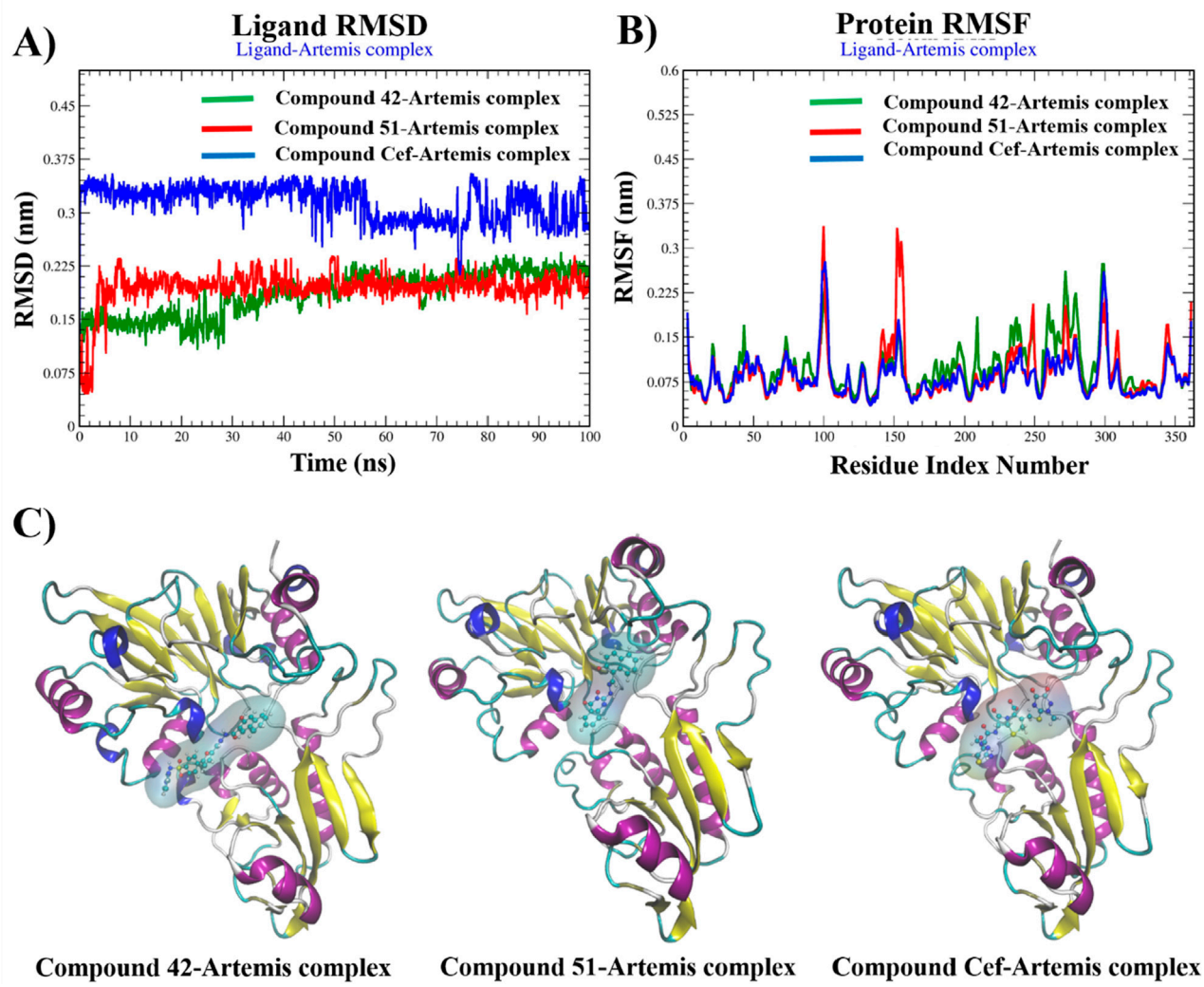


FIGURE 10
Graphical plots of **(A)** ligand RMSD (nm) versus time (100 ns), **(B)** protein RMSF (nm) versus residue index number, and **(C)** Snapshots of MD-trajectories for compounds 42, 51, and ceftriaxone in complex with Artemis protein.

Figure 10 illustrates the RMSD, RMSF plots, and MD snapshots of top hits, providing valuable insights into the binding stability of these compounds with the target protein. The average RMSD value of 0.35 nm was recorded from 0 ns to 55 ns for ceftriaxone. The structural stability was increased with RMSDs of about 0.3 nm up to 80 of simulation, and fluctuation was observed at the end of the simulation. In contrast, the compounds 42 and 51 were equilibrated at 2 ns and 10 ns of simulation, respectively, and maintained stability, demonstrating minimal deviation in RMSD values (~2.5 nm) for the rest of the time period. The binding stability was further validated by aligning MD snapshots, representing that compounds remained stably bound to the protein during the simulation.

Protein Root-Mean-Square Fluctuation (RMSF) is invaluable for determining the structural variation of the Artemis protein during complex formation. The RMSF plots revealed the structural stability of the Artemis protein complex, with fluctuations recorded to be less than 2.0 nm for most of the residues. The complex-42 displayed fluctuations greater than 2.0 nm for amino acid residues 100-101, 278-279, and 297–300, representing flexible loops in protein structure. Complex 51 displayed significant variation in amino acid residues such as 100 and 152-156 with RMSF >3.0 nm. However, the key amino acid residues within the binding pocket remained stable in all complexes over 100 ns of the time period and showed RMSF values less than 2.0 nm.

The binding stability of complexes relayed on the intermolecular interactions, such as H-bonding with crucial amino acid residues and distortion of these interactions under dynamic conditions, is a key factor of complex instability. Supplementary Figure S12 Illustrates the H-bond interaction analysis of complexes over a 100 ns time period. The complex-42 exhibited 3-4 no. Of H-bonds with three consistent H-bonds for most of the simulation time period. A similar H-bonding pattern is observed for ceftriaxone, reflecting their significant stability during the simulation. Compound 51 displayed only one H-bond number for up to 10 ns and gained stability with two H-bonding interactions for the rest of the simulation. To gain further insights and assess the stability of these interactions, we

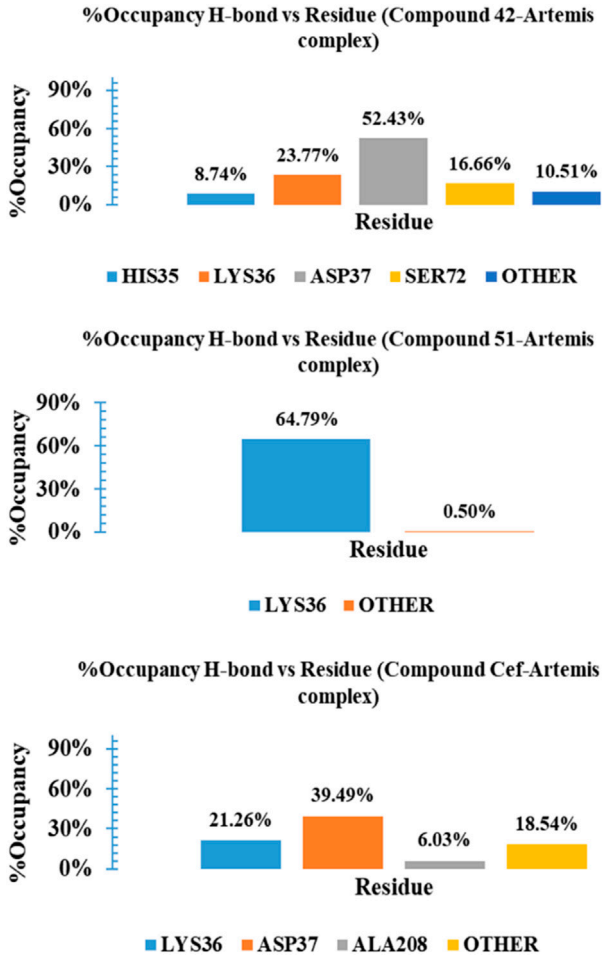


FIGURE 11
Histogram representation of %occupancies of the H-bond versus residues in protein-ligand contacts for compounds 42, 51, and ceftriaxone in complex with Artemis protein.

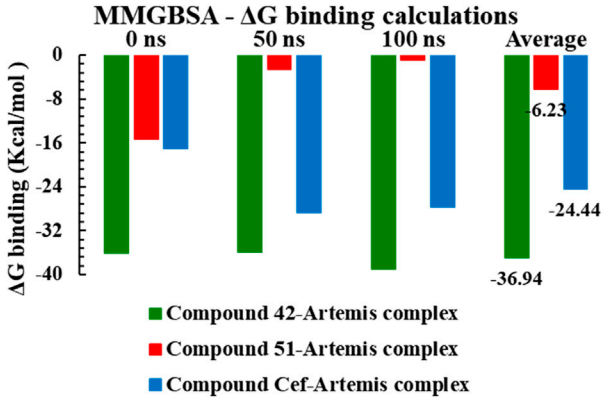


FIGURE 12
The graphical representation of MMGBSA ΔG binding energy calculations for compounds 42, 51, and ceftriaxone in complex with Artemis protein (PDB ID: 7ABS).

calculated the percentage occupancies of specific residues involved in H-bonding interactions. Figure 11 presented a histogram of the % occupancy of hydrogen bond contacts formed by compounds 42, 51, and ceftriaxone in complex with Artemis protein. Compound 42 exhibited significant H-bonding interactions among residues ASP37 and LYS36 with occupancy rates of 52.43% and 23.77%, respectively. The H-bonding interaction is also recorded with another catalytic amino acid residue, HIS35, showing 8.74% occupancy. In contrast, compound 51 exhibited H-bonding interaction with LYS36 for most of the simulation time, demonstrating a 64.79% occupancy rate. The reference compound, ceftriaxone, showed 21.26% and 31.29% H-bonding occupancy for LYS36 and ASP37, respectively. These findings concluded the greater effective binding of compound 42, showcasing substantial interaction with catalytic amino acid residues of the target protein.

The MM-GBSA method was employed for Gibbs free energy (ΔG) calculations at 0 ns, 50 ns and 100 ns simulation trajectories, tabulated in Supplementary Table S5, to estimate the binding stability of investigated complexes in a dynamic environment. The binding free energy for complex 42 ranged from −38.56 kcal/mol to −37.48 kcal/mol at different simulation trajectories, indicating the complex stability with an average ΔG value of −36.94 kcal/mol. The ceftriaxone complex displayed higher binding affinities for time, maximum at 50 ns of simulation, with an average ΔG value of −24.44 kcal/mol. In contrast, the complex-51 displayed significant binding free energy with ΔG calculated to be −15.58 kcal/mol at 0 ns of trajectory. However, high binding energies of −5.58 kcal/mol and −2.67 kcal/mol were recorded at 50 ns and 100 ns intervals, suggesting that new conformations of compound 51 were found to be energetically less favorable. Figure 12 illustrated the graphical representation of MM-GBSA Gibbs free energy calculations for studied complexes.

Principle component analysis

Molecular dynamics (MD) simulations are crucial for assessing the flexibility of ligands and receptors. However, the receptor conformations can shift within nanoseconds, so identifying suitable conformations for MD to screen millions of compounds for potential inhibitors with high efficacy poses a significant challenge. By combining these simulations with theoretical models, certain receptor conformations emerge as promising ones, warranting deeper investigation. Despite this, achieving the necessary accuracy in calculations is difficult. The challenge lay in selecting the most promising conformations while managing the long computational times, even though simulations typically span only microseconds (Adcock and McCammon, 2006; Robson, 2022).

To address this, several advanced techniques have been developed to reduce the number of frames needed while retaining critical data. Among these techniques, principal component analysis (PCA) (Das and Mukhopadhyay, 2007), and wavelet analysis (Heidari et al., 2016) were employed to interpret complex data. PCA, in particular, is widely used to simplify the high dimensionality of datasets by focusing on the most relevant principal components. These components capture the key variations in protein motion, enabling the global dynamics of the protein to be represented without losing essential details. PCA reveals

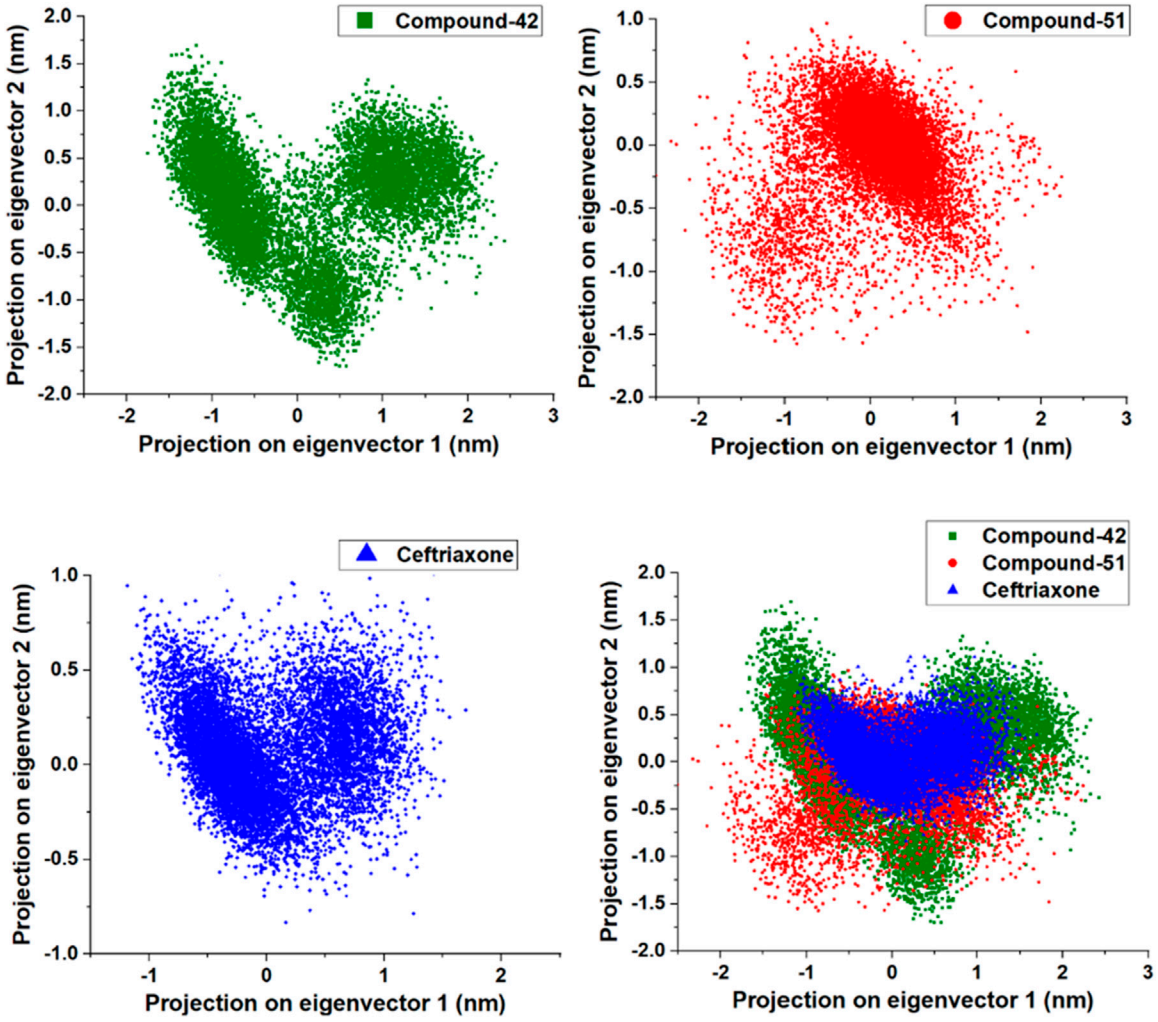


FIGURE 13
Principal Component analysis for compound-42, compound-51 and cefriaxone in complex with target protein (PDB ID: 7ABS).

important structural variations occurring in the protein's trajectory by analyzing eigenvalues from the covariance matrix. Through this process, the most dominant protein motions can be identified, highlighting significant conformational changes throughout the simulation (David and Jacobs, 2014).

This study conducted a two-dimensional (2D) PCA to compare the dynamics of three systems: 7ABS-42 complex, 7ABS-51 complex, and 7ABS-ceftriaxone complex. The goal was to understand how compound-42, compound-51, and ceftriaxone binding influences protein motion. As shown in Figure 13, the binding of compound-42 to 7ABS confined the protein's motion to a compact phase space with a narrow binding site volume, indicating stronger binding interactions than ceftriaxone. In contrast, the binding of compound-51 led to increased internal motions, resulting in a new configuration with a wider binding site volume. A comparison of the PCA results with the RMSF (Root Mean Square Fluctuations) values for the 7ABS-42 and 7ABS-51 complexes indicated that the 7ABS-51 complex occupied a wider phase space, likely due to higher fluctuations in the 100-150 region. Overall, the PCA results highlighted that the binding site volume decreased in the order of the 7ABS-51 > 7ABS-ceftriaxone > 7ABS-42 complexes, indicating a strong interaction of compound-42 with the target protein.

Free energy landscape (FEL) analysis

Based on PCA, free energy landscape (FEL) analysis provides a more accurate representation of the protein's conformational space in terms of energy and time. FEL is constructed from the probability distribution of specific data points, which are then transformed into free energy values using a straightforward mathematical relationship (Papaleo et al., 2009). Figure 14 illustrated FEL projections onto the first two principal components for the 7ABS-42, 7ABS-51, and 7ABS-ceftriaxone complexes, focusing on the Cα-atoms of 7ABS. Deep blue areas represented the lowest energy conformations in these plots, while red areas indicated the highest. For the 7ABS-42 complex, a more compact blue region covering a larger surface area is suggested to be a stable cluster. The conformational state with energy minima of varying depths, separated by an energy barrier, indicated that 7ABS-42 could

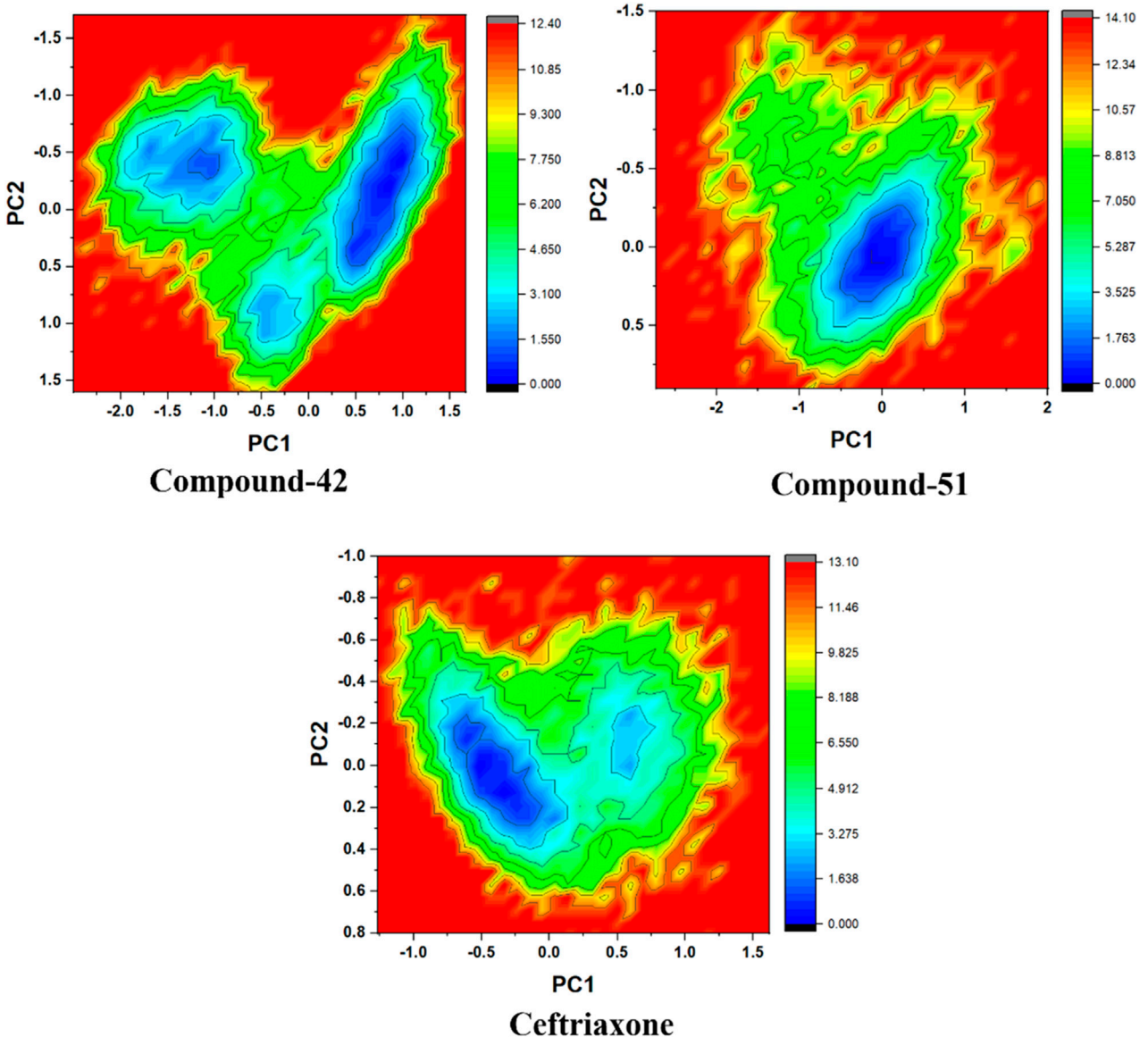


FIGURE 14
Gibbs free energy landscape for compound-42, compound-51, and cefriaxone in complex with target protein (PDB ID: 7ABS).

adopt several thermodynamically favorable conformations, allowing for more significant interactions over time.

In contrast, the 7ABS-51 complex displayed a single deep blue region, indicating greater stability with fewer conformational changes than the reference. This is further supported by the 7ABS-51 complex's low RMSD, which showcases only minor fluctuations throughout the simulation. Meanwhile, the 7ABS-ceftriaxone complex exhibited two distinct blue regions, separated by a small energy barrier, suggesting that it existed in two different energetically favorable conformational states.

The FEL results align well with the hydrogen bonding (H-bonding) analysis. The less conformationally dynamic 7ABS-51 complex consistently maintained two H-bonds throughout the simulation, whereas the 7ABS-ceftriaxone complex displayed up to four H-bonds over time. Similarly, the conformational flexibility of the 7ABS-42 complex resulted in the formation of four H-bonds for most of the simulation period, indicating a more favorable conformational shift than the 7ABS-ceftriaxone complex.

Conclusion

Our experiments showed that Artemis deficiency in CJ179 cells would leave some DNA breaks unrepaired, as observed by the increase in micronucleus frequency. Overall, Artemis inhibition in most target cell lines should, in principle, radiosensitize them and increase target cell lethality upon irradiation. Experiments with siRNA inhibition of Artemis also exhibited a 40 percent decrease in Artemis gene expression level as compared to control in 1MOS and 1PTNC. In 2PTN, 30 percent, whereas around a 20 percent decrease in 3PRF and 2PRF samples was observed. The increase in DNA PK gene expression shown by IMOS was not significant as compared to

2PRF. whereas other primary cell lines had a downregulation effect. 1PTN showed no decreasing trend as compared to 2PTN and 3PRF, which showed almost up to 15 percent and 30 percent decrease, respectively. Gene expression analysis of TP53 showed that 2PTN had the highest increase in p53 gene expression, which was almost 46%. Almost similar trend was observed in 2PRF, whereas 1PTN and 1MOS showed a similarity in increased expression of 38%. We selected one primary Artemis inhibitor and tested it against 5 primary cell lines derived from invasive ductal carcinomas and found that Artemis inhibition does not affect the DNA repair process, but inhibition results in increased DNA damage as evident from the COMET assay data. This increased DNA damage puts the irradiated cell on a path of apoptosis, notwithstanding the heavy damage. The *in vitro* analysis revealed small molecule (HMAD) as an inhibitor of Artemis protein, further motivating us to conduct an *in silico* screening of the compound library in search of a more potent inhibitor. In the current study, a small molecule library of 69 compounds, retrieved from the ZINC database, was investigated for their inhibiting potential against the endonuclease protein Artemis (PDB ID: 7ABS) to boost the effect of ionizing radiation in cancer therapy. The sixteen compounds were recognized as top hits through docking studies with ΔG-scores greater than −8.0 kcal/mol, which exposed physicochemical and pharmacokinetic properties for further screening. Furthermore, the DFT studies unveiled the electronic properties of top-hit compounds, suggesting the notable reactivity of compounds 42 and 51 with softness values of 0.29 eV and 0.27 eV, respectively. MEP analysis shows these compounds demonstrated the nucleophilic attack sites highlighted with blue color coding, indicating their potential involvement in intermolecular interactions. Based on docking studies along with ADMET and DFT analysis, compounds 42 and 51 were subjected to MD simulation for 100 ns. Compound 42 showed stable trajectories throughout the simulation, evidenced by consistent H-bonding interactions with key amino acid residues. Furthermore, the Gibbs free energies were calculated by the MM-GBSA method, showing higher binding affinities for compound 42 with average ΔG values of −36.94 kcal/mol, suggesting it to be a promising candidate in potentiating the effect of radiotherapy. Furthermore, the PCA and FEL analysesW support the simulation results, indicating the significant potential of these compounds as radiosensitizers in cancer therapy. Future studies could benefit from incorporating MM-PBSA to refine binding energy estimations and to further validate lead compound selection.

Data availability statement

The datasets presented in this study can be found in online repositories. The names of the repository/repositories and accession number(s) can be found in the article/Supplementary Material.

Ethics statement

Ethical approval was not required for the studies on humans in accordance with the local legislation and institutional requirements because only commercially available established cell lines were used.

Author contributions

MB: Data curation, Formal Analysis, Visualization, Methodology, Software, Investigation, Writing – review and editing, Writing – original draft. UA: Writing – review and editing, Formal Analysis, Validation, Writing – original draft, Data curation, Investigation. SN: Data Curation, Formal Analysis, Methodology, Investigation, Visualization, Writing – original draft. FS: Writing – original draft, Resources, Project administration, Conceptualization, Writing – review and editing, Validation, Supervision. NJ: Project administration, Supervision, Conceptualization, Writing – review and editing, Investigation, Formal Analysis, Writing – original draft, Resources.

Funding

The author(s) declare that no financial support was received for the research and/or publication of this article.

Acknowledgments

The authors extend their appreciation to the Owner and founder of Hangzhou Baiao Kuntai Biotechnology, Office 314, Building 1, China-Europe Innovation Center, Gongshu district, Zhejiang, 310000 P.R. China, for the research work and development of the study. We are also thankful to the Computer Aided Drug Design Facility at the Department of Pharmaceutical Chemistry, Faculty of Pharmacy, Bahauddin Zikriya University, Multan, 60800, Pakistan.

Conflict of interest

The authors declare that the research was conducted in the absence of any commercial or financial relationships that could be construed as a potential conflict of interest.

Generative AI statement

The author(s) declare that no Generative AI was used in the creation of this manuscript.

Publisher's note

All claims expressed in this article are solely those of the authors and do not necessarily represent those of their affiliated organizations, or those of the publisher, the editors and the reviewers. Any product that may be evaluated in this article, or claim that may be made by its manufacturer, is not guaranteed or endorsed by the publisher.

Supplementary material

The Supplementary Material for this article can be found online at: https://www.frontiersin.org/articles/10.3389/fchem.2025.1597454/full#supplementary-material

References

Abdi, H., and Williams, L. J. (2010). Principal component analysis. *Wiley Interdiscip. Rev. Comput. Stat.* 2 (4), 433–459. doi:10.1002/wics.101

Abel, R., Wang, L., Harder, E. D., Berne, B. J., and Friesner, R. A. (2017). Advancing drug discovery through enhanced free energy calculations. *Accounts Chem. Res.* 50 (7), 1625–1632. doi:10.1021/acs.accounts.7b00083

Abraham, M. J., Murtola, T., Schulz, R., Páll, S., Smith, J. C., Hess, B., et al. (2022). *GROMACS: high performance molecular simulations through multi-level parallelism from laptops to supercomputers*. (Elsevier: Netherlands) GROMACS Development Team, 19–25. Available online at: www.gromacs.org.

Adcock, S. A., and McCammon, J. A. (2006). Molecular dynamics: survey of methods for simulating the activity of proteins. *Chem. Rev.* 106 (5), 1589–1615. doi:10.1021/cr040426m

Agoni, C., Olotu, F. A., Ramharack, P., and Soliman, M. E. (2020). Druggability and drug-likeness concepts in drug design: are biomodelling and predictive tools having their say? *J. Mol. Model.* 26, 120–11. doi:10.1007/s00894-020-04385-6

Allen, W. J., Balius, T. E., Mukherjee, S., Brozell, S. R., Moustakas, D. T., Lang, P. T., et al. (2015). DOCK 6: impact of new features and current docking performance. *J. Comput. Chem.* 36 (15), 1132–1156. doi:10.1002/jcc.23905

Anwar, T., Kumar, P., and Khan, A. U. (2021). "Modern tools and techniques in computer-aided drug design," in *Molecular docking for computer-aided drug design* (Elsevier), 1–30.

Arshad, M., Ahmed, K., Bashir, M., Kosar, N., Kanwal, M., Ahmed, M., et al. (2021). Synthesis, structural properties and potent bioactivities supported by molecular docking and DFT studies of new hydrazones derived from 5-chloroisatin and 2-thiophenecarboxaldehyde. *J. Mol. Struct.* 1246, 131204. doi:10.1016/j.molstruc.2021.131204

Aziz, M., Ejaz, S. A., Rehman, H. M., Alsubaie, A. S., Mahmoud, K. H., Siddique, F., et al. (2023). Identification of NEK7 inhibitors: structure based virtual screening, molecular docking, density functional theory calculations and molecular dynamics simulations. *J. Biomol. Struct. Dyn.* 41 (14), 6894–6908. doi:10.1080/07391102.2022.2113563

Aziz, M., Ejaz, S. A., Tamam, N., Siddique, F., Riaz, N., Qais, F. A., et al. (2022b). Identification of potent inhibitors of NEK7 protein using a comprehensive computational approach. *Sci. Rep.* 12 (1), 6404. doi:10.1038/s41598-022-10253-5

Aziz, M., Ejaz, S. A., Zargar, S., Akhtar, N., Aborode, A. T., A. Wani, T., et al. (2022a). Deep learning and structure-based virtual screening for drug discovery against NEK7: a novel target for the treatment of cancer. *Molecules* 27 (13), 4098. doi:10.3390/molecules27134098

Badar, M. S., Shamsi, S., Ahmed, J., and Alam, A. (2022). "Molecular dynamics simulations: concept, methods, and applications," in *Transdisciplinarity* (Springer), 131–151.

Becke, A. D. (1993). Density-functional thermochemistry. III. The role of exact exchange. *J. Chem. Phys.* 98 (7), 5648–5652. doi:10.1063/1.464913

Bilal, M. S., Ejaz, S. A., Zargar, S., Akhtar, N., Wani, T. A., Riaz, N., et al. (2022). Computational investigation of 1, 3, 4 oxadiazole derivatives as lead inhibitors of VEGFR 2 in comparison with EGFR: density functional theory, molecular docking and molecular dynamics simulation studies. *Biomolecules* 12 (11), 1612. doi:10.3390/biom12111612

Burdak-Rothkamm, S., Rothkamm, K., and Prise, K. M. (2008). ATM acts downstream of ATR in the DNA damage response signaling of bystander cells. *Cancer Res.* 68 (17), 7059–7065. doi:10.1158/0008-5472.can-08-0545

Chattaraj, P., Nath, S., and Maiti, B. (2003). Reactivity descriptors. Computational medicinal chemistry for drug discovery. 11, 295.

Clark, T., Chandrasekhar, J., Spitznagel, G. W., and Schleyer, P. V. R. (1983). Efficient diffuse function-augmented basis sets for anion calculations. III. The 3-21+G basis set for first-row elements, Li–F. *J. Comput. Chem.* 4 (3), 294–301. doi:10.1002/jcc.540040303

Cross, S. S. (2005). Improved FlexX docking using FlexS-determined base fragment placement. *J. Chem. Inf. Model.* 45 (4), 993–1001. doi:10.1021/ci050026f

Das, A., and Mukhopadhyay, C. (2007). Application of principal component analysis in protein unfolding: an all-atom molecular dynamics simulation study. *J. Chem. Phys.* 127 (16), 165103. doi:10.1063/1.2796165

David, C. C., and Jacobs, D. J. (2014). Principal component analysis: a method for determining the essential dynamics of proteins. *Protein Dyn. Methods Protoc.* 1084, 193–226. doi:10.1007/978-1-62703-658-0_11

Ejaz, S. A., Aziz, M., Ahmed, A., Alotaibi, S. S., Albogami, S. M., Siddique, F., et al. (2023). New Insight into the pharmacological importance of atropine as the potential inhibitor of AKR1B1 via detailed computational investigations: DFTs, ADMET, molecular docking, and molecular dynamics studies. *Appl. Biochem. Biotechnol.* 195 (8), 5136–5157. doi:10.1007/s12010-023-04411-2

Farhan, S., Aqdas, A., Bashir, M., Nadeem, S., and Rawat, R. (2024). Harnessing the potential of natural products in cancer treatment: a comprehensive review. *J. Biol. Regul. Homeost. Agents* 38 (2), 873–897. doi:10.23812/j.biol.regul.homeost.agents.20243802.72

Friesner, R. A., Banks, J. L., Murphy, R. B., Halgren, T. A., Klicic, J. J., Mainz, D. T., et al. (2004). Glide: a new approach for rapid, accurate docking and scoring. 1. Method and assessment of docking accuracy. *J. Med. Chem.* 47 (7), 1739–1749. doi:10.1021/jm0306430

Frisch, M. J., Trucks, G. W., and Schlegel, H. B. (2009). *Gaussian 09, revision A.02*. Wallingford, CT: Gaussian, Inc.

Glorieux, M. (2020). *Combining radiotherapy with DNA repair inhibitors as novel treatment strategy for head and neck cancers*. KU Leuven. London, United Kingdom: Nature Portfolio.

Heidari, Z., Roe, D. R., Galindo-Murillo, R., Ghasemi, J. B., and Cheatham, T. E., III (2016). Using wavelet analysis to assist in identification of significant events in molecular dynamics simulations. *J. Chem. Inf. Model.* 56 (7), 1282–1291. doi:10.1021/acs.jcim.5b00727

Huang, S.-Y., and Zou, X. (2010). Advances and challenges in protein-ligand docking. *Int. J. Mol. Sci.* 11 (8), 3016–3034. doi:10.3390/ijms11083016

Huey, R., Morris, G. M., Olson, A. J., and Goodsell, D. S. (2007). A semiempirical free energy force field with charge-based desolvation. *J. Comput. Chem.* 28 (6), 1145–1152. doi:10.1002/jcc.20634

Humphrey, W., Dalke, A., and Schulten, K. (1996). VMD: visual molecular dynamics. *J. Mol. Graph.* 14 (1), 33–38. doi:10.1016/0263-7855(96)00018-5

Irwin, J. J., and Shoichet, B. K. (2005). ZINC– a free database of commercially available compounds for virtual screening. *J. Chem. Inf. Model.* 45 (1), 177–182. doi:10.1021/ci049714+

Jorgensen, W. L., Chandrasekhar, J., Madura, J. D., Impey, R. W., and Klein, M. L. (1983). Comparison of simple potential functions for simulating liquid water. *J. Chem. Phys.* 79 (2), 926–935. doi:10.1063/1.445869

Karim, M. F., Liu, S., Laciak, A. R., Volk, L., Koszelak-Rosenblum, M., Lieber, M. R., et al. (2020). Structural analysis of the catalytic domain of Artemis endonuclease/SNM1C reveals distinct structural features. *J. Biol. Chem.* 295 (35), 12368–12377. doi:10.1074/jbc.ra120.014136

Krempler, A. (2004). *A pathway of double-strand break rejoining dependent upon ATM*. Artemis. Cambridge, MA: Cell Press.

Kunnakkattu, I. R., Choudhary, P., Pravda, L., Nadzirin, N., Smart, O. S., Yuan, Q., et al. (2023). PDBe CCDUtils: an RDKit-based toolkit for handling and analysing small molecules in the Protein Data Bank. *J. Cheminformatics* 15 (1), 117. doi:10.1186/s13321-023-00786-w

Li, S., Chang, H. H., Niewolik, D., Hedrick, M. P., Pinkerton, A. B., Hassig, C. A., et al. (2014). Evidence that the DNA endonuclease ARTEMIS also has intrinsic 5′-exonuclease activity. *J. Biol. Chem.* 289 (11), 7825–7834. doi:10.1074/jbc.m113.544874

Li, Z., Huang, Y., Wu, Y., Chen, J., Wu, D., Zhan, C. G., et al. (2019). Absolute binding free energy calculation and design of a subnanomolar inhibitor of phosphodiesterase-10. *J. Med. Chem.* 62 (4), 2099–2111. doi:10.1021/acs.jmedchem.8b01763

Lindahl, E., Hess, B., and Van Der Spoel, D. (2001). GROMACS 3.0: a package for molecular simulation and trajectory analysis. *Mol. Model. Annu.* 7, 306–317. doi:10.1007/s008940100045

Liu, H., Wang, X., Huang, A., Gao, H., Sun, Y., Jiang, T., et al. (2018). Silencing artemis enhances colorectal cancer cell sensitivity to DNA-damaging agents. *Oncol. Res.* 27 (1), 29–38. doi:10.3727/096504018x15179694020751

Ma, Y., Schwarz, K., and Lieber, M. R. (2005). The Artemis: DNA-PKcs endonuclease cleaves DNA loops, flaps, and gaps. *DNA repair* 4 (7), 845–851. doi:10.1016/j.dnarep.2005.04.013

MacKerell, A. D., Jr., Bashford, D., Bellott, M., Dunbrack, R. L., Jr., Evanseck, J. D., Field, M. J., et al. (1998). All-Atom empirical potential for molecular modeling and dynamics studies of proteins. *J. Phys. Chem. B* 102 (18), 3586–3616. doi:10.1021/jp973084f

Melenotte, C., Pontarotti, P., Pinault, L., Mège, J. L., Devaux, C., and Raoult, D. (2021). Could β-lactam antibiotics block humoral immunity? *Front. Immunol.* 12, 680146. doi:10.3389/fimmu.2021.680146

Pagadala, N. S., Syed, K., and Tuszynski, J. (2017). Software for molecular docking: a review. *Biophys. Rev.* 9, 91–102. doi:10.1007/s12551-016-0247-1

Papaleo, E., Mereghetti, P., Fantucci, P., Grandori, R., and De Gioia, L. (2009). Free-energy landscape, principal component analysis, and structural clustering to identify representative conformations from molecular dynamics simulations: the myoglobin case. *J. Mol. Graph. Model.* 27 (8), 889–899. doi:10.1016/j.jmgm.2009.01.006

Podrimaj-Bytyqi, A., Borovečki, A., Selimi, Q., Manxhuka-Kerliu, S., Gashi, G., and Elezaj, I. R. (2018). The frequencies of micronuclei, nucleoplasmic bridges and nuclear buds as biomarkers of genomic instability in patients with urothelial cell carcinoma. *Sci. Rep.* 8 (1), 17873. doi:10.1038/s41598-018-35903-5

Potdar, P., and Chaugule, S. (2011). Establishment and molecular characterization of breast cancer mesenchymal stem cell line derived from human non-metastasis breast cancer tumor. *Stem Cell Discov.* 1 (02), 21–28. doi:10.4236/scd.2011.12003

Prieto-Martínez, F. D., López-López, E., Juárez-Mercado, K. E., and Medina-Franco, J. L. (2019). "Computational drug design methods—current and future perspectives," in *In silico drug design*, 19–44.

RCSB (2025). Redesigned PDB statistics support enhanced functionality. Available online at: https://www.rcsb.org/.

Reimers, J. R., Cai, Z., Bilić, A., and Hush, N. S. (2003). The appropriateness of density-functional theory for the calculation of molecular electronics properties. *Ann. N. Y. Acad. Sci.* 1006 (1), 235–251. doi:10.1196/annals.1292.017

Riballo, E., Kühne, M., Rief, N., Doherty, A., Smith, G. C., Recio, M. J., et al. (2004). A pathway of double-strand break rejoining dependent upon ATM, Artemis, and proteins locating to γ-H2AX foci. *Mol. cell* 16 (5), 715–724. doi:10.1016/j.molcel.2004.10.029

Robson, B. (2022). *De novo* protein folding on computers. Benefits and challenges. *Comput. Biol. Med.* 143, 105292. doi:10.1016/j.compbiomed.2022.105292

Sambrook, J., Fritsch, E. F., and Maniatis, T. (1989). Molecular cloning: a laboratory manual.

Schmidtke, P., and Barril, X. (2010). Understanding and predicting druggability. A high-throughput method for detection of drug binding sites. *J. Med. Chem.* 53 (15), 5858–5867. doi:10.1021/jm100574m

Schulz-Gasch, T., and Stahl, M. (2004). Scoring functions for protein–ligand interactions: a critical perspective. *Drug Discov. Today Technol.* 1 (3), 231–239. doi:10.1016/j.ddtec.2004.08.004

Siddique, F., Anwaar, A., Bashir, M., Nadeem, S., Rawat, R., Eyupoglu, V., et al. (2024). Revisiting methotrexate and phototrexate Zinc15 library-based derivatives using deep learning in-silico drug design approach. *Front. Chem.* 12, 1380266. doi:10.3389/fchem.2024.1380266

Soubeyrand, S., Pope, L., De Chasseval, R., Gosselin, D., Dong, F., de Villartay, J. P., et al. (2006). Artemis phosphorylated by DNA-dependent protein kinase associates preferentially with discrete regions of chromatin. *J. Mol. Biol.* 358 (5), 1200–1211. doi:10.1016/j.jmb.2006.02.061

Sun, H., Li, Y., Shen, M., Tian, S., Xu, L., Pan, P., et al. (2014). Assessing the performance of MM/PBSA and MM/GBSA methods. 5. Improved docking performance using high solute dielectric constant MM/GBSA and MM/PBSA rescoring. *Phys. Chem. Chem. Phys.* 16 (40), 22035–22045. doi:10.1039/c4cp03179b

Tandon, H., Chakraborty, T., and Suhag, V. (2019). A brief review on importance of DFT in drug design. *Res. Med. Eng. Sci.* 7 (4), 791–795. doi:10.31031/RMES.2019.07.00068

Tirado-Rives, J., and Jorgensen, W. L. (2008). Performance of B3LYP density functional methods for a large set of organic molecules. *J. Chem. theory Comput.* 4 (2), 297–306. doi:10.1021/ct700248k

Tuma, C., Boese, A. D., and Handy, N. C. (1999). Predicting the binding energies of H-bonded complexes: a comparative DFT study. *Phys. Chem. Chem. Phys.* 1 (17), 3939–3947. doi:10.1039/a904357h

Turner, P. (2005). XMGRACE, version 5.1. 19. Center for coastal and land-margin research, Oregon graduate Institute of science and technology. *Beavert. OR* 2 (5), 19.

Valencia, E., Olarte, W., and Sastoque, F. (2023). *In silico* study of the admet properties of potential inhibitors of new Delhi methalo-ß-lactamase-1 (NDM-1). *Seven Ed.* São José dos Pinhais, Brazil: part of Seven Publicações Ltda. doi:10.56238/uniknowindevolp-013

van de Kamp, G., Heemskerk, T., Kanaar, R., and Essers, J. (2021). DNA double strand break repair pathways in response to different types of ionizing radiation. *Front. Genet.* 12, 738230. doi:10.3389/fgene.2021.738230

Verdonk, M. L., Cole, J. C., Hartshorn, M. J., Murray, C. W., and Taylor, R. D. (2003). Improved protein–ligand docking using GOLD. *Proteins Struct. Funct. Bioinforma.* 52 (4), 609–623. doi:10.1002/prot.10465

Vogt, M., and Bajorath, J. (2017). Modeling tanimoto similarity value distributions and predicting search results. *Mol. Inf.* 36 (7), 1600131. doi:10.1002/minf.201600131

Watanabe, G., Lieber, M. R., and Williams, D. R. (2022). Structural analysis of the basal state of the Artemis: DNA-PKcs complex. *Nucleic Acids Res.* 50 (13), 7697–7720. doi:10.1093/nar/gkac564

Xiong, G., Wu, Z., Yi, J., Fu, L., Yang, Z., Hsieh, C., et al. (2021). ADMETlab 2.0: an integrated online platform for accurate and comprehensive predictions of ADMET properties. *Nucleic acids Res.* 49 (W1), W5–W14. doi:10.1093/nar/gkab255

Węglarz, L., Molin, I., Orchel, A., Parfiniewicz, B., and Dzierżewicz, Z. (2006). Quantitative analysis of the level of p53 and p21WAF1 mRNA in human colon cancer HT-29 cells treated with inositol hexaphosphate.

Xiong, X., Du, Z., Wang, Y., Feng, Z., Fan, P., Yan, C., et al. (2015). 53BP1 promotes microhomology-mediated end-joining in G1-phase cells. *Nucleic acids Res.* 43 (3), 1659–1670. doi:10.1093/nar/gku1406

Yang, X., Wang, Y., Byrne, R., Schneider, G., and Yang, S. (2019). Concepts of artificial intelligence for computer-assisted drug discovery. *Chem. Rev.* 119 (18), 10520–10594. doi:10.1021/acs.chemrev.8b00728

Yaqoob, F., Aftab, H., Sadeghian, N., Taslimi, P., Siddique, F., Nadeem, S., et al. (2025). Design, synthesis, antidiabetic evaluation and computational modeling of phenylnaphthalene-2-sulfonate derived hydrazones. *J. Mol. Struct.* 1335, 141883. doi:10.1016/j.molstruc.2025.141883

Yasaei, H., and Slijepcevic, P. (2010). Research Defective Artemis causes mild telomere dysfunction.

Yosaatmadja, Y., Baddock, H., Newman, J., Bielinski, M., Gavard, A., Mukhopadhyay, S. M. M., et al. (2021). Structural and mechanistic insights into the Artemis endonuclease and strategies for its inhibition. *Nucleic acids Res.* 49 (16), 9310–9326. doi:10.1093/nar/gkab693

Zadorozhnii, P. V., Kiselev, V. V., and Kharchenko, A. V. (2022). *In silico* ADME profiling of salubrinal and its analogues. *Future Pharmacol.* 2 (2), 160–197. doi:10.3390/futurepharmacol2020013

Zang, Q., Mansouri, K., Williams, A. J., Judson, R. S., Allen, D. G., Casey, W. M., et al. (2017). *In silico* prediction of physicochemical properties of environmental chemicals using molecular fingerprints and machine learning. *J. Chem. Inf. Model.* 57 (1), 36–49. doi:10.1021/acs.jcim.6b00625

Zhang, X., Succi, J., Feng, Z., Prithivirajsingh, S., Story, M. D., and Legerski, R. J. (2004). Artemis is a phosphorylation target of ATM and ATR and is involved in the G2/M DNA damage checkpoint response. *Mol. Cell. Biol.* 24, 9207–9220. doi:10.1128/mcb.24.20.9207-9220.2004

Zhang, X., Zhu, Y., Geng, L., Wang, H., and Legerski, R. J. (2009). Artemis is a negative regulator of p53 in response to oxidative stress. *Oncogene* 28 (22), 2196–2204.

Zoete, V., Grosdidier, A., and Michielin, O. (2009). Docking, virtual high throughput screening and *in silico* fragment-based drug design. *J. Cell. Mol. Med.* 13 (2), 238–248. doi:10.1111/j.1582-4934.2008.00665.x

frontiers | Frontiers in Chemistry

TYPE Original Research
PUBLISHED 05 September 2025
DOI 10.3389/fchem.2025.1627186

Check for updates

OPEN ACCESS

EDITED BY
Md. Palashuddin S. K.,
Aligarh Muslim University, India

REVIEWED BY
Abbas Hassan,
United Arab Emirates University, United Arab Emirates
Ata Makarem,
University of Hamburg, Germany
Mohammed Mahbubul Matin,
University of Chittagong, Bangladesh

*CORRESPONDENCE
Ahmed Sabt,
sabt.nrc@gmail.com
Jarosław Dziadek,
jdziadek@cbm.pan.pl

RECEIVED 12 May 2025
ACCEPTED 21 August 2025
PUBLISHED 05 September 2025

CITATION
Ebaid MS, Farag H, Abdelraof M, Saleh AM, Thabit MG, Dziadek J, Youssef AA and Sabt A (2025) Design, synthesis, and biological assessment of a novel series of coumarin-tethered thiazole derivatives as potential antibacterial agents.
Front. Chem. 13:1627186.
doi: 10.3389/fchem.2025.1627186

COPYRIGHT
© 2025 Ebaid, Farag, Abdelraof, Saleh, Thabit, Dziadek, Youssef and Sabt. This is an open-access article distributed under the terms of the Creative Commons Attribution License (CC BY). The use, distribution or reproduction in other forums is permitted, provided the original author(s) and the copyright owner(s) are credited and that the original publication in this journal is cited, in accordance with accepted academic practice. No use, distribution or reproduction is permitted which does not comply with these terms.

Design, synthesis, and biological assessment of a novel series of coumarin-tethered thiazole derivatives as potential antibacterial agents

Manal S. Ebaid[1], Hanaa Farag[2], Mohamed Abdelraof[3], Abdulrahman M. Saleh[4], Mohamed G. Thabit [5], Jarosław Dziadek[6]*, Ahmed A. Youssef[7,8] and Ahmed Sabt [9]*

[1]Department of Chemistry, College of Science, Northern Border University, Arar, Saudi Arabia, [2]Pesticide Chemistry Department, Chemical Industries Research Institute, National Research Centre, Cairo, Egypt, [3]Microbial Chemistry Department, National Research Centre, Biotechnology Research Institute, Giza, Egypt, [4]Department of Pharmaceutical Chemistry, Faculty of Pharmacy, Cairo University, Cairo, Egypt, [5]Pharmaceutical Chemistry Department, Faculty of Pharmacy, Pharos University (PUA), Alexandria, Egypt, [6]Laboratory of Genetics and Physiology of Mycobacterium, Institute of Medical Biology of the Polish Academy of Sciences, Lodz, Poland, [7]Department of Biochemistry, Faculty of Pharmacy, Egyptian Russian University, Cairo, Egypt, [8]Department of Laboratory Science, College of Pharmacy, University of Kut, Wasit, Iraq, [9]Chemistry of Natural Compounds Department, Pharmaceutical and Drug Industries Research Institute, National Research Centre, Cairo, Egypt

Since the discovery of penicillin in the 1930s, antibiotics have been the primary treatment for bacterial infections. However, antimicrobial resistance (AMR) has escalated due to antibiotics overuse and misuse. To address this concern, a new series of coumarin-thiazole derivatives was synthesized and evaluated against *Serratia fonticola, Campylobacter jejuni, Enterococcus faecalis, and Achromobacter xylosoxidans*. Most compounds showed selective activity, with compounds 6a and 6c exhibiting potent effects against *E. faecalis* (MICs: 25, 12.5 µg/mL) and *A. xylosoxidans* (MICs: 50, 25 µg/mL), comparable to ciprofloxacin. Further studies revealed that 6a and 6c effectively disrupted bacterial biofilms with a low resistance risk. Mechanistically, they induced ROS production, thereby impairing redox homeostasis and reducing lipid peroxidation. Additionally, compound 6a inhibited *E. coli* DNA gyrase (IC_{50} = 23.75 µg/mL). Molecular docking studies (PDB ID: 4duh) and dynamics simulations confirmed the stable binding of these compounds to DNA gyrase, suggesting their potential as novel antibacterial agents. These findings highlight promising avenues for the development of new therapeutic agents to combat AMR.

KEYWORDS

Coumarin-thiazole derivatives, Antibacterial activity, Drug Resistance, Biofilm, DNA Gyrase, molecular docking, molecular dynamics

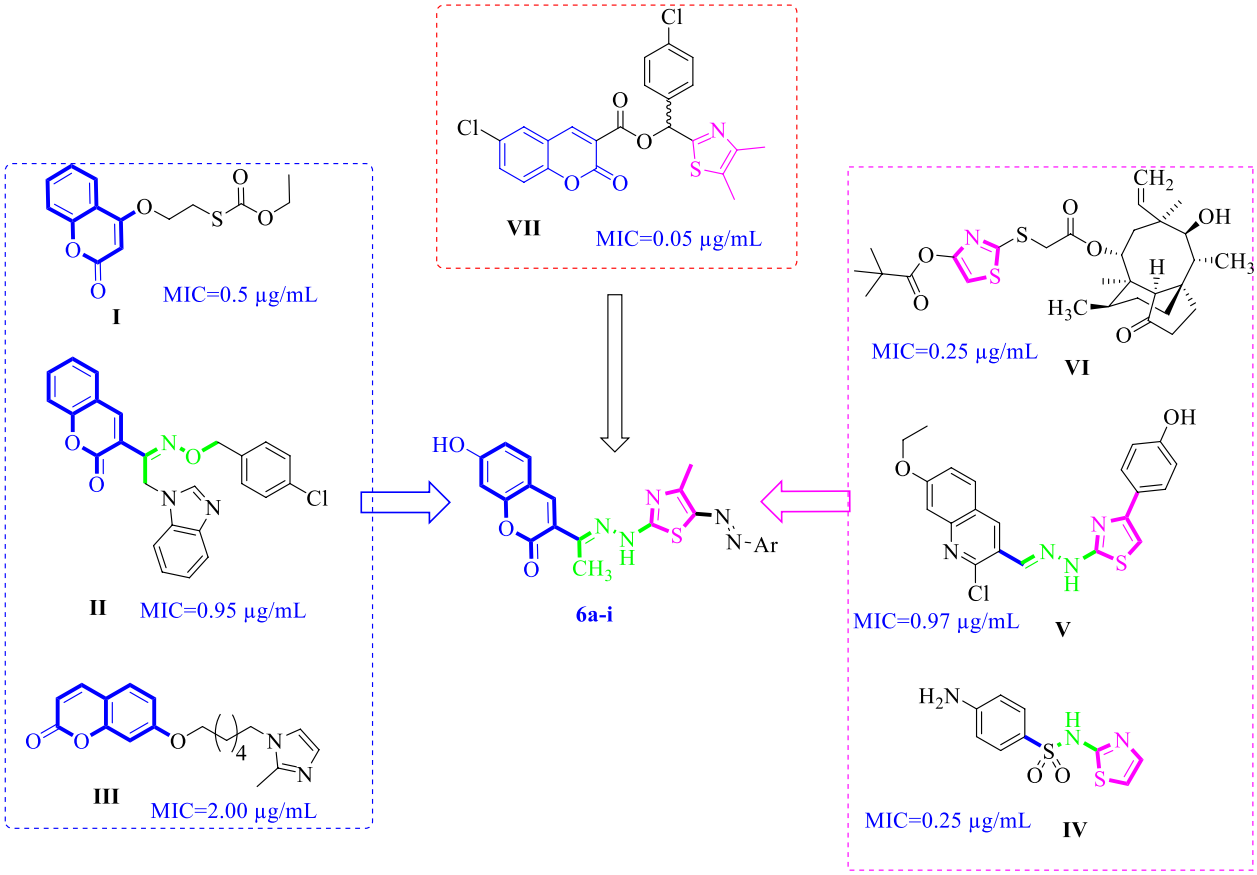
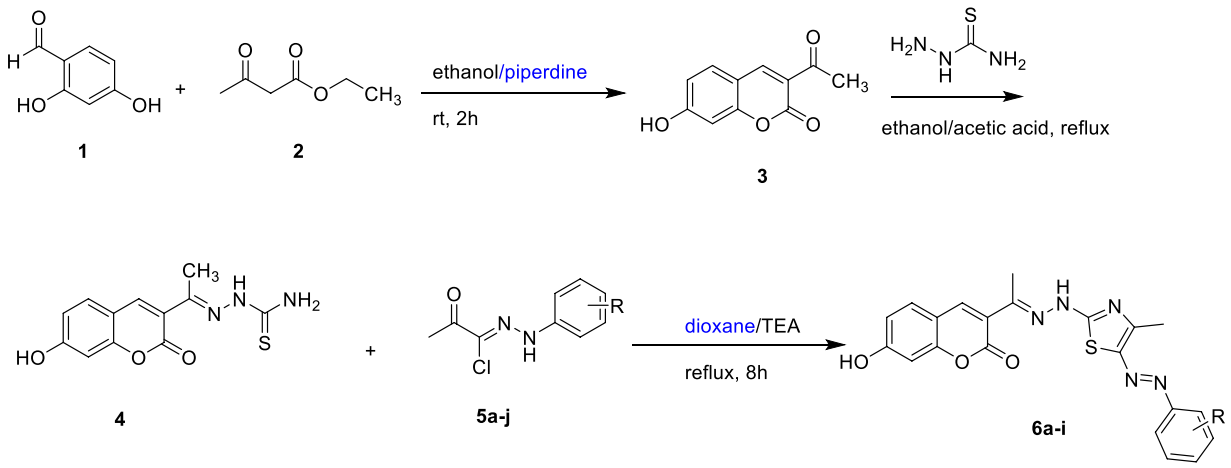


FIGURE 1
Reported antibacterial agents containing bioactive cores coumarin I-III, thiazole IV-VI, Coumarin-thiazole VII and our newly target compounds 6a-i.

1 Introduction

Infectious diseases remain a leading cause of global mortality, with antimicrobial resistance (AMR) posing a critical threat to public health (Naghavi et al., 2024). The rise of multidrug-resistant (MDR) bacterial strains has rendered many conventional antibiotics ineffective, leading to increased morbidity and mortality (Llor and Bjerrum, 2014; Prestinaci et al., 2015). In 2019 alone, AMR was associated with nearly 5 million deaths, underscoring the urgent need for novel therapeutic strategies (Antimicrobial Resistance Collaborators, 2022; Salam et al., 2023). Despite ongoing research efforts, the development of new antibiotics has been hindered by toxicity, limited efficacy, and rapid resistance emergence (Huemer et al., 2020; Ayukekbong et al., 2017; Prestinaci et al., 2015). As a pharmaceutical chemist, I propose a multifaceted approach to combat AMR through innovative drug design, alternative antimicrobial agents, and strategic resistance mitigation (Lungu et al., 2023; Silver, 2011). The development of drug resistance remains a critical challenge in pharmaceutical chemistry, particularly in antimicrobial and anticancer therapies. Single-target agents are highly susceptible to resistance due to the ease with which pathogens or cancer cells can mutate or activate alternative pathways (Sabt et al., 2023; Sabt et al., 2024a; Sabt et al., 2024b). In contrast, multi-targeting agents—particularly those designed via molecular hybridization—demonstrate superior efficacy and a reduced likelihood of resistance development (Singh H. et al., 2017).

Natural products have been utilized for the treatment of diseases for millennia and are becoming increasingly significant in the realms of drug discovery and development. Notably, a substantial proportion of anti-infective agents are derived from natural sources (Li et al., 2013; Weinmann, 1997). Coumarin, a natural product and the simplest representative of the oxygen-containing heterocycles known as benzo [*b*]pyran-2-one, is a secondary metabolite found in various plant families, including *Apiaceae*, *Fabaceae*, *Asteraceae*, *Solanaceae Rubiaceae*, *Rosaceae*, and *Rutaceae* (Sharifi-Rad et al., 2021). Compounds containing a coumarin nucleus have been documented to demonstrate a variety of biological functions, such as anticoagulant, anti-fungal, anticancer, antileishmanial, antiviral effects in addition to carbonic anhydrase inhibitors (Batran et al., 2023; Hassan et al., 2023; Ibrahim et al., 2022; Koley et al., 2024; Sabt et al., 2024c). Furthermore, researchers have focused on the antimicrobial properties of coumarins (Bhagat et al., 2019; Cheke et al., 2022; Hu et al., 2018; Ranjan et al., 2021). For instance, Coumarin–carbonodithioate hybrid I exhibited significant antibacterial efficacy, with MICs of 0.5 μg/mL against *S. aureus* and *B. subtilis*, and 1 μg/mL against *E. coli* and *P. aeruginosa* (Mangasuli et al., 2018). Similarly, the coumarin-benzimidazole



5, 6 a, R = H
b, R = 4-CH_3
c, R = 4-F
d, R = 4-Br
e, R = 4-OCH_3
f, R = 2,4-Cl
g, R = 4-$COCH_3$
h, R = 2-Cl-4-NO_2
i, R = 4-SO_2NH_2

SCHEME 1
Synthesis of the target compounds 6a-i.

hybrid II demonstrated significant antibacterial agent with a wide range of efficacy against *Staphylococcus aureus, Pseudomonas aeruginosa, Proteus vulgaris and Bacillus subtilis*. Importantly, this compound exhibited no cytotoxic effects or hemolytic activity at concentrations 10-fold greater than the MIC (Singh L. R. et al., 2017). Additionally, the coumarin-imidazole derivative III revealed strong and extensive antimicrobial activity (Hu et al., 2018) (Figure 1).

It has been reported that the thiazole moiety serves as a crucial element in numerous natural compounds, including vitamin B (thiamine) and antibiotics such as penicillin (Eryılmaz et al., 2020). Moreover, the thiazole nucleus has demonstrated a diverse array of pharmacological activities, including antileishmanial (Queiroz et al., 2020), antiviral (Farghaly et al., 2022), anticancer (Sabt et al., 2018), antidiabetic (Abid et al., 2025), and significant antibacterial properties (Ahmad et al., 2020; Sayed et al., 2023) (e.g., compound IV) (Figure 1) (Qi et al., 2025). Additionally, thiazole nucleus can possess the capability to inhibit several enzymes, such as carbonic anhydrase (Karakaya et al., 2024) and dihydrofolate reductase, as inhibited by compound V (Figure 1) (Ammar et al., 2021). Previous studies have indicated that thiazole can impede bacterial growth by disrupting the biosynthesis of specific bacterial lipids, as exemplified by sulphathiazole VI (Figure 1) (Desai et al., 2013).

It is worth noting that thiazoles and similar N-heterocycles (e.g., triazoles, oxazoles) are widely used in organic synthesis and medicinal chemistry (Joule and Mills, 2010; Klika et al., 2021; Klika et al., 2022). DNA gyrase is classified within the DNA topoisomerase protein family and is responsible for facilitating the interconversion of various topological forms of DNA. This enzyme is crucial for processes such as DNA replication and transcription, as well as other cellular functions (Rajakumari et al., 2024). Consequently, the inhibition of DNA gyrase presents a promising target for the development of antibacterial agents. For instance, compounds such as coumarin-thiazole VII specifically inhibit DNA gyrase, highlighting the enzyme's importance in combating bacterial infections (Liu et al., 2020).

This study focuses on the design and synthesis of new coumarin-based derivatives conjugated with thiazole scaffolds, aiming to incorporate diverse pharmacophoric features into a single molecular framework. The primary goal of this approach was to develop innovative coumarin-thiazole hybrids with enhanced antibacterial activity. The synthesized compounds were evaluated against multiple bacterial strains, with minimum inhibitory concentration (MIC) assays and antibacterial efficacy assessments conducted for the most promising candidates. Furthermore, their potential to disrupt bacterial biofilms was investigated. To explore the mechanistic basis of their antibacterial action, preliminary studies were performed, focusing on intracellular oxidative stress markers, including reactive oxygen species (ROS) production and lipid peroxidase activity. The most active derivatives were further analyzed for their inhibitory effects on the DNA gyrase enzyme. To elucidate binding interactions and target engagement, molecular docking simulations were employed, supported by molecular dynamics studies to validate the docking results and provide deeper insights into the binding stability.

TABLE 1 Antibacterial activity of the targeted molecules using agar-well diffusion.

Compound	Inhibition zone (mm)			
	Serratia fonticola (Gram-negative)	*Campylobacter jejuni* (Gram-positive)	*Enterococcus faecalis* (Gram-positive)	*Achromobacter xylosoxidans* (Gram-negative)
6a	2 ± 0.02	ND	6 ± 1.02	4 ± 1.11
6b	ND	ND	5 ± 0.38	5 ± 0.82
6c	2 ± 0.16	ND	7 ± 0.44	5 ± 0.25
6d	ND	ND	5 ± 0.18	4 ± 0.31
6e	ND	ND	5 ± 0.52	3 ± 0.73
6f	ND	ND	4 ± 0.61	2 ± 0.12
6g	ND	ND	ND	ND
6h	2 ± 0.31	ND	2 ± 0.07	3 ± 0.91
6i	ND	ND	2 ± 0.21	ND
Ciprofloxacin[a]	4 ± 0.56	3 ± 0.42	4 ± 0.78	5 ± 0.22
Cephradine	ND[b]	ND	ND	ND
Ampicillin	ND	ND	ND	2 ± 0.01
Polymexine B	3 ± 0.12	ND	3 ± 0.29	4 ± 0.65
Kanamycin	ND	2 ± 0.06	ND	ND
Erythromycin	ND	ND	3 ± 0.15	2 ± 0.18

[a]Kanamycin, Ciprofloxacin, Ampicillin, Polymexine B, kanamycin, Erythromycin and Cephradine were used as standard antibacterial agents at 20 μg/mL.
[b]ND: not determined.

2 Results and discussion

2.1 Chemistry

The synthesis of coumarin derivatives 6a-i was executed in accordance with the methodologies delineated in Scheme 1, which also illustrates the formation of the precursor compound, 3-acetyl-7-hydroxy-2*H*-chromen-2-one (3). In this investigation, a Knoevenagel condensation reaction was employed, wherein 2,4-dihydroxybenzaldehyde (1) was reacted with ethyl acetoacetate (2) at ambient temperature, facilitated by a minimal quantity of piperidine in ethanol, yielding 3-acetyl-7-hydroxy-2*H*-chromen-2-one (3) (Hassan et al., 2023). Subsequently, this compound underwent reflux with thiosemicarbazide in absolute ethanol, with the addition of several drops of glacial acetic acid, resulting in the formation of the corresponding thiosemicarbazone 4. The heterocyclization of thiosemicarbazone derivative 4, an important intermediate, was successfully accomplished by refluxing it with a range of hydrazonoyl chloride derivatives 5a-I. These derivatives were synthesized using established methods that involve the reaction of diazonium chloride with appropriately activated halogenated methylene groups, which is an efficient approach for generating various hydrazonoyl halides (Osman et al., 2023). The reaction was conducted in dioxane, with the addition of a few drops of triethylamine (TEA), resulting in the formation of the desired compounds, 6a-i. The structural characterization of the newly synthesized derivatives was performed utilizing ^{1}H-NMR and ^{13}C-NMR spectroscopy, as detailed in the Experimental section.

2.2 Biological activity

2.2.1 Antibacterial screening

Recently, the drug-resistant bacteria represented a distinctive hindrance, especially those having the capability to proliferate in the presence of several antibiotic groups (Matin et al., 2019). The resistance of bacterial pathogens toward at least one agent in three or more antibacterial families was characterized as MDR. Moreover, the bacterial pathogen was called XDR when it's non-susceptible to at least one agent in all but two or fewer antimicrobial categories. In this regard, our vision is aimed at investigating the ability of the targeted compounds to cause bactericidal effects against the clinically important bacterial pathogens. In which, these models were isolated from different urinary tract infected samples, which had a significant resistance toward the classical antibacterial agents as mentioned in the antibiotic profile for each pathogen (Table 1). The new coumarin-based derivatives conjugated with the thiazole scaffold were examined as a potential drug against these pathogens due to the potential antibacterial activity of coumarin and thiazole derivatives.

The target compounds 6a-i were prepared, and their antibacterial activities were investigated against XDR and MDR pathogens. As can be seen in Supplementary Figure S1, the

TABLE 2 Minimum inhibitory concentration (MIC) of the potent synthesized derivatives.

Sample no.	Minimum inhibitory concentration (MIC, µg/mL)	
	Enterococcus faecalis (Gram-positive)	*Achromobacter xylosoxidans* (Gram-negative)
6a	22.8 ± 2.66	46.9 ± 3.82
6b	49.1 ± 0.79	162.3 ± 2.99
6c	10.9 ± 2.16	24.6 ± 0.36
6d	48.7 ± 2.11	47.9 ± 2.87
6e	49.2 ± 0.77	128.4 ± 3.41
8f	47.8 ± 2.58	173.4 ± 1.11
Ciprofloxacin	22.8 ± 0.25	18.5 ± 1.56

sensitivity of the XDR pathogens (*C. jejuni* and *S. fonticola*) towards the tested compounds was found to be negligible, as no inhibition zone appeared around all tested molecules. High resistance demonstrated by these pathogens emphasized the ineffective action of the tested compounds; hence, those were excluded from our examination. Interestingly, the efficiency of the targeted compounds was notably performed toward the MDR pathogens (*A. xylosoxidans*) and XDR (*E. faecalis*) (Table 1). A significant activity was clearly indicated in the case of most tested compounds against both pathogens except for compound 6g. On the other hand, the activity of some tested compounds was relatively preferred when compared to the standard antibacterial agents. Since some compounds of this group obtained an inhibition zone higher than that carried out by the potent antibacterial standards. Surprisingly, compounds 6a-e had higher sensitivity towards *E. faecalis* than that obtained by ciprofloxacin (4 mm). In addition, the ability of these compounds to inhibit *A. xylosoxidans* was observed in the equal efficacy of the reference drug (5 mm) as occurred in compounds 6b and 6c. Our results clearly showed that compounds 6a-f and h were very effective against *A. xylosoxidans* and *E. faecalis*. Therefore, further studies using potent compounds were implemented against *A. xylosoxidans* and *E. faecalis* to establish more details about their activity.

The ability of the potent compounds to inhibit the targeted bacterial pathogens at the lowest concentration (MIC) could be determining the optimal dosage that maximizes the killing of bacterial colony-forming units (CFUs). Accordingly, stock solutions of each potent compound were prepared at different concentrations and incubated with each bacterial pathogen. Bacterial growth was measured using turbidimetric methods, and the percentage of survival inhibition was calculated based on the reduction of CFUs. The activity of the potent compounds 6a and 6b was clearly observed at significant MIC values, which were sometimes close to the values of the standard antibiotic Ciprofloxacin (see Table 2). Comparatively, the potency of the most active compounds was significantly greater against *E. faecalis* than against *A. xylosoxidans*, indicating the specificity of these compounds in combating *E. faecalis*. Notably, compound 6c demonstrated the highest MIC values, with 12.5 µg/mL against *E. faecalis* and 25 µg/mL against *A. xylosoxidans*. Overall, the superiority of compounds 6a and 6c, with MIC values not exceeding 50 µg/mL, positions them as promising candidates for application in the pharmaceutical industry.

2.2.2 Biofilm activity assay

Bacterial biofilms are slimy structures created by the aggregation of bacteria that can protect bacterial cells from outside influences and enhance resistance to antimicrobial agents (Yang et al., 2022). Commonly, microbial pathogens utilize this mechanism to increase their virulence and evade adverse conditions. The assessment of biofilm formation by the treated bacterial pathogens was performed using both qualitative and quantitative methodologies.

Preliminarily, the evaluation of bacterial biofilm formation was conducted at a fixed concentration of 50 µg/mL (which considered an effective concentration for the potent molecules) for all potent molecules using a Congo red plate assay. After incubating each bacterial pathogen with the targeted molecule, the resulting bacterial suspension was cultivated on the Congo red plate and incubated for 48 h. The colonial growth was then observed. Notably, the black pigment of the growth colonies was clearly visible in the untreated samples after 24 h Supplementary Figure S2. Variable antibacterial activity was observed in all treated samples, indicating the efficacy of the tested compounds at this concentration, particularly compounds 6a and 6c. The bacterial cells appeared stressed and exhibited difficulty in growth. Furthermore, the black pigment did not develop in any of the treated samples, with only a slight appearance noted in the cases of P25 and P100.

Indeed, the qualitative assay demonstrated that compounds 6c and 6a have the potential to act as strong antagonists against bacterial biofilm formation, particularly against *E. faecalis* (Supplementary Figure S2).

Quantitative assay methodologies were utilized to assess the effectiveness of the potent compounds 6a and 6c in inhibiting biofilm formation by specific bacterial pathogens. Initially, the assessment of microbial biofilm formation was conducted at a fixed concentration of 50 µg/mL. The target compound 6c demonstrated greater effectiveness against both bacterial pathogens, as shown in Table 3. Both compounds yielded significant results regarding the inability of bacterial

TABLE 3 Antibiofilm activity of the potent molecules at MIC value.

Sample no.	Biofilm inhibition (%)	
	Enterococcus faecalis (Gram-positive)	*Achromobacter xylosoxidans* (Gram-negative)
6a	46.57 ± 2.06	30.21 ± 0.96
6c	55.03 ± 3.11	41.81 ± 2.85
Ciprofloxacin	66.21 ± 0.56	48.33 ± 0.56

TABLE 4 ROS determination of the potent molecules inside the bacterial cell's pathogens.

Sample No	ROS determination (DCF level, counts) using spectrofluorometric (excitation and emission wavelength at 485 nm and 530 nm, respectively)	
	Enterococcus faecalis (Gram-positive)	*Achromobacter xylosoxidans* (Gram-negative)
6a	268.79 ± 1.76	178.02 ± 0.88
6c	284.54 ± 3.92	136.19 ± 2.17
Ciprofloxacin	277.93 ± 1.52	217.57 ± 2.16
Control	89.53 ± 0.99	97.36 ± 2.02

pathogens to produce biofilm while maintaining cell proliferation without negative consequences. The assessment of biofilm formation demonstrated a significantly enhanced ability to suppress biofilm formation in both Gram-positive and Gram-negative bacteria compared to the standard drug. The percentage of bacterial biofilm inhibition exceeded 50% for *E. faecalis*, indicating that it is a promising antibiofilm agent. Conversely, it is noteworthy that 6a exhibited moderate antibiofilm efficacy against *A. xylosoxidans*, with inhibition levels below 40%. The observed differences in biofilm production among the tested pathogens in the presence of these potent molecules may be attributed to variations in the composition of the embedded biofilm.

2.2.3 Intracellular oxidative stress

2.2.3.1 The generation of reactive oxygen species (ROS)

The generation of intracellular oxidative stress, characterized by the presence of reactive oxygen species (ROS), has been identified as a significant factor influencing the antibacterial effectiveness of various antibiotics (Sui et al., 2021). To determine whether compounds 6a and 6c cause membrane damage that results in oxidative stress, the levels of intracellular ROS were measured using a fluorometric assay employing DCFH-DA dye. The findings revealed that the treatment of *Enterococcus faecalis* and Achromobacter xylosoxidans with compounds 6a and 6c resulted in a notable increase in intracellular ROS production, as demonstrated in Table 4. The results displayed that the highest levels of DCF detected in *E. faecalis* demonstrated a substantial induction of ROS by compound 6c, followed closely by compound 6a. Importantly, the ROS release was found to exceed that induced by ciprofloxacin, indicating a pronounced oxidative stress response triggered by these compounds in *E. faecalis*. Conversely, the intracellular ROS levels in *A xylosoxidans* were significantly lower in comparison to the reference drug. Additionally, an increase in ROS was particularly noted in the context of Gram-positive bacteria.

2.2.3.2 Lipid peroxidation (LPO)

Malondialdehyde (MDA) is a crucial parameter that reflects the antioxidant potential of organisms and the extent of cellular peroxidation damage (Cui et al., 2016). The cell membrane is one of the most vital components of bacterial structure due to its role in protecting against external inhibitors. Disintegration of the cell membrane inevitably leads to the death of bacterial cells, as it facilitates the inhibition of protein and nucleic acid synthesis. The oxidation of fatty acid content is considered a significant marker indicating the disruption of the cell membrane. Therefore, investigating the lipid oxidation levels in each bacterial pathogen by comparing them with untreated samples can provide valuable insights into the pathways through which targeted molecules are eradicated.

As shown in Table 5, The oxidation potential associated with the bacterial cell membrane by the potent molecules 6a and 6c dramatically increased against both pathogens, particularly in the case of *E. faecalis*. A notable difference in LPO activity was observed among the most active compounds; the lipid oxidation level in Gram-positive *E. faecalis* was remarkably close to that observed with the standard antibiotic. However, the effect of the targeted compounds on the fatty acid content of Gram-negative *A. xylosoxidans* was found to be lower than that caused by the standard antibiotic, except for compound 6a, suggesting their efficacy against Gram-positive bacteria. Furthermore, the cell membrane structure of each bacterial type reflects the performance of the potent compounds. Notably, the ability of both compounds to induce significant oxidation of lipid content

TABLE 5 Lipid peroxidation activity for each potent molecule at MIC values.

Sample No	Lipid peroxidation efficiency (malondialdehyde, nmol mL^{-1})	
	Achromobacter xylosoxidans (Gram-negative)	*Enterococcus faecalis* (Gram-positive)
6a	6.352 ± 0.08	7.673 ± 0.26
6c	5.252 ± 0.33	8.815 ± 0.18
Ciprofloxacin	7.724 ± 0.51	9.07 ± 0.32
Control	2.145 ± 0.08	1.664 ± 0.01

TABLE 6 Inhibitory activities of the most active compounds (6a and 6c) against E.*Coli* DNA gyrase (supercoiling).

Compound	IC_{50} (μg/mL)
6a	23.75 ± 0.77
6c	40.87 ± 1.33
Ciprofloxacin	15.95 ± 0.52

in *E. faecalis* was greater than in *A. xylosoxidans*, attributed to differences in cell membrane composition. The variations in cell membrane composition were discussed, which may be due to the presence of a lipopolysaccharide layer surrounding the Gram-negative outer membrane.

2.2.4 DNA gyrase inhibitory activity

An assay to evaluate the inhibition of *E. coli* DNA gyrase was conducted for the two most potent compounds, 6a and 6c, with Ciprofloxacin serving as a reference control. The findings are presented in Table 6, indicating the IC_{50} values in μg/mL. Compound 6a exhibited notable inhibitory activity against DNA gyrase, with an IC_{50} value of 23.75 μg/mL, relative to the Ciprofloxacin control, which recorded an IC_{50} of 15.95 μg/mL. Conversely, compound 6c demonstrated a comparatively lower level of inhibition, being approximately 2.5 times less effective than the control.

2.3 Molecular modeling simulation

2.3.1 Molecular docking of the tested compounds against DNA Gyrase B

The suggested binding mode of compound 6a demonstrated a binding energy of −8.35 kcal/mol in relation to DNA Gyrase B (PDB ID: 4duh). A total of fifteen interactions were identified, including hydrophobic π-π, π-cation, π-anion, π-alkyl, and π-sigma interactions with Val120, Ile94, Lys103, Ile78, Gly77, Glu50, Pro50, and Arg76 amino acids sidechain. Moreover, compound 6a formed five hydrogen bonds with Ala100, Gly101, Asp73, Thr165, and Arg136 with a distance of 3.29, 1.76, 1.82, 2.37, and 2.42 Å, Figure 2. The binding mode of compound 6c showed a binding energy that was not constrained (ΔG) equal of −7.14 kcal/mol. fourteen hydrophobic π-π, π-anion, π-cation, and π-alkyl interactions were conducted with Pro79, Arg76, Glu50, Lys103, Ile94, Val120, Val43, Val167, Ile78, and Asn46. Additionally, the interaction of Compound 6c was stabilized by the formation of three hydrogen bonds with Arg76, Gly77, and Asp73 with distances of 2.59, 2.50, and 2.05 Å

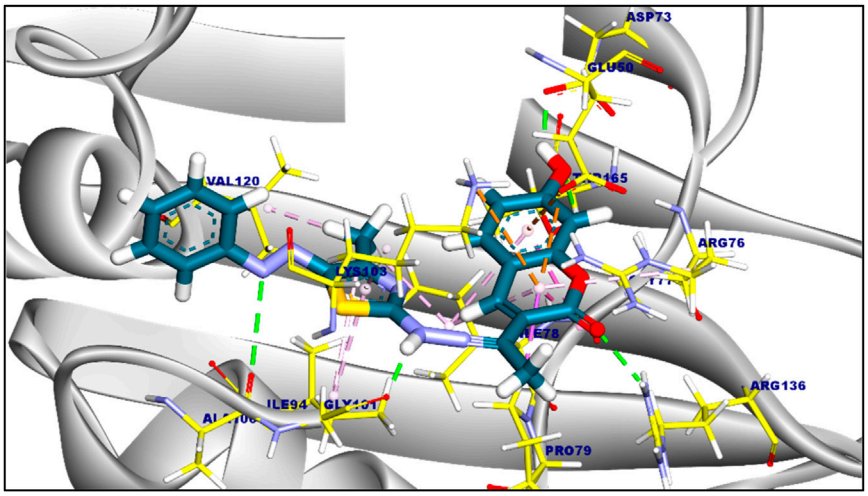


FIGURE 2
3D figure of the proposed binding mode of compound 6a against DNA Gyrase B. The tested compound is colored by (Blue), and amnio acid side chain by (yellow).

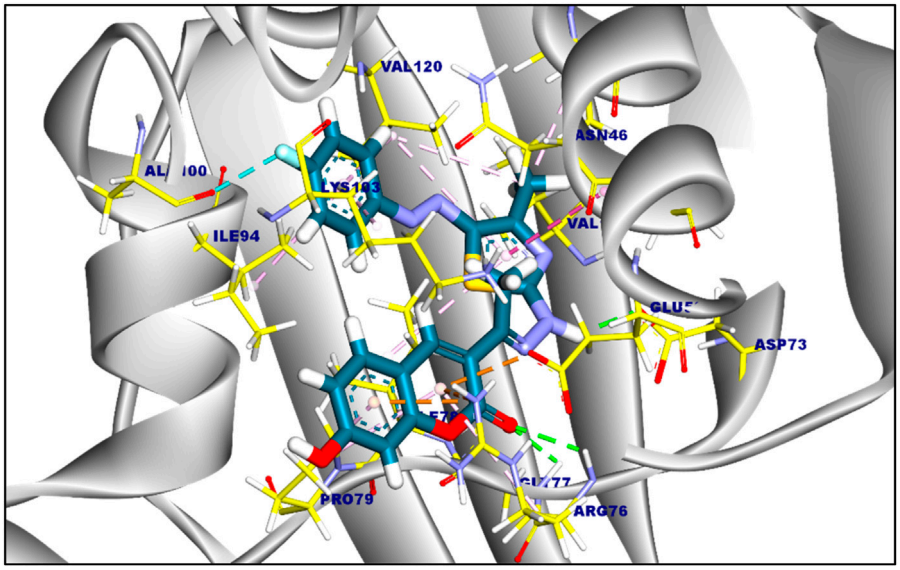


FIGURE 3
3D figure of the proposed binding mode of compound 6c against DNA Gyrase B. The tested compound is colored by (Blue), and amnio acid side chain by (yellow).

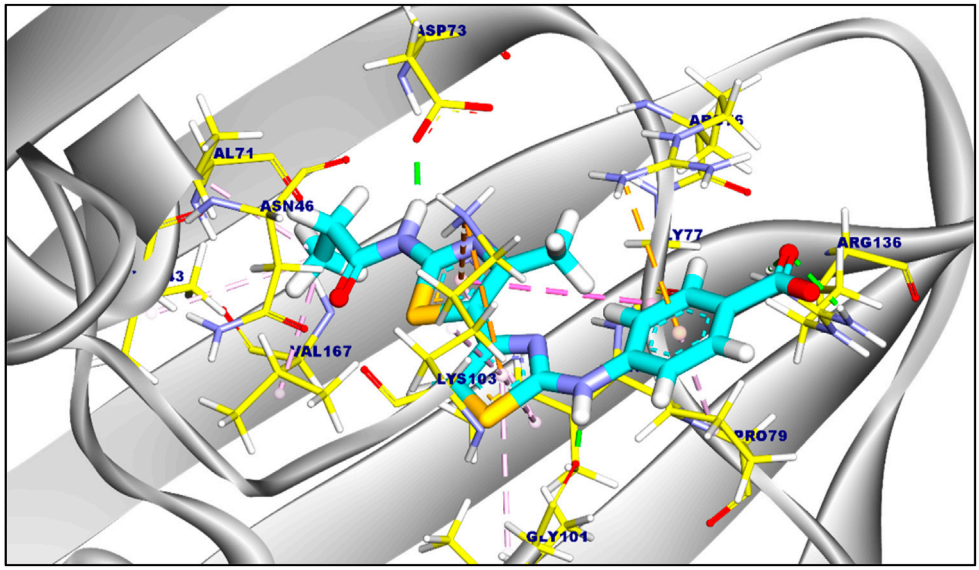


FIGURE 4
the proposed binding mode of the co-crystalized ligand complexed with DNA Gyrase (B). Ligand is colored by (turquoise), and amnio acid side chain colored by (yellow).

(Figure 3). Furthermore, The co-crystalized ligand complexed with DNA Gyrase B exhibited an affinity score of −8.12 kcal/mol with RMSD value equal 1.12 Å, the co-crystalized ligand formed twelve hydrophobic π-alkyl, π-cation, and π-π interactions with Val167, Val43, Val71, Asn46, Gly77, Ile78, Lys103, Ile94, Pro79, and Arg76, additionally, the interaction was supported by three hydrogen bonds with Asp73, Arg136, and Gly101 with distances of 1.87, 2.19 and 1.81 Å (Figure 4).

2.3.2 Molecular dynamic (MD) simulation study for ligand 6a

Molecular dynamics (MD) simulations were performed over duration of 100 nanoseconds to investigate the molecular stability of the ligand 6a, which exhibited the most favorable docking results, in relation to the DNA Gyrase B target pocket. The resulting root mean square deviation (RMSD) values for both the complex and the ligand, in comparison to their initial positions within the active site, were

TABLE 7 Molecular Docking Analysis of the tested ligands 6a and 6c against DNA Gyrase B.

Compounds	RMSD value (Å)	Docking (affinity) score (kcal/mol)
6a	1.54	−8.35
6c	1.67	−7.14
The co-crystalized ligand	1.15	−8.12

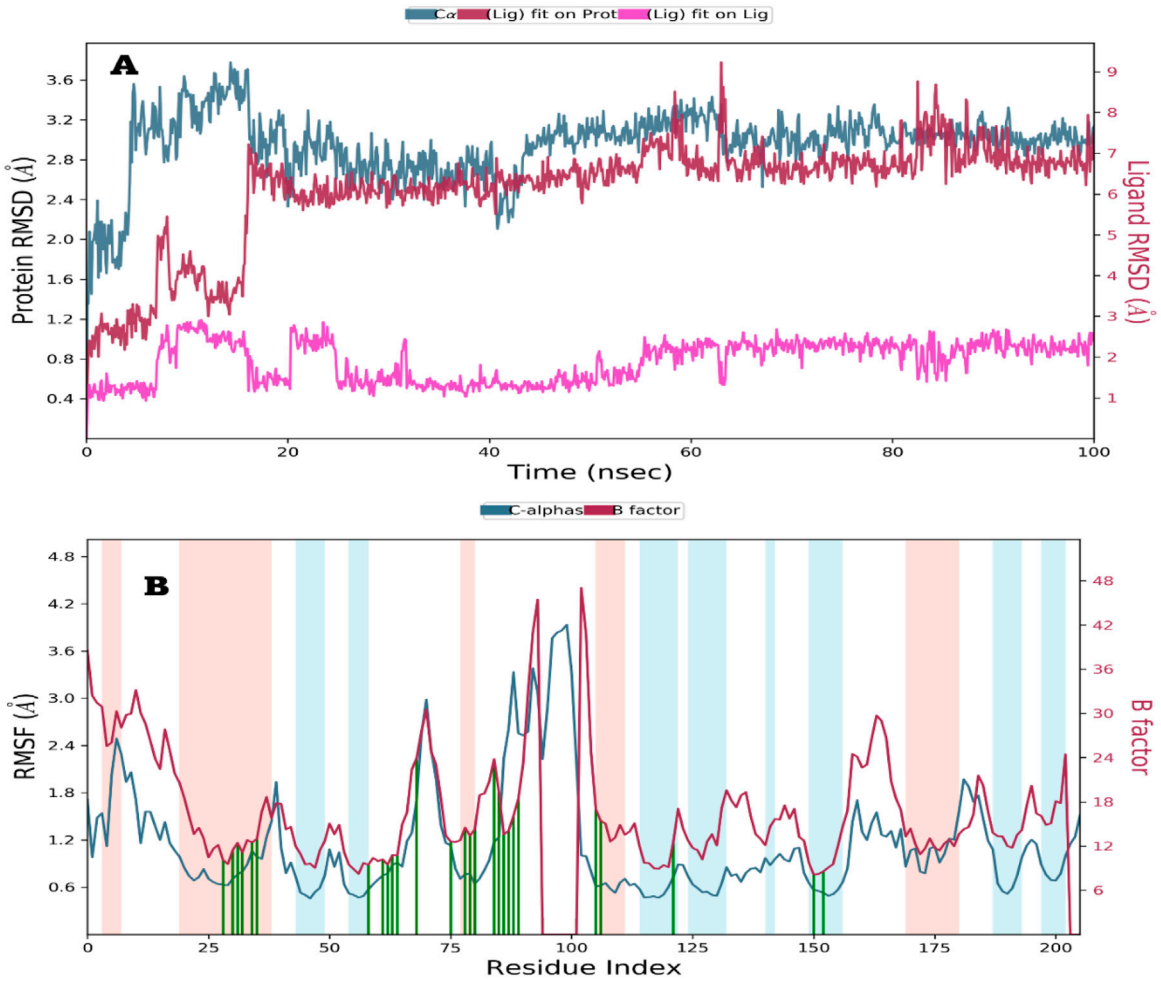


FIGURE 5
Showed the RMSD and RMSF of Compound 6a against DNA Gyrase B over 100 ns.

documented and subjected to analysis. Additionally, the interactions of the lead compound 6a were thoroughly examined and assessed (Table 7).

2.3.2.1 Analysis of root mean square deviation (RMSD) and root mean square fluctuation (RMSF) for proteins and ligands

Following molecular docking, ligand 6a, which formed a complex with DNA Gyrase B, was chosen for molecular dynamics (MD) simulation. The conformational stability of the protein structure was assessed by tracking the Cα atoms (indicated by the blue line) in relation to their initial positions. As illustrated in Figure 5A, ligand 6a demonstrated stability within the binding pocket of DNA Gyrase B through the simulation time with fluctuation at 10–20 ns, at this time, target protein loops exhibited many movements at 60–65, 80–110, and 155–170 amino acids areas, which leads to many conformational changes in protein skeleton, that can affect the protein ligand interactions especially at 60–65 amino acids area. Additionally, the protein ligand complex showed stability over the simulation time (20–100 ns) which the ligand reaches equilibrium and fluctuated at 6–7 Å (within RMSD value = 1 Å) (Figure 5B).

2.3.2.2 Analysis of protein-ligand interactions

2.3.2.2.1 Analysis of protein-ligand interaction histograms. Compound 6a demonstrated significant stability when interacting with DNA Gyrase B, with numerous interactions identified between the compound and the amino acids within the target pocket, which are

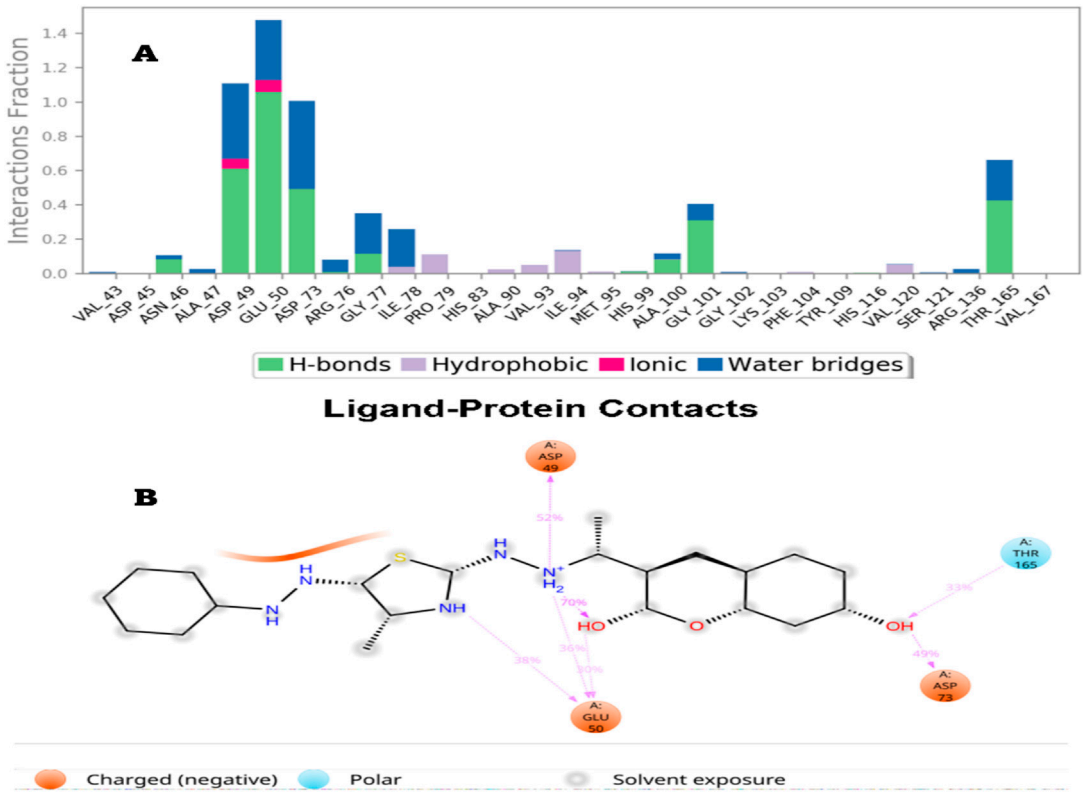


FIGURE 6
Histogram analysis describing the binding interactions of ligand 6a with DNA Gyrase B during the simulation time (100 ns).

elaborated upon in detail. Ligand 6a established π-interactions with the subsequent residues: Ile78 (~5%), Pro79 (~10%), Val93 (~5%), and Ile94 (~20%), As illustrated in Figure 6. Additionally, Ligand 6a exhibited interactions with DNA Gyrase B through multiple polar hydrogen bonds and water-mediated hydrogen bonds. The presence of crystallization water molecules facilitated connections between the protein residues and the ligands, as demonstrated by the specific residues involved, Asn46 (~15%), Asp49 (~60%), Glu50 (~110%), Asp73 (~50%), Ala100 (~10%), Gly101 (~35%), and Thr165 (~50%). Moreover, Ligand 6a demonstrated the capacity to establish ionic interactions with the residues Asp49 and Glu50.

Another method used to monitor these interactions involves plotting the number of interactions concerning time, a heat map Figure 7 indicates the number of interactions at each frame of Compound 6a with DNA Gyrase B, whereas the dark color indicates more interactions. From the heat maps figures, it was observed that the highest number of conformations of the protein of DNA Gyrase B formed up to nine interactions, the most interacted amino acids of DNA Gyrase B with ligand 6a are Asp49, Glu50, Asp73, Gly77, Ile78, Ile94, Gly101 and Thr165.

3 Conclusion

The synthesized coumarin-thiazole derivatives showed variable antibacterial activity against drug-resistant pathogens. While ineffective against *Campylobacter jejuni* and *Serratia fonticola*, compounds 6a and 6c exhibited strong activity against *Enterococcus faecalis* and *Achromobacter xylosoxidans* (MICs: 12.5–50 μg/mL). These compounds also inhibited biofilm formation (>50% in *E. faecalis*), induced lipid peroxidation and ROS production, and disrupted bacterial cell integrity. 6a acted as a DNA gyrase inhibitor (IC_{50}: 23.75 μg/mL). Molecular docking and dynamics simulations confirmed stable binding of 6a/6c to DNA gyrase, mimicking known inhibitors. These findings highlight 6a and 6c as promising candidates against resistant bacteria.

4 Materials and methods

4.1 Chemistry

Melting points were determined on electrothermal IA 9000 apparatus and were uncorrected. The NMR analysis including ^{1}H and ^{13}C-NMR, spectra were recorded using Bruker 500 NMR (Japan) spectrometers (MA, United States) in Faculty of Pharmaceutical Science, Tokushima Bunri University, Japan. The chemical shifts were given in δ (ppm), and coupling constants were reported in Hz. Mass spectrum (Direct Inlet part to mass analyzer in Thermo Scientific GCMS model ISQ) and Elemental analyses (FLASH 2000 CHNS/O analyzer, Thermo Scientific (United States) were carried out at the Regional Center for

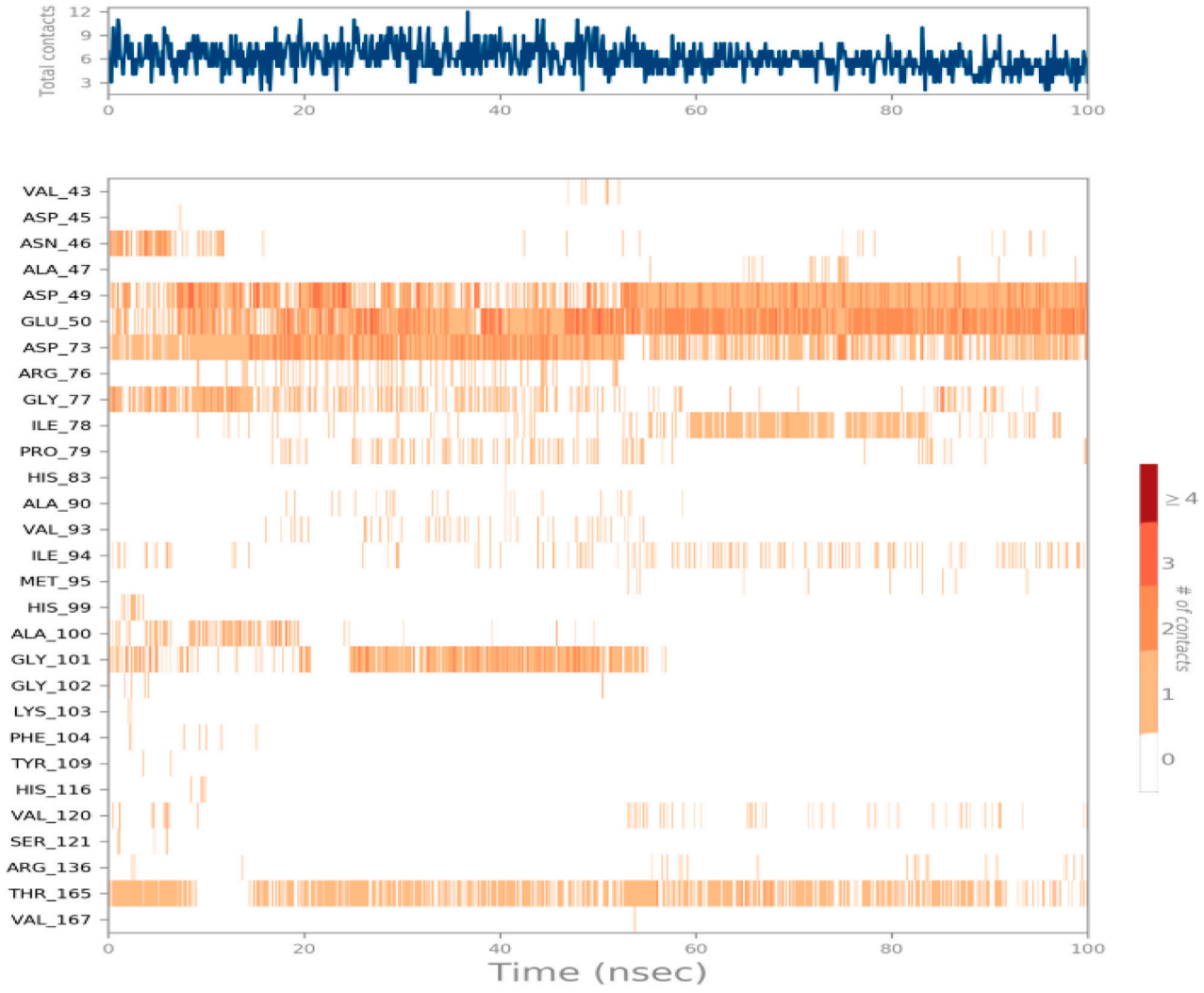


FIGURE 7
Heat map describing the total interactions within ligand 6a with DNA Gyrase B during the simulation time.

Mycology and Biotechnology (RCMB), Al-Azhar University, Nasr City, Cairo. The reactions were followed by TLC (silica gel, aluminum sheets 60 F254, Merck) using chloroform/methanol (9.8:0.2 v/v) as eluent and sprayed with iodine-potassium. Compounds 3, 4 and 5a-i were previously prepared (Ebaid et al., 2025; Osman et al., 2023).

4.1.1 General procedure for the preparation of target compounds 6a-i

A reaction was performed utilizing a combination of thiosemicarbazones 4 (0.001 mol) and their corresponding hydrazonoyl chloride derivatives 5a-i (0.001 mol) (These derivatives were synthesized using established methods that involve the reaction of diazonium chloride with appropriately activated halogenated methylene groups) in 15 mL of dioxane, with triethylamine (TEA) employed as a catalytic agent. The reaction mixture underwent reflux for a period of 8 h. Following the cooling phase, the resulting precipitate was filtered and subsequently recrystallized from ethanol, leading to the synthesis of the desired compounds 6a-i.

4.1.1.1 7-Hydroxy-3-(-1-{2-[4-methyl-5-(phenyldiazenyl) thiazol-2-yl]hydrazono}ethyl)-2*H*-chromen-2-one (6a)

Red powder, m. p. 228 °C–230 °C, yield (78%). ^{1}H NMR (500 MHz, DMSO-d_6): δ = 2.06 (s, 3H, CH_3), 2.35 (s, 3H, CH_3-thiazole), 6.69 (s, 1H, H-Ar), 6.77 (d, 1H, *J* = 8.5 Hz, H-Ar), 7.08-7.14 (m, 1H, H-Ar), 7.37 (d, 2H, *J* = 8.5 Hz, H-Ar), 7.58 (d, 1H, *J* = 8.00 Hz, H-Ar), 7.74 (d, 2H, *J* = 8.5 Hz, 1H, H-Ar), 7.76 (d, 1H, *J* = 1.5 Hz, H_4 of coumarin), 10.54 (s, 1H, NH), 10.72 (s, 1H, OH). ^{13}C NMR (126 MHz, DMSO) δ = 14.25 (CH_3), 15.49 (CH_3), 104.10, 119.37, 121.03, 121.44, 125.07, 125.77, 128.25, 128.66, 129.75, 132.21, 134.58, 138.63, 147.28, 158.51, 159.60(C-OH), 160.64(C=O), 171.50(C=N). Analysis for $C_{21}H_{17}N_5O_3S$ (419.45), Calcd.: % C, 60.13; H, 4.09; N, 16.70; Found: % C, 60.24; H, 4.21; N, 16.82. MS m/z (R.A.%): 419 (M^+) (34.33%), 368 (100.00%).

4.1.1.2 7-Hydroxy-3-(-1-{2-[4-methyl-5-(*p*-tolyldiazenyl) thiazol-2-yl]hydrazono}ethyl)-2*H*-chromen-2-one (6b)

Brown powder, m. p. 197 °C–199 °C, yield (85%). ^{1}H NMR (500 MHz, DMSO-d_6): δ = 2.29 (s, 3H, CH_3), 2.35 (s, 3H, CH_3), 2.45 (s, 3H, CH_3-thiazole), 6.95 (s, 1H, H-Ar), 7.20 (d, 1H, *J* = 8.0 Hz,

H-Ar), 7.30 (d, 1H, *J* = 8.5 Hz, H-Ar), 7.68 (d, 2H, *J* = 8.5 Hz, H-Ar), 7.83 (s, 1H, H_4 of coumarin), 7.87 (d, 2H, *J* = 8.5 Hz, 1H, H-Ar), 10.12 (s, 1H, NH), 10.91 (s, 1H, OH). ^{13}C NMR (126 MHz, DMSO) δ = 14.54 (CH_3), 16.05 (CH_3), 20.00 (CH_3), 101.82, 106.22, 113.81, 121.76, 125.53, 125.97, 128.82, 130.07, 131.98, 137.33, 141.89, 150.89, 154.45, 155.89, 155.97, 161.26 (C=O), 171.19(C=N). Analysis for $C_{22}H_{19}N_5O_3S$ (433.48), Calcd.: % C, 60.96; H, 4.42; N, 16.16;. Found: % C, 61.06; H, 4.54; N, 16.25. MS m/z (R.A.%): 433 (M^+) (19.01%), 81 (100.00%).

4.1.1.3 3-(-1-{2-[5-((4-fluorophenyl)diazenyl)-4-methylthiazol-2-yl]hydrazono}ethyl)-7-hydroxy-2*H*-chromen-2-one (6c)

Red powder, m. p. 207 °C–209 °C, yield (77%). ^{1}H NMR (500 MHz, DMSO-d_6): δ = 2.26 (s, 3H, CH_3), 2.41 (s, 3H, CH_3-thiazole), 6.88 (s, 1H, H-Ar), 7.00 (d, 1H, *J* = 8.0 Hz, H-Ar), 7.42 (d, 2H, *J* = 8.5 Hz, H-Ar), 7.59 (d, 1H, *J* = 8.0 Hz, H-Ar), 7.80 (d, 2H, *J* = 8.5 Hz, H-Ar), 7.98 (s, 1H, H_4 of coumarin), 10.25 (s, 1H, NH), 11.15 (s, 1H, OH). ^{13}C NMR (126 MHz, DMSO) δ = 14.16 (CH_3), 17.65(CH_3), 101.82, 106.22, 113.81, 125.53, 125.97, 128.84, 130.07, 131.98, 137.33, 141.80, 141.89, 150.62, 154.51(C-OH), 155.97(C9), 159.21(C=O), 161.26(C-F), 171.94(C=N). Analysis for $C_{21}H_{16}FN_5O_3S$ (437.44), Calcd.: % C, 57.66; H, 3.69; N, 16.01. Found: % C, 57.77; H, 3.82; N, 16.13. MS m/z (R.A.%): 437 (M^+) (18.75%), 225 (100.00%).

4.1.1.4 3-(1-{2-[5-(4-Bromophenyl)diazinyl]-4-methylthiazol-2-yl}hydrazono)ethyl-7-hyd- roxy-2*H*-chromen-2-one (6d)

Red powder, m. p. 215 °C–217 °C, yield (88%). ^{1}H NMR (500 MHz, DMSO-d_6): δ = 2.29 (s, 3H, CH_3), 2.35 (s, 3H, CH_3-thiazole), 6.72 (d, 1H, *J* = 8.0 Hz, H-Ar), 6.93 (s, 1H, H-Ar), 7.53 (d, 1H, *J* = 8.5 Hz, H-Ar), 7.68 (d, 2H, *J* = 8.0 Hz, H-Ar), 7.84 (s, 1H, H4 of coumarin), 7.87 (d, 2H, *J* = 8.0 Hz, H-Ar), 10.32 (s, 1H, NH), 11.33 (s, 1H, OH). ^{13}C NMR (126 MHz, DMSO) δ = 13.09 (CH_3), 15.75(CH_3), 101.70, 111.09, 111.64, 113.44, 113.70, 118.64, 120.45, 121.52, 124.08, 129.97, 130.29, 130.37, 142.79, 155.71, 156.25, 160.71(C=O), 172.20 (C=N). Analysis for $C_{21}H_{16}BrN_5O_3S$ (498.35), Calcd.: % C, 50.61; H, 3.24; N, 14.05. Found: % C, 50.73; H, 3.33; N, 14.16. MS m/z (R.A.%): 498 (M^+) (39.46%), 163 (100.00%).

4.1.1.5 7-Hydroxy-3-(1-{2-[5-(4-methoxyphenyl)diazinyl]-4-methylthiazol-2-yl}hydrazono) ethyl-2*H*-chromen-2-one (6e)

Red powder, m. p. 226 °C–227 °C, yield (91%). ^{1}H NMR (500 MHz, $CDCl_3$): δ = 2.23 (s, 3H, CH_3), 3.33 (s, 3H, CH_3-thiazole), 3.85 (s, 3H, OCH_3), 6.74 (s, 1H, H-Ar), 6.80 (d, 1H, *J* = 8.0 Hz, H-Ar), 6.94 (d, 2H, *J* = 8.5 Hz, H-Ar), 7.44 (d, 1H, *J* = 8.0 Hz, H-Ar), 7.70 (d, 2H, *J* = 8.5 Hz, H-Ar), 8.00 (s, 1H, H4 of coumarin), 10.13 (s, 1H, NH), 10.97 (s, 1H, OH). ^{13}C NMR (126 MHz, $CDCl_3$) δ 14.13 (CH_3), 14.96 (CH_3), 55.37 (OCH_3), 102.58, 112.31, 113.61, 113.91, 114.08, 119.17, 119.64, 122.07, 127.21, 130.08, 132.05, 144.78, 155.95, 159.44 (C-OH), 160.93(C=O), 161.39(C-OCH_3), 172.05 (C=N). Analysis for $C_{22}H_{19}N_5O_4S$ (449.48), Calcd.: % C, 58.79; H, 4.26; N, 15.58. Found: % C, 58.91; H, 4.33; N, 15.67. MS m/z (R.A.%): 449 (M^+) (29.80%), 62 (100.00%).

4.1.1.6 3-(1-{2-[5-(2,4-Dichlorophenyl)diazinyl]-4-methylthiazol-2-yl}hydrazono)ethyl-7-hydroxy-2*H*-chromen-2-one (6f)

Red powder, m. p. 194 °C–196 °C, yield (89%). ^{1}H NMR (500 MHz, DMSO-d_6): δ = 2.29 (s, 3H, CH_3), 2.46 (s, 3H, CH_3-thiazole), 6.95 (s, 1H, H-Ar), 7.17-7.21 (m, 2H, H-Ar), 7.32 (s, 1H, H-Ar), 7.53 (d, 1H, *J* = 8.5 Hz, H-Ar), 7.69 (d, 1H, *J* = 8.0 Hz, H-Ar), 8.05 (s, 1H, H4 of coumarin), 10.06 (s, 1H, NH), 10.97 (s, 1H, OH). ^{13}C NMR (126 MHz, DMSO), δ = 13.06 (CH_3), 14.31(CH_3), 101.69, 101.90, 102.20, 107.79, 111.02, 111.77, 113.73, 114.97, 121.10, 130.35, 132.23, 142.95, 147.41, 148.40, 156.06, 158.89, 160.86(C-OH), 162.64(C=O), 170.31(C=N). Analysis for $C_{21}H_{15}C_{l2}N_5O_3S$ (488.34), Calcd.: % C, 51.65; H, 3.10; N, 14.34. Found: % C, 51.76; H, 3.21; N, 14.44. MS m/z (R.A.%): 488 (M^+) (22.92%), 240 (100.00%).

4.1.1.7 3-(1-{2-[5-(4-Acetylphenyl)diazinyl]-4-methylthiazol-2-yl}hydrazono)ethyl-7-hydroxy-2*H*-chromen-2-one (6g)

Red powder, m. p. 205 °C–207 °C, yield (76%). ^{1}H NMR (500 MHz, DMSO-d_6): δ = 2.29 (s, 3H, CH_3), 2.34 (s, 3H, CH_3-thiazole), 2.46 (s, 3H, $COCH_3$), 6.72 (d, 1H, *J* = 8.0 Hz, H-Ar), 7.32 (s, 1H, H-Ar), 7.54 (d, 1H, *J* = 8.5 Hz, H-Ar), 7.68 (d, 2H, *J* = 8.0 Hz, H-Ar), 7.83 (s, 1H, H4 of coumarin), 7.87 (d, 2H, *J* = 8.0 Hz, H-Ar), 10.22 (s, 1H, NH), 11.16 (s, 1H, OH). ^{13}C NMR (126 MHz, DMSO) δ = 14.31(CH_3), 16.05 (CH_3-thiazole), 22.38 (CH_3-CO), 101.69, 107.79, 111.77, 113.73, 114.97, 121.10, 130.35, 132.23, 142.95, 148.40, 156.06, 158.89, 160.86, 161.10, 162.64 (C2 of coumarin), 171.94(C=N), 196.13 (C=O). Analysis for $C_{23}H_{19}N_5O_4S$ (461.49), Calcd.: % C, 59.86; H, 4.15; N, 15.18;. Found: % C, 59.96; H, 4.24; N, 15.30. MS m/z (R.A.%): 461 (M^+) (17.32%), 191 (100.00%).

4.1.1.8 3-(1-{2-[5-(2-chloro-4-nitrophenyl)diazinyl]-4-methylthiazol-2-yl}hydrazono) ethyl-7-hydroxy-2*H*-chromen-2-one (6h)

Brown powder, m. p. 237 °C–239 °C, yield (88%). ^{1}H NMR (500 MHz, DMSO-d_6): δ = 2.18 (s, 3H, CH_3), 2.41 (s, 3H, CH_3-thiazole), 6.29 (s, 1H, H-Ar), 6.92 (d, 1H, *J* = 8.0 Hz, H-Ar), 7.26 (d, 1H, *J* = 7.5 Hz, H-Ar), 7.44 (d, 1H, *J* = 8.0 Hz, H-Ar), 7.59 (s, 1H, H-Ar), 7.88 (d, 1H, *J* = 8.0 Hz, H-Ar), 8.30 (s, 1H, H-Ar), 10.11 (s, 1H, NH), 11.41 (s, 1H, OH). ^{13}C NMR (126 MHz, DMSO) δ = 13.09 (CH_3), 15.75 (CH_3-thiazole), 101.70, 111.09, 111.64, 113.70, 113.44, 118.64, 120.45, 121.52, 129.97, 130.29, 130.37, 142.79, 156.25, 159.08, 160.37, 160.71, 160.78 (C2 of coumarin), 172.20 (C=N). Analysis for $C_{21}H_{15}ClN_6O_5S$ (498.89), Calcd.: % C, 50.56; H, 3.03; N, 16.85; Found: C, 50.67; H, 3.14; N, 16.95. MS m/z (R.A.%): 498 (M^+) (35.06%), 148 (100.00%).

4.1.1.9 4-(2-{2-[1-(7-Hydroxy-2-oxo-2*H*-chromen-3-yl) ethylidene]hydrazinyl}-4-methyl thiazol-5-yl) diazinyl benzenesulfonamide (6i)

Red powder, m. p. > 300 °C, yield (74%). ^{1}H NMR (500 MHz, DMSO-d_6): δ = 2.40 (s, 3H, CH_3), 2.47 (s, 3H, CH_3-thiazole), 6.74 (s, 1H, H-Ar), 6.81 (d, 1H, *J* = 8.5 Hz, H-Ar), 6.94 (d, 2H, *J* = 7.0 Hz, H-Ar), 7.26-7.31 (m, 4H, H-Ar, NH_2), 7.63 (d, 1H, *J* = 8.5 Hz, H-Ar), 8.24 (s, 1H, H4 of coumarin), 10.56 (s, 1H, NH), 10.84 (s, 1H, OH). ^{13}C NMR (126 MHz, DMSO) δ = 14.26 (CH_3), 15.52(CH_3), 103.28,

119.09, 121.06, 121.52, 125.04, 125.67, 127.94, 128.26, 128.69, 129.62, 133.12, 134.61, 141.87, 147.92, 149.81, 152.23, 171.24 (C=N). Analysis for $C_{21}H_{18}N_6O_5S_2$ (498.53), Calcd.: % C, 50.59; H, 3.64; N, 16.86; Found: C, 50.70; H, 3.72; N, 16.95. MS m/z (R.A.%): 498 (M^+) (18.83%), 366 (100.00%).

4.2 Biological activity

4.2.1 Antibacterial activity of the prepared coumarin derivatives

To assess the antibacterial effectiveness of the synthesized coumarin derivatives, various extensively drug-resistant (XDR) bacterial pathogens were employed. In this regard, two Gram-positive (*Campylobacter jejuni* and *Enterococcus faecalis*) and two Gram-negative (*Serratia fonticola* and *Achromobacter xylosoxidans*) bacteria were supplemented by faculty of medicine (Boys), Al-Azhar University. Antibiogram sensitivity profile demonstrated highly resistance of these pathogens towards at least three groups of classical antibiotic references. Activation of each of pathogen prior to screening of the targeted compounds was implemented Cultivating in Mueller Hinton broth for 24 h at 37 °C with shaking. The rationale for the inoculum size for each pathogen was determined through the use of the McFarland scale and precisely quantified in terms of colony forming units (CFU/mL) to ensure a constant bacterial concentration across all experimental assays. Thus, The agar-well diffusion method was developed in accordance with the guidelines established by the Clinical and Laboratory Standards Institute (CLSI) (Yassin et al., 2025). Subsequently, screening of each of targeted molecule was performed at fixed concentration (50 μg/mL). Incubation of each tested pathogen was carried out and the observed inhibition zone diameter (mm) were conducted in triplicate and subsequently compared to established standard antibacterial agents (Ahmed et al., 2024).

4.2.2 Determination of MIC values

The most-active compounds that efficiently inhibited the tested bacterial pathogens were subjected to determine the MIC using broth microdilution procedure according to CLSI protocol. Briefly, a predetermined quantity, 10 mg of each compound and standard drug was solubilized in 1 mL of dimethyl sulphoxide (DMSO) to create a stock solution. Ten successive dilutions were prepared with a concentration 10 times greater than the final solution of the targeted compounds. The dilutions were further diluted to 1:5 in Mueller Hinton broth medium and 100 μL aliquots were sequentially dispensed into the microdilution plates to obtain the desired concentrations ranging from 20 to 250 μg/mL. In comparison, the standard antibacterial drug was also prepared as same as the targeted compounds and determined its MIC value. After incubation period, 80 μL of each microbial cell was swapped onto nutrient agar plates. The determination of the minimum inhibitory concentration (MIC) for each targeted compound is defined as the lowest concentration of each sample that results in a minimum number of colony-forming units (CFUs) when compared to the untreated samples (Mohamed et al., 2023).

Briefly, 10 mg of each selected compound and reference drugs were dissolved in 1 mL of dimethyl sulphoxide (DMSO) to prepare the stock solution. Ten successive dilutions were prepared with a concentration 10 times greater than the final solution of the synthesized compounds. The dilutions were further diluted to 1: 5 in PDB and 100 μL aliquots were sequentially dispensed into the microdilution plates to get the desired concentrations ranging from10–400 μg/mL. Each tested compound was incubated with the tested fungal strain for 48 h at 28 °C. The PDB mixed with DMSO was served as the control growth samples. After that, inoculated of each treated sample with 50 μL to Potato dextrose agar plate and incubated for 72 h at 28 °C

4.2.3 Biofilm inhibitory activity

4.2.3.1 Qualitative method using Congo red agar plate

The Congo Red Agar (CRA) method was employed to qualitatively evaluate biofilm formation in bacteria subjected to a fixed concentration of polymer (20 μg/mL). The CRA medium was formulated with brain heart infusion broth (37 g/L), sucrose (50 g/L), agar (10 g/L), and Congo red indicator (0.8 g/L). Bacterial cultures that had been treated with the polymer were inoculated onto CRA plates and incubated aerobically at 37 °C for a duration of 24 h. The presence of black colonies exhibiting a dry, crystalline morphology indicated successful biofilm production, while red colonies were indicative of inhibited biofilm formation (Ragab et al., 2023).

4.2.3.2 Quantitative method using crystal violet assay

Quantitative evaluation of biofilm inhibition was conducted using crystal violet assay. Anti-biofilm activity of each potent molecule was investigated at MIC value, which mixed with 170 μL Mueller Hinton broth and then inoculated with 15 μL of bacterial pathogen in 96-well plate and incubated at 37 °C for 24 h. The culture medium was removed, and the wells were rinsed with 200 μL of phosphate-buffered saline (PBS) at pH 7.2 to eliminate any planktonic cells, followed by a drying period of 1 hour in a sterilized laminar flow hood. Subsequently, 200 μL of a 0.1% (w/v) crystal violet solution was added to each well and allowed to incubate for 1 hour. Excess stain was then removed by washing the wells three times with PBS, after which the plates were dried. Finally, 200 μL of ethanol was introduced to elute the crystal violet, and the absorbance was measured at 590 nm (Basnet et al., 2023).

The biofilm mass inhibition % was calculated according to the following formula:

$$\text{Biofilm mass inhibition } (\%) = [(C - S)/C] \times 100$$

Where C is the optical density at 590 nm (OD_{590}) of the untreated bacterial cells and S is the OD_{590} of the treated bacterial cells.

4.2.4 Measurement of intracellular reactive oxygen species (ROS) inside the treated microbial cells

Reactive Oxygen Species is one of the assumed mechanisms that may responsible for the antibacterial activity of the Sulfa drugs. ROS are known as a group of highly reactive molecules like molecular oxygen (O_2), superoxide anion ($O_2^{\bullet}$), hydrogen peroxide (H_2O_2) and hydroxyl radicals ($OH^{\bullet}$) having an ability to induced an

oxidative stress onto the bacterial cells. Therefore, the susceptibility of the potent compounds to induced ROS toward the microbial pathogens was assessed intracellularly. In this regard, ROS could be quantifying using a fluorescent prop 2′,7′-Dichlorodihydrofluorescein diacetate (DCFH-DA). Briefly, the treated microbial samples were subjected to permeabilization process by ultrasonciation of cells and the resultant supernatant was harvested and reacted with 10 μM DCFH-DA for 30 min at 37 °C (Farid et al., 2024). At the same time, the microbial cells were treated with hydrogen peroxide H_2O_2 at 155 μM as a positive control. Immediately, the DCF fluorescence intensity was measured by Spectrofluorometric apparatus (JASCO FP-6500, light source Xenon arc lamp, Japan). The fluorescence intensity for each sample was measured with an excitation and emission wavelength at 485 nm and 530 nm, respectively.

4.2.5 Effect of coumarin derivatives on the bacterial lipid peroxidation (LPO)

A treated bacterial cell using the most potent molecules was subjected to investigate the LPO process. Utilizing the LPO colorimetric kit assay, a particular reagent called thiobarbituric acid (TBA) was utilized to indicate the fatty acid peroxidation byproduct, malondialdehyde (MDA), producing a pink color complex known as MDA-TBA (Mallique Qader et al., 2021). In this study, a consistent concentration of each potent molecule (20 μg/mL) was employed to evaluate the level of oxidation occurring in the lipids of the bacterial cell membrane. To assess lipid peroxidation (LPO), 1 mL of each treated bacterial pathogen was combined with 300 μL of malondialdehyde (MDA) lysis buffer at 4 °C. Subsequently, 3 μL of Butylated Hydroxytoluene (BHT) was added to mitigate interference from pigments generated by the decomposition of lipophilic peroxides. Each sample was then subjected to centrifugation at 8,000 rpm for 10 min, after which the insoluble materials were discarded. A volume of 200 μL of the clear supernatant was mixed with 600 μL of thiobarbituric acid (TBA) solution and incubated at 95 °C for 60 min. Following incubation, the samples were cooled to 25 °C, and the resultant pink color was quantified using a spectrophotometer (Agilent Cary 100, Germany) at a wavelength of 532 nm. Treatment of both bacterial pathogens using 5% hydrogen peroxide for 20 min as a positive control was also involved. The increase in the malondialdehyde concentration in the tested sample indicated the increase of the lipid peroxidation activity of SL towards bacterial cell membrane, malondialdehyde concentration was calculated based on the following equation:

$$\mathbf{Malondialdehyde\,(nmol/mL)} = \mathbf{A}\,\text{sample}/\mathbf{A}\,\text{standard} \times \mathbf{10} \ldots$$

Where A sample is the lipid peroxidation absorbance in the treated bacterial cells and A standard is the absorbance of the standard lipid peroxidation sample.

4.2.6 Enzyme inhibitory effects against *E.Coli* DNA Gyrase

The *in vitro* assessment of enzyme inhibition for the most active derivative 6a and 6c was performed against *E. coli* DNA gyrase B. The anticipated assay was done *using E. coli* DNA gyrase microplate assay kit (Inspiralis) according to the optimized protocol of the manufacturer. Ciprofloxacin was used as a reference drug for *E. coli* DNA gyrase B according to the previously reported methods (Fayed et al., 2022). The obtained data are tabulated as IC_{50} values in Table 6.

4.3 Molecular modeling

4.3.1 Molecular docking analysis

Molecular docking studies were conducted to evaluate the potential binding affinity of the compounds 6a and 6c towards DNA Gyrase B. the tested compounds were docked against DNA Gyrase B obtained from Protein Data Bank (PDB ID: 4duh) (Brvar et al., 2012).

Initially, water molecules and extraneous components were eliminated from the protein complex. Subsequently, crystallographic disorders and unoccupied valence atoms were rectified. The energy of the protein structure was minimized and subsequently saved in a PDBQT file format. The two-dimensional structures of each compound were constructed utilizing Chem-Bio Draw Ultra 16.0, saved as SDF files, and subsequently converted into three-dimensional structures. Protonation and energy minimization were performed, with the results also saved as PDBQT files. The docking processes were executed using AutoDock Vina version 1.5.7, employing a rigid docking technique in which the receptor remained fixed while the ligands were permitted to adopt flexible conformations. Furthermore, each molecule was allowed to generate twenty distinct poses. The docking scores, representing the affinity energy of the most favorable poses in relation to the target protein, were documented, and both three-dimensional and two-dimensional representations were produced using Discovery Studio 2024 for visualization purposes (El-Demerdash et al., 2024).

4.3.2 Molecular dynamic (MD) simulation

The Desmond simulation package developed by Schrödinger LLC was employed to perform molecular dynamics (MD) simulations (Kumar et al., 2022). All simulations were conducted using the NPT ensemble, maintaining a temperature of 300 K and a pressure of 1 bar throughout the experimental runs. Each simulation was executed for a duration of 100 ns, with a relaxation time of 1 ps allocated for the ligands under investigation. The OPLS_2005 force field parameters were utilized for all simulations. Long-range electrostatic interactions were calculated using the particle mesh Ewald method, with a cutoff radius of 9.0 Å designated for Coulomb interactions (Ivanova et al., 2018).

Water molecules were represented explicitly through the simple point charge model. Pressure regulation was achieved using the Martyna–Tuckerman–Klein chain coupling scheme, characterized by a coupling constant of 2.0 ps, while temperature regulation was conducted via the Nosé–Hoover chain coupling scheme. Nonbonded interactions were computed utilizing the r-RESPA integrator, wherein short-range forces were updated at every time step and long-range forces were updated every three-time steps. Trajectories were recorded at intervals of 4.8 ps for further analysis.

The interactions and behavior of ligands and proteins were analyzed using the Simulation Interaction Diagram tool available in the Desmond molecular dynamics (MD) package. The stability of the MD simulations was evaluated by tracking the root mean square deviation (RMSD) of the positions of ligand and protein atoms over time (Case et al., 2008).

Data availability statement

The datasets presented in this study can be found in online repositories. The names of the repository/repositories and accession number(s) can be found in the article/Supplementary Material.

Author contributions

ME: Data curation, Funding acquisition, Methodology, Resources, Writing – review and editing. HF: Conceptualization, Data curation, Formal Analysis, Investigation, Writing – review and editing. MA: Data curation, Formal Analysis, Methodology, Validation, Writing – original draft. AS: Data curation, Investigation, Methodology, Software, Visualization, Writing – original draft. MT: Formal Analysis, Investigation, Methodology, Validation, Writing – review and editing. JD: Conceptualization, Data curation, Formal Analysis, Funding acquisition, Investigation, Supervision, Writing – review and editing. AY: Formal Analysis, Methodology, Software, Validation, Visualization, Writing – review and editing. AS: Conceptualization, Data curation, Formal Analysis, Investigation, Methodology, Supervision, Writing – original draft, Writing – review and editing.

Funding

The author(s) declare that financial support was received for the research and/or publication of this article. The authors extend their appreciation to the Deanship of Scientific Research at Northern Border University, Arar, KSA, for supporting this work through the project number "NBU-FFR-2025-80-04" -JD was supported by the Ministry of Science and Higher Education, POL-OPENSCREEN, 2024/WK/06.

Conflict of interest

The authors declare that the research was conducted in the absence of any commercial or financial relationships that could be construed as a potential conflict of interest.

Generative AI statement

The author(s) declare that no Generative AI was used in the creation of this manuscript.

Any alternative text (alt text) provided alongside figures in this article has been generated by Frontiers with the support of artificial intelligence and reasonable efforts have been made to ensure accuracy, including review by the authors wherever possible. If you identify any issues, please contact us.

Publisher's note

All claims expressed in this article are solely those of the authors and do not necessarily represent those of their affiliated organizations, or those of the publisher, the editors and the reviewers. Any product that may be evaluated in this article, or claim that may be made by its manufacturer, is not guaranteed or endorsed by the publisher.

Supplementary material

The Supplementary Material for this article can be found online at: https://www.frontiersin.org/articles/10.3389/fchem.2025.1627186/full#supplementary-material

References

Ayukekbong, J. A., Ntemgwa, M., and Atabe, A. N. (2017). The threat of antimicrobial resistance in developing countries: causes and control strategies. *Antimicrob. Resist. and Infect. Control* 6, 47–48. doi:10.1186/s13756-017-0208-x

Abid, M. A., Abed, A. A., Musa, M., Izuagie, T., and Agwamba, E. C. (2025). Anti-diabetic, anti-bacterial and anti-oxidant potential of new biologically active thiazole-derivatives: experimental and molecular docking studies. *J. Mol. Struct.* 1321, 139482. doi:10.1016/j.molstruc.2024.139482

Ahmad, H., Ahmad, F., Parveen, S., Ahmad, S., Azam, S. S., and Hassan, A. (2020). A combine approach of chemical synthesis, biological evaluation and structural dynamics studies revealed thiazole substituted arylamine derivatives as potent FabH enzyme inhibitors. *Bioorg. Chem.* 105, 104426. þ. doi:10.1016/j.bioorg.2020.104426

Ahmed, A. H., Ghareeb, M. A., Kelany, A. K., Abdelraof, M., Kabary, H. A., Soliman, N. R., et al. (2024). Induction of antimicrobial, antioxidant metabolites production by co-cultivation of two red-sea-sponge-associated Aspergillus sp. CO_2 and Bacillus sp. COBZ21. *BMC Biotechnol.* 24, 3. doi:10.1186/s12896-024-00830-z

Ammar, Y. A., Abd El-Hafez, S. M. A., Hessein, S. A., Ali, A. M., Askar, A. A., and Ahmed, R. (2021). One-pot strategy for thiazole tethered 7-ethoxy quinoline hybrids: synthesis and potential antimicrobial agents as dihydrofolate reductase (DHFR) inhibitors with molecular docking study. *J. Mol. Struct.* 1242, 130748. doi:10.1016/j.molstruc.2021.130748

Antimicrobial Resistance Collaborators (2022). Global burden of bacterial antimicrobial resistance in 2019: a systematic analysis. *Lancet* 399, 629–655. doi:10.1016/s0140-6736(21)02724-0

Basnet, A., Tamang, B., Shrestha, M. R., Shrestha, L. B., Rai, J. R., Maharjan, R., et al. (2023). Assessment of four *in vitro* phenotypic biofilm detection methods in relation to antimicrobial resistance in aerobic clinical bacterial isolates. *PLoS ONE* 18 (11), e0294646. doi:10.1371/journal.pone.0294646

Batran, R. Z., Sabt, A., Khedr, M. A., Allayeh, A. K., Pannecouque, C., and Kassem, A. F. (2023). 4-Phenylcoumarin derivatives as new HIV-1 NNRTIs: design, synthesis, biological activities, and computational studies. *Bioorg. Chem.* 141, 106918. doi:10.1016/j.bioorg.2023.106918

Bhagat, K., Bhagat, J., Gupta, M. K., Singh, J. V., Gulati, H. K., Singh, A., et al. (2019). Design, synthesis, antimicrobial evaluation, and molecular modeling studies of novel indolinedione–coumarin molecular hybrids. *ACS omega* 4 (5), 8720–8730. doi:10.1021/acsomega.8b02481

Brvar, M., Perdih, A., Renko, M., Anderluh, G., Turk, D., and Solmajer, T. (2012). Structure-based discovery of substituted 4, 5′-bithiazoles as novel DNA gyrase inhibitors. *J. Med. Chem.* 55 (14), 6413–6426. doi:10.1021/jm300395d

Case, D. A., Darden, T. A., Cheatham, T. E., Simmerling, C. L., Wang, J., Duke, R. E., et al. (2008). *Amber 10*. University of California.

Cheke, R. S., Patel, H. M., Patil, V. M., Ansari, I. A., Ambhore, J. P., Shinde, S. D., et al. (2022). Molecular insights into coumarin analogues as antimicrobial agents: recent developments in drug discovery. *Antibiotics* 11 (5), 566. doi:10.3390/antibiotics11050566

Cui, S. F., Addla, D., and Zhou, C. H. (2016). Novel 3-aminothiazolquinolones: design, synthesis, bioactive evaluation, SARs and preliminary antibacterial mechanism. *J. Med. Chem.* 59, 4488–4510. doi:10.1021/acs.jmedchem.5b01678

Desai, N. C., Bhatt, N., Somani, H., and Trivedi, A. (2013). Synthesis, antimicrobial and cytotoxic activities of some novel thiazole clubbed 1,3,4-oxadiazoles. *Eur. J. Med. Chem.* 67, 54–59. doi:10.1016/j.ejmech.2013.06.029

El-Demerdash, A. S., Kamel, S. A., Elariny, E. Y., Henidi, H., Mahran, Y., Alahdal, H., et al. (2024). Natural inhibitors of Salmonella MDR efflux pumps AcrAB and AcrD: an integrated *in silico*, molecular, and *in vitro* investigation. *Int. J. Mol. Sci.* 25 (23), 12949. doi:10.3390/ijms252312949

Ebaid, M. S., Korycka-Machala, M., Shaldam, M. A., Thabit, M. G., Kawka, M., Dziadek, B., et al. (2025). Exploring antitubercular activity of new coumarin derivatives targeting enoyl acyl carrier protein reductase (InhA): synthesis, biological evaluation

and computational studies. *J. Mol. Struct.* 1336, 142074. doi:10.1016/j.molstruc.2025.142074

Eryılmaz, S., Türk Çelikoglu, E., Idil, Ö., Inkaya, E., Kozak, Z., Mısır, E., et al. (2020). Derivatives of pyridine and thiazole hybrid: synthesis, DFT, biological evaluation via antimicrobial and DNA cleavage activity. *Bioorg. Chem.* 95, 103476. doi:10.1016/j.bioorg.2019.103476

Farghaly, T. A., Alsaedi, A. M., Alenazi, N. A., and Harras, M. F. (2022). Anti-viral activity of thiazole derivatives: an updated patent review. *Expert Opin. Ther. Pat.* 32 (7), 791–815. doi:10.1080/13543776.2022.2067477

Farid, M. S., Ahmed, F. E.-S., and Mohamed, A. (2024). Design, synthesis, structure elucidation, antimicrobial, molecular docking, and SAR studies of novel urea derivatives bearing tricyclic aromatic hydrocarbon rings. *Arch. Pharm.* 357 (6), 2300738. doi:10.1002/ardp.202300738

Fayed, E. A., Nosseir, E. S., Atef, A., and El-Kalyoubi, S. A. (2022). *In vitro* antimicrobial evaluation and *in silico* studies of coumarin derivatives tagged with pyrano-pyridine and pyrano-pyrimidine moieties as DNA gyrase inhibitors. *Mol. Divers.* 26 (1), 341–363. doi:10.1007/s11030-021-10224-4

Hassan, N. W., Sabt, A., El-Attar, M. A., Ora, M., Bekhit, A. E., Amagase, K., et al. (2023). Modulating leishmanial pteridine metabolism machinery via some new coumarin-1, 2, 3-triazoles: design, synthesis and computational studies. *Eur. J. Med. Chem.* 253, 115333. doi:10.1016/j.ejmech.2023.115333

Hu, Y., Shen, Y., Wu, X., Tu, X., and Wang, G. X. (2018). Synthesis and biological evaluation of coumarin derivatives containing imidazole skeleton as potential antibacterial agents. *Eur. J. Med. Chem.* 143, 958–969. doi:10.1016/j.ejmech.2017.11.100

Huemer, M., Mairpady Shambat, S., Brugger, S. D., and Zinkernagel, A. S. (2020). Antibiotic resistance and persistence-Implications for human health and treatment perspectives. *EMBO Rep.* 21 (12), e51034. doi:10.15252/embr.202051034

Ibrahim, H. S., Abdelrahman, M. A., Nocentini, A., Bua, S., Abdel-Aziz, H. A., Supuran, C. T., et al. (2022). Insights into the effect of elaborating coumarin-based aryl enaminones with sulfonamide or carboxylic acid functionality on carbonic anhydrase inhibitory potency and selectivity. *Bioorg. Chem.* 126, 105888. doi:10.1016/j.bioorg.2022.105888

Ivanova, L., Tammiku-Taul, J., García-Sosa, A. T., Sidorova, Y., Saarma, M., and Karelson, M. (2018). Molecular dynamics simulations of the interactions between glial cell line-derived neurotrophic factor family receptor GFRα1 and small-molecule ligands. *ACS omega* 3 (9), 11407–11414. doi:10.1021/acsomega.8b01524

Joule, J. A., and Mills, K. (2010). *Heterocyclic chemistry*. 5th ed. John Wiley and Sons.

Karakaya, A., Ercetin, T., Yıldırım, S., Kocyigit, Ü. M., Rudrapal, M., Rakshit, G., et al. (2024). New thiazole derivatives: carbonic anhydrase I–II and cholinesterase inhibition profiles, molecular docking studies. *ChemistrySelect* 9 (28), e202401587. doi:10.1002/slct.202401587

Klika, K. D., Da Pieve, C., Kopka, K., Smith, G., and Makarem, A. (2021). Synthesis and application of a thiol-reactive HBED-type chelator for development of easy-to-produce Ga-radiopharmaceutical kits and imaging probes. *Org. Biomol. Chem.* 19 (8), 1722–1726. doi:10.1039/d0ob02513e

Klika, K. D., Alsalim, R., Eftekhari, M., and Makarem, A. (2022). Synthesis of a polyaminocarboxylate-based aluminum complex and its structural studies using 1 H {13 C}-HMBC NMR and a Karplus-type function. *Dalton Trans.* 51 (33), 12436–12441. doi:10.1039/d2dt01702d

Koley, M., Han, J., Soloshonok, V. A., Mojumder, S., Javahershenas, R., and Makarem, A. (2024). Latest developments in coumarin-based anticancer agents: mechanism of action and structure–activity relationship studies. *RSC Med. Chem.* 15 (1), 10–54. doi:10.1039/d3md00511a

Kumar, B. K., Faheem, F., Sekhar, K. V. G. C., Ojha, R., Prajapati, V. K., Pai, A., et al. (2022). Pharmacophore based virtual screening, molecular docking, molecular dynamics and MM-GBSA approach for identification of prospective SARS-CoV-2 inhibitor from natural product databases. *J. Biomol. Struct. Dyn.* 40 (3), 1363–1386. doi:10.1080/07391102.2020.1824814

Li, W., Sun, Y. N., Yan, X. T., Yang, S. Y., Kim, E. J., Kang, H. K., et al. (2013). Coumarins and lignans from zanthoxylum schinifolium and their anticancer activities. *J. Agric. Food Chem.* 61, 10730–10740. doi:10.1021/jf403479c

Liu, H., Xia, D. G., Chu, Z. W., Hu, R., Cheng, X., and Lv, X. H. (2020). Novel coumarin-thiazolyl ester derivatives as potential DNA gyrase Inhibitors: design, synthesis, and antibacterial activity. *Bioorg. Chem.* 100, 103907. doi:10.1016/j.bioorg.2020.103907

Llor, C., and Bjerrum, L. (2014). Antimicrobial resistance: risk associated with antibiotic overuse and initiatives to reduce the problem. *Ther. Adv. Drug Saf.* 5 (6), 229–241. doi:10.1177/2042098614554919

Lungu, L., Blaja, S., Cucicova, C., Ciocarlan, A., Barba, A., Kulcițki, V., et al. (2023). Synthesis and antimicrobial activity evaluation of homodrimane sesquiterpenoids with a benzimidazole unit. *Molecules* 28, 933. doi:10.3390/molecules28030933

Mallique Qader, M., Ahmed, A. H., Soldatou, S., Abdelraof, M., Elawady, M. E., Ahmed, S. I. H., et al. (2021). Antimicrobial and antibiofilm activities of the fungal metabolites isolated from the marine endophytes epicoccum nigrum M13 and *Alternaria alternata* 13A. *Mar. Drugs* 19 (4), 323. doi:10.3390/md19040232

Mangasuli, S. N., Hosamani, K. M., Satapute, P., and Joshi, S. D. (2018). Synthesis, molecular docking studies and biological evaluation of potent coumarin-carbonodithioate hybrids via microwave irradiation. *Chem. Data Collect.* 15-16, 115–125. doi:10.1016/j.cdc.2018.04.001

Matin, M. M., Bhattacharjee, S. C., Chakraborty, P., and Alam, M. S. (2019). Synthesis, PASS predication, *in vitro* antimicrobial evaluation and pharmacokinetic study of novel n-octyl glucopyranoside esters. *Carbohydr. Res.* 485, 107812. doi:10.1016/j.carres.2019.107812

Mohamed, A., Mohamed, F., Hashem, A. H., El-Naggar, M. E., and Rashdan, H. R. M. (2023). Insight into novel anti-mucormycosis therapies: investigation of new anti-mucormycosis laser-induced photodynamic therapy based on a sulphone bis-compound loaded silica nanoemulsion. *RSC Adv.* 13, 20684–20697. doi:10.1039/d3ra02775a

Naghavi, M., Vollset, S. E., Ikuta, K. S., Swetschinski, L. R., Gray, A. P., Wool, E. E., et al. (2024). Global burden of bacterial antimicrobial resistance 1990–2021: a systematic analysis with forecasts to 2050. *Lancet* 404 (10459), 1199–1226. doi:10.1016/s0140-6736(24)01867-1

Osman, S. A., Abdallah, M., Bassiony, H., and Rashdan, H. (2023). Insight into the synthesis, biological impact and convenient routes of hydrazonoyl halides for synthesis of novel bioactive heterocycles: mini-review. *Egypt. J. Chem.* 66 (13), 2371–2378. þ. doi:10.21608/ejchem.2024.249272.8883

Prestinaci, F., Pezzotti, P., and Pantosti, A. (2015). Antimicrobial resistance: a global multifaceted phenomenon. *Pathog. Glob. Health* 109, 309–318. doi:10.1179/2047773215y.0000000030

Qi, X. L., Zhang, H. C., Xu, X., Liu, X. W., Yang, Y. J., Li, Z., et al. (2025). Discovery of novel thiazole-pleuromutilin derivatives with potent antibacterial activity. *Eur. J. Med. Chem.* 8, 117374. doi:10.1016/j.ejmech.2025.117374

Queiroz, C. M., de Oliveira Filho, G. B., Espíndola, J. W., do Nascimento, A. V., Aliança, A. S., de Lorena, V. M., et al. (2020). Thiosemicarbazone and thiazole: *in vitro* evaluation of leishmanicidal and ultrastructural activity on Leishmania infantum. *Med. Chem. Res.* 29, 2050–2065. doi:10.1007/s00044-020-02619-z

Ragab, S. S., Abdelraof, M., Elrashedy, A. A., and Sweed, A. M. K. (2023). Design, synthesis, molecular dynamic simulation studies, and antibacterial evaluation of new spirocyclic aminopyrimidines. *J. Mol. Struct.* 1278, 134912. doi:10.1016/j.molstruc.2023.134912

Rajakumari, K., Aravind, K., Balamugundhan, M., Jagadeesan, M., Somasundaram, A., Devi, P., et al. (2024). Comprehensive review of DNA gyrase as enzymatic target for drug discovery and development. *Eur. J. Med. Chem. Rep.* 12, 100233. doi:10.1016/j.ejmcr.2024.100233

Ranjan, S. C., Sahoo, J., Mahapatra, M., Lenka, D., Kumar, S. P., Dehury, B., et al. (2021). Coumarin derivatives as promising antibacterial agent (s). *Arab. J. Chem.* 14 (2), 102922. doi:10.1016/j.arabjc.2020.102922

Sabt, A., Abdelhafez, O. M., El-Haggar, R. S., Madkour, H. M., Eldehna, W. M., El-Khrisy, E. E., et al. (2018). Novel coumarin-6-sulfonamides as apoptotic anti-proliferative agents: synthesis, *in vitro* biological evaluation, and QSAR studies. *J. Enzyme Inhibition Med. Chem.* 33 (1), 1095–1107. doi:10.1080/14756366.2018.1477137

Sabt, A., Abdelraof, M., Hamissa, M. F., and Noamaan, M. A. (2023). Antibacterial activity of quinoline-based derivatives against methicillin-resistant *Staphylococcus aureus* and *Pseudomonas aeruginosa*: design, synthesis, DFT and molecular dynamic simulations. *Chem. Biodivers.* 20 (11), e202300804. doi:10.1002/cbdv.202300804

Sabt, A., Abdulla, M. H., Ebaid, M. S., Pawełczyk, J., Abd El Salam, H. A., Son, N. T., et al. (2024a). Identification of 2-(N-aryl-1, 2, 3-triazol-4-yl) quinoline derivatives as antitubercular agents endowed with InhA inhibitory activity. *Front. Chem.* 12, 1424017. doi:10.3389/fchem.2024.1424017

Sabt, A., Khaleel, E. F., Shaldam, M. A., Ebaid, M. S., Badi, R. M., Allayeh, A. K., et al. (2024b). Discovery of new quinoline derivatives bearing 1-aryl-1, 2, 3-triazole motif as influenza H1N1 virus neuraminidase inhibitors. *Bioorg. Chem.* 151, 107703. doi:10.1016/j.bioorg.2024.107703

Sabt, A., Khedr, M. A., Eldehna, W. M., Elshamy, A. I., Abdelhameed, M. F., Allam, R. M., et al. (2024c). New pyrazolylindolin-2-one based coumarin derivatives as anti-melanoma agents: design, synthesis, dual BRAF V600E/VEGFR-2 inhibition, and computational studies. *RSC Adv.* 14 (9), 5907–5925. doi:10.1039/d4ra00157e

Salam, M. A., Al-Amin, M. Y., Salam, M. T., Pawar, J. S., Akhter, N., Rabaan, A. A., et al. (2023). Antimicrobial resistance: a growing serious threat for global public health. *Healthc. (Basel)* 11 (13), 1946. doi:10.3390/healthcare11131946

Sayed, M. T., Elsharabasy, S. A., and Abdel-Aziem, A. (2023). Synthesis and antimicrobial activity of new series of thiazoles, pyridines and pyrazoles based on coumarin moiety. *Sci. Rep.* 13 (1), 9912. þ. doi:10.1038/s41598-023-36705-0

Sharifi-Rad, J., Cruz-Martins, N., López-Jornet, P., Lopez, E. P., Harun, N., Yeskaliyeva, B., et al. (2021). Natural coumarins: exploring the pharmacological complexity and underlying molecular mechanisms. *Oxid. Med. Cell Longev.* 2021, 6492346. doi:10.1155/2021/6492346

Silver, L. L. (2011). Challenges of antibacterial discovery. *Clin. Microbiol. Rev.* 24 (1), 71–109. doi:10.1128/cmr.00030-10

Singh, H., Singh, J. V., Gupta, M. K., Saxena, A. K., Sharma, S., Nepali, K., et al. (2017a). Triazole tethered isatin-coumarin based molecular hybrids as novel antitubulin

agents: design, synthesis, biological investigation and docking studies. *Bioorg. Med. Chem. Lett.* 27, 3974–3979. doi:10.1016/j.bmcl.2017.07.069

Singh, L. R., Avula, S. R., Raj, S., Srivastava, A., Palnati, G. R., Tripathi, C. K. M., et al. (2017b). Coumarinbenzimidazole hybrids as a potent antimicrobial agent: synthesis and biological elevation. *J. Antibiot.* 70, 954–961. doi:10.1038/ja.2017.70

Sui, Y. F., Ansari, M. F., Fang, B., Zhang, S. L., and Zhou, C. H. (2021). Discovery of novel purinylthiazolylethanone derivatives as anti-Candida albicans agents through possible multifaceted mechanisms. *Eur. J. Med. Chem.* 221, 113557. doi:10.1016/j.ejmech.2021.113557

Weinmann, I. (1997). *History of the development and applications of coumarin and coumarin-related compounds, coumarins: biology, applications and mode of action*. New York, NY: John Wiley and Sons, Inc.

Yang, X. C., Hu, C. F., Zhang, P. L., Li, S., Hu, C. S., Geng, R. X., et al. (2022). Coumarin thiazoles as unique structural skeleton of potential antimicrobial agents. *Bioorg. Chem.* 124, 105855. doi:10.1016/j.bioorg.2022.105855

Yassin, M. A., Komber, H., Mohamed, N., Mohamed, A., Appelhans, D., and Voit, B. (2025). Antimicrobial polymer via ROMP of a bioderived tricyclic oxanorbornene lactam derivative. *ACS Appl. Bio Mater.* 8, 1720–1731. doi:10.1021/acsabm.4c01924

frontiers | Frontiers in Chemistry

TYPE Original Research
PUBLISHED 16 September 2025
DOI 10.3389/fchem.2025.1638489

Check for updates

OPEN ACCESS

EDITED BY
Belgin Sever,
Anadolu University, Türkiye

REVIEWED BY
Narva Deshwar Kushwaha,
Wayne State University, United States
Tanmay Pati,
Rensselaer Polytechnic Institute, United States

*CORRESPONDENCE
Bahaa G. M. Youssif,
bgyoussif2@gmail.com
Stefan Bräse,
braese@kit.edu

RECEIVED 30 May 2025
ACCEPTED 01 September 2025
PUBLISHED 16 September 2025

CITATION
Al-Wahaibi LH, Abou-Zied HA, Nieger M, Bräse S, Youssif BGM and Tawfik H (2025) Design, synthesis, antiproliferative assessments, and computational studies of new quinolin-2(1*H*)-ones as dual EGFR/HER-2 inhibitors. *Front. Chem.* 13:1638489. doi: 10.3389/fchem.2025.1638489

COPYRIGHT
© 2025 Al-Wahaibi, Abou-Zied, Nieger, Bräse, Youssif and Tawfik. This is an open-access article distributed under the terms of the Creative Commons Attribution License (CC BY). The use, distribution or reproduction in other forums is permitted, provided the original author(s) and the copyright owner(s) are credited and that the original publication in this journal is cited, in accordance with accepted academic practice. No use, distribution or reproduction is permitted which does not comply with these terms.

Design, synthesis, antiproliferative assessments, and computational studies of new quinolin-2(1*H*)-ones as dual EGFR/HER-2 inhibitors

Lamya H. Al-Wahaibi[1], Hesham A. Abou-Zied[2], Martin Nieger[3], Stefan Bräse[4]*, Bahaa G. M. Youssif[5]* and Hendawy Tawfik[6,7]

[1]Department of Chemistry, College of Sciences, Princess Nourah bint Abdulrahman University, Riyadh, Saudi Arabia, [2]Medicinal Chemistry Department, Faculty of Pharmacy, Deraya University, Minia, Egypt, [3]Department of Chemistry, University of Helsinki, Helsinki, Finland, [4]Institute of Biological and Chemical Systems, IBCS-FMS, Karlsruhe Institute of Technology, Karlsruhe, Germany, [5]Department of Pharmaceutical Organic Chemistry, Faculty of Pharmacy, Assiut University, Assiut, Egypt, [6]Chemistry Department, Faculty of Science, Minia University, El Minia, Egypt, [7]Unit of Occupational of Safety and Health, Administration Office of Minia University, El-Minia, Egypt

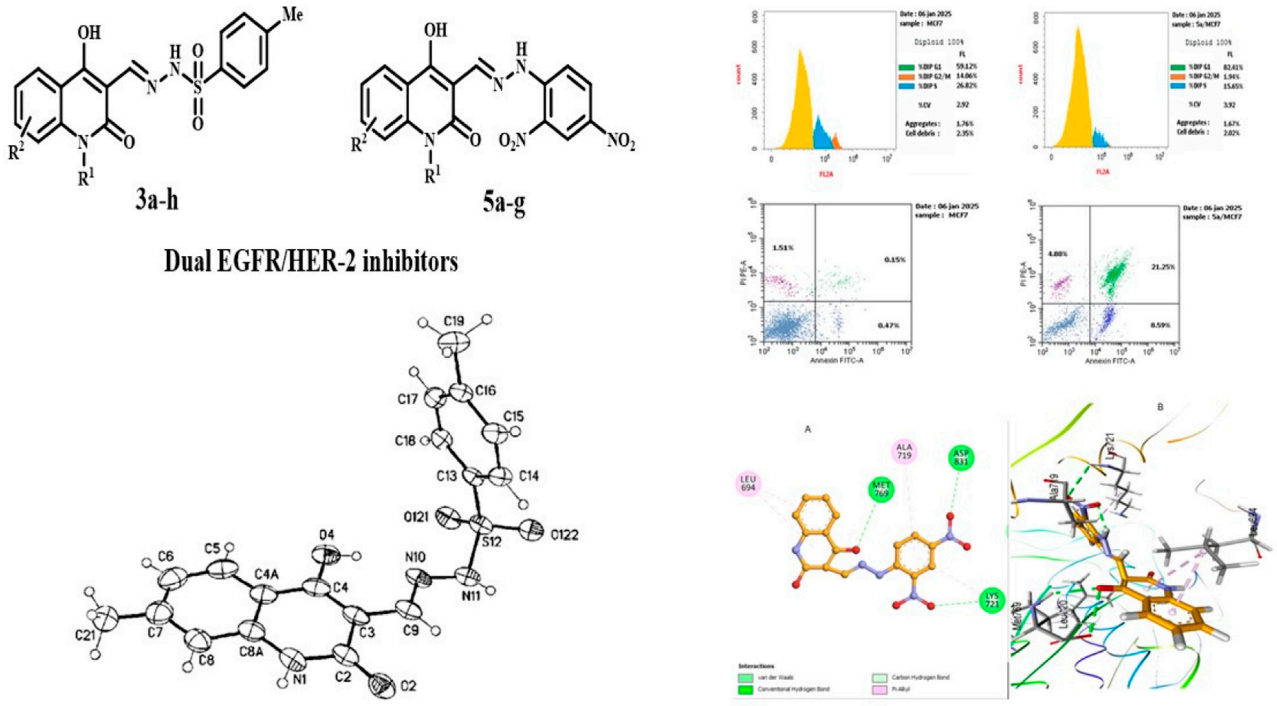
Introduction: A novel series of quinolin-2(1*H*)-one derivative was rationally designed, synthesized, and characterized as potential dual inhibitors of EGFR and HER-2.

Methods: Structural elucidation was achieved through IR, NMR, mass spectrometry, elemental analysis, and single-crystal X-ray crystallography. The synthesized compounds were screened for antiproliferative activity against four human cancer cell lines.

Results and Discussion: Compound **5a** exhibited the most potent antiproliferative profile, particularly against MCF-7 breast cancer cells (IC_{50} = 34 nM), outperforming erlotinib (IC_{50} = 40 nM). Kinase inhibition assays further confirmed dual activity of **5a**, with IC_{50} values of 87?nM and 33?nM against EGFR and HER-2, respectively. Compound **5a** induced apoptosis via activation of caspase-3, -8, and -9, along with upregulation of Bax, downregulation of Bcl-2, and increased cytochrome c release. Flow cytometry analysis demonstrated that **5a** caused significant G0/G1 phase arrest in MCF-7 cells, indicating a cytostatic mechanism of action. Computational studies provided structural validation of the observed biological activities. Molecular docking studies showed a strong binding affinity **5a** within the ATP-binding pockets of EGFR and HER-2, supported by key hydrogen bonding and hydrophobic interactions. These findings were further corroborated by 100 ns molecular dynamics simulations, which confirmed the structural stability and compactness of the **5a**-HER-2 complex, as evidenced by low RMSD, consistent RMSF, and favorable radius of gyration and potential energy profiles. Additionally, ADME predictions revealed that **5a** possesses favorable physicochemical and pharmacokinetic properties. Density Functional Theory (DFT) calculations provided insights into the electronic structure of **5a**, highlighting favorable HOMO–LUMO distribution and electrostatic potential surfaces that support its dual-binding behavior.

KEYWORDS

quinoline, kinases, X-ray, DFT, anticancer, EGFR, HER-2



GRAPHICAL ABSTRACT

A series of new methylbenzene sulfonohydrazide and (2,4-dinitrophenyl)hydrazono based quinolin-2(1*H*)-one derivatives was designed and synthesised. The Structures of new compounds were validated by IR, NMR, elemental analysis and X-ray crystallography. The new compounds were evaluated as antiproliferative agent targeting EGFR and HER-2.

Highlights

- A series of new Quinoline-based derivatives was designed and synthesised.
- The Structures of new compounds were validated by IR, NMR, elemental analysis and X-ray crystallography.
- The new compounds were evaluated as antiproliferative agent targeting EGFR, and HER-2.
- Antiproliferative activities were evaluated against four human cancer cell lines.

1 Introduction

The initial development and progression of cancer include several receptors and signaling pathways, demonstrating that multitargeting agents are more favorable than individual therapies (Al-Wahaibi et al., 2023a; Al-Wahaibi et al., 2024a). Multitargeting anticancer drugs aim to engage various biological receptors, anticipating synergistic effects and reduced toxicity compared to conventional therapy (Al-Wahaibi et al., 2023b). The two primary methods for identifying multitargeting drugs are screening techniques and knowledge-based strategies, wherein a rational design is established based on some pharmacophores that are retained while introducing another to produce hybrid compounds (Mahmo et al., 2024; Ravikumar et al., 2025).

HER-2 belongs to the EGFR family of tyrosine kinases, a broad category of proteins involved in various processes related to cell growth, proliferation, and differentiation (Hao et al., 2024). HER-2 plays an important role in a variety of cell signaling pathways. Gene amplification and transcriptional dysregulation cause HER-2 overexpression in breast cancer (BC), resulting in 25–50 copies of the gene. This causes a 40- to 100-fold increase in HER-2 expression, resulting in the development of up to 2 million HER-2 receptors on the cell surface (Gutierrez and Schiff, 2011). Additionally, HER-2-positive breast cancer exhibits a propensity for metastasis, particularly to the brain (Zimmer et al., 2022).

In addition to HER-2, there are three forms of EGFRs: EGFR, HER-3, and HER-4. Several investigations indicate that EGFR and HER-2 experience coamplification in numerous cancer types, including those of the breast, ovaries, prostate, colon, and other tissues (Alkahtani et al., 2020; Luhtala, 2019; Maennling et al., 2019). Overexpression of the HER-2 receptor in breast cancer is often associated with improper diagnosis and treatment resistance. Co-overexpression of EGFRs contributes to suboptimal diagnosis and treatment resistance in BC. According to the reports, simply suppressing HER-2 is insufficient for treating HER-2+ breast cancer. The complementary functions and interrelationships among HER-2 family members justify simultaneously targeting HER-2 and EGFR (Ghorab et al., 2018; Soliman et al., 2019).

Lapatinib (Compound **I**, Figure 1) is an FDA-approved dual inhibitor of HER-2 and EGFR for HER2-positive breast cancer, granted approval in 2007. However, multiple cases of lapatinib-resistant breast cancer have emerged recently (Pernas and Tolaney, 2019; Tsang et al., 2011). Neratinib (Compound **II**, Figure 1) is a multi-targeting inhibitor of the EGFR family, which received FDA

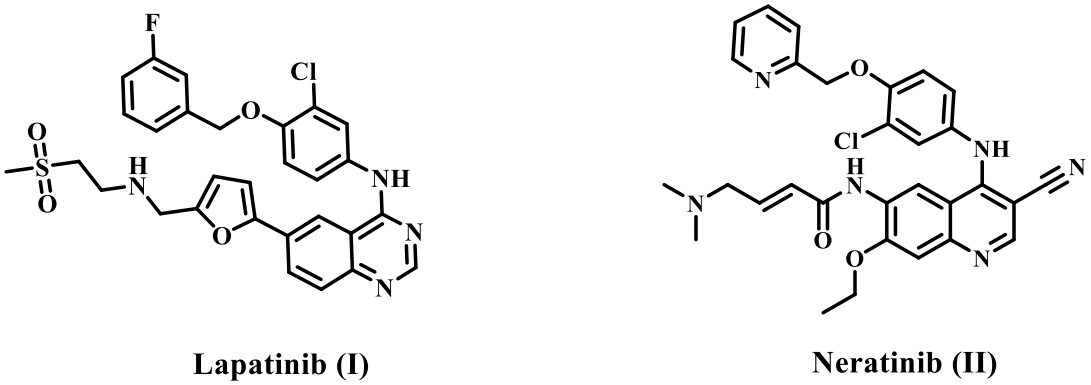


FIGURE 1
Structures of dual EGFR/HER-2 inhibitors lapatinib and neratinib.

approval in 2017 for HER-2-positive breast cancer (Abourehab et al., 2021; Wu et al., 2023). Phase III study data indicate that neratinib presents multiple adverse effects, such as diarrhea, gastrointestinal tract toxicity, and other side effects, mostly linked to heightened cytochrome P4503A4 activity during metabolism (Harding et al., 2023; Piha-Paul et al., 2023).

Our recent work (Voigtlaender et al., 2018) describes the design, synthesis, and antiproliferative efficacy of novel quinoline-based compounds functioning as dual EGFR/HER-2 inhibitors. Compound **III** (Figure 2B) was recognized as the most effective dual inhibitor of EGFR and HER-2, with IC_{50} values of 71 and 31 nM, respectively. Compound **III** had more potency than erlotinib as an EGFR inhibitor, displaying equivalent efficacy to Lapatinib as a HER-2 inhibitor. Compound **III** demonstrated significant antitumor activity against a panel of cancer cell lines, with a GI_{50} value of 25 nM, compared to erlotinib's GI_{50} of 33 nM. Compound **III** was evaluated on four cancer cell lines, with the breast (MCF-7) cancer cell line being the most sensitive, it demonstrated an IC_{50} value of 23 nM against the MCF-7 cell line, 1.8 times more potent than erlotinib (IC_{50} = 40 nM).

1.1 Rational design

Lapatinib **I** and Neratinib **II** (Figure 1) are strong inhibitors of both EGFR and HER-2. They obtained FDA approval as a monotherapy or in combination with other chemotherapeutics for the treatment of HER-2-positive metastatic breast cancer (Deeks, 2017; Voigtlaender et al., 2018). According to reports, lapatinib must be dissolved as a tosylate salt due to its limited water solubility. Consequently, clinical applications use lapatinib ditosylate. Simultaneously, the treatment of breast cancer has revealed the negative effects of lapatinib ditosylate, or Neratinib, which include gastrointestinal disorders, hepatic impairment, and arrhythmia (Deeks, 2017). In response to these limitations, researchers developed innovative EGFR/HER-2 dual inhibitors that fight cancers, have fewer side effects, and have enhanced water solubility.

Weissner et al. reported that the nitrogen atom at position three of the quinazoline ring could be replaced by a C-X, where X represents an electron-drawing group (Wissner et al., 2000). Accordingly, this paper describes the design, synthesis, and biological evaluation of new EGFR and HER-2 **3a-h** and **5a-g** dual inhibitors (Figure 2C). We chose lapatinib (quinazoline-based drug) and neratinib (quinoline-based drug) as the lead molecules for these inhibitors. The proposal calls for a quinoline core scaffold with an Azomethine (Schiff base) group at position 3, and a hydrophobic tail containing a benzene ring (Figure 2C), which shows that the hydrophobic tail may contain a *p*-toluene sulphonyl moiety (**3a-h**) or a dinitrobenzene ring (**5a-g**).

2 Results and discussion

2.1 Chemistry

The present study focuses on the synthesis of a new series of (*E*)-*N*'-((4-hydroxy-7-2-oxo-1,2-dihydroquinolin-3-yl)methylene) benzenesulfonohydrazides **3a-h** and (*E*)-3-((2-(2,4-dinitrophenyl) hydrazono)methyl)-4-hydroxyquinolin-2(1*H*)-ones **5a-g** which were obtained in 79%–92% and 76%–90% yields, respectively. The reaction occurs through a straightforward condensation between quinoline-3-carbaldehydes **1a-h** and 4-methylbenzene sulfonohydrazide **2**, along with (2,4-dinitrophenyl)hydrazine **4**, conducted in absolute ethanol and few drops of glacial acetic acid, as depicted in Scheme 1.

The structures of the new compounds were elucidated using various spectroscopic techniques, such as IR, NMR spectroscopy, elemental analysis, and mass spectrometry. At the same time, geometrical configuration is validated using X-ray crystallographic studies. Compound **3a**, as a representative example, exhibit a molecular formula $C_{18}H_{17}N_3O_4S$, with a molecular weight *m/z* = 371. This result were confirmed by elemental analysis and mass spectrometry. On the other hand, to complete the proof of our results, the ^{1}H NMR spectrum of compound **3a** revealed a three broad singlet signals at a downfield shift of δ_H = 12.90, 11.71, and 8.36 ppm, attributed to the quinolone-OH proton (Al-Wahaibi et al., 2024b), the hydrazonyl-NH proton (Al-Wahaibi et al., 2023c), and CH = N-proton (Al-Wahaibi et al., 2024b), respectively. Additionally,

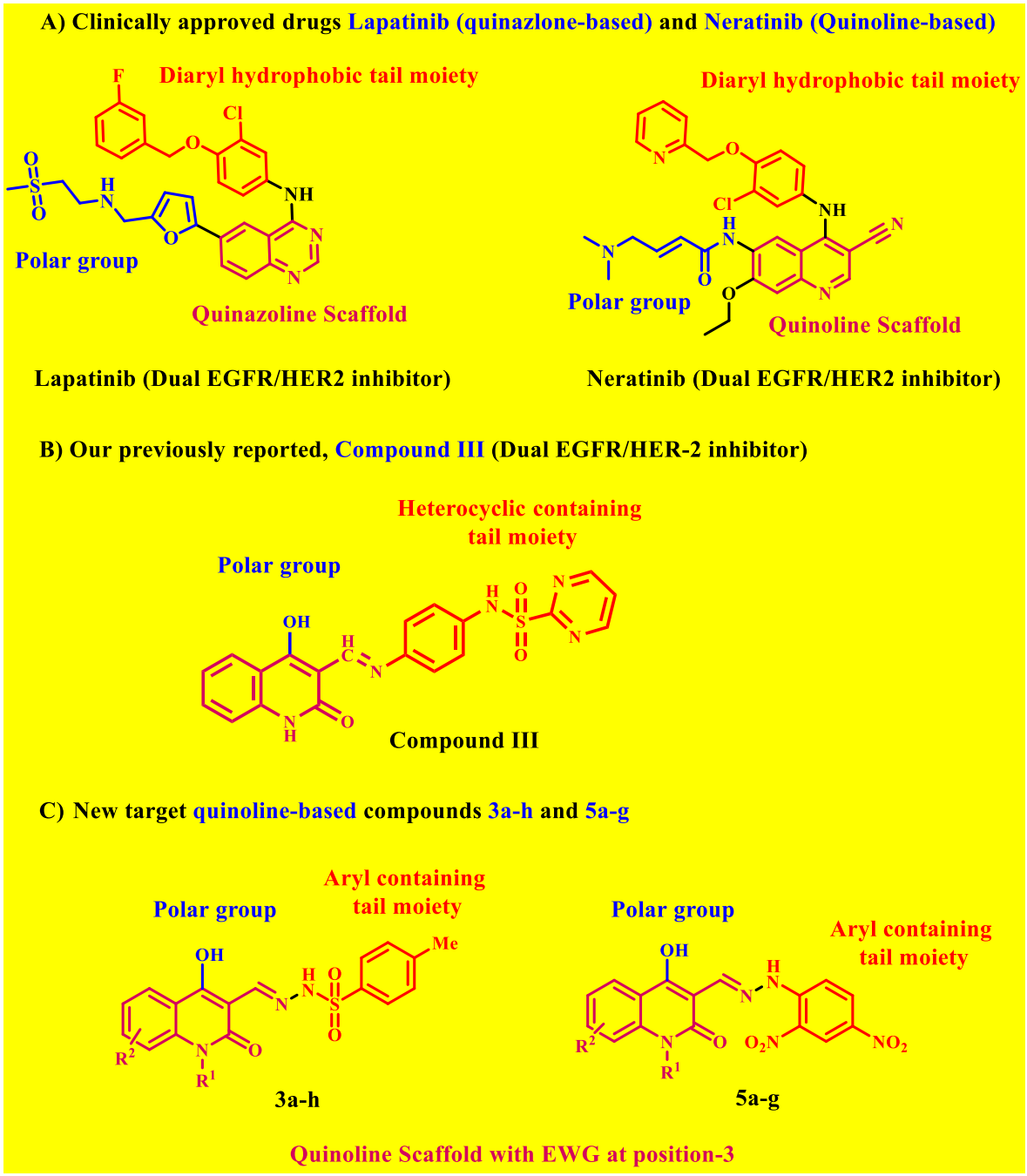
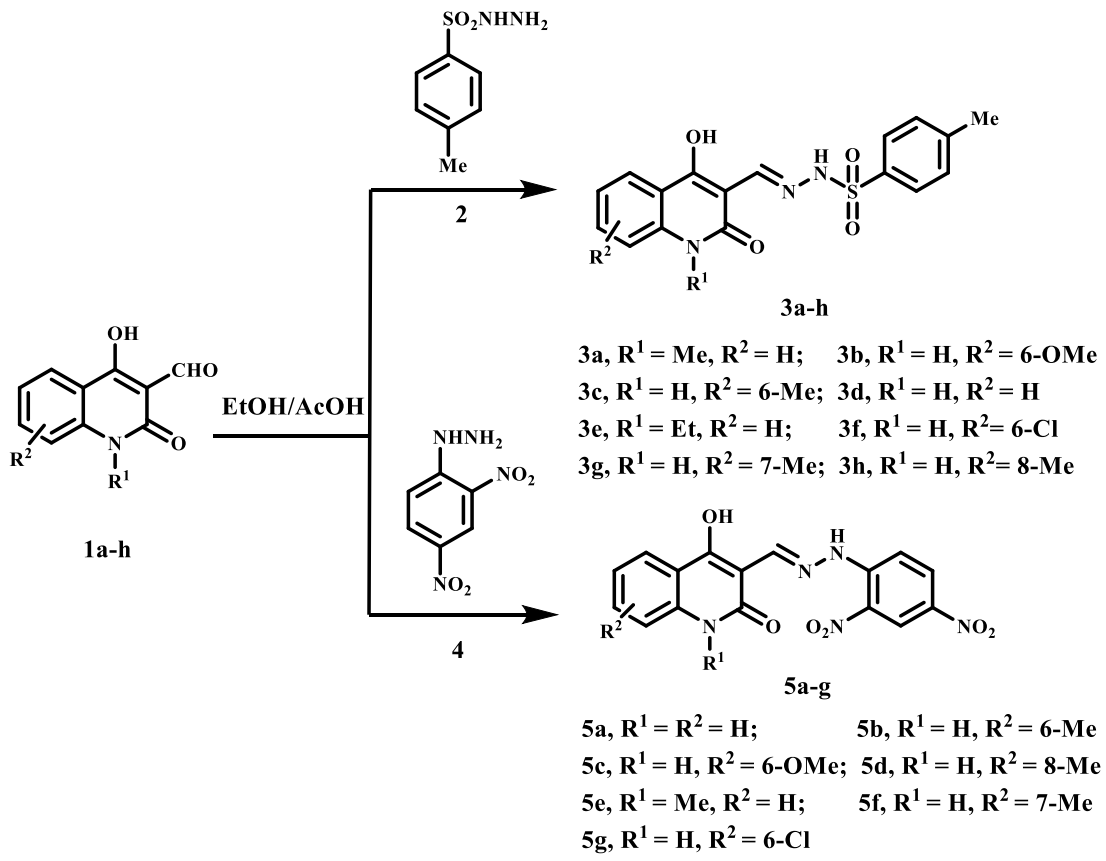


FIGURE 2
Rational design of **(A)** Lapatinib and Neratinib; **(B)** previously reported compound **III**; **(C)** New target compounds **3a-h** and **5a-g**.

the tosyl-ring protons exhibit two doublet signals attributed to the 1,4-disubstituted benzene ring system; one signal is observed at δ_H = 7.45–7.47 ppm (d, J = 8.0 Hz, 2H), while the other doublet is noted at δ_H = 7.73–7.75 ppm (d, J = 8.0 Hz, 2H). The four protons of the quinolone ring appear within the range of δ_H = 7.26–7.76 ppm. Also, two singlet signals exhibiting upfield shifts were found at δ_H = 2.36 and 3.52 ppm, which were assigned as the methyl group of the tosyl ring and the *N*-methyl groups, respectively.

The ^{13}C NMR spectrum of **3a** exhibited two signals resonating upfield at δ_C = 21.05 and 28.96 ppm, attributed to the methyl groups of the *p*-tosyl moiety and the N-methyl, respectively. Additionally, two downfield shift values with δ_C = 164.47 and 160.60 ppm are designated as amide-CO and C-4 linked to the hydroxyl group. Additionally, the CH = N was detected resonating at δ_C = 149.69 ppm. The aromatic-CH resonated at δ_C = 122.15, 124.02, 127.18, and 130.10 ppm. The quaternary carbons resonate at 115.10, 133.16, 134.93, 140.06, and 144.27 ppm.

Additionally, the X-ray study dispelled any uncertainties regarding the validity of our findings. The geometric configuration of the produced compounds was validated using



SCHEME 1
Synthesis of hydrazone derivatives **3a-h** and **5a-g**.

X-ray crystallographic analysis of compound **3g**, which displayed the predominant *E*-geometry as evidenced by the crystal molecular structure. The X-ray crystallographic analysis reveals that compound **3g** exists as two positional isomers: (*E*)-*N*'-((4-hydroxy-7-methyl-2-oxo-1,2-dihydroquinolin-3-yl)methylene)-4-methylbenzenesulfono-hydrazide (**3g**) and (*E*)-*N*'-((4-hydroxy-5-methyl-2-oxo-1,2-dihydroquinolin-3-yl)methylene)-4-methylbenzenesulfonohydrazide (**3g′**), as illustrated in Figures 3, 4, respectively.

Conversely, the condensation reactions of quinoline-3-carbaldehydes **1a-h** with (2,4-dinitrophenyl)hydrazine (**4**) result in the synthesis of a novel series of (*E*)-3-((2-(2,4-dinitrophenyl) hydrazono)-methyl)-4-hydroxyquinolin-2(1*H*)-ones **5a-g**, which were obtained in high to exceptional yields. We choose compound **5a** as an example which was assigned as (*E*)-3-((2-(2,4-dinitro-phenyl)hydrazono)methyl)-4-hydroxyquinolin-2(1*H*)-one. The structure was assigned based on spectral data, elemental analysis as well as mass spectrometry. The elemental analysis shows that this compound has a molecular formula $C_{16}H_{11}N_5$ and its molecular formula completed by its mass spectrometry which give m/z = 369 to give its actual molecular formula as $C_{16}H_{11}N_5O_6$. Also, the mass spectrometry fragmentation for the obtained product was studied under electron ionization. The following common features of the fragmentation patterns lend support to the assigned structures: Loss $2NO_2$ groups giving rise to ion m/z = 278 (M^+ - 92), m/z = 208 (M^+ - 4-hydroxy-2-quinolinone), m/z = 202 (M^+ - dinitrobenzene), and m/z = 168 (dinitrobenzene) (Figure 5). Compound **5a** was further confirmed from the ^{1}H NMR spectrum which clearly shows the presence of four broad singlet signals at δ_H = 8.35, 11.18, 11.33 and 12.77 ppm., with the ratio (1:2:1) which were assigned as CH = N, quinolinon-NH, hydrazono-NH and hydroxyl group, respectively. Other two doublet signals with the ratio (2:2) at δ_H = 7.18–7.19 and 7.89–7.91 ppm, which were assigned as quinolinon-2H and dinitrobenzene-2H, respectively. In addition to other protons which appeared as multiplet at δ_H = 7.20–7.77 (m, 3H). Furthermore, the ^{13}C NMR spectrum for compound **5a** exhibit common signals at δ_C = 101.10, 140.06, 144.28, 149.69, 161.10, and 166.43 ppm., which were assigned as (C-3), (Ar-C), (CH = N), (C-4) and quinolinone-C2, respectively.

2.2 Biology

2.2.1 Cell viability assay

The MCF-10A normal cell line from the human mammary gland was used to study the impact of new targets **3a-h** and **5a-g** on cellular survival. The MTT assay was employed to determine the viability of **3a-h** and **5a-g** cells after 4 days of incubation with MCF-10A cells (El-Sherief et al., 2019; Ramadan et al., 2020). Table 1 shows that none of the tested compounds caused cell death, with over 86% of cells surviving at a 50 μM concentration.

10.3389/fchem.2025.1638489

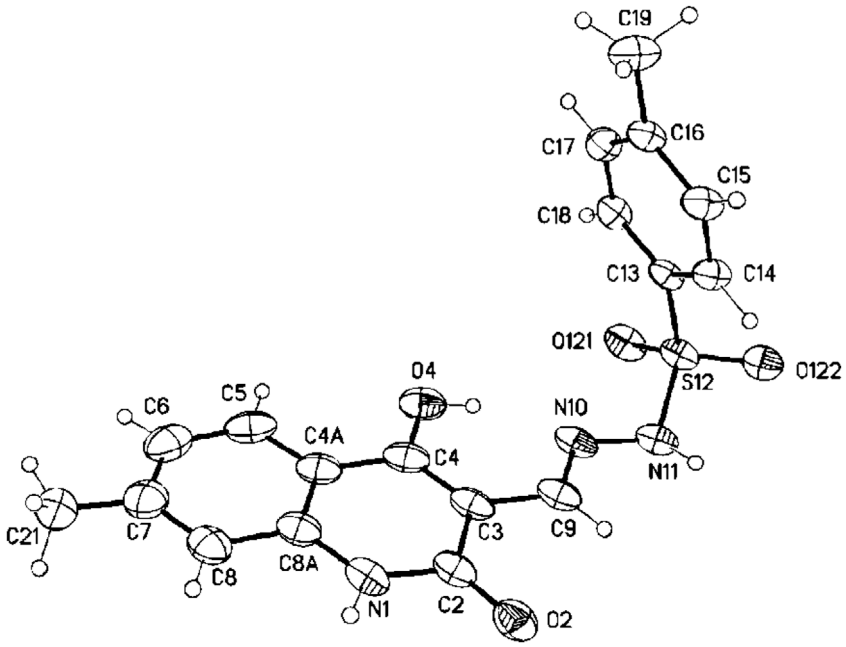


FIGURE 3
Molecular structure of (*E*)-*N*′-((4-hydroxy-7-methyl-2-oxo-1,2-dihydro-quinolin-3-yl)methylene)-4-methylbenzenesulfonohydrazide **3g** (approx. 30% displacement parameters are drawn at 30% probability level).

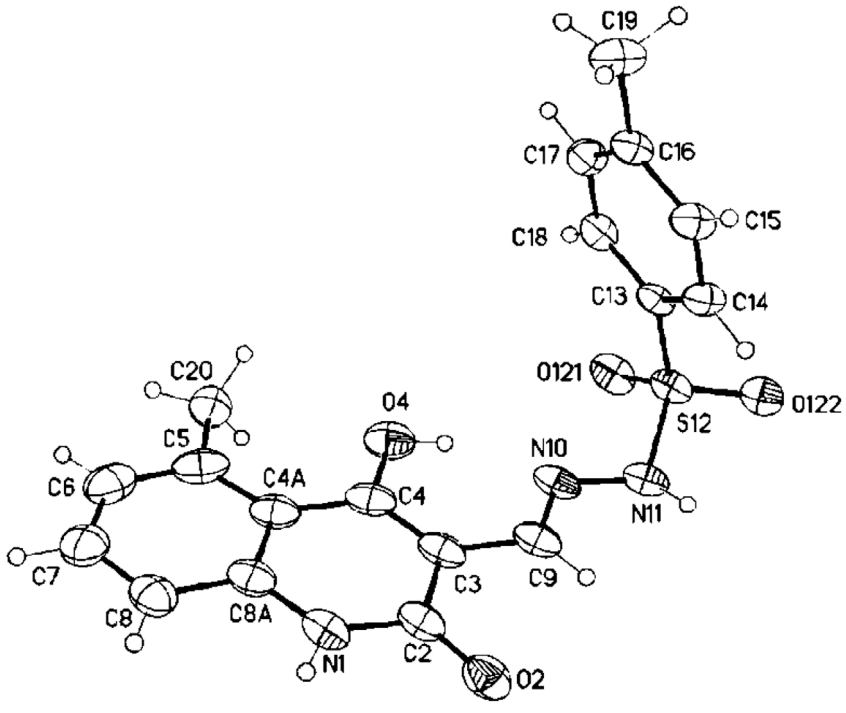


FIGURE 4
(*E*)-*N*′-((4-hydroxy-5-methyl-2-oxo-1,2-dihydroquinolin-3-yl)methylene)-4-methylbenzenesulfonohydrazide **3g`** (approx. 70%, displacement parameters are drawn at 30% probability level).

10.3389/fchem.2025.1638489

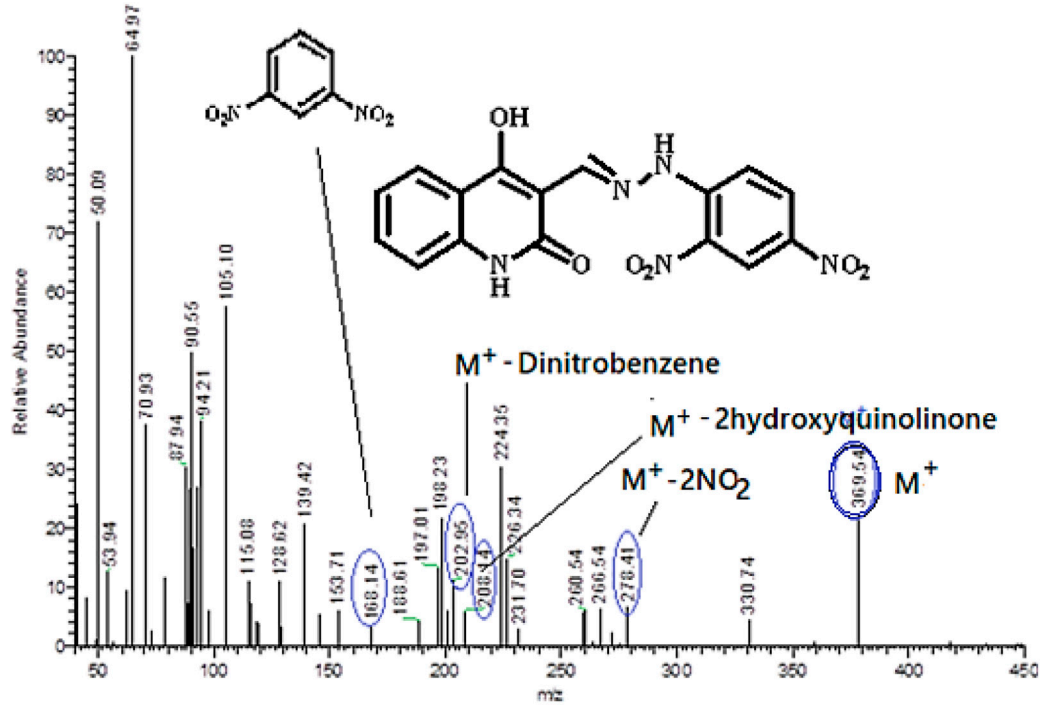


FIGURE 5
Mass spectrometry and fragmentation patterns for compound (*E*)-3-((2-(2,4-dinitrophenyl)hydrazono)methyl)-4-hydroxyquinolin-2(1*H*)-one (**5a**).

TABLE 1 Cell Viability and IC_{50} values of compounds 3a-h and 5a-g.

Comp.	Cell viability %	Antiproliferative activity IC_{50} ± SEM (nM)				
		A-549	MCF-7	Panc-1	HT-29	Average (GI_{50})
3a	90	92 ± 9	89 ± 8	94 ± 9	94 ± 9	92
3b	92	56 ± 5	52 ± 5	56 ± 5	58 ± 5	56
3c	86	50 ± 5	48 ± 4	53 ± 5	52 ± 4	51
3d	91	40 ± 3	37 ± 3	43 ± 4	42 ± 4	41
3e	89	62 ± 6	61 ± 6	64 ± 6	64 ± 6	63
3f	90	46 ± 4	43 ± 4	46 ± 4	48 ± 4	46
3g	87	94 ± 9	90 ± 9	94 ± 9	96 ± 9	94
3h	90	>100	>100	>100	>100	>100
5a	88	36 ± 3	34 ± 3	38 ± 3	38 ± 3	37
5b	90	52 ± 5	50 ± 5	54 ± 5	54 ± 5	53
5c	89	65 ± 6	62 ± 6	69 ± 6	68 ± 6	66
5d	92	71 ± 7	67 ± 6	74 ± 7	74 ± 7	72
5e	87	76 ± 7	74 ± 7	76 ± 7	78 ± 7	76
5f	90	85 ± 8	83 ± 8	86 ± 8	86 ± 8	85
5g	91	81 ± 8	78 ± 7	82 ± 8	82 ± 8	81
Erlotinib	ND	30 ± 3	40 ± 3	30 ± 3	30 ± 3	33

2.2.2 Antiproliferative assay

The MTT assay (Al-Wahaibi et al., 2022; Mahmoud et al., 2023) was employed to assess the antiproliferative effects of compounds **3a-h** and **5a-g** on four human cancer cell lines: colon (HT-29) cancer, pancreatic (Panc-1) cancer, lung (A-549) cancer, and breast (MCF-7) cancer cell lines. Erlotinib was applied as a reference. Table 1 presents the median inhibitory concentration (IC_{50}) and average IC_{50} (GI_{50}) values for each compound evaluated on the four cancer cell lines.

Compounds **3a-h** and **5a-g** had significant antiproliferative activity, with GI_{50} values ranging from 37 to 100 nM, compared to the reference erlotinib (GI_{50} = 33 nM). In all cases, the compounds under investigation have lower potency than erlotinib. Moreover, all examined compounds have a higher affinity for breast cancer (MCF-7) cell line than the other cell lines studied. Compounds **3c**, **3d**, **3f**, **5a,** and **5b** had the highest antiproliferative activity, with GI_{50} values between 37 and 53 nM. Derivatives **3d** and **5a** are more effective than erlotinib against the MCF-7 breast cancer cell line. Their IC_{50} values were 37 nM and 34 nM, respectively, while erlotinib exhibited an IC_{50} value of 40 nM.

Compound **5a** (R^1 = R^2 = H, Scaffold B) surpassed all other tested compounds. It exhibited a GI_{50} of 37 nM, rendering it 1.2 times less effective than erlotinib (GI_{50} = 33 nM) against the four cancer cell lines tested. Compound **5a** exhibited substantial antiproliferative activity against the MCF-7 breast cancer cell line, with an IC_{50} value of 34 nM, 1.2 times more effective than erlotinib's IC_{50} value of 40 nM. Furthermore, compound **5a** has marginally reduced potency compared to erlotinib against the other three cell lines, as seen in Table 1.

The substitution pattern of the quinoline moiety markedly influences the antiproliferative efficacy of compounds **3a-h** and **5a-g**. For instance, compound **5e** (R^1 = Me, R^2 = H, Scaffold B), an *N*-methyl derivative, had lower efficacy as an antiproliferative agent than **5a** (R^1 = R^2 = H, Scaffold B). Compound **5e** exhibited a GI_{50} of 76 nM, which is twice as low as that of **5a**, indicating that the presence of a free nitrogen atom at position 1 (N-1) of the quinoline moiety is more supportive of antiproliferative activity than the *N*-methyl group.

A different example is the 6-methyl derivative, compound **5b** (R^1 = H, R^2 = 6-Me, Scaffold B), the 6-methoxy derivative, **5c** (R^1 = H, R^2 = 6-OMe, Scaffold B), and the 6-chloro derivative, **5g** (R^1 = H, R^2 = 6-Cl, Scaffold B), all of which were found to be less efficient than the unsubstituted derivative, **5a** (R^1 = R^2 = H, Scaffold B). Compounds **5b**, **5c**, and **5g** exhibit IC_{50} values of 53, 66, and 81 nM, respectively, signifying their reduced potency compared to **5a** (GI_{50} = 37 nM). These findings indicate that derivatives possessing an unsubstituted quinoline moiety at the six position exhibit greater efficiency than those substituted with either electron-donating methyl and methoxy groups or an electron-withdrawing chlorine atom. Also, the 8-methyl derivative, compound **5d** (R^1 = H, R^2 = 8-Me, Scaffold B), and the 7-methyl derivative, **5f** (R^1 = H, R^2 = 7-Me, Scaffold B), were both shown to be less efficient than the unsubstituted derivative, **5a**. To establish an optimal structural-activity relationship (SAR), derivatives of the quinoline moiety's phenyl ring must be modified with an electron-withdrawing group, such as a halogen atom or nitro group, at various positions of the quinoline structure. These specific modifications are now under investigation in our laboratory.

Compound **3d** (R^1 = R^2 = H, Scaffold A) exhibited the second greatest activity, with a GI_{50} value of 41 nM, 1.3-fold less active than erlotinib (GI_{50} = 33 nM). However, **3d** had superior activity to erlotinib against the MCF-7 breast cancer cell line, as indicated in Table 1. Replacing the C6-H of the quinoline moiety in compound **3d** with C6-methoxy in compound **3b** (R^1 = H, R^2 = 6-OMe, Scaffold A), a methyl group in compound **3c** (R^1 = H, R^2 = 6-Me, Scaffold A), or a chlorine atom in compound **3f** (R^1 = H, R^2 = 6-Cl, Scaffold A) led to a marked reduction in antiproliferative activity. The GI_{50} values for **3b**, **3c**, and **3f** were 56, 51, and 46 nM, respectively, demonstrating a potency reduction of 1.4-, 1.3-, and 2.5-fold compared to **3d** (GI_{50} = 41 nM). This corroborates the idea that the quinoline molecule's unsubstituted phenyl ring exhibited greater activity tolerance.

It is noteworthy that the *N*-methyl derivative, **3a** (R^1 = Me, R^2 = H, Scaffold A), the C7-Me derivative, **3g** (R^1 = H, R^2 = 7-Me, Scaffold A), and the C8-Me derivative, **3h** (R^1 = H, R^2 = 8-Me, Scaffold A), demonstrate the lowest antiproliferative effect against all tested cell lines. The GI_{50} values for **3a**, **3g**, and **3h** were 92, 94, and >100 nM, respectively, indicating a potency decrease of at least 2.3-fold relative to **3d** (GI_{50} = 41 nM).

2.2.3 EGFR inhibitory assay

The most effective antiproliferative derivatives, **3c**, **3d**, **3f**, **5a,** and **5b,** were evaluated for their ability to inhibit EGFR using the EGFR-TK test (Abou-Zied et al., 2023). The results are presented in Table 2. Erlotinib operated as the reference compound.

The assay results align with those of the antiproliferative assay, indicating that compounds **5a** (R^1 = R^2 = H, Scaffold B) and **3d** (R^1 = R^2 = H, Scaffold A), the most potent antiproliferative agents, were the most efficient derivatives of EGFR inhibitors, exhibiting IC_{50} values of 87 ± 5 and 91 ± 6 nM, respectively, in comparison to erlotinib's IC_{50} value of 80 ± 5 nM. Results revealed that compounds **3d** and **5a** were less potent as EGFR inhibitors than the reference drug erlotinib. Compounds **3c** and **3f** inhibited EGFR significantly, with IC_{50} values of 95 and 99 nM, respectively, and were 1.2-fold less effective than the reference erlotinib. Ultimately, compound **5b** exhibited the lowest potency as an EGFR inhibitor, with an IC_{50} value of 106 ± 7 nM.

These data suggest that compounds **3d** and **5a** are effective antiproliferative candidates that could operate as EGFR inhibitors.

2.2.4 HER-2 inhibitory assay

Compounds **3c**, **3d**, **3f**, **5a** and **5b** were evaluated for their capacity to inhibit HER-2 by a kinase assay (Al-Wahaibi et al., 2025). The findings are displayed in Table 2. Lapatinib functioned as the reference drug. The findings indicated that the investigated compounds markedly suppressed HER-2, exhibiting IC_{50} values between 33 and 56 nM, in contrast to lapatinib's IC_{50} of 26 nM. The evaluated compounds exhibited lower potency in each case than the lapatinib reference medication. Compound **5a** was the most efficient HER-2 inhibitor, with an IC_{50} value of 33 nM, 1.3 times less potent than lapatinib. The data indicate that compound **5a** is a promising antiproliferative candidate with dual inhibitory activity against EGFR and HER-2, necessitating structural modifications for lead optimization.

TABLE 2 IC_{50} values of compounds 3c, 3d, 3f, 5a and 5b against EGFR and HER-2.

Compound	EGFR inhibition IC_{50} ± SEM (nM)	HER-2 inhibition IC_{50} ± SEM (nM)
3c	99 ± 6	49 ± 3
3d	91 ± 6	38 ± 2
3f	95 ± 6	44 ± 3
5a	87 ± 5	33 ± 2
5b	106 ± 7	56 ± 4
Erlotinib	80 ± 5	--
Lapatinib	--	26 ± 1

TABLE 3 Apoptotic markers assays of compounds 3d and 5a.

Compd. No.	Caspase-3		Caspase-8		Caspase-9		Cytochrome C	
	Conc (pg/mL)	Fold change	Conc (ng/mL)	Fold change	Conc (ng/mL)	Fold change	Conc (ng/mL)	Fold change
3d	515 ± 5	8.0	2.10 ± 0.20	23	21 ± 3	21	0.65	13
5a	570 ± 5	9.0	2.65 ± 0.25	29	24 ± 1	24	0.85	17
Staurosporine	465 ± 4	7.0	1.85 ± 0.15	21	20 ± 1	20	0.50	10
Control	65	1.0	0.09	1	1	1	0.05	1

2.2.5 Apoptotic markers assay

Deficiencies in apoptosis within cancer cells significantly hinder the therapeutic effectiveness of anticancer drugs; therefore, developing of new therapies that target programmed cell death has become an essential objective for clinical use (Hisham et al., 2019; Bräse). Consequently, to reveal the pro-apoptotic potential of our target compounds, compounds **3d** and **5a** were evaluated for their capacity to initiate the apoptosis cascade.

2.2.5.1 Activation of caspases 3, 8, and 9

Activating caspases is crucial in initiating and concluding the apoptotic process (Wu et al., 2025). Caspase-3 is a crucial enzyme that cleaves several proteins within cells, resulting in apoptotic cell death (Kouwenhoven et al., 2025). The impact of compounds **3d** and **5a** on caspase-3 was assessed and matched with Staurosporine as a reference medication (Table 3.

The findings indicated that **5a** was the most potent derivative, exhibiting a significant overexpression of caspase-3 protein levels (570 ± 5 pg/mL) compared to the reference staurosporine (465 ± 4 pg/mL). Compound **3d** exhibited a 9-fold rise in active caspase-3 levels compared to control cells and induced caspase-3 levels surpassing those of staurosporine, the reference medication. Compound **3d** demonstrated an 8-fold increase in active caspase-3 levels (515 ± 5 pg/mL) compared to the control untreated cells, as shown in Table 3.

To elucidate the apoptotic mechanism of compounds **3d** and **5a**, whether *via* the intrinsic or extrinsic pathway, their impact on caspase-8 and caspase-9 was evaluated. The results indicated that compound **5a** elevates the levels of caspase-8 and caspase-9 by 29 and 18-fold, respectively, while compound **3d** increases the levels of caspase-8 and caspase-9 by 23 and 15-fold, respectively, in comparison to the control cells. This suggests activation of both intrinsic and extrinsic pathways, with a more pronounced effect on the extrinsic pathway, as evidenced by the elevated levels of caspase-8 (Table 3).

2.2.5.2 Cytochrome C assay

The level of Cytochrome C within the cell is crucial for activating caspases and initiating the intrinsic apoptosis pathway (Jan et al., 2025).

Compounds **3d** and **5a** were assessed for their activity against cytochrome C in the MCF-7 human breast cancer cell line, with results in Table 3. Compounds **3d** and **5a** induce a 13-fold and 17-fold increase in cytochrome C levels in MCF-7 human breast cancer cells compared to the control. The results above show that apoptosis may be linked to the overexpression of cytochrome C and the activation of intrinsic and extrinsic apoptotic pathways initiated by the compounds studied.

2.2.5.3 Bax and Bcl-2 levels assay

Compounds **3d** and **5a** were further investigated for their impact on Bax and Bcl-2 levels in the MCF-7 human breast cancer cell line, using staurosporine as a reference, as detailed in Table 4.

The results indicated that **3d** and **5a** significantly elevated Bax levels compared to staurosporine. Compound **5a** demonstrated an induction of Bax at 320 pg/mL, comparable to staurosporine at 290 pg/mL, and exhibited a 35-fold increase relative to untreated MCF-7 cancer cells, followed by compound **3d** at 310 pg/mL with a 34-fold rise. Ultimately, compound **5a** induced a reduction in the anti-apoptotic Bcl-2 protein level (0.70 ng/mL), preceded by compound **3d** (0.80 ng/mL) in the MCF-7 cell line, in comparison to staurosporine (1.00 ng/mL).

TABLE 4 Bax and Bcl-2 levels for 3d, 5a, and Staurosporine on human breast (MCF-7) cancer cell line.

Compd. No.	Bax		Bcl-2	
	Conc (pg/mL)	Fold change	Conc (ng/mL)	Fold reduction
3d	310 ± 2	34	0.80	6
5a	320 ± 2	35	0.70	7
Staurosporine	290 ± 2	32	1.00	5
Control	9.00	1	5.00	1

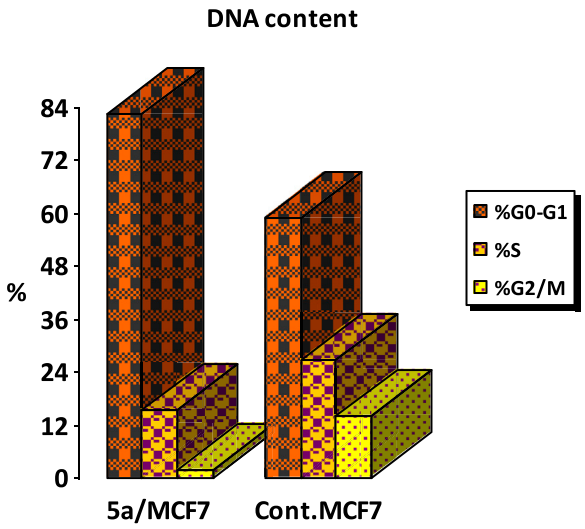


FIGURE 6
Cell cycle analysis of compound **5a** against the MCF-7 cancer cell line.

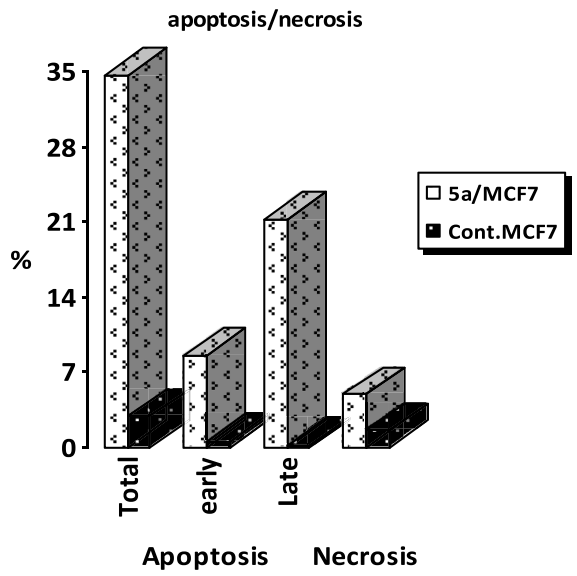


FIGURE 7
Percentage of apoptosis and necrosis of **5a** against the MCF-7 cancer cell line.

2.2.6 Flow cytometric cell cycle analysis

Cell cycle analysis has been done for the most potent compound **5a** against the MCF-7 human breast cancer cell line. The percentage of MCF-7 cells in the G0/G1 phase of the cell cycle in the control was 59.12%, which significantly increased to 81.42% following treatment with compound **5a**. In comparison, the percentage of cells in the S phase decreased slightly with compound **5a** (15.65%) compared to the control (26.82%) (Figure 6). The percentage of MCF-7 human breast cancer cells in the G2/M phase diminishes to 1.94% following treatment with compound **5a**. The data indicate that compound **5a** primarily induced cell cycle arrest in the G1 phase. Furthermore, it is evident that the examined compound is not cytotoxic; rather, it exhibits antiproliferative properties, inducing programmed cell death and cell cycle arrest (Figures 7, 8).

2.3 Docking study of EGFR and HER-2 enzymes

A comprehensive computational docking study was conducted to explore the binding interactions of compound **5a** with EGFR and HER-2 enzymes (Al-Wahaibi et al., 2025). The crystallographic structures of EGFR (PDB ID: 1M17) and HER-2 (PDB ID: 3PP0) were obtained and utilized as structural templates for the docking simulations, which were performed using the Discovery Studio software (Jejurikar and Rohane, 2021). Erlotinib and lapatinib were selected as reference ligands for EGFR and HER-2 (Al-Wahaibi et al., 2024b).

The docking simulations were performed using the OPLS-AA (Optimized Potentials for Liquid Simulations–All Atom) force field during the energy minimization process to ensure conformational stability of the ligand-protein complexes (R et al., 2022). This step is critical in enhancing the accuracy and reliability of computational predictions. Before the docking procedure, an extensive protein preparation protocol was followed, including appropriate protonation of the protein structures to improve their geometrical accuracy and optimize the docking results (Buccheri et al., 2025).

To assess the validity of the docking protocol, the co-crystallized ligand erlotinib was re-docked into the EGFR binding site (Fayed et al., 2023). This validation step yielded a binding energy (S-score) of −8.05 kcal/mol, with a root mean square deviation (RMSD) value of 0.91 Å, indicating a reliable docking method. The re-docking simulation confirmed a key hydrogen bond interaction between the pyrimidine nitrogen of erlotinib and the Met769 residue in the

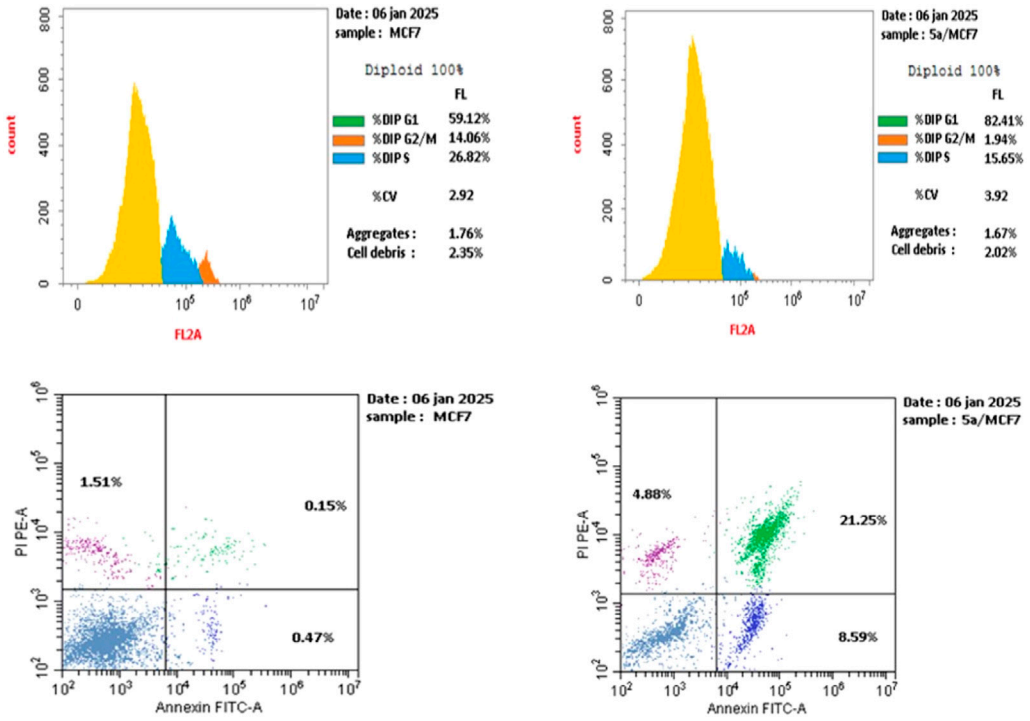


FIGURE 8
Cell cycle analysis and apoptosis induction of **5a** against the MCF-7 breast cancer cell line.

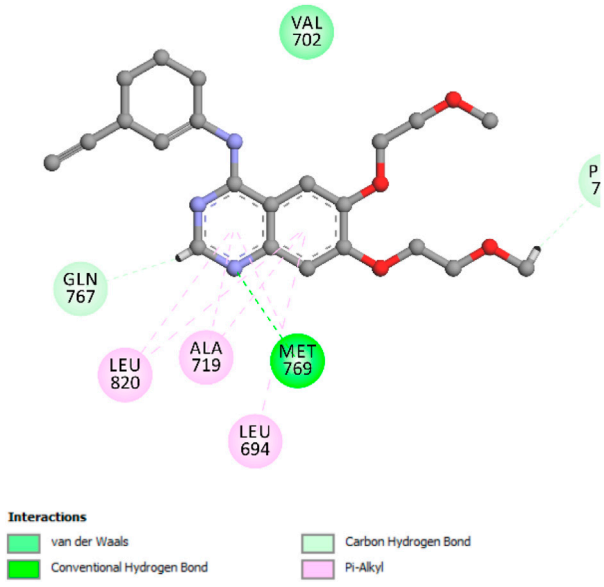


FIGURE 9
Two-dimensional docking model illustrating the binding orientation of erlotinib within the active site of EGFR.

EGFR active site, a crucial interaction that plays a significant role in stabilizing the ligand within the protein pocket (Figure 9).

The docking scores obtained for compound **5a** demonstrated a strong correlation with the *in vitro* inhibition activity of EGFR, thereby validating the predictive power of the docking methodology used in this study. This consistency between docking results and biological activity highlights the reliability of the docking protocol and its utility in identifying promising inhibitors for EGFR and HER-2 enzymes.

The docking analysis of compound **5a** within the ATP-binding site of EGFR revealed a highly favorable binding pose with a docking score of −7.33 kcal/mol, with a root mean square deviation (RMSD) value of 1.44 Å. The interaction profile shows that compound **5a** forms a pivotal hydrogen bond with the Met769 residue through its enol oxygen, anchoring the ligand within the active site (Figure 10). Additionally, two significant hydrogen bond interactions with the Asp831 and Lys721 residues further stabilize the compound. Notably, Pi-alkyl stacking interactions between the aromatic ring of quinolone and Leu694 strengthen the binding affinity by securing the ligand within the hydrophobic pocket (Figure 10).

Also, Pi-alkyl interaction with residue Ala719 further reinforces stability in the ATP-binding site. The 3D visualization depicts the precise orientation of 5a within the ATP-binding pocket, where the di-nitro phenyl core and hydrazone moiety are optimally aligned to maximize both hydrophobic and hydrogen-bonding interactions. The planar structure promotes effective alignment with the pocket, further enhancing binding efficacy (Figure 10).

To check the validity of the docking protocol for HER-2, the co-crystallized ligand was re-docked into the HER-2 binding site (Metibemu et al., 2021). This validation process yielded a binding energy (S-score) of −7.86 kcal/mol, with a root mean square deviation (RMSD) value of 1.24 Å, confirming the reliability of the docking procedure.

The re-docking simulation revealed a key hydrogen bond interaction between the pyrimidine nitrogen of the ligand and

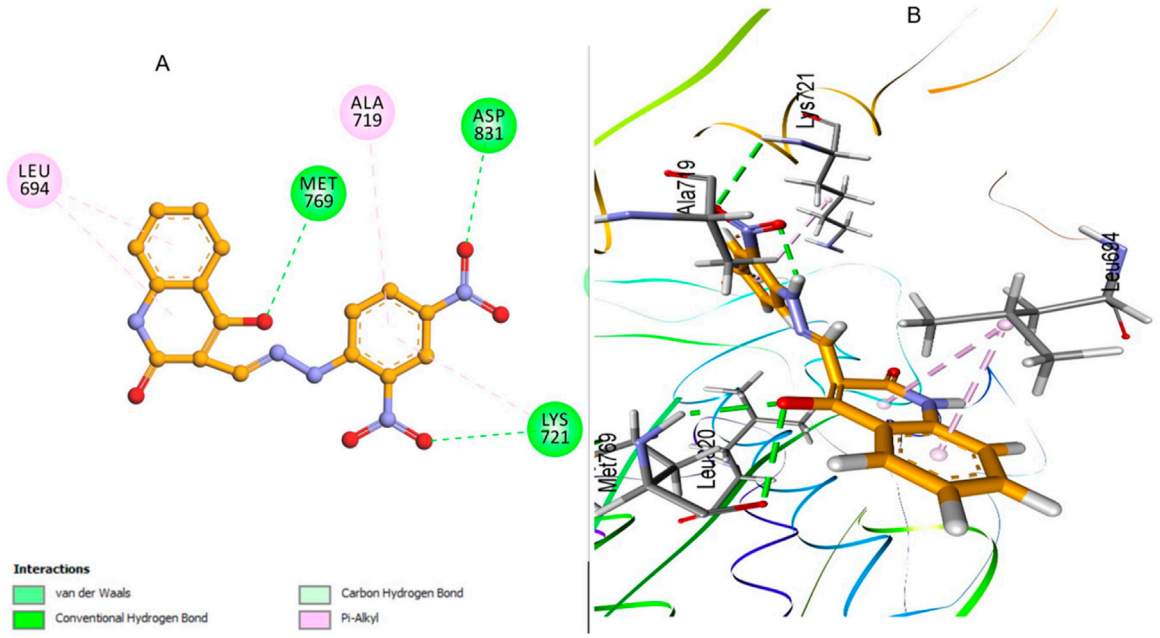


FIGURE 10
Two-dimensional **(A)** and three-dimensional **(B)** docking representations showing the binding interactions of compound 5a within the ATP-binding pocket of EGFR.

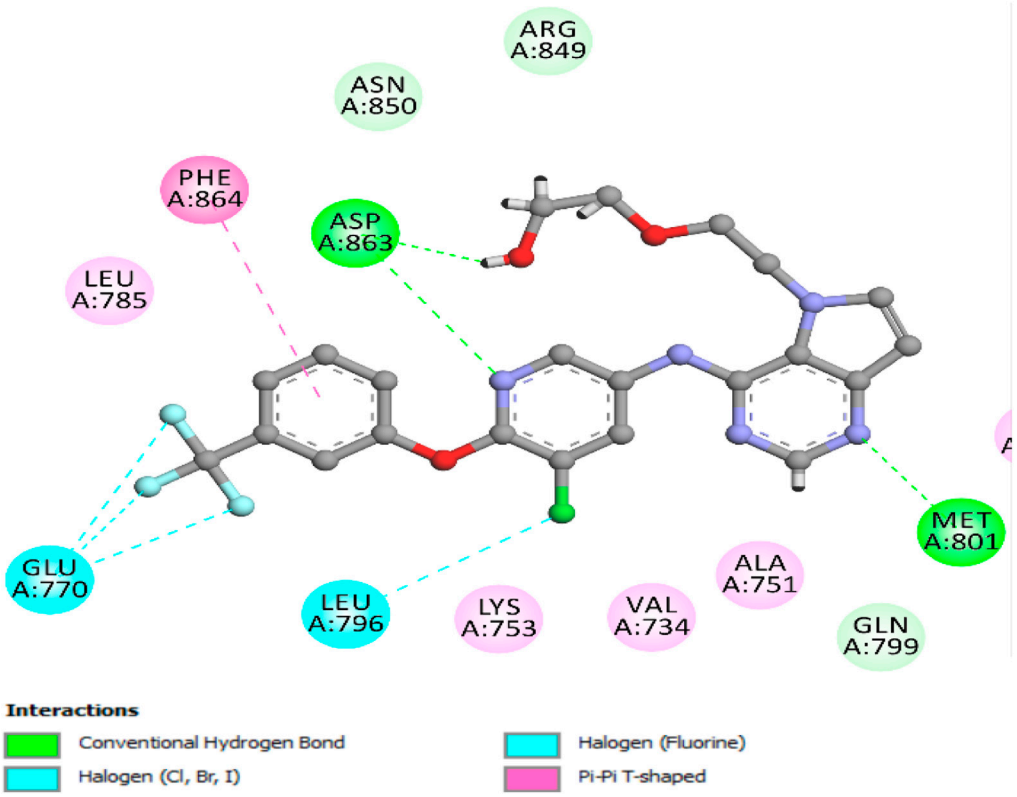


FIGURE 11
Two-dimensional docking model highlighting the binding interactions of the validated co-crystallized ligand within the HER-2 binding site.

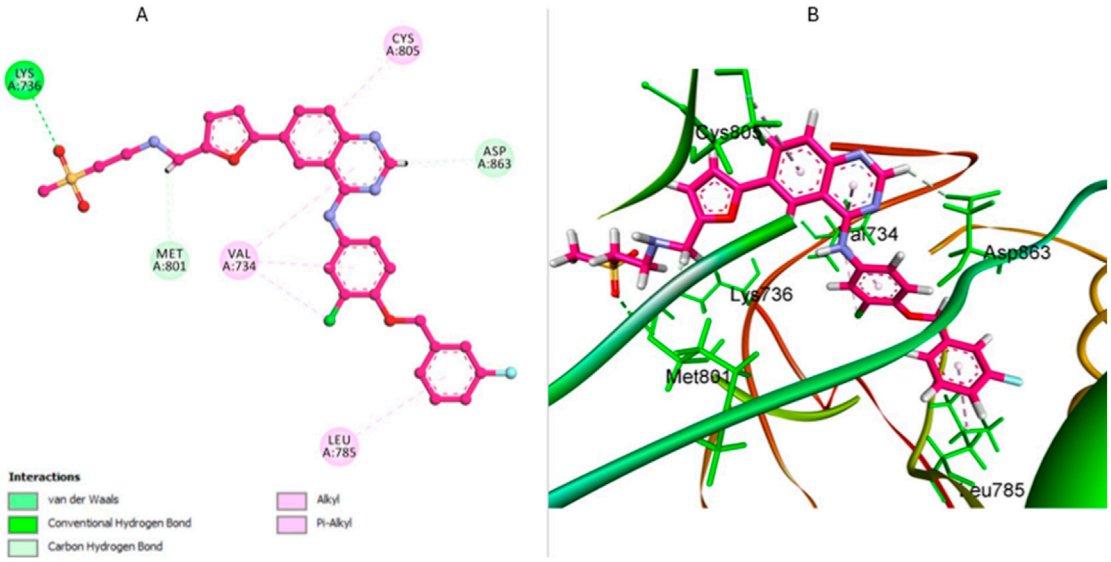


FIGURE 12
Docking representation of lapatinib within the HER-2 binding site; **(A)** 2D representation **(B)** 3D representation.

the Met801 residue, which plays a crucial role in stabilizing the ligand within the HER-2 active site (Figure 11). The re-docking simulation revealed crucial interactions within the HER-2 binding pocket, including a key hydrogen bond between the nitrogen of the pyridine ring of the ligand and the Asp863 residue, contributing significantly to ligand stabilization. The docking interactions highlighted additional hydrogen bonds with Met801 and pi-pi T-shaped interactions with Phe864. Notably, halogen interactions with Glu770 and Leu796 further reinforced the binding within the active site (Figure 11).

The docking analysis of lapatinib, a reference drug for HER-2 inhibition in our *in vitro* studies, provides valuable insights into its binding mode within the HER-2 active site. Lapatinib exhibits a favorable binding energy of −7.47 kcal/mol with an RMSD value of 1.45 Å, indicating a stable pose within the HER-2 binding pocket. The analysis reveals the formation of an essential hydrogen bond between the sulfone oxygen atoms of lapatinib and Lys753. Also, lapatinib can form other carbon-hydrogen bonds with Met801 residue and Asp863, significantly stabilizing the binding site's ligand (Figure 12). Also, lapatinib forms extensive hydrophobic interactions with key residue Leu785, contributing to a stable hydrophobic core. Pi-alkyl interactions with residue Val734 further enhance the binding stability. These pi-alkyl interactions establish a robust network, ensuring a tight fit of lapatinib within the HER-2 active site and improving its inhibitory potential against HER-2 (Figure 12).

The docking analysis of compound **5a** against HER-2 revealed a binding energy of −7.24 kcal/mol, indicating a strong affinity for the HER-2 active site with an RMSD value of 1.63 Å, confirming a stable pose within the HER-2 binding site—compound **5a** forms several key interactions within the binding pocket, contributing to its stability and binding efficacy.

The most notable interactions include two important hydrogen bonds that enhance the stabilization within the HER-2 binding site. The first hydrogen bond is observed between the nitro group and Met801, reinforcing its position and stabilizing the binding conformation. The second hydrogen bond is established between the nitrogen of the quinolone and Thr862, securing the ligand within the pocket (Figure 13). In addition to these hydrogen bonds, 5a engaged in significant hydrophobic interactions between the di-nitro phenyl ring of **5a** with Leu726, Leu852, and Val734, contributing further to the overall conformational stability of the ligand.

The quinolone ring of **5a** also exhibited extensive hydrophobic contacts with residues such as Met801 and Lys753, which enhanced the tight fit of the compound within the HER-2 active site. The combination of these interactions ensured that **5a** maintained a secure and stable orientation within the binding site. When compared to lapatinib, the reference drug used in HER-2 inhibition studies, compound **5a** displayed a comparable binding profile with key differences in interaction patterns. Lapatinib demonstrated a binding energy, slightly higher than that of **5a**, indicating a comparable binding affinity. Both compounds exhibit crucial interactions with residues such as, Met801, and Val734, contributing to the overall binding stability.

Overall, the comparison between **5a** and lapatinib suggests that **5a** has a binding mode that is distinct yet similarly effective to that of the reference drug. Both compounds demonstrate strong hydrophobic interactions and hydrogen bonding, ensuring stable binding within the HER-2 binding pocket. These findings highlight the potential of **5a** as a promising HER-2 inhibitor with binding characteristics comparable to the clinically used reference drug, lapatinib, suggesting its possible utility in targeted HER-2 therapies.

The docking results for compound **5a** align well with the *in vitro* inhibition data, where **5a** demonstrated an IC_{50} of 33 ± 2 nM against HER-2, indicating potent inhibitory activity. In comparison, lapatinib, the reference drug for HER-2 inhibition, showed an IC_{50} of 26 ± 1 nM, slightly more potent than **5a**. When comparing compound 5a and erlotinib, the docking and *in vitro* results differ in their selectivity profiles. Erlotinib displayed an IC_{50}

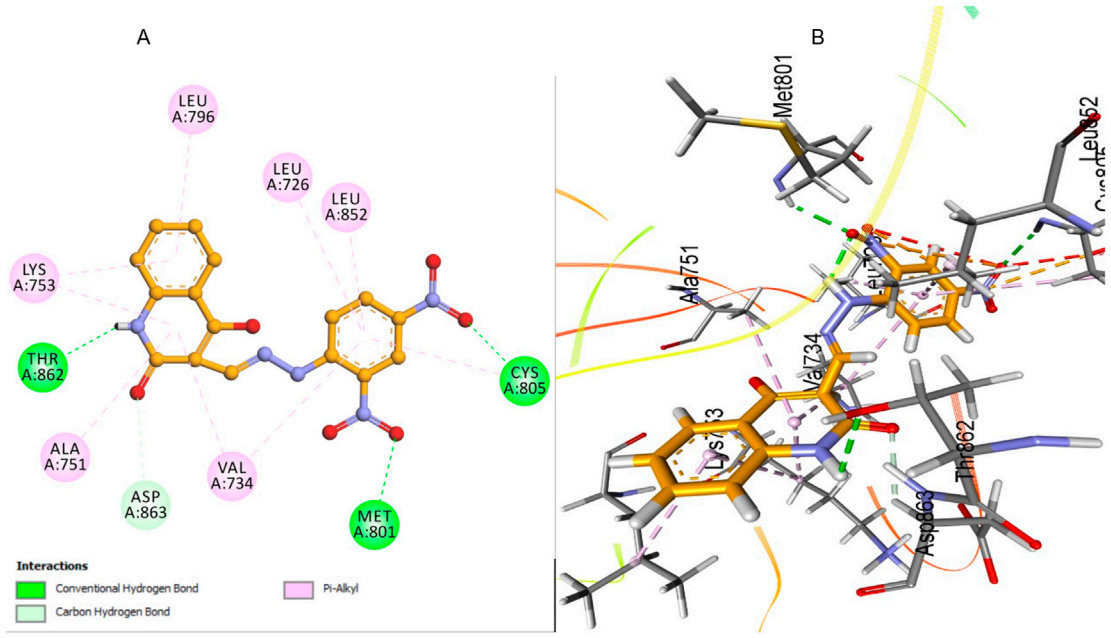


FIGURE 13
Docking representation of 5a within the HER-2 binding site; **(A)** 2D representation **(B)** 3D representation.

of 80 ± 5 nM against EGFR, highlighting its higher potency against EGFR than HER-2. On the other hand, **5a** demonstrated dual inhibition activity, with an IC_{50} of 87 ± 5 nM against EGFR and a more potent IC_{50} of 33 ± 2 nM against HER-2. This suggests that **5a** has a more balanced inhibitory effect on both targets than erlotinib and lapatinib. These findings highlight **5a** as a potential candidate for further development as a dual HER-2/EGFR inhibitor.

2.4 Molecular dynamics discussion of HER-2 for compounds **5a** and lapatinib

Molecular Dynamics (MD) simulations serve as a critical complement to docking studies in drug discovery by providing detailed insights into the stability and dynamics of ligand-protein interactions (Bozorgpour et al., 2023; Kumar et al., 2024). While docking predicts a ligand's initial binding pose and interactions within the active site, it offers a rigid snapshot of the complex (Stanzione et al., 2021). MD simulations, on the other hand, incorporate time-dependent molecular movements and environmental factors, allowing for a more realistic evaluation of the ligand-protein system (Adelusi et al., 2022). Through MD, key parameters such as stability (*via* RMSD), flexibility (*via* RMSF), compactness (*via* radius of gyration), and binding strength (*via* potential energy) can be assessed, offering a deeper understanding of the behavior of the ligand under physiological conditions (Tripathi et al., 2025). This dynamic perspective validates docking results and identifies critical interactions that stabilize the complex, helping to refine and prioritize drug candidates for experimental validation (Ghahremanian et al., 2022; Haider et al., 2020). By bridging the gap between computational predictions and experimental outcomes, MD simulations enhance the reliability and accuracy of virtual screening workflows (Kumar et al., 2025). The RMSD plot indicates the stability of the **5a** and lapatinib in the HER-2 binding pocket over a simulation period of 100 ns. Compound **5a** (blue) exhibits a significantly lower RMSD value, stabilizing at approximately 0.4–0.5 nm, compared to lapatinib (red), which fluctuates around 0.7–0.9 nm (Figure 14). The lower RMSD for 5a suggests a more stable binding conformation and less structural deviation during the simulation. Despite being a clinically established HER-2 inhibitor, Lapatinib shows higher fluctuations, indicating that compound **5a** may form a more rigid and stable complex with HER-2 under the tested conditions.

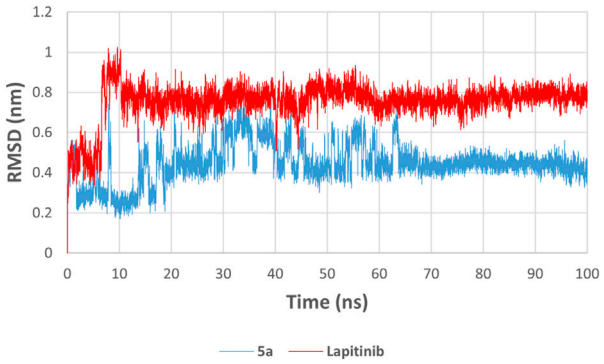


FIGURE 14
RMSD of HER-2-ligand complexes for **5a** (blue) and lapatinib (red) over a 100 ns molecular dynamics simulation.

The RMSF plot highlights residue-level flexibility within HER-2 upon binding with **5a** and lapatinib. Both compounds exhibit similar fluctuations for most regions, particularly in flexible loop

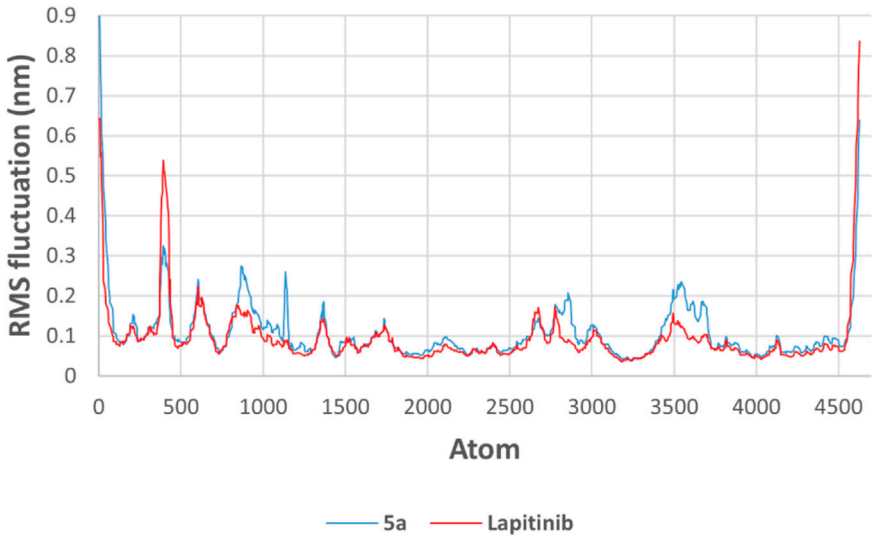


FIGURE 15
RMSF of HER-2 residues in complexes with **5a** (blue) and lapatinib (red).

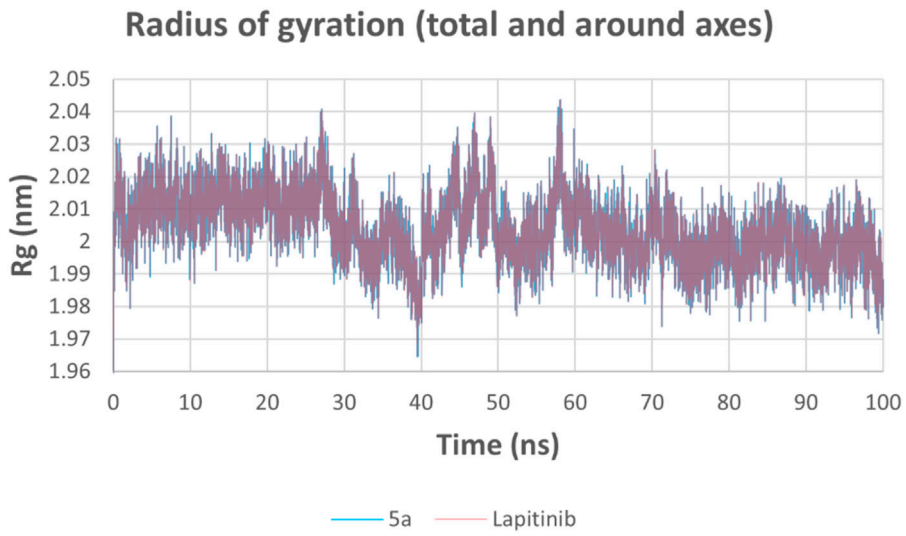


FIGURE 16
Radius of gyration (Rg) of HER-2-ligand complexes for **5a** (blue) and lapatinib (red).

regions and solvent-exposed residues. These findings suggest tighter binding and stabilization of the HER-2 active site of **5a** (Figure 15).

The Rg plot measures the compactness of the HER-2-ligand complex during the simulation. Both complexes maintain consistent Rg values around 2.00–2.03 nm, indicating that the overall HER-2 protein structure remains stable throughout the simulation for both compounds. There is no significant difference in the fluctuation of Rg between **5a** and lapatinib, suggesting that **5a** stabilizes the HER-2 conformation comparably well (Figure 16).

The potential energy analysis evaluates the stability of the HER-2-ligand systems. Both compounds exhibit consistent potential energy values throughout the 100 ns simulation, with no significant conformational disruptions observed (Figure 17).

The molecular dynamics simulations reveal compound **5a** and lapatinib demonstrate stable binding interactions with HER-2. **5a**'s lower RMSD and reduced flexibility indicate its potential as a promising HER-2 inhibitor. These findings highlight the need for further experimental validation of **5a**'s inhibitory efficacy against HER-2, as it shows comparable interaction dynamics relative to the clinically established lapatinib.

2.5 ADME studies

SwissADME was employed to predict the pharmacokinetic properties of compounds **5a** and reference drug lapatinib,

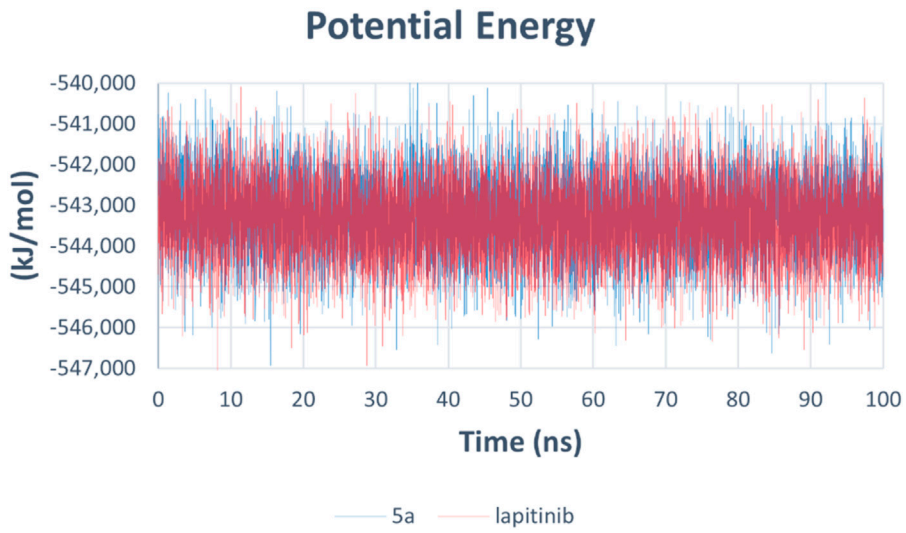


FIGURE 17
Potential energy of HER-2-ligand complexes for **5a** (blue) and lapatinib (red).

focusing on their Absorption, Distribution, Metabolism, and Excretion (ADME) characteristics (Khaled et al., 2023). The analysis sheds light on their drug-like behaviors, identifying distinct features and shared attributes that could influence the performance **5a** as a dual EGFR/HER-2 inhibitor. The analysis can also guide its potential for further development.

The ADME profiles of compound **5a** and lapatinib reveal significant differences and similarities. Compound **5a** exhibits a lower molecular weight (369.29 g/mol) than lapatinib (581.06 g/mol), enhancing its likelihood of better absorption and permeability. Additionally, **5a** has fewer rotatable bonds (5 vs 11 for lapatinib), indicating reduced molecular flexibility, which may improve binding stability within the target sites. Regarding solubility, **5a** is moderately soluble, whereas lapatinib is poorly soluble, a key limitation that could impact its bioavailability. Both compounds show low gastrointestinal (GI) absorption. However, the higher polar surface area **5a** (TPSA: 169.12 $Å^2$) than lapatinib (TPSA: 114.73 $Å^2$) may limit its permeability.

Lapatinib, while clinically effective, inhibits several CYP450 enzymes (CYP2C19, CYP2C9, CYP2D6, and CYP3A4), indicating a higher risk for drug-drug interactions, whereas **5a** shows no CYP450 inhibition, highlighting its safer pharmacokinetic profile. Both compounds have comparable bioavailability scores (0.55), but the lower consensus LogP of **5a** (1.26 vs 5.19 for lapatinib) suggests better hydrophilicity, which may support its drug-likeness. Furthermore, **5a** demonstrates easier synthetic accessibility (score: 3.22) compared to lapatinib (score: 4.05), which could simplify manufacturing processes. A safer profile of **5a**, better solubility, and lack of CYP450 inhibition suggest it could be a promising alternative to lapatinib.

2.6 DFT analysis of compound **5a**

To gain deeper insight into the electronic characteristics and reactivity profile of compound **5a**, Density Functional Theory (DFT) calculations were carried out using Gaussian 09 software with visualizations generated through Gauss View 6.0 (Ozcelik et al., 2023). The geometry optimization and vibrational frequency analyses were performed at the B3LYP level of theory with the 6-311+G (d,p) basis set, which incorporates diffuse and polarization functions to capture electron distribution and non-covalent interactions (Ozcelik et al., 2023) more accurately. The optimized structure of compound **5a** was confirmed as a true energy minimum since no imaginary vibrational frequencies were detected (Janani et al., 2021). The calculated geometry reveals that the molecule adopts a nearly planar conformation across the quinoline–hydrazone–di-nitrophenyl scaffold, which facilitates extended π-conjugation and supports the intermolecular interactions observed in the molecular docking studies with EGFR and HER-2 (Figure 18).

Frontier Molecular Orbital (FMO) analysis provided further evidence of the dual inhibitory potential of compound **5a** (Figure 19). The HOMO (Highest Occupied Molecular Orbital) was found to be located primarily over the quinoline core and hydrazone linker, indicating their role in electron donation during interaction with key amino acid residues, particularly those forming hydrogen bonds in the EGFR binding site (e.g., Met769 and Lys721). In contrast, the LUMO (Lowest Unoccupied Molecular Orbital) was predominantly located over the di-nitrophenyl ring, especially the nitro substituent, suggesting these regions function as electron acceptors and may be involved in stabilizing interactions with HER-2 residues such as Met801 and Thr862. The HOMO–LUMO energy gap (ΔE) was calculated as 3.15 eV, a moderate value indicating a balance between chemical stability and biological reactivity both of which are desirable properties for bioactive small molecules.

A molecular electrostatic potential (ESP) map was generated to complement the orbital analysis and visualize the distribution of electrostatic charges on the molecular surface. In this ESP surface, red regions indicate areas of highest negative electrostatic potential, blue regions signify the most positive potential, and green represents

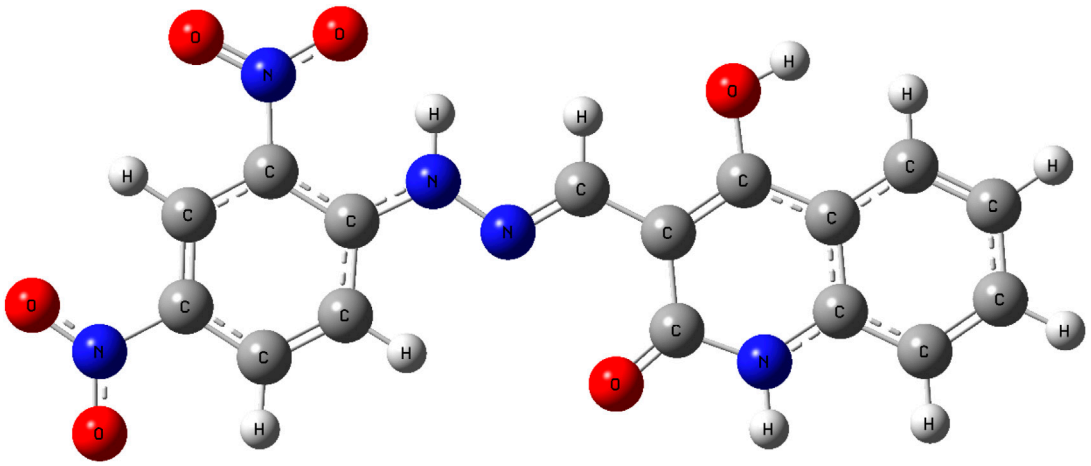


FIGURE 18
Optimized molecular geometry of compound **5a** at the B3LYP/6-311+G (d,p) level showing planarity and conjugation across the quinoline–hydrazone–di-nitrophenyl scaffold.

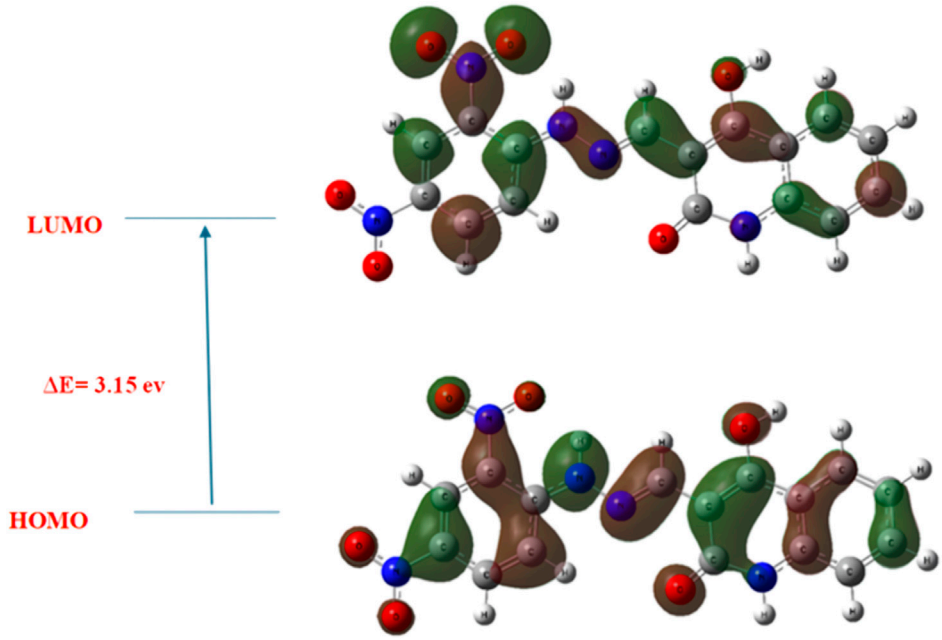


FIGURE 19
Frontier Molecular Orbitals (HOMO and LUMO) of compound **5a** with an energy gap (ΔE) of 3.15 eV, highlighting electron-rich (HOMO) and electron-deficient (LUMO) regions relevant to EGFR and HER-2 binding.

regions of neutral potential (Figure 20). The red zones were prominently located around the oxygen atoms of the nitro groups and carbonyl functionalities, marking them as favorable sites for hydrogen bond acceptance. Meanwhile, the blue zones were observed around the hydrazone NH and enol OH groups, which serve as potential hydrogen bond donors. These findings correlate closely with the docking results, where such groups engage in crucial hydrogen bonding interactions with residues in both EGFR and HER-2 active sites. Additionally, the extended green zones around the aromatic rings represent regions with relatively neutral electrostatic potential, supporting π-π stacking and hydrophobic interactions observed in the docking models with residues like Leu694 (EGFR) and Val734 (HER-2).

The electronic features derived from DFT calculations provide strong mechanistic support for compound 5a's dual EGFR/HER-2 inhibitory activity. The HOMO-LUMO orbital distribution highlights the complementary donor-acceptor regions essential for stable protein-ligand interactions. At the same time, the ESP map reveals an electrostatic profile conducive to binding within the ATP-binding pockets of both kinases. Together, these DFT findings reinforce the docking-based conclusions and confirm the structural

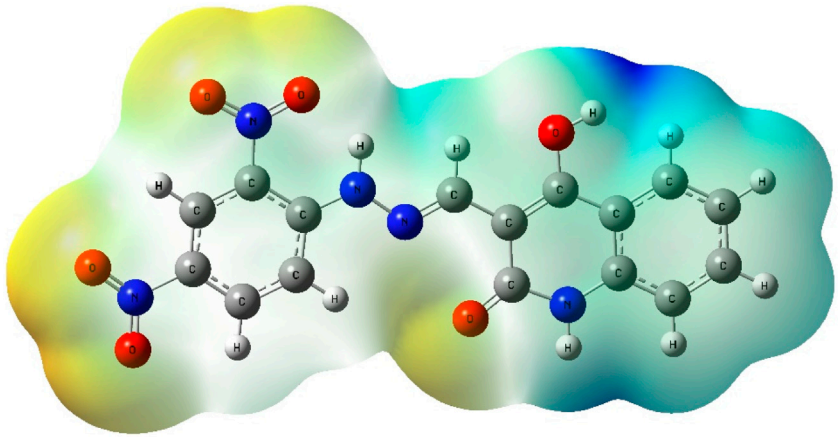


FIGURE 20
Molecular Electrostatic Potential (ESP) map of compound **5a** indicating zones of nucleophilic (red), electrophilic (blue), and neutral (green) potential character correlating with observed docking interactions in HER-2 and EGFR.

suitability of compound **5a** for further development as a dual-targeted anticancer agent.

3 Conclusion

This comprehensive study reports the successful synthesis, characterization, biological evaluation, and computational analysis of a new class of quinolin-2(1H)-one derivatives designed to function as dual inhibitors of EGFR and HER-2; two critical tyrosine kinases implicated in various cancers, including breast carcinoma. The lead compound, **5a**, demonstrated potent antiproliferative activity across multiple human cancer cell lines, with superior efficacy against the MCF-7 breast cancer cell line compared to the reference drug erlotinib. Enzymatic assays validated its dual-target inhibitory profile, exhibiting potent activity against EGFR and HER-2. Mechanistic investigations confirmed that compound **5a** promotes apoptosis through intrinsic and extrinsic pathways. Furthermore, **5a** induced G0/G1 phase arrest in MCF-7 cells, reinforcing its role in halting cancer cell proliferation. Molecular docking revealed that **5a** forms multiple stabilizing interactions within the active sites of both kinases. Molecular dynamics simulations over 100 ns confirmed the conformational stability of the ligand–protein complexes. Pharmacokinetic predictions from SwissADME indicated that **5a** exhibits favorable drug-like properties. DFT analysis further supported the electronic suitability of **5a** for dual kinase interaction. In summary, compound **5a** emerges as a compelling dual-target anticancer agent, combining potent antiproliferative efficacy, dual enzymatic inhibition, apoptosis induction, and favorable pharmacokinetic and electronic profiles. These results strongly support the continued preclinical development of **5a** as a lead compound for targeted therapy in EGFR/HER-2-overexpressing cancers.

4 Experimental

4.1 Chemistry

General Details: See Appendix A (Supplementary Material).

4.1.1 Materials and methods

4-Hydroxy-2-oxo-1,2-dihydroquinoline-3-carbaldehydes **1a-h** (Tang and Shi, 2008), 4-methylbenzene-sulfonohydrazide (**2**) (Şenkardeş et al., 2020) were prepared as previously described. (2,4-Dinitrophenyl)hydrazine (**4**) was purchased from Sigma Aldrich.

4.1.2 Synthesis of (*E*)-*N*′-((4-hydroxy-7-2-oxo-1,2-dihydroquinolin-3-yl) methylene) benzenesulfonohydrazides 3a-h and (*E*)-3-((2-(2,4-dinitrophenyl) hydrazono)methyl)-4-hydroxyquinolin-2(1*H*)-ones **5a-g**

In a round-bottomed flask, the appropriate quinolone-carbaldehydes **1a-h** (1 mmol) were dissolved in absolute ethanol (10 mL), to which a few drops of glacial acetic acid were added. A solution of 4-methylbenzenesulfonohydrazide (**2**, 186 mg) or (2,4-dinitrophenyl)hydrazine (**4**, 198 mg), dissolved in 10 mL of absolute ethanol, was added to the resultant mixture. The entire reaction was subjected to reflux for 4 hours. Following the completion of the reaction and the disappearance of the starting materials, the precipitates were collected and recrystallized from a mixture of ethanol/DMF in ratio (5:2) to yield the desired products **3a-h** and **5a-g** in good to excellent yields.

4.1.2.1 (*E*)-*N*′-((4-hydroxy-1-methyl-2-oxo-1,2-dihydroquinolin-3-yl)methylene)-4-methylbenzenesulfonohydrazide (**3a**)

Yellow crystals, yield (83%), mp. 245–247 °C; IR (KBr): ν = 3286 (NH), 3012 (Ar-CH), 2857 (ali-CH), 1668 (C=O), 1609 (C=N), 1568 (Ar-C=C), 1344, 1163 (SO_2) cm^{-1}; ^{1}H NMR (400 MHz, DMSO-d_6): δ_H = 2.36 (s, 3H, CH_3), 3.52 (s, 3H, CH_3), 7.26–7.30 (m, 1H, Ar-H), 7.45–7.47 (d, 2H, *J* = 8 Hz, Ar-H), 7.46–7.48 (d, 1H, *J* = 8 Hz, Ar-H), 7.65–7.69 (m, 1H, Ar-H), 7.73–7.75 (d, 2H, *J* = 8, Ar-H), 7.95–7.98 (m, 1H, Ar-H), 8.36 (s, 1H, CH = N), 11.71 (br, s, 1H, hydrazono-NH), 12.90 (br, s, 1H, OH) ppm; ^{13}C NMR (100 MHz, DMSO-d_6): δ_C = 21.05 (CH_3), 28.96 (CH_3), 101.61 (C-3), 122.15, 124.02, 127.18, 130.10 (Ar-CH), 115.10, 133.16, 134.93, 140.06, 144.27 (Ar-C), 149.69 (CH = N), 160.60 (C-4) 164.47 (C=O) ppm; MS (*m/z*):

10.3389/fchem.2025.1638489

391 ($M^+ + H_2O$, 5),154 (100), 92 (13). *Anal. Calcd. For* $C_{18}H_{17}N_3O_4S$ (371.41): C, 58.21; H, 4.61; N, 11.31; S, 8.63. Found: C, 58.16; H, 4.74; N, 11.33; S, 8.58.

4.1.2.2 (*E*)-*N*′-((4-hydroxy-6-methoxy-2-oxo-1,2-dihydroquinolin-3-yl) methylene)-4-methyl benzenesulfonohydrazide (**3b**)

Yellow crystals, yield (90%), mp. 272–273 °C; IR (KBr): ν = 3275 (NH), 3004 (Ar-CH), 2948, 2881 (ali-CH), 1662 (C=O), 1602 (C=N), 1566, 1492 (Ar-C=C), 1416, 1240 (SO_2) cm^{-1}; ^1H NMR (400 MHz, DMSO-d_6): δ_H = 2.37 (s, 3H, CH_3), 3.79 (s, 3H, OCH_3), 7.20–7.26 (m, 3H, Ar-H), 7.45–7.47 (d, 2H, *J* = 8, Ar-H), 7.73–7.75 (d, 2H, *J* = 8, Ar-H), 8.30 (s, 1H, CH = N), 11.37 (s, 1H, quinolone-NH) 11.68 (br, s, 1H, hydrazono-NH), 12.91 (br, s, 1H, OH) ppm; ^{13}C NMR (100 MHz, DMSO-d_6): δ_C = 21.07 (CH_3), 55.48 (OCH_3), 102.13 (C-3), 104.23, 114.71, 117.25, 122.51, 127.16, 130.13 (Ar-CH), 133.90, 134.94, 144.42 (Ar-C), 149.49 (CH = N), 154.29 (C-OMe), 160.88 (C-4) 165.88 (C=O) ppm; MS (*m/z*): 391 (M^+, 5), 220 (5), 190 (14), 154 (100), 92 (13). Anal. Calcd. For $C_{18}H_{17}N_3O_5S$ (387.41): C, 55.80; H, 4.42; N, 10.85; S, 8.28. Found: C, 55.77; H, 4.37; N, 10.87; S, 8.25.

4.1.2.3 (*E*)-*N*′-((4-hydroxy-6-methyl-2-oxo-1,2-dihydroquinolin-3-yl)methylene)-4-methylbenzenesulfonohydrazide (**3c**)

Yellow crystals, yield (92%), mp. 280–282 °C; IR (KBr): ν = 3196 (NH), 3104 (Ar-CH), 2915 (ali-CH), 1670 (C=O), 1610 (C=N), 1591, 1463 (Ar-C=C), 1404, 1159 (SO_2) cm^{-1}; ^1H NMR (400 MHz, DMSO-d_6): δ_H = 2.33 (s, 3H, CH_3), 2.38 (s, 3H, CH_3), 7.14–7.25 (m, 2H, Ar-H), 7.46–7.48 (d, 2H, *J* = 8, Ar-H), 7.55–7.59 (m, 1H, Ar-H), 7.74–7.76 (d, 2H, *J* = 8, Ar-H), 8.31 (s, 1H, CH = N), 11.47 (s, 1H, quinolone-NH) 11.66 (br, s, 1H, hydrazono-NH), 12.88 (br, s, 1H, OH) ppm; ^{13}C NMR (100 MHz, DMSO-d_6): δ_C = 20.55 (CH_3), 21.08 (CH_3), 98.26 (C-3), 114.90, 122.18, 125.54, 127.67, 129.30 (Ar-CH), 130.11, 132.05, 136.13, 137.22, 143.21 (Ar-C), 162.32 (CH = N) 163.49 (C-4), 167.98 (C=O) ppm; MS (*m/z*): 371 (M^+, 20), 201 (4), 174 (10), 154 (100), 92 (17). Anal. Calcd. For $C_{18}H_{17}N_3O_4S$ (371.41): C, 58.21; H, 4.61; N, 11.31; S, 8.63. Found: C, 58.13; H, 4.57; N, 11.33; S, 8.59.

4.1.2.4 (*E*)-*N*′-((4-hydroxy-2-oxo-1,2-dihydroquinolin-3-yl) methylene)-4-methyl benzenesulfonohydrazide (**3d**)

Yellow crystals, yield (85%), mp. 255–257 °C; IR (KBr): ν = 3201 (NH), 3011 (Ar-CH), 2952, 2833 (ali-CH), 1656 (C=O), 1613 (C=N), 1591, 1493 (Ar-C=C), 1404, 1159 (SO_2) cm^{-1}; ^1H NMR (400 MHz, DMSO-d_6): δ_H = 2.38 (s, 3H, CH_3), 7.18–7.22 (t, 1H, *J* = 16 Hz, Ar-H), 7.25–7.27 (d, 1H, *J* = 8 Hz, Ar-H), 7.46–7.48 (d, 2H, *J* = 8 Hz, Ar-H), 7.55–7.58 (t, 1H, *J* = 12 Hz, Ar-H), 7.75–7.77 (d, 2H, *J* = 8 Hz, Ar-H), 7.86–7.88 (d, 1H, *J* = 8 Hz, Ar-H), 8.33 (s, 1H, CH = N), 11.48 (s, 1H, quinolone-NH) 11.80 (br, s, 1H, hydrazono-NH), 12.91 (br, s, 1H, OH) ppm; ^{13}C NMR (100 MHz, DMSO-d_6): δ_C = 21.65 (CH_3), 98.29 (C-3), 114.90, 115.68, 122.01, 123.75, 127.24, 130.12 (Ar-CH), 102.01, 132.93, 139.46, 144.29 (Ar-C), 149.69 (CH = N) 161.38 (C-4), 166.64 (C=O) ppm; MS (*m/z*): 357 (M^+, 6), 188 (4), 154 (100), 92 (16). Anal. Calcd. For $C_{17}H_{15}N_3O_4S$ (357.38): C, 57.13; H, 4.23; N, 11.76; S, 8.97. Found: C, 55.08; H, 4.30; N, 11.78; S, 8.91.

4.1.2.5 (*E*)-*N*′-((1-Ethyl-4-hydroxy-2-oxo-1,2-dihydroquinolin-3-yl)methylene)-4-methyl benzenesulfonohydrazide (**3e**)

Yellow crystals, yield (82%), mp. 265–267 °C; IR (KBr): ν = 3222 (NH), 3066 (Ar-CH), 2977, 2872 (ali-CH), 1673 (C=O), 1607 (C=N), 1566, 1499 (Ar-C=C), 1335, 1165 (SO_2) cm^{-1}; ^1H NMR (400 MHz, DMSO-d_6): δ_H = 1.13–1.16 (t, 3H, *J* = 12, CH_3), 2.36 (s, 3H, CH_3), 4.16–4.19 (q, 2H, *J* = 12 Hz, CH_2), 7.25–7.29 (t, 1H, *J* = 12 Hz, Ar-H), 7.45–7.47 (d, 2H, *J* = 8 Hz, Ar-H), 7.49–7.52 (d, 1H, *J* = 12, Ar-H), 7.65–7.69 (t, 3H, *J* = 16 Hz, Ar-H), 7.75–7.77 (d, 2H, J = 8 Hz, Ar-H), 7.97–7.99 (d, 1H, *J* = 8 Hz, Ar-H), 8.38 (s, 1H, CH = N), 11.74 (br, s, 1H, hydrazono-NH), 12.91 (br, s, 1H, OH) ppm; ^{13}C NMR (100 MHz, DMSO-d_6): δ_C = 12.71 (CH_3), 21.05 (CH_3), 36.46 (CH_2), 101.54 (C-3), 115.21, 122.04, 124.28, 127.18, 130.10, 133.23 (Ar-CH), 114.81, 134.96, 138.96, 144.25 (Ar-C), 149.42 (CH = N), 160.16 (C-4), 164.15 (C=O) ppm. MS (*m/z*): 385 (M^+, 9), 154 (100), 92 (18). Anal. Calcd. For $C_{19}H_{19}N_3O_4S$ (385.44): C, 59.21; H, 4.97; N, 10.90; S, 8.32. Found: C, 59.17; H, 4.89; N, 10.87; S, 8.27.

4.1.2.6 (*E*)-*N*′-((6-chloro-4-hydroxy-2-oxo-1,2-dihydroquinolin-3-yl)methylene)-4-methyl benzenesulfonohydrazide (**3f**)

Yellow crystals, yield (79%), mp. 270–272 °C; IR (KBr): ν = 3230 (NH), 3047 (Ar-CH), 2900, 2823 (ali-CH), 1665 (C=O), 1595 (C=N), 1589, 1459 (Ar-C=C), 1410, 1187 (SO_2) cm^{-1}; ^1H NMR (400 MHz, DMSO-d_6): δ_H = 2.39 (s, 3H, CH_3), 7.24–7.26 (d, 1H, *J* = 8 Hz, Ar-H), 7.46–7.48 (d, 2H, *J* = 8 Hz, Ar-H), 7.59–7.62 (dd, 1H, J = 12 Hz, Ar-H), 7.73–7.75 (d, 2H, *J* = 8 Hz, Ar-H), 7.81–7.83 (d, 1H, *J* = 8 Hz, Ar-H), 8.28 (s, 1H, CH = N), 11.56 (s, 1H, quinolone-NH) 11.68 (br, s, 1H, hydrazono-NH), 12.86 (br, s, 1H, OH) ppm; ^{13}C NMR (100 MHz, DMSO-d_6): δ_C = 21.09 (CH_3), 102.56 (C-3), 116.15, 122.77, 126.06, 127.28, 130.15 (Ar-CH), 117.76, 132.77, 134.69, 138.24, 144.41 (Ar-C), 150.14 (CH = N) 161.28 (C-4), 166.36 (C=O) ppm; MS (*m/z*): 371 (M^+, 100), 201 (21), 188 (30), 154 (100), 91 (4). Anal. Calcd. For $C_{17}H_{14}ClN_3O_4S$ (391.83): C, 52.11; H, 3.60; Cl, 9.05; N, 10.72; S, 8.18. Found: C, 52.07; H, 3.52; Cl, 9.00; N, 10.65; S, 8.20.

4.1.2.7 (*E*)-*N*′-((4-hydroxy-7-methyl-2-oxo-1,2-dihydroquinolin-3-yl)methylene)-4-methyl benzenesulfonohydrazide (**3g**)

Yellow crystals, yield (91%), mp. 224–225 °C; IR (KBr): ν = 3642/3519 (OH), 3182 (NH), 3029 (Ar-CH), 2977, 2864 (ali-CH), 1642 (C=O), 1597 (C=N), 1497, 1484 (Ar-C=C), 1382, 1163 (SO_2) cm^{-1}; ^1H NMR (400 MHz, DMSO-d_6): δ_H = 2.34 (s, 3H, CH_3), 3.17 (s, 3H, CH_3), 6.90–6.92 (d, 1H, *J* = 8, Ar-H), 7.07–7.09 (d, 1H, *J* = 8 Hz, Ar-H), 7.35–7.38 (t, 1H, *J* = 12 Hz, Ar-H), 7.45–7.47 (d, 2H, *J* = 8 Hz, Ar-H), 7.73–7.75 (d, 2H, *J* = 8 Hz, Ar-H), 8.30 (s, 1H, CH = N), 11.38 (br, s, 1H, quinolone-NH), 11.50 (br, s, 1H, hydrazono-NH), 13.14 (br, s, 1H, OH) ppm; ^{13}C NMR (100 MHz, DMSO-d_6): δ_C = 21.52 (CH_3), 23.42 (CH_3), 102.15 (C-3), 114.01, 115.35, 125.18, 127.24, 127.34, (Ar-CH), 114.19, 130.11, 132.38, 138.34, 151.47 (Ar-C), 159.63 (CH = N), 161.57 (C-4), 166.77 (C=O) ppm; Anal. Calcd. For $C_{18}H_{17}N_3O_4S$ (371.41): C, 58.21; H, 4.61; N, 11.31; S, 8.63. Found: C, 58.13; H, 4.57; N, 11.33; S, 8.59.

4.1.2.8 (*E*)-*N*′-((4-hydroxy-8-methyl-2-oxo-1,2-dihydroquinolin-3-yl)methylene)-4-methyl benzenesulfonohydrazide (**3h**)

Yellow crystals, yield (90%), mp. 234–236 °C; ^{1}H NMR (400 MHz, DMSO-d_6): δ_H = 1.90 (s, 3H, CH_3), 2.37 (s, 3H, CH_3), 7.09–7.13 (t, 1H, *J* = 16 Hz, Ar-H), 7.41–7.43 (d, 1H, *J* = 8 Hz, Ar-H), 7.45–7.47 (d, 2H, *J* = 8 Hz, Ar-H), 7.74–7.76 (d, 3H, *J* = 8 Hz, Ar-H), 8.32 (s, 1H, CH = N), 11.69 (br, s, 1H, quinolone-NH), 11.95 (br, s, 1H, hydrazono-NH), 12.88 (br, s, 1H, OH) ppm; ^{13}C NMR (100 MHz, DMSO-d_6): δ_C = 17.40 (CH_3), 21.10 (CH_3), 101.72 (C-3), 121.55, 121.77, 124.07, 127.19, 130.14 (Ar-CH), 134.05, 134.90, 137.96, 144.29, 149.61 (Ar-C), 161.64 (CH = N), 166.22 (C-4), 172.09 (C=O) ppm; *Anal. Calcd. For* $C_{18}H_{17}N_3O_4S$ (371.41): C, 58.21; H, 4.61; N, 11.31; S, 8.63. Found: C, 58.23; H, 4.55; N, 11.28; S, 8.60.

4.1.2.9 (*E*)-3-((2-(2,4-Dinitrophenyl)hydrazono)methyl)-4-hydroxyquinolin-2(1*H*)-one (**5a**)

Orange crystals, yield (86%), mp. = 327–329 °C; ^{1}H NMR (400 MHz, DMSO-d_6): δ_H = 7.18–7.20 (d, *J* = 8.0 Hz, 2H, quinolinone-H), 7.22–7.77 (m, 3H, quinolinone-H, Ar-H), 7.89–7.91 (d, 2H, *J* = 8.0 Hz, dinitrobenzene-H), 8.35 (s, 1H, CH = N), 11.18 (br, s, 1H, quinolone-NH), 11.33 (br, s, 1H, hydrazono-NH), 12.77 (br, s, 1H, OH) ppm; ^{13}C NMR (100 MHz, DMSO-d_6): δ_C = 101.10 (C-3), 115.10, 121.16, 124.03, 126.19, 130.11, 132.16, 134.06 (Ar-CH), 140.06, 144.28 (Ar-C), 149.69 (CH = N) 161.10 (C-4), 166.43 (C=O) ppm. *Anal. Calcd. For* $C_{16}H_{11}N_5O_6$ (369.29): C, 52.04; H, 3.00; N, 18.96. Found: C, 51.97; H, 3.05; N, 18.00.

4.1.2.10 (*E*)-3-((2-(2,4-Dinitrophenyl)hydrazono)methyl)-4-hydroxy-6-methyl quinolin-2(1*H*)-one (**5b**)

Orange crystals, yield (89%), mp. 338–340 °C; ^{1}H NMR (400 MHz, DMSO-d_6): δ_H = 2.54 (s, 3H, CH_3), 7.18–7.41 (m, 4H, quinolinone-H, Ar-H), 7.42–7.43 (d, 2H, quinolinone-H, Ar-H), 8.74 (s, 1H, CH = N), 11.19 (br, s, 1H, quinolone-NH), 11.62 (br, s, 1H, hydrazono-NH), 12.69 (br, s, 1H, OH) ppm; *Anal. Calcd. For* $C_{17}H_{13}N_5O_6$ (383.32): C, 53.27; H, 3.42; N, 18.27. Found: C, 53.19; H, 3.45; N, 18.18.

4.1.2.11 (*E*)-3-((2-(2,4-Dinitrophenyl)hydrazono)methyl)-4-hydroxy-6-methoxy quinolin-2(1*H*)-one (**5c**)

Orange red crystals, yield (90%), mp. 313–315 °C; ^{1}H NMR (400 MHz, DMSO-d_6): δ_H = 3.84 (s, 3H, OCH_3), 7.20–7.43 (m, 6H, quinolinone-H, Ar-H), 8.43 (s, 1H, CH = N), 11.20 (br, s, 1H, quinolone-NH), 11.60 (br, s, 1H, hydrazono-NH), 12.93 (br, s, 1H, OH) ppm; *Anal. Calcd. For* $C_{17}H_{13}N_5O_6$ (399.31): C, 51.13; H, 3.28; N, 17.54. Found: C, 51.05; H, 3.30; N, 17.49.

4.1.2.12 (*E*)-3-((2-(2,4-Dinitrophenyl)hydrazono)methyl)-4-hydroxy-8-methyl quinolin-2(1*H*)-one (**5d**)

Orange red crystals, yield (87%), mp. 338–340 °C; ^{1}H NMR (400 MHz, DMSO-d_6): δ_H = 1.91 (s, 3H, CH_3), 7.19–7.49 (m, 2H, Ar-H), 7.62–7.71 (m, 2H, Ar-H), 7.87–7.95 (m, 1H, Ar-H), 8.28–8.48 (m, 1H, Ar-H), 8.83–8.90 (d, 1H, Ar-H), 9.19 (s, 1H, CH = N), 10.84 (br, s, 1H, quinolone-NH), 11.95 (br, s, 1H, hydrazono-NH), 12.99 (br, s, 1H, OH) ppm; *Anal. Calcd. For* $C_{17}H_{13}N_5O_6$ (383.32): C, 53.27; H, 3.42; N, 18.27. Found: C, 53.17; H, 3.45; N, 18.19.

4.1.2.13 (*E*)-3-((2-(2,4-Dinitrophenyl)hydrazono)methyl)-4-hydroxy-1-methyl quinolin-2(1*H*)-one (**5e**)

Orange crystals, yield (77%), mp. 295–297 °C; ^{1}H NMR (400 MHz, DMSO-d_6): δ_H = 3.62 (s, 3H, NCH_3), 7.36–7.74 (m, 3H, Ar-H), 8.07–8.11 (m, 2H, Ar-H), 8.44–8.46 (d, 1H, *J* = 8.4 Hz, Ar-H), 8.86–8.92 (d, 1H, Ar-H), 9.20 (s, 1H, CH = N), 11.88 (br, s, 1H, hydrazono-NH), 12.67 (br, s, 1H, OH) ppm; 13C NMR (100 MHz, DMSO-d6): δ_C = 28.83 (NCH3), 114.79, 115.21, 115. 31, 121.92, 123.69, 129.82 (Ar-CH), 129.91, 132.92, 137.24 (Ar-C), 149.98 (CH = N), 161.09 (C-4), 164.31 (C=O) ppm; *Anal. Calcd. For* $C_{17}H_{13}N_5O_6$ (383.32): C, 53.27; H, 3.42; N, 18.27. Found: C, 53.29; H, 3.38; N, 18.31.

4.1.2.14 (*E*)-3-((2-(2,4-Dinitrophenyl)hydrazono)methyl)-4-hydroxy-7-methyl quinolin-2(1*H*)-one (5f)

Orange red crystals, yield (88%), mp. 332–334 °C; ^{1}H NMR (400 MHz, DMSO-d_6): δ_H = 3.00 (s, 3H, CH_3), 7.01–7.39 (m, 6H, quinolinone-H, Ar-H), 8.42 (s, 1H, CH = N), 11.17 (br, s, 1H, quinolone-NH), 11.41 (br, s, 1H, hydrazono-NH), 12.76 (br, s, 1H, OH) ppm; *Anal. Calcd. For* $C_{17}H_{13}N_5O_6$ (383.32): C, 53.27; H, 3.42; N, 18.27. Found: C, 53.29; H, 3.38; N, 18.30.

4.1.2.15 (*E*)-6-Chloro-3-((2-(2,4-dinitrophenyl)hydrazono) methyl)-4-hydroxy quinolin-2(1*H*)-one (**5g**)

Orange red crystals, yield (76%), mp. 328–330 °C; ^{1}H NMR (400 MHz, DMSO-d_6): δ_H = 7.23–7.43 (m, 6H, quinolinone-H, Ar-H), 8.73 (s, 1H, CH = N), 11.22 (br, s, 1H, quinolone-NH), 11.77 (br, s, 1H, hydrazono-NH), 12.97 (br, s, 1H, OH) ppm; *Anal. calcd. for* $C_{16}H_{10}ClN_5O_6$ (403.73): C, 47.60; H, 2.50; Cl, 8.78; N, 17.35. Found: C, 47.62; H, 2.48; Cl, 8.71; N, 17.38.

4.1.3 Crystal X-ray structure determination of 3g

Single crystals of **3g** were obtained by recrystallization from CH_3CH_2OH. The single-crystal X-ray diffraction study was carried out on a Bruker D8 Venture diffractometer with a Photon II detector at 173 (2) K (λ = 1.54178 Å). Dual space methods (SHELXT) (Sheldrick, 2015) were used for structure solution, and refinement was carried out using SHELXL-2014 (full-matrix least-squares on F2). Hydrogen atoms were refined using a riding model (H(N, O) free). A semi-empirical absorption correction was applied. The methyl group is disordered (5-methyl vs 7-methyl, approximately 73:27; see cif-file for details).

Compound **3g**: $C_{18}H_{17}N_3O_4S{\cdot}H_2O$, Mr = 389.42 g mol^{-1}, yellow crystals, size 0.20 × 0.12 × 0.08 mm, Monoclinic, $P2_1/n$ *(no.14)*, a = 7.8378 (5) Å, b = 9.1161 (6) Å, c = 26.7859 (17) Å, β = 97.797 (2)°, V = 1896.2 (2) Å^3, λ = 1.54178 Å, Z = 4, D_{calcd} = 1.364 Mg m^{-3}, *F* (000) = 816, μ = 1.82 mm^{-1}, T = 173 K, 21,753 collected reflection ($2\theta_{max}$ = 144.0°), of which 3729 were reflection unique (R_{int} = 0.030), 261 parameters, 216 restraints, R1 [for 3401 I > 2σ(I)] = 0.043, wR2 (for all data) = 0.125, S = 1.03, largest diff. peak and hole = 0.30 e Å^{-3}/-0.33 e Å^{-3}. CCDC 2451182 (**3g**) contains the supplementary crystallographic data for this paper. These data can be obtained free from The Cambridge Crystallographic Data Centre *via* www.ccdc.cam.ac.uk/data_request/cif.

4.2 Biology

4.2.1 Cell viability assay

The MTT assay was used to assess the viability of **3a-h** and **5a-g** cells after 4 days of incubation with MCF-10A (a normal human mammary gland cell line) (El-Sherief et al., 2019; Ramadan et al., 2020). For more experimental details, refer to Supplementary Appendix A.

4.2.2 Antiproliferative assay

Compounds **3a-h** and **5a-g** were tested for their antiproliferative activities on four human cancer cell lines: colon (HT-29), pancreatic (Panc-1), lung (A-549), and breast (MCF-7) using the MTT assay (Al-Wahaibi et al., 2022; Mahmoud et al., 2023). Erlotinib was applied as a reference. See Supplementary Appendix A for more experimental details.

4.2.3 EGFR inhibitory assay

The most efficient antiproliferative derivatives, **3c**, **3d**, **3f**, **5a,** and **5b,** were evaluated for their ability to inhibit EGFR using the EGFR-TK test, with Erlotinib as the reference drug (Abou-Zied et al., 2023). Refer to Supplementary Appendix A for more details.

4.2.4 HER-2 inhibitory assay

Compounds **3c**, **3d**, **3f**, **5a,** and **5b** were evaluated for their capacity to inhibit HER-2 by a kinase assay (Al-Wahaibi et al., 2025). Lapatinib functioned as the reference drug. See Supplementary Appendix A for more experimental details.

4.2.5 Caspases-3, -8, and -9 activation assay

The MCF-7 human breast cancer cell line was acquired from ATCC. RPMI 1640 with 10% FBS was used to assist the cells grow at 37 °C, and then the cells were treated with the compounds being studied to check the activity of caspase-3, -8, and -9 (Hisham et al., 2019). Refer to Supplementary Appendix A.

4.2.6 Evaluation of Bax and Bcl-2 levels

RNA isolation was performed using the RNeasy extraction kit with up to 1 × 10^7 cells. They were disturbed and homogenized in Buffer RLT (Mitupatum et al., 2016). See Supplementary Appendix A for more details.

4.2.7 Cytochrome C assay

Cells were obtained from the American Type Culture Collection and grown at 37 °C in RPMI 1640 supplemented with 10% fetal bovine serum before being stimulated with **3d** and **5a** to test cytochrome C (Abdelbaset et al., 2019). Refer to Supplementary Appendix A for more details on the experimental process.

4.2.8 Flow cytometry and cell cycle analysis

Apoptosis was detected using flow cytometry with an annexin-V-fluorescein isothiocyanate (FITC) and propidium iodide (PI) staining kit (BD Pharmingen, San Diego, United States) (Mohamed et al., 2024). See Supplementary Appendix A for more details.

Data availability statement

The original contributions presented in the study are included in the article/Supplementary Material, further inquiries can be directed to the corresponding authors.

Author contributions

LHA-W: Writing – review and editing, Software, Funding acquisition, Resources. HAA-Z: Writing – review and editing, Formal Analysis, Visualization, Data curation, Software, Writing – original draft. MN: Resources, Writing – original draft, Software. SB: Writing – review and editing, Data curation, Visualization. BY: Investigation, Conceptualization, Validation, Supervision, Writing – review and editing, Visualization, Formal Analysis, Writing – original draft, Methodology. HT: Methodology, Writing – original draft, Writing – review and editing.

Funding

The author(s) declare that financial support was received for the research and/or publication of this article.

Acknowledgements

The authors acknowledge support from Princess Nourah bint Abdulrahman University Researchers Supporting Project Number (PNURSP2025R3), Princess Nourah bint Abdulrahman University, Riyadh, Saudi Arabia, and the KIT-Publication Fund of the Karlsruhe Institute of Technology.

Conflict of interest

The authors declare that the research was conducted in the absence of any commercial or financial relationships that could be construed as a potential conflict of interest.

Generative AI statement

The author(s) declare that no Generative AI was used in the creation of this manuscript.

Any alternative text (alt text) provided alongside figures in this article has been generated by Frontiers with the support of artificial intelligence and reasonable efforts have been made to ensure accuracy, including review by the authors wherever possible. If you identify any issues, please contact us.

Publisher's note

All claims expressed in this article are solely those of the authors and do not necessarily represent those of their

affiliated organizations, or those of the publisher, the editors and the reviewers. Any product that may be evaluated in this article, or claim that may be made by its manufacturer, is not guaranteed or endorsed by the publisher.

Supplementary material

The Supplementary Material for this article can be found online at: https://www.frontiersin.org/articles/10.3389/fchem.2025.1638489/full#supplementary-material

References

Abdelbaset, M. S., Abdel-Aziz, M., Abuo-Rahma, G. E. D. A., Abdelrahman, M. H., Ramadan, M., and Youssif, B. G. (2019). Novel quinoline derivatives carrying nitrones/oximes nitric oxide donors: design, synthesis, antiproliferative and caspase-3 activation activities. *Arch. Pharm.* 352 (1), 1800270. doi:10.1002/ardp.201800270

Abourehab, M. A., Alqahtani, A. M., Youssif, B. G., and Gouda, A. M. (2021). Globally approved EGFR inhibitors: insights into their syntheses, target kinases, biological activities, receptor interactions, and metabolism. *Molecules* 26 (21), 6677. doi:10.3390/molecules26216677

Abou-Zied, H. A., Beshr, E. A., Gomaa, H. A., Mostafa, Y. A., Youssif, B. G., Hayallah, A. M., et al. (2023). Discovery of new cyanopyridine/chalcone hybrids as dual inhibitors of EGFR/BRAFV600E with promising antiproliferative properties. *Arch. Pharm.* 356 (4), 2200464. doi:10.1002/ardp.202200464

Adelusi, T. I., Oyedele, A.-Q. K., Boyenle, I. D., Ogunlana, A. T., Adeyemi, R. O., Ukachi, C. D., et al. (2022). Molecular modeling in drug discovery. *Inf. Med. Unlocked* 29, 100880. doi:10.1016/j.imu.2022.100880

Al-Wahaibi, L. H., Mostafa, Y. A., Abdelrahman, M. H., El-Bahrawy, A. H., Trembleau, L., and Youssif, B. G. (2022). Synthesis and biological evaluation of indole-2-carboxamides with potent apoptotic antiproliferative activity as egfr/cdk2 dual inhibitors. *Pharmaceuticals* 15 (8), 1006. doi:10.3390/ph15081006

Al-Wahaibi, L. H., Mahmoud, M. A., Mostafa, Y. A., Raslan, A. E., and Youssif, B. G. (2023a). Novel piperine-carboximidamide hybrids: design, synthesis, and antiproliferative activity via a multi-targeted inhibitory pathway. *J. Enzyme Inhibition Med. Chem.* 38 (1), 376–386. doi:10.1080/14756366.2022.2151593

Al-Wahaibi, L. H., Mohammed, A. F., Abdelrahman, M. H., Trembleau, L., and Youssif, B. G. (2023b). Design, synthesis, and biological evaluation of indole-2-carboxamides as potential multi-target antiproliferative agents. *Pharmaceuticals* 16 (7), 1039. doi:10.3390/ph16071039

Al-Wahaibi, L. H., El-Sheref, E. M., Hassan, A. A., Bräse, S., Nieger, M., Youssif, B. G., et al. (2023c). Synthesis and structure determination of substituted thiazole derivatives as EGFR/BRAFV600E dual inhibitors endowed with antiproliferative activity. *Pharmaceuticals* 16 (7), 1014. doi:10.3390/ph16071014

Al-Wahaibi, L. H., Elshamsy, A. M., Ali, T. F., Youssif, B. G., Bräse, S., Abdel-Aziz, M., et al. (2024a). Design and synthesis of new dihydropyrimidine derivatives with a cytotoxic effect as dual EGFR/VEGFR-2 inhibitors. *ACS Omega* 9 (32), 34358–34369. doi:10.1021/acsomega.4c01361

Al-Wahaibi, L. H., El-Sheref, E. M., Tawfeek, H. N., Abou-Zied, H. A., Rabea, S. M., Bräse, S., et al. (2024b). Design, synthesis, and biological evaluation of novel quinoline-based EGFR/HER-2 dual-target inhibitors as potential anti-tumor agents. *RSC Adv.* 14 (45), 32978–32991. doi:10.1039/d4ra06394e

Al-Wahaibi, L. H., Hafez, H. M., Edrees, F. H., Abou-Zied, H. A., Youssif, B. G., and Bräse, S. (2025). Design, synthesis, and computational studies of novel pyrazoline-based dual EGFR/HER-2 inhibitors with apoptotic antiproliferative activity. *J. Mol. Struct.* 1339, 142364. doi:10.1016/j.molstruc.2025.142364

Alkahtani, H. M., Abdalla, A. N., Obaidullah, A. J., Alanazi, M. M., Almehizia, A. A., Alanazi, M. G., et al. (2020). Synthesis, cytotoxic evaluation, and molecular docking studies of novel quinazoline derivatives with benzenesulfonamide and anilide tails: dual inhibitors of EGFR/HER2. *Bioorg. Chem.* 95, 103461. doi:10.1016/j.bioorg.2019.103461

Bozorgpour, R., Sheybanikashani, S., and Mohebi, M. (2023). Exploring the role of molecular dynamics simulations in most recent cancer research: insights into treatment strategies. *arXiv preprint arXiv. 2310, 19950*.

Bräse, S. *Privileged scaffolds in medicinal chemistry: design, synthesis, evaluation*. Cambridge, England: Royal Society of Chemistry2015.

Buccheri, R., Coco, A., Pasquinucci, L., Amata, E., Marrazzo, A., and Rescifina, A. (2025). Enhancing HDAC inhibitor screening: addressing zinc parameterization and ligand protonation in docking studies. *Int. J. Mol. Sci.* 26 (2), 850. doi:10.3390/ijms26020850

Deeks, E. D. (2017). Neratinib: first global approval. *Drugs* 77, 1695–1704. doi:10.1007/s40265-017-0811-4

El-Sherief, H. A., Youssif, B. G., Abdelazeem, A. H., Abdel-Aziz, M., and Abdel-Rahman, H. M. (2019). Design, synthesis and antiproliferative evaluation of novel 1, 2, 4-triazole/schiff base hybrids with EGFR and B-RAF inhibitory activities. *Anti-Cancer Agents Med. Chem.* 19 (5), 697–706. doi:10.2174/1871520619666181224115346

Fayed, E. A., Gohar, N. A., Bayoumi, A. H., and Ammar, Y. A. (2023). Novel fluorinated pyrazole-based heterocycles scaffold: cytotoxicity, *in silico* studies and molecular modelling targeting double mutant EGFR L858R/T790M as antiproliferative and apoptotic agents. *Med. Chem. Res.* 32 (2), 369–388. doi:10.1007/s00044-022-03004-8

Ghahremanian, S., Rashidi, M. M., Raeisi, K., and Toghraie, D. (2022). Molecular dynamics simulation approach for discovering potential inhibitors against SARS-CoV-2: a structural review. *J. Mol. Liq.* 354, 118901. doi:10.1016/j.molliq.2022.118901

Ghorab, M. M., Alsaid, M. S., and Soliman, A. M. (2018). Dual EGFR/HER2 inhibitors and apoptosis inducers: new benzo [g] quinazoline derivatives bearing benzenesulfonamide as anticancer and radiosensitizers. *Bioorg. Chem.* 80, 611–620. doi:10.1016/j.bioorg.2018.07.015

Gutierrez, C., and Schiff, R. (2011). HER2: biology, detection, and clinical implications. *Archives Pathol. Lab. Med.* 135 (1), 55–62. doi:10.5858/2010-0454-rar.1

Haider, S., Barakat, A., and Ul-Haq, Z. (2020). Discovery of potential chemical probe as inhibitors of CXCL12 using ligand-based virtual screening and molecular dynamic simulation. *Molecules* 25 (20), 4829. doi:10.3390/molecules25204829

Hao, S., Wang, J.-h., Hou, L., Liang, J.-w., Yan, J.-h., Niu, Y.-f., et al. (2024). Design, synthesis and biological evaluation of novel quinazoline-derived EGFR/HER-2 dual-target inhibitors bearing a heterocyclic-containing tail as potential anti-tumor agents. *Bioorg. Chem.* 151, 107686. doi:10.1016/j.bioorg.2024.107686

Harding, J. J., Piha-Paul, S. A., Shah, R. H., Murphy, J. J., Cleary, J. M., Shapiro, G. I., et al. (2023). Antitumour activity of neratinib in patients with HER2-mutant advanced biliary tract cancers. *Nat. Commun.* 14 (1), 630. doi:10.1038/s41467-023-36399-y

Hisham, M., Youssif, B. G., Osman, E. E. A., Hayallah, A. M., and Abdel-Aziz, M. (2019). Synthesis and biological evaluation of novel xanthine derivatives as potential apoptotic antitumor agents. *Eur. J. Med. Chem.* 176, 117–128. doi:10.1016/j.ejmech.2019.05.015

Jan, A., Sofi, M. S., and Mir, M. A. (2025). Cytochrome c and cancer cell metabolism: a new perspective. *Adv. Cancer biology-Metastasis* 14, 100134.

Janani, S., Rajagopal, H., Muthu, S., Aayisha, S., and Raja, M. (2021). Molecular structure, spectroscopic (FT-IR, FT-Raman, NMR), HOMO-LUMO, chemical reactivity, AIM, ELF, LOL and Molecular docking studies on 1-Benzyl-4-(N-Boc-amino) piperidine. *J. Mol. Struct.* 1230, 129657. doi:10.1016/j.molstruc.2020.129657

Jejurikar, B. L., and Rohane, S. H. (2021). *Drug designing in discovery studio*.

Khaled, N. A., Ahmed, N. S., Abdelazem, A. Z., Mohamed, N. A., El-Sayed, A. F., and Ahmed, S. A. (2023). Design, synthesis, biological evaluation, *in silico* ADME prediction and molecular docking of pyrazole-benzamides as multitargeting protien kinase inhibitors. *J. Mol. Struct.* 1288, 135753. doi:10.1016/j.molstruc.2023.135753

Kouwenhoven, W. M., Robinson, E. J., Hamberg, D., von Oerthel, L., Smidt, M. P., and van der Heide, L. P. (2025). The absence of Pitx3 results in postnatal loss of dopamine neurons and is associated with an increase in the pro-apoptotic Bcl2 factor Noxa and cleaved caspase 3. *Cell Death Dis.* 16 (1), 230. doi:10.1038/s41419-025-07552-w

Kumar, M., Tripathi, M. K., and Kaur, P. (2024). Molecular dynamics and its significance in drug discovery. *Structure-Based Drug Des.* 149–175. doi:10.1007/978-3-031-69162-1_6

Kumar, A., Bharadwaj, T., Muthuraj, L., Kumar, J., Kumar, P., Lalitha, R., et al. (2025). Molecular dynamics simulation and docking studies reveals inhibition of NF-kB signaling as a promising therapeutic drug target for reduction in cytokines storms. *Sci. Rep.* 15 (1), 15225. doi:10.1038/s41598-024-78411-5

Luhtala, S. (2019). *Novel biomarkers in HER2-amplified breast cancer: histopathological and clinical associations*.

Maennling, A. E., Tur, M. K., Niebert, M., Klockenbring, T., Zeppernick, F., Gattenlöhner, S., et al. (2019). Molecular targeting therapy against EGFR family in breast cancer: progress and future potentials. *Cancers (Basel)* 11 (12), 1826. doi:10.3390/cancers11121826

Mahmoud, M. A., Mohammed, A. F., Salem, O. I., Almutairi, T. M., Bräse, S., and Youssif, B. G. (2024). Design, synthesis, and apoptotic antiproliferative action of new 1, 2, 3-triazole/1, 2, 4-oxadiazole hybrids as dual EGFR/VEGFR-2 inhibitors. *J. Enzyme Inhibition Med. Chem.* 39 (1), 2305856. doi:10.1080/14756366.2024.2305856

Mahmoud, M. A., Mohammed, A. F., Salem, O. I., Rabea, S. M., and Youssif, B. G. (2023). Design, synthesis, and antiproliferative properties of new 1, 2, 3-triazole-carboximidamide derivatives as dual EGFR/VEGFR-2 inhibitors. *J. Mol. Struct.* 1282, 135165. doi:10.1016/j.molstruc.2023.135165

Metibemu, D. S., Akinloye, O. A., Omotuyi, I. O., Okoye, J. O., Popoola, M. A., and Akamo, A. J. (2021). Carotenoid-enriched fractions from Spondias mombin demonstrate HER2 ATP kinase domain inhibition: computational and *in vivo* animal model of breast carcinoma studies. *Front. Oncol.* 11, 687190. doi:10.3389/fonc.2021.687190

Mitupatum, T., Aree, K., Kittisenachai, S., Roytrakul, S., Puthong, S., Kangsadalampai, S., et al. (2016). mRNA expression of Bax, Bcl-2, p53, cathepsin B, caspase-3 and caspase-9 in the HepG2 cell line following induction by a novel monoclonal Ab Hep88 mAb: cross-talk for paraptosis and apoptosis. *Asian Pac. J. Cancer Prev.* 17 (2), 703–712. doi:10.7314/apjcp.2016.17.2.703

Mohamed, A. M., Abou-Ghadir, O. M., Mostafa, Y. A., Dahlous, K. A., Bräse, S., and Youssif, B. G. (2024). Design and synthesis of new 1, 2, 4-oxadiazole/quinazoline-4-one hybrids with antiproliferative activity as multitargeted inhibitors. *Front. Chem.* 12, 1447618. doi:10.3389/fchem.2024.1447618

Ozcelik, F., Sertbakan, T. R., and Yalcin, S. (2023). Spectroscopic and *in silico* characterization of irınotecan-loaded nanoparticles: *in vitro* evaluation for breast cancer treatment. *Russ. J. Phys. Chem. A* 97 (13), 3089–3103. doi:10.1134/s0036024423130095

Pernas, S., and Tolaney, S. M. (2019). HER2-positive breast cancer: new therapeutic frontiers and overcoming resistance. *Ther. Adv. Med. Oncol.* 11, 1758835919833519. doi:10.1177/1758835919833519

Piha-Paul, S. A., Tseng, C., Tran, H. T., Gao, M., Karp, D. D., Subbiah, V., et al. (2023). A phase I trial of the pan-ERBB inhibitor neratinib combined with the MEK inhibitor trametinib in patients with advanced cancer with EGFR mutation/amplification, HER2 mutation/amplification, HER3/4 mutation or KRAS mutation. *Cancer Chemother. Pharmacol.* 92 (2), 107–118. doi:10.1007/s00280-023-04545-4

Rego, T., Silva, G. M., Goldmann, M., Filipe, E. J., and Morgado, P. (2022). Optimized all-atom force field for alkynes within the OPLS-AA framework. *Fluid Phase Equilibria* 554, 113314. doi:10.1016/j.fluid.2021.113314

Ramadan, M., Abd El-Aziz, M., Elshaier, Y. A., Youssif, B. G., Brown, A. B., Fathy, H. M., et al. (2020). Design and synthesis of new pyranoquinolinone heteroannulated to triazolopyrimidine of potential apoptotic antiproliferative activity. *Bioorg. Chem.* 105, 104392. doi:10.1016/j.bioorg.2020.104392

Ravikumar, B., Cichońska, A., Sahni, N., Aittokallio, T., and Rahman, R. (2025). Advancements in rational multi-targeted drug discovery: improving the efficacy-safety balance of small molecule cancer therapeutics. *Polypharmacology Strategies Multi-Target Drug Discov.*, 109–125.

Şenkardeş, S., Han, M. İ., Kulabaş, N., Abbak, M., Çevik, Ö., Küçükgüzel, İ., et al. (2020). Synthesis, molecular docking and evaluation of novel sulfonyl hydrazones as anticancer agents and COX-2 inhibitors. *Mol. Divers.* 24, 673–689. doi:10.1007/s11030-019-09974-z

Sheldrick, G. M. (2015). *SHELXT*– Integrated space-group and crystal-structure determination. *Acta Crystallogr. A* 71, 3–8. doi:10.1107/s2053273314026370

Soliman, A. M., Alqahtani, A. S., and Ghorab, M. M. (2019). Novel sulfonamide benzoquinazolinones as dual EGFR/HER2 inhibitors, apoptosis inducers and radiosensitizers. *J. Enzyme Inhibition Med. Chem.* 34 (1), 1030–1040. doi:10.1080/14756366.2019.1609469

Stanzione, F., Giangreco, I., and Cole, J. C. (2021). Use of molecular docking computational tools in drug discovery. *Prog. Med. Chem.* 60, 273–343.

Tang, X.-Y., and Shi, M. (2008). Vilsmeier– haack reaction of 1-cyclopropyl-2-arylethanones. *J. Org. Chem.* 73 (21), 8317–8320. doi:10.1021/jo801492k

Tripathi, K. L., Dwivedi, V. D., and Badoni, H. (2025). Pharmacophore modeling and molecular dynamics simulations to study the conformational stability of natural HER2 inhibitors in breast cancer therapy. *Mol. Divers.*, 1–25. doi:10.1007/s11030-025-11165-y

Tsang, R. Y., Sadeghi, S., and Finn, R. S. (2011). Lapatinib, a dual-targeted small molecule inhibitor of EGFR and HER2, in HER2-amplified breast cancer: from bench to bedside. *Clin. Med. Insights Ther.* 3. CMT. S3783. doi:10.4137/cmt.s3783

Voigtlaender, M., Schneider-Merck, T., and Trepel, M. (2018). Lapatinib. *Small Mol. Oncol.* 211, 19–44. doi:10.1007/978-3-319-91442-8_2

Wissner, A., Berger, D. M., Boschelli, D. H., Floyd, M. B., Greenberger, L. M., Gruber, B. C., et al. (2000). 4-Anilino-6, 7-dialkoxyquinoline-3-carbonitrile inhibitors of epidermal growth factor receptor kinase and their bioisosteric relationship to the 4-anilino-6, 7-dialkoxyquinazoline inhibitors. *J. Med. Chem.* 43 (17), 3244–3256. doi:10.1021/jm000206a

Wu, Z., Wang, J., You, F., Li, X., and Xiao, C. (2023). The role of irreversible pan-HER tyrosine kinase inhibitors in the treatment of HER2-Positive metastatic breast cancer. *Front. Pharmacol.* 14, 1142087. doi:10.3389/fphar.2023.1142087

Wu, X., Gu, R., Tang, M., Mu, X., He, W., and Nie, X. (2025). Elucidating the dual roles of apoptosis and necroptosis in diabetic wound healing: implications for therapeutic intervention. *Burns Trauma* 13, tkae061. doi:10.1093/burnst/tkae061

Zimmer, A. S., Van Swearingen, A. E., and Anders, C. K. (2022). HER2-positive breast cancer brain metastasis: a new and exciting landscape. *Cancer Rep.* 5 (4), e1274. doi:10.1002/cnr2.1274

frontiers | Frontiers in Chemistry

TYPE Original Research
PUBLISHED 23 September 2025
DOI 10.3389/fchem.2025.1650302

Check for updates

OPEN ACCESS

EDITED BY
Naohiko Yoshikai,
Tohoku University, Japan

REVIEWED BY
Mattan Hurevich,
Hebrew University of Jerusalem, Israel
Sagnik Sengupta,
University of Texas Southwestern Medical Center, United States

*CORRESPONDENCE
Shang-Cheng Hung,
schung@gate.sinica.edu.tw

RECEIVED 19 June 2025
ACCEPTED 13 August 2025
PUBLISHED 23 September 2025

CITATION
Lin J-S, Tzeng Z-H, Dumalaog JS and Hung S-C (2025) A streamlined synthetic approach to the truncated linear trisaccharide fragment of QS-21.
Front. Chem. 13:1650302.
doi: 10.3389/fchem.2025.1650302

COPYRIGHT
© 2025 Lin, Tzeng, Dumalaog and Hung. This is an open-access article distributed under the terms of the Creative Commons Attribution License (CC BY). The use, distribution or reproduction in other forums is permitted, provided the original author(s) and the copyright owner(s) are credited and that the original publication in this journal is cited, in accordance with accepted academic practice. No use, distribution or reproduction is permitted which does not comply with these terms.

A streamlined synthetic approach to the truncated linear trisaccharide fragment of QS-21

Jhe-Sian Lin[1,2], Zheng-Hao Tzeng[2], Jasper S. Dumalaog[2,3] and Shang-Cheng Hung[2,3,4,5]*

[1]Institute of Biochemistry and Molecular Biology, National Yang Ming Chiao Tung University, Taipei, Taiwan, [2]Genomics Research Center, Academia Sinica, Taipei, Taiwan, [3]Department of Chemistry, National Tsing Hua University, Hsinchu, Taiwan, [4]Department of Applied Science, National Taitung University, Taitung, Taiwan, [5]Department of Chemistry, National Cheng Kung University, Tainan, Taiwan

QS-21, a potent immunostimulatory saponin obtained from *Quillaja saponaria* Molina, a soapbark tree native to Chile, has undergone extensive study for its broad application as a vaccine adjuvant against various infectious diseases and cancers. The structure of QS-21, which features a linear oligosaccharide moiety, provides a critical attachment site for both the labile acyl side chain and the distinctive sugar unit that defines each major saponin variant. In this study, we present an efficient synthetic approach to the truncated linear trisaccharide fragment of QS-21, circumventing the challenges associated with the synthesis of the rare sugar D-fucose. The synthesis of this linear trisaccharide enables streamlined access to a homogeneous QS-21.

KEYWORDS

QS-21, linear trisaccharide, glycosylation, carbohydrate chemistry, vaccine adjuvant

1 Introduction

Adjuvants play a crucial role in enhancing vaccine effectiveness by stimulating the immune system to produce a robust response (Reed et al., 2013). Among vaccine adjuvants, QS-21 stands out for its potent immunostimulatory properties. It is a natural saponin derived from the bark of the Chilean soapbark tree, *Quillaja saponaria* (QS) Molina, which contains over 100 structurally related QS saponins due to its diverse composition (Reed et al., 2023). QS-21 is identified as the 21st fraction of 22 obtained from the reverse-phase high-performance liquid chromatography (HPLC) of the semi-purified QS extract with potent adjuvant activity, hence its name (Kensil et al., 1991; Martin et al., 2024). Currently, QS-21 has been the most extensively studied saponin adjuvant for over 28 years (Ragupathi et al., 2011). It has been shown to stimulate both cellular (Th1) and humoral (Th2) immune responses, making it highly effective in enhancing immunogenicity (Fernández-Tejada et al., 2014; Pink and Kieny, 2004). In 2017, QS-21 was first licensed for human use as a vaccine adjuvant, specifically for the herpes zoster vaccine Shingrix® (Lacaille-Dubois, 2019). Extensive clinical studies have demonstrated its strong immunostimulatory effects, significantly improving vaccine efficacy against a range of infectious diseases and cancers (Garçon and Van Mechelen, 2011; Gin and Slovin, 2011).

The structure of QS-21, as illustrated in Figure 1, consists of a quillaic acid triterpene attached to branched trisaccharide and linear oligosaccharide moieties. QS-21 is a mixture of two isomers, apiose- (65%) and xylose-containing (35%) oligosaccharides, attached to the D-xylose ring of the linear trisaccharide group. These two isomers were found to have

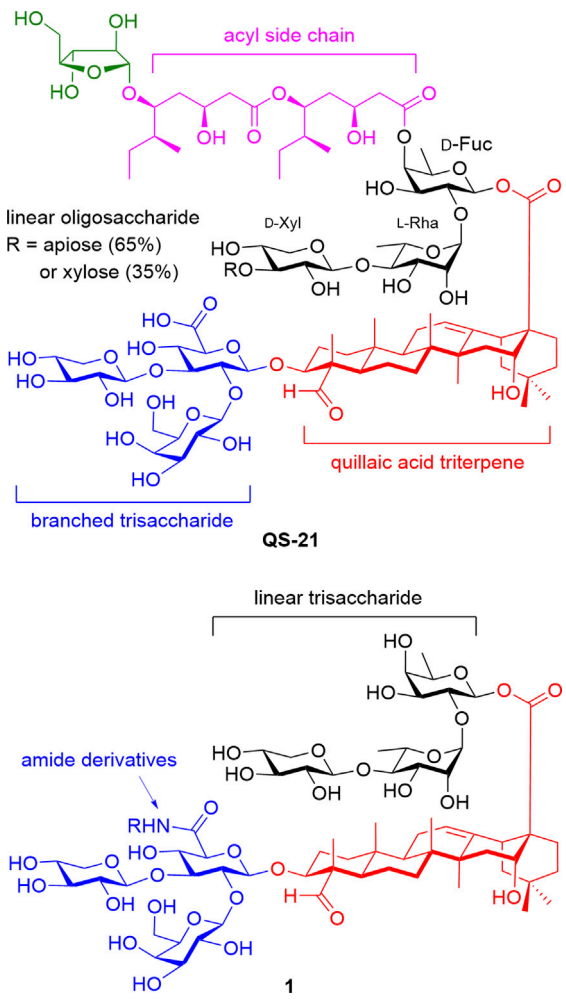


FIGURE 1
Structure of QS-21 and its saponin conjugate **1**.

similar adjuvanticity and toxicity (Ragupathi et al., 2010). A labile acyl side chain containing an arabinofuranose ring is connected to the D-fucose ring of the linear oligosaccharide. Despite its immunostimulatory properties, the instability of the acyl side chain and the challenges associated with its low-yielding purification limit the broader application of QS-21. Moreover, the loss of the lipophilic side chain due to the hydrolysis of the ester linkage results in the loss of its adjuvanticity (Marciani et al., 2001).

Numerous efforts have been undertaken to synthesize analogs of QS-21 with comparable or enhanced potency to mitigate these challenges. Wang et al. (2005) achieved the pioneering total synthesis of QS-21 and its definitive structural characterization. Additionally, they conducted an efficient semi-synthesis of various QS-21 variants to develop immunoadjuvants with improved chemical stability (Chea et al., 2012; Fernández-Tejada et al., 2016). Liang et al. (2020) patented the synthesis of saponin conjugates, including the truncated QS-21 moiety **1** (Figure 1), which enhances efficacy in both humoral and cell-mediated immunity. The structure of **1** comprises a truncated linear trisaccharide featuring a *β*-D-Xyl*p*-(1→4)-*α*-L-Rha*p*-(1→2)-*β*-D-Fuc*p* moiety linked to the quillaic acid triterpene.

In this study, we present an efficient and streamlined synthesis of the linear trisaccharide moiety derived from saponin conjugate **1**, offering an alternative approach to the synthesis of these QS-21 oligosaccharide units. Two complementary strategies, pre- and post-glycosylation deoxygenation, were explored to address key synthetic challenges. These included the efficient incorporation of the rare sugar D-fucose and the stereoselective construction of oligosaccharides featuring 1,2-*trans*-glycosidic bonds, both of which are pivotal for constructing the biologically relevant glycan structure.

2 Materials and methods

2.1 General procedures

All moisture-sensitive reactions were carried out under an N_2 atmosphere in flame-dried glassware. Solvents such as dichloromethane (CH_2Cl_2), acetonitrile (CH_3CN), and tetrahydrofuran (THF) were distilled using a purification system with activated Al_2O_3. All commercially obtained reagents were used without additional purification, unless specified otherwise. All distilled water used was purified using a Milli-Q system. Prior to all glycosylations, the starting materials were thoroughly dried under high vacuum in a desiccator. Thin-layer chromatography (TLC) analysis was conducted on Silica Gel 60G F_{254} glass plates (0.25 mm, E. Merck from Germany). TLC analysis was performed with visualization under ultraviolet light (UV-254 nm), and staining was carried out by spraying with a solution of Hanessian's reagent containing $Ce(NH_4)_2(NO_3)_6$, $(NH_4)_6Mo_7O_{24}$, and H_2SO_4 in water, followed by heating on a hot plate. Flash column chromatography was conducted on Silica Gel 60 (230–400 mesh, E. Merck).

Specific rotations were measured at ambient temperature using a HORIBA SEPA-300 High-Sensitive Polarimeter from Kyoto, Japan at 589 nm (sodium D line) and reported in 10^{-1}·deg·cm^2·g^{-1}, with sample concentrations given in g·dL^{-1}. IR spectra were recorded on KBr plates using a PerkinElmer Spectrum 100 FT-IR Spectrometer from Waltham, Massachusetts, USA. 1D and 2D NMR spectra were acquired using a Bruker Avance III 600 MHz spectrometer from Billerica, Massachusetts, USA at ambient temperature. Data were recorded as follows: chemical shift in ppm from the solvent resonance used as the internal standard ($CDCl_3$ at 7.26 ppm), multiplicity (s, singlet; d, doublet; t, triplet; q, quartet; m, multiplet), coupling constant in Hz, and integration. ^{13}C NMR spectra were obtained using a 150 MHz spectrometer, and chemical shifts were recorded in ppm relative to the solvent resonance used as the internal standard ($CDCl_3$ at 77.0 ppm). Mass spectra were acquired using an ESI Finnigan LCQ Mass Spectrometer (Thermo Finnigan from Waltham, Massachusetts, USA), performed at the Genomics Research Center.

2.2 Synthetic procedures and characterization data

2.2.1 Benzyl 2,3,4,6-tetra-*O*-acetyl-*β*-D-galactopyranoside (**9**)

To a stirred suspension of **14** (2.0 g, 5.12 mmol) in BnOH (1.1 mL), BF_3•Et_2O (2.6 mL, 20.5 mmol) was added at 0 °C under an

N_2 atmosphere. Upon completion of the reaction after 16 h, the mixture was diluted with CH_2Cl_2, washed with H_2O and brine, dried over $MgSO_4$, and then concentrated *in vacuo*. The residue was purified by column chromatography (silica gel; ethyl acetate/hexane = 1/4) to afford **9** (2.24 g, 75%). The IR spectrum (thin film) showed absorption bands at ν 2,924, 1,749, 1,369, and 1,221 cm^{-1}. The ^1H NMR spectrum (600 MHz, $CDCl_3$) exhibited signals at δ 7.35–7.22 (m, 5H, Ar-H), 5.36 (dd, J = 3.5, 1.2 Hz, 1H, H-4), 5.26 (dd, J = 10.5, 7.9 Hz, 1H, H-2), 4.96 (dd, J = 10.5, 3.5 Hz, 1H, H-3), 4.89 (d, J = 12.4 Hz, 1H, Ar-CH_2), 4.61 (d, J = 12.3 Hz, 1H, Ar-CH_2), 4.49 (d, J = 8.0 Hz, 1H, H-1), 4.22–4.09 (m, 2H, H-6), 3.86 (td, J = 6.7, 1.2 Hz, 1H, H-5), 2.14 (s, 3H, CH_3), 2.04 (s, 3H, CH_3), 1.99 (s, 3H, CH_3), and 1.95 (s, 3H CH_3). The ^{13}C NMR spectrum (150 MHz, $CDCl_3$) displayed resonances at δ 170.4 (C), 170.3 (C), 170.1 (C), 169.4 (C), 136.7 (C), 128.4 (CH), 127.9 (CH),127.7 (CH), 99.8 (CH), 70.9 (CH), 70.8 (CH_2), 70.7 (CH), 68.8 (CH), 67.0 (CH), 61.2 (CH_2), 20.8 (CH_3), 20.7 (CH_3), 20.7 (CH_3), and 20.6 (CH_3). High-resolution mass spectrometry (HRMS) (ESI) analysis showed a peak at m/z 456.1869, which is consistent with the calculated value of m/z 456.1864 for $C_{21}H_{26}O_{10}NH_4$ ($[M + NH_4]^+$).

2.2.2 Benzyl 3,4-*O*-isopropylidene-β-D-galactopyranoside (**8**)

Compound **9** (493.3 mg, 1.83 mmol) and MeOH (6 mL) were added to the flask, and the mixture was stirred at 0 °C for 30 min. NaOMe (19.4 mg, 0.36 mmol) was slowly added to the reaction mixture in 10 mg portions at 10 min intervals, and the mixture was then allowed to warm to room temperature (RT) and react overnight. The reaction progress was monitored by TLC (ethyl acetate/hexane = 1/2). The reaction mixture was neutralized with Dowex® 50W × 8 resin to pH 5–6, filtered directly, and concentrated (45 °C, below 25 mbar) to obtain an off-white solid. The solid was vacuum-dried for over 16 h and used directly in the following steps without additional purification.

To a stirred suspension of the crude intermediate in anhydrous CH_3CN (6 mL), 2,2-dimethoxypropane (2,2-DMP, 1.35 mL, 3.65 mmol) and 10-camphorsulfonic acid (CSA, 0.13 g, 0.55 mmol) were added at RT under an N_2 atmosphere. Upon completion of the reaction after 30 min, the mixture was diluted with CH_2Cl_2, washed with H_2O and brine, dried over $MgSO_4$, and then concentrated under reduced pressure. The residue was purified by column chromatography (silica gel; ethyl acetate/hexane = 3/2) to yield **8** (301 mg, 53%). The specific rotation was $[\alpha]^{29}_D$ +6.16 (*c* 0.6, $CHCl_3$). The IR spectrum (thin film) showed absorption bands at ν 3,400, 2,919, 1,454, and 1,040 cm^{-1}. The ^1H NMR spectrum (600 MHz, $CDCl_3$) exhibited signals at δ 7.34 (d, J = 4.4 Hz, 4H, Ar-H), 7.30 (ddt, J = 8.4, 6.9, 3.6 Hz, 1H, Ar-H), 4.90 (d, J = 11.7 Hz, 1H, Ar-CH_2), 4.64 (d, J = 11.7 Hz, 1H, Ar-CH_2), 4.27 (d, J = 8.2 Hz, 1H, H-1), 4.13 (dd, J = 5.5, 2.1 Hz, 1H, H-5), 4.07 (dd, J = 7.4, 5.5 Hz, 1H, H-3), 3.97 (dd, J = 12.8, 8.2 Hz, 1H, H-6a), 3.82 (qd, J = 5.4, 4.2, 2.2 Hz, 2H, 4-H, H-6b), 3.60 (t, J = 7.8 Hz, 1H), 2.43 (s, 1H, 2-OH), 2.07–2.02 (m, 1H, 6-OH), 1.59 (s, 3H, CH_3), and 1.32 (s, 3H, CH_3). The ^{13}C NMR spectrum (150 MHz, $CDCl_3$) displayed resonances at δ 136.6 (C), 128.4 (CH), 128.1 (CH), 127.9 (CH), 110.3 (C), 101.1 (CH), 78.6 (CH), 73.7 (CH), 73.5 (CH), 73.3 (CH), 71.2 (CH_2), 62.3 (CH_2), 27.9 (CH_3), and 26.1 (CH_3). HRMS (ESI) analysis showed a peak at m/z 328.1757, which is consistent with the calculated value of m/z 328.1755 for $C_{16}H_{22}O_6NH_4$ ($[M + NH_4]^+$).

2.2.3 Benzyl 6-*O*-acetyl-3,4-*O*-isopropylidene-β-D-galactopyranoside (**5**)

To a stirred suspension of **8** (76 mg, 0.25 mmol) in anhydrous CH_2Cl_2 (0.7 mL), Et_3N (0.23 g, 1.0 mmol) and Ac_2O (24 μL, 0.26 mmol) were added at 0 °C under an N_2 atmosphere. Upon completion of the reaction after 2 h, the mixture was diluted with CH_2Cl_2, washed with H_2O and brine, dried over $MgSO_4$, and then concentrated under reduced pressure. The residue was purified by column chromatography (silica gel; ethyl acetate/hexane = 1/2) to yield **5** (66.9 mg, 76%). The specific rotation was $[\alpha]^{28}_D$ +12.1 (*c* 1.0, $CHCl_3$). The IR spectrum (thin film) showed absorption bands at ν 3,454, 2,987, 1,741, 1,242, and 1,076 cm^{-1}. The ^1H NMR spectrum (600 MHz, $CDCl_3$) exhibited signals at δ 7.34 (d, J = 4.3 Hz, 4H, Ar-H), 7.30 (q, J = 4.4 Hz, 1H, Ar-H), 4.91 (d, J = 11.5 Hz, 1H, Ar-CH_2), 4.60 (d, J = 11.6 Hz, 1H, Ar-CH_2), 4.41–4.35 (m, 2H, H-6), 4.21 (d, J = 8.4 Hz, 1H, H-1), 4.13–4.09 (m, 1H, H-4), 4.04 (t, J = 6.5 Hz, 1H, H-3), 3.94 (t, J = 6.0 Hz, 1H, H-5), 3.60 (t, J = 7.9 Hz, 1H, H-2), 2.45 (s, 1H, 2-OH), 2.10 (d, J = 1.5 Hz, 3H, CH_3), 1.50 (s, 3H, CH_3), and 1.32 (s, 3H, CH_3). The ^{13}C NMR spectrum (150 MHz, $CDCl_3$) displayed resonances at δ 170.8 (C), 136.7 (C), 128.5 (CH), 128.3 (CH), 128.1 (CH), 110.6 (C), 101.8 (CH), 78.6 (CH), 73.5 (CH), 73.4 (CH), 71.2 (CH), 70.9 (CH_2), 63.5 (CH_2), 28.1 (CH_3), 26.3 (CH_3), and 20.9 (CH_3). HRMS (ESI) analysis showed a peak at m/z 370.1861, which is consistent with the calculated value of m/z 370.1860 for $C_{18}H_{24}O_7NH_4$ ($[M + NH_4]^+$).

2.2.4 Benzyl 6-*O*-methanesulfonyl-3,4-*O*-isopropylidene-β-D-galactopyranoside (**20**)

To a stirred suspension of **8** (60 mg, 0.194 mmol) in anhydrous CH_2Cl_2 (2.4 mL), Et_3N (27.1 μL, 0.194 mmol) and MsCl (15.1 μL, 0.388 mmol) were added at 0 °C under an N_2 atmosphere. Upon completion of the reaction after 1 h, the mixture was diluted with CH_2Cl_2, washed with H_2O and brine, dried over $MgSO_4$, and then concentrated under reduced pressure. The residue was purified by column chromatography (silica gel; ethyl acetate/hexane = 1/3) to afford **20** (47.5 mg, 63%). The specific rotation was $[\alpha]^{28}_D$ +7.80 (*c* 0.5, $CHCl_3$). The IR spectrum (thin film) showed absorption bands at ν 3,492, 2,922, 1,712, 1,355, and 1,073 cm^{-1}. The ^1H NMR spectrum (600 MHz, $CDCl_3$) exhibited signals at δ 7.34 (s, 3H, Ar-H), 7.38–7.27 (m, 2H, Ar-H), 4.90 (d, J = 11.6 Hz, 1H, Ar-CH_2), 4.62 (d, J = 11.6 Hz, 1H, Ar-CH_2), 4.51–4.42 (m, 2H, H-6), 4.25 (d, J = 8.3 Hz, 1H, H-1), 4.13 (dd, J = 5.6, 2.3 Hz, 1H, H-4), 4.11–4.04 (m, 2H, 3-H, H-5), 3.60 (td, J = 7.9, 1.9 Hz, 1H, H-2), 3.04 (s, 3H, SO_2CH_3), 2.40 (d, J = 2.4 Hz, 1H, OH), 1.50 (s, 3H, CH_3), and 1.32 (s, 3H, CH_3). The ^{13}C NMR spectrum (150 MHz, $CDCl_3$) displayed resonances at δ 136.5 (C), 128.61 (CH), 128.28 (CH), 128.24 (CH), 110.7 (C), 100.83 (CH), 78.6 (CH), 73.4 (CH), 73.0 (CH), 71.2 (CH_2), 68.7 (CH_2), 37.38 (CH_3), 28.00 (CH_3), and 26.31 (CH_3). HRMS (ESI) analysis showed a peak at m/z 406.1535, which is consistent with the calculated value of m/z 406.1530 for $C_{17}H_{24}O_8SNH_4$ ($[M + NH_4]^+$).

2.2.5 Benzyl 6-deoxy-6-iodo-3,4-*O*-isopropylidene-β-D-galactopyranoside (**21**)

To a solution of **20** (20.2 mg, 0.059 mmol) in DMF (2.0 mL), tetrabutylammonium iodide (TBAI) (19.2 mg, 0.059 mmol) and KI (29.7 mg, 0.179 mmol) were added. The solution was stirred at 120 °C for 26 h, then cooled to RT, diluted with water, and extracted

using ethyl acetate. The combined organic layer was washed with saturated aqueous $Na_2S_2O_3$ and brine and then dried over anhydrous Na_2SO_4. The organic layer was evaporated, and the residue was purified by silica gel chromatography (silica gel; ethyl acetate/hexane = 1/3) to afford **21** (24.8 mg, 72%). The specific rotation was $[\alpha]^{28}_D$ +12.1 (*c* 0.5, $CHCl_3$). The IR spectrum (thin film) showed absorption bands at ν 3,432, 2,920, and 1,065 cm^{-1}. The ^1H NMR spectrum (600 MHz, $CDCl_3$) exhibited signals at δ 7.40–7.32 (m, 4H, Ar-H), 7.34–7.27 (m, 1H, Ar-H), 4.95 (d, *J* = 11.6 Hz, 1H, Ar-CH_2), 4.65 (d, *J* = 11.7 Hz, 1H, Ar-CH_2), 4.27 (dd, *J* = 5.5, 2.3 Hz, 1H, H-4), 4.22 (d, *J* = 8.3 Hz, 1H, H-1), 4.05 (dd, *J* = 7.4, 5.4 Hz, 1H, H-3), 3.88 (ddd, *J* = 7.3, 6.7, 2.3 Hz, 1H, H-5), 3.59 (ddd, *J* = 8.3, 7.4, 2.3 Hz, 1H, H-2), 3.43 (dd, *J* = 7.0, 0.9 Hz, 2H, H-6a, H-6b), 2.34 (d, *J* = 2.3 Hz, 1H, OH), 1.50 (s, 3H, CH_3), and 1.34 (d, *J* = 0.8 Hz, 3H, CH_3). The ^{13}C NMR spectrum (150 MHz, $CDCl_3$) displayed resonances at δ 136.6 (C), 128.6 (CH), 128.5 (CH), 128.2 (CH), 110.29 (C), 100.62 (CH), 78.7 (CH), 74.0 (CH), 73.8 (CH), 73.5 (CH), 70.79 (CH_2), 28.1 (CH_3), 26.2 (CH_3), and 1.86 (CH_2). HRMS (ESI) analysis showed a peak at *m/z* 438.0777, which is consistent with the calculated value of *m/z* 438.0772 for $C_{16}H_{21}IO_5NH_4$ ([M + NH_4]$^+$).

2.2.6 Benzyl 3,4-*O*-isopropylidene-β-D-fucopyranoside (**10**)

To a solution of **21** (10.1 mg, 0.024 mmol) in THF/MeOH = 10/1 (2 mL), $Pd(OH)_2$/C (20% wt, 10.1 mg) was added. The resulting suspension was stirred under $H_{2(g)}$ at room temperature and atmospheric pressure for 6 h. The reaction mixture was filtered through Celite and concentrated under reduced pressure. The residue was purified by silica gel chromatography (silica gel; ethyl acetate/hexane = 1/3) to afford **10** (6.72 mg, 95%). The specific rotation was $[\alpha]^{29}_D$ −28.5 (*c* 0.1, $CHCl_3$). The IR spectrum (thin film) showed absorption bands at ν 3,445, 2,926, and 1,071 cm^{-1}. The ^1H NMR spectrum (600 MHz, $CDCl_3$) displayed signals at δ 7.37–7.31 (m, 4H, Ar-H), 7.29 (ddt, *J* = 8.8, 6.6, 3.0 Hz, 1H, Ar-H), 4.92 (dd, *J* = 11.6, 1.6 Hz, 1H, Ar-CH_2), 4.57 (dd, *J* = 11.6, 1.8 Hz, 1H Ar-CH_2), 4.21 (dd, *J* = 8.3, 1.6 Hz, 1H, H-1), 4.03–3.98 (m, 1H, H-3), 4.00–3.96 (m, 1H, H-4), 3.84 (qd, *J* = 6.6, 3.5 Hz, 1H, H-5), 3.61–3.55 (m, 1H, H-2), 2.35 (s, 1H, OH), 1.52 (s, 3H, CH_3), 1.43 (dd, *J* = 6.6, 1.7 Hz, 3H, H-6), and 1.34 (s, 3H, CH_3). The ^{13}C NMR spectrum (150 MHz, $CDCl_3$) exhibited resonances at δ 137.0 (C), 128.5 (CH), 128.3 (CH), 128.0 (CH), 109.9 (C), 100.9 (CH), 78.7(CH), 76.3 (CH), 73.6 (CH), 70.8 (CH_2), 69.2 (CH), 28.2 (CH_3), 26.3 (CH_3), and 16.6 (CH_3). HRMS (ESI) analysis showed a peak at *m/z* 312.1810, which is consistent with the calculated value of *m/z* 312.1805 for $C_{16}H_{22}O_5NH_4$ ([M + NH_4]$^+$).

2.2.7 2,3,4-Tri-*O*-acetyl-α,β-D-xylopyranoside (**12**)

A 12-L reaction flask and a 1-L addition funnel were dried and allowed to cool to room temperature. D-Xylose (500 g, 3.33 mol), Et_3N (2.8 L, 19.9 mol), and DMAP (40.7 g, 0.33 mol) were added to the flask, and the mixture was cooled to 0 °C and stirred for 30 min. Ac_2O (1.57 L, 16.6 mol) was placed in an addition funnel and added dropwise over approximately 1 h. The mixture changed from pale yellow and turbid to dark brown while remaining turbid. The reaction was stirred for approximately 3 h. The reaction progress was monitored by TLC (ethyl acetate/hexane = 1/1). The reaction mixture was quenched by pouring into 2 L of ice water, extracted with ethyl acetate, and washed with saturated aqueous $NaHCO_3$ solution. The organic layer was dried over $MgSO_4$, filtered, concentrated (45 °C, below 20 mbar), and used directly in the subsequent steps. Mechanical stirring was set up for a 20-L reaction flask. Compound **12** and THF were added to the flask, and the mixture was cooled to 0 °C and stirred for 30 min. $BnNH_2$ (610.2 g, 5.59 mol) was added dropwise using a 1-L addition funnel. The mixture was allowed to warm to room temperature and react overnight. The reaction progress was monitored by TLC (ethyl acetate/hexane = 1/1). The reaction mixture was quenched with 1 N $HCl_{(aq)}$ and neutralized to a pH of 0–2. The mixture was extracted twice with ethyl acetate/brine, dried over $MgSO_4$, filtered, and concentrated (45 °C, below 30 mbar). The crude product was then subjected to 151G3 flash column chromatography in three batches. The 151G3 flash column (diameter: 18 cm; height: 20 cm; volume: approximately 5 L) was loaded with crude product (approximately 300 g) that had been premixed with silica gel (approximately 300 g) in an ethyl acetate/hexane = 1/2 mixture. The column was packed with 2 L of silica gel, followed by the addition of the crude solution. The column was eluted with an ethyl acetate/hexane = 1/2 mixture (approximately 3 L per 8 fractions). The eluent was concentrated (45 °C, below 15 mbar) and allowed to stand overnight, yielding a precipitate. The solid was washed with hexane, dried under vacuum, and afforded a white solid (561 g) with a yield of 62% (over two steps). The specific rotation was $[\alpha]^{28}_D$ +58.4 (*c* 1.0, $CHCl_3$). The IR spectrum (thin film) showed absorption bands at ν 3,393, 2,947, 1,757, 1,230, and 1,052 cm^{-1}.

2.2.8 *p*-Methylphenyl 2,3-*O*-isopropylidene-1-thio-α-L-rhamnopyranoside (**7**)

A 5-L reaction flask was dried and allowed to cool to room temperature. Compound **13** (300 g, 0.757 mol) and MeOH (3 L) were added to the flask, and the mixture was stirred at 0 °C for 30 min. NaOMe (40.9 g, 0.757 mol) was slowly added to the reaction mixture in 10 g portions at 10 min intervals, and the mixture was allowed to warm to room temperature and react overnight. The reaction progress was monitored by TLC (ethyl acetate/hexane = 2/1). The reaction mixture was neutralized with Dowex® 50W × 8 resin (prewashed twice with MeOH, approximately 330 g) to a pH of 5–6, filtered directly, and concentrated (45 °C, below 25 mbar) to obtain an off-white solid. The solid was dried under vacuum for over 16 h and then used directly in the subsequent steps without further purification.

Crude intermediates, CH_3CN, 2,2-DMP (182.4 mL, 1.48 mol), and CSA (51.6 g, 0.222 mol), were added to the dried 5-L reaction flask, and the mixture was stirred at room temperature for 60 min. The reaction progress was monitored by TLC (ethyl acetate/hexane = 2/1 and ethyl acetate/hexane = 1/3). If the reaction was incomplete, the mixture was directly concentrated to dryness and step 2 was repeated with the addition of CH_3CN and 2,2-DMP. Upon completion of the reaction, the mixture was quenched with Et_3N, concentrated to dryness, and subjected to thin-layer chromatography using ethyl acetate/hexane = 1/2 as the eluent. The concentrated product was then subjected to azeotropic distillation with toluene (45 °C, below 25 mbar). The resulting solid was allowed to precipitate and washed thrice with hexane. The product was dried under vacuum to obtain **7** (169.2 g, 72% over two steps) as a yellow solid. The specific rotation was $[\alpha]^{28}_D$ −196.2 (*c* 1.0, $CHCl_3$). The IR spectrum (thin film) showed absorption bands at ν 3,447, 2,984, and 1,065 cm^{-1}.

2.2.9 *p*-Methylphenyl 2,3,4-tri-*O*-acetyl-*β*-D-xylopyranosyl-(1→4)-2,3-*O*-isopropylidene-1-thio-*α*-L-rhamnopyranoside (**15**)

Compound **12** (50 g, 0.181 mol), CCl_3CN (500 mL), and Cs_2CO_3 (176.9 g, 0.543 mol) were sequentially added to the reaction flask and stirred at RT for approximately 30 min. The reaction progress was monitored by TLC (ethyl acetate/hexane = 1/2). The reaction mixture was filtered through Celite and concentrated to obtain crude product **6**. This crude product was then subjected to vacuum drying for 16 h together with compound **7** (56.2 g, 0.181 mol). Then, 5 Å molecular sieve powder was activated by heating and allowed to cool to room temperature. It was then added to the reaction flask along with CH_2Cl_2, and the mixture was stirred for 1 h. The reaction mixture was cooled to −78 °C, followed by the addition of 6.5 mL of TMSOTf. The mixture was stirred for 2 h. The temperature of the reaction mixture was gradually increased to 0 °C, and an additional 16.4 mL of TMSOTf was added. The mixture was stirred for 3 h. The reaction progress was monitored by TLC (ethyl acetate/hexane = 1/2). The reaction mixture was filtered through Celite, neutralized with $Na_2CO_{3(aq)}$, and extracted with CH_2Cl_2. The organic layer was dried over $MgSO_4$, filtered, and concentrated. The residue was purified by column chromatography (silica gel; ethyl acetate/hexane = 2/3) to yield **15** (42.73 g, 53%). The specific rotation was $[\alpha]^{28}_D$ −193.6 (*c* 1.0, $CHCl_3$). The IR spectrum (thin film) showed absorption peaks at *ν* 2,984, 1,757, 1,230, and 1,054 cm^{-1}. The ^1H NMR spectrum (600 MHz, $CDCl_3$) displayed signals at δ 7.36–7.30 (m, 2H, Ar-H), 7.10 (d, *J* = 7.9 Hz, 2H, Ar-H), 5.62 (s, 1H, H-1), 5.18 (t, *J* = 8.5 Hz, 1H, H-2′), 4.99 (d, *J* = 6.8 Hz, 1H, H-1′), 4.96–4.86 (m, 2H, H-4′, H-3′), 4.27 (d, *J* = 5.5 Hz, 1H, H-2), 4.13–4.02 (m, 3H, H-3, H-5, H-5a′), 3.57 (dd, *J* = 10.0, 7.5 Hz, 1H, H-4), 3.33 (dd, *J* = 11.8, 8.6 Hz, 1H, H-5b′), 2.31 (s, 3H, CH_3), 2.08 (s, 3H, CH_3), 2.02 (s, 6H, CH_3), 1.49 (s, 3H, CH_3), 1.33 (s, 3H, CH_3), and 1.18 (d, *J* = 6.2 Hz, 3H, H-6). The ^{13}C NMR spectrum (150 MHz, $CDCl_3$) exhibited resonances at δ 170.1 (C), 169.9 (C), 169.7 (C), 138.0 (C), 132.7 (CH), 129.9 (CH), 129.3 (C), 109.6 (C), 99.4 (CH), 84.05 (CH), 79.0 (CH), 77.9 (CH), 77.0 (CH), 71.4 (CH), 71.0 (CH), 69.1 (CH), 65.56 (CH), 62.0 (CH_2), 27.9 (CH_3), 26.5 (CH_3), 21.2 (CH_3), 20.8 (CH_3), 20.7 (CH_3), 17.3 (CH_3), and 14.2 (CH_3). HRMS (ESI) analysis showed a peak at *m/z* 586.2319, which is consistent with the calculated value of *m/z* 586.2317 for $C_{27}H_{36}O_{11}SNH_4$ ($[M + NH_4]^+$).

2.2.10 *p*-Methylphenyl 2,3,4-tri-*O*-acetyl-*β*-D-xylopyranosyl-(1→4)-2,3-di-*O*-acetyl-1-thio-α-L-rhamnopyranoside (**4**)

A solution of **15** (4.6 g, 8.1 mmol) in 2% HCl/MeOH (100 mL) was prepared and stirred for 16 h. The resulting mixture was evaporated and then azeotropically distilled with toluene (50 mL) twice under reduced pressure. After drying under high vacuum, the crude syrup was treated with Ac_2O (2.2 mL, 23.1 mmol), Et_3N (5.2 mL, 38.1 mmol), and DMAP (9 mg, 0.074 mmol) in CH_2Cl_2 under an N_2 atmosphere at RT. Upon completion of the reaction after 2 h, the mixture was diluted with CH_2Cl_2, washed with H_2O and brine, dried over $MgSO_4$, and then concentrated under reduced pressure. The residue was purified by column chromatography (silica gel; ethyl acetate/hexane = 2/3) to yield **4** (3.8 g, 81%). The specific rotation was $[\alpha]^{28}_D$ −132.9 (*c* 1.0, $CHCl_3$). The IR spectrum (thin film) showed absorption bands at *ν* 2,940, 1,751, 1,223, and 1,054 cm^{-1}. The ^1H NMR spectrum (600 MHz, $CDCl_3$) exhibited signals at δ 7.34–7.30 (m, 2H, Ar-H), 7.09 (d, *J* = 7.9 Hz, 2H, Ar-H), 5.37 (dd, *J* = 3.4, 1.6 Hz, 1H, H-2), 5.24 (d, *J* = 1.6 Hz, H-1), 5.20 (dd, *J* = 9.7, 3.4 Hz, 1H, 1H, H-3), 5.12 (t, *J* = 9.2 Hz, 1H, H-3′), 4.94 (td, *J* = 9.3, 5.4 Hz, 1H, H-4′), 4.88 (dd, *J* = 9.5, 7.6 Hz, 1H, H-2′), 4.64 (d, *J* = 7.6 Hz, 1H, H-1′), 4.22 (dq, *J* = 9.5, 6.2 Hz, 1H, H-5), 4.10 (dd, *J* = 11.7, 5.4 Hz, 1H, H-5′a), 3.70 (t, *J* = 9.6 Hz, 1H, H-4), 3.32 (dd, *J* = 11.8, 9.6 Hz, 1H, H-5′b), 2.29 (s, 3H, CH_3), 2.08 (d, *J* = 13.0 Hz, 6H, CH_3), 2.03–1.98 (m, 9H, CH_3), and 1.29 (d, *J* = 6.2 Hz, 3H, CH_3). The ^{13}C NMR spectrum (150 MHz, $CDCl_3$) displayed resonances at δ 170.3 (C), 169.9 (C), 169.9 (C), 169.6 (C), 169.6 (C), 138.2 (C), 132.7 (CH), 129.9 (CH), 129.3 (C), 101.07 (CH), 85.7 (CH), 76.5 (CH), 72.2 (CH), 71.7 (CH), 71.6 (CH), 71.1 (CH), 69.2 (CH), 68.1(CH), 62.5 (CH_2), 21.1 (CH_3), 21.0 (CH_3), 20.9 (CH_3), 20.8 (CH_3), 20.7 (CH_3), 20.5 (CH_3), and 17.4 (CH_3). HRMS (ESI) analysis showed a peak at *m/z* 630.2215, which is consistent with the calculated value of *m/z* 630.2215 for $C_{28}H_{36}O_{13}SNH_4$ ($[M + NH_4]^+$).

2.2.11 Benzyl 2,3,4-tri-*O*-acetyl-*β*-D-xylopyranosyl-(1→4)-2,3-di-*O*-acetyl-*α*-L-rhamnopyranosyl-(1→2)-6-*O*-acetyl-3,4-*O*-isopropylidene-*β*-D-galactopyranoside (**16**)

To a stirred suspension of **4** (53.0 mg, 0.086 mmol), **5** (25.4 mg, 0.072 mmol), and activated 5 Å molecular sieve powder in anhydrous CH_2Cl_2 (1.6 mL), NIS (19.5 mg, 0.086 mmol) and TfOH (1.5 μL, 0.017 mmol) were added at 0 °C under an N_2 atmosphere. Upon completion of the reaction after 30 min, the reaction was quenched by the addition of Et_3N, saturated $NaHCO_3$, and 10% $Na_2S_2O_3$ aqueous solution. After warming and stirring at RT for 1 h, the reaction mixture was filtered, diluted with CH_2Cl_2, washed with 10% $Na_2S_2O_3$ aqueous solution, saturated $NaHCO_3$, and brine, dried over $MgSO_4$, and concentrated under reduced pressure. The residue was purified by column chromatography (silica gel; ethyl acetate/hexane = 1/2) to yield **16** (46.1 mg, 76%) as a white solid. The specific rotation was $[\alpha]^{26}_D$ −70.2 (*c* 1.5, $CHCl_3$). The IR spectrum (thin film) showed absorption peaks at *ν* 2,935, 1,748, 1,223, and 1,051 cm^{-1}. The ^1H NMR spectrum (600 MHz, $CDCl_3$) exhibited signals at δ 7.37–7.32 (m, 2H, Ar-H), 7.32–7.27 (m, 3H, Ar-H), 5.23–5.16 (m, 2H, H-2′, H-3′), 5.13–5.05 (m, 2H, H-1′, H-3′), 4.93 (td, *J* = 9.0, 5.3 Hz, 1H, H-4′), 4.89–4.80 (m, 2H, H-2″, Ar-CH_2), 4.64–4.57 (m, 2H, H-1″, Ar-CH_2), 4.39–4.26 (m, 3H, H-1, H-6a, H-6b), 4.15–4.10 (m, 1H, H-3), 4.07 (ddd, *J* = 11.5, 6.0, 3.5 Hz, 3H, H-4, H-5′, H-5a”), 3.87 (ddd, *J* = 7.3, 4.7, 2.2 Hz, 1H, H-5), 3.74–3.68 (m, 1H, H-2), 3.58 (t, *J* = 9.6 Hz, 1H, H-4′), 3.31 (dd, *J* = 11.9, 9.2 Hz, 1H, H-5b”), 2.10 (d, *J* = 7.8 Hz, 6H), 2.05 (s, 3H, CH_3), 2.01 (s, 3H, CH_3), 1.97 (d, *J* = 9.4 Hz, 6H, CH_3), 1.47 (s, 3H, CH_3), 1.27 (s, 3H, CH_3), and 1.07 (d, *J* = 6.1 Hz, 3H, H-6′). The ^{13}C NMR spectrum (150 MHz, $CDCl_3$) displayed resonances at δ 170.79 (C), 170.25 (C), 170.03 (C), 169.88 (C), 169.86 (C), 169.28 (C), 136.45 (C), 128.57 (CH), 128.53 (CH), 128.05 (CH), 110.62 (C), 101.02 (CH), 98.72 (CH), 96.24 (CH), 79.72 (CH), 76.49 (CH), 75.80 (CH), 73.65 (CH), 72.15 (CH), 71.70 (CH), 71.14 (CH), 70.80 (CH), 70.48 (CH_2), 70.01 (CH), 69.30 (CH), 66.82 (CH), 63.45 (CH_2), 62.41 (CH_2), 27.87 (CH_3), 26.32 (CH_3), 21.03 (CH_3), 20.88 (CH_3), 20.74 (CH_3), 20.69 (CH_3), 20.42 (CH_3), and 17.20 (CH_3). HRMS (ESI) analysis showed a peak at *m/z* 858.3399, which is consistent with the calculated value of *m/z* 858.3390 for $C_{39}H_{52}O_{20}NH_4$ ($[M + NH_4]^+$).

2.2.12 Benzyl 2,3,4-tri-*O*-acetyl-*β*-D-xylopyranosyl-(1→4)-2,3-di-*O*-acetyl-*α*-L-rhamnopyranosyl-(1→2)-6-*O*-methanesulfonyl-3,4-*O*-isopropylidene-*β*-D-galactopyranoside (**17**)

To a stirred suspension of **16** (50.3 mg, 0.059 mmol) in anhydrous CH_2Cl_2 (5.0 mL), 7%–8% $Mg(OMe)_2$ (0.5 mL) was added at 0 °C under an N_2 atmosphere. Upon completion of the reaction after 1 h, the mixture was diluted with CH_2Cl_2, washed with H_2O and brine, dried over $MgSO_4$, and then concentrated under reduced pressure. The resulting mixture was evaporated and then azeotropically distilled with toluene (50 mL) twice under reduced pressure to generate crude intermediate **3**. After drying under high vacuum, the crude syrup containing **3** was treated with Et_3N (16.6 μL, 0.119 mmol) and MsCl (9.2 μL, 0.119 mmol) at 0 °C in anhydrous CH_2Cl_2 (5 mL) under an N_2 atmosphere. Upon completion of the reaction after 1 h, the mixture was diluted with CH_2Cl_2, washed with H_2O and brine, dried over $MgSO_4$, and then concentrated under reduced pressure. The residue was purified by column chromatography (silica gel; ethyl acetate/hexane = 2/3) to yield **17** (36.2 mg, 70% over two steps). The specific rotation was $[\alpha]^{28}_D$ −38.2 (*c* 1.0, $CHCl_3$). The IR spectrum (thin film) showed absorption bands at *ν* 2,935, 1,693, 1,295, and 1,193 cm^{-1}. The ^1H NMR spectrum (600 MHz, $CDCl_3$) exhibited signals at δ 7.39–7.33 (m, 2H, Ar-H), 7.30 (td, *J* = 6.4, 1.7 Hz, 3H, Ar-H), 5.23–5.16 (m, 2H, H-2′, H-3′), 5.14–5.08 (m, 2H, H-1′, H-3″), 4.94 (td, *J* = 9.1, 5.4 Hz, 1H, H-4″), 4.89–4.82 (m, 2H, 2-H″, $ArCH_2$), 4.64–4.60 (m, 2H, H-1′, $ArCH_2$), 4.49–4.39 (m, 2H, H-6a, H-6b), 4.34 (d, *J* = 8.1 Hz, 1H, H-1), 4.17 (dd, *J* = 6.9, 5.6 Hz, 1H, H-3), 4.10–4.03 (m, 3H, H-4, H-5′, H-5a), 4.00 (ddd, *J* = 7.7, 4.4, 2.2 Hz, 1H, H-5), 3.71 (dd, *J* = 8.2, 6.9 Hz, 1H, H-2), 3.59 (t, *J* = 9.6 Hz, 1H, H-4′), 3.31 (dd, *J* = 11.8, 9.3 Hz, 1H, H-5b"), 3.04 (s, 3H, SO_2CH_3), 2.11 (s, 3H, CH_3), 2.06 (s, 3H, CH_3), 2.02 (s, 3H, CH_3), 1.98 (s, 3H, CH_3), 1.97 (s, 3H, CH_3), 1.47 (s, 3H, CH_3), 1.27 (s, 3H, CH_3), and 1.09 (d, *J* = 6.2 Hz, 3H, H-6′). The ^{13}C NMR spectrum (150 MHz, $CDCl_3$) displayed resonances at δ 170.2 (C), 169.9 (C), 169.8 (C), 169.7 (C), 169.3 (C), 136.2 (C), 128.6 (CH), 128.5 (CH), 128.1 (CH), 110.8 (C), 101.0 (CH), 98.9 (CH), 96.3 (CH), 79.8 (CH), 76.4 (CH), 75.7 (CH), 73.1 (CH), 72.1 (CH), 71.6 (CH), 71.1 (CH), 70.8 (CH_2), 70.7 (CH), 69.9 (CH), 69.3 (CH), 68.7 (CH_2), 66.9 (CH), 62.4 (CH_2), 37.4 (CH_3), 27.8 (CH_3), 26.3 (CH_3), 20.9 (CH_3),20.7 (CH_3), 20.6 (CH_3), 20.4 (CH_3), and 17.2 (CH_3). HRMS (ESI) analysis showed a peak at *m/z* 894.3065, which is consistent with the calculated value of *m/z* 894.3060 for $C_{38}H_{52}O_{21}SNH_4$ ($[M + NH_4]^+$).

2.2.13 Benzyl 2,3,4-tri-*O*-acetyl-*β*-D-xylopyranosyl-(1→4)-2,3-di-*O*-acetyl-*α*-L-rhamnopyranosyl-(1→2)-6-deoxy-6-iodo-3,4-*O*-isopropylidene-*β*-D-galactopyranoside (**18**)

To a solution of **17** (10.2 mg, 0.012 mmol) in DMF (2 mL), tetrabutylammonium iodide (TBAI) (4.3 mg, 0.012 mmol) and KI (5.8 mg, 0.034 mmol) were added. The solution was stirred at 120 °C for 26 h, then cooled to room temperature, diluted with water, and extracted using ethyl acetate. The combined organic layer was washed with saturated aqueous $Na_2S_2O_3$ and brine and then dried over anhydrous Na_2SO_4. The organic layer was concentrated *in vacuo*, and the residue was purified by silica gel chromatography (silica gel; ethyl acetate/hexane = 2/3) to yield **18** (6.3 mg, 58%). The specific rotation was $[\alpha]^{27}_D$ 29.4 (*c* 0.25, $CHCl_3$). The IR spectrum (thin film) showed absorptions bands at *ν* 3,401, 2,920, 1,749, 1,221, and 1,052 cm^{-1}. The ^1H NMR spectrum (600 MHz, $CDCl_3$) exhibited signals at δ 7.33 (td, *J* = 13.9, 7.0 Hz, 5H, Ar-H), 5.20 (dd, *J* = 9.0, 2.6 Hz, 2H, H-2′, H-3), 5.14–5.06 (m, 2H, H-1′, H-3″), 4.97–4.85 (m, 3H, H-2″, H-4″, Ar-CH_2), 4.68 (d, *J* = 11.7 Hz, 1H, Ar-CH_2), 4.63 (d, *J* = 7.5 Hz, 1H, H-1″), 4.28 (d, *J* = 8.2 Hz, 1H, H-1), 4.21 (dd, *J* = 5.6, 2.3 Hz, 1H, H-3), 4.15–4.05 (m, 3H, H-4, H-5″, H-5a"), 3.81 (dt, *J* = 10.1, 3.9 Hz, 1H, H-5), 3.71 (t, *J* = 7.5 Hz, 1H, H-2), 3.59 (t, *J* = 9.4 Hz, 1H, H-4′), 3.41 (td, *J* = 9.7, 9.2, 6.9 Hz, 2H, H-6a, H-6b), 3.32 (dd, *J* = 11.8, 9.2 Hz, 1H, H-5b"), 2.11 (d, *J* = 1.8 Hz, 3H, CH_3), 2.02 (d, *J* = 1.7 Hz, 3H, CH_3), 1.98 (s, 3H, CH_3), 1.97 (s, 3H, CH_3), 1.47 (s, 3H, CH_3), 1.29 (s, 3H, CH_3), and 1.10 (d, *J* = 6.0 Hz, 3H, H-6′). The ^{13}C NMR spectrum (150 MHz, $CDCl_3$) displayed resonances at δ 170.2 (C), 170.0 (C), 169.7 (C), 169.2 (C), 136.4 (C), 128.6 (C), 128.5 (CH), 128.1 (CH), 110.4 (C), 101.0 (CH), 98.6 (CH), 96.1 (CH), 79.8, 75.5(CH), 74.2 (CH), 73.4 (CH), 72.1 (CH), 71.6 (CH), 71.1 (CH), 70.4 (CH_2), 70.0 (CH), 69.3 (CH), 66.8 (CH), 62.4 (CH_2), 27.8 (CH_3), 26.3 (CH_2), 21.0 (CH_2), 20.7 (CH_3), 20.7 (CH_3), 20.4 (CH_3), and 17.2 (CH_3). HRMS (ESI) analysis showed a peak at *m/z* 926.2298, which is consistent with the calculated value of *m/z* 926.2302 for $C_{37}H_{49}IO_{18}NH_4$ ($[M + NH_4]^+$).

2.2.14 Benzyl 2,3,4-tri-*O*-acetyl-*β*-D-xylopyranosyl-(1→4)-2,3-di-*O*-acetyl-*α*-L-rhamnopyranosyl-(1→2)-3,4-*O*-isopropylidene-*β*-D-fucopyranoside (**19**)

From **4** and **10**: A mixture of acceptor **10** (5.0 mg, 0.017 mmol, 1 equiv), donor **4** (17.7 mg, 1.7 equiv, 0.029 mmol), and freshly activated AW-500 MS (25 mg) in dry CH_2Cl_2 (1.5 mL) was stirred at room temperature for 1 h under an N_2 atmosphere and then cooled to 0 °C. NIS (6.5 mg, 1.7 equiv, 0.029 mmol) and TfOH (0.3 μL, 0.2 equiv, 0.003 mmol) were added to the reaction mixture. After constant stirring at 0 °C for 2 more hours, the mixture was filtered through a pad of Celite, the solids were washed with CH_2Cl_2, and the filtrate was washed with a mixture of saturated $NaHCO_{3(aq)}$ and 20% $Na_2S_2O_3$ solution and then with water. The organic layer was dried over anhydrous $MgSO_4$, filtered, and concentrated *in vacuo*. The residue was purified by flash column chromatography (silica gel; ethyl acetate/hexane = 2/3) to afford trisaccharide **19** (12.7 mg, 95%).

From **18**: To a solution of **18** (10.1 mg, 0.011 mmol) in a co-solvent of THF/MeOH (10/1, 2 mL), $Pd(OH)_2/C$ (20% wt, 20.2 mg) was added. The resulting suspension was stirred under $H_{2(g)}$ at room temperature and atmospheric pressure for 6 h. The reaction mixture was filtered through Celite and concentrated under reduced pressure. The residue was purified by silica gel chromatography (silica gel; ethyl acetate/hexane = 2/3) to yield **19** (8.2 mg, 95%).

The specific rotation was $[\alpha]^{28}_D$ +38.0 (*c* 0.1, $CHCl_3$). The IR spectrum (thin film) showed absorption bands at *ν* 2,919, 1,750, 1,222, and 1,073 cm^{-1}. The ^1H NMR spectrum (600 MHz, $CDCl_3$) exhibited signals at δ 7.34 (t, *J* = 7.0 Hz, 2H, Ar-H), 7.31–7.26 (m, 3H, Ar-H), 5.24–5.17 (m, 2H, H-2′, H-3′), 5.13–5.07 (m, 2H, H-1′, H-3″), 4.97–4.90 (m, 1H, H-4″), 4.90–4.83 (m, 2H, H-2″, Ar-CH_2), 4.62 (dd, *J* = 7.4, 2.1 Hz, H-1″), 4.58 (dd, *J* = 11.7, 2.0 Hz, 1H, Ar-CH_2), 4.29 (dd, *J* = 8.2, 1.8 Hz, 1H, H-1), 4.12–4.04 (m, 3H, H-3, H-5′, H-5a"), 3.93 (dt, *J* = 4.6, 2.0 Hz, 1H, H-4), 3.77 (qd, *J* = 6.6, 3.5 Hz, 1H, H-5), 3.73–3.67 (m, 1H, H-2), 3.57 (td, *J* = 9.6, 2.1 Hz, 1H, H-4′), 3.31 (ddd, *J* = 11.5, 9.1, 2.0 Hz, 1H, H-5b"), 2.11 (s, 3H, CH_3), 2.05 (s, 3H, CH_3), 2.02 (s, 3H, CH_3), 1.97 (s, 3H, CH_3), 1.96 (s, 3H, CH_3), 1.49 (s, 3H, CH_3), 1.40 (dd, *J* = 6.5, 1.8 Hz, 3H, H-6), 1.29 (s, 3H, CH_3), and 1.05 (dd, *J* = 6.5, 2.2 Hz, 3H, H-6′). The ^{13}C NMR spectrum (150 MHz, $CDCl_3$) displayed resonances at δ 170.2 (C), 170.0 (C), 169.8 (C), 169.8 (C), 169.2(C), 136.8 (C), 128.6 (CH), 128.4 (CH), 127.9 (CH), 110.0 (C),

100.9 (CH), 98.8 (CH), 96.2 (CH), 79.9 (CH), 75.8 (CH), 72.1 (CH), 71.8 (CH), 71.1 (CH), 70.3 (CH_2), 70.1 (CH), 69.3 (CH), 68.8 (CH), 66.7 (CH), 62.4 (CH_2), 28.0 (CH_3), 26.4 (CH_3), 21.0 (CH_3), 20.7 (CH_3), 20.7 (CH_3), 20.4 (CH_3), 17.2 (CH_3), and 16.6 (CH_3). HRMS (ESI) analysis showed a peak at *m/z* 800.3337, which is consistent with the calculated value of *m/z* 800.3335 for $C_{37}H_{50}O_{18}NH_4$ ($[M + NH_4]^+$).

2.2.15 2,3,4-tri-*O*-acetyl-*β*-D-xylopyranosyl-(1→4)-2,3-di-*O*-acetyl-*α*-L-rhamnopyranosyl-(1→2)-3,4-*O*-isopropylidene-*β*-D-fucopyranoside (**2**)

From **18:** To a solution of **18** (7.1 mg, 0.008 mmol) in THF/MeOH (1/1, 1 mL), $Pd(OH)_2/C$ (20% wt, 35.5 mg) was added. The resulting suspension was stirred under $H_{2(g)}$ at room temperature and atmospheric pressure for 7 h. The reaction mixture was filtered through Celite and concentrated under reduced pressure. The residue was purified by silica gel chromatography (silica gel; ethyl acetate/hexane = 2/3) to yield **2** (4.8 mg, 89%, *α:β* = 1.1:1.0).

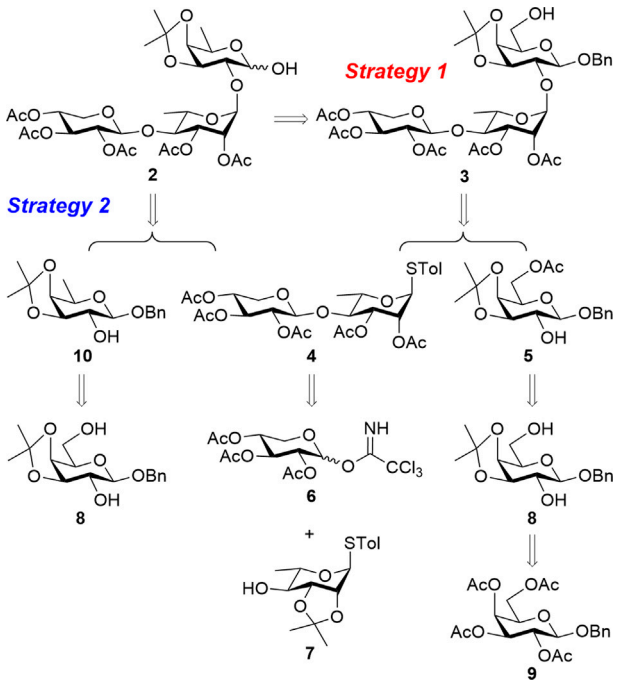
From **19:** To a solution of **19** (10.4 mg, 0.012 mmol) in THF/MeOH (1/1, 1 mL), $Pd(OH)_2/C$ (20% wt, 52.0 mg) was added. The resulting suspension was stirred under $H_{2(g)}$ at room temperature and atmospheric pressure for 4 h. The reaction mixture was filtered through Celite and concentrated under reduced pressure. The residue was purified by silica gel chromatography (silica gel; ethyl acetate/hexane = 2/3) to afford **2** (7.4 mg, 89%, *α:β* = 1.5:1.0).

The IR spectrum (thin film) showed absorption bands at *ν* 2,919, 1,750, 1,222, and 1,073 cm^{-1}. The ^1H NMR spectrum (600 MHz, $CDCl_3$) exhibited signals at δ 5.24 (ddd, *J* = 22.0, 3.8, 1.8 Hz, 2H), 5.21–5.15 (m, 3H), 5.11 (td, *J* = 9.1, 2.8 Hz, 2H), 5.06 (d, *J* = 2.1 Hz, 2H), 4.96–4.90 (m, 2H), 4.85 (dd, *J* = 9.5, 7.7 Hz, 2H), 4.61 (td, *J* = 7.1, 6.5, 2.7 Hz, 3H), 4.37 (d, *J* = 7.1 Hz, 1H), 4.31 (dd, *J* = 7.2, 5.7 Hz, 1H), 4.15 (t, *J* = 6.2 Hz, 1H), 4.10 (dd, *J* = 11.8, 5.4 Hz, 2H), 4.07–4.02 (m, 2H), 3.98 (dd, *J* = 5.8, 2.1 Hz, 1H), 3.82–3.75 (m, 2H), 3.62 (t, *J* = 9.6 Hz, 2H), 3.57 (t, *J* = 7.1 Hz, 1H), 3.36–3.29 (m, 2H), 3.26 (dd, *J* = 6.3, 1.2 Hz, 1H), 2.85 (d, *J* = 4.1 Hz, 1H), 2.13 (d, *J* = 1.6 Hz, 6H), 2.05 (d, *J* = 1.6 Hz, 6H), 2.01 (d, *J* = 1.5 Hz, 6H), 1.99 (d, *J* = 1.5 Hz, 6H), 1.98 (d, *J* = 4.6 Hz, 6H), 1.49 (d, *J* = 7.7 Hz, 6H), 1.38 (d, *J* = 6.5 Hz, 3H), 1.33 (d, *J* = 6.6 Hz, 3H), 1.31 (d, *J* = 2.9 Hz, 6H), and 1.28–1.26 (m, 6H). The ^{13}C NMR spectrum (150 MHz, $CDCl_3$) displayed resonances at δ 170.2 (C), 170 (C), 169.9 (C), 169.8 (C), 169.6 (C), 169.5 (C), 110.0 (C), 109.1 (C), 101.1 (CH),101.0 (CH), 97.5 (CH), 97.1 (CH), 96.1 (CH), 94.8 (CH), 91.6 (CH), 78.6 (CH), 76.3 (CH), 76.3 (CH), 75.9 (CH), 75.4 (CH), 75.3 (CH), 75.1 (CH), 72.2 (CH), 72.1 (CH), 71.4 (CH), 71.2 (CH), 71.1 (CH), 70.1 (CH), 70.0 (CH), 69.2 (CH), 68.7 (CH), 67.3 (CH), 67.1 (CH), 63.4 (CH), 62.5 (CH_2), 62.4 (CH_2), 28.0 (CH_3), 27.9 (CH_3), 26.2 (CH_3), 26.1 (CH_3), 21.0 (CH_3), 20.9 (CH_3), 20.7 (CH_3), 20.6 (CH_3), 20.5 (CH_3), 17.6 (CH_3), 17.5 (CH_3), 16.6 (CH_3), and 16.5 (CH_3). HRMS (ESI) analysis showed a peak at *m/z* 710.2867, which was consistent with the calculated value of *m/z* 710.2866 for $C_{30}H_{44}O_{18}NH_4$ ($[M + NH_4]^+$).

3 Results and discussion

3.1 Retrosynthesis

A linear trisaccharide of interest consists of D-xylose, L-rhamnose, and the rare D-fucose. Key challenges, such as the synthesis of the rare D-fucose unit and the stereocontrolled installation of 1,2-*trans* glycosidic bonds between each sugar ring, must be addressed to effectively generate the target linear trisaccharide. The target linear trisaccharide **2** can be synthesized using two [2 + 1] glycosylation strategies between a common disaccharide donor **4** and acceptors **5** and **10**, as shown in Scheme 1.

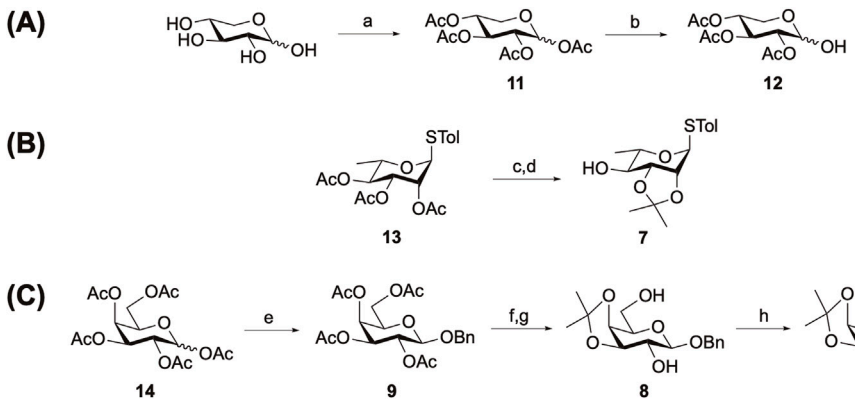


Scheme 1
Structure of linear trisaccharide moiety **2** from QS-21 and its retrosynthesis. Ac, acetyl; Bn, benzyl; Tol, *p*-methylphenyl.

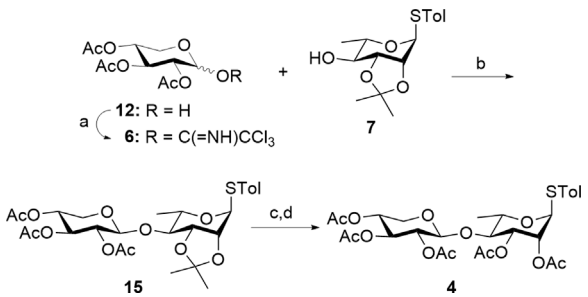
In the first retrosynthetic strategy, the target trisaccharide was envisioned to be obtained through a glycosylation reaction between glycosyl donor **4** and glycosyl acceptor **5**. The latter can be derived via regioselective acetylation of compound **8**, which, in turn, can be obtained through deacylation, followed by acetonide protection of compound **9**. After glycosylation, the D-galactose reducing end in **3** would be converted into a D-fucose moiety through deoxygenation at the C6 position. On the other hand, the second retrosynthetic strategy was to synthesize the target trisaccharide from donor **4** and acceptor **10**. Prior to glycosylation, D-galactose in **8** would be converted into a D-fucose acceptor **10**. Disaccharide donor **4**, used in both approaches, is synthesized via [1 + 1] glycosylation of D-xylose-derived donor **6** with L-rhamnose-derived acceptor **7**, ensuring efficient assembly. The glycosylation reactions are anticipated to yield 1,2-*trans*-glycosidic linkages facilitated by the adjacent acetyl (Ac) group at the C2 position.

3.2 Synthesis of the monosaccharide precursors

The truncated linear trisaccharide domain was synthesized beginning with the preparation of monosaccharide building blocks. In Scheme 2A, D-xylose building block **12** was synthesized starting from DMAP-catalyzed per-*O*-acetylation of D-xylose to generate **11** in 93% yield. Regioselective anomeric deacetylation with benzylamine ($BnNH_2$) then afforded **12** in 68% yield. To prepare L-rhamnose-derived acceptor



Scheme 2
Synthesis of the monosaccharide building blocks **12 (A)**, **7 (B)**, and **5 (C)**. Reagents and conditions: (a) Ac_2O, DMAP, Et_3N, 0 °C, 3 h, 93%; (b) $BnNH_2$, THF, 0 °C, 16 h, 68%; (c) NaOMe, MeOH, 0 °C, 1 h; (d) 2,2-DMP, CSA, MeCN, RT, 1 h, 72% over 2 steps; (e) BnOH, BF_3•Et_2O, 0 °C, 16 h, 75%; (f) NaOMe, MeOH, 0 °C to RT, 5 h; (g) 2,2-DMP, CSA, MeCN, RT, 30 min, 48% over two steps; (h) Ac_2O, Et_3N, CH_2Cl_2, 0 °C to RT, 3 h, 76%. DMAP, 4-dimethylaminopyridine; $BnNH_2$, benzylamine; THF, tetrahydrofuran; Me, methyl; 2,2-DMP, 2,2-dimethoxypropane; CSA, 10-camphorsulfonic acid.



Scheme 3
Synthesis of the common disaccharide donor **4**. Reagents and conditions: (a) Cl_3CCN, Cs_2CO_3, RT, 0.5 h; (b) TMSOTf, AW-500, CH_2Cl_2, −78 °C to 0 °C, 5 h, 53%; (c) 2% HCl/MeOH, RT, 16 h; (d) Ac_2O, DMAP, Et_3N, EtOAc, 0 °C, 16 h, 81% over two steps. TMSOTf, trimethylsilyl trifluoromethanesulfonate; EtOAc, ethyl acetate.

7 (Scheme 2B), an acetonide protecting group was introduced via a sequential two-step process involving Zemplén deacylation, followed by isopropylidenation of the 2,3-*cis*-diol group using 2,2-DMP and CSA. This acetonide protection sequence resulted in the formation of **7** in 72% yield over two steps.

In Scheme 2C, per-*O*-acetylated D-galactose underwent BF_3•Et_2O-catalyzed benzyl group substitution at the anomeric position using benzyl alcohol (BnOH) to afford **9** in 75% yield. Subsequently, acetonide protection of **9** was performed analogously to the synthesis of **7**, resulting in the formation of **8** in 48% yield over two steps. The acetonide group was installed to protect the target trisaccharide prior to its final functionalization, when it was attached to the acyl side chain of QS-21. Finally, regioselective acetylation of the primary alcohol at the C6 position produced 2-alcohol **5** in 76% yield.

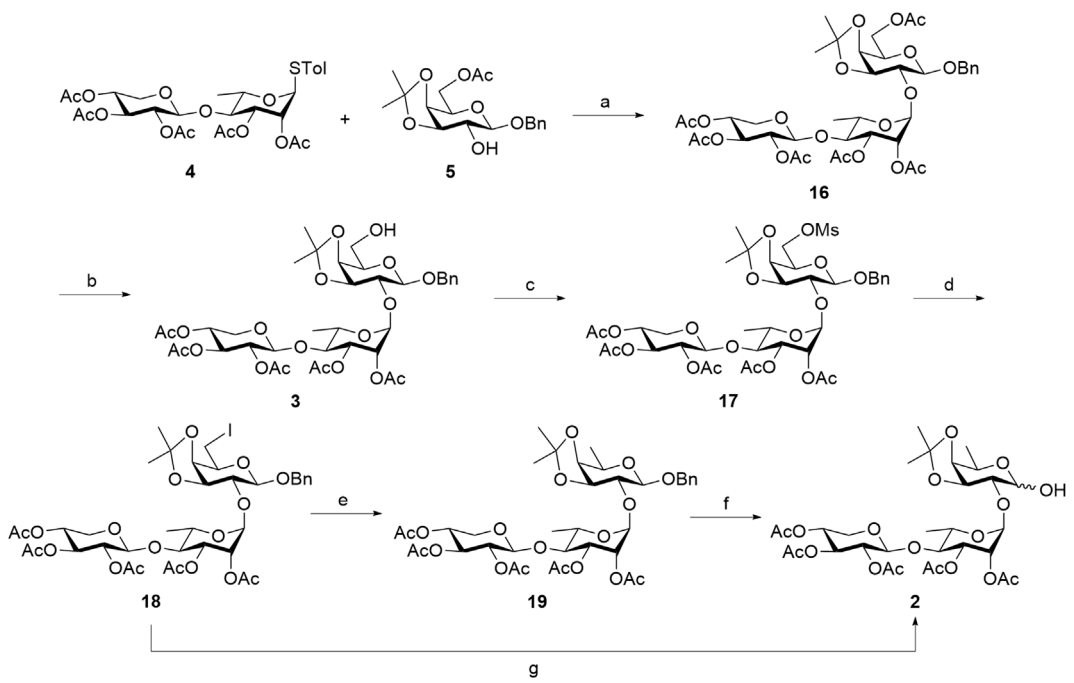
3.3 Synthesis of the common disaccharide donor

The synthesis of common disaccharide donor **4** depicted in Scheme 3 involves the efficient assembly of compounds **6** and **7**. Conversion of **12** to a glycosyl trichloroacetimidate **6** using Cl_3CCN was carried out, and then it was directly coupled with **7** through a TMSOTf-promoted glycosylation to afford disaccharide **15** in 53% yield. Neighboring group participation of the 2-*O*-Ac group from D-xylose resulted in a *β*-linked disaccharide ($^1J_{C-H}$ = 162.9 Hz). Analysis of the nondecoupled HSQC spectra distinguished the *α*- and *β*-anomers, with the α-anomers displaying a J_{C1-H1} coupling of approximately 170 Hz for the anomeric carbon and proton, while the *β*-anomers exhibited around 160 Hz (Bock and Pedersen, 1974). Hydrolysis of the isopropylidene ketal in **15** using 2% HCl/MeOH, followed by acetylation, afforded common disaccharide donor **4** in 81% yield over two steps.

3.4 Synthesis of the truncated linear trisaccharide

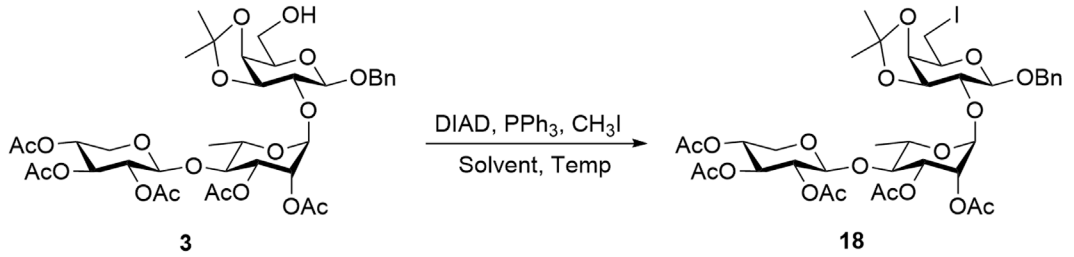
The synthesis of linear trisaccharide **2** was conducted using two distinct approaches. The first strategy, illustrated in Scheme 4, involved an NIS/TfOH-promoted [2 + 1] glycosylation between thioglycoside donor **4** and acceptor **5**. This reaction resulted in the successful formation of *α*-1→2-linked L-Rha-D-Gal **16** in 76% yield ($^1J_{C-H}$ = 172.5 Hz), through the neighboring group participation of the 2-*O*-Ac moiety from the donor.

Upon obtaining D-galactose-containing trisaccharide **16**, post-glycosylation deoxygenation at the C6 position was performed to transform the reducing end into a rare D-fucose moiety. First, the primary 6-*O*-Ac group of D-galactose was selectively removed using 7%–8% $Mg(OMe)_2$ in MeOH, generating 6-alcohol **3**, which was used directly in the next step without further purification. From this intermediate, deoxygenation was initially planned by introducing an iodide group at the C6 position, which could then be removed via hydrogenolysis (Lemieux and Levine, 1962). However, attempts to directly substitute the 6-hydroxy group in compound **3** with iodine on a 50 mg scale using the Mitsunobu reaction [PPh_3, diisopropyl azodicarboxylate (DIAD), and methyl iodide] were unsuccessful. No product formation was observed, even after varying the solvent or increasing the reaction temperature. As shown in Table 1, the reaction in CH_2Cl_2 at 0 °C–22 °C (Entry 1) and 22 °C (Entry 2) failed to produce



Scheme 4
First approach in the synthesis of truncated linear trisaccharide domain **2**. Reagents and conditions: (a) NIS, TfOH, AW-500, CH_2Cl_2, 0 °C, 2 h, 76%; (b) 7%–8% $Mg(OMe)_2$ in MeOH, CH_2Cl_2, 0 °C, 1 h; (c) Et_3N, MsCl, CH_2Cl_2, 0 °C, 1 h, 70% (over two steps); (d) TBAI, KI, DMF, 120 °C, 22 h, 58%; (e) $H_{2(g)}$, $Pd(OH)_2$/C, THF/MeOH (10/1), RT, 6 h, 95%; (f) $H_{2(g)}$, $Pd(OH)_2$/C, THF/MeOH (1/1), RT, 4 h, 89%; (g) $H_{2(g)}$, $Pd(OH)_2$/C, THF/MeOH (10/1), RT, 7 h, 89%. NIS, *N*-iodosuccinimide; TfOH, trifluoromethanesulfonic acid; MsCl, methanesulfonyl chloride; TBAI, tetra-*n*-butylammonium iodide; DMF, *N*,*N*-dimethylformamide.

TABLE 1 Direct substitution of the iodine atom through the Mitsunobu reaction.



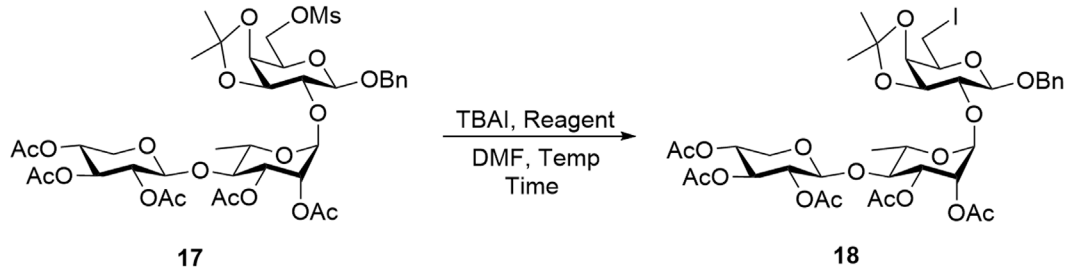
Entry[a]	Solvent	Time	Temperature (°C)	Yield (%)
1	CH_2Cl_2	16 h	0–22	0
2	CH_2Cl_2	16 h	22	0
3	THF	16 h	0–22	0
4	THF	16 h	60	0

[a]All reactions were carried out using 1.5 equiv DIAD, 3 equiv PPh_3, and 1.5 equiv CH_3I.

desired product **18**, and the starting material was largely recovered. Changing the solvent to THF and conducting the reaction at 0 °C–22 °C (Entry 3) or 60 °C (Entry 4) also did not lead to successful installation of a 6-iodo group at the reducing-end sugar. This may be attributed to the low reactivity of the hydroxy group toward direct iodine substitution.

To overcome this key synthetic challenge, a methanesulfonyl (or mesyl) group was introduced at the O6 position prior to substitution with iodine to convert the hydroxy group to a more reactive leaving group. Following the deprotection of the 6-*O*-Ac group in trisaccharide **16** to form compound **3**, mesylation with mesyl chloride (MsCl) furnished **17** in 70% yield over two steps. Various reaction conditions were then explored to convert **17** into the C6-iodinated trisaccharide **18**, as summarized in Table 2. At a 10 mg scale, treatment of **17** with TBAI (1 equiv) and NaI (3 equiv) in DMF at 90 °C (Entry 1) did not yield **18**, even after 48 h, and the starting material remained unreacted. Increasing the temperature to 120 °C (Entry 2) also

TABLE 2 Substitution of the iodine atom with mesylated compound 17.



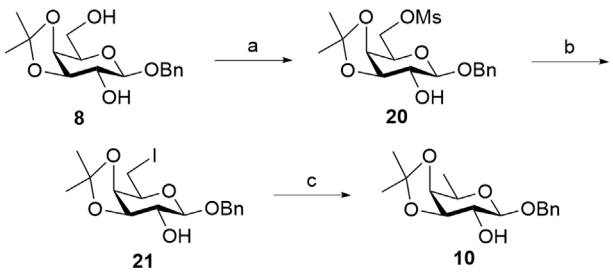
17 18

Entry[a]	Reagent	Temperature (°C)	Time (h)	Yield (%)
1	NaI (3 equiv)	90	48	0
2	NaI (3 equiv)	120	48	0
3	KI (3 equiv)	90	22	Trace
4	KI (3 equiv)	120	22	58

[a]All reactions were carried out using 1 equiv TBAI in 10 mg.

failed to produce the desired product. A trace amount of **18** was observed when KI (3 equiv) was used in place of NaI at 90 °C for 22 h (Entry 3). Gratifyingly, increasing the temperature to 120 °C under these conditions (Entry 4) successfully afforded the C6-iodinated trisaccharide **18** in 58% yield. This likely results from the higher solubility and enhanced nucleophilicity of iodide ions from KI in DMF at elevated temperature, facilitating more efficient substitution. The conversion from mesyl to iodide caused an upfield shift of the two H6 protons to 3.41 ppm and the disappearance of the mesyl CH_3 proton signal at 3.04 ppm, suggesting the efficient formation of **18**. The final functionalization of trisaccharide **18** involves hydrogenolysis to remove the benzyl group and transform the galactosyl iodide moiety into a rare D-fucose residue. In our initial attempt, hydrogenolysis of compound **18** was carried out using $Pd(OH)_2/C$ (Degussa type, 20 wt%) at a loading rate of 1 g catalyst per gram of **18** under a hydrogen atmosphere. Under the initial conditions, using THF as the solvent, the reaction proceeded very slowly. Switching to an increased catalyst loading of 2 g $Pd(OH)_2$ per gram of **18** and THF/MeOH (10/1) as co-solvent significantly improved the reaction efficiency, enabling selective removal of the iodine atom while preserving the benzyl group and affording compound **19** with a D-fucose-reducing end in 95% yield. The formation of D-fucose in **19** from the D-galactose-reducing end in **18** was evidenced by the presence of methyl protons at the C6 position (^{1}H NMR: d, δ 1.44 ppm, J = 6.5 Hz). Furthermore, hydrogenolysis of **19** in the THF/MeOH (1/1) co-solvent using $Pd(OH)_2/C$ at a loading rate of 5 g catalyst per gram of starting material then furnished target linear trisaccharide **2** in 89% yield (α:β = 1:1).

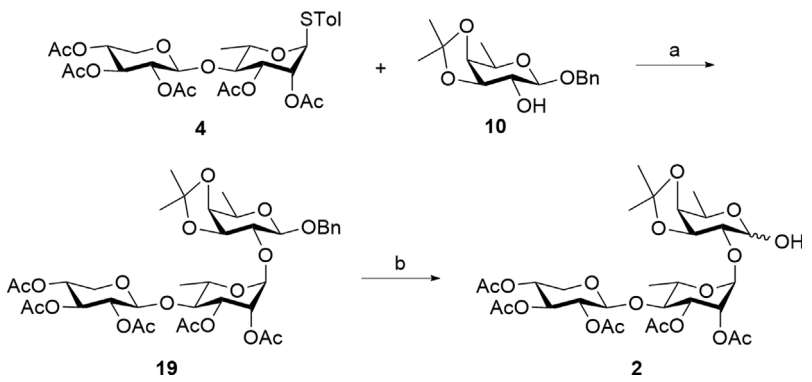
In our second attempt to carry out the final functionalization, we tried to synthesize trisaccharide **2** directly from **18** by investigating the effect of $Pd(OH)_2/C$ loading on the hydrogenolysis reaction. Hydrogenolysis of C–O bonds, such as those in benzyl protecting groups, typically requires harsher conditions than the cleavage of C–I bonds (Ahluwalia, 2023). Hydrogenolysis was performed using $Pd(OH)_2/C$ at a loading rate of 5 g catalyst per gram of **18** under an H_2 atmosphere, with THF/MeOH (1/1) as the co-solvent. This condition effectively removed both the iodine atom and the benzyl protecting group from **18**, directly producing trisaccharide **2** in 89% yield. The successful synthesis of final compound **2** from **18** was confirmed by the disappearance of benzyl proton-NMR peaks and the detection of methyl protons at the C6 position (^{1}H NMR: d, δ 1.38 ppm, J = 6.5 Hz).



Scheme 5
Synthesis of acceptor **10** through pre-glycosylation deoxygenation. Reagents and conditions: (a) Et_3N, MsCl, CH_2Cl_2, 0 °C, 2 h, 63%; (b) TBAI, KI, DMF, 120 °C, 22 h, 72%; (c) $H_{2(g)}$, $Pd(OH)_2/C$, THF/MeOH (10/1), RT, 7 h, 95%.

Our second strategy in the synthesis of the truncated linear trisaccharide domain of QS-21 utilizes a pre-glycosylation deoxygenation approach from Scheme 1. Conversion of the D-galactose unit into rare D-fucose was conducted prior to [2 + 1] glycosylation with D-xylose and L-rhamnose-derived donor **4**. This strategy was anticipated to be more efficient than the initial approach due to its reduced number of steps since the 6-deoxygenation reaction is only conducted on a monosaccharide.

The pre-glycosylation deoxygenation strategy commenced with the transformation of isopropylidenated D-galactose **8** into D-fucose through a series of mesylation, iodine substitution, and selective hydrogenolysis reactions (Scheme 5). Mesylation of 2,6-diol **8** at the C6 position furnished **20** in 63% yield, as indicated by the presence of mesyl methyl protons at 3.04 ppm. Following the optimized conditions from Table 2, the substitution of the OMs group with an iodine atom using TBAI and KI in DMF afforded **21** in 72% yield. Finally, D-fucose acceptor **10** was obtained following selective hydrogenolysis at the



Scheme 6
[2 + 1] glycosylation approach for the synthesis of truncated linear trisaccharide **2** using the pre-glycosylation deoxygenation strategy. Reagents and conditions: (a) NIS, TfOH, AW-500, CH_2Cl_2, 0 °C, 2 h, 95%; (b) $H_{2(g)}$, $Pd(OH)_2$/C, THF/MeOH (1/1), RT, 7 h, 89%.

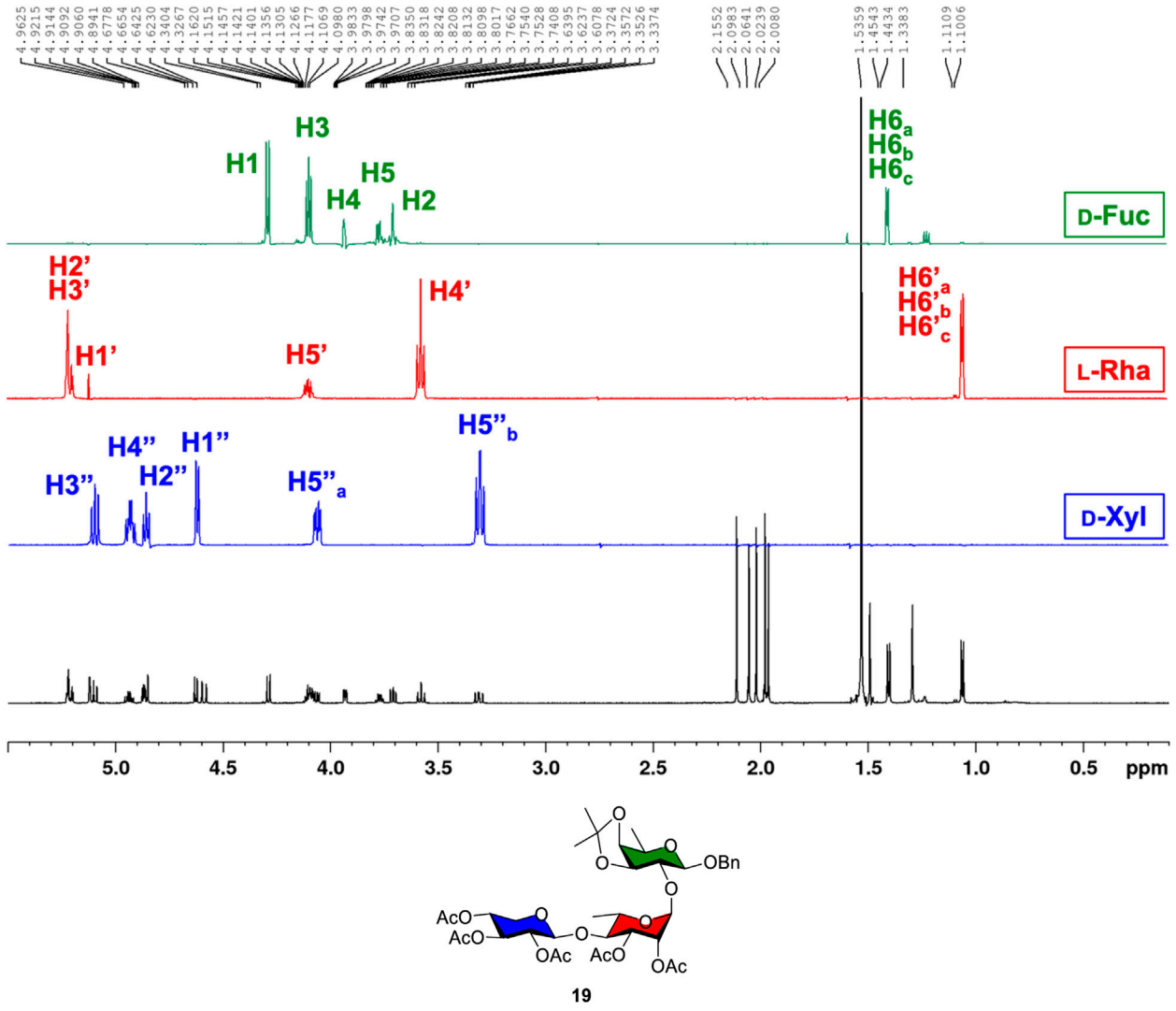


FIGURE 2
1D TOCSY analysis of trisaccharide **19** resolving the complex ^{1}H NMR spectrum into three resolve spectra corresponding to the ring protons of D-xylose (blue), L-rhamnose (red), and D-fucose (green).

C6 position in THF/MeOH (10/1), preserving the integrity of the benzyl group prior to the [2 + 1] glycosylation step. The reaction was carried out using 1 g of $Pd(OH)_2/C$ per gram of **21** to achieve a high yield of 95% for compound **10**, mirroring the synthesis of trisaccharide **19**. The detection of an upfield chemical shift for the methyl C6-protons at 1.43 ppm of **10** indicates the successful conversion of D-galactose into rare D-fucose.

With synthesized D-fucose acceptor **10** and disaccharide donor **4** in hand, we proceeded with [2 + 1] glycosylation to generate the trisaccharide unit **19** (Scheme 6). Using NIS/TfOH in CH_2Cl_2 at 0 °C, glycosylation proceeded with exclusive α-stereoselectivity ($^1J_{C-H}$ = 173.2 Hz) to furnish trisaccharide **19** in 95% yield. Neighboring group participation of the 2-*O*-Ac group led to α-selectivity. Afterward, benzyl group deprotection through hydrogenolysis with H_2 and $Pd(OH)_2/C$ in THF/MeOH (1/1) produced target linear trisaccharide **2** in 89% yield (α:β = 1.5:1.0). The structures of the final compound were confirmed through NMR spectroscopic and mass spectrometric analyses (see Supplementary Material).

Using trisaccharide **19** as a representative example, all glycan backbone ^{1}H protons were examined through the ^{1}H, ^{13}C, COSY, HSQC, HMBC, and 1D total correlation spectroscopy (1D TOCSY) experiments in detail. Following the identification of anomeric carbons and protons using HSQC, the complex ^{1}H NMR spectrum was then deconvoluted into three distinct spectroscopic patterns by selectively exciting anomeric ^{1}H nuclei at a given frequency using 1D TOCSY NMR. Figure 2 depicts the identification of protons from D-xylose (blue spectrum), L-rhamnose (red spectrum), and D-fucose (green spectrum) through a combined 1D TOCSY NMR and 2D COSY analysis. This combined analysis, along with HSQC and HMBC, confirms the connectivity of each sugar ring from trisaccharide **19**, as shown in Figure 2.

Comparing the post-glycosylation and pre-glycosylation deoxygenation strategies, target trisaccharide **2** was obtained in overall yields of 7.8% and 15.6%, respectively. The pre-glycosylation deoxygenation route required only a single-step transformation after the [2 + 1] glycosylation reaction to reach the final product, whereas the post-glycosylation pathway involved three additional steps. Although the pre-glycosylation approach includes a three-step synthesis of the deoxygenated D-fucose acceptor, this added effort is offset by the reduced number of steps following glycosylation. Overall, the higher yield and greater step economy highlight the pre-glycosylation deoxygenation strategy as the more efficient route to the truncated linear trisaccharide fragment of QS-21.

4 Conclusion

We have successfully accomplished an efficient synthesis of the truncated linear trisaccharide domain **2** of QS-21. Two synthetic strategies were used: post-glycosylation and pre-glycosylation deoxygenation. The latter proved to be more efficient, yielding a higher overall yield with fewer reaction steps. En route, we established an efficient synthesis of the rare D-fucose moiety from D-galactose. We believe that this efficient synthesis of the linear trisaccharide domain will be applicable to the synthesis of pure and homogeneous QS-21 structures and their analogs for use as vaccine adjuvants.

Data availability statement

The original contributions presented in the study are included in the article/Supplementary Material, further inquiries can be directed to the corresponding author.

Author contributions

J-SL: Data curation, Formal analysis, Writing – original draft, Methodology. Z-HT: Data curation, Formal analysis, Investigation, Writing – review and editing, Methodology, Conceptualization. JD: Data curation, Formal analysis, Writing – original draft, Writing – review and editing. S-CH: Writing – original draft, Visualization, Conceptualization, Project administration, Writing – review and editing, Funding acquisition, Supervision.

Funding

The author(s) declare that financial support was received for the research and/or publication of this article. This work was supported by the National Science and Technology Council (NSTC) of Taiwan (NSTC 111-2639-M-001-001-ASP and NSTC 112-2639-M-001-001-ASP). S-CH also acknowledges being awarded the Taiwan Bio-Development Foundation (TBF) Chair in Biotechnology.

Conflict of interest

The authors declare that the research was conducted in the absence of any commercial or financial relationships that could be construed as a potential conflict of interest.

Generative AI statement

The author(s) declare that no Generative AI was used in the creation of this manuscript.

Any alternative text (alt text) provided alongside figures in this article has been generated by Frontiers with the support of artificial intelligence and reasonable efforts have been made to ensure accuracy, including review by the authors wherever possible. If you identify any issues, please contact us.

Publisher's note

All claims expressed in this article are solely those of the authors and do not necessarily represent those of their affiliated organizations, or those of the publisher, the editors and the reviewers. Any product that may be evaluated in this article, or claim that may be made by its manufacturer, is not guaranteed or endorsed by the publisher.

Supplementary material

The Supplementary Material for this article can be found online at: https://www.frontiersin.org/articles/10.3389/fchem.2025.1650302/full#supplementary-material

References

Ahluwalia, V. K. (2023). "Hydrogenolysis," in *Reduction in organic synthesis*, 115–121. doi:10.1007/978-3-031-37686-3_4

Bock, K., and Pedersen, C. A. (1974). Study of 13C–H Coupling Constants in Hexopyranoses. *J. Chem. Soc. Perkin Trans.* 2 (293), 293–297. doi:10.1039/P29740000293

Chea, E. K., Fernández-Tejada, A., Damani, P., Adams, M. M., Gardner, J. R., Livingston, P. O., et al. (2012). Synthesis and preclinical evaluation of QS-21 variants leading to simplified vaccine adjuvants and mechanistic probes. *J. Am. Chem. Soc.* 134, 13448–13457. doi:10.1021/ja305121q

Fernández-Tejada, A., Chea, E. K., George, C., Pillarsetty, N., Gardner, J. R., Livingston, P. O., et al. (2014). Development of a minimal saponin vaccine adjuvant based on QS-21. *Nat. Chem.* 6, 635–643. doi:10.1038/nchem.1963

Fernández-Tejada, A., Tan, D. S., and Gin, D. Y. (2016). Development of improved vaccine adjuvants based on the saponin natural product QS-21 through chemical synthesis. *Acc. Chem. Res.* 49, 1741–1756. doi:10.1021/acs.accounts.6b00242

Garçon, N., and Van Mechelen, M. (2011). Recent clinical experience with vaccines using MPL- and QS-21-containing adjuvant systems. *Expert Rev. Vaccines* 10, 471–486. doi:10.1586/erv.11.29

Gin, Y., and Slovin, F. (2011). Enhancing immunogenicity of cancer vaccines: QS-21 as an immune adjuvant. *Curr. Drug. Ther.* 6, 207–212. doi:10.2174/157488511796391988

Kensil, C. R., Patel, U., Lennick, M., and Marciani, D. (1991). Separation and characterization of saponins with adjuvant activity from *Quillaja saponaria* Molina cortex. *J. Immunol.* 146, 431–437. doi:10.4049/jimmunol.146.2.431

Lacaille-Dubois, M.-A. (2019). Updated insights into the mechanism of action and clinical profile of the immunoadjuvant QS-21: a review. *Phytomedicine* 60, 152905. doi:10.1016/j.phymed.2019.152905

Lemieux, R. U., and Levine, S. (1962). The products of the prevost reaction on D-glucal triacetate. *Can. J. Chem.* 40, 1926–1932. doi:10.1139/v62-296

Liang, P.-H., Lai, Y.-H., Chang, C.-K., and Chaw, C.-W. (2020). Saponin conjugate and vaccine or pharmaceutical composition comprising the same.

Marciani, D. J., Pathak, A. K., Reynolds, R. C., Seitz, L., and May, R. D. (2001). Altered immunomodulating and toxicological properties of degraded *Quillaja saponaria* Molina saponins. *Int. Immunopharmacol.* 1, 813–818. doi:10.1016/S1567-5769(01)00016-9

Martin, L. B. B., Kikuchi, S., Rejzek, M., Owen, C., Reed, J., Orme, A., et al. (2024). Complete biosynthesis of the potent vaccine adjuvant QS-21. *Nat. Chem. Bio.* 20, 493–502. doi:10.1038/s41589-023-01538-5

Pink, J. R., and Kieny, M.-P. (2004). 4th Meeting on novel adjuvants currently in/close to human clinical testing. *Vaccine* 22, 2097–2102. doi:10.1016/j.vaccine.2004.01.021

Ragupathi, G., Damani, P., Deng, K., Adams, M. M., Hang, J., George, C., et al. (2010). Preclinical evaluation of the synthetic adjuvant SQS-21 and its constituent isomeric saponins. *Vaccine* 28, 4260–4267. doi:10.1016/j.vaccine.2010.04.034

Ragupathi, G., Gardner, J. R., Livingston, P. O., and Gin, D. Y. (2011). Natural and synthetic saponin adjuvant QS-21 for vaccines against cancer. *Expert Rev. Vaccines* 10, 463–470. doi:10.1586/erv.11.18

Reed, S. G., Orr, M. T., and Fox, C. B. (2013). Key roles of adjuvants in modern vaccines. *Nat. Med.* 19, 1597–1608. doi:10.1038/nm.3409

Reed, J., Orme, A., El-Demerdash, A., Owen, C., Martin, L. B. B., Misra, R. C., et al. (2023). Elucidation of the pathway for biosynthesis of saponin adjuvants from the soapbark tree. *Science* 379, 1252–1264. doi:10.1126/science.adf3727

Wang, P., Kim, Y.-J., Navarro-Villalobos, M., Rohde, B. D., and Gin, D. Y. (2005). Synthesis of the potent immunostimulatory adjuvant QS-21A. *J. Am. Chem. Soc.* 127, 3256–3257. doi:10.1021/ja0422007

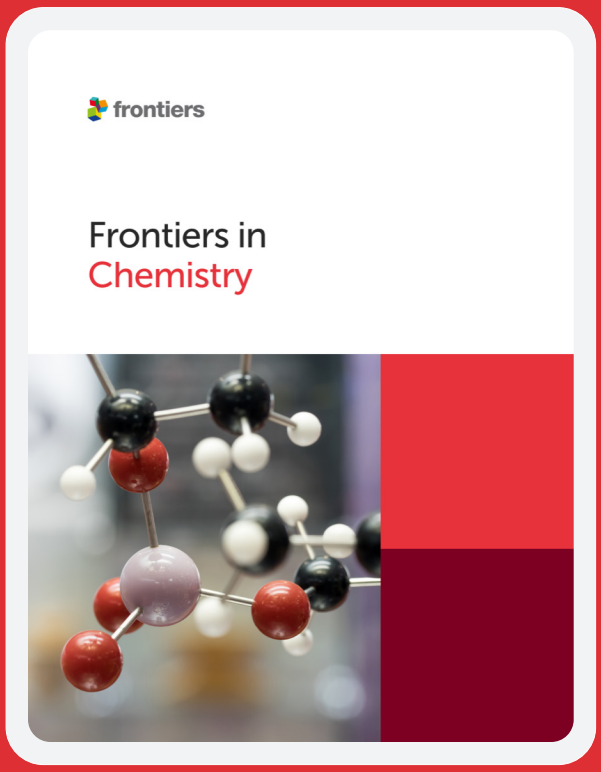
Frontiers in Chemistry

Explores all fields of chemical science across the periodic table

Advances our understanding of how atoms, ions, and molecules come together and come apart. It explores the role of chemistry in our everyday lives - from electronic devices to health and wellbeing.

Discover the latest Research Topics

See more →



Frontiers

Avenue du Tribunal-Fédéral 34
1005 Lausanne, Switzerland
frontiersin.org

Contact us

+41 (0)21 510 17 00
frontiersin.org/about/contact